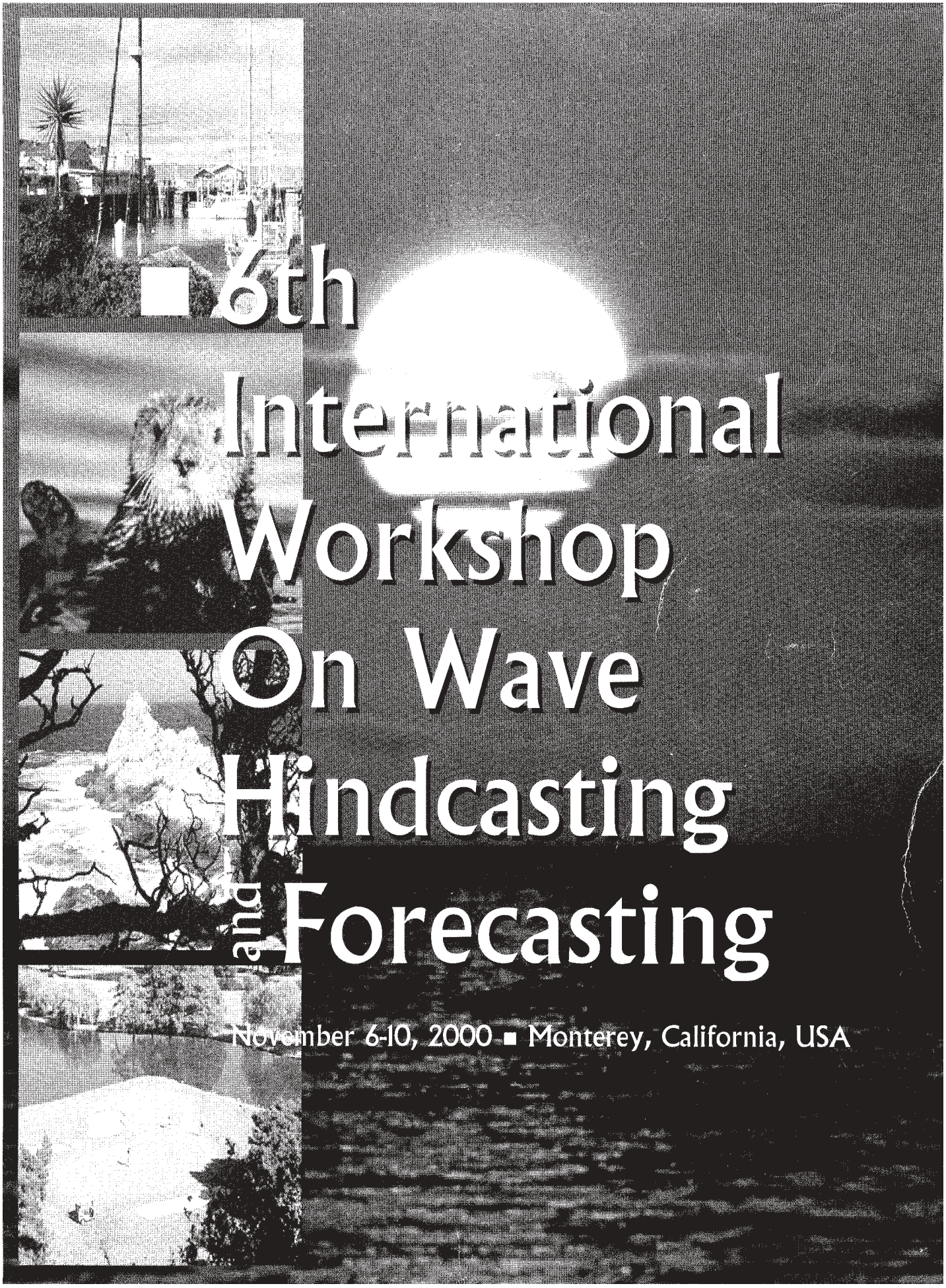

6th International Workshop On Wave Hindcasting and Forecasting

November 6-10, 2000 ■ Monterey, California, USA

PREPRINTS

6th INTERNATIONAL WORKSHOP ON WAVE HINDCASTING AND FORECASTING

MONTEREY, CALIFORNIA
NOVEMBER 6-10, 2000

Published by:

Meteorological Service of Canada
Environment Canada
4905 Dufferin Street
M3H 5T4

AUTHOR INDEX

TABLE OF CONTENTS

ACKNOWLEDGMENTS

The organizers are indebted to many people who provided valuable assistance in planning of this workshop. We would especially like to thank the sponsors: the U.S. Army Engineer Research and Development Center, Coastal and Hydraulics Laboratory, the Fleet Numerical Meteorological Oceanography Center, and the Meteorological Service of Canada. The committee would also like to thank those who submitted papers and posters for the workshop program, and those who served as chairmen for various sessions. Special thanks are due to Ms. Claudette Doiron who assembled and produced the camera-ready copy of the preprints and Ms. Patricia Oldham and Ms. Regina Gailani for preparing the cover.

D.T. Resio, Chairman, Workshop Organizing Committee.

Workshop Coordination By:

SHIP TO SHORE TRAVEL & EVENTS

With over 20 years experience, SHIP TO SHORE is in business of professional event planning (so you can get back to your business). Call toll-free 800-809-6623.

- Hotel Selection & Negotiation
- Special Activity Planning (banquets, day trips)
- Participant Communications & Registration
- Event Programs, Marketing Materials & Signage
- On-site Event Assistance

Ship-to-Shore

TABLE OF CONTENTS

*abstract only – full paper not available
#abstract only – if received in time will appear at back of book

Session C: Performance of Existing Prediction Systems
Chair: Al Osborne, University of Torino

Session D: Wave Prediction for Tropical Systems
Chair: Linwood Vincent, Office of Naval Research and Naval Research Laboratory

*abstract only – full paper not available
#abstract only – if received in time will appear at back of book

AUTHOR INDEX

Session E: Wave Climate: Estimation and Implication I
Chair: Val Swail, Environment Canada

Session F: Wave Climate: Estimation and Implication II
Chair: Donald Resio, U.S. Army Engineer Research & Development Center

*abstract only – full paper not available
#abstract only – if received in time will appear at back of book

Session G: Deep Model Formulation I
Chair: Paul Wittmann, Fleet Numerical Meteorology and Oceanography

Session H: Deep Model Formulation II
Chair: Roop Lalbeharry, Meteorological Service of Canada

Session I: Shallow Model Formulation I
Chair: W. Erick Rogers, Naval Research Laboratory

*abstract only – full paper not available
#abstract only – if received in time will appear at back of book

Session J: Shallow Model Formulation II
Chair: William C. O'Reilly, U.S. Naval Postgraduate School

Session K: Shallow Model Formulation III
Chair: Nico Boij, Delft University

*abstract only – full paper not available
#abstract only – if received in time will appear at back of book

Session L: Nonlinear Wave Phenomena
Chair: Robert Jensen, U.S. Army Engineer Research & Development Center

Poster Session

*abstract only – full paper not available
#abstract only – if received in time will appear at back of book

AUTHOR INDEX

*abstract only – full paper not available
#abstract only – if received in time will appear at back of book

AUTHOR INDEX

Author Index

*abstract only – full paper not available

#abstract only – if paper received in time will appear at back of book

TABLE OF CONTENTS

*abstract only – full paper not available

#abstract only – if paper received in time will appear at back of book

THE AES40 NORTH ATLANTIC WAVE REANALYSIS: VALIDATION AND CLIMATE ASSESSMENT

V.R Swail[1], E.A Ceccacci[2] and A.T. Cox[2]

[1]Environment Canada
Downsview, Ontario

[2]Oceanweather, Inc.
Cos Cob, CT

1. INTRODUCTION

The advent of long-term climate reanalysis projects undertaken by major numerical weather prediction centres has significantly changed the approach to the investigation of climate variability and trend on decadal and longer time scales. Swail and Cox (2000) evaluated the suitability of the NCEP-NCAR Reanalysis Project (NRA) wind fields to generate a long-term wave hindcast of the North Atlantic Ocean (NA). Swail *et al.* (1998) described in detail a project undertaken by Oceanweather Inc. for the Meteorological Service of Canada (formerly Atmospheric Environment Service (AES)) to produce the first 40-year (1958-1997) wind and wave hindcast of the North Atlantic (AES40). The objective of the study was to use the NRA products (Kalnay *et al.*, 1996) to drive a third-generation wave model adapted to the NA on a high-resolution grid to produce a high-quality, homogeneous, long term wind and wave data base for assessment of the wave climate of the NA, its trend and variability. The most important feature of the hindcast was the rigorous attention devoted to producing the wind fields used to drive the wave model. To remove potential biases in the historical wind fields, all wind observations from ships and buoys were re-assimilated into the analysis taking account of the method of observation, anemometer height and stability. Wind fields for all significant storms were then painstakingly kinematically reanalyzed with the aid of an interactive Wind Workstation (Cox *et al.*, 1995). Furthermore, high-resolution surface wind fields for all tropical cyclones, as specified by a proven tropical cyclone boundary layer model, were assimilated into the wind fields to provide greater skill and resolution in the resulting wave hindcasts.

This paper describes the validation of the AES40 hindcast wind and wave fields, and analysis of the wave climate, its trend and variability. The wave model is described in Section 2. The generation of the homogeneous, high-quality wind fields used as input to the wave model is described in detail in Section 3. Section 4 describes the extensive evaluation of the model winds and waves compared to both *in situ* and satellite observations. Finally, Section 5 shows results of the climate assessment, including both engineering-type analyses and climate trend analysis.

2. WAVE MODEL

The wave model used for this hindcast is a discrete spectral type called OWI 3-G. The spectrum is resolved at each grid point in 24 directional bins and 23 frequency bins. The bin centre frequencies range from 0.039 Hz to 0.32 Hz increasing in geometric progression with a constant ratio 1.10064. Deep-water physics is assumed in both the propagation algorithm and the source terms. The propagation scheme (Greenwood *et al.*, 1985) is a downstream interpolatory scheme that is rigorously energy conserving with great circle propagation effects included. The source term formulation and integration is a third-generation type (WAMDI, 1988) but with different numerics and with the following modifications of the source terms in official WAMDI. First, a linear excitation source term is added to the input source term to allow the sea to grow from a flat calm condition without an artificial warm start sea state. The exponential wind input source is taken as the Snyder *et al.* (1981) linear function of friction velocity, as in WAMDI. However, unlike WAM, in which friction velocity is computed from the input 10-m wind speed following the drag law of Wu (1982), a different drag law is used in OWI 3-G. That law follows Wu closely up to wind speed of 20 m/s and then becomes asymptotic to a constant at hurricane wind speeds. The dissipation source term is taken from WAMDI except that the frequency dependence is cubic rather than quadratic. Finally, the discrete interaction approximation to the non-linear source term is used as in WAMDI except that two modes of interaction are included (in WAMDI the second mode is ignored). Further details on this model and its validation may be found in Khandekar *et al.* (1994), Cardone *et al.* (1996) and Forristall and Greenwood (1998). This wave model has been shown to reproduce observed wave heights

very well when driven by accurate wind fields (Cardone *et al.*, 1995, 1996).

OWI 3-G is adapted on a latitude-longitude grid consisting of a 122 (in latitude) by 126 (in longitude) array of points. The grid spacing is 0.625° in latitude by 0.833° in longitude, which is within 10% of square (i.e. $\Delta x = \Delta y$) between 38° and 45° N. The eastern boundary is at 20°E longitude and the northern boundary is at 75.625°N latitude. After deductions for land there are 9023 grid points. The south edge of the grid is at the equator. This boundary was treated as open; wave spectra interpolated from the output of a lower resolution (2.5 degrees at a 3-hour time step) global second generation model driven by unmodified NRA 10 m wind fields (Cox and Swail, 2000) are used as boundary conditions along the equator to preserve any South Atlantic swells. The basic model integration time step is 0.5 hours and consists of one 30 minute propagation time step and two 15 minute growth cycles.

The hindcast was carried out in monthly segments using the OWI 3-G wave model in deep water mode driven by the final kinematically reanalyzed wind fields as described in the next section. A spectral save file was generated at the end of each month of integration and used to initialize the spectrum for the run of the succeeding month (warm start). Ice cover was specified for each month from mid-monthly ice tables specified on the wave grid from Walsh & Johnson (1979) (prior to 1972), Arctic and Antarctic Sea Ice Data CD-ROM 1972-1994, and hand-digitized maps produced from the joint Navy/NOAA Ice Center data sets. The 5/10-ice concentration contour was used as the definition of the ice edge - points with ice concentrations greater than 5/10 were considered as land by the model, those with concentrations 5/10 or less were considered as open water. The output of the model consists of 17 'fields' quantities (e.g. significant wave height, peak period, vector mean direction, partitioned fields, directional and angular spreading) at all grid points and the full two-dimensional spectrum at 233 grid points. The spectral save points were selected to allow even coverage of the basin (every 5° of latitude and longitude), as well as to allow the possibility to drive finer mesh models for the US East Coast, the Scotian Shelf and Grand Banks of Newfoundland and the European West Coast. Spectra were also saved at the locations of selected moored buoys and offshore platforms.

3. WIND FIELDS

The most important, and unique, element of the AES40 hindcast was the enormous effort devoted to producing the wind fields for the wave model; this effort accounted for more than 10,000 meteorologist-hours of effort spent in manual and interactive kinematic analysis. Details of the wind field generation are given in Swail and Cox (2000); however, a brief description will be included here for completeness.

In the first step of the wind field generation, NRA surface (10 m) winds are brought into the Wind WorkStation every 6 hours in monthly segments, after first being converted to an equivalent neutral wind using the NRA 2 m surface temperature and sea-surface temperature fields and the algorithm described by Cardone *et al.* (1990).

In the second step of the wind analysis, all available historical marine surface data, including buoy observations, ship reports, coastal stations and ERS 1/2 scatterometer winds are displayed in the Wind WorkStation. A crucial feature of the AES40 hindcast concerns the treatment of these surface observations. The NRA assimilation scheme (as with most numerical weather prediction schemes) treated all observations at a 10 m reference level, whereas ship and drilling platform observations may actually range from about 15 m to more than 100 m, and buoy observations are typically taken about 5 m. Over the 40 year duration of the NRA this may introduce biases similar to those found by Cardone *et al.* (1990) due to the increasing heights of shipboard anemometers and the higher fraction of wind measurements compared to wind estimates. To overcome any potential bias in this project, all surface wind data were first adjusted to effective neutral 10-m winds.

It was found in the NRA hindcasts that tropical storms are poorly resolved in the NRA wind fields. In the third step of the wind analysis, high resolution surface wind fields for all tropical cyclones, as specified by a proven tropical cyclone boundary layer model (Cardone *et al.*, 1994; Thompson and Cardone, 1996), are assimilated into the wind fields to provide greater skill and resolution in the resulting wave hindcasts. Track and initial estimates of intensity are taken, with some modification, from the NOAA Tropical Prediction Center's (TPC) HURDAT database. The radius of maximum wind is determined using a pressure profile fit to available surface observations and aircraft reconnaissance data. Reconnaissance data are taken from TPC's Annual Data and Verification Tabulation diskettes from 1989-1996, digitally scanned from manuscript records for the period 1974-1988, and

manually scanned from reconnaissance microfilm for periods prior to 1974. Surface winds generated from the model are then evaluated against available surface data and aircraft reconnaissance wind observations adjusted to the surface as described by Powell *et al.* (1989). Model winds within 240 nautical miles from the centre are then exported on a 0.5° latitude-longitude grid for inclusion and blending using the Wind WorkStation.

The fourth, and most labour-intensive and time-consuming, but also the most important step, was the detailed kinematic analysis incorporating all of the wind information noted above. The interactive wind analysis methodology used follows similar previous hindcast studies (Cardone *et al.,* 1995, 1996). Particular attention is spent on strong extra-tropical systems, blending tropical model winds into the NCEP surface wind field, and in the quality control of surface data. Kinematically analyzed winds from previous hindcasts of severe extratropical storms in the northwest Atlantic (Swail *et al.*, 1995) are incorporated into the present analysis on the North Atlantic wave model grid.

Altimeter wave measurements are used in an inverse modelling approach as follows. Hindcast wave heights over the North Atlantic Ocean derived from the global 2-G model described in Section 2 are compared to altimeter wave measurements. Areas where the resulting wave fields are deficient, as indicated by the altimeter, are brought to the analysts' attention and the analyst subjectively rectifies the deficiencies in the backward space-time evolution of the NRA wind field causing the discrepancy.

Final wind fields for each month were interpolated onto the 0.625° by 0.833° latitude-longitude wave model grid using the IOKA (Interactive Objective Kinematic Analysis) algorithm (Cox *et al.*, 1995) and then time interpolated to a one-hour time step.

4. VALIDATION

4.1 Validation Data Sets

4.1.1. Buoys and Platforms

The *in situ* validation data set included buoys and measurement platforms mainly located along the continental margins. The *in situ* measured wind and wave data came from a variety of sources. U.S. buoy data came from the NOAA Marine Environmental Buoy Database on CD-ROM; the Canadian buoy data came from the Marine Environmental Data Service marine CD-ROM; the remaining buoy and platform data (notably the northeast Atlantic) came from the Comprehensive Ocean Atmosphere Data Set (COADS) data set described by Slutz *et al.* (1985). Comparisons were restricted to well-exposed deep-water sites with the longest records. The wave measurements are comprised of 20-minute samples (except for Canadian buoys which were 40 minutes) once per hour. The wind measurements were taken as 10-minute samples, scalar averaged, except vector averaged at the Canadian buoys, also once per hour. The wind and wave values selected for comparison with the hindcast were 3-hour mean values centered on each six-hour synoptic time with equal (1,1,1) weighting. All wind speeds were adjusted to 10-m neutral winds following the approach described in Cardone *et al.* (1990).

4.1.2. Satellite Data

Altimeters from the ERS-1, ERS-2 and TOPEX/Poseidon instruments were used for wind and wave comparisons. The ERS-1/2 altimeter data sets were obtained from the Ifremer CD-ROM data set, while TOPEX data (GDR Generation-B CD-ROM set) was obtained from the NASA Physical Oceanography Distributed Active Archive Center at the Jet Propulsion Laboratory/California Institute of Technology. Both data sets were decoded using the recommended quality controls described in each respective documentation. Further adjustments and quality control measures were used as recommended by Cotton and Carter (1994) to make the observations from differing platforms consistent with each other. Individual data points were then spatially binned onto the wave model grid, and output on to 6-hour synoptic times using a ±3-hour window. Additional quality control was performed for measurements along land and ice edges where some contamination of the altimeter wave measurements was encountered despite rigorous checking of ice/quality control flags available with each data set.

4.2 *In situ* Comparisons

Individual buoys and platforms were grouped by region for comparison against the AES40 hindcast. Table 1 shows regional grouped statistics and represents more than 200,000 wind and wave observations. Highest scatter indices (SI) are from the northeast Atlantic regions, which were made up exclusively of COADS data. The COADS data lacks both the time resolution (3/6 hours versus 1 hour) and coding accuracy (winds nearest 1 knot, waves 0.5 m) than the other regions obtained from the CD-ROM marine data sets, which may explain some of the differences in SI. The Canadian and U.S. buoys were grouped into one data set since they represented the best science quality validation data set. These statistics show very good

agreement with a mean bias of 0.31 m/s for winds and 0.10 m for waves and SI of 0.23 for both winds and waves. Wind speed scatter at the Canadian buoys is high, 0.31, mainly due to questionable data from one buoy which was left out in the wind assimilation but left in the comparisons shown here.

Table 1. Regional statistical comparison of AES40 vs. *in situ* buoy and platform observations.

	Number of Points	Mean Meas	Mean Hind	Diff (H-M)	RMS Error	Std. Dev.	Scatter Index	Corr. Coeff.
U.S. Buoys								
Ws (m/s)	169927	6.92	7.18	0.26	1.31	1.28	0.19	0.94
Wd (°)	169925	240.47	251.65	0.99	N/A	16.65	0.05	N/A
Hs (m)	164834	1.83	1.94	0.12	0.43	0.42	0.23	0.93
Canadian Buoys								
Ws (m/s)	49272	7.94	8.41	0.46	2.54	2.50	0.31	0.84
Wd (°)	49272	263.46	268.87	1.58	N/A	29.48	0.08	N/A
Hs (m)	48890	2.51	2.53	0.03	0.53	0.53	0.21	0.93
East Atlantic Buoys								
Ws (m/s)	11019	9.75	9.71	-0.04	1.64	1.64	0.17	0.93
Wd (°)	11027	245.40	244.27	-0.44	N/A	17.98	0.05	N/A
Hs (m)	8071	3.73	3.47	-0.27	1.68	1.65	0.44	0.74
North/Norwegian Sea Platforms and Buoys								
Ws (m/s)	117198	8.58	9.14	0.56	2.24	2.17	0.25	0.88
Wd (°)	117204	240.17	239.27	-1.09	N/A	22.64	0.06	N/A
Hs (m)	107301	2.47	2.67	0.20	0.96	0.94	0.38	0.83
U.S. and Canadian Data Combined								
Ws (m/s)	219199	7.15	7.45	0.31	1.67	1.64	0.23	0.91
Wd (°)	219197	247.72	257.67	1.11	N/A	20.14	0.06	N/A
Hs (m)	213724	1.98	2.08	0.10	0.46	0.45	0.23	0.93

A quantile-quantile comparison of wind speed and wave height for the combined U.S. and Canadian buoys (Figure 1) shows excellent agreement from the 1st to 99th percentile. There is a small overestimation of both the winds and waves (mean difference is 0.31 m/s and 0.10 meters), however the near-linear comparison indicates that AES40 is properly describing the wind and wave climate at the buoy locations up to and including the 99th percentile.

While overall statistics are useful for evaluating the skill of a hindcast, they don't indicate how the hindcast has changed over time relative to the *in situ* data. A comparison of seasonal wave height bias and scatter over the 1975-1997 period (Figure 2) shows any trends that may exist in the hindcasts. Of course, trends may also occur in the measurements themselves (number of observations available, differing instrumentation, etc.) and the measured data must be evaluated carefully. These plots were produced by computing bias and SI for each region for every 3 months and plotting the resulting time series. Figure 2 shows good agreement between the buoy observations and AES40 over time. The plots show nearly linear bias and SI over time indicating that AES40 has remained consistent over the 22 years that the buoy measurements are available. Highest SI values occur in the data from COADS, while the US and Canadian comparisons are more consistent. Early US buoy comparisons show more bias and slightly higher SI, which may be due to the relatively few experimental buoys available in late 70's/early 80's.

4.3 Satellite Comparisons

Altimeter wind and wave measurements provide the best spatial coverage to evaluate wave hindcasts. Statistics and plots from the individual instruments (ERS-1, ERS-2, and TOPEX) showed very good agreement between each other, so the data sets were

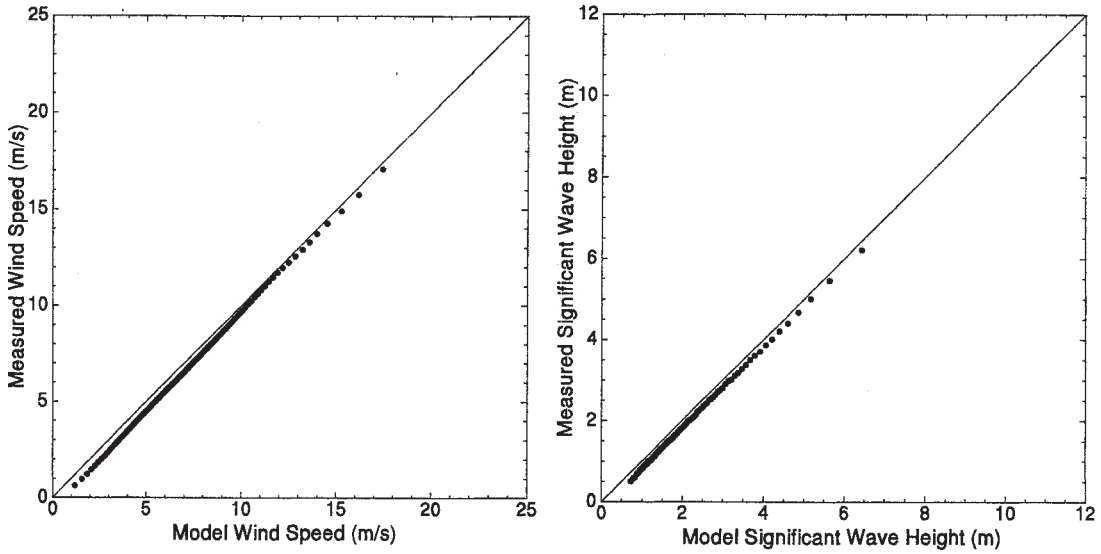

Figure 1. Quantile-Quantile comparison from 1 to 99% for combined U.S. and Canadian buoys vs. AES40 wind speed (m/s, left) and significant wave height (meters, right).

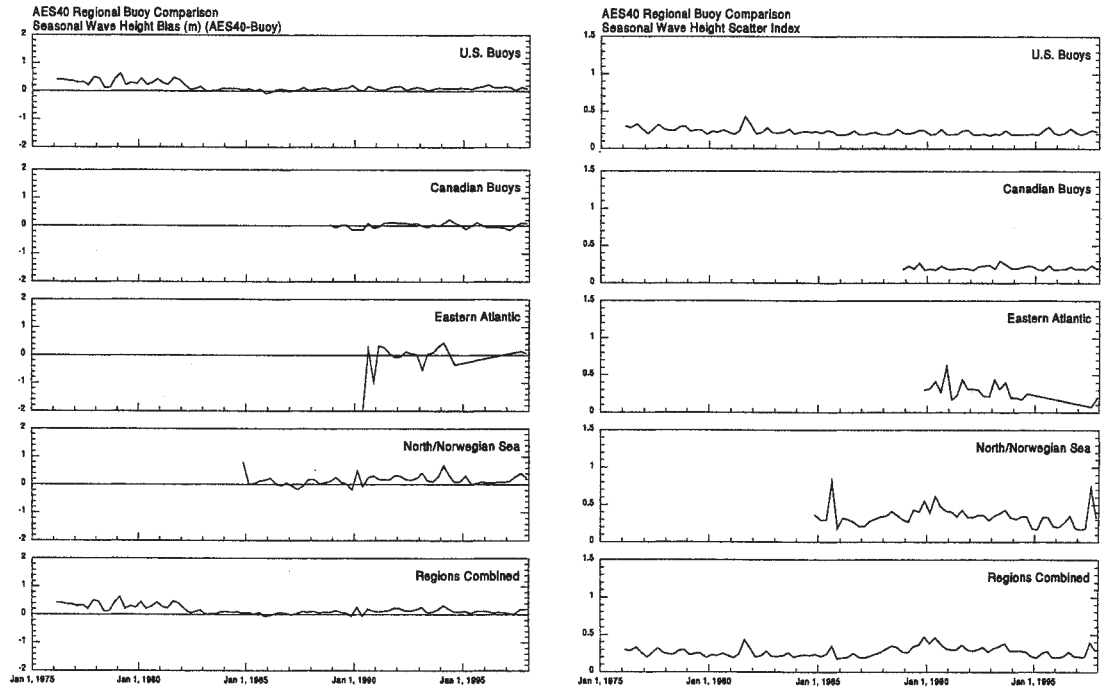

Figure 2. Seasonal wave height bias (m) (left) and scatter (right) comparison of AES40 vs. buoys by region

combined for these comparisons. Comparisons were done for the full basin only. Statistics are summarized in Table 2. The wave height comparisons showed near-zero bias, while the model winds were slightly higher than the satellite values. Scatter indices were of comparable magnitude to the *in situ* comparisons.

Table 2. Regional statistical comparison of AES40 vs. altimeter measurements.

	Number of Points	Mean Meas	Mean Hind	Diff (H-M)	RMS Error	Std. Dev.	Scatter Index	Corr. Coeff.
Ws (m/s)	3471109	7.66	7.81	0.15	1.94	1.94	0.25	0.86
Hs (m)	3523575	2.52	2.51	-0.01	0.56	0.56	0.22	0.93

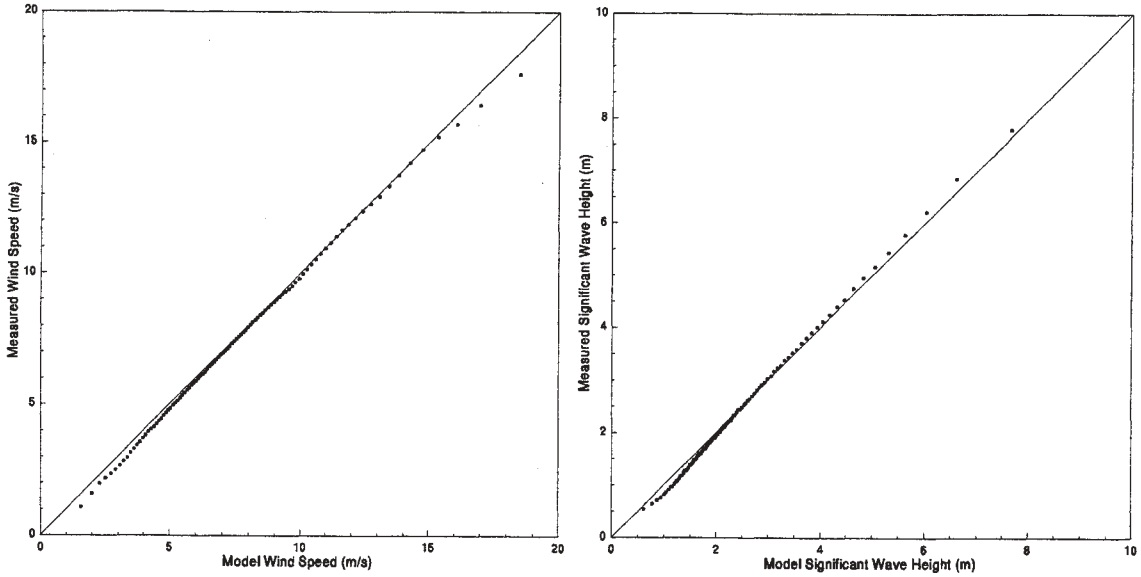

Figure 3. Q-Q wind speed (m/s) and wave height (m) comparisons of AES40 and altimeter measurements.

Quantile-quantile (Q-Q) plots of the combined altimeter versus AES40 (Figure 3) show excellent agreement for both wind speed and wave height. At the highest percentiles, winds appear to be over-predicted while waves track up to the 99th percentile. This is suspected to be a wind speed saturation problem with the altimeter in wind speeds above 15 m/s.

The extensive coverage of the altimeter measurements makes it possible to plot contours of wave bias on a basin-wide projection. A spatial wave bias plot of AES40 (Figure 4) shows that over most of the North Atlantic AES40 has very little bias. The largest feature is the underestimation in Baffin Bay and in the Denmark Strait. This is suspected to be a result of ice edge effects, and to some degree an underestimation of the wind speed in the NRA winds. While the AES40 winds were kinematically enhanced, the lack of data in these areas made it difficult to track all significant systems. When sufficient data were available, large discrepancies of the wind speed were found and corrected in the NRA winds. Grid scale effects explain most other areas of bias near island chains or in the shallow Southern North Sea.

A basin map of wave height scatter index (SI) (Figure 5) shows many of the same patterns as the wave height bias map. In general, the SI is very small (near or under .20 for most of the basin) with larger values at the coasts and along water/ice boundaries.

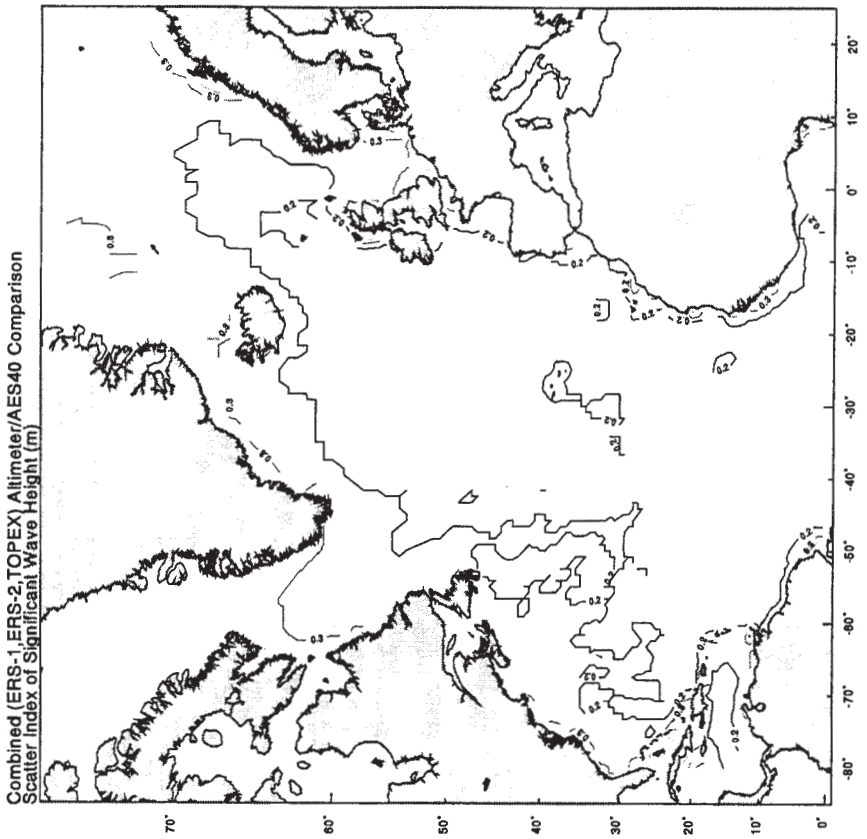

Figure 5. Comparison of wave height scatter index (RMS/Mean Altimeter) for combined ERS 1/2 and TOPEX wave measurements vs. AES40 for period 1991-1997.

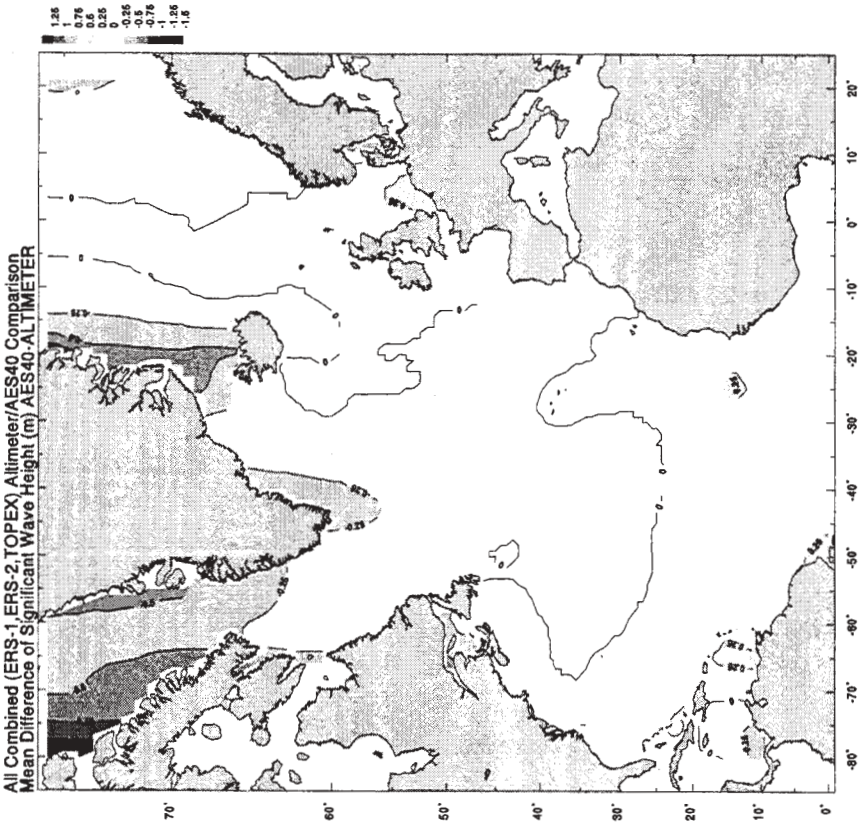

Figure 4. Mean difference of wave height (m) between AES40 and altimeter measurements (AES40-Altimeter)

AUTHOR INDEX TABLE OF CONTENTS

5. CLIMATE ASSESSMENT

5.1 Trend and Variability Analysis

Fifteen statistics were computed for both the input wind fields and resultant wave heights on monthly, seasonal and annual time scales; trend and variability analysis was carried out for every grid point in the hindcast. Among the statistics computed were: mean, standard deviation, skew, kurtosis, 50th, 90th, 95 and 99th percentiles, and exceedance above selected thresholds.

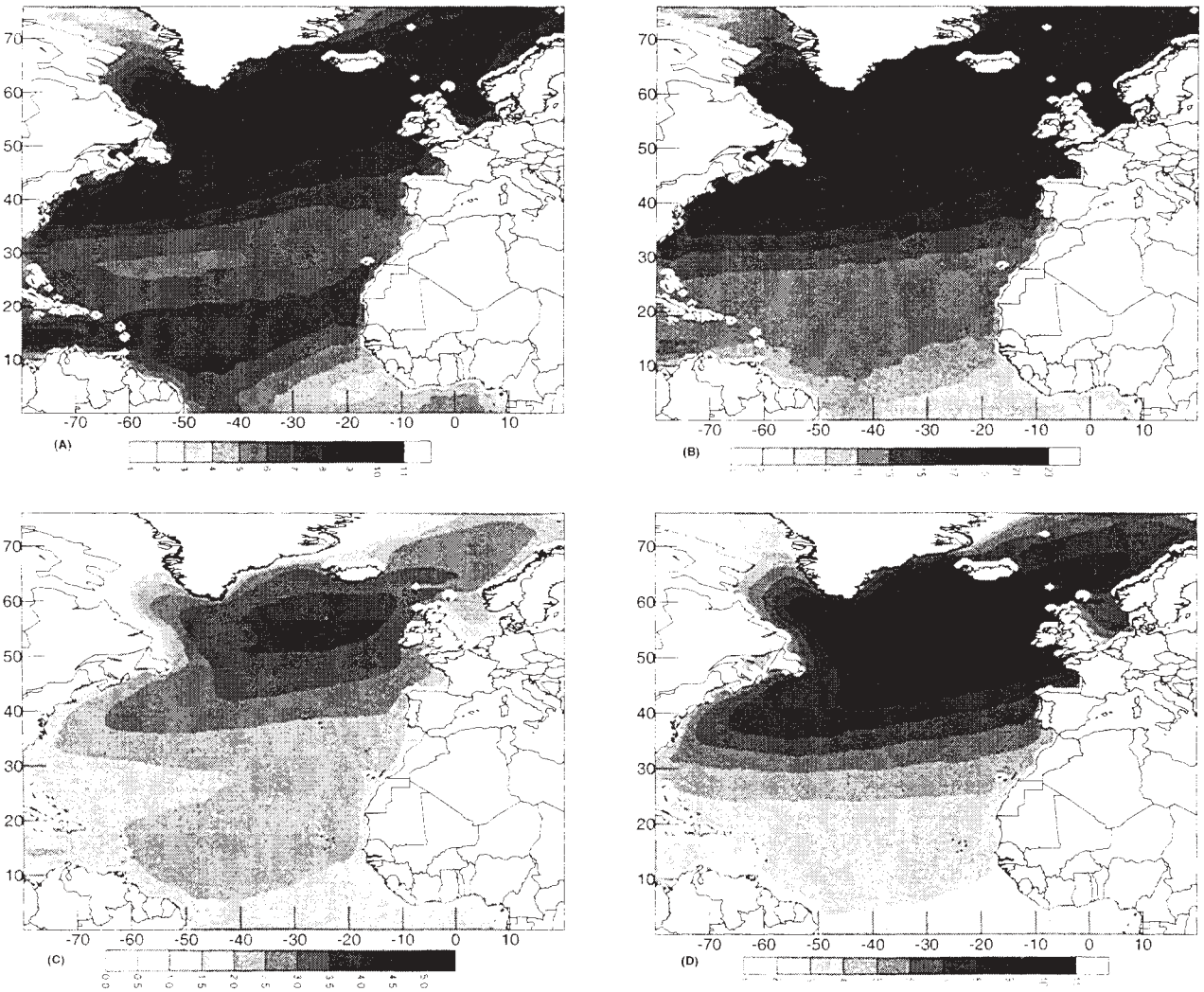

Figure 6. Wind speed and wave height statistics over the period 1958-1997: (a) annual mean wind speed; (b) 99th percentile wind speed; (c) annual mean wave height; (d) 99th percentile wave height

Figure 6 (a,b) shows the mean annual wind speed and wave height distribution for the period 1958 to 1997. The maxima in the high latitude areas and along the prevailing storm tracks are very evident in these charts.

Figure 6 (c,d) shows the geographical distribution of the annual 99th percentile wind speed and wave height for 1958-1997. The patterns are very similar to those for the means, although the areas of highest wind speed and wave height are even more accentuated.

A series of statistical analyses of the wind and wave trends was carried out at each grid point. Trends were computed as simple linear trends over the 40 years of the hindcast using least squares fitting techniques; 99% statistical significance levels were also computed. Figure 7 shows the trends in the mean and 99th percentile wind speed and wave heights; trends are expressed as the inferred change over the 40-year

period 1958-1997 based on the slope of the linear trend line. Increasing trends are most noticeable in the northeast Atlantic Ocean. Negative trends in wave height are found in the Labrador Sea. Particularly noticeable is the bi-polar nature of the trends in the North Atlantic, with strong increases in the northeast, and strong decreases in the south central North Atlantic. This pattern follows the dominant mode of the North Atlantic Oscillation. The trends are much more pronounced for the extreme wave heights (99th percentile) than for the mean conditions, with large areas of increases of wave height more than 1 m.

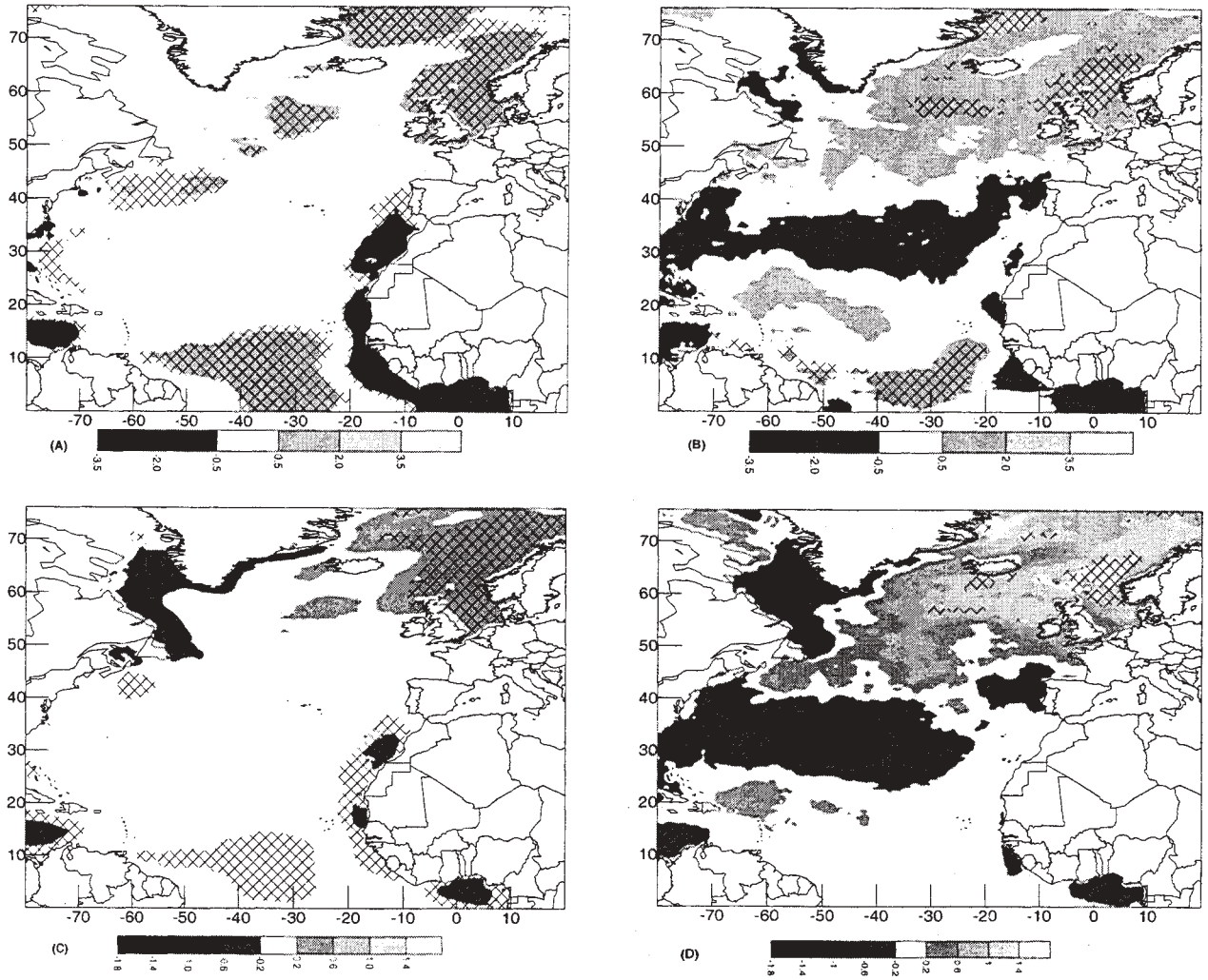

Figure 7. Inferred change over the period 1958-1997 with 99% statistical significance in (a) annual mean wind speed; (b) 99th percentile wind speed; (c) annual mean wave height; (d) 99th percentile wave height

5.2 Extreme Value Analysis

Three populations of storms were used for the extremal analysis. "Tropical" refers to any peak which occurred within 240 nmi of a tropical system center location at any intensity. "Extratropical" refers to any peak that is not considered "Tropical." Finally, "combined" contains every peak. A peak is defined as any event that greater than the minimum significant wave height threshold, and must be separated from any other peak by at least 48 hours. The length of a storm for the maximum wave and crest computations is defined as the time when significant wave height is greater than one-half of the peak of that particular event, or a maximum of 48-hours, where the peak is at the midpoint. The minimum significant wave height threshold varied with latitude, 2.5 m from 0-31.25°N and 3.0 m from 31.25°N-75.625°N. For locations covered often by ice and very sheltered locations along

the African coast, a lower threshold of 0.5 m was used to achieve a minimum of 4 peaks.

Peaks were produced for seven time slices: 1958-1997 (all 40 years); 1958-1977 and 1978-1997; 1958-1967, 1968-1977, 1978-1987, and 1988-1997. All peaks were processed using two extremal distributions, Gumbel and Weibull (Borgman, 1973; Forristall, 1978; Gumbel, 1958; Haring *et al.*). In each case, the top 40 peaks (with a minimum of four peaks) were used to produce a fit at each of the 9023 grid points. Seven return periods were computed: 2, 5, 10, 20, 40, 50, and 100 years for each of the following six variables: significant wave height (SWH), maximum wave, maximum crest, peak period (associated with SWH), wind speed that occurred at the same time as SWH, and maximum wind speed (can occur independently of SWH but within the storm length as defined above). Figure 8 shows the 100-year Gumbel analysis of the entire 40-year period for significant and maximum wave height, associated wind speed and peak period; the wave height and wind speed contours were smoothed using an evenly weighted 9-point average. Unsmoothed SWH values were used to develop the regression analysis for peak period, but smoothed values were used to derive the associated peak period values shown in the figure.

From Figure 8 it can be seen that the highest wind and wave conditions are expected to occur west of the United Kingdom and south of Iceland. Also, tropical system "trails" can be seen extending along 15-20°N and towards the northwest to the southern U.S. The other time slices showed similar results (not shown) and were dictated by the relative storminess. The tropical system "trail" would grow or shrink accordingly as would the strongest area over the North East Atlantic. In fact, the strong North East Atlantic area shifted to the south and west and was centered along 50°N during the first and most recent decades.

5.3 Redundancy Analysis

Like canonical correlation analysis (CCA), redundancy analysis is a technique that is used to associate patterns of variation in a predictor field with patterns of the predictand field through a regression model. It differs from CCA because it seeks to find pairs of predictor and predictand patterns that maximize the associated predictand variance, rather than the correlation only. Redundancy analysis techniques (described by Wang *et al.*, 1999) were used to carry out detailed seasonal spatial statistical analyses. Significant increases in the northeast Atlantic in the 90th and 99th percentile wave heights were matched by significant decreases in the subtropical North Atlantic, for the winter (JFM) season. Linear trends detected for the 99th percentiles are generally less significant than those for the 90th percentiles. The correlation between sea level pressure (SLP) and the 90th percentile wave height (H90) is significant at the 99th confidence level. Both time series possess a significant increasing trend at the 95% confidence level, indicating that the Icelandic low has deepened during the recent decades while the Azores high intensified, and consequently, SWH extremes have increased in the northeast NA, accompanied by decreases of SWH extremes in the subtropical NA. Both SLP and H90 are highly significantly correlated with the NAO index. Similar results were also found for winter (JFM) 99th percentile wave heights. No significant trends of seasonal SWH extremes are found for the last century, though significant changes do exist in the last four decades; multi-decadal fluctuations are quite noticeable. These results are summarized in Figure 9. A more detailed description of these results can be found in Swail and Wang (2000).

5.4 Assessment of Homogeneity

While the NRA used the same numerical prediction scheme for the entire 40-year period, thus removing the bias associated with ever-changing operational models, there still remain probable biases due to increased observational quality and densities (Schmidt and von Storch, 1993). These are often referred to as "creeping inhomogeneities", and are potentially serious constraints to any attempt to derive long-term trends. Therefore, we would like to verify the trend analyses derived from the hindcast against some long time histories of homogeneous measured data at selected points. Unfortunately, there are very few such locations in the global ocean.

One location for which we do have reasonably homogeneous wind measurements over the 40-year period is at Sable Island, just off the east coast of Canada. We are also able to analyze the surface atmospheric pressure record from Sable Island, along with records from two other sites in Nova Scotia (Halifax, Sydney), to compute pressure triangle wind records. As shown by Schmidt and von Storch (1993), the pressure triangle winds are likely the least biased wind estimator available, since inhomogeneities in pressure records are much less than for most atmospheric variables.

Figure 10 shows the trends for the Sable Island area from the AES40 hindcast, Sable Island and the pressure triangle. In both the Sable Island measurements and the triangle winds the trends in the percentiles are decreasing; the magnitude of the decreasing trend is comparable in both analyses, with the triangle wind

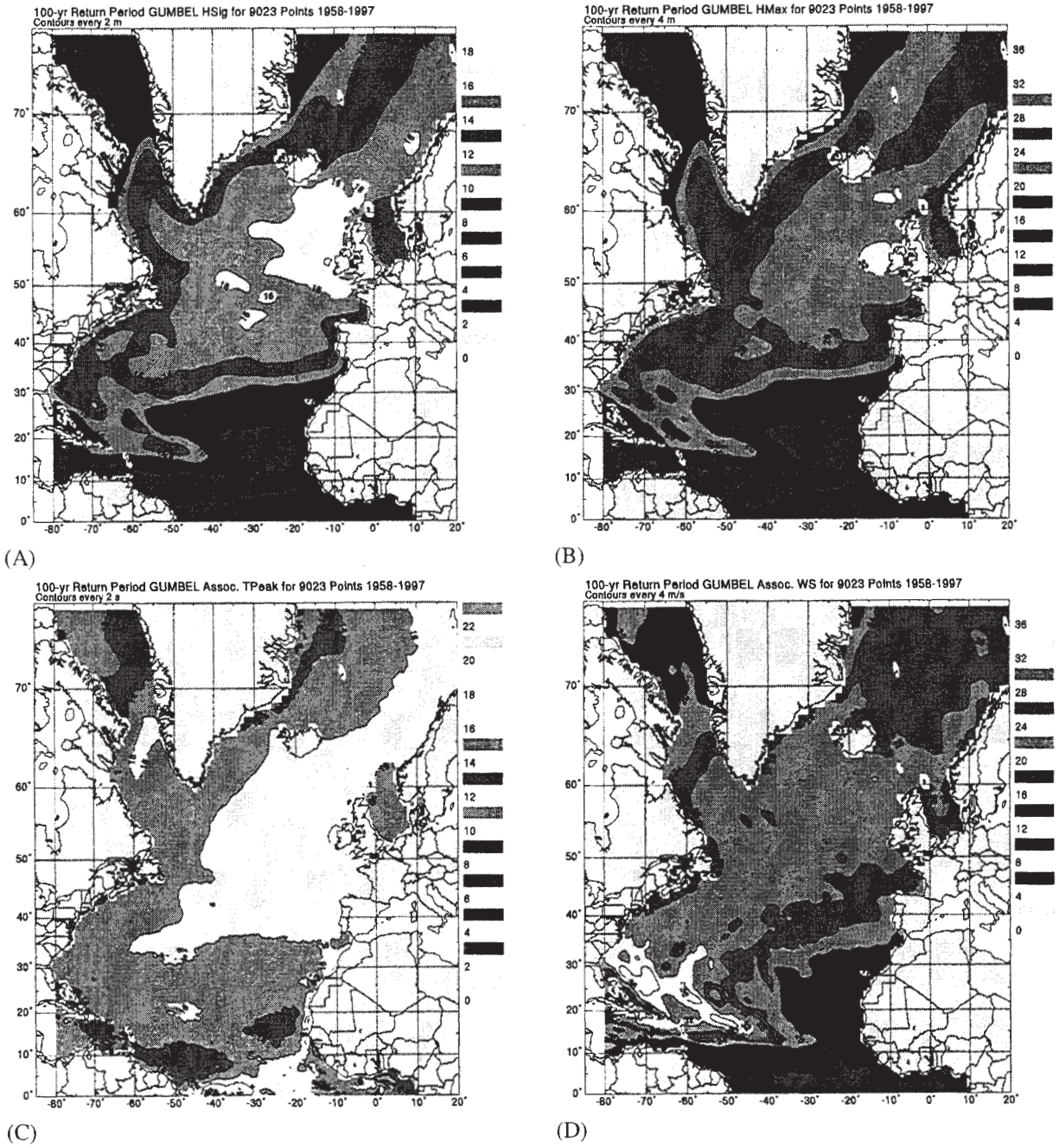

Figure 8. 100-year return period statistics for AES40 hindcast 1958-1997. All peaks combined. Gumbel analysis. (A) significant wave height; contours every 2 m; (B) maximum wave height, contours every 4 m; (C) peak period associated, contours every 2 s; (D) wind speed associated, contours every 4 m/s

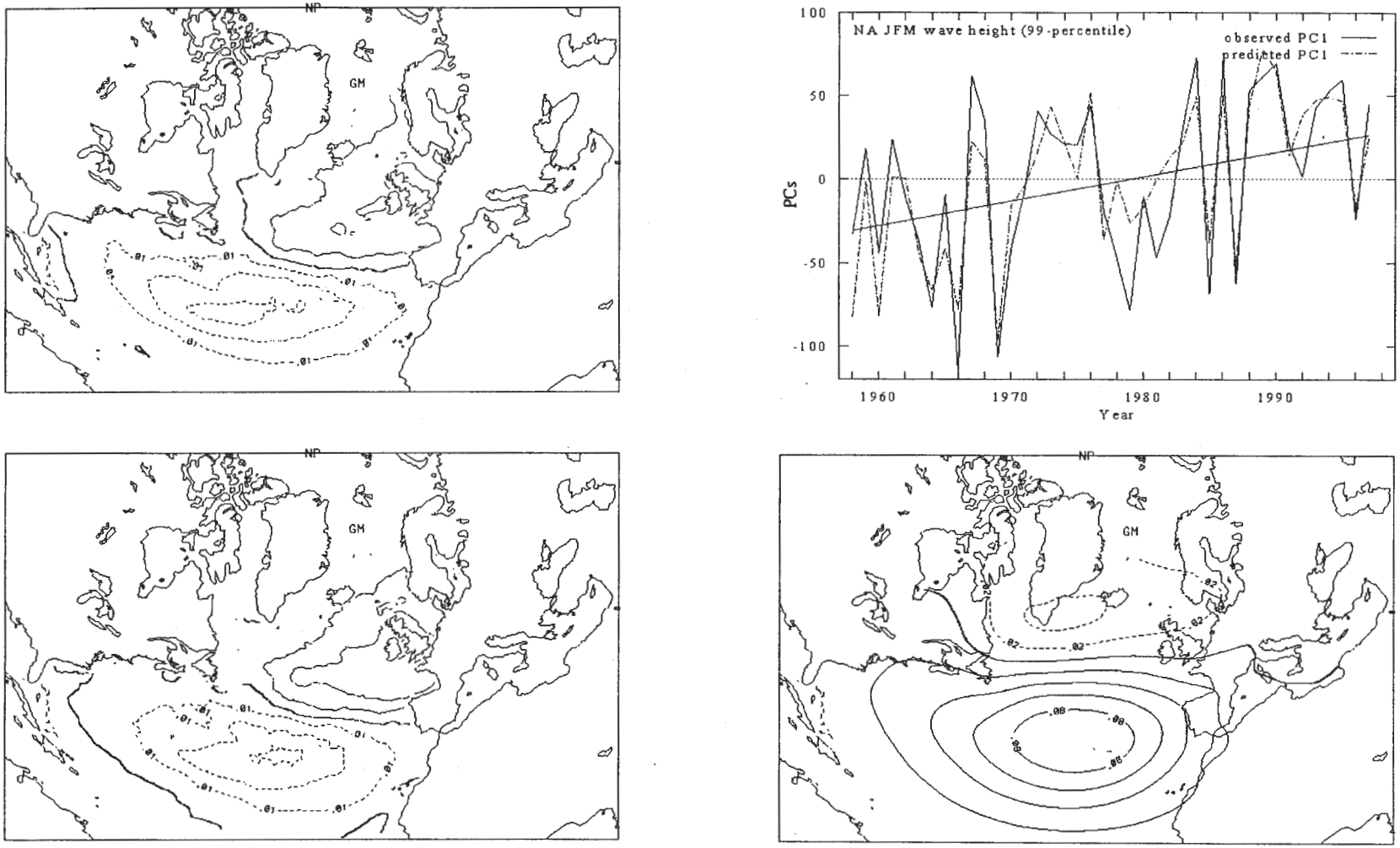

Figure 9. (top left, top right). First Empirical Orthogonal Function (EOF1) and first principal component (PC1) of winter (JFM) seasonal significant wave height extremes (H_{99}). The observed and predicted PC1s are PC1s of the numerical and statistical reconstruction, respectively. The trends shown were estimated from the numerical PC1. The contour interval is 0.01 m; solid, bold and dashed lines are positive, zero and negative contours, respectively. (bottom left, bottom right). The best predicted mode of winter seasonal 99-percentiles of significant wave height (H_{99}) in the North Atlantic and the associated predictor (SLP) mode, respectively. In the 1958-1997 period, both the predictor and predictand time series (SLP-T1 and H99-T1; normalized) have a significant increasing trend at 95% confidence level.

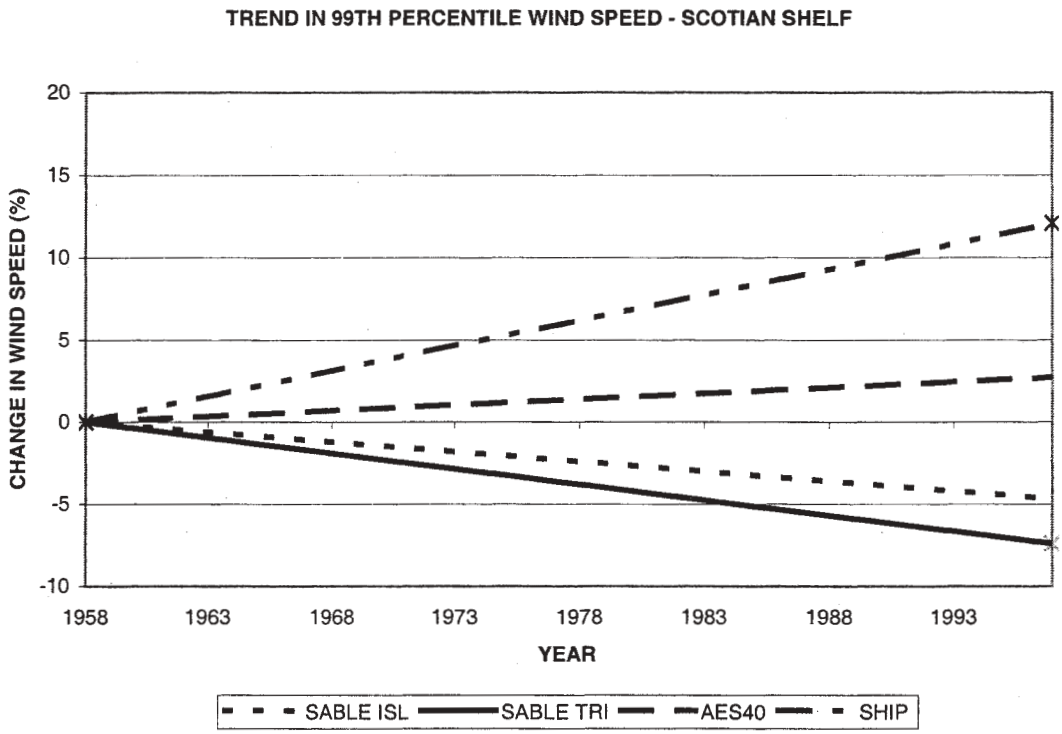

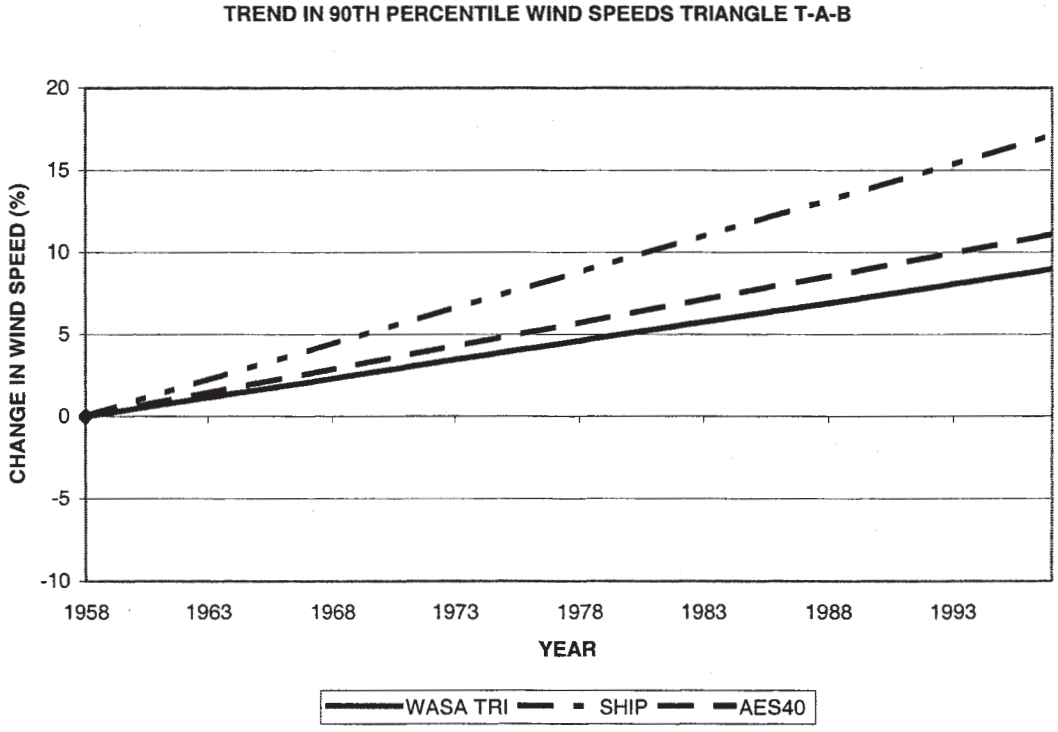

Figure 10. Trends in AES40 wind speeds and corresponding point trends expressed as the inferred percent change in 99th (lower panel 90th) percentile wind speed over the period 1958-1997 for the Sable Island area (upper) and the WASA triangle Thorshavn-Aberdeen-Bergen (lower)

trend being slightly more negative. The hindcast wind speed trend shows a near-zero, but very slightly positive trend. This likely indicates an inhomogeneity introduced into the NRA winds. The AES40 trends should be a reasonable indication of the intangible creeping inhomogeneities in the reanalysis process, such as increased data density, since the other sources such as changing anemometer heights have been mostly removed. Figure 10 also shows the trends from Comprehensive Ocean-Atmosphere Data Set (COADS) ship observations. These wind speeds have been corrected where possible following the approach of Cardone *et al.* (1990). However, there remains a strong positive trend in wind speeds, particularly at the higher percentiles. Based on the Sable Island and triangle winds, this trend is likely spurious, indicating that even these methods are unable to remove all of the artificial trend introduced by changing observational procedures on ships.

A second area for which "ground truth" information is available for trends is off the Norwegian coast. WASA (1998) computed winds from two pressure triangles: (1) T-B-M (Thorshavn-Bergen-Mike (OWS)); and (2) T-A-B (Thorshavn-Aberdeen-Bergen). Figure 10 shows the comparative results of the hindcast and the T-A-B triangle. In this area both trends are strongly positive, the hindcast winds being slightly more positive than the triangles. This indicates that the hindcast trends are reasonable, but probably slightly too high, or a good upper bound on real trends. Trends from adjusted ships in these areas similarly show too-strong increases in wind speed, especially in the higher percentiles. Results from the T-B-M triangle (not shown) were similar.

6. SUMMARY

This study describes the first engineering-quality 40-year wind and wave hindcast produced for the entire North Atlantic Ocean using a long term, consistent wind field forcing based on the NCEP re-analysis. The NRA surface wind fields have been kinematically reanalyzed to account for differences in wind observations, to reproduce small-scale features such as tropical storms, and to reduce the inherent low bias in extreme extratropical storms due to the limited grid resolution in the NRA wind fields. The wind fields are used to drive a 3rd generation wave model on a fine mesh grid covering the entire North Atlantic Ocean. The output from the wave model, consisting of 17 different fields is archived at 6-hour intervals at each grid location; 2-D wave spectra are archived every 6 hours at 233 grid points covering the entire basin, but particularly along the continental margins.

In situ and satellite observations have been used to evaluate the wind and wave hindcast. The hindcast compares well against the available buoy, platform, ocean weather ship and satellite measurements in all parts of the North Atlantic, not only in terms of bias and scatter, but over the entire frequency distribution out to and beyond the 99th percentiles of both winds and waves. Comparisons of *in situ* data over the full 1958-1997 period show that the hindcast has remained consistent with the observations. The wind and wave data are considered to be of sufficiently high quality to be used in the analysis of long return period statistics, and other engineering applications.

Extremal analysis was performed for the entire basin. Highest winds and waves are shown to occur over the North East Atlantic west of the United Kingdom and south of Iceland.

The trend analysis showed statistically significant areas of both increasing and decreasing winds and waves. The increasing trend in the North East Atlantic and decreasing trend in the Central North Atlantic are particularly well defined and consistent with changes reported in previous studies, which were linked to reported changes in the North Atlantic Oscillation. The apparent creeping inhomogneities in the NRA winds highlight the need for additional investigation of the sources and magnitudes of the inhomogeneities, by comparing the results of this (and subsequent) hindcasts to other long-term homogeneous data sets such as pressure triangles.

7. REFERENCES

Borgman, L.E. 1973. Probabilities for the highest wave in a hurricane. *J. Waterways, Harbors and Coastal Engineering Div.*, ASCE, 185-207.

Cardone, V.J., A.T. Cox, J.A. Greenwood, and E.F. Thompson, 1994. *Upgrade of tropical cyclone Surface wind field model.* U.S. Corps of Engineers Misc. Paper CERC-94-14.

Cardone, V.J., H.C. Graber, R.E. Jensen, S. Hasselmann, and M.J. Caruso, 1995. *In search of the true surface wind field in SWADE IOP-1: ocean wave modeling perspective.* The Global Ocean Atmosphere System, **3**, 107-150.

Cardone, V.J., J.G. Greenwood and M.A. Cane, 1990. *On trends in historical marine wind data.* J. Climate, **3**, 113-127.

Cardone, V.J., R.E. Jensen, D.T. Resio, V.R. Swail and A.T. Cox, 1996. *Evaluation of Contemporary Ocean Wave Models in Rare Extreme Events: "Halloween Storm of October, 1991; "Storm of the Century" of March, 1993."* J. Atmos. Ocean. Tech., **13**, 1, 198-230.

Cotton, P.D., and D.J.T. Carter, 1994. *Cross calibration of TOPEX, ERS-1, and Geosat wave heights.* J. of Geophysical Research, **99**, C12, 25,025-25,033.

Cox, A.T., and V.R. Swail, 2000. *A global wave hindcast over the period 1958-1997: validation and climate assessment.* J. of Geophys. Res., (in press).

Cox, A.T., J.A. Greenwood, V.J. Cardone and V.R. Swail, 1995. *An interactive objective kinematic analysis system.* Proceedings 4th International Workshop on Wave Hindcasting and Forecasting, October 16-20, 1995, Banff, Alberta, p. 109-118.

Forristall, G.Z. 1978. *On the statistical distribution of wave heights in a storm.* J. of Geophys. Res., **83**, 2353-2358.

Forristall, G.Z. and J. A. Greenwood, 1998. *Directional spreading of measured and hindcasted wave spectra.* Proc. 5th International Workshop on Wave Hindcasting and Forecasting, Melbourne, FL, January 26-30, 1998.

Greenwood, J.A., V.J. Cardone and L.M. Lawson, 1985. *Intercomparison test version of the SAIL wave model.* Ocean Wave Modelling, the SWAMP Group, Plenum Press, 221-233.

Gumbel, E.J. 1958. *Statistics of Extremes.* Columbia University Press, New York, 375 pp.

Haring, R.E., A.R. Osborne, and L.P. Spencer. 1976. *Extreme wave parameters based on continental shelf storm wave records.* Proceedings of the 15th Coastal Engineering Conference, Honolulu, July 11-17, 1976.

Kalnay, E., *et al*, 1996. *The NCEP/NCAR 40-Year reanalysis project.* Bull. Amer. Meteor. Soc., **77**, 3, 437-471.

Khandekar, M.L., R. Lalbeharry and V.J. Cardone, 1994. *The Performance of the Canadian Spectral Ocean Wave Model (CSOWM) During the Grand Banks ERS-1 SAR Wave Spectra Validation Experiment.* Atmosphere-Ocean, **32**, 1, 31-60.

Powell, M.D., and P.G. Black, 1989. *The relationship of hurricane reconnaissance flight-level wind measured by NOAA's oceanic platforms.* 6th National Conference on Wind Engineering, March 7-10, 1989.

Schmidt, H. and H. von Storch, 1993. German Bight storms analyzed. Nature: **365**:791.

Snyder, R., F.W. Dobson, J.A. Elliott and R.B. Long, 1981. *Array measurements of atmospheric pressure fluctuations above surface gravity waves.* J. Fluid Mech., **102**, 1-59.

Stutz, R.J., S.J. Lubker, J.D. Hiscox, S.D. Woodruff, R.L. Jenne, D.H. Joseph, P.M. Steurer, and J.D. Elms, 1985. *Comprehensive Ocean-Atmosphere Data Set Release 1.* NOAA Environmental Research Laboratories, Boulder, Colo., 268 pp. (NTIS PB86-105723).

Swail, V.R. and A.T. Cox, 2000. *On the use of NCEP/NCAR reanalysis surface marine wind fields for a long term North Atlantic wave hindcast.* J. Atmos. Ocean. Technol., **17**, 532-545..

Swail, V.R. and X.L. Wang, 2000. Trends of Atlantic wave extremes as simulated in a 40-year wave hindcast using kinematically reanalyzed wind fields. Submitted to J. Climate.

Swail, V.R., M. Parsons, B.T. Callahan and V.J. Cardone, 1995. *A revised extreme wave climatology for the east coast of Canada.* Proceedings 4th International Workshop on Wave Hindcasting and Forecasting, October 16-20, 1995, Banff, Alberta, p. 81-91.

Swail, V.R., V.J. Cardone and A.T. Cox, 1998. *A Long Term North Atlantic Wave Hindcast.* Proc. 5th International Workshop on Wave Hindcasting and Forecasting, Melbourne,.FL, January 26-30, 1998.

Thompson, E.F., and V.J. Cardone, 1996. *Practical modeling of hurricane surface wind fields.* Journal of Waterway, Port, Coastal, and Ocean Engineering, July/August 1996, pp. 195-205.

Walsh, J.E., and C.M. Johnson, 1979. *An analysis of Arctic sea ice fluctuations, 1953-1977.* J. Phys. Ocean., **9**, 580-591.

WAMDI Group, 1988. *The WAM model - a third generation ocean wave prediction model.* J. Phys. Ocean. **18**: 1775-1810.

Wang, X.L., F.W. Zwiers and H. von Storch, 2000. Using Redundancy analysis to improve dynamic seasonal mean 500 hPa geopotential forecasts. Submitted to J. Climate.

WASA Group, 1998. *Changing waves and storms in the Northeast Atlantic?* Bull. AMS., **79**(5), 741-760.

Wu, J., 1982. *Wind-stress coefficients over the sea surface from breeze to hurricane.* J. Geophys. Res., **87**, 9704-9706.

EFFECT OF WIND ESTIMATION METHOD ON LONG TERM WAVE HINDCAST AT THE COASTAL AREA AROUND JAPAN

Masataka Yamaguchi, Yoshio Hatada and Hirokazu Nonaka

Department of Civil and Environmental Engineering
Faculty of Engineering, Ehime University
Matsuyama, Ehime Prefecture, Japan

1. INTRODUCTION

Yamaguchi et al. (1990, 1992, 1995) and Hatada & Yamaguchi (1992, 1997) established a long term shallow water wave hindcast system for the estimation of wave climate in coastal waters around Japan. In this system, a weather chart analysis method is applied for wind evaluation. The system makes it possible to consecutively follow wave conditions over several years with reasonable accuracy, but tremendous efforts are required to extend wind data sets over more several years. From this reason, Hatada & Yamaguchi (1998) reconstructed a long term wave hindcast system in which analysis surface wind data sets provided by ECMWF (European Centre for Medium-range Weather Forecasts) are used in place of wind data estimated by a weather chart analysis method.

In this study, wave hindcast over a long term of about 10 years or more using two systems is conducted at almost all wave measurement stations around the coasts of Japan, and comparisons are made among wave climate parameters and error statistic estimated from hindcasts and measurement on various time scales such as separate months and a whole year period for the purpose of verifying the validity of each system.

2. WIND DATA SETS

2.1 *Data Sets of Sea-Level Pressure and Wind*

Wind field at height of 10 m is estimated by the Bijvoet (1957) model which uses sea-level pressure data on a regular grid with a size of 80 km. The pressure data sets are made by spatial interpolation using a weighted linear function method to sea-level pressure data which were gathered every 3 hours at irregularly-distributed locations on a weather chart. Figure 1 illustrates a grid system divided into 28 by 41 with a grid distance of 80 km for the computation of pressure and wind distributions over the Japan Sea, whose coordinate system is rotated 45 degrees counterclockwise from the north direction. The figure includes 46 pressure measurement locations with the WMO location number and the WMO local area code number enclosed with a circle. The input pressure data sets over 13 years from 1982 to 1994 consist of the data at the measurement locations and those at central positions of lows and highs.

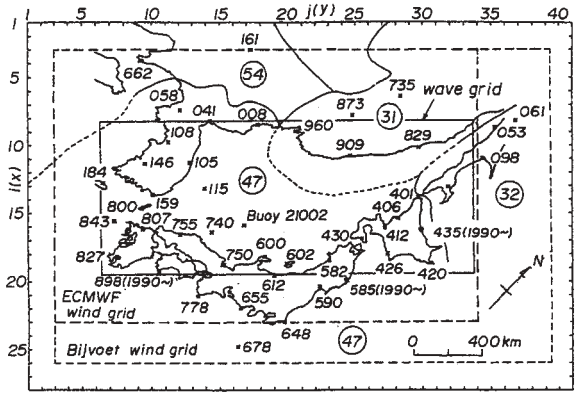

Figure 1 Grid for computing wind distribution over the Japan Sea by the Bijvoet model and input points of sea-level pressure.

Also, Figure 2 shows a grid system of 45 by 51 divisions with an 80 km grid distance over the Northwestern Pacific Ocean, which includes 43 pressure measurement locations with the WMO location number and 11 properly-selected locations with names of A to I. The pressure data are reinforced by those at the centers of lows and highs.

AUTHOR INDEX TABLE OF CONTENTS

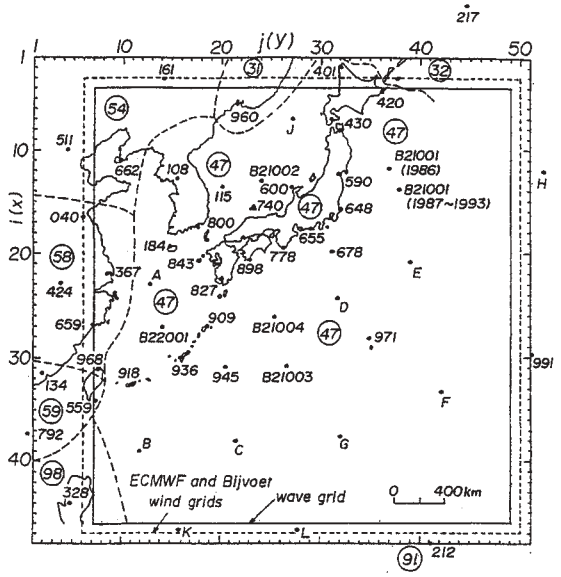

Figure 2 Grid for computing wind distribution over the Northwestern Pacific Ocean by the Bijvoet model and input points of sea-level pressure.

The period of the data sets is 9 years from 1986 to 1994.

In wind estimation by the Bijvoet(1957) model, a yearly-varying value from -3 to 0° C is given for air-water temperature difference, so that hindcast waves are in close agreement with measured waves at the coastal stations to the highest possible degree. Also, in cases where typhoons with central pressure less than 980 hPa exist in the Pacific Ocean region, the wind distribution estimated by a parametric typhoon model is embedded into the original wind field as a remedy for unrealistic estimates of wind field associated with strong typhoons. The wind data obtained by use of the Bijvoet model is referred to the Bijvoet wind data.

2.2 *ECMWF Wind Data Sets*

Wind data at 10 m height every 6 hours over a 13 year period of 1982 to 1994 is gathered from the uninitialized analysis surface wind data sets offered by ECMWF. This is hereafter called the ECMWF wind data. The original ECMWF data in this case are provided on a spherical grid with a space resolution of 1.125 degrees for a period of Jan. 1982 to Sept. 1991 and with a space resolution of 0.5625 degrees for a period of Oct. 1991 to Dec. 1994. For use in wave hindcasting, the ECMWF wind data is interpolated onto the Cartesian grid using a numerical table which gives the relation between location of grid point with the spherical coordinate and location of grid point with the Cartesian orthogonal grid. The range of the grid system with a 40 km grid distance on the Japan Sea area and that with an 80 km grid distance on the Pacific Ocean area are indicated in Figure 1 and Figure 2 respectively. As was mentioned above, the grid system on the Japan Sea area is rotated 45 degrees counterclockwise from the north direction. The ECMWF wind speed data used in wave hindcast on the Japan Sea coasts is tuned by multiplying a spatially-varying coefficient from 1.05 to 1.35 in a narrow strait area situated between southwestern Japan and the Korean Peninsula or from 1.20 to 2.0 in a small coastal sea area of central Japan strongly sheltered by a peninsula and island, because the data excessively receives the effect of land topography resulting in considerably underestimated wind speed.

3. Wave Model and Condition of Wave Hindcast

A shallow water wave model(Yamaguchi et al., 1987) called a single point model(SPM) is applied for long-year wave hindcast in order to save computer processing time. The model follows the change of directional spectrum along a refracted ray of each component wave focusing on a hindcast point. The source function consists of linear and exponential growth terms, energy dissipation terms during the following winds and the opposing winds and a linear bottom friction term. Energy dissipation due to wave breaking during the wave growth is evaluated by imposing the limitation of a saturated directional spectrum.

Each wave ray is traced on a nesting grid composed of the Japan Sea or the Northwestern Pacific Ocean with a medium grid size of 5 km and a small sea area surrounding the hindcast point with a fine grid size of 1 or 0.5 km. Wind components are bi-linearly interpolated onto a wave ray of each component every 1 hour using the Bijvoet wind data or the ECMWF wind data on a regular grid for wave hindcast. At the land boundary, the directional spectrum is set at zero.

AUTHOR INDEX TABLE OF CONTENTS

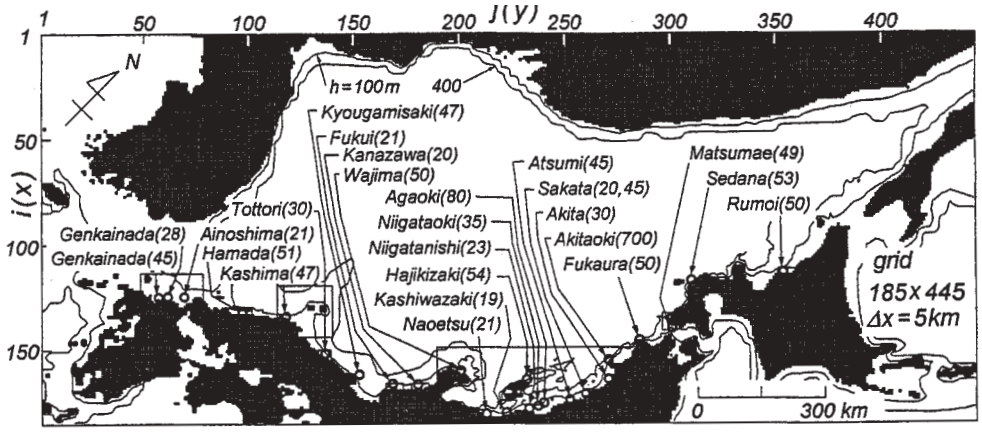

Figure 3 Computation area in the Japan Sea and location of wave hindcast points.

At the open boundary, the directional spectrum calculated by a parametric model using local wind speed and direction is prescribed. The model is a decoupled propagation model classified into the first generation. Accuracy of the model is comparable to the third generation model WAM at the level of significant waves for ocean waves and the usage of a nesting grid system with high topographical resolution easily enables a realistic estimation over WAM for coastal waves (Hatada et al., 2000).

Figure 3 illustrates the computation area in the Japan Sea divided by a 5 km grid distance, an extent of each embedded small sea area and the location of hindcast points with water depth in parentheses where measurement data over long years are acquired. The region is rotated 45 degrees counterclockwise from the north direction in order to approximate the bottom bathymetry to the best possible degree with use of a constant grid distance. As input wave conditions, 25 frequency components from 0.055 to 0.75 Hz and 37 direction components on the full circle are prescribed. One-hourly wave hindcast is separately conducted over 13 years from 1982 to 1994 at 25 measurement stations deployed along the Japan Sea coasts.

As well, Figure 4 provides the computation area in the Pacific Ocean and the like. The conditions of 23 frequency data from 0.04 to 0.50 Hz and 37 direction data on the full circle are used. One hourly waves over 9 years from 1986 to 1994 are separately hindcast at 29 measurement stations along the Pacific Ocean coasts.

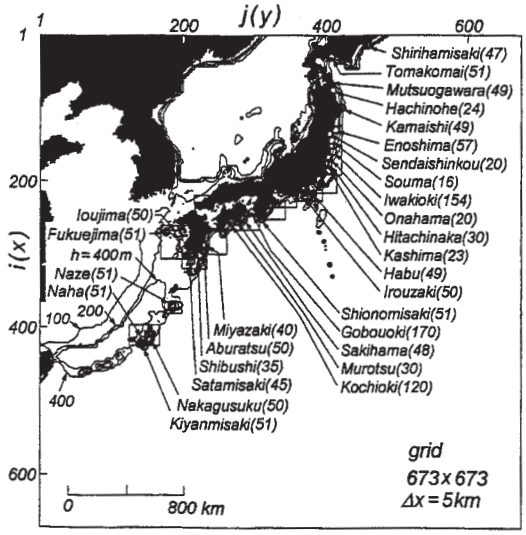

Figure 4 Computation area in the Northwestern Pacific Ocean and location of wave hindcast points.

4. COMPARISON OF WAVE CLIMATE STATISTICS

4.1 *Wave Climate at a Selected Point*

At Wajima situated on the central part of the Japan Sea coast, accuracy of the long term wave hindcast using 2 kinds of wind data is investigated in detail. Hereafter wave data hindcast under the Bijvoet wind conditions and the ECMWF wind conditions are referred to the Bijvoet wave data and the ECMWF wave data respectively. Figure 5 indicates a scatter diagram between hindcast H_{cal} and measurement H_{obs} for 2 hourly wave height

AUTHOR INDEX TABLE OF CONTENTS

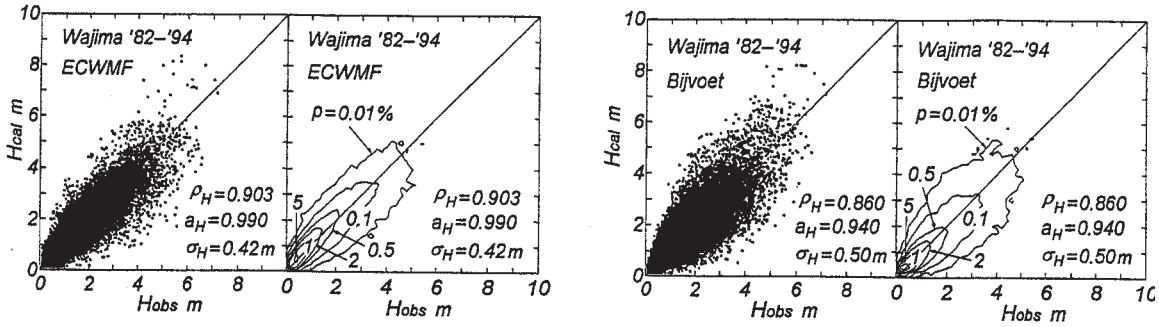

Figure 5 Scatter diagram between hindcast and measurement for wave height, and contour plot for relative occurrence frequency of wave height at Wajima on the Japan Sea coast.

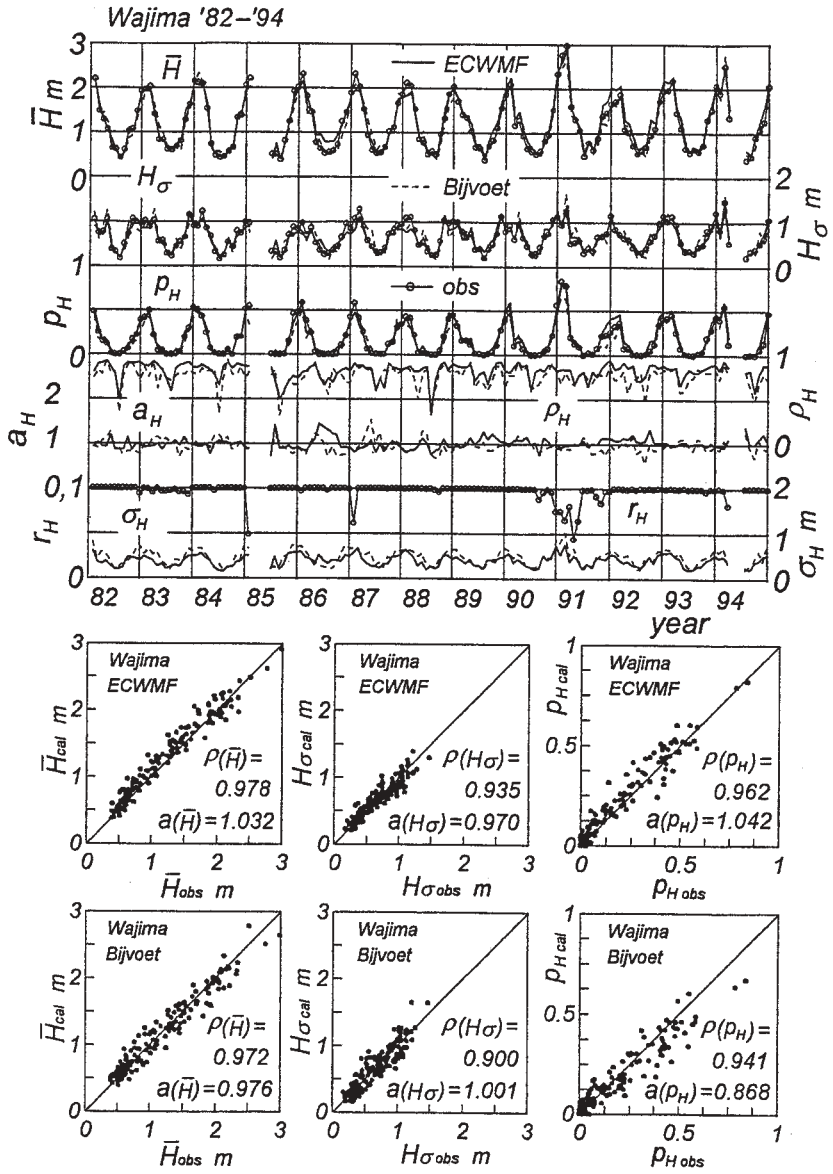

Figure 6 Yearly variation of monthly-grouped wave climate parameters for wave height and error statistics, and correlation plot between wave climate parameters at Wajima on the Japan Sea coast.

data over 13 years from 1982 to 1998 and a contour plot for relative occurrence frequency of wave height. Close gathering of individually plotted data around the 45 degree-inclined perfect correlation line suggests a rather high accuracy of the hindcast data in both cases. In a more detailed aspect, the ECMWF wave data yields less-scattered plots around the perfect correlation line and a flatter ellipse-shaped contour than the Bijvoet wave data, which means slightly higher accuracy of the ECMWF wave data over the Bijvoet wave data. For the ECMWF wave data and the Bijvoet wave data, the correlation coefficient between hindcast and measurement ρ_H is (0.903, 0.860), the slope value of a straight line passing through the origin best-fitted to the data in the scatter diagram a_H is (0.990, 0.940) and the root mean square error (RMSE) of wave height σ_H is (0.42 m, 0.50 m). These figures support higher accuracy of the ECMWF wave data over the Bijvoet wave data.

Figure 6 shows comparison for 13-year variation of wave climate parameters and error statistics estimated using monthly-grouped hindcast and measurement data, and a correlation plot between wave climate parameters based on hindcast and measurement data. The selected wave climate parameters are mean and standard deviation of wave height ($\overline{H}$, $H_{1/3}$), those of wave period ($\overline{T}$, $T_{1/3}$) and the occurrence rate of high waves greater than 2 m p_H, and then the error statistics for wave height or wave period are the above-mentioned correlation coefficient (ρ_H, ρ_T), the slope value of a straight line (a_H, a_T) and the RMSE (σ_H, σ_T). The figure includes measurement rate to total run n_H. Other indices of error statistics are the correlation coefficient between hindcast and measurement for monthly-grouped wave climate parameters and the slope value of a straight line passing the origin in the correlation diagram, as shown in the lower panels of the figure. The notations are exemplified as $\rho(\overline{H})$ and $a(\overline{H})$ for mean value of wave height. Two kinds of wave hindcast follow closely the measurement for cyclic yearly-change of wave climate parameters which reflects specific property of wind climate conditions in the Japan Sea. The correlation coefficient and slope value in the correlation diagram for each of the wave climate parameters indicate generally higher accuracy of the ECMWF wave data over the Bijvoet wave data. Also, a whole year average $\overline{\rho_H}$ and standard deviation $\sigma(\rho_H)$ of monthly-separated correlation coefficient ρ_H for the ECMWF wave data and the Bijvoet wave data are (0.790 ± 0.188, 0.735 ± 0.186), average $\overline{a_H}$ and standard deviation $\sigma(a_H)$ of slope value a_H are (1.021 ± 0.125, 0.962 ± 0.147), and average $\overline{\sigma_H}$ and standard deviation $\sigma(\sigma_H)$ of RMSE σ_H are (0.39 ± 0.15 m, 0.45 ± 0.19 m). These figures support the above-mentioned result again.

4.2 *Wave Climate along the Japan Sea Coasts*

Figure 7 illustrates the wave climate parameters and error statistics processed over the longest measurement period of 13 years at 25 measurement stations along the Japan Sea coasts. The following descriptions may be drawn from the figure.

1) Either of the hindcast data for wave height is in close agreement with the measurement in which wave climate becomes gradually severe from southern coasts toward northern coasts.

2) The ECMWF wave height data gives a correlation coefficient of about 0.85, a slope value of nearly 1.0 and a RMSE less than 0.5 m over the entire area, whereas the Bijvoet wave height data tends to yield a smaller correlation coefficient and a greater RMSE toward northern coasts.

3) Wave climate parameters for wave period hardly change along the Japan Sea coasts. Either of the hindcast wave data coincides closely with the measurement data for mean value of wave period, while it provides a consistently smaller estimate compared to the measurement data for standard deviation of wave period probably due to wide scatter of individual measurement data of wave period in the case of low wave height.

4) Both the ECMWF and Bijvoet wave period data have a slope value close to 1 at any station, which suggests gross agreement between hindcast and measurement for wave period. But a larger correlation coefficient and a smaller RMSE in the ECMWF wave period data at all stations located north of Tottori indicate that the ECMWF wave period data is a more proper estimate than the Bijvoet wave period data.

In order to have a closer look at the comparison between hindcast and measurement, alongshore variation of error statistics for monthly-separated wave climate parameters is shown in Figure 8. The error statistics used have been illustrated in

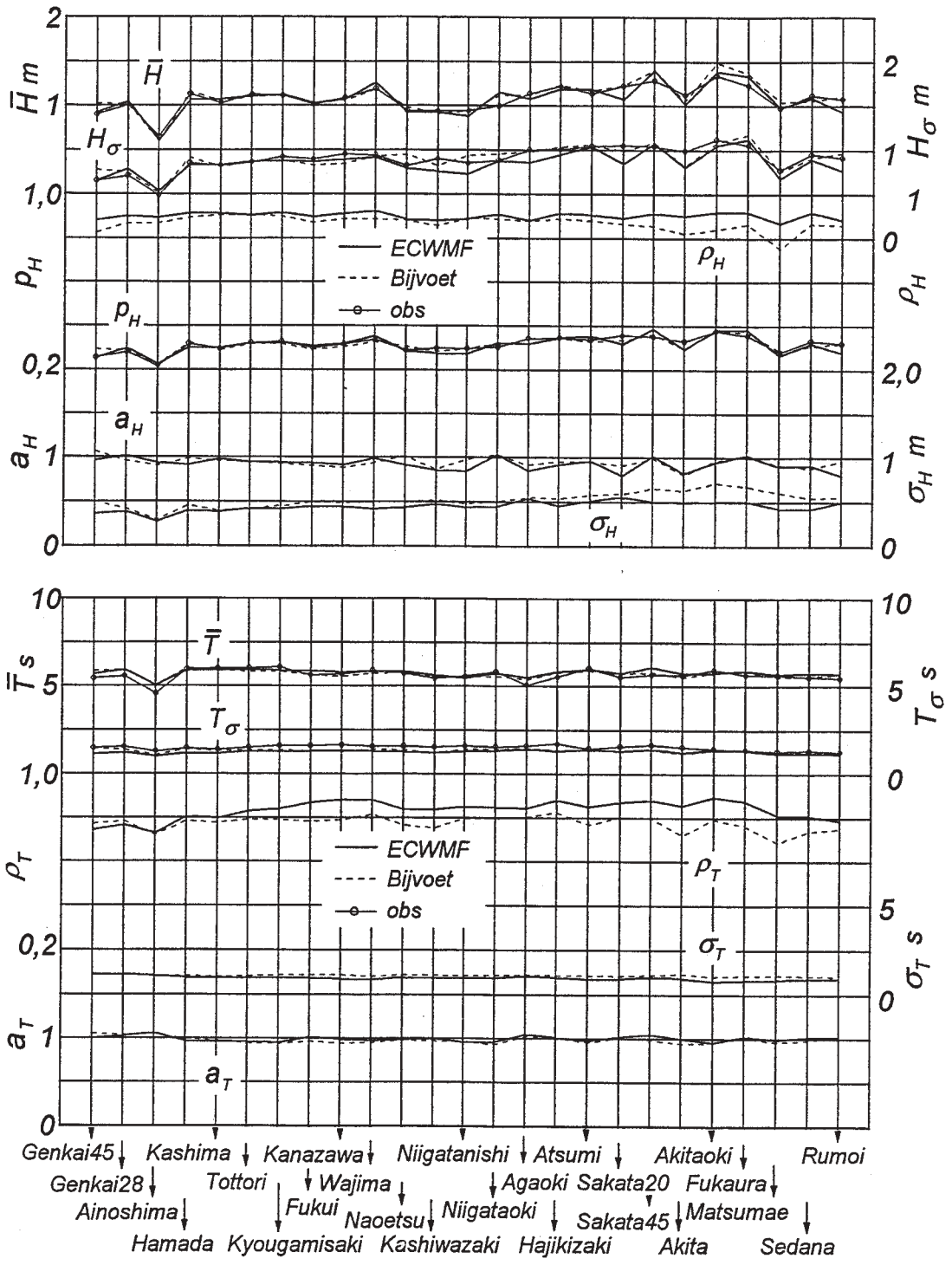

Figure 7 Variation of wave climate parameters and error statistics processed over whole year period along the Japan Sea coasts.

AUTHOR INDEX TABLE OF CONTENTS

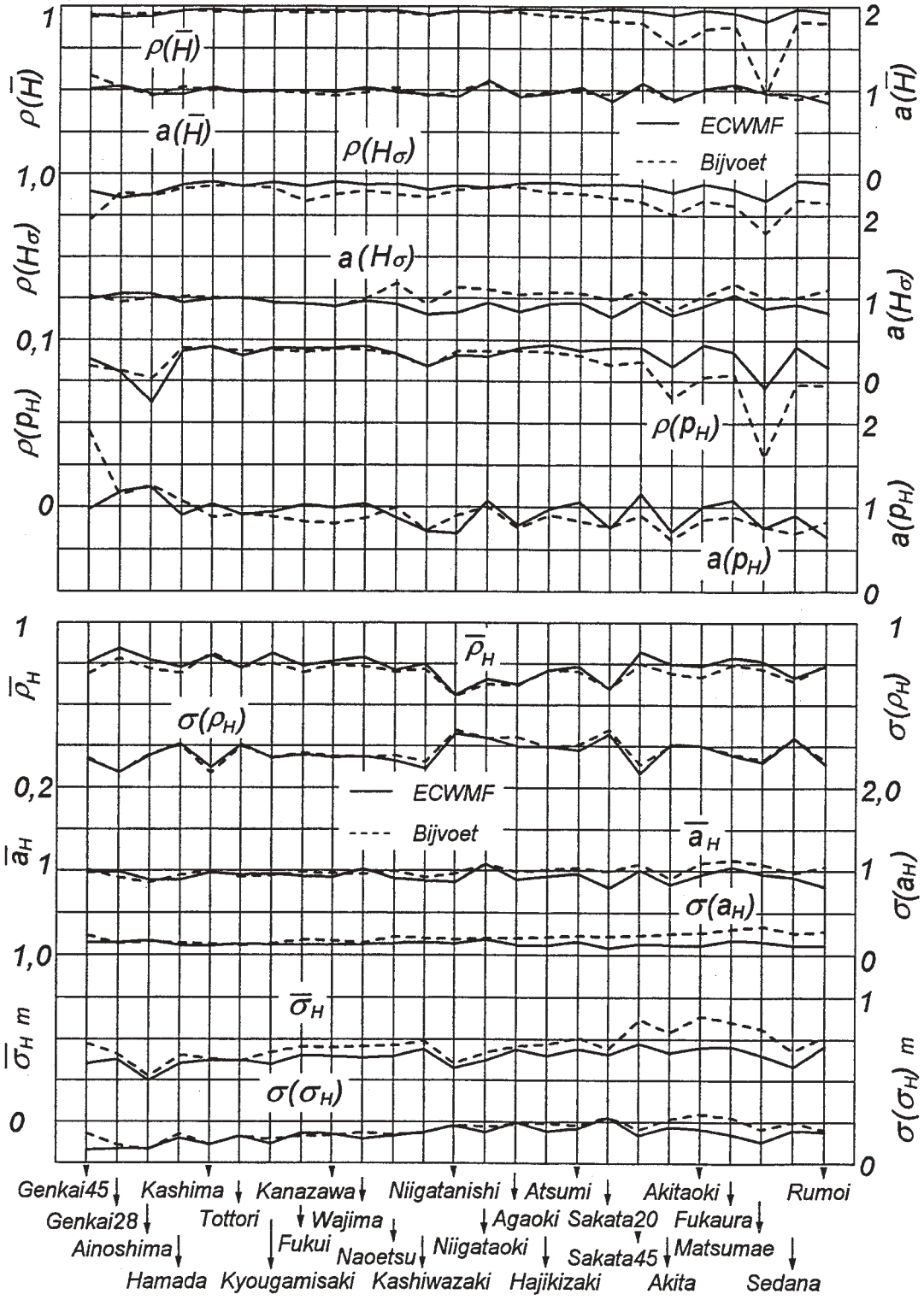

Figure 8 Variation of whole year period averages on monthly-grouped error statistics for wave height along the Japan Sea coasts.

AUTHOR INDEX TABLE OF CONTENTS

Figure 6 and the related description. The ECMWF wave data yields a larger correlation coefficient and a slope value closer to 1 for monthly-separated wave parameters ($\overline{H}$, H_{σ}, p_H) compared to the Bijvoet wave data at almost all stations. Another indication is that whole year averages and standard deviations for monthly-separated error statistics ($\overline{\rho_H}$, $\sigma(\rho_H)$, $\overline{a_H}$, $\sigma(a_H)$, $\overline{\sigma_H}$, $\sigma(\sigma_H)$) take more appropriate values in the ECMWF wave data than in the Bijvoet wave data, as is represented by a larger averaged correlation coefficient, a smaller averaged RMSE and the like. The above-mentioned results suggest that accuracy of the ECMWF wave data is rather high on the entire area of the Japan Sea coasts, while accuracy of the Bijvoet wave data becomes lower in northern coasts.

Figure 9 gives comparison for the occurrence rate of directionally-grouped high waves greater than 2 m over a whole year period. It should be noted that the measurement data of mean wave direction may include error within one direction range of 22.5 degrees, because the data happens to show discrepancy of one direction range at two locations situated within a short distance of several kilometers. The measurement data indicates directional distribution almost restricted to 3 direction ranges. Both the ECMWF wave direction data and the Bijvoet wave direction data tend to yield directional distribution analogous to the measurement data on the whole if a difference of one direction range would be allowable. However, it is not easy to judge whether either of the data provides a better estimate of mean wave direction because of the correspondence between hindcast and measurement which varies station by station.

4.3 *Wave Climate along the Pacific Ocean Coasts*

Similar hindcast over 9 years from 1986 to 1994 and comparison with measurement are conducted at 29 coastal stations along the Pacific Ocean coasts. Wave climate along the coasts varies location by location, depending on geographical conditions and dominant storm type. Alongshore variation of wave climate parameters and error statistics for wave height and wave period processed over a whole year period are presented in Figure 10. The ECMWF wave data provides reasonable agreement with the measurement data for wave climate parameters, but tends to give rise to slightly overestimated values for standard deviation of wave height and occurrence rate of high waves. On the other hand, the Bijvoet wave data yields larger discrepancy with the measurement data for individual wave climate parameter than the ECMWF wave data. Also, the ECMWF wave data take a larger correlation coefficient, a slope value closer to 1 and a smaller RMSE for either wave height or wave period, compared with the Bijvoet wave data. These results indicate that accuracy of the ECMWF wave data is consistently higher than that of the Bijvoet wave data on the Pacific Ocean coasts, but correlation between hindcast and measurement on the Pacific Ocean coasts is lower than that on the Japan Sea coasts. This may be due to more complicated and diverse meteorological conditions in the Pacific Ocean and wave hindcast which imposes a parameterized input condition on open boundary in an arbitrarily-limited domain.

Figure 11 demonstrates alongshore variation of error statistics for monthly-separated wave climate parameters to provide a more detailed comparison between hindcast and measurement as does Figure 8 on the Japan Sea coasts. The ECMWF wave data yields larger correlation coefficients $\rho(\overline{H})$, $\rho(H_{\sigma})$, $\rho(p_H)$ and slope values closer to 1 $a(\overline{H})$, $a(H_{\sigma})$, $a(p_H)$ in correlation diagrams between hindcast and measurement for wave climate parameters, compared with the Bijvoet wave data at almost all stations. A similar tendency can be found for a whole year average and standard deviation of the correlation coefficient, slope value and RMSE which indicate the error statistics for monthly-separated wave height data.

Figure 12 illustrates directionally-grouped occurrence rate of high waves. Occurrence of high waves on the Pacific Ocean coasts concentrates to a narrow range of 2 to 3 direction segments except for some stations with more than 5 direction segments. The ECMWF wave data as well as the Bijvoet wave data gives rise to directional distribution of high waves analogous to the measurement data at all stations within an acceptable range of one direction segment.

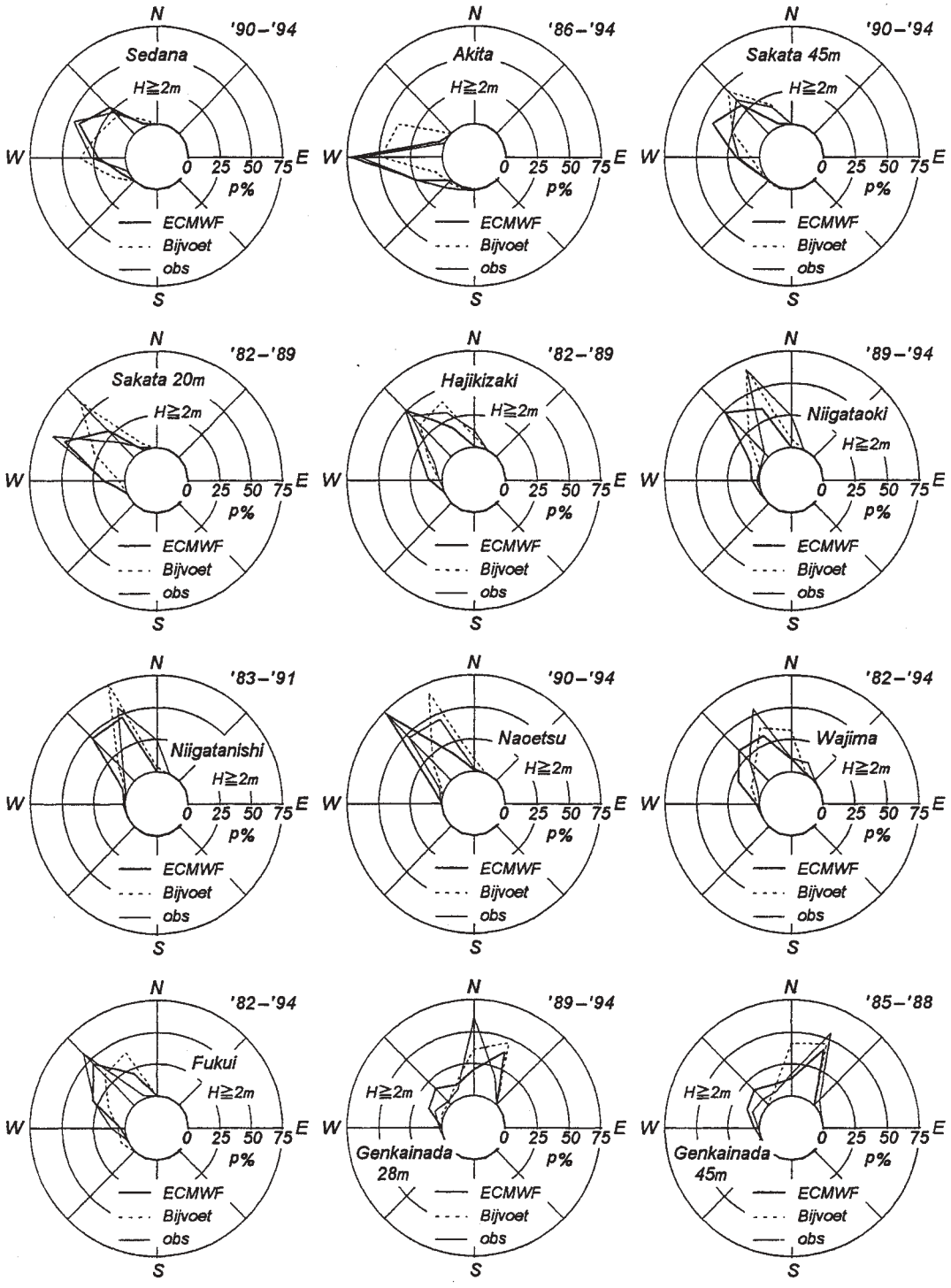

Figure 9 Directionally-grouped occurrence rates of high waves at measurement stations on the Japan Sea coasts.

AUTHOR INDEX

TABLE OF CONTENTS

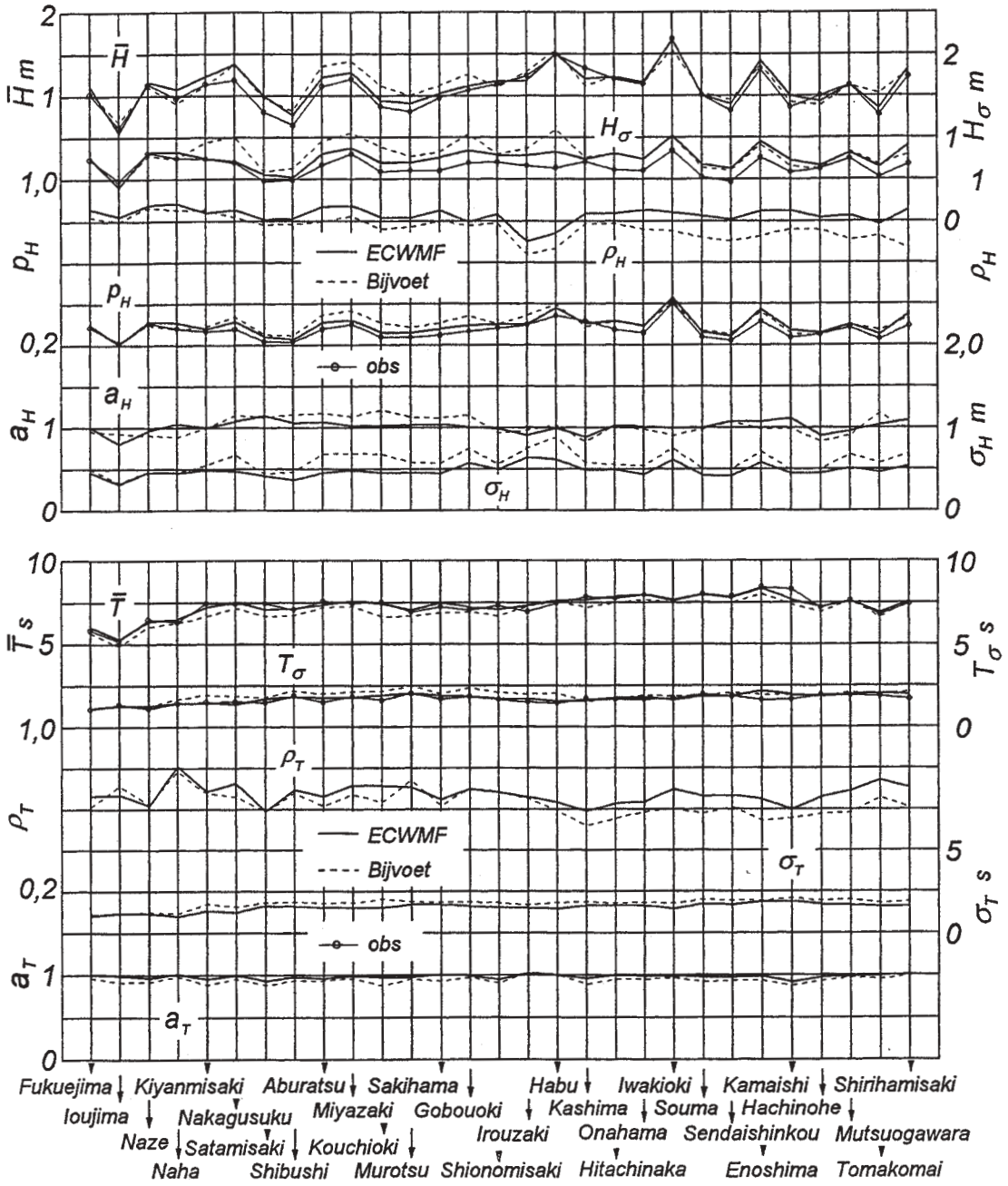

Figure 10 Variation of wave climate parameters and error statistics processed over whole year period along the Pacific Ocean coasts.

AUTHOR INDEX TABLE OF CONTENTS

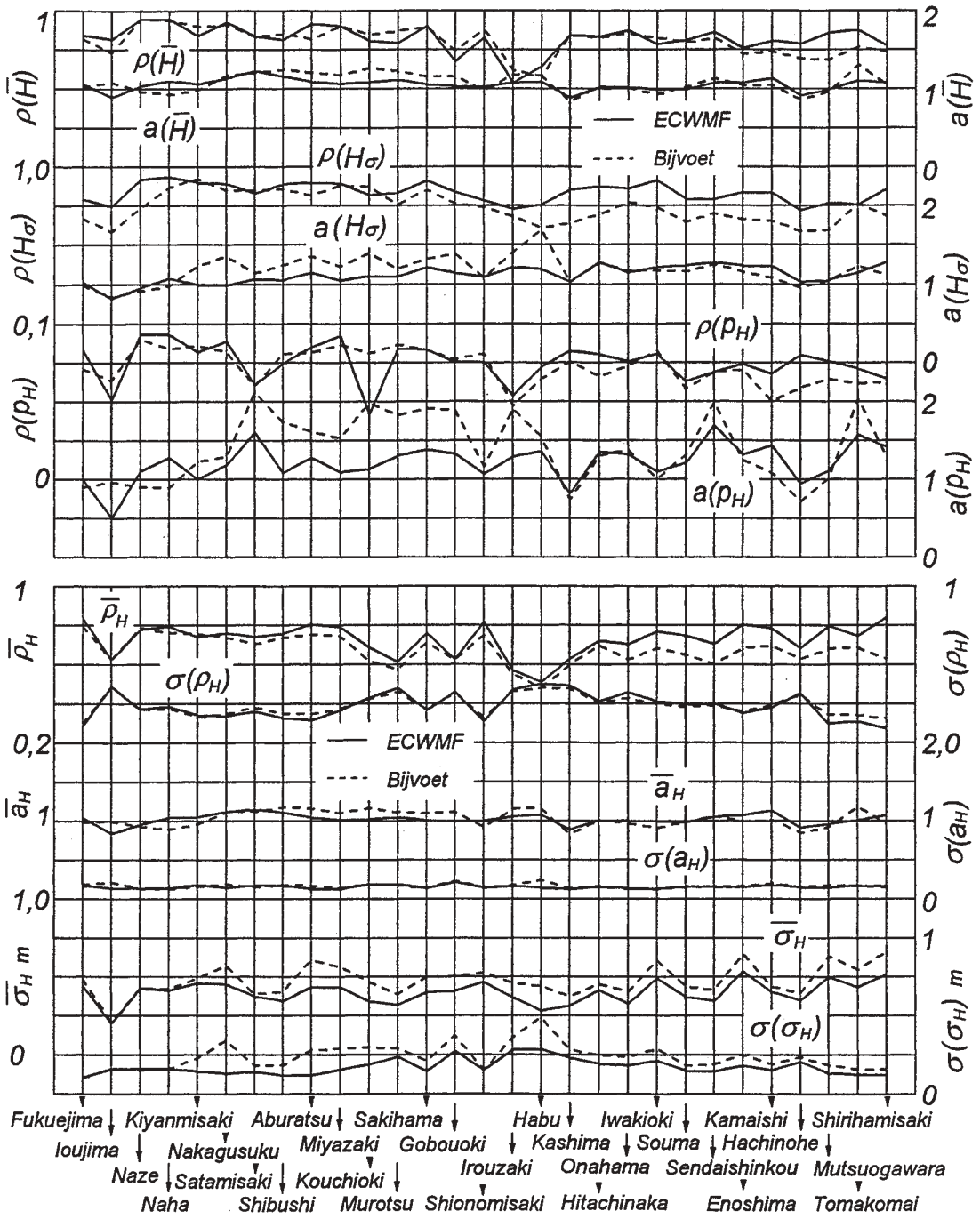

Figure 11 Variation of whole year period averages on monthly-grouped error statistics for wave height along the Pacific Ocean coasts.

AUTHOR INDEX TABLE OF CONTENTS

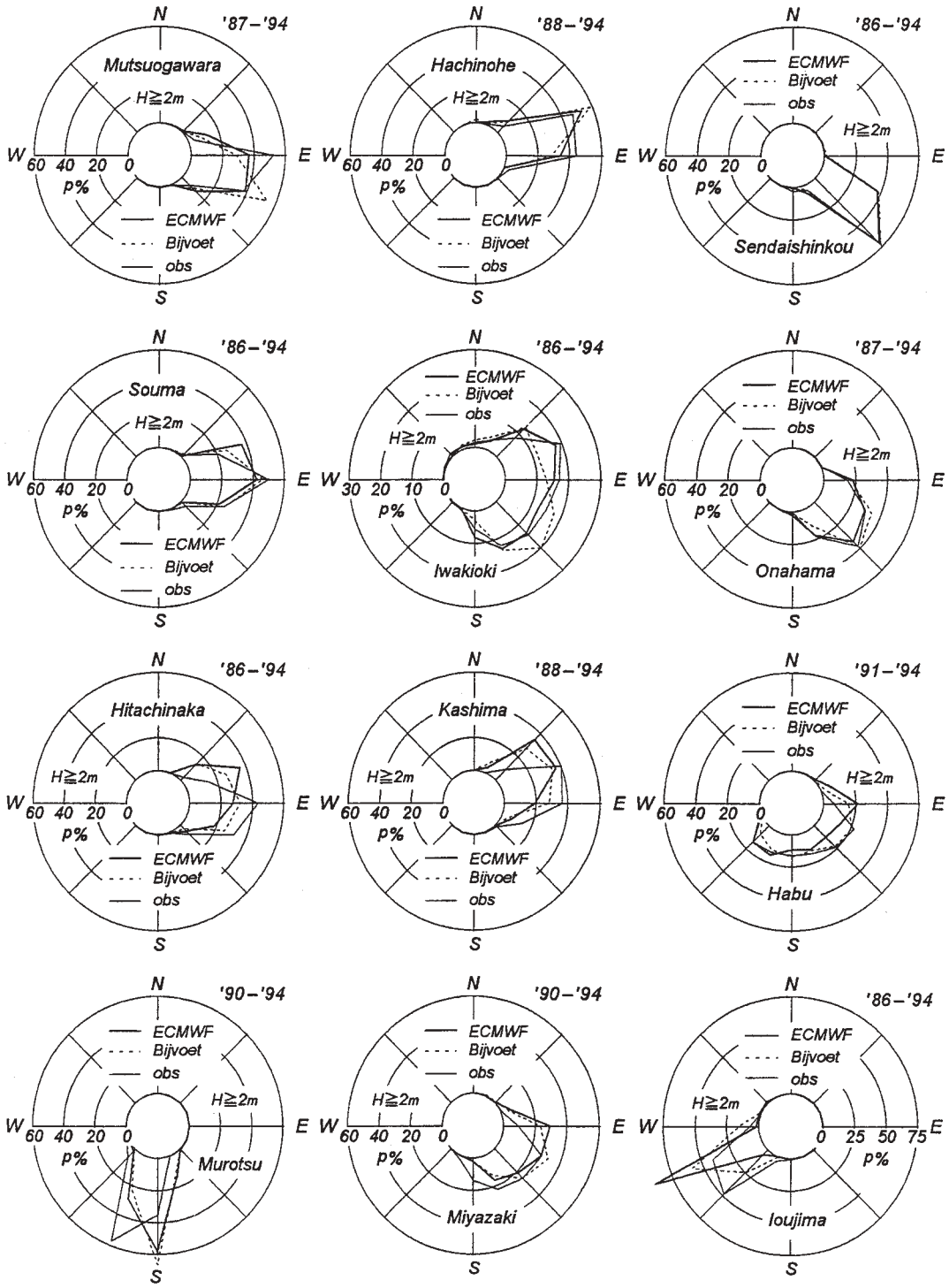

Figure 12 Directionally-grouped occurrence rate of high waves at measurement stations along the Pacific Ocean coasts.

AUTHOR INDEX TABLE OF CONTENTS

5. CONCLUSIONS

The main results drawn from this study are that the SPM system with use of either of the ECMWF wind data or the Bijvoet wind model data is fairly useful for the evaluation of long term waves at any coastal location of Japan directly facing the open sea and that the system with use of the ECMWF wind data yields more appropriate evaluation of waves, particularly on the Pacific Ocean coasts of Japan.

ACKNOWLEDGEMENTS

The authors give their thanks to the ECMWF which provided ECMWF analysis surface wind data sets. Thanks are also due to the Coastal Development Institute of Technology for use of NOWPHAS measurement data.

REFERENCES

Bijvoet, H. C., 1957: A new overlay for the determination of the surface wind over sea from surface weather charts. KNMI Mededelingen en Verhandelingen, 71, 1-35.

Hatada, Y. and M. Yamaguchi, 1992: Eight years wave hindcast and analysis of wave climate. Proc. 23rd ICCE, 1, 267-280.

Hatada, Y. and M. Yamaguchi, 1997: Eight years wave hindcast at the coastal area of the East China Sea and estimation of wave climate. Proc. WAVES97, 2, 911-924.

Hatada, Y. and M. Yamaguchi, 1998: A long term wave hindcast system using ECMWF winds. Proc. 26th ICCE, 1, 509-522.

Hatada, Y., M. Yamaguchi and H. Nonaka, 2000: One year comparison of wave hindcasts by backward ray tracing model and WAM. Proc. 6th Int. Workshop on Wave Hindcasting and Forecasting.

Yamaguchi, M., Y. Hatada and Y. Utsunomiya, 1987: A shallow water wave prediction model at a single location and its applicability. Proc. JSCE, 381/II-7, 151-160 (in Japanese).

Yamaguchi, M., Y. Hatada, M. Ohfuku and K. Nishioka, 1990: Estimation of wave climate along the coast of the Japan Sea based on wave hindcasting. Natural Disas. Sci., 9-3, 18-42 (in Japanese).

Yamaguchi, M., Y. Hatada and T. Hioki, 1992: Applicability of a long term shallow water wave hindcast system to the estimation of wave climate along the coast of the Japan Sea. Natural Disas. Sci., Jour. Japan Soc. Natural Disas. Sci., 11-3, 157-174 (in Japanese).

Yamaguchi, M., Y. Hatada and S. Ohsako, 1995: Applicability of long term shallow water wave hindcast system. Proc. Japanese Coastal Eng., 42, 331-335 (in Japanese).

IMPROVING WIND INPUT INFORMATION FOR GREAT LAKES WAVE HINDCAST STUDY

Lihwa Lin and Donald T. Resio

U. S. Army Engineer Research and Development Center
Waterways Experiment Station
Vicksburg, Mississippi, USA

1. INTRODUCTION

Accurate long-term wind information with homogeneous high quality and fine resolution is essential to wave hindcasting. For the Great Lakes, the surface wind information has been routinely derived from one or a combination of four sources: (1) nearby weather observation stations on land, (2) buoy wind measurements, (3) ship observation, and (4) computer modeling wind database. In general, the buoy wind measurements are more reliable and accurate than ship and land station observations. The buoy wind measurements became available at the Great Lakes after a network of buoys was established by the National Data Buoy Center (NDBC) in 1980. More wind data were collected later under a buoy program managed by the Atmospheric Environment Service (AES), Canada after 1989. The buoy data were usually not collected during the winter when buoys were retrieved for maintenance.

The wind database generated by computer models generally covers a longer, continuous time period. However, the quality of model wind information is relatively poor with low resolution in both time and space, as compared to other wind sources. For instance, a reanalysis project of wind information conducted by the National Centers for Environmental Prediction (NCEP) has produced a computer model wind database for the 50-year period from 1950 to 1999 (Kalnay *et al.* 1996). The quality of the NCEP winds is normally poor at the Great Lakes because the wind fields were generated at 6-hour intervals, which is too large for quick moving storms, and approximately 2-deg resolution, which is considerably too coarse for modeling lake winds.

Surface wind information is also available from weather observation stations around the lakes (Hubertz *et al.* 1991). Both the National Meteorological Center (NMC) and Canadian Climate Center (CCC) have collected long-term wind data from land weather stations since early 1930s. Because the anemometer technology has improved frequently over the time, the quality of these wind data is strongly affected by the type and model of the anemometers that measure the winds. Similarly, the quality of ship wind observations is also influenced from different anemometers that were used for the wind measurement. The ship observations are likely to miss the storms due to the hazardous weather condition for boating. The ship observation data were often not collected regularly in time and space.

It is apparent that the quality and characteristics of wind information can vary with different wind sources. To generate accurate long-term wind information, it seems logical to improve the wind data from individual sources and combine them as the final wind product for wave hindcasting.

2. RECREATION OF BUOY WINDS

Generation of accurate wind information as input to wave modeling can depend on four components:

(1) quality control of various types of wind observation data
(2) adjustment of observation data, including land to lake and air-water temperature corrections, to a fixed height over the water surface

(3) recreation of accurate and continuous wind information at a number of key locations
(4) interpolation of a network of irregularly spaced observation data into a continuous wind field database

Among these four components, the third component is probably the most important but normally neglected one. To include this third component in the generation of wind field information can improve significantly the quality of the final wind product from the interpolation routine.

This paper is aimed at recreating accurate and continuous winds at a number of selected key locations in the Great Lakes. The natural choice of key locations is from the existing buoy stations for three reasons. First, most buoys have been deployed at the critical locations to collect meteorological data for the Great Lakes. Second, the wind data collected by buoys generally have the best quality among various sources of wind information available at the Great Lakes. Third, many buoys have collected wind data for more than 15 years, which are sufficient for recreation of missing data during winter seasons. The same procedure is also valid for recreation of wind information at buoy locations before the NDBC and AES buoys were installed for wind data collection. Table 1 summarizes the location, depth, and operational time period of NDBC and AES buoys at the Great Lakes. Figure 1 shows the location map of the NDBC buoys, AES buoys, and NWS stations.

Figure 2 compares the windrose diagrams constructed from buoy and NWS data at Lake Superior for April-November, 1993. This windrose diagram comparison shows that wind distribution patterns are very different between the buoy and NWS stations. The wind data quality from buoys is better than the NWS since the wind data collected from buoys show more smoothed distribution than the NWS. Figures 3 and 4 show more windrose comparisons at Lake Huron, Lake Erie, and Lake Ontario for the same time period. It is noticed that buoy windrose patterns usually resemble the local geometry of the lakes. The resemblance between the windroses and shoreline geometry is caused by the sudden change of surface roughness across the land-to-lake boundaries. Since winds over the lake surface experience less friction, they tend to follow the long axis of a lake rather than short axis.

The method for recreating winds at a buoy station is based on the transformation of NCEP reanalyzed winds interpolated at the buoy location. Despite that the NCEP winds are usually underestimated and wind direction misestimated, they have better consistent and long-term quality than the ship and land observations. Figure 5 shows an example comparing the monthly root-mean-square (RMS) wind speeds from Buoys 45003 and 45008 at Lake Huron and the NCEP winds interpolated at the two buoy locations for 1980-1999. Figure 6 compares the monthly RMS wind speeds from Buoys 45002 and 45007 at Lake Michigan and the NCEP winds at the two buoy locations for 1980-1999. The reason the RMS wind speed is calculated instead of the arithmetic mean is because the RMS wind speed is computed based on the average of kinematics energy, which is equal to the square of wind speed. The RMS quantity is considered a better statistic than the mean value to present the monthly variation of wind speed. Figures 5 and 6 clearly show that the NCEP winds are underestimated as compared to the buoy data. Despite NCEP winds are underestimated, the overall variation of NCEP winds is very consistent in time, which is a good property for the long-term hindcast.

3. METHODOLOGY

Recreation of buoy winds is based on the transformation of wind magnitude and direction of NCEP winds through the development of windrose transformation diagrams. The windrose transformation diagrams contain information of correction factors and constants for wind magnitude and direction in 36 equally spaced direction bands, each at 10-deg intervals. The windrose transformation diagrams consists of a wind speed correction diagram and a wind direction correction diagram. These windrose transformation

diagrams, which need to be prepared for each buoy station, are developed by a linear regression of buoy and NCEP winds in each of the 36 direction bands. Since correction factors and constants are likely to change more significantly from month to month, it is determined to generate windrose transformation diagrams on the monthly basis. The windrose transformation diagrams developed for a month is based on the linear regression method using all of the available buoy data measured in that month and the corresponding NCEP winds.

Figure 7 displays the example windrose transformation diagrams generated at Buoy 45003 for the month of October. The diagrams are developed using all the wind data collected by Buoy 45003 for October from 1980-1999 and the corresponding NECP winds interpolated at the buoy station. The wind speed correction diagram contains information of correction factors whereas the wind direction correction diagram contains the correction constants. The direction defined in the diagrams is according to the meteorological convention. That is, 0-deg is from the north, and 90-deg is from the east, etc. The direction is adjusted clockwise for positive correction constant and counterclockwise for negative correction constant.

Figure 8 illustrates the use of linear versus nonlinear regression methods to compute wind speed correction factor and a simple algorithm to calculate direction correction constant at the Buoy 45003 station in the 80 to 90-deg direction band for October. The wind speed correction factor is determined using all buoy and corresponding NCEP wind speeds appeared in the same direction band. The direction correction constant is computed from the mean difference of NCEP wind directions found in a direction band and corresponding buoy winds that are fallen in one standard deviation of errors between the buoy and NCEP wind directions to the averaged NCEP wind direction. It appears that the temporal change of field wind direction is less steady than wind speed. To use buoy data with wind directions fallen in one standard errors to NCEP wind directions shall improve the estimation of direction correction constant.

Using the windrose correction diagrams the surface wind information can be recreated at a buoy station by transforming the NCEP winds to the buoy location. Figure 9 compares the windroses generated from the buoy, NCEP, and recreated wind data at Buoy 45003 for October 1998. Figure 10 compares the time series of wind speed and direction of the buoy, NCEP and recreated at Buoy 45003 for October 1998. It is evident that surface winds can be recreated well by using the windrose transformation diagrams on the NCEP winds.

4. RESULTS

Long-term wind information can be recreated at buoy stations by the method using windrose transformation diagrams on the NCEP winds. Ideally, the method should be applied to fill the gap of missing buoy wind data before a buoy was installed or during the winter seasons when buoy was retrieved for maintenance. However, in the present paper the actual buoy data will not replace the recreated winds when they both exist for the same time to demonstrate the recreated winds. In the case that there are too few measured buoy data to compute the wind correction factor or constant at a direction band, which can happen for the winter months, the correction factor or constant is then interpolated from the neighbor bands or the same band from the neighbor months.

Figure 11 shows the monthly RMS wind speed comparison of the measured, recreated, and NCEP winds at Buoys 45003 and 45008 in Lake Huron for 1980-1999. Figure 12 shows the corresponding windrose diagrams for the same data. It should be noted that both the RMS wind speed statistics and windroses from the NCEP and created winds have included the winter data that were generally not measured by buoys.

There are about 14 buoy stations at the Great Lakes that have collected wind data for more than 5 years. These buoys are ideal for the development of windrose transformation diagrams. Each lake has at least two of these buoys. Therefore, the approach using windrose transformation diagrams in the generation of

good long-term winds at buoy stations is feasible at the Great Lakes. More examples are shown in Figures 13-20 to compare the recreated wind properties. Figures 13 and 14 show the monthly RMS wind speed and windrose comparisons at Buoys 45002 and 45007 in Lake Michigan for 1980-1999. Figures 15 and 16 show the similar comparisons at Buoys 45001 and 45006 in Lake Superior. Figures 17 and 18 compare the monthly RMS wind speed statistics and corresponding windrose diagrams at Buoys 45005 and 45132 in Lake Erie. Figures 19 and 20 compare the monthly RMS wind speeds and windroses at Buoys 45135 and 45139 in Lake Ontario. In these figures, the recreated winds were generated directly from NCEP winds, interpolated at buoy locations and 3-hour intervals, by using the windrose transformation diagrams. The buoy data were not assimilated in the recreated winds. Both NCEP and recreated winds include winter season whereas buoy data generally exclude the winter months.

5. SUMMARY

This study aims at recreating surface winds at the Great Lakes buoy stations when buoy data are missing. The recreation of wind data at the buoy stations is designed for generation of long-term wind information as the input to the wave hindcast. Recreation of wind data is based on the mapping of the NCEP winds to a buoy station through windrose transformation diagrams developed by the linear regression of buoy data and NCEP winds. It is demonstrated that surface winds recreated at buoy stations resemble well the actual buoy data with consistent seasonal change pattern from year to year in the Great Lakes. Windrose diagrams were generated and compared between the measured and recreated winds to show the improved wind information at buoy locations for the Great Lakes.

REFERENCES

Hubertz, M.J., D.B. Driver and R.D. Reinhard, 1991: Hindcast wave information for the Great Lakes - Lake Michigan. WIS Report 24, U.S. Army Engineer Waterways Experiment Station, Vicksburg, MS.

Kalnay, E., *et al.* 1996: The NCEP/NCAR 40-year Reanalysis Project. *Bulletin, American Meteorological Society*, 77(3), 437-471.

Table 1. Summary of buoy stations for wind data measurement

Region	Station*	Latitude, N	Longitude, W	Depth (m)	Data duration
Lake Superior	45001	48.0	87.7	249	4/80 - 11/99
	45004	47.6	86.5	213	4/80 - 11/99
	45006	47.3	89.8	186	6/81 - 11/99
	45136	48.535	86.952	183	9/89 - 10/99
Lake Michigan	45002	45.3	86.4	194	5/80 - 11/99
	45007	42.7	87.1	194	7/81 - 12/99
	45010	43.0	87.8	19	6/93 - 11/95
	45011	43.02	86.27	17	8/97 - 11/97
Lake Huron	45003	45.3	82.8	162	5/80 - 11/99
	45008	44.3	82.4	58	9/81 - 11/99
Georgian Bay	45137	45.545	81.015	55	10/89 - 7/99
	45143	44.92	80.63	37	8/97 - 7/99
Lake Erie	45005	41.7	82.4	14	6/80 - 11/99
	45132	42.467	81.217	21	9/89 - 11/99
	45142	42.73	79.29	27	7/94 - 11/99
Lake Ontario	45135	43.845	78.337	47	9/89 - 11/99
	45139	43.265	79.542	41	5/91 - 9/99
* 45000 series are NDBC buoys and 45100 series are AES buoys					

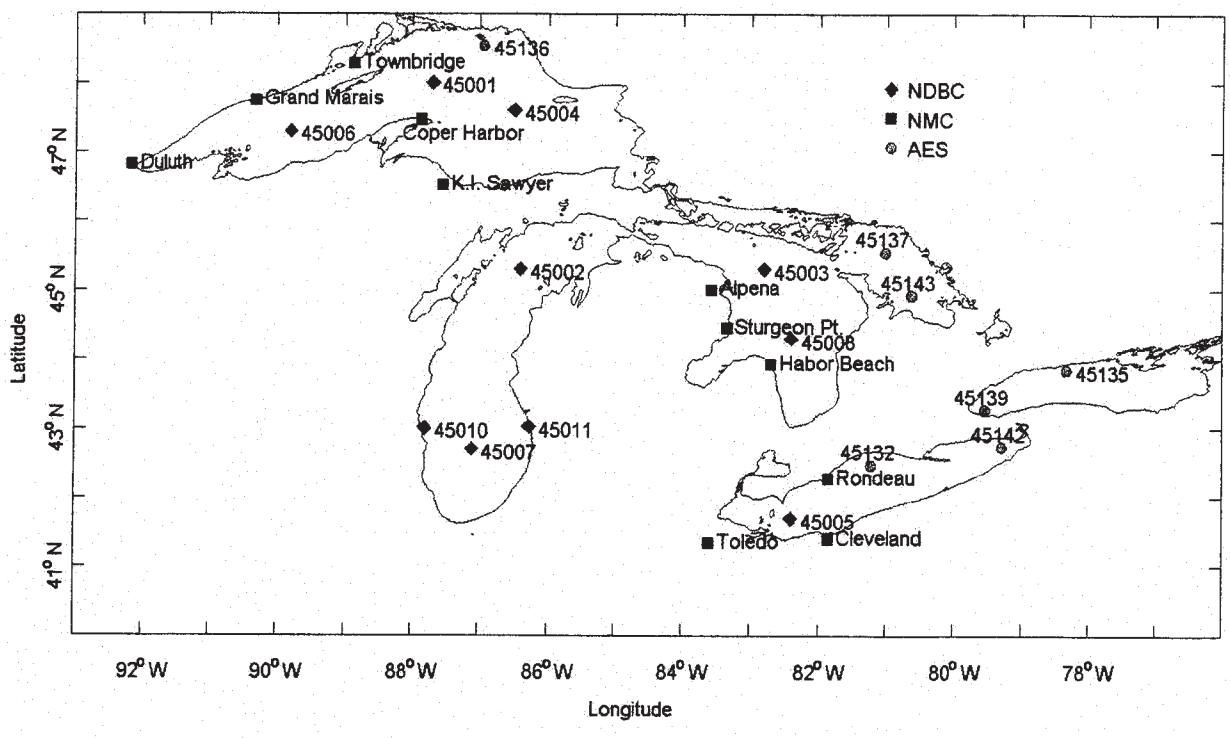

Figure 1. Location of NMC stations, NDBC and AES buoys

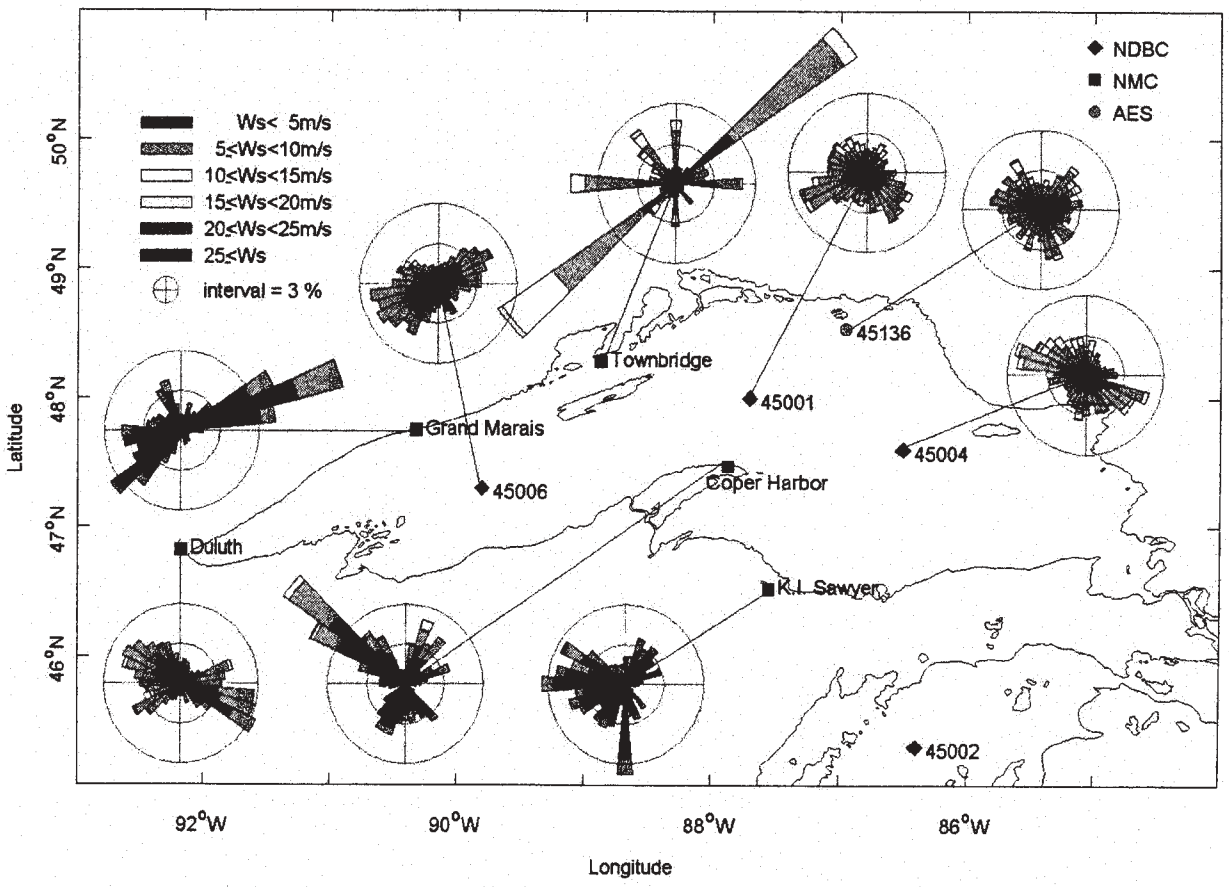

Figure 2. Comparison of NMC, NDBC and AES windrose diagrams at Lake Superior

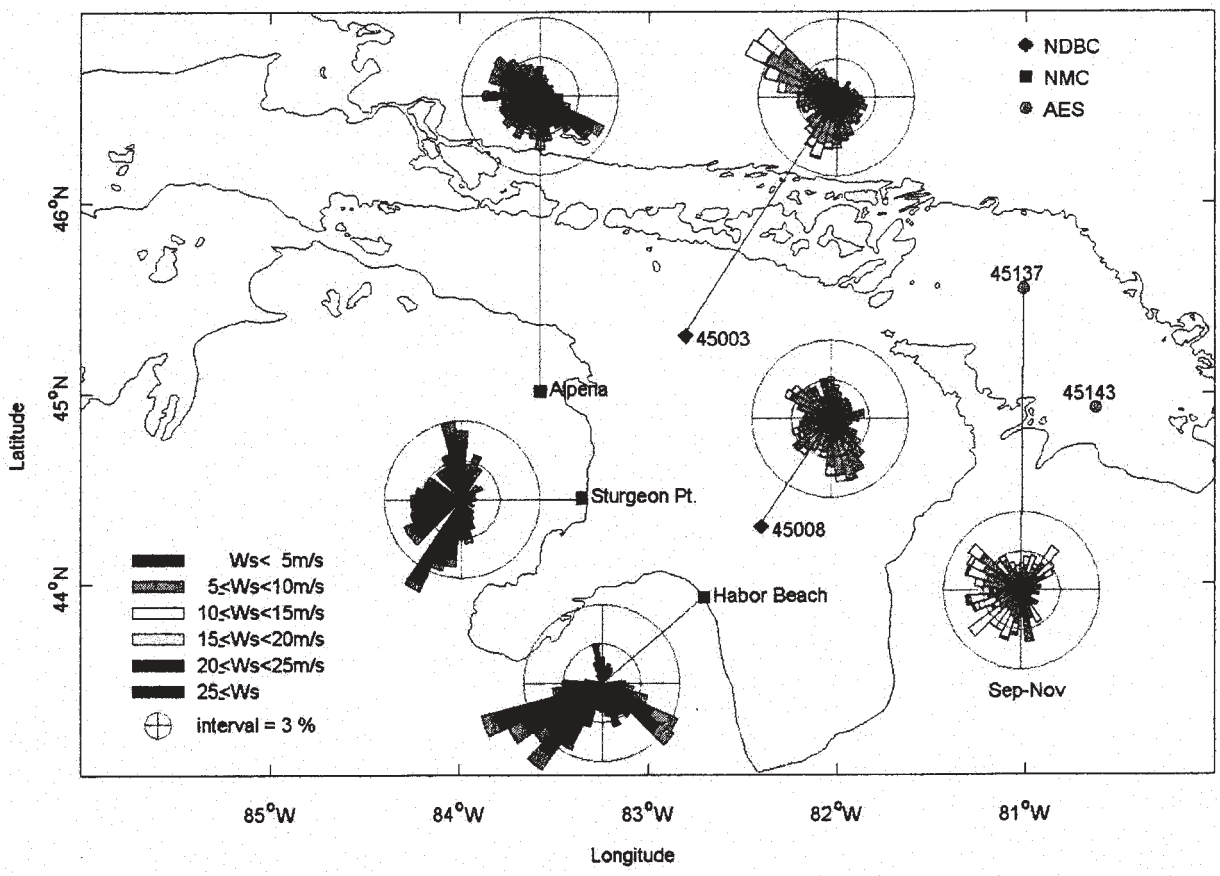

Figure 3. Comparison of NMC, NDBC and AES windrose diagrams at Lake Huron

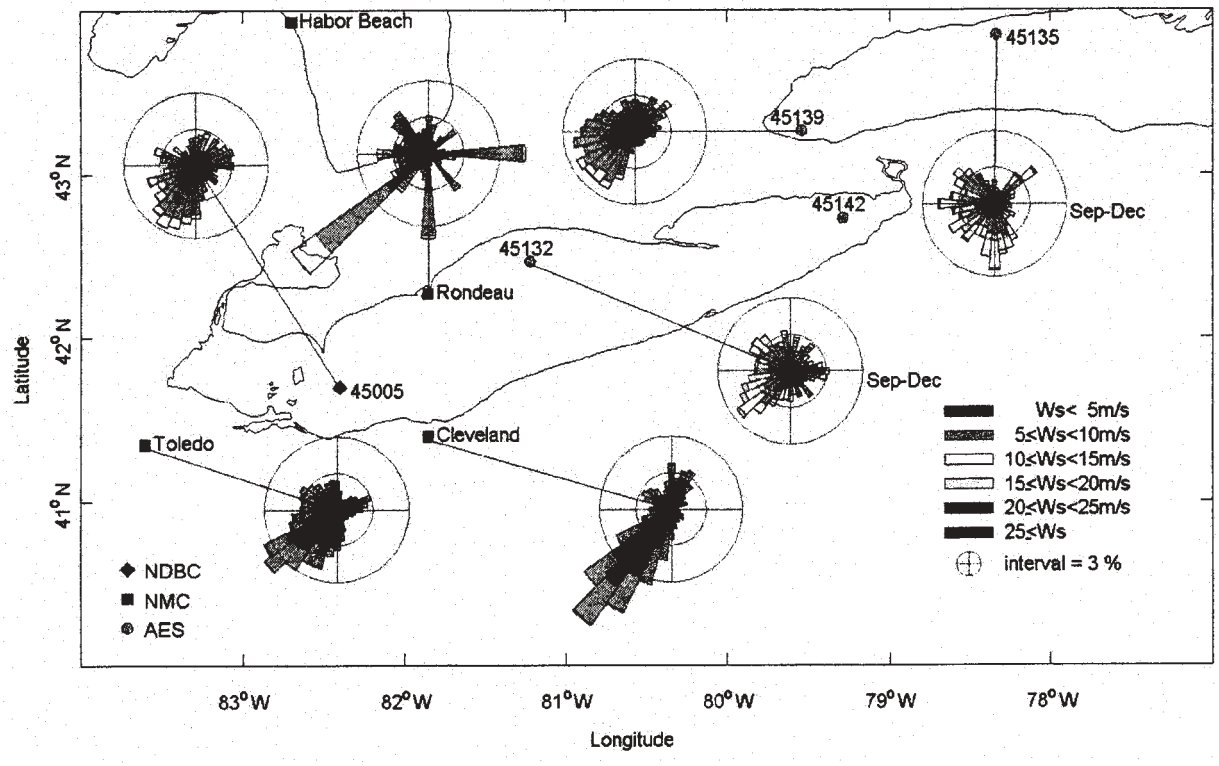

Figure 4. Comparison of NMC, NDBC, and AES windroses at Lake Erie and Lake Ontario

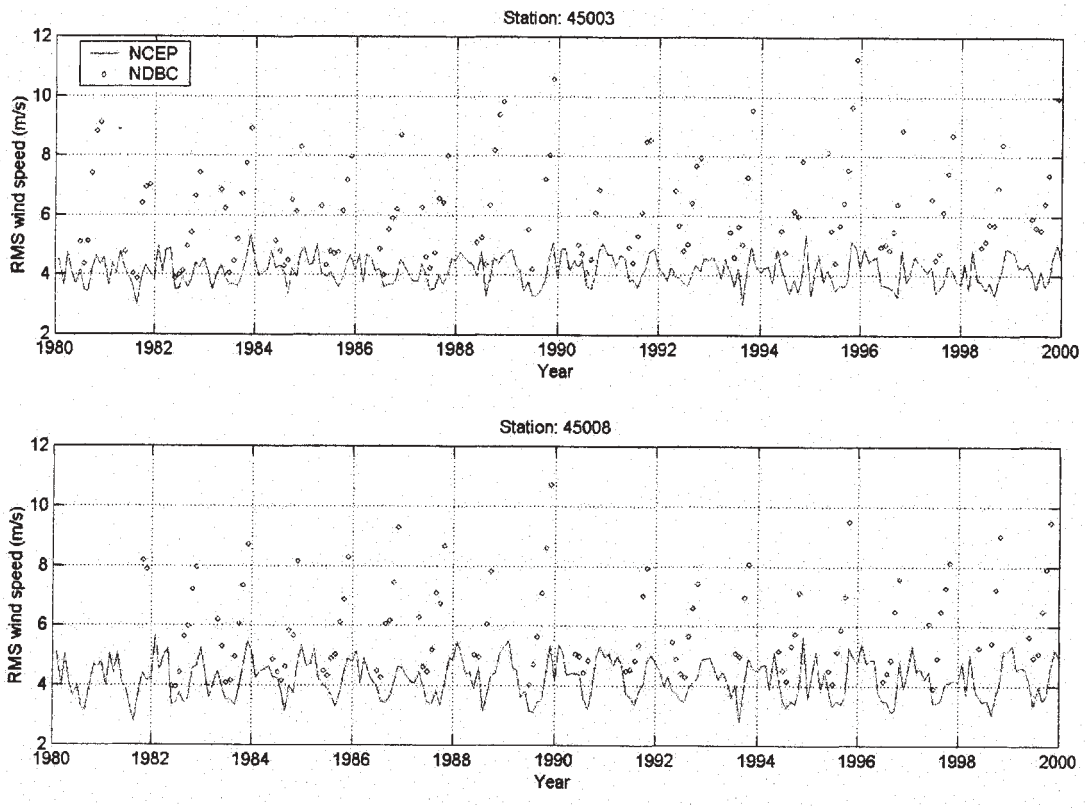

Figure 5. Monthly RMS wind speeds for NCEP and NDBC data at Buoys 45003 and 45008

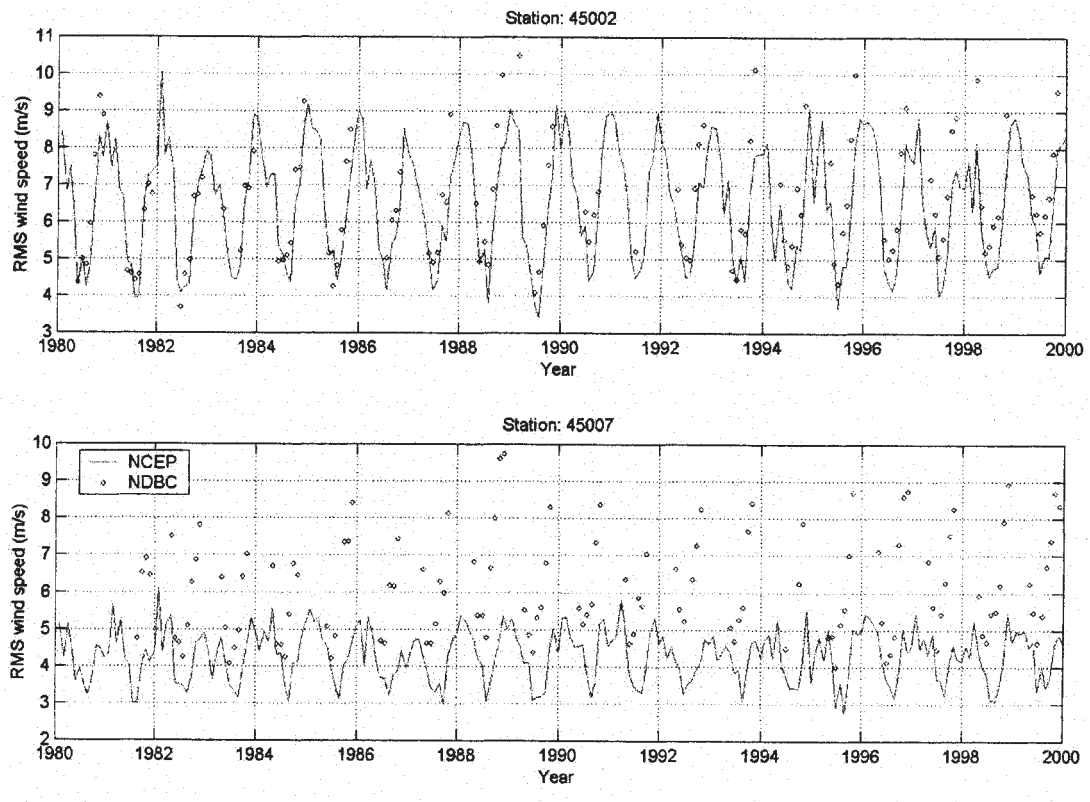

Figure 6. Monthly RMS wind speeds for NCEP and NDBC data at Buoys 45002 and 45007

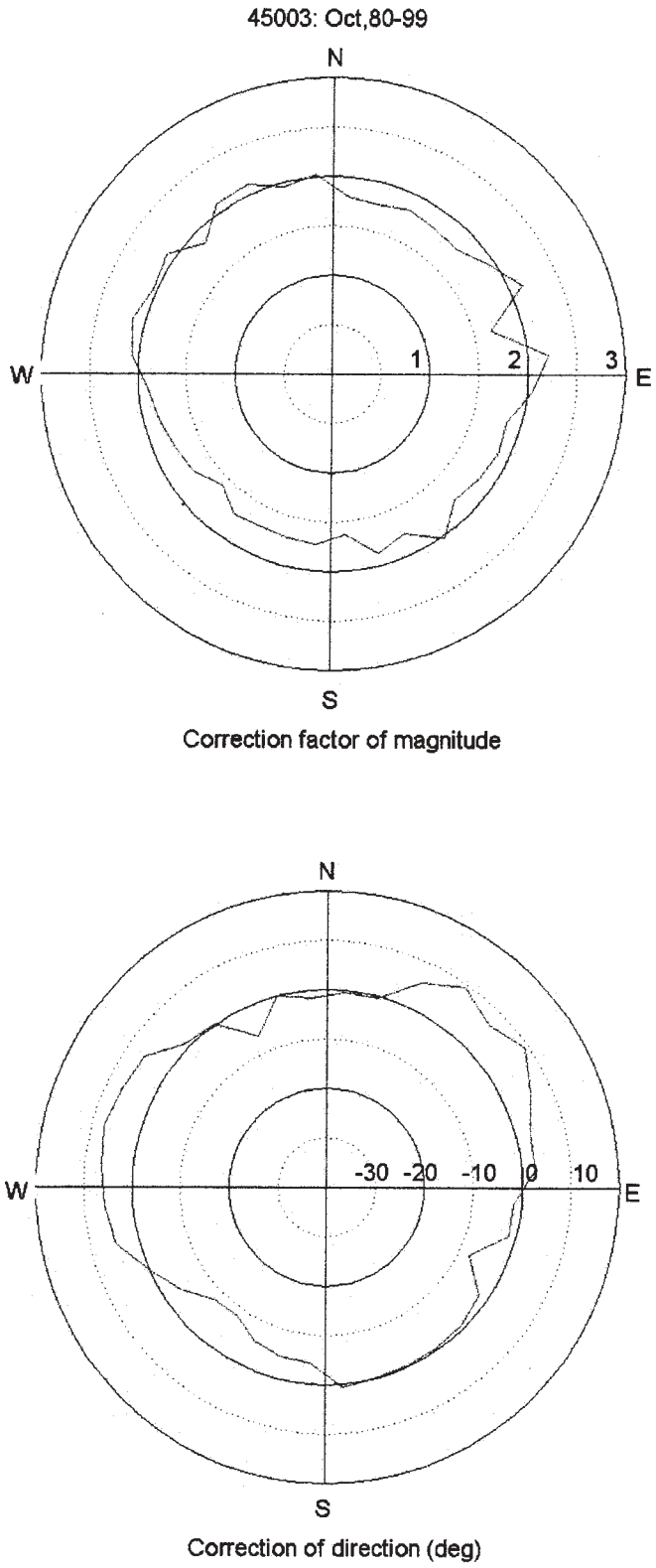

Figure 7. Windrose transformation diagrams at Buoy 45003 for October, based on 1980-1999 data

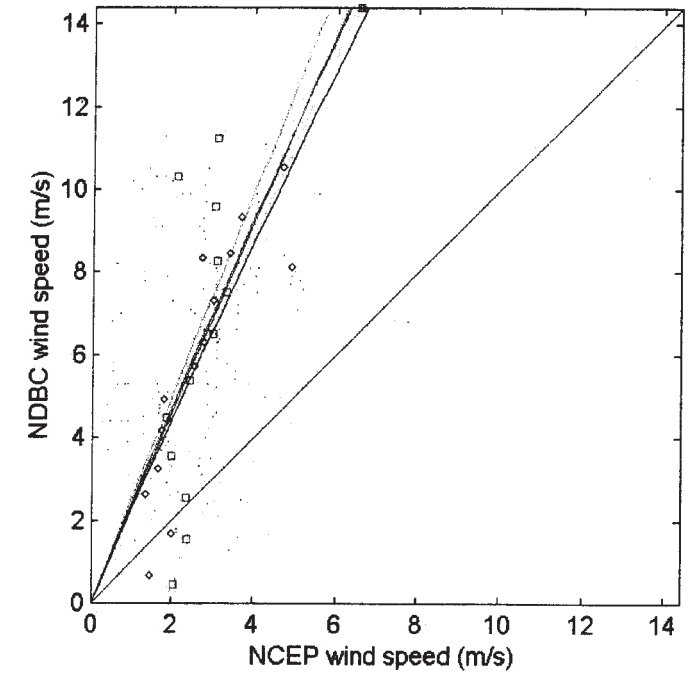

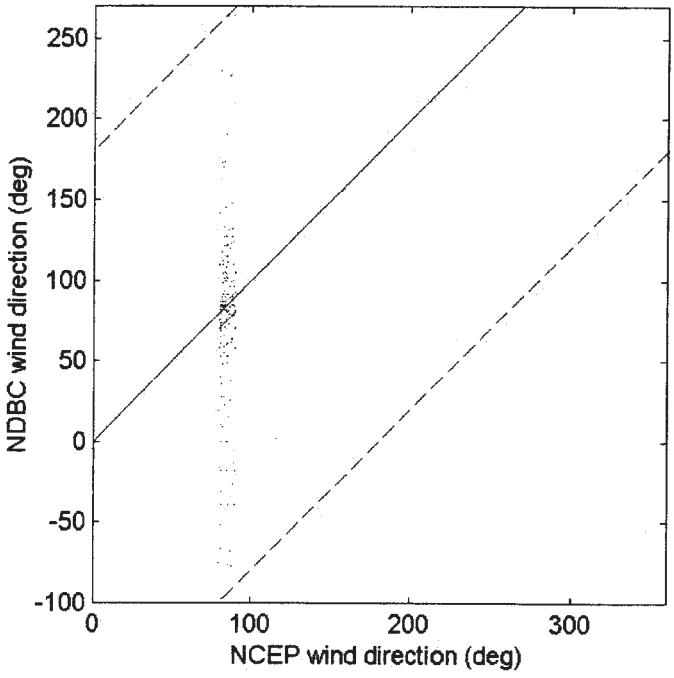

Figure 8. Regression of NDBC and NCEP wind data in 80-90 deg sector for October

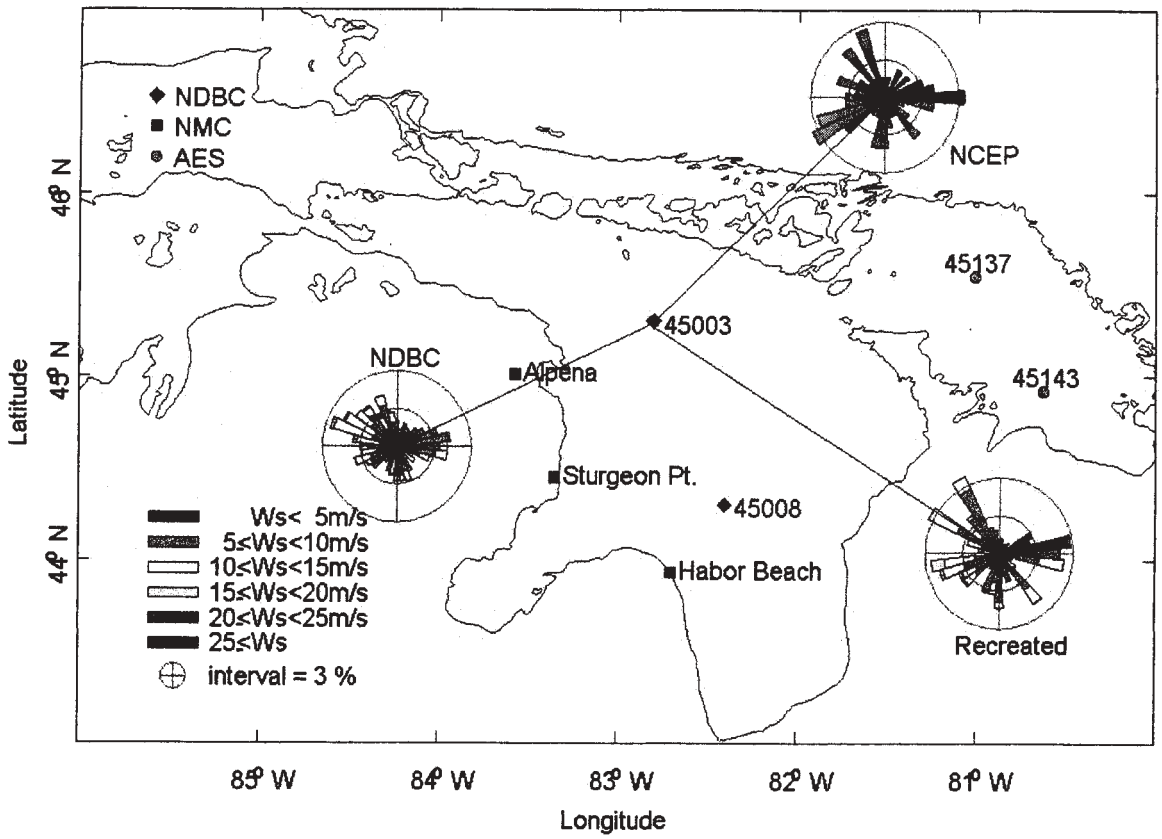

Figure 9. Comparison of NCEP, NDBC and recreated windroses at Buoy 45003 for October, 1998

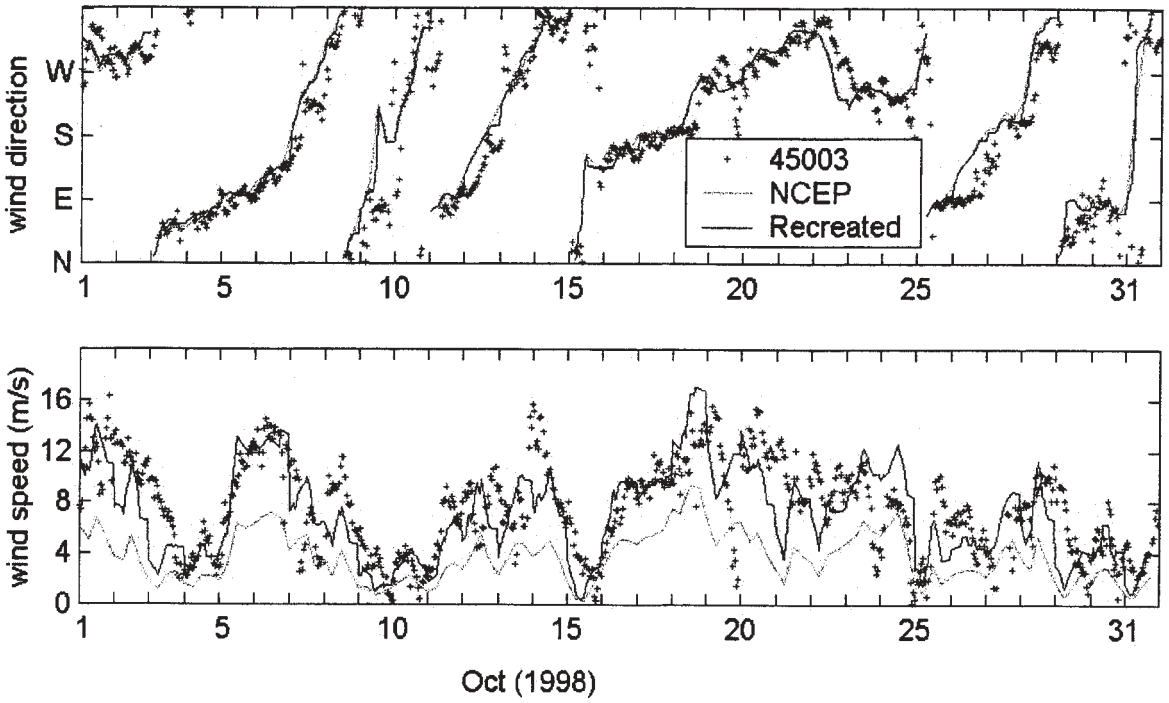

Figure 10. Comparison of NCEP, NDBC and recreated wind data at Buoy 45003 for October, 1998

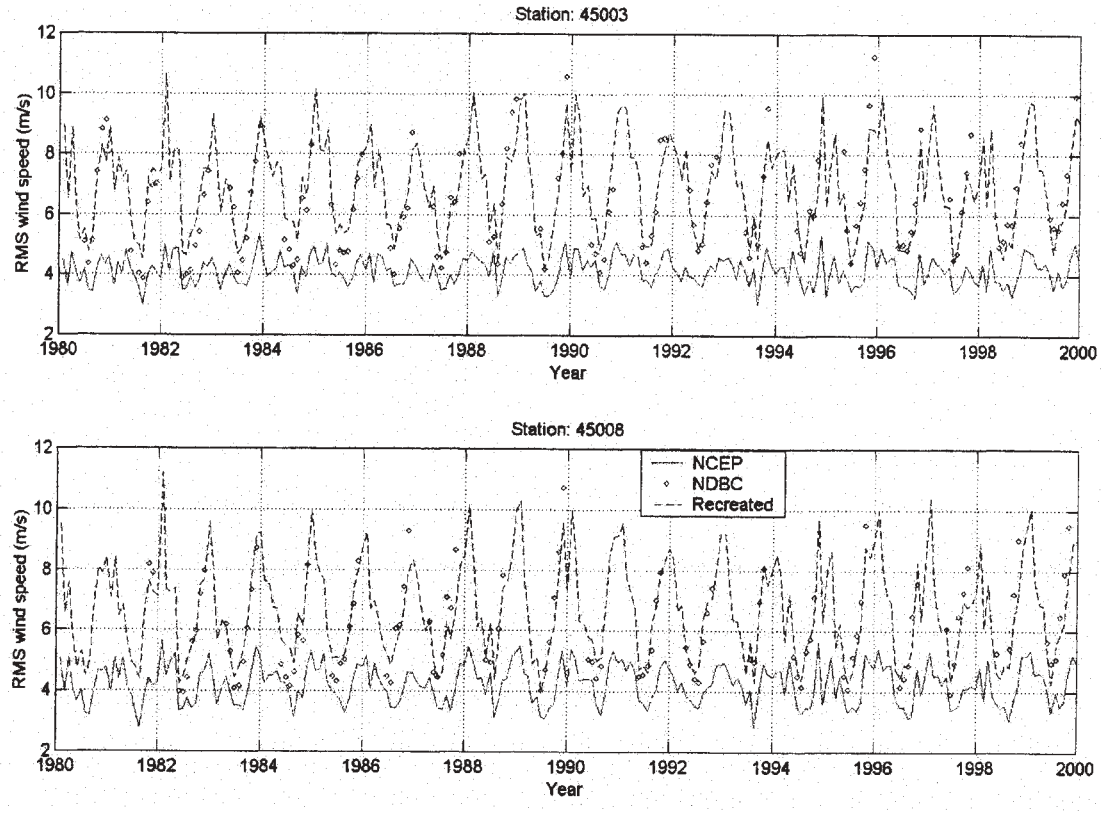

Figure 11. Comparison of NCEP, NDBC and recreated RMS wind speeds at Buoys 45003 and 45008

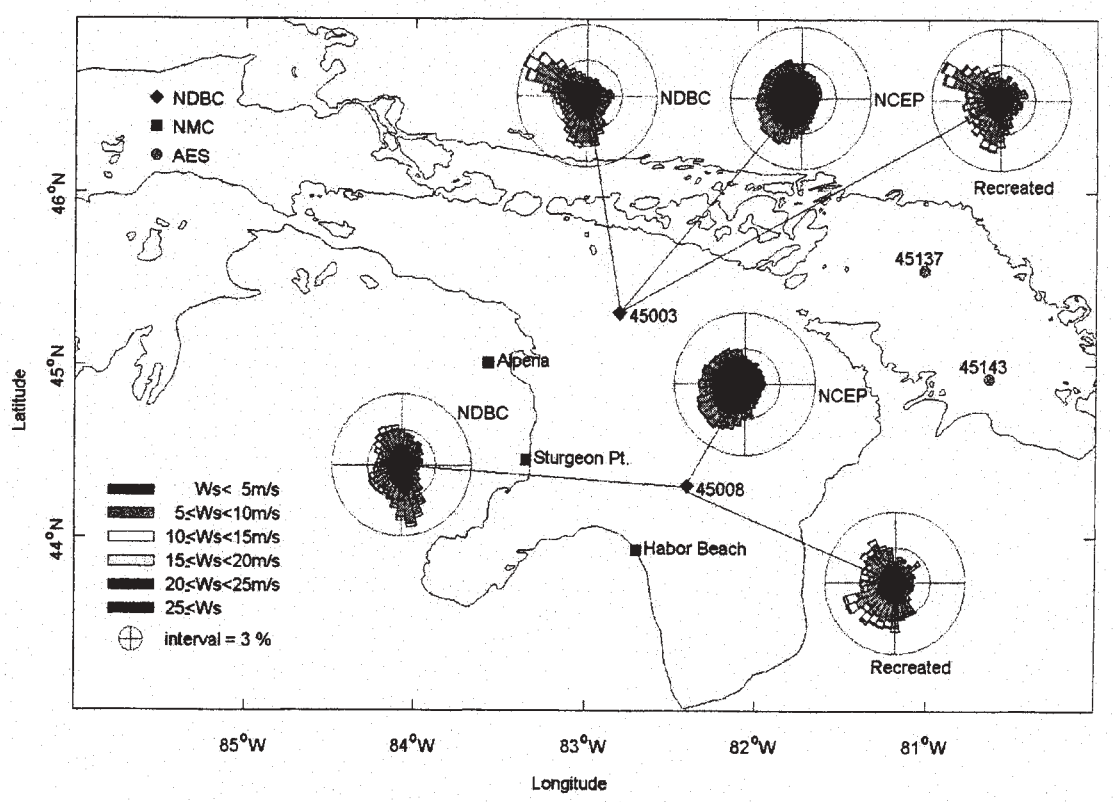

Figure 12. Comparison of NCEP, NDBC and recreated windroses at Buoys 45003 and 45008, 1980-1999

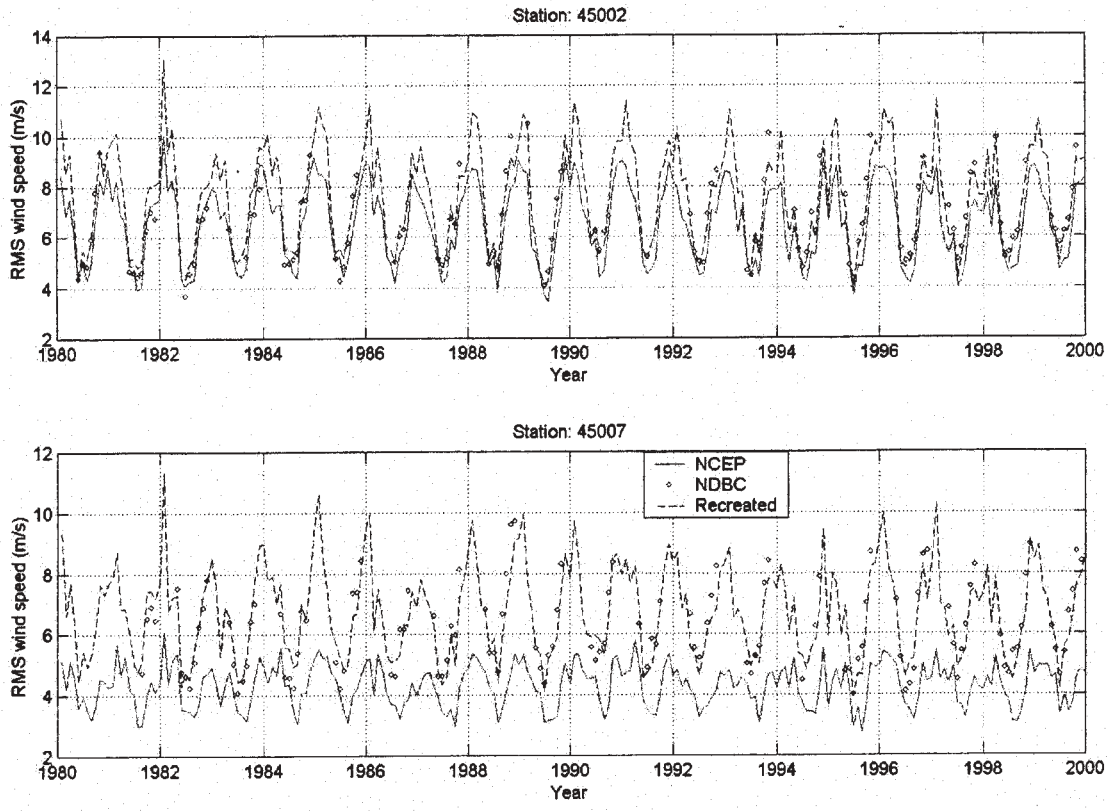

Figure 13. Comparison of NCEP, NDBC and recreated RMS wind speeds at Buoys 45002 and 45007

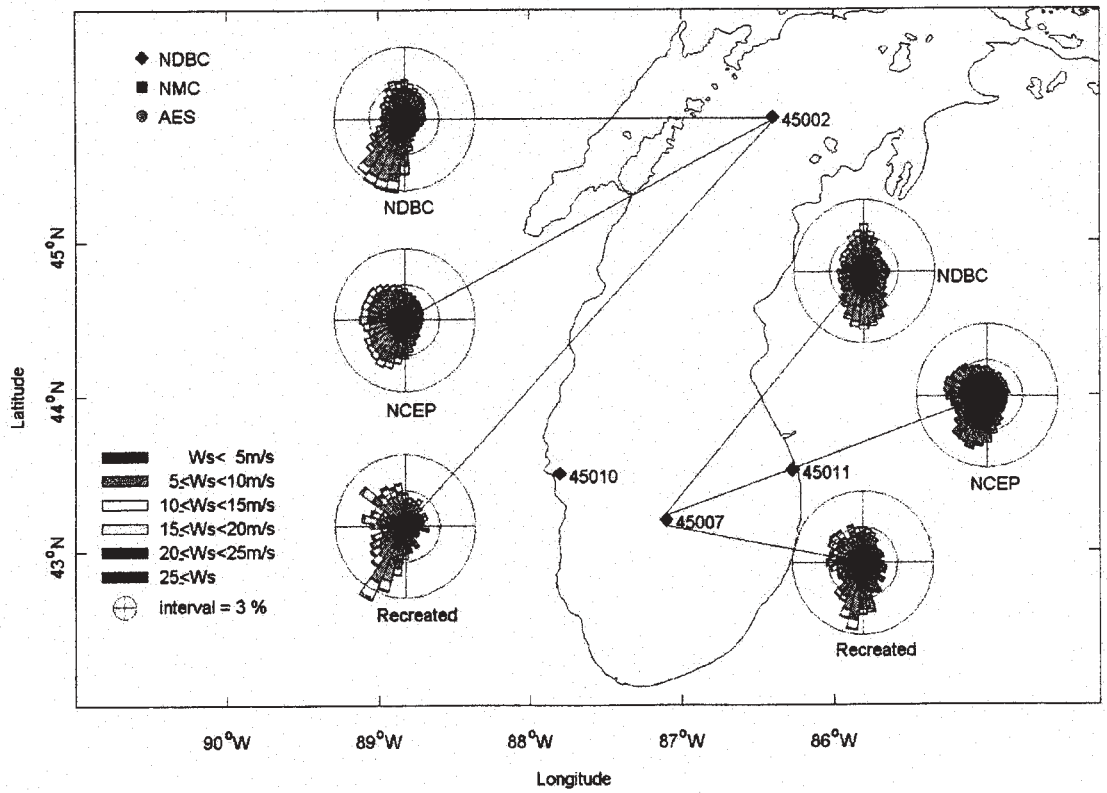

Figure 14. Comparison of NCEP, NDBC and recreated windroses at Buoys 45002 and 45007, 1980-1999

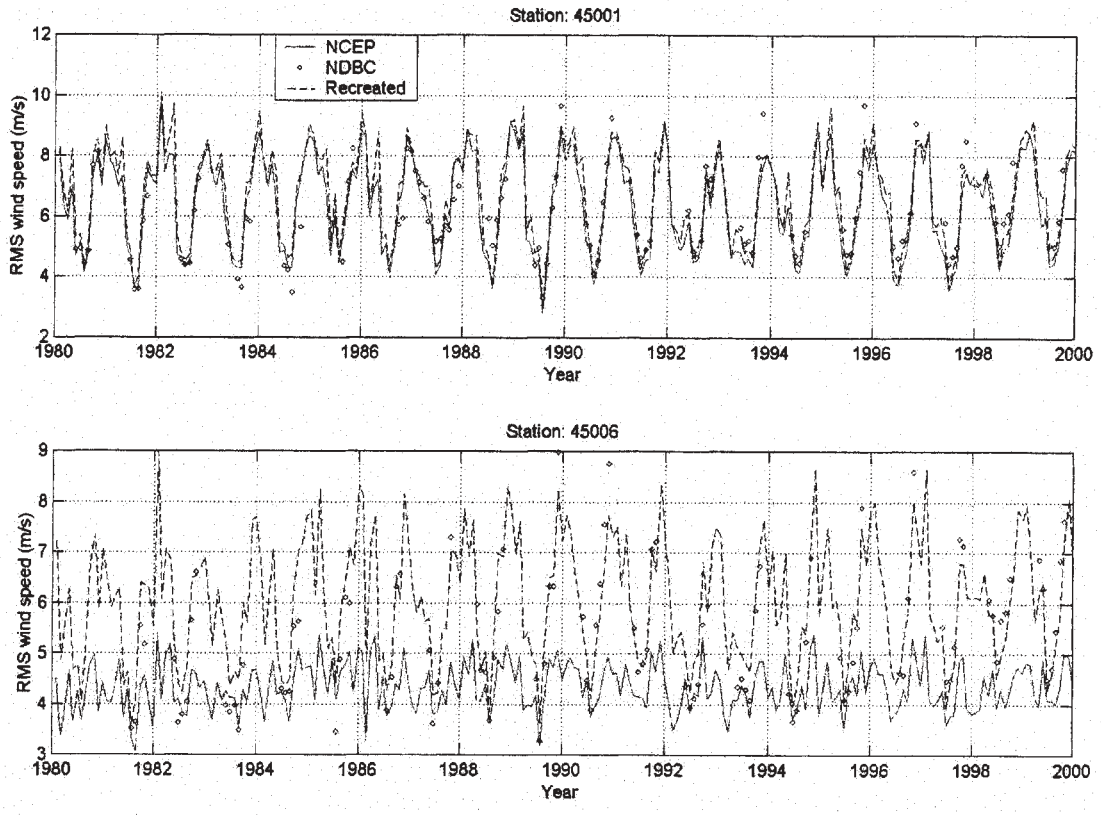

Figure 15. Comparison of NCEP, NDBC and recreated RMS wind speeds at Buoys 45001 and 45006

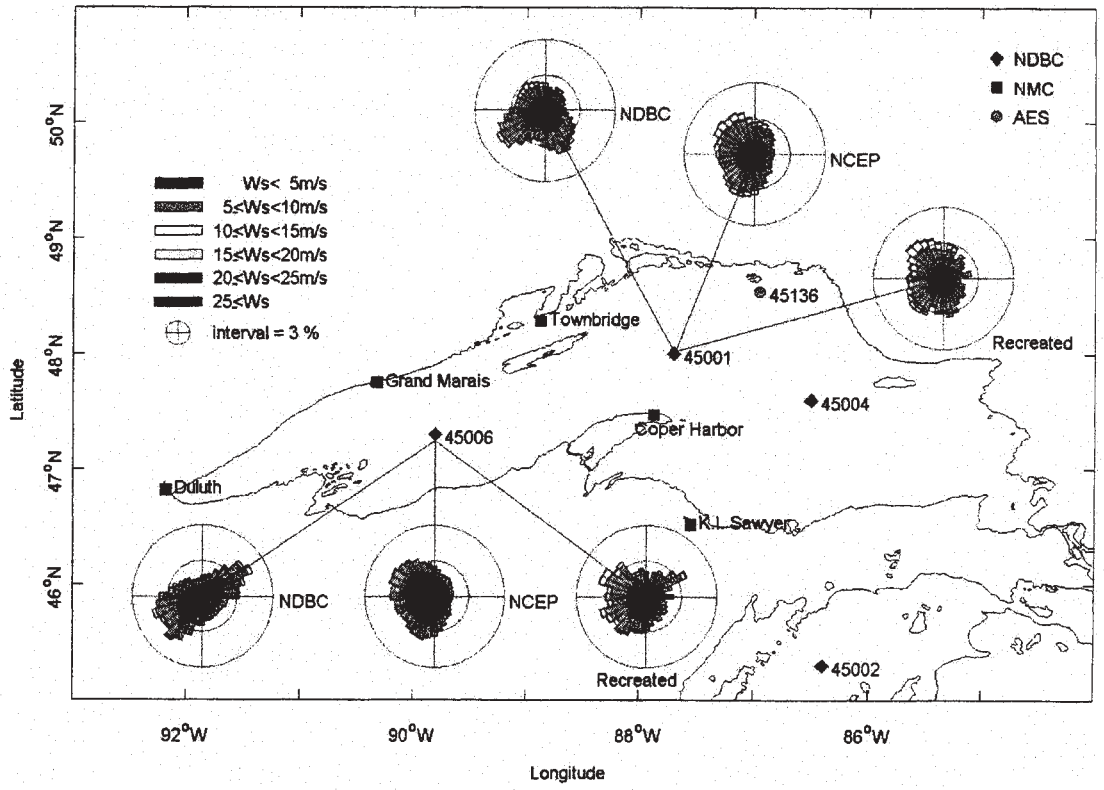

Figure 16. Comparison of NCEP, NDBC and recreated windroses at Buoys 45001 and 45006, 1980-1999

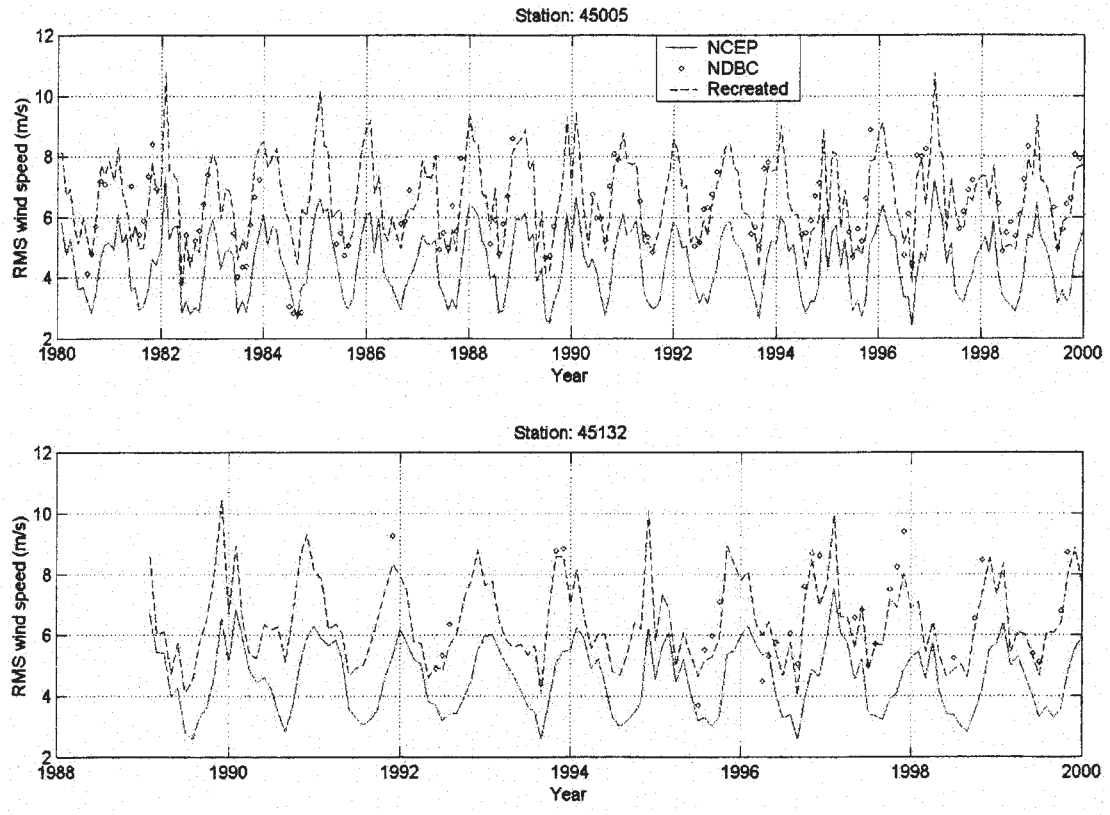

Figure 17. Comparison of NCEP, NDBC and recreated RMS wind speeds at Buoys 45005 and 45132

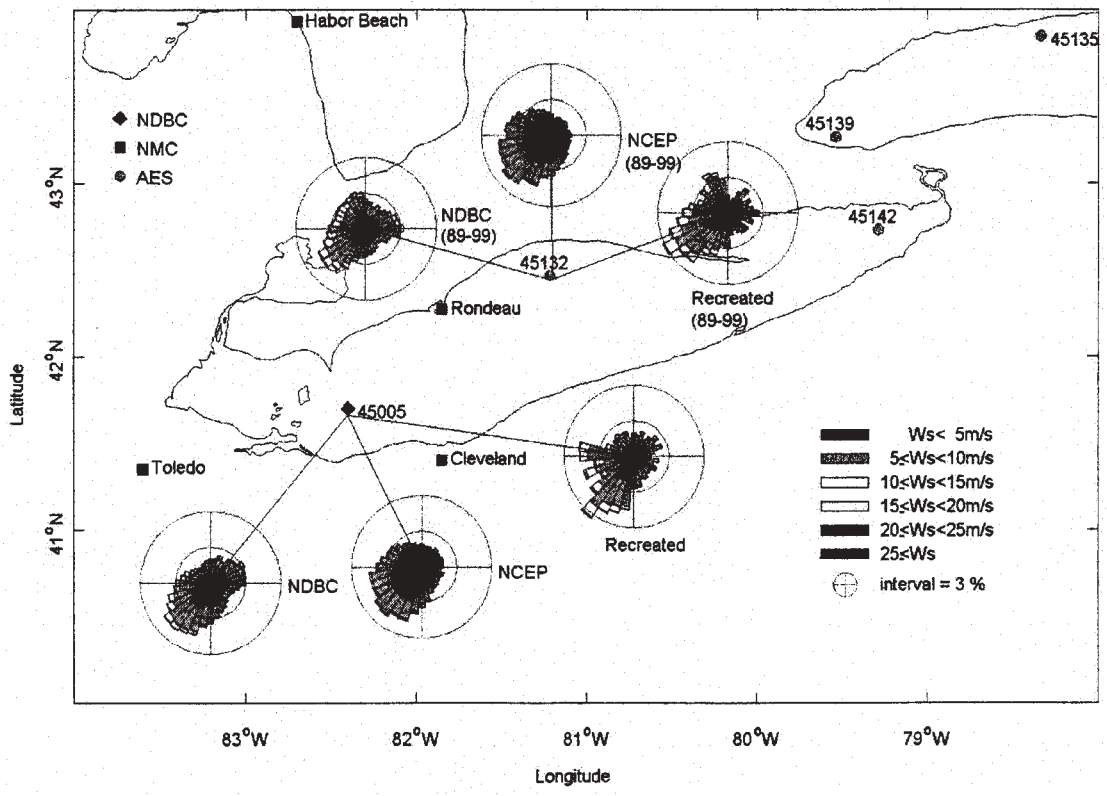

Figure 18. Comparison of NCEP, NDBC and recreated windroses at Buoys 45005 and 45132, 1980-1999

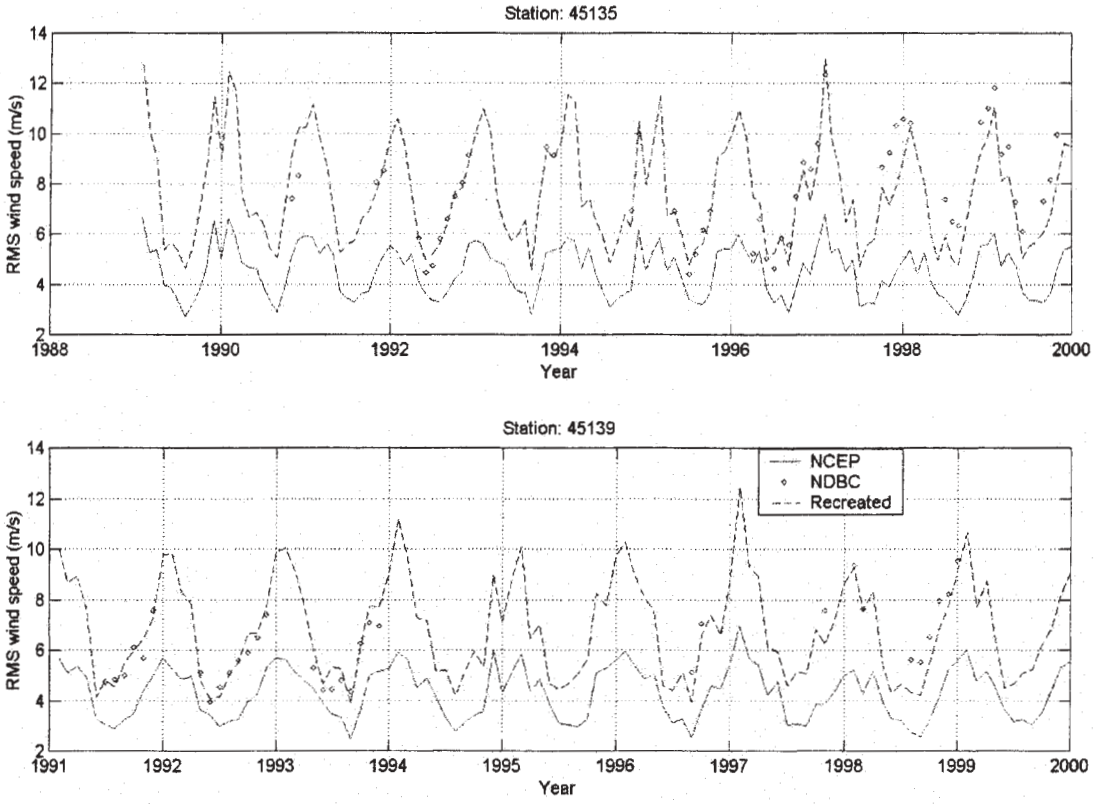

Figure 19. Comparison of NCEP, NDBC and recreated RMS wind speeds at Buoys 45135 and 45139

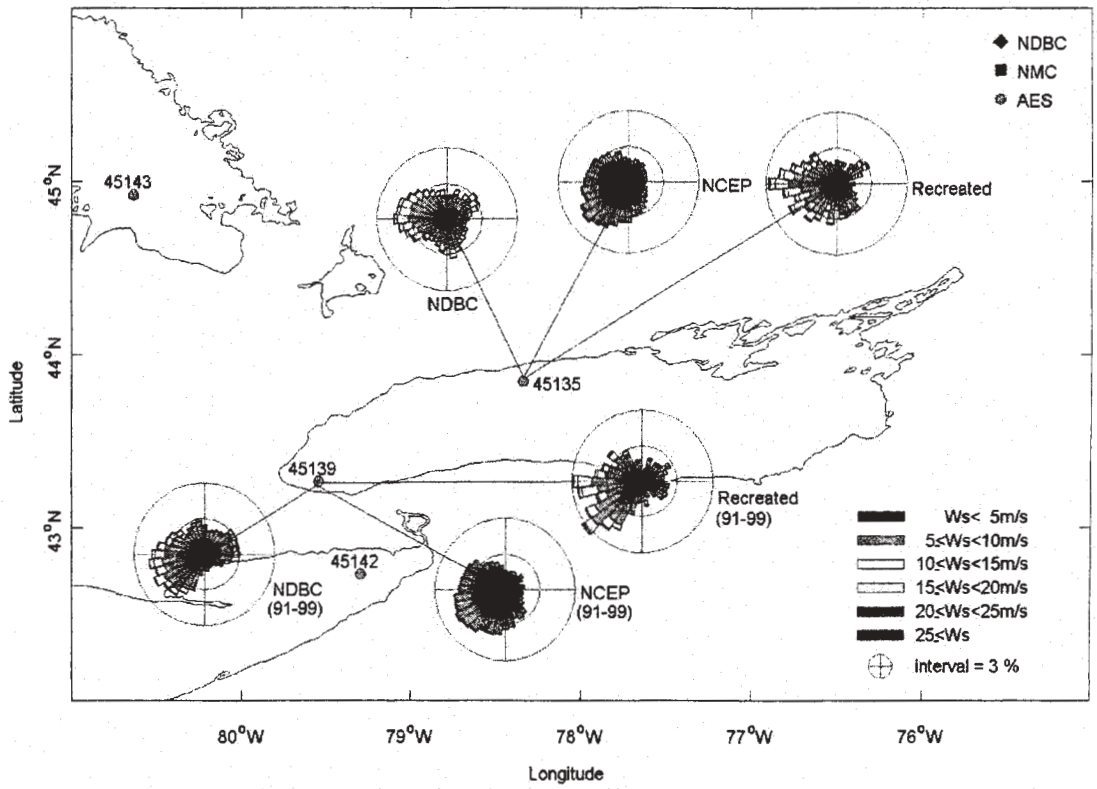

Figure 20. Comparison of NCEP, NDBC and recreated windroses at Buoys 45135 and 45139, 1989-1999

AIRBORNE OPTICAL MEASUREMENTS FOR ESTIMATING DIRECTIONAL WAVE SPECTRA, CURRENTS AND WATER DEPTH

J.Z. Williams, C.C. Piotrowski, J.P. Dugan, and D.C. Campion

Areté Associates
Arlington, VA

1. INTRODUCTION

Measurements of environmental parameters are vital to evaluating the performance of shoaling wave models. Unfortunately, most *in situ* collections of wave heights and currents are spot measurements obtained from a single point or small number of points in the wavefield. In addition, bathymetry is usually obtained from a survey performed prior to the time of interest and may be weeks, months or even years old. To properly characterize the accuracy of a wave model, measurements of the wavefield covering a large area with moderate resolution are needed. These measurements must include a self-consistent set of bathymetry, currents and directional spectra. All these fields exist in concert in the ocean, and should be included in realistic models and the data sets for evaluating them.

One approach is to use a passive EO sensor to image the surface waves by measuring their effect on the brightness distribution, with the space-time behavior of the measured radiance replicating the space-time behavior of the waves. Cameras have for many years provided qualitative and/or quantitative information on a number of parameters and physical processes associated with waves and wind. Since cameras and other optical imaging systems typically have excellent spatial resolution, data can be collected that easily resolve the band of wavelengths associated with gravity waves. Also, the imagery can simultaneously be used for bathymetry and current measurements.

Passive optical imagers have been mounted on towers and used for estimating 2D wavenumber spectra (Barber 1949; Stilwell 1969), and 3D ω-κ spectra (Kasevich et al 1972; Lubard et al 1980). These imagers collect the radiance that is emitted and reflected at the surface. At modest grazing angles, the modulations in the radiance are dominated by the reflection of the sky radiance by the changing wave slopes (Walker 1994). Since the wavelengths of visible light are much shorter than the lengths of the waves on the surface, the reflection mechanism is mostly specular and the measured radiance modulations closely replicate the line-of-sight wave slope modulations. The precise magnitude of the radiance modulations depends upon the wave slopes and the radiance gradient of the background sky. The latter typically is not known in absolute units, so these measurements cannot be utilized to retrieve the actual wave slope magnitudes. However, this uncertainty in the actual slopes does not affect the temporal or spatial distribution of the modulating radiance, so the distribution of variance in spectral space is not affected. The wave height power spectral density can be extracted from measured power spectral density if the proper modulation transfer function (MTF) is applied or a single wave amplitude measurement is made somewhere in the field.

Although shallow grazing angles can result in wave hiding for tower-mounted sensors, this can be avoided by mounting the sensor on an airborne platform. The methodology is to collect a series of geographically referenced images, compute the 3D frequency-wavenumber spectrum of the waves, estimate the location of the wave dispersion surface, and extract the bathymetry and currents from the location of this surface. There is some urgency in pursuing concepts for remotely estimating these particular parameters, as there is a need by the U.S. Naval Oceanographic Office for this type of information in regions that are observable from a distance but not immediately accessible. In this case, remote retrievals of the waves, water depth, and currents along defended coastlines would be useful for assimilation into operational coastal ocean wave and circulation forecasting models. Reasonably accurate bathymetry is a fundamental input for these models. A primary technological issue to doing this operationally from an airborne platform is the registration of the imagery. In addition, although the general methodology for extracting bathymetry and current information from the imagery is now well known, the quality of inexpensive optical data and the accuracy and robustness of algorithms to do this with any reliability are uncertain.

With the above motivation, a camera system was developed on an airborne platform to provide both

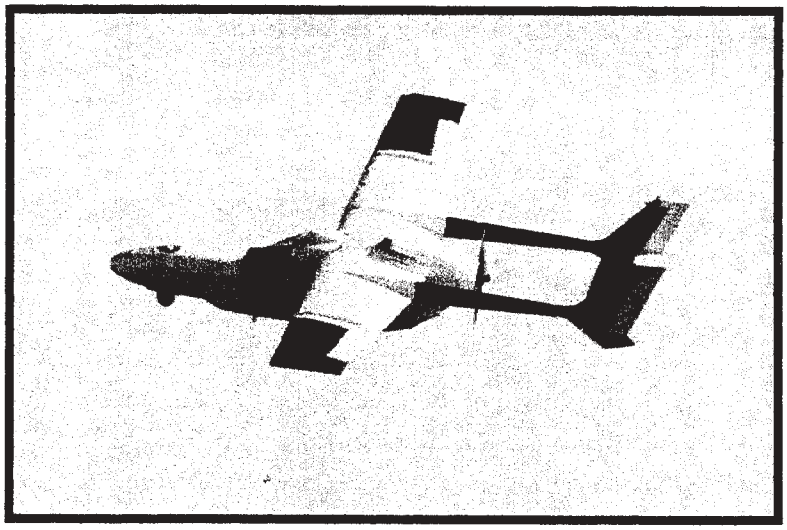

Figure 1: AROSS in flight

portability and moderate grazing angles. To be successful in this application, the system had to exhibit a number of specific characteristics. Accurate registration of the imagery was deemed most crucial, so that spatial and temporal aspects would be accurately separated and the derived data have appropriate characteristics for measuring the location of the dispersion surface in the resulting spectra. Adequate spatial resolution, field of view, dwell, and dynamic range were also identified as important elements. Given these characteristics, the data obtained by this system could potentially be used to estimate bathymetry and currents, as information on these parameters is encoded in the ω-κ luminance spectra. The directional properties of the waves also are contained in these luminance spectra, although the absolute spectral variance densities remain in units of radiance and not wave amplitudes, as stated earlier. A second goal of this effort was to construct the system so that it could be used on small single-engine aircraft and ultimately moved to unmanned aerial vehicles (UAVs).

The Airborne Remote Optical Spotlight System (AROSS) has been designed and constructed with this specific purpose in mind (Dugan et al 2000a). Imagery data sets were collected during the SHOaling Wave EXperiment (SHOWEX), which was conducted near the U.S. Army Corps of Engineers Waterways Experiment Station (WES) Field Research Facility (FRF) located on the North Carolina (USA) Outer Banks in October - December 1999. Data from SHOWEX have been used to retrieve bathymetry, currents and directional wave spectra for comparison with *in situ* measurements.

2. SYSTEM DESIGN

The design approach was to utilize a commercial off-the-shelf (COTS) turret-type positioner, digital framing camera, and integrated Global Positioning System/inertial measurement unit (GPS/IMU), with a computer-based data acquisition and control system. Attitude and position information are provided by the GPS/IMU, which was mounted within the turret rather than on the airframe. The control system uses this information, along with differential GPS corrections, to calculate the camera pointing direction and maintain the intended geodetic location of the aim point in close proximity to the center of the image.

The specifications for this GPS/IMU result in absolute turret position and attitude errors of approximately 3 meters in turret location and 2-4 milliradians in elevation and azimuth. For the nominal viewing geometry given by an aircraft altitude of 2.8 km and a ground distance to the target of 5.6 km, yielding a grazing angle of 30°, these errors translate to absolute pointing accuracy of about 20 meters and interframe accuracy of better than 5 meters in both range and azimuth. For the intended application, these values meet the requirements that most of the imaged area is retained in continuous view over the dwell and the jitter is small. Most importantly, the accuracy of the mapping can be improved by post-processing when there is a stationary target in the FOV.

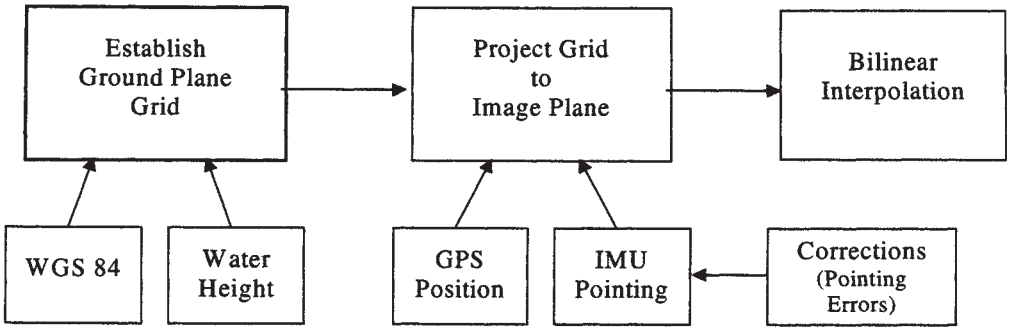

Figure 2: Block diagram of mapping software

The camera has a 1024 x 1024 pixel CCD array that can be sampled at a frame rate of up to 8 Hz. The 12-bit quantization of the camera provides sufficient sensitivity to resolve ocean wave contrast while maintaining the generally brighter coast on the digitizer scale. The imaging lens on the camera is anamorphic, with a FOV of 18.6° in azimuth and 9.4° in elevation. The two-to-one aspect ratio approximately accounts for the projection of the FOV onto a level geodetic surface from the nominal grazing angle of approximately 30° relative to the ocean surface. With the nominal viewing geometry, this camera provides spatial resolution of 2 meters per pixel and a 2 kilometer by 2 kilometer FOV. A 100 nm optical bandpass filter centered at 600 nm restricts the response of the camera to the red to green region of the spectrum.

An external turret-type positioner currently used on the Predator surveillance UAV (Mulford 1994) was modified for this application. This positioner is a four-axis gimbaled turret that houses the camera/lens system, and it provides unlimited motion in azimuth and +20° to -90° in elevation. It was mounted to the underside of the payload bay in the nose of a modified Cessna 337 Skymaster that is operated by the Naval Postgraduate School (NPS) Center for Interdisciplinary Remotely Piloted Aircraft Studies (CIRPAS). The payload bay also contains support electronics, the system data acquisition/control computer, the data storage medium, and a GPS antenna. The plane is called the *Pelican* (Bluth et al 1995) and is shown in flight in Figure 1.

The camera and GPS/IMU are interfaced through the turret slip ring to the data acquisition and turret control computer and the GPS antenna. A RAID system comprised of three 18 GB drives, formatted in RAID type 0, provides over 50 GB of data storage capacity. The RAID capacity is large enough to record continuously for over three hours at the 2 Hz rate.

3. DATA COLLECTION AND PROCESSING

The selected image data are mapped by transforming them to a uniform rectilinear grid at the WGS84 vertical level of the mean ocean surface, using laboratory-derived optical distortion data for the lens and the camera attitude and position data from the GPS/IMU. This processing technique is summarized in the block diagram in Figure 2.

Further processing of the mapped data consists of frame-by-frame mean normalization, a 3D de-trend, and an 80% cosine window to reduce the effects of spectral leakage. The data are then Fourier transformed in time and two spatial dimensions to obtain the 3D ω-κ spectrum. This is typically done for sub-images of 64, 128, or 256 pixels on a side, and for 64, 128, or 256 frames. Each resulting spectral estimate is averaged over three adjacent values in both wavenumber and frequency. The result for even a single sub-patch is reasonably smooth, as shown in the example discussed below.

SHOWEX was conducted near the U.S. Army Corps of Engineers' Waterways Experiment Station FRF on the Outer Banks at Duck, NC. The primary emphasis of this experiment was the energy budget for the surface wave spectrum as the waves propagate across the wide, shallow shelf near Duck, but our imagery was largely focused on the nearshore at FRF. The water depth at this location varies from the beach to about 15 m. The depths were measured by coordinated surveys before and after our experiment by a combination of the FRF Coastal Research Amphibious Buggy (CRAB), which crawls on the bottom and uses a kinematic GPS (KGPS) receiver for measuring the geodetic height of the bottom (see Birkemeier and Mason (1984) for an

early description), and the FRF LARC (Lighter Amphibious Resupply Cargo), a wheeled amphibious vehicle which uses a combination of a KGPS receiver and a fathometer for measuring these heights/depths (Dugan et al 1999). The surveyed heights were adjusted to account for the local tide level at the times of the remote observations, so that a direct comparison can be made between the retrieved depths and the survey depths. *In situ* water current profiles were measured by an ADCP mounted on a jet-ski, which was deployed simultaneously with AROSS observations on two occasions. FRF measured the frequency-directional wave spectrum using an array of bottom pressure sensors near 8 m water depth, and also the wind vector using an anemometer near the seaward end of their long pier. The measured wave spectra are valid only for frequencies lower than about 0.3 Hz due to the exponential loss of pressure modulations over the 8 m depth, but they are accurate for the longer and lower frequency waves.

4. BATHYMETRY RETRIEVAL

The data that are utilized for bathymetry retrieval in this paper were collected at 1527 UTC on 19 October 1999, with the nominal distance from the aircraft to the center of FRF's 8-meter pressure array (36° 11.23' N, 75° 44.57' W) of about 5.6 km. At this time, the sun was at an azimuth of 43° east of south and elevation of 33°. The sky was clear, with little obvious haze. The wind speed measured by the FRF anemometer was 4.6 m/s from 43.5° relative to true north (°T). The aircraft circled the array for approximately 8 minutes, acquiring 1000 frames of data, and a two-minute segment was selected for processing. Figure 3 is a plot of a data frame that has been mapped to the vertical

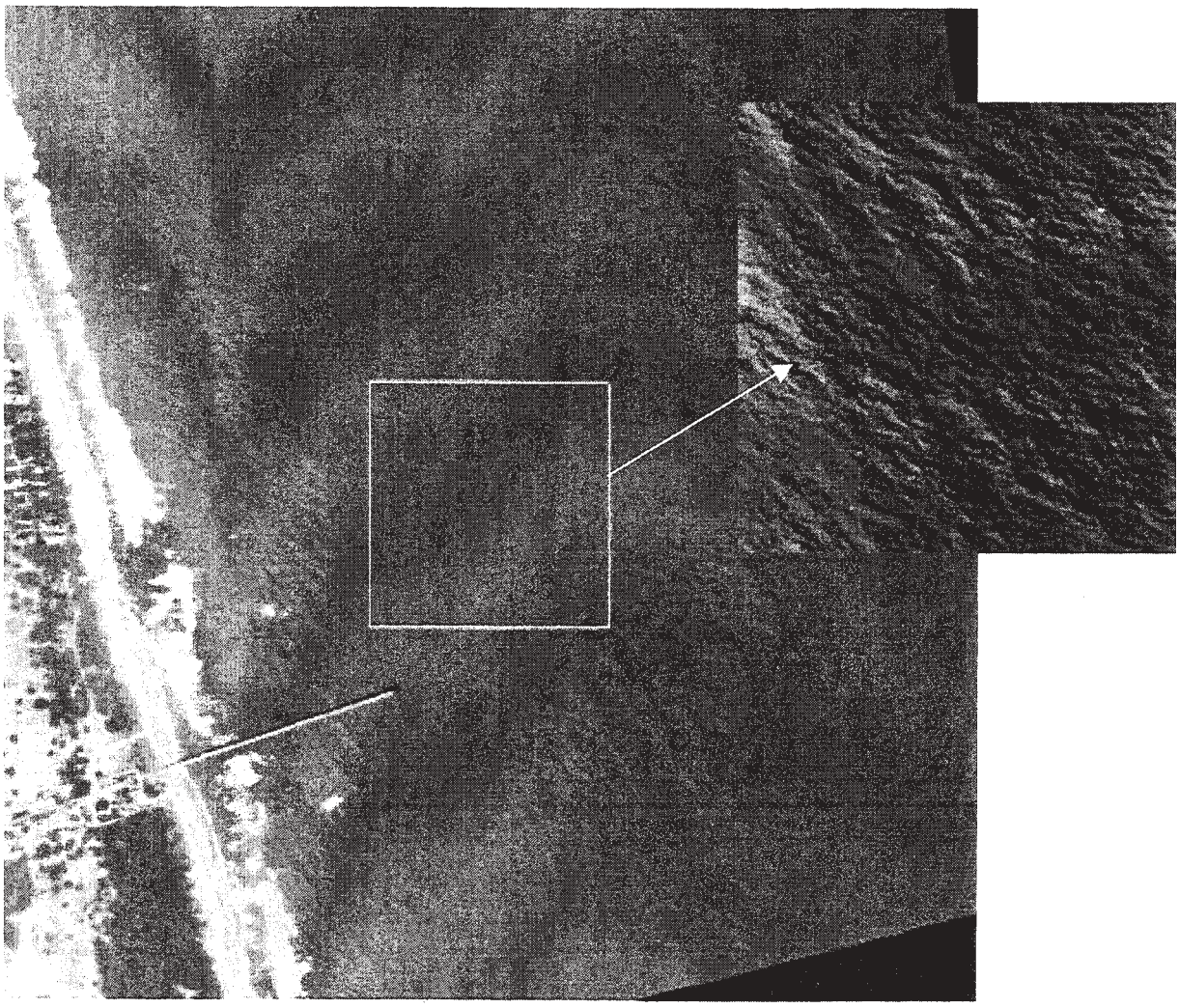

Figure 3: Mapped AROSS image with a closeup of the processed subset

level of the local mean ocean surface. In the full frame, the waves are not immediately obvious because of the large range of luminance levels that are required to keep the bright land on scale in the image. Thus, Figure 3 also illustrates a portion of the scene outside the surf line centered on the 8 m array. The scale has been expanded and the histogram of the wave luminance data has been stretched to cover the same brightness scale as the rest of the image. Waves having a broad range of lengths are readily apparent. Note the linearity of the coastline, which implies that the bathymetry contours are also parallel to the beach, though likely with some variability in the vicinity of the nearshore bar and trough.

Figure 4 shows a 2D slice through the 3D ω-κ spectrum. For this spectrum, 256 pixels were transformed in the two spatial dimensions and 256 frames in the temporal, or about 500 m in space and 2 minutes in time. This slice is in the primary direction in which the swell is propagating, and it shows that the waves occupy a wide range of frequencies from the swell near 0.1 Hz (wavelength near 100 m) almost all the way out to a frequency of about 0.5 Hz (wavelength near the Nyquist of 4 m). This is much more apparent in color graphics. Note the narrowness of the ridge of energy (the dispersion surface) that lies along the smooth line which represents the fit to this dispersion surface with depth $h = 8.2$ m and current (in the direction of the slice) $U = 0.14$ m/s. The theoretical dispersion surface for zero current and infinite water depth is shown as the dashed curve. There also are interesting side bands near the primary waves that are about 10-15 dB below the level of the energy on the ridge.

For comparison, the average water depth measured by the FRF LARC over this 500 m region near the 8 m array was precisely 8.0 m, so the error of the retrieval for this case is less than 3%. Note also that there is much lower amplitude but clearly noticeable wave energy that is propagating in the opposite direction, presumably having been reflected by processes near the beach and/or in the surf. The reflected wave energy is also apparent Figure 5, which displays slices through the 3D spectrum at constant frequency. The solid circular line in these plots is the intersection of the dispersion surface (assuming infinite water depth and no current) and the spectral surface. Figure 5(a) displays the slice at 0.12 Hz, near the dominant swell frequency, and clearly shows the direction of propagation of the incoming swell and the broad distribution of reflected waves at this frequency. The proportion of energy in the reflected waves relative to the incoming waves can be obtained by separately integrating the left and right sides of this spectral slice and taking the ratio of the two. In this particular case, the reflected wave energy is about 8% of the onshore

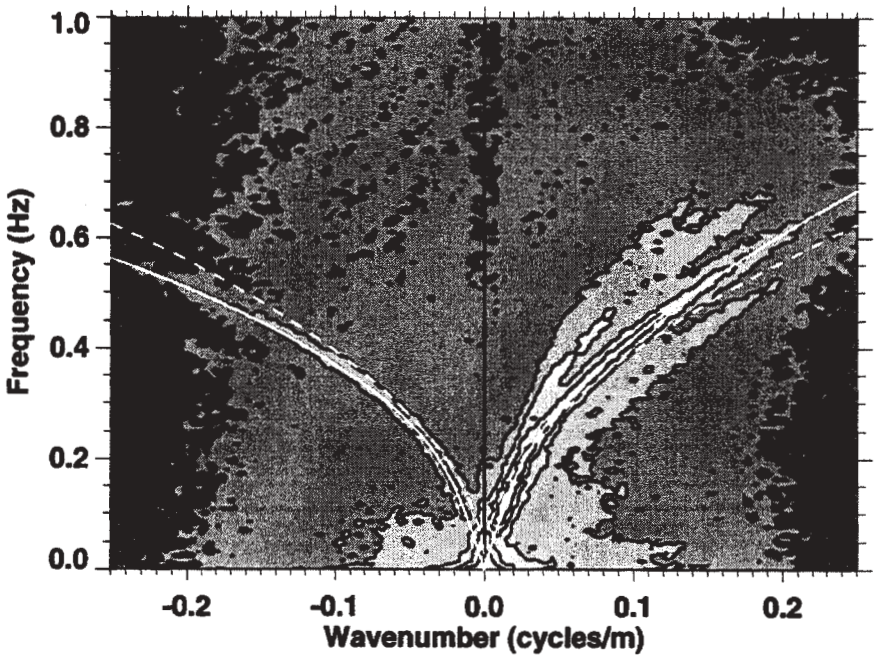

Figure 4: An ω–κ slice in the direction of the swell, with both the deep water dispersion curve (dashed curve) and empirical fit (solid curve) to the spectrum with $h = 8.2$ m and $U = -0.14$ m/s in the direction of the swell.

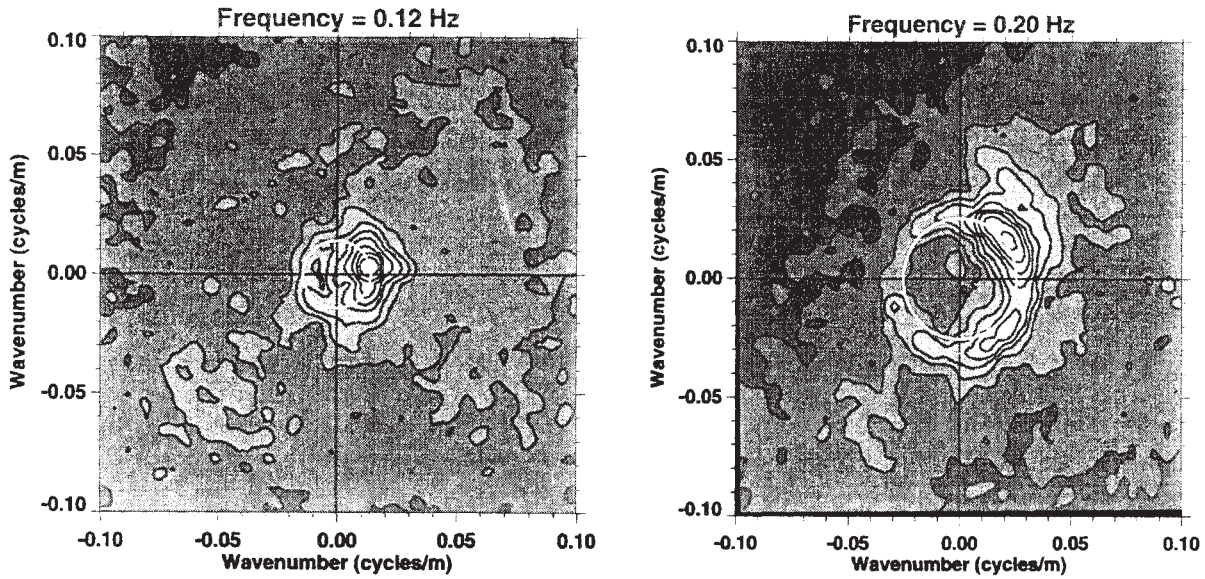

Figure 5: κ_x- κ_y slices through the 3-D spectrum at (a) the swell frequency of 0.12 Hz and (b) the wind wave frequency of 0.2 Hz

energy. Figure 5(b) shows the directional situation at 0.2 Hz, in the wind wave band. We believe that this is the first estimate of reflected wave energy obtained from optical imagery collected from an airborne platform, and this was possible because of the high fidelity of the measurement system.

In order to obtain a depth profile for comparison with the FRF bathymetry survey, overlapping sub-patches were chosen. Figure 6 shows a cross-shore plot of the depth profiles from three nearby survey lines, and also the retrieved depths for each of the sub-patches. The differences are rather small, and summary statistics are given in Table 1.

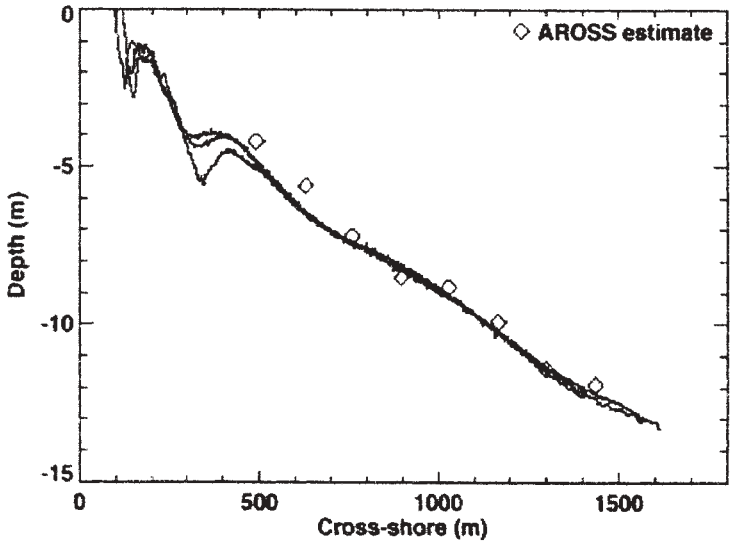

Figure 6: Comparison of AROSS estimated depths with ground truth bathymetry survey data (AROSS estimates were adjusted for a tide of –0.2 m at the time of data collection).

Table 1 : Summary statistics of the comparison of AROSS bathymetry estimates and the ground truth survey

Statistic	Ground Truth Comparison
Bias	0.12 m
RMS	0.48 m
Mean relative Error	5%

5. CURRENT RETRIEVAL

An analysis of current retrievals was performed for data collected on 4 Nov 1999 during SHOWEX when *in situ* currents were available. The significant wave height was 0.6 m with a modest swell coming from ~80°, almost directly onshore, and a smaller wind wave spectrum from the NE. The wind actually was 3.7 m/s from 204°, almost in the opposite direction, and there were few clouds. The primary *in situ* instrumentation was a 1.2 MHz RDI ADCP that was mounted on the stern of an instrumented personal water craft (jet ski) along with a real time kinematic GPS (Dugan et al 1999, 2000b) to provide precise navigation. This small boat was run back and forth perpendicular to the shore. The ADCP was equipped with bottom-tracking capability so that the data could be corrected for boat motion and heading using the velocity vector of the bottom reflection. On 4 Nov 1999, the current magnitude increased with distance from shore, from a value of ~10 cm/s near the surf at about 3 m water depth (near 300 m cross shore in the FRF coordinate system) to a value of about 50 cm/s farther out at 12 m water depth. The currents were nearly parallel to the shore and the vertical shear was small.

AROSS images taken simultaneously with the ADCP data were each mapped to the mean ocean surface using the onboard navigation and turret attitude data as the initial estimates for the location and attitude of the camera. Known fixed locations of features on the beach and the pier were found to be in error by as much as 20 m, and series of frames have been observed to drift by as much as 20 cm/s. This drift must be removed in order to obtain accurate current estimates. This was achieved using ground control points that were visible in each frame to determine the corrections to the attitude angles which forced the ground control points to remain stationary, at least within the 2 m resolution of the images, and remapping using the corrected angles. This correction was verified by generating a 'movie' loop and observing the waves moving as one expects and noting that the FRF pier and features on the beach do not move.

Cubical stacks of 256 pixels on a side (512 m) and 256 frames (128 seconds dwell) were Fourier transformed to form the 3-D ω-κ spectra used in the subsequent analyses. The specific sub-regions under analysis were centered along a line about 350 m north of the FRF pier, and these sub-regions were stepped 128 m in the offshore direction and the analysis repeated, from a mean depth of 5 m to 12 m. The two-dimensional slice through the three-dimensional frequency-wavenumber spectra in the cross shore direction (which in this case happens to be in the direction of the swell) at the location nearest 8 m depth (~900 m cross shore) is shown in Figure 7. The band of wave energy on the dispersion surface is well above the noise floor from about 7 m to 100 m wavelength. The shoreward-propagating energy on the right side of the plot is ~30 dB above the noise floor and the reflected seaward-propagating energy on the left is still observable above the nearby noise level. The linear spectral feature below the dispersion surface on the left is due to the presence of the jet ski in the imagery, travelling in the offshore direction at a speed of 2.5 m/s. Figure 8 shows the accompanying slice in the alongshore direction, and the Doppler shift due to the current clearly tilts the dispersion surface asymmetrically. In each figure, the best fit to the theoretical dispersion surface is shown as the smooth white line. The fit was obtained by locating the maximum value of the spectrum at each wavenumber between the shortest wave clearly resolved above the noise level (about 5 m) and a wavelength of about 30 m. Then the theoretical dispersion surface was fit to this series of values using a nonlinear least squares procedure having depth and current vector as free parameters. The dashed curve indicates the dispersion surface for infinite depth and no current.

It is important to note that a requirement for estimating the current is that there be a measurable component of the waves traveling parallel to the direction of the current. This does not seem to be a limitation in the nearshore data analyzed to date, as there are detectable waves of relatively high frequency propagating in practically all directions in each case. An example of the slice at a constant frequency of 0.2 Hz through the 3-D spectrum for the sub-patch located at 8 m depth was shown in Figure 5(b). This plot clearly indicates that there is a wide distribution of directions of waves having this frequency. We believe this is a result of

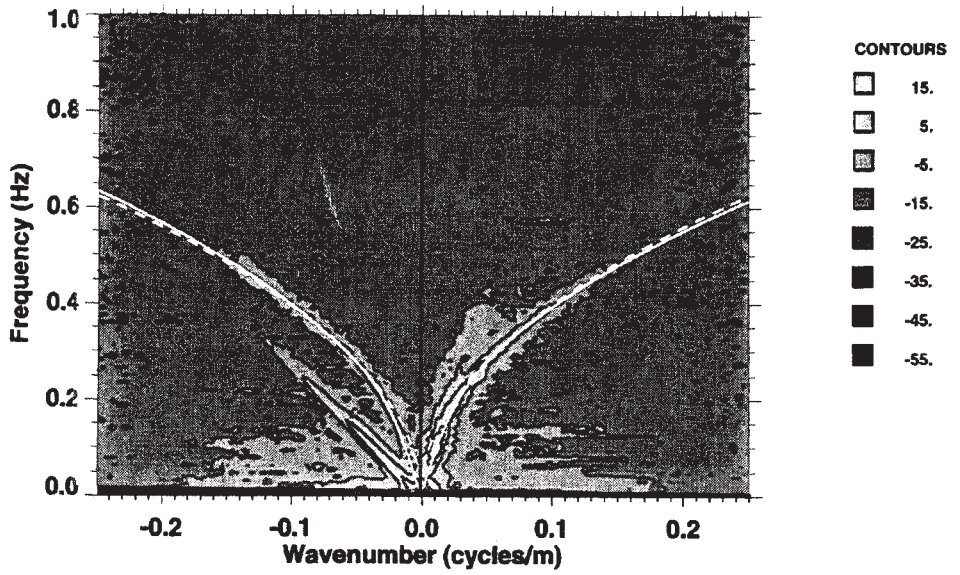

Figure 7: Frequency-wavenumber slice through the 3-D spectrum in the cross shore direction (which is also the swell direction, in this case) used to extract the current.

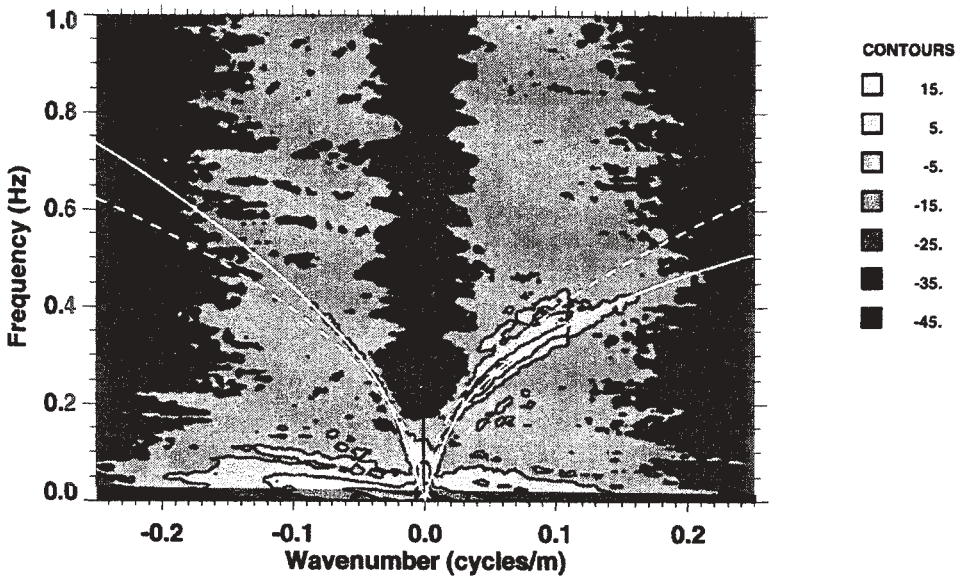

Figure 8: Along shore slice through the 3-D spectrum at 8 meters depth used for current extraction.

significant scattering effects in the surf zone, as close examination of the time series of images in this vicinity shows waves being radiated (in more or less circular patterns) from each of the breakers.

In Figure 9, the retrieved velocity vector (solid) for each sub-patch is plotted as a function of the offshore distance of the patch center, along with the ADCP current velocity measurement at 1.5 m depth (dash).

The ADCP measurements were averaged over each sub-patch for a 30-minute interval centered on the AROSS collection time and adjusted for a wind-driven surface current. An empirical rule of thumb is that the wind-driven surface current is given by ~3% of the wind speed in a direction up to 15° to the right of the wind. Neglecting the Coriolis deflection and using the measured wind speed during the time of the AROSS data collection, we assumed that this wind-driven

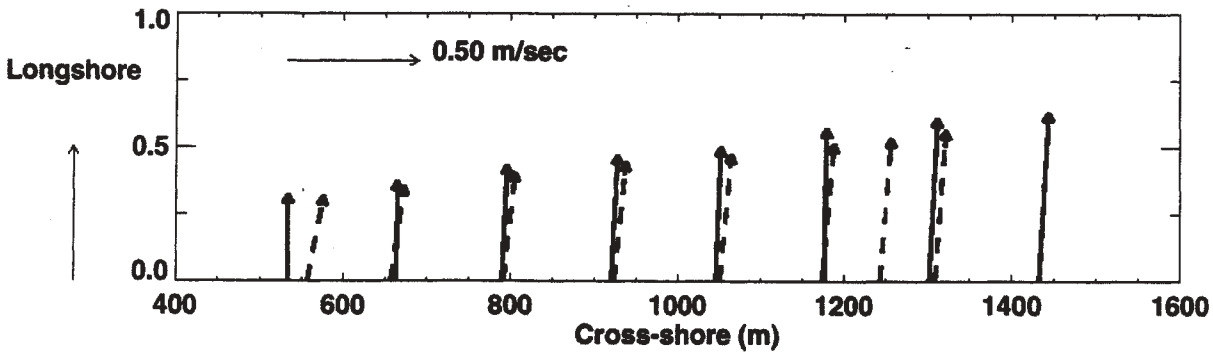

Figure 9: Comparison of AROSS current vector estimates (solid) and averaged ADCP current measurements at 1.5 meters depth adjusted for a wind-driven surface current (dash).

surface current may be vector-added to the underlying current measured by the ADCP to obtain the total surface current. The AROSS current vectors were on average within 5-6% in magnitude and 5° in direction of the adjusted ADCP measurements, with RMS errors of 3 cm/s in magnitude and 6° in direction. These differences are much smaller than typical comparisons between shipboard ADCPs and HF radar-derived surface currents (Chapman et al 1997).

6. DIRECTIONAL SPECTRUM

Automated software produces a directional spectrum from the FRF array every 3 hours. As part of the data collection runs during SHOWEX, data were collected during most of the AROSS flights with the center of the array as an aim point.

AROSS data collected on 4 November 1999 at 2045 UTC were used to produce a 3D ω–κ spectrum using the same methodology as described above. The data cube consisted of a 500x500 meter patch and 256 frames (~2 minutes). A directional-frequency spectrum was produced by integrating the 3D spectrum over an angular increment of 2° and over all κ, excluding the region near the origin.

Assuming a linear sky-gradient and no look dependence for the observed wavefield, the resulting spectrum is a directional slope spectrum with an unknown gain. These assumptions should be valid since the data were collected with the sun behind the sensor and with an angular change of 90° in the look direction. Thus, the AROSS spectrum was divided by κ^2, the appropriate scaling between amplitude and slope power spectral density, based on small amplitude wave theory. The directional-frequency wave spectra from both the FRF array and AROSS are shown in Figure 10. In these plots, the horizontal axis is the direction the waves are coming from, using a coordinate system aligned with the coastline in the vicinity of FRF. In this coordinate system, 0° is normal to the pressure array, 90° is parallel to the array from the north, and -90° is parallel to the array from the south (true north is ~72°). The high frequency cutoff was set to 0.32 Hz, since the FRF pressure array can only resolve waves with this frequency or lower with reasonable accuracy, due to the depth of the array. The agreement between the two plots is excellent, except at higher frequencies. The integrated frequency and direction spectra are shown in Figure 11. In this figure, the AROSS spectra have been multiplied by a constant gain factor in order to match the peak of the FRF frequency spectrum.

This result confirms the validity of assuming a linear sky-gradient and no look dependence in the MTF for this data set. Therefore, the luminance spectra measured by AROSS can be used to provide a reasonable measurement of the wave amplitude spectra provided the data is collected to avoid highly non-linear effects (such as reflected sunlight) and collected with a moderate change in the look vector. By integrating the κ^2 corrected luminance spectra over all angles, a simple measurement of the wave amplitude spectrum at a single point can be used to provide the MTF gain. This provides a unique ability to obtain the wave amplitude spectrum over large areas as opposed to the spot measurements provided by directional arrays and buoys. Using this capability provides a means for testing shoaling wave models through observation of the change in the wave amplitude spectra as a function of the change in bathymetry and currents.

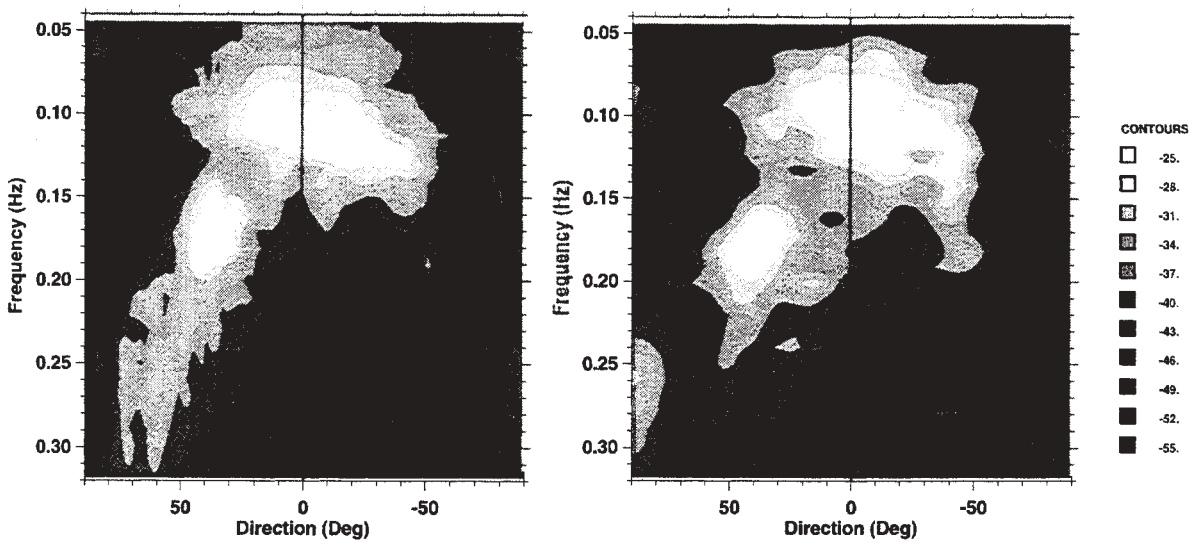

Figure 10: Comparison of the directional spectra from AROSS and the FRF 8 m array. The AROSS spectrum is on the left and has been corrected by the slope-to-amplitude MTF, k^2. The contours are in dB of power.

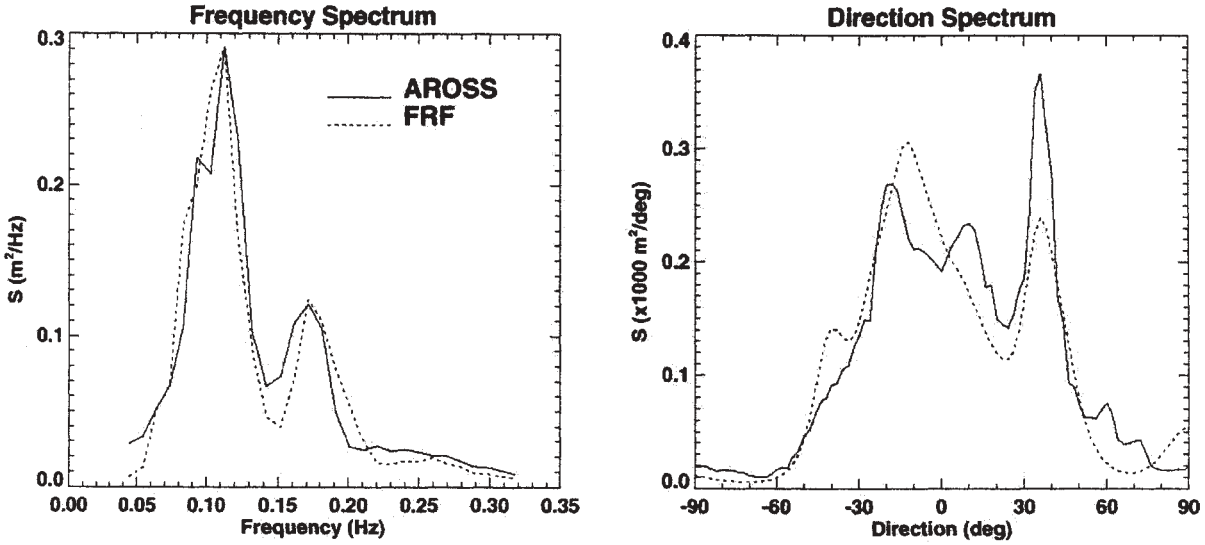

Figure 11: Comparison of the integrated directional spectra from AROSS and the FRF 8 m array. The AROSS spectra have been multiplied by a constant to match the peak in the FRF frequency spectrum.

7. CONCLUSION

AROSS provides useful image data that are collected at modest grazing angles with enough control that they can be mapped successfully to a level geodetic surface. The ω-κ spectrum is highly resolved, which could only result from the combination of the high quality camera, accurate mapping, fine sampling, long dwell, and large sub-patch that was analyzed. All of these elements are necessary to obtain high resolution and a narrow ridge of energy that represents the dispersion surface. The narrowness of this ridge and the resulting high power level relative to the noise (i.e., high wave 'contrast') enable a very accurate and precise estimate to be made of the location of the dispersion surface.

The theoretical dispersion surface was fit to the observed surface, and quite accurate depth and current retrievals obtained. Between 4 and 12 m depths, the retrievals compare very well with the survey depths and currents, having rms errors of about 5%. This is quite adequate for quick survey applications.

In addition, comparisons between the directional spectra obtained from AROSS and the FRF 8 m array are in excellent agreement. This new capability represents a unique ability to obtain all the critical fields (wave amplitude spectrum, bathymetry, and current vector) over large regions of shoaling waves. Such measurements can provide new opportunities for testing shoaling wave models as well as the possibility of use in driving shoaling wave and circulation models through data assimilation.

8. ACKNOWLEDMENTS

This development was supported by an Office of Naval Research SBIR. Bob Bluth and the personnel of the NPS CIRPAS were particularly cooperative and helpful with flight testing and operations. The U.S. Army Corps of Engineers FRF provided excellent facilities, support, and *in situ* data.

9. REFERENCES

Barber, N. F., 1949: A diffraction analysis of a photograph of the sea. *Nature*, **164**, 485.

Birkemeier, W. A. and C. Mason, 1984: The CRAB: A unique nearshore surveying device, *J. Surveying Eng.*, **110**, 1-7.

Bluth, R. T., P. A. Durkee, J. H. Seinfeld, R. C. Flagan, and L. M. Russell, 1995: The Center for Interdisciplinary Remotely-Piloted-Aircraft Studies (CIRPAS). *Bull. Amer. Meteor. Soc.*, **77**, 2691-2699.

Chapman, R. D., L. K. Shay, H. C. Graber, J. B. Edson, A. Karachintsev, C. L. Trump and D. B. Ross, 1997, On the accuracy of HF radar current measurements: intercomparisons with ship-based sensors, J. Geophys. Res., 102 (C8), 18737-18748

Dugan, J. P., K. C. Vierra, W. D. Morris, G. J. Farruggia, D. C. Campion, and H. C. Miller, 1999: Unique vehicles used for bathymetry surveys in exposed coastal regions, *Hydro'99*, U.S. Hydrographics Conf., Mobile, AL, May 1999.

Dugan, J. P., G. J. Fetzer, J. Bowden, G. J. Faruggia, J. Z. Williams, C. C. Piotrowski, K. Vierra, D. Campion and D. N. Sitter, 2000a, Airborne optical spotlight system for remote sensing of ocean waves, J. Atmos. and Oceanic Technol., submitted

Dugan, J. P., W. D. Morris, K. Vierra, C. C. Piotrowski, G. Farruggia and D. Campion, 2000b, Jet ski based nearshore bathymetry and current survey system, J. Coastal Res., submitted

Kasevich, R. S, C. H. Tang, and S.W. Henriksen, 1972: Analysis and optical processing of sea photographs for energy spectra. *IEEE Trans. Geosci. Remote Sens.*, **10 (1)**, 51-58.

Lubard, S. C., J. E. Krimmel, L. R. Thebaud, D. D. Evans, and O. H. Shemdin, 1980: Optical image and laser slope meter intercomparison of high-frequency waves. *J. Geophys. Res.*, **85**, 4996-5002.

Mulford, L., 1994: Skyball: the eyes for Predator. *Unmanned Systems*, **12 (4)**, 30-31.

Stilwell, D., 1969: Directional energy spectra of the sea from photographs. *J. Geophys. Res.*, **74**, 1974-1986.

Walker, R. E., 1994: *Marine Light Field Statistics*. Wiley, N.Y., 675 pp.

Wave Information Inferred From Synthetic Aperture Radar Images Used To Improve Numerical Simulation Of Directional Wave Spectra In The Coastal Zone

F. J. Ocampo-Torres and P. Rosales

Departmento de Oceanografía Física, CICESE
Km 107 Carretera Tijuana-Ensenada, Enesnada BC, 22860 México
Tel: +52(6)175050 Fax: +52 (6) 1750547 E-mail: ocampo@cicese.mx

ABSTRACT

The use of synthetic aperture radar (SAR) images of the ocean surface to improve the results of hindcasting wave spectra in the coastal zone is being explored. Even though SAR image spectra are constrained within the azimuth cut-off region, spatial variability of the wave field can be determined, both in terms of the two-dimensional shape of the spectrum as well as of the resolved direction of wave propagation. Furthermore, a good number of analysed images provide supporting evidence on the continuous detectability of waves within the region of interest, a coastal region in the north west of Baja California.

Spatial variability of the wave field is being investigated by means of an alternative analysis, which does not impose the condition for an homogeneous process, and specific cases for range and azimuth travelling waves are discussed. When in terms of typical FFT spectral analysis, the spatial variability is also detected through SAR images. This is of prime concern for considering initial and/or boundary conditions for fine spatial wave modelling.
Hindcast cases are presented where an advance third generation wave model (SAWN) is being used. Procedures to incorporate the characteristic spatial variability observed into the model are being addressed.

BIMODAL DIRECTIONAL DISTRIBUTION OF OCEAN WAVES IN MIXED SEAS

David W. Wang, Paul A. Hwang, James M. Kaihatu and W. Erick Rogers
Oceanography Division, Naval Research Laboratory, Stennis Space Center, MS 39529

1. INTRODUCTION

Until recently, wave energy directional distributions have been treated as a unimodal function. Intuitively, the wind wave energy propagates mainly in the wind direction and decreases monotonically with increasing angle to the wind. Field studies by Mistuyasu et al. (1975), Hasselmann et al. (1980), and Donelan et al. (1985) provide parameterizations of such unimodal directional distributions with directional spreading narrowest at the peak frequency and broader toward both higher and lower frequencies. The bimodal directional distribution, unlike the unimodal function, indicates that most wave energy is in two sidelobes symmetrically located about the wind direction. Numerical simulations by Banner and Young (1994) show that the presence of a bimodal directional spreading is a robust feature at wavenumbers above the spectral peak. The mechanism that maintains the bimodal feature is believed to be the directional transfer of energy through nonlinear wave-wave interactions (e.g., Hasselmann 1962; Young and Van Vledder 1993). This bimodal feature with most wave energy propagating at two directions oblique to the wind direction has been observed by spatial measurements using stereo-photography and scanning radar or lidar (Phillips 1958; Cote et al. 1960; Holthuijsen 1983; Jackson et al. 1985; Hwang et al. 2000a). The directional bimodality has also been observed in temporal measurements of directional buoys and wave gauges (Young et al. 1995; Ewans 1998; Ewans and Van der Vlugt 1999).

Using directional buoy data at Maui, New Zealand, Ewans (1998) investigates the bimodal directional distribution of stationary wave fields under fetch-limited conditions. His results show no clear wave age dependence on the bimodal distribution parameters, which indicates that the bimodal directional distribution is an invariant property of a steady wind-generated wave field. More recently, Wang and Hwang (2000a) carry out a comprehensive data analysis on the transient evolution of the wave directional distribution during two active wave growth periods in the Lake Michigan. Their study shows that the bimodal distribution is a distinctive and persistent feature over a broad frequency range throughout the wave growth process. The characteristics of directional bimodality are quantified by parameters related to the separation angles and the amplitudes of the sidelobes. In general, the values of the parameters are smallest near the peak frequency and increase toward both lower and higher frequencies. This frequency-dependent pattern appears to be invariant to the change of wave age throughout the wave growth process.

The presence of swell affects wind wave evolution and air-sea momentum flux (Donelan 1987; Masson 1993; Dobson et al. 1994; Donelan et al. 1997; Mitsuyasu 1997). Depending on the interaction angle between wind sea and swell, the wind wave is subject to different levels of swell modulation. Qualitatively, a wave system propagating normal to the swell will experience minimal hydrodynamic modulation (Hwang et al. 2000b). To examine the invariant bimodal directional distribution of wind sea in the presence of swells will provide important information towards the understanding of the interaction of wind sea and swell. Most field studies on the wave directional distribution are conducted in conditions minimizing the swell influence. In this study, we conduct data analysis on the directional distribution of actively growing wind sea in the presence of high swell. The directional wave data are collected from a buoy located off the coast of California (Buoy ID 46024). The buoy measurement systems are described in Section 2. Also presented in this section is an empirical method for estimating the directional distribution using buoy's heave, pitch and roll measurements. The marine environmental conditions and wave directional distributions during the events are discussed in Section 3. Parameterization of the wave directional bimodality and its dependence on frequency are examined in Section 4. A summary is given in Section 5.

2. MEASUREMENT SYSTEMS AND DATA PROCESSING METHODS

2.1. Measurement systems

In this study, directional wave data are acquired from a heave-pitch-roll buoy deployed and operated by the National Data Buoy Center (NDBC) in the coastal waters off the California coast. This buoy is equipped with a Datawell Hippy 40 Mark II sensor measuring

buoy's heave, pitch and roll over a specified 40-min period each hour. The hourly buoy motion data are processed by an on-board NDBC's wave analyzer to obtain co- and quad-spectra of buoy's heave and the north-south and east-west slopes. Local wind speed and direction are acquired by a propeller-type wind anemometer mounted on the mast of the buoy at approximately 5 m above the design waterline of the buoy hull. Average wind speed and direction, sampled over an 8-minute period immediately after the buoy motion data acquisition, are computed. The hourly measured spectra and other measured meteorological and oceanographic parameters are relayed through the Geostationary Environmental Satellite (GOES) to NDBC for further processing and quality control. Details of the NDBC meteorological and directional wave measurement systems can be found in Steele et al. (1992) and Earle (1996). The archived co- and quad-spectra have 24 degrees of freedom (DOF). In this study, a 3-band running average is applied to the archived spectra to further reduce data variability. This procedure increases the degrees of freedom to 72.

2.2 Processing methods for estimating the directional distribution

The 2D directional spectrum $E(f,\theta)$, which is a function of frequency f and direction θ, is often expressed as the product of the omnidirectional wave spectrum $S(f)$ and the frequency-dependent directional distribution $D(f,\theta)$,

$$E(f,\theta) = S(f)D(f,\theta), \tag{1}$$

where

$$\int_{-\pi}^{\pi} D(f,\theta)d\theta = 1, \tag{2}$$

Longuet-Higgins et al. (1963) approximate the directional distribution by Fourier series expansion,

$$D(f,\theta) = \frac{1}{2} + \sum_{n=1}^{\infty}\left[a_n(f)\cos n\theta + b_n(f)\sin n\theta\right], \tag{3}$$

where a_n and b_n are the Fourier coefficients of the n^{th} harmonic component. The Fourier coefficients of the first two harmonic terms can be computed from the co- and quad-spectra of buoy's heave, north-south and east-west slopes. A frequency-dependent directional parameter, referred to as the mean wave direction θ_1, is computed from the Fourier coefficients of the first harmonic term,

$$\theta_1 = \tan^{-1}\left(\frac{b_1}{a_1}\right). \tag{4}$$

The mean wave direction θ_1 associated with the peak frequency f_p of $S(f)$ is referred to as the peak wave direction θ_p. To coincide with the established convention for wind direction measurements, NDBC reports the wave direction as the angle that the wave is coming from, measured clockwise from true north.

In addition to the Fourier series approximation, several data-adaptive methods providing higher directional resolutions have been proposed to estimate the directional distribution from the co- and quad-spectra of buoy's heave and the north-south and east-west slopes. However, the estimated directional distributions vary significantly depending on the selected method (Benoit 1992). This method-dependent variation has caused significant disputes over the interpretation of the characteristics of the estimated directional distribution from buoy's temporal measurements, especially in cases of multi-modal distributions. In this study, the directional distributions are from an empirical directional distribution estimates (EMP) obtained by averaging the directional distribution estimates of the Maximum Entropy Method (MEM, Lygre and Krogstad 1986) and the Maximum Likelihood Method (MLM, Oltman-Shay and Guza 1984). The EMP estimate, by averaging the sharp and high-amplitude MEM estimate with the broader MLM estimate, seems to provide a practical compromise and shows a better agreement in the comparison with spatially measured directional wave data (Hwang et al. 2000b). Wang and Hwang (2000a) conduct a numerical simulation to show that the EMP provides a better estimate of directional distribution than the MLM and MEM. Detailed discussions about the EMP can be found in Wang and Hwang (2000a).

3. RESULTS

The mixed sea often occurs in costal areas facing open oceans, where the wind sea generated locally often coexists swell radiated from distant storms. In this study, we use directional wave data collected from a buoy moored off the California coast at a water depth of approximately 300 m. Figure 1 shows the time history of buoy wind and wave data from a three-day period (December 12-14, 1993). Due to the constant arrival of strong westerly swells with peak period varying between 12 to 15 s, the variation of sea state deviates significantly from the local wind conditions. In the first 24 hours, the westerly swell coexists with wind sea generated by the southeasterly wind with speed increasing from 5 to 15 m s^{-1}. As the wind starts a gradual shift toward northwest at earlier hours of December 13, the wind speed drops to 1 m s^{-1} at midday of December 13 and increases to 10 m s^{-1} at the end of the day. For the most part of December 14, the strong westerly swell coexists with the wind

sea generated by the northwesterly wind with speed varying between 10 to 12 m s^{-1}. Two active wave growth events by a steady wind in the presence of heavy swell are selected for the study. Detailed statistics are listed in Table1. As marked by the vertical lines in Fig. 1, the first event covers a 15 hours period from 0800 to 2200 UTC, December 12, when the wind sea generated by the offshore southeasterly wind encounters the westerly swell at an average angle of about 154°. The second event covers an 8 hours period from 0900 to 1600 UTC, December 14 when the wind sea generated by the onshore northwesterly wind interacts with the westerly swell at an average angle of about 47°.

Figure 2 shows the wave spectrum and the mean wave direction θ_1 at 2200 UTC, December 12 during the first event. As indicted by the mean wave direction, the wave spectrum shows a dominant and a secondary peaks at about 0.07 and 0.2 Hz corresponding to the westerly swell and the southeasterly wind sea, respectively. Figure 3 shows the shaded image of the 2D directional distribution by the EMP method at the same hour. The directional distribution is normalized by the maximum value at each frequency and displayed in logarithmic scale. Brighter image corresponds to higher level of the distribution density. The wind and peak wave directions are marked as the vertical dashed-and-dotted and dashed lines, respectively. The shaded 2D image shows that the directional spreading of wind sea is narrowest at its peak frequency and broadens as frequency moves toward higher frequency region. Most wave energy concentrates at two sides of the wind direction. The angular separation between the two energy concentration peaks is smallest near the peak frequency of wind sea and increases as the wave frequency moves away from the peak frequency. The directional spreading of swell remains narrower and has no noticeable bimodal directional spreading. To further illustrate details of the directional distribution, frequency slices extracted from the 2D directional distribution at five frequencies are plotted in Fig. 4.

Figure 5 shows the wave spectrum and the mean wave directions θ_1 at 10 UTC, December 14 during the second event. The wave spectrum shows a dominant low-frequency swell peak at about 0.06 Hz. The spectral peak of the wind sea at higher frequencies is rather broad and indistinctive. Using the wind sea and swell separation method by Wang and Hwang (2000b), the wind sea peak is estimated at about 0.16 Hz. Figure 6 shows the shaded image of the 2D directional distribution at the same hour. The wind direction is about 20° from the peak direction of the westerly swell. The shaded 2D image shows that the directional spreading of wind sea is narrowest at its peak frequency and broadens as frequency moves toward higher frequency region. However, the directional distribution is rather asymmetric with most wave energy concentrates only at one side of the wind direction, which is the side away from the swell direction. The wave energy at the other side of the wind direction is closer to the swell direction and suppressed by the swell modulation effect. More details can be shown in the frequency slices of the directional distribution at five frequencies (Fig. 7). Very similar results are also observed in the rest of the period.

4. DISCUSSIONS

4.1. Definition of bimodal parameters

To quantify the characteristics of the directional bimodality, parameters related to the angular locations and the amplitudes of the sidelobes are defined in Fig. 8. Based on their respective locations in the coordinate system shown, the lobe on the left-hand side when following the wind direction is referred to as $Lobe_1$ and the other lobe is referred to as $Lobe_2$. As the wind direction is generally at the center of the bimodal directional distribution, for the southerly wind event, $Lobe_1$ is at a more southeasterly direction and $Lobe_2$ is at a more southwesterly direction. Likewise, for the northerly wind event, $Lobe_1$ is at a more northwesterly direction and $Lobe_2$ is at a more northeasterly direction. The peaks of $Lobe_1$ and $Lobe_2$ are at directions α_1 and α_2, respectively. The lowest point between the two lobe peaks is at direction α_0. The lobe angles θ_{Lobe1} and θ_{Lobe2} are defined as the angular separation distances from α_1 and α_2 to α_0, respectively. The ratios $D(f,\alpha_1)/D(f,\alpha_0)$ and $D(f,\alpha_2)/D(f,\alpha_0)$ are referred to as r_{Lobe1} and r_{Lobe2}, respectively. The lobe ratio r_{Lobe} is the average of r_{Lobe1} and r_{Lobe2},

$$r_{Lobe} = \frac{r_{Lobe1} + r_{Lobe2}}{2}, \tag{5}$$

and the lobe separation angle θ_{Lobe} is the average of θ_{Lobe1} and θ_{Lobe2},

$$\theta_{Lobe} = \frac{\theta_{Lobe1} + \theta_{Lobe2}}{2}. \tag{6}$$

To quantify the asymmetry of bimodal directional distribution, we use the skewness γ of the distribution function, defined as (Kuik et al. 1988)

$$\gamma = \frac{\mu_3}{\sigma^3}, \tag{7}$$

where σ defined as

$$\sigma = \mu_2^{1/2}, \quad (8)$$

is equivalent to the root-mean-square angular deviation (Longuet-Higgins et al. 1963), and

$$\mu_n = \int_{\theta_m-\pi}^{\theta_m+\pi} (\theta - \theta_m)^n D(f,\theta) d\theta, \quad (9)$$

is the *nth* moment centered at mean direction, θ_m, defined as

$$\theta_m = \int_{-\pi}^{\pi} \theta D(f,\theta) d\theta. \quad (10)$$

For a perfectly symmetric distribution with respect to θ_m, the skewness is zero. A larger value of skewness The skewness can be positive or negative depending on the location of the mode of distribution with respect to θ_m.

4.2 Lobe separation angle

Because of the dependence of θ_{Lobe} on f/f_p is invariant to the wave age (Wang and Hwang 2000a), the θ_{Lobe} of hourly measured directional distribution throughout the duration of the two events listed in Table 1 are then grouped into f/f_p bins with a 0.2 f/f_p bin width. The peak frequency f_p is the spectral peak of wind sea. Figure 9 shows the bin-averaged lobe separation angle, $\langle\theta_{Lobe}\rangle$, versus f/f_p for the two events. The dashed curves represent the calculated results of a nonlinear wave-wave interaction model (Plate 1 of Young et al. 1995; Fig. 11 of Ewans 1998). The dashed-and-dotted curves in the range $1.3 < f/f_p < 2.65$ represent the ATM results (Hwang et al. 2000a). The two dotted curves at $f/f_p > 1$ are, respectively, the upper and lower bounds of the results of the Maui buoy data reported by Ewans (1998). At $f/f_p > 1$, all four curves show that lobe separation angle increases with increasing frequency. At $f/f_p < 1$, the model curve shows that lobe separation angle increases rapidly and linearly as frequency decreases from the peak frequency. In general, at $f/f_p > 1$, the pattern of the f/f_p dependence of $\langle\theta_{Lobe}\rangle$ for the four events is consistent with the results of the model, ATM and Ewans. For the event of the southeasterly wind sea against the westerly swell (Fig. 9a), $\langle\theta_{Lobe}\rangle$ has its smallest value of about 25° at $f/f_p = 1$ and increases toward both higher and lower frequencies. At $f/f_p < 1$, the trend of increasing $\langle\theta_{Lobe}\rangle$ is consistent with the model results. At $f/f_p > 1$, $\langle\theta_{Lobe}\rangle$ is very close to the upper bound of the Ewans' results and higher than the model and ATM curves. For the event of northwesterly wind sea in the presence of the westerly swell (Figs. 9b), $\langle\theta_{Lobe}\rangle$ shows a weaker dependence on f/f_p in the range $1 \le f/f_p < 1.5$ as compared to that in Fig 9a. In the range $1.5 \le f/f_p \le 2$, $\langle\theta_{Lobe}\rangle$ is close to the upper bound of Ewans' results and higher than the model and ATM curves. As frequency moves closer to $f/f_p = 3$, the $\langle\theta_{Lobe}\rangle$, model and ATM curves gradually converge to the middle of the upper and lower bounds of the Ewans' results. These two events with two interaction angles between wind sea and swell show that the swell modulation has very limited effect on the frequency dependence pattern of the lobe separation angle.

4.3 Lobe ratio

Figure 10 shows the bin-averaged lobe ratio, $\langle r_{Lobe}\rangle$, versus f/f_p for the two events. The dashed curves represent the model results (case Y10UT in Table 1 of Banner and Young 1994, data provided by Young). The dashed-and-dotted curves represent the ATM results (Hwang et al. 2000a). The dotted curves represent the results of the empirical bimodal Gaussian distribution function proposed by Ewans (1998). All three curves show that r_{Lobe} increases with increasing frequency from $f/f_p = 1$. At $1 < f/f_p < 2$, the model curve is very close to the ATM curve. At $f/f_p \ge 2$, the model curve shows a much slower rate of increase than the ATM curve. The Ewans' curve is very similar to the ATM curve but with a larger offset in f/f_p indicating no directional bimodality ($r_{Lobe} > 1$) until $f/f_p = 2$, which is higher than $f/f_p = 1.3$ for the ATM results. For the event of the southeasterly wind sea against the westerly swell (Fig. 10a), $\langle r_{Lobe}\rangle$ has a local minimum near $f/f_p = 1$ and increases as frequency increases. This pattern is qualitatively consistent with the results of the model, the ATM, and the Ewans' empirical function but at a much larger rate of increase. For the event of northwesterly wind sea following the westerly swell (Fig. 10b), $\langle r_{Lobe}\rangle$ shows much weaker frequency dependence as compared to that in Fig. 14a. $\langle r_{Lobe}\rangle$ is higher than the curves of model, ATM and Ewans's results and remain almost constant at $f/f_p > 1.5$. Even though the general frequency dependent pattern of lobe ratio is not affected significantly by the presence of swell, the swell effect on the lobe ratio is more evident than those on the lobe separation angle. When the swell moves in the direction of the local wind, the frequency dependence of lobe ratio of wind sea is much weaker than that when the swell moves in the direction against the local wind.

4.4 Asymmetry of bimodal directional distribution

Young et al. (1995), Ewans (1998) and Wang and Hwang (2000a) observe asymmetric directional distributions of wind sea in conditions of limited swell influence. Wang and Hwang (2000a) report asymmetric bimodal distributions during two wave growth events at a nearshore buoy in the Lake Michigan. They suggests that inhomogeneous wind

fields due to land proximity, slant fetch effects, and difference in wind and wave directions all could contribute to the asymmetric wave directional distributions. For the bimodal directional distribution of wind sea in the presence of strong swell of the two events, the degree of directional distribution asymmetry varies. Figure 11 shows the bin-averaged skewness, $\langle\gamma\rangle$, versus f/f_p for the two events. For event of wind sea against swell (southeasterly wind sea and westerly swell), the directional distribution of wind sea is generally symmetric with $\langle\gamma\rangle$ near zero at $f/f_p <$ 2. For the event of wind sea following swell (northwesterly wind sea and the westerly swell), the directional distribution of wind sea is asymmetric with $\langle\gamma\rangle$ near –0.2. These various degrees asymmetry of bimodal directional distribution may be due to the direction-dependent swell modulation. Depending their relative directional separations with respect to the swell direction, the two wave systems concentrating at the two side lobes of the bimodal directional distribution could experience different levels of swell modulation effects. Based on a numerical simulation, Masson (1993) shows that the strength of the nonlinear coupling between wind sea and swell depend on the difference of their mean directions. Qualitatively, the wave system with direction generally following the swell direction will be significantly suppressed while the wave system with direction opposing to the swell direction will be enhanced. The wave system moves at a normal angle to the swell will have smallest modulation effect. The relative intensity and frequency separation between the wind sea and swell could also contribute to the variations.

5. SUMMARY

In this study, we present an analysis on the directional distribution of wind sea under the influence of swells. The directional wave data are acquired from a heave-pitch-roll buoy off the California coast during two strong wind wave growth events by the steady onshore and offshore winds in the presence of strong westerly swell. The study shows that the bimodal distribution of wind sea is a distinctive and persistent feature over a broad frequency range under various swell conditions. The characteristics of the directional bimodality are quantified by the parameters related to the separation angle and the amplitude of the sidelobes. In the presence of strong swell, the dependence of the directional parameters on frequency is in general qualitatively consistent with those observe in the absence of swell. The parameters of lobe separation angle and lobe ratio are smallest at the peak frequency and increase as frequency moves to both lower and higher frequencies. This frequency-dependent pattern is invariant to the presence of swells. The persistent nature of the directional bimodality of wind sea indicates that the nonlinear wave-wave interaction are not significantly affected by the swell modulation. The swell modulation could cause asymmetry in the bimodal directional distribution depending on the interaction direction between wind sea and swell. More quantitative comparisons will be presented in a later paper.

ACKNOWLEDGMENTS

This work is supported by the Office of Naval Research (Naval Research Laboratory Program Element N62435, "Phase Resolved Nonlinear Transformation of Shoaling Waves" NRL Contribution PP/7330-00-0050)

REFERENCES

Banner, M. L., and I. R. Young, 1994: Modeling spectral dissipation in the evolution of wind waves. Part I: Assessment of existing model performance. *J. Phys. Oceanogr.*, **24**, 1550-1571.

Benoit, M., 1992: Practical comparative performance survey of methods used for estimating directional wave spectra form heave-pitch-roll data. *Proc. 23rd Int. Conf. Coastal Eng.*, **2**, 162-75.

Cote, L. J., *et al.*, 1960: The directional spectrum of a wind generated sea as determined from data obtained by the Stereo Wave Observation Project. *Meteor. Papers, New York Univ.*, **2**, W. J. Pierson (ed.), 88 pp.

Dobson F.W., S.D. Smith, and R.J. Anderson, 1994: Measuring the relationship between wind stress and sea state in the open ocean in the presence of swell. *Atmos.-Ocean,* **32** (1), 237-236.

Donelan, M., 1987: The effect of swell on the growth of wind waves. *Johns Hopkins APL Tech. Dig.*, 8(1), 18-23.

Donelan, M. A., J. Hamilton, and W. H. Hui, 1985: Directional spectra of wind-generated waves. *Phil. Trans. Roy. Soc. Lond.*, **A315**, 509-562.

Donelan, M. A., W. M. Drennan and K. B. Katsaros, 1997: The air-sea momentum flux in conditions of wind sea and swell. *J. Phys. Oceanogr.,* **27,** 2087-2099.

Earle, M. D., 1996: Nondirectional and directional wave data analysis procedures. *NDBC Tech. Doc.*, 96-01, 35 pp.

Ewans, K. C., 1998: Observations of the directional spectrum of fetch-limited waves. *J. Phys. Oceanogr.,* **28,** 495-512.

Ewans, K. C. and T. Van der Vlugt, 1999: Estimating bimodal frequency-direction spectra from surface buoy data recorded during tropical cyclones. *J. Offshore Mech. and Arctic Eng.* **121**, 172-180.

Hasselmann, K., 1962: On the non-linear energy transfer in a gravity-wave spectrum. 1: General

theory. *J. Fluid Mech.*, **15**, 273-281.

Hasselmann, D. E., M. Dunckel, and J. A. Ewing, 1980: Directional wave spectra observed during JONSWAP 1973. *J. Phys. Oceanogr.*, **10**, 1264-1280.

Holthuijsen, L. H., 1983: Observations of the directional distribution of ocean-wave energy in fetch-limited conditions. *J. Phys. Oceanogr.*, **13**, 191-207.

Hwang, P. A., D. W. Wang, E. J. Walsh, W. B. Krabill, and R. N. Swift, 2000a: Directional wavenumber spectra of ocean surface waves. Part 2. Directional distribution. *J. Phys. Oceanogr.* (in press).

Hwang, P. A., D. W. Wang, E. W. Rogers, and J. M. Kaihatu, 2000b: A discussion on the directional distribution of wind-generated ocean waves. *Proc. 6th Int. Workshop on Wave Hindcasting and Forecasting*, (in press).

Jackson, F. C., W. T. Walton, and C. Y. Peng, 1985: A comparison of in situ and airborne radar observations of ocean wave directionality. *J. Geophys. Res.*, **90**, 1005-1018.

Kuik, A. J., G. Ph. Van Vledder, and L. H. Holthuisen, 1988: A method for the routine analysis of pitch-and-roll buoy wave data. *J. Phys. Oceanogr.*, **18**, 1020-1034.

Longuet-Higgins, M. S., D. E. Cartwright, and N.D. Smith, 1963: Observations of the directional spectrum of sea waves using the motions of a floating buoy. *Ocean Wave Spectra,* Prentice Hall, Englewood Cliffs, N. J., 111-136.

Lygre, A., and H. E. Krogstad, 1986: Maximum entropy estimation of the directional distribution in ocean wave spectra. *J. Phys. Oceanogr.*, 16, 2052-2060.

Masson, D, 1993: On the nonlinear coupling between swell and wind waves. *J. Phys. Oceanogr.*, 23, 1249-1258.

Mitsuyasu, H., et al., 1975: Observations of the directional spectrum of ocean waves using a cloverleaf buoy. *J. Phys. Oceanogr.*, **5**, 750-760.

Mitsuyasu, H., 1997: On the contribution of swell to sea surface phenomena. *Proc. 7th Int. Offshore and Polar Eng. Con.,* Honolulu, 1-7.

Oltman-Shay, J., and R. T. Guza, 1984: A data-adaptive ocean wave directional spectrum estimator for pitch-roll type measurements. *J. Phys. Oceanogr.*, **14**, 1800-1810.

Phillips, O. M., 1958: On some properties of the spectrum of wind-generated ocean waves. *J. Mar. Res.*, **16**, 231-240.

Phillips, O. M., 1985: Spectral and statistical properties of the equilibrium range in wind-generated gravity waves. *J. Fluid Mech.,* **156**, 505-531.

Steele, K. E., C. C. Teng, and D. W. Wang, 1992: Wave direction measurements using pitch-roll buoys. *Ocean Eng.*, **19**, 349-375.

Walsh, E. J., D. W. Hancock, D. E. Hines, R. N. Swift, and J. F. Scott, 1989: An observation of the directional wave spectrum evolution from shoreline to fully developed. *J. Phys. Oceanogr.*, **19**, 670-690.

Wang, D. W., and P. A. Hwang, 2000a: Evolution of the bimodal directional distribution of ocean waves. *J. Phys. Oceanogr.* (in press).

Wang, D. W., and P. A. Hwang, 2000b: An opertatona method for separating wind sea and swell from ocean wave spectra. *J, Atmos. Oceanic Technol.,* (submitted).

Young, I. R., and G. Ph. Van Vledder, 1993: A review of the central role of nonlinear interactions in wind-wave evolution. *Phil. Trans. Roy. Soc. Lond.*, **A342**, 505-524.

Young, I. R., L. A. Verhagen, and M. L. Banner, 1995: A note on the bimodal directional spreading of fetch-limited wind waves. *J. Geophys. Res.*, **100**, 773-778.

Table 1. Statistics of wind and wave measurements at the buoy station.

EVENT	**1**	**2**
Buoy ID	**46024**	**46024**
Duration (h)	15	8
Starting time (UTC/day/month/year)	0800/12/12/93	0900/14/12/93
Avg. wind speed (m s^{-1})	12.1	11.0
Avg. wave height, H_s (m)	3.6	4.7
Avg. swell peak period, T_p (s)	13.5	15.9
Avg. swell direction(°)	286	274
Avg. wind direction (°)	132	321
Avg. diff. wind & swell direction (°)	154	47

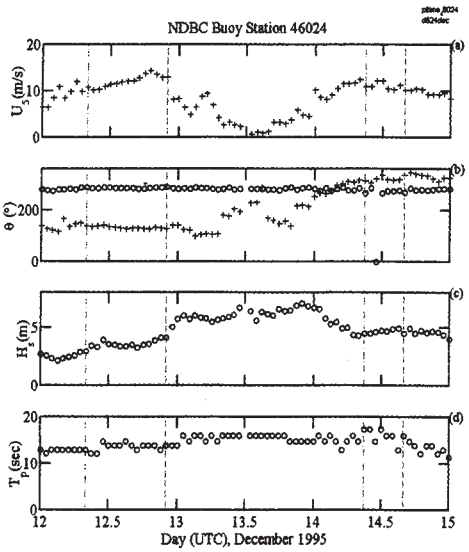

Fig. 1. Time series of hourly wind and wave measurements at the offshore buoy (ID 46024): (a) significant wave height H_s, (b) wind speed U, (c) wind direction θ_w (o) and peak wave direction θ_p (+), (d) peak wave period T_p . The vertical dashed-and-dotted and dashed lines, respectively, mark the beginning and the end of the two wave growth events used.

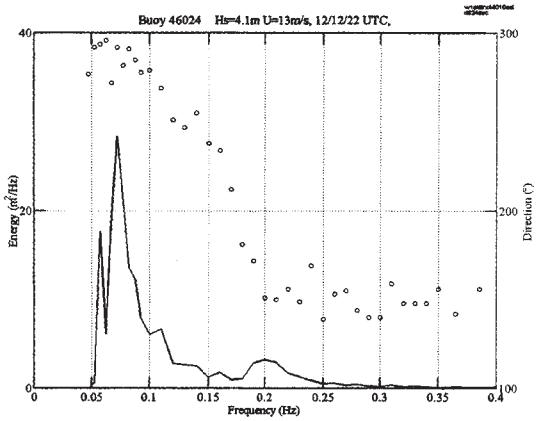

Fig 2. Wave energy spectrum (solid line) and the mean wave direction (circles) at 1200 UTC, December 12 1993, from the offshore buoy (ID 46024) when the westerly swell coexists with the southeasterly wind sea.

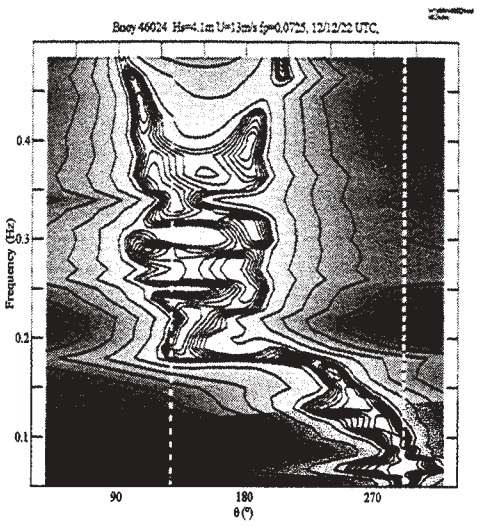

Fig. 3. Shaded image of the 2D directional distributions of the same hour as that in Fig. 2. The wind and peak wave directions are marked as dashed-and-dotted and dashed lines, respectively. The directional distribution is normalized by the maximum value at each frequency and displayed in logarithmic scale. Brighter image corresponds to higher level of the normalized distribution density.

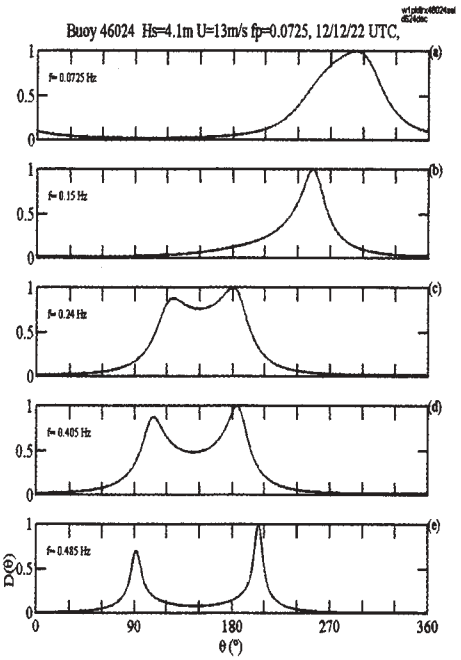

Fig. 4. Frequency slices from the 2D directional distribution at frequencies of 0.0725, 0.15, 0.24, 0.405, and 0.485 Hz (a-e).

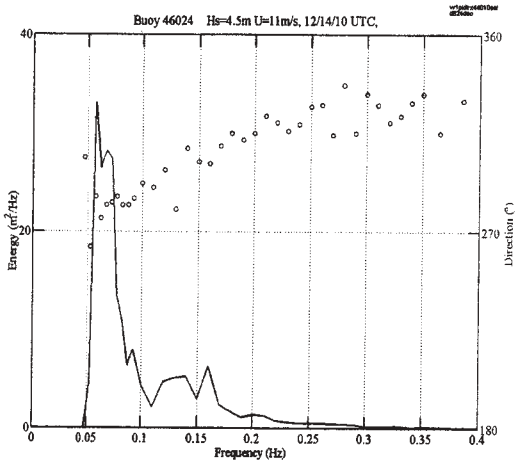

Fig 5. Wave energy spectrum (solid line) and the mean wave direction (circles) at 1000 UTC, December 14 1993, from the offshore buoy (ID 46024) when the westerly swell coexists with the northwesterly wind sea.

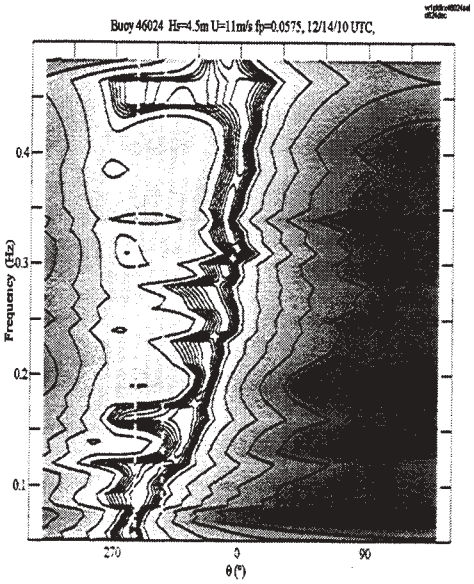

Fig. 6. Shaded image of the 2D directional distributions of the same hour as that in Fig. 5. The line styles and color image scales are the same as those in Fig. 3.

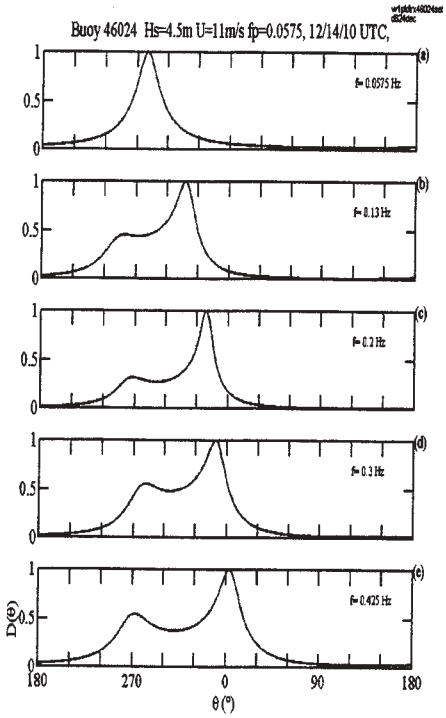

Fig. 7. Frequency slices from the 2D directional distribution at frequencies of 0.0575, 0.13, 0.2, 0.3, and 0.425 Hz (a-e).

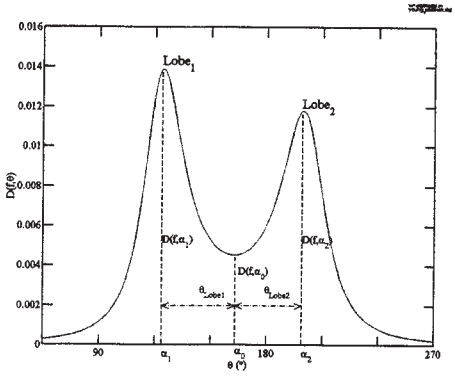

Fig. 8. Definition sketch of the parameters used to characterize the bimodal distribution.

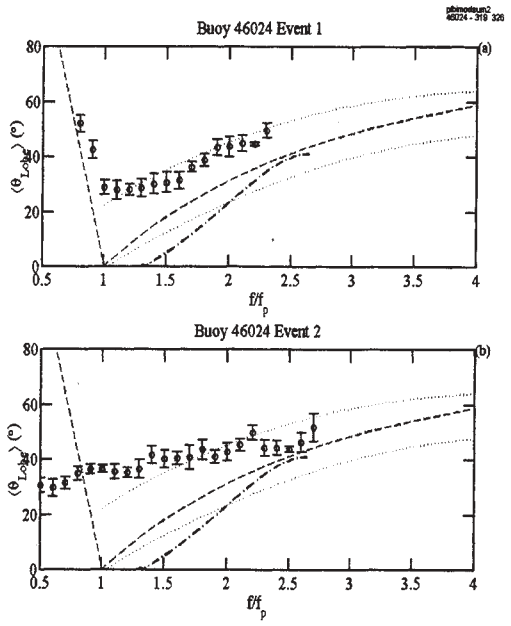

Fig. 9. Bin-averaged separation angle, $\langle\theta_{Lobe}\rangle$, versus f/f_p at the buoy 46024 for (a) Event 1 and (b) Event 2; The bin width is 0.2 f/f_p. The mean value of θ_{Lobe} is marked at the center frequency of each bin as an open circle, the error bar represents one standard deviation. Dashed curve: the model results (Young et al. 1995; Ewans 1998), dashed-and-dotted curve: the ATM results (Hwang et al. 2000a), dotted curves: the upper and lower bounds of the Maui data (Ewans 1998).

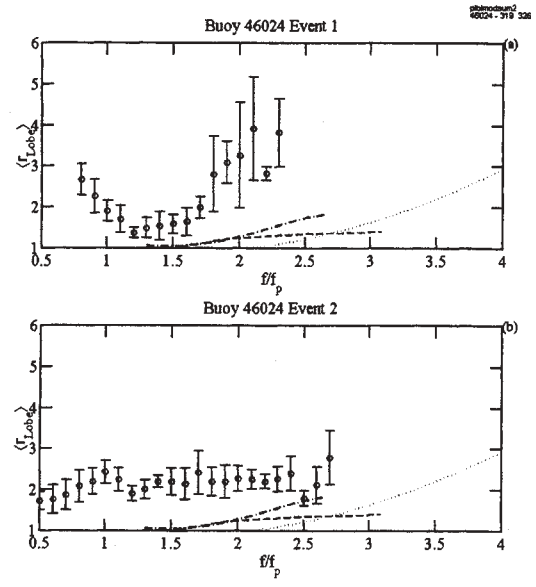

Fig. 10. Bin-averaged lobe ratio, $\langle r_{Lobe}\rangle$, versus f/f_p at the buoy 46024 for (a) Event 1 and (b) Event 2; The bin width, symbols and line styles are the same as those in Fig 9.

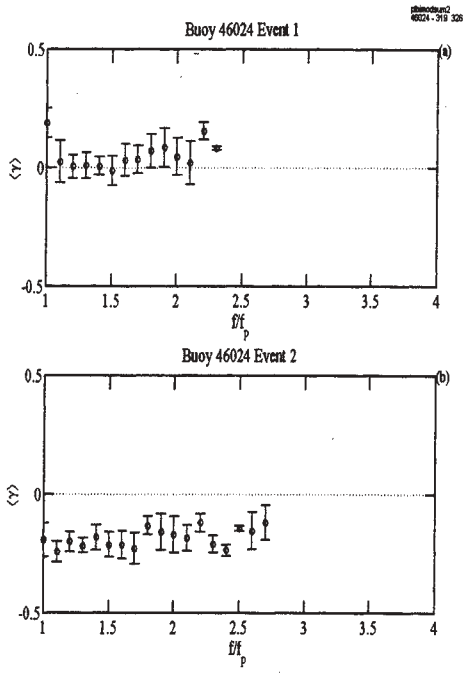

Fig. 11. Bin-averaged skewness, $\langle\gamma\rangle$, versus f/f_p. at the buoy 46024 for (a) Event 1 and (b) Event 2; The dotted lines indicate $\langle\gamma\rangle$=0 for symmetric directional distribution. The bin width and symbols are the same as those in Fig 9.

Validation of the Doppler Shifted Dispersion Relation for Waves in the Presence of Strong Tidal Currents, using ADCP Wave Directional Spectra and Comparison Data.

B. Strong and B. Brumley
RD Instruments
9855 Business Park Ave.
San Diego, CA, USA 92131
Bstrong@rdinstruments.com

E.A. Terray
Department of Applied Ocean Physics and Engineering
Woods Hole Oceanographic Institution
Woods Hole, MA, USA 02543

N. C. Kraus
U.S. Army Corps of Engineers
CEERD – HC, 3909 Halls Ferry Rd.
Vicksburg, MS, USA 39180

1. Introduction

Waves propagating through regions of strongly varying mean flows, such as occur at the edges of ocean boundary currents, or the mouths of harbors and estuaries, are modified substantially by their interaction with the flow (this is nicely illustrated by Figure 1, which shows ADCP observations taken off the southern coast of England near Eastbourne, Sussex). The sea states that result, particularly in the case of adverse waves and currents, can be a hazard to mariners, present challenges in the design of coastal structures, and are active transporters of sediment in the nearshore region. Wave-current interaction has been investigated in the laboratory (Thomas, 1981), and several authors (Battjes, 1982; Gonzalez, 1984) have studied it in the field (interestingly, neither of the latter studies included direct measurements of near-surface currents, relying instead on tidal models to provide this information).

Although originally developed for current measurement,, upward-looking acoustic Doppler current profilers (ADCPs) have proven also to be useful for sensing waves. Recent work has demonstrated that they are capable of measuring the frequency-directional distribution of surface waves with a fidelity equivalent, and in many cases superior, to those obtained from bottom-mounted PUV wave gages (Strong *et al.*, 2000; Terray *et al.*, 1999, 1997 1990; Gordon *et al.*, 1998; Hashimoto, 1997). A unique strength of this approach is that a single compact instrument yields simultaneous information about the waves in conjunction with full water column profiles of the current.

In this contribution we show that both kinematic and dynamic aspects of the modulation of waves by currents can be seen in measurements obtained from an ADCP "Wave Gage". Our purpose is to illustrate, by means of a few examples, the utility of this sensor for addressing questions related to wave-current interaction. We conclude the paper with a slightly different application, in which we use time series of measured wave height spectra to estimate the direction, range and duration of distant storm events.

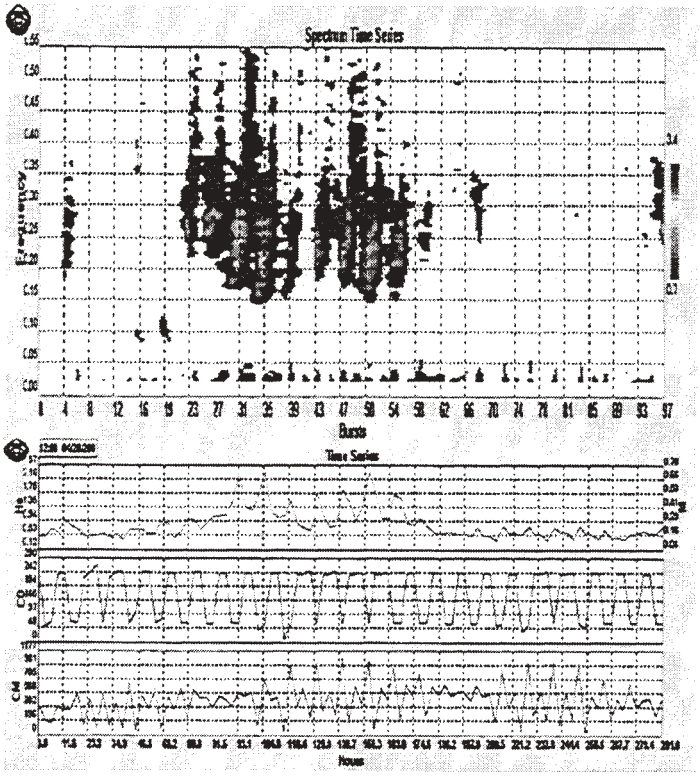

Figure 1. ADCP data showing the modulation of wave amplitude by tidal currents. Top panel: spectrogram of wave height (time is in 4 hr. "bursts"). Bottom panel: time series of significant height H_s (ft), current direction CD (degT), and current magnitude CM (mm/s). The water depth was 5m.

2. Kinematics of Waves on Currents

The dispersion relation for waves travelling on a vertically-sheared current U(z) has been analyzed by Kirby and Chen (1989) for the case of weak currents. Expanding in terms of the small parameter ε=U/c, where c is the wave phase speed, they found that through O(ε)

$$(\omega - kU\cos\alpha)^2 = gk\tanh(kH) \qquad (2.1)$$

where ω and k are the bottom-relative radian frequency and wavenumber (*i.e.* those observed in a fixed reference frame), H is the water depth, and α denotes the included angle between the directions of wave propagation and the current. Note that equation (2.1) is just the usual dispersion relation for arbitrary water depth applied to the frequency observed in a reference frame moving with the current (*i.e.* the *intrinsic* frequency ω-**k**·**U**). Kirby and Chen show that at this order U should be taken to be the depth average of U(z) over the normalized energy distribution of the waves

$$U = \int_{-H}^{0} dzE(\omega,z)U(z) \Big/ \int_{-H}^{0} dzE(\omega,z)\ . \qquad (2.2)$$

We remark that the ADCP is particularly useful in this regard because it can measure the current profile over the region in which wave energy is concentrated.

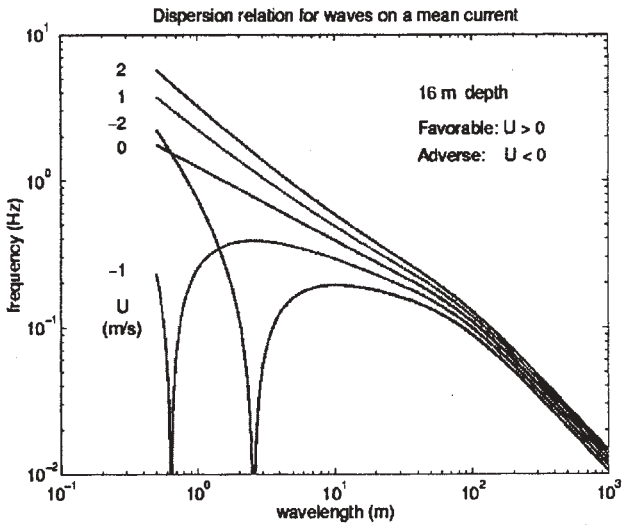

Figure 2. Relation between wavenumber and measured frequency in 16 m water depth for co-linear waves and currents (with and against), and current speeds between ±2 m/s.

We plot the dispersion relation (2.1) in Figure 2. When the current flows in the same direction as the waves (U>0) there is a unique solution for k at each frequency. For adverse currents (U<0) the frequency ω(k) vanishes for waves having a phase speed ω/k equal to the current speed, and has a local maximum for the wave whose group velocity dω/dk equals U. For frequencies above this local maximum the solution for the wavenumber k(ω) is seen to be unique, whereas at lower frequencies there are three solutions. In the latter case we use the smallest wavenumber solution since we are interested in the energy-containing part of the spectrum. The dispersion relation is used in several ways. We estimate the wave directional spectrum by the Iterative Maximum Likelihood Method (Krogstad *et al.*, 1988) which requires a model of the ADCP response, H(**k**), to a monochromatic wave propagating at an arbitrary angle. Consequently at each frequency we compute k(ω,α) over all angles from 0–360° (typically in 4° increments), and use this to determine the response function H. To calculate the non-directional spectrum of surface displacement from either pressure or orbital velocity we use the wavenumber $k_p(\omega)$ corresponding to the direction α_p of the dominant wave at that frequency. Use of the correct wavenumber is important when computing spectra of surface displacement from subsurface pressure or velocity measurements. For example, in the case of a bottom-mounted pressure gage, the Fourier amplitudes of wave height and pressure are related (via linear theory) by

$$\hat{p}(\omega \mid z=-H) = \rho g\hat{a}(\omega)\cosh(kH)\ . \qquad (2.3)$$

Hence the amplitude spectrum of wave height, A(ω), estimated using the true wavenumber, k, and the corresponding quantity $A_o(\omega)$, computed from equation (2.3) using the wavenumber k_o obtained from (2.1) when the current is neglected, are related by

$$A(\omega)/A_0(\omega) = \cosh(kH)/\cosh(k_0H)\ . \qquad (2.4)$$

In the case of a favorable current (U > 0), Figure 2 shows that $k < k_o$, so that $A < A_o$. The situation is reversed for an adverse current (U < 0), in which case $A > A_o$.

3. Grays Harbor Data

We illustrate the kinematics and dynamics of waves riding on currents using data collected during two deployments of a bottom-mounted ADCP at Grays Harbor, WA (roughly 46.8°N, 124.2°W – see Figure 3). The first deployment took place from 13 September through 11 October, 1999 near the mouth of the harbor in a nominal water depth of 17m, and included a co-located ADV (PUV-type) wave gage. For the second deployment (15 October - 15 November, 1999) the ADCP was placed on the bottom farther east into the channel at 15 m depth. In both deployments data were collected every four hours in bursts of roughly 34 minutes (4096 points at a 2 Hz sample rate). The maximum current in the first data set was roughly 1 m/s, reaching almost 2m/s during the second deployment.

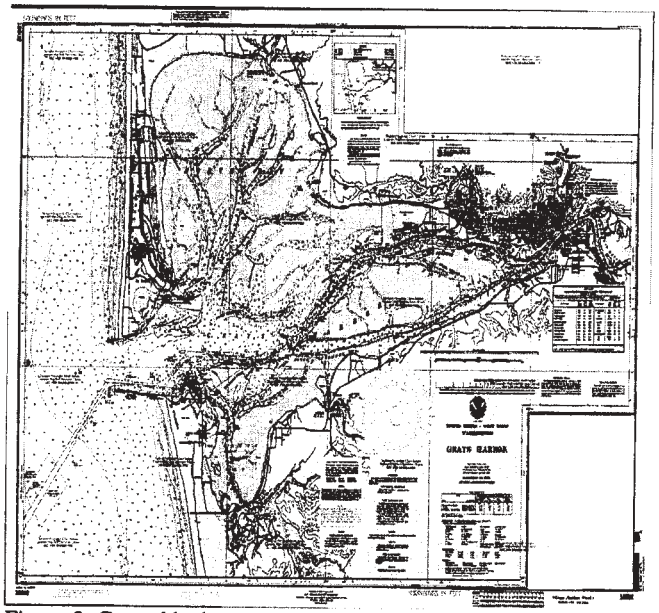

Figure 3. Coastal bathymetry in the vicinity of Grays Harbor, WA. The shore normal is approximately 260°T.

4. Observations of Wave Kinematics

Time series of significant wave height, peak period, peak direction, and tidal excursion during the first deployment are shown in Figure 4. The time series of significant height is seen to be modulated at the tidal period, although the degree of modulation is less than that shown in Figure 1 due to the relatively longer wavelengths of the waves in this case. A similar periodicity is also evident in the spectrogram of wave height shown in Figure 5. A careful examination of that figure shows that the spectrum at higher frequencies is enhanced during outgoing (ebb) and reduced during incoming (flood) tides.

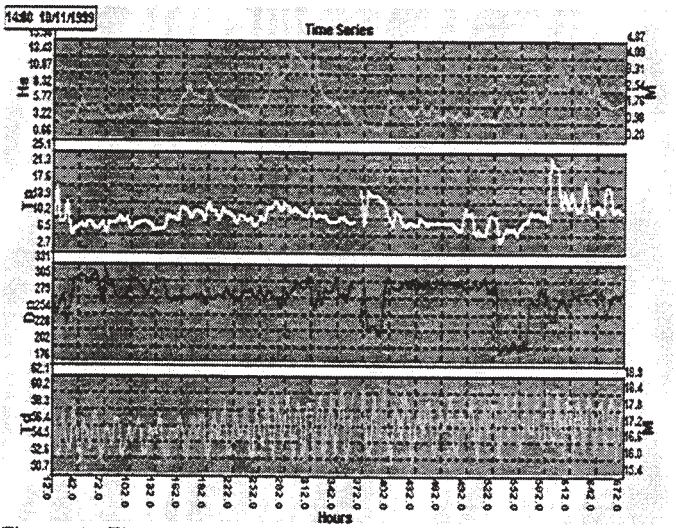

Figure 4. Time-series of significant wave height (Hs, ft), peak period (Tp), peak direction (Dp, degrees), and tidal elevation (Td, ft) as a function of time (hours). The right-hand scale gives wave height and tidal elevation in meters.

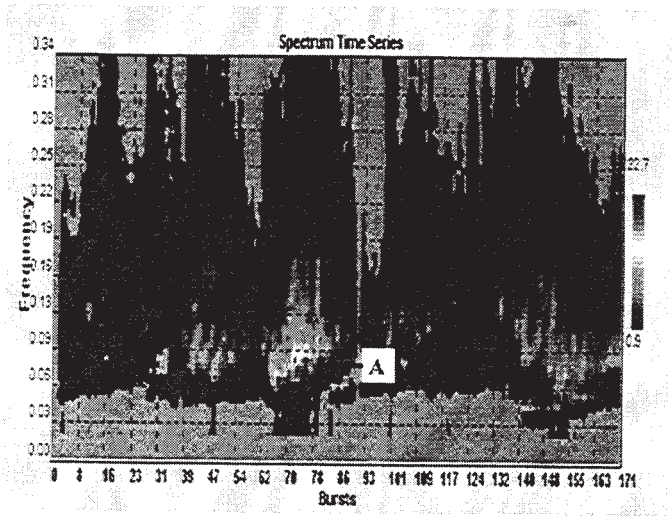

Figure 5. Spectrogram of wave height computed from 34 minute bursts of data taken every 4 hours.

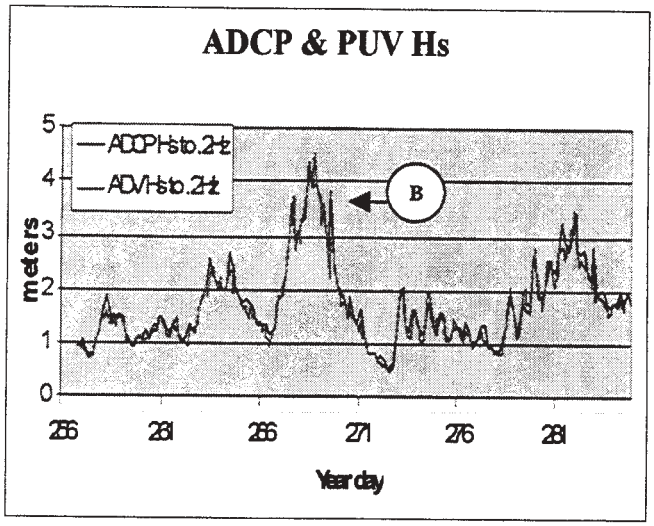

Figure 6. Time-series of significant wave height computed from frequency components below 0.2 Hz. The ADCP estimate was obtained from range cells close to the surface, and wave height was estimated using the correct wavenumber. The presence of a current was not included in the analysis of the ADV-PUV measurements.

The first Grays Harbor deployment included a co-located ADV-PUV directional wave gage. The PUV data were analyzed using software that did not account for the presence of the tidal current. Although the ADCP-derived wave parameters compared well most of the time with those estimated from the PUV gage (Strong, *et al.*, 2000), there were discrepancies during periods of maximal current. This can be seen in Figure 6 which shows the significant wave height for waves with frequencies below 0.2 Hz estimated from both the ADCP and PUV sensors. The difference between these two estimates is shown in Figure 7, where it is seen to correlate strongly with the tidal current.

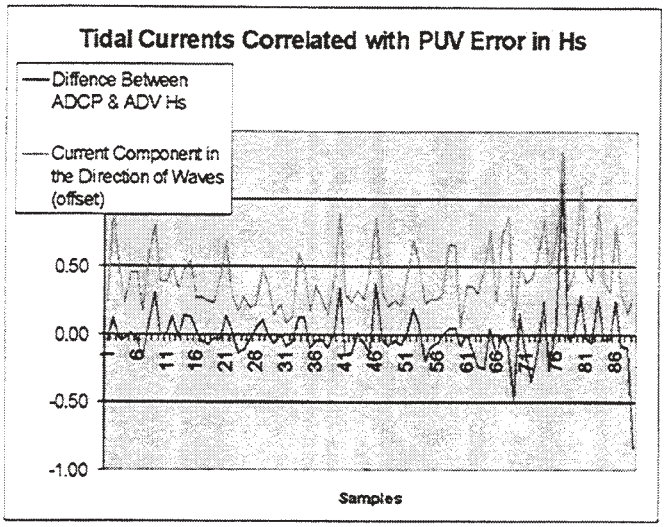

Figure 7. The difference between ADCP and PUV estimates of significant wave height shown in Figure 6. The component of the tidal current in the direction of the waves is also shown (this curve has been shifted upward, and the scale is arbitrary).

We focus on a case where the disagreement between the two sensors is large. This is marked "B" in Figure 6, and occurred at 1400 PDT on 26 September, 1999. Figure 8, below, shows the measured current profile and wave direction for this burst.

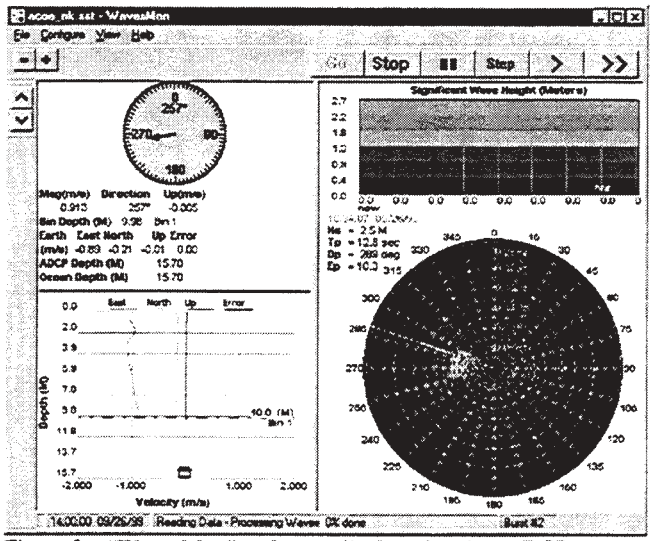

Figure 8. "WavesMon" software display showing ADCP currents and waves for the burst at 1400 (PDT) on 26 September, 1999.

The depth-averaged current is flowing west out of the harbor at roughly 1 m/s. The shear at depths below 3 m is close to linear with a value of roughly 4×10^{-2} s^{-1}. This extrapolates to a near-bed velocity of 0.5 m/s, which is in agreement with the average velocity measured by the co-located PUV gage. Current shear contributes directly to the dispersion relation. For a linear shear, the right hand side of equation (1.1) is multiplied by a factor $[1-(c-U_s)\nabla U/g]$, where ∇U denotes the vertical shear, and U_s is the current at the surface (Kirby and Chen, 1989). In our case,

$$|(U_s-C)\nabla U/g| < 5\times10^{-2} << 1\ ,$$

and therefore the direct effect of shear can be neglected. However, shear has another implication when the only estimate of the current available has been obtained near the bed. As an illustration, using a current speed of 0.5 m/s instead of 1 m/s in the dispersion relation (in 17m water depth) produces wavenumbers in error by 6%, 19% and 46% at frequencies of 0.1, 0.2, and 0.3 Hz, respectively. This example shows that even for the case of modest shears, using a measurement of the current near the bed can introduce significant errors.

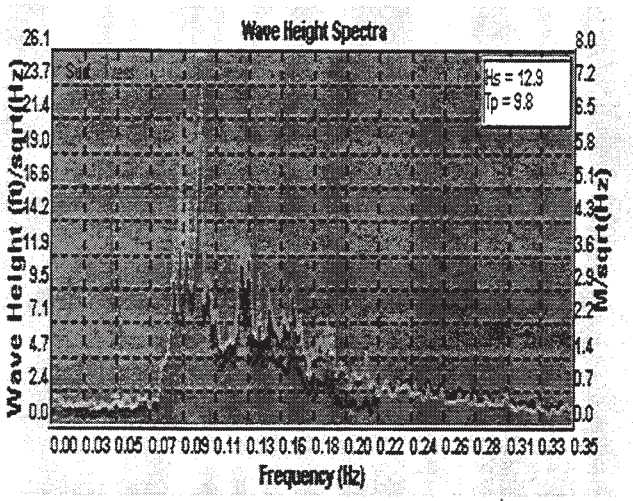

Figure 9. Estimates of the amplitude spectrum (ft/√Hz) of surface displacement derived from surface echolocation and subsurface orbital velocities (both extend over all frequencies shown), and pressure (to 0.21 Hz) during an adverse (ebb) current of 1 m/s. The presence of a current has been neglected in computing surface spectra from the pressure and velocity measurements.

The ADCP Wave Gage yields three independent estimates of the non-directional wave height spectrum based on pressure, orbital velocity, and echo-location of the surface ("surface-track"). Note that echo-location is a direct measurement of the surface and does not depend on knowing the correct wavenumber.

The wave height spectra derived from these measurements, but neglecting the current, are shown in Figure 9. The pressure measurement (taken at 17m depth) is seen to underestimate the true height spectrum in an adverse current. The magnitude of the discrepancy is a function of frequency, in agreement with our earlier discussion in connection with equation (2.4). For example, in a co-linear adverse current of 1 m/s, 17 m water depth, and for a frequency of 0.18 Hz, we find $k = 0.175m^{-1}$, and $k_o = 0.133m^{-1}$. Applying equation (2.4) gives $A/A_o \sim 2$, which is in reasonable agreement with the ratio of echolocation to pressure-derived amplitude

spectra shown in Figure 9. In contrast, at 0.1 Hz, we compute $k = 0.062 m^{-1}$ and $k_o = 0.055\ m^{-1}$, so that $A/A_o \sim 1.1$, a value also in agreement with the observations. Although wave height spectra also should be computed from ADCP velocity measurements using the correct wavenumber, in this case the velocity measurements were taken at depths of 1, 2 and 3 m, and hence are relatively insensitive to the effect of the current.

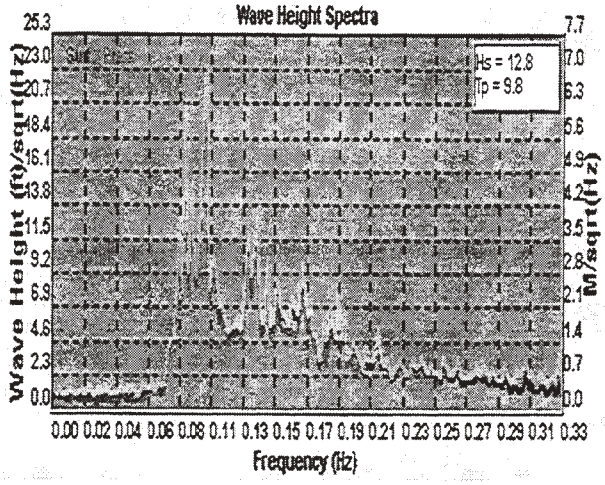

Figure 10. Amplitude spectra as in Figure 8, but the pressure and velocity data now have been converted to surface spectra using the current-dependent wavenumber determined from equation (2.1).

Figure 10 shows the result of using the Doppler corrected wavenumber in the conversion of pressure (and velocity) to wave height at all frequencies. The agreement between the three measurements is excellent, validating equation (2.4).

Table 1. Significant Wave Height on 09/26/99 at 1400 PDT

ADCP Corrected for Currents with 0.35 Hz. cut-off	3.95 m
ADCP Corrected for Currents with 0.22 Hz. cut-off	3.87 m
ADCP Not Corrected for Currents with 0.22 Hz. Cut-off, Using Pressure	2.87 m
ADV Not Corrected for Currents with 0.22 Hz. Cut-off, Using Pressure	2.94 m
Buoy (not co-located)	2.46 m

Although the Doppler correction of the wavenumber mainly affects the higher frequencies in the spectra, its integrated effect on the estimation of significant wave height is not negligible. This is illustrated in Table 1, from which we conclude that when the current is strong, neglecting it can introduce a significant error into the estimate of H_s derived from pressure measurements at the bed.

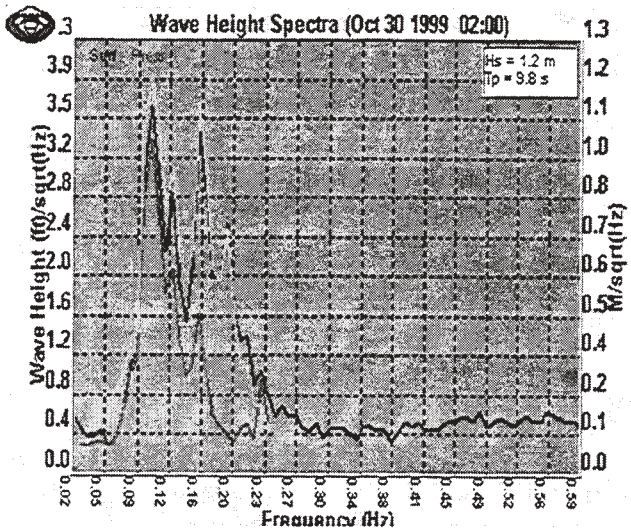

Figure 11. Estimates of the amplitude spectrum (ft/√Hz) of surface displacement derived from surface echolocation (all frequencies), subsurface orbital velocities (to 0.25 Hz), and pressure (to 0.2 Hz) during an adverse (outflow) current of 1.7 m/s.

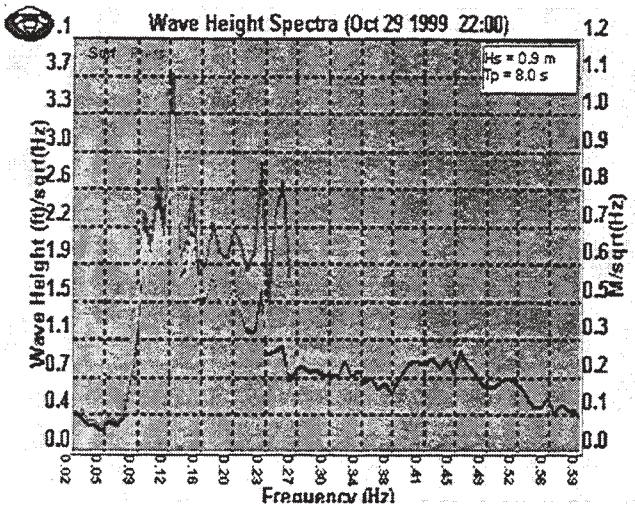

Figure 12. As in Figure 11, but estimated during a favorable (inflow) current of 0.9 m/s.

Figures 11 and 12 show another example of wave height amplitude spectra derived from the pressure, velocity and surface-track by neglecting the effect of the current on the wavenumber. The pressure-derived height is seen to underestimate the true spectrum when the waves and currents are adverse, and to overestimate it when the current is flowing in the same direction as the waves. This behavior is in accord with our conclusions following equation (2.4).

5. Dynamics of Waves on Currents

So far we have only considered kinematic effects, such as the change in wavelength. To determine amplitude changes requires consideration of the dynamics. This problem has been addressed using field observations by Battjes (1982) and Gonzalez (1984). We follow the latter reference here. Energy does not provide the required relation, since the energy of waves propagating through an inhomogeneous current is not conserved due to the rate of working on the current by the wave ("radiation") stresses. However, if the variation of the current is slow compared to the scale of the waves (*i.e.* the system is only weakly nonlinear) a related quantity, the wave action $\Lambda=E/\sigma$, is conserved (here E denotes the wave energy density computed from linear theory, and $\sigma = \omega-\mathbf{k}\cdot\mathbf{U}$ is the intrinsic frequency). We write this as

$$\frac{\partial \Lambda}{\partial t} + \nabla \bullet \left[\left(\mathbf{U} + \mathbf{c}_g \right) \Lambda \right] = 0 \qquad (5.1)$$

where $\mathbf{c}_g$ is the group velocity $d\sigma/dk$. Then $\mathbf{U}+\mathbf{c}_g$ is the propagation velocity of energy or action in a fixed reference frame (*i.e.* relative to the bottom). The time scale, T, for temporal changes in action density is roughly a tidal period. Hence $\partial\Lambda/\partial t$ can be neglected relative to the flux divergence if the spatial scale of the current, L, is much less than $c_gT \sim O(200)$ km. We assume that this condition is satisfied, and neglect the time dependent term. Making the further assumption that the flux balance is approximately one-dimensional, we find that the local (E) and offshore (E_o), energy densities are related by

$$\frac{E}{E_0} = \frac{U_0 + c_{g0}\cos\vartheta_0}{U + c_g \cos\vartheta} \frac{\sigma}{\sigma_0} \qquad (5.2)$$

where ϑ and ϑo are the angles, respectively, between the wave propagation directions and the shore normal at the local and offshore locations which, by definition in this case, coincides with the direction of the current (Gonzalez, 1984). These angles are related by refraction due either to the bathymetry or the current.

Since we do not have simultaneous measurements of the unperturbed waves (in the absence of currents), it is not possible to use our data to make a direct test of equation (5.2). Instead we use the latter relation to estimate what the offshore wave energy must have been in a region with negligible current ($U_o = 0$, $\sigma_o = \omega$, and $c_{go} = \omega/2k_o$). Assuming the action is conserved, and the system one-dimensional, we expect the offshore energy E_o to be independent of the local current. The result of this exercise, applied to a narrow band of waves centered at 0.3 Hz, is shown in Figure 13.

Note that changes in wave amplitude due to bottom refraction, while contained in the general equation (5.1), are not important for waves of this frequency since, even at the location of the ADCP, they are not depth limited. It is evident that whereas the local enegy exhibits a tidal modulation, much of this signature has been removed from the estimate of the offshore energy. The residual modulation can be due to several factors not accounted for in our simple calculation. First, we used the component of the current in the direction of the dominant wave, rather than the mean direction of the waves in the frequency band around 0.3 Hz. This appears to be a reasonable approximation for many of the spectra, but has not been checked thoroughly. Second, equation (5.2) is based on a one-dimensional model, and neglects lateral current variation (see Battjes, 1982, for a discussion). Third, we do not include wind forcing of either the waves or currents (for action to be conserved, the combined wave-current system be stationary). Fourth, there might be a non-negligible offshore tidal current that is coherent with the flow at our measurement site. Fifth, although bottom-refraction for waves in this band is not important, U/c~0.2, so that refraction by the current might be important. Lastly, we used the mean current rather than using the vertical-weighting given by equation (2.2). The sensitivity of our result to these factors has not been explored. However, the simple analysis here removes much of the tidal modulation, suggesting that the effects listed above amount to a relatively small correction.

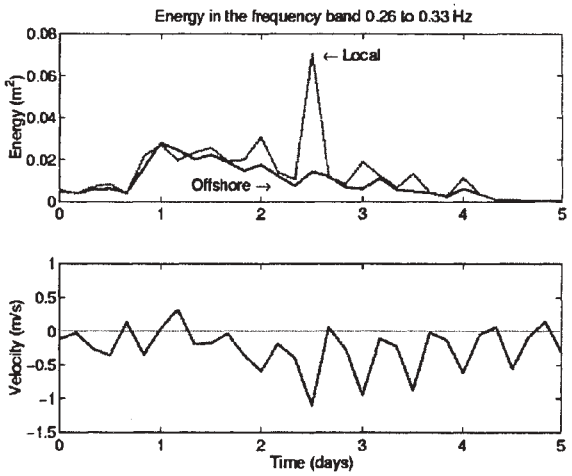

Figure 13. Top panel: Offshore energy E_o (*i.e.* in deep water with negligible current) of waves in the frequency band 0.26-0.33 Hz deduced from the locally-measured energy E using equation (5.2). Note that offshore energy was calculated and then band-averaged. Bottom panel: Component of the local current in the dominant wave direction. U < 0 represents an adverse (outgoing) current.

6. Refraction Due to Bathymetry

"Point" wave direction sensors, such as PUV triplets and directional buoys (either 3-D acceleration, or pitch-roll-heave) yield estimates of the first three (complex) coefficients in the Fourier expansion of the directional distribution, and hence these sensors cannot resolve multidirectional spectra without additional modeling assumptions.

In contrast, the ADCP measures wave velocities at a number of horizontal positions (and depths) within the wave field. The collection of these measurement volumes constitutes a compact spatial array from which the directional distribution of the waves can be estimated by applying the Iterative Maximum Likelihood Method (Krogstad *et al.*, 1988) to "invert" the forward model for the expected array cross-spectra. As a result, for the frequencies encountered here, the ADCP wave gage produces relatively high directional resolution (this, of course, is also a function of the analysis technique), and as a result resolve multimodal directional distributions (within a given frequency band).

The utility of the ADCP for studying wave refraction is illustrated by Figure 14, which shows the average directional distribution of the waves over the period 2-5 October, 1999. An energetic band of waves (at frequencies above 0.1 Hz) arriving from the northwest (~305°T) is evident, as well as a second weaker system from a more southerly direction (~210°T). The very longest waves have been turned to propagate in the shore-normal direction (~260-265°T).

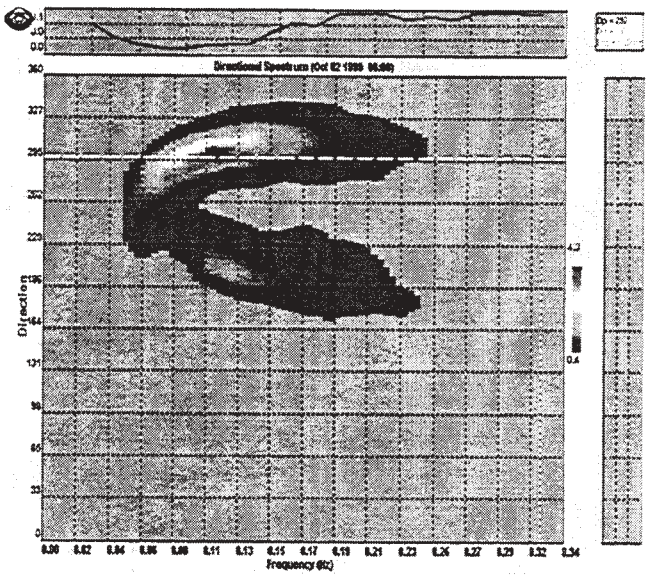

Figure 14. Average ADCP directional spectrum from Grays Harbor in 17m water depth for the period 2-5 October, 1999. The shore normal is approximately 260-265°T.

Although properly speaking, to model this result one should integrate the ray equations from deep water to the nearshore measurement site, in practice the shelf is relatively narrow and consequently Snell's law provides a reasonable first order approximation. We assume that the local depth contours are straight. Then the component of the wavenumber along the contours is constant, and therefore

$$k \sin \vartheta = k_0 \sin \vartheta_0 \qquad (6.1)$$

where (k_o,ϑ_o) and (k,ϑ) are respectively the offshore and local wavenumber and propagation directions (relative to the shore normal). We take the water depth to be 17 m, and use a coastline normal of 265°T. The offshore direction of each of the two wave systems observed in Figure 14 is taken to be the direction of the higher frequency waves. Equation 6.1 is then employed to determine the local wave direction at lower frequencies. The result, shown in Figure 15, is seen to be in reasonable agreement with the data. From the figure it appears that the waves are independent of the bathymetry for wave frequencies above roughly $0.25\sqrt{g/H}$ ~ 0.2 Hz.

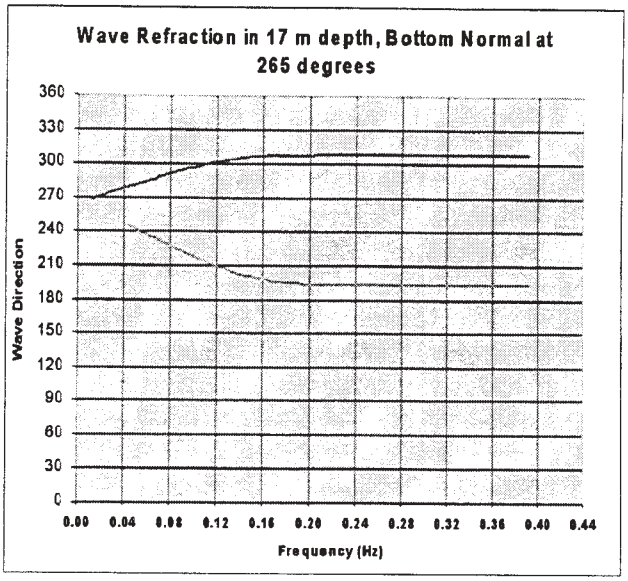

Figure 15. Modeled refraction computed using Snell's law for the wave systems shown in Figure 14.

7. Dispersive Propagation

Because gravity waves in all but the shallowest waters are dispersive, waves generated by a distant storm will arrive in a temporal succession that is determined by their group velocity (and hence frequency), with the lower frequencies preceding the higher. This phenomenon was pointed out, and thoroughly studied, in the pioneering work of Munk *et al.* (1963), and Snodgrass *et al.* (1966). The latter investigators set up a series of observing stations across the Pacific from New Zealand to Alaska, and were able to track swell generated in the Southern Ocean as it propagated northward along a great circle into the Gulf of Alaska.

Following the development in Munk *et al.* (1963), the propagation time T for a wave of frequency f to travel a distance R is

$$T(f) = R/C_g = (4\pi R/g)f \qquad (7.1)$$

where we have used the deep water form of the group velocity C_g. The travel time for waves to arrive is given by T(f=0). Alternatively viewing (7.1) as a relationship for f(T), we define the slope S = df/dT. Then the range to the generation region is given by

$$R = g/(4\pi S) = (67.4 \text{ km-Hz/day})/S \quad . \qquad (7.2)$$

In this section we identify the dispersive propagation of waves generated (we hypothesize) by a distant storm. The data we examine are the group of arrivals marked as "A" on Figure 5. Various frequency components arrive over roughly a 4-5 day interval from 24-28 September, 1999 (spanning bursts 63-89). A plot of the peak frequency of the non-directional spectrum as a function of time (measured every four hours) is shown in Figure 16. A least squares fit to the data gives a slope S of 1 Hz per 119 days. This gives a range of roughly 8800 km, and a propagation time of 9 days for the lowest frequency waves, which first arrived at 1300Z on 24 September. Taking a deep-water direction of 281°T, we use spherical geometry to estimate that the storm was located slightly west of Guam around 13°N, 140°E.

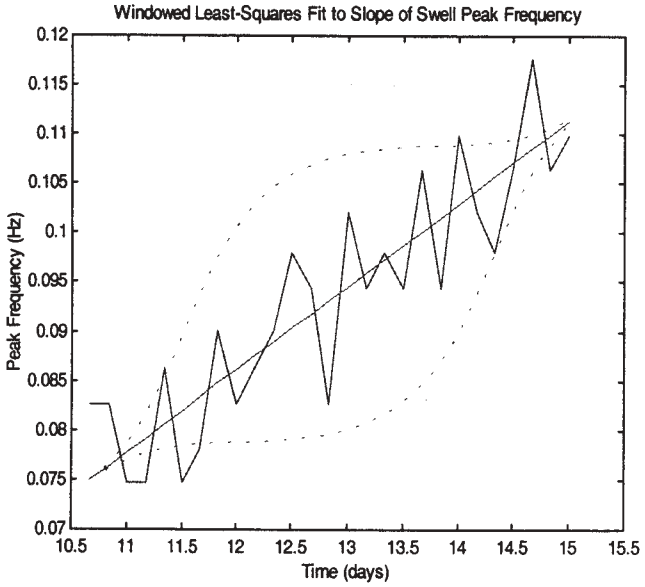

Fig. 16. Least-squares fit to slope of ridge, using the peak frequency of the non-directional spectrum measured every four hours. A cosine-squared weighting window (indicated with dashed lines) was applied to make the estimate insensitive to the choice of endpoints. Day 10.5 is 9/24/99, and the first data point shown corresponds to burst 63 in Figure 5.

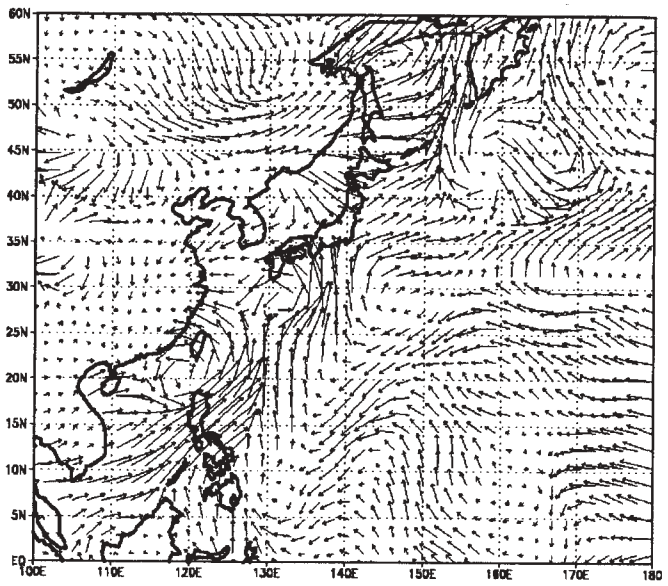

Figure 17. 12-hour average 10 m wind vectors for 1200Z September 13 taken from the 1999 NCEP/NCAR Reanalysis CD-ROM (Kalnay *et al.*, 1996). A moderate wind event can be seen in the eastern Pacific around 15°N, 125°E. This figure was produced using the GrADS visualization package v1.4 (Doty, 1994).

We used the NCEP/NCAR reanalysis output (Kalnay, 1996) to look for a possible generation event. There was a moderate cyclonic disturbance with 20-30 kt winds in the vicinity of the Phillipines lasting from September 11-14. This is somewhat earlier and farther west than our earlier estimate of the source location. However, Snodgrass *et al.* (1966) noted that arrivals typically build up in amplitude over several days before reaching a plateau. Therefore this weather pattern might still be consistent with the data shown in Figure 5, although a detailed analysis of the time dependence of amplitude, which we have not carried out, would be required to determine this. Lastly, we note that the NCEP/NCAR output indicates several intense storms in the eastern Pacific during the period 15-23 September. The effect of these wind fields on the propagation of the waves is unknown, and adds a considerable degree of ambiguity to our conclusions as to their origin.

We close by noting that another example of disperive propagation is provided by the very long waves seen at the start of the data shown in Figure 5 (spanning bursts 4-24). The shallower slope of the f(T) curve in that case suggests waves arriving from the southern hemisphere. The frequency changes from .050 Hz to .075Hz over a period of 108 hours, and a range calculation places the storm at a distance of about 13000 ± 1000 km. Waves in this frequency range will experience substantial refraction due to the bottom. Applying a refraction model to the observed direction of 240°T (and assuming a coast normal of 260°T), gives a deep water direction of about 190°T.

8. Conclusions

We have used observations of waves and currents obtained with an ADCP to illustrate several aspects of wave-current interaction. Our measurements show that the kinematic effect of the change in wavelength of waves riding on currents must be accounted for in order to obtain the correct wave height spectrum from subsurface pressure or velocity measurements. In addition, there is a dynamical effect whereby the waves are changed in amplitude through their interaction with the current. We have shown that in a tidally-driven current regime the observed modulation of wave amplitude at the dominant tidal frequency can largely be explained by this mechanism. We have also shown that because of its directional resolution, an ADCP wave gage is a useful tool for studying refractive effects. Lastly we have revisited the dispersive arrival of waves from a distant storm.

Acknowledgments

We thank Drs. K.R. Stapleton and S. Redford of Emu Environmental Ltd. for permission to include Figure 1. N.C. Kraus acknowledges permission by Headquarters, U.S. Army Corps of Engineers, to publish this information supported by the Coastal Inlets Research Program. E. Terray was partially supported by NSF grant OCE-9811316, and ONR grant N00014-97-10483. This is WHOI contribution number 10326.

References

Battjes (1982): A case study of wave height variations due to currents in a tidal entrance. *Coastal Engr.*, **6**, 47-57.

Doty, Brian (1994): GrADS (Grid Analysis and Display System), v.1.4. Center for Ocean-Land-Atmosphere Interactions, Institute of Global Environment and Society, 4041 Powder Mill Rd., Suite 302, Calverton, MD 20705-3106. http://grads.iges.org/ (192.239.84.50).

Kalnay, E., M. Kanamitsu, R. Kistler, W. Collins, D. Deaven, L. Gandin, M. Iredell, S. Saha, G. White, J. Woollen, Y. Zhu, A. Leetmaa, R. Reynolds, M. Chelliah, W. Ebisuzaki, W. Higgins, J. Janowiak, K. C. Mo, C. Ropelewski, J. Wang, Roy Jenne, and Dennis Joseph, (1996): The NCEP/NCAR 40-Year Reanalysis Project. *Bull. Am. Met. Soc.*, **77**(3), 437-471. NCEP/NCAR Reanalysis CD-ROM: 1999.

Gonzalez, F.I. (1984): A case study of wave-current-bathymetry interactions at the Columbia River entrance. J. Phys. Oceanogr. , **14**, 1065-1078.

Gordon, R.L., E. Terray and B. Brumley (1998): Observing wave height and direction with conventional (Janus-style) ADCPs. *Proc. Oceanology International'98*, **2**, 261-269, ISBN 0 900254 21 1.

Hashimoto, N. (1997): Analysis of the directional wave spectrum from field data. Advances in Coastal and Ocean Engineering., vol. **3**, pp. 103-143. World Science Press.

Kirby, J.T. and T-M. Chen (1989): Surface waves on vertically sheared flows: approximate dispersion relations. J. *Geophys. Res.*, **94**(C1), 1013-1027.

Krogstad, H.E., R.L. Gordon and M.C. Miller (1988): High-resolution directional wave spectra from horizontally-mounted acoustic Doppler current meters. *J. Atmos. and Oceanic Technol.*, **5**, 340-352.

Munk, W.H., G.R. Miller, F.E. Snodgrass and N.F. Barber (1963): Directional recording of swell from distant storms. *Proc. Roy. Soc.* **A255**, 505-584.

Snodgrass, F.E., G.W. Groves, K.F. Hasselmann, G.R. Miller, W.H. Munk and W.H. Powers (1966): Propagation of ocean swell across the Pacific. *Proc. Roy. Soc.* **A259**, 431-497.

Strong, B., B. Brumley, E.A. Terray, and G.W. Stone (2000): The performance of ADCP-derived wave directional spectra and comparison with other independent measurements. *Proc. Oceans2000*, IEEE Press, 1195-1203.

Terray, E.A., B.H. Brumley and B. Strong (1999): Measuring waves and currents with an upward-looking ADCP. *Proc. IEEE 6th Working Conference on Current Measurement*, IEEE Press, 66-71.

Terray,E.A., R.L. Gordon and B.H. Brumley (1997): Measuring wave height and direction using upward-looking ADCPs. *Proc. Oceans'97*, IEEE Press, 287-290.

Terray, E.A., H.E. Krogstad, R. Cabrera, R.L. Gordon and A. Lohrmann (1990): Measuring wave direction using upward-looking Doppler sonar. *Proc. IEEE 4th Working Conference. on Current Measurement*, IEEE Press, 252-257

Thomas, G.P. (1981): Wave-current interactions: An experimental and numerical study. Part 1. Linear Waves. *J. Fluid Mech.*, **110**, 457-474.

MEASUREMENT OF WAVE FIELD HISTORIES IN HYDRAULIC MODELS USING PHASE PROFILOMETRY

Dr. Cary Cox
Dr. Barry McCleave
Mr. James Troupe
Dr. Charles R. Welch
Mr. William Seabergh
Mr. William Curtis

U.S. Army Engineer Research and Development Center
Waterways Experiment Station
3909 Halls Ferry Road
Vicksburg, MS 39180
Phone: 601.634.2599
Fax: 601.634.2747
Email: mccleab@wes.army.mil

1. INTRODUCTION

Hydraulic scale-model studies are used to understand, to verify numerical models for, and to predict wind waves near coastal structures. Hudson et al. (1979) present many examples of such studies and present much of the supporting science and practical considerations on the use of hydraulic models. Hughes (1993) provides a brief history of the use of scale models in hydraulic studies, and relationships among the various scale parameters.

A primary diagnostic tool for hydraulic model studies is wave height measurements. Usually wave heights are measured using capacitance or resistor wave gages that measure the wave fields at discrete locations. Wave gages and their supporting tripod stands protrude into the water causing perturbations of the wave fields. A sensing method that could measure the wave height histories over continuous areas, and do so without contact with the water, would be preferable to these traditional "at-a-point" methods. Typically, wave measurements in the field are accurate to 30 mm, which implies that in 1:100-scale models, waves should be measured to about 0.3 mm for similar accuracy.

We performed a feasibility study on the use of Phase Profilometry to provide a spatially continuous measurement of wave heights of wave fields. Phase Profilometry is a general, non-contacting method for measuring surface topographies. It uses periodic shadows from visible light falling onto a surface to measure that surface's topography (see Figure 1). An example of a periodic shadow is the shadow cast by a common window blind. An observer, not on-line with the light source and shadow, sees a modulation of the shadows caused by changes in surface elevation. The change in phase between the modulated and unmodulated shadow patterns can be used to calculate the surface elevation.

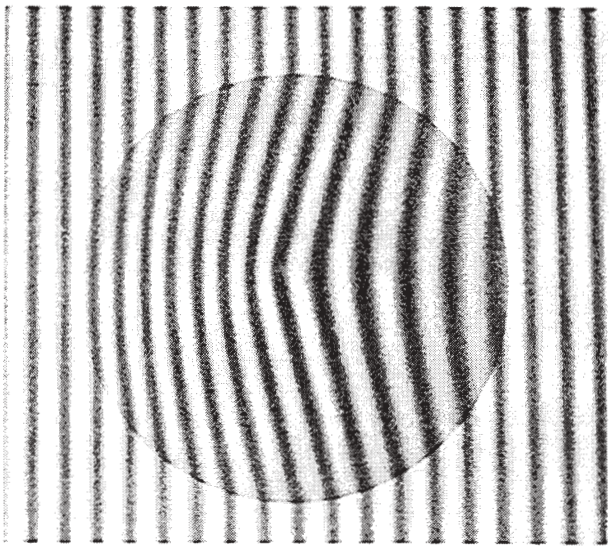

Figure 1. Ronchi Pattern Projected on Cone

The physics underlying the distortion of shadows by non-planar surfaces has been known for several hundreds of years. Automatic surface topography

analyses using this phenomenon became practical only since the early 1980s as a result of the widespread availability of scanners, which allowed photographs to be converted into digital form, and inexpensive, powerful computers, which could perform the necessary numerical operations. These technologies were augmented by the recent advent of digital cameras that made shadow analysis expedient for a wide range of surface topography measurements.

Some of the more important research in shadow topography, encouraged by the technological advances, is as follows. Takeda, Ina, and Kobayashi (1982) developed an algorithm for extracting phase information of fringe-pattern images using Fast Fourier Transforms. This development influenced later research. Takeda and Mutoh (1983) present a method for deriving surface profiles using periodic shadows cast onto a surface, and analyze these distorted shadows using Fast Fourier Transforms similar to Takeda, Ina, and Kobayashi (1982). The method, which they called "Fourier Transform Profilometry," is the method used in this study. Haliouva and Srinivasan (1987) describe a non-contacting method to measure surface topography using periodic shadows of sinusoidally varying intensity. The phase of the illuminating pattern is varied, and the surface topography is rendered via addition of the returned pixel intensity, using trigonometric identities. Henderson and Boudreaux (1999) report on feasibility experiments in which Phase Profilometry was used to measure the surface topography of craters in concrete and in sand. They show that Phase Profilometry was applicable to a wide range of problems.

Other optical techniques besides Phase Profilometry have been used to measure water surface topography. For example, shadow and Projection Moiré Topography techniques produced results on physical models that agreed in surface shape with those obtained by intrusive instruments and numerical simulations (Grant, Padilla-Perez and Stewart, 1990; Grant, Stewart, and Padilla-Perez, 1990). In these techniques, two sets of periodic shadows are used simultaneously to discern surface topography. Shadow Moiré topography capitalizes on the presence of Moiré fringes (incoherent light) observed when a shadow of a reference grid is cast on an object and observed by a camera through a single reference grid. Projection Moiré topography projects a reference grid onto an object, and the Moiré pattern is observed on the image plane of the camera through a second reference grid. The geometry of both the shadow and projection Moiré methods are similar to that of a stereo photogrammetry arrangement. The elegance of the Moiré process is that parallax information required to recover the third or vertical spatial dimension is encoded in a single image (see Karara, 1989). To oversimplify, the interference fringes are contours of elevation relative to a reference plane.

Monoscopic photogrammetric techniques have been used on laboratory hydraulic models to accurately measure the spatial and temporal evolution of wave frequency and direction (e.g., Curtis, Hathaway, and Seabergh, 2001). The methodology used in the laboratory is derived from principles of photogrammetry and image processing, which are documented by Holland et al. (1997). Standard stereo photogrammetric methods may be applied to map the model's free surface topography, but is rarely attempted. Determination of 3-D spatial coordinates from 2-D image coordinates using this method requires geometric constraints on the free surface and homologous patterns or points in the stereo pair of images (Wolf, 1983). Stereo photogrammetry's lack of practical application arises from the absence of distinguishable points observed in the stereo images corresponding to a location in 3-D space.

The objectives of the experiments were to determine if Phase Profilometry could be used to measure water surface topography and to define the areas where future development is needed. The Phase Profilometry system used provided the equivalent of an array of approximately 500,000 surface point wave height measurements covering an area of about 5 sq m at a rate of 30 times per second. The system employed a Ronchi grating shadow projected onto the water surface. The images were recorded using a digital video camera, and the water surface elevations were derived from the digital images via analysis of the Ronchi shadow distortions. The accuracy of this first-generation system was on the order of ±3.0 mm.

These experiments and their results are described below. The governing equations for the technique are provided, and comparisons are made to traditional wave gage measurements. Recommendations are made for future research and development.

2. EXPERIMENTS

The experiments were performed in model basins of the Coastal and Hydraulics Laboratory of the U.S. Army Engineer Research and Development Center. These concrete basins can be a few hundred feet in length and breadth and several feet in depth. If the model is of a

particular coastal site, the scaled bathymetry of the model is the same as the coastal site. Regions that require wave measurements typically cover square decameters. Wave measurements at up to 20 points are collected for a given experiment. Usually many wave conditions, water levels, and current conditions are combined to create a matrix of at least a few hundred experimental conditions for a study.

In all the Phase Profilometry experiments, the recording camera was centered above and perpendicular to the surface field to be contoured (Figure 2). The projector that cast the Ronchi grating shadow onto the water surface was offset from the camera centerline by about 15 deg.

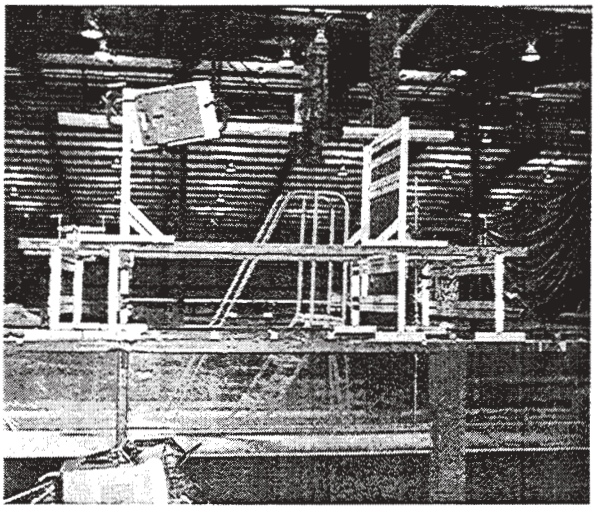

Figure 2. Phase Profilometry Setup

This angle was chosen to minimize interference on the pattern projected on the surface due to the reflection of the projector's lightbulb. This reflection is from the projector's glowing lens system reflected by the water surface. The angle was increased to the point that the disrupting reflection was on the edge of the projected pattern. The projector was positioned the same distance above the water surface as the camera and was aimed at the center of the camera's field of view, resulting in a right-triangle geometry. The projected lines were perpendicular to a line between the camera and projector, and the lines were continually increased in separation as they got further from the projector. Generally, it is desirable to keep the angle between the camera and projector as small as possible to minimize the difference in phase shift between lines as viewed by the camera; thus, 15 deg was a compromise between good geometry and interference elimination. This geometric phenomenon of phase shift due to projection angle was accounted for in the processing algorithm. The perpendicular distance from the surface to the camera lens entrance pupil and the projector lens exit pupil was about 2 m for flume studies, and about 4 m for the open-water model studies.

The camera used in all tests was a Sony DSR-130 and was composed of two parts: (1) video camera head DXC-D30 and (2) DVCAM cassette tape. The DXC-D30 incorporates Sony's proprietary digital signal processing chip that processes brightness, hue, and saturation to achieve maximum dynamic range. The camera's video resolution was 800 TV lines, with a 63-dB signal-to-noise ratio. The video sensor system of the camera was a 3-chip, 17-mm CCD sensor combination with 811 x 508 pixels (768 x 494 effective). Three-chip CCD cameras give higher true resolution than one-chip masked CCD cameras because each pixel of the image has actual sensor information for red, green, and blue. One-chip cameras interpolate to give their stated resolution and have actually one-third their specified resolution. Maximum shutter speed for the DXC-D30 was 1/2000 second, and minimum illumination was 0.5 lux. The camera produced 60 Hz interlaced NTSC images as output, stored in DV25 compressed format for transfer by IEEE 1394 (fire wire) interface to the processing computer. Since DV25 and JPEG both use Discrete Cosine Transform Compression, the images were converted to JPEG for input to the Phase Profilometry software to reduce compression loss.

The projector used was a Kodak Ektagraphic III E Plus slide projector with a Buhl 35-mm F2.5 economical series lens. The projector used a 300-watt halogen bulb. The Buhl lens and Kodak projector combination projected a 1.2 m by 0.9 m pattern at 1.5 m. The Ronchi grating slides were common 50.8-mm × 50.8-mm slides available commercially. Several Ronchi gratings were used in the experiments, with 127 lines per centimeter producing the best results.

A 1-m-wide single paddle wave generator, similar to the larger ones shown in Figure 3, was used to produce waves in the flume Phase Profilometry experiments. The generator on the left is fluid-powered and can be operated in translation or rotation configuration. It has an articulated wave board that can be programmed to operate in basic translation, as the upper half rotates. The maximum translational stroke is 686 mm in the 102-m-long by 1.8-m-wide flume. The generator in the right half of Figure 3 is fluid-powered and operates in translation mode only. The 3.0-m-wide board has a

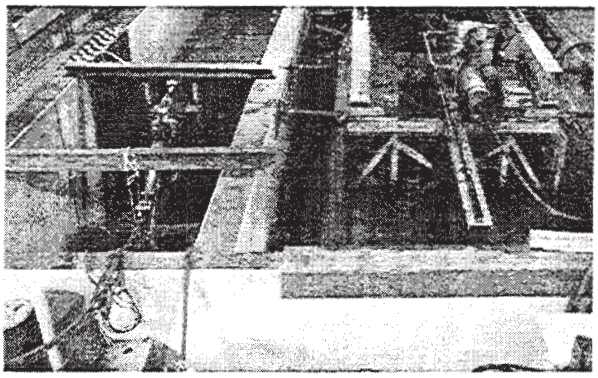

Figure 3. Single Paddle Generators

stroke of 102 mm with velocity of up to 356 mm per second.

Directional spectral wave generators (Figure 4) are often used to produce waves in open water models. The one shown in Figure 4 is composed of 60 individual surfaces joined at the sides to form a continuous surface. It can produce spectral waves over a range of angles from -70 to 70 deg. A fixed model can thus be tested with spectral wave action impacting from a number of different directions.

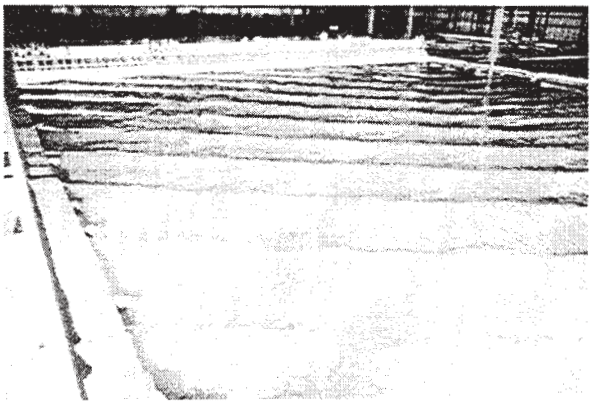

Figure 4. Monochromatic Directional Wave From a Directional Spectral Wave Generator

The data for the experiments were recorded on videotape and converted to JPEG digital files for processing. For each experiment, a brief recording of still water was made for use as the zero reference. Each experiment was recorded for several minutes with about 20 seconds of each experiment used for analysis.

To apply Phase Profilometry to water surface motion, the Ronchi grating must be reflected from the water's surface. Thus, the water used in hydraulic models was "colored" to prevent light transmission to the bottom.

The initial feasibility experiments were performed using 25-micron hollow glass spheres to "color" the water. However, these glass spheres had an average density of 1.15, and most of the reflected light was returning from several centimeters below the surface.

A product search uncovered similar ceramic spheres (Extendospheres SF-14, from PQ Corporation, Chattanooga, TN) with slightly larger diameters and specific gravity less than one. Being less dense than water, they would float, causing most of the reflected light to come from the water surface. The particle size varied from 10 to 90 microns, with mean of 50 microns, and a density range of 0.7 to 0.85 g/cm^3. This material reflected light from the water surface better than the other agents tested. The dust from the spheres presented a potential breathing hazard and required special handling during deployment. The spheres also clung to the walls of the models which complicated clean-up. Even though the effects on wave action by introducing this substance appeared negligible, further testing is recommended to ensure that wave action is unaffected.

Because of these concerns, other dyes that dissolve in the water were also tested. Only chemicals that were certified safe for use in or around potable water were examined. Two certified potable fluorescent dyes were purchased (Forestry Suppliers of Jackson, MS):
(1) Fluorescent Yellow-Green Fluorescein Dye
(2) Fluorescent Red FWT Dye.

The yellow-green dye was too transparent, and visual inspection verified that reflections were coming mostly from the bottom. The red dye, on the other hand, colored the water completely so that no visually discernable light was transmitted to the bottom. Combinations of red and yellow-green dye were tested, as well as combinations of the ceramic spheres with the fluorescent dyes. The combination most promising visually was a light coat of ceramic spheres floating on the surface of the red dye solution. A problem with a light coat of spheres is that the spheres tended to separate from points of wave action after a few minutes of testing, requiring that new spheres be continually added during the experiment. The optimum coloring method has yet to be determined.

3. DATA ANALYSIS

The analysis was preformed using programs written with the mathematical interpreter MATLAB. The analysis began by cropping the files to include only areas that contained good reflectivity and no

miscellaneous objects. The same area for each data file was saved from an associated zero reference file (that is, an unmodulated grid). The data were analyzed using the Fourier Transform Profilometry algorithm. This algorithm accepts the zero reference file, a data file, and the geometry of the camera setup as inputs, and delivers a 2-D matrix that describes the height of the object (wave) being analyzed for each pixel in the picture.

The Fourier Transform Profilometry algorithm is presented in Takeda and Mutoh (1983). In this method each line of the photograph is analyzed separately. If a line perpendicular to the Ronchi grating lines of the non-deformed grid is viewed as a space versus amplitude (light intensity) plot, it would look like a square wave. Analytically this line can be written as

$$g_0(x,y) = \sum_{n=-\infty}^{\infty} A_n \, e^{j(2\pi \cdot f_n \cdot x + \phi_n(x))}, \quad (1)$$

where j is the imaginary number, $(-1)^{1/2}$. This is the Fourier Series Expansion of the square wave, where the coefficients A_n are present at the fundamental frequency of the wave and its odd harmonics. If all but the fundamental frequency is filtered out, the remaining term will be

$$g_0(x,y) = A_0 \, e^{j(2\pi \cdot f_0 \cdot x + \phi(x))}, \quad (2)$$

where A_0 is the coefficient of the fundamental frequency.

When an object is illuminated by the Ronchi grid, the deformed grid can be expressed by a similar formula:

$$g(x,y) = r(x,y) \sum_{n=-\infty}^{\infty} A_n \, e^{j(2\pi \cdot f_n \cdot x + \phi_n(x,y))}, \quad (3)$$

where $r(x,y)$ is the non-uniform distribution of reflectivity on the object surface.

If the same filter is applied to these data, the equation becomes

$$g(x,y) = A_0 \cdot r(x,y) \cdot e^{j(2\pi \cdot f_0 \cdot x + \phi(x,y))}. \quad (4)$$

The problem is to find the phase change from a line of the non-deformed grid to the deformed grid. Multiplying each line of the non-deformed grid by the complex conjugate of the deformed line, we obtain:

$$g(x,y) \cdot g_0'(x,y) = |A_0|^2 \, r(x,y) \cdot e^{j\Delta\phi(x,y)}, \quad (5)$$

where $g_0'(x,y)$ denotes the complex conjugate of $g_0(x,y)$.

Taking the log of this product yields:

$$\log\left(|A_0|^2 \, r(x,y)\right) + j\,\Delta\phi(x,y). \quad (6)$$

The imaginary part will yield the change in phase,

$$\Delta\phi(x,y). \quad (7)$$

As can be seen from the diagram in Figure 5, the camera and projector are separated from each other by a distance d. They are located a distance L from the background reference plane, and a grid of f_0 cycles per unit distance is projected onto the background.

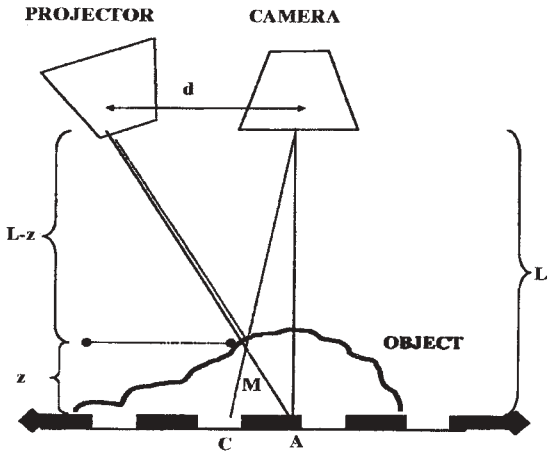

Figure 5. Phase Profilometry Analysis Geometry

To understand the 3-D measurements, consider the example of one pixel when there is no object in the picture. Light, modulated by the grid, travels from the projector to point A on the background and is then recorded by the camera. When an object is placed in front of the background, the light strikes the object at location M. When the 2-D camera views this change, it appears that the grid has moved to point C.

The relationship between the distance, AC, and the change in phase of the grid ($\Delta\phi$) from its reference plane value at this point is given by:

$$\Delta\phi = -2\pi \cdot AC \cdot f_0 \quad (8)$$

AUTHOR INDEX
TABLE OF CONTENTS

or,

$$AC = -\frac{\Delta\phi}{2\pi \cdot f_0}. \quad (9)$$

The object of these measurements is to obtain *Z*, the height, at each pixel on the photograph. Notice that the triangle formed by the camera, the projector, and *M*, and the triangle formed by *A*, *C*, and *M*, are similar triangles. The heights of these triangles are then proportional to the sides *d* and line *AC*, as shown in the formula:

$$\frac{d}{AC} = \frac{L-Z}{Z}. \quad (10)$$

By substituting the calculated value of line *AC* and solving for *Z*, we obtain the Profilometry formula:

$$Z = \frac{L \cdot \Delta\phi}{\Delta\phi - 2\pi \cdot d \cdot f_0}. \quad (11)$$

This formula relates the phase of each pixel to the geometry of the Profilometry setup so that the 3-D distance, *Z*, can be calculated. When this type of Profilometry is used, the deformed grid and the picture are separated from each other so that the phase of the grid can be measured and used to calculate the depth at each pixel of the picture. Additionally, intra- and inter-frame geometrical line tracking is used to eliminate the 2π phase jump problem.

4. PHASE PROFILOMETRY RESULTS

A sample of the water surface profiles derived using Phase Profilometry from the digital video images is shown in Figure 6. Each profile was derived independently of the profiles that came before and after it in time and converted into AVI files for display as a movie. The surface profiles showed smooth transitions in the wave structure with time and visually appeared to agree with the wave structure seen in the experiments. These observations provided qualitative support that the Phase Profilometry was accurately measuring wave heights. To provide quantitative support, comparisons were made between the Phase Profilometry results and traditional wave heights measuring sensors, namely capacitance wave gages.

Capacitance wave gages (Figure 7) have been used in hydraulic models for over 40 years to measure wave surface profiles. The wave gage operates in the 1- to 2-MHz range and consists of a submerged, insulated wire rod (McCleave, Greer, and Briggs, 1999). The time-varying height of the water surface in the model (i.e., effective ground) creates a varying capacitance that detunes the oscillator, linearly producing a difference frequency of 1 to 10 kHz. The optically isolated signal is transmitted by digital current loop to a voltage-to-frequency converter on the signal conditioner board. The output analog voltage is proportional to the wave height. Wire length may vary from a few centimeters to a meter. The capacitance of the wires is a function of the conductor and insulation's diameter and dielectric constant. Twenty-four-gage Teflon or PVC-insulated wire is commonly used for the wave rod.

A wave gage is calibrated by mechanically driving the rod up and down in fixed increments about zero and recording the wave gage voltage. A linear or second-order equation is least squares fit to the acquired data. Figure 8 shows a typical wave gage calibration curve.

There are 21 data points (zero, 5 down, 10 up, 4 down, zero) at 11 points on the curve. The duplication of points measured while the rod is being driven through a point on the curve through opposite directions reduces the effect of meniscus on the calibration.

Figure 9 displays data from a Phase Profilometry experiment shown as a "Virtual Wave Gage." These data were produced by taking the wave height values at the same point in the wave field from a consecutive series of images. The fact that the data are continuous when displayed in this fashion provides additional support to the robustness of the Phase Profilometry process in that, as mentioned before, each image was analyzed independently of the other images.

Data from a wave gage are compared with Phase Profilometry data in Figure 10. The wave gage could not be placed in the field imaged by Phase Profilometry because the gage would obstruct the field of view. Therefore, the wave gage was placed slightly to the right of this area. Samples were taken from the Profilometry data near the center of the imaged area and at the end furthest from the wave gage. This gave three measurements: the wave gage at the far right, a Profilometry reading 0.15 m to the right of the wave gage, and a second Profilometry reading 0.3 m to the right of the wave gage. The results from the reading closest to the wave gage are displayed in Figure 10. Based on the wave height trends seen in the Phase Profilometry data when approaching the wave gage, the small differences in the wave heights seen in Figure 10 are attributed to differences in the wave field at the two locations.

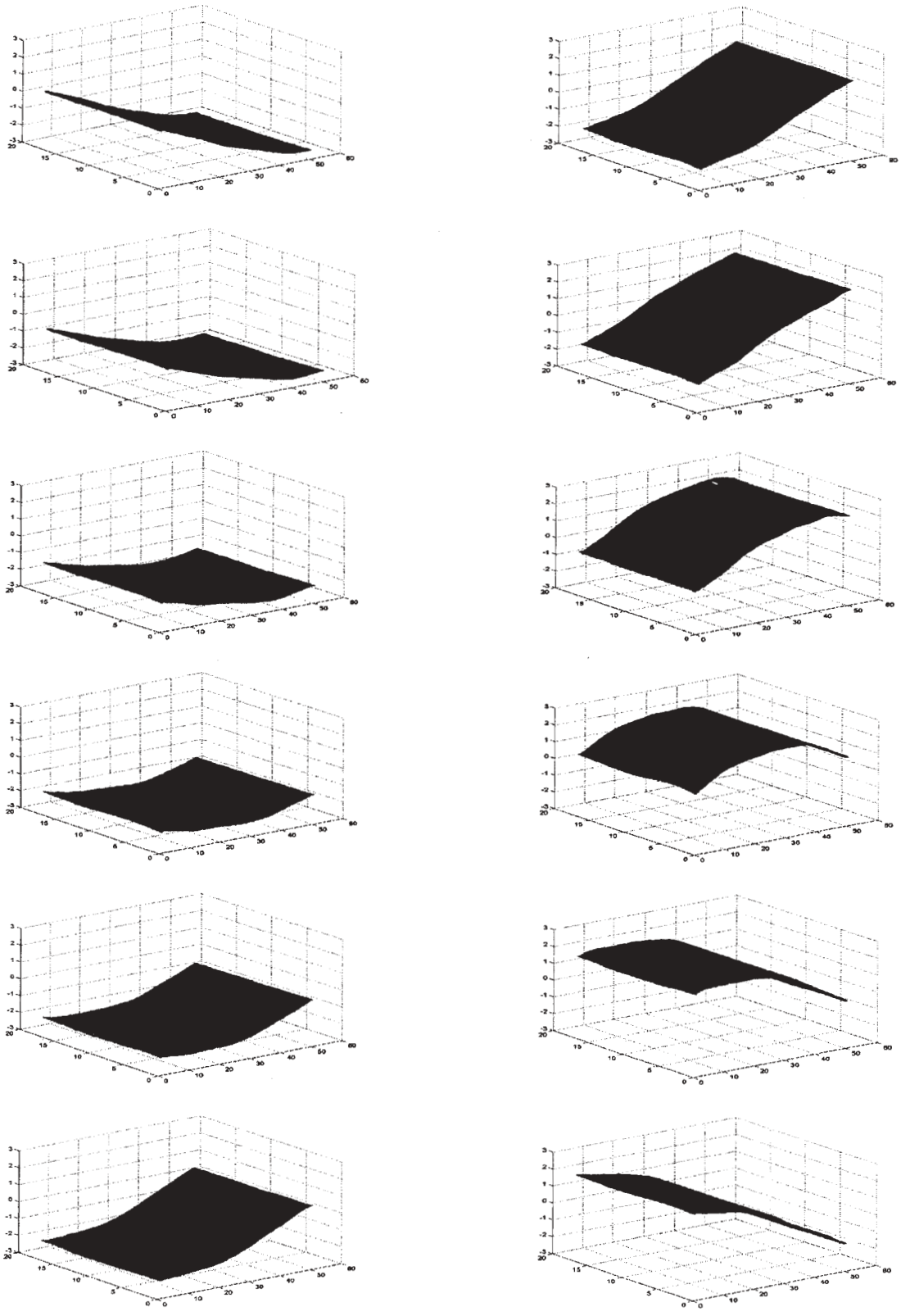

Figure 6. Water Surface Profiles at 0.13-second Intervals Determined via Phase Profilometry (Scales are in 25.4-mm [1-in.] intervals)

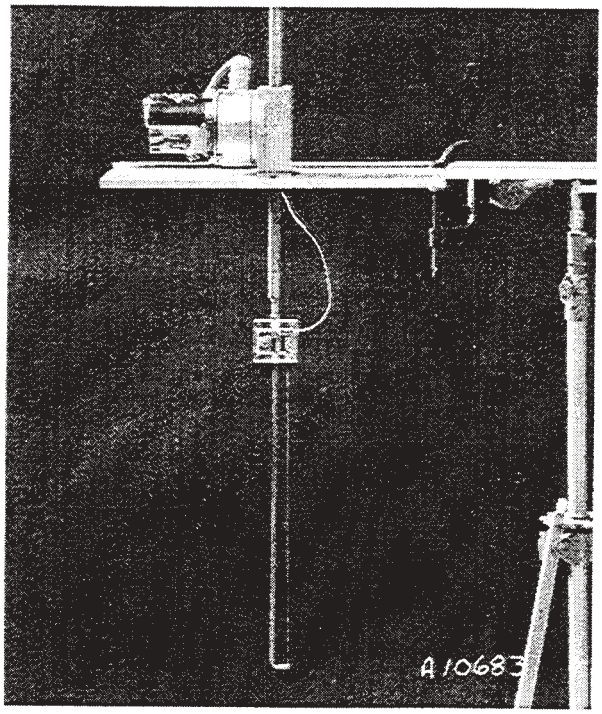

Figure 7. Capacitance Wave Gage

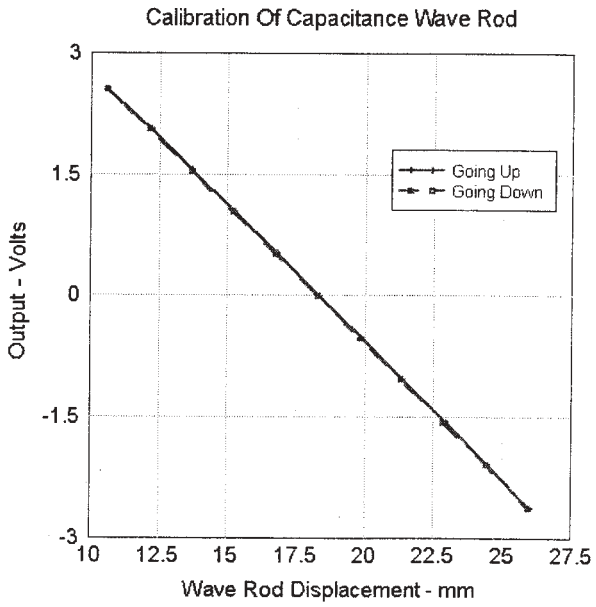

Figure 8. Wave Gage Calibration Curve

An additional experiment was conducted to determine within an order-of-magnitude the accuracy of Phase Profilometry for measuring wave heights. For this experiment, a sheet of corrugated fiberglass was used to simulate a standing wave. The Profilometry system used in the experiment was different from the one used

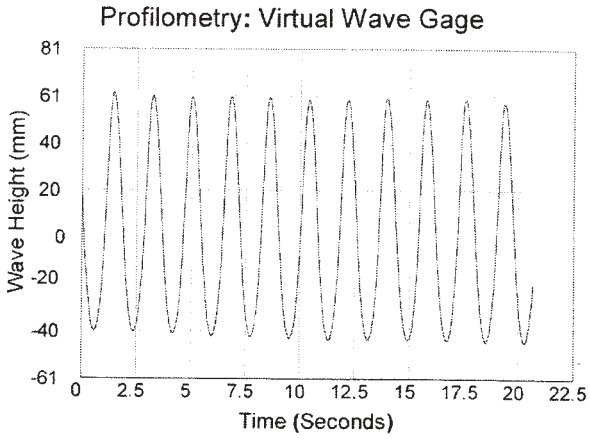

Figure 9. Phase Profilometry Virtual Wave Gage

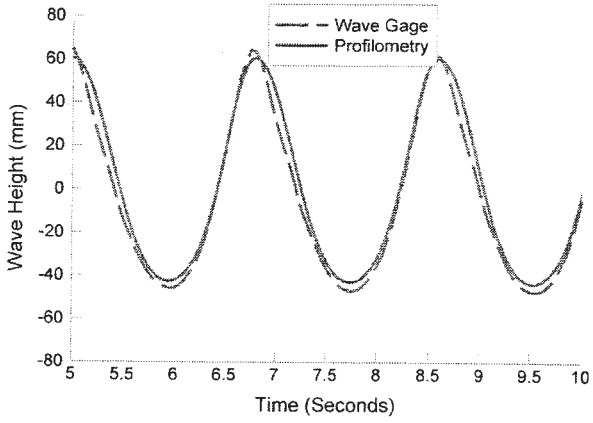

Figure 10. Phase Profilometry Data Compared to Wave Gage Data

in the dynamic wave tests. A digital still camera was used in place of the digital video camera. This still camera had a resolution of over one million pixels, significantly greater than the video camera used in the wave test. Also, the surface area measured in the static test was approximately 0.09 sq m as compared to the 0.3-sq-m area of some of the dynamic wave experiments. Shown in Figure 11 are the results of the Phase Profilometry measurement of the corrugated fiberglass section.

Figure 12 displays a cross-section through the Phase Profilometry data. Hand measurements using a micrometer yielded a thickness of 0.9 mm. The average peak height was measured to be 16 mm using Phase Profilometry, with a value of 15 mm given by hand measurements using a ruler.

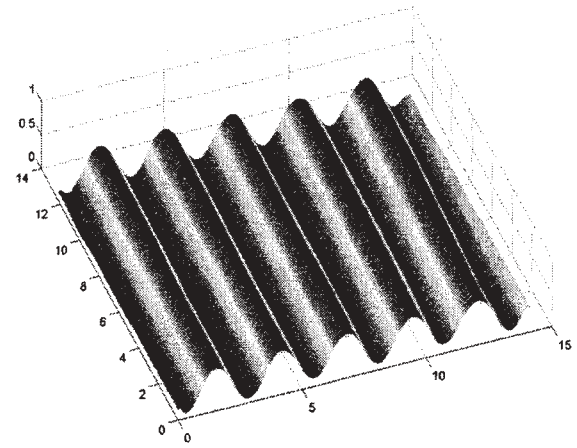

Figure 11. Phase Profilometry Profile Results for Sheet of Corrugated Fiberglass

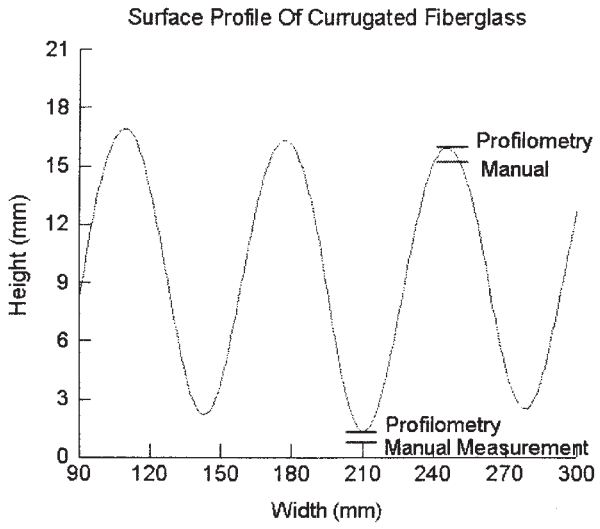

Figure 12. Fiberglass Cross-Section

The thickness of the fiberglass was measured to be 1.3 mm. The small differences are believed caused by the fiberglass sheet not resting on the supporting plane at all places.

5. RECOMMENDATIONS FOR FUTURE WORK

A thorough and comprehensive study needs to be performed of the precision and accuracy of Phase Profilometry as a function of the frequency of the Ronchi gratings, lens aberrations, pixel spatial and intensity resolution, and measurement errors of the camera-projector-target geometry. Other shadow patterns and other methods to unfold the water wave height, such as the use of sinusoidally varying intensity patterns, need to be investigated. Better methods or materials for causing strong reflectance of the projected Ronchi patterns off the water surface need to be developed. Faster algorithms need to be developed so that the water wave profiles can be displayed real-time. This would hasten considerably the overall development of Phase Profilometry for water wave field profiling.

6. CONCLUSIONS

These results demonstrate the feasibility of using Phase Profilometry to provide spatially and temporally continuous measurements of wave field profiles in hydraulic models. Phase Profilometry can be a significant improvement in the measurement tools used in hydraulic modeling. Additional research and development are needed in several areas of Phase Profilometry to finalize its utility for this area.

7. ACKNOWLEDGMENTS

We thank the U.S. Army Engineer Research and Development Center, and the associated Coastal and Hydraulics Laboratory and Information Technology Laboratory, for their support during the conduct of this study. Permission was granted by the Chief of Engineers to publish this paper.

8. BIBLIOGRAPHY

Curtis, W. R., K. Hathaway and W. C. Seabergh, 2001 (in preparation): Video-based physical model directional wave measurements. Submitted to *Proceedings, Coastal Dynamics 2001*, Lund, Sweden.

Grant, I.; I. Padilla-Perez and N. Stewart, 1990: Application of optical techniques to water surface measurements. *Proceedings of the Ninth International Conference on Offshore Mechanics and Arctic Engineering*, Volume 1 – Part A, 27-35.

Grant, I., N. Stewart and I. Padilla-Perez, 1990: Topographical measurements of water waves using the Projection Moiré Method. *Applied Optics*, 29(28), 3981-3983.

Haliouva, M. and V. Srinivasan, 1987: Method and apparatus for surface profilometry. U.S. Patent 4,641,972, U.S. Patent & Trademark Office, Washington, DC.

Henderson, M. and G. Boudreaux, 1999: Waterways Experiment Station demonstration of Fourier Transform Profilometry (FTP/WES). U.S. Army Engineer Research and Development Center Contract Report DACW39-99-P-0585, 3909 Halls Ferry Rd., Vicksburg, MS.

Holland, K. T., R. A. Holman, T. C. Lippmann, J. Stanley and N. Plant, 1997: Practical use of video imagery in nearshore oceanographic field studies. *IEEE Journal of Oceanic Engineering*, 22(1), 81-92.

Hudson, R. Y., F. A. Herrmann, R. A. Sager, R. W. Whalin, G. H. Keulegan, C. E. Chatham and L. Z. Hales, 1979: Coastal hydraulic models. Special Report No. 5, U.S. Army Engineer Waterways Experiment Station, Vicksburg, MS.

Hughes, S. A., 1993: *Physical models and laboratory techniques in coastal engineering.* World Scientific, Singapore.

Karara, H. M., 1989: Handbook of non-topographic photogrammetry. H. M. Karara (ed.), American Society of Photogrammetry and Remote Sensing, Falls Church, VA.

McCleave, B. W., H. C. Greer and M. J. Briggs, 1999: Wave generation instrumentation in hydraulic models. *Proceedings of Oceans '99 Conference*, Seattle, WA.

Takeda, M., H. Ina and S. Kobayashi, 1982: Fourier-Transform Method of fringe pattern analysis for computer-base topography and interferometry, *Journal of the Optical Society of America,* 72(1), 156-160.

Takeda, M. and K. Mutoh, 1983: Fourier Transform Profilometry for the automatic measurement of 3-D object shapes, *Applied Optics, Optical Society of America*, 22(24), 3977-3982.

Wolf, P. R., 1983: *Elements of photogrammetry.* McGraw Hill, Inc., New York, 628p.

WAVE MODELLING IN ARCHIPELAGIC SEAS
The Aegean Sea case

S. Christopoulos and C. Koutitas

Abstract

The wave forecast model DAUT is implemented on a fine space scale for the demands of wave forecasting in the Aegean Sea. The wave model takes into account the propagation of waves in open sea, the wind input source, the wave dissipation sink and the nonlinear wave energy transfer sources and sinks.

For the implementation of the wave model there are used winds from the SKIRON atmospheric model. The special orography of the area is very sensitive for the analyzed wind fields and the resulting wave fields, so the discretization of 1/10 of a degree is adopted.

The wave model is implemented for a period of six months, ie the second half of 1999. The model results are compared with in situ directional measurements from the recently established network of measuring stations POSEIDON in Aegean Sea. Results of the 2d wind and wave fields as well as the time series of important wave parameters are presented. Statistical analysis of the results emphasizing aspects about the wave intensity, the wave variability, the wave modelling and the wind modelling efficiency in this area, are presented.

Communication elements:
Dr. S. Christopoulos
ARISTOTLE UNIVERSITY OF THESSALONIKI,
Division of Hydraulics & Environmental Engineering,
540 06 Thessaloniki, Greece.
Tel: 30-31-995710 or 30-31-459966
e-mail: schristo@civil.auth.gr

PROVIDING OPERATIONAL WAVE/SURF SUPPORT DURING NATO EXERCISE LINKED SEAS 2000

Richard Allard
Naval Research Laboratory
Stennis Space Center, MS, USA

Michael Brooking, James Dykes
Naval Oceanographic Office
Stennis Space Center, MS

Kelley Miles
Sverdrup Technology, Inc.
Stennis Space Center, MS

1. INTRODUCTION

The Naval Oceanographic Office's Warfighting Support Center (WSC), in cooperation with the Naval Research Laboratory, provided wave and surf forecasts for the amphibious component of the NATO Linked Seas 2000 (LS2K) Exercise held near Pinheiro da Cruz, Portugal during the period 24 APR - 18 MAY 2000. Model support included a 1/12° resolution WAM model, the steady-state spectral wave model (STWAVE) and the Navy Standard Surf Model (SURF3.0). The wave and surf models were forced by the US Navy's Coupled Ocean Atmosphere Mesoscale Prediction System (COAMPS). Bathymetry and beach profiles collected in mid-April 2000 during the Rapid Environmental Assessment (REA) phase of LS2K were obtained from the Scanning Hydrographic Operational Airborne Lidar Survey System (SHOALS). This represented the first time that SHOALS was used to support operational US Navy wave and surf prediction. This paper will discuss the WAM, STWAVE and SURF3.0 coupling and discuss a preliminary analysis of the model outputs.

2. MODELS

2.1 WAM

The Naval Oceanographic Office runs WAM Cycle 4 (Wittman and Farrar 1997) for domains scanning the globe. WAM is a 3rd Generation spectral wave prediction model described by the WAMDI group (1988; also Komen et al. 1994) and international consortium of wave modelers. WAM describes the sea surface as a discretized two-dimensional (2D) spectrum of sea surface elevation density.

In a typical operational configuration, WAM is run with 25 frequency bands with center frequencies ranging from 0.0433 Hz to 0.3283 Hz, with the each frequency 1.1 times that of the next lower band. WAM computes the wind-generated energy density of each spectral wave component. Energy is also propagated in space, with refraction due to depth variation, and dispersion due to the nature of the waves. WAM's spatial resolution does not resolve bathymetric variations close to the coast, typically, a shallow-water wave refraction model (see Sec. 2.2) is utilized.

For Navy applications, Global and Basin scale WAM operational runs are forced with winds from the Navy Operational Global Atmospheric Prediction System (NOGAPS) which provides truly global coverage at a resolution of 1.0. For embedded nests of higher resolution (typically ≥¼°), COAMPS winds are used when available.

A triple-nested WAM configuration, as shown in Fig. 1, was used in support of LS2K. A basin-scale 1.0° Atlantic basin WAM was forced with NOGAPS wind stresses. A second 1/4° Mediterranean nest was forced with 27km COAMPS wind stresses. This second nest was chosen to coincide with the Mediterranean COAMPS wind fields which extended only to 12 °W. The inner-most 1/12° nest was also forced with Mediterranean COAMPS winds. Bathymetry from NAVO's Digital Bathymetric Data Base Variable Resolution (DBDB-V) was used for all three WAM nests.

2.2 STWAVE

The spectral wave transformation model STWAVE (Smith et al. 1999) can be implemented to transform offshore wave spectra into the nearshore and the surf zone. STWAVE is formulated as a steady-state model. This type of model is appropriate for wave conditions that vary more slowly than the time it takes for waves to transit the computational grid. For wave generation, the steady-state assumption means that the winds have remained steady sufficiently long for the waves to attain fetch-limited or fully developed conditions.

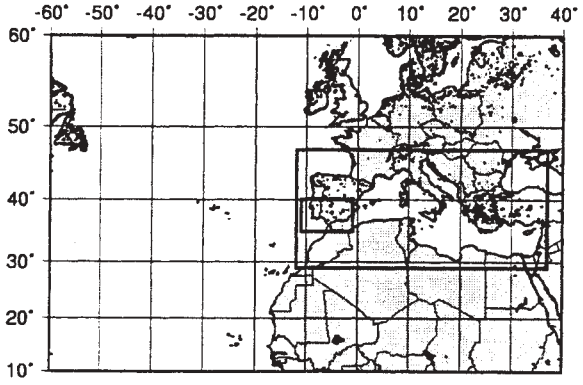

Figure 1. WAM nests used in support of NATO Exercise LS2K. Outer nest covers entire Atlantic Basin (not all shown) and provides boundary conditions (BC) to Mediterranean Sea 1/4° nest which in turn provides BC for inner 1/12° Western Europe nest.

STWAVE is a half-plane model, meaning that wave energy propagates from the offshore toward the nearshore (+/- 87.5°) from the x-axis of the grid, which is typically the approximate shore-normal direction.

COAMPS wind speed and direction were used as wind forcing for STWAVE. Only one value of wind speed and direction representative of wind conditions over the model grid was used (i.e., winds do not vary spatially). WAM spectra saved from the 1/12° nest were applied on the outer (seaward) boundary. Fig. 2 shows the STWAVE grid and prominent bathymetric features near the area of interest.

Bathymetry from the Instituto Hidrografico in Lisbon and data collected from SHOALS in April 2000 were used to generate a 100m STWAVE grid.

Tides were not considered for this application of STWAVE.

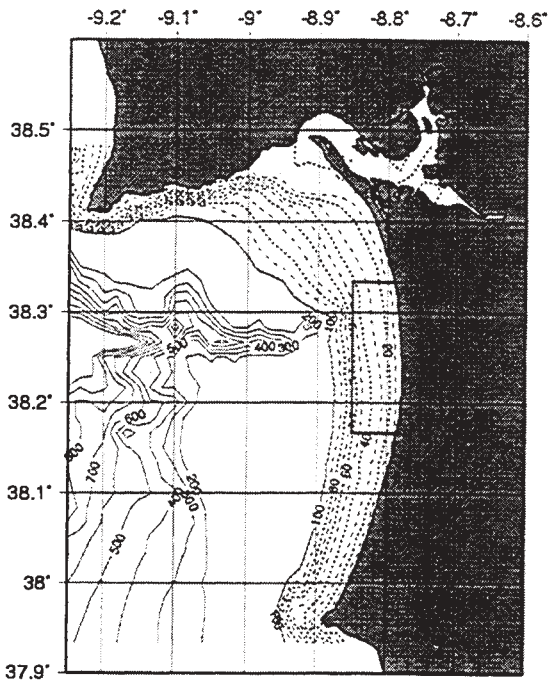

Figure 2. STWAVE grid (rectangle) for Pinheiro da Cruz region in Portugal. WAM deep-water spectra are applied along STWAVE outer model boundary. STWAVE spectra were saved at selected locations for subsequent surf model forecasts. Contours show DBDB-V 1 minute bathymetry (m).

2.3 SURF3.0

SURF3.0, a parametric one-dimensional model developed by Earle (1988, 1989), is based largely on the work of Thornton and Guza (1983, 1986). Thornton and Guza developed several models for random wave processes including a wave height transformation model and a longshore current model. These models contain both numerical and analytical solutions which provide cross-shore distributions of various wave parameters such as wave height, longshore current velocity, and wave length.

The model is designed to operate in a variety of modes to provide both military and civilian users with local surf and current forecasts. SURF3.0 requires four standard inputs to perform calculations: (1) depth or beach profile, (2) a directional wave spectrum, (3) water level, and (4) wind direction and speed. The beach profile can be based on a recent NAVY SEAL Team survey, inferred from remotely sensed means (e.g., SHOALS) or a sediment-based profile.

For LS2K, STWAVE directional spectra saved at requested locations were used to initialize

SURF3.0. Hourly tidal predictions were provided by the Instituto Hidrografico in Lisbon. Beach profiles were extracted from SHOALS using the Surface-water Modeling System (SMS). The SMS interface (Smith et al. 1999) supports grid generation, interpolation of current fields (for wave-current interaction studies), and visualization of model output. Wind speed and direction from COAMPS were used in the calculation of the longshore current.

3. DISCUSSION

Overall, feedback on the WAM, STWAVE and SURF3.0 forecast products was very favorable. During the Rapid Environmental Assessment (REA) phase in APR 2000, there were many bouts of bad weather and high seas, generating much interest in the wave products. The twin-otter which flew SHOALS was able to operate in poor weather conditions and collect data over a two-day period for the Pinheiro da Cruz area. A NATO hyrdrographic survey of the same area was cancelled due to poor weather; SHOALS proved itself to be invaluable.

During the planning meetings leading up to LS2K, it was anticipated that assets from NATO countries would be available to provide some in-situ data to compare the models against. However, due to budget limitations, prior commitments and some unfortunate circumstances, little data has been available.

The Instituto Hidrogfico operates a network of buoy and tide stations and provides access to hourly wave height, period and direction for selected locations along the Portugal coast (http://www.insthidrografico.pt/wwwbd/Boias/BoiasUltimoRegisto.asp) Fig. 3 shows the locations of wave buoys maintained by the Instituto Hidrografico. The closest buoy to the STWAVE modeling area near Sines (37 55' 16" N, 8 55' 44" W), located at a water depth of 97m, was damaged just prior to the LS2K exercise. A replacement buoy did not become available until a few days before the end of the exercise. Another buoy located along the Northwest coast of Portugal near Leixões (41 19" 00" N, 8 59 00" W) at a depth of 83m, provided continuous hourly wave data from the beginning of the exercise through 2 MAY 2000, at which time is was deactivated. A third buoy near Faro (36 54' 17" N, 7 53' 54" W) on the southern "Algarve" Portuguese Coast is located at a water depth of 93 m. The Faro buoy began providing nearly-continuous hourly data in late March 2000. The authors are in the process of obtaining available data for the buoys for the period of record coincident with LS2K. This will permit a comparison of the 1/12° WAM which provided boundary conditions for STWAVE.

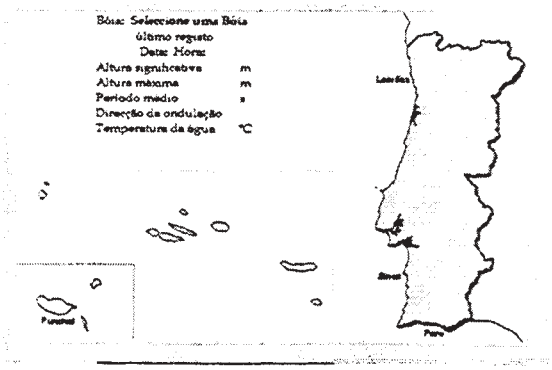

Figure 3. Wave buoy network operated by Instituto Hydrografico in Lisbon. The Sines buoy was out of service for most of the LS2K Exercise.

The wave climate for this area is swell-dominated due to frequent storms to the north (Paillard et. al, 2000). Winds are predominantly north to northwesterly. Wave directions are typically northwesterly but some southern storms can cause directions to be from the southwest as well. Wave heights are typically at their highest during late autumn through early spring due to a more active storm track.

Fig. 4 shows Regional WAM analyses (1/12° inner-nest) for a 3-day period for 27-29 APR 2000. Predicted wave heights in the exercise area reach a maximum of 2.5m at 12Z on 27 APR, decreasing to 1.25m 48 hours later. Wave directions during this period shift from northwesterly, to westerly, to finally southwesterly on 29 APR 12Z near the Pinheiro da Cruz region.

The bathymetry for the STWAVE modeling area shows a generally gently sloping bottom with depth contours fairly parallel to the coast. Note the predominant canyon feature (Fig. 2) which runs east-west near 38.275°N). This lies outside of the STWAVE grid domain.

STWAVE provided high-resolution (100m) 48-hr forecasts for an area covering 25km alongshore and about 8 km cross-shore. Fig. 5 shows a black & white depiction of significant wave height and wave direction for 27 APR 00Z. Wave directions become more shore-normal closer to shore.

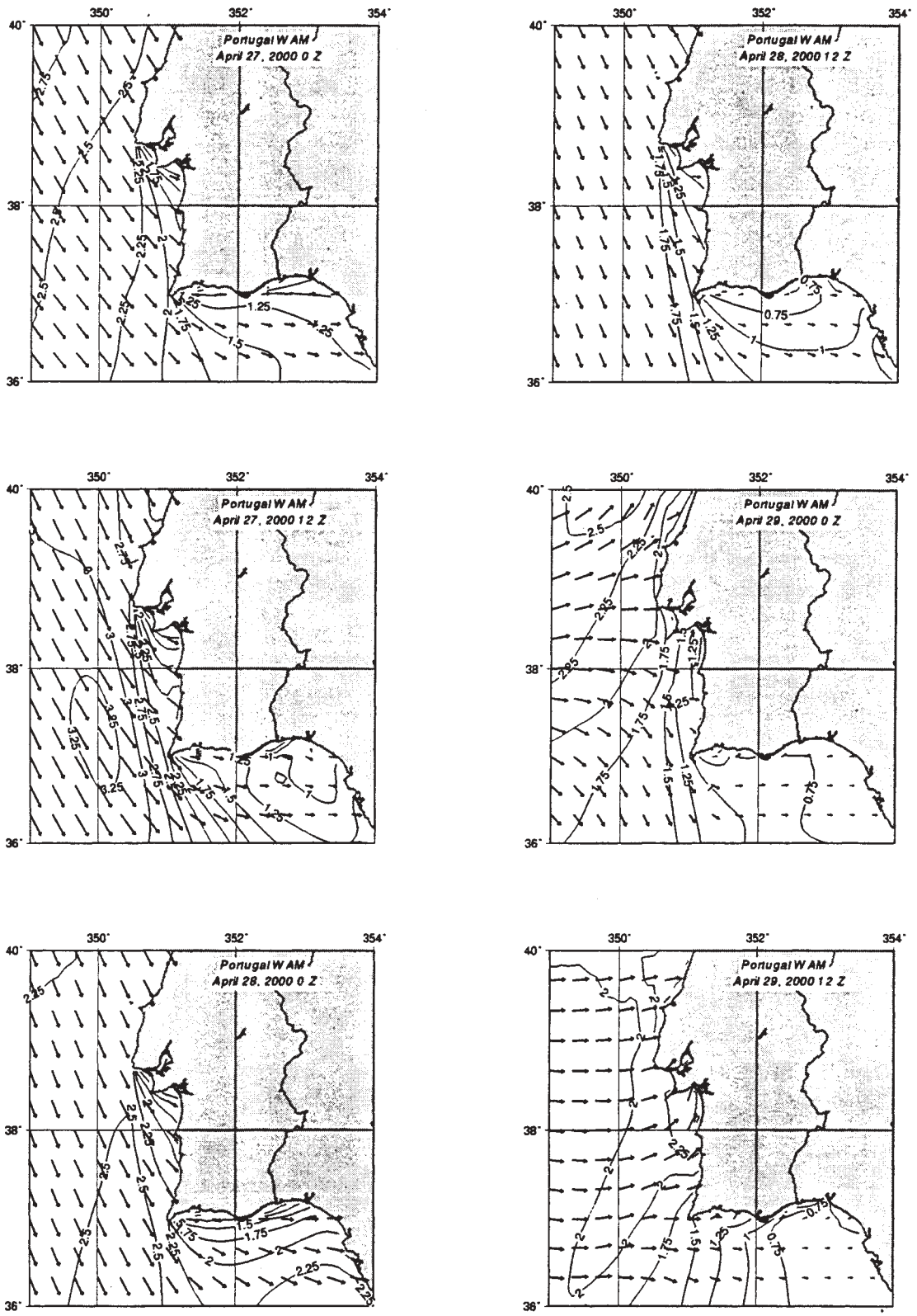

Figure 4. Inner-nest of WAM wave model for LS2K operating area; 00Z and 12Z analyses for 27-29 April 2000. Contours represent wave height at 0.25m intervals. Arrows denote direction waves are moving toward.

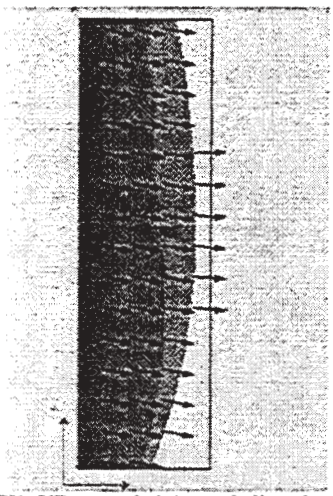

Figure 5. STWAVE wave height and direction for 27 APR 2000. Higher (darker colors) wave heights are offshore.

Fig. 6 shows a SURF3.0 48-hr forecast for a beach landing area for 27 APR 2000. The panel on the upper left depicts the very-high resolution SHOALS beach profile. COAMPS winds show a wind directed toward the southeast coast initially, which gradually veers toward the northeast near the end of the forecast period. The longshore current reflects the changing wind and wave directions with a shift from a 1-2 cm/s right flank directed current to a weak left flank current. The tidal range during this forecast period was +/- 0.75m.

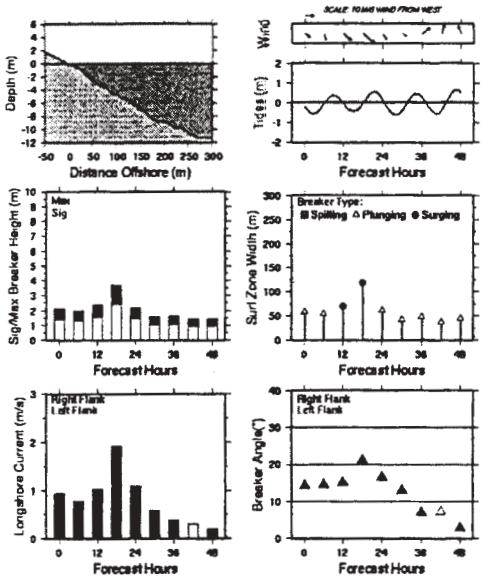

Figure 6. SURF3.0 48-hr forecast for a landing beach on the Portugal coast valid 27-29 APR 2000. In the lowest panel, right flank longshore currents and breaker angles are depicted in solid black.

Of note in Fig. 6 is the peak in significant wave height that occurs at 18Z on 27 APR 2000. It can be seen in Fig. 4b (12Z 27 APR) as a 3.25m contour offshore (in the vicinity of the STWAVE region shown in Fig. 2) and in Fig. 4c (00Z 28 APR) as a 2.0m contour near the shoreline. This passing wave height feature is communicated through WAM to STWAVE and finally to SURF3.0 as evidenced by the peaks in significant wave height, longshore current, and breaker angle at 18Z in the surf output shown in Fig. 6. Since the passage does not correspond with a directional shift, the longshore current remains directed toward the right flank. The intensity doubles from 1 to 2 m/s while the breaker angle increases from 15 to 21°.

4. SUMMARY & FUTURE PLANS

The WAM, STWAVE and SURF3.0 model implementation for LS2K worked well and provided valuable information to the operational community. The models were run twice per day, producing 48-hr forecasts during the period 24 APR – 18 MAY 2000. High resolution wind forcing, bathymetry and beach profiles added to the success of this effort. Unfortunately, little data has been available to quantify the success of the modeling effort.

Plans are underway to validate STWAVE during the Northern Gulf Littoral Initiative (NGLI) in Mississippi Sound. NGLI will offer three directional wave buoys, additional sensors and high-resolution bathymetry. In addition to additional STWAVE work, plans are underway to evaluate the SWAN (Simulation of Waves Nearshore) wave model, a full-plane model (onshore and offshore winds and waves) which can run for both time dependent and steady-state modes.

5. ACKNOWLEDGMENTS

Special thanks to Mr. Jeff Lillycroft for providing the SHOALS data, Mr. Pat Wilz of Planning Systems, Inc. who assisted in getting the STWAVE and SURF3.0 models running at NAVO, and Jarrell Smith (CHL, Vicksburg) who offered assistance with SMS. This work was sponsored by the Space and Naval Warfare Systems Command (SPAWAR) Program Element PE 0603207N.

6. REFERENCES

Earle, M.D., "Surf Forecasting Software Scientific Reference Manual", NORDA Technical Note 351, Naval Research Laboratory, Stennis Space Center, MS, 1989, 261 pp.

Earle, M.D., "Surf Forecasting Software User's Manual", NORDA Technical Note 352, Naval Research Laboratory, Stennis Space Center, MS, 1988, 194 pp.

Thornton, E.B., and R.T. Guza, "Transformation Of Wave Height Distributions", *J. Geo. Res*, **88** (C10), 1983, 5925-5938.

Thornton, E.B., and R.T. Guza, "Surf Zone Longshore Currents And Random Waves: Field Data And Models", *J. Phys. Oceanogr.*, **16**, 1986, 1165-1178.

Komen, G.J., L. Cavaleri, M. Donelan, K. Hasselmann, S. Hasselmann, and P.A.E.M. Janssen, "Dynamics and Modelling of Ocean Waves", Cambridge University Press, Cambridge, U.K., 1994, 532 pp.

Paillard, M., M. Prevosto, S. Barstow and C.G. Soares. "Field Measurements of Coastal Waves and Currents in Portugal and Greece", *C. Eng.*, **40**, 2000, 285-296.

Smith, J. M., D.T. Resio and A.K. Zundel, "STWAVE: Steady-State Spectral Wave Model, Report 1 User's Manual for STWAVE Version 2.0", Instruction Report CHL-99-1, April 1999, 57 pp.

WAMDI Group, "The WAM Model – A Third-Generation Ocean Wave Prediction Model", *J. Phys. Ocean.* **18**, 1988, 1775-1810.

Wittmann, P.A. and P.D. Farrar, "Global, Regional and Coastal Wave Prediction", *MTS Journal*, **31**, 1997, 76-82.

COMPARISON OF TWO YEARS OF WIND AND WAVE HINDCASTS VIA WAM BASED OPERATIONAL FORECASTING SYSTEM VERSUS FIELD AND OTHER MODELS DATA

I. Gertman[1], D.S. Rosen[1], S. Kariel[2] and L. Raskin[1].

[1] Israel Oceanographic & Limnological Research,
National Institute of Oceanography
Tel Shikmona, P.O.Box 8030, Haifa 31080, Israel
Tel: (+972) 48515202, Fax: (+972) 48511911
E-mail: isaac@ocean.org.il, rosen@ocean.org.il, lazar@ocean.org.il
[2] Israel Defense Forces, Israel Navy, Hydrographic Service, Tel Aviv, Israel.

1. INTRODUCTION

An operational wind and wave 48-hours forecasting system for the Eastern Mediterranean (EMWW) has been implemented since fall 1997 in Israel. The core of this operational system is the WAM numerical wave model Cycle 4 (Gunter at al., 1991), run on a coarse space grid resolution of 1/2 degree and on a fine space grid resolution of 1/6 degree.

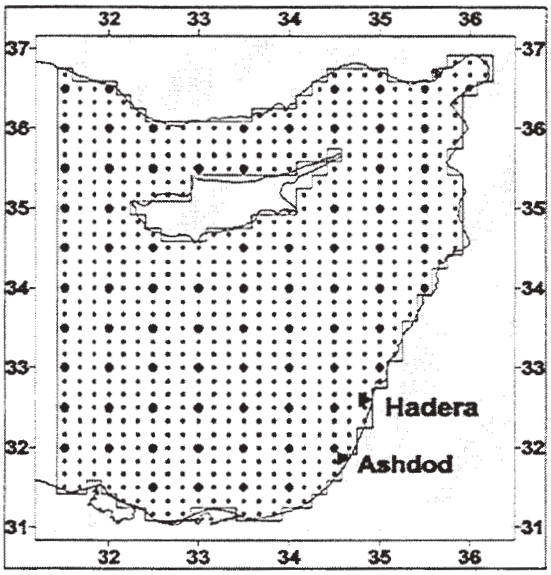

Fig. 1: WAM fine grid (1/6°×1/6°) embedded in coarse grid (1/2°×1/2°) and position of Hadera and Ashdod wave stations.

The estimation of the input wind field is obtained from sea-surface atmospheric pressure fields (SSP). These are calculated using a regional atmospheric model MM4 (Anthes at al., 1987), run by the Israel Military Meteorological Center (IMMC) every 12 hours, providing a 48 hours forecast. The SSP forecast has a time step of 1 hour and covers the Mediterranean region with a spatial resolution of 80 km. A sea surface wind (SSW 10 m) computation is performed according to equations of geostrophic wind and empirical relationships between SSW 10 m and the geostrophic wind. The whole system description and SSW 10m model validation are given in Gertman at al. (1999).

The aim of the investigation is an estimation of the reliability of EMWW results by comparison against data from ground true observations and from EMWW runs with SSP and SSW from ECMWF .

2. GROUND TRUE WIND AND WAVE DATA

For ground true comparison of the computed EMWW atmospheric pressure, wind and wave parameters we used data obtained at Hadera GLOSS station number 80. The station is located about 2.2 km offshore in 27 m water depth. It gathers wind, atmospheric pressure as well as directional waves, currents and accurate sea-levels data on a routine hourly basis. Due to the station position, the observed data are considered to be almost representative of open sea conditions and hence suitable for comparison with the outcome of the EMWW system. The only additional requirement for correct comparison with the coarse grid WAM results, is to account for wave refraction from deep water to – 27 m depth. Prior to the performance of the comparison, the Hadera wave data were back refracted to deep water using Snell wave refraction and Airy linear wave theory (Wiegel, 1964), since the bottom contour lines seaward of the station are almost straight and parallel to the coast. Results of wave measurements at Hadera station are in good agreement with results obtained at Ashdod wave station. For this reason it is assumed that using only the Hadera data is sufficient for estimation of the accuracy of the wind and wave prediction system at the Mediterranean coast of Israel.

3. SEA SURFACE PRESSURE AND WIND DATA

Since January 1998 the EMWW system logs and manages an archive of SSP fields providing the capability of wind and wave hindcasting and of comparison between computed and observed time series of atmospheric pressure, wind and wave data at locations of available ground true observations or other models estimates. The hindcasts in this paper were obtained using SSP with forecasting index 12-24 hours. This choice was taken according to estimation of IMMC meteorologists, that these fields give the most reliable description of true SSP over the Eastern Mediterranean, in contrast with fields with forecasting index 0-12 hours, which contain a certain amount of noise, related to errors in the initial meteorological model fields. Using these SSP fields we ran EMWW for the period January 1998 - January 2000, and derived time series of SSP, SSW 10 m and of the significant wave height at the coordinates of the Hadera station, at 1 hour time step interval.

Furthermore, results of weather reanalysis carried out by the ECMWF for the Mediterranean region, for the period 1979 to 2000, so called "***ECMWF Re-Analysis (ERA)***", prepared within the framework of the Mediterranean Forecasting System (MFS) project (http://www.cineca.it/~mfspp000) were also used for the present comparison. These data contain SSW 10 m and SSP fields with space resolution 1/2°×1/2° and time step 6 hours. Using these fields, we carried out another wave hindcast for the Eastern Mediterranean with the EMWW using the coarse grid and we also built time series of SSP, SSW 10m (6 hours interval) and significant wave height (1 hour interval) at the coordinates of the Hadera station for period from January 1998 to January 2000.

4. COMPARISON BETWEEN MEASURED AND MODELED SSP

SSP is an important input parameter used for estimation of SSW 10 m. Correlation between measured and model SSP is necessary for providing a reliable wind input, but is not sufficient, because reliable wind field estimation requires a reliable horizontal gradient of SSP as input. The results of the SSP comparison are given in scatter diagrams in Fig. 2. Values of statistical parameters used in the comparison are shown in table 1 (negative values of bias indicate that the measured pressure is less than that modeled). The results indicate that the SSP computed via ECMWF model are significantly closer to the ground true values measured at Hadera station than the SSP computed via the EMWW. However, we must remind that the SSP fields computed via EMWW are not re-analyses, but direct forecasts with forecasting index from12 to 24 hours, and consequently such differences seem reasonable. For example, Lavrenov (1998) got root mean square error (RMSE) values of 3.07 millibars and correlation coefficient 0.97, while carrying out a comparison between measured and modeled ECMWF SSP values with forecasting index 48 hours.

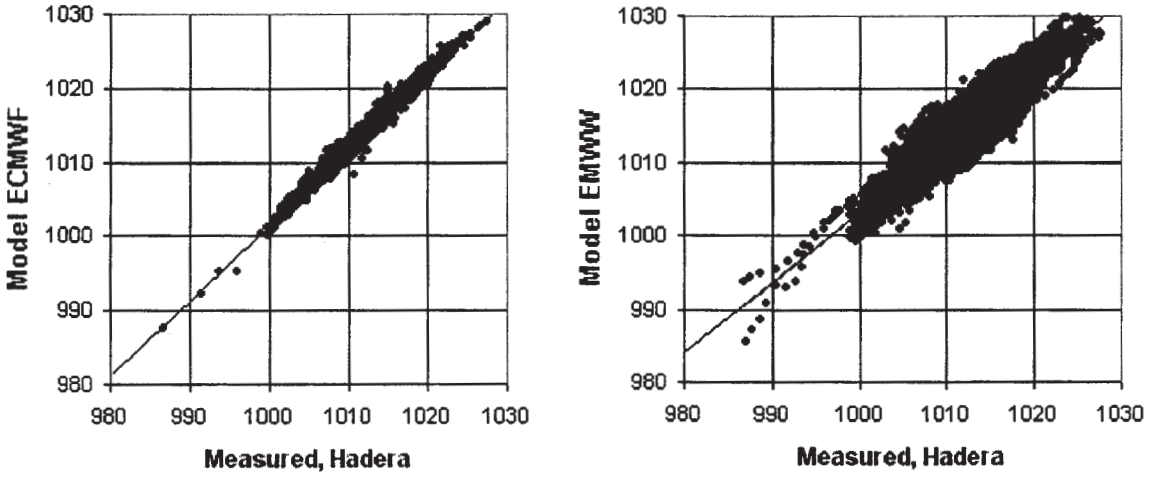

Fig. 2: Scatter diagrams between measured and modeled SSP (in millibars)

Thus, we can conclude that the accuracy of EMWW pressure fields with forecasting index 12-24 hours is similar to the accuracy of ECMWF SSP fields with forecasting index about 48 hours

Tab. 1: Statistical parameters of comparison between SSP (millibars) measured at Hadera and those estimated by models.

Statistical parameters	Model	
	ECMWF	EMWW
Count	2983	16388
Bias	-1.6	-2.9
RMSE	1.8	3.15
Correlation coefficient	0.99	0.94

5. COMPARISON BETWEEN MEASURED AND MODELED SSW 10M

For estimation of the accuracy of the directions of the modeled winds we selected cases with measured wind speed above 5 m/s. For calm weather conditions, the differences in direction of measured and modeled winds are irregular. As a criterion of accuracy of the modeled wind direction, we used the declination of modeled wind vectors from measured wind vector (less than 180°), without any respect to a relative position of the vectors. Hence, a smaller declination means a better modeled wind direction. Fig. 3 shows histograms of the declinations. These histograms show an apparent advantage to the ECMWF wind, because a maximum probability (about 30%) is found for the declination interval of 20-40°. However, at the same time the distribution of the declination of EMWW wind has lower values of maximum probability (about 20%), and is positioned at a higher declination interval 40-60°.

For estimation of the accuracy of the modeled wind speed obtained from the above two sources against the wind measured at Hadera, we built two two-dimensional histograms of their distributions (in percentages from the amount of compared wind speed couples) (tab. 2,3). These histograms provide a more reliable evaluation than that obtained using simple scatter diagrams, for cases like our, of significant dispersion of the compared parameters. One-dimensional histograms of measured wind speed (in the most upper row) and modeled wind speed (in the most right column) are also shown.

In an ideal case (equal measured and modeled values) it would be filled only on the diagonal squares of the histograms with equal interval values. As expected, the results of the comparison of both models are far from the ideal case. The histogram of comparison with ECMWF wind (tab.2) has significantly smaller dispersion than the histogram of the EMWW. The peak of the distribution of modeled ECMWF wind speed is found in the same interval as the peak of the distribution of measured wind (2-4 m/s). However, for wind speeds above 4 m/s the ECMWF wind speed is usually underestimated by about 2-4 m/s. The ECMWF wind did not reach the maximum wind speed in intervals 16-20 m/s, while these wind speeds were measured at Hadera station. On the other hand, the wind speeds estimated by EMWW do not show a constant problem of speed underestimation in intervals 6-16 m/s, but the dispersion of the modeled wind speed versus the measured wind speed is relatively larger (±6 m/s). EMWW wind also did not

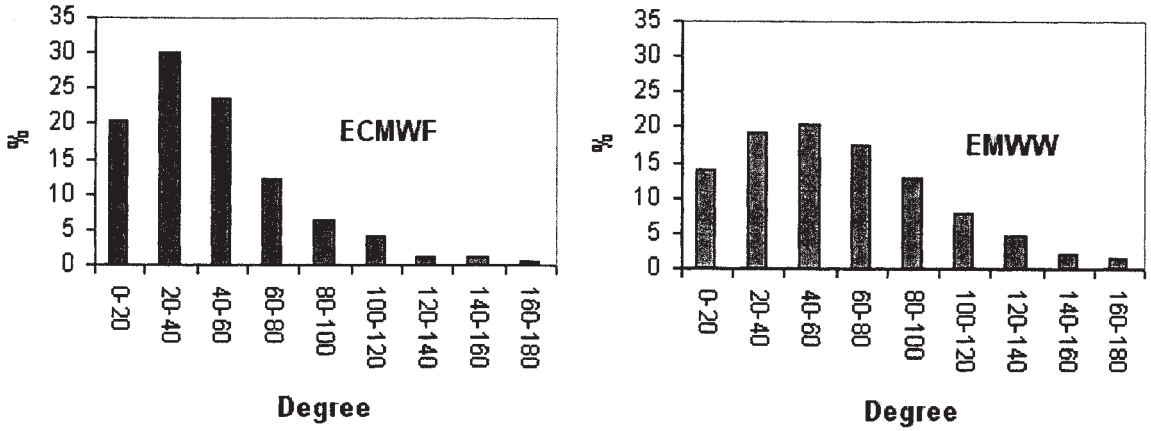

Fig. 3: Histograms of declination of modeled wind direction from measured wind direction.

reach maximum values of 18-20 m/s, but was much closer to these values (16-18 m/s). In the speed intervals of 0-6 m/s EMWW wind speed has an overestimation problem of about 2-4 m/s and the peak of the distribution of EMWW wind is found in interval 6-8 m/s, but not in the interval of the peak of the measured wind (2-4 m/s).

We have also explored the perfomance of the models in time. For this purpose we computed the bias (measured value minus modeled one), the root mean square error and the coeficient of correlation (R) for each month during the hindcasted period. According to these parameters, it is possible to conclude that during summer months, the correlation between measured and modeled wind speeds was poorer. Apparently, this result is connected with the lesser definition of meteorological situations in summer. RMSE of summer months is also a little bit lower than for winter RMSE, but we have to take into account that during summer months wind speed in the Eastern Mediterranean is usually lower than 8 m/s.

According to the results presented in tab. 4 we can also conclude, that ECMWF wind speed has a significantly better correlation with the measured wind speed and also significantly lower bias and RMSE. We want to note that values of bias and RMSE for all hindcast period for both models are a little bit lower than similar estimates obtained from comprehensive comparisons between modeled ECMWF and measured wind speed in the Adriatic Sea (Cavaleri at al. 1996)

6. COMPARISON BETWEEN MEASURED AND MODELED SIGNIFICANT WAVE HEIGHT

To derive time series (January 1989 – January 2000) of significant wave height at the coordinates of the Hadera wave gauge, we carried out the computation by WAM (0.5°x0.5°) using the same sets of input SSW 10 m fields (ECMWF and EMWW) from which we extracted and analyzed the above mentioned wind time series. Using the modeled values obtained in two separate WAM runs and the measured time series of data, we also built two two-dimension distributions of measured and modeled significant wave height (tab. 5,6) and computed their statistics comparison for each month of the hindcasting period (tab. 7).

It is found that as in the case of the wind speed distribution, also the ECMWF wave histogram (tab. 5) has a significantly smaller dispersion than the EMWW wave histogram (tab. 6). However, the maxima of the probability for each interval of the measured wave height (identified by bold font values) lie significantly lower than the "ideal" diagonal squares. This means that at least for the Mediterranean coast of Israel, using ECMWF wind for wave computation by WAM leads to a systematic underestimation of wave heights and requires introduction of a correction factor. The wave height distribution derived using EMWW wind also has the underestimation problem, but to a much lesser degree and in particular for wave height intervals above 3 m. Another problem found for the EMWW distribution is the shift of the position of the probability peak of the modeled wave height for the one–dimensional histogram, from interval 0-0.5 m to interval 0.5-1 m, while the measured wave height one–dimensional histogram peak is in the interval 0-0.5 m.

Both modeled significant wave height time series show a good correlation with the measured one. As it was expected, correlations during winter months are better than during summer months. Again we can see that ECMWF wind led to higher coefficients of correlation and smaller RMSE in wave height comparison. The small values of bias correspond to the high probabilities of the low wave heights and we think that the two-dimensional histograms provide a better estimation of the results of the hindcast performed.

7. CONCLUSIONS

- On the basis of two years comparison of atmospheric pressure, wind speed, wind direction and significant wave height, computed by wind and wave forecasting system EMWW with ground true measurements off the Mediterranean coast of Israel, it was found that the results of the comparison are similar to the results obtained for similar experiments in marginal seas (e.g. Cavaleri at al., 1996 and Lavrenov, 1998). Average values of RMSE and coefficient correlation for wind speed are 3.2 m/s and 0.5. The same statistics for significant wave height are 0.5 m and 0.7.
- The analogous comparison carried out using input wind fields extracted from "***ECMWF Re-Analysis (ERA)***" revealed a significantly lower dispersion between all modeled and measured parameters.

- Both comparisons show underestimation of wind speed and significant wave height in intervals of maximal values, but the underestimation of wind speed and wave height modeled with wind from ECMWF is significantly larger.

8. ACKNOWLEDGMENTS

The present study has been partially funded by the Israel Ministry of Defense. Permission to publish this paper is gratefully acknowledged.

We gratefully acknowledge MFSPP program for making available ECMWF wind and pressure fields, and IOLR for providing the Hadera data.

Tab. 2: Distribution measured wind speed relative wind speed modeled by ECMWF

Model	8.76	**38.57**	31.74	12.14	5.11	2.69	0.69	0.24	0.03	0.03	100.00
14-16								0.07	**0.03**	**0.03**	0.14
12-14						0.17	0.07	**0.14**			0.38
10-12	0.03	0.07	0.07	0.24	0.41	0.66	**0.28**	0.03			1.79
8-10	0.07	0.21	0.48	0.76	1.00	**0.79**	0.10				3.41
6-8	0.14	1.72	2.83	3.93	1.41	0.45	0.14				10.62
4-6	1.38	9.18	12.94	**4.73**	**1.55**	0.55	0.10				30.42
2-4	**5.04**	**20.73**	**13.59**	2.28	0.69	0.07					**42.39**
0-2	2.10	6.66	1.83	0.21	0.03						10.83
Speed m/s	0-2	2-4	4-6	6-8	8-10	10-12	12-14	14-16	16-18	18-20	**Measured**

Table 3: Distribution measured wind speed relative wind speed modeled by EMWW

Model	8.42	**38.76**	30.82	12.42	5.56	2.94	0.83	0.13	0.08	0.04	100.00
18-20					0.01	0.01	0.01	0.01			0.04
16-18				0.01	0.01	0.06	0.02	0.01	0.01	**0.03**	0.16
14-16	0.01	0.04	0.04	0.10	0.08	0.24	0.19	**0.06**	**0.03**	0.01	0.80
12-14	0.03	0.21	0.50	0.56	0.52	0.55	**0.21**	0.01	0.02		2.61
10-12	0.18	0.99	2.11	2.17	1.30	**0.76**	0.17	0.03	0.01		7.72
8-10	0.57	3.57	5.18	2.98	1.33	0.60	0.11	0.01	0.01		14.35
6-8	1.98	11.94	**10.88**	**3.55**	**1.37**	0.50	0.09	0.01			**30.32**
4-6	**2.88**	**12.70**	7.76	2.09	0.71	0.18	0.03	0.01			26.36
2-4	2.08	6.69	3.40	0.74	0.18	0.04					13.12
0-2	0.69	2.63	0.96	0.21	0.03						4.53
Speed m/s	0-2	2-4	4-6	6-8	8-10	10-12	12-14	14-16	16-18	18-20	**Measured**

Tab. 4: Values of statistical parameters of the comparison between SSW 10 m (in m/s) meassured in Hadera and estimated by models.

Year	Month	ECMWF				EMWW			
		Count	Bias	RMSE	R	Count	Bias	RMSE	R
1998	1	124	0.4	2.1	0.7	744	-2.2	3.9	0.5
1998	2	105	0.5	2.2	0.5	381	-2.1	3.5	0.6
1998	3	121	0.4	2.1	0.8	725	-2.9	4.0	0.7
1998	4	101	0.4	2.0	0.6	602	-2.2	3.6	0.5
1998	5	105	0.3	1.9	0.5	635	-2.1	3.5	0.3
1998	6	94	0.6	1.3	0.6	551	-2.2	3.2	0.2
1998	7	122	0.3	1.2	0.7	728	-1.6	2.9	0.4
1998	8	124	0.5	1.3	0.5	743	-1.5	2.9	-0.1
1998	9	120	0.5	1.9	0.5	36			
1998	10	122	0.7	2.0	0.5	728	-1.4	2.9	0.3
1998	11	111	0.7	2.3	0.4	668	-1.1	2.7	0.3
1998	12	123	0.0	2.2	0.7	742	-1.5	3.1	0.6
1999	1	110	0.4	1.9	0.7	662	-1.3	2.9	0.4
1999	2	104	0.0	2.3	0.7	612	-1.8	3.2	0.5
1999	3	116	0.0	2.3	0.4	696	-2.7	4.0	0.3
1999	4	120	0.4	2.3	0.5	720	-2.8	3.9	0.4
1999	5	120	0.7	2.2	0.5	723	-2.4	3.5	0.5
1999	6	120	0.3	1.2	0.7	720	-2.4	2.9	0.5
1999	7	119	0.7	1.4	0.7	677	-2.1	2.5	0.6
1999	8	124	0.6	1.3	0.6	576	-1.9	2.5	0.3
1999	9	120	0.4	1.7	0.5	360	-1.5	2.6	0.0
1999	10	124	0.8	2.0	0.6	744	-1.1	2.5	0.4
1999	11	120	0.0	2.2	0.5	720	-1.0	2.7	0.4
1999	12	112	-0.2	1.9	0.6	669	-1.8	3.2	0.5
2000	1	118	-0.9	2.6	0.7	709	-1.8	3.6	0.6
All Period		2899	0.3	2.0	0.6	15871	-1.9	3.2	0.5

Tab. 5: Distribution of measured significant wave heights versus those computed by WAM with ECMWF wind

Model	**51.01**	30.03	10.65	4.38	2.00	0.98	0.50	0.29	0.10	0.02	0.03	0.01	100.00
3.5-4								0.01	0.01	0.01			0.02
3-3.5									0.01	0.01	**0.01**	**0.01**	0.03
2.5-3					0.01	0.01	0.07	0.11	0.02	**0.01**	0.01		0.24
2-2.5				0.04	0.11	0.19	0.20	**0.14**	**0.06**	0.01	0.01		0.74
1.5-2	0.01		0.04	0.39	0.76	**0.54**	**0.22**	0.03	0.01				1.98
1-1.5	0.11	0.24	1.51	**2.22**	**0.91**	0.22	0.01	0.01					5.23
0.5-1	4.34	12.34	**7.49**	1.65	0.21	0.02	0.01						26.06
0-0.5	**46.55**	**17.45**	1.60	0.09									**65.69**
Hs meter	0-0.5	0.5-1	1-1.5	1.5-2	2-2.5	2.5-3	3-3.5	3.5-4	4-4.5	4.5-5	5-5.5	5.5-6	**Measured**

Tab. 6: Distribution of measured significant wave height versus those computed by WAM with EMWW wind

Model	**50.99**	29.07	10.88	4.62	2.25	1.11	0.57	0.33	0.11	0.03	0.03	0.01	100.00
4-4.5				0.01				0.03	0.01	0.01	0.01		0.06
3.5-4	-		0.01	0.01	0.05	0.02	0.01	0.05	0.01	**0.01**	**0.01**	**0.01**	0.17
3-3.5	0.01	0.01	0.06	0.11	0.12	0.11	0.08	0.05	0.01	0.01	0.01		0.57
2.5-3	0.01	0.06	0.26	0.26	0.44	0.26	0.13	0.10	**0.04**				1.55
2-2.5	0.20	0.46	0.64	0.69	0.49	**0.35**	**0.25**	**0.09**	0.03				3.19
1.5-2	0.89	2.40	2.84	**1.68**	**0.57**	0.25	0.10	0.01	0.02				8.75
1-1.5	8.27	11.12	**5.35**	1.62	0.51	0.10	0.01						26.97
0.5-1	**33.10**	**14.37**	1.73	0.25	0.08	0.03							**49.57**
0-0.5	8.52	0.65											9.17
Hs meter	0-0.5	0.5-1	1-1.5	1.5-2	2-2.5	2.5-3	3-3.5	3.5-4	4-4.5	4.5-5	5-5.5	5.5-6	**Measured**

Table 7: Values of statistical parameters of the comparison between significant wave height (in meters) measured at Hadera and that estimated by WAM with different wind fields.

Year	**Month**	**Wind from ECMWF**				**Wind from EMWW**			
		Count	**Bias**	**RMSE**	**R**	**Count**	**Bias**	**RMSE**	**R**
1998	1	646	0.1	0.3	0.9	646	-0.6	0.8	0.7
1998	2	669	0.3	0.4	0.9	130	-0.3	0.4	0.7
1998	3	742	0.3	0.5	0.9	742	-0.3	0.6	0.8
1998	4	618	0.1	0.3	0.9	618	-0.3	0.5	0.7
1998	5	697	0.1	0.2	0.9	697	-0.4	0.5	0.6
1998	6	493	0.2	0.4	0.9	469	-0.5	0.6	0.8
1998	7	740	0.1	0.2	0.8	740	-0.4	0.5	0.6
1998	8	741	0.2	0.3	0.7	718	-0.3	0.4	0.7
1998	9	719	0.2	0.2	0.8	0			
1998	10	741	0.2	0.4	0.7	740	-0.3	0.4	0.7
1998	11	710	0.2	0.3	0.8	709	-0.2	0.3	0.7
1998	12	741	0.3	0.5	0.9	741	-0.4	0.6	0.8
1999	1	740	0.2	0.4	0.9	739	-0.2	0.5	0.6
1999	2	656	0.3	0.5	0.9	656	-0.1	0.6	0.7
1999	3	703	0.2	0.3	0.9	703	-0.4	0.6	0.7
1999	4	717	0.1	0.2	0.9	717	-0.6	0.7	0.6
1999	5	742	0.1	0.3	0.7	742	-0.6	0.7	0.5
1999	6	717	0.0	0.2	0.9	717	-0.6	0.7	0.7
1999	7	742	-0.1	0.2	0.5	527	-0.6	0.6	0.7
1999	8	743	0.2	0.4	0.7	526	-0.3	0.5	0.5
1999	9	720	0.1	0.2	0.8	359	-0.3	0.4	0.6
1999	10	742	0.2	0.3	0.8	741	-0.3	0.4	0.8
1999	11	720	0.2	0.4	0.9	720	-0.2	0.4	0.8
1999	12	724	0.2	0.4	0.9	734	-0.3	0.4	0.9
2000	1	735	0.5	0.7	0.9	740	0.0	0.6	0.8
All Period		17658	0.2	0.4	0.9	15571	-0.3	0.5	0.7

9. REFERENCES

Anthes, R.A., E.Y.Hsie and Y.H. Kuo, 1987: Description of the Penn State/NCAR Mesoscale Model Version 4 (MM4), *NCAR Technical Note*, TCAR/TN-282+STR.

Cavaleri, L., L. Bergamasco, L. Bertotti at al., 1996: Wind and waves in the Northern Adriatic Sea, *In book: "Wind and waves in Northern Adriatic Sea", edited by L. Cavalieri.* Venice, 195 p.

Gertman, I., S. Kariel, L. Raskin and D.S. Rosen, 1999: Sea Surface Wind and Wave Forecasting System for the Eastern Mediterranean, *Proc. Of the Intl. MEDCOAST Conference on Wind and Wave Climate of Mediterranean and Black Sea, WIND & WAVE CLIMATE '99, March 30-April 2, 1999;Antalya,Turkey. Abdalla, Ozhan(Editors)*, pp. 171-179.

Gunter, H., S. Hasselmann and P.A.E.M. Janssen, 1991: Wamodel cycle 4, *DKRZ report no. 4*, Hamburg.

Lavrenov, I.,V., 1998: Mathematic Modeling of Wind Waves in Spatial-Inhomogeneous Ocean. (in Russian), St.Peterburg, Izd. HYDROMETEOIZDAT, 500 p.

Wiegel, R.L., 1964: Oceanographical Engineering, Prentice-Hall, Inc., Englewood Cliffs, New Jersey, USA, 532 p.

EVALUATION OF THE CMC REGIONAL WIND AND WAVE FORECASTING SYSTEM DURING A 3-YEAR PERIOD

Roop Lalbeharry

Recherche en Prévision Numérique, Meteorological Service of Canada
Downsview, Ontario, Canada M3H 5T4
E-mail: Roop.Lalbeharry@ec.gc.ca

1. INTRODUCTION

In December 1990, the Canadian Meteorological Centre (CMC) of the Meteorological Service of Canada (MSC), formerly the Atmospheric Environment Service and Program (AES/AEP), implemented in its forecasting system the operational first generation (1G) wave model called the Canadian Spectral Ocean Wave Model (CSOWM) (Cardone et al., 1976) which operated on two separate oceanic regions, namely, the northwest Atlantic and the northeast Pacific. An evaluation of the performance of the CSOWM against buoy data is presented in Khandekar and Lalbeharry (1996) and Khandekar et al. (1994). The development of the third generation (3G) wave model called WAM (WAMDI Group, 1988) led to a gradual replacement of earlier 1G and 2G wave models in most deep water prediction systems since 1988. The current Cycle-4 version of the WAM, hereinafter referred to as WAM4, is based on the ideas of Janssen (1991) in which the winds and waves are coupled, that is, there is feedback of growing waves on the wind profile. The effect of this feedback is to enhance the wave growth of younger wind seas over that of older wind seas for the same wind. Validation studies (Wittmann et al., 1994, 1995; Cardone et al., 1995, 1996; Janssen et al., 1997; and Bidlot et al., 1998) on the performance of WAM4 against buoy observations indicate that the analyzed wave heights generated by WAM4 are of good quality and in good agreement with the buoy observations while the quality of the wave forecasts shows a slow deterioration with projection time. In February 1996, the CMC implemented the WAM4 in an operational mode in its wave forecasting system, replacing the 1G CSOWM in operation since December 1990. Two regional versions of the WAM4 were implemented, one for the northwest Atlantic ocean extending from 25°N to 70°N and from 80°W to 15°W (Fig. 1a) and the other for the northeast Pacific ocean bounded by latitudes 25°N and 60°N and longitudes 160°E and 120°W (Fig. 1b). Each version has a grid spacing of 1.0° in both latitude and longitude directions and is driven by 10 m level surface winds provided by the CMC global and regional operational atmospheric weather prediction models. The primary purpose of this paper is to assess how well the regional version of the WAM4 implemented at the CMC performed during the 3-year period December 1996 - November 1999.

Section 2 presents a brief description of the CMC regional wave forecasting system and its wind forcing. Changes in the wind forcing due to changes in the operational weather prediction models are also described. The buoy data used for verification and the generation of the wave model data sets for comparison are described in section 3 while section 4 gives the definitions of the statistical parameters used in the present study. Section 5 describes the results and compares the performance of the regional WAM4 with the performance of the global WAM4. Section 6 briefly summarizes the main findings of this study.

2. CMC OCEAN WAVE FORECASTING SYSTEM

2.1 The ocean wave model

The ocean wave model in operational use at the CMC is a regional version of the global WAM4 (WAMDI Group, 1988; Janssen, 1991). The WAM4 is based on the explicit solution of the energy balance equation for the two-dimensional surface wave spectrum written in standard notation as

$$\frac{\partial E}{\partial t} + \nabla.(\vec{C}_g E) = S \qquad (1)$$

where $E = E(f,\theta,\varphi,\lambda,t)$ is the two dimensional spectral energy density which is a function of frequency f,

direction of wave propagation θ, latitude φ, longitude λ and time t. Here, C_g is the group velocity of the surface waves which can be expressed in terms of the phase speed C, wavenumber k and water depth h ($C_g = \frac{1}{2}C[1 + 2kh/\sinh(2kh)]$) ; in deep water the group velocity is a function of frequency only, that is, $C_g = \frac{1}{2}C = g/4\pi f$ where g is acceleration due to gravity. The assumptions made include no bottom friction, no shoaling, no depth refraction, no diffraction and reflection, and no ocean currents. The wave spectrum is locally modified by the net source term $S = S(f,\theta,\varphi,\lambda,t)$ which represents the physical processes that transfer energy to and from the wave spectrum. The source term S can be written as

$$S = S_{in} + S_{in} + S_{ds} \qquad (2)$$

where S_{in} represents the wind energy input to the wave field, S_{nl} the energy redistribution associated with the nonlinear wave-wave interactions, and S_{ds} the energy dissipation due to whitecapping. All the source terms are functions of E. Equation (2) is solved for 25 frequencies logarithmically spaced from 0.042 Hz to 0.41 Hz at intervals of $\Delta f/f = 0.1$ and 24 directional bands of 15° each so that at each model grid point there are 600 spectral estimates at any given time. The solution requires the specification of the forcing winds at each grid point for each time and the initial and boundary conditions. The winds are obtained from the numerical weather prediction models. The model's boundary points along the coasts are treated as fully absorbing. For a regional model with open boundaries the integration area is chosen large enough, and the forecast period short enough, to minimize contamination of the waves inside the area of interest by waves propagating into the area from outside. When the model starts from a flat sea, its initial state is parameterized using an empirically derived spectrum, a directional spreading function, and the wind speed at run time. In an operational environment, the initial field is saved after 12 hours of integration time into the forecast for input to the model's next run. Both the propagation and integration time steps are each set to 1200 s and with the grid resolution of 1.0° the Courant-Friedrichs-Lewy (CFL) stability criterion is more than adequately satisfied. The solution of (1) is for deep water physics in which C_g and C are both functions of frequency only. The WAM4 grid spacing $\Delta\phi = 1.0°$ latitude is equivalent to a spacing of 111 km and $\Delta\lambda = 1.0°$ longitude to a spacing that varies from 100 km at 25°N to 38 km at 70°N.

The WAM4 grid is partially covered with sea ice mainly in the winter months. For each run the ice field for input to the WAM4 is obtained from the CMC sea ice analyses. The WAM4 model grid point is considered to be a sea ice point if the ice fraction at that point > 0.5. Once this determination is made at the beginning of each model run, the ice field remains unchanged during the 48-hour forecast period. At all land points, and at all sea ice points, the wave energy of each spectral component is set equal to zero.

2.2 Wind forcing

Both regional WAM4s were initially driven by winds obtained from the two operational numerical weather prediction models in use at the CMC. The Atlantic WAM4 was originally forced by winds from the regional finite element (RFE) model producing short-range forecasts up to 48 hours. The horizontal grid is a variable resolution grid with a central domain of uniform grid spacing of 50 km covering most of North America and adjacent waters. The vertical discretization consists of 28 σ ($= p/p_s$, where p is pressure and p_s is surface pressure) levels with the lowest prognostic level being $\sigma = 0.995$ (about 40 m above the surface). In December 1992 the regional data assimilation system (RDAS) based on multivariate optimum interpolation was implemented (Chouinard et al. 1994) to provide an analysis at run time following a 12h spin-up cycle initiated from the global data analysis 18 hours earlier. In December 1995 the RFE model resolution in the central window was increased to 35 km. Details of the RFE model, the changes made to it, and its physical parameterization are described in Mailhot et al. (1995, 1997). On the other hand, the Pacific WAM4 was forced by winds generated by the medium range (> 2 days) global spectral finite element (SEF) model. It has a uniform grid spacing of about 0.9° (about 100 km), a spectral representation of 199 waves for the model fields and 21 σ levels in the vertical (Ritchie and Beaudoin, 1994) with the lowest prognostic level being $\sigma = 0.990$ (about 80 m above the surface). The SEF model served both as the global data assimilation model and the medium range forecast model.

The Global Environmental Multiscale (GEM) model replaced the RFE model as the regional model on 24 February 1997 without a RDAS. It uses the static analysis from the global SEF model as its initial conditions to produce short-range (up to 2 days) forecasts. The GEM model has a global variable resolution latitude-longitude mesh which can be arbitrarily rotated to permit resolution to be focused over the area of interest and 28 η ($= (p - p_t)/(p_s - p_t)$, where p_t is the top pressure) levels in the vertical with

the lowest prognostic level being $\eta = 0.995$ (about 40 m above the surface). The model can be used in uniform resolution mode for medium range forecasting or in focused mode for short range regional forecasting (Côté et al., 1998a,b). For its initial operational implementation in the regional cycle, the GEM model had a grid resolution of 0.33° (about 35 km). On 18 June 1997 a new global 3D variational (3DVAR) analysis (Gauthier et al., 1999) replaced the SEF-driven global optimum interpolation analysis, while in September 1997 the 3DVAR data assimilation system was implemented for the GEM regional analyses (Laroche et al., 1999). In September 1998, the regional model resolution in the uniform window was increased to 0.22° (about 24 km) and in October 1998, the SEF model was replaced by the global GEM model with the same uniform grid resolution as the SEF model. This unified system for short-range and medium-range forecasting allows the global cycle and the regional cycle to share the same code, the same physics library, and the same data assimilation system code (Steenbergen et al., 1998). However, the physics options used operationally are not all the same in the two models.

The CMC weather prediction models use the dynamic variables at their lowest prognostic σ or η level, the Monin-Obukov similarity theory for the surface layer, the surface temperature and moisture, and the turbulent kinetic energy in the planetary boundary layer to diagnose the winds at the base of the models, nominally at σ or $\eta = 1$. The winds at this level represent the winds at the 10 m level. The WAM4 considers the wind field provided by the atmospheric model to be the equivalent neutral wind field.

3. MODEL AND BUOY DATA

3.1 Model data

In late 1995, the European Centre for Medium-Range Weather Forecasts (ECMWF), the Fleet Numerical Meteorology and Oceanography Center (FNMOC), the United Kingdom Meteorological Office (UKMO), and the CMC started a project aimed at exchanging model data at selected geographical locations. They were joined in May 1996 by the National Centers for Environmental Prediction (NCEP). All centres use the wave model WAM4, except the UKMO which has its own 2G wave model (Golding, 1983; Holt, 1994), and their own atmospheric models to produce the surface wind forcing for driving their operational wave models. The model data exchanged in this project are the significant wave height, wind speed and direction, and the peak period. The model two-dimensional spectral energy is integrated over all wave directions to obtain the model energy as function of model frequency only. The frequency corresponding to the peak one-dimensional energy is defined as the peak frequency and its inverse is the peak period.

The CMC WAM4 for each oceanic basin is run twice daily at 0000 and 1200 UTC and generates wave forecasts at 3-hourly intervals up to 48 hours. For each run and each day of the month the model data are bilinearly interpolated to the selected buoy locations. The interpolated forecast data valid for each of 3 projection times 00h, 24h and 48h from the model run time are stored in separate files. At the end of each month these files which contain model monthly time series of interpolated data at buoy locations are transferred by each participating centre via "ftp" to the UKMO computer server, where they are combined with the observations and processed by the ECMWF. The combined data files are then retrieved from the UKMO server by each participating centre. The results shown in this study pertain to the wind and wave data provided by CMC, ECMWF, and FNMOC and processed by the ECMWF in the data exchange project for the period December 1996 to November 1999. The results valid at the 00h, that is, at the analysis or run time, are based on the 0000 and 1200 UTC model runs while those valid at the 24h and 48h projections are based only on the 1200 UTC model run. This is done to facilitate comparison with the verification statistics of the ECMWF wave model which is run once per day at 1200 UTC. The ECMWF also produces a daily 0000 UTC wave analysis which is used in the computation of the 00h statistics. Hence, for the 24h and 48h forecasts the number of observations used is approximately half that used for the 00h forecast.

3.2 *Buoy data*

The Marine Environmental Data Service (MEDS) in Canada and the National Buoy Data Centre (NDBC) in the United States operate a network of moored buoys in the coastal and shelf regions of the Atlantic and Pacific coasts of North America. Table 1 gives the buoy identification numbers and their names while Fig. 1 shows their corresponding geographical locations. The buoys shown in Fig. 1 are well within the grids of the two regional wave models in relatively deep waters ranging from 40 m to well over 1000 m and have a high rate of data availability. The buoys listed in Table 1 are the buoys selected for validation of model results. The buoy data are transmitted to the ECMWF via the Global Telecommunication System (GTS). From the buoy records, monthly time series of wind speed and

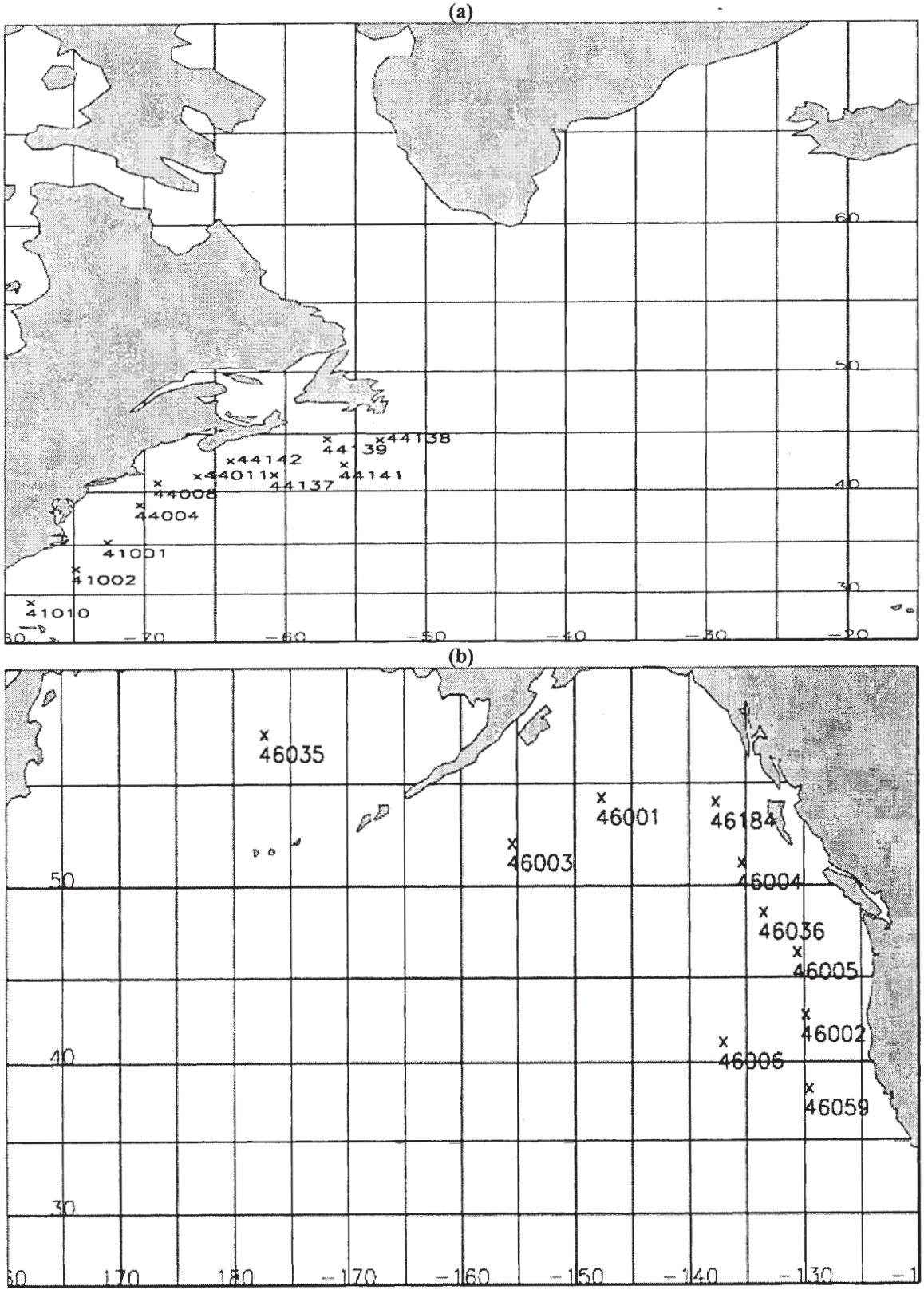

Fig. 1. Areas covered by the CMC regional WAM4 and geographical locations and identification numbers of the buoys given in Table 1 for (a) the North Atlantic and (b) the North Pacific.

direction, significant wave height, and peak period are constructed and used to perform a basic quality check on the data. This quality control procedure described in Bidlot et al. (1998) and Janssen et al. (1997) includes removal of data due to faulty instruments and removal of outliers. The buoy wind speed, usually measured at a height of 5 m, is multiplied by a factor of 1.07 to adjust it to the 10 m level for a neutrally stable atmosphere (Smith, 1988). However, during the winter months the atmosphere is generally unstable with cold air over warm waters. This implies a different wind profile than the neutrally stable one so that during these months this adjustment would also have errors (Zambresky, 1989).

Table 1: Buoy identification numbers and their names

North Atlantic (NATL) buoys		North Pacific (NPAC) buoys	
Buoy ID	Buoy name	Buoy ID	Buoy name
41001	East Cape Hatteras	46001	Gulf of Alaska
41002	South Cape Hatteras	46002	Oregon
41010	East Cape Canaveral	46003	South Aleutians
44004	Hotel	46004	Middle Nomad
44008	Nantuket	46005	Washington
44011	Georges Bank	46006	SE Papa
44137	East Scotia Slope	46035	Bering Sea
44138	SW Grand Banks	46036	South Nomad
44139	Banquereau Bank	46059	California
44141	Laurentian Fan	46184	North Nomad
44142	La Have Bank		

4. STATISTICAL ANALYSIS PROCEDURE

The buoy data provide an independent data set to objectively evaluate the accuracy or quality of the model wave forecasts. Let F be the model forecast value, O the observed buoy value, $\overline{F} = 1/N\Sigma F$ the model mean, $\overline{O} = 1/N\Sigma O$ the buoy mean, $\Delta F = (F - O)$ the difference between the model and observed values, and N the number of observations. Then, for each of the parameters of wind speed, significant wave height, and peak spectral period, the following statistics are computed:

mean error or

$$\text{bias} = 1/N\Sigma\Delta F \quad (3)$$

root mean square error

$$\text{rmse} = [1/N\Sigma\Delta F^2]^{\frac{1}{2}} \quad (4)$$

standard deviation

$$\text{stdev} = [1/(N-1)\Sigma(\Delta F - \mu)^2]^{\frac{1}{2}} \quad (5)$$

linear correlation coefficient

$$r = [1/N\Sigma(F - \overline{F})(O - \overline{O})]/\sigma_f\sigma_o \quad (6)$$

scatter index

$$SI = \text{rmse}/\overline{O} \quad (7)$$

symmetric slope

$$s = [\Sigma F^2/\Sigma O^2]^{\frac{1}{2}} \quad (8)$$

slope of best fit line

$$b = [N\Sigma FO - \Sigma F\Sigma O] / [N\Sigma O^2 - (\Sigma O)^2] \quad (9)$$

intercept of best fit line

$$a = \overline{F} - b\overline{O} \quad (10)$$

overprediction ratio

$$Ra = 1/N\Sigma\delta; \quad \delta = 1 \text{ if } F \geq O \text{ and } \delta = 0 \text{ if } F < O \quad (11)$$

anomaly correlation

$$AC=\Sigma[(F - \overline{O})(O - \overline{O})]/[\Sigma(F - \overline{O})^2(O - \overline{O})^2]^{1/2} \quad (12)$$

reduction of variance

$$RV = 1 - [\Sigma(F - O)^2/\Sigma(\overline{O} - O) \quad (13)$$

where σ_f is the standard deviation of F and σ_o that of O. The overprediction ratio Ra gives the fraction of the total observations N overpredicted by the model while the scatter index SI is the ratio of the rmse relative to the mean observations. The symmetric slope s is the mean ratio between the modelled and observed values. It is the coefficient of the linear regression line constrained to pass through the origin and is invariant with respect to an interchange between F and O (Bauer et al., 1992; Romeiser, 1993). On the other hand, the standard regression line whose slope is given by (9) and intercept by (10) gives the optimal linear transformation from one data set to another. The anomaly correlation measures the correlation between the forecast and observed deviations from climatology, that is, it measures how much skill the forecast has over climatology. When it falls below 60%, the wave forecast is regarded to be of little use (Janssen et al., 1997), the same criterion as used in weather forecast. The reduction of variance is a skill score that compares the mean squared error of the forecast to the mean squared error of the unskilled estimate based on climatology. For RV > 0 the forecast is better than climatology but for RV < 0 climatology gives a better representation of the forecast.

5. RESULTS

5.1 CMC Atlantic and Pacific statistics

The data for the verification period (December 1996 - November 1999) are divided into seasons, namely, winter (December - February), spring (March - May), summer (June - August) and fall (September - November). This division gives time series consisting of three winters, three springs, three summers, and three falls and permits the examination of the seasonal variations of the various statistical parameters for each of the two oceans. The results are presented in Figs. 2-3 in which the upper panel in each Figure highlights the similarities and differences in the North Atlantic (NATL) and the North Pacific (NPAC) model-generated statistics for the 00h projection time since the wind input to the WAM4 comes from different CMC weather prediction models. The NATL and the NPAC statistics for the 3 projection times 00h, 24h and 48h are shown separately in the middle and lower panels, respectively.

The results of the statistical parameter of rmse are presented in Fig. 2(a) for the significant wave height SWH, in Fig. 2b for the wind speed U_{10} and in Fig. 2c for the wave peak period T_p based on the buoys shown in Table 1. An examination of Fig. 2a indicates an oscillatory pattern of the SWH rmse values for both oceans with maximum in winter and minimum in summer. The NPAC winter rmse values, however, are larger than those of the NATL, which suggests the higher variability of the Pacific ocean-wave systems during the winter months, while in both oceans the wave systems in winter are more variable than those in summer. A comparison of the three NATL winter rmse values reveals that the 1997 and 1998 winter values are nearly the same but slightly larger than the 1999 value, suggesting that both the RFE and regional GEM models show little difference in impact on the WAM4 output. This is expected because both models have basically the same physics and grid resolution. The impact of the increased grid resolution of the regional GEM model on the SWH rmse is also less obvious. On the other hand, the Pacific winter rmse value of 1999 is somewhat higher than the winter 1997 and 1998 values, which indicates that the implementation of the global GEM model and the global 3DVAR analysis did not produce any positive impact on the Pacific SWH rmse. In the Atlantic the analyzed rmse varies from 0.4 m to 0.6 m while in the Pacific, it varies from 0.35 m to 0.95 m. In both oceans the 24h forecast is quite reliable as it shows little or no degradation while the 48h forecast shows a more significant deterioration.

The seasonal variations of the wind speed rmse statistics are presented in Fig. 2b in which the atmospheric systems in both oceans have more variability in winter than in summer. The fluctuations of the NPAC winter rmse are significantly larger than those of the NATL rmse, which indicates that Pacific winter atmospheric systems are more intense and, hence, show a higher variability than the Atlantic ones. In summer the NATL U_{10} rmse is slightly larger than the NPAC rmse and this may be the result of the occasional extratropical storms passing close to the US and Canadian buoy network during the Atlantic hurricane season (June - October). This is also reflected in the SWH rmse. When the regional GEM model replaced the RFE model without the spin up cycle in the regional analysis in February 1997, the wind speed rmse values for the spring and summer 1997 were unusually large but these were significantly reduced after 24 hours into the forecast. The rmse improved also from fall 1997 and remained steady close to 2 m s^{-1} for the rest of the period. This improvement in the rmse is due mainly to the effect of the spin up cycle of the RDAS based on 3DVAR. A comparison of the NATL

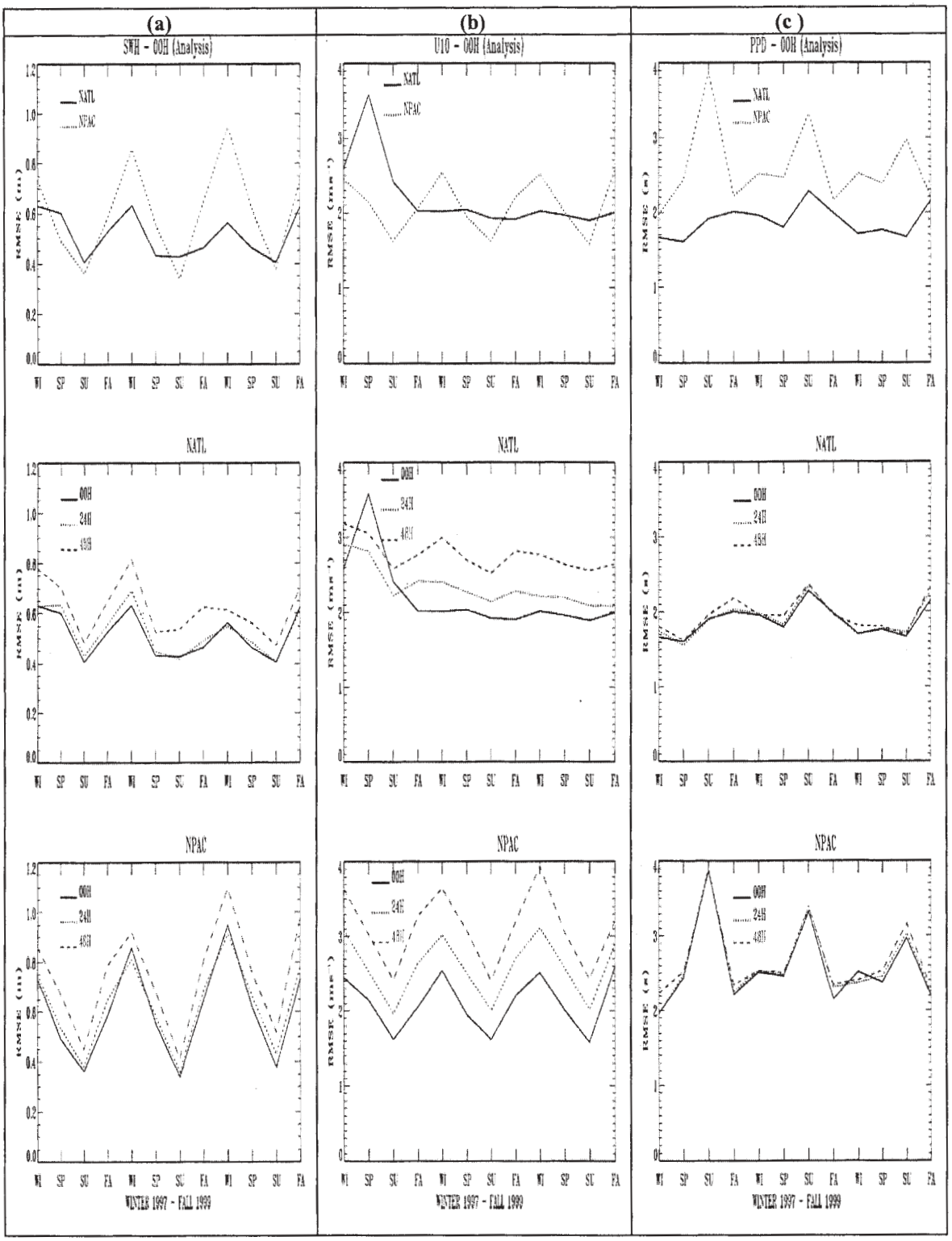

Fig. 2. Seasonal variations of the rmse parameter for (a) the significant wave height SWH, (b) the wind speed U_{10}, and (c) the peak period T_p for the period winter 1997 - fall 1999. In each panel, the upper plot compares the North Atlantic (NATL) and the North Pacific (NPAC) 00H forecasts, the middle plot the forecasts for the 00H, 24H, and 48H projection times for the NATL, and the lower plot those for the NPAC. Here, the upper case "H" denotes hour.

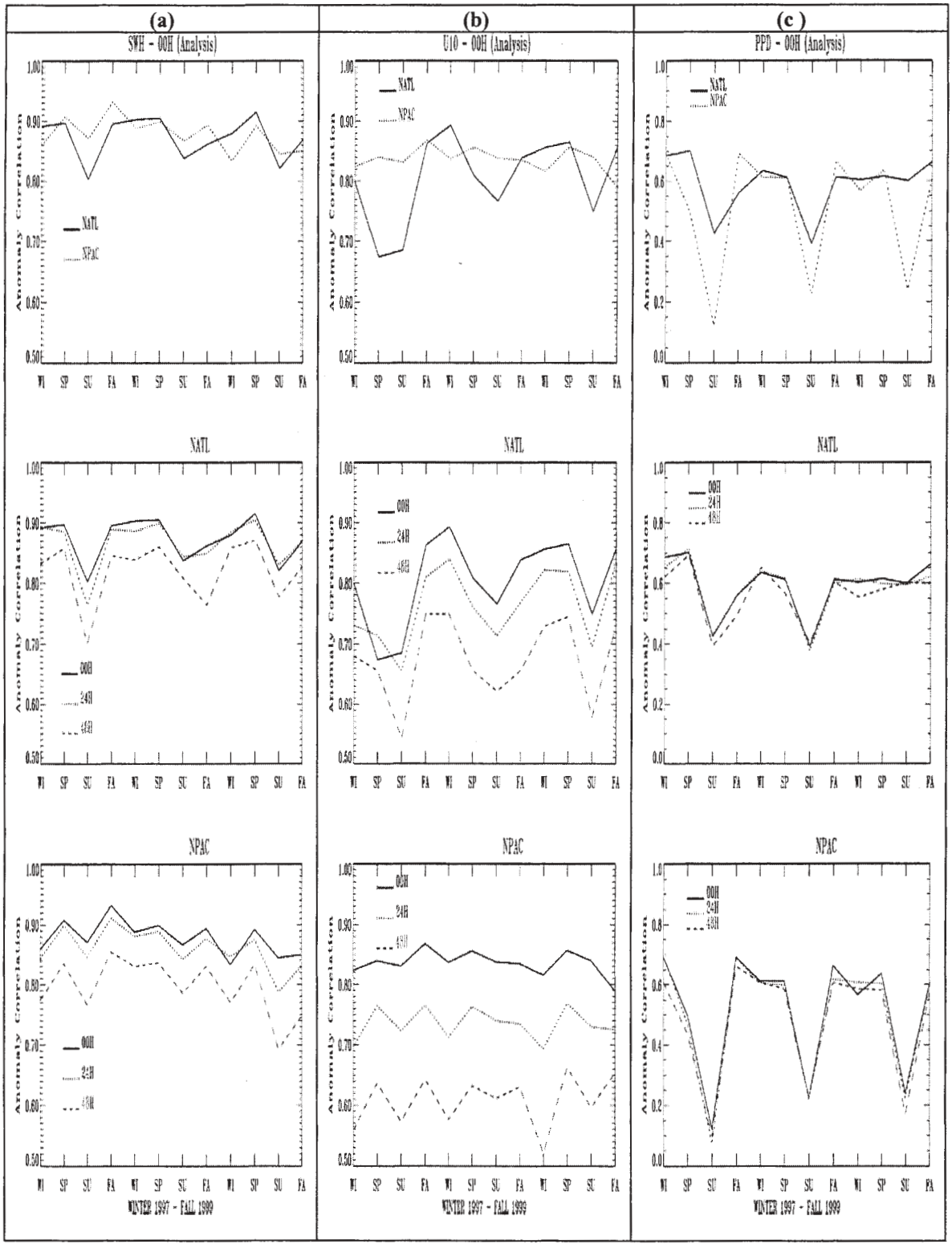

Fig. 3. Same as Fig 2 but for the anomaly correlation (AC) parameter.

winter 1997 rmse value with the corresponding 1998 and 1999 values indicates a slightly better performance of the regional GEM model over the RFE model in operation up to February 1997. The impact of the increased grid resolution of the regional GEM model from 35 km to 24 km from fall 1998, however, is not too noticeable. On the other hand, the switch from the global SEF to the global GEM in October 1998 had little or no impact on the NPAC U_{10} rmse since the physics and grid resolutions of the two global models are basically the same. The Pacific wind forecasts show more significant deterioration than the Atlantic forecasts and this is also reflected in the wave forecasts. For the Pacific the maximum rmse varies from 2.5 m s^{-1} for the 00h forecast to about 4.0 m s^{-1} for the 48h forecast while for the Atlantic it varies from 2.0 m s^{-1} to 3.25 m s^{-1} if the spring and summer 1997 rmse values are excluded.

The wave peak period T_p rmse statistics for both oceans are given in Fig. 2c. The wave model has a tendency to predict more accurately the winter T_p than the summer T_p. A possible reason is that during summer winds are lighter and directions change more frequently and this may give rise to ill-defined spectral peaks. The NPAC T_p rmse shows a stronger oscillatory behaviour than the NATL rmse. Its analyzed rmse ranges from 2.0 s to a maximum close to 4.0 s in summer while for the Atlantic it is more steady with a value close to 2.0 s. The mean peak period (not shown here) for the Pacific is larger than that for the Atlantic, making the former more swell dominated. The Pacific swells measured by the buoy network may come from the west and southwest from outside the grid area and may not be well predicted by the regional WAM4, especially during the summer season leading to large rmse. It is interesting to note that the T_p rmse shows little or no degradation with time for both oceans.

The anomaly correlation (AC) is a verification tool which is used as an indicator of the quality of a forecast since it is a skill score that provides a measure of how much more skill the forecast has over climatology. The forecast is considered to be useful if the AC exceeds the threshold value of 0.6 or 60% (Janssen et al., 1997). The AC for SWH, U_{10}, and T_p is presented in Fig. 3. This parameter shows seasonal variations in each of the two oceans. In Fig. 3a the SWH analyses and forecasts are of good quality since the AC averages close to 90%. However, the 48h wave forecast tends to approach climatology more rapidly than the 24h forecast but it is still useful. In the Pacific the seasonal fluctuations are more regular while in the Atlantic the summer fluctuations are more pronounced indicating that the Atlantic summer wave forecasts are of poorer quality than its winter forecasts. In Fig. 3b the low AC values for the U_{10} analysis during the Atlantic spring and summer of 1997 are attributable to the absence of a spin up cycle in the regional GEM model. Except for this period the Pacific and Atlantic analyses are quite comparable with the AC averaging close to 0.8. The Pacific 48h forecast, however, is barely useful with the AC hovering near the threshold value of 60 %. Fig. 3c indicates that the T_p forecasts in both oceans are generally of poor quality, especially during the summer when climatology would give adequate or better representation of the forecast.

5.2 CMC regional WAM4 versus global WAM4

The CMC regional WAM4 SWH rmse values are compared with those obtained from the global WAM4 in operations at the ECMWF and FNMOC using the data sets from the global models and the verification data from the buoys given in Table 1 for the same period in order to assess how well the regional WAM4 performed against the global WAM4. The ECMWF WAM4 has an effective grid resolution of 55 km and a spectral resolution of 25 frequencies and 12 directional bands. The model is driven by 10 m level winds provided by the ECMWF atmospheric model and includes assimilation of ERS-2 altimeter wave height data to generate an enhanced initial wave state. In June 1998 the WAM4 was dynamically coupled to the ECMWF atmospheric model. The FNMOC global WAM4 has a spatial resolution of 1.0° in both latitude/longitude directions and a spectral resolution of 25 frequency and 24 directional bands. The FNMOC Operational Global Atmospheric Prediction System (NOGAPS) provides to the FNMOC WAM4 the surface wind stress which is converted to a neutral U_{10} field given the 10 m level neutral drag coefficient. The latter is obtained using the surface roughness computed from the Charnock relation (Charnock, 1955) with the Charnock parameter set to a constant value of 0.0185.

The rmse values for the 00h, 24h, and 48h projection times for the three centres are presented in Fig. 4a for the Atlantic and Fig. 4b for the Pacific. An examination of Fig. 4 indicates that the statistics for the three centres show generally similar seasonal behaviour for both oceans whether the wind forcing provided to the WAM4 is in the form of 10 m level winds or surface wind stress. The three models show higher rmse values for winter than for summer for both oceans. Also, the NPAC winter values are larger than the NATL winter values while NATL summer values are slightly larger than the NPAC summer values. This confirms the earlier conclusion that wave systems have more variability in winter than in summer and that the Pacific

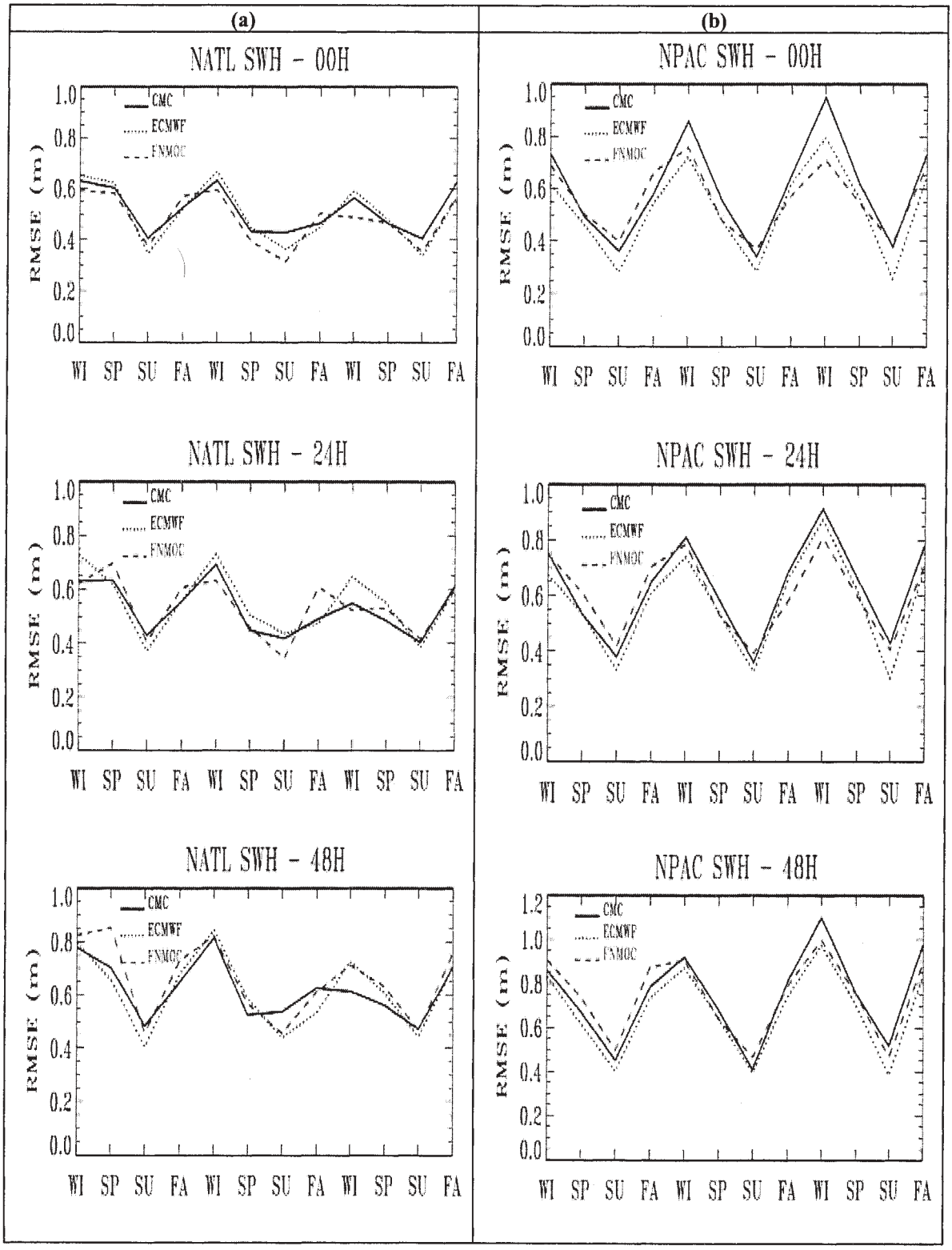

Fig. 4. The seasonal variations of the CMC SWH rmse statistics for (a) the NATL and (b) the NPAC are compared with those of the ECMWF and FNMOC for the period winter 1997 - fall 1999. In each panel, the upper plot gives the projection time 00H, the middle plot the 24H, and the lower plot the 48H where the upper case "H" denotes hour.

Table 2. SWH, U_{10} and T_p verification statistics for the North Atlantic for the period December 1996 - November 1999 for the forecast hours 00H, 24H, and 48H. Here, the upper case "H" denotes hour.

		North Atlantic Wave Height Statistics		
Season	Parameter	00H	24H	48H
All	Buoy Mean (m)	1.991	1.999	2.000
	Model mean (m)	1.771	1.801	1.829
	Lsq fit:Slope b	.840	.830	.791
	Lsq fit:Intr a	.099	.141	.246
	Symmetric slope s	.896	.903	.914
	Bias (m)	-.220	-.199	-.171
	Rmse (m)	.517	.530	.623
	Stdev (m)	.468	.492	.599
	SI	.235	.246	.299
	r	.920	.912	.868
	AC	.902	.897	.857
	RV	.812	.804	.730
	Ra	.340	.373	.412
	N (No. of obs)	15721	8053	8052

		North Atlantic Wind Speed Statistics		
Season	Parameter	00H	24H	48H
All	Buoy mean ($m\ s^{-1}$)	7.181	7.218	7.217
	Model mean ($m\ s^{-1}$)	7.279	7.323	7.461
	Lsq fit:Slope b	.839	.763	.692
	Lsq fit:Intr a	1.251	1.816	2.468
	Symmetric slope s	1.015	1.003	1.019
	Bias ($m\ s^{-1}$)	.098	.105	.244
	Rmse ($m\ s^{-1}$)	2.261	2.348	2.766
	Stdev ($m s^{-1}$)	2.259	2.346	2.755
	SI	.315	.325	.382
	r	.822	.796	.719
	AC	.822	.795	.717
	RV	.636	.606	.453
	Ra	.505	.518	.535
	N (No. of obs)	15419	7896	7895

		North Atlantic Peak Period Statistics		
Season	Parameter	00H	24H	48H
All	Buoy mean (s)	8.375	8.386	8.389
	Model mean (s)	7.760	7.780	7.791
	Lsq fit:Slope b	.597	.582	.555
	Lsq fit:Intr a	2.759	2.902	3.133
	Symmetric slope s	.926	.926	.927
	Bias (s)	-.615	-.607	-.598
	Rmse (s)	1.888	1.921	1.973
	Stdev (s)	1.785	1.823	1.880
	SI	.213	.217	.224
	r	.655	.644	.619
	AC	.627	.617	.594
	RV	.287	.275	.237
	Ra	.346	.352	.365
	N (No. of obs)	15054	7690	7690

Table 3. Same as Table 2 but for the North Pacific.

		North Pacific Wave Height Statistics		
Season	Parameter	00H	24H	48H
All	Buoy Mean (m)	2.900	2.891	2.897
	Model mean (m)	2.832	2.794	2.729
	Lsq fit:Slope b	.932	.917	.854
	Lsq fit:Intr a	.130	.142	.256
	Symmetric slope s	.985	.975	.950
	Bias (m)	-.068	-.098	-.168
	Rmse (m)	.626	.645	.766
	Stdev (m)	.622	.637	.747
	SI	.215	.220	.258
	r	.915	.910	.873
	AC	.914	.908	.867
	RV	.825	.814	.738
	Ra	.474	.447	.422
	N (No. of obs)	16782	8429	8397

		North Pacific Wind Speed Statistics		
Season	Parameter	00H	24H	48H
All	Buoy mean (m s^{-1})	8.301	8.283	8.297
	Model mean (m s^{-1})	8.319	8.078	8.008
	Lsq fit:Slope b	.911	.769	.650
	Lsq fit:Intr a	.754	1.709	2.614
	Symmetric slope s	1.014	.981	.971
	Bias (m s^{-1})	.018	-.205	-.290
	Rmse (m s^{-1})	2.124	2.593	3.117
	Stdev (m s^{-1})	2.124	2.585	3.103
	SI	.256	.312	.374
	r	.849	.761	.650
	AC	.849	.760	.648
	RV	.669	.513	.295
	Ra	.483	.462	.452
	N (No. of obs)	15434	7767	7735

		North Pacific Peak Period Statistics		
Season	Parameter	00H	24H	48H
All	Buoy mean (s)	10.688	10.712	10.721
	Model mean (s)	10.473	10.514	10.495
	Lsq fit:Slope b	.516	.502	.482
	Lsq fit:Intr a	4.954	5.132	5.325
	Symmetric slope s	.974	.975	.972
	Bias (s)	-.216	-.198	-.226
	Rmse (s)	2.657	2.696	2.739
	Stdev (s)	2.648	2.689	2.729
	SI	.248	.251	.255
	r	.577	.566	.549
	AC	.575	.564	.547
	RV	.226	.212	.188
	Ra	.527	.530	.514
	N (No. of obs)	16769	8424	8392

winter wave systems show more variability than the Atlantic winter wave systems. On the other hand, the NATL summer wave systems are slightly more variable than the NPAC summer wave systems and this may the related to the occasional hurricanes which become extratropical storms as they traverse the buoy network along the Atlantic seaboard.

In Fig. 4a the agreement among the three models is quite good for the NATL SWH rmse for the three forecast hours shown. Generally, the CMC SWH rmse lies between the rmse values of the ECMWF and FNMOC. No one model significantly outperforms the other two models. In Fig 4b the CMC NPAC SWH winter rmse values are significantly larger than those of the ECMWF and FNMOC for the 00h forecast but the differences become smaller for the 24h and 48h forecasts. Nevertheless, for the Pacific area the global models seem to have an edge over the regional model. The Pacific is more swell dominated and the larger CMC SWH rmse may be partly due to the fact that the two global wave models are better able to simulate the Pacific swells than the CMC Pacific WAM4. The FNMOC and CMC WAM4s have the same grid and spectral resolutions and the FNMOC SWH rmse is in better agreement with that of the ECMWF model which has a finer spatial resolution but coarser spectral angular resolution.

Overall, despite some differences the performances of the CMC Atlantic and Pacific WAM4s follow closely the performances of the two global WAM4s. The northwest Atlantic is wind sea dominated and the regional WAM4 generated rmse values that generally lie between the rmse values of the two global WAM4s. For the Pacific the analysis suggests that the CMC WAM4 generates SWH rmse values that are quite comparable and consistent with those produced by the two global models, in particular, as the forecast period increases.

5.3 *North Atlantic and North Pacific overall statistics*

The overall statistics for the entire period for the North Atlantic are presented in Table 2 and those for the North Pacific in Table 3. The buoy and model mean values suggest that the Pacific wave and weather systems are more intense than the Atlantic systems. The SWH and U_{10} bias and rmse values are not too large but with the U_{10} SI > 0.25 for both oceans, more accurate specifications of the wind forcings are needed for driving the WAM4. The differences in SWH and U_{10} bias and rmse values between the two oceans are rather small. The smaller Pacific SWH bias, however, may be attributed to the longer Pacific fetches. The AC is well above the threshold value of 60% and the RV is mostly above 0.5 for both SWH and U_{10}. This indicates that the SWH and U_{10} forecasts beat climatology in a meaningful way and that they are useful and of good quality. The decay of the SWH AC from 91% for day 1 to 86% for day 2 is in close agreement with the typical AC decay from 95% for day 1 to 80% for day 3 as pointed out by Komen (1999) for the northern hemisphere.

The mean values of T_p indicate that the Pacific wave systems have longer wave periods than the Atlantic systems due to the presence of more Pacific swells leading to larger rmse values. The AC is barely above 60% for the NATL region and just below for the NPAC region while the RV > 0 but somewhat small. The T_p forecasts beat climatology in the mean but not for individual seasons and are barely useful.

The higher U_{10} Ra values are not reflected in the SWH Ra values for the Atlantic but are better reflected for the Pacific. Wave heights are both duration-limited and fetch-limited and need either long fetch or long time, or both, to reach equilibrium values. Fetches associated with Pacific storm systems are generally longer than those associated with Atlantic storm systems.

6. CONCLUDING REMARKS

The CMC wave forecasting system consists of two regional versions of the global WAM4, one operating in the North Atlantic and one in the North Pacific. During the period December 1996 to November 1999, the 10 m level winds obtained from the operational global SEF/GEM model were used to drive the Pacific WAM4 while those obtained from the operational RFE/regional GEM model were used to drive the Atlantic WAM4. The significant wave heights and the peak periods from the WAM4 and the wind speeds from the atmospheric models interpolated onto the WAM4 grid are validated against wave/wind data measured by buoys located in the coastal and shelf regions of the Atlantic and Pacific coasts of North America for that period. The main conclusions from the results presented in this study are briefly summarized below.

The replacement of the global SEF model by the global GEM model in October 1998 did not show any significant impact on the verification statistics of the wind and wave parameters, most likely because both models have nearly the same physics and grid resolution. When the regional GEM model replaced the RFE model without the spin up cycle in the regional

analysis system in February 1997, the wind speed rmse was unusually large but this was significantly reduced after the spin up cycle was implemented in September 1997. Although the impact on the SWH in this case was not too noticeable, the spin up cycle is, nevertheless, an important component of the CMC regional data assimilation system. The results also show that there was little or no impact on the wind and wave forecasts following the increase of the grid resolution of the regional GEM model from 35 to 24 km in September 1998.

The Pacific winter atmospheric and wave systems have higher variability than the winter systems for the Atlantic but in each of the oceans they exhibit higher variability in winter than in summer. The Pacific consists of longer period swells throughout the year and is more swell dominated than the Atlantic. The WAM4 seems to have some difficulty in predicting the swells since some of these may originate from well outside the grid area, especially in the Pacific. The anomaly correlation and reduction of variance analyses indicate that the forecasts are useful and of good quality and show skill when compared with climatology.

The wave statistics generated by the regional WAM4 are quite comparable with those obtained from the global WAM4 run by the international wave forecasting centres at ECMWF and FNMOC. They all show similar seasonal behaviour for both oceans. Overall, the performances of the CMC regional Atlantic and Pacific WAM4s follow closely the performances of the ECMWF and FNMOC global WAM4s, taking into consideration the somewhat different wave model grid configurations, inclusion of data assimilation to create enhanced initial sea state, coupled model system, and wind forcings from different atmospheric prediction models. The global models, however, seem to handle the Pacific swells slightly better and appear to have an edge over the CMC Pacific WAM4.

7. REFERENCES

Bauer E., S. Hasselmann and K. Hasselmann, 1992: Validation and assimilation of Seasat altimeter wave heights using the WAM wave model. J. Geophys. Res., 98C, 12671-12692.

Bidlot, J.R., M. Holt, P.A. Wittmann, R. Lalbeharry, and H.S. Chen, 1998: Towards a systematic verification of operational wave models. Proc. Third Int. Symposium on WAVES'97, November 3-7, 1997, Virginia Beach, Va., U.S.A. Edited by B.L. Edge and J.M. Hemsley, America Society of Engineers.

Cardone, V.J., W.J. Pierson and E.G. Ward, 1976: Hindcasting the directional spectra of hurricane generated winds. J. Petr. Technol., 28, 385-394.

——, H.C. Graber, R.E. Jensen, S. Hasselmann and M.J. Caruso, 1995: In search of true surface wind field in SWADE IOP-1: Ocean wave modelling perspective. The Global Atmosphere and Ocean System, 3, 107-150.

——, R.E. Jensen, D.T. Resio, V.R. Swail and A.T. Cox, 1996: Evaluation of comtemporary ocean wave models in rare extreme events: The "Halloween Storm" of October 1991 and the "Storm of the Century" of March 1993. J. Atmos. Oceanic Technol, **13**, 198-230.

Charnock, H., 1955: Wind stress on a water surface. Quart. J. Roy. Meteor. Soc., **81**, 639-640.

Chouinard, C., J. Mailhot, H.L. Mitchell, A. Staniforth and R. Hogue, 1994: The Canadian data assimilation system: Operational and research applications. Mon. Wea. Rev., 122, 1306-1325.

Côté, J., S. Gravel, A. Methot, A. Patoine, M. Roch and A. Staniforth, 1998a: The operational CMC-MRB Global Environmental Multi-scale (GEM) model. Part I: Design considerations and formulation. Mon. Wea. Rev., 126, 1373-1395.

---------, J.G. Desmarais, S. Gravel, A. Methot, A. Patoine, M. Roch and A. Staniforth, 1998b: The operational CMC-MRB Global Environmental Multi-scale (GEM) model. Part II: Results. Mon. Wea. Rev., 126, 1397-1418.

Gauthier, P., C. Charette, L. Fillion, P. Koclas and S. Laroche, 1999: Implementation of a 3D variational data assimilation system at the Canadian Meteorological Centre. Part I: The global analysis. Atmosphere-Ocean, 37, 103-156.

Golding, B., 1983: A wave prediction system for real time sea state forecasting. Quart. J. Roy. Meteor. Soc., 393-416.

Holt, M.W., 1994: Improvement to the UKMO wave model swell dissipation and performance in light wind. UKMO Forecasting Res. Div. Tech. Report, 119.

Janssen, P.A.E.M., 1991: Quasi-linear theory for wind-wave generation applied to wave forecasting. J. Phys. Oceanogr., **21**, 1631-1642.

——, P.A.E.M., B. Hansen, and J. R. Bidlot, 1997: Verification of the ECMWF wave forecasting system against buoy and altimeter data. Wea. Forecasting, **12**, 763-784.

Khandekar, M.L. and R. Lalbeharry, 1996: An evaluation of Environment Canada's operational wave model based on moored buoy data. Wea. Forecasting, 11, 139-152.

——, —— and V. Cardone, 1994: The performance of the Canadian Spectral Ocean Wave Model (CSOWM) during the Grand Banks ERS-1 wave spectra validation experiment. Atmosphere-Ocean, 32, 31-60.

Komen, G., 1999: The physics of ocean waves. Proceedings on Atmosphere-surface interaction, 8-12 September 1997, European Centre for Medium-Range Weather Forecasts, Shinfield Park, Reading RG2 9AX, UK, 67-84.

Laroche, S., P. Gauthier, J. St-James and J. Morneau, 1999: Implementation of a 3D variational data assimilation system at the Canadian Meteorological Centre. Part II: The regional analysis. Atmosphere-Ocean, 37, 281-307.

Mailhot, J., R. Sarrazin, B. Bilodeau, N. Brunet, A. Methot, G. Pellerin, C. Chouinard, L. Garand, C. Girard and R. Hogue, 1995: Changes to the Canadian regional forecast system: Description and evaluation of the 50-km version. Atmosphere-Ocean, 33, 55-80.

Mailhot, J., R. Sarrazin, B. Bilodeau, N. Brunet and G. Pellerin, 1997: Development of the 35km version of the Canadian regional forecast system. Atmosphere-Ocean, 35, 1-28.

Ritchie, H. and C. Beaudoin, 1994: Approximations and sensitivity experiments with a baroclinic spectral model. Mon. Wea. Rev., 122, 2391-2399.

Romeiser, R., 1993: Global validation of the wave model WAM over an one-year period using Geosat wave height data. J. Geophys. Res., 98C, 4713-4726.

Smith, S., 1988: Coefficients for sea surface wind stress, heat flux and wind profiles as a function of wind speed and temperature. J. Geophys. Res., 93C, 15467-15472.

Steenbergen, D., A. Simard and P. Dubreuil, 1998: Towards operational 10 km forecasts at the Canadian Meteorological Centre (CMC). CMOS Bulletin, 26, 41-43.

WAMDI Group, 1988: The WAM model - A third generation ocean wave prediction model. J. Phys. Oceanogr., **18**, 1775-1810.

Wittman, P.A., C. Kunitani and R.M. Clancy, 1994: Visualizations of the WAM third generation wave models. Preprints, 10th Int. Conf. on Interactive Information and Processing Systems for Metoerology, Oceanography and Hydrology, Nashville, TN, Am. Meteor. Soc., 17-22.

——, R.M. Clancy and T. Metlach, 1995: Operational wave forecasting at Fleet Numerical Meteorology and Oceanography Center, Monterey, CA. 4TH International Workshop on Wave Hindcasting and Forecasting, Banff, Alberta, Canada, Atmospheric Environment Service, 335-342.

Zambresky. L., 1989: A verification study of the Global WAM model. December 1987-November 1988. ECMWF Tech. Rep. 63, ECMWF, Reading, United Kingdom, 86pp.

8. *ACKNOWLEDGEMENTS*

The author wishes to express his sincere thanks to Laurie Wilson and to Drs. Venkata Neralla, Jocelyn Mailhot, and Weimin Luo of the Meteorological Service of Canada and to Dr. Jean Bidlot of the European Centre for Medium-Range Weather Forecasts for their helpful comments and suggestions for the improvement of the paper. Thanks are also due to the ECMWF and FNMOC for allowing the use of their global WAM4 data acquired through collaborative exchange.

WIND WAVE FORECASTING ON THE GREAT LAKES

W. K. Luo, R. Lalbeharry and L. Wilson

Recherche en Prévision Numérique, Meteorological Service of Canada
Downsview, Ontario, Canada M3H 5T4

1. INTRODUCTION

Increased commercial and recreational activities on the Great Lakes require accurate and timely forecasts of significant wind and wave to reduce potential risks. Currently, the Great Lakes marine forecasts are scientifically supported by the Canadian Meteorological Centre (CMC) regional version of the Global Environmental Multiscale (GEM) model, which produces forecasts twice daily up to 48 hours with a resolution of 24 km. Wave forecasts on the Great Lakes from the Regional Center at Thunder Bay (RCTB) are estimated using the empirical Bretschneider methods as developed in the 1950's. The existing atmospheric model resolution may not achieve the results needed to mitigate potential Search And Rescue (SAR) events. The CMC also runs once daily a 10-km version of the regional GEM model producing forecasts up to 24 hours as part of the High-resolution Model Applications Project (HIMAP).

In the framework of the Meteorological Service of Canada (MSC) and SAR Project, the objectives of this study are to:

- evaluate wind forecasts from the 24-km regional GEM model and the 10-km HIMAP model against buoy measurements
- develop, test, and implement a high-resolution wave model for forecasts on the Great Lakes
- evaluate and validate wave forecasts from the new high resolution Great Lakes wave model

The wave model chosen for the Great Lakes region is a high resolution version of the WAM Cycle-4 (hereinafter referred to as WAM) (WAMDI Group, 1988: Janssen, 1991). The test runs were carried out for the selected period from 2 September to 2 October 1999. The effect of the resolution of wind field on the WAM wave forecasts is investigated. The present status of wind wave modeling is assessed by comparing the results from the WAM, the second generation Great Lakes Environmental Research Laboratory (GLERL) wave model and the empirical Bretschneider method employed by the RCTB in its wave forecast system with the actual buoy measurements in Lake Superior, Lake Ontario, Lake Huron and Georgian Bay, and Lake Erie.

In this paper, section 2 presents a brief description of the wave models while section 3 gives a description of the model implementation areas and the buoy network of the four Lakes. Section 4 presents the wind fields used to drive the WAM. The quality of the wind data is assessed by comparing the GEM and HIMAP model winds with the buoy measurements for the selected one-month period. Section 5 presents the evaluation and validation of the WAM results against the present RCTB and GLERL model wave forecasts and the buoy data. The impact of the resolution of the wind forcings on the model results is also addressed. Section 6 is devoted to conclusions.

2. DESCRIPTION OF THE WAVE MODELS

2.1 The WAM

The WAM is the state-of-the-art third generation wave model, at least up to intermediate water depths, and is definitely suitable for the Great Lakes applications but with some limitations for shallow water and near-shore areas (Luo *et al.*, 1997). For shallow water and near-shore applications, the third generation SWAN wave model (Holthuijsen *et al.*, 1993), introduces adaptations so as to be more computationally efficient, especially when running on the Unix- and PC-based platforms.). It is believed that the coding structure of WAM is more suitable for high performance computing (vector processing),

which makes it attractive for operational real time modeling.

A general description of the WAM is outlined here with more details given in Günther *et al.* (1992) and Komen *et al.* (1994). The WAM solves the action density balance equation (1) explicitly without any presumptions on the shape of the wave spectrum governed by:

$$\frac{\partial N}{\partial t}+\frac{1}{\cos\phi}\frac{\partial}{\partial\phi}(c_\phi\cos\phi N)+\frac{\partial}{\partial\lambda}(c_\lambda N)+\frac{\partial}{\partial\sigma}(c_\sigma N)+\frac{\partial}{\partial\theta}(c_\theta N)=\frac{S_{tot}}{\sigma} \tag{1}$$

where the action density is equal to the energy density divided by the relative frequency σ, that is, $\mathbf{N(\phi,\lambda,\sigma,\theta,t) = F(\phi,\lambda,\sigma,\theta,t)/\sigma}$. The first term on the left-hand side of (1) represents the local rate of change of the wave action. The second and third terms are the propagation of wave action in the (ϕ,λ) space including bottom- and current-induced straining. The bottom-induced straining is commonly called shoaling. The last two terms account for depth and current refraction, and describe the redistribution of action density over the spectrum. The right-hand side of (1) is the sum of several source terms, namely,

$$S_{tot} = S_{in} + S_{ds} + S_{nl} + S_{bf} \tag{2}$$

where S_{in} is the wind input, S_{ds} is the decay of wave energy due to whitecapping, S_{nl} is the wave energy transfer due to quadruplet non-linear wave interactions, S_{bf} is the wave energy dissipation due to the bottom friction.

The WAM can run for deep and shallow water conditions, can include depth and current refraction (steady and current field only), and can be set up for any local and global grid with a prescribed topographic dataset. The source term integration and the propagation of the wave energy are solved with different numerical methods and time steps. A semi-implicit scheme is used for the source term integration while the first-order upwind flux scheme is used for the propagation scheme. The wind input time step can be chosen arbitrarily, but it has to be a multiple of 1 minute. The source term integration time step has to be smaller than or equal to the propagation time step and also has to be a mutilple of 1 minute. The ratio of the propagation time step and the source term integration time step must be an integer greater than or equal to 1.

2.2 The GLERL/Donelan Model

Based on the observation that the sea states affect the drag of the wind on the water surface, Donelan (1977) developed a simple parametric second-generation wave prediction model. This model differs from other second-generation wave model in two ways. First, it is based on a local momentum equation rather than an energy transport equation. Second, the momentum input results from the drag on the waves. Schwab et al. (1984) provided the required numerical framework to make the model operational for general wind wave prediction applications over the Great Lakes. The momentum balance equation for the momentum vector, $\boldsymbol{M}$, is given as:

$$\frac{\partial M}{\partial t} + v \bullet \nabla M = \tau_w \tag{3}$$

where ∇ is the horizontal gradient operator, v is the group velocity vector corresponding to $\boldsymbol{M}$, and τ_w represents the part of the momentum input from the wind that produces net wave momentum growth. The momentum vector is expressed by

$$M = \rho_w g \iint \frac{F(\omega,\theta)}{c(\omega)} \begin{pmatrix} \cos\theta \\ \sin\theta \end{pmatrix} d\theta d\omega \tag{4}$$

where ρ_w is the water density, $c(\omega)$ the phase speed, and $F(\omega,\theta)$ the two-dimensional spectrum of energy density as a function of angular frequency ω and direction θ. A detailed description of the GLERL/Donelan model can be found in Donelan (1977) and Schwab *et al.* (1984).

The main assumption in the GLERL/Donolan model is the linear deep-water theory. This means that shoaling, refraction and breaking are ignored. The waves in the coastal area are assumed to be unaffected by finite water depth. This is not a severe limitation in most of the lakes, but it may be of importance in Lake St. Clair and certain parts of Lake Erie.

2.3 The Bretschneider method

At present, the Great Lakes wave forecasts issued by the RCTB are estimated using Bretschneider's empirical methods, which were developed in the 1950's. The wave forecast system uses statistical wind forecasts as input to the Bretschneider's empirical equations (Bretschneider, 1952) for forecasting wave height. Forecasts are made at some

selected locations around the lakes. The existing forecasting system may not meet the accurate and timely forecasts requirement needed to mitigate potential SAR events over a complex waterway such as the Great Lakes.

3. MODEL IMPLEMENTATION AREA AND BUOY NETWORK

The wave model integrates the wave energy transport equation over a certain region and so a definition of the model area (coastline geometry) is required. The WAM is implemented over the Great Lakes except Lake Michigan. The grid area covered by each of the 4 lakes and the corresponding spatial resolution are given in Table 1 while the corresponding spectral resolution is given in Table 2. In the shallow water area, the energy propagation and the dissipation source terms all depend on the water depth and, therefore, a definition of the model bathymetry is also required. An example of the computational domain and bathymetry is shown in Figure 1 for Lake Erie. The WAM is set up to run in both deep and shallow water modes for each of the 4 lakes. The shallow water option can be easily switched on/off. For the first phase of this study, only the deep-water results presented.

In order to attest to the quality of the wave model results, the NOAA buoy data are used for the evaluation. There are 13 buoy stations deployed in the four lakes with identification numbers 45001, 45003, 45004, 45005, 45006, 45008, 45132, 45135, 45136, 45137, 45139, 45142, 45143 as shown in Table 3. The wave measurements are available for the one-month period 2 September to 2 October 1999, except for the buoys 45137, 45139 and 45143, which were not operational. The evaluation is, therefore, based on the remaining 10 buoy data archived by the RCTB.

Table. 1: Grid specifications for each of the 4 lakes

	Lake Erie	Lake Huron & Georgian Bay	Lake Ontario	Lake Superior
Northern Boundary	43.00° N	46.34727° N	44.18805° N	48.97957° N
Southern Boundary	41.30° N	42.93603° N	43.16421° N	46.31845° N
Western Boundary	83.60° W	84.77321° W	79.85073° W	92.31230° W
Eastern Boundary	78.75° W	79.37810° W	76.07423° W	84.34343° W
ΔLat.	0.05°	0.05502°	0.05688°	0.05544°
ΔLon.	0.05°	0.07819°	0.07553°	0.08187°
NX x NY	98 x 35	70 x 63	51 x 19	102 x 49
Note: ΔLat. / ΔLon.	Grid size in latitude / longitude direction (in degree)			
NX / NY	Number of bathymetry grid points in longitude / latitude direction			

Table. 2: Spectral resolution of the WAM for each of the 4 lakes

	L. Erie	L. Huron & Georgian Bay	L. Ontario	L. Superior
NANG	12	12	12	12
NFRE	25	25	25	25
NGX	98	70	51	102
NGY	35	63	19	49
Time Step (s)	300	300	300	300
f_{i+1}/f_i	1.1	1.1	1.1	1.1
f_1 (Hz)	0.05	0.05	0.05	0.05
Note: NANG / NFRE	Number of directions / frequencies			
NGX / NGY	Number of model grid points in longitude / latitude direction			
f_1	First frequency			
f_i	ith frequency			

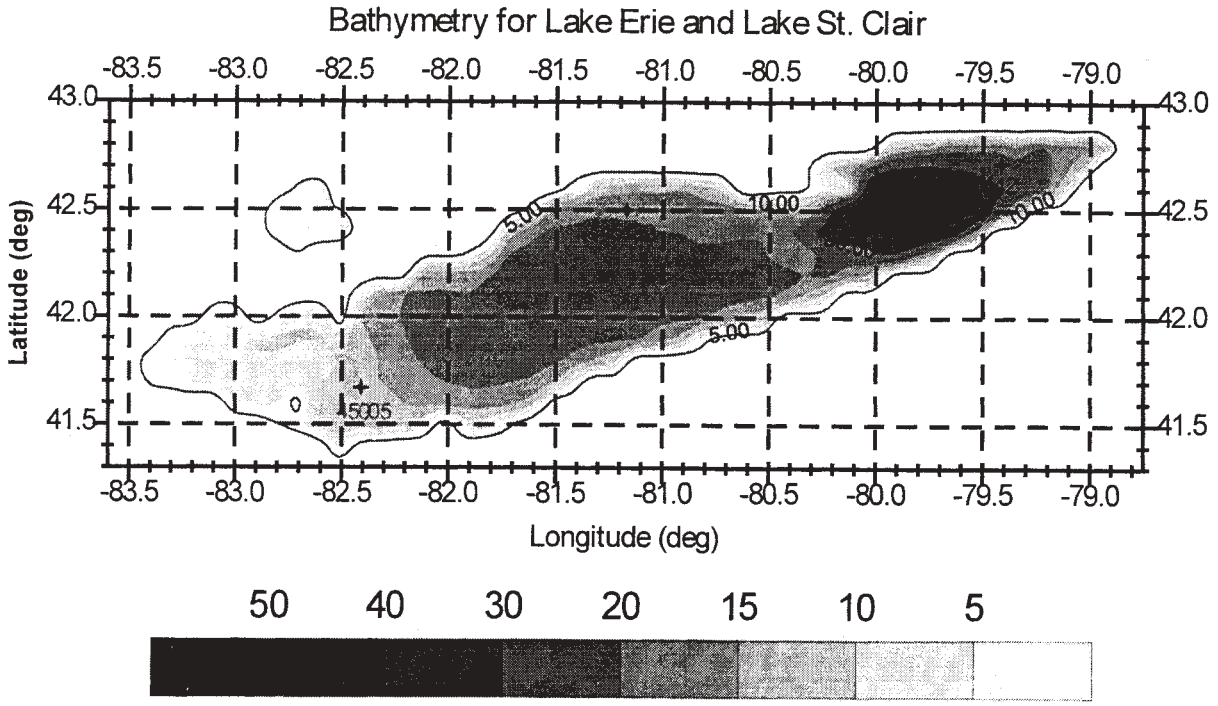

Figure 1: Lake Erie Bathymetry in meters and Locations of Buoy Stations

Table. 3: Buoy identification (ID) numbers and location coordinates.

Station ID	Station Name	Latitude	Longitude	Lake Name
45005	N/A	41.6975° N	82.3902° W	Erie
45132	Port Stanley	42.5208° N	81.1912° W	Erie
45142	Pt. Colborne	42.7048° N	79.3381° W	Erie
45003	N/A	45.3440° N	82.9226° W	Huron
45008	N/A	44.2642° N	82.3562° W	Huron
45137	Georgian Bay	45.4661° N	81.0054° W	Georgian Bay
45143	South Georgian Bay	44.9201° N	80.6414° W	Georgian Bay
45135	Prince Edward Pt	43.7600° N	76.9198° W	Ontario
45139	West Lake Ontario	43.3966° N	79.3948° W	Ontario
45001	Northeast Hancock	48.0772° N	87.7116° W	Superior
45004	N/A	47.5290° N	86.5199° W	Superior
45006	N/A	47.2539° N	89.8948° W	Superior
45136	Slate Island	48.5336° N	86.9506° W	Superior

4. *EVALUATION OF THE WIND DATA*

The main input required by the WAM is the time series of the surface wind field. An accurate representation of the wind field is one of the most important elements in a successful wave forecast. A 10 percent error in the estimation of surface wind speed can lead to 20 percent errors in significant wave height and 40 percent in wave energy (Cavaleri, 1994). In this study, the wind field over the four lakes during a one-month period from September 2, 1999 to October 2, 1999 when detailed wind and wave measurements were available is used. The wind forcings used are based on the HIMAP winds with a spatial resolution of 10-km and the regional GEM model winds with a spatial resolution of 24-km.

To verify the reliability and quality of the wind field data, time series of the GEM model winds, the

HIMAP winds, the RCTB forecast winds and the buoy measurements are presented. Also presented are the corresponding wind speed statistics. For this analysis the buoy data serve as reference data. The buoy wind speeds were all adjusted to a uniform 10-m height based on the study of Smith (1981).

4.1 Wind speed statistics

The statistical parameters used in the validation were taken from Zambresky (1989), Romeiser (1993) and Luo (1995). Let X_i represents the buoy measurements and Y_i the corresponding model values. The bias or mean error is defined as

$$Bias = \frac{1}{n}\sum(X_i - Y_i) \tag{5}$$

where positive bias indicates underestimation by the model and negative bias overestimation. The root-mean-square error is given by

$$RMSE = \sqrt{\frac{1}{n}\sum(X_i - Y_i)^2} \tag{6}$$

Tables 4 and 5 give, respectively, the wind speed bias and RMSE. The GEM model and the HIMAP winds are underestimated while the RCTB wind forecasts are overestimated when compared with the buoy measurements. The GEM model winds have a bias (RMSE) of the order of 0.45 m/s (2.21 m/s) for all the ten stations, 0.38 m/s (2.42 m/s) for the HIMAP winds and –0.6 m/s (3.09 m/s) for the RCTB forecast winds. Overall, the GEM and HIMAP winds are very similar, the higher resolution of the HIMAP winds indeed improve a little the quality of the wind data in terms of the statistical bias. In the cross-comparison with the buoy winds and RCTB forecast winds, the GEM model winds and the HIMAP winds were found to be of good quality.

4.2 Time series of model versus buoy wind data

Figure 2a shows the time series of the wind speed and Figure 2b the wind direction for buoy station 45142 on Lake Erie during the period from 2 September 2 to 2 October 1999. There is overall good agreement between the GEM model and the HIMAP winds and the buoy measurements. The GEM model and the HIMAP winds are very similar. They tend to underestimate the wind speed, especially for strong wind conditions (wind speed > 12 m/s). The RCTB wind forecasts tend to overestimate the wind speed at the high-speed range or in the storm conditions.

5. WAVE MODEL VALIDATION AGAINST BUOY DATA

Buoy wave measurements have played an important and reliable role mainly as a means of validating wave models at a few measurement stations in meteorology and oceanography. The first validation exercise in this study is executed for the selected period 2 September to 2 October 1999. The significant wave height and the peak wave period are only used since the wave direction measurements are not available from the buoys. The comparison of the model results between the WAM and the GLERL/Donelan wave model is discussed along with the effect of the resolution of atmospheric model wind on the wave hindcasts.

5.1 *Wave model statistics found in other studies*

Since many different wave models were developed during the past years and were tested in many different situations, it would be a good practice to compare the statistical results from this study with those found in other studies. Table 6 shows the bias and the RMSE of the significant wave height and the peak wave period where available. The wave height bias ranges from –0.6 m to 0.67 m and the RMSE from 0.2 m to 0.78 m, while the wave period has values from –0.71 s to 1.08 s for bias and from 0.57 s to 2.66 s for the RMSE.

5.2 Significant wave height (SWH) and peak wave period statistics

Tables 7 and 8 depict, respectively, the results of the bias and RMSE analyses for the chosen period and for all stations. In general, the GLERL model and RCTB forecasts both overpredict the wave height while the WAM underestimates the wave height at most of the stations. The underestimation of the wave height from WAM matches the trends of the underestimation of the winds used to drive the model at most of the stations, except at stations 45003, 45005, 45132 and 45135. Another reason for the underestimation may be due to the fetch-limited / duration-limited feature in the Great Lakes. Unlike the open sea, there is not enough fetch/time for waves to grow to reach equilibrium values in the Great Lakes.

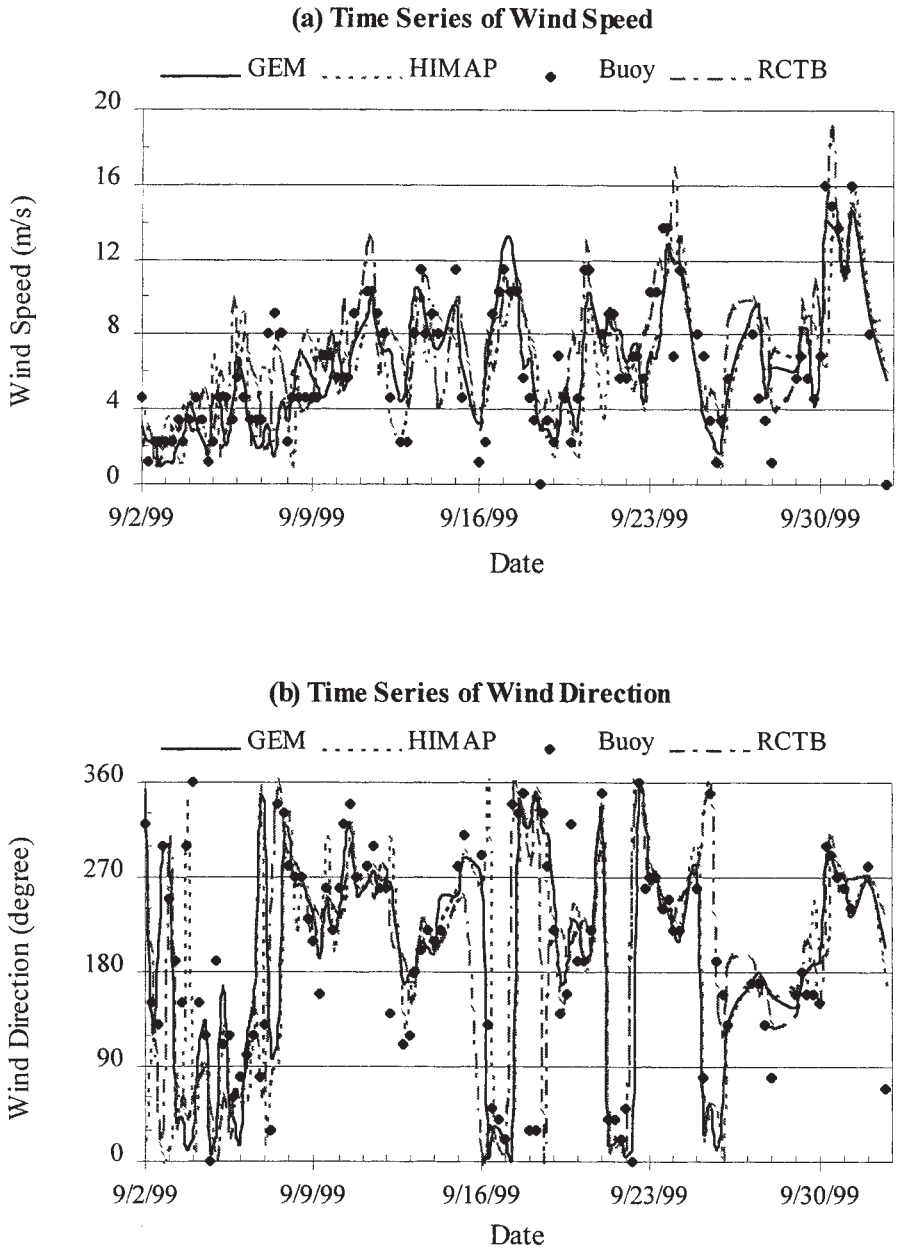

Figure 2: The GEM model, HIMAP and RCTB forecast (a) wind speed and (b) wind direction time series compared against the buoy measurements at station 45142.

Table. 4: Wind speed bias between the buoy and the model winds

Station ID	GEM Model (m/s)	HIMAP Model (m/s)	RCTB Forecast (m/s)
45001 Lake Superior	0.56	0.38	-0.27
45003 Lake Huron	0.24	0.14	-0.47
45004 Lake Superior	0.39	0.57	-0.05
45005 Lake Erie	0.38	0.31	-0.74
45006 Lake Superior	0.28	0.24	-0.71
45008 Lake Huron	0.74	0.36	-0.19
45132 Lake Erie	0.27	-0.02	-0.64
45135 Lake Ontario	0.35	0.36	-1.02
45136 Lake Superior	1.27	1.39	-0.80
45142 Lake Erie	0.01	0.03	-1.12
Average for 10 Stations	**0.45**	**0.38**	**-0.60**

Table 5. Same as Table 4 but for wind speed RMSE.

Station ID	GEM Model (m/s)	HIMAP Model (m/s)	RCTB Forecast (m/s)
45001 Lake Superior	2.39	2.47	2.90
45003 Lake Huron	2.09	2.33	2.82
45004 Lake Superior	2.14	2.46	2.60
45005 Lake Erie	1.93	2.17	3.04
45006 Lake Superior	2.40	2.38	2.97
45008 Lake Huron	2.10	2.28	2.50
45132 Lake Erie	2.28	2.49	3.03
45135 Lake Ontario	2.22	2.49	3.19
45136 Lake Superior	2.41	2.69	4.81
45142 Lake Erie	2.17	2.46	3.02
Average for 10 Stations	**2.21**	**2.42**	**3.09**

Table. 6: Wave model statistics found in other studies.

Model	Significant Wave Height		Mean or Peak Period		Reference/Area
	Bias (m)	RMSE (m)	Bias (s)	RMSE (s)	
DWAVE	NA	0.3/0.43	NA	1.06/1.07	Liu et al., 1999/Great Lakes
GLERL	NA	0.32/0.41	NA	0.85/1.07	Liu et al., 1999/Great Lakes
SHALWV	NA	0.41/0.52	NA	1.91/1.96	Liu et al., 1999/Great Lakes
NEDWAM	-0.61/-0.13	.32/0.74	-0.71/-0.01	1.44/1.99	Mastenbroek et al., 1994 / S. North Sea
WAM	-0.14/0.67	0.21/0.78	1.08/-0.1	0.57/1.62	Luo, 1995 / North Sea
CMC	0.07	0.63	0.22	2.66	Lalbeharry, 2000 / Pacific Ocean
WAM	0.22	0.52	0.62	1.89	Lalbeharry, 2000 / Atlantic Ocean
Note:	The numbers separated by "/" indicate the range of values. NA denotes "not available".				

Table 7. SWH bias between the buoy observations and the model outputs.

Station ID	WAM (GEM Model Wind) (m)	WAM (HIMAP Wind) (m)	GLERL/Donelan (m)	RCTB Forecast (m)
45001 Lake Superior	0.11	0.11	-0.05	-0.13
45003 Lake Huron	-0.02	-0.04	-0.02	-0.27
45004 Lake Superior	0.01	0.02	-0.23	-0.30
45005 Lake Erie	-0.07	-0.09	-0.33	-0.22
45006 Lake Superior	0.01	0.02	-0.10	-0.24
45008 Lake Huron	0.02	-0.02	-0.09	-0.28
45132 Lake Erie	-0.04	-0.07	-0.14	-0.22
45135 Lake Ontario	-0.16	-0.18	-0.34	-0.35
45136 Lake Superior	0.19	0.22	-0.06	0.09
45142 Lake Erie	0.02	-0.01	-0.09	-0.30
Average for 10 Stations	**0.01**	**0.01**	**-0.15**	**-0.22**

Table 8. Same as Table 7 but for the RMSE.

Station ID	WAM (GEM Model Wind) (m)	WAM (HIMAP Wind) (m)	GLERL/Donelan (m)	RCTB Forecast (m)
45001 Lake Superior	0.40	0.41	0.27	0.58
45003 Lake Huron	0.23	0.26	0.22	0.55
45004 Lake Superior	0.32	0.34	0.35	0.61
45005 Lake Erie	0.25	0.30	0.43	0.48
45006 Lake Superior	0.30	0.30	0.19	0.51
45008 Lake Huron	0.24	0.30	0.23	0.54
45132 Lake Erie	0.24	0.28	0.20	0.50
45135 Lake Ontario	0.32	0.34	0.42	0.64
45136 Lake Superior	0.37	0.40	0.24	0.99
45142 Lake Erie	0.23	0.28	0.21	0.62
Average for 10 Stations	**0.29**	**0.32**	**0.28**	**0.60**

At buoy stations 45003, 45005, 45132 and 45135, the model winds are underestimated, but the model waves are overestimated. The possible reason for this opposite match may be related to shallow water effects, especially at stations 45005 and 45132 where the water depth is quite shallow in Lake Erie. The effect of shallow water on the wave prediction will be investigated in the second phase of this study.

The WAM driven by the GEM model winds produces bias of the order of 0.1 m and RMSE of the order of 0.3 m. The GLERL model has bias of the order of –0.15 m and RMSE of the order of 0.28 m while the RCTB forecast results in bias of the order of –0.22 m and 0.6 m for RMSE. When compared to the statistics of –0.6 m to 0.67 m for bias and 0.2 m to 0.78 m for RMSE found in other studies shown in Table 6, the WAM results are quite good. It produces significant wave height much closer to the buoy measurements than the RCTB wave forecast system, even better than the GLERL model in terms of bias. The RMSE values of the WAM are very similar to those of the GLERL model.

The statistical results of the bias and RMSE analysis for the peak wave period can be found in Tables 9 and 10, respectively, for the chosen period and for the stations with peak wave period measurements. The RCTB forecast system does not produce the information about the peak period and is, therefore,

not included in the discussion. From Tables 9 and 10, it can see that the GLERL model underpredicts the wave period for most of the stations with a bias of the order of 0.23 s and produces a RMSE value of the order of 1.09 s. The WAM also underestimates the wave period but with a much smaller bias and a lower RMSE value than the GLERL model. Its bias and RMSE are of the order of 0.02 s and 0.97 s, respectively. The WAM with different wind inputs (i.e., the GEM model or HIMAP winds) produces similar statistical results in terms of both bias and RMSE. When compared with the wave period statistics found in Table 6 (–0.71 s to 1.08 s for bias and 0.57 s to 2.66 s for RMSE), the WAM results are reasonable. It produces peak wave period closer to the buoy measurements than the GLERL model forecast system.

Table. 9: Peak wave period bias between the buoy observations and the model outputs

Station ID	WAM (GEM Model Wind) (s)	WAM (HIMAP Wind) (s)	GLERL/Donelan (s)
45001 Lake Superior	0.27	0.31	0.52
45003 Lake Huron	-0.18	-0.23	0.26
45004 Lake Superior	0.13	0.10	0.12
45005 Lake Erie	-0.58	-0.68	-0.70
45006 Lake Superior	-0.34	-0.36	-0.01
45008 Lake Huron	-0.11	-0.19	0.17
45132 Lake Erie	0.14	0.16	0.31
45135 Lake Ontario	0.31	0.23	0.43
45136 Lake Superior	0.37	0.36	0.65
45142 Lake Erie	0.26	0.21	0.51
Average for 10 Stations	**0.03**	**-0.01**	**0.23**

Table. 10: Same as Table 9 but for the RMSE.

Station ID	WAM (GEM Model Wind) (s)	WAM (HIMAP Wind) (s)	GLERL/Donelan (s)
45001 Lake Superior	0.92	0.94	1.04
45003 Lake Huron	1.01	1.00	1.24
45004 Lake Superior	0.78	0.76	0.94
45005 Lake Erie	1.49	1.62	1.26
45006 Lake Superior	1.31	1.34	1.11
45008 Lake Huron	1.03	1.08	1.11
45132 Lake Erie	0.64	0.68	0.84
45135 Lake Ontario	0.71	0.69	0.95
45136 Lake Superior	0.96	0.91	1.28
45142 Lake Erie	0.73	0.72	1.09
Average for 10 Stations	**0.96**	**0.97**	**1.09**

5.2 *Time series plots of wave model result versus buoy data*

Figures 3a-b present the time series of the significant wave height and peak wave period from the buoy observations, the WAM results, the GLERL model data and the RCTB forecasts at station 45142. The Figures indicate that the wave heights produced by the WAM and the GLERL model agree well with each other and with the buoy data. The RCTB forecasts tend to overpredict the wave height, especially in rough weather conditions. During the one month period, the strong wave activities (wave height > 1.5 m) were hindcast by the model and observed by the buoy measurements on September 14, 15, 22, 27 and October 1, 1999. In most cases, the WAM captures the strong waves, but at some stations especially at 45001, 45008 and 45136, the WAM underestimates the highest waves. When checking the time series of the wind speed, it is found that the wind speed is clearly underestimated by the GEM and HIMAP models, especially at the strong wind conditions (wind speed > 12 m/s) . The good quality of the wind data indeed plays an important role on the reliable wave forecasts.

5.3 *Effect of the atmospheric model wind resolution on the wave model output.*

There is no doubt that higher the atmospheric model resolution, the more accurate the wind data, and thus the more reliable the wave calculation. But the question is to what extent the atmospheric model resolution produces improvement in the wave hindcasts/forecasts. When comparing the wind speed statistical analysis results (see Tables 4 and 5), it is found that the GEM model (24-km resolution) and the HIMAP (10-km resolution) winds are very similar and the improvement of the wind speed is not too obvious. The impact of the increased resolution of the atmospheric model resolution on the wave model results is not too significant. Figures 4a-b show the time series of the significant wave height and the peak wave period for station 45142. The WAM wave hindcasts based on the GEM model and HIMAP winds are similar. There are some improvements in several occurrences when using the high resolution HIMAP winds, but there is no systematic indication that the HIMAP winds outperforms the GEM model winds. The possible reason may be due to smoothing of the wind data interpolated from the atmospheric model grid onto the higher resolution (4-6 km) wave model grid.

6. *CONCLUSIONS*

The quality of wind data is assessed by comparison between the results from the GEM and HIMAP models and the buoy measurements for the selected one-month period from 2 September 2 October 1999. From the statistical analysis conducted, it is found that there is a good agreement among the GEM model winds, the HIMAP winds and the buoy data. However, the GEM model and HIMAP winds are underestimated while the RCTB wind forecast is overestimated when compared against the buoy measurements. The GEM model winds have a bias and RMSE of the order of **0.45 m/s** and **2.21 m/s**, respectively, the HIMAP winds **0.38 m/s** and **2.42 m/s** and the RCTB forecasts **–0.6 m/s** and **3.09 m/s**.

The third generation WAM has been implemented on Lake Superior, Lake Ontario, Lake Huron and Gerogian Bay, and Lake Erie and tested for the one-month period mentioned above. The present status of wind wave modeling over the Great Lakes is assessed by comparing the results from the third generation WAM, the second generation GLERL model and the RCTB forecasts based on the empirical Bretschneider method with the actual buoy measurements. The results indicate that the wave heights and peak periods produced by the WAM and the GLERL model agree well with each other and with the buoy data. The RCTB forecasts tend to overpredict the wave height, especially in rough weather conditions. Moreover, the WAM tends to produce closer results to the buoy data than the RCTB forecasts.

The statistical analysis between the buoy data and the model results showed that the WAM underestimates the significant wave height with a bias of the order of **0.01 m** and RMSE of the order of **0.3 m**. Both the GLERL model and the RCTB forecast overpredict the wave heights. The bias and the RMSE are of the order of **–0.15 m** and **0.28 m,** respectively, for the GLERL model while the RCTB forecast results in a bias of the order of **–0.22 m** and a RMSE of **0.6 m**. When compared with the statistics found in other studies, the WAM, as well as the GLERL model, results are satisfactory. Both the WAM and the GLERL model underestimates the wave period, but the WAM results in a much smaller bias and a lower RMSE value than the GLERL model. The bias and RMSE are of the order of **0.02 s** and **0.97 s,** respectively, for the WAM and **0.23 s** and **1.09 s** for the GLERL model. The WAM clearly outperforms the GLERL model and the RCTB forecasts in terms

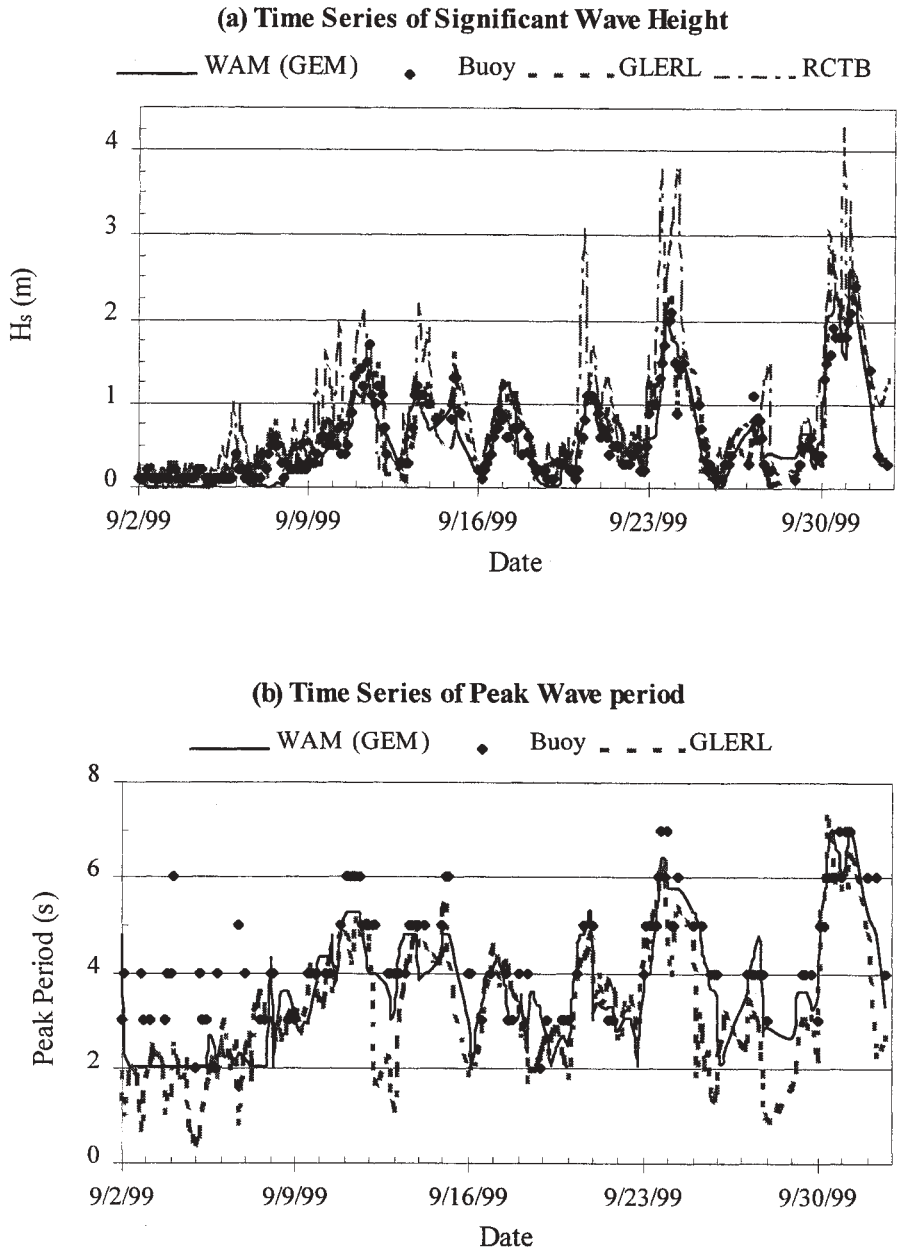

Figure 3: The WAM model, GLERL model and RCTB forecast (a) significant wave height and (b) peak wave period time series compared against the buoy measurements at station 45142. Note that for the RCTB forecasts the peak period is not available and that the WAM data are based on the GEM model winds.

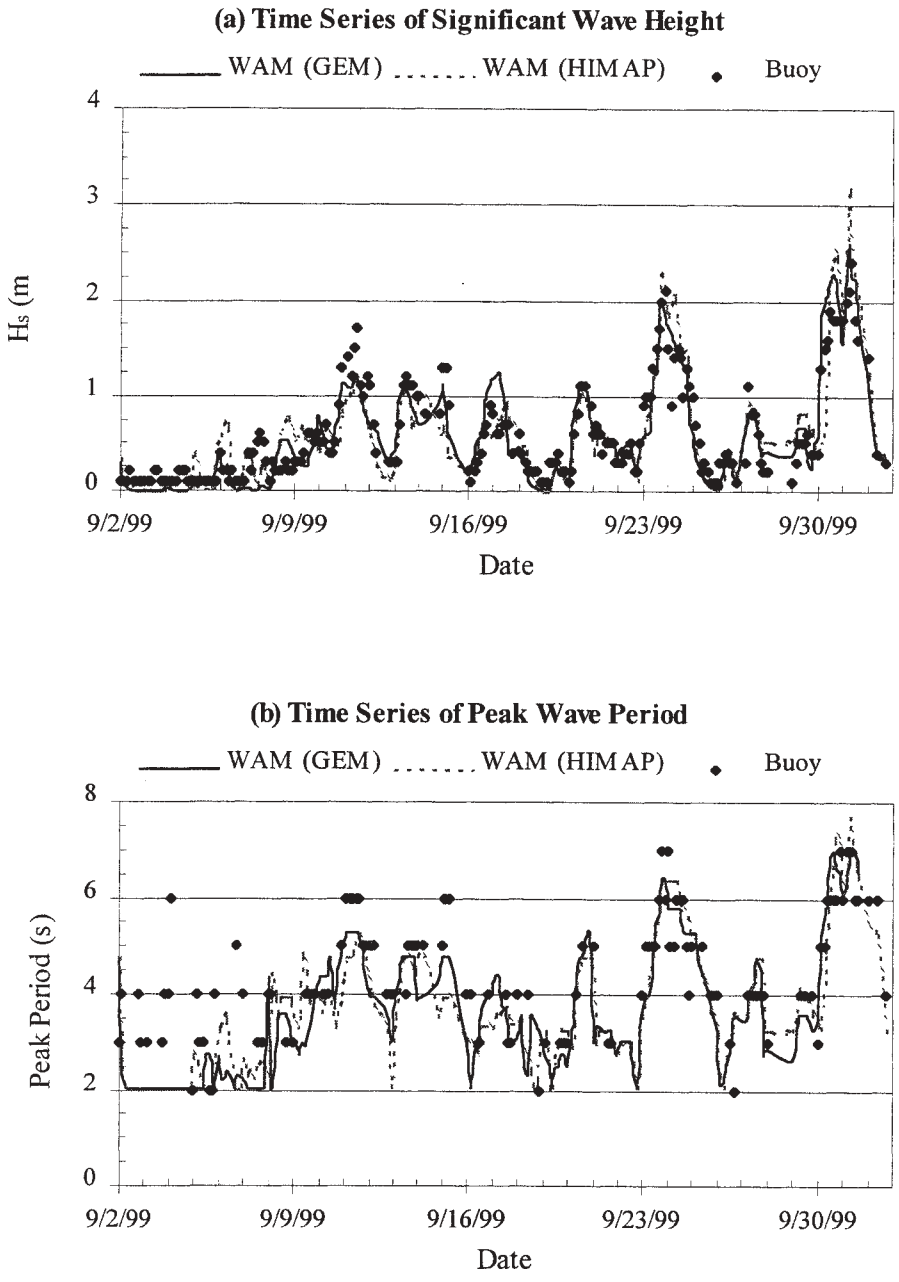

Figure 4: The WAM model and RCTB forecast (a) significant wave height and (b) peak wave period time series compared against the buoy measurements at station 45142. Note that for the RCTB forecasts the peak period is not available and that the WAM data are based on both the GEM model and HIMAP wind forcings.

of the bias and the RMSE.

The main reason for the underestimation of the significant wave height lies in the underprediction of the wind speed by the atmospheric models. Another reason may be due to the fetch-limited / duration-limited feature in the Great Lakes. Unlike the open sea, there is not enough fetch / time for waves to grow in the Great Lakes to reach equilibrium conditions.

The effect of the increased resolution of wind field on the WAM forecasts is not significant. One possible reason may be the fact that the wind data on the WAM grid are smoothed versions of the wind data on the lower resolution atmospheric model grid.

The next phase of this study is to implement a shallow water version of the WAM on Lake Erie and to further evaluate the quality of the GEM model and HIMAP model winds.

7. *ACKNOWLEDGEMENTS*

The authors are grateful to Dr. D. J. Schwab of Great Lakes Environmental Research Laboratory, NOAA, for providing the GLERL model results and to the Regional Center of Thunder Bay for providing the buoy data and its wind and wave forecasts. This study is supported by funds made available under Contract No. KM156-9-6793.

8. *REFERENCES*

Bretschneider, C. L., 1952: The generation and decay of wind waves in deep water, *Trans. Amer. Geophys. Union*, **33**, 381-389.

Cavaleri, L., 1994: Wave models and input wind, in Dynamics and Modelling of Ocean Waves, Komen *et al.* (eds.), Cambridge, 283-284.

Donelan, M. A., 1977: A simple numerical model for wave and wind stress prediction, National Water Research Institute manscript, Burlington, Ontario, Canada, 28 pp.

Günther, H., S. Hasselmann and P. A. E. M. Janssen, 1992: The WAM model Cycle 4, Report No. 4, Hamburg.

Holthuijsen, L. H., N. Nooij and R. C. Herbers, 1993: A spectral wave model for the coastal zone, *Proc. In. Conf. WAVES '93*, New Orleans, 630-641.

Janssen, P.A.E.M., 1991: Quasi-linear theory of wind-wave generation applied to wave forecasting, *J. Phys. Oceanogr.*, **21**, 1631-1642.

Komen, G. J., L. Cavaleri, M. A. Donelan, K. Hasselmann, S. Hasselmann and P. A. E. M. Janssen, 1994: Dynamics and Modelling of Ocean Waves, Cambridge University Press, Cambridge, 532 pp.

Lalbeharry, R., 2000: Evaluation of the CMC regional wave forecasting system against buoy data. Submitted to Atmosphere-Ocean.

Liu, P. C., D. J. Schwab and R. E. Jensen, 2000: Has wind-wave modeling reached its limit?, Ocean Engineering (*in press*).

Luo, W., 1995: Wind wave modeling in Shallow Water. Ph. D. Thesis, Dept. of Civil Engineering, Catholic University of Leuven, Belgium, 195 pp.

Mastenbroek, C., V. K. Makin, A. C. Voorips and G. J. Komen, 1994: Validation of ERS-1 altimeter wave heights measurements and assimilation in a North Sea wave model, *Glob. Oc. Atm. Sys.*, **2**, 143-161.

Romeiser, R., 1993: Global validation of the wave model WAM over a one-year period using geosat wave height data. *J. Geophys. Res.*, **98**, (*C3*), 4713-4726.

Schwab, D. J., J. R. Bennett, P. C. Liu and M.A. Donelan, 1984: Application of a simple numerical wave prediction model to Lake Erie, *J. Geophys. Res.*, **89**, 3586-3592.

Smith, S. D., 1981: Factors for adjustment of wind speed over water to a 10-meter height. Report Series/BI-R-81-3/March 81, Bedford Institute of Oceanography, Bedford, NS, Canada, 29 pp.

WAMDI Group, 1988: The WAM model – a third generation ocean wave prediction model, *J. Phys. Oceanogr.*, **18**, 1775-1810.

Zambresky, L. F., 1989: A verification study of the global WAM: December 1987 - November 1988. ECMWF Tech. Report **63**, ENMWF, Reading, U.K.

A WAVE MODELLING STUDY OF AN INTENSE STORM IN BASS STRAIT, AUSTRALIA

Diana J. M. Greenslade

Bureau of Meteorology Research Centre
Melbourne, VIC, Australia

1. INTRODUCTION

This paper describes a case study of a storm which passed over the Bass Strait area (see Figure 1) during December 1998. This particular storm attracted much media attention due to the fact that it devastated the fleet of the 1998 Sydney to Hobart yacht race. This race turned out to be the most disastrous event in the race's 54-year history, and indeed of any offshore race in Australian waters. Of the 115 yachts departing Sydney Harbour at 1pm on December 26th, only 44 reached their destination. Sixty-six boats retired from the race and five were lost completely. Tragically, six people lost their lives during the storm and another fifty-five people were rescued in the biggest maritime rescue operation ever undertaken in Australian waters (Cruising Yacht Club of Australia, 1999, hereafter CYC99).

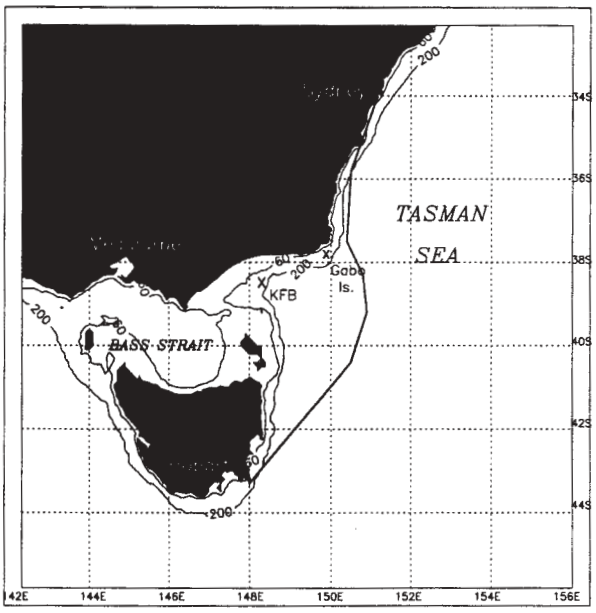

Figure 1. This map shows the area of the Sydney to Hobart yacht race. 60m and 200m bathymetric depth contours are marked. The thick black line shows the trajectory taken by one of the yachts to complete the race.

Figure 1 shows a map of the race region with a few depth contours outlined. The thick line on this figure represents the trajectory taken by one of the 44 yachts to finish the race. It can be seen that after reaching Gabo Island, the yacht was subsequently blown off course by the storm. Also marked on the map is Kingfish B oil platform (KFB), from which marine observations were available.

The aim of this paper is to examine the evolving sea-state during the yacht race. Section 2 describes the wave model and wind forcing fields used for this study. The modelled wave fields are described in Section 3, along with a discussion of some potentially important factors governing the development of the sea-state. In Section 4, the surface winds and wave model results are compared with the available observations and possible causes for discrepancies are discussed, and Section 5 presents the conclusions.

2. DESCRIPTION OF THE WAVE MODEL

The wave model used for this study is a high-resolution version of the wave model, WAM. The WAM model (Komen *et al.*, 1994) is a third generation wave model, i.e., the wave transport equation is solved explicitly without assuming a form for the evolving wave spectrum. The wave transport equation is:

$$\frac{\partial F}{\partial t} + \nabla\left(c_g F\right) = S_{in} + S_{nl} + S_d + S_{bot} \qquad (1)$$

where F is the wave spectrum, c_g is the group velocity and the terms on the right hand side represent the source terms: S_{in} is the energy input due to wind forcing, S_{nl} the non-linear energy transfer between groups of resonant waves, S_d the dissipation of energy due to whitecapping, and S_{bot} the dissipation of energy due to bottom friction. The WAM model is implemented operationally at many forecasting centres around the world, including a version at the Australian Bureau of Meteorology (AUSWAM).

AUSWAM currently comprises a global model at 3° spatial resolution, a regional model at 1° resolution and a mesoscale model at 0.25° resolution. The mesoscale model is nested inside the regional model, which is in turn nested inside the global model. The regional model spans the oceans around Australia and covers an area from 60°S to 12°N and from 69°E to 180°. The mesoscale model covers the southeast of Australia and ranges from 50°S to 24°S and from 126°E to 164°E.

For the global and regional models the source terms are integrated every 10 minutes and the propagation terms every 20 minutes, while for the mesoscale model, the timestep is 5 minutes for both source and propagation terms. In terms of the wave spectrum, the directional resolution is 30° and there are 25 frequency bins ranging from 0.0418 Hz to 0.4114 Hz. This represents wave periods from approximately 24 seconds to 2.5 seconds. At spatial resolutions of 1° or greater, very few of the wave model gridpoints are in water depths of less than 100m and so the regional and global wave models are run with deep-water physics only, while the mesoscale model includes shallow-water physics. The global and regional versions include the assimilation of Significant Wave Height (SWH) data from the ERS-2 altimeter. A major difference between AUSWAM and other versions of WAM is that the deep-water versions of AUSWAM are run with 3rd-order propagation numerics (Bender, 1996).

Winds used to force AUSWAM are 10m surface wind velocities obtained from the Bureau of Meteorology's operational global, regional and mesoscale atmospheric models, GASP (Seaman *et al.*, 1995), LAPS (Puri *et al.*, 1998) and MESO_LAPS (National Meteorological and Operations Centre, 1999), respectively. The 10m surface winds are obtained from the lowest levels of the atmospheric models via Monin-Obukhov theory with empirical stability functions (Garratt, 1992).

2.1 Model Configuration

For this particular study, some details of the wave model's configuration were altered. The spatial domain is centred on Bass Strait and ranges from 45°S to 33°S and from 143°E to 155°E. Although most of the domain is more than 200m deep, the depth throughout Bass Strait is less than 80m, indicating that shallow water effects will be important in this area. The bathymetry used for this study was obtained from a 30 arc-second bathymetric dataset of the Australian continental shelf produced by the Australian Geological Survey Organisation. The spatial resolution of the wave model was increased to 0.1°, or approximately 10km. The source terms and propagation terms were integrated every 5 minutes. In terms of the wave spectrum, the directional resolution was increased to 15° while the frequency resolution remained the same as in the operational models. Fields of SWH, mean wave direction and other diagnostic variables are output every hour.

2.2 Wind Forcing

It is generally acknowledged that most of the errors in wave prediction fields arise from errors in the wind forcing fields (Cardone *et al.*, 1996, Komen and Smith, 1999). Therefore, for a detailed wave modelling study, it is desirable to obtain the best possible surface wind fields. In this case, they were provided by a very high resolution (0.05°) atmospheric model documented in Mills (2000). Mills (2000) shows that the hindcast is of very high quality, and we can be confident that the surface wind fields obtained from this atmospheric model are a good representation of the true conditions. This assertion will be examined more closely in Section 4.

New wind forcing fields were provided at hourly intervals. The lowest level of the atmospheric model was very close to 10m and the 10m winds were obtained in a similar way as for the operational models. Since the spatial resolution of the atmospheric model is simply twice the spatial resolution of the wave model, no interpolation of the wind fields to the wave model grid was necessary. Surface wind fields are not presented here, but the general synoptic situation was as follows.

A cold front passed through the region during the morning of December 26th, prior to the start of the yacht race. A low-pressure system formed within Bass Strait during the 26th, became cut-off at about midnight and continued to move eastwards. A small-scale secondary low developed over northern Tasmania in the early morning of the 27th, and rapidly intensified, with a band of very strong westerly winds on its northern side. It was these strong winds and the waves forced by these winds that contributed to major problems for the race fleet. A detailed description of the meteorological situation can be found in Mills (2000).

2.3 Boundary and Initial Conditions

To obtain boundary conditions for the Bass Strait model it was necessary to rerun the global and regional wave models with increased spectral resolution. These were forced with operational hindcast winds. The regional model provided wave spectra at 1° intervals along the edges of the high-resolution grid to use as boundary conditions.

To initialise the wave model for a cold start, JONSWAP spectra (Hasselmann *et al.*, 1973), were defined at each model gridpoint from the local initial winds according to fetch laws with a $\cos^2$ directional distribution (Gunther *et al.*, 1992). In this case, an initial fetch of 30km was imposed at all gridpoints. This ensured that some swell energy was present in the model at the beginning of the spin-up period. Initialisation for all three domains (global, regional and Bass Strait) occurred at Dec. 20th 11am (local time) and the models were spun up for 6.5 days, using the operational hindcast surface winds as forcing fields. After the initial spin-up period, the model was then run for 36 hours over the time period of interest, from Dec. 26th, 11pm until Dec. 28th, 11am.

3. EVOLUTION OF SWH FIELD

The predominant influence on the sea-state at any time is the local wind forcing, however there are other important elements that must be taken into consideration. In this section, three factors affecting the development of the sea-state during the yacht race are considered: 1) the wave conditions in the Tasman Sea, i.e., the area surrounding the race region, 2) the East Australian Current system and 3) the local wind forcing.

3.1 Tasman Sea

We first consider the wave conditions of the area surrounding the race region for the time period leading up to the yacht race. Figure 2 shows the SWH field obtained from the regional wave model at 11am on Dec. 26th, a few hours before the commencement of the race. Note that only a portion of the regional model

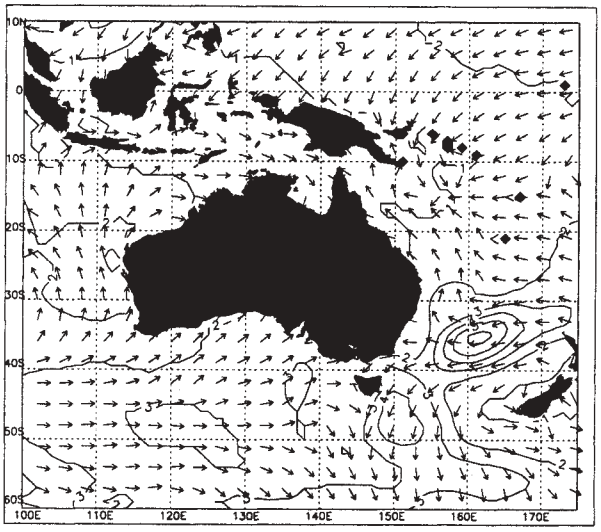

Figure 2. SWH (m) and mean wave directions from the regional wave model at 11am on Dec. 26th, just before the start of the yacht race. An area of high SWH is present in the Tasman Sea at around (160°E, 35°S), and the mean wave directions indicate that these waves are propagating towards the Australian coast.

domain is shown here. This figure shows that a region of high SWH has developed in the Tasman Sea, at around (160°E, 35°S) caused by strong winds associated with a low-pressure system in this area. The maximum SWH at this time is greater than 6m. The arrows on this plot represent the mean wave direction at every third model gridpoint. The mean wave direction is defined as the energy-weighted average direction of all spectral wave components. This means that if there is more than one wave system present, there may be no waves actually propagating in the 'mean' direction. However, inspection of the directional wave spectrum near the peak of this storm indicates that the vast majority of the wave energy here is propagating towards the west, with only a small directional spread.

During Dec. 27th, this area of strong winds and high SWH moves southward, while the mean wave direction turns towards the southwest. Although the area of maximum SWH remains some distance away from Bass Strait, this storm still has a significant influence over the sea-state near the coast. During the period of the yacht race, swell with a period of approximately 11 seconds propagates towards the Australian coast and into the race region.

3.2 East Australian Current

Another potentially important factor governing the development of the sea-state in the area is the East Australia Current (EAC). The EAC is a western boundary current carrying warm water from the Coral Sea southwards along the east coast of Australia. Eddies pinch off from the meanders of the EAC and the current speeds at the edge of these eddies can be up

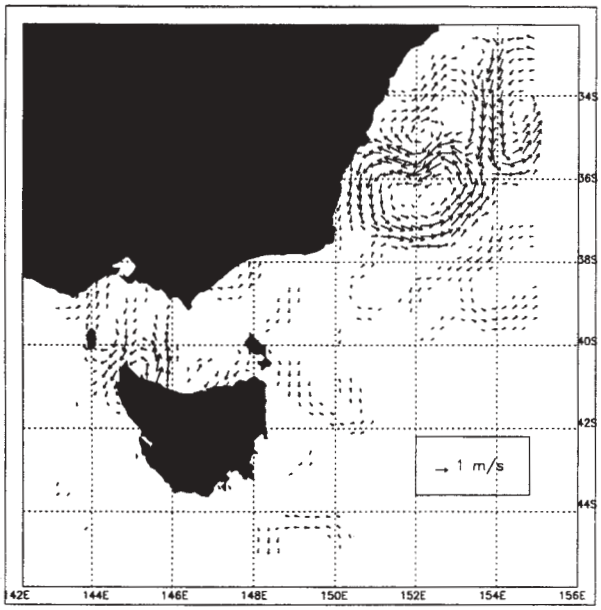

Figure 3. Surface geostrophic currents from satellite altimetry for a 15-day time period centred on Dec. 30th 1998.

to 2m/s (Andrews and Scully-Power, 1976). Although no direct *in situ* measurements of the velocity field of the EAC are available for the time period of the yacht race, it is possible to estimate geostrophic surface currents from satellite altimeter measurements of relative sea-surface height. Figure 3 shows surface velocities estimated from combined ERS-2 and Topex/Poseidon sea-surface height data during a 15-day time window centred on Dec. 30th, 1998. It should be noted that in depths of less than approximately 1000m, errors in correcting the observed sea-surface height for tides are too large for reliable estimates of surface currents to be made. Therefore the currents within Bass Strait are unlikely to be accurate.

It can be seen that during this time period, there was a large anti-cyclonic eddy centred at about (152°E, 36.5°S). There are strong currents around the boundary of this eddy with speeds of up to 2m/s. Note in particular an eastward-flowing current at around 37.5°S. Images of SST from infrared sensors aboard NOAA satellites confirm this diagnosis for the time period of the yacht race (G. Cresswell, personal communication).

The effect of an adverse current on a wave field is to decrease the wavelength and increase the SWH. This therefore has the effect of steepening the waves, although the amount by which the waves are altered is uncertain. Previous studies have suggested that the SWH can be increased by up to 50% in extreme cases although it is more likely to be closer to 10% (Komen *et al.*, 1994). The eastward flowing current described above will therefore cause the westerly propagating swell (from the Tasman Sea storm) to steepen.

It is currently not feasible to include the effect of surface currents in an operational wave model due to the difficulty in obtaining observed or modelled surface currents in real-time. This situation may be improved with the implementation of projects such as the Global Ocean Observing System (GOOS) or the Global Ocean Data Assimilation Experiment (GODAE) (Swail *et al.*, 1999).

3.3 Sea-state Development

It is not possible to present the entire time series of SWH fields here. A fuller description of the evolution of the sea-state can be found in Greenslade (2001). Figures 4 (a) (b) and (c) show several fields of SWH from the high resolution Bass Strait wave model during the time of interest. In Figure 4(a), a clear distinction can be seen at around 152°E between the waves propagating generally towards the southwest and waves propagating towards the east. This is the signature of the cold front passing over the area. The mean wave directions take some time to adjust to the

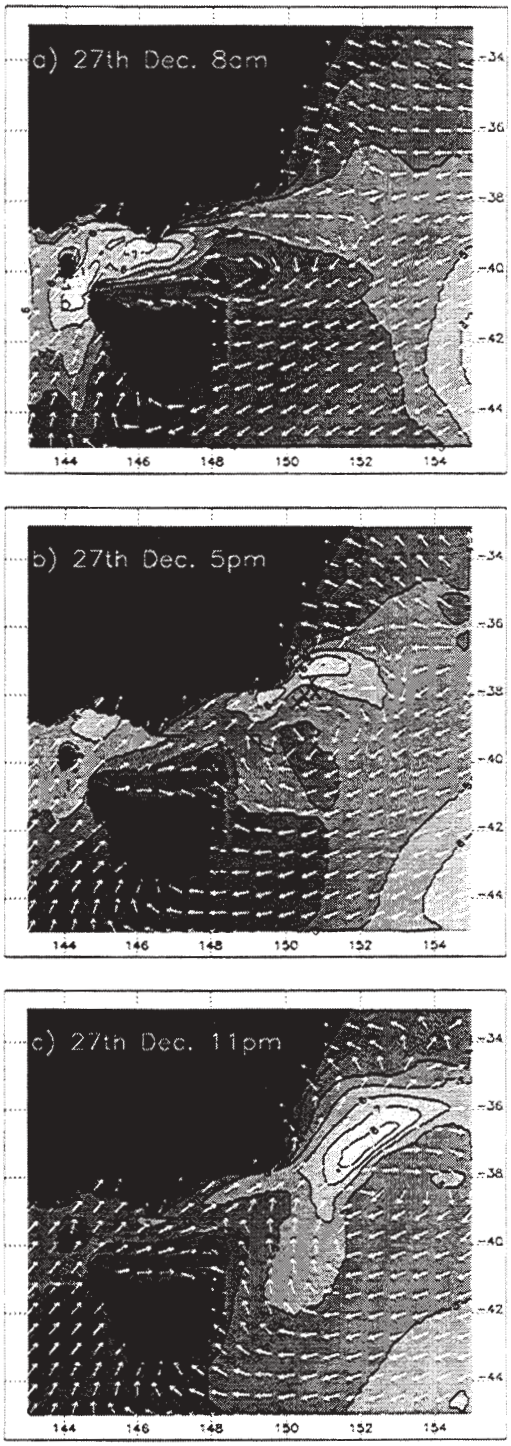

Figure 4. SWH (m) from the high-resolution wave model. Arrows show mean wave directions. The crosses on panel (b) show the approximate locations where several of the yachts capsized or were dismasted.

change in wind direction. The position of the 'front' in Figure 4(a) occurred in the wind field at 4am, i.e. 4 hours earlier.

After the front has swept through the Bass Strait region, the SWH in the western half of Bass Strait increases significantly, reaching a maximum of over 8m, just south of Melbourne at 11am. The mean wave direction here at this stage is towards the north, and during the afternoon of Dec. 27th, the SWH in the western half of Bass Strait abates somewhat.

The strong westerly winds associated with the small-scale secondary low pressure system over northern Tasmania cause a build-up in SWH in the eastern half of Bass Strait and by 2pm on the 27th, the SWH off the southeast corner of the continent is over 6m. By this time the passage of the low-pressure system has caused winds over most of Bass Strait to strengthen and swing to the southwest and this causes the SWH off Gabo Island to increase further (Figure 4(b)). By 11pm on Dec. 27th, the peak SWH has started to move slightly offshore (Figure 4(c)). A maximum SWH of 8.5m is reached between 10pm and 1am. During the early hours of the 28th, the area of peak SWH continues to move off into the Tasman Sea. SWH in the race region, southeast of Gabo Island remains fairly high at approximately 5m.

Figure 4(b) shows the locations where several of the yachts capsized (CYC99). These all occurred between 3pm and 7pm on Dec. 27th. It can be seen that the problems for the yachts occurred close to the area of highest SWH. However, another important consideration is the fact that multiple wave systems were present here. In particular, the easterly propagating wave systems created by the strong westerly winds combined with the westerly propagating swell arising from the earlier Tasman Sea storm, possibly steepened by the EAC. These multiple wave systems can be seen in a plot of the directional wave spectrum in Figure 5(a). This spectrum is representative of the sea-state at the second most southerly location marked in Figure 4(b). Note that the mean wave direction here is 68°, i.e., east-northeast. This is not representative of the actual sea-state, as the directional wave spectrum shows there is also a large amount of wave energy propagating towards the west.

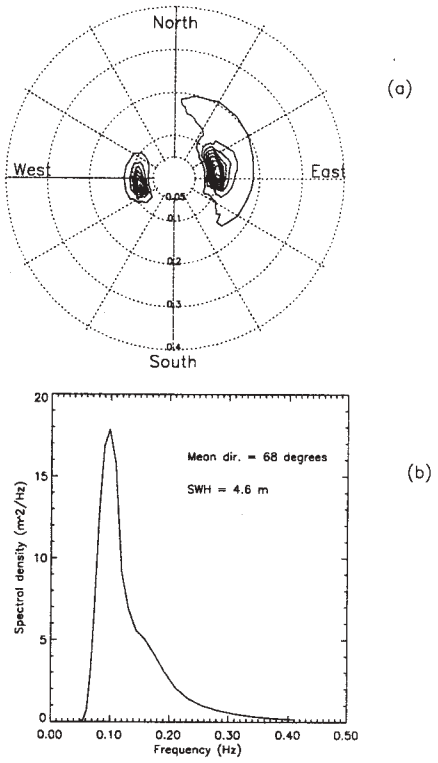

Figure 5. (a) Directional wave spectrum (m^2/Hz) from the wave model at (150°E, 38.1°S) on Dec. 27th at 5pm. (b) Directional average of the spectrum shown in (a).

The term 'crossing seas' or a 'confused sea' is used to describe the situation in which wave systems propagating in more than one distinct direction are present in a wave field. The existence of large waves propagating in many different directions causes the water surface to become highly irregular. These large, steep and chaotic waves can thus become hazardous to marine vessels. In addition, the situation depicted in Figure 5(a) shows that the 2 wave systems are propagating in almost opposite directions. Although the predominant wave direction is towards the east (the eastward peak has a higher spectral density), single waves propagating in the opposite direction will occasionally appear. These individual waves are sometimes termed 'rogue waves' (Torum and Gudmestad, 1990).

For operational purposes, marine forecasts are usually summarized in terms of SWH and mean wave direction. Further work would be required to develop techniques to summarize the sea-state when more than one wave system is significant in a region. This would need to take into account the relative significance of the superimposing wave systems and the likely impact of their combined effect on local wave characteristics.

4. COMPARISON WITH OBSERVATIONS

There are few reliable observations of SWH available in this area at this time - a reflection of the general difficulty in obtaining *in situ* marine observations. The locations of the ERS-2 and Topex/Poseidon satellite overpasses unfortunately do not coincide with the area of interest. We concentrate here on the data available from KFB at (148.2°E, 38.6°S) in Bass Strait (see Figure 1). In addition, some reports from the yacht fleet are considered. These, however, are subjective visual observations and are therefore less reliable than instrumented measurements.

4.1 Surface Winds

We first consider the accuracy of the forcing fields and compare the surface winds obtained from the atmospheric model with the observed winds at KFB. Wind speeds were measured by an anemometer mounted 44m above the sea-surface on the KFB platform. These winds need to be extrapolated to a height of 10m to enable comparison with the 10m surface winds used to force the wave model. In neutrally stable conditions, a logarithmic wind profile applies. In this particular situation, air and water temperature measurements from KFB show that after the passage of the cold front on Dec. 26th, the water was several degrees warmer than the air, resulting in low static stability. This is likely to contribute to deviations from a logarithmic wind profile. The following analysis can nevertheless provide a useful assessment of any major differences occurring between the modelled and observed surface winds.
So, assuming a logarithmic wind profile:

$$\frac{\partial u(z)}{\partial z} = \frac{u_*}{\kappa z} \qquad (2)$$

where $u(z)$ is wind speed at height z above the sea-surface, u_* is friction velocity and κ is von Karman's constant (= 0.41), wind speed at 44m can therefore be converted to wind speed at 10m via:

$$u(10) = u(44) - \frac{u_*}{\kappa} \ln\left(\frac{44}{10}\right) \qquad (3)$$

Using the drag law $u_*^2 = C_D\, u(10)^2$, we find:

$$u(10) = \frac{u(44)}{1 + \frac{\sqrt{C_D}}{\kappa} \ln\left(\frac{44}{10}\right)} \qquad (4)$$

The fact that C_D is itself a function of 10m wind speed again complicates these calculations, but a more detailed examination of the structure of the surface boundary layer is outside the scope of this paper. Here, C_D is taken to be 0.0015, which is an appropriate value for a 10m wind speed of approximately 15m/s (Large and Pond, 1981).

Figure 6(a) shows a comparison of 10m wind speed from the atmospheric model at the location of KFB, the wind speed measured at the anemometer, and the measured wind speed extrapolated to 10m. Validation statistics are shown in the first row of Table 1.

Table 1. Validation statistics for surface winds and SWH when compared to observations at KFB.

	Bias	R	*rms*	SI
u_{10} (KFB)	-1.3 m/s	0.58	3.6 m/s	0.23
u_{10} (pt2)	-1.3 m/s	0.86	2.7 m/s	0.16
SWH (pt2)	-0.34 m	0.93	0.68 m	0.16

Here, bias is (observed - modelled), *rms* is the root-mean-square difference, SI is the Scatter Index and R is the linear correlation coefficient. The SI is defined as the ratio of standard deviation of error to mean observed u_{10} (or SWH) and is given by:

$$SI = \frac{\sqrt{\frac{1}{N}\sum_{i=1}^{N}\left(u_m^i - u_o^i - bias\right)^2}}{\frac{1}{N}\sum_{i=1}^{N} u_o^i} \qquad (5)$$

where u_m is the modelled 10m wind speed and u_o is the observed 10m wind speed.

The relatively poor match between modelled and observed wind speeds at KFB could be because the assumption of neutral stability is not appropriate in this situation. However, there is also the possibility that the small-scale features of the wind field are simply slightly displaced in the model. Upon inspection of the modelled winds from the surrounding gridpoints, it was found that the best correlation with the observations occurred at (147.8°E, 38.5°S). The 10m wind speed from this location (pt2) is shown in Figure 6(b) and the validation statistics are also shown in Table 1.

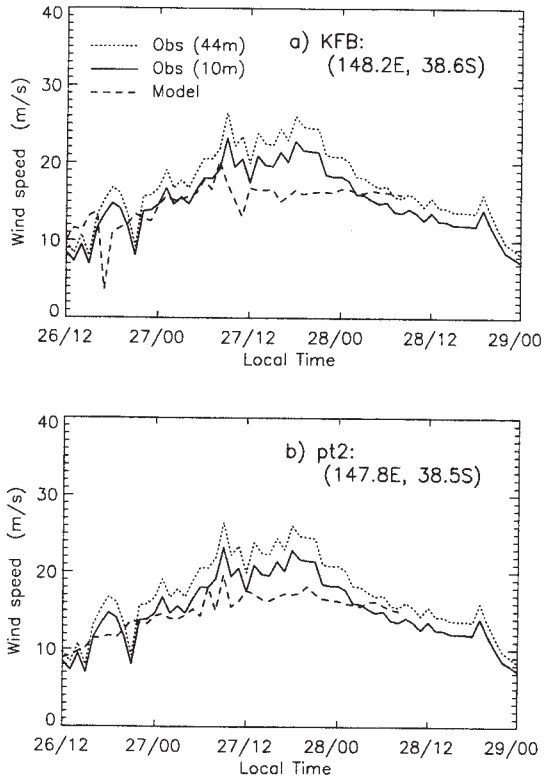

Figure 6. (a) Comparison between 10m wind speed from the atmospheric model (dashed line) and wind speed measured by a 44m-high anemometer at Kingfish B platform (dotted line). The solid line shows the observations extrapolated to 10m assuming a logarithmic wind profile. (b) The same as (a) but modelled wind speeds are at (147.8°E, 38.5°S).

It can be seen that although the bias is the same, there is a much greater correlation between the modelled and observed winds at this second location. This suggests that the small-scale characteristics of the wind forcing fields may be displaced slightly to the west in the atmospheric model. Following this implication, comparisons between modelled wave fields and KFB observations were performed using wave model output at this second location.

4.2 Significant Wave Height

Figure 7 shows a comparison between hourly SWH measured by a wave sensor at KFB and the SWH generated by the high-resolution wave model. Overall, there is good phase agreement between the modelled SWH and the data. The rapid increase during Dec. 27th is represented very well by the wave model, however the SWH is slightly underestimated overall, and the

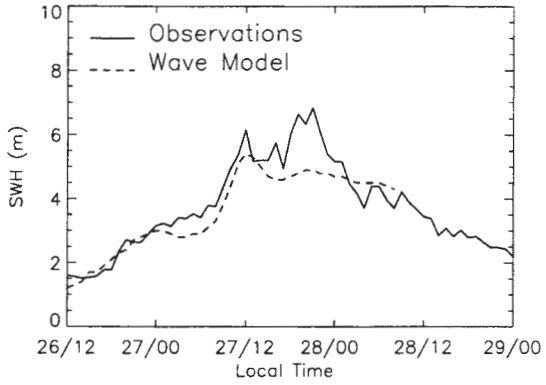

Figure 7. Comparison between SWH from the high-resolution wave model (dashed line) and SWH measured at Kingfish B platform (solid line).

second, larger peak is not present in the modelled SWH. In addition, the model appears to decay on a slower scale than the observations. Overall, the modelled SWH appears smoother than the observed SWH. This is to be expected as the model represents an expected value of SWH over a 10km by 10km area, rather than a value at a single location.

Validation statistics are shown in Table 1. Although the *rms* error seems high when compared to a typical operational *rms* error of about 0.4m, this is mainly due to the fact that the mean SWH here is high. The time-varying errors indicated by SI and R, show that the skill of the model in this case is very good. Note that a large portion of the bias and *rms* error here arises from the wave model not capturing the second peak in SWH. This is very similar to the pattern occurring in the wind speeds, i.e., the atmospheric model generally underpredicts wind speeds with most of the underestimation occurring during the second peak. From this, we may conclude that a large portion of the SWH bias is likely to be due to errors in the wind field.

One factor missing from the growth term within the wave model is the effect of the 'gustiness' in the wind, i.e., variability that occurs on time scales shorter than the temporal resolution of the wind fields. Generally, gusts are defined to be random wind oscillations with periods of up to 20-30 minutes. In this study, new wind fields were provided at hourly intervals and so gusts are likely to be important here. This is particularly true since this is a situation of low static stability, which implies that there will be more turbulence in the atmosphere. It has been shown that variability or gustiness in the wind speed can enhance wave growth by up to 10% (Komen *et al.*, 1994), and so this could also help explain the underprediction in the modelled SWH.

To be able to completely explain the differences between the modelled and observed SWH, it would be necessary to compare total wave spectra. This would indicate at which frequencies and in which directions the wave model is lacking in energy, i.e., whether the deficiencies are in the swell or wind-sea components of the spectrum. However, observations of wave spectra are very difficult to obtain and there were none available here during this time period.

One possible cause for underprediction of swell from the Tasman Sea storm is the 'sprinkler effect' (Booij and Holthuijsen, 1987). This is due to poor resolution in the wave spectrum and causes the disintegration of swell energy as it propagates long distances across the ocean. This can eventually result in an unrealistic spatial distribution of swell energy from distant storms. In this study, the directional resolution of the wave spectrum has been doubled from the usual operational resolution in an attempt to minimize this effect.

Another possible source of error is the lack of current or depth refraction in the wave model. It has been shown however, that depth refraction contributes very little to model performance statistics (Komen *et al.*, 1994) and it is seldom included in operational wave models. As discussed in Section 3.2, the EAC may have some effect on the development of the sea-state by steepening the westerly propagating swell arising from the Tasman Sea storm. The effects of surface currents are not included in this study. It is not clear whether the potential alteration to this swell system would still be detected at the location of the KFB platform.

4.3 Yacht Fleet Reports

CYC99 presents summaries of some visual reports from competitors made in their post-race surveys. Although highly subjective, these reports do provide some interesting information that can be useful in a general examination of the sea-surface conditions.

The average wave height reported by the fleet was 9.4m This presumably was during the worst conditions that the boats encountered, and compares fairly well with the modelled SWH of 8.5m. Assuming a Rayleigh distribution of waveheights, one might expect a maximum wave 1.91 times the SWH every 1500 waves. Assuming a peak period of 9 seconds, this would therefore be encountered on average every 3.75 hours. Most of the fleet reported that they endured the most severe conditions for at least 4 hours, so according to the wave model, it would not be unusual for individual waves of over 15m to be encountered. In fact, the average maximum wave height reported by the fleet was 14m.

The yacht fleet reported that the direction of propagation of the waves was irregular, but that the average direction was 60°. This is consistent with the modelled sea-state depicted in Section 3.3, and particularly that shown in Figure 5, where the mean wave direction is 68°. In addition, the yachts that experienced problems reported that 'exceptional' waves were responsible for causing knockdowns, and that these waves always came from a direction other than the prevailing wave pattern. This agrees with the idea of rogue waves, described previously.

Competitors in the race also commented that the 'waves had no back to them'. This effect is likely to be due to the steepening of the westerly-propagating swell by the EAC (see Section 3.2).

5. CONCLUSIONS

A high-resolution (0.1°) wave model has been run for the Bass Strait region over the period of the 1998 Sydney to Hobart yacht race. The maximum SWH reached in the wave model is 8.5m, east of Gabo Island during the evening of Dec. 27th. The model compares well with observations of Significant Wave Height (SWH) at Kingfish B Platform in Bass Strait. There is an underprediction of SWH at this location of approximately 0.34m. This is likely to be due to residual errors in the wind forcing fields. The wave model results are also consistent with visual observations of the sea-state made by competitors in the race.

Examination of the ambient sea-state conditions and directional wave spectra during the race shows that in addition to the strong winds and high SWH experienced by the fleet, there were multiple wave systems present. At times, and particularly during the peak of the storm, these wave systems were propagating in almost opposite directions. This situation is termed 'crossing seas' and has the potential to create hazardous conditions for mariners.

Acknowledgements
Lawson and Treloar provided the wave data from Kingfish B platform. The author wishes to thank George Cresswell for his comments on the EAC during the period of the yacht race and David Griffin for providing the gridded TP/ERS-2 surface velocity dataset. Thanks also to Rick Smith for providing the 0.1° bathymetry.

REFERENCES

Andrews, J. C. and Scully-Power, P.D. 1976. The structure of an East Australia Current anti-cyclonic eddy, J. Phys. Oc., 6, 756 - 765.

Bender, L., 1996. Modification of the physics and numerics in a third-generation ocean wave model. J. Atmos. Oc. Tech., 13, 726 – 750.

Booij, N. and Holthuijsen, L. H. 1987. Propagation of ocean waves in discrete spectral wave models, J. Comp. Phys., 68, 307 - 326.

Cardone, V.J., Jensen, R.E., Resio, D.T., Swail, V.R. and Cox, A.T. 1996. Evaluation of contemporary ocean wave models in rare extreme events: The 'Halloween Storm' of October 1991 and the 'Storm of the Century' of March 1993, J. Atmos. Oc. Tech., 13, 198 - 230.

Cruising Yacht Club of Australia. 1999. Report of the 1998 Sydney to Hobart Race Review Committee.

Garratt, J.R. 1992. The Atmospheric boundary layer, Cambridge Univ. Press, Cambridge, U.K., 316pp.

Greenslade, D.J.M. 2001. A wave modelling study of the 1998 Sydney to Hobart Yacht race, Aus. Met. Mag., (accepted).

Gunther, H., Hasselmann, S. and Janssen, P.A.E.M. 1992. Wamodel Cycle 4, DKRZ Report No. 4., Hamburg.

Hasselmann, K., Barnett, T.P., Buows, E., Carlson, H., Cartwright, D.E., Enke, K., Ewing, J.A., Gienapp, H., Hasselmann, D.E., Kruseman, P., Meerburg, A., Muller, P., Olbers, D.J., Richter, K., Sell, W. and Walden, H. 1973. Measurements of wind-wave growth and swell decay during the Joint North Sea Wave Project (JONSWAP), Dtsch. Hydrogr. Z. Suppl. A., 8(12), 95p.

Komen, G.J. and Smith, N.R. 1999. Wave and sea level monitoring and prediction in the service module of the Global Ocean Observing System (GOOS), J. Mar. Sys., 19, 235 - 250.

Komen, G.J., Cavaleri, L., Donelan, M., Hasselmann, K., Hasselmann, S. and Janssen, P.A.E.M. 1994. Dynamics and modelling of ocean waves. Cambridge University Press, Cambridge, UK, 532 pp.

Large, W.G. and Pond, S. 1981. Open ocean momentum flux measurements in moderate to strong winds, J. Phys. Oc., 11, 324 - 336.

Mills, G. A Synoptic/diagnostic study of the 1998 Sydney-Hobart yacht race storm - a warm-cored extratropical cyclone, BMRC Research Report No. 76, Bur. Met., Australia

National Meteorological Operations Centre. 1999. The operational implementation of MESO_LAPS_PT125 in NMOC, Operations Bulletin No. 49, Bur. Met., Australia.

Puri, K., Dietachmayer, G.S., Mills, G.A., Davidson, N.E., Bowen, R.A.and Logan, L.W. 1998. The new BMRC Limited Area Prediction System, LAPS, Aust. Met. Mag., 47, 203 - 233.

Seaman, R., Bourke, W., Steinle, P., Hart, T., Embery, G., Naughton, M. and Rikus L. 1995. Evolution of the Bureau of Meteorology's Global Assimilation and Prediction System, Part 1: Analyses and Initialization, Aust. Met. Mag., 44, 1 - 18.

Swail, V., Komen, G., Ryabinin, V., Holt, M., Taylor, P.K. and Bidlot, J. 1999. Wind waves in the Global Ocean Observing System, in OCEANOBS99, Proc. of the Int. Conf on the Ocean Observing System for Climate, St. Raphael, France, 1999.

Torum, A. and Gudmestad, O.T. (eds), 1990. Water wave kinematics., Kluwer Academic Publishers, Dordrecht, Holland, 771pp.

DETERMINATION OF OCEANOGRAPHIC RISKS FROM HURRICANES ON THE MEXICAN COAST

R. Silva, G. Díaz, A. Contreras, G. Bautista & C. Sánchez
Instituto de Ingeniería, Universidad Nacional Autónoma de México.
Cd. Universitaria. Apdo. Postal 70-472. 04510. México, D. F.
Email. rodo@litoral.iingen.unam.mx

1. INTRODUCTION

Following hurricanes Gilbert (1988) and Pauline (1997) various projects are underway which provide Mexico with an integrated coastal management programme (ICMP), Silva et al. (2000). The starting point for these has been what information should be used in order to establish criteria for the coastal zone management.

This paper presents numerical results for different probabilities of presentation for significant wave heights, peak periods, maximum winds and minimum pressures caused by hurricanes over the Gulf of Mexico and the Pacific Ocean.

In order to obtain these parameters, two computational grids were designed corresponding to the Gulf of Mexico area (latitude 14° N to 35° N and longitude 75° W to 100° W) and the Pacific coast (latitude 10° N to 35° N and 89° W to 129° W) both with a resolution of 0.1° that is nearly 11 km, as shown in figure 1.

The database used goes back 50 years, covering 1225 hurricanes; 711 hurricanes on the Pacific and 514 on the Gulf of Mexico. The source data for every report and for each hurricane are central pressure, cyclostrophic radius, velocity displacement and the geographic position of the eye. The wave propagation data is based on digitalised bathymetry of both oceans.

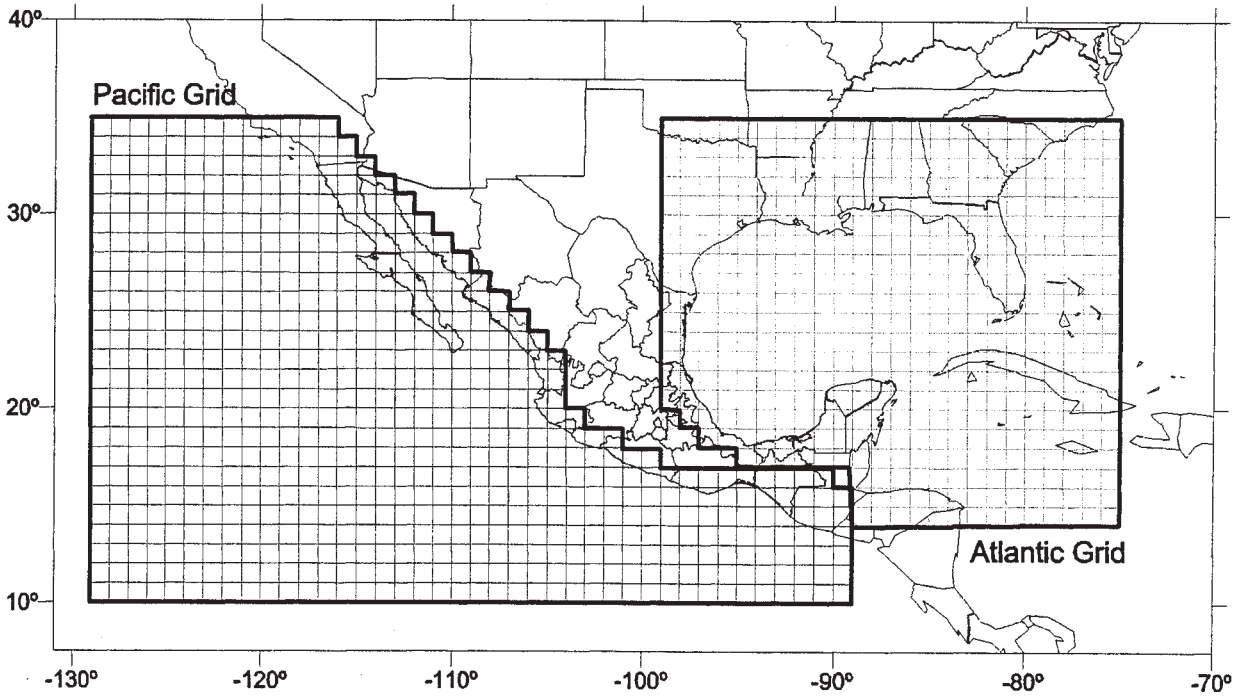

Figure 1. Computational Grids designed for the Pacific Ocean and the Gulf of Mexico.

For the synthetic estimation of the pressure, winds and wave parameters in deep waters models offered by the Hydromet – Rankin Vortex, Bret-Model X and Bretchsneider, reported in Bretchsneider (1990) and verified by Sanchez et al. (1998) were used. For the wave propagation from deep to shallow waters a model of refraction, Dalrymple (1988), was taken.

2. GOAL

To develop an oceanographic database, using meteorological information in order to evaluate the statistical risks generated by the presence of hurricanes affecting Mexico, thus improving coastal planning.

3. METHODOLOGY

The methodology described can be divided in three stages: data standardization, hydro-meteorology field estimation and statistical parameter evaluation. This last allows the study of meteorological and oceanic features of the Mexican oceans.

3.1 Data standardization

In order to apply all the models described certain data and specific spatial distance are required:

- Central pressure
- Cyclostrophic radius
- Displacement velocity
- Displacement direction
- Geographic position (latitude-longitute)

First, the blank field data from the bulletins provided by the NOAA were completed using the following criteria:

3.1.1 Central pressure

Until 1972 some of the reports provided by the NOAA web site omitted the central pressure. To solve this problem, two curves were generated based on the 50 year historical record and fixed with a best fit line. In figure 2 the correlation between central pressure and maximum wind speed, is presented. On the right is the correlation for to the Gulf of Mexico on the left that corresponding to the Pacific.

The equations that represent central pressure and maximum wind velocity are:

- For the Gulf of Mexico:

$$Pc = 1015.46 - 0.128758Vv - 0.000856224Vv^2 \quad (1)$$

- For the Pacific Ocean:

$$Pc = 991.7 - 24.2363Vv - 3.91299Vv^2 \quad (2)$$

where

Pc – Central Pressure of the Hurricane [mb]
Vv – Maximum wind speed [km/h]

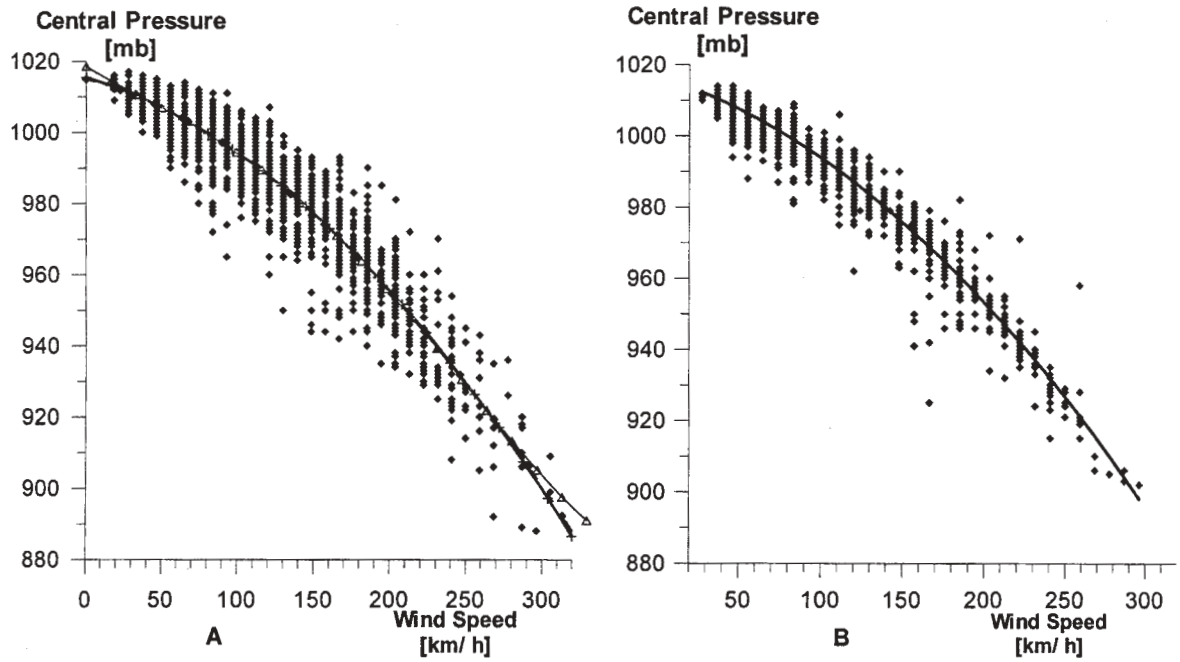

Figure 2. Maximum wind speed vs. central pressure. (**A**) *Gulf of Mexico and* (**B**) *Pacific Ocean*

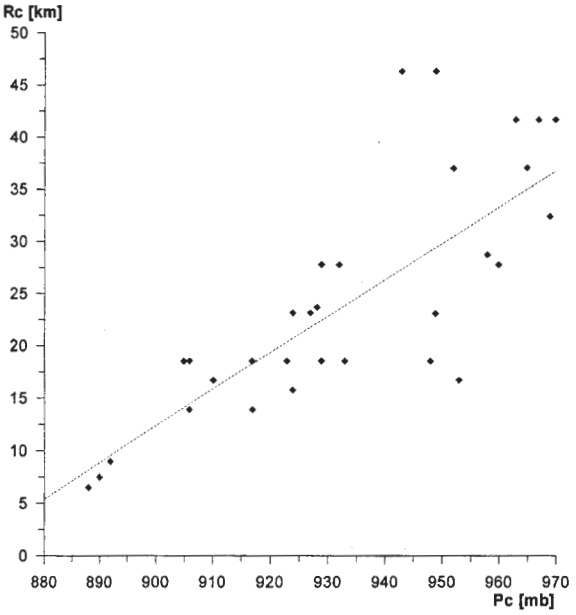

Figure 3. Cyclostrophic Radius vs hurricane central pressure.

3.1.2 Cyclostrophic radius

Normally, the cyclostrophic radius is not reported in the meteorological bulletins used. To rectify this a best fit line that relates central pressure and cyclostrophic radius was found for 26 hurricanes over the 50 year period.

Equation (3) represents the best fit line presented in figure 3:

$$Rc = -301.201 + 0.348383\,Pc \qquad (3)$$

Where

Rc - Cyclostrophic radius [km]

3.1.3 Data interpolation

Even where all the necessary data is present in the bulletins, the information recorded is really not enough for the resolution required in the statistical grid (0.1° x 0.1°), since the NOAA reports are made every six hours and in some cases a hurricane may move distances of over 2° (about 222 km) in that time. Therefore we interpolate linearly between bulletins all the base data with a resolution of 0.1° before applying the numerical models.

3.2 Hydro-meteorology field evaluation

For this stage, we developed three modules: pressure, wind and wave models, described below.

3.2.1 Pressure Model

Here we summarized the main feature of the mathematical Hydromet Rankin-Vortex Model, Bretchsneider (1990). This model represents the pressure field by a series of concentric circles that represent lines of equal pressure. The slope of the pressure configuration yields the pressure gradient that is used on the hurricane wind equation. The mathematical expressions that describe the pressure field are the following:

$$\frac{P_r - P_0}{P_\infty - P_0} = Ae^{-B(R/r)} \qquad (4)$$

$$\frac{P_r - P_0}{P_\infty - P_0} = 1 - \left[1 + a\left(\frac{r}{R_c}\right)^2\right]^{-b} \qquad (5)$$

where

Po - Pressure at the hurricane centre
Pr - Pressure within a distance r from the centre point of the hurricane
P_∞ - Pressure at an infinite distance
R_c – Cyclostrophic radius

The parameters A, B, a and b depend on the value of the Rankin Vortex number: Details of how this can be evaluated are reported in Bretchsneider (1990) and Sanchez et al. (1998).

3.2.2 Wind model

The model used is known as the Bret Model-X, Bretchsneider (1990). In summary, the main equations for evaluating the wind field are:

$$P_r = P_0 + \left(\frac{(r/R_C)^2}{1+(r/R_C)^2}\right)(P_N - P_0) \qquad (6)$$

$$R_c \frac{dp}{dr} = (P_N - P_0)\frac{2(r/R_C)^2}{(1+2(r/R_C)^2)^2} \qquad (7)$$

$$r\frac{dp}{dr} = (P_N - P_0)\frac{2(r/R_C)^2}{(1+2(r/R_C)^2)^2} \qquad (8)$$

$$V_{cr} = \left(\frac{P_N - P_0}{\rho_a}\frac{(r/R_C)}{1+2(r/R_C)^2}\right)^{1/2} \qquad (8)$$

where

V_{cr} - velocity of the wind
P_N - pressure in a selected distance

3.2.3 Wave model

This is the simplified mathematical model known as HIDROMET, which was originally developed by Bretchsneider (1990). From this, the significant wave height and associated significant wave period in deep water, based on the cyclonic wind, are obtained.

.

The significant sea wave height depends on a K' value which in turn depends on the value of the Rankin Vortex number, Nc which is obtained through the next equation:

$$H_{Rs\_Sta} = K'\sqrt{R_C \Delta P_0} \qquad (9)$$

The wave height can be obtained as well as any wind velocity for any radius r. The wave field for the hurricane is obtained with the following equation:

$$H_{r\theta} = H_r\left[1+\frac{0.5V_F\cos(\beta)}{U_r}\right] \qquad (10)$$

Where

V_F - Hurricane advance speed
β - Angle between the hurricane and the wind *Ur*.
U_r - Hurricane wind

The velocity field for winds 10 meters over the mean sea water level can be estimated through the equation:

$$V_{10\vartheta} = 0.865(U_r + 0.5V_F\cos(\beta)) \qquad (11)$$

For the propagation from deep to intermediate and shallow waters we used the Refract model developed by Dalrymple (1988).

3.3 Statistical parameter Evaluation

Using the data which had been interpolated from the standardized reports; the first step was to create four different grids for: pressure, winds, significant waves and for associated wave period fields.

Figures 4 and 5 show the maps for wind and wave height fields, obtained for the case of hurricane Gilbert. The dots represent the original points for which we have information from the NOAA bulletins. As can be seen, the maximum velocity of the hurricane was reached when Gilbert hit the Yucatan Peninsula (Cancun).

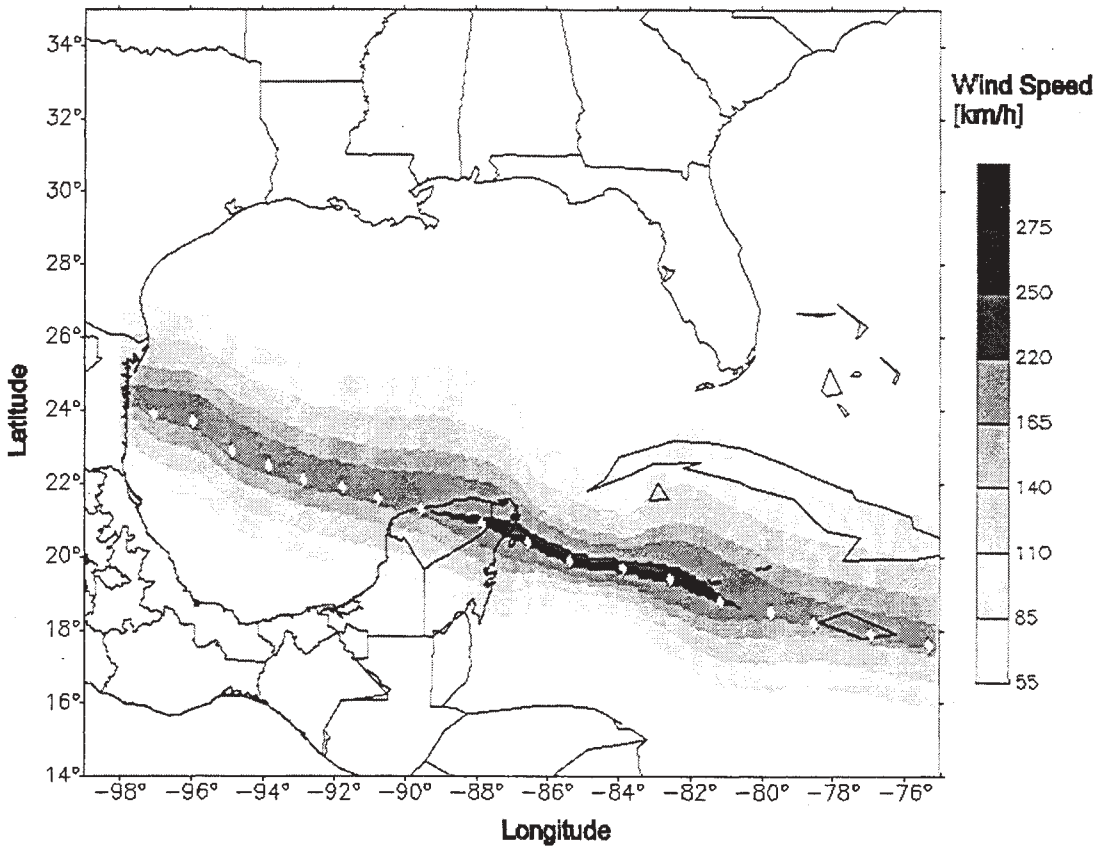

Figure 4. Map of maximum wind velocities generated by hurricane Gilbert (1988).

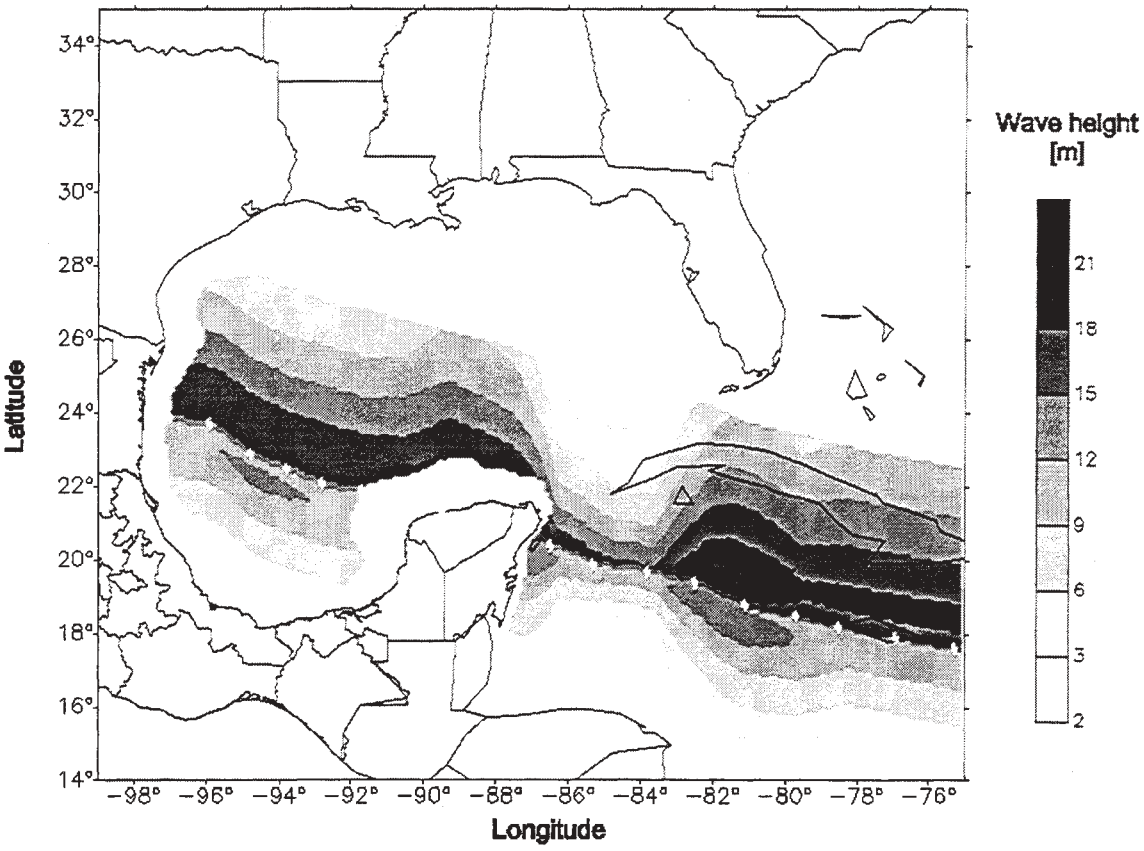

Figure 5. Map of maximum wave heights generated by hurricane Gilbert (1988).

Color	Category	Wind Velocity [km/h]	Storm Surge [m]
TD (1)	Tropical Depression	< 64	< 0.86
TS (2)	Tropical Storm	64 < > 118	0.86 < > 1.0
H1 (3)	Hurricane type 1	118 < > 154	1.00 < > 1.8
H2 (4)	Hurricane type 2	154 < > 178	1.80 < > 2.7
H3 (5)	Hurricane type 3	178 < > 210	2.70 < > 3.9
H4 (6)	Hurricane type 4	210 < > 250	3.90 < > 5.6
H5 (7)	Hurricane type 5	250 <	5.6 <

Table 1. Saffir-Simpson tropical cyclone classification

Table 1 shows the Saffir – Simpson scale used in order to characterize cyclone intensity from a tropical depression to a hurricane of class 5. This scale is based on the wind speed and gives a good idea of the storm surge magnitude.

Once all the hurricane information was processed, we were able to evaluate different kind of parameters for any specific location or for the whole grid.

The system was designed to evaluate the following parameters in each grid and for the

whole period or for a specific year, season or month:

- Number of hurricanes of any given intensity
- Minimum pressure presented
- Maximum significant wave height
- Wave period associated with the maximum wave height
- Maximum wind velocity
- Mean and maximum velocity displacement of hurricanes

It is also possible to evaluate any statistical feature, like return periods, for any particular location or for the whole grid.

4. RESULTS

Figures 6 and 7 show the full series of hurricane tracks reported in the last 50 years in the Pacific Ocean and the Gulf of Mexico. As can be seen from the figure, in the Pacific Ocean most of the hurricanes travel a great distance from the Mexican coast and much of the area of influence is between latitudes 15° and 25°. For the case of the Gulf of Mexico, there are some definite paths preferred by the hurricanes. These figures do not give us any conclusive findings but we can see that there are some areas where it is more common to observe the presence of hurricanes.

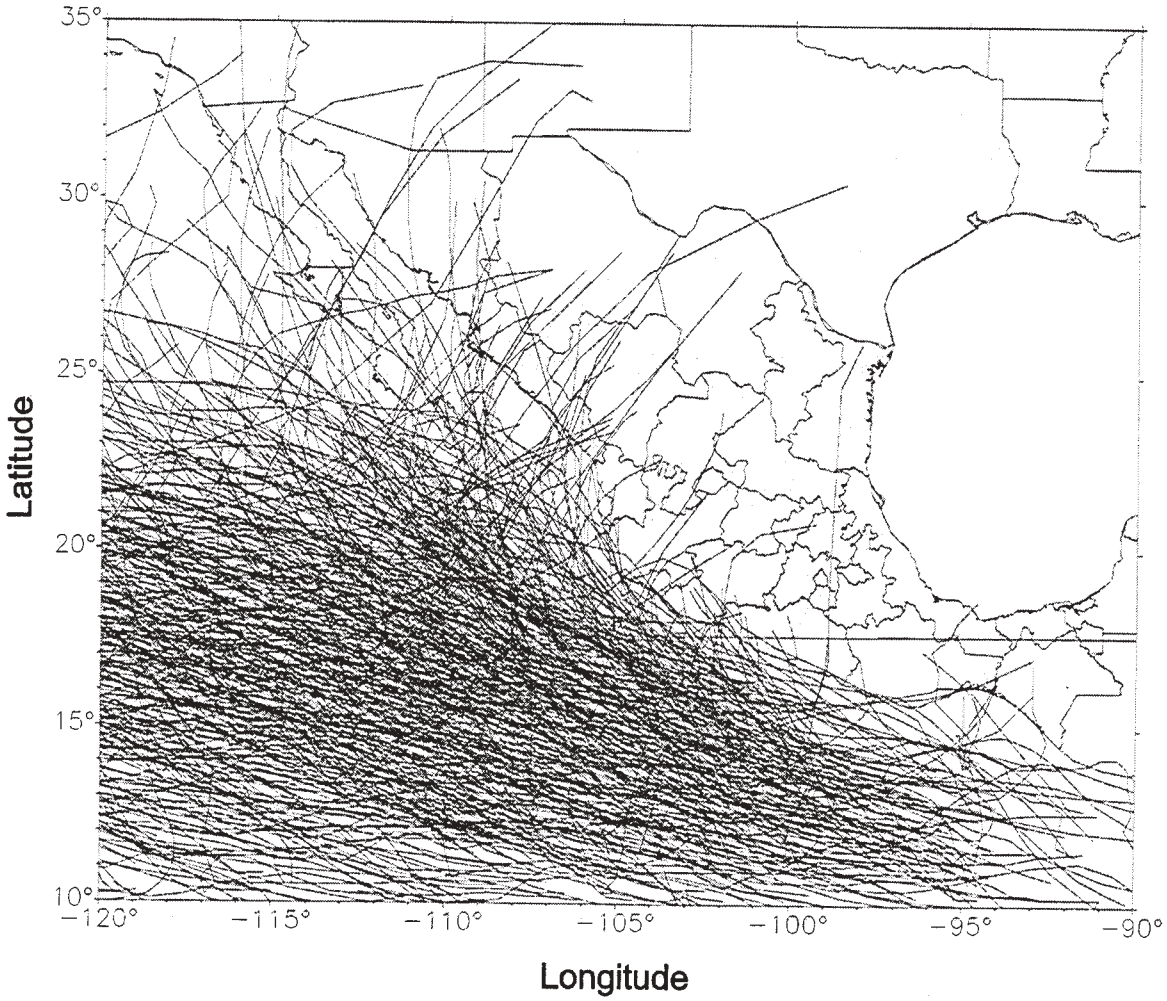

Figure 6. Pacific hurricane tracking

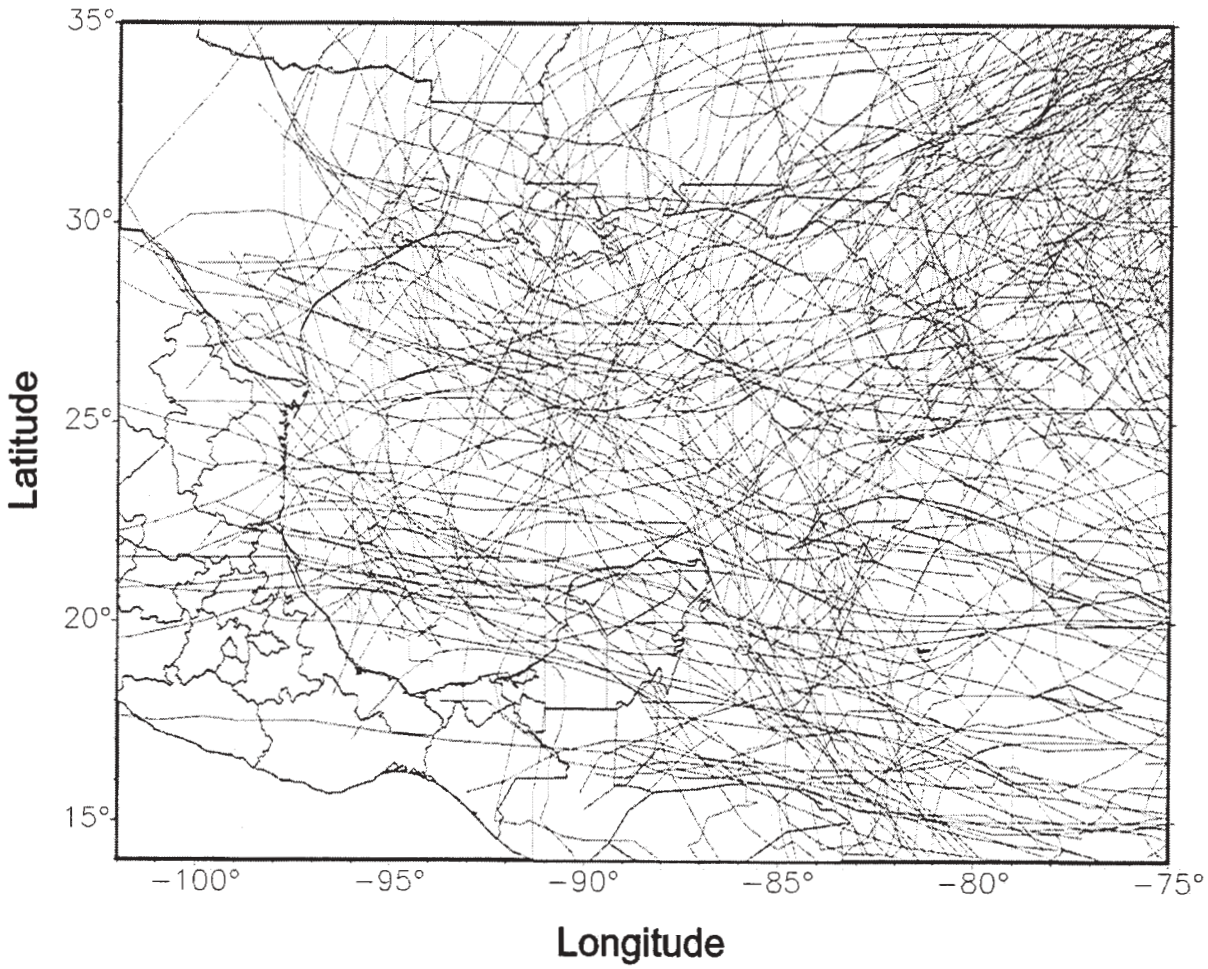

Figure 7. Gulf of Mexico hurricane tracking

Figures 8 and 9 are maps showing the number of hurricanes (type 1 to 5) for the Gulf of Mexico and the Mexican Pacific. From the first of these figures we can observe that there two areas in which more than 10 hurricanes in the last 50 years have occurred (latitude 28° to 33° North and longitude 75° to 82° West and latitude 16° to 21° North and longitude 83° to 86° South).

For the case of the Pacific Ocean, there is an area between latitude 15° to 20° North and longitude 108° to 119° West where more than 40 hurricanes are registered, in other words nearly one hurricane every year.

Figures 10 and 11 show the minimum hurricane pressures presented in the Gulf of Mexico and Mexican Pacific Ocean, using the whole database. From the first figure, we can detect five areas where very intense hurricanes occur: two in the Gulf of Mexico (one near Louisiana and the other close to the border between Mexico and the United States) and another three in the Caribbean Sea (two near and over the Yucatan Peninsula and another in front of the Nicaraguan coast), generated by hurricanes Beulah (1959), Camille (1969), Allen (1980), Gilbert (1988) and Mitch (1998).

For the case of the Pacific ocean, the most intensive areas are in the open sea, with the

possible exception of four narrow paths near the Mexican states of Baja California Sur, Sinaloa, Jalisco and Oaxaca

Again using the Saffir-Simpson scale, Figures 12 and 13 show the maximum intensities recorded in the Gulf of Mexico and the Pacific Ocean. In both cases, there are areas where some hurricanes have reached velocities of over 250 km/hr, but only one hurricane, Gilbert (1988), hit land with that velocity (Cancun).

Figures 14 and 15 are maps showing an estimation of maximum wave heights in the Gulf of Mexico and Pacific. In the first figure maximum values are clearly visible in a zone in front of the Peninsula of Yucatan (near Cancun in the state of Quintana Roo).

Comparing the results presented in figures 14 and 15, we can see that the order of magnitude of maximum waves are about the same in both seas, around 20 meters. However the coast line of the Gulf of Mexico is more vulnerable to higher waves, especially the peninsulas of Yucatan and Florida.

Associated with the maximum wave data, figures 16 and 17 show maps of wave periods with the maximum significant wave height for the Gulf of Mexico and the Pacific. In both cases the wave period can reach values of as much as twenty seconds.

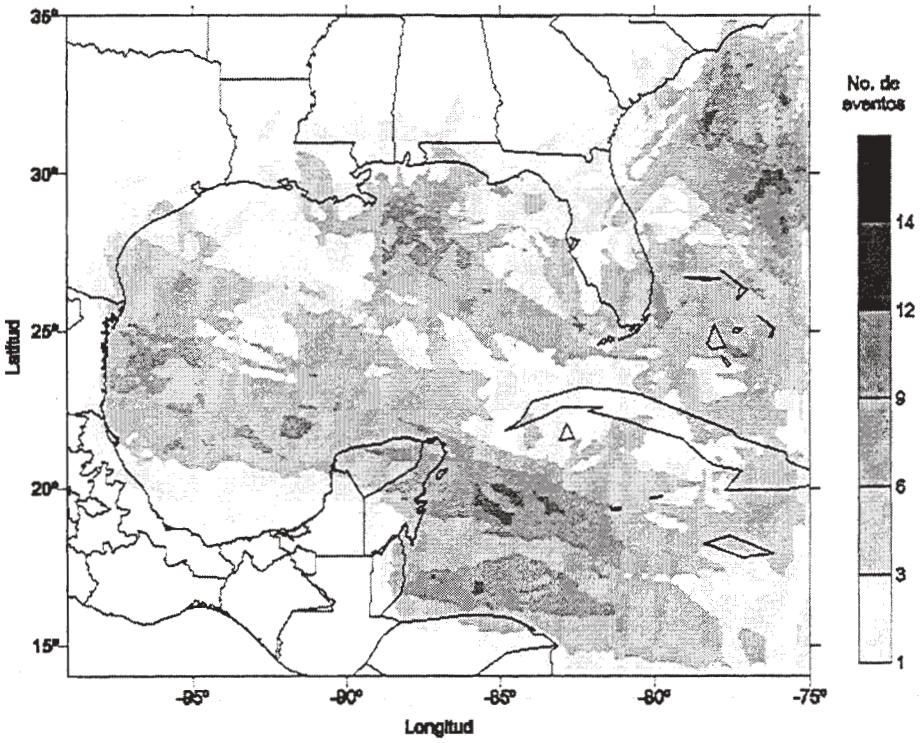

Figure 8. Map of the number of hurricanes type 1 -5 for the Gulf of Mexico.

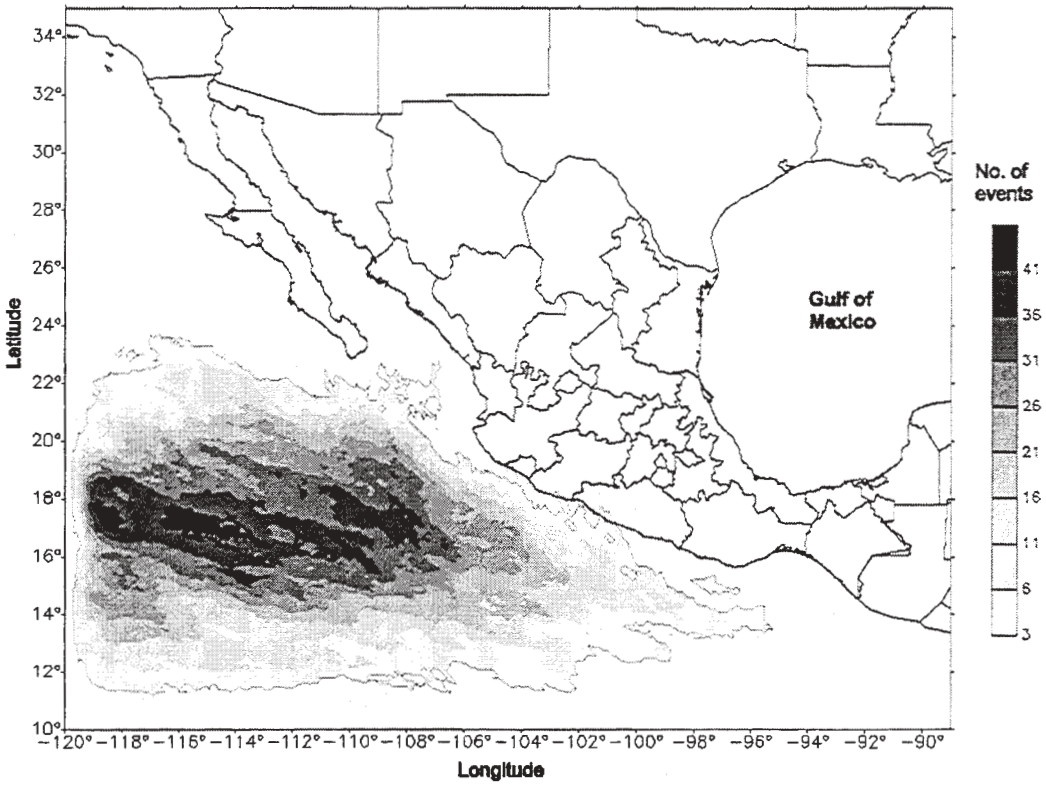

Figure 9. Map of the number of hurricanes type 1 - 5 for the Pacific Ocean.

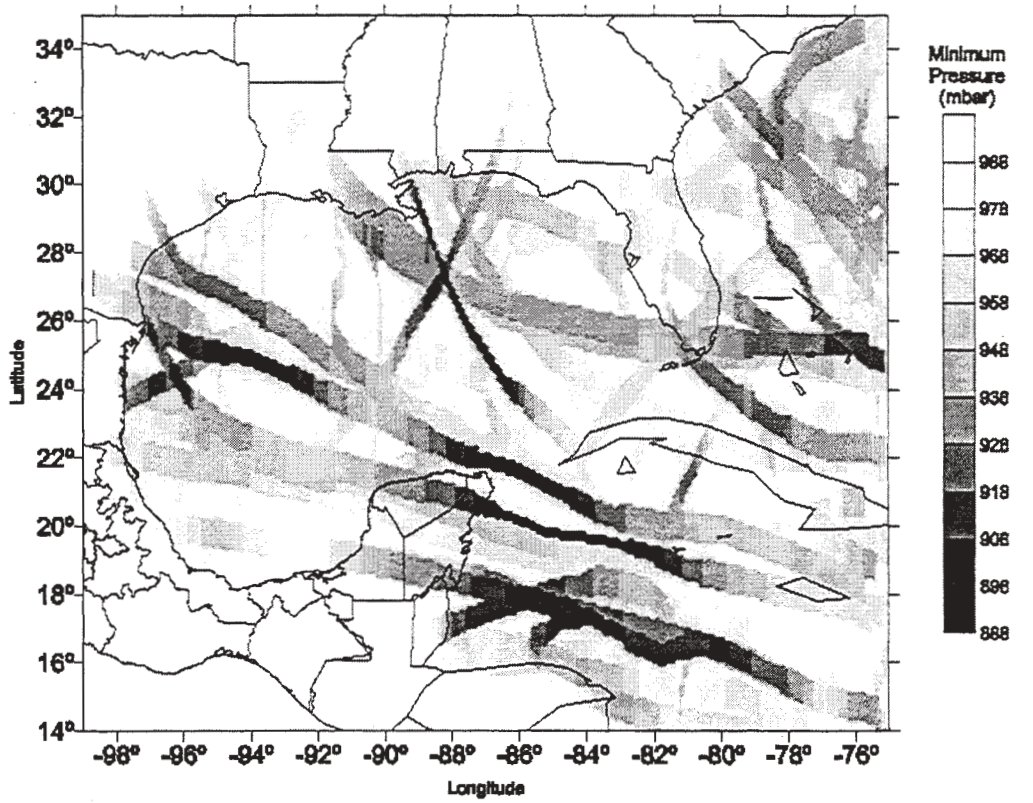

Figure 10. Map of minimum hurricane pressure presented in the last 50 years in the Gulf of Mexico.

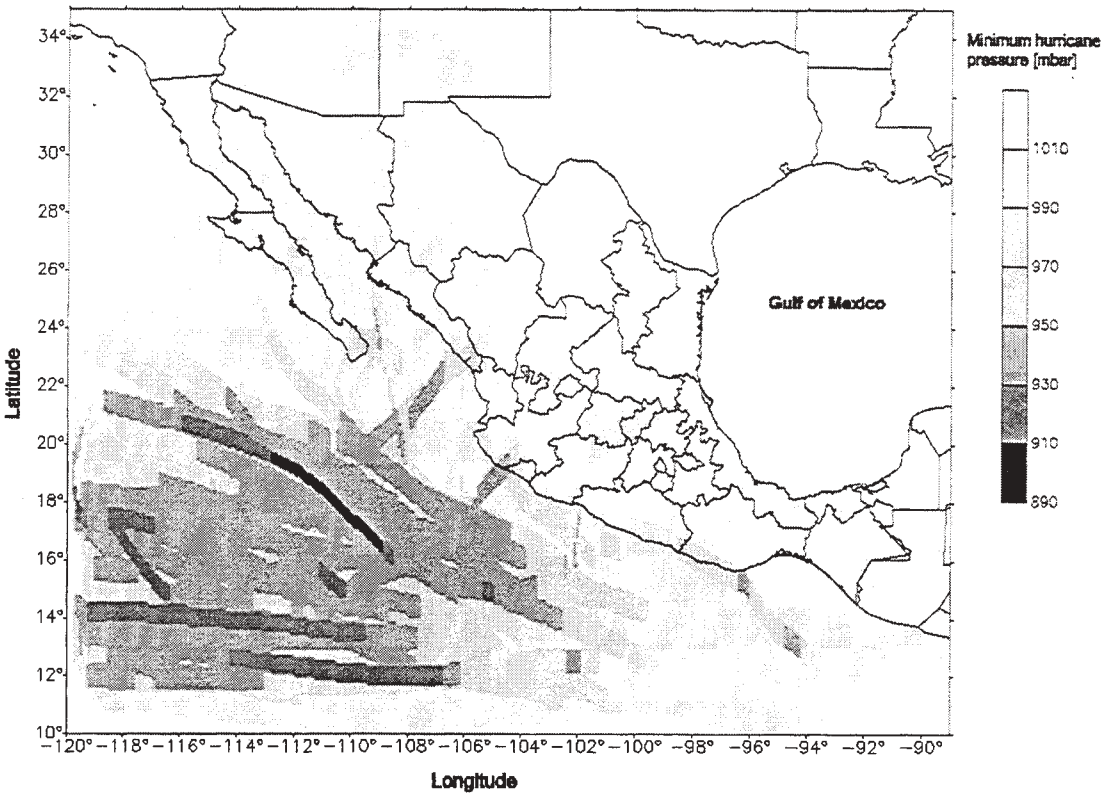

Figure 11. Map of minimum hurricane pressure presented in the last 50 years in the Pacific Ocean.

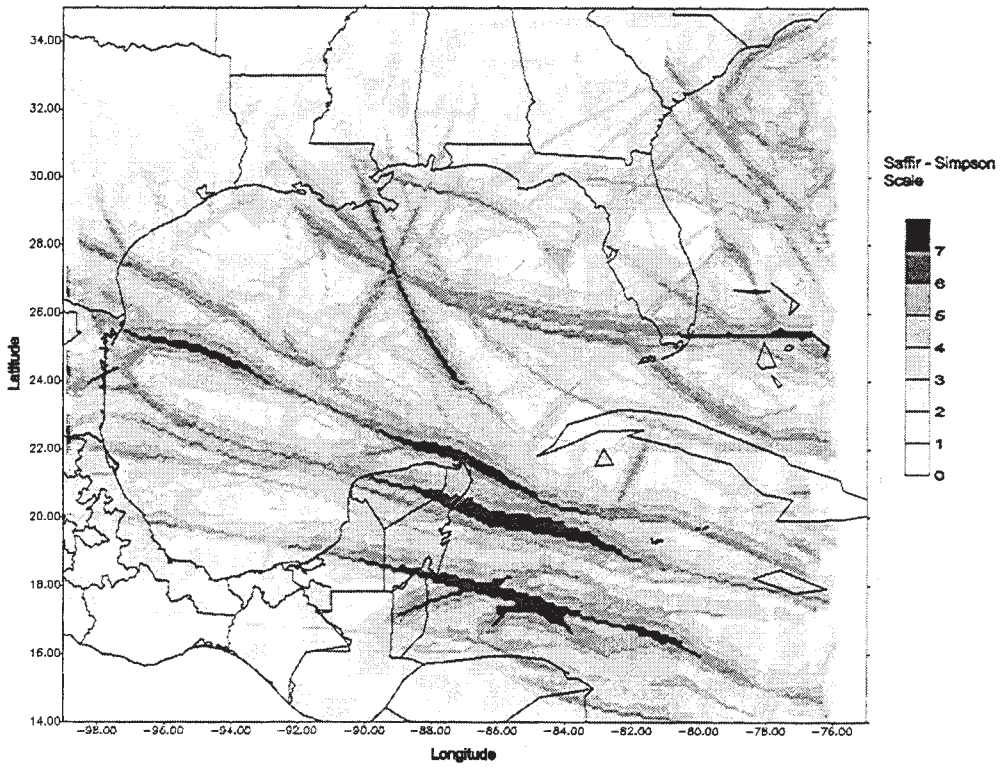

Figure 12. Maximum intensity recorded in the Gulf of Mexico.

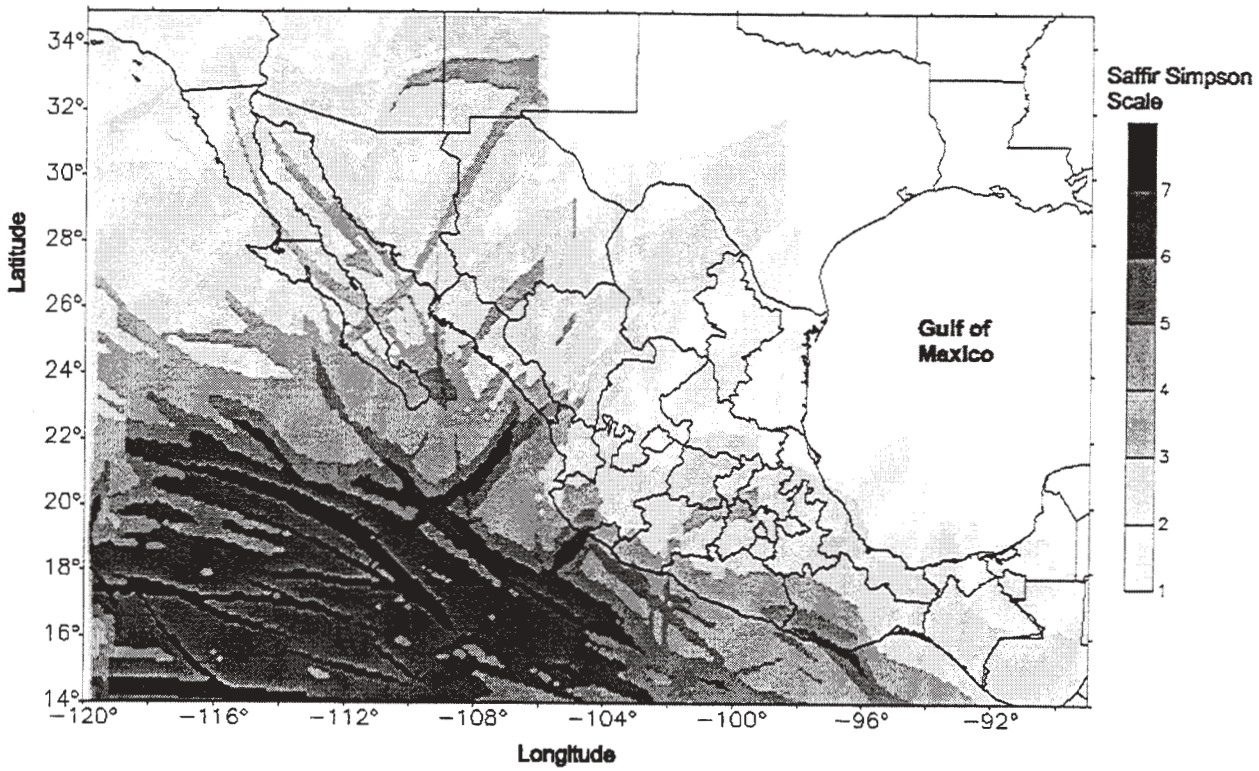

Figure 13. Maximum intensity recorded in the Pacific Ocean

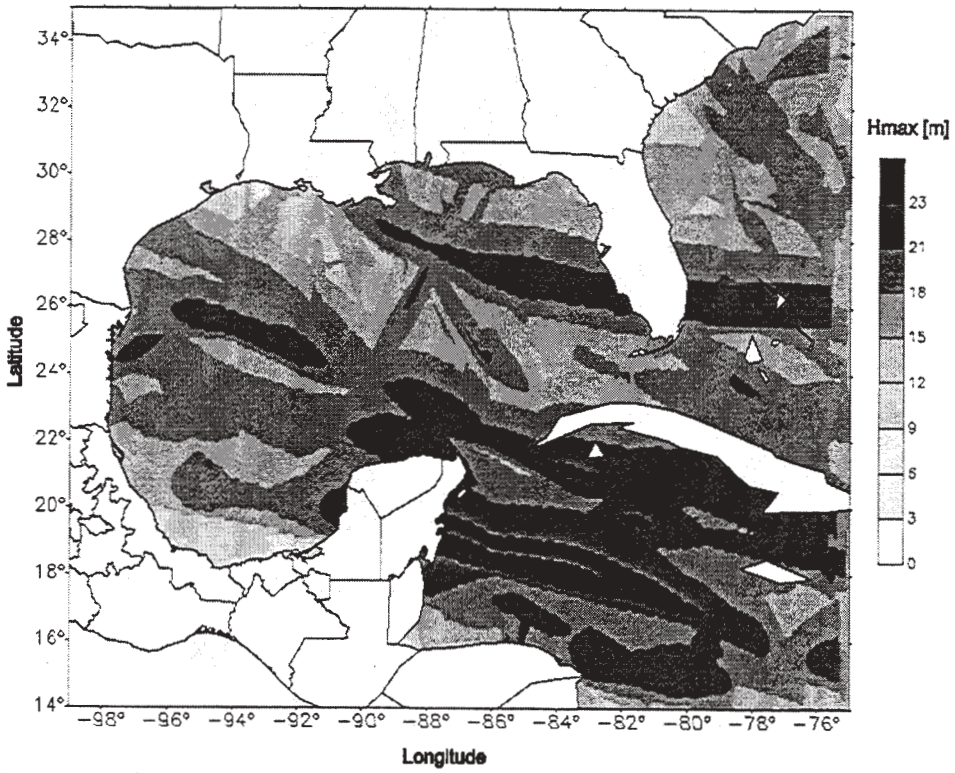

Figure 14. Map of maximum wave heights generated by hurricanes in the Gulf of Mexico.

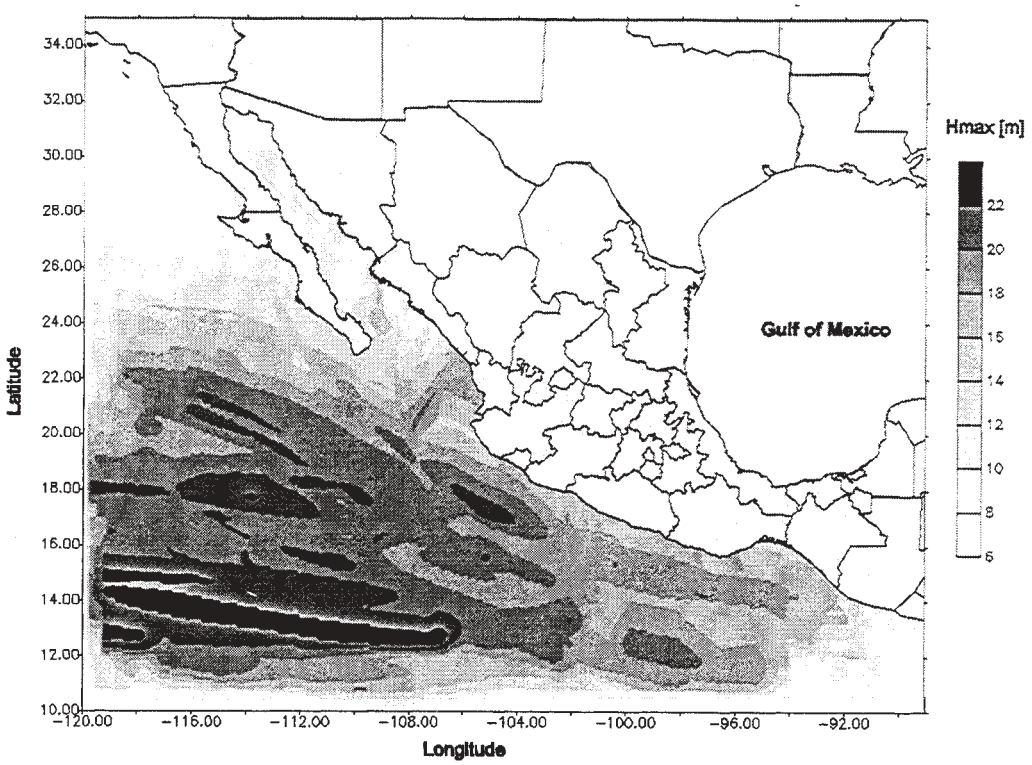

Figure 15. Map of maximum wave heights generated by hurricanes in the Pacific Ocean.

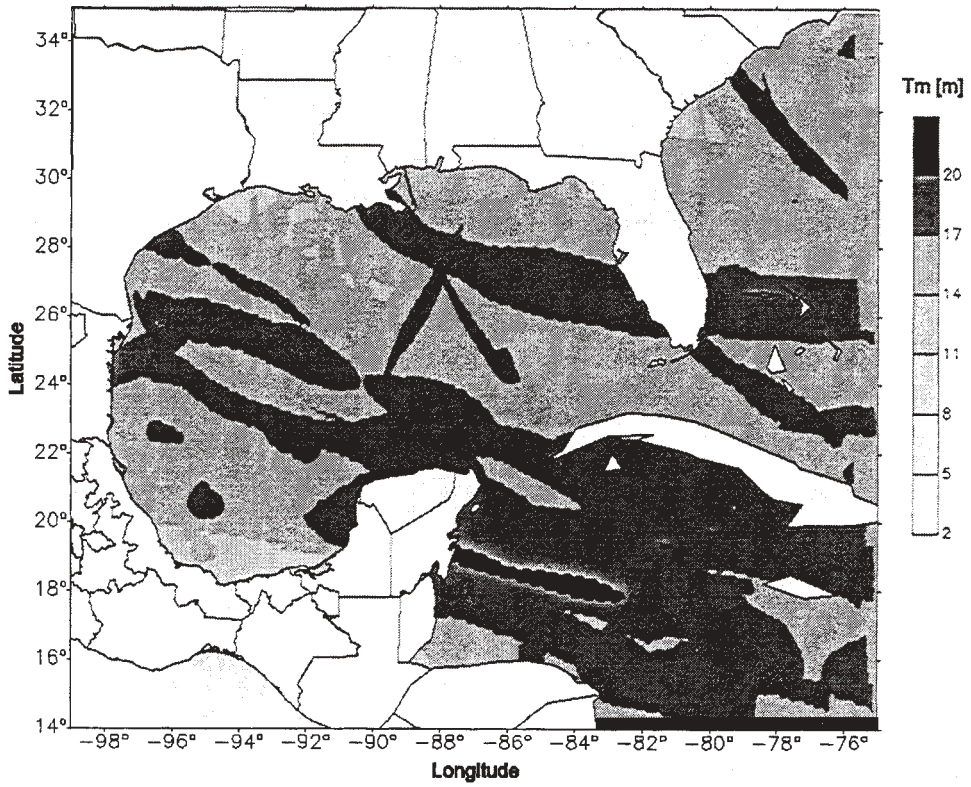

Figure 16. Map of wave periods associated with the maximum significant wave heights in the Gulf of Mexico.

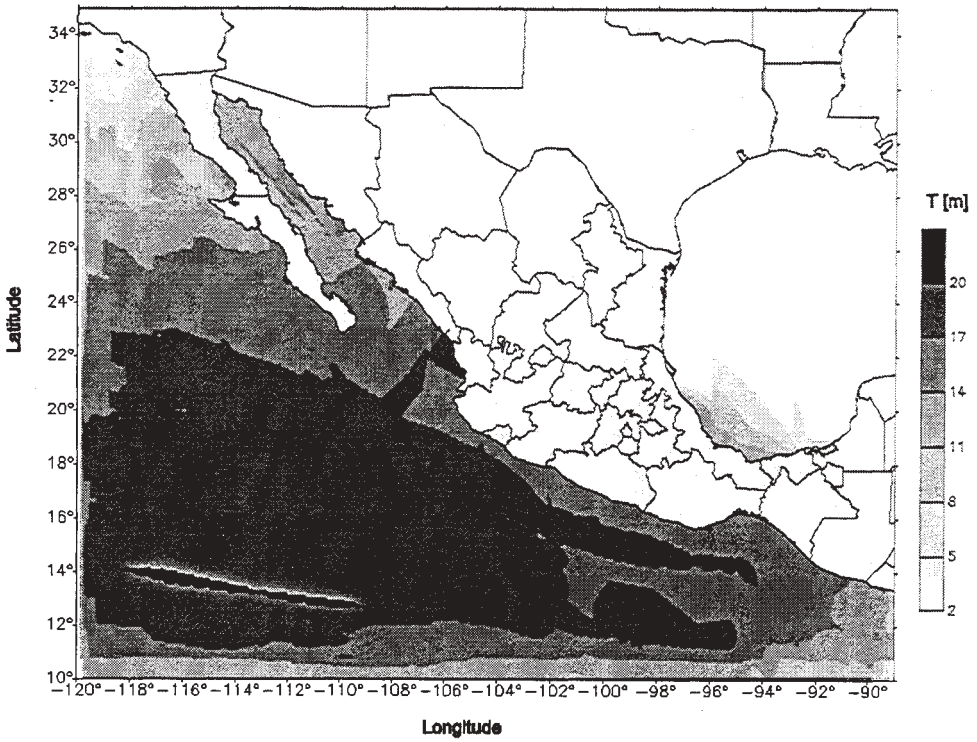

Figure 17. Map of wave periods associated with the maximum significant wave heights in the Pacific Ocean.

5. CONCLUSIONS

The information that can be obtained with this system could have a direct consequence for the redefinition of land use guidelines for Mexico.

While the probable presentation of a hurricane is greater in the Pacific Ocean, the vulnerability of the coast of the Gulf of Mexico is more important. For Mexican authorities this is of great importance given that this is both the main area of petroleum exploitation and the busiest route of international commerce.

One of the most important tourist developments in Mexico is found on the Peninsula of Yucatan, the Riviera Maya, where there is a high probability of intense hurricanes.

As part of this research we found that the mean number of hurricanes per year are ten for the Gulf of Mexico and sixteen for the Pacific Ocean.

Figure 18 shows the number of hurricanes per year for the Gulf of Mexico and the Pacific Ocean over the last 50 years. The solid lines represent the evolution of the mean values in both cases. From this figure we can see that there are now on average of ten more hurricanes annually over the Pacific Ocean while there has been little change in the number of hurricanes in the Gulf of Mexico. Perhaps global warming (Contreras (2000) reported 2° C in the last 20 years) has affected the atmosphere increasing the frequency and the intensity of hurricanes in the Pacific.

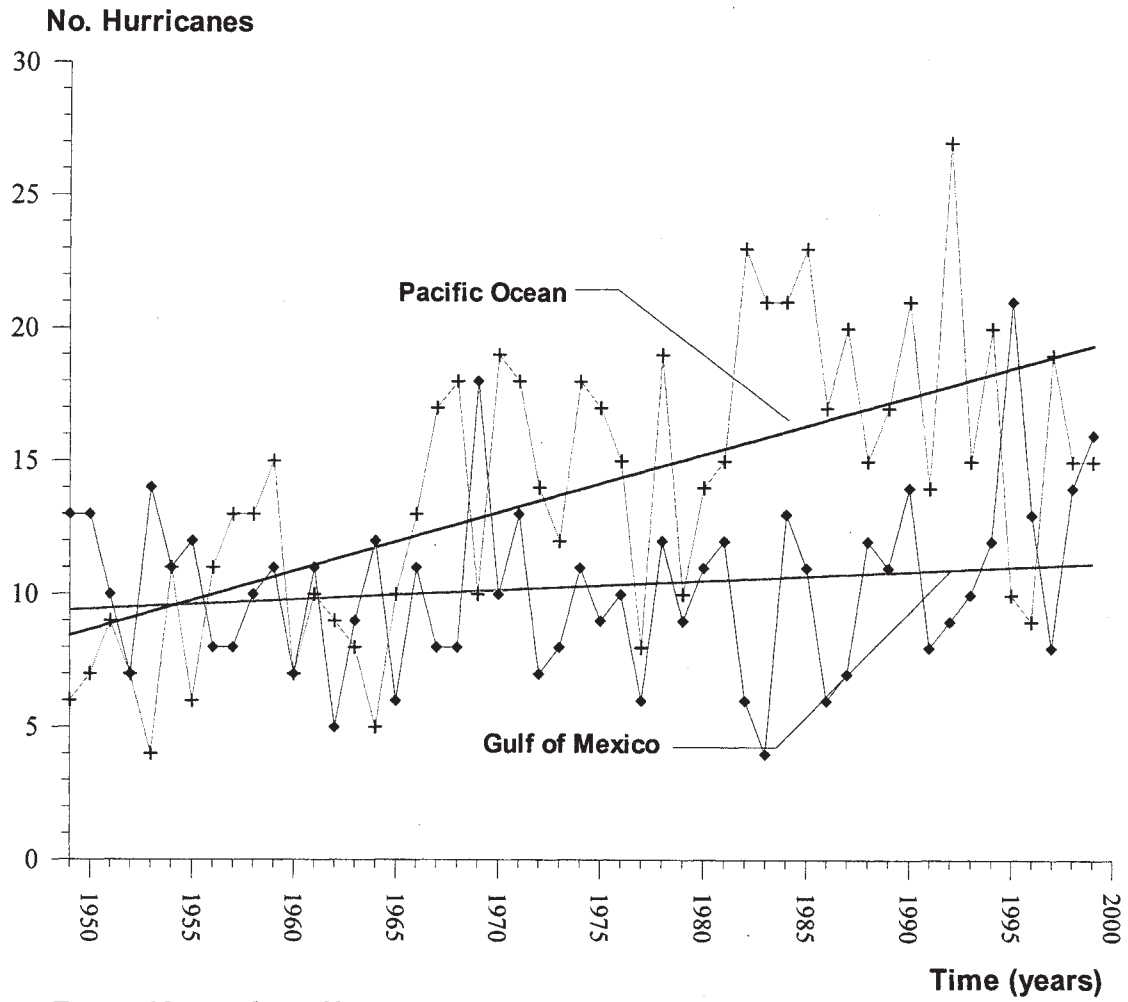

Figure 18. Number of hurricanes per year in Gulf of Mexico and Pacific Ocean.

6. REFERENCES

1. Bretchsneider, C.L., 1990, "Tropical Cyclones". Handbook of Coastal and Ocean Engineering Vol. 1.pp. 249-370.
2. Contreras, A. 2000, "Estudio océano-meteorológico del riesgo generado por ciclones en el litoral mexicano". Faculty of Engineering, National University of Mexico, MS. Disertation (In Spanish).
3. Dalrymple, R.A. 1988, "A model for the refraction of water waves". Jour. Of waterways, Port, Coastal and Ocean Engineering. ASCE. 114, 4.
4. NOAA. www.noaa.gov
5. Sanchez, C, Silva, R. et al. 1998, "Comparison of 4 wave prediction models". 5th International Workshop on Wave Hindcasting and Forecasting. Melbourne Fl. Pp. 134-145.
6. Silva R. et al. 2000, "Development of an M.I.S. for the prevention of hurricane damage on the Mexican Coast. Management Information Systems 2000". GIS and Remote Sensing. WIT press. UK. Pp. 471-4

COUPLED OCEAN WAVE-ATMOSPHERE SIMULATIONS USING THE NAVY'S COAMPS

James D. Doyle

Naval Research Laboratory, Monterey, CA

1. INTRODUCTION

The exchange of heat, momentum and moisture between the air and sea has long been recognized as a fundamental process in the development of a number of mesoscale atmospheric phenomena such as tropical cyclones, extratropical cyclones, boundary layer jets, coastal fronts, and precipitating systems. Numerical prediction of these phenomena is often critically dependent on the fidelity of surface flux representation (e.g., Emanuel 1995). This air-sea exchange takes place at the fluid interface in the wave boundary layer (WBL), which underscores the potential importance of ocean waves in air-sea interaction processes.

The conventional representation of the surface roughness effects over the sea due to ocean waves, based on the scaling arguments of Charnock (1955), is used by nearly all atmospheric research and operational models, and is valid only for fully-developed ocean wave conditions. Under high-wind conditions, however, wind direction and speed are often time dependent, such as for a tropical cyclone or topographically driven flows of the coastal zone. In these fetch-limited conditions, surface ocean waves have an increasingly important impact on the momentum flux in the atmospheric and oceanic boundary layers (Donelan 1990). In situations when the wave age is small, the wave-induced stress comprises a significant fraction of the total stress. A number of previous studies using field measurements have documented this dependence of the atmospheric momentum flux on the ocean wave age (e.g., Smith et al. 1992). The interaction between the sea and air is especially complex at high wind speeds where flux exchange processes may be impacted by sea spray and spume (Kepert et al. 1999).

Wave-induced stress may be a significant component of the total momentum stress in the atmospheric boundary layer over the ocean (e.g., Donelan 1990; Janssen 1991) and has been suggested to enhance the decay of extratropical systems (e.g., Doyle 1995). However, the impact of wind-generated ocean waves on the structure and evolution of mesoscale phenomena that are primarily forced by i) air-sea fluxes such as tropical cyclones, and ii) orography has received considerably less attention. In this study, three tropical cyclones and a Bora event are investigated using NRL's Coupled Ocean-Atmosphere Mesoscale Prediction System (COAMPS) coupled with the Wave Model (WAM) to examine the significance of coupling on the mesoscale.

Corresponding Author Address: James D. Doyle, NRL, 7 Grace Hopper Ave., Monterey, CA 93943-5502
e-mail: doyle@nrlmry.navy.mil

2. NUMERICAL MODEL DESCRIPTION

The atmospheric model used in this study is NRL's COAMPS (Hodur 1997; Hodur and Doyle 1999). Finite-difference approximations are used in the model to represent the fully compressible, nonhydrostatic equations that govern atmospheric motions. The equations are solved in three dimensions, with a nested-grid mesh capability, using a terrain-following vertical coordinate transformation. The finite difference schemes are of second-order accuracy in time and space. The compressible equations are integrated efficiently through the use of a time splitting technique that features a semi-implicit treatment in the vertical for the acoustic modes (Klemp and Wilhelmson 1978).

The parameterization of short- and long-wave radiation processes is formulated following Harshvardhan et al. (1987). The planetary boundary-layer and free-atmospheric turbulent mixing and diffusion are parameterized using a prognostic equation for the turbulent kinetic energy (TKE), e, budget based on the level 2.5 formulation of Mellor and Yamada (1982) as follows,

$$\frac{\partial e}{\partial t} = -u\frac{\partial e}{\partial x} - v\frac{\partial e}{\partial y} - \dot{\sigma}\frac{\partial e}{\partial \sigma} + BP + SP + D + K_H \nabla^4 e - \varepsilon, \quad (1)$$

where u and v are the horizontal wind velocity components, BP is the buoyancy production, SP is the shear production, D is the subgrid-scale vertical mixing, K_H is the horizontal diffusion coefficient, and ε is the dissipation rate. The buoyancy production is defined as,

$$BP = -\frac{GgK_h}{\theta}\frac{\partial \theta_v}{\partial \sigma}, \quad (2)$$

where G is the coordinate transformation metric defined as $\partial\sigma/\partial z$, g is the acceleration of gravity, K_h is the vertical eddy mixing coefficient for heat, and θ is the potential temperature. The shear production is defined as,

$$SP = K_m\left[\left(G\frac{\partial u}{\partial \sigma}\right)^2 + \left(G\frac{\partial v}{\partial \sigma}\right)^2\right], \quad (3)$$

where K_m is the vertical eddy mixing coefficient for momentum. The dissipation rate is parameterized in (1) as,

$$\varepsilon = \frac{\mu}{\ell}e^{3/2}, \quad (4)$$

where μ is a constant of 0.17, and ℓ is a mixing length based on Mellor and Yamada (1982). Accurate representation of the TKE is necessary because the eddy diffusivity coefficients for heat and momentum, K_h and K_m, are directly proportional to $e^{1/2}$. Counter gradient correction terms to the vertical fluxes are included for the potential temperature and water vapor equations. The surface fluxes are computed following the Louis et

al. (1982) formulation, which makes use of Monin-Obukhov similarity theory. In the standard application of COAMPS when a predictive ocean-wave model is not used in a tightly coupled manner, z_o is approximated over the open sea by the Charnock relationship (Charnock 1955)

$$z_o = \alpha \frac{\tau}{g\rho}, \quad (5)$$

where τ is the magnitude of the turbulent stress, ρ is the density and α is the Charnock parameter taken to be 0.0185.

A force-restore method is used to parameterize the surface energy budget. The subgrid-scale moist convective processes are parameterized using a modified approach following Kain and Fritsch (1990). Budget equations for cloud water, cloud ice, rain drops, snow flakes, and water vapor are used to represent the grid-scale evolution of the moist processes (Rutledge and Hobbs 1983).

Multivariate optimum interpolation analysis of upper-air sounding, surface, aircraft (ACARS) and satellite data that are quality controlled is the basis for the initial state for the nonhydrostatic model. Navy Operational Global Analysis and Prediction System (NOGAPS, Hogan et al. 1991) forecast fields are used for lateral boundary conditions following Davies (1976). The application of COAMPS in this type of manner closely emulates a real-time numerical prediction system in spite of the simulations being performed in a hindcast mode. The atmospheric topographic data are based on the U.S. Defense Mapping Agency's 100-m resolution data set.

The atmospheric model is coupled in an interactive mode to the 3rd generation (cycle 4) of the Wave Model (WAM) (WAMDI Group 1988). The quasi-linear theory of wind-wave generation following Janssen et al. (1989) and Janssen (1991) is applied. The transport equation is integrated to solve for the wave variance spectrum for 25 frequencies and 24 directions. The processes represented in WAM include wind-generated ocean waves, transfer of energy within the wave spectrum, wave propagation and dissipation by whitecapping.

The coupling methodology follows Janssen et al. (1989) and Janssen (1991) and includes the processes represented by mutual interaction of the wind waves and boundary-layer stress. The roughness length used in the coupled simulation is represented by,

$$z_o = \beta \frac{\tau}{g\rho(1 - \tau_w/\tau)^{0.5}} \quad (6)$$

where τ is the total stress and τ_w is the wave-induced stress. The constant β is chosen as 0.01 implying that (6) reduces to the standard Charnock relationship (5). The wave-induced stress is defined as the integral over all directions and spectral components of the atmospheric momentum flux to the wind-generated wave field (Janssen 1989). It follows, for a young windsea, the effective Charnock parameter can be enhanced by an order of magnitude. The simultaneous coupling is physically achieved through communicating the atmospheric stress to the wave model every WAM time step. An iterative technique is then used to calculate τ_w based on the 10-m wind speed, drag coefficient and τ. The new wave-induced Charnock parameter is subsequently used in the Louis et al. (1982) flux calculations in the atmospheric model. This coupling technique using the WAM and an atmospheric model has been applied previously to study air-sea interaction in extratropical cyclones by Doyle (1995), Lionello et al. (1998) and Desjardins et al. (2000) and Lalbeharry et al. (2000). The coupling technique is currently being applied operationally at the European Center for Medium Range Forecasts (ECMWF) and is used as part of the Ensemble Prediction System as well (Janssen, personal communications 1999). In this study, the uncoupled simulations are performed with simultaneous integration of the WAM except the standard Charnock parameter of 0.0185 is used in the atmospheric model flux calculations.

3. COUPLED SIMULATIONS

In this series of simulations, the impact of the wave-induced stress on the evolution of the atmospheric and surface ocean wave fields are investigated. To isolate the importance of the wave coupling, two experiments are performed for each case. The first simulation makes use of the conventional Charnock parameter in the atmosphere and includes a wave simulation based on the atmospheric winds every WAM time step. The second simulation includes the wave-induced stress effects in the modified Charnock formulation following (6) and also includes the feedback of the atmospheric winds, already modified by wave-induced roughness, back to the waves.

Two coupled COAMPS/WAM simulations were performed for tropical cyclones Mitch, Bonnie and Bret for a 48-h duration initialized at 0000 UTC 25 October 1998. A horizontal grid increment of 12 km was used for both COAMPS and the WAM model grids for the Mitch and Bret simulations. Two nested grids were used for the simulations of Bonnie that featured a grid increment of the finest mesh of 6 km and an identical resolution on the single WAM mesh. The simulation of the Bora event made use of a grid increment of 5 km.

3.1 Tropical Cyclone Mitch Simulations

Tropical cyclone Mitch was responsible for over nine thousand deaths, making it one of the deadliest Atlantic tropical cyclones in history. At the peak intensity, the minimum central pressure was estimated to be 905 hPa with sustained surface wind speed in excess of 80 m s^{-1}, making Mitch the strongest October hurricane in the Atlantic Basin on record.

	Uncoupled	Coupled	Observed
SLP (24 h)	960.1 hPa	958.2 hPa	923 hPa
SLP (48 h)	933.6 hPa	925.7 hPa	910 hPa
U_{max} (24 h)	62.6 m s^{-1}	59.9 m s^{-1}	67.0 m s^{-1}
U_{max} (48 h)	77.0 m s^{-1}	73.8 m s^{-1}	77.0 m s^{-1}
H_s (24 h)	14.9 m	13.9 m	
H_s (48 h)	17.2 m	15.1 m	
α_{max}	0.0185	0.30	
α_{max}	0.0185	0.32	

Table 1. Summary of the simulated central pressure (SLP), 500-m wind speed maximum (U_{max}), significant wave height maximum (H_s) and maximum Charnock parameter value (α_{max}) for tropical cyclone Mitch at 0000 UTC 26 October (24 h) and 0000 UTC 27 October 1998 (48 h). Available observed estimates are included.

The simulated central pressure, maximum wind speed at 500 m, maximum significant wave height and maximum Charnock parameter for 0000 UTC 26 October (24-h simulation time) and 0000 27 October (48-h simulation time) 1998 are summarized in Table 1. The central pressure is approximately 8 hPa lower in the coupled simulation than in the uncoupled case. As a result of the enhanced surface stress, the momentum flux increases considerably due to the coupled response. In the parameterization of the surface fluxes, the roughness length for heat is an order of magnitude smaller than that of momentum. Even with this reduction to the roughness length for heat, the wave-induced effects increase the surface heat flux by nearly a factor of 2, from a maximum of 506 W m^{-2} to 946 W m^{-2} at 0000 UTC 27 October. This increase in the heat flux apparently accounts for the 8 hPa reduction in central pressure in the coupled simulation. However, because of the increased drag due to the young ocean waves, the maximum wind speed at 500 m and the surface is less for the coupled simulation.

As a result of weaker surface winds due to enhanced roughness associated with the young ocean waves, the significant wave height maximum is 2 m less in the coupled simulation, as shown in Table 1 and Fig. 1 for 0000 UTC 27 October. The increased stress associated with the young ocean waves does not appear to have a large impact on the structural character of the ocean wave response. Unfortunately, no observed estimates of the wave fields are available for this time. The Charnock parameter is shown in Fig. 2 for 0000 UTC 27 October. The maximum Charnock parameter is 0.32, which is over an order of magnitude larger than the conventional parameter valid for the open ocean featuring a mature wave state. It is noteworthy that the Charnock parameter is a maximum near the eye wall structure coincident with the highest wind speeds and a minimum within the eye. Additionally, the enhanced roughness effects due to the young wave state have a minimal impact on the tropical cyclone track, in spite of the significant changes in the central pressure. For example, at 0000 UTC 27 October (48 h), the position of the tropical cyclone differs by 1 grid point (12 km).

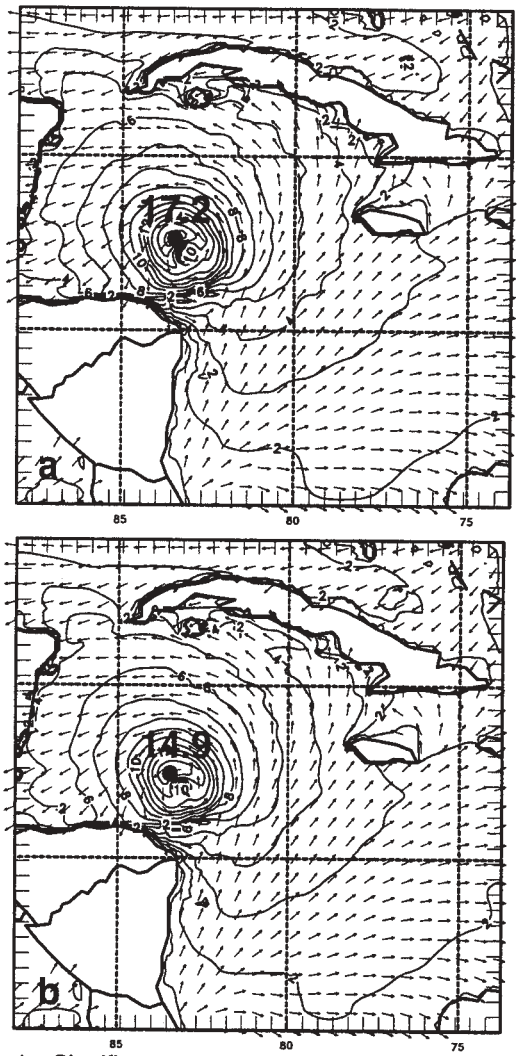

Fig. 1. Significant wave height and direction for a) uncoupled and b) coupled simulations of tropical cyclone Mitch at 0000 UTC 27 October 1998 (48-h time).

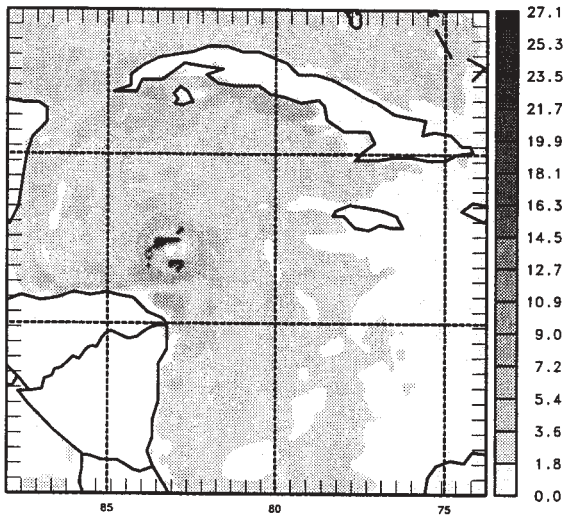

Fig. 2. Charnock parameter (x10^{-2}) for tropical cyclone Mitch at 0000 UTC 27 October 1998 (48-h time).

3.2 Tropical Cyclone Bonnie Simulations

Tropical cyclone Bonnie strengthened to hurricane force at 0600 UTC 22 August when it was located 400 km north of Hispaniola. Bonnie moved on a general west-northwest heading reaching maximum strength of 51 m s^{-1} and a central pressure of 954 hPa. Eventually, Bonnie made landfall near Wilmington, NC around 0330 UTC 27 August. The focus of this simulation is during an earlier phase of the tropical cyclone on 24 August. On this day, the sea surface directional wave spectrum was measured using the NASA airborne Scanning Radar Altimeter (SRA) carried aboard a NOAA WP-3D hurricane research aircraft at a height of 1.5 km (Wright 2000).

Relevant aspects of the Bonnie simulation for 1200 UTC 24 August (24-h simulation time) and 0000 25 August (36-h simulation time) 1998 are summarized in Table 2. The central pressures for the coupled and uncoupled simulations are quite similar and within 1.5 hPa of each other. Once again, the tropical cyclone track is nearly identical between the coupled and uncoupled simulations. Similar maximum velocities are attained in the two simulations. These velocities were taken at 500 m and are considerably greater than the surface estimated values.

The most substantial differences between the simulations exist in the simulated significant wave height maximum. The coupled simulation has a significant wave height maximum that is ~15% reduced relative to the uncoupled case. Both the coupled and uncoupled simulations make use of new atmospheric winds every wave model time step. The SRA derived significant wave height and dominant wave length superimposed on the NOAA/AOML/HRD surface wind field analysis are shown in Fig. 3 (from Wright 2000). The maximum significant wave height derived from this composite analysis of 5 flight segments is 10.7 m. The dominant waves propagate at significant angles to the low-level wind direction. The significant wave height maximum is located in the northeast quadrant (Fig. 3a) where the wavefield is dominated by swell (Fig. 3b). In the southern half of the tropical cyclone, the wavelength is considerably shorter.

	Uncoupled	Coupled	Observed
SLP (24 h)	982.6 hPa	983.2 hPa	962 hPa
SLP (36 h)	980.2 hPa	978.7 hPa	964 hPa
U_{max} (24 h)	54.1 m s^{-1}	52.2 m s^{-1}	37.0 m s^{-1}
U_{max} (36 h)	49.7 m s^{-1}	54.7 m s^{-1}	37.0 m s^{-1}
H_s (24 h)	12.8 m	10.9 m	10.7 m
H_s (36 h)	12.6 m	11.0 m	
α_{max}	0.0185	0.15	
α_{max}	0.0185	0.11	

Table 2. Summary of the simulated central pressure (SLP), 500-m wind speed maximum (U_{max}), significant wave height maximum (H_s) and maximum Charnock parameter value (α_{max}) for tropical cyclone Bonnie at 1200 UTC 24 August (24 h) and 0000 UTC 25 August 1998 (36 h). Observed estimates are shown as well.

The simulated significant wave heights for the uncoupled and coupled simulations of Bonnie are shown in Fig. 4. As noted above, the significant wave height maximum in the northeastern quadrant is considerably reduced in the coupled simulation, in spite of the dominance of the swell. The coupled simulation is in overall closer agreement with the SRA derived wave field than the uncoupled case. The dominant wavelength for the coupled simulation is shown in Fig. 5. Considering the complexity of both the wave and wind fields, the simulated wavelength contains many common characteristics with the SRA composite wavelength field (Fig. 3b) including the swell in the northern half and shorter wavelengths in the southern portion of the tropical cyclone.

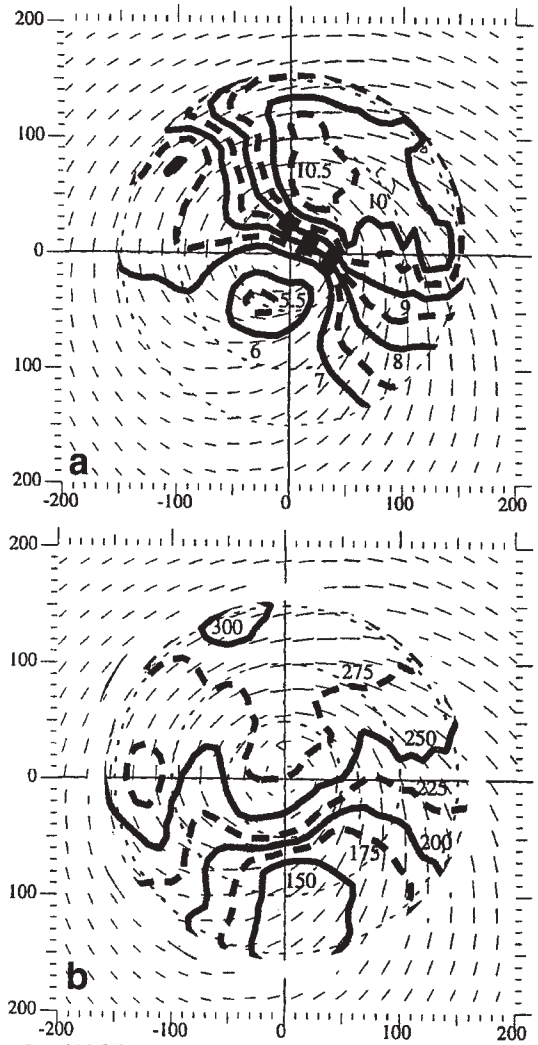

Fig. 3. NASA airborne Scanning Radar Altimeter derived (a) significant wave height (m) and (b) dominant wavelength (m) based on NOAA WP-3D research aircraft data from 24 August 1998 (from Wright 2000).

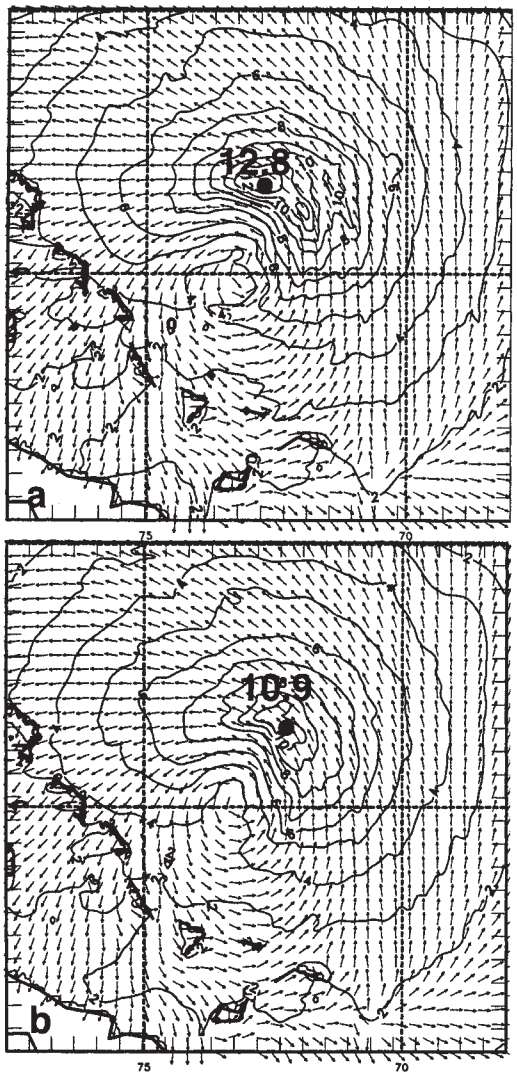

Fig. 4. Simulated significant wave height (m) for the (a) uncoupled and (b) coupled simulations for 1200 UTC 24 August 1998 (24 h).

3.3 Tropical Cyclone Bret Simulations

Tropical cyclone Bret was a small hurricane that formed in the Gulf of Mexico and eventually made landfall along the south Texas coast. Near the time of peak intensity, hurricane force winds were confined to a narrow radius of approximately 50 km wide in the northern portion of the cyclone and 25 km to the south.

The simulated characteristics of the atmospheric and wave fields are summarized in Table 3. The central pressure of the tropical cyclone is approximately 3 hPa lower in the coupled simulation than in the uncoupled case, in better agreement with the estimated values based on in situ observations. The maximum wind speed at 500 m is similar in both simulations. The significant wave height maximum is ~0.5 m lower in the coupled simulation. The simulated track for Bret is insensitive to any wave coupling issues.

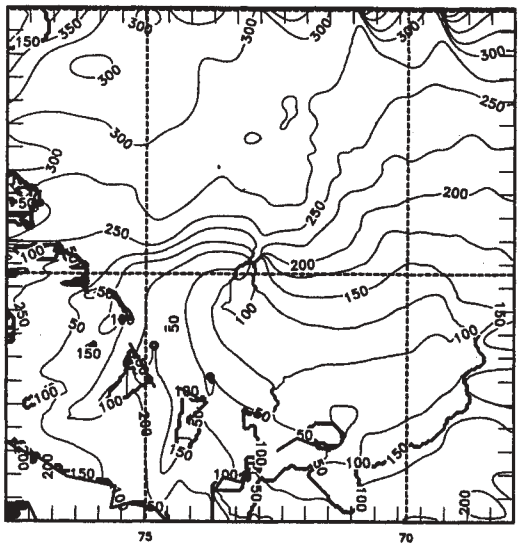

Fig. 5. Wavelength (m) of the wave spectrum peak for 1200 UTC 24 August 1998 (24h) for the coupled model.

	Uncoupled	Coupled	Observed
SLP (24 h)	987.2 hPa	983.9 hPa	979 hPa
SLP (48 h)	955.2 hPa	952.1 hPa	944 hPa
U_{max} (24 h)	45.7 m s^{-1}	47.4 m s^{-1}	41.0 m s^{-1}
U_{max} (48 h)	66.9 m s^{-1}	66.2 m s^{-1}	64.0 m s^{-1}
H_s (24 h)	8.3 m	7.6 m	
H_s (48 h)	12.3 m	11.8 m	
α_{max}	0.0185	0.10	
α_{max}	0.0185	0.32	

Table 3. Summary of the simulated central pressure (SLP), 500-m wind speed maximum (U_{max}), significant wave height maximum (H_s) and maximum Charnock parameter value (α_{max}) for tropical cyclone Bret at 1200 UTC 21 August (24 h) and 1200 UTC 22 August 1999 (48 h). Available observed estimates are included.

3.4 Bora Event Simulations

The Mesoscale Alpine Programme (MAP) was a field campaign that took place during fall 1999 with the objective to measure and understand the meteorology in the vicinity of the Alps (Bougeault et al. 2000). On 7 November 1999, a strong wind event occurred in the lee of the Dnirac Alps of Slovenia and Croatia, often referred to as a Bora. Several research aircraft took low-level measurements and found wind speeds in excess of 30 m s^{-1} along the coast above the Adriatic Sea at 1.5 km.

Coupled and uncoupled simulations of the Bora were performed using COAMPS with a horizontal grid increment of 5 km. In general the simulated fields are quite comparable. For example, the wind speed difference at 10 m between the coupled and uncoupled simulations is shown in Fig. 5. The wind speeds differ by less than 4.0 m s^{-1}, which is comparatively small to the maximum Bora speed of 22 m s^{-1} near the surface. Overall the coupling appears to have minimal impact.

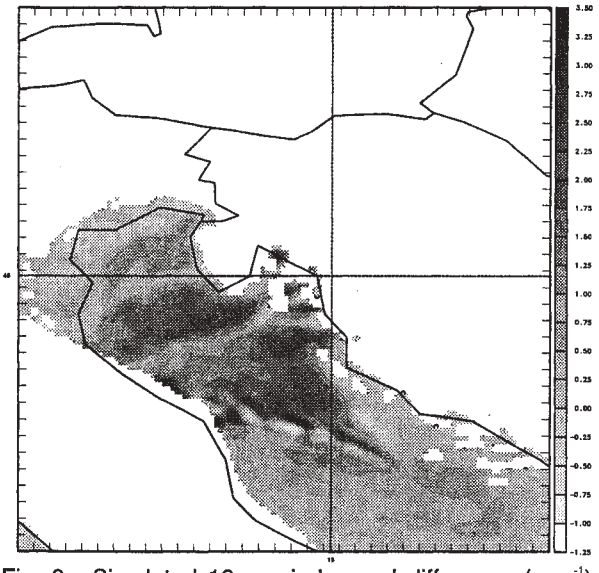

Fig. 6. Simulated 10-m wind speed difference (m s^{-1}) between uncoupled and coupled simulations for 1200 UTC 7 November 1999 (12 h).

4. CONCLUSIONS

In this study, three major tropical cyclones and a topographically forced Bora event over the Mediterranean Sea were simulated using a coupled atmosphere-ocean surface wave model, COAMPS. The model consists of a nonhydrostatic atmospheric model coupled with the WAM. The models were integrated simultaneously and on identical grids with horizontal grid increments ranging from 12 km to 5 km. The impact of the wave-induced stress was largest for the strongest of the three tropical cyclones, Mitch. The central pressure in the coupled simulation in this particular case was 8 hPa more intense than the uncoupled simulation due to larger surface heat flux effects. Significant wave height maxima were typically ~15% lower in the coupled simulations. In general, the low-level wind speeds were remarkably insensitive to the coupling in spite of a Charnock parameter increase by more than a factor of 20. The tracks of the tropical cyclones were especially insensitive to wave coupling effects. Finally, the Bora event was least sensitive of all the cases to the enhanced roughness due to fetch-limited conditions.

ACKNOWLEDGEMENTS

This research was supported by ONR PE0602435N and PE0601153N. Computing time was supported by a grant of HPC time from the DoD HPC MSRCs at Stennis, MS and Aberdeen, MD, and performed on a Cray T-90. Beneficial discussions with Paul Wittmann concerning the WAM coupling contributed to this study.

REFERENCES

Bougeault, P., P. Binder, A. Buzzi, R. Dirks, R. Houze, J. Kuettner, R.B. Smith, R. Steinacker, and H. Volkert, 2000: The Mesoscale Alpine Programme (MAP), submitted to *Bull. Amer. Met. Soc.*

Charnock, H., 1955: Wind stress on a water surface. Quart. J. Roy. Meteor. Soc., 81, 639-640.

Davies, H.C., 1976: A lateral boundary formulation for multi-level prediction models. *Quart. J. Roy. Meteor. Soc.*, **102**, 405-418.

Desjardins, S. J. Mailhot, R. Lalbeharry, 2000: Examination of the impact of a coupled atmospheric and ocean wave system. Part I. Atmospheric aspects. *J. Phys. Oceanogr.*, **30**, 385-401.

Donnelan, M., 1990: Air sea interaction. *Surface Waves and Fluxes, Vol. 1.* Edited by G.L. Geernaert and W.J. Plant, 336 pp., Kluwer Acad., Norwell Mass.

Doyle, J. D., 1995: Coupled ocean wave/atmosphere mesoscale model simulations of cyclogenesis. *Tellus*, **47A**, 766-788.

Emanuel, Kerry A., 1995: Sensitivity of tropical cyclones to surface exchange coefficients and a revised steady-state model incorporating eye dynamics. *J. Atmos. Sci.*, **52**, 3969–3976.

Harshvardhan, R. Davies, D. Randall, and T. Corsetti, 1987: A fast radiation parameterization for atmospheric circulation models. *J. Geophys. Res.*, **92**, 1009-1015.

Hodur, R.M., 1997: The Naval Research Laboratory's Coupled Ocean/Atmosphere Mesoscale Prediction System (COAMPS). *Mon. Wea. Rev.*, **125**, 1414-1430.

Hodur, R. M., and J. D. Doyle, 1999: The coupled ocean/atmosphere mesoscale model prediction system (COAMPS). *Coastal Ocean Prediction*, Coastal and Estuarine Studies 56, 125-155.

Hogan, T.F., and T.E. Rosmond, 1991: The description of the U.S. Navy Operational Global Atmospheric Prediction System's spectral forecast model. *Mon. Wea. Rev.*, **119**, 1786-1815.

Janssen, P.A.E.M., 1989: Wave-induced stress and the drag of air flow over sea waves. *J. Phys. Oceanogr.*, **19**, 745-754.

Janssen, P.A.E.M., 1991: Quasi-linear theory of wind-wave generation applied to wave forecasting. *J. Phys. Oceanogr.*, **21**, 1631-1642.

Kain, J.S., and J.M. Fritsch 1993: Convective parameterization for mesoscale models: The Kain-Fritsch scheme. *The Representation of Cumulus Convection in Numerical Models, Meteor. Monogr.*, **46**, Amer. Meteor. Soc., 165-170.

Kepert, J.D, C.W. Fairall and J.W. Bao, 1999: Modelling the interaction between the atmospheric boundary layer and evaporating sea spray droplets. *Air-Sea Fluxes of Momentum, Heat and Chemicals.* editor G.L Geeraert. Kluwer.

Klemp, J., and R. Wilhelmson, 1978: The simulation of three-dimensional convective storm dynamics. *J. Atmos. Sci.*, **35**, 1070-1096.

Lalbeharry, R., J. Mailhot, S. Desjardins, and L. Wilson, 2000: Examination of the impact of a coupled atmospheric and ocean wave system. Part II: Ocean wave aspects. *J. Phys. Oceanogr.*, **30**, 402-415.

Lionello, P., P. Malguzzi and A. Buzzi, 1998: Coupling between the atmospheric circulation and ocean wave field: An idealized case. *J. Phys. Oceanogr.*, **28**, 161-177.

Louis, J.F., M. Tiedtke, and J.F. Geleyn, 1982: A short history of the operational PBL-parameterization at ECMWF. *Workshop on Planetary Boundary Layer Parameterization.* ECMWF, Reading, 59-79 (Available from ECMWF, Shinfield Park, Reading RG2 9AX, UK).

Mellor, G.L. and T. Yamada, 1982: Development of a turbulence closure for geophysical fluid problems. *Rev. Geophys. and Space Phys.*, **20**, 851-875,

Rutledge, S.A., and P.V. Hobbs, 1983: The mesoscale and microscale structure of organization of clouds and precipitation in mid-latitude cyclones. VIII: A model for the "seeder-feeder" process in warm-frontal rainbands. *J. Atmos. Sci.*, **40**, 1185-1206.

Smith, S.D., R.J. Anderson, W.A. Oost, C. Kraan, N. Maat, J. De Cosmo, K.B. Katsaros, K. Davidson, K. Bumke, L. Hasse, and H.M. Chadwick, 1992: Sea surface wind stress and drag coefficients. The HEXOS results. *Bound-layer Meteor.*, **60**, 109-142.

Wright, W., 2000: Open ocean and landfalling hurricane directional wave spectra from a scanning radar altimeter. *Sixth International Conference on Remote Sensing for Marine and Coastal Environments.* Amer. Meteor. Soc., Charleston, SC, 1-3 May.

Operational System for the Prediction of Tropical Cyclone Generated Winds and Waves

Andrew T. Cox and Vincent J. Cardone

Oceanweather Inc.
Cos Cob, CT

1. Introduction

It is well known that the details of the circulation of tropical cyclones are typically poorly resolved in surface wind analyses and forecasts produced by NWP centers. At many centers this shortcoming is addressed by a process of "bogussing" within a specified radius of the cyclone centers using solutions of simple parametric models. This paper describes an operational system used for determining inputs to a dynamical tropical wind field model and generation of tropical wind fields. The system is presently used for both hindcasting and real time global and regional wind and wave forecasting.

Sections 2 and 3 of this paper describe the tropical wind model and analysis/blending tool used in the generation of tropical cyclone winds. Section 4 is dedicated to the methodology used in determining inputs to the tropical wind model. A case study of Hurricane Floyd (1999) is presented in section 5, and is followed by a brief section on conclusions.

2. Tropical Wind Model

This model (TC96) was first developed into a practical tool in the Ocean Data Gathering Program (ODGP) (Cardone *et al.* 1976). It can provide a fairly complete description of time-space evolution of the surface winds in the boundary layer of a tropical cyclone. The model is an application of a theoretical model of the horizontal airflow in the boundary layer of a moving vortex. That model solves, by numerical integration, the vertically averaged equations of motion that govern a boundary layer subject to horizontal and vertical shear stresses. The equations are resolved in a Cartesian coordinate system whose origin translates at constant velocity, V_f with the storm center of the pressure field associated with the cyclone. Variations in storm intensity and motion are represented by a series of quasi-steady state solutions. The original theoretical formulation of the model is given by Chow (1971), a similar model was described more recently in the open literature by Shapiro (1983).

The version of the model applied in this paper is the result of two major upgrades, one described by Cardone *et al.* (1992) and the second by Cardone *et al.* (1994) and Thompson and Cardone (1996). The first upgrade mainly involved replacement of the empirical scaling law by a similarity boundary layer formulation to link the surface drag, surface wind and the model vertically averaged velocity components. The second upgrade added spatial resolution and generalized the pressure field specification. A more complete description of the theoretical development of the model as upgraded is given by Thompson and Cardone (1996).

The model pressure field is described as the sum of an axially symmetric part, and a large-scale pressure field of constant gradient. The symmetric part is described in terms of an exponential pressure profile from Holland (1980):

$$p(r) = p_0 + \sum_{i=1}^{n} dp_i \, e^{-\left(\frac{Rpi}{r}\right)^{Bi}}$$

where
n = number of components
dp_i = pressure anomaly for the *i'th* component
R_{pi} = scale radius for the *i'th* component
B_i= Holland's B coefficient for the *i'th* component
p_0= central pressure

The model is driven from parameters that are derived from data in meteorological records and the ambient pressure field. The entire wind field history is computed from knowledge of the variation of those parameters along the storm track by computing solutions, or so-called "snapshots", on the nested grid as often as is necessary to describe different stages of intensity. The entire time history is then interpolated from the snapshots. The snapshot input parameters to TC96 are shown in Table 1.

Table 1. Model parameters for TC96.

Parameter	Description
V_{spd}, V_{dir}	speed and direction of vortex motion
V_{gs}, D_{gs}	equivalent geostrophic flow of the ambient PBL pressure field in which the vortex propagates
D_p	total storm pressure anomaly
dp_1	pressure anomaly associated with the first component of the exponential radial pressure profile
R_{p1}, R_{p2}	scale radii of the up to two components of the exponential radial pressure profile
B_1, B_2	Holland's profile peakedness parameter for each component

The model was originally validated against winds measured in several ODGP storms. It has since been applied to nearly every recent hurricane to affect the United States offshore area, to all major storms to affect the South China Sea since 1945, and to storms affecting many other foreign basins including the Northwest Shelf of Australia, Tasman Sea of New Zealand, Bay of Bengal, Arabian Sea and Caribbean Sea. Comparisons with over-water measurements from buoys and rigs support an accuracy specification of ± 20 degrees in direction and ± 2 meters/second in wind speed (1-hour average at 10-meter elevation). Many comparisons have been published (see e.g., Ross and Cardone, 1978; Cardone and Ross, 1979; Forristall *et al.*, 1977; 1978; 1980; Cardone and Ewans, 1992; Cardone and Grant, 1994).

The wind model is free of arbitrary calibration constants that might link the model to a particular storm type or region. For example, differences in latitude are handled properly in the primitive equation formulation through the Coriolis parameter. The variations in structure between tropical storm types manifest themselves basically in the characteristics of the pressure field of the vortex itself and of the surrounding region. The interaction of a tropical cyclone and its environment, therefore, can be accounted for by a proper specification of the input parameters. The assignable parameters of the planetary boundary layer (PBL) formulation, namely planetary boundary layer depth and stability, and of the sea surface roughness formulation, can safely be taken from studies performed in the Gulf of Mexico, since tropical cyclones world-wide share a common set of thermodynamic and kinematic constraints.

3. Wind WorkStation

The Wind WorkStation (WWS) is a graphical analysis tool developed in 1995 for the analysis of marine surface wind fields. The WWS was originally developed for the analysis of extra-tropical systems, but it has been extended to the analysis of tropical wind fields as well. Details on the use and objective analysis algorithm used in the WWS can be found in Cox *et al.* (1995).

The purpose of the WWS in tropical wind field generation is two-fold: First, the WWS can be used to assimilate marine surface, aircraft, and satellite observations into a tropical wind field. Where high-quality aircraft reconnaissance data are available, the WWS can be used as a direct analysis tool much in the same way as the Wind Analysis Distributed Application (WANDA) system developed by the National Hurricane Research Division (HRD) of NOAA (Powell,*et al.* 1998). Aircraft winds are reduced to the surface using a method described by Powell and Black (1990), and used directly to produce a snapshot wind field. In the absence of aircraft data, or as a supplement to the reconnaissance observations, wind fields from the tropical wind model are included in the WWS to define the tropical winds. The second purpose of the

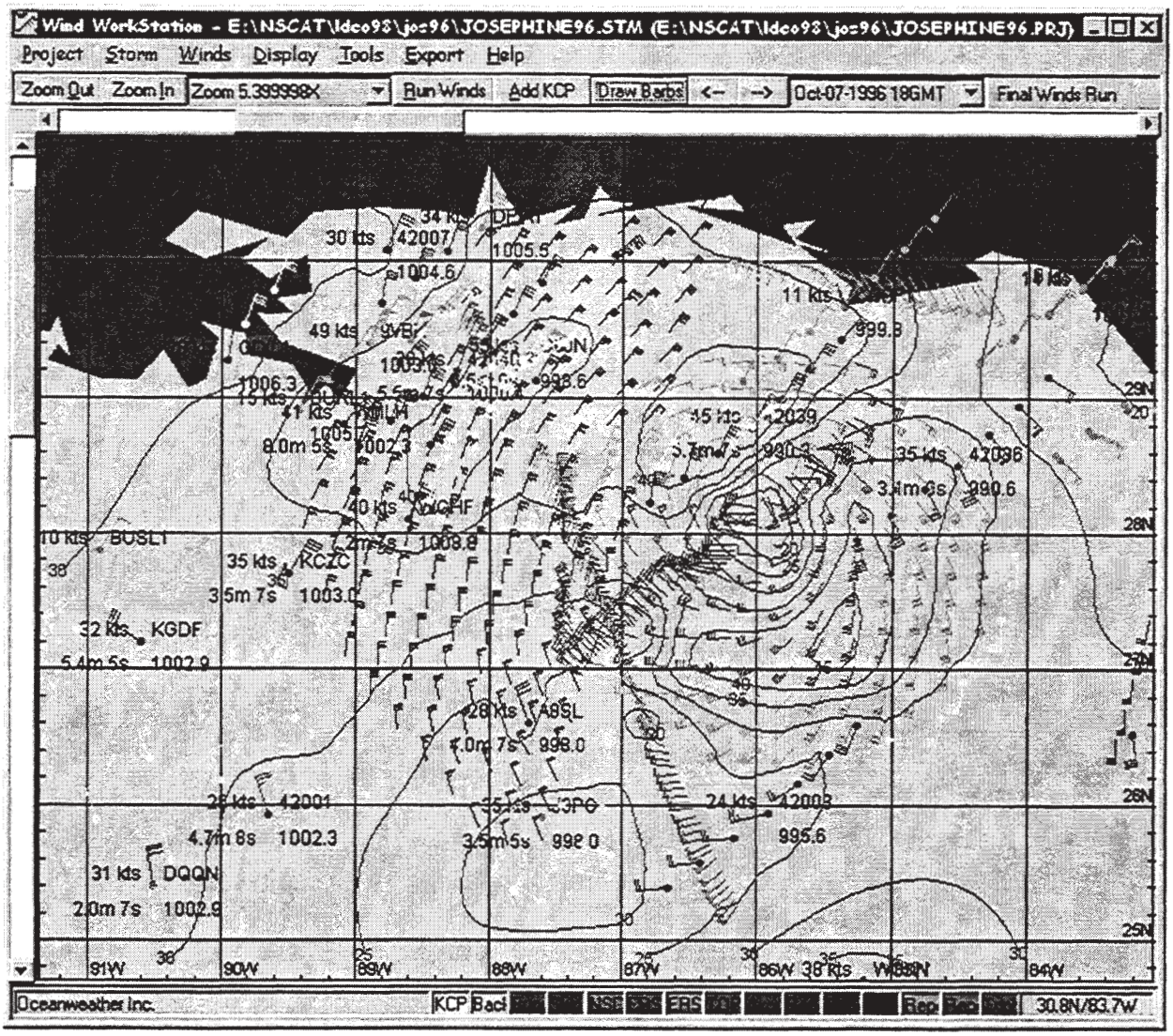

Figure 1. Wind WorkStation analysis of Hurricane Josephine (1996) valid for October 7th, 1996 at 18 GMT. Winds shown in knots, some wind inputs have been repositioned (with respect to Josephine) to synoptic time.

WWS is to blend the tropical winds with the synoptic-scale atmospheric flow to produce a basin-wide wind field for use in wave modeling. Figure 1 shows a WWS analysis of hurricane Josephine (1996) in the Gulf of Mexico. The analysis is a blend of buoy and ship winds, TOPEX altimeter winds, NSCAT scatterometer winds, TC96 model inputs, NOAA reconnaissance winds, and analyst's input.

4. Methodology

4.1 General Approach

The approach for developing tropical wind fields in both a hindcast and forecast mode is essentially the same. The relative storm motion (V_{spd}, V_{dir}) and intensity (D_p) are taken directly from best track data or from forecasts issued by warning centers such as the Tropical Prediction Center (TPC) and Joint Typhoon Warning Center (JTWC). The geostrophic flow of the ambient PBL pressure field in which the vortex propagates (V_{gs}, D_{gs}) can be estimated from

surface analyses. The remaining model parameters, the scale radii of the exponential radial pressure profile (R_{p1}, R_{p2}) and Holland's B parameter (B_1, B_2), are the most difficult to determine. Except in cases where high quality aircraft reconnaissance indicate otherwise, typically only the single-exponential cases (R_{p1}, B_1) are considered.

In the case of aircraft reconnaissance, the surface pressure profile (reduced from flight level) can be used to fit an R_{p1}/B_1 curve to the data. Such a methodology is outlined in section 4.2. Otherwise, either wind radii information or actual wind measurements can be used to determine the R_{p1}/B_1 model parameters in an "inverse modeling" sense. A database of more than 30,000 iterations of the TC96 model runs were compiled by varying the parameters found in Table 2. Output from each model solution was saved for parameters listed in Table 3.

Table 2. Value of input parameters used in TC96 database.

Input Parameter	Value
Latitude	20 degrees
V_{spd}, V_{dir}	stationary
V_{gs}, D_{gs}	stationary
D_p	2 to 120 mb in 2 mb increments
R_p	5 nmi to 120 nmi in 4 nmi increments
B	1 to 2.5 in 0.1 increments
H	500 m (boundary layer depth)
Tempurature Difference	-2 C (air-sea temperature)

Table 3. Saved output in TC96 database.

Output Parameter
Maximum surface wind
Radius of maximum wind
Azimuthally averaged wind speed in 5 nm bins
Radius (maximum) of 35 knot winds
Radius (maximum) of 50 knot winds

Once the model inputs are determined and the model run, the winds surrounding the center (typically within 180 nmi) are brought into the WWS. The model winds are then compared to the available *insitu*, satellite, and aircraft wind observations. In a hindcast mode, it is common to iterate the model inputs based on the measured winds. Once the model winds have been finalized, they are blended into the surrounding synoptic wind field using selective deletion of peripheral model inputs and the use of kinematic control points (KCPs) which are highly weighted winds added by the analyst for use in the objective analysis.

4.2 Model Inputs Derived from Aircraft Reconnaissance

When available, aircraft reconnaissance can be used to fit the pressure profile directly. Currently, aircraft reconnaissance is only available in the North Atlantic. Historically, a large database of aircraft data is also available for the North Pacific (JTWC discontinued aircraft reconnaissance 1986). In real time, typically vortex and supplementary vortex messages are available, while high-resolution observations (every 30 seconds or 1 minute) are available for hindcast studies. Aircraft pressure and wind measurements taken at flight level are reduced to the surface using techniques described by Jordan (1958) and Powell and Black (1990). Recent development of the GPS Dropwindsonde (Hock and Franklin, 1999) not only promises to measure the 10 meter surface wind directly, but to sample the entire wind sheer profile which may lead to better adjustment procedures for reducing flight level winds.

Figure 2 shows a sample fit of the real-time aircraft reconnaissance estimated pressures during Hurricane Dennis (1999). The upper left panel shows the supplementary vortex message winds plotted as distance from the center of Dennis (center position computed from closest vortex messages interpolated to wind observation time). The map in the upper right shows the track of Dennis from vortex messages with wind barbs (in knots) indicating the adjusted surface ten-minute wind. The lower

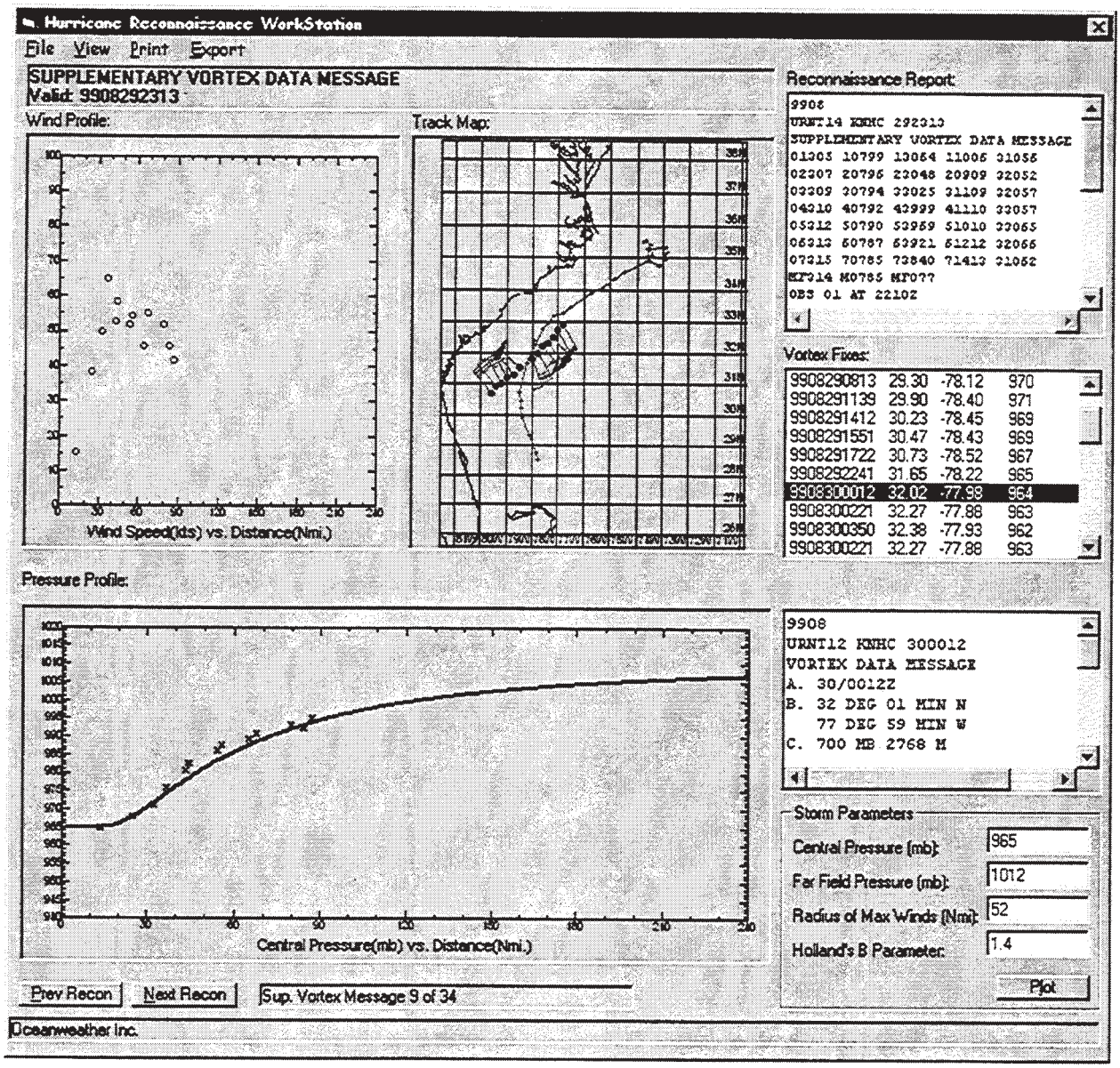

Figure 2. Real-time pressure profile fit to aircraft reconnaissance surface pressures reduced from flight level.

panel shows the reduced aircraft surface pressures with a profile fit. The fit profile of D_p=47 (1012-965), R_p=52 and B_1=1.4 corresponds to a TC96 model maximum one-minute wind of 88.4 knots. The closest vortex message indicates that a surface wind of 86 knots (one-minute) was observed at this time.

4.3 Model Inputs Derived from Official Forecast Guidance Wind Radii

Official forecasts from both TPC and JTWC for global tropical systems include forecast track, intensity and radii of 35 and 50 knots. It is desirable for an operational wind/wave forecast to as closely match as possible the official forecasts, both for consistency and for derivative

forecast products which are based on an individual warning center's error statistics (such as a probabilistic wind/wave forecast).

To make use of the official forecast parameters, the TC96 database is first searched for all model solutions with a D_p matching the official forecast intensity with a maximum wind solution +/- 2 m/s from the adjusted forecast intensity. The forecast intensity is adjusted for forward speed since the database assumes a stationary system. The resulting model solutions are then sorted by the radii of 50 (preferred) or 35 knots, and the model parameters are then interpolated from the closest 2 snap inputs. In cases were the tropical wind radii in a particular quadrant are enhanced by a synoptic-scale feature, the non-affected quadrant is used to determine the snap parameters and synoptic enhancement is modeled through the WWS.

This wind radii technique was recently applied in a hindcast mode. The GROW2000 (Global Reanalysis of Ocean Waves) project involved hindcasting the global ocean for the period 1979 to 1998. While the resolution of the global model (.625 by 1.25 degrees) was relatively course for tropical modeling, tropical systems were added to base GROW2000 wind fields to better predict the swells generated by tropical systems. A database of wind radii analyzed by JTWC was obtained for much of the Northern and Southern Pacific Oceans and was used to determine TC96 model parameters (Atlantic systems had already been analyzed in a previous project). The resulting tropical winds were more accurate than could be expected from using a simple climatological R_p/B_1 ratio since they reflected an individual storm's wind radii as analyzed by JTWC.

4.4 Model Inputs Derived from QUIKSCAT Wind Measurements

The global coverage and wide-swath of surface marine winds available from the QUIKSCAT scatterometer make this instrument well suited for the detection and analysis of tropical cyclone winds. However, this instrument suffers from both rain contamination and model function saturation that limits its use in winds over 20 m/s. Recent studies (Jones *et al.* 1999 and Cardone *et al.* 1999) indicate that a neural net algorithm for tropical cyclone winds may extend this limit to 25 m/s, but it is not yet clear that wind speed above 30 m/s will be retrievable.

While the radii of 35 knot winds can be determined from QUIKSCAT data (and perhaps someday the 50 knot radii) and the methodology in section 4.2 applied, the wide swath data make it possible to fit the model winds across the entire wind profile sampled by QUIKSCAT. Figure 2 shows QUIKSCAT wind measurements vs. distance from the center of hurricane Floyd (1999) for one pass. The thick line is the azimuthally averaged QUIKSCAT wind in 5 nmi bins. The dashed lines are a family of TC96 model solutions for a given D_p where $B_1 = 1.00$ (representing $1/15^{th}$ of the total possible combinations in the TC96 database for this D_p). While the range of maximum winds for this D_p / B_1 combination has a 5 m/s range, the wind speed difference outside the radius of maximum winds is as much as 25 m/s.

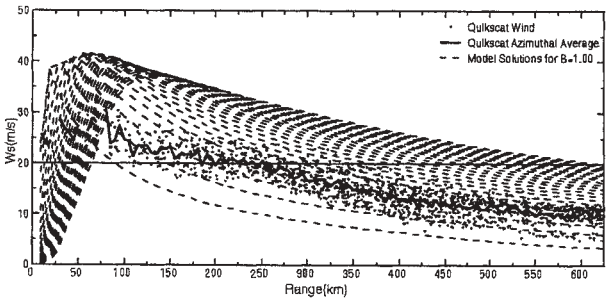

Figure 3. Family of TC96 model solutions (dashed) for D_p=90, B_1 = 1.00 vs. azimuthally averaged QUIKSCAT data (solid) during hurricane Floyd (1999).

Figure 4 shows a best root mean squared (RMS) fit (left) of a TC96 database solution to the azimuthally averaged QUIKSCAT data for September 14^{th} at 12 GMT. Only azimuthally averaged QUIKSCAT winds below 20 m/s were considered in this fit to minimize the influence of model retrieval underestimation. Twenty-two snapshots were derived during the lifetime of

Floyd using this methodology where sufficient QUIKSCAT was available. The resulting tropical wind field, when compared directly to QUIKSCAT observations, had a mean difference of .81 m/s with a scatter index (SI) of .23 and correlation coefficient of .87.

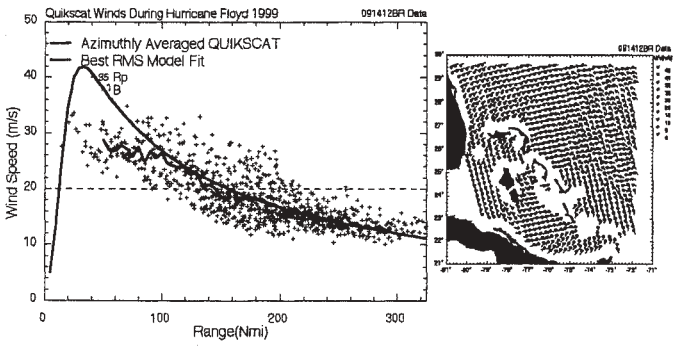

Figure 4. Best RMS fit to QUIKSCAT azimuthally averaged winds on September 14th 12 GMT.

5. Case Study during Hurricane Floyd (1999)

Hurricane Floyd is an excellent test case for determining TC96 parameters from scatterometer measurements. The QUIKSCAT data allowed the selection of 22 snapshots during the lifetime of Floyd where there was sufficient data in all quadrants. These snapshots, along with the best track from NHC were used to construct the tropical wind field for Floyd without the direct use of reconnaissance data (although reconnaissance data was used by NHC to determine the track and intensity).

During Floyd, HRD produced 24 wind field snapshots using the WANDA system. While the HRD winds do not constitute an absolute standard for verification, they do provide a measure of the success of the QUIKSCAT inverse modeling technique. The TC96 model winds were compared to the HRD winds at the time of the HRD analyses. Overall, the TC96 model winds were biased high by 2.79 m/s with a SI of .17 and correlation coefficient of .92. Wind directions were biased by -5.6 degrees. These statistics indicate a close statistical match between the QUIKSCAT derived inverse model winds and the HRD- aircraft derived winds. Differences within a given snapshot occasionally display large spatially coherence differences. These differences may arise from a number of causes including: (1) failure of the TC96 model to simulate smaller scale spiral bands which are sensed by the aircraft; (2) HRD wind errors in storm quadrants not probed by the aircraft and (3) slight positioning errors in wind field features which have been qualitatively well modeled by both wind fields.

The HRD and TC96 wind fields were both imbedded into a synoptic-scale wind field using the WWS, and run through a .25-degree 3rd generation wave model adapted to the Western North Atlantic. A comparison of the winds and waves during Floyd at NOAA buoy 41002 (Figure 5) show similar characteristics from the HRD and TC96 winds and waves. There is a slight underestimation of the winds and waves by the HRD winds and a slight overestimation by the TC96 model at this buoy. Overall, both hindcasts verify well. Wind comparisons to buoy 41010 (not shown), which was closest to the center of Floyd, show that the TC96 model winds tracked the measured wind speed very closely, except at the peak of the storm. The storm peak was overestimated by 7.5 m/s. The overestimation occurs when the modeled waves were greater than 9 meters (wave measurements at 41010 were not available). Given the extreme waves that the buoy likely encountered, coupled with the higher estimation of maximum winds by NHC (Table 4), it is likely that the buoy measurements are biased low and may have pulled down the peak winds in the HRD analysis which assimilated the buoy winds.

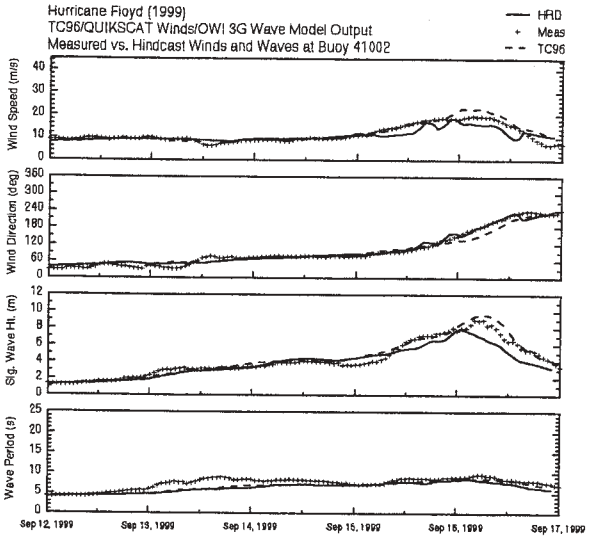

Figure 5. Comparison of wind and waves from HRD (solid) and TC96 (dashed) at Buoy 41002.

Table 4. Comparison of peak 10-minute, 10 meter wind speeds (m/s) during Floyd.

TC96	HRD	Buoy	NHC Best Track
43.0	38.0	35.5	41.2

Overall, the TC96 model winds during Floyd show very good skill when compared directly against QUIKSCAT, HRD, and buoy winds and indirectly compared to buoy wave measurements. Given the global coverage of QUIKSCAT, this technique shows promise for the increased skill of tropical wind fields where aircraft reconnaissance is not available.

6. Conclusion

This paper describes the system and techniques used to specify the surface wind field in tropical cyclones. The system is designed about the TC96 model, a well-proven tool that has been applied and validated in tropical basins worldwide. Methodologies applicable in both hindcasting and forecasting settings have been presented and have shown to be skillful when compared to measured wind and wave datasets.

References

Cardone, V. J., W. J. Pierson, and E. G. Ward, 1976. Hindcasting the directional spectra of hurricane generated waves. J. of Petrol. Technol., 28, 385-395.

Cardone, V. J. and D. B. Ross, 1979. State-of-the-art wave prediction methods and data requirements. Ocean Wave Climate ed. M. D. Earle and A. Malahoff. Plenum Publishing Corp., 1979, 61-91.

Cardone, V.J., C.V. Greenwood, and J.A. Greenwood, 1992. Unified program for the specification of hurricane boundary layer winds over surfaces of specified roughness. Final Report. Contract Report CERC-92-1. Dept. of the Army,Waterways Experiment Station, Vicksburg, MS.

Cardone, V.J. and K.C. Ewans. 1992. Validation of the hindcast approach to the specification of wave conditions at the Maui location off the west coast of New Zealand. Preprints of the Third International Workshop on Wave Hindcasting and Forecasting, May 19-22, 1992, Montreal, Quebec, 232-247.

Cardone, V.J., A.T. Cox, J.A. Greenwood and E.F. Thompson, 1994. Upgrade of Tropical Cyclone Surface Wind Field Model Misc. Paper CERC-94-14, US Army Corps of Engineers.

Cardone, V.J. and C.K. Grant, 1994. Southeast Asia Meteorological and oceanographic hindcast study (SEAMOS). OSEA 94132. 10th Offshore Southeast Asia Conference, 6-9 December, 1994.

Cardone, V.J., A.T. Cox, W.J. Pierson, W.B. Sylvester, W.L. Jones and J. Zec, 1999. NASA Scatterometer High Resolution Winds for Hurricane Lili. IEEE 1999 International Geoscience and Remote Sensing Symposium (IGARRS'99) 28 June-2 July, 1999, Hamburg.

Chow, S. H., 1971. A study of the wind field in the planetary boundary layer of a moving tropical cyclone. Master of Science Thesis in

Meteorology, School of Engineering and Science, New York University, New York, N.Y.

Cox, A.T., J.A. Greenwood, V.J. Cardone and V.R. Swail, 1995. An Interactive Objective Kinematic Analysis System Fourth International Workshop on Wave Hindcasting and Forecasting. October 16-20, 1995. Banff, Alberta, Canada.

Forristall, G.Z., R.C. Hamilton and V.J. Cardone, 1977. Continental shelf currents in tropical storm Delia: observations and theory. J. of Phys. Oceanog. 7, 532-546.

Forristall, G.Z., E.G. Ward, V.J. Cardone, and L.E. Borgman. 1978. The directional spectra and kinematics of surface waves in Tropical Storm Delia. J. of Phys Oceanog., 8, 888-909.

Forristall, G.Z., E.G. Ward and V.J. Cardone., 1980. Directional spectra and wave kinematics in hurricanes Carmen and Eloise. 17th International Conference on Coastal Engineering, Sydney, Australia.

Jones, L.W., V.J. Cardone, W.J. Pierson, J. Zec, L.P. Rice, A.T. Cox and W.B. Sylvester, 1999. NSCAT High Resolution Surface Wind Measurements In Typhoon Violet J. Geophys. Res. (Oceans), vol. 104, no.C5, pp. 11247-11259, May 15, 1999.

Jordon, C.L., 1958. Estimation of Surface Central Pressures in Tropical Cyclones from Aircraft Observations. Bul. of Amer. Met. Soc. 39, pp. 345-352.

Hock, T.F., and J.L. Franklin, 1999: The NCAR GPS dropwindsonde. Bull. Amer. Meteor. Soc., 71, 1410-1428.

Holland, G. J., 1980. An analytical model of the wind and pressure profiles in hurricanes. Mon. Wea. Rev. 1980, 108, 1212-1218.

Ross, D. B. and V. J. Cardone, 1978. A comparison of parametric and spectral hurricane wave prediction products. Turbulent Fluxes through the Sea Surface, Wave Dynamics, and Prediction, A. Favre and K. Hasselmann, editors, 647-665.

Shapiro, L. J.,1983. The asymmetric boundary layer flow under a translating hurricane. J. of Atm. Sci. 39 (February).

Powell, M.D., and P.G. Black (1990). The relationship of hurricane reconnaissance flight-level wind measurements to winds measured by NOAA's oceanic platforms. J. Wind Engrg. and Industrial Areodynamics, 36, 381-392.

Powell, M.D., S.H. Houston, L.R. Amat and N. Morisseau-Leroy, 1998. The HRD real-time hurricane wind analysis system. J. of Wind Eng. and Ind. Areodynamics. 77&78, pp. 53-63.

Thompson, E. F. and V. J. Cardone, 1996. Practical modeling of hurricane surface wind fields. ASCE J. of Waterway, Port, Coastal and Ocean Engineering. 122, 4, 195-205.

NUMERICAL EXPERIMENTS ON PREDICTING HURRICANE GENERATED WIND WAVES*

Yung Y. Chao and Hendrik L. Tolman

Ocean Modeling Branch, Environmental Modeling Center
National Centers for Environmental Prediction, NOAA
Camp Springs, Maryland, USA

1. INTRODUCTION

It is necessary to develop an advanced technique to forecast ocean surface waves generated by tropical cyclone to ensure the safety and economic welfare of marine activities over the ocean and in coastal communities. Because of cyclone's relatively small size, yet highly intense and rapidly varying wind fields, it requires the use of sufficiently high-resolution state-of-the-art dynamical weather and wave models to provide reliable numerical forecasts.

An improved third generation wave model is used presently at NCEP for operational global and regional wave forecasts. It uses wind data derived from the aviation run (AVN) of the operational global atmospheric model to drive the wave model. The intrinsic spatial resolution of the global atmospheric model, however, is about 1° latitude-longitude and is too coarse to resolve in a realistic manner the surface wind field structure associated with a hurricane vortex (Surgi et al., 1998). As a result, forecast wave conditions in the area under the influence of a tropical storm or hurricane usually are unrealistically low when AVN model winds are used to force the wave model. Also predictions of the direction and arriving time of swells in the coastal areas tend to be inaccurate.

In order to improve the accuracy of predicting storm tracks, intensity and wind distribution, NCEP uses a separate hurricane model during the hurricane season to produce forecast guidance. It is a regional multiply nested movable mesh model (MMM) involving variable grid resolutions developed at the Geophysical Fluid Dynamics Laboratory (GFDL). The current prediction system, however, only deals with one individual storm at a time. If multiple storms exist simultaneously within the domain of concern, the model is integrated independently for each storm. As a result, in dealing with a specific storm, only the coarse outer mesh resolves the other storms and the details of their structures are lost. Consequently, the combined effects of various wind fields associated with multiple storms on ocean waves cannot be adequately predicted.

---

* OMB contribution No. 194.

The purpose of this study is to develop a practical prediction system for producing realistic wind fields to provide forecast guidance regarding hurricane generated ocean surface waves. As a first step towards achieving this goal, the feasibility of combining winds obtained from NCEP's operational global atmospheric model (AVN) with those obtained from GFDL model run for a single hurricane if only one is present of from separate GFDL model runs for each hurricane if more than one hurricane is present in the Atlantic Ocean is considered to drive the operational western North Atlantic regional wave model.

In the following sections, a brief description of GFDL hurricane model and its output data sets related to the present study are presented first. The strategy of specifying hurricane wind fields based on AVN and GFDL models output for driving the wave model is described next. Then the results of predicted ocean wave fields associated with specified hurricane wind fields are presented. Finally a summary and concluding remarks on remaining tasks including further improvement of the prediction system are presented.

2. THE GFDL HURRICANE PREDICTION SCHEME AND PRODUCTS

The development and succeeding improvements of GFDL/MMM hurricane model are described in detail in a series of papers by Kurihara and associates (see e.g. Kurihara, et al. 1980, 1990, 1995, and 1998). In what follows, the basic feature of the system relevant to the present study is summarized.

The model is a three-dimensional primitive equation model formulated in latitude, longitude, and sigma coordinates, with 18 levels in the vertical. The lowest level is at approximately 42-meter height from the surface. The model domain consists of three grids with horizontal resolutions ranging from 1° to 1/3° to 1/6° longitude-latitude covering an area of 75°x75°, 11°x11° and 5°x5° in longitude and latitude, respectively. The domain of the outermost grid extends from 10°S to 65°N in the latitudinal direction. The time dependent lateral boundary in the zonal (longitudinal) direction of the domain is determined by the National Hurricane Center (NHC). The center provides official forecast of the storm's initial and 72-h positions based on NCEP global model analysis and forecasts. It remains fixed during the forecast cycle and is open to receive the forecast information from the global model. The two inner meshes are movable following the movement of the storm center at all times.

An important aspect of the model depends on its scheme of specifying a vortex to represent a tropical cyclone initially. Initial conditions for the model, basically are determined from the NCEP global model analysis and the observational information on the tropical cyclone structure prepared at NHC. The former is used to specify the environmental field and the latter is utilized to generate an empirical realistic (bogus) vortex involving axisymmetric and asymmetric components so as to replace a crudely resolved tropical cyclone in the global model analysis.

The hurricane prediction system is initiated with a request from NHC that specifies which storm to predict and the initial forecast time. At present, it runs four times a day and produces forecast output at six-hour intervals up to 78 hours for each cycle run. Products in Grib form are available only for 1° and 1/6° grids. The contents of output include but are not limited, to mean sea level

pressure and wind components at 35-meter height. The AVN model whose output data sets provide initial fields for the GFDL model is also run four times a day but at three-hour interval up to 126 hours for each cycle run.

Examples showing the mean sea level pressure field and wind distribution on 1° and 1/6° resolution moving grids are given in Figure 1a and 1b, respectively. They are extracted from the model run using initialized fields for Hurricane Floyd (September 1999). The hurricane center is located around 79°W and 30°N, just off the East Coast of Florida at the forecast valid time. It is of interest to note that the presence of another tropical storm is also seen in Fig. 1a near 50°W and 18°N. This low-pressure system, in fact, represents another hurricane named 'Gert'. An independent run of the model using initialized fields for this tropical storm Gert resulted in somewhat different distribution of pressure and wind fields for Hurricanes Floyd and Gert as shown in Fig. 2a and 2b.

3. STRATEGY OF HURRICANE WIND FIELD SPECIFICATION FOR DRIVING THE REGIONAL WAVE MODEL

The first step toward specifying hurricane wind fields for driving the wave model is to interpolate needed data from AVN and GFDL grids onto the regional Western North Atlantic wave model(WNA) domain. The domain of wave model extends from 98° W to 30° W in longitude and from 0° N to 45° N covering the entire western North Atlantic including the Gulf of Mexico. The domain was so defined in order to cover the entire ocean area that might be affected by tropical storms occurred in the Northern Atlantic Ocean. The grid resolution of the wave model is 1/4° latitude-longitude. A bi-linear interpolation scheme is employed to interpolate GFDL data to generate required hurricane wind field on the wave model domain. For the portion of the wave model domain in which interpolated values can be derived from both GFDL 1° and 1/6° resolution grids, data obtained from 1/6° grid are used.

As shown in Fig. 1(a) and Fig. 2(a), if multiple storms co-exist, wind and pressure fields produced by the hurricane model for different storms can have considerable discrepancy in the area of storm influence. This is the result of the initialization of the selected storm in the model. In order to resolve this problem, the concept of an area of influence for each storm is introduced. Various definitions of the area of influence are considered and tested. It is found that the area that is determined based on the following procedure would provide the most realistic and consistent wind field structure. The procedure involves:

(a) Determining a box area which has the shortest distance from the storm center to a specified maximum isobar;
(b) Determining a box area extending from the storm center (out of the hurricane eye) to four sides on which the wind speed decreases to a specified wind speed or less;
(c) Forming a new box area with each side taken from the corresponding side of the above two boxes which ever has greater distance from the center;
(d) Restricting the new box area to be less than or equal to a maximum allowable longitude-latitude box;
(e) Once the area of influence of a storm is determined, wind data in the box are used to replace AVN wind data in the same area. A weighted average procedure is

used to ensure a smoothly varying wind field over four boundaries of the box area.

Numerical experiments are made using various combinations of maximum isobar (ranging from 1020 to 1000 mb), minimum wind speed (ranging from 10 to 5 m/s) and maximum allowable box size for the area of storm influence (ranging from 10° to 15°). It is found that the use of 1015.0 mb mean sea level pressure, 5.5 m/s wind speed at 10 meter height and the maximum box size of 12.5° in latitude-longitude, would provide most realistic and smooth hurricane wind fields. Figure 3a and 3b show the area of influence for Hurricane Floyd and Gert, respectively. Figure 4a shows the result of blending the hurricanes wind field with AVN wind field. And for comparison, the original AVN wind field that is used in regular operational wave model runs is shown in Fig. 4b. The most significant difference on the wind field between these two figures is in the area near the hurricane center. The excessive size of the hurricane eye displayed in AVN wind field is replaced by much small one with high wind surrounding it.

It is of interest to mention in passing an empirical criterion that was used in the GFDL model for determining the extent of an analyzed storm. It involves the conditions that the tangential component of the disturbance wind is less than 6 m/s from the storm center or bounded by 1200 km in radius (Kurihara et al., 1995). These values are close to the values of our best choice for the area of influence of a storm.

4. SIMULATION OF HURRICANE WAVES

The Western North Atlantic regional wave model (WNA) is developed based on the global wave model (NCEP WAVEWATCH-III, NWW3) currently operational at NCEP. The specific features of this third generation model differing from the well known WAM model (WAMDIG, 1988, Komen et al. 1994) include: (a) an addition of diffusion terms to the propagation equation to account for wave dispersion within discrete spectral bins (Booij and Holthuijsen, 1987), (b) the use of a new wave generation formulation (Chalikov and Belevich, 1993), (c) the use of a new dissipation formulation (Tolman and Chalikov, 1996), and (d) the use of a third order finite differencing method to solve wave propagation (Leonard, 1979,1991). The resolution of directional frequency spectrum of the model consists of 24 directions and 25 frequencies ranging from the lowest frequency of 0.042 Hz (23.9 sec.) to 0.41 Hz (2.4 sec.). More detailed description of the model can be found in Tolman (1999).

Wind fields constructed according to the procedure described in Section 3 are used to drive the wave model during the period when both Hurricanes Floyd and Gert appeared simultaneously in the wave model domain. Wave field simulations are made by using: (1) AVN winds only; (2) blended AVN and GFDL's Floyd winds; (3) blended AVN and GFDL's Gert winds; and (4) blended AVN and GFDL's Floyd and Gert winds. Preliminary evaluation shows that using wind fields obtained according to (4) provides the most realistic result.

Examples showing differences in wave fields between forecasts with and without GFDL hurricane wind data are shown in Figures 5 through 8. Figures 5a and 5b show the significant wave heights for 24-h forecasts obtained using AVN wind alone and those obtained using AVN and GFDL wind fields. Figure 6 shows similar results for the 72-h forecast. For the 24-h forecast (Fig.

5a), the AVN winds result in maximum wave heights for Floyd of 10m around 77W and 32N, and for Gert of 5m around 52W and 19N. Combining AVN and GFDL winds results in maximum wave heights of 15m for both systems at roughly the same location (contours truncated at 12m). For the 72-h forecast (Fig. 6), inclusion of GFDL winds results in much higher wave heights for Gert at roughly the same location (6 vs. 15m around 56W and 22N). For Floyd, the maximum wave height is moved from about 65W 44N to 72W 40N and is slightly increased from 7 to 8m. The difference in position is due to different tracks predicted by the AVN and GFDL models. Note furthermore that the local maximum east of 65W in Fig. 6b is due to the fact that Floyd in the AVN is not completely covered by the area of influence calculated from the GFDL results. This maximum is therefore spurious and will be dealt with in a newer version of the wind-blending algorithm.

Figures 7 and 8 show the corresponding peak periods for the 24 and 72-h forecasts. The peak period is defined as the period at which the energy density of the one-dimensional frequency spectrum is maximum. Inside the storm, this parameter indicates the wind sea period. Outside the storm, this period tracks the dominant swell system. Note that the peak period is discontinuous, and shows "fronts" where many contour lines coincide. Such a front identifies locations where a different swell system (generally from a different source) becomes dominant. Figures 7a and 8a show that the AVN winds result in a dominant swell system associated with Gert with periods of 10 to 11s in a large area. For the 72-h forecast (Fig. 8a) this swell field is dominant from about 55W to 72W and from 10N to 32N. Because Gert moves slowly, it's swells travel ahead of it. When using GFDL winds, much longer (and higher) swells are generated with periods of typically 15s. Such swells travel faster, and will therefore result in earlier and higher swells at the coast. Addition of GFDL winds also results in increased swell production by Floyd. Because, however, much of the swells generated by Floyd travel directly to the coast where they are dissipated, differences in peak periods for swells associated with Floyd are less dramatic.

Note that both runs start from identical initial conditions. If the model is continuously run with GFDL winds even larger impact might be expected. This is particularly important in forecasting coastal swell from hurricanes that are still far offshore since a great number of fatalities near beaches might be attribute to this cause.

5. SUMMARY AND CONCLUDING REMARKS

A strategy to empirically determine the area of influence of a tropical storm based on the prediction of GFDL hurricane model has been developed. Once the area of influence of each storm is determined, it is possible to construct realistic wind fields over the wave model domain by blending the wind fields from either a single storm or multiple storms with those from the large-scale AVN model. Since this approach accounts for the intensity of all storms without favoring any particular one, the wave conditions predicted by these wind fields would be more realistic.

Although the present experimental study has revealed quite encouraging results, some additional tasks still need to be done before the system can be used to provide operational forecast guidance of hurricane generated waves. These tasks include but are not limited to the following:

1. Increasing the frequency of GFDL model output, preferably hourly intervals instead of current six-hr intervals so that a smooth temporal and spatial variation of wave field can be obtained.
2. Validating wind and wave data with observed data obtained from buoys and satellites.
3. Adjusting the size of the area of influence obtained from GFDL model so that it is consistent with the area of influence specified on the storm predicted by AVN model. This step is required only when there is a significant difference between AVN and GFDL models in forecasting storm location and size.

REFERENCES

Booij, N, and L.H. Holthuijsen, 1987: Propagation of ocean waves in discrete spectral wave models. J, Comput. Phys. **68**, 307-326.

Chalikov, D.V., and M.Y. Belevich, 1993: One-dimensional theory of the wave boundary layer. Bound. Layer Metero. **63**, 65-96.

Komen, G.J., L. Cavaleri, M. Donelan, K. Hasselmann, S. Hasselmann and P.E.A.M. Janssen, 1994: *Dynamics and modeling of ocean waves*. Cambridge University Press, 532 pp.

Kurihara, Y., and M. A. Bender, 1980: Use of a movable nested mesh model for tracking a small vortex. Mon. Wea. Rev.**108**, 1792-1809.

Kurihara, Y., M.A. Bender, R.E. Tuleya and R.J. Ross, 1990: Prediction experiments of Hurricane Gloria (1985) using a multiply nested movable mesh model. Mon. Wea. Rev., **118**, 2185-2198.

Kurihara, Y., M.A. Bender, R.E. Tuleya and R. J. Ross, 1995: Improvements in the GFDL hurricane prediction system. Mon. Wea. Rev., **123**, 2791-2801.

Kurihara, Y., R.E. Tuleya and M. A. Bender, 1998: The GFDL hurricane prediction system and its performance in the 1995 hurricane season. Mon. Wea. Rev., **126**, 1306-1322.

Leonard, B.P., 1979: A stable and accurate convective modeling procedure based on quadratic upstream interpolation. Comput. Methods Appl. Mech. Engng. **19**, 59-98.

Leonard, B.P., 1991: The ULTIMATE conservative difference scheme applied to unsteady one-dimensional advection. Comput. Methods Appl. Mech. Engng.,**88**, 17-74.

Surgi, N., H.-L. Pan and S.J. Lord, 1998: Improvement of the NCEP global model over the tropics: an evaluation of model performance during the 1995 hurricane season. Mon. Wea. Rev. **126**, 1287-1305.

WAMDIG, 1988: The WAM model - a third generation ocean wave prediction model. J. Phys. Oceanogr. **18**, 1775-1810.

Tolman, H.L., 1999: User manual and system documentation of WAVEWATCH-III version 1.18. Tech. Note. No.166, Ocean Modeling Branch, NCEP/NWS/NOAA, U.S. Department of Commerce, 110 pp. [Available at http://polar.wwb.noaa.gov/waves/wavewatch/].

Tolman, H. L. and D.V. Chalikov, 1996: source terms in a third-generation wind wave model. J. Phys, Oceanogr. **18**,1775-1810.

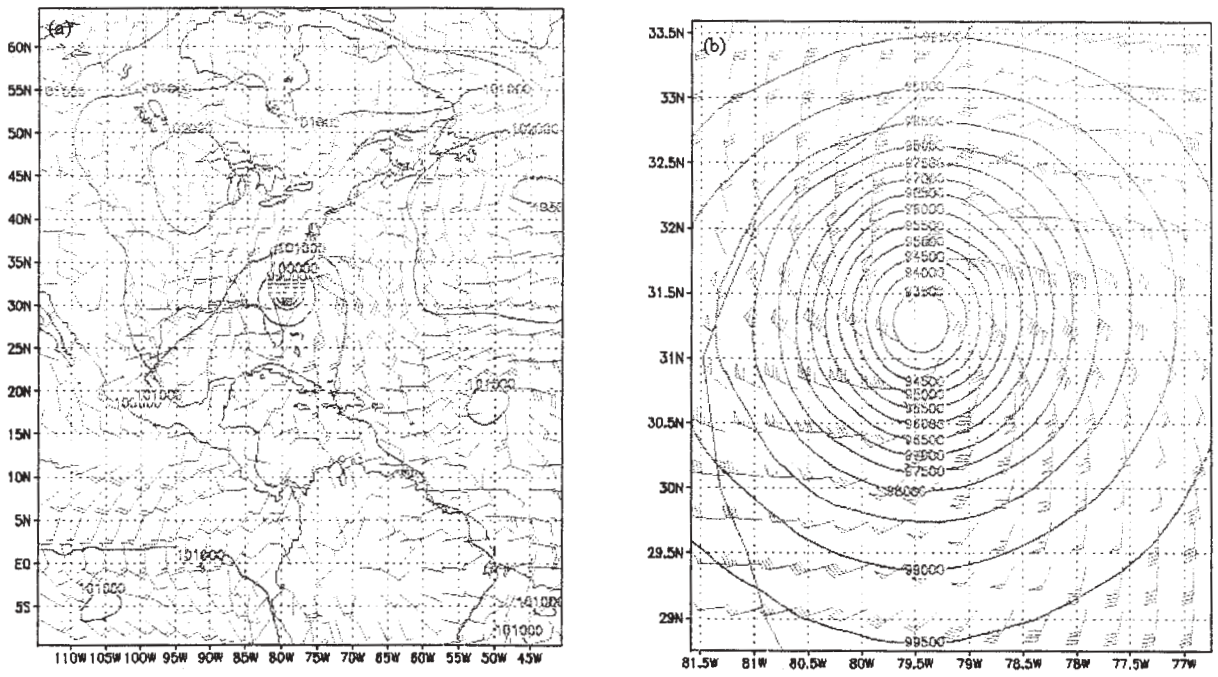

Fig. 1 GFDL model 24-h forecast of Hurricane Floyd's MSL pressure and wind fields valid for 1999/09/1600z: (a) coarse grid; (b) find greid.

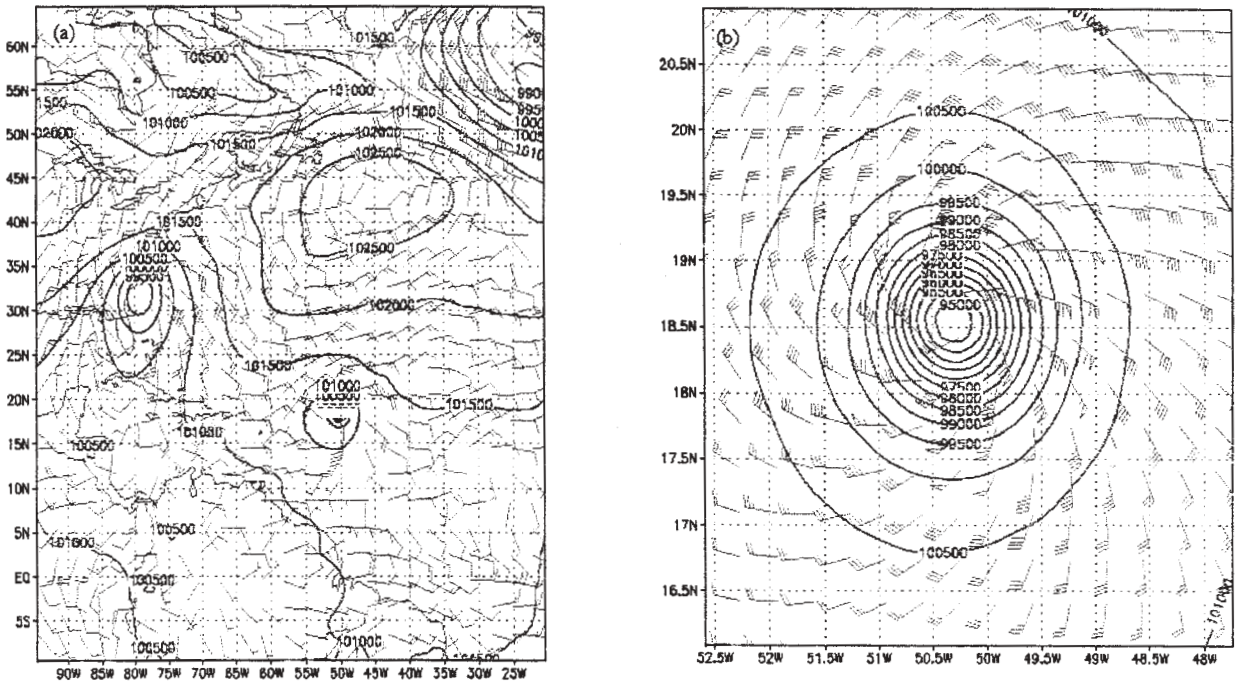

Fig. 2 GFDL model 24-h forecast of Hurricane Gert's MSL pressure and wind fields valid for 1999/09/1600z: (a) coarse grid; (b) find greid.

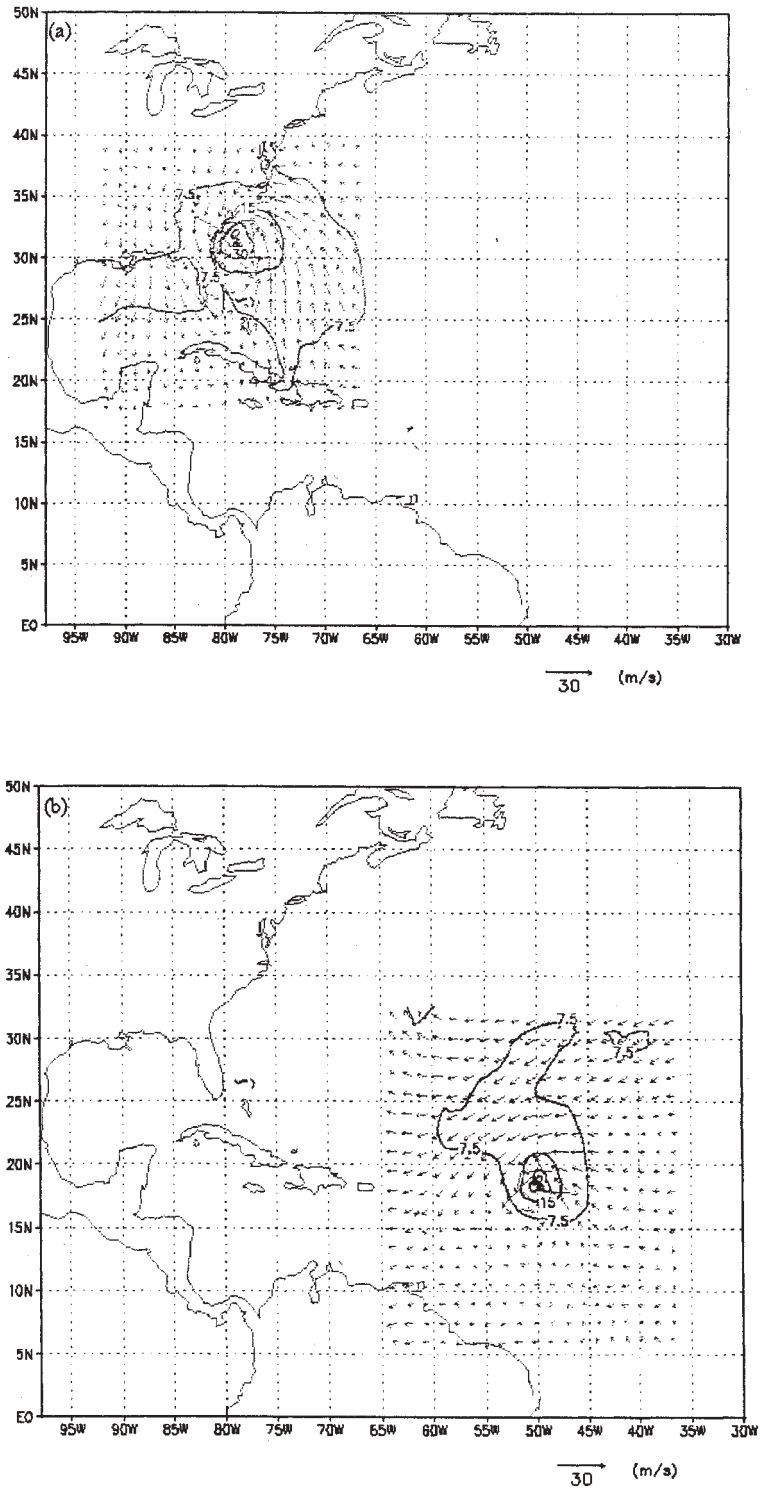

Fig. 3 Specified areas of influence for GFDL 24-h forecast of Hurricanes:(a) Floyd; (b)Gert. Valid 1999/09/1600z.

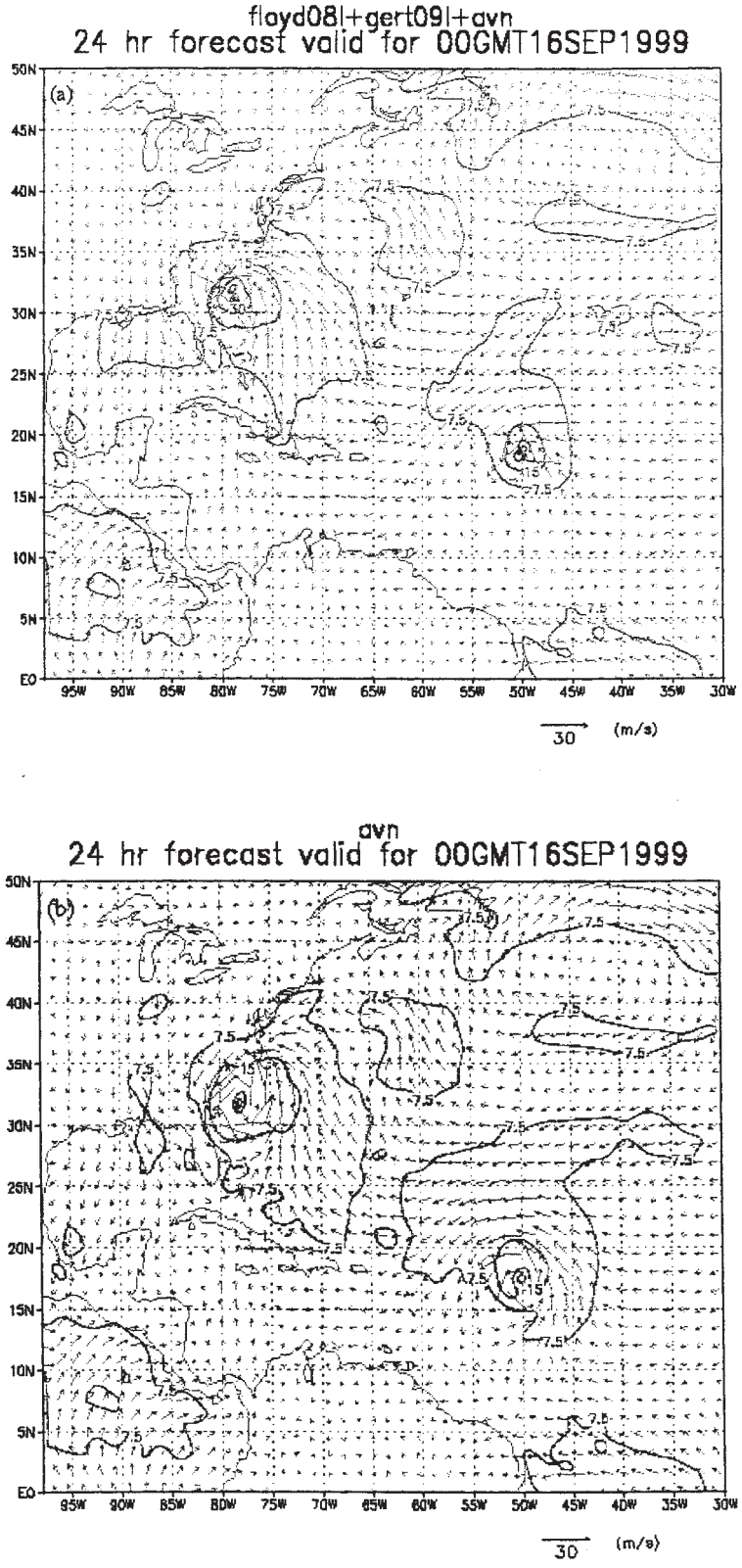

Fig. 4 Comparison of blended AVN and GFDL's Floyd and Gert winds (a) with the original AVN wind field (b).

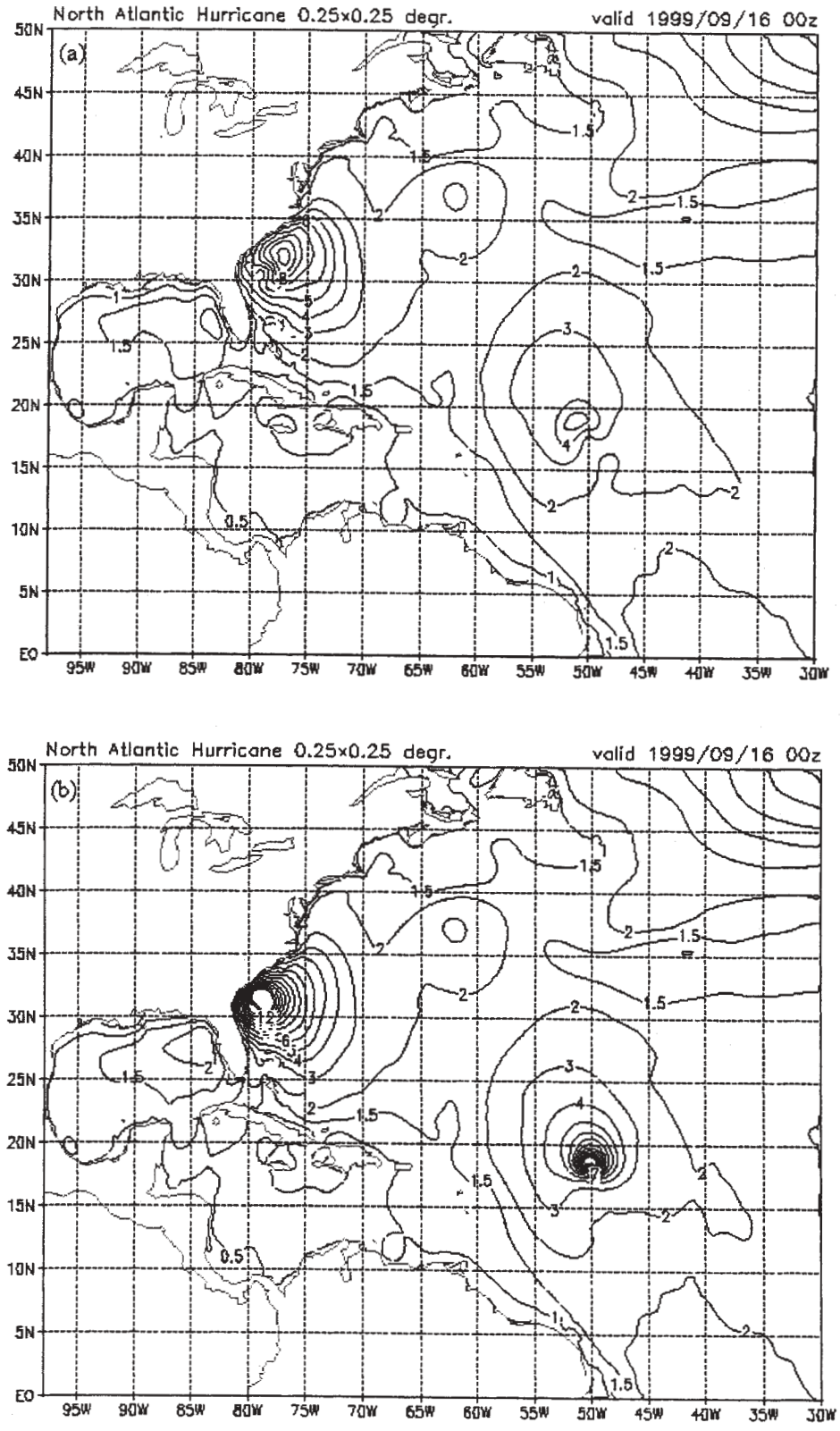

Fig. 5 24-h forecast of the significant wave height (m) forced by: (a) AVN winds only; (b) blendid AVN and GFDL's Floyd and Gert winds.

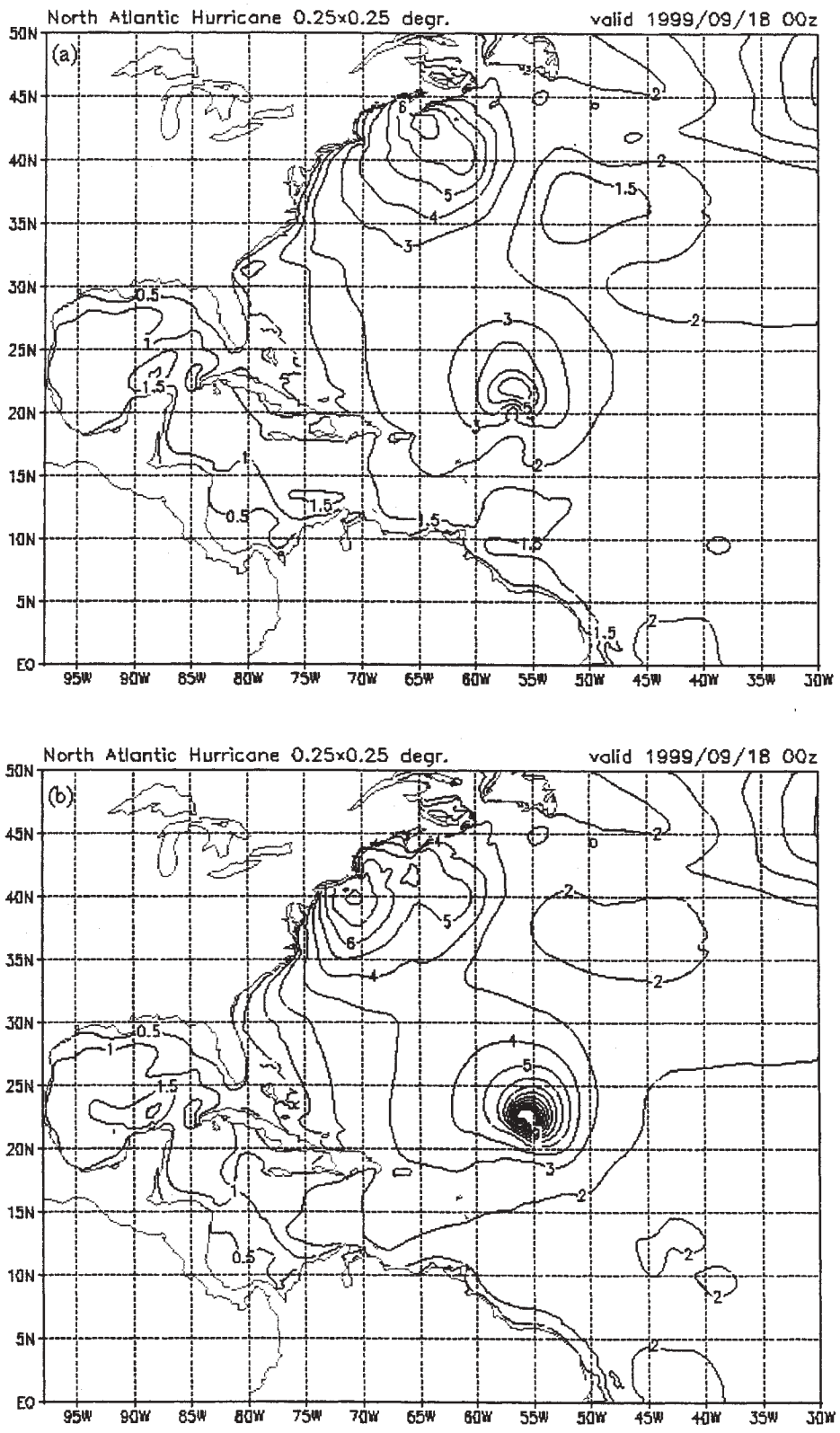

Fig. 6 72-h forecast of the significant wave hieght(m) forced by: (a) AVN winds only; (b) blendidd AVN and GFDL's Floyd and Gert winds.

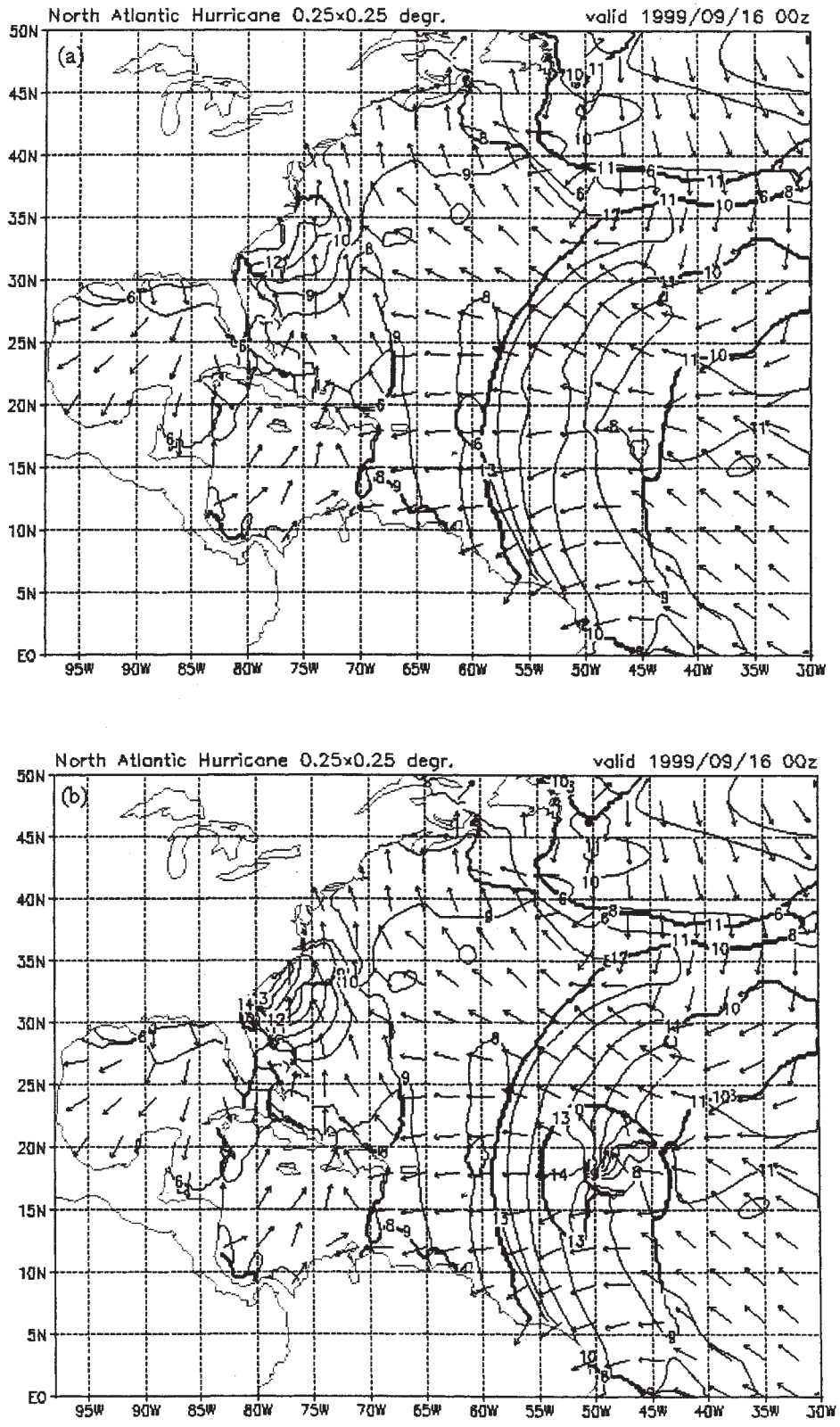

Fig. 7 24-h forecast of the peak wave period forced by: (a) AVN winds only; (b) blended AVN and GFDL's Floyd and Gert winds.

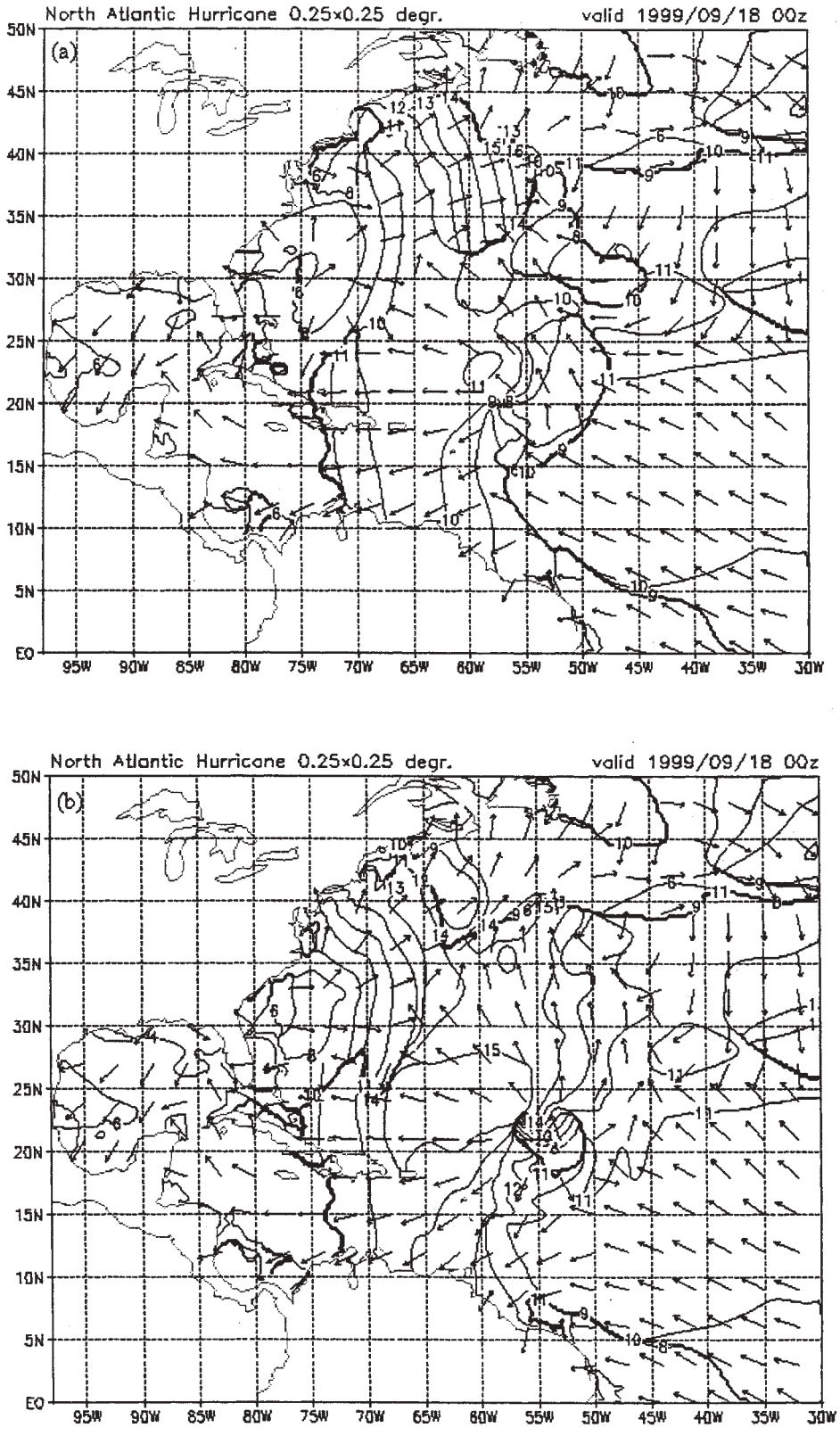

Fig. 8 72-h forecast of the peak wave period forced by: (a) AVN winds only; (b) blended AVN and GFDL's Floyd and Gert winds.

DESIGN WAVE EVALUATION FOR COASTAL PROTECTION STRUCTURES IN THE WADDEN SEA

Hanz D. Niemeyer, Ralf Kaiser & Bettina Weiler

Coastal Research Station of the Lower Saxon Central State Board for Ecology (CRS)
Fledderweg 25, D-26506 Norddeich/East Frisia, Germany (email: niemeyer.crs@t-online.de)

1. INTRODUCTION

The design of coastal protection structures depends highly on a proper evaluation of design waves in respect of both safety and economical benefit-cost ratio. Any uncertainty endangers safety of goods and sometimes even human life or leads to an inappropriate spending of tax payer's money. Nevertheless in many regions of the world and not only in developing countries the basis for the evaluation of design waves is rather poor.

The length of time series of wave measurements is generally insufficient with respect to a proper evaluation by probabilistic methods since the therefore remaining ranges of uncertainty are enormously high. Additionally the density of wave measuring nets is in most cases insufficient in order to cover the local variability of wave climate.

The classical wave prediction methods basing on wind input incorporate also inaccuracies, which grow the more the area of interest is characterized by enormous changes of morphological features, which is particularly valid for Wadden Sea coasts. As well the complex morphology as the superposition of several wave systems aggravate the application of conventional forecasting methods or make it even useless in these areas.

Though mathematical wave models have proven their capability even in these morphologically complex coastal areas the implementation of reliable boundary conditions like e. g. the offshore design wind or wave conditions remains a problem if the evaluation of design waves is required.

Therefore the design of coastal protection structures at the Wadden Sea coasts of the southern North Sea is still semi-empirical, particularly for the determination of design wave run-up on sea dykes. Major reason is usually the lack of reliable design wave parameters (Niemeyer et al. 1995).

2. TASKS AND PROBLEMS

The CRS Hydrodynamics Section is generally involved in the design of protection structures at the Lower Saxon coast at the southern North Sea (fig. 1). Its particular task is the evaluation of water level heights, wave parameters and wave run-up being appropriate for design conditions with respect to both technical state of the art and legal boundary conditions.

In the recent past local authorities asked for assistance by the design of coastal protection structure which implied specific requirements for the evaluation of coastal design waves.

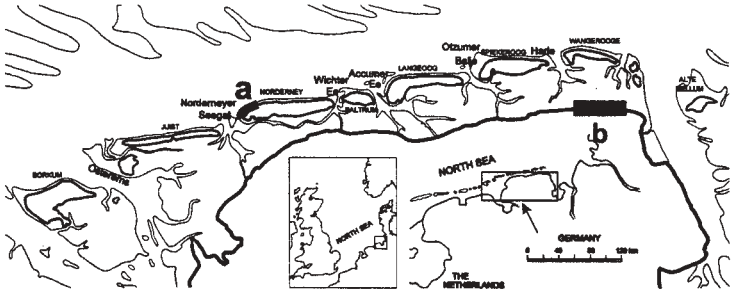

Fig.1: Location of the investigation areas at the Frisian North Sea coast: a) Island of Norderney; b) Elisabethgroden-dyke

In the first case the ultimate aim was the design height of dyke at a stretch of about 10 kilometers at the Frisian mainland coast (fig. 1) which shall be strengthened during forthcoming years. In order to keep the maintenance cost of the new dyke as low as possible beforehand to stretches of 250 m each were planned with pilot constructions of dyke revetments. The responsible dyke community asked therefore additionally to determination of design wave run-up by the extrapolation-method (Niemeyer et al. 1995) for an estimation of local design wave conditions in order to get the necessary basics for the revetment design.

In the second case parts of the seawall on the island of Norderney (fig. 1) had to be investigated with respect to a probably needed redesign. The core of the construction was erected at about 1860; afterward numerous extensions and improvements have been carried out due to increasing wave loads or due to damages during storm surges (Niemeyer et al. 1996). Therefore model tests in the large wave flume at Hannover University (Führböter 1982) were planned in order to evaluate the wave loads the seawall will experience if design conditions occur. As necessary boundary conditions for the model tests wave spectra on the island's shoreface were required from CRS Hydrodynamics Section.

In the first case the spectral shape is of lower importance since the formulas for the determination of wave run-up and the evaluation on revetments usually do not consider multipeak spectra. For the second one the spectral shape for design conditions was regarded as rather important, since the steering of the wave paddle is controlled either by wave trains or by spectra. Furthermore the input of spectral information is expected to deliver an improved basis for the evaluation of wave loads on structures.

The evaluation of design waves in the inner part of estuaries by mathematical modeling has been carried out earlier with success (Niemeyer 1997; Niemeyer & Kaiser 1999, 2001) by applying the third-generation model SWAN (Ris et al. 1995; Holthuijsen et al. 1998; Booij et al. 1999). This has proven its applicability in Wadden Sea areas delivering reliable results both for normal and storm conditions (fig. 2a + b) if driven by measured spectra at its offshore boundary. But there are no wave measuring data available matching design conditions in the southern North Sea.

It is possible to create in SWAN a parametric spectra for chosen offshore wave parameters. Therefore chosen offshore design wave parameters can be transferred into such a parametric spectrum as boundary condition for a model run. Major disadvantage of this procedure is that specific regional features of wave spectra like e. g. multipeaks get lost and any of their possible impacts on local design waves also.

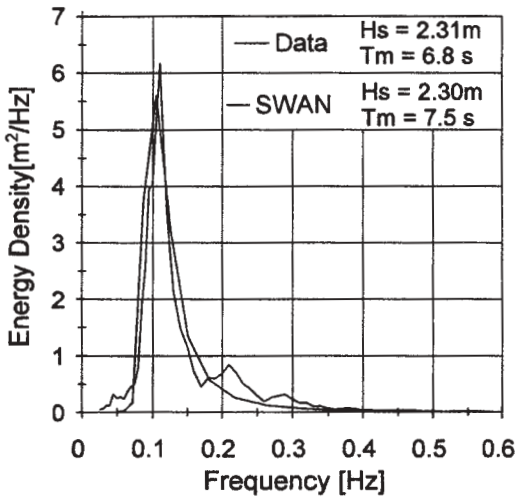

Fig. 2a: Comparison of field data and model results (ordinary tide), island shoreface of norderney

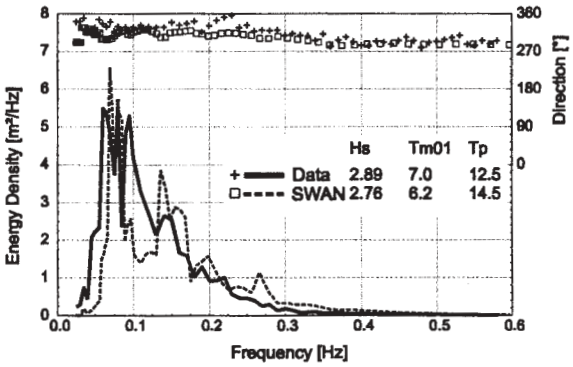

Fig.2b: Comparison of field data and model results (storm surge), island shoreface of norderney

3. PROBLEM APPROACH

3.1 Mainland coast

3.1.1 Feasibility study

Field measurements highlighted that waves in Wadden Sea areas are on the one hand strongly depth-controlled (fig. 3). On the other hand local water depths are also determined by local wave climate (Niemeyer 1991): The relation of wave parameters and water depths are in a dynamical equilibrium. If the water depth is larger than the waves need, sedimentation takes place. Vice versa an unsteady non-continuing increase of wave energy input beyond the level of established dynamical equilibrium will only create a higher rate of dissipation. If this holds also stand for design conditions the use of measured spectra as a seaward boundary condition for model runs could lead to reliable results. It must be stressed that such an approach would only be

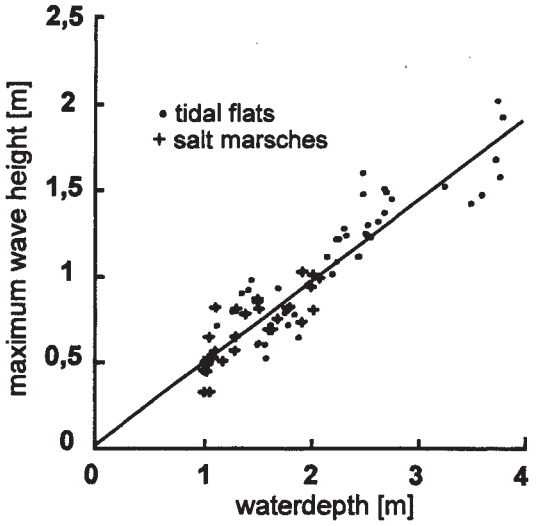

Fig.3: Wave height / water depth- relation in Wadden Sea areas (Niemeyer 1983)

valid for wave parameters but not for the spectral shape. It is therefore only then successfully applicable, if the transfer of spectral shape into wave loads is not required.

Therefore tests have been carried out comparing the results of runs with SWAN for the design water level with distinct seaward boundary conditions:

1. Measured directional wave spectra from storm surges (fig. 4),
2. Parametric wave spectra with higher waves and longer periods for matching design conditions (fig. 4).

The comparison of the results of the two model runs is here presented as well for significant wave heights (fig. 5) as for mean wave periods (fig. 6) and for mean directions (fig. 7) for the whole model area. The results highlight that particularly in the areas of interest i. e. on the tidal flats and salt marshes in front of the sea dyke at the mainland coast the differences for the wave parameters are very small (fig. 5 - 7). They are always within the range of the model accuracy to be expected. In any case the margin of 5 % is not exceeded in the vicinity of the sea dyke.

The closer the mainland coast the more the differences of local wave parameters diminish: In the course of wave propagation to the mainland coast gradually an increasing tendency towards a uniform wave climate develops independently from the offshore wave conditions. The interactions of waves and tidal flat morphology determine dominantly local wave conditions, as already highlighted by the strong linear relationship between wave heights and water depths (fig. 3). The results of this comparison give emphasis to the effect of morphological filtering of storm waves traveling from offshore across the tidal flats. The water depth on tidal flats is determined by the mid-term dynamical equilibrium of strong waves and morphology; but during singular events it acts as a limiter. This effect facilitates enormously the choice of suitable offshore boundary conditions for mathematical modeling of design waves for dykes at the mainland coast of Wadden Sea areas by implementing measured storm surge spectra.

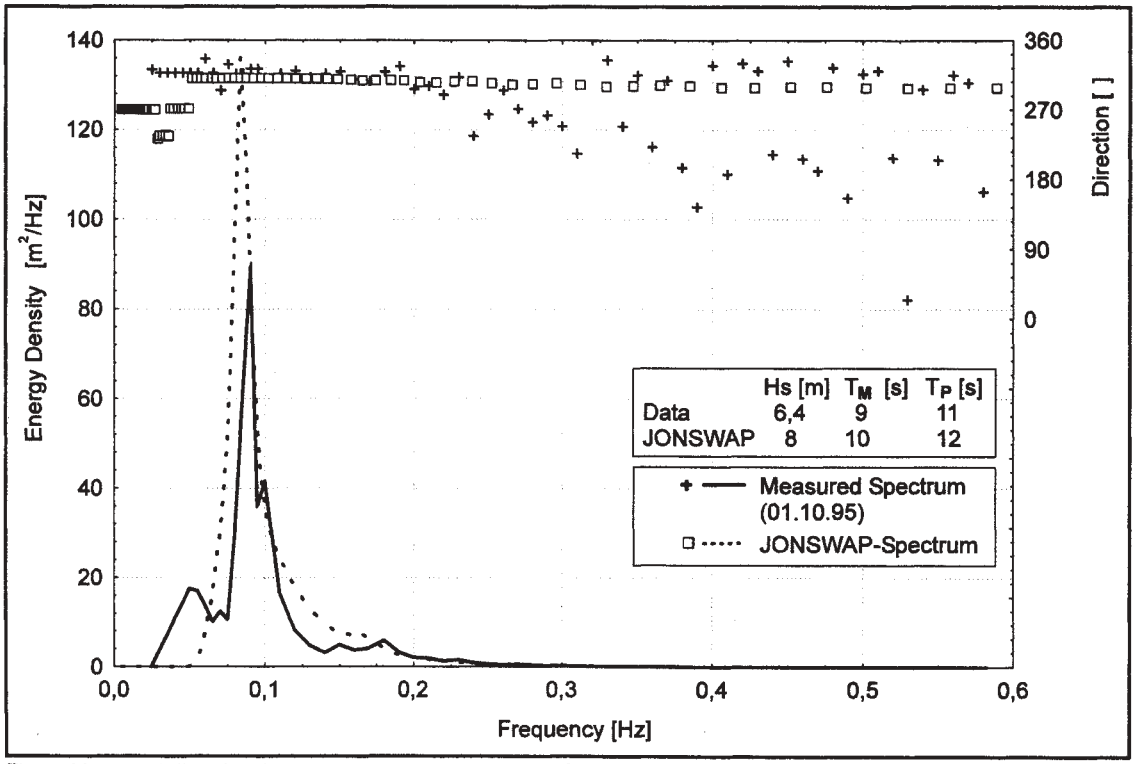

Fig.4: Measured directional wave spectrum (storm surge of January 10th, 1995) and chosen JONSWAP-Spectrum)

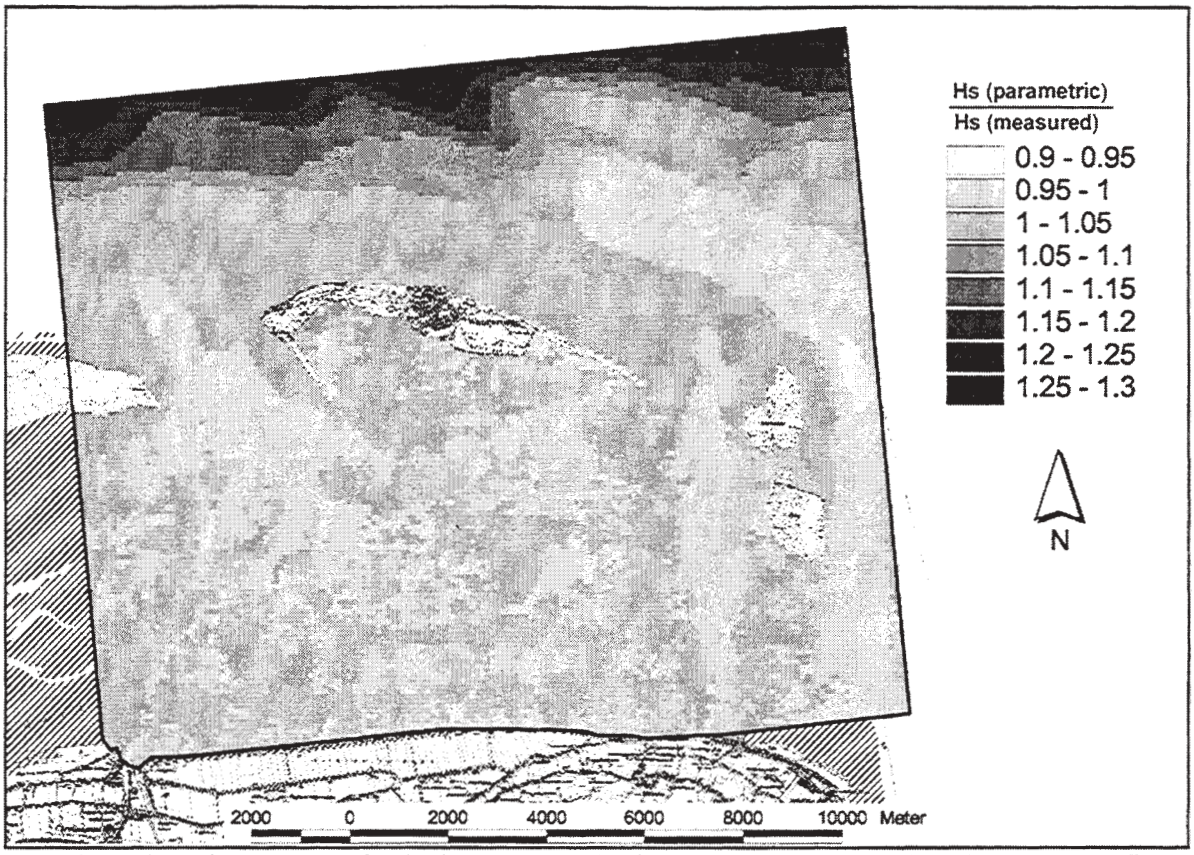

Fig.5: Comparison of model results for significant wave heights for measured and parametric design spectra as offshore boundary conditions

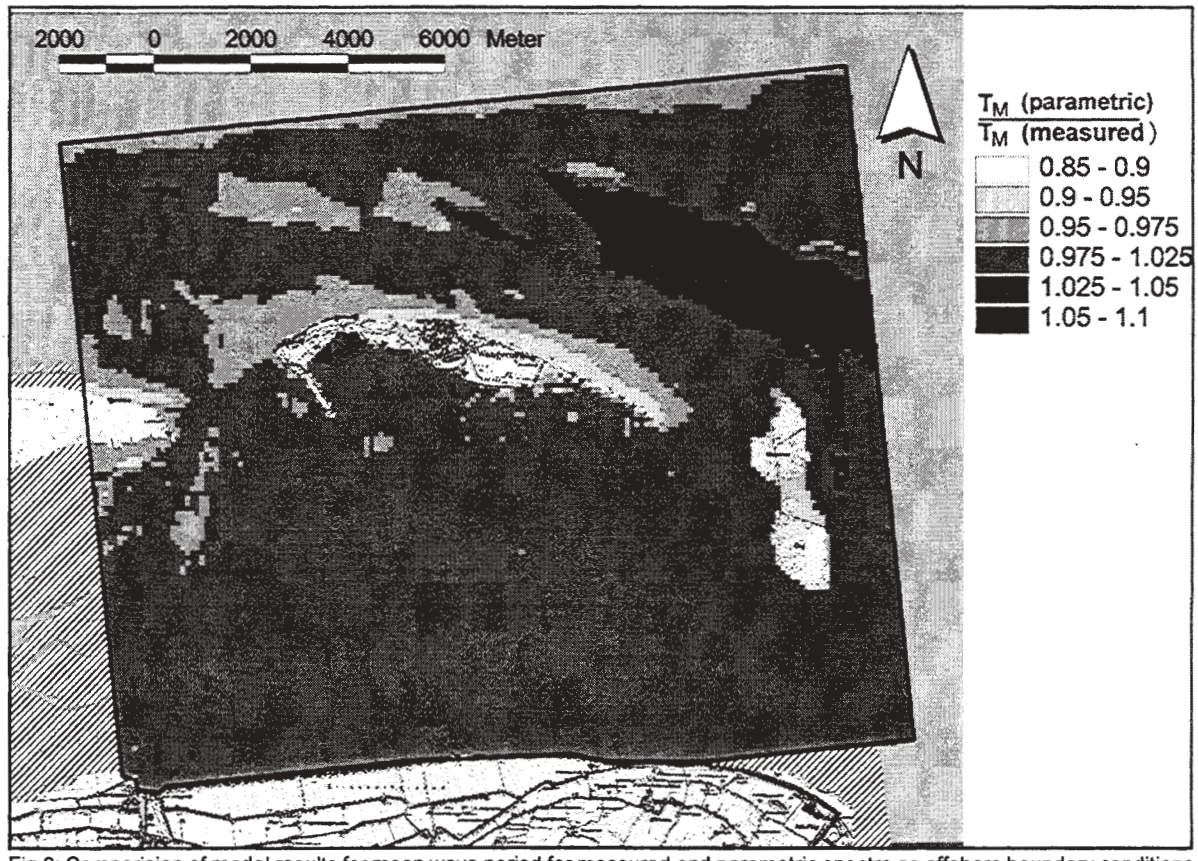

Fig.6: Comparision of model results for mean wave period for measured and parametric spectra as offshore boundary conditions

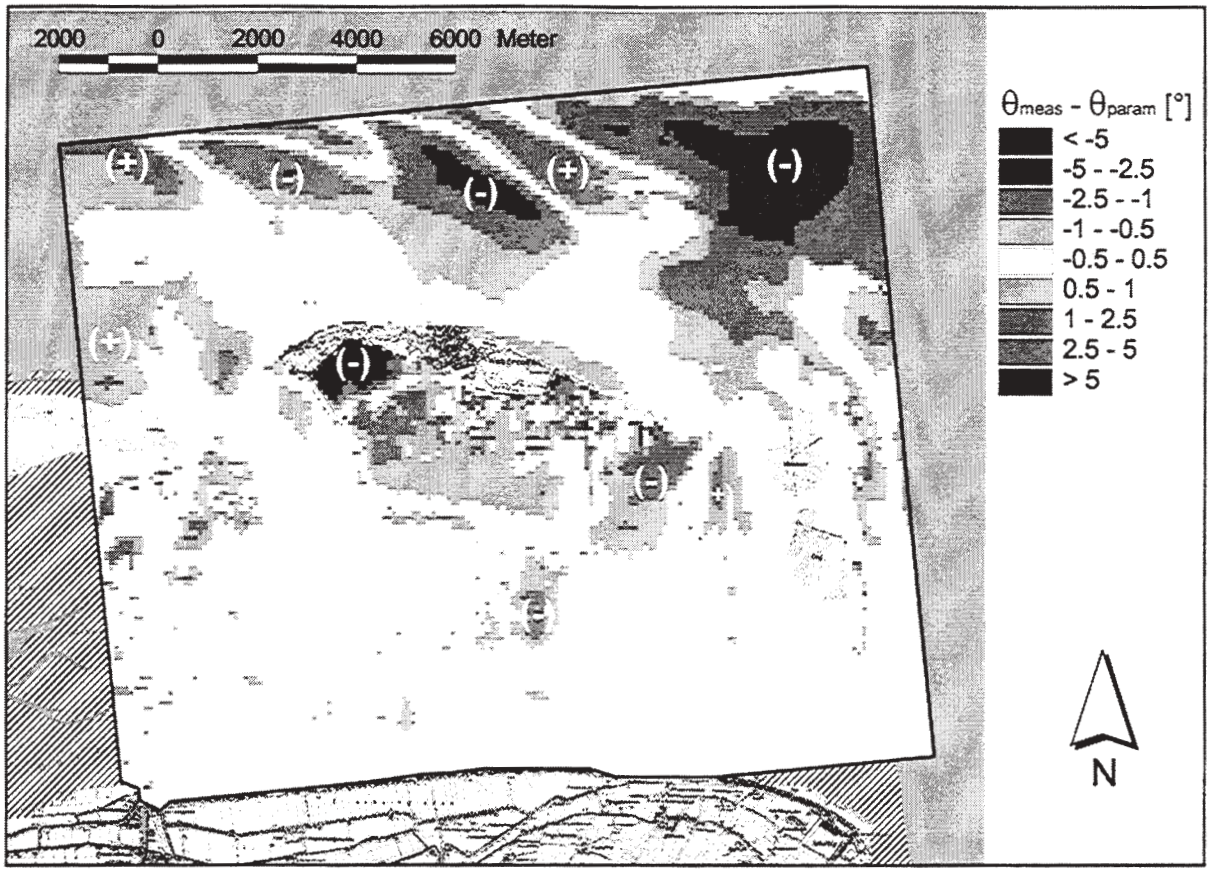

Fig. 7:Comparison of model results for mean wave direction for measured and parametric spectra as offshore boundary conditions

3.1.2 Modeling of design waves

For the modeling of design waves an overall model representing an area of 14 x 20 km with a grid size of 100 x 100 m was established; in the vicinity of the dykes a smaller nested model for an area of 4,25 x 12,5 km and a grid size of 50 x 50 m was additionally implemented (fig. 8).

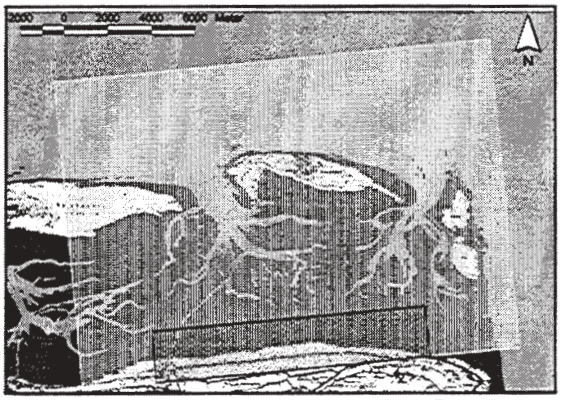

Fig. 8: Model areas and grid size- East Frisian coast seaward of the Elisabethgroden Dyke

Beside the choice of the offshore wave spectrum driving the model, water level, wind velocity and direction must be introduced as governing boundary conditions. The design water level is about

SWL = G. D. + 5,6 m

and the equivalent wind velocity and direction are:

u = 30 m/s

D = 315°

Though it is a well known fact, that the wind field is significantly affected in the coastal area (Kaiser & Niemeyer 1999) the reduction of velocity is not taken into consideration. On the one hand this assumption is on the safe side. On the other hand local wind generation is much lesser important for wave climate on tidal flats than the interaction of waves entering from offshore with local morphology.

The results of the overall model for the significant wave heights and mean directions make evident the tremendous changes waves experience propagating from offshore coastward in barrier island sheltered Wadden Sea areas (fig. 9): An enormous wave energy dissipation takes place on the ebb deltas of the tidal inlets and on the islands' shorefaces. Furthermore the barrier islands shadow large areas of the tidal flats against direct wave intrusion. Waves from offshore penetrate only towards the tidal flat area

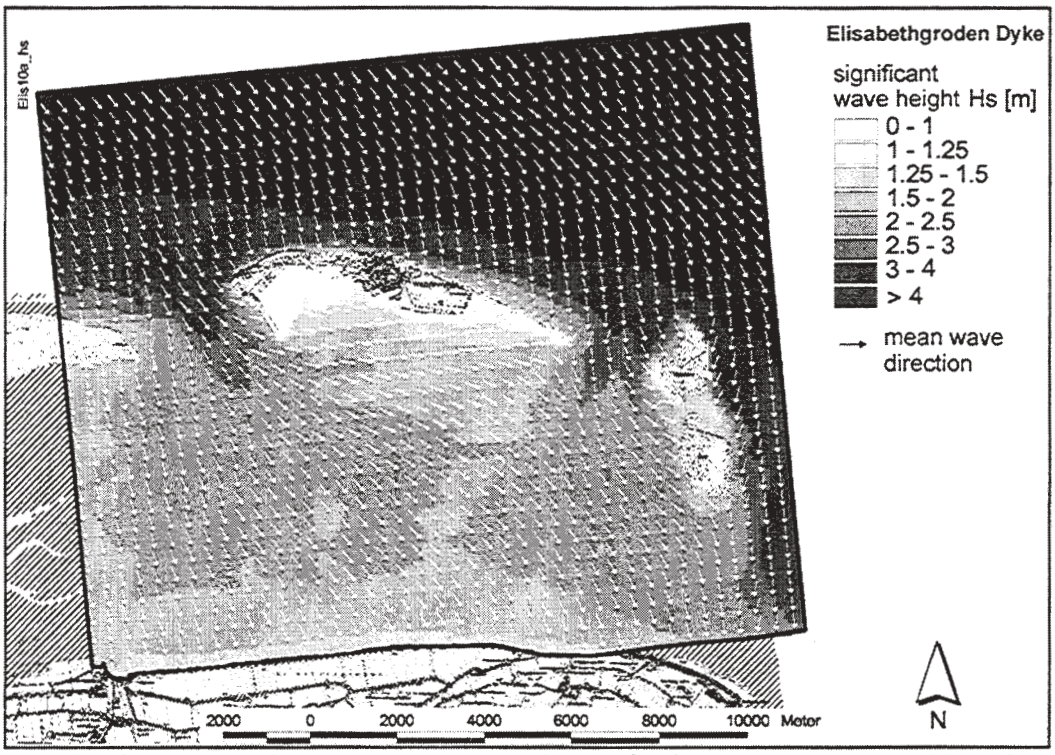

Fig. 9: Significant wave heights H_S and mean wave direction θ_m (SWL: G. D. + 5,6 m; u = 30 m/s from 315°) in the Wadden Sea area seaward of the Elisabethgroden Dyke

and the mainland coast via the tidal inlets. From there they are spreading out across the flats. The wave heights decrease there the more the farther from the inlet.

The evaluation of the design wave parameters in front of the dyke was carried out with the nested model (fig. 10 + 11) in order to consider sufficiently any variation for dimensioning the dyke and the revetments properly. The uniformity in local variation of the wave parameters features again the filtering effects due to interactions of waves and tidal flat morphology.

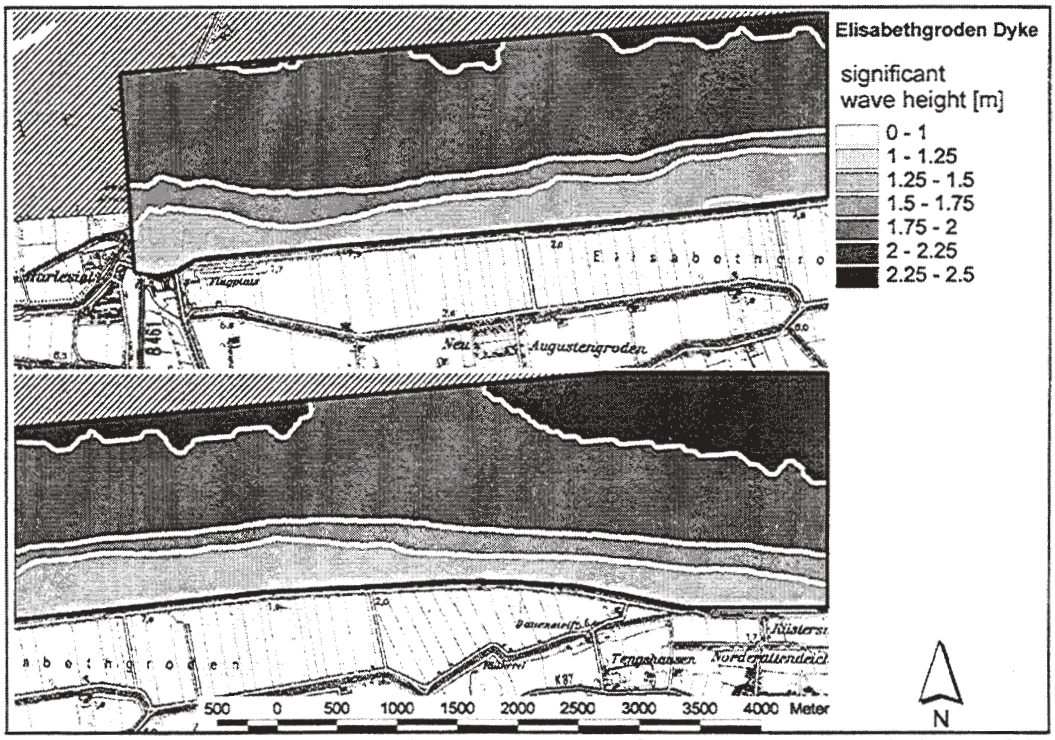

Fig. 10: Significant wave heights H_S (nested model) in the Wadden Sea area close to the Elisabethgroden Dyke

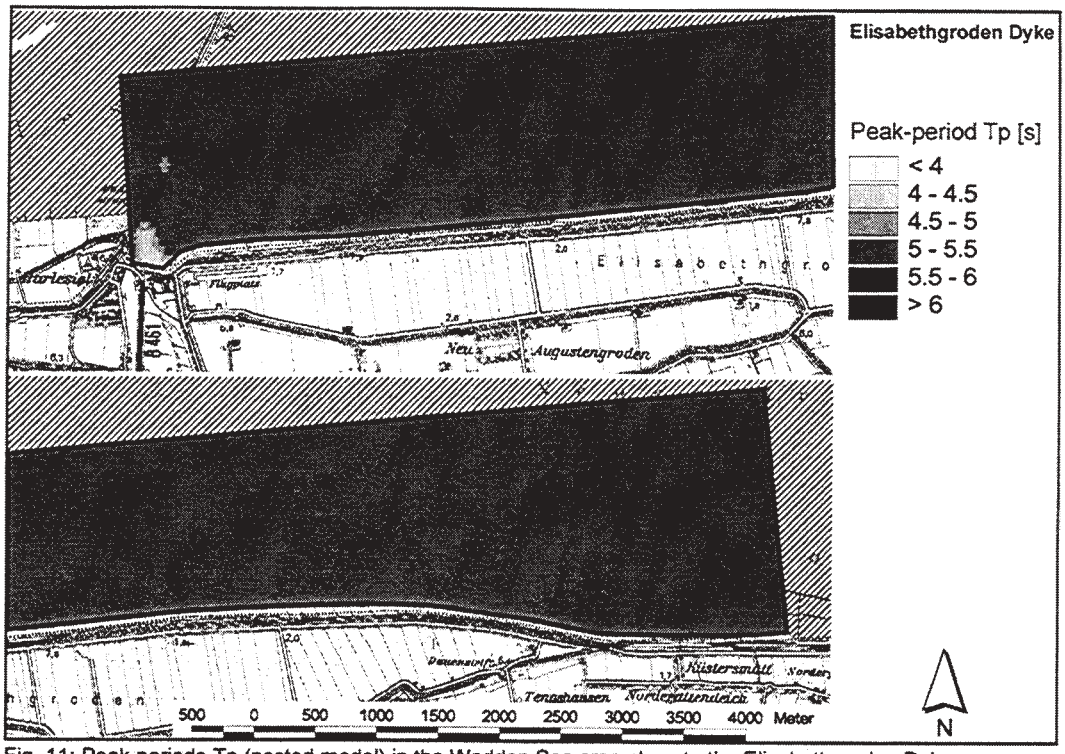

Fig. 11: Peak periods Tp (nested model) in the Wadden Sea area close to the Elisabethgroden Dyke

3.2 Island shoreface

3.2.1 Offshore design wave evaluation

The modeling of the design waves for the Elisabethgroden Dyke taught already the lesson that the wave-morphology-interactions act not everywhere in the coastal area as a limiter. Particularly seaward of the barrier islands an increase of wave energy has an impact on local wave climate. This is in accordance with experience gained earlier from field measurements (Niemeyer 1983).

In line with this perception as a preliminary for the modeling of design waves the effect of distinct offshore wave conditions on the wave climate in the area of interest was investigated. As offshore boundary conditions for the modeling three distinct wave spectra were chosen:

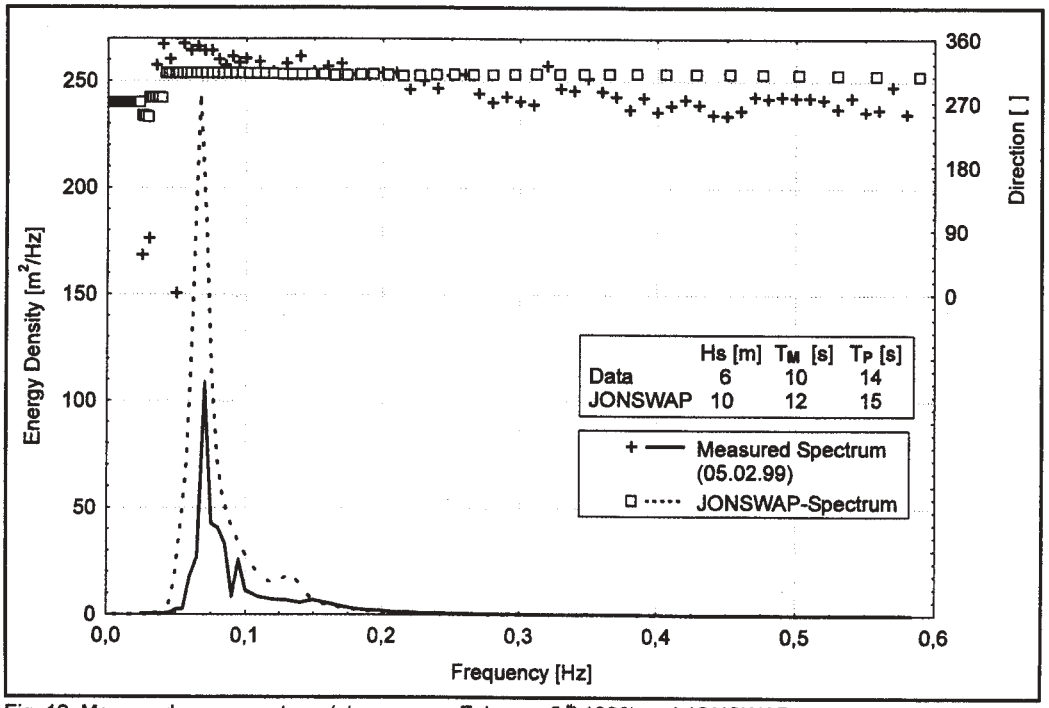

Fig. 12: Measured wave spectrum (storm surge, February 5 th.1999) and JONSWAP-spectrum (H_S =10 m; T_P = 15 s) offshore area

1. Measured spectrum
   with H_S = 6 m; T_P = 14 s; T_M = 10 s;

2. JONSWAP-spectrum
   with H_S = 8 m; T_P = 12 s; T_M = 10 s;

3. JONSWAP-spectrum
   with H_S = 10 m; T_P = 12 s; T_M = 10 s;

The measured spectrum (fig. 12) was chosen since for this storm surge a verification of the SWAN-model is available (fig. 2b). Additionally to the first case another JONSWAP-Spectrum with higher wave energy (fig. 12) was introduced which represents the wave parameters evaluated by statistical relationships for design wind conditions (Niemeyer 1983).

The morphology of the investigation area was reproduced by a model bathymetry covering an area of approximately 6,7 x 12,6 km with a grid size of 80 x 80 m. In order to avoid boundary effect the output area was reduced to approximately 5,9 x 7,4 km. For the computation of the design wave spectra a nested model with a grid size of 20 x 20 m was embedded in the shoreface area (fig. 13).

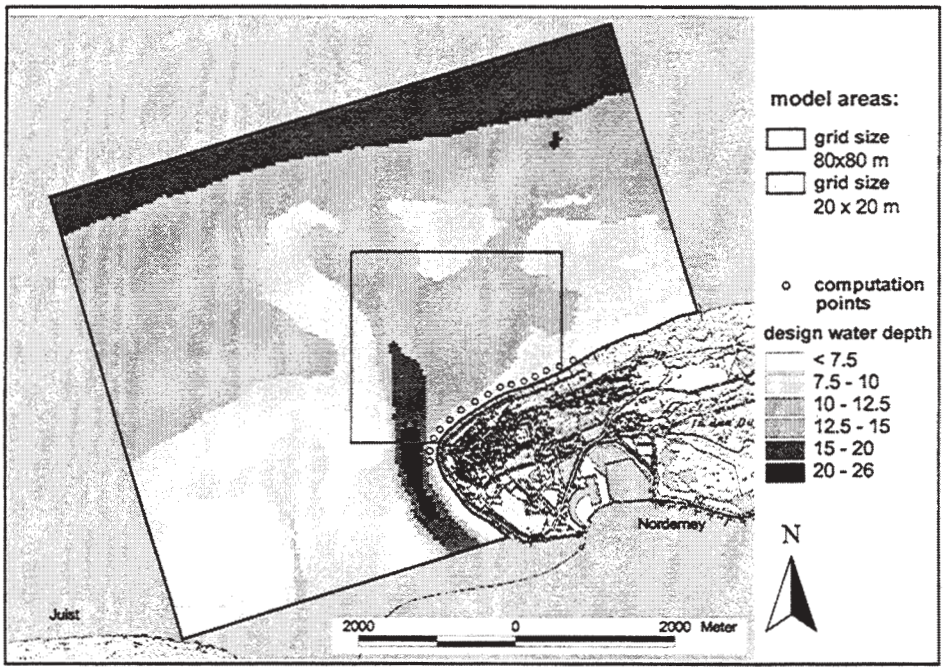

Fig. 13: Dimensions and bathmetry of the wave models Norderney: overall model: grid size 80 x 80 m (output dimensions); nested model: shoreface 20 x 20 m

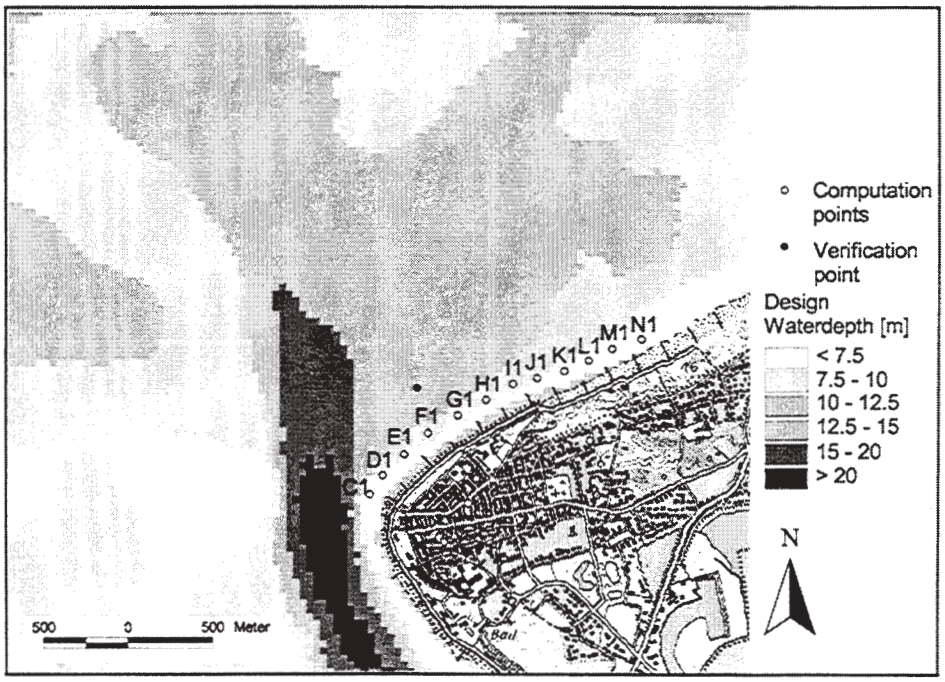

Fig. 14: Bathymetry in the model area with computation points for data transfer

For the data transfer for the steering of the large wave flume tests in the nested model computation points were chosen being representative for stretches of the island's northwestern shore (fig. 14).

Comparing the results at computation points of the model runs with distinct boundary conditions highlights that an increase of offshore wave energy has significant effects on the wave climate on the island's shoreface for the design water level which could not be neglected (fig . 15 + 16): The significant wave heights increase there for the assumed extreme offshore wave condition up to approximately 19% (fig. 15). For the mean periods the figure is even higher with a maximum of about 24% (fig. 16). The consideration of these extreme offshore wave conditions for the redesign of the seawall at the northwestern shore of the island of Norderney is therefore indispensable.

With respect to required input signal for the large wave flume tests beside the wave parameters the spectral shape is also highly important. Since the measured spectra in the offshore area del area have a more complex structure than the JONSWAP-spectrum it is urgently necessary to check if such boundary conditions would create unacceptable simplifications of the design spectra on the island's shoreface. In order to solve this question the spectra modeled with SWAN at the computation point H_1 (fig. 14) by applying the measured spectra on the one hand and the JONSWAP-spectrum for extreme conditions on the other hand as offshore boundary condition were compared (fig. 17).

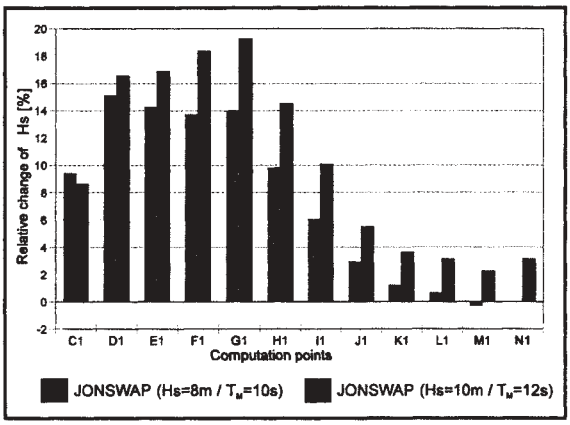

Fig. 15: Relative changes of significant wave heights on the island's shoreface due to higher wave energy in the offshore area (reference: measured spectrum)

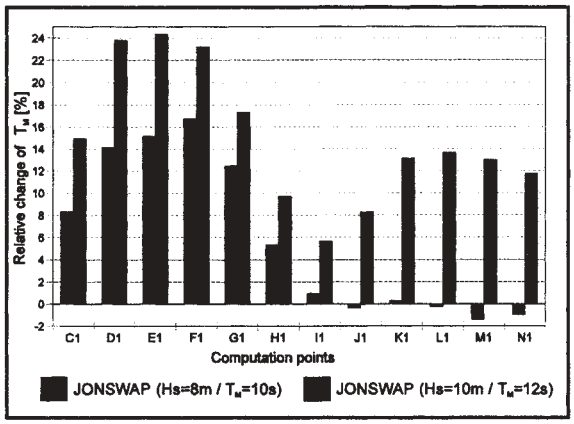

Fig. 16: Relative changes of mean wave periods on the island's shoreface due to higher wave energy in the offshore area (reference: measured spectrum)

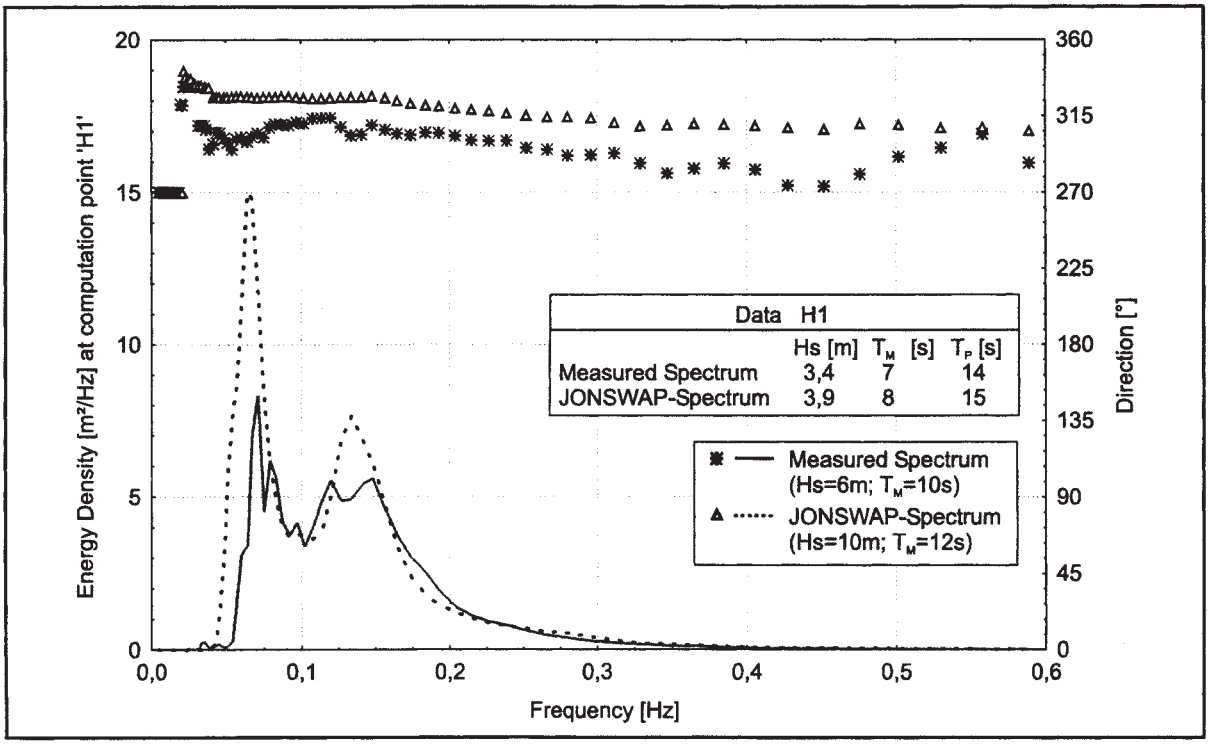

Fig. 17: Comparison of modeled wave spectra at computation point H_1 with distinct offshore boundary conditions

The spectra on the island's shoreface have the same characteristic features: the main energy is bound in two narrow frequency ranges of the same order of magnitude. The measured spectrum has furthermore multi-peaks, but they are on a considerably lower scale than the major ones and are therefore of low importance with respect to loads on structures. Summing up the use of a parametric spectrum for the representation of extreme offshore wave conditions is acceptable for the modeling of design waves in this environment; neglected effects are of minor importance. Major reason are the strong interactions between waves and morphology between the offshore area and the island's shoreface, particularly the intense wave breaking on the ebb delta shoals of the tidal inlet (Niemeyer 1987).

3.2 Design wave evaluation

The model run for the chosen offshore boundary conditions produced the following results for design significant wave heights (fig. 18): From offshore in landward direction first a slightly gradual decrease takes place which is characterized by long stretched contours of wave height isobaths. They get a highly irregular shape after meeting the ebb delta area where they reflect the differences in local wave breaking. Obvious is the penetration of relatively high waves onto the island's northwestern shoreface. This is a resulting effect of the erosion of the ebb delta shoals which has taken place in that area during the last 25 years leading to a significant increase of local wave energy (Niemeyer et al. 1997; Kaiser & Niemeyer 1999). In consequence the seawall experiences in that part of the island's shoreface the relatively highest wave loads.

The change of mean periods due to decreasing water depths in the investigation area is much lesser accentuated than for wave heights (fig. 19): The relative changes from offshore to the island's shoreface are smaller and the pattern of isobaths has a less pronounced irregularity. Therefore the variabilty of the mean periods in the area of interest is rather small.

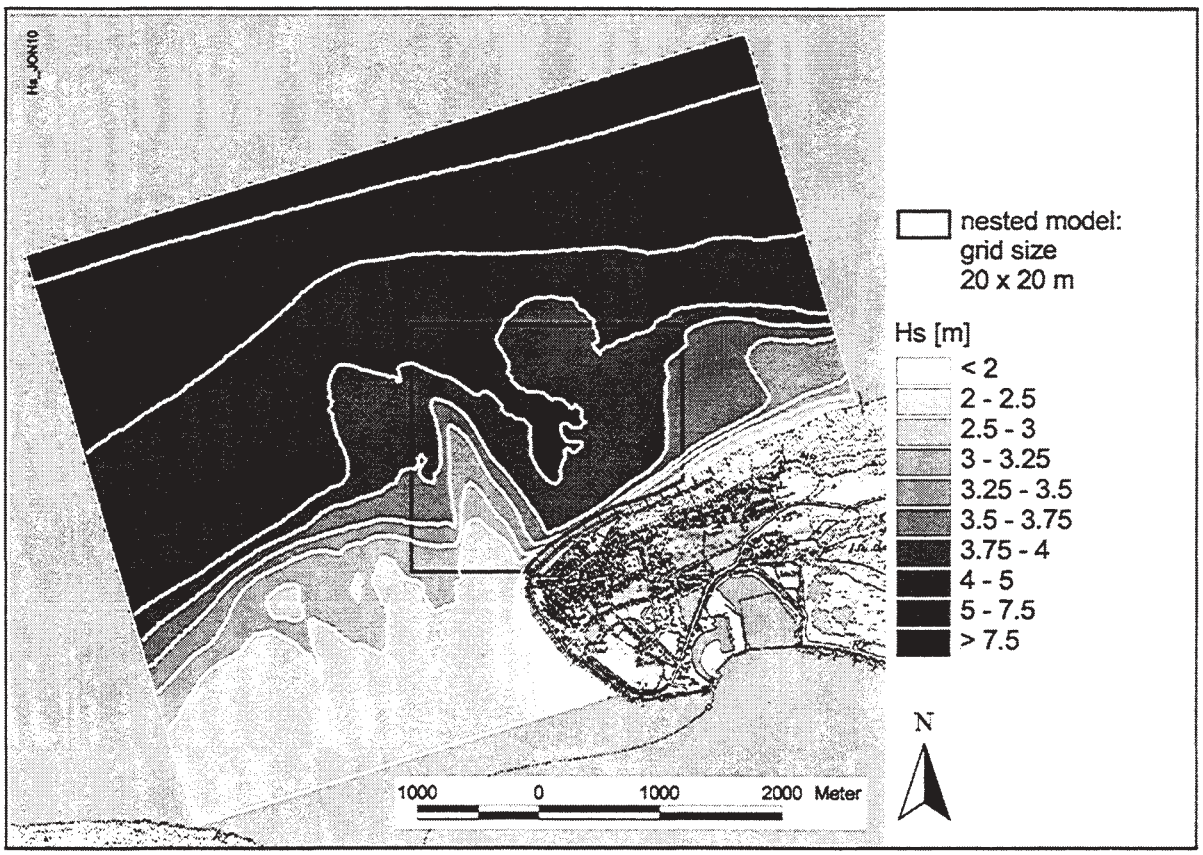

Fig. 18: Significant wave heights for design conditions in the offshore area, in the ebb delta region and on the island's shoreface of the island of Norderney

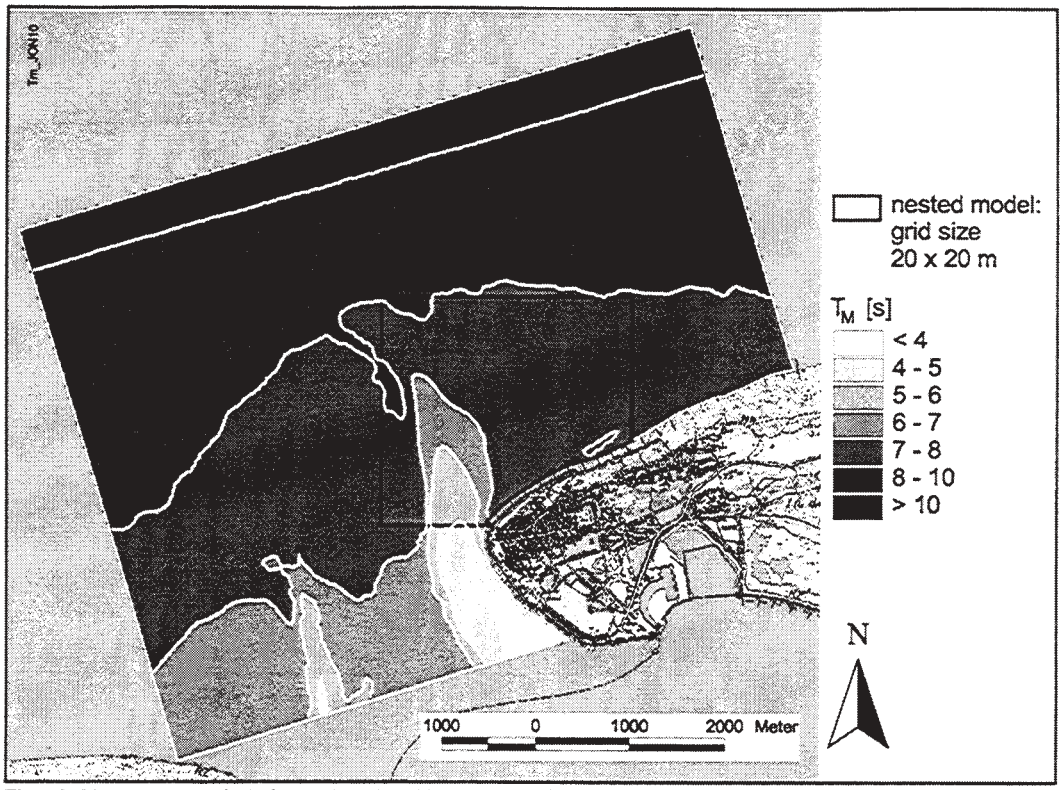

Fig. 19: Mean wave periods for design cionditions in the offshore area, in the ebb delta region and on the island's shoreface of the island of Norderney

3.3 Study of further ebb delta and shore erosion

With respect to experienced changes of local wave climate due to ebb delta erosion additional tests were carried out by implementation of further erosion in the ebb delta area (fig. 20) on the one hand and of the shoreface and beach (fig. 21) on the other hand was implemented in the model topography.

In the ebb delta area a fictitious erosion was step by step introduced: first up to 0,5 m and then up to 0,75 m (fig. 20). After both steps no significant increase of wave parameters on the island's shoreface took place: Obviously the decrease of the ebb delta shoals had already exceeded the ultimate treshhold beyond which no further impact on the landward wave climate will happen.

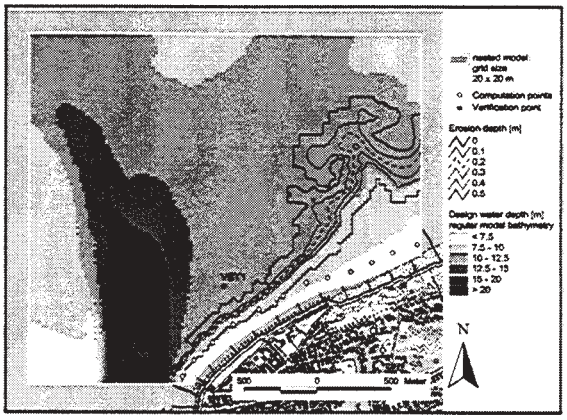

Fig. 21: Implementation of an fictitious erosion on the shoreface and on the beach of the island of Norderney

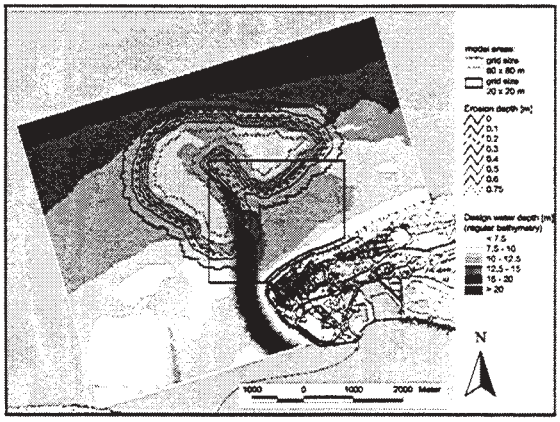

Fig. 20: Implementation of an fictitious erosion on the shoreface and on the beach of the island of Norderney

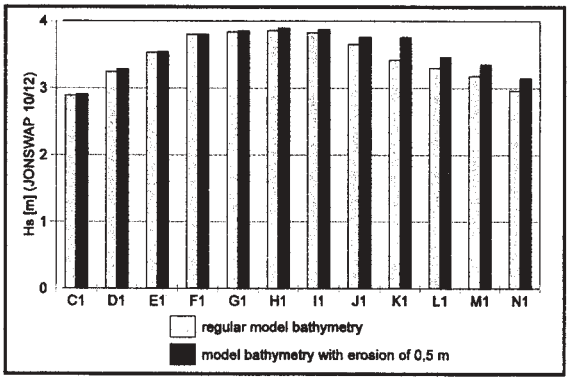

Fig. 22: Effect of a fictitious erosion of shoreface and beach (Fig. 21) on significant wave height

The fictitious beach erosion (fig. 21) had no remarkable effect in the areas with the relatively high wave loads and only a limited one on the significant wave heights in the eastern part of the investigation area (fig. 22).

4. CONCLUSIONS

The evaluation of design waves for coastal protection structures in Wadden Sea areas requires specific feasibility studies in order to overcome the lack of sufficiently long time series of measurements. The application of reliable mathematical wave models is very beneficial; crucial for their successful practical use is the introduction of reliable boundary conditions. Their derivation and introduction for to regions with distinct morphological features was displayed.

The morphology of tidal flats which levels are determined by mid-term interactions with from offshore penetrating waves act during extreme storm surges as a limiter for waves. Therefore wave spectra measured during storm surges can be used to drive mathematical wave models for the evaluation of design waves for dykes at the Wadden Sea mainland coast.

The ebb deltas of tidal inlets act as well as a limiter on waves penetrating from offshore into the coastal areas as tidal flats do. But wave energy dissipation in the ebb delta region is not everywhere sufficiently high for absorbing the effects of extreme offshore wave conditions in total. This is particularly the case if the ebb delta effect on attenuating waves is weakened by severe erosion as happened in the area of the island of Norderney. But obviously there is even for continuous erosion a threshold beyond which a further increase of the from offshore penetrating wave energy does not take place.

The investigations highlighted the enormous progress in the evaluation of design waves for coastal protection structures being achievable by application of third generation wave models with the capabilities of SWAN.

The successful application of SWAN in the Wadden Sea area was possible because

a. verification data were available,

b. the knowledge gained from process-oriented analysis of field measurements was successfully introduced into the set-up of modeling.

5. ACKNOWLEDGEMENTS

These studies were carried out for the 3rd Dyke Community of Oldenburg and the Lower Saxon Agency for Water Management and Coastal Protection-Division Norden. Additionally basic investigations were undertaken in the framework of the research project "Design Waves for Coastal Protection Structures and Dunes" of the GERMAN COMMITTEE FOR COASTAL ENGINEERING RESEARCH (Sponsor: GERMAN FEDERAL MINISTRY FOR EDUCATION AND RESEARCH via the carrier BEO; project-code KIS 004). The authors are greatly indebted to their colleagues Günther Brandt, Detlef Glaser, Anja van Hettinga, Holger Karow and Georg Münkewarf from the CRS Hydrodynamics Section for their assistance and support.

6. REFERENCES

Booij, N.; Ris, R.C. and Holthuijsen, L.H., 1999: A Third-Generation Wave Model for Coastal Regions, Part I, Model description and validation, J. Geoph. Research, 104, C4

Führböter, A, 1982: The Research Facility 'Large Wave Flume' and its tasks. Intermaritec ,82, Hamburg (in German)

Holthuijsen, L.H.; Ris, R.C. and Booij, N., 1998: A Verification of the Third-Generation Wave Model "SWAN". Proc. 5th Int. Worksh. Wave Hindcast. a. Forecast., Melbourne, Fl./USA

Kaiser, R. and Niemeyer, H. D., 1999: Change of Local Wave Climate due to Ebb Delta Migration. Proc. 26th Int. Conf. Coast. Engrg., Copenhagen/Denmark, ASCE, New York

Kaiser, R.; Weiler, B. and Niemeyer, H. D., 2001: Evaluation of Design Waves for Coastal Protection Structures in the Wadden Sea. Proc. 27th Int. Conf. Coast. Engrg., Sydney/Australia, ASCE, New York (in preparation)

Niemeyer, H.D., 1983: Wave Climate at an Island Sheltered Wadden Sea Coast. Res. Rep. MF 0203 Germ. Fed. Min. f. Res. & Techn. (in German)

Niemeyer, H.D., 1987: Changing of Wave Climate due to Breaking on a Tidal Inlet Bar. Proc. 20th Int. Conf. Coast. Engrg., Taipei/R.o.C. Taiwan, ASCE, New York

Niemeyer, H.D., 1991: Case Study Ley Bay: an Alternative to Traditional Enclosure. Proc. 3rd Conf. Coast. a. Port Engrg. i. Devel. Countr., Mombasa/Kenia

Niemeyer, H.D., 1997: Check of the Design Height of Dykes at the Lower Ems Estuary. CRS-Rep. 05/97 (in German)

Niemeyer, H.D.; Gärtner, J.; Kaiser, R.; Peters, K.H. and Schneider, O., 1995: Estimation of Design Wave Run-up on Sea Dykes under Consideration of Overtopping Security by Using Benchmarks of Flotsam. Proc. 4th Conf. Coast.

a. Port Engrg. i. Devel. Countr., Rio de Janeiro/Brazil
Niemeyer, H.D. and Kaiser, R., 1998: Investigations on the design of test slopes of the Elisabethgroden Dyke, Wangerland. CRS-Rep. 10/98 (in German)
Niemeyer, H.D. and Kaiser, R., 1999: Investigations on the Safety of Dykes at the Lower Ems estuary. Arb. Forsch.-Stelle Küste, 13 (in German)
Niemeyer, H.D. and Kaiser, R., 2001: Evaluation of Design Water Levels and Design Wave Run-up for an Estuarine Coastal Protection Masterplan. Proc. 27th Int. Conf. Coast. Engrg., Sydney/Australia, ASCE, New York (in preparation)
Niemeyer, H.D.; Kaiser, R. and Knaack, H., 1997: Effectiveness of a Combined Beach and Shoreface Nourishment on the Island of Norderney/ East Frisia, Germany. Proc. 25th Int. Conf. Coast. Engrg., Orlando,Fl./USA, ASCE, New York
Ris, R.; Holthuijsen, L. H. and Booij, N. (1995): A Spectral Model for Waves in the Near Shore Zone. Proc. 24th Int. Conf. Coast. Engrg., Kobe/Japan, ASCE, New York

WAVE CLIMATE STUDIES FOR THE SOUTHERN INDIAN OCEAN

R. Douglas Scott[1], Rob Del Core[2] and Tad Murty[1]

1. Baird & Associates Coastal Engineers Ltd.
Ottawa, Ontario, Canada
2. Hydrogenics
Toronto, Ontario, Canada

1. INTRODUCTION

Reliable wave information is essential to the design of any coastal facility. A detailed investigation of the wave climate in the southern Indian Ocean in the vicinity of Madagascar has been carried out in support of preliminary design for a port project. Specific objectives of the study included the development of a statistical wave climate that was used to assess port performance, such as harbour wave disturbance and vessel motion, and an extreme wave climate utilized for the design of the port structures.

The site of interest is located along the southeast shores of Madagascar, as shown in Figure 1. Given the limited availability of wave measurements in this region of the world, it proved essential to hindcast the local wave conditions. Madagascar is subject to both swells created within the Southern Indian Ocean as well as seas generated by the southeast trade winds. Tropical cyclones spawned within the southern equatorial region can also impact the island. Based on the these considerations, two types of hindcasts were completed:

1. A ten-year hindcast of the general wave climate within the southern Indian and Atlantic Oceans. The NCEP/NCAR Re-analysis 10 m winds were utilized as the starting point for development of the wind forcing for this modeling effort. As discussed later in this paper, specific modifications were carried out to the NCEP/NCAR winds in order to better simulate the more severe storm events.

2. Simulation of historical tropical cyclone events that have impacted southern Madagascar.

This paper summarizes the methodology and findings of the wave climate study.

2. METEOROLOGICAL CONDITIONS

Madagascar extends from 12°S to 25°S and is about 1,650 km in length, see Figure 1. A dorsal mountain ridge reaching 1,200 to 1,500 m in height, with three isolated massifs above 2,600 m runs north south the length of the island (Griffiths and Ranaivoson, 1972). Two distinct climatic seasons can be distinguished in Madagascar, the winter from May to October and the summer from November to April. Two short intermediate seasons separate these but they are each of less than one-month duration. During winter, or the cool season, the main activity stems from the tropical anticyclonic belt, which is often subject to perturbations from the passage of moving pressure systems from the west to the east. These high pressures produce a deep southeast trade wind and variable patterns over Madagascar.

During summer, the hot season, the situation is more complex: the oceanic anticyclone weakens and subdivides and a ridge of the Arabian anticyclone intermittently affects the north of the Mozambique Channel, while the inter-tropical convergence zone extends its influence over Madagascar. The trade-wind circulation becomes less regular and convective instability develops almost daily in all regions. It is during this season that the depressions and tropical cyclones spawned in the southwest Indian Ocean can, if conditions are right, affect Madagascar (Griffiths and Ranaivoson, 1972).

The principal wind field of Madagascar is the southeasterly trade wind, which stems from the semi-permanent anticyclone (see Figure 2) of the Indian Ocean and exhibits a remarkable regularity from June to August. The trade winds are very humid and bring abundant precipitation to the coast of the easterly slopes. The lower layers of the trade winds are strongly diverted by the topography towards the south of the island. The wind speed has a very marked diurnal variation.

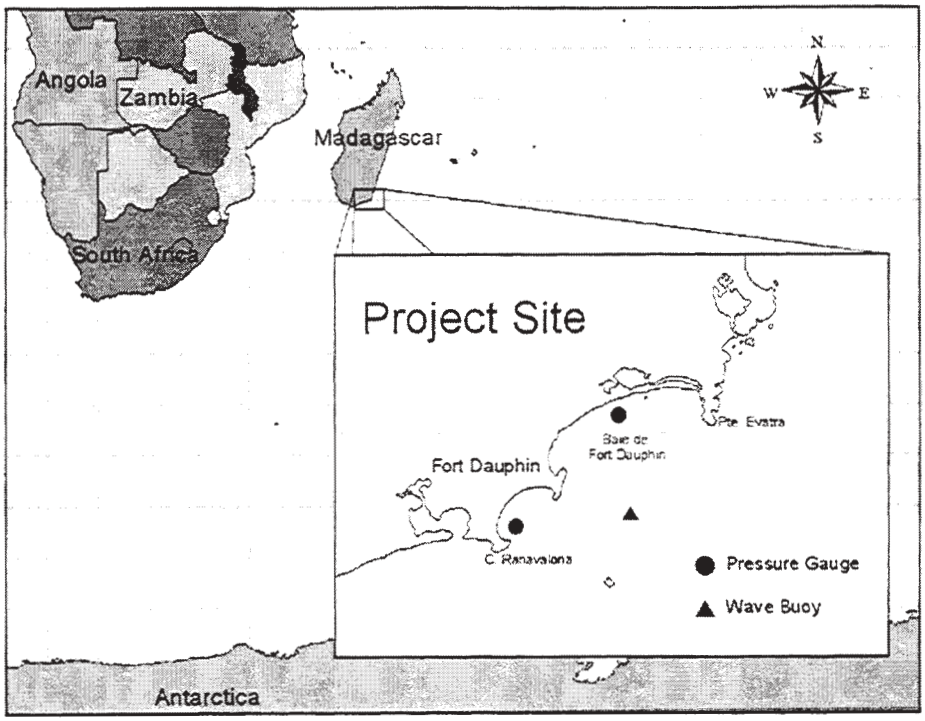

Figure 1. Location Plan

Land and sea breezes are observed, to a greater or lesser extent, around the whole coast. They are especially well defined on the west coast, sheltered from the trade winds, and where the hinderland is such that large diurnal temperature variation results.

Despite the predominance of southeast trade winds in Madagascar, the major wave-generating systems resulting in large wave conditions are due to the passage of cold fronts with their associated low pressure systems that pass to the south of the continent of Africa. There are two permanent high pressure systems, the South Atlantic high (located of the west of South Africa) and the Indian Ocean high (located southeast of Madagascar), that, in conjunction with the cold fronts, dominate the wave generation processes in this region of the world. The low pressure systems that travel from west to east, shift towards the north in winter causing an increase in wave conditions at that time of the year.

Extratropical cyclones affecting Madagascar usually originate in the South Atlantic Ocean between 30°S and 40°S. Their centres travel east-southeastwards and are followed by anticylones travelling eastwards and very often, especially in summer, moving northeastwards around the South African and Madagascar coasts.

Tropical cyclones are especially prevalent during the warm season, and it is principally in the northern half and on the east coast of Madagascar where they are the most violent; however, there is not an area of the island that is sheltered from their influence. Their intensity usually diminishes when they travel over land, but they can be regenerated on reaching the sea again.

3. AVAILABLE WAVE MEASUREMENTS

3.1 Site-Specific Wave Records

Historical wave data for the region were very limited. A few periods of non-directional Waverider measurements were conducted at the project site by others in the period from 1990 to 1992; however, the total data recovery was poor and the Waverider was generally placed in shallow water locations where topographic effects would significantly impact the wave climate.

In support of the port design process, a wave measurement program was initiated in October 1999. A TriAxys directional wave buoy was deployed seven kilometers offshore in 66 metres of water, as shown in Figure 1. In addition, two non-directional pressure wave recorders were installed in approximately 10 meters depth at two nearshore

locations, representing two potential port sites. The nearshore recorders have been in continuous operation since deployment with data retrieval on a monthly basis; however, the buoy has experienced a significant portion of downtime due to mooring failure and subsequent electronic malfunction.

The short period of wave buoy measurements have shown the complexity of the incicdent wave climate in southern Madagascar. In particular, detailed evaluation of the directional spectra from the buoy has shown that the wave climate is often bi-modal in nature with long period swells from southern to southwestern directions, and shorter period seas from easterly to southeasterly directions, representing the contributions of the southern extratropical cyclones and the local trade winds, respectively. Figure 3 presents a wave rose for the TriAxys buoy measurements. It may be noted from this figure that the wave conditions during the measurement period (October to December 1999) were more dominated by south and south-southwest swells. The median significant wave height and peak wave period at the buoy were 1.9 metres and 10.5 s, respectively, for the

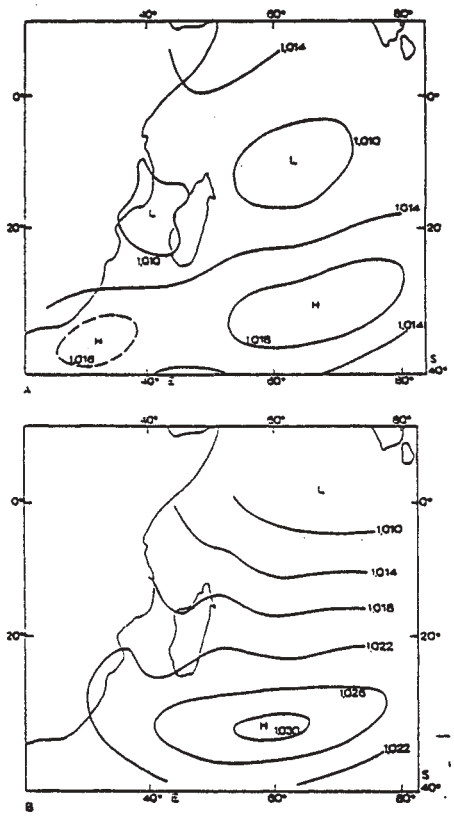

Figure 2. Mean Pressure Patterns
Top: January; Bottom: July
[from Griffiths and Ranaivoson, 1972]

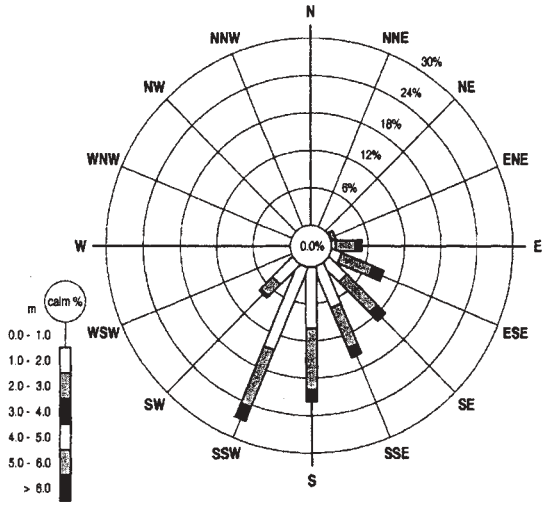

Figure 3. Wave Rose from Buoy Measurements

time period from October 1999 to March 2000 (with some gaps in data coverage).

The data from the existing wave measurement program have been extensively compared to the results of the wave hindcast model, as is discussed later in this report.

3.2 Other Regional Wave Data

The South African Centre for Scientific and Industrial Research (CSIR) maintains a series of wave buoys along the coast of South Africa. The CSIR kindly supplied summary statistics and digital wave time series data for a buoy located in 50 metres of water offshore of Durban. The buoy has been operational over an eight year period with 78% data recovery. The median significant wave height at the buoy was 1.6 metres and the largest recorded significant wave height was 5.6 metres.

3.3 Satellite Wave Data

Satellite altimeter wave data from the Geosat and Topex/Poseidon missions were also employed in the wave climate study. Several quality control procedures were applied to the altimeter data in order to eliminate spurious measurements prior to statistical analysis of the data. The satellite data were derived from the average wave height measurement in each satellite pass through a two degree box (25-27°S, 46-

48°E) at southern Madagascar. The Topex data had median and maximum significant wave heights of 2.7 metres and 6.4 metres, respectively.

Figure 4 gives a summary of wave height exceedence for the various offshore wave data sources. Note that the wave buoy was located a distance of approximately 7 km from shore while the satellite data was for a 2° by 2° region to the south of the site.

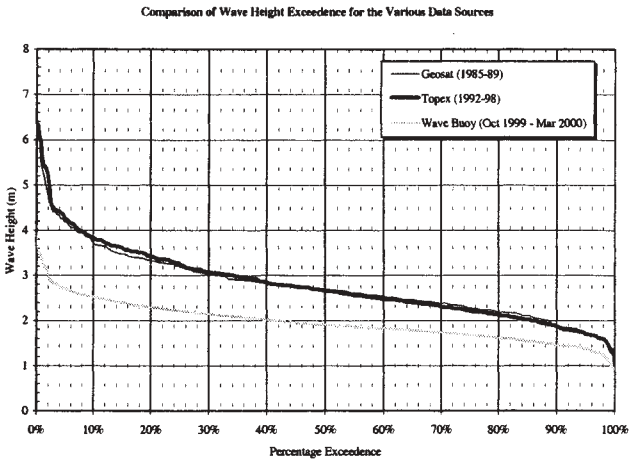

Figure 4. Exceedence Plot of Data Sources

4. WAVE MODELLING OF THE SOUTHERN INDIAN OCEAN

4.1 Model Description

The WAVAD wave model, as summarized in Resio (1981) and Resio and Perrie (1989), was used for all of the hindcasting carried out in this study. WAVAD is a second generation (2G) spectral wave model that maintains an equilibrium between the wind source and non-linear wave energy flux with an assumed f^4 shape for the wave spectrum. The non-linear wave interactions are represented as a momentum flux to the forward face (frequencies less than spectral peak) of the spectrum based on a constant proportion of the energy transferred out of the mid-range frequencies. Wave-wave interactions also transfer energy to the high frequency region of the spectrum where it is assumed that energy is lost due to breaking processes. Wave propagation is handled in WAVAD by means of a first order upwinding scheme. The model can simulate both deep and shallow water physics (refraction); however, only deep water processes were considered in this investigation.

In the wave hindcast model, the directional wave energy spectrum is computed at each grid point from which wave statistical parameters (eg. Hmo, Tp, MWD) were derived for pre-selected archival points within the grid area.

Various sizes and resolutions of model grids were tested in the preliminary stages of this study. The final numerical model grid covered a domain extending from 50.0° W to 110.0° E and from 0.0° to 70.0° S with a resolution of 1.0°. The model bathymetry for much of the Southern Indian Ocean was derived from a global (ETOPO30) database. Figure 5 shows a plan view of the final numerical model grid.

A total of twenty-three frequencies were used for the hindcasts in conjunction with a directional resolution of 22.5° (16 direction bands). The frequencies were spaced at a constant ratio of 1.1 starting at 0.038 Hz.

A one-hour time step was employed for all of the simulations, and the ten year hindcast required approximately 35 hours of computation time on a high-end PC.

4.2 The Wind Field

Wind fields derived from the NCEP/NCAR Reanalysis Project data set (Kalanay et al., 1996) were used as the primary driving mechanism for the wave model. The U (east-west) and V (north-south) wind fields at 10 m elevation above ground were extracted from the NCEP/NCAR global database for a grid network that covered the eastern South Indian Ocean region and the South Atlantic Ocean. The NCEP data are available on a 6-hourly basis for a grid resolution of 1.875° longitude by an average 1.905° latitude (actual grid is Gaussian), and were interpolated onto the more refined WAVAD input grid using a four-point bi-linear interpolation scheme. This approach provided a driving wind field for the model at six-hour intervals. The WAVAD model automatically interpolated the six-hour wind fields to the selected model time step of one hour.

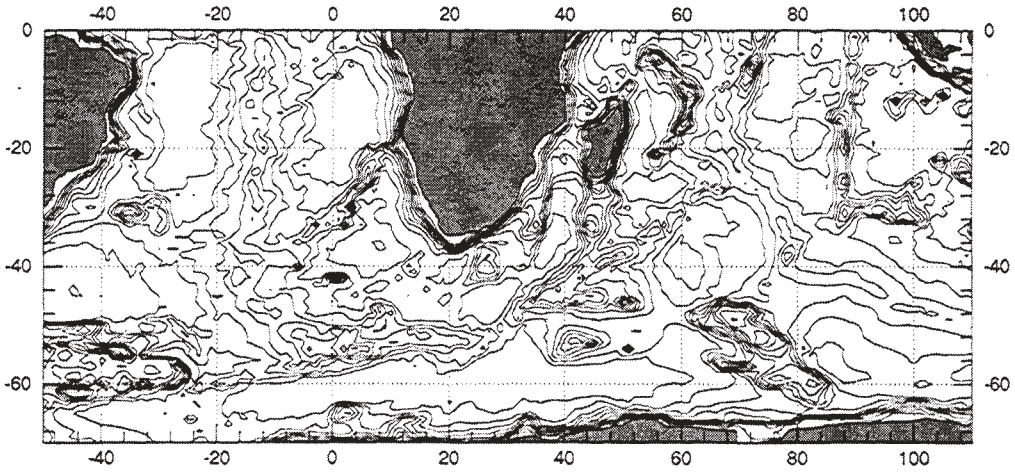

Figure 5. The Numerical Model Grid

4.3 Initial Model Calibration

Cox et al. (1998) showed that NCEP 10 m surface wind fields produced the least biased and most skilled hindcasts of the various NCEP parameters; however, it was noted that the hindcasts tended to systematically underestimate storm peaks. It has been long recognized that wind data provided in global databases such as that of the NCEP/NCAR Reanalysis project cannot appropriately represent certain meteorological phenomena due to limitations in spatial and temporal resolution. In particular, the intensity of severe extratropical cyclones and tropical cyclones will tend to be underestimated. As such, it was recognized early on in the study that tropical cyclones would be hindcast separately using a much more refined wave model grid and a specialized model for tropical cyclone winds.

As noted previously, the swells generated by extratropical events in the southern ocean are critical to defining the wave climate in southern Madagascar. As a first step in the modeling process, the winds provided in the NCEP data set were compared to measured winds in the southern oceans, and a series of short trial and error wave simulations carried out in which a wind speed adjustment factor was applied to the NCEP wind speeds at each grid point. This wind speed factor, suggested D. Resio (2000), had the form of:

$$U_{model} = U_{NCEP} * (1 + (U_{NCEP}-U_{threshold})*F) \quad (1)$$

Where U_{model} is the wind speed input to the wave model, U_{NCEP} is the 10 m wind speed as interpolated from the NCEP data set, $U_{threshold}$ is the minimum wind speed at which the factor is applied and F is the wind speed factor. The final wave model simulation used a factor of 0.028 and a $U_{threshold}$ of 15 m/s. The effect of this factoring expersion was to enhance wind events only above the predetermined threshold.

Some initial difficulties were experienced in the magnitude of the swell developed within the model, and experimentation was carried out with the proportionality factors affecting the momentum flux from the mid-frequencies to the forward face of the spectrum. The impact of variations in these factors was explored through numerous model runs and comparisons with recorded datasets.

The WAVAD output was systematically compared to wave buoy measurements at the site as well as Topex altimeter data. Time series of height and period as well as wave height and period exceedence plots where used to assess model performance. Statistical calculations such as the root mean square error (rms) and bias between measured and computed data provided an additional performance metric for comparison.

Figure 6 shows a typical snapshot of the modeling results.

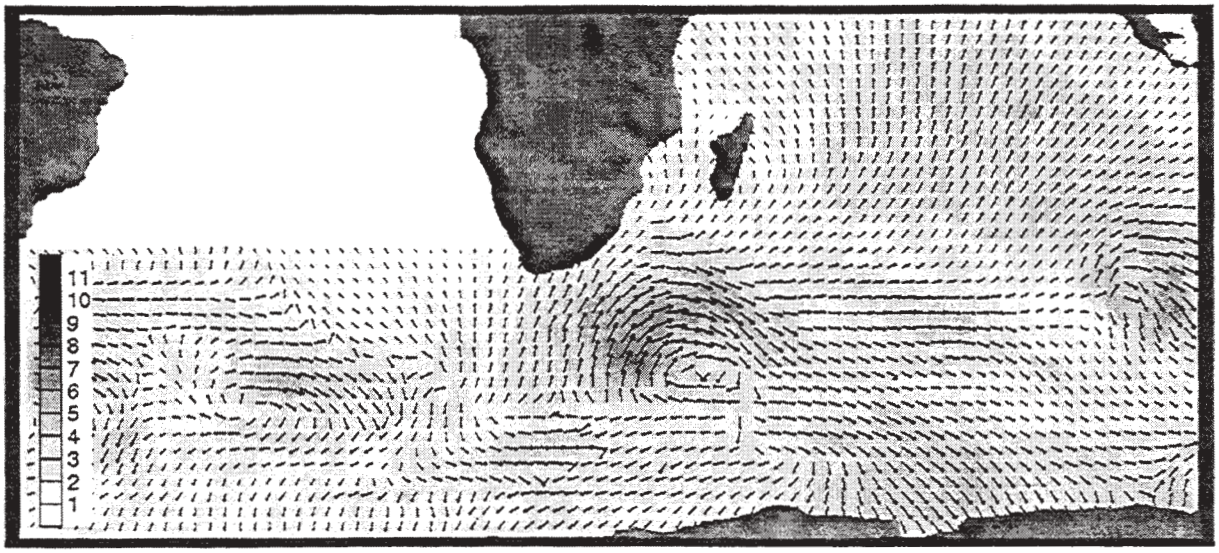

Figure 6. Typical Model Result (June 1990)
[Note: mid-Atlantic waves not computed in model]

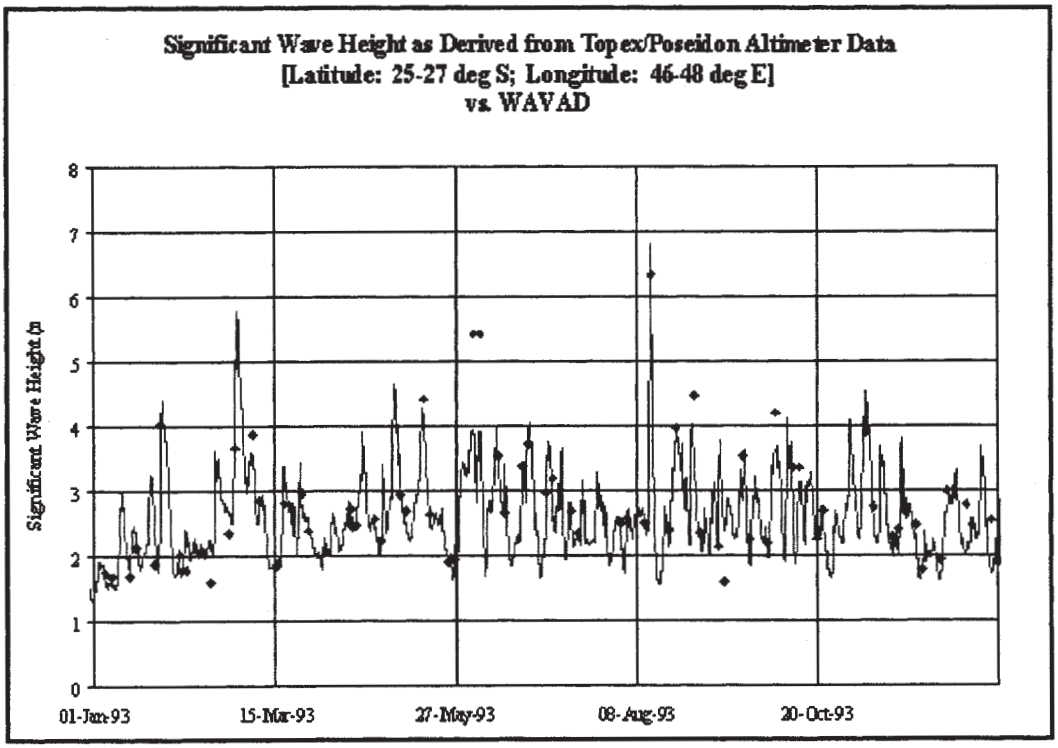

Figure 7. Comparison of Hindcast Results to Topex Data

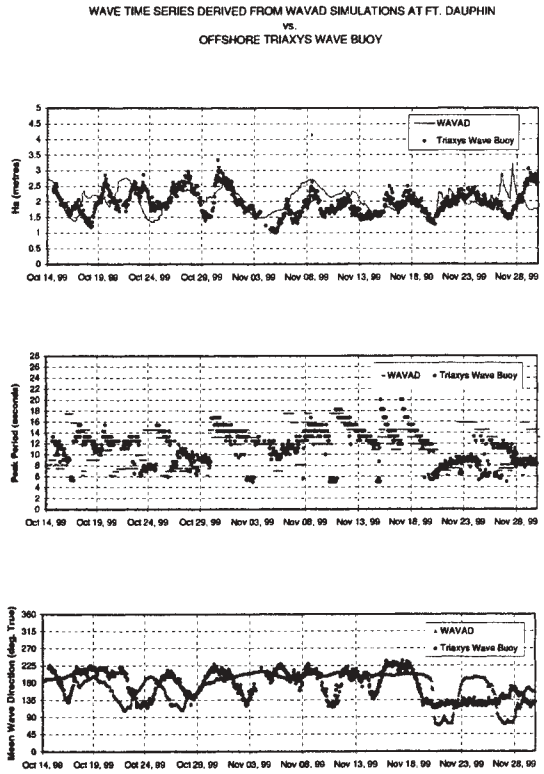

Figures 7 to 9 present comparisons of the modeling results against the Topex altimeter data and the short

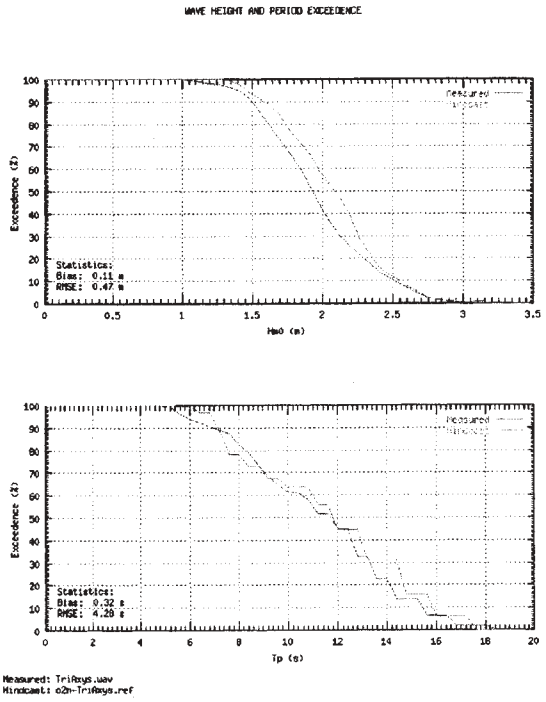

Figure 9. Comparison of Exceedence Plots for WAVAD Results and Buoy

record of measured waves at the site. The Topex comparison showed that the calibrated model underestimated the wave height with a bias of 0.2m and an associated RMS error of 0.6m. The A three month period of comparison between the numerical model and the measured buoy data indicated a bias in significant wave height of 0.1 metres and in peak wave period of 0.3 s. Model parameters that yielded the above results where used as calibrated parameters for the subsequent more detailed analysis of storms and the final hindcast simulation.

4.4 Detailed Analysis of Key Storms

Once the initial calibration of the wind field had been completed, detailed analysis of the wind fields was conducted for twenty of the largest storms. These analyses were supported by synoptic charts obtained from the South Africa Weather Bureau, and ship- and land-based observations of meteorological conditions. The vessel observations were relatively sparse in this region.

Based on principals of meteorological continuity, the NCEP wind fields input to the WAVAD model were

Figure 8. Time Series Comparisons with Buoy

varied and the individual storms re-run. The storm time series were then re-incorporated into the overall wave hindcast time series.

4.5 Hindcast Results

The final results of the10 year hindcast showed the complex, bi-modal nature of the wave climate in Southern Madagascar, and the seasonal variation in magnitude between the swells generated in the lower latitudes versus the waves created by the southeast trade winds (see Figure 10).

The 10-year hourly wave climate was subsequently transformed to nearshore using a nearshore spectral model and various analyses of vessel motion and port downtime performed.

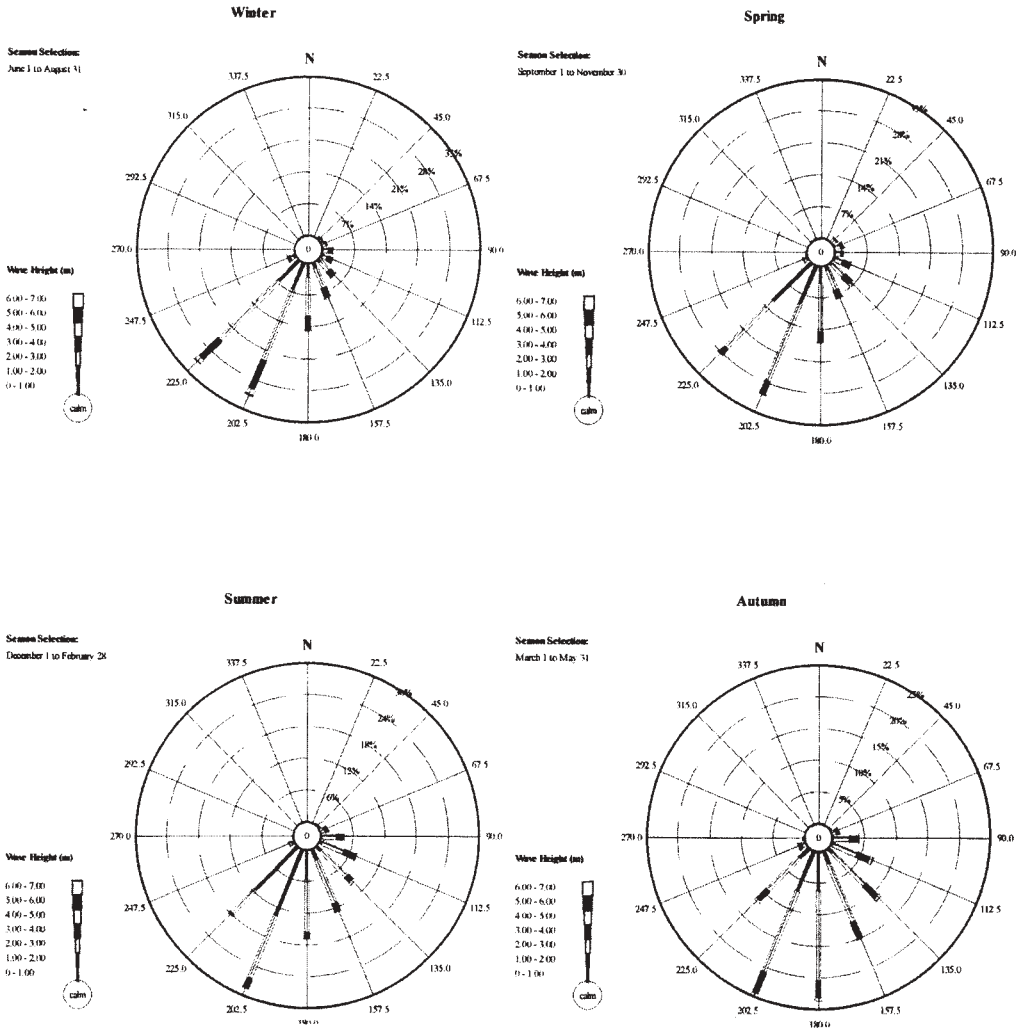

Figure 10. Seasonal Wave Roses Developed from Model Results

5. TROPICAL CYCLONES

5.1 Introduction

A key consideration in development of an extreme wave climate at the Madagascar site was the passage of tropical cyclones. Tropical cyclones are generated in the southern equatorial belt of the Indian Ocean, generally traveling westward and southward. The cyclones often re-curve to the south and east prior to reaching the island of Madagascar and the cyclone intensity typically diminishes with latitude; however, there have been a number of severe tropical cyclone events that have severely impacted the southern island. Figure 11 shows the tracks for all tropical cyclones of greater than Category 3 intensity from 1950 to 1995.

Historical tropical cyclone data from the Indian Ocean is limited compared to other regions of the world. A global database of tropical cyclones was obtained from the U.S. National Oceanographic and Atmospheric Administration (NOAA), covering the period from 1848 to 1998. For time periods prior to 1980, there is information on the cyclone tracks and the magnitude of the storm is often only documented at the location of the storm's greatest intensity.

In a review of the historical cyclones, it was noted that the average number of cyclones per year prior to about 1950 was significantly less than recent years, possible due to the reduced detection and tracking technology. As a consequence, data prior to 1950 were not considered due to the lack of detailed information, in addition to the suspicion of unreported events.

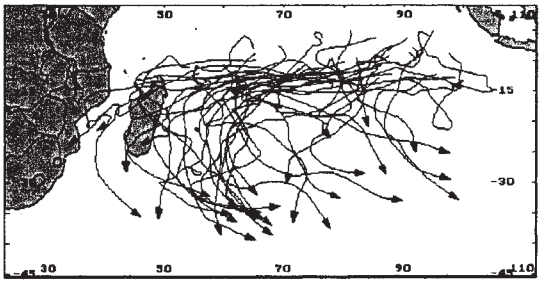

Figure 11. Tracks of Tropical Cyclones Greater Than Category 3 (1950-95)

As a starting point in the cyclone analysis, a simplified parametric model of hurricane wave generation was run for all of the historical tropical cyclones in the period from 1950 to present. Using this technique, the tropical cyclones that most significantly impacted southern Madagascar during that period could be determined. The identified tropical cyclones were then simulated in detail using the WAVAD numerical model.

5.2 Numerical Modelling of Historical Tropical Cyclones

The WAVAD 2nd Generation wave model was used for the simulations. In this case, a much more refined numerical grid was employed that focused on the southern shoreline of Madagascar. The grid had 100 longitudinal grid points and 80 latitude grid points at an equal resolution of 0.135°. A time step of 15 minutes was used in all of the simulations. A total of 23 frequencies were employed in conjunction with a directional resolution of 11.25° (32 sectors).

The wave fields used to drive the WAVAD model were derived from a parametric representation based on the work of Holland (1980). Inputs to the procedure included the tropical cyclone track, the maximum wind speed, the central and ambient atmospheric pressure and the estimated radius to maximum winds. The Holland formulation includes two scaling parameters which allow the cyclone pressure and wind fields to be altered to fit any available measured data.

5.3 Detailed Simulation of Tropical Cyclones

From the cyclones identified to be the most significant at Fort Dauphin, ten selected events were simulated using the WAVAD model. Wave statistics were recorded at the site in order to assess the wave height, period and direction as the cyclone event progressed. Table 1 presents the maximum wave heights that were recorded during each of the storm simulations.

Table 1
Wave Heights from Top Ten Recent Storms

Storm	Maximum Hm0 (m)	Tp (s)
Deborah 75	6.33	10
Edwige 80	4.11	8.3
Kolia 80	4.89	10
Helyette 81	5.52	10
Jinabo 89	2.29	12.5
Aliberi 90	2.25	11
Dessili 93	3.05	8.3
Litanne 94	2.81	12.5
Edwige 96	2.64	11
Gretell 97	6.05	10

None of the tropical cyclone-generated wave conditions could be verified against recorded data, although it is noted that the approach employed in this study has been successfully at other locations around the world (notably the Caribbean).

The peak wave heights from these wave simulations were combined with the results from lesser tropical cyclone events identified using the parametric model, and the composite list of independent cyclone wave events was statistically analyzed using a peak over threshold (POT) extreme value analysis. This analysis gave an estimate of the 100 year significant wave height as 7.0 metres.

5.4 Tropical Cyclone Deborah

Tropical cyclone Deborah in 1975 was identified as the most severe event to impact the region of interest in the last 50 years. This was also supported by local anecdotal evidence. The peak of the storm occurred at 24.7° S latitude, 51.4° E longitude, at a position approximately 440 km east of the site on January 24, 1975 at 12:00 UTC. At the peak of the storm, maximum wind speeds were approximately 108 knots, and the central pressure was 960 hPa. The path of the track was marginally south of being a

direct hit on the site, with the point of closest approach about 25 km south of the site at about 04:00 UTC on January 25th.

There were no land-based or airborne observations of maximum wind speed or central pressure of Deborah as it approached the site of interest; however, wind estimates and pressure measurements from the single ship observation in the region provided some confirmation that the tropical cyclone maintained its intensity as it approached landfall on Madagascar. Based on the above information, it was assumed that the strength of the cyclone did not significantly diminish as the cyclone approached the site. An estimate of 100 knots and 960 hPa was used to describe the storm as it passed Fort Dauphin. The WAVAD model provided an estimate of the maximum wave height immediately offshore in the order of 6.3 m.

6. CONCLUSIONS

Statistical and extreme wave climates in the vicinity of Southern Madagascar have been estimated by means of a second generaton wave model. This has been achieved using two levels of wave hindcasting involving (1) the simulation of waves generated in the Southern Indian Ocean and (2) detailed modeling of critical tropical cyclone events using a locally refined grid. The 10 m winds produced in the NCEP/NCAR Re-analysis Project were successfully employed as the basis for the overall hindcast; however, modifications to the wind fields were carried out to enhance the hindcast performance.

Where possible the wave model has been calibrated or verified against available data; however, it has been noted that there is a paucity of meteorological and wave data in this region of the world.

As further data are collected through the active wave measurement program, the hindcast will be updated and improved.

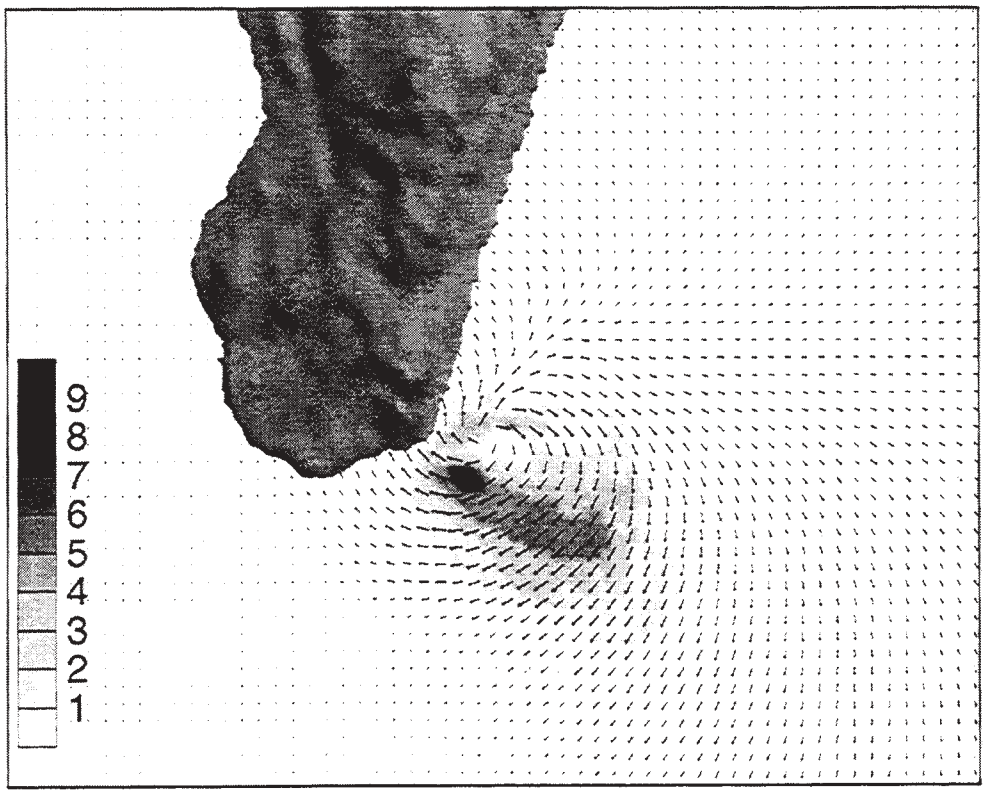

Figure 12. Simulation of Tropical Cyclone Deborah

7. REFERENCES

Cox et al., 1998 : Evaluation of NCEP/NCAR Reanalysis Project Marine Surface Wind Products for a Long Term North Atlantic Wave Hindcast. Proceedings of the 5th International Workshop on Wave Hindcasting and Forecasting. Melbourne, Fl. January 26-30.

Griffiths, J.F. and R. Ranaivoson, 1972 : Madagascar, " World Survey of Climatology". Vol 10, Chapter 14. Edited by J.F. Griffiths, Elsevier.

Kalnay, E. et al. 1996 : The NCEP/NCAR 40-Year Reanalysis Project. Bull. AMS. 77(3). 437-471.

Holland, G., 1980 : An Analytic Model of the Wind and Pressure Profiles in Hurricanes. Monthly Weather Review. Volume 108. 1212-1218.

Ramage, C.S., 1984 : Climate of the Indian Ocean North of 35.5°S, "World Survey of Climatology". Edited by H. Van Loon, Elsevier. 603-671

Resio, D., 2000 : Personal Communication.

AN APPROACH TOWARDS A 40-YEAR HIGH-RESOLUTION WAVE HINDCAST FOR THE SOUTHERN NORTH SEA

Ralf Weisse and Gerhard Gayer

GKSS Research Center
Institute of Hydrophysics
Geesthacht, Germany

1. INTRODUCTION

In the marine environment the planing of the sustainable development of economic activities requires long term information about the prevailing environmental conditions. Detailed knowledge on local wave conditions is an essential prerequisite for designing marine and coastal protection structures. To estimate the risk which emerges from local wave conditions knowledge on both, the wave climatology and the extreme events is necessary.

Thus a couple of attempts have been undertaken within the last few years to provide reasonable reconstructions of the past wave conditions. One of the more prominent attempts to reconstruct the wave and storm climate over a longer period was provided by the WASA Group (WASA 1998). Their goal was to prove or disprove hypotheses of a worsening storm and wave climate in the Northeast North Atlantic. The changes in the wave climate were assessed using a state-of-the-art wave model driven by wind analyses over a period of 40 years (1955-1994) (Günther et al. 1998).

Since the project was mainly focused on changing waves and storms (i.e. on identifying trends) only limited attention was paid to the exact hindcast of a particular wave or storm event. In addition, the atmospheric forcing suffered from a lack of inhomogeneities along the reconstruction period (Günther et al. 1998) and for coastal applications the spatial and the temporal resolution of the reconstruction is relatively coarse (0.5° × 0.75°). However, even with these shortcomings the WASA data set has proven to be extremely useful and was requested frequently, often being the only source of information available for wave climate studies at many places along the European Coast.

In this study we introduce the European project HIPOCAS (Hindcast of Dynamic Processes of the Ocean and Coastal Areas of Europe) which was set up to overcome several of the shortcomings of the WASA record. The project is focused on high-resolution wave hindcasts and climatologies in European Coastal Areas using a more homogeneous wind forcing. We present and discuss the approach and the work that will/has been undertaken for that part of the project which is focused on the Southern North Sea. In section 2 we briefly describe the methodology and the general approach towards the wave hindcast. Some preliminary results are presented in section 3. A summary and preliminary conclusions are provided in section 4.

2. METHODS AND GENERAL APPROACH

The purpose of the study is to provide a reasonable reconstruction of the wave conditions and the wave climate over the past decades for the European Coastal Areas. For the Southern North Sea we therefore have adopted the following approach:

AUTHOR INDEX TABLE OF CONTENTS

2.1 *Atmospheric forcing*

An essential prerequisite for obtaining a reasonable reconstruction of the wave conditions and the wave climate is the high-quality of the driving wind fields. While the wind analysis used in WASA still suffered from some inhomogeneities due to changes in the analysis system or the migration from manual to automatic analysis (Günther et al. 1998) these problems have been overcome recently when the data from the global reanalyses projects (Kalnay et al. 1996, Gibson et al. 1996) became available. In these reanalysis projects global atmospheric circulation models were used for reanalyzing existing observational data back in time for some decades using a frozen state-of-the-art data assimilation system and an enhanced observational data base which additionally comprises observations which were not available in real time. Presently such global reanalyses products have typical spatial resolutions of roughly 200 km and the data are provided every 6 hours. So far, the NCEP reanalysis (Kalnay et al. 1996) comprises the longest available reanalyzed data set (1948 until now).

While these reanalyses provide a useful product for a variety of studies, their spatial and temporal resolution is too coarse for wave studies in coastal areas. For this project, we therefore introduced an additional step to obtain high-resolution wind fields from the NCEP reanalysis and to simulate the regional features of the wind field in more detail: A regional atmospheric model (RAM) was nested and driven by the NCEP reanalyses at the lateral boundaies. The model covers Europe, the entire North Sea and large parts of the North Atlantic (von Storch et al. 2000). The spatial resolution applied was about 50 × 50 km and the modeled wind fields were stored every hour. This way the spatial resolution was increased by a factor of about 16 and the temporal resolution by a factor of 6 compared to the driving NCEP reanalysis. The model was integrated for the entire NCEP reanalysis period.

In order to obtain the best possible reconstruction of the local wind fields a method called spectral nudging (von Storch et al. 2000) was used for the RAM integrations. It differs from the conventional approach for RAM integrations in the following way: In the conventional approach boundary conditions are forced upon the RAM at the lateral boundaries only. In the spectral nudging approach an additional forcing in the interior of the model domain is provided besides the forcing at the lateral boundaries. The additional forcing is provided by adding nudging terms in the spectral domain which have maximum efficiency for large scales and no effect for small scales. Also the efficiency varies with height and the variable considered such that there is no forcing for heights below 850 hpa.

The effect of the spectral nudging is demonstrated in Figure 1. A number of ensemble calculations with slightly varying initial conditions were carried out for January 1993 using the conventional and the spectral nudging approach (Weisse et al. 2000b). These simulations clearly demonstrate the high internal variability of the RAM at some synoptic situations and its sensitivity to the initial conditions (cf. eg., Rinke and Dethloff 2000 or Weisse et al. 2000a). While there is a large variability of the deviations between the modeled and the observed wind field when the conventional approach is used this variability is clearly reduced in the spectral nudging approach. For periods with high internal variability the deviations between the modeled and the observed wind speeds are on average smaller if the spectral nudging approach is used. Sometimes the deviation of an individual realization from the ensemble using the conventional approach may be smaller, however, the solutions for the spectral nudging approach stay closer together. Since ensemble calculations are much too expensive for a multidecadal reconstruction of the wind field the spectral nudging approach provides higher confidence if only one realization of each ensemble can be computed. Weisse et al. (2000b) showed that such numbers as bias or root-mean-square error were on average indeed reduced if the spectral nudging approach was used.

For the purpose of weather forecast spectral nudging comprises a sub-optimal method since ideally one would like to directly assimilate local

AUTHOR INDEX TABLE OF CONTENTS

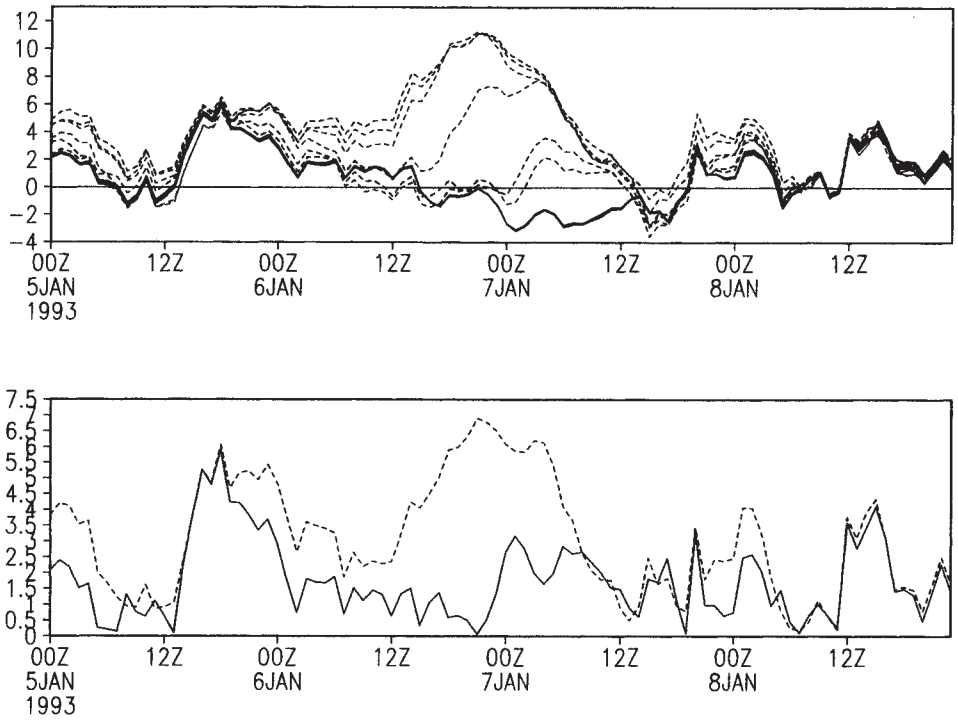

Figure 1: Top: Difference between the observed and modeled wind speed in ms^{-1} at Scharhoern from 05 January 1993 until 09 January 1993 for 6 simulations using the conventional approach (dashed) and 6 simulations using the spectral nudging approach. The 6 simulations for each approach differ by their initial conditions. Bottom: Root-mean-square distance between the observed and the modeled wind speed in ms^{-1} at Scharhoern for the 6 simulations using the conventional approach (dashed) and 6 simulations using the spectral nudging approach (solid).

observational data which had little or no impact on the global reanalysis (von Storch et al. 2000). Since such a scheme is technically demanding and often not feasible, spectral nudging may be considered as a "zero-order" data assimilation technique.

2.2 Hydrodynamical Modeling

For waves the Southern North Sea must be considered as being primarily a shallow water area. Therefore the tidal water level fluctuations will comprise an important constituent for the quality of the wave reconstructions. This is demonstrated in Figure 2. It can be obtained that in general the observed wave height is reproduced reasonably by the simulation. However, the observations clearly show some fluctuations which are associated with the water level fluctuations due to tides. If these fluctuations are removed from the observations by averaging over the tidal period a much better agreement between observations and simulations can be obtained.

However, for this study we want to reproduce also the tidal fluctuations since we are interested also in the extreme wave events. Therefore we are going to use the wind fields produced and described in section 2.1 in cooperation with the Bundesanstalt für Wasserbau (BAW) to drive a high-resolution hydrodynamical model for the North Sea. This model is a finite element model (TELEMAC2D) used routinely by some German coastal authorities and has a resolution of a view kilometers in the Northern North Sea which increases towards the German Bight were it finally reaches a few hundred meters. The model domain comprises the entire North Sea. External surges will be taken into account by assimilating water level observations at Aberdeen. Initial simulations for a 3 month test period showed

AUTHOR INDEX TABLE OF CONTENTS

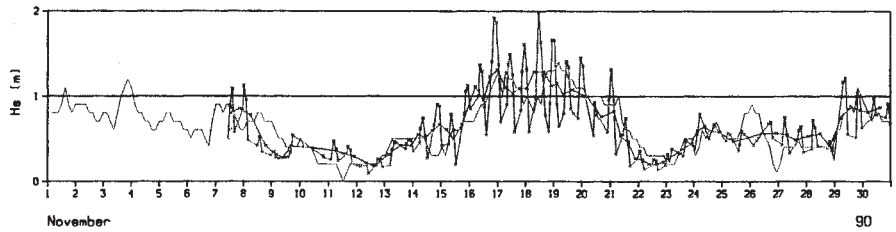

Figure 2: Observed (red) and modeled (blue) significant wave height in m at station Vogelsand. The green line shows the observations averaged over the tidal period.

that reasonable reconstructions of the water levels along the German coast could be obtained this way (Pluess pers. comm. 2000).

2.3 Waves

The wind fields and the water levels described above will be used to force the wave model WAM (WAMDI 1988) for the period from 1958 until now. The model was set up for the Southern North Sea with a horizontal resolution of about 5 × 5 km. We use essentially the same topography as in the simulations of the water levels.

The wave model WAM was modified such that time varying water levels may be taken into account. Lateral boundary conditions were obtained from the WASA integrations (Günther et al. 1998) which were linearly interpolated in time between two WASA output time steps (3 hours). Compared to the WASA simulations the frequency grid was extended by 2 more frequencies in the high frequency domain. In order to obtain suitable boundary spectra from the WASA simulations the WASA spectra were extended at these frequencies using a f^{-5} tail.

The wave model will be integrated from 1958 onwards using hourly wind fields to force the model.

3. RESULTS

Only some preliminary results are presented here.

We used the complex correlation ρ (Kundu 1976) between the observed $U_t^{\mathrm{obs}} = u_t^{\mathrm{obs}} + \mathrm{i}v_t^{\mathrm{obs}}$ and the modeled wind field $U_t^{\mathrm{mod}} = u_t^{\mathrm{mod}} + \mathrm{i}v_t^{\mathrm{mod}}$ to assess the quality of the numerical wind hindcast

$$\rho = \frac{\mathcal{E}(U_t^{\mathrm{obs}}, U_t^{\mathrm{mod}^*})}{\sigma_{U_t^{\mathrm{obs}}} \sigma_{U_t^{\mathrm{mod}}}}. \qquad (1)$$

Here U denotes the complex representation of the two dimensional wind field at 10 m height, u and v are the zonal and the meridional wind component respectively, t is time, $\mathrm{i} = \sqrt{-1}$, and the indices "obs" and "mod" denote the winds taken from observation or simulation. $\mathcal{E}$ denotes the expectation operator, $*$ the complex conjugate, $\sigma_{U_t^{\mathrm{obs}}}$ is defined as $\sigma^2_{U_t^{\mathrm{obs}}} = \mathcal{E}(U_t^{\mathrm{obs}}, U_t^{\mathrm{obs}^*})$ and $\sigma^2_{U_t^{\mathrm{mod}}}$ is defined similarly. The correlation $\rho = \rho_{Re} + \mathrm{i}\rho_{Im}$ can be written in polar coordinates as

$$\rho = R \exp(\mathrm{i}\phi) \qquad (2)$$

where the length R represents a measure of the overall magnitude of the correlation and the phase angle ϕ is a measure of the average relative angular displacement (veering) between a pair of two dimensional vector time series (cf. Kundu 1976).

Monthly complex correlations between the observed and the modeled winds at 10 m height at Ocean Weather Ship Mike (66.0°N, 2.0°E) are shown in Figure 3. In general the complex correlations indicate a good agreement between the observations and the simulation. For the entire period from 1958 until 1991 the magnitude of the complex correlation is in the order of 0.8. The relative angular displacement between the observations and the simulations is about 10° to 15° throughout the simulation period with slightly smaller variability at the end of the simulation. Additionally, monthly biases and root-

AUTHOR INDEX TABLE OF CONTENTS

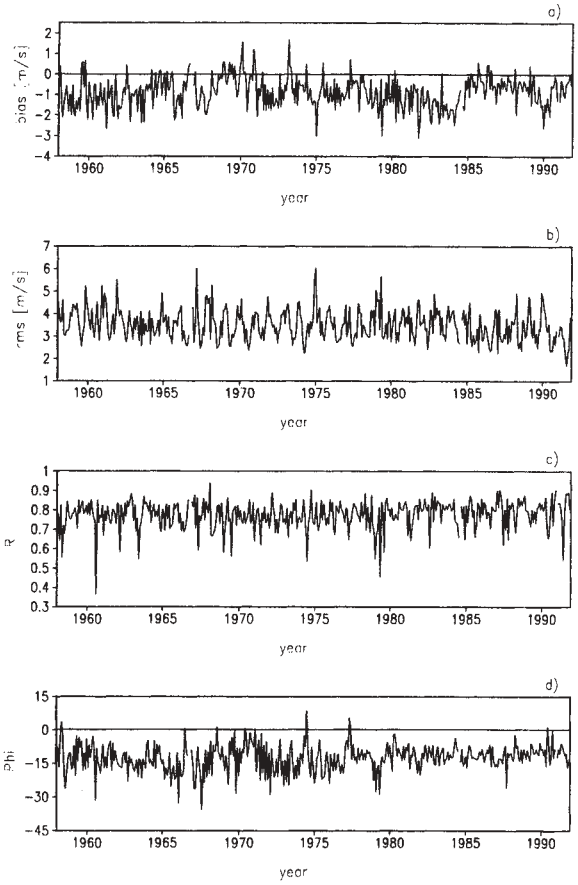

Figure 3: Monthly bias (a), root-mean-square error (b), magnitude (c) and veering angle (d) of the complex correlation between the observed and the modeled wind at Ocean Weather Ship Mike for the period 1958-1991.

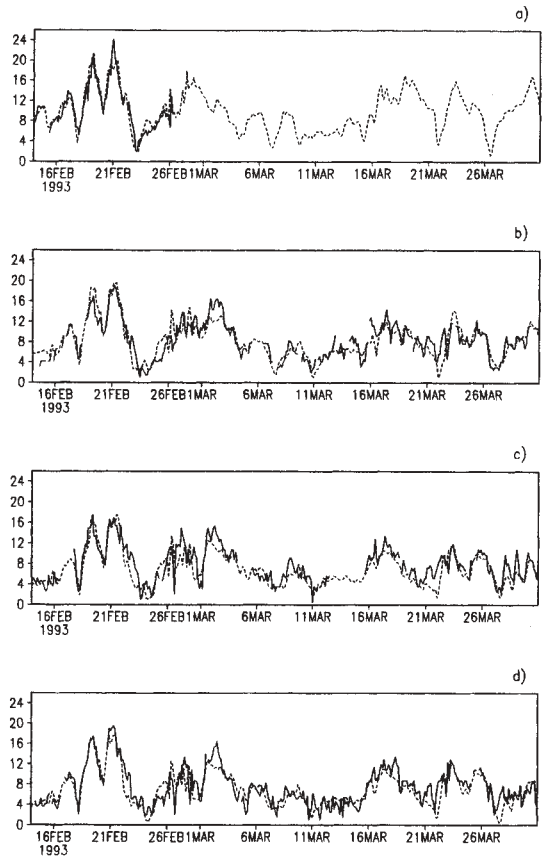

Figure 4: Comparison of modeled (dashed) and observed (solid) wind speed at (a) AUK (56.4°N, 2.1°E), (b) K13 (53.2°N, 3.2°E), (c) EUR (52.0°N, 3.3°E), and (d) YM6 (52.6°N, 4.1°E) for the period 14 February until 31 March 1993.

mean-square errors are shown in Figure 3. It can be obtained that on average the simulation underestimates the observations by 1 ms^{-1} or so. However, the bias is rather sensitive on how the observations have been reduced to 10 m height. The monthly root-mean-square error is in the order of 3 to 4 ms^{-1} with a slight tendency towards smaller values at the end of the simulation period.

The agreement between observed and modeled wind speed is illustrated in more detail for a number of buoys and platforms scattered across the North Sea (Figure 4). Again a good agreement between observations and simulations can be inferred. However, since the period for which data were available is limited the conclusions that can be drawn from this comparison are limited.

A more detailed comparison of the modeled wind fields for a three month period in winter 1993 at the oil platform Ekofisk (56.5°N 3.2°E) is presented in von Storch et al. (2000). They compared the observed wind speed with those modeled using a conventional and a spectral nudging approach and found that in general there is a very good agreement among the model results and the observations. Additionally, they showed that sometimes the spectral nudging approach performed remarkably better.

The wind fields discussed above have been used to perform some initial wave simulations for the North Sea (Figure 5). For significant wave height, peak period, and wave direction the agreement between observations and simulation

AUTHOR INDEX TABLE OF CONTENTS

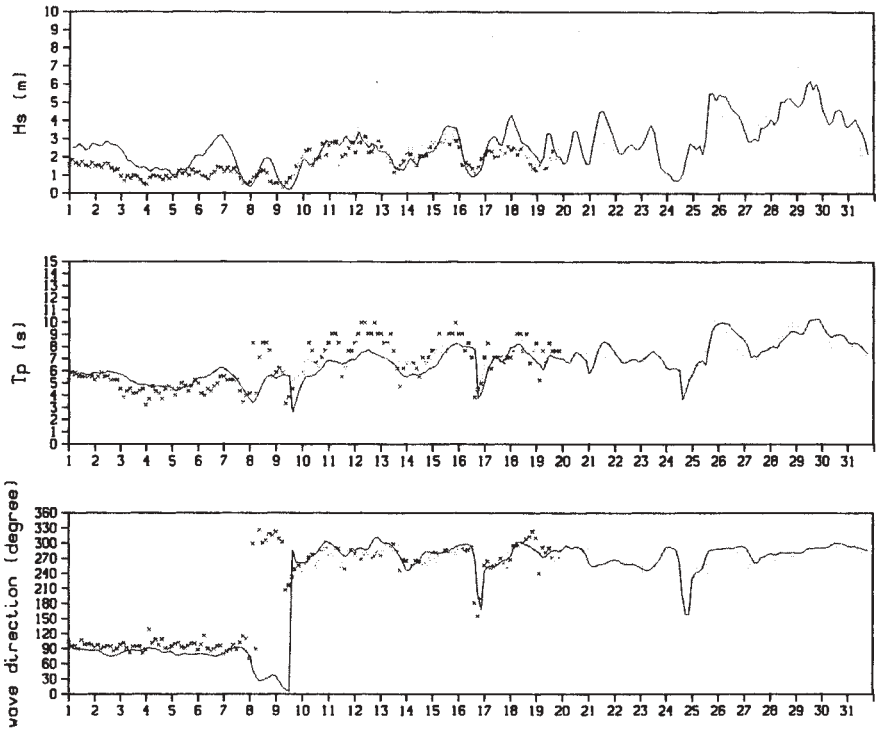

Figure 5: Significant wave height in m (top), peak period in s (middle), and wave direction in degrees (bottom) at Helgoland (54.3°N, 7.9°E) for October 1998 as modeled (blue) and measured by a wave rider buoy (red) and the radar system WAMOS (yellow).

was found to be remarkably. Especially the large wave heights and peak periods at the end of October are captured reasonably. However, compared to the observations wave height and peak period decrease too slowly after 26 October. This is a result of overestimated winds in the atmospheric simulation at this time.

4. SUMMARY

An approach towards a 40-year high-resolution wave hindcast for the Southern North Sea was presented. The approach is embedded in the European project HIPOCAS (Hindcast of Dynamic Processes of the Ocean and Coastal Areas of Europe) which is focused on high-resolution wave hindcasts for European Coastal Seas. The approach is based on driving a high-resolution wave model (about 5 × 5 km) for the Southern North Sea using an improved meteorological forcing and taking the effects of tidal water level fluctuations on the waves in shallow waters into account.

The high-resolution wind fields are available hourly and are obtained from a regional atmosphere model driven by the NCEP reanalysis (Kalnay et al. 1996). A spectral nudging technique (von Storch et al. 2000) is applied to assure an improved reconstruction of the regional atmospheric conditions compared to the conventional approach in which the RAM is driven by the large scale reanalysis at the lateral boundaries only.

Preliminary results suggest that a good quality wind field and a reasonable wave hindcast can be obtained this way.

Acknowledgements. This research is supported by the European Union under EVK2-1999-00248 (HIPOCAS).

5. REFERENCES

Gibson, R., P. Kålberg, and S. Uppala, 1996: The ECMWF Re-Analysis (ERA) project. ECMWF Newsl.,73, 7-17.

Günther, H., W. Rosenthal, M. Stawarz, J.C. Carretero, M. Gomez, I. Lozano, O. Serrano, and M. Reistad, 1998: The wave climate of the Northeast Atlantic over the period 1955-1994: The WASA wave hindcast. Global Atmos. Oc. System, 6, 121-164.

Kalnay, E., M. Kanamitsu, R. Kistler, W. Collins, D. Deaven, L. Gandin, M. Iredell, S. Saha, G. White, J. Woollen, Y. Zhu, M. Chelliah, W. Ebisuzaki, W. Higgins, J. Janowiak, K.C. Mo, C. Ropelewski, J. Wang, A. Leetmaa, R. Reynolds, R. Jenne, and D. Joseph, 1996: The NCEP/NCAR reanalysis project. Bull. Am. Meteorol. Soc., 77, 437-471.

Kundu, P.K., 1976: Ekman veering observed near the ocean bottom. J. Phys. Oceanogr., 6, 238-242.

Rinke, A. and K. Dethloff, 2000: On the sensitivity of a regional arctic climate model to initial and boundary conditions. Clim. Res., 14, 101-113.

von Storch, H., H. Langenberg, and F. Feser, 2000: A spectral nudging technique for dynamical downscaling purposes. Mon. Wea. Rev., 128, 3664-3673.

The WAMDI Group, 1988: The WAM model - a third generation ocean wave prediction model. J. Phys. Oceanogr., 18, 1776-1810.

The WASA Group, 1998: Changing waves and storms in the Northeast Atlantic? Bull. Am. Meteorol. Soc.,79, 741-760.

Weisse, R., H. Heyen, and H. von Storch, 2000a: Sensitivity of a regional atmospheric model to a sea state dependent roughness and the need of ensemble calculations. Mon. Wea. Rev., 128, 3631-3642.

Weisse, R. and F. Feser, 2000b: The impact of spectral nudging on numerical wind hindcasts using a regional atmospheric model. in prep.

SPECIFICATION OF GLOBAL WAVE CLIMATE: IS THIS THE FINAL ANSWER?

V. J. Cardone[1], A.T. Cox[1] and V.R. Swail[2]

[1]Oceanweather Inc.
Cos Cob, CT

[2]Environment Canada
Downsview, Ontario

1. INTRODUCTION

By the beginning of the decade of the 1980s, the so-called hindcast approach for specification of environmental data for the design of offshore structures was well established. For example, a U.S. National Research Council Marine Board review (National Academy of Sciences, 1980) concluded that: "Hindcasting techniques using verified environmental models coupled with statistical treatment of occurrences of natural events gives an appropriate and adequate technical basis for determining environmental exposure". This 6th in a series of international workshops since 1986 on the subject of wave hindcasting further attests to the acceptance of this approach. This paper reviews briefly the development of wave hindcasting and explores whether it is capable of and ready to provide a complete and accurate description of the global wave climate for all practical engineering and scientific purposes.

The hindcast approach was first applied in the decades of the 70s and 80s to develop sea state extremes for engineering design in specific areas of offshore development such as, for example, the US Gulf of Mexico as part of the ODGP program (Cardone *et al.*, 1976, Ward *et al.*, 1979) and to the Hibernia, Grand Banks design (Cardone *et al.*, 1989). These early programs almost always included a dedicated measurement program and hindcast model calibration and validation activities. Over the next decade (i.e. 1990s) the approach was applied to develop definitive wind and wave criteria for entire basins of mature or planned offshore development, usually within Joint Industry Projects (JIP) supported by consortia of oil companies. Major JIPs (acronyms noted) have addressed the Gulf of Mexico (GUMSHOE and WINX), the Bering and Chukchi Seas (BSCOMP, CSCOMP), Russian Arctic Seas (RASMOS), Sakhalin Island (SIMOS), the South China Sea (SEAMOS, Cardone and Grant, 1994), the west coast of Africa (WAX, Cardone *et al.*, 1995), the North Sea (NESS; Peters *et al.*, 1993), the east Coast of Canada (CCC-91; Swail *et al.*, 1995), Brazil (Cardone and Lima, 2000). JIPs are currently underway for the Mediterranean Sea Nile Delta and the Caspian Sea. Many of these JIPs have undergone recent updates as the passage of time has allowed the simulation of an additional decade or so of history and use of newer 3G wave models. For example, CCC-91 was updated to include the many severe storms observed through 1995, with all previous and new storms (a total of 82 events between 1957-1995) rehindcast with Oceanweather's third generation model (OWI3G) model (Swail *et al.*, 1995). The updates to the NESS, CCC-91, SEAMOS and the more recent JIPs (all carried out by OWI) have utilized a new interactive PC-based wind workstation (WWS) to hindcast the surface winds fields following an Interactive Objective Kinematic Analysis (IOKA) (Cox *et al.*, 1995). WWS greatly reduces the degree of manual labor over classical kinematic analysis required to develop the most accurate wind fields possible for a given historical meteorological data set.

The JIPs noted above have typically included the application of the hindcast method to

simulate several continuous years in addition to the core study hindcast of many (20-100) individual high-ranked historical storms. The continuous hindcasts provided time series and statistical summaries useful for the development of wind and wave normals for use in fatigue analysis and planning of routine operations in areas where a sufficiently long-term measured database does not exist. Recently, we have explored the convergence of the storm and continuous hindcast approaches through simulation of multi-decade continuous periods on an oceanic or global scale using high–resolution wave models and reanalyzed wind fields. This approach has been stimulated in part by a resurgence of interest in wave climate within the scientific community as a result of indications of a worsening storm wave regimes in some areas (Bacon and Carter, 1991) and evidence that trends and variability in wave climate on a regional basis may be linked to more familiar modes of atmospheric climate trend and variability such as the North Atlantic Oscillation (NAO) (Kushnir*et al.*, 1997; Wang and Swail (2000)). A sufficiently accurate global 40-50 year hindcast has the potential to describe the global deep water wave climate and its trend and variability and to provide extremal and operational wave deep water wave statistics at a considerable saving compared to the cost of many separate site-specific or basin studies.

In Section 2, we review several recently completed continuous hindcasts, including the new 40-year AES40 and GROW and 20-year GROW2000 simulations. The skill thresholds which must be attained before any simulation may be dubbed the "final answer", are discussed in Section 3. Section 4 gives a critical assessment of these new continuous hindcasts and Section 5 gives our conclusions and outlook.

2. CONTINUOUS HINDCAST PROJECTS

The first attempts to develop long-term wave climatologies from continuous integrations of spectral ocean wave models applied to Northern Hemisphere basins only. These include the U.S. Navy 20-year (1956-1975) Northern Hemisphere project using the SOWM model (Naval Oceanography Command, 1983), the U.S. Army 20-year (1956-1975) North Atlantic and North Pacific Wave Information Study (WIS) project using the WIS wave model (Corson *et al.*, 1981), a 35-year simulation of the North Atlantic Ocean carried out by the Norwegian Meteorological Institute using the WINCH model (Eide*et al.*, 1985) and a 40-year hindcast of the northeast North Atlantic Ocean using the WAM model (Gunther*et al.*, 1998). Since the mid-1980's several major NWP centers (U.S. Navy FNMOC, ECMWF, U.S. NCEP) have operated global spectral ocean wave models in real time and have accumulated the analysis products to form preliminary estimates of the global wave climate. Recently the ECMWF global wave model was applied to hindcast a 15-year period 1979-1983 (Sterl *et al.*, 1998).

An unfortunate property of the earlier hindcast studies and of real time NWP operations is that changes over time in data sources, improvements in data analysis techniques and evolution and upgrades in numerical models have tended to impart a temporal or "creeping" inhomogeneity into the real time products of such centers which naturally feed into the wave simulations. Therefore, output data not only vary in quality but also vary over time and subtle changes in climate may be masked.

Known deficiencies in archived real time atmospheric analyses have led to several major attempts to produce a consistent analysis of the atmosphere spanning a 40-year period. The first of these projects to be completed is the NOAA/NCEP/NCAR Reanalysis project (henceforth NRA, Kalnay *et al.*, 1996). The NRA products to date have been used to drive three continuous wave hindcasts: AES40, GROW, GROW2000.

AES40. The OWI3G spectral wave model was used for this hindcast with the spectrum resolved at each grid point in 24 directional bins

and 23 frequency bins covering the range .039 Hz to .32 Hz. Deep-water physics is assumed in both the propagation algorithm and the source terms. OWI3G is adapted on a latitude-longitude grid consisting of a 122 (in latitude) by 126 (in longitude) array of points with grid spacing of 0.625° in latitude by 0.833° in longitude. The eastern boundary is at 20° E longitude and the northern boundary is at 75.625° N latitude. After deductions for land there are 9023 grid points. The south edge of the grid is at the equator. This boundary was treated as open; wave spectra were interpolated from the output of a lower resolution (2.5 degrees at a 3-hour time step) global model (GROW, see below). The hindcast was carried out in monthly segments. Ice cover was specified for each month from mid-monthly ice tables specified on the wave grid from the best available historical ice data. The output of the model consists of 17 'fields' quantities (e.g. significant wave height, peak period, vector mean direction, partitioned fields, directional and angular spreading) at all grid points and the full two-dimensional spectrum at 233 grid points. The spectral save points were selected to allow even coverage of the basin (every 5 of latitude and longitude), as well as to allow the possibility to drive finer mesh models for the US East Coast, the Scotian Shelf and Grand Banks of Newfoundland and the European West Coast. Spectra were also saved at the locations of selected moored buoys and offshore platforms.

The most important, and unique, element of the AES40 hindcast was the enormous effort devoted to producing the wind fields for the wave model; this effort accounted for more than 10,000 meteorologist-hours of effort spent in manual and interactive kinematic analysis. Details of the wind field generation are given in Swail and Cox (2000). Briefly, the process included the transformation of the NRA Surface (10m) winds to effective neutral stability, the re-assimilation at proper equivalent 10 m height of high quality wind observations from buoys, ships, coastal stations and ERS1/2 scatterometers and the assimilation of winds in tropical cyclones generated in a separate mesoscale model simulation of each such cyclone within the 40 years modeled. The very labor intensive detailed kinematic analysis effort noted above was devoted to incorporation of all the wind information noted above into the final analysis with particular attention spent on strong extra-tropical systems, blending tropical model winds into the NCEP surface wind field, and in the quality control of surface data. As part of this process, kinematically analyzed winds from previous storm hindcasts of severe extratropical storms in the northwest Atlantic (Swail *et al.*, 1995) were incorporated into AES40 wind fields. Final wind fields for each month were interpolated onto the 0.625° by 0.833° latitude-longitude wave model grid using the IOKA (Interactive Objective Kinematic Analysis) algorithm (Cox *et al.*, 1995) and then time interpolated from the 6-hourly analysis interval to a one-hour time step. The validation of this database is described at this workshop by Swail *et al.*, (2000).

GROW (Global Reanalysis of Ocean Waves). This database was generated in 1998 by OWI on a global grid using its ODGP2 deep-water wave model with spectral resolution as noted above for AES40. GROW is the first global 40-year hindcast based upon NRA products. The grid spacing is 1.25 degrees latitude by 2.5 degrees longitude. Winds were specified on the wave model grid directly from the 40-year (1958-1997) NRA surface 10-m 6-hourly wind file, except for transformation of wind speeds to effective neutral stratification using NRA 2-meter air temperature and sea surface temperature fields. That is, no attempt was made to re-assimilate wind observations or to modify wind fields kinematically in tropical or extratropical storms. The ice edge was specified on a monthly basis using a long-term monthly mean ice climatology. Winds were input at 6-hourly intervals for use with the model time step of 3 hours. Output wind and wave fields (again 17 "fields" variables) are archived at 6-hourly intervals at all model grid points, while spectra are archived at 6-hourly intervals only at 10 degree latitude-longitude intervals. GROW

SWH specifications were validated on a global basis against all available buoy, platform, ship and satellite altimeter (Cox and Swail, 2000). That validation showed that GROW provides reasonably accurate global (SWH) statistics and estimates of recent trends in global wave climate.

GROW2000. The experience of AES40 and GROW has been applied to an update of GROW called GROW2000. GROW2000 attempts to correct the main deficiencies of GROW but stops short of the enormous expenditure of labor which would be required to extend the AES40 wind hindcast methodology to the globe. To date GROW2000 has simulated the continuous 20-year period 1979-1998. First, the grid resolution was substantially increased by decreasing the grid spacing to 0.625 degrees latitude by 1.25 degrees longitude, yielding a global grid of 46,529 points. The higher resolution was needed to decrease obvious GROW model biases in SWH in the vicinity of major island groups and chains. Next, the systematic errors observed in NRA winds in GROW were addressed by applying to NRA wind speeds spatially varying regressions developed from global evaluation of NRA wind against adjusted in-situ data and corrected satellite scatterometer winds. Separate wind adjustment algorithms have been developed for three regions: Northern Hemisphere (NH) Extratropical, Southern Hemisphere (SH) Extratropical and Tropical Belt. In addition to the correction of the NRA winds, the time and space evolution of the wind field about each tropical cyclone was specified using OWI's mesoscale vortex model. For each cyclone, the parameters for the tropical cyclones (that is the inputs to the mesoscale model) were taken from the best source available. Therefore, for virtually all storms in the greater North Atlantic basin, the inputs are developed (as in AES40) by analysis of raw source data as analyzed by OWI analysts. The same is true for several hundred Western North Pacific tropical cyclones. In other areas (e.g Indian Ocean, Australia etc.) OWI used mainly its newly developed algorithm (Cox and Cardone, 2000) to extract the OWI model parameters from standard historical sources (Global Tropical and Extratropical Cyclone CD-ROM) and products of major warning centers (e.g. Navy's Joint Typhoon Warning Center, NOAA National Hurricane Center, Australian Bureau of Meteorology, Royal Observatory Hong Kong). However, no manual intervention was applied to blend cyclone winds into the adjusted NRA background or to modify winds in intense extratropical cyclones. Finally, the latest available historical ice data from the National Ice Center were manipulated to provide boundaries of monthly 50% ice cover grids for each individual month over the 20-year period simulated. A variant of OWI's ODGP wave model was used for the hindcast with the same spectral resolution as adopted for AES40 and GROW. This variant incorporates a new formulation of the Pierson-Moskowitz fully developed sea theory (Resio*et al.*, 1999). The new wind scaling used therein operates within a 1G or 2G model to correct the tendency of all previous wave models, including 3G models, to under specify very extreme sea states in a special class of storms characterized by resonant dynamic fetches or very long physical fetches and durations. The archive of GROW2000 consists of time sorted "fields" of 17 wind and wave variables at 3-hourly intervals at all grid points and time histories of full 2-D spectra at grid points at 5 degree latitude-longitude intersections.

3. HINDCAST SKILL THRESHOLDS

Storm Peak Skill The skill of storm hindcasts that is necessary in order for a hindcast database to provide extrapolation of reliable sea state extremes for design has been demonstrated and achieved in hindcast model validation studies. For example, validation of the ODGP hindcast model against high quality wave measurements acquired in tropical cyclones and severe extratropical cyclones (Reece and Cardone, 1982) demonstrated that ODGP when driven by high-quality winds typically specifies peak significant

wave height (SWH) at an arbitrary site in a storm with bias of less than 0.5 m, mean absolute error of less than 1.0 m and scatter index (SI) of 10-15% (SI= 100 x sd/avg where sd is the standard deviation of differences between hindcast and measured peak wave heights and avg is the average of measured heights in the validation population of heights; SI is also often expressed fractionally as sd/avg). The peak spectral period (TP) appeared to be specified with comparably small bias but with greater scatter. Since ODGP, the same hindcast methodology has been validated in a wide range of wave regimes including arctic and sub-arctic basins, mid-latitude NH and SH regimes, tropical cyclone regimes and subtropical regimes such as the Gulf of Mexico, South China Sea and Arabian Gulf (e.g. Cardone *et al.*, 1989; Swail *et al.*, 1992; Cardone and Ewans, 1992; Eid *et al.*, 1992). Oceanweather's 3G model (the alternative wave model physics of OWI3G is described by Khandekar *et al.* (1994) and Forristall and Greenwood (1998)) has also demonstrated excellent skill in both tropical and extratropical settings. Where OWI3G was used to validate hindcasts against many of the same storms used to validate ODGP as well as more recent storms measured by US and Canadian buoys the mean error in SWH and (TP) was found to be -.13 m (-.27 sec), the rms error .98 m (1.64 sec) and the scatter index 14% (15%). The skill seems to be invariant with wave height at least up to SWH of about 12 m, with a tendency to underestimate peak sea states in the most extreme storms in which SWH exceeds about 12 m. This under-specification in peak states was also observed with other wave models (Cardone *et al.*, 1996) and may be associated with one or more of the following possibilities: (1) wind speeds measured from buoys in high seas states, which feed into operational as well as kinematically reanalyzed wind fields may be biased low; (2) wave model growth reaches saturation prematurely (3) the source terms in wave models used for atmospheric input and wave dissipation, which are tuned even in 3G models, are being extrapolated beyond their applicable range; (4) spatially coherent small scale wind field features, such as rapidly propagating surface wind "jet streaks", which seem to be associated with several known occurrences of extreme storm sea states (Cardone *et al.*, 1996) are not resolved accurately in even the best wind fields. The concept of a fully developed sea continues to play a large role in wave models. In 1G and 2G models this limit to growth is usually explicitly invoked. In most 3G models, the dissipation source term is tuned such that when the model is driven by constant winds the detailed balance leads to an equilibrium or very slowly evolving spectrum at large fetch or duration. Resio *et al.* (1999) have shown that a rescaling of the reference wind speed in a fully developed spectrum formulation in terms of a dynamic reference height which increases with increasing wave height may explain the tendency of all models to underestimate extreme sea states. As noted above this revised scaling has been incorporated into ODGP2 for GROW2000.

Relatively few studies have been reported which compare model and measured directional spectra. For example, Jensen *et al.* (1995) compared WAM-4 hindcast and measured 2-D spectra at several data buoys off the US East Coast in two storm events (one tropical, one extratropical) in terms of mean wave direction and rms spreading. While generally good agreement was found for mean wave direction, systematic differences were often found for spreading. Forristall and Greenwood (1998) investigated the directional spread of various models as compared to measurements in both simple fetch and duration wave generation regimes and in tropical and extratropical storm hindcasts. To represent spreading, they adopted a measure based on second trigonometric moments of the wave spectrum which is equivalent to the square root of the "in-line variance ratio" defined by Haring and Heideman (1978). This ratio is an important measure of the wave load on an offshore structure. In comparisons of 2-D spectra from simulations of simple duration growth for a 20 m/s wind speed with various models and indications from measured data, Forristall and Greenwood show that the model spreading factors near the peak frequency of the model spectra differed little from each other but all models yield spreading factors less than (therefore too broadly spread)

the measured spreading. In the tail of the spectrum, the WAM model has a lower spreading factor than the measurements, while the OWI3G agrees more closely with the data. The spreading exhibited by ODGP2 actually agreed best with the measured data, but this is not surprising because in that model the spreading is constrained to follow a prescribed empirical form. Forristall and Greenwood (1998) also found good agreement between modeled and measured spreading factors at two sites in the northern North Sea in a 5-year continuous hindcast made with OWI3G, but not so good agreement between hindcasts and measurements at a site in the northern Gulf of Mexico on the left side of the track of severe hurricane Opal (1995). Lower skill has also been seen in OWI3G and WAM hindcasts than of ODGP2 of the details of the 2-D spectra on the left side of tracks of tropical cyclones Frederic (1979) and Luis (1995).

Skill in Continuous Hindcasts The recent SWADE hindcast study carried out using data acquired off the US East Coast (Cardone *et al.*, 1995b) demonstrated that where surface wind fields are specified using kinematic reanalysis techniques which take advantage of the enhanced data coverage in areas of dense buoy and/or offshore platform measurement arrays (e.g. off the east and west coasts of North America and in and around the North Sea), well calibrated wave models may specify the evolution of SWH with negligible bias and scatter near the lower limit set by accuracy and sampling variability in the wave measurements. It is not yet as clear that the details of the 2-D spectrum and hence mean or peak spectral wave period or wave direction and angular spreading of waves are as well simulated. Within the core of the dense SWADE buoy array, the SWH scatter index (SI) found of 14% is unprecedented for continuous hindcasts. However, the mean negative error of about 0.4 seconds in peak period is apparently a real characteristic of this hindcast and may be caused by use of 3G wave model physics. Errors in hindcasts validated against wave measurements over the larger area comprising the SWADE and NOAA buoy arrays increased to levels (SWH SI of 18%-25%) probably more typical of continuous hindcasts of mid-latitude extratropical weather regimes in the open ocean with kinematically reanalyzed winds. Errors were generally larger (SWH SI 26%-40%) when the same hindcast was repeated with wind fields produced operationally at major analysis centers at the time (October, 1990). This study suggests that an acceptable skill level for continuous hindcasts is represented by SWH SI in the range of 18-25% and bias of less than 0.5 m. More recent validation studies have added hindcast-measured parameter distributional comparisons as a skill measure, usually in terms of SWH quantile-quantile scatter plots (Cox *et al.*, 1999).

4. CRITICAL EVALUATION OF NRA BASED HINDCASTS

A comprehensive validation of the AES40 hindcast against in-situ wind and wave measurements at data buoys and against wind speed and SWH measurements from ERS1/2 and TOPEX satellite altimeters is reported at this workshop by Swail *et al.* (2000). Basin-wide 100-year extremes of wind speed, SWH, associated TP and maximum wave height were also reported. Against the best science quality measurements, namely 213,724 comparisons at US and Canadian buoys, the mean difference (bias), SI and correlation coefficient (CC) between AES40 and buoy SWH were found to be .10 m, 23% and .93 respectively. For the same comparison data base, a quantile-quantile scatter plot comparison of SWH height over the range of cumulative non-exceedance probability of 1% to 99% showed a near linear match and average difference of only 0.10 m at all sites. The satellite comparisons (over 3 million data pairs were used over the whole basin) were found to be quite consistent with the in-situ comparisons with bias, SI and CC of -.01m, 22% and .93 respectively. Spatial maps of these difference measures derived from the satellite comparisons exhibit very good consistency in skill at these

levels over virtually all parts of the AES40 hindcast domain. Storm peaks are also well specified as reflected in the close match between 100-year extremes derived from the top-40 peaks of the AES40 hindcast and extremes developed from previous detailed storm hindcast studies. Table 1 compares 100-year SWH at several such locations, including a location (West of Shetlands) in the most severe part of the North Atlantic and several sites off the East Coast of North America. Extremes in all of these areas are dominated by extratropical cyclones. The extremes match closely in all areas with differences within the expected sensitivity of the extrapolation process to details such as peak threshold and fit uncertainty (the AES40 extremes are based upon the GUMBEL distribution fitted with the method of moments; see Swail *et al.*, 2000).

Table 1. Comparison of 100-Year Significant Wave Height (m) from AES40 Hindcast and Dedicated Site-Specific Studies.

Area	Study	AES40
West of Shetlands	18	17
Hibernia, Grand Banks	15	15
Scotian Shelf Deep	13	14
Georges Bank Deep	13	14

Thus we may conclude that AES40 provides a data base for the specification of SWH normals and extremes in all regions of the North Atlantic dominated by extratropical weather to a level of accuracy comparable to that provided by dedicated site-specific hindcast studies. AES40 also provides reasonable estimates of extremes in regions dominated by tropical cyclones, though no public domain estimates from detailed hindcast studies were available for comparisons with the AES40 extremes here. However, we may legitimately ask: is the AES40 SWH wave climate specified with the minimum uncertainty possible especially in areas subject to "extreme storm seas" (SWH > 12 m) and are the other integrated properties of the spectrum important for engineering applications such as TP, directional spreading and 'swell' content specified with comparable accuracy? Until this question is answered in the affirmative, and it cannot at this time, AES40 may be considered to be a state-of-the-art hindcast but perhaps not quite yet the "final answer" for the North Atlantic.

Next, we explore how closely GROW and its refinement GROW2000 approach, on a global basis, the skill of AES40 at least with regard to SWH. Cox and Swail (2000) include a comprehensive validation of the GROW hindcast against in-situ wind and wave measurements at data buoys and against wind speed and SWH measurements from ERS1/2 and TOPEX satellite altimeters. The evaluation of GROW2000 is underway and only preliminary results are given here with more complete results to be presented at the workshop itself. For the highest quality measured data, namely 453,750 comparisons over all US and Canadian buoys, the SWH bias, SI and CC were found to be .10 m, 27% and .90 respectively. These statistics (and similar statistics for smaller buoy groupings) indicate only a relatively small deterioration of these skill measures in GROW in the deep water areas off the east and west coasts of North America, in the central Bering Sea and Gulf of Mexico, relative to that achieved off the east coast by AES40. However, the regional SWH distributional comparisons for GROW showed less linearity than the AES40, suggesting biases which vary systematically from region to region in certain SWH ranges. For example, near Hawaii and west of Chile, GROW SWH is biased low in the 10%-99% (percentiles) by up to 1 m, while in the Gulf of Mexico and western Caribbean GROW SWH is biased high by up to 1 m in the same probability range. In NH mid-latitudes, GROW appears biased high by up to 0.5 m in the 25 – 75% range.

Cox and Swail (2000) include altimeter comparisons stratified over broad regions (NH extratropics, SH extratropics and tropical belt (20N-20S)). These difference statistics showed little variation when averaged over broad regions. For all regions combined (8,662,504 comparisons), the bias, SI and CC were -.04 m,

24% and .89, which are again only slightly less skillful than AES40. The altimeter comparison database allows resolution of the skill measures spatially over regions as small as one grid point box. Figure 1 shows the SWH bias (hindcast – altimeter) so computed as contoured in 0.25 m intervals (dashed lines negative, solid lines positive). The bias is less than 0.25 m over virtually the entire North Atlantic and North Pacific and generally varies between +0.50 m and - 0.50 m in the SH. The narrow belt of -0.25 m to -0.50 m bias along the northern border of the Southern Oceans which extends around the globe near 30 S is confirmed in in-situ comparisons using a NOAA buoy moored west of Chile. Cox and Swail (2000) speculate that this bias pattern may reflect a small deficiency of SH swell. Figure 1 also gives the global bias distribution based on the GROW2000 hindcast. GROW2000 virtually eliminates the positive bias seen in GROW on both sides of the Aleutian and Kurile island chains and the small chains and larger islands which define the Caribbean basin. This is a logical result of the greater resolution of GROW2000. The positive bias of GROW is also reduced along the Antarctic ice edge, probably a result of both the greater model resolution and the more accurate ice edge specification of GROW2000. Over other regions the spatial distribution and magnitude of the bias is little changed between GROW and GROW2000. However, this is not to say that hindcasts are equivalent in these regions. In general GROW2000 SWH is more energetic than GROW because of the inflation of NRA wind speeds, the revised P-M wind scaling and the explicit assimilation and resolution of tropical cyclones. For example, Figure 2 compares the GROW (upper) and GROW2000 (lower) monthly maximum SWH for a typical month (October, 1998). The peaks of SWH in the several severe storms in the SH "roaring forties" are 20-30% greater in GROW2000 than in GROW. The signatures of tropical cyclones are also indicated in GROW2000 (and absent in GROW) in the western Caribbean (Hurricane Mitch), off the west coast of Mexico and in the vicinity of the Philippines Islands. The systems in the Chukchi and Beaufort Seas are resolved in GROW2000 and absent in GROW, a result again of more accurate ice specification.

One area where one would expect a definite bias in GROW and possibly GROW2000 relative to AES40, is in specification of storm peaks and derivative return period extremes. In Figure 3, we compare 100-year SWH extremes computed from GROW with extremes derived in detailed hindcast studies with kinematically reanalyzed winds. The GROW extremes are based upon fits to the top-ranked 40 events over 40 years using the GUMBEL distribution and method of moments fitting. This process is comparable to the method used in the detailed basin studies. The points on this plot represent 15 widely separated areas distributed over the following basins: North Atlantic Ocean, Gulf of Mexico, South Atlantic Ocean, North Pacific Ocean, Bering Sea, Sea of Okhotsk, South China Sea, Southern Ocean. These comparisons are restricted to extremes associated with non-tropical cyclones. The smallest extreme on this plot (3.8 m) is associated with pure southwest swell offshore Nigeria (Cardone *et al.*, 1995a). The largest extreme on this plot (18 m) is associated with West of Shetlands (Archer, 1999/2000). The correlation between the GROW and the "studies" extremes is remarkable (CC = .99) and as expected the GROW extremes are biased low. The bias is –1.5 m in an absolute sense and about 12% as a percentage. It is expected that extremes from GROW2000, when similarly analyzed, will yield comparably skillful extremes with less bias. For example, Figure 4 compares GROW2000 and altimeter wind speed and SWH in terms of scatter plots, difference statistics and q-q plots in the northeast North Atlantic west of Shetlands, where we would expect the hindcast to be quite good, and Figure 5 gives the same for a grid points in the Tasman Sea west of central New Zealand where skill is much more challenging to achieve. However, we find that at both sites the scatter index is 23% or less, the overall bias is less than 0.5 m and the match at the 99 percentile between model and altimeter SWH is within 0.1 m. The matches in wind speed at the same percentile are not very close, with the model greater than the altimeter,

but this is largely a result of the saturation of altimeter wind speeds above about 15 m/s.

5. CONCLUSIONS AND OUTLOOK

5.1 Conclusions

Are these latest continuous long term hindcasts based on NRA products the "final answer" to global wave climate specification? Not quite! But these products constitute considerable progress toward that ideal. With regard to specification of SWH normals and extremes in the North Atlantic Ocean, AES40 provides wave statistics accurate enough for most engineering purposes and a database ripe for mining in research on climate change and variability. Additional spatial and temporal resolution is required for the most accurate representation of tropical cyclones and of course higher resolution and shallow water physics are needed for near shore applications. Also, the issue of a possible bias of SWH in rare "extreme sea states" needs to be resolved. Finally, the period and directional properties of the seaway are probably not specified as skillfully and with as little bias as SWH and further improvements in these areas will depend at least in part on further improvement in wave model source term physics and propagation schemes.

The global hindcast products described provide remarkably skillful hindcasts of SWH on a global basis and estimates of normals and extremes, which compare well with those derived in dedicated local studies and (in the North Atlantic) from AES40. Extremes of SWH derived from GROW are biased low in general but the bias appears to be correctible through the use of local in-situ data sets (if available), altimeter data or, as a last resort, the linear regression indicated in Figure 3. So unbiased, GROW normals and extremes may be adequate for engineering applications involving planning and feasibility and initial assessments of global wave climate change and variability. However, we do not recommend the use of GROW derived extremes for final design. GROW2000 provides higher resolution global hindcast data at least as skillful as GROW and extremes with much less bias than GROW.

5.2 Outlook

Wave Models. Despite the great progress in wave modeling over the past two decades, several problem areas have been revealed mainly through the biases in 3G model specification of the wave heights in very high sea states, biases in specification of details of the 2-D spectrum such as TP and angular spreading in simple regimes, and larger errors in specification of 2-D spectra in more complicated wave regimes such as tropical cyclones. In fact, in some of these respects, well-tuned 2G models may outperform 3G models, the latter admittedly constrained by empirical rather than physical formulations for spectral shape. There is certainly a need for further refinement of the source terms for input and dissipation and more accurate numerical approximation of wave-wave interactions. Fortunately, there is a growing base of high-quality wind fields and measured wave data becoming available to wave modelers to allow testing of more physically based source terms, including data sets in a number of well documented extratropical and tropical cyclones and the new global wind data sets such as the NRA and modified NRA wind fields described in this paper. The international wave modeling community has, in fact, embarked on the development of a virtual wave model test bed facility that assembles the drivers for the standard tests and the above noted wind fields and measured wave data sets for the real test cases in a convenient form for alternative wave model evaluation. This facility will also include a standard package for the statistical evaluation of model performance.

Convergence. The continuous hindcast studies described in this paper point the way, say within the next five years, to a definitive hindcast of the time and space evolution of the global wave climate over the past fifty years, at least for deep-water open coast exposures. This "final" hindcast data set will have incorporated and be entirely consistent with available in-situ historical

measured data sets and global satellite data sets. The data set will be free of bias in all properties of the 2-D spectrum of interest to the offshore industry such as SWH, TP, mean wave direction and wave directional spreading and correctly specify swell after propagation basin scale distances. However, it is unlikely that this database can be extended any further back in time, except for tropical cyclone extremes in limited areas. And since current design practices demand estimates of extremes for even rarer return periods (up to 10,000 years) additional research is needed to understand the influence of climate variability and trend on extremes estimated from only 50 years of history, and to define the possible physical constraints on storm intensities and ocean response which might place an upper limit on the extremes predicted by distributional extrapolations.

Access. The products of the earliest hindcast studies (e.g. ODGP, Hibernia) consisted typically of a hard-copy report containing a few tables of estimates of extremes of wave height and period for return periods up to 100 years at specific concession blocks of interest to the study sponsor. The earliest JIPs (e.g. ODGP, BSCOMP) included the derivation of extremes over larger areas and included delivery on 9-track tape of actual hindcast time series in bit-packed binary form. The most recently conducted JIPs, such as the SEAMOS and NESS updates, include derivation of extremes and normals at thousands of grid points in the study basin and delivery of digital files of the derivative products and all hindcast time series at all model grid points. All files are placed on CD-ROM and delivered together with access software for browsing and exporting of either derivative products or the hindcasts themselves. As the hindcast databases become even larger, such as produced for example by the AES40 study, it will be more convenient for the user to access the data base for the grid points needed at any given time over the Internet from a central server.

REFERENCES

Archer, S., 1999/2000: *6th Atlantic Frontier Workshop: Waves, Steep Waves and Statistics-Operating in Harsh Environment, Report on Meeting*. Underwater Technology, **24**, p. 73-80.

Bacon, S. and D.J.T. Carter, 1991: *Wave climate changes in the North Atlantic and North Sea*. Intl J. of Climate, **11**, p. 545-558.

Cardone, V. J., W. J. Pierson and E. G. Ward, 1976: *Hindcasting the directional spectra of hurricane generated waves*. J. Petrol. Technol., **28**, 385-394.

Cardone, V. J., D. Szabo and F. J. Dello Stritto, 1989: *Development of extreme wind and wave criteria for Hibernia.* Proc. 2nd Int'l Workshop on Wave Hindcasting and Forecasting Vancouver, BC, 25-28 April, 1989, 75-88.

Cardone, V. J. and K. C. Ewans, 1992: *Validation of the hindcast approach to the specification of wave conditions at the Maui location off the west coast of New Zealand.* Proc. 3rd International Workshop on Wave Hindcasting and Forecasting, May 9-22, Montreal, Quebec, p. 232-247.

Cardone, V.J. and C. K. Grant, 1994: *Southeast Asia meteorological and oceanographic hindcast study (SEAMOS).* OSEA 94132. Offshore South East Asia 10th Conference & Exhibition, Dec 6-9,1994, p. 6-9

Cardone, V.J., C.K. Cooper and D. Szabo, 1995a: *A hindcast study of the extreme wave climate of offshore West Africa (WAX).* OTC 007687 Offshore Technology Conference, Houston, 1-4 May, p. 439 -451.

Cardone, V. J., H.C. Graber, R.E. Jensen, S. Hasselmann and M. J. Caruso 1995b: *In search of the true surface wind field in SWADE IOP-1: ocean wave modeling perspective*. The Global Atmosphere and Ocean System, **3** p. 107-150.

Cardone, V.J., R.E. Jensen, D.T. Resio, V.R. Swail and A.T. Cox. 1996: *Evaluation of*

contemporary ocean wave models in rare extreme events: the "Halloween Storm' of October, 1991 and the "Storm of the Century" of March, 1993." J. Atmos. Oceanic. Technol. **13,**p. 198-230.

Cardone, V. J. and J. Lima, 2001: *Wave and wind hindcast study for southeast Brazil.* Submitted to Offshore Technology Conference, 30 April-3 May, 2001, Houston, TX.

Corson, W. D., D. T. Resio, R. M. Brooks, B. A. Ebersole, R. E. Jensen, D. S. Ragsdale and B. A. Tracy, 1981: *Atlantic coast hindcast deepwater significant wave information.* WIS Report 2, U.S. Army Engineer Waterways Experiment Station, Vicksburg, MS.

Cox, A.T., J.A. Greenwood, V.J. Cardone and V.R. Swail. 1995: *An interactive objective kinematic analysis system.* Proc. 4th International Workshop on Wave Hindcasting and Forecasting. Banff, Alberta, 16-20 October, p. 109-118.

Cox, A.T., V. J. Cardone and V. R. Swail, 1998: *Evaluation of NCEP/NCAR Reanalysis Project marine surface wind products for a long term North Atlantic wave hindcast.* Proc. 5th International Workshop on Wave Hindcasting and Forecasting, Melbourne, FL, January 26-30, 1998, p.30-40.

Cox, A.T., Cardone, V.J. and V.R. Swail, 1999. *On the Use of In-Situ and Satellite Wave Measurements for Evaluation of Wave Hindcasts.* CLIMAR 1999 Preprints, Sept. 8-15, 1999, Vancouver, Canada. p. 130-138.

Cox, A.T. and V.R. Swail, 2000: *A Global Wave Hindcast over the Period 1958-1997: Validation and Climate Assessment.* J.Geophys. Res. (Oceans), in press.

Cox, A.T. and V. J. Cardone, 2000: *Operational system for the prediction of tropical cyclone generated winds and waves.* Proc. 6th International Workshop on Wave Hindcasting and Forecasting. 6-10 November, Monterey, CA.

Eid, B., V. J. Cardone, and V. K. Swail, 1992: *Beaufort Sea extreme wind/wave hindcast study.* Proc.3rd International Workshop on Wave Hindcasting and Forecasting. Montreal, Quebec. May 9-22, 1992, p. 351-361.

Ewans, K.C. 1995: *Observations the directional spectrum of fetch-limited waves off the west coast of New Zealand.* Proc. 4th International Workshop on Wave Hindcasting and Forecasting. Banff, Alberta. 16-20 October, p. 263-278.

Forristall, G.Z. and J. A. Greenwood, 1998: *Directional spreading of measured and hindcasted wave spectra.* Proc. 5th International Workshop on Wave Hindcasting and Forecasting, Melbourne, FL, January 26-30, 1998, p. P5-P15.

Haring, R.E. and J. C. Heideman, 1980: *Gulf of Mexico rare wave return periods.* J. Petrol. Tech ., p. 35-37.

Jensen, R.E., C.M. Holmes and C.L. Doiron, 1995: *An evaluation of two extreme storm events in the mid-Atlantic coastal waters: measurement and 3GWAM assessment.* Proc. 4th International Workshop on Wave Hindcasting and Forecasting, Banff, Alberta, 16-20 October, p. 235-249.

Kalnay, E. *et al.*, 1996: *The NCEP/NCAR 40-year reanalysis project.* Bull. AMS, 77(3), p. 437-471.

Khandekar, M.L., R. Lalbeharry and V.J. Cardone, 1994: *The performance of the Canadian spectral ocean wave model (CSOWM) during the Grand Banks ERS-1 SAR wave spectra validation experiment.* Atmosphere-Ocean, **32,**p. 31-60.

National Academy of Sciences, 1980: *Environmental exposure and design criteria for offshore oil and gas structures.* A report prepared by the Marine Board of the Assembly of Engineering. National Academy of Sciences, Washington, DC. 215 pages.

Peters, D.J., C.J. Shaw, C.K. Grant, J.C. Heideman and D. Szabo, 1993: *Modeling the*

North Sea through the North European Storm Study. OTC 7130, Offshore Technology Conference, Houston, 3-6 May. p. 479-493.

Reece, A. M. and V. J. Cardone. 1982: *Test of wave hindcast model results against measurements during four meteorological systems*. Offshore Technology Conference. OTC 4323, p. 269-.

Resio, D. T., V. R. Swail, R. E. Jensen and V. J. Cardone, 1999: *Wind speed scaling in fully developed seas*. J. Phys. Oceanog., **29**, p. 1801-1811.

Sterl, A., G. Komen and P. D. Cotton, 1998: *Fifteen years of global wave hindcasts using winds from the European Center for Medium Range Weather Forecasts reanalysis: validating the reanalyzed winds and assessing the wave climate.* J. of Geophys. Res. (Oceans), **103**, (C3), p. 5477-5492.

Swail, V. R., V. J. Cardone and B. Eid, 1992: An extremes wind and wave hindcast off the west coast of Canada. Proc. 3rd International workshop on Wave Hindcasting and Forecasting, Montreal, Quebec, 19-22 May, p. 339-350.

Swail, V.R., M. Parsons, B.T. Callahan and V.J. Cardone, 1995: *A revised extreme wave climatology for the Canadian east coast*". Proc. 4th International Workshop on Wave Hindcasting and Forecasting. Banff, Alberta. 16-20 October, p. 81 - 92.

Swail, V. R., V. J. Cardone and A. T. Cox, 1998. *A long term North Atlantic wave hindcast*. Proc. 5th International Workshop on Wave Hindcasting and Forecasting, Melbourne, FL, January 26-30, 1998.

Swail, V.R. and A.T. Cox, 2000. *On the use of NCEP/NCAR Reanalysis Surface Marine Wind Fields for a Long Term North Atlantic Wave Hindcast.* J. Atmos. Ocean. Tech.., **17 (C3)**, p. 532–545.

Swail, V. R., E.A. Ceccacci and A. T. Cox, 2000: *The AES40 North Atlantic wave reanalysis: validation and climate assessment*. Proc. 6th International Workshop on Wave Hindcasting and Forecasting, 6-10 November, 2000, Monterey, CA.

U.S. Naval Oceanography Command, 1983: *Hindcast spectral ocean wave model climate atlas: North Atlantic Ocean*. Prepared by Naval Oceanographic Command Detachment, Asheville, NC.

Wang, X.L. and V.R. Swail, 2000. Changes of extreme wave heights in Northern Hemisphere oceans and related atmospheric circulation regimes. J. Climate, in press.

Ward, E. G., L. E. Borgman and V. J. Cardone, 1978. *Statistics of hurricane Waves in the Gulf of Mexico*. OTC 3229. 10th Annual Offshore Technology Conference, 8-11 May, 1978, Houston, TX. (also appeared in J.Petrol. Tech., 1979)

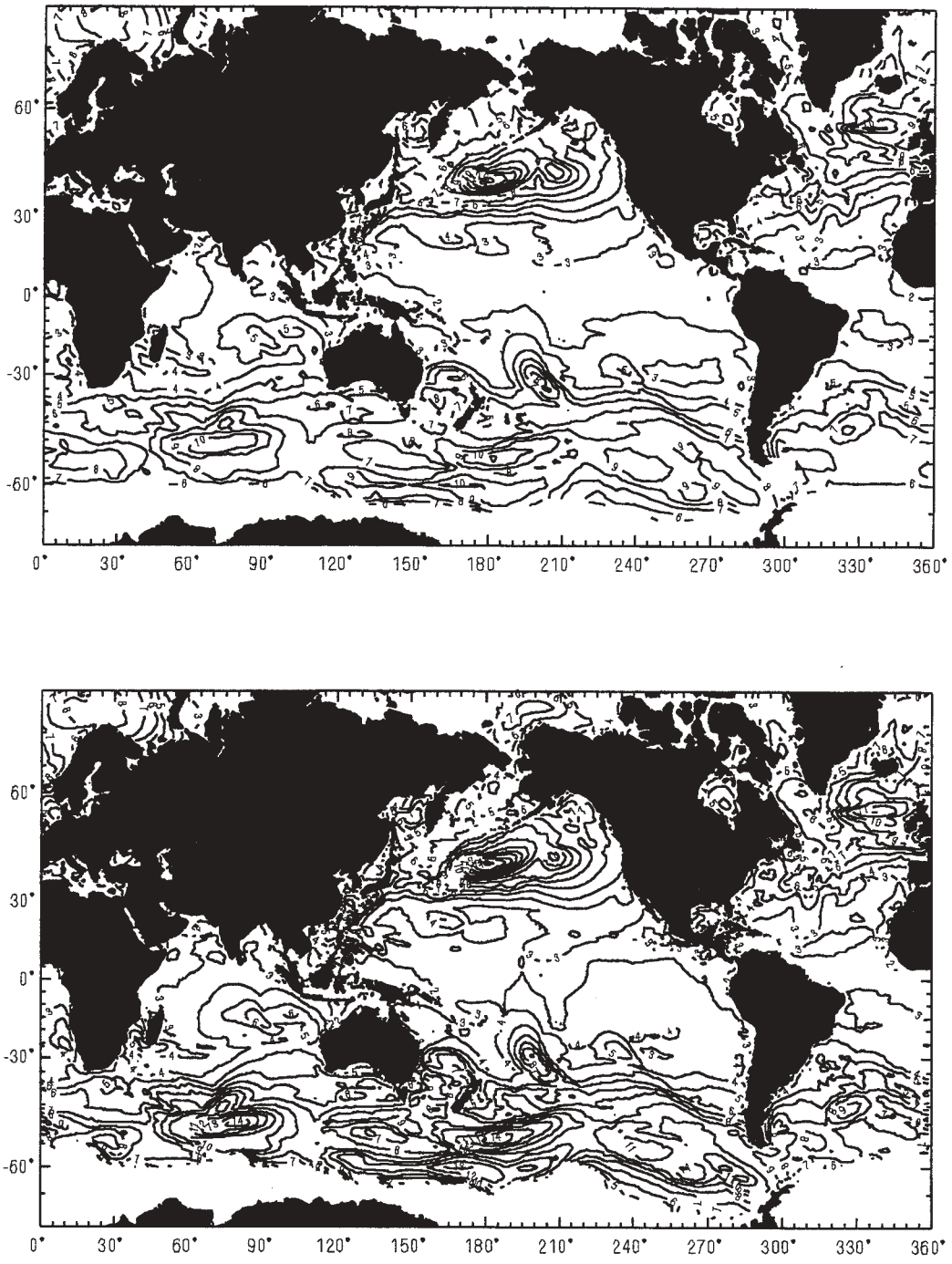

Figure 2. Maximum significant wave height (meters) hindcast for October 1998 for GROW (top) and GROW2000 (bottom).

AN EFFICIENT APPROACH TO WAVE CLIMATE ANALYSIS IN COASTAL WATERS

Mauro Sclavo (1), G.A. Athanassoulis (2), S. Barstow (3) and Luigi Cavaleri (1)

(1) CNR-ISDGM, S.Polo 1364, 30125 Venice, Italy Tel. +39-041-5216814; Fax +39-041-2602340; e-mail: sclavo@flux.isdgm.ve.cnr.it (2) Dept. of Naval Arch. and Mar. Engng, NTUA, Zographos 157 10, Athens, Greece (3) Oceanor, Pir-Senteret, N-7005, Trondheim, Norway.

1. INTRODUCTION

With the ever-growing activity in coastal waters and concerns related to the marine environment, the coastal engineer and marine scientist faces more and more the problem of obtaining the wave information he needs for his work. The typical solution is to ask an experienced third party to carry out a site specific study of the local wave conditions. Short cuts are often made, however, as the provision of such information is frequently either too expensive or takes too long.

Eurowaves, an EU funded MAST project, is aiming at providing a different, simplified alternative to engineers and others interested in coastal wave data, which will allow reliable coastal wave data to be provided in a timely manner. The project exploits the fact that the different information and software required to carry out the job are actually already available for a relatively modest investment. The main task of the project has been to assemble the different components into a sophisticated software package, which is at the same time user-friendly enough to be used by a person who is not necessarily an expert in the field. In this paper, we describe the general structure of the project, and its main component parts.

We start, in section 2, with a description of the construction of the offshore wave data base and statistics. This is followed, in section 3, by a description of the geographic software, which defines the bathymetry and coastline and allows the user to zoom in to the area of interest.

In section 4 the numerical models, which are used by Eurowaves to transfer the offshore information to the chosen location are described. Section 5 outlines the statistical package which can provide full information on the local wave statistics at the location of interest. In section 6 a sample of the capability of EUROWAVES is given. The potential for expanding Eurowaves at the next stage to any region world-wide is discussed in the final section on future developments.

2. OFFSHORE WAVE DATA

The area of interest for Eurowaves includes the whole European coast, starting from the Barents Sea in the North, down along the Atlantic coast, including the North Sea and the Baltic, ending in the Mediterranean and the Black Sea. Iceland and all the major islands (Faeroes, Azores, Canaries, etc.) are also included. For the enclosed seas and the Barents Sea, it was also natural to extend the interest to other non-European countries (Cavaleri et al, 1999).

Three major sources of wave data can be considered: 1) Local measurements, 2) Remotely sensed measurements, 3) Wave model simulations. We will briefly discuss the availability for the Eurowaves area of each type of data and discuss their characteristics.

2.1 Local measurements

This has been, for several decades, the only objective source of wave data. Many different instruments have been devised, the most common by far being the wave measuring buoy. Various different technologies are used by the manufacturers of wave buoys. Although there is no co-ordinated European-wide wave data collection paralleling the network operated by NOAA in the US, most countries have embarked on data collection for different reasons over the years, with responsibility for data banking resting with the different countries.

Through a network of contacts known to the Eurowaves partners, available wave measurements have been sought from throughout Europe. Agreement has been reached with holders of wave data in 15 countries and many of these data are currently being received, archived and documented. Despite the rather successful data acquisition, the number and location of the measurement sites (with dense coverage in some areas and sparse in others) are still far too limited for an extensive statistics to be built up along all European coastlines. Therefore, while the data they provide are locally very useful,

their use in Eurowaves is mainly for validation of the wave model data. This will be discussed later in the paper.

2.2 Remotely sensed measurements

Remote sensing can be used both at close and far range. At close range, a radar, for example, may be installed on the coast or on a high structure offshore. The back-scattered signal, properly interpreted, can provide information over an area around the source (from a few metres to hundreds of kilometres depending on the technique employed). However, the real breakthrough for our purposes came with the advent of microwave radar instruments on board of orbiting satellites, capable of providing accurate wave measurements along a ground track at nadir or swath to the side of the satellite. Currently the most useful satellite wave measuring instrument is the satellite altimeter. This instrument can provide significant wave height measurements close to the accuracy of a buoy from an orbit of typically 1,000 km. Measurements are provided each second, whilst the satellite covers a repeated net of ground tracks at about 6 km/s. This provides enormous amounts of wave data worldwide, and with, at present, a steady flow of new data from 3 or more operational satellites, millions of new observations are becoming available each month. Altimeter measurements have been performed during 1985-1989 (US Navy's Geosat), from 1991 by ESA's ERS-1 and ERS-2 satellites, and from the US/French Topex/Poseidon mission since 1992.
Algorithms for the correct interpretation of the back-scattered radar return pulse have been gradually improved, and the values presently derived show an accuracy close to buoy data (see Figure 1 and Krogstad and Barstow, 1999). However, some uncertainty still exists in the high wave height range, and this can, in particular, influence the evaluation of extreme conditions when extrapolating satellite data alone or using the altimeter data to calibrate wave model data.
All methods and instruments have their own particular drawbacks. It is important to be aware of the error sources and to combine the different information into a single data set to provide the best possible overall information. This leads naturally to the discussion of wave model data in the next sub-section.

2.3 Wave model data

Wave modelling relies on the description of wave growth, decay and propagation by a system of mathematical equations and given the availability of sufficient information on the initial conditions and external input, solving the system provides, in principle, the evolution of the process in time and space. Steady improvements both in theory and computer power have led to today's very sophisticated models, which are presently used to produce daily wave forecasts on global, regional and sometimes site specific scales. With respect to wave measurements, the biggest advantage of wave modelling is its capability to operate in the past (hindcast). The key point is that the meteorological information, in practice the surface wind fields, are available for the recent past, over a period up to tens of years.

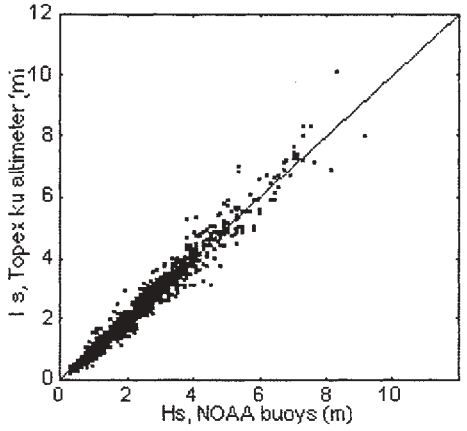

Figure 1. Comparison of significant wave height between the Topex altimeter and NOAA buoys for 1,365 coincident data (from Krogstad and Barstow, 1999).

These fields can be used to derive, through the wave model, similarly extended wave results, although the model results can be verified strictly only for the period and location where measured wave data are available. In offshore waters, it should be noted that we can verify the hindcast practically anywhere for the time period when altimeter missions have been operational (i.e., 1986-89 and 1991 to present). In addition, if no substantial discontinuity is present in the quality of the wind fields, we can assume the same to be also true for the wave fields, in practice allowing validating the results for the whole hindcast period.
In practice, the limiting factor is the accuracy of the input wind fields, to which the wave results are extremely sensitive. As a result, while we have quite good results in the open ocean (see Figure 2a), the quality decreases in the Mediterranean Sea (Figure 2b), and more generally in the enclosed basins.
This is where the synergy between the different sources steps in. As the accuracy of the measurements, both buoys and satellites, is

independent of the dimensions of the basin, we can use them to validate and calibrate the model data. The result of this merging of data sets is then a reliable long-term data set, expanded in time and space relative to the measurements alone, and providing exactly what is required for the first component of Eurowaves.

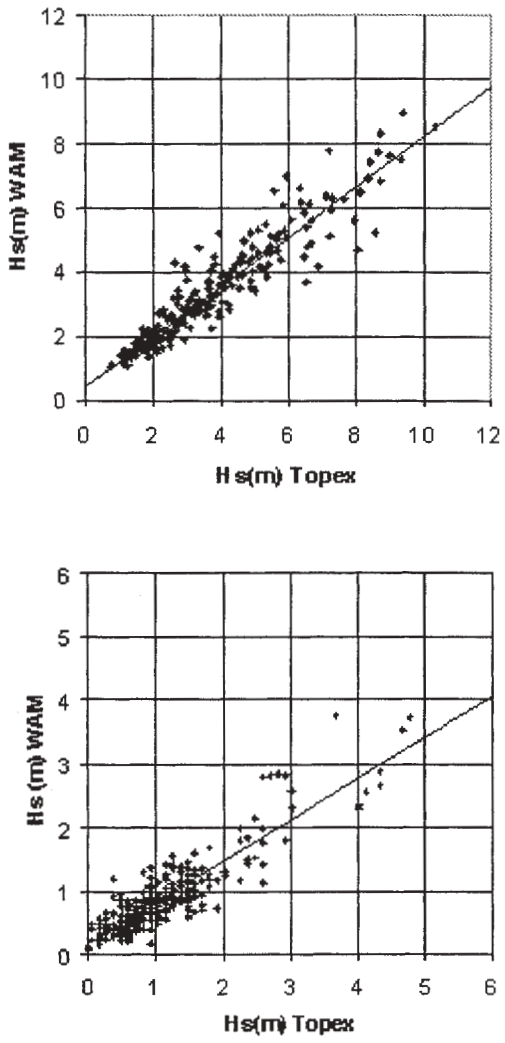

Figure 2. Comparison of significant wave height between WAM model data (y) against altimeter data from Topex for: top) the West of Ireland and bottom) the Mediterranean off Libya (after Mørk and Barstow, 1998a and 1998b).

For our purposes, the main source of data is the European Centre for Medium-Range Weather Forecasts (ECMWF, Reading, UK), where the WAM wave model (Komen *et al.*, 1994) has been operational since 1992. The data are available at 6 hourly intervals, with a resolution that has been changed in time, from 3 to 1.5 then 0.5 degrees in the open ocean, and from 0.5 to 0.25 degrees in the Mediterranean and the Baltic. In addition, hindcast data sets, at both large and local scale, are being considered as a source in Eurowaves, namely the ERA hindcast at ECMWF and the WASA project hindcast (Gunther *et al.*, 1997), the latter spanning a period of 40 years.

The model data, calibrated using the satellite and buoy data, provides the material for the next step, i.e. the statistics offshore.

Figure 3 shows, for part of the Atlantic coast of Europe, the points where wave information is available. The points close to the coast are 0.5° spanned, which assures enough definition in space for the boundary conditions. For each point information is, for the time being, available from July 1992 to June 1999 at 6 hour interval, summing up to more than ten thousand events per point. When, due to the WAM model resolution that has been changed in time, data were available with a coarse resolution (1.5°), the data have been interpolated on a finer grid (0.5° step). Interpolated data are a small fraction of the obtained data base.

The Mediterranean, North Sea and Black Sea model coverage (not shown here) was assured on a 0.5 degree space span basis from 1992 onward.

3. GEOGRAPHICAL DATA

To obtain the final results at the nearshore location, the user is able to interact with the system, and easily indicate the location of interest. A specific software has been developed that, starting from an overall view of the Eurowaves area, allows the user to zoom progressively in to the area of interest, and to choose the exact location by using the mouse.

Towards this objective, two pieces of information had to be assembled. First, full bathymetric information and an accurate description of the coastline for the whole Eurowaves area was needed. After a careful search of the available data sets, the DBDB-V data base was selected for the bathymetry. This data set was released in 1996 and was last updated in 1998. It covers the whole area of interest and numerous tests have shown that it is the data set presenting the best overall quality and least compatibility problems with the definition of the coastline. The coastline data were extracted from the GMT High Resolution Coastline Database (GMT-HRCD), released in 1995. It has a working scale of 1:250000, containing vector information in a polygon format. As expected, the coastline database, derived from detailed satellite images, is much more accurate than the bathymetry. Close to the coast, in

AUTHOR INDEX TABLE OF CONTENTS

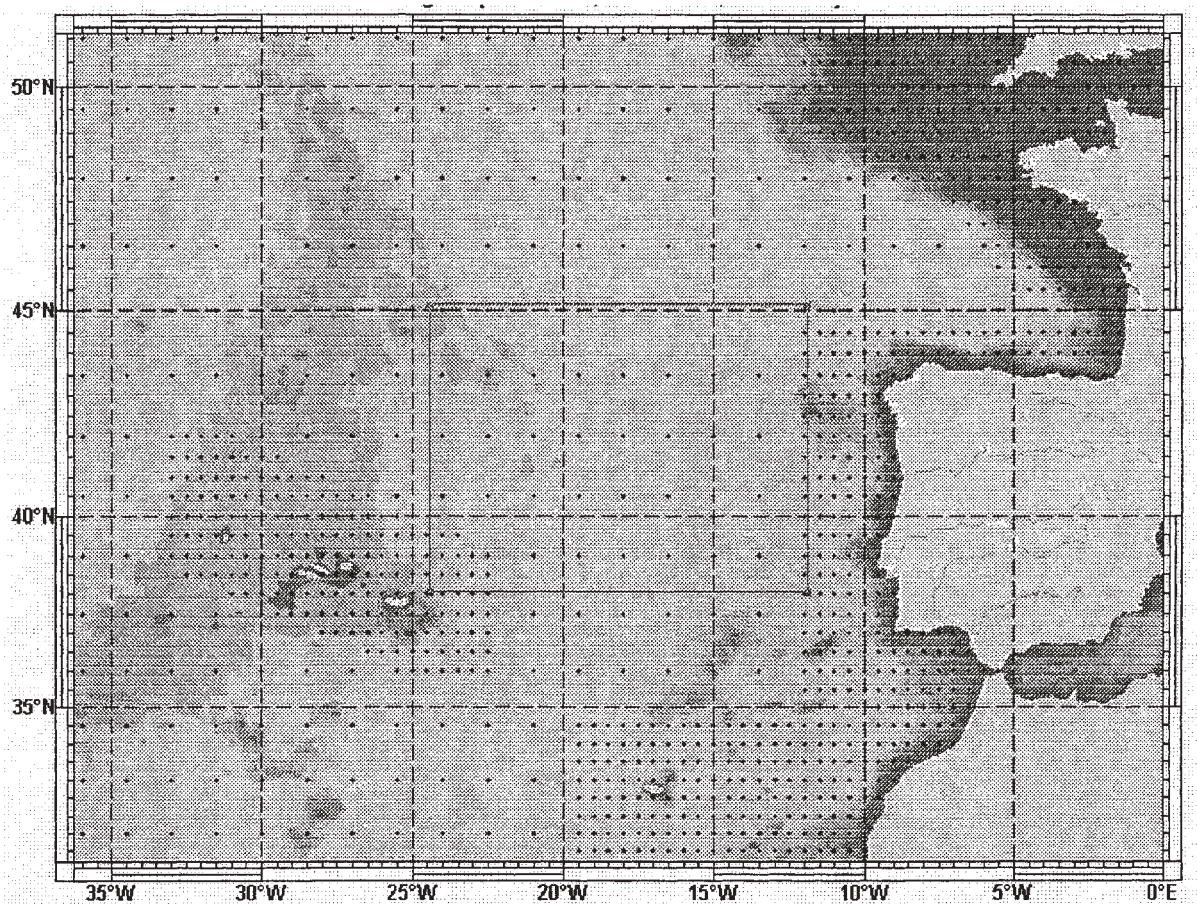

Figure 3. Data point distribution in the Atlantic.

areas rarely explored with ship sounding campaigns, the bathymetric data often seem to have been interpolated from offshore values to some reference point on the land. This can lead to erroneous isobaths close to the coast. A good example is shown in Figure 4 (top panel), where there is an overlap of the depth and coastline areas.

Based on the fact that the GMT-HRCD database is the more accurate one of the two, a procedure has been devised to optimise the overall information. Towards this aim, the coastline points are considered as points with zero depth. A triangulation is performed that represents the sea bottom surface (Figure 4-middle). This enhanced data set is used to obtain, by interpolation, a finer local grid for the examined area, which in turn serves as a basis for estimating the new isolines of constant depth (Figure 4-bottom). This results in a marked improvement of the shallow water bathymetry.

The second piece of software which was required is an interface with the user that, starting from the overall map of Europe, can zoom gradually in to the area of interest and allow the user to choose the location after inspecting the detailed local bathymetry, and geometry of the coast. The user is also allowed to introduce his own local bathymetric information, should he have a more accurate one.

4. WAVE TRANSFORMATION

Once the offshore information is available, and after the user has indicated on the screen the area and the specific point P where he requires the results, the transfer of the wave conditions to P may be performed. This involves the following steps 1) A fine local grid is established; 2) The most suitable wave model is run; 3) Statistics for P are calculated. The last point will be discussed further in the next section 5. Here we deal with points 1 and 2.

4.1 Establishing the grid

In Eurowaves, it is planned to provide results at least as close as five kilometres from the coast and down to five metres depth. This is basically connected to the practical accuracy with which we know the bathymetry close to the whole European

AUTHOR INDEX TABLE OF CONTENTS

coastline. If, as mentioned in the previous section, more detailed local information is introduced, the user can move even closer to the coast and ease the restriction.

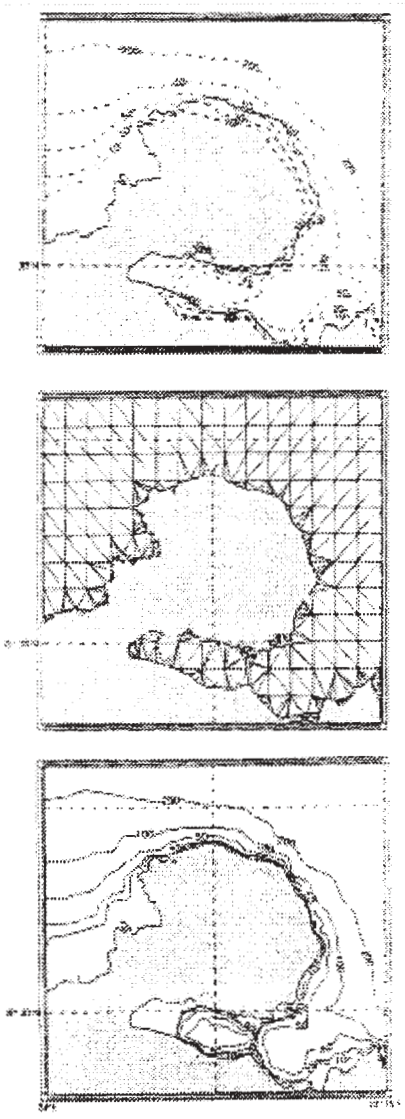

Figure 4. Top) original isolines and coastline profile; middle) triangulation of the coastline and bathymetric data; bottom) the new isobaths after interpolating from the triangulation.

However, a practical difficulty may be the computer time required for the calculations. The point is that, moving closer to the coast, the grid must have enough resolution to describe the predominant local details. On the other hand the grid must extend offshore at least to the points where the wave conditions are known (see the second section) in order to provide the necessary boundary conditions. A finer grid will lead to a rapid increase of the number of points, and hence of the time required for the calculations.

The time will depend in a critical way also on the type of model selected by the user. Eurowaves offers two models to the user, ranging from the simple back-tracing ray technique which considers only refraction, shoaling and generation by wind (VENICE model), to the advanced third generation models that take full consideration of all the relevant processes that govern wave evolution in both deep and shallow water (SWAN model).

The VENICE model (Cavaleri and Malanotte Rizzoli, 1981) is a backward ray-tracing model. Before its implementation in EUROWAVES, the model code has been fully revised and optimized for efficiency.

The SWAN model is a recently developed third generation model, specifically designed for shallow-water applications, available in public domain at http://swan.ct.tudelft.nl. A full description of the model is provided by Booij et al, 1999 and by Ris et al, 1999.

Presently, on PIII 600MHz, one run of the SWAN model with about 300 grid points takes about 10 seconds. With six hourly data, about 1500 wave conditions have to be transferred each year. For a ten year time series, the cpu time is about one day. The user can perform the transformation on a subsample of the time series (e.g. consider two or one events per day) and obtain sensible results in a night time. The VENICE model allows a complete time series transformation in less than 2 minutes (i.e. is about 1000 times faster!).

As a rule, the more sophisticated models should produce better results, at least in complicated bathymetric areas, very close to the coast and for extreme wave conditions. Therefore, the choice will often be a trade off between the resolution at the coast, the accuracy of the results and the time required for the calculations. A possible optimum strategy for the user could be to attack the problem first with a simple (and fast) model, followed, possibly, by a more elaborate approach for the final calculations and/or for analysis of special events such as extremes sea conditions.

As the "best" solution depends on the specific problem, on the geometry of the area, the local bathymetry, on the wave climate offshore and obviously on the requirements of the user, we offer to the user more than one approach, with guidelines as far as the implications in terms of accuracy and computer time.

4.2 Wave modelling

It is clear that the user must be given suitable information on the possible accuracy of the different

models. For this purpose a lot of effort in Eurowaves was put on validation, testing the various models against measured data. For this purpose, multiple measurements are required.

Given a suitable location with certain characteristics, e.g. a bay with a sloping bottom, we need contemporary wave data taken offshore, say at A, and at a more inshore location B. Using the A data as input, we can model the transfer to B and verify the model results against the data from B.

One of these data sets being used for this purpose has been collected at Holderness, on the East Coast of England. Prandle et al. (1996) give a full description of the measurement campaigns and the available data. A sample of the results from the SWAN simulations (the number of runs of the model amounts to several tens of thousands) is given in Figure 5.

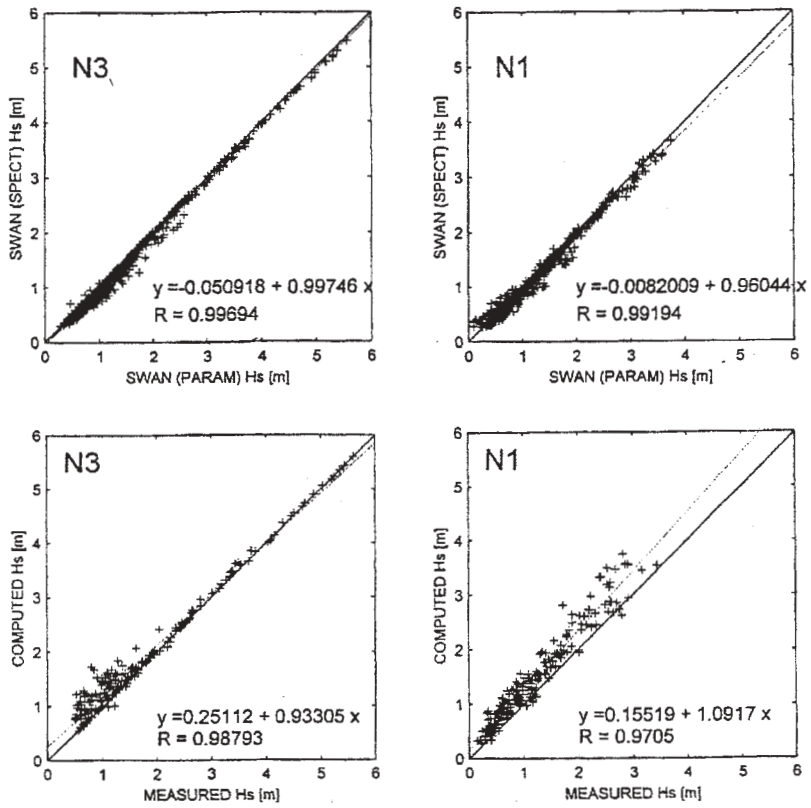

Figure 5. Wave model simulations of the data collected at Holderness, UK. N3 offshore buoy, N1 inshore buoy. Top, left and right: comparison between the spectral and the parametric approach; bottom, left and right: comparison between the measured and modelled wave height, taking wind into account.

The A and B buoys mentioned above (N3 and N1 in the figure) were moored at about 12 and 1.6 kilometres off the coast, at respectively 30 and 12 metres depth. Among other possibilities, we explored 1) the effect of having as input a two-dimensional spectrum or only the summarising parameters (H, T, θ); 2) the influence of the local wind on the results. We note from top panels (left and right) that the parametric approach leads to higher values at the inner buoys with respect to the spectral approach. The reason is that, considering only the cases with dominant waves moving towards the shore, and summarising the wave conditions at A (N3) by a single triplet, we include inherently into the model onshore propagating input also the wave components, which were actually moving offshore.

A similar argument applies to the effect of the wind (bottom panels in Figure 5). A wind towards the shore leads generally to higher waves closer to the coast, hence at B (N1). However, this can also occur with the model even with an offshore blowing wind. For the same reason as that explained above, if the dominant wave system is moving onshore, the buoy will add up the two systems into the triplet (H, T, θ), providing an apparent input to shore larger than the actual.

Sclavo and Cavaleri (1999) give a fuller discussion on this. It is clear that these effects need careful consideration when deriving and interpreting coastal statistics from a wave model. From the WAM model, we have 6 parameters, 3 each for wind sea and swell. Using all 6 parameters potentially solve this problem. Using the 6 parameters as input, a spectral reconstruction procedure has been devised, which can also infer a sensible wind speed and direction (from the 3 wind sea parameters). The procedure has been tested and validated reconstructing, from the 6 parameters of the EUROWAVES data base more than 100 spectra and then compared with the original (f, θ) spectra of the ECMWF archive. The devised method is quite capable to reconstruct also the bi-modal spectra from the 6 parameter information of the EUROWAVES data base, as shown in Figure 6.

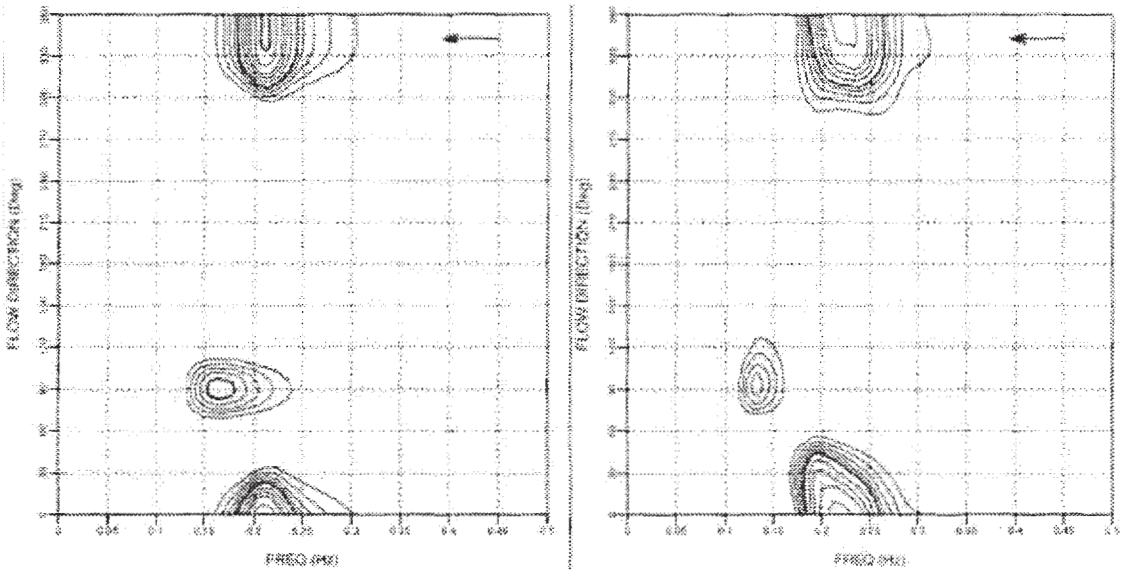

Figure 6. spectrum left) as reconstructed from the 6-parameters of the EUROWAVES data base and right) as in the ECMWF archive.

The Figure (left panel) represents a bunch of swell ($fp \cong 0.17$ Hz, $\theta p \cong 90°$N) propagating at almost cross angle with respect to a wind-sea system ($fp \cong 0.21$ Hz, $\theta p \cong 315°$N), as reconstructed from the 6-parameters of the EUROWAVES data base. The right hand panel shows the fully (f, θ) spectrum from the ECMWF archive, referred to the same time and location. It is evident that the devised reconstruction procedure catch the main features of the spectrum, both in frequency and direction. In the case shown here, both the swell and wind sea directional spreading are underestimate by the reconstruction, but must be considered that the parameters governing the spreading have been optimized to suit at best the more than 100 spectra used for the tuning.

Similar model validation work has been carried out against other data sets in Europe (e.g., Figuera da Foz Portugal and Montalto di Castro, Italy) where buoy data are available in offshore and coastal waters simultaneously (these test are described by Sclavo and Cavaleri, 2000).

5. STATISTICAL PACKAGE

Ideally, we would like to transfer the full offshore six hourly time series to the nearshore location P. With a perfect model, and given all the necessary local information, this would correspond to having had a wave measuring instrument operational at P for the corresponding length of time. A simple transformation of the offshore series in this way leads to some difficulties. In practice, all the input data have been provided under the condition that the time series data are not to be transferred to third parties (i.e., the actual time series cannot be included with the Eurowaves package) , i.e. the actual time series cannot be included with the Eurowaves package. The solution has been to scramble the data in time, destroying their actual time sequence. Scrambling is done on a monthly basis, so that the average yearly distribution is available, and uniformly in space, so that the structure of the single fields is maintained. Running a wave model for the whole time series provides the corresponding results at P, suitable for statistical analysis.

A complete package is provided for this purpose, supplying all the fundamental one- and two-dimensional distributions concerning the basic parameters and their combinations, e.g. the wave steepness

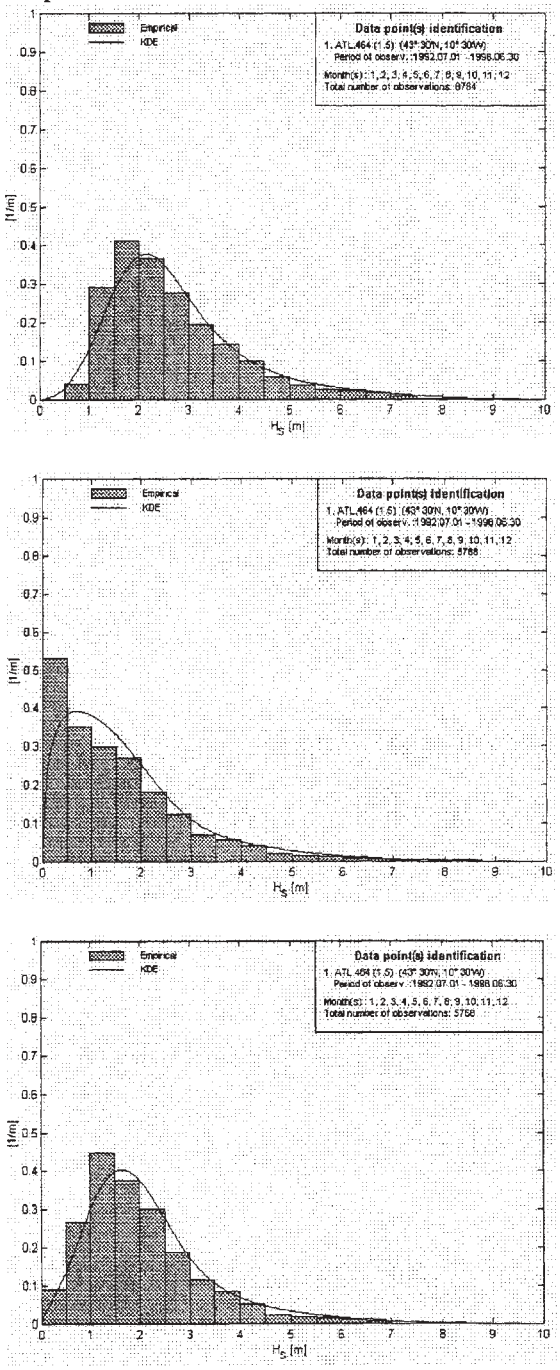

Figure 7: Hs distribution for point P (43.5°N, 10.5° W). Top: overall sea. Middle: wind sea. Bottom: swell. All months have been taken into account.

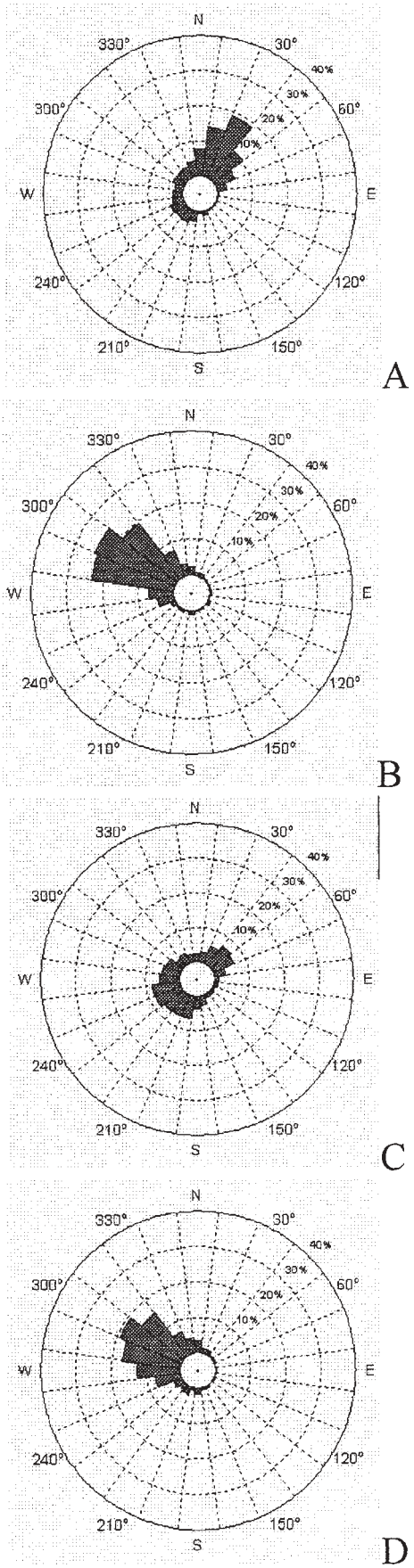

Figure 8 (right): Directional wave distribution of a) summer wind sea; b) of summer swell; c) winter wind sea and d) winter swell.

AUTHOR INDEX TABLE OF CONTENTS

The statistical results, available as plots and tables, can be exported for further analysis by the user. Figure 7 shows the Hs statistics for a point off the Portuguese coast (43.5°N, 10.5° W), for the overall sea and , separately, for swell and wind sea.

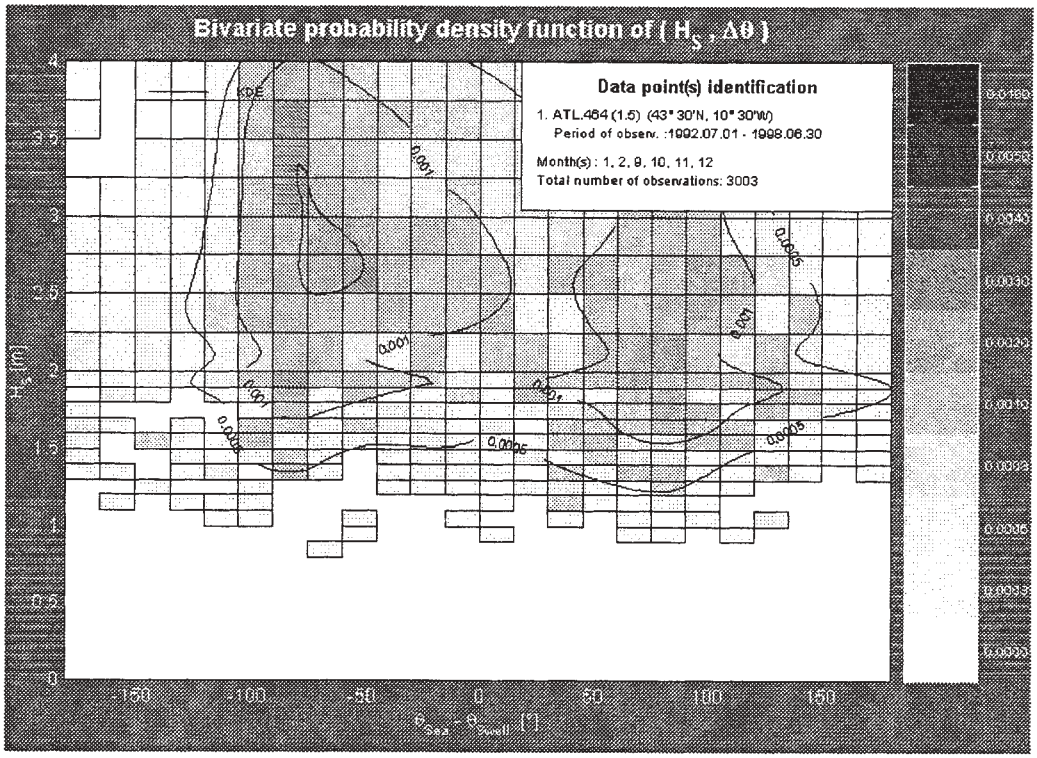

Figure 9. Bivariate probability density function of (Hs, Δθ), with Δθ =difference between the wind sea direction and swell direction. Winter.

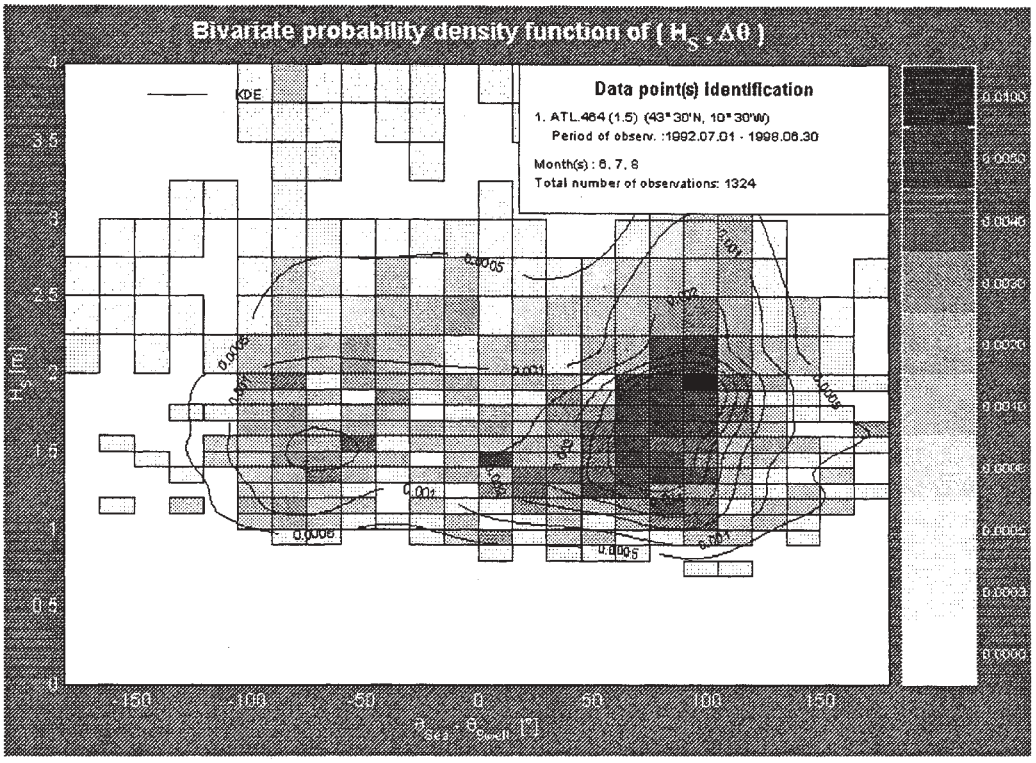

Figure 10. As Figure 9, but for Summer months.

AUTHOR INDEX TABLE OF CONTENTS

The statistical package allows, for all the available statistics, several data interpolation procedures; as an example Figure 7 shows, together the "empirical" data, the fit obtained with a Kernel Density Estimation (KDE) procedure.
The statistics separated for wind sea and swell are, as expected, more informative than the one referred to the overall sea. For example, the Raleight-like distribution of the wind waves, is evidenced only in the split statistics.
As a further example, Figures 8a-8d report wave direction statistics for the same point, separately for winter and summer season and for swell and wind sea.
While the prevailing swell direction is roughly constant (N-W), the wind sea directional distribution exhibits a seasonal pattern (from N-E in summer and from S-W in winter). This feature is further evidenced by one of the bivariate statistical analysis the Eurowaves can perform. In fact the joint distribution of wave height and difference in direction between wind sea and swell exhibits different pattern for winter and summer.
In winter, Figure 9, the wind sea is distributed at both side of the swell with a prevalence of wind sea from the right of the swell (θ wind sea < θ swell) in conjunction with more severe sea states.
In summer, Figure 10 , the wind sea is prone to come from the left of the swell, at a 90° angle. This cross sea condition seems to be a summer feature both for low and severe sea states.

6. A CASE STUDY

As an example, Figures 11 and 12 show the layout and some results of a nearshore statistics reconstruction from offshore data.

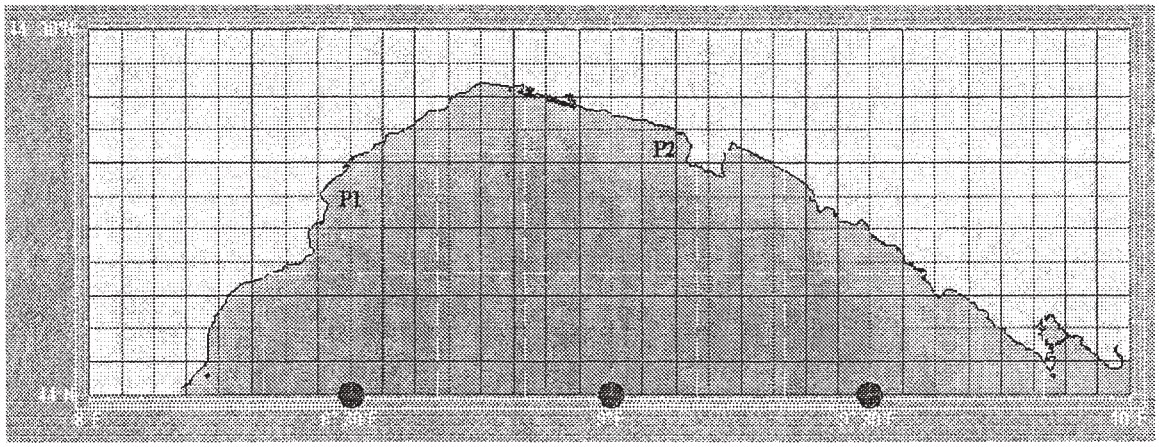

Figure 11: The Genua Gulf layout (Tyrrenian sea), with superimposed the computational grid obtained with the default EUROWAVES setting. The three dots on the lower side show the locations (0.5° spanned) where the long term time series are available. P1 and P2 are the nearshore locations selected for the transferring.

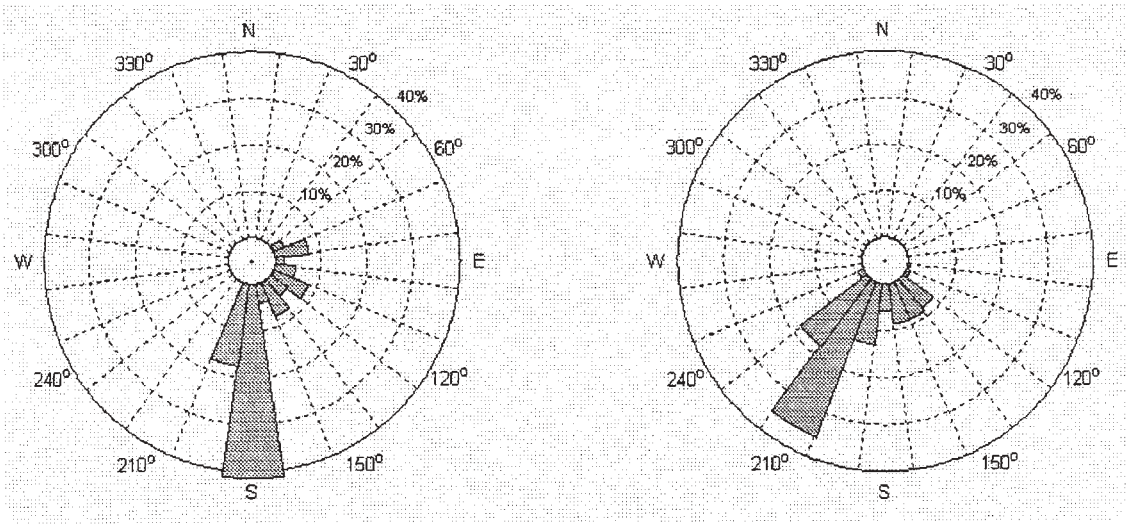

Figure 12: Directional wave distribution at locations P1 (left) and P2 (right) in Figure 11.

Figure 11 shows the Genua Gulf layout (Tyrrenian sea), with superimposed the computational grid obtained with the default EUROWAVES setting. The rationale of EUROWAVES is to suggest a grid that take into account the main bathymetric features with an eye on the required cpu time. Should the user want to give more consideration to one of this aspects, he is allowed to increase or decrease the grid resolution. The three dots on the lower side show the locations (0.5° spanned) where the long-term time series are available. The user can select the points he want to be considered in the definition of the boundary condition. EUROWAVES then takes care of the interpolation. When defining the boundary conditions from the built in data base the user is obviously stuck, for the choice of the grid dimension, to a 0.5° space spanning. The user can also introduce his own input data, and in this case the choice of he grid is completely free.

As for the grid choice, EUROWAVES suggests sensible default values for all the relevant inputs (e.g. wind velocity and direction, bottom friction coefficient). The experienced user can change this values to better suit the simulation to his needs.

P1 and P2, in Figure 11, are the nearshore locations selected for the transferring. When the target point for the nearshore statistics is selected, a nested grid (not shown), finer than the main computational grid is automatically created and centred on the target point. The aim is to take into account the bathymetry details with the minimum cpu surcharge. As for the main grid, the user can change the default settings.

Figure 12 shows, for the situation outlined in Figure 11, the directional wave distribution at P1 and P2, as obtained with EUROWAVES using the SWAN model and as input conditions the time series from the EUROWAVES data base.

7. FUTURE DEVELOPMENTS

In practice, all the important components being used to construct Eurowaves; i.e., the wave model data, satellite altimeter data, bathymetric and coastline data as well as the wave models themselves can be put together for any country or region globally. The Eurowaves group has already extended to one new area, the Black Sea (Cavaleri et al., 1999), although, in this case, hindcast data were not previously available and a new hindcast was therefore performed to provide the basic offshore time series. As an example, the model grid points and the satellite ground tracks are shown for the area of the western South Africa and Namibia in Figure 13.

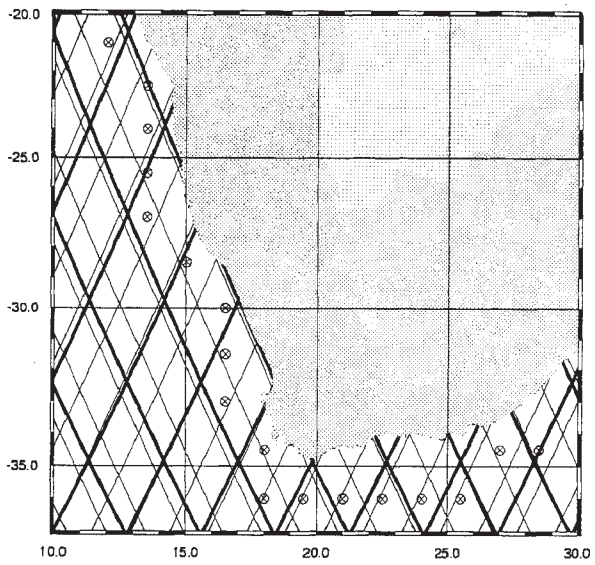

Figure 13. Satellite altimeter (Topex: thick lines, Geosat: thin lines) and offshore wave model grid points from the WAM model for an area off Southern Africa.

8. ACKNOWLEDGEMENTS

This work has been carried out under the MAST project Eurowaves, contract MAST3-CT97-109.

9. REFERENCES

Booij, N., R.C. Ris and L.H. Holthuijsen, 1999: A third-generation wave model for coastal regions – 1. Model description and validation. J. Geophys. Res, 104, 7649-7666 .

Cavaleri, L. and P. Malanotte Rizzoli, 1981: Wind wave prediction in shallow water – theory and applications. J. Geoph. Res., 8b, C11, 10961 – 10973.

Cavaleri, L., L. Bertotti, J. Bidlot, M. Sclavo, G. Mørk, S. Barstow, G. Athanassoulis and C. Stefanakos, 1999: Hindcast and calibration of the wave conditions in the Black Sea. Proc. International Medcoast Conference on the Wind and Wave Climate in the Mediterranean Sea and the Black Sea., Antalya, Turkey.

Gunther, H., Rosenthal, W., Stawarz, M., Carretero, J.C., Gomez, M., Lozano, I., Serrano, O. and Reistad, M. ,1997: The wave climate of the Northeast Atlantic over the period 1955-1994: the WASA wave hindcast. GKSS Report 97/E/73, 34 pp.

Komen, G.J., Cavaleri, L., Donelan, M., Hasselmann, K., Hasselmann, S. and Janssen,

P.A.E.M. ,1994: Dynamics and Modelling of Ocean Waves. Cambridge University Press, 532 pp.

Krogstad, H.E. and Barstow, S.F, 1999: Satellite Wave Measurements in Coastal Engineering Applications. To be published in Coastal Engineering.

Mork, G. and S. Barstow, 1998a: Comparison of WAM estimates of H_s with TOPEX/ POSEIDON altimeter data in the Mediterranean Sea; a comparison of low and high resolution wind models. OCN R-98019, 10 pp.

Mork, G. and S. Barstow, 1998b: Comparison of WAM estimates of Hs with Topex/Poseidon altimeter data in European Atlantic waters; a comparison of low and high resolution wind models. OCN R-98025, 10 pp.

Prandle, D., Harrison, A., Hunphrey, J., Lane, A., Player, R., Williams, J.J. and Wolf , J.(1996): The Holderness Coastal Experiment '93-'96, POL, Report 44, 48 pp.

Ris, R.C. , N. Booij and L.H. Holthuijsen, 1999: A third-generation wave model for coastal regions – 2. Verification. J. Geophys. Res, 104, 7667-7681.

Sclavo, M. and L. Cavaleri, 1999: Sensitivity analysis of the of the offshore wave conditions to a coastal location. Proc. Medcoast Conference, Antalya, Turkey.

Sclavo, M. and L. Cavaleri, 2000: The transfer of wind waves from the shelf to the coastal zone. Il Nuovo Cimento, 23C n°3, 315-325.

JOINT DISTRIBUTION FOR WAVES AND CURRENT IN THE NORTHERN NORTH SEA

Kenneth Johannessen
Einar Nygaard
Sverre Haver
Per Strass

Statoil
Stavanger, Norway

1. INTRODUCTION

For design purposes, the 100-year response is traditionally estimated by combining the 100-year wind, 100-year wave and 10-year current. This method of estimating the response will most probably be conservative and we will therefore address the following work to show that current speed associated with the 100-years significant wave height, H_{m0}, is significant lower than the current speed, U, with a return period of 10 years. In accordance with NORSOK (1999), a joint distribution for waves and current may be used if sufficient joint data are available. By producing contour lines for wave height versus current speed, the worst combinations of waves and current may be identified. The expected current speed for given significant wave height with a return period of 100 years, is in the following defined as "associated current". By using the contour lines, the variability in the current speed will be revealed. Figure 1 shows a map of the area of interest. The Snorre, Kvitebjørn and Oseberg fields (Statfjord area) are shown (BODC, 1998).

2. DATA SOURCES

Table 1 gives a general view of the environmental data that have been used in this analysis and the periods they cover. The current data have been smoothed and resampled to give average current over 1 hour. Wave data were interpolated to give H_{m0}, with an interval of 1 hour. Poor quality data or instrument failure during the measuring periods reduced the simultaneous period of wave and current data to 1.8 years. This may be somewhat limited in view of the design lifetime.

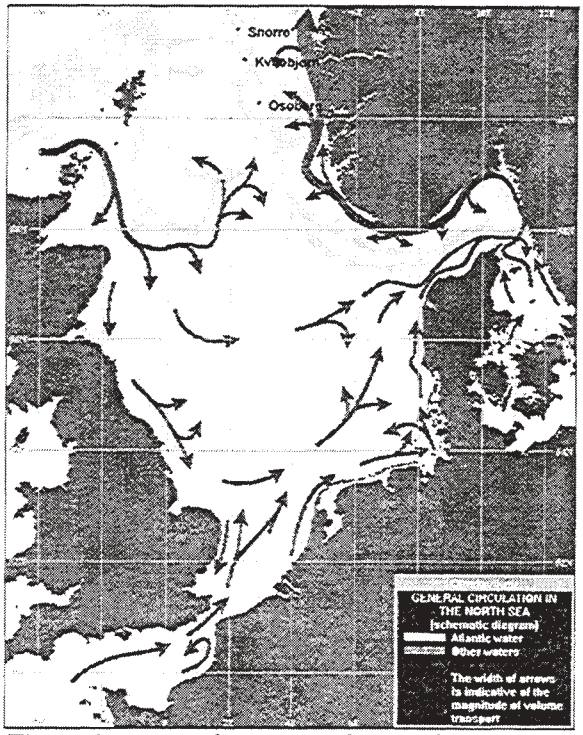

Figure 1. *Area of interest and general circulation, (BODC, 1998).*

Table 1. *Time series for waves and current in the Northern North Sea.*

	Period	Depth	Instrument
Current			
Snorre	1984-1985	20 m	UCM *
Snorre	1985-1987	20 m	UCM
Oseberg	1982-1983	25 m	UCM
Waves			
Statfjord	1982-1987	0 m	Wave buoy

*Ultrasonic current meter

Table 2. Simultaneous data of significant wave height versus current speed in the Northern North Sea.

U (cm/s)	H_{m0} (m)												
	0 - 1	**1 - 2**	**2 - 3**	**3 - 4**	**4 - 5**	**5 - 6**	**6 - 7**	**7 - 8**	**8 - 9**	**9- 10**	**10- 11**	**11- 12**	**Total**
2.5	238	990	640	306	166	76	27	7	0	0	0	0	2 450
7.5	407	1 470	1 395	739	414	165	93	29	4	0	0	0	4 716
12.5	249	1 193	1 044	691	417	218	105	23	3	4	2	0	3 949
17.5	100	712	666	494	261	229	88	31	8	7	1	0	2 597
22.5	44	305	306	250	171	121	43	12	19	9	11	0	1 291
27.5	12	112	140	97	101	53	12	8	3	2	0	0	540
32.5	2	32	43	28	30	15	7	6	2	0	0	0	165
37.5	0	9	12	19	14	10	2	0	0	0	0	0	66
42.5	0	3	2	3	9	5	0	0	0	0	0	0	22
47.5	0	2	2	1	4	1	0	0	0	0	0	0	10
52.5	0	0	0	0	4	0	0	0	0	0	0	0	4
Sum	**1 052**	**4 828**	**4 250**	**2 628**	**1 591**	**893**	**377**	**116**	**39**	**22**	**14**	**0**	**15 810**

3. METHOD

The long term variation of the wave-current climate is assumed to be properly described by a joint density distribution for H_{m0} and U; $f_{H_{m0}U}(h_{m0},u)$. Based on simultaneous wave and current data, a scatter plot (Table 2) for H_{m0} versus U was established. The scatter plot shows that the highest current speeds generally correspond to wave heights of 4 to 5 meters while the current speeds associated with the highest waves were in the interval 20 to 25 cm/s. The conditional mean current is however, increasing with increasing significant wave height. The largest current speeds are found at moderate wave heights. This is mainly due to frequent observations of these sea states. In addition, the conditional standard deviation of current speed attains the largest value at moderate sea states. Figure 2 shows the mean current speed and standard deviation for given values of significant wave height based on the simultaneous data.

Based on the wave data in Table 2 a three-parameter Weibull distribution was fitted by use of the method of moments. H_{m0} with a return period of 100 years was estimated to 14.5 m.

A combined Log-Normal and a 2-parameter Weibull distribution (LoNoWe-distribution) was chosen. The computer program PHT was used (Haver et. al, 1998). Normally, this distribution gives an equivalent or better fit to the data than the three parameter Weibull distribution. Figure 3 shows the cumulative distribution of H_{m0} based on measured data, a 3-parameter Weibull distribution and a LoNoWe distribution.

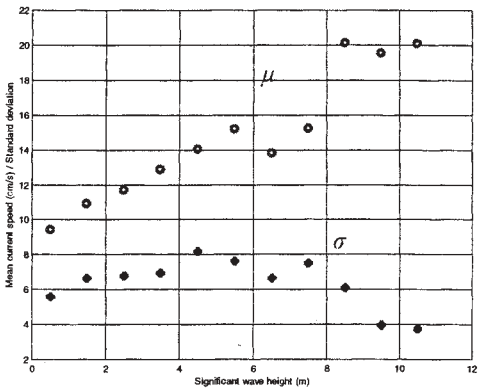

Figure 2 *Mean current speed (μ) and standard deviation (σ) versus significant wave height, based on simultaneous data from the Northern North Sea.*

To describe the conditional variation of current speed given the significant wave height a 2-parameter Weibull distribution was used. A plot showing the cumulative distribution of the current speeds for given classes of wave heights is given in Figure 4. Figure 4 shows also the resulting cumulative Weibull distributions obtained by using the parameterisation described in the following. The Weibull *shape* and *scale* parameters are expressed as follows:

AUTHOR INDEX TABLE OF CONTENTS

Scale : $\kappa(h_{m0}) = a_1 + a_2 \cdot h_{m0}^{a_3}$ (1)

Shape: $\xi(h_{m0}) = b_1 + b_2 * arctan(b_3 * (h_{m0} - b_4))$ (2)

where a_1, a_2, a_3, b_1, b_2, b_3 and b_4 are constants and h_{m0} is the significant wave height. The parameterisation of the *scale* parameter is based on the assumption that the parameter value would continue to increase also for wave heights above the range of measurements. By looking at the data points in Figure 5 the *shape* parameter seem to increase to very large values for large wave heights. This means that the conditional variability of the current will decrease with increasing wave heights. This is also shown in Figure 2. There is no reason to assume that the current speed will be deterministic for large wave heights even if the degree of correlation is expected to increase for increasing sea states. The *shape* parameter has therefore been parameterised in such a manner that it will converge to a reasonable value and thereby maintain a certain conditional variability of the current speed also for the largest wave heights.

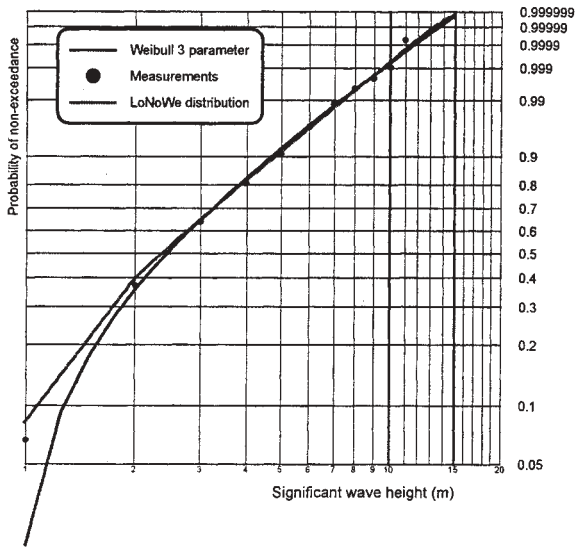

Figure 3. *Cumulative distribution of H_{m0} based on measurements during the period 1982 to 1987 for the Northern North Sea.*

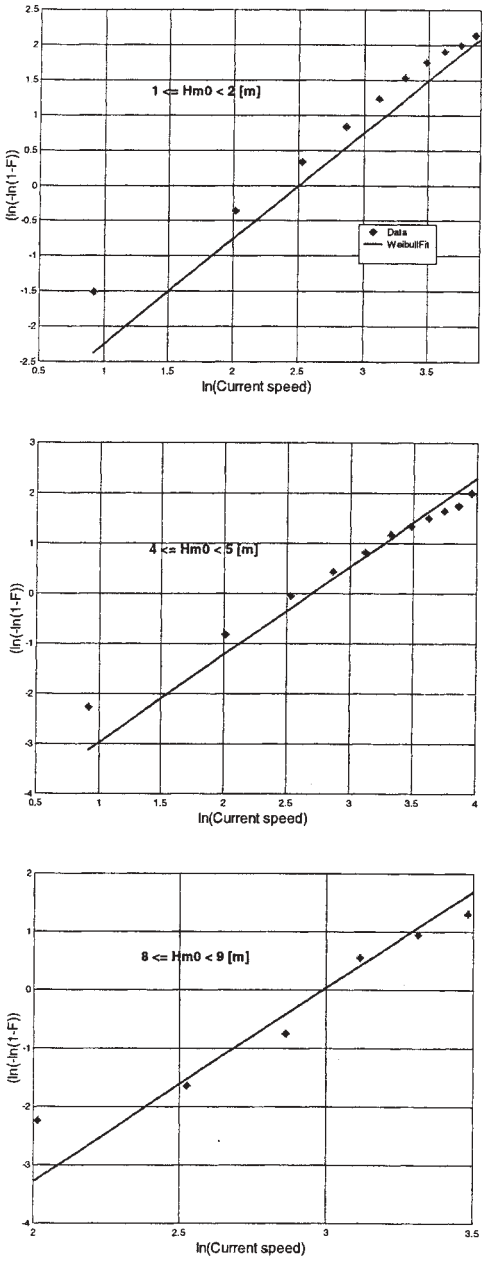

Figure 4. *Cumulative distribution of current speed for given wave height classes. Based on simultaneous data and a smoothed parameterisation.*

The program *PHT* was used to calculate the *scale* and *shape* parameters based on the measurements and thereafter a regression analysis/engineering judgement was used in order to estimate the coefficients a_1, a_2, a_3, b_1, b_2, b_3. and b_4 . Figure 5 shows how the *shape* and *scale* parameters vary with the wave height

AUTHOR INDEX TABLE OF CONTENTS

and how the smoothed curve fits to values obtained from the measurements.

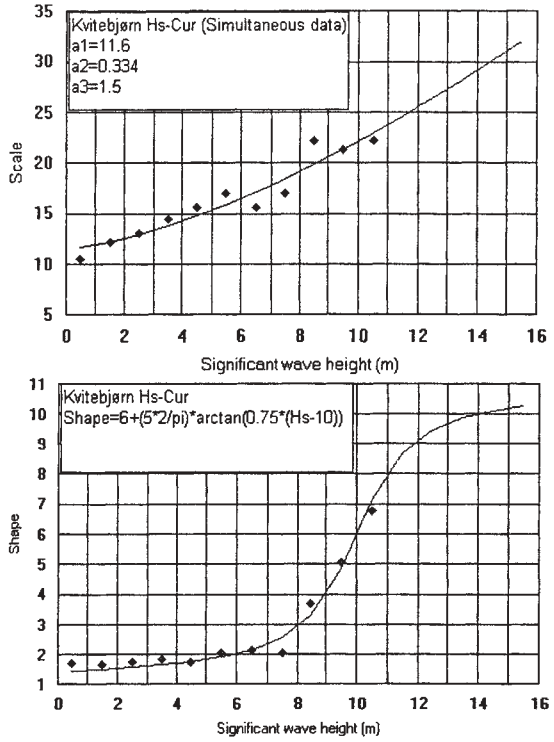

Figure 5. *Fitted shape and scale parameters in the distribution of U based on measured data and by a smoothed parameterisation.*

The mean current value and the variance of the current speed can then be calculated by:

Mean value:
$$\mu = \kappa \cdot \Gamma\left(\frac{\xi+1}{\xi}\right) \quad (3)$$

Variance:
$$\sigma^2 = \kappa^2\left[\Gamma\left(\frac{\xi+2}{\xi}\right) - \Gamma^2\left(\frac{\xi+1}{\xi}\right)\right] \quad (4)$$

where the parameters κ and ξ are functions of h_{m0} as given in Eq. (1 and 2). Γ is the Gamma function.

To examine how good the smoothed Weibull *shape* and *scale* parameters describe the conditional current speed characteristics, the mean and standard deviation obtained from Eqs. (3 and 4) were plotted in the same figure as the mean value and standard deviation based on the measured data (shown in Figure 2). The result is shown in Figure 6 and shows that the parameterisation is fairly good.

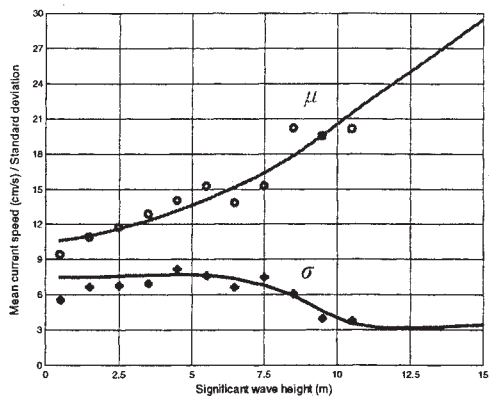

Figure 6. *Mean current speed and standard deviation versus significant wave height, based on simultaneous wave and current data and a smoothed parameterisation.*

Figure 7 shows all measured combinations of H_{m0} and U in addition to conditional expectation of U given H_{m0} both from measurements and the Weibull distribution. It also shows a 90% confidence interval for U given H_{m0} based on the Weibull distribution.

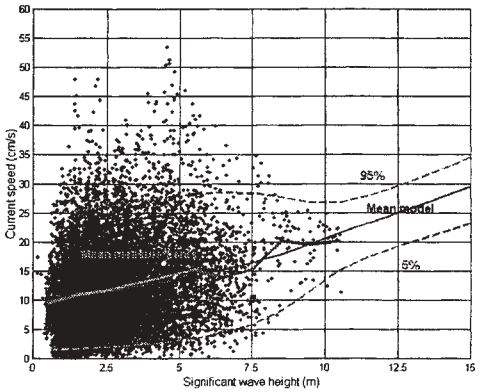

Figure 7. *Simultaneous measured combinations of H_{m0} and U, marked with dots. Mean U for given wave class is marked with a fat solid line. Expected U for given wave class based on a 2-parameter Weibull distribution is given with a thin solid line. A 90% confidence interval for U given wave class is given with broken lines.*

The suggested joint distribution function for significant wave height and current speed will be as follows:

$$f_{H_{m0}U}(h_{m0}, u) = f_{H_{m0}}(h_{m0}) \cdot f_{U|H_{m0}}(u|h_{m0}) \quad (5)$$

where

$$f_{H_{m0}}(h_{m0}) = \frac{1}{\sqrt{2\pi}\cdot a\cdot h_{m0}} \cdot \exp(-\frac{(\ln(h_{m0})-\theta)^2}{2\cdot a^2}) \quad \text{for } h_{m0} \le \eta \qquad (6)$$

and

$$f_{H_{m0}}(h_{m0}) = \frac{\beta}{\rho}\left(\frac{h_{m0}}{\rho}\right)^{\beta-1} \cdot \exp\left(-\left(\frac{h_{m0}}{\rho}\right)^{\beta}\right) \quad \text{for } h_{m0} > \eta \qquad (7)$$

and

$$f_{U|H_{m0}}(u|h_{m0}) = \frac{\xi}{\kappa}\left(\frac{u}{\kappa}\right)^{\xi-1} \cdot \exp\left(-\left(\frac{u}{\kappa}\right)^{\xi}\right) \qquad (8)$$

where the parameters κ and ξ are functions of h_{m0} as given in Eq. (1 and 2).

Table 3. *Parameter values in the joint density distribution for significant wave height and current speed (Eq. 5).*

α	θ	η	β	ρ	a_1	a_2	a_3	b_1	b_2	b_3	b_4
0.61	0.85	3.07	1.61	2.87	11.6	0.33	1.5	6	3.18	0.75	10

As the joint distribution of significant wave height and current speed is available, the long term distribution of a response quantity reads:

$$F_X(x) = \int\int w(h_{m0},u) F_{X|H_{m0}U}(x \mid h_{m0},u) f_{Hm0}(h_{m0},u) dh_{m0} du$$

where $F_{X|H_{m0}U}(x \mid h_{m0},u)$ is the short term distribution of response maxima given a particular combination of H_{m0} and U. Further, $w(h_{m0},u)$ is a weight function that should be included since the expected frequency of response maxima may vary from sea state to sea state.

In principle one should of course also include the spectral peak wave period in the joint modelling. However, joint models for H_{m0} and T_p are available, see e.g. Johannessen and Nygaard (2000). By assuming that U and T_p are statistically independent, a joint model for H_{m0}, T_p and U can be established from $f_{H_{m0}T_p}(h_{m0}t_p)$ and $f_{H_{m0}U}(h_{m0}u)$.

If the response quantity under consideration is a non-linear function of waves and current, and additionally, is of a dynamic nature, it is rather time consuming to establish the short term distribution, $F_{H_{m0}U}(x \mid h_{m0},u)$, for all important combinations of H_{m0} and U. This will in principle require a considerable amount of non-linear time domain simulations. For complicated response problems it is therefore more convenient to base the response calculations on the environmental contour concept. For a further discussion of this approach, reference is made to Haver et. al (1988). The contour line (line corresponding to constant probability density of the joint model) referred to as the n-year contour line is herein defined as the contour line that goes through the point defined by the 100-year significant wave height and the corresponding conditional mean current speed. It can be shown that the most unfavorable sea state along the contour line is a convenient sea state to be used for estimating long term extremes by means of a short term response analysis, see e.g. Winterstein et. al. (1994), Haver et al. (1988).

Based on the joint density distribution, contour lines for sea states with return periods of 1, 10 and 100 years were established. These lines show that the current speed associated with the 100-years significant wave height is 30 cm/s, while the marginal 10-years current speed seem to be 60 cm/s. As an indication of the adequacy of the contour lines, the contour lines were plotted together with the measured combinations of H_{m0} and U. The contour lines and data points are shown in Figure 8.

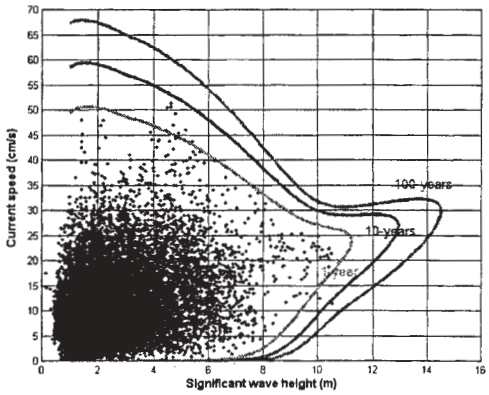

Figure 8. *1, 10 and 100-years extreme contour lines in the H_{m0} - U space. Measured combinations of H_{m0} and U are shown with dots. Duration: H_{m0} - 3 hours, U - 1 hours mean current.*

4. VALIDATION

The method described in Chapter 3 is based on simultaneous data of current and waves. Remembering that the values for H_{m0} have been interpolated to give data for every hour instead of every 3 hour and that the current speed have been smoothed to give 1 hour mean current, we can not be sure that the data values are 100% simultaneous.

To investigate the importance of not having exact simultaneous data, a new analysis was performed. The worst combinations of all wave and current data within 24-hour intervals were used (Johannessen and Nygaard, 2000). The current speed corresponding to the 100 years extreme significant wave height was approximately the same as from the analysis where simultaneous data were used.

By use of the DnV wind induced current profile (DnV, 1991) and using the 1 hour wind speed associated to the 100-years wave height (35 m/s, Johannessen et. al, 1999) the wind induced current speed at 20 meters water depth will be 32 cm/s. The tidal current speed may be as high as 16 cm/s, but is normally in the range 3 – 6 cm/s. By assuming that the strong winds break down density driven currents (McClimans and Eidnes, 1983), the current speed during a 100-years storm should be slightly below 40 cm/s. Compared to the data used in this analysis the DnV profile (DnV, 1991) seem to give somewhat conservative current speed.

The maximum measured current speed was 55 cm/s and the simultaneous wave height was 5 m, Figure 7. The wind induced current speed 20 m below the surface should in accordance with the DnV profile (DnV, 1991) be approximate 15 cm/s. This means that the maximum currents in the Statfjord area are mainly density driven.

5. ERROR SOURCES

The constructed simultaneous series of waves and current describes 1.8 years of data. It may be questioned if this is sufficient to describe the long term wave/current climate. However, the wave distribution from this period is in good accordance with the wave distribution based on a 25 years long wave time serie from the Northern North Sea (Johannessen and Nygaard, 2000). Accounting for temporal correlation, the information corresponds to much less than 1.8 years of data. Further work is therefore recommended before a joint approach is fully utilised.

Wave and current measurements have been collected at different sites. However, wave samples is representative for a large area in this region. Therefore, the current and wave measurements may be assumed simultaneous both with respect to time and space.

The current and wave directions have not been included in the analysis. The directional distribution of current at 25 m and waves shows that both waves and current mainly travel to Northeast (Johannessen and Nygaard, 2000) indicating that there is a correlation between waves and current.

6. CONCLUTIONS

Contour lines based on measurements from waves and current indicates that the current speed in 25 m depth "associated" with the 100-years significant wave height is approximately 30 cm/s in the Statfjord area.

Due to the limited amount of joint data, and since current measurements are not available at the same location, there are uncertainties connected to the "associated current speed". In order to account for the scatter around the conditional mean, the "associated current" has to be taken somewhat larger than the conditional mean value. Further work is therefore recommended before joint occurrence is fully utilized.

There are no indications that the 10-years current (59 cm/s) will act simultaneously to the 100-years significant wave height.

7. REFERENCES

BODC, 1998: United Kingdom Digital Marine Atlas, British Oceanographic Datasenter, UK.

DnV Classification Note 30.5, 1991: Environmental Conditions and Environmental Loads.

Haver, S., Dalane, J. I., Anfindsen, M., 1988: Uncertainties in the modelling of ocean waves and their effects on the structural response, Statoil report F&U - ST 88006.

Johannessen, K., Stokka Meling, T., Haver, S. and Andersen, O. J., 1999: Joint distribution for wind and waves at Veslefrikk, Statoil report 99s9626183.

Johannessen K. and Nygaard E., 2000: Metocean Design Criteria at Kvitebjørn, Rev. 4. Statoil report C-193-KVB-N-FD-0001.

McClimans T. A. and Eidnes G., 1983: Three paradoxes of tile winds over baroclinic coastal current. Ocean Mod. 50, 12-13.

NORSOK STANDARD 1999: Action and Actions effects, N-003. http://www.nts.no/norsok/n/n000301/n003_01.htm

Winterstein, S. R., Ude, T.C., Cornell, C. A., Bjerager, P., Haver, S., 1994: Environmental parameters for extreme response: Inverse form with omission factors.Structural Safety & Reliability, Schueller, Shinozuka & Yao (eds), Balkema, Rotterdam, ISBN 9054103574.

Integrating Metocean Models with Structural Response Models

Don Smith
UK Health and Safety Executive
Rose Court
2 Southwark Bridge
London
SE1 2HS

Tel: 0207 717 6894
Fax: 0207 717 6678
E-Mail: don.smith@hse.gsi.gov.uk

ABSTRACT

The need to design and operate increasingly more efficient and safe offshore oil and gas installations is forcing the industry to develop more sophisticated tools to support the decision making process.

Whereas in the past, the standard output from forecast and hindcast models have been sufficient to drive design models and operational decision making tools, there are benefits to be had in integrating the metocean and structural response models in order to provide an output closer to the desired final product. For example, for floating installations, what is often required is not only forecast wind, wave and current conditions, but forecasts of the response of the installation to the forecast weather conditions. Typical response parameters being the heave, roll and pitch of an FPSO.

Embodied in API's latest fixed structure design guideline, and soon to be included in the corresponding ISO design standard, is the option to design installations on the basis of the 100 year response of the installation (eg base shear or overturning moment) to the metocean environment in which it is to be located. Such an approach requires the use of high quality hindcast databases which drive simplified structural response models. The challenges which faced metocean engineers to produce extreme metocean parameters, has now been subsumed into an overall design approach. However, it remains essential that the limitations of the hindcast databases are not lost within this new design environment.

Clearly the integration of forecast/hindcast models with response models present a number of new challenges for two parts of an industry which, up to now, have had limited interaction.

This paper reviews work underway to integrate forecast and hindcast products with structural response models. In particular it reviews efforts currently underway to produce response based forecasts for use on floating installations, and to use hindcast data for the production of load factors for use in the forthcoming ISO standard for the design of fixed jacket structures. The problems encountered in both of these areas are discussed.

RAPIDLY SIMULATED SHIP BUOYANCY AND WAKE IN WAVES, FROM GRAPHICS HARDWARE

Anthony B. Williams

Independent Consultant
245 Dundee Drive
Monterey, CA 93940-5418

1. METHOD

Among the uses of our ability to forecast and hindcast waves, we should include consideration of the impact of waves upon ships. In forecasting, we want to predict ship motions, to provide a decision aid that helps users understand the likely results of a possible course of action. A timely simulation is particularly appropriate as operational models such as WAM and WaveWatch III become more precise and more widely available. In hindcasting, an ability to visualize what might have happened to a vessel can assist failure analysis, and help us to understand historical circumstance. As we learn more about wind-driven ocean waves, we would like to inform naval architects and marine engineers, so they can design better hulls, especially above the waterline (Larson & Eliasson, 1994). This paper and video record demonstrate a rapid means to estimate the response of a specific hull to specified waves. Rapidity is paramount to the cybernetic application, where shipboard sensors might estimate approaching waves in near real time, to advise best helm.

Computer software methods to estimate the hydrostatic forces and torques on a ship at sea employ a numerical model of the ship hull (Stephens, 1999). The hull may be subdivided into small plane elements, as many as 100,000 triangles. The vertical component of water pressure applied to the exterior area of each submerged triangle because of its depth below the waterline contributes the element's buoyant force. Summing these forces over the canoe hull (no keel or other appendages) yields the total vertical force for the current depth of immersion. This depth must be adjusted using some iterative procedure to cause the computed total force to converge to the design weight of the ship.

After reaching equilibrium in vertical position (heave), similar forces are summed as products of horizontal distances from the ship's center of gravity, to obtain righting torques for the given attitude. For still water, attitude (roll, pitch) is iteratively adjusted in a similar fashion to reach torque equilibrium. Execution on typical computers may take more than several seconds for a given attitude and depth of immersion. It seems difficult to improve the speed of the method without a faster or more sophisticated machine.

This sort of method is straightforward for an unmoving ship in a flat calm sea. Calculating the hydrodynamic forces for just the wave motion is difficult (Kim *et al.*, 1997). The case of a moving ship in a moving sea has only recently become feasible on very large machines (Sclavounos, 1996; Celebi & Beck. 1997), and despite preconditioning to turn an order N squared into an order N problem. Still involves considerable computer expense (Xue, 1997). Breaking waves may require construction of actual physical scale models and testing in a wave tank (Claughton, 1999).

Alternative buoyancy algorithms such as various quadratures for piece-wise analytic surfaces handle only limited special cases, and mostly improve volumetric precision (of the buoyancy calculation) rather than speed of execution.

One alternative to better algorithms or faster general-purpose computers is some purpose-built computer hardware, in which specialization and absence of compromise can deliver more than 10 times the performance available from typical central processing units. Hydrostatics is such a small part of the naval architecture task that the initial expense of this sort of application-specific hardware prohibits development. The computer graphics industry, however, has developed specialized tools with just this high performance, which are normally incorporated into many existing personal computer and workstation displays, and which can be adapted for rapid solution of linear hydrostatics problems. These tools are the fast matrix multiplier or graphics engine, and the Depth- or Z-Buffer (Neider & Woo, 1993). They are fast enough to allow video animation of a linearized interaction of ship and sea, and suitable for rapidly estimating the resulting time-varying behavior.

A graphics engine often consists of pipelined multiply-and-add floating point architectures, for the rotation, scale, translation, and projection of three-dimensional object coordinate descriptions prior to rasterizing and display on screen. The Z-Buffer helps to render scenes of three-dimensional objects by ensuring that objects further away are hidden by nearer objects along the line of sight. The Z-Buffer is composed of auxiliary memory aligned with display memory, and records distance from eye to object at each pixel. As parts of display objects are rendered (after rotate, scale, translate, and project operations), distance from the eye is tested against recorded distance. If it is further, the object is not drawn, but if it is nearer, then the pixel is colored accordingly and the Z-buffer is updated with the new distance. These functions are implemented in very fast hardware to provide the illusion of animation, and are well supported in graphics software which allows the user to recover these distance data by reading back the Z-Buffer depth contents after rendering. This hardware may be used to calculate instantaneous displacement.

The process requires choosing an orientation and position for the canoe hull, described by, say, triangular facets, although any form acceptable to the graphics system will work, such as non-uniform rational B-spline patches. A description of the instantaneous ocean surface is needed. For still water, a plane suffices, while for a specific sea state we need to describe water height. In this simulation, a regular grid of water heights includes the waves, and is paved with rows of triangle strips. From a graphics window opened with an orthographic projection looking along the vertical axis, the depth component recovered from the Z-Buffer is the vertical height, or water depth, within a scale factor. The process renders the ocean surface, recovers its heights, then renders the canoe hull at the attitude and location supplied to the graphics engine, and recovers the heights again. To obtain the appropriate ordering of eye-distance, the view may be rendered from below, or rendered from above with the distance test function in the Z-Buffer reversed in value. The results take the form of a regularly sampled array of floating point values, suitable for further calculations.

The descaled difference of these two height fields is zero, except within the instantaneous waterline, where we obtain a set of regularly gridded samples of the depth of water displaced by the hull. Since the axis of view is vertical, the grid heights are also vertical, suitable for the calculation of moments about the center of gravity. Summing this height field difference times the per-pixel grid cell area times density of water produces the instantaneous buoyancy heave force, and summing the same values times distances from the ship's center of gravity produces buoyancy torque (or righting moment) in pitch and roll. Summing the fore-to-aft change in displacement with the simplified lift equations (Prandtl and Tietjens, 1934) estimates the heave force, and similarly the pitch torque, resulting from the ship's forward velocity. Here we are using the flat plate model, where a plate is defined for each pair of triangular elements constructed inside a rectangular grid cell. Drag forces (Wang *et al.*, 1997) and torques are not incorporated into this simulation, as we assume equilibrium with propulsion force, and as we are more concerned with modeling the disturbance to the ship's steady motion by wave action, to look at consequent hull (and propulsion) inefficiency.

An initial pass through the process, using a flat calm sea with the ship oriented to lie at her still waterline provides an estimate of the total displacement or the ship mass. Averaging the weighted centroids of each element of volume provides the three-dimensional location of the center of buoyancy, and the horizontal location of the ship center of gravity. Determining the vertical coordinate of the center of gravity and the true moments of inertia about that center requires more knowledge, essentially the complete distribution of all mass within the ship. For the ship model simulated in this report, moments were not available, so the canoe hull was assumed weightless, but filled with water to the waterline. This provides the total displacement or ship weight, and the three dimensional location of the center of buoyancy. The ship center of gravity was then assumed to lie 1/3 m above center of buoyancy. We sum the elementary masses times the squares of distances from centroids to axes to provide working moments of inertia, probably underestimating the true moments.

Given a vertical coordinate for center of gravity, moments of inertia, and a satisfactory stimulus wave field, the simulation proceeds by solving the highly linearized equations of motion at discrete time steps. The hull is moved forward a distance equal to this step multiplied by a chosen constant speed. The lift and buoyant forces for the wave field at this location are calculated as described, and divided by the effective mass to get the vertical acceleration at the center of gravity. The accelerations multiplied by the time step gives the vertical velocities, which in turn multiplied by the time step gives the next-employed set of vertical coordinates of the ship model. Similarly, integrating the pitch and roll torques versus moments of inertia provides the angular accelerations, which give angular velocities, to yield new attitudes by rotation about the center of gravity.

Horizontal forces were derived from the attitude, as if the ship were sliding along a frictionless plane fitted to her instantaneous waterline, and similarly integrated for the next horizontal coordinates, all applied before the next time step. Torque about the vertical axis results from the horizontal component of force on the hull from the depth of water at each grid sample, multiplied by the horizontal distance from ship's center of gravity. Since motion of the hull drags water with it, an "added mass" equal to the mass of the ship is used, linearly adjusted with the instantaneous departure in heave to reach zero in the case that the motion were sufficiently violent that the hull left the water. Further, mild viscous damping was applied to all motion except yaw. Since yaw has no restoring force, the hull would quickly turn to lie beam-on to the swell, so the yaw motion was heavily damped and spring-loaded to simulate steering control as might be provided by an alert helmsman, or some directional GPS feedback from a device such as the Trimble Advanced Navigation Sensor (Trimble, 1996).

Taking the most exterior points where the two height fields differ (first and last by row and column) indicates the intersection of the hull with the water surface, which marks a dynamic waterline or foam line as shown. Finally, finding the volume of water displaced at each cross section provided a disturbing source for a propagating wave system forced by the hull motion, both translational and rotational, leading to a simulation of a time-varying Kelvin wake, described next.

2. WAVE & WAKE MODELING

We simulate a suitable stimulus wave field by a linear sum of some collection of sinusoidal waves. For each discrete time step, traveling waves are propagated by advancing their phases according to the deep-water dispersion law, period in seconds ~ 0.8 times square root of wavelength in meters. We employ a two-dimensional, backwards, complex-to-complex Fast Fourier Transform (Bracewell, 1986) to build the instantaneous height field from an initial sampled spectrum of ocean waves (Martin *et al.*, 1987). Typical 2D Fourier spectra are available for equilibrium wind-driven seas, with amplitude and directional distribution specified for each wavenumber, dependent upon wind speed and direction, that agree moderately well with observation (Bratos, 1997; Krogstad *et al.*, 1997). The amplitudes of such a spectrum are held constant for the simulation run, while the repeatable pseudo-random distribution of phase steps forward at each frame time.

The stimulus height fields generated by this method are periodic in space on the computational grid employed, so that adjoining copies may be rendered via a display list to simulate a larger patch of ocean without further computer expense. In addition, two copies of the spectrum at the current time step were premultiplied by the X and Y wavenumber. Their FFT then provides X and Y slopes of the waves at each grid point. The total slope allows checking for the breaking wave condition, local wave slope exceeding unity (Lee *et al.*, 1992). To enhance the graphics, the X and Y slopes provide the water surface normal vectors to show smooth specular highlights.

The adjoining copy and breaking wave check above were tested as an exercise, but were not used in the video record for this simulation. Another exercise was excluded in the present simulation: orbital particle velocities associated with the incident waves were computed at each grid point, by premultiplying two more copies of the spectrum in the X and Y directions by the wave phase speed appropriate to each wavelength and back transforming to get the speed components at the water surface. The speeds were found to be small, less than about one m/s for reasonable sea states, since large particle speed requires long wavelength with large amplitude. Particle speeds at the submerged hull surface would have been smaller, after the hyperbolic tangent correction for the depth beneath the mean free surface water elevation relevant to the individual wavenumber of interest.

Two by-products of the displacement information are introduced into the simulation; differential displacement due to change in ship attitude, and differential displacement due to ship forward motion. For both cases, the total change in volume of water at each grid interval cross-section was transferred laterally and aft along the instantaneous flow trajectory to the location of the dynamic waterline found above.

The resulting "excess water" was treated as a height field on an otherwise flat grid, smoothed, and forward transformed to be merged with the initial sampled spectrum. Since this disturbance is propagated exactly as if it were composed of ordinary ocean waves, the result appears similar to the classical Kelvin wake (Lighthill, 1978). Although hidden in the high sea state cases described below, this wake does show up clearly in the low sea state cases, with longer wavelengths curving ahead of the shorter wavelengths nearer to the centerline of the wake. The fastest forward speed run at low sea state also shows a diamond pattern along the centerline of the wake, characteristic of the "rooster-tail" aft of a semi-planing hull (Sorenson, 1966). In the low speed run at low sea state, the wake crests are seen to lie athwartships instead.

Two strategies are available for generating the steps between successive frames of the simulation, constant velocity (as shown in the video record) or fully variable velocity. In the constant velocity case, we assumed an equilibrium between propulsion and drag, so each time step must correspond to a nearly constant change in position, and the ship model is permitted to move about within the boundaries of the grid as a result of the time-varying forces applied to it.

In the variable velocity case, if we had a more complete accounting of motive power, we would correspondingly modify the equations of motion. For example, a Velocity Prediction Program might deduce the instantaneous motive power available from the ship's propeller or sail at the simulated attitude, generate the available forces and torques after accounting for drag and wavemaking resistance, and thus supply refined velocities at each time step. The components of motion on the grid then would determine the corresponding wave phase speed to account for ship motion, and some bookkeeping would be required to keep the hull approximately centered in the Z-Buffer.

3. CONDITIONS OF SIMULATION

Since the spectrum is uniformly sampled in wavenumber, consideration for grid size or sample spacing density with respect to the hull involves trading off realistic appearance of the ocean wave animation, truncating ripples at large wavenumber and swell at small wavenumber. This in turn affects the time step permissible in the simulation, to avoid aliasing the wavenumbers retained. For the equipment and hull described below, a 64 x 64 grid gave recognizable ocean waves, 512 x 512 overtaxed the machinery, and a 256 x 256 grid was used for the video record. The simulation time step was set at 100 ms, as playback to video was supported at this rate, and GPS navigation devices can provide attitude data and control signals to throttle (or to sheet winches) and helm at this rate.

In addition to the orthographic projection window for the calculation, a perspective projection window was used to display the ship model, the water waves, and sets of 2 m high rectangular marker buoys at rest in the ocean. We simulate the forward motion of the ship along with the viewpoint for this window by moving the buoys and water backwards relative to the ship, the latter by incrementing the wave phase in the complex spectrum. Here the phase change in each time step was determined by the distance required to move the fore and aft component of each wavelength aft, so that the entire height field moves away from the viewer, along with the markers. The ship seems to remain at nearly constant distance from the viewer, as if the camera position continually moves ahead.

To make the video record, we anti-aliased the image by jittering display objects in all three dimensions. We saved results to a display file at each time step. This file was then played back into a videocassette recorder, with image interval equal to simulation time step, so that the video record appears to be in real time. Without the perspective graphics, the simulation took less than a second of wall clock time per simulated time step, mostly spent updating the water surface. With perspective graphics of good enough detail for quality control, each frame took 3 seconds; the final video product was rendered at 5 seconds per frame.

Two sea states were modeled for the video record, both truncated at 0.174 and 5.580 radians/meter, with a cell size of 0.563 m for the 256 x 256 grid. The higher of the two sea states had amplitude (half of the maximum minus the minimum heights observed on the grid) of 4.9 m, rms height 1.42 m; the lower sea state had amplitude 0.75 m, rms height 0.23 m. The center of the wave propagation direction was from 57 degrees off the port bow, or from behind the right shoulder of the observer, power concentrated in the 32.25 m wavelength band. For each sea state, forward speeds of 11.8, 5.9, 2.95, and 0.0 m/s were modeled, and the zero speed case was rerun without the ship. Each simulation run consists of 360 frames (36 seconds), plus a fade from and to black of 16 frames each.

For a given hull, speed, and sea state, the code reports extreme, mean, and moment for the simulated and derived variables, such as wave height, ship acceleration, velocity, and position in six axes, as file streams sampled at each time step, along with a summary at the end of the run. Although these features were included to assist debugging, even a condensed graphic display of the variables may be rather confusing unless it is keyed to the imagery. Since each user has specific and different details of engineering interest, no further discussion of calculated output need be given here.

4. CONCERNS & LIMITATIONS

The gridded samples obtained from this process form a single-valued height field, and so the method must be modified for re-entrants in the submerged part of a hull, for example extreme tumblehome or a bulb bow. The limitation is not that the canoe hull be a convex hull, merely that for all attitudes of interest, the hull be single-valued along any submerged vertical; even a coach roof or cabin stepped up from the deck is

permissible at extreme roll, provided that submerged parts do not overlap in a plan view. If the multiple-valued condition obtains, the submerged parts can be sliced horizontally, for example with the graphics hardware clipping planes, and the problem parts rendered into the Z-Buffer viewed from below, tested against an artificial still water plane at the depth of the clip. For some submerged near-ellipsoidal volume, for example, a single cut through the equatorial plane will work for many attitudes. Problems that are more complicated may arise in damage hydrostatics and partial flooding, requiring that the numerical hull model carefully be tailored to the work at hand.

Multi-hull models (tunnel-hull, catamaran, trimaran, *etc.*) require modification to the "excess water" lateral transfer code that generates the Kelvin wake and foam line decoration. Rather than scan for the grid extremes, we would test for more than one connected region that displaces water, find the boundaries of each region, and proceed as before for each such region.

Precision clearly depends upon the grid size: the hull used in this study produced displacements that varied by less than 2% for arbitrary attitudes across grids of 64x64 to 256x256. Typical displays allow resolutions of 1280x1024, although a slender hull will not use all of this screen area. Rendering and recovering data for several adjacent parts of the height field, one at a time, may obtain higher resolutions. Alternatively, one could render the calculation buffer off-line, although this fails to take advantage of the hardware capability. Careful control of the Z-Buffer parameters helps where available, such as selecting 32-bit depth rather than 16-bit, and ensuring that any adaptive distance scale feature is turned off, controlled, or tested to determine the actual scale in use. Additional hints for the most precise operation of the Z-Buffer and graphics engine should be obtained from user documentation. Precision will of course be reduced for components that have near-vertical slopes at the attitude of interest, or that have significant detail that is smaller than the cell size.

The choice of spectral power, phase structure, and sampling for a particular simulation supports a large body of oceanographic literature, not limited to recent history of the wind speed and direction, fetch, duration, water salinity, aeration, ocean and air temperatures, degree and type of surface contamination, rainfall, and neighboring storm history. These are all ignored for this simulation and video record. Breaking waves, steep slopes, and waves of sufficient amplitude to deserve trochoidal appearance are ignored as well, although some experiments to test for these conditions were conducted.

The procedure described in this paper is nearly independent of the mechanisms behind the simulated wave field, which employed an artificial spectrum analogous to the Pierson family of equilibrium wind generated seas. If the products of any of the methods of wave forecasting or hindcasting are to be employed, the simulation can read the appropriate spectral amplitude decomposition. Care must be taken when interpolating from a frequency domain specification to the wavenumber domain employed here.

If specific phases or locked phase relationships can be supplied, these can replace the pseudo-random phases and deep-water law phase advance speeds actually employed. Likewise, any appropriate hull model may be substituted, if its numerical description in triangular facets is available, especially if the location of the true center of gravity and the actual moments of inertia in the loaded condition can be stated. In addition, the OpenGL graphics software and associated hardware are widely available, so the code can be ported to other platforms such as the Microsoft Windows NT® Workstation environment.

We ignored wind and spray-related phenomena, stem splash, centerline wake, foam, slick trails or vortices shed beside the hull path, bound waves other than the wake, reflected waves, and many other of the real problems of computational fluid dynamics which provide a convincing verisimilitude of real ship motion (Robertson, 2000). Because of the periodic nature of the grid, modeled wake from the earlier part of the faster runs "wraps around" to disturb the ship model near the end of the run. In effect, this simulation really models an infinite checkerboard of identical ships seeing the identical waves. Depending upon the needs of the simulator, various ameliorations such as virtual absorber walls or opposing and canceling wave trains could be employed, not further discussed here.

5. COMPUTER EQUIPMENT & SHIP MODEL

This entire project was executed in six months on an SGI O2 Desktop Workstation from Silicon Graphics Developer Program, with MIPS R10000 CPU, 32 Mb memory, 4Gb hard disk, DAT tape and diskette, CD-ROM, internal video package, and IRIX 6.3 operating system, from Silicon Graphics, Inc., 2011 N. Shoreline Blvd., Mountain View, CA 94043-1389.

Software was written as outlined above, mixing library calls, Fortran and C++ to drive the OpenGL graphics. Output went directly to a Panasonic PV-S4670 videocassette recorder in S-VHS format.

Edward M. Stanley used MultiSurf 3D Design Software at AeroHydro, Inc., PO BOX 684, Southwest Harbor, ME 04679-0684 to construct the ship model. It is a modern, bilge-fin-stabilized ocean-going motor yacht, 36 m length overall, of about 175 m^3 displacement. The hull and superstructure were output from MultiSurf (supported by Insignia Solutions SoftWindows '95 on the SGI O2) as a POV file (Rule, 1996) of triangle coordinates and vertex normals, and exported into the Unix system. Additional software was written for the O2 to convert the triangles into a more compact triangle strip form, to take advantage of the OpenGL graphics (Neider *et al.*, 1993). I am grateful for help from Ms Jane Cortez, SGI and Dr John S. Letcher, jr., AeroHydro, Inc. and their associates. Thanks also to members of TRW Ocean Technology Department, Redondo Beach, CA for stimulating discussions.

BIBLIOGRAPHICAL REFERENCES

AeroHydro, Inc. Staff, 1997; MultiSurf 3D surface design software documentation, version 3.0. Southwest Harbor, ME

Bracewell, R.N., 1986; The Fourier transform and its applications. McGraw-Hill, NY

Bratos, S.M., 1997; Comparison of 3G (WAM) and 2G (WISWAVE) wave models in deep water. Ocean wave measurement and analysis, volume one, Edge, B.L., and J. M. Hemsley, eds., Proc. 3rd Int. Symp., ASCE, Reston, VA, 92-106

Celebi, M.S. and R.F. Beck, 1997; Geometric modeling for fully non-linear ship-wave interactions. J. Ship Res., 41, No. 1, 17

Claughton, A., 1999; The stability of yachts in large breaking waves. Bruce, P. ed., Adlard Coles' heavy weather sailing, McGraw-Hill, Blacklick, OH, 17

Kim, M.H., M.S. Celebi, and J.C. Park, 1997; A numerical wave tank for nonlinear wave simulation. Ocean wave measurement and analysis, volume one, Edge, B.L., and J. M. Hemsley, eds., Proc. 3rd Int. Symp., ASCE, Reston, VA, 716-724

Krogstad, H.E., S.F. Barstow, O. Haug, and D.J.H. Peters, 1997; Directional distributions in wave spectra. Ocean wave measurement and analysis, volume two, Edge, B.L., and J. M. Hemsley, eds., Proc. 3rd Int. Symp., ASCE, Reston, VA, 883-895

Larson, L. and R.E. Eliasson, 1994; Principles of yacht design. International Marine, Camden, ME

Lee, P.H.Y., J.D. Barter, K.L. Beach, C.L. Hindman, B.M. Lake, H. Rungaldier, J.C. Schatzman, J.C. Shelton, R.N. Wagner, A.B. Williams, R. Yee, and H.C. Yuen, 1992, Recent advances in ocean surface characterization by a scanning laser slope gauge. SPIE 1749, 234-244

Lighthill, J., 1978; Waves in fluids. Cambridge University Press, Cambridge

Martin, G.A., P.A. Watterberg and J. Mareda, 1987; Fourier synthesis of ocean scenes. IEEE Comp. Graphics & Applications, 3, 16-23

Neider, J., T. Davis and M.Woo, 1993; OpenGL programming guide. Addison-Wesley, Reading, MA

Prandtl, L. and O.G. Tietjens, 1934; Applied Hydro- and aeromechanics. Dover

Robertson, B., 2000; Sea change: ILM's effects crew plunged deep into state-of-the-art technology to create digital water for *The Perfect Storm*. Comp. Graphics World, 23, No. 7, 38

Rule, K., 1996; 3D graphics file formats. Addison-Wesley, NY

Sclavounos, P.D., 1996; Computations of wave ship interactions. Ch. 4, Advances in marine hydrodynamics, M. Ohkusa, ed., Computational Mechanics Publications, 233-278

Sorensen, R.M., 1966; Investigation of ship-generated waves. UCB, Berkeley, CA

Stephens, O.J.II, 1999; Yacht design and construction for heavy weather. Bruce, P. ed., Adlard Coles' heavy weather sailing, McGraw-Hill, Blacklick, OH, 5

Trimble Navigation Ltd. Staff, 1996; TANS Vector GPS attitude determination system, 10 Hz output version, specification and user's manual. Trimble Navigation Ltd., Sunnyvale, CA

Wang, C-T., S-J. Horng and F-C. Chin, 1997; Hydrodynamic forces on the advancing slender body with speed effects. Int. Shipbuilding Prog., 44, No. 438, 105-126

Xue, M., 1997; Three-dimensional fully-nonlinear simulations of waves and wave-body interactions. Ph. D. Thesis, Dept. of Ocean Eng., MIT, Cambridge, MA

COMPARISON OF HINDCAST RESULTS AND EXTREME VALUE ESTIMATES FOR WAVE CONDITIONS IN THE HIBERNIA AREA – GRAND BANKS OF NEWFOUNDLAND

E. P. Berek[1], V. J. Cardone[2], and V. R. Swail[3]

[1]Metocean, Coastal, and Offshore Technologies, LLC, Flower Mound, TX, USA,
[2] Oceanweather, Inc., Cos Cob, CT, USA,
[3]Climate Research Branch, Meteorological Service of Canada, Downsview, ONT, CANADA.

1. INTRODUCTION

Since the mid 1980s, Oceanweather Inc. has performed four separate wind and wave hindcast studies that included the area around the Hibernia offshore oil development on the Grand Banks of Newfoundland. These studies are: 1) the site specific hindcast study for Hibernia prepared for Mobil Research and Development Corporation (1982-86), 2) the "Wind/Wave Hindcast Extremes for the East Coast of Canada," performed around 1992 by Oceanweather and MacLaren Plansearch Limited, for the Atmospheric Environment Service (AES), under funding from the Federal Program of Energy Research and Development (PERD), 3) an 82 storm hindcast covering the years 1957-1995, using the Canadian Spectral Ocean Model (CSOWM), and 4) the so-called AES-40, a 1999-2000 study that hindcasted 40 continuous years of winds and waves, again for the Atmospheric Environment Service (now Meteorological Service of Canada). The four studies covered different years, the wind and wave models used in the four studies were not the same, and the first three studies were storm studies having different populations while the fourth study modelled continuous years. The present report compares the results obtained from these four disparate studies for the Hibernia area, along with the extreme value estimates for wave conditions.

2. OVERVIEW OF THE STUDIES

The Mobil study is comprehensively described in a series of four papers published in the proceedings of the 2nd International Workshop on Wave Hindcasting and Forecasting, held in Vancouver, B.C., on April 25-28, 1989. A total of 29 severe storms occurring between January 1951 and December 1984 were selected from archived meteorological charts, early regional hindcasts, and recorded data. Winds were first calculated from hand-drawn pressure maps based on synoptic measurements that were available in real-time. These were then modified through kinematic analysis and the inclusion of pressure and wind data not reported in real-time. Waves were hindcast using the ODGP 1-G deep model. Different wave model grids were used in the study, beginning with a 2° latitude by 2° longitude spacing for storms 1 to 20, covering an area from 81°W to 6°E, and 26.45°N to 64.63°N. The remaining storms, 21 through 29, used a nested grid with a coarse grid of 1.25° latitude by 2.5° longitude, covering most of the North Atlantic west of 20° W, and a fine grid of spacing half that of the coarse covering 60°W to 45°W, and 41°N to 50°N.

The PERD study was intended to develop a hindcast data base and extreme wave estimates for the Canadian east coast offshore exploration areas: the Grand Banks, the Scotian Shelf, and Georges Bank. The time period covered in the storm selection process was 1957 – 1988. A total of 68 storms covering the three areas were included in the study. The winds were modelled using a blend of surface pressure analysis and kinematic analysis wind fields. Waves were hindcast using a deepwater ODGP wave model. A nested model grid was used with the coarse grid spacing of 1.25° latitude by 2.5° longitude extending from 25°N to 67.5°N and 20°W to 80°W, and a fine grid of half the spacing of the coarse and covering the are between 38.75°N to 53.75°N and 42.5°W to the coast.

The CSOWM study was performed in 1995 and 1996 as an update to the PERD study wherein the time period of the hindcast was extended and the wave model was changed. The CSWOM study used the third generation, shallow water version of the Canadian Spectral Ocean Wave Model and hindcasted 82 storms covering the time period from 1957 to 1995. A nested grid

was used having a coarse grid spacing of 1.084° longitude on the assumed equator (at 51°W) and a nested fine grid with spacing of about 0.361° of longitude. The study was done using Oceanweather's 1GDdeep, 3GDdeep, and 3GShallow wave models. The results discussed in this paper are from the 3Gshallow model. This study is thoroughly described in the paper ***"A Revised Extreme Wave Climatology for the East Coast of Canada,"*** by V. R. Swail, M. Parsons, B. T. Callahan, and V. J. Cardone, and presented at the 4th International Workshop on Wave Hindcasting and Forecasting, held in Banff, Alberta, in October 1995.

The AES 40 study modelled the entire 40 year time period from 1958 to 1997, with an update to 1998 and 1999 in progress. The study utilized the results of the NCAR/NCEP (U.S. National Centers for Environmental Prediction) global re-analysis for 1958-97 wind fields as input to a third generation deep water wave model. The winds were modified by adding measured winds from high quality buoys, platforms, and C-MAN stations. Cyclone wind fields were also generated and added to the background winds. Lastly, the wind fields were refined using Oceanweather's Interactive Objective Kinematic Analysis System (IOKA). The wave model grid spacing was 0.625° latitude by 0.833° longitude, which is within 10% of a square grid between 38° and 45° North, over a grid domain from 80°W to 20°E, and the Equator to 76°N.

3. THE STORM POPULATIONS

As discussed previously, the storm populations in the first three studies differed from each other, and the fourth study was continuous, but covered a different time period. The following Table 1 gives the peak significant wave height for the different storm populations. For the AES 40 study, all storms generating peak significant wave heights exceeding 9.5 meters at the grid point nearest Hibernia are included in the present comparison. Interestingly, two of the storms included in the three storm studies, 08 – 13 March 1974 and 16 – 20 March 1976, have no results for the grid point nearest Hibernia (grid point 5622) in the AES 40 study due to the presence of at least 50 percent ice cover. For these storms results from another grid point (5551), just to the southeast of the point previously used to represent Hibernia, have been included.

	Mobil	PERD	CSOWM	AES 40 5622
Date				
10 - 14 Nov 52	7.1			
08 - 11 Feb 54	11.6			
20 - 23 Sep 55	9.5			
09 - 13 Dec 55	10.7			
16 Jan 59				9.6
07 - 08 Feb 59		9.3	8.6	10.4
17 Feb 59				9.7
09 - 10 Jan 60		8.8	9.3	10.0
20 - 23 Jan 61	11.7	11.1	9.5	11.1
15 - 18 Dec 61	9.7	10.3	10.9	11.5
05 Jan 62				9.5
26 Feb 62				9.5
02 May 62				10.1
26 Feb 63				10.7
16 Nov 63		10.3	10.0	10.5
20 Dec 63			8.0	8.8
10 - 14 Jan 64	6.3	10.9	10.0	9.8
09 - 10 Feb 64		9.3	8.4	10.8
14 - 18 Mar 64	8.4	9.2	8.7	8.1
24 Jan 65		7.4	7.0	8.4
17 - 20 Feb 65	9.9			9.9
29 Mar 65				10.0
09 - 10 Jan 66		8.8	9.1	10.1
29 Jan 66			9.4	9.7
13 - 17 Feb 66	10.4	12.0	12.6	13.7
21 - 24 Feb 66	8.9			8.7
20 Apr 66				10.8
17 Feb 67				10.8
20 - 24 Feb 67	11.9	12.6	11.4	13.2
05 - 06 Jan 68		10.1	9.4	11.3
26 Dec 69			7.1	5.6
20 - 24 Jan 70	12.1	9.8	9.2	10.1
28 Dec 70			6.2	5.8
06 - 07 Jan 71				10.6
16 - 19 Jan 71	11.8	12.0	11.2	12.8
04 Mar 71			7.4	7.5
06 Dec 71				11.0
04 Jan 72				11.1
21 Feb 72			6.3	6.8
18 Dec 72			7.4	8.6
26 - 29 Oct 73	11.1	10.8	9.2	10.4
03 Nov 73			6.2	7.0
04 Jan 74		9.6	10.1	10.6
07 Feb 74			7.1	7.2
08 - 13 Mar 74	10.4	10.0	8.9	10.0
23 Feb 76				9.9
16 - 20 Mar 76	10.3	12.4	10.3	9.5
19 Oct 76				11.1
07 Nov 76			7.2	6.5
05 Dec 76				9.6
19 - 22 Jan 77	12.1	11.0	10.0	11.5
07 Feb 77		9.8	8.7	7.3
14 Feb 78				9.9
17 Feb 78				10.3
01 - 05 Mar 78	10.2	11.5	11.0	9.7
04 Feb 79			6.1	6.0
02 - 06 Jan 80	8.9			8.8
11 - 12 Feb 80		8.4	8.0	9.5
27 Feb 80				10.5
19 - 20 Nov 80		9.5	9.6	11.2
29 Nov 80				9.8
08 Mar 81			8.1	9.8
07 Dec 81			9.8	4.1
30 - 31 Dec 81		10.2	7.9	11.3
13 - 18 Jan 82	11.7	12.6	11.0	13.0
01 - 04 Feb 82	9.2			8.0
11 - 16 Feb 82	13.4	13.4	13.0	12.1
25 Feb 82				9.8

Date	Mobil	PERD	CSOWM	AES 40 5622
07 - 12 Dec 82	8.6			6.5
12 Feb 83			11.9	9.1
16 - 17 Feb 83		10.3	8.4	12.1
05 - 11 Mar 83	9.2			10.1
25 - 30 Nov 83	8.8	10.2	10.2	11.3
18 - 23 Dec 83	11.2	13.3	12.6	13.4
24 - 27 Dec 83	8.8			9.0
27 Jan 84				9.6
29 Mar 84			6.3	6.6
06 - 07 Jan 85		9.0	8.0	9.9
28 - 29 Jan 85		11.4	11.3	12.7
16 Dec 85		9.9		9.6
19 Dec 85			9.4	10.5
05 Jan 86		9.2	7.5	8.7
15 Nov 86				10.8
09 Dec 86				11.2
15 Feb 87				10.6
26 Feb 87				9.6
18 Feb 88				10.6
09 Mar 88			7.7	8.5
05 Jan 89			8.0	10.0
22 Jan 89				10.3
09 Dec 89			7.3	7.3
22 Dec 89				9.6
30 Dec 89				10.0
03 Jan 90				9.9
20 Jan 90				11.3
29 Oct 91			6.3	7.5
04 Dec 91				10.0
02 Mar 92			9.3	10.1
03 Nov 92				11.6
05 Dec 92			9.9	11.8
26 Dec 92			6.3	8.0
18 Jan 93			6.8	7.5
15 Mar 93			6.7	8.2
28 Dec 93			10.6	10.6
31 Dec 93			9.6	12.5
07 Jan 94				10.6
10 Dec 94			7.1	8.1
14 Feb 95			10.3	11.7
05 Apr 95			6.0	6.8
03 Nov 95				9.7
25 Sep 96				10.1
22 Nov 97				9.7
16 Dec 97				10.9
25 Sep 96				10.1
22 Nov 97				9.7
16 Dec 97				10.9

Table 1. The Storm Populations

A total of 17 storms are found in all four hindcast studies. These are summarized in Table 2 below:

Date	Mobil	PERD	CSOWM	AES 40	Mean	Variation	Variation /Mean
20 - 23 Jan 61	11.7	11.1	9.5	11.1	10.9	1.6	0.15
15 - 18 Dec 61	9.7	10.3	10.9	11.5	10.6	1.8	0.17
10 - 14 Jan 64	6.3	10.9	10.0	9.8	9.3	4.6	0.50
14 - 18 Mar 64	8.4	9.2	8.7	8.1	8.6	1.1	0.13
13 - 17 Feb 66	10.4	12.0	12.6	13.7	12.2	3.3	0.27
20 - 24 Feb 67	11.9	12.6	11.4	13.2	12.3	1.8	0.15
20 - 24 Jan 70	12.1	9.8	9.2	10.1	10.3	2.9	0.28
16 - 19 Jan 71	11.8	12.0	11.2	12.8	12.0	1.6	0.13
26 - 29 Oct 73	11.1	10.8	9.2	10.4	10.4	1.9	0.18
08 - 13 Mar 74	10.4	10.0	8.9	10.0 *	9.8	1.5	0.15
16 - 20 Mar 76	10.3	12.4	10.3	9.5 *	10.6	2.9	0.27
19 - 22 Jan 77	12.1	11.0	10.0	11.5	11.2	1.1	0.10
01 - 05 Mar 78	10.2	11.5	11.0	9.7	10.6	1.8	0.17
13 - 18 Jan 82	11.7	12.6	11.0	13.0	12.1	2.0	0.17
11 - 16 Feb 82	13.4	13.4	13.0	12.1	13.0	1.3	0.10
25 - 30 Nov 83	8.8	10.2	10.2	11.3	10.1	2.5	0.25
18 - 23 Dec 83	11.2	13.3	12.6	13.4	12.6	2.2	0.17
Mean						2.11	0.20

* "ice" storms – data from Point 5551

Table 2. Peak Hs in the 17 Storms Included in All Four Populations

The following figure shows the peak significant wave height values for these 17 storms in each of the four studies:

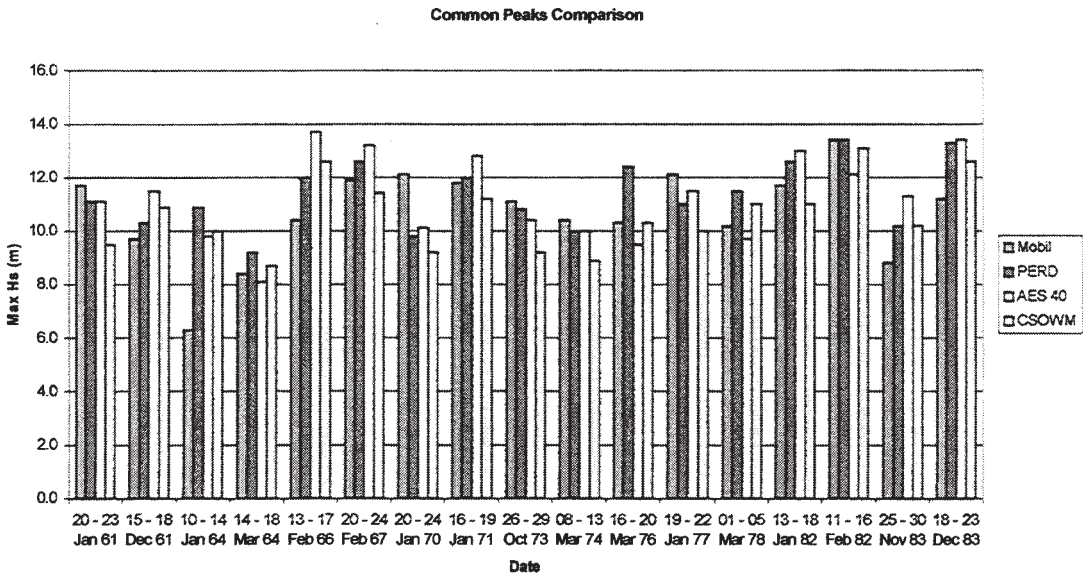

4. COMPARISON OF RESULTS

Generally, the comparison of the peak results for these 17 storms is quite good. Defining the "variation" as the difference between the highest and the lowest (standard deviation is not particularly meaningful for a sample set of four values), the mean variation is 2.11 meters. Another measure of variation might be the "variation" defined above divided by the mean value of the results for a given storm in all four studies. By this measure, the mean value of "variation over mean" is 0.20 or 20%. Remembering that this variation is defined as the difference between the lowest and highest hindcast values for a storm, this 20% value for variation over mean is similar to a variation of plus and minus 10% from the mean value.

The most obvious exception to the generally favorable comparisons is the 10 – 14 January 1964 storm. The peak of this storm appears to be substantially underestimated in the Mobil study compared to the other two studies: a peak Hs of 6.3 meters for the Mobil study compared to 10.9 in the PERD study, 10.0 in the CSOWM, and 9.8 in the AES 40 study. The variation between the Mobil and PERD results is more than 4 meters, or about 50% of the mean value from the four studies. Ignoring the Mobil study, the variation is only 0.9 meters, and the mean value is 10.2. It seems likely that the Mobil result is erroneous.

Four other storms show "variation over mean" values in excess of 20%. These are:

13 – 17 February 1966
20 – 24 January 1970
16 – 20 March 1976
25 – 30 November 1983.

In two of these (February 1966 and November 1983) the Mobil study results are lowest and the AES 40 results are highest, with the PERD and CSOWM results agreeing very well with each other and falling approximately mid-way between the Mobil and AES 40 results. For the January 1970 storm, the Mobil results are the highest, the CSOWM is the lowest, and the AES 40 and PERD results are in excellent agreement with each other. In the last case (March 1976), the PERD result is much higher than the other three results, with these agreeing reasonably well with each other.

The Mobil, PERD, and CSOWM studies are all storm hindcasts, thereby involving a storm selection process. It is interesting to compare the storm populations in these three studies during the overlapping years, 1957 to 1984. During this time it appears that the Mobil storm selection process did not include a total of four events that had peak significant wave heights in excess of 10 meters in the PERD results. These were the following storms:

16 November 1963
5 - 6 January 1968
30 – 31 December 1981
16 – 17 February 1983.

With regard to the reverse of this, the PERD study included all the Mobil storms where the hindcast Hs exceeded 10 meters during the overlap period. In each of the four 10 meter events found in the PERD study but not the Mobil study, the AES 40 results for these storms all exceed the PERD results, but the CSOWM results are all lower than the PERD results. In three of the four events the AES 40 results exceed the PERD results by more than one meter in peak Hs. Considering that the Mobil study had only 15 events where Hs exceeded in 10 meters, this storm comparison would probably lead to an expectation that the AES 40 extreme wave estimates are likely be larger than the Mobil study results.

Looking at the annual occurrence rates of storms producing significant wave heights in excess of varying thresholds is also interesting. This is summarized in the following table 3:

	Mobil (34 years)		PERD (30 years)		CSOWM (37 years)		AES 40 (40 years)	
Threshold Hs (m)	N	λ	N	λ	N	λ	N	λ
10	15	0.44	20	0.67	19	0.51	58	1.45
11	10	0.29	11	0.37	10	0.27	25	0.60
12	3	0.088	7	0.23	4	0.11	10	0.25
12.5	1	0.029	4	0.13	3	0.081	7	0.18
13	1	0.029	2	0.067	1	0.027	4	0.10

Table 3. Exceedances of Threshold Significant Wave Heights at Hibernia in the Four Studies

The trend is very apparent: the Mobil study appears to indicate a substantially lower rate of exceeding the various thresholds, than the PERD and AES 40 studies, i.e., these large storms are less frequent than we see in either of the other studies. With the exception of the 12.5 m threshold, the CSOWM threshold exceedances are very similar to those seen in the Mobil study. Generally the AES 40 study indicates that the thresholds are exceeded about three times more often than what was indicated in the Mobil results. This may or may not affect the extreme value estimates (return periods for various rare events) but it undoubtedly has an influence on operations planning.

For example, suppose that a storm with Hs greater than 10 meters causes the cessation of a certain operation on the Hibernia platform. The Mobil study indicated that this would occur, on average, once every 2.3 years, while the AES 40 study indicates that it would occur, on average, 1.45 times each year. Over a 25 year platform life this translates into an expected 11 exceedances in the Mobil study versus 36 exceedances in the AES 40 study. It is possible that this could have an effect when considering project life cycle economics, which is often important both for development scenario selection as well as estimating the expected economic value of a project.

5. EXTREME VALUE ESTIMATES OF HS FROM THE FOUR STUDIES

Estimates of extreme significant wave heights using the results of the four studies have been made using the Gumbel and Borgman (Gumbel on H_s^2) extreme value distributions. The distributions were fit using the method of moments as defined by Oceanweather.

The following data sets were analyzed:

1) The 26 Mobil hindcast storms used by Mobil in estimating extremes. The two storms that produced the lowest peak Hs values (6.3 and 7.1 m) are excluded, following the procedure outlined in Mobil's series of published papers.

2) The Mobil hindcast storms producing Hs values exceeding 9.5 meters. There are 18 such events.

3) The 30 storms designated as Grand Banks storms hindcast in the PERD study having hindcast Hs values of 9.0 meters or higher.

4) All PERD storms in which the maximum Hs exceeded 9.5 meters. The total number of such storms was 25.

5) All CSOWM storms where the peak Hs value is greater than or equal to one half

of the maximum Hs in the study. The number of such storms is 58.

6) All CSOWM storms where the peak Hs value is equal to greater than 9.5 meters. This is a sample size of 24 storms.

7) All AES 40 storms having maximum Hs values exceeding 9.5 meters. This totaled 81 events.

8) All storms found in the PERD study that had hindcast maximum Hs values greater than 9.5 meters in the AES 40 study. There were 28 such events.

9) All storms found in the PERD study that had hindcast maximum Hs values greater than 9.5 meters in the AES 40 study, including Hs values from an adjacent grid point for the two PERD storms that occurred with greater than 50% ice coverage in the AES 40 study. There were 30 such events.

10) All storms in the AES-40 study with maximum Hs greater than 9.5 meters, occurring during the years covered by the PERD study (1957 – 1988). This totaled 62 events. Comparison of this data set to the PERD storm set qualitatively assesses the effect of storm selection. The comparison is not perfect however, since the wind and wave modeling changed between PERD and AES 40.

	Gumbel Distribution, Method of Moments Hs (m)									
Return Period										
2	9.7	9.6	10.5	10.5	9.8	9.9	11.3	10.9	10.9	11.3
5	11.2	11.3	11.8	11.8	11.2	11.2	12.1	12.2	12.2	12.2
10	12.1	12.1	12.6	12.6	12.2	12.0	12.7	13.0	13.0	12.8
20	13.0	12.8	13.4	13.4	13.2	12.7	13.3	13.8	13.8	13.5
25	13.3	13.0	13.7	13.6	13.5	12.9	13.5	14.1	14.1	13.7
50	14.2	13.7	14.5	14.4	14.5	13.5	14.1	14.9	14.9	14.3
100	15.0	14.4	15.3	15.1	15.5	14.2	14.7	15.7	15.7	14.9
	Mobil	Mobil	PERD	PERD	CSOWM	CSOWM	AES 40	AES 40	AES 40	AES
								PERD storms	PERD storms *	PERD years *
		Hs > 9.5		All Hs > 9.5	All Hs > 0.5 * max Hs	All Hs > 9.5	All Hs > 9.5	Hs > 9.5	Hs > 9.5	Hs > 9.5
	N = 26	N = 18	N = 30	N = 25	N = 58	N = 24	N = 81	N = 28	N = 30	N = 62

	Borgman Distribution, Method of Moments Hs (m)									
Return Period										
2	9.7	9.5	10.6	10.5	9.8	9.7	11.3	11.0	11.0	11.4
5	11.3	11.4	11.8	11.9	11.1	11.2	12.1	12.2	12.2	12.4
10	12.1	12.1	12.6	12.6	12.0	11.9	12.7	13.0	13.0	13.0
20	12.9	12.7	13.3	13.3	12.7	12.5	13.2	13.7	13.7	13.6
25	13.1	12.9	13.5	13.5	13.0	12.7	13.4	13.9	13.9	13.8
50	13.8	13.5	14.2	14.1	13.7	13.3	13.8	14.5	14.5	14.4
100	14.4	14.1	14.8	14.7	14.3	13.9	14.3	14.7	15.1	14.9
	Mobil	Mobil	PERD	PERD	CSOWM	CSOWM	AES 40	AES 40	AES 40	AES
								PERD storms	PERD storms *	PERD years *
		Hs > 9.5		All Hs > 9.5	All Hs > 0.5 * max Hs	All Hs > 9.5	All Hs > 9.5	Hs > 9.5	Hs > 9.5	Hs > 9.5
	N = 26	N = 18	N = 30	N = 25	N = 58	N = 24	N = 81	N = 28	N = 30	N = 62

* "ice" storms included

Table 4. Extreme Value Estimates of Hs

The results for extreme value estimates of significant wave height from these ten data sets, for both the Gumbel and Borgman distributions, are summarized in Table 4.

Comparing first the AES 40 PERD storms, with and without the two "ice" storms, clearly shows that the addition of these two storms, both having peak Hs values near the middle of the storms used in the analyses, did not effect the extreme value estimates at all.

Perhaps the most remarkable observation based on review of table 4 is the high degree of consistency among the results for the ten data sets. This is summarized in table 5 below:

	Gumbel			Borgman		
Return Period (years)	Mean	Std. Dev.	COV	Mean	Std. Dev.	COV
2	10.4	0.66	0.063	10.5	0.72	0.069
5	11.7	0.45	0.039	11.8	0.47	0.040
10	12.5	0.38	0.031	12.5	0.44	0.035
20	13.3	0.38	0.028	13.2	0.44	0.033
25	13.5	0.40	0.030	13.4	0.43	0.032
50	14.3	0.45	0.032	14.0	0.42	0.030
100	15.1	0.52	0.034	14.5	0.38	0.026

Std. Dev. – standard deviation
COV – coefficient of variation

Table 5. Statistical Summary of Hs Estimates from the Ten Data Sets.

In the earlier discussion regarding the storm selection process, a foundation was laid for the expectation that the results from the Mobil hindcast study might yield low estimates for extreme wave heights. Comparing first the Gumbel distribution, it is seen that this is only marginally true. For all 26 Mobil storms the 100-year Hs value is 15.0 meters, actually 0.3 meters higher than the AES 40 value for all peaks above 9.5 meters. Compared to the AES 40 results for all PERD storms where Hs exceeded 9.5 m, the Mobil value is only 0.7 meters, or about 5%, lower than the largest 100-year Hs determined for the eight data sets. The estimate obtained using the subset of Mobil results where Hs exceeded 9.5 meters resulted in an even lower 100-year Hs value, 14.4 meters, but this is still only 9% less than the largest 100-year Hs. Essentially the same results are found from comparisons of the Borgman distribution results.

[An important point to note is that the Hibernia platform was designed to a 100-year Hs value of 15.9 meters, based on the 90% control level value obtained using the Borgman distribution fit. The AES 40 results for all storms exceeding 9.5 meters, fit with the Gumbel distribution using the method of moments, would define this Hs as having a return interval of 125 years. For the other data sets, the return period would be longer.]

Examination of the other return periods shows that, at 2 years for example, the Mobil hindcast is much lower than the PERD and AES40. This difference indicates that the mean value of the extreme storms is much lower in the Mobil study (as seen in the earlier discussion), but that the standard deviation of the storm peaks is much higher. This creates a larger slope to the return period line. Another result is that the confidence intervals will also be much larger.

6. EXTREME VALUE ESTIMATES OF HMAX FROM THE FOUR STUDIES

Estimates of extreme significant and maximum wave heights using the results of the three studies have been made using the Gumbel and Borgman (Gumbel on H_m^2) extreme value distributions. The distributions were fit using the method of moments as defined by Oceanweather.

The following data sets were analyzed:

1) The 26 Mobil hindcast storms used by Mobil in estimating extremes. The two storms that produced the lowest peak Hs values (6.3 and 7.1 m) are excluded, following the procedure outlined in Mobil's series of published papers..

2) The Mobil hindcast storms producing Hmax values exceeding 17.5 meters. There are 18 such events.

3) The 30 storms designated as Grand Banks storms hindcast in the PERD study having hindcast Hs values of 9.0 meters or higher.

4) All PERD storms in which Hmax exceeded 17.5 meters. The total number of such storms was 25.

5) All CSOWM storms where the Hmax value is greater than or equal to one-half of the maximum Hmax in the study. The number of such storms is 60.

6) All CSOWM storms where the Hmax value is equal to greater than 17.5 meters. This is a sample size of 22 storms.

7) All AES 40 storms having Hmax values exceeding 17.5 meters. This totaled 93 events.

8) All storms found in the PERD study that had hindcast maximum Hmax values greater than 17.5 meters in the AES 40 study. There were 28 such events.

9) All storms found in the PERD study that had hindcast maximum Hmax values greater than 17.5 meters in the AES 40 study, including Hmax values from an adjacent grid point for the two PERD storms that occurred with greater than 50% ice coverage in the AES 40 study. There were 30 such events.

10) All storms in the AES study with Hmax values greater than 17.5 meters, occurring during the years covered by the PERD study (1957 – 1988). This totaled 68 events. Comparison of this data set to the PERD storm set qualitatively assesses the effective of storm selection. The comparison is not perfect however, since the wind and wave modeling changed between PERD and AES 40.

Table 6 summarizes the Hmax results from the four studies. Immediately after Table 6, the results for extreme value estimates of maximum wave height from these ten data sets, for both the Gumbel and Borgman distributions, are summarized in table 7.

The most remarkable observation based on review of table 7 is again the high degree of consistency among the results for the eight data sets. This is summarized in table 8.

Again the presence of the two PERD "ice" storms in the AES 40 results for the PERD storms, both having Hmax values near the middle of the storms used in the analyses, did not affect the extreme value estimates at all.

In the earlier discussion regarding the storm selection process, a foundation was laid for the expectation that the results from the Mobil hindcast study would yield low estimates for extreme wave heights. Comparing first the Gumbel distribution, it is again seen that the Mobil study yields only slightly lower values. For all 26 Mobil storms the 100 year Hmax value is 27.4 meters, actually 0.3 meters lower than the AES 40 value for all storms where Hmax is above 17.5 meters. Compared to the AES 40 results for all PERD storms where Hmax exceeded 17.5 m, the Mobil value is 1.9 meters, or about 7%, lower than this largest 100 Hmax determined for the ten data sets. The estimate obtained using the subset of Mobil results where Hs exceeded 17.5 meters resulted in an even lower 100 year Hmax value, 26.4 meters, nearly 10% less than the largest 100-year Hmax. Essentially the same results are found from comparisons of the Borgman distribution results.

[An important point to note is that the Hibernia platform was designed to a 100 year Hs value of 29.3 meters, based on the 90% control level value obtained using the Borgman distribution fit. This turns out to exactly equal the highest Hmax estimate in the present comparisons, that derived from the AES 40 results for all the PERD storms with an Hmax exceeding 17.5 meters fit with the Gumbel distribution using the method of moments.]

The variation in the estimates obtained for the 2-year return period is significantly greater than what is seen for the 100-year return period. For example, for the Gumbel distribution the variation is 1.7 meters, or equivalently, about 16%. At first consideration this is a counterintuitive result. Since the time period covered with each data set is on the order of 30 to 40 years, the estimate of the values corresponding to return periods well within this time period would be expected to be consistent among the data sets. More careful review of the results reveals that the high estimates of 2-year return period come from the continuous study (AES 40) as opposed to the storm studies. This occurs because the continuous study by default includes many more storm events that produce moderately high waves than are found in storm studies since, by definition, the storm studies focus on the most extreme events.

Date	Mobil	PERD	CSOWM	AES 40 5622
10 - 14 Nov 52	13.2			
08 - 11 Feb 54	20.6			
20 - 23 Sep 55	17.6			
09 - 13 Dec 55	19.8			
16 Jan 59				18.2
07 - 08 Feb 59		17.1	16.4	19.6
17 Feb 59				17.6
09 - 10 Jan 60		16.2	17.3	19.2
20 - 23 Jan 61	21.6	20.4	17.3	20.8
15 - 18 Dec 61	18.4	19.0	20.6	22.3
05 Jan 62				17.7
26 Feb 62				17.7
02 May 62				18.7
26 Feb 63				20.1
16 Nov 63		19.0	18.6	19.6
27 Dec 63			8.0	17.9
10– 14 Jan 64	12.4	20.1	18.7	18.2
09 - 10 Feb 64		17.1	15.5	19.6
14 - 18 Mar 64	15.8	16.9	16.7	15.3
24 Jan 65		13.6	13.7	15.8
17 - 20 Feb 65	18.0			18.7
29 Mar 65				18.7
03 Jan 66				17.5
09 - 10 Jan 66		16.2	17.0	19.2
29 Jan 66			17.1	18.2
13 - 17 Feb 66	19.8	22.1	23.5	25.5
21 - 24 Feb 66	16.6			16.5
20 Apr 66				20.3
17 Feb 67				20.0
20 - 24 Feb 67	21.4	23.2	20.8	24.3
05 - 06 Jan 68		18.6	17.4	21.1
26 Dec 69			12.6	10.7
20 - 24 Jan 70	22.3	18.0	17.1	19.4
28 Dec 70			11.4	11.0
06 - 07 Jan 71				20.1
16 - 19 Jan 71	21.6	22.1	22.1	24.2
04 Mar 71			13.8	13.9
06 Dec 71				20.6
02 Jan 72				20.2
04 Jan 72				20.7
21 Feb 72			11.7	12.7
03 Dec 72				17.5
18 Dec 72			13.6	15.6
26 - 29 Oct 73	20.2	19.9	17.4	19.4
03 Nov 73			11.6	13.2
04 Jan 74		17.7	19.1	20.2
07 Feb 74			13.0	13.2
08 - 13 Mar 74	18.7	18.4	16.8	18.7
23 Feb 76				18.1
16 - 20 Mar 76	18.2	22.8	18.6	17.9
19 Oct 76				20.5
07 Nov 76			13.1	13.3
05 Dec 76				18.0
19 - 22 Jan 77	22.5	20.2	19.2	21.6
07 Feb 77		18.0	16.5	13.8
14 Feb 78				18.8
17 Feb 78				19.9
01 - 05 Mar 78	18.7	21.2	20.1	17.7
05 Oct 78				17.5
04 Feb 79			11.7	11.9
10 Dec 79				17.6

Date	Mobil	PERD	CSOWM	AES 40 5622
02 – 06 Jan 80	16.3			17.1
11 - 12 Feb 80		15.5	14.6	17.7
27 Feb 80				19.6
19 - 20 Nov 80		17.5	18.2	21.2
29 Nov 80				18.4
08 Mar 81			15.9	18.9
07 Dec 81			18.2	13.8
30 - 31 Dec 81		18.8	18.2	21.2
13 - 18 Jan 82	21.5	23.2	20.4	23.9
01 - 04 Feb 82	16.9			14.9
11 - 16 Feb 82	24.7	24.7	23.0	23.1
25 Feb 82				17.8
07 - 12 Dec 82	15.8			12.4
16 - 17 Feb 83		19.0	22.2	23.1
05 - 11 Mar 83	16.9			19.0
25 - 30 Nov 83	16.2	18.8	18.7	21.0
14 Dec 83				17.2
18 - 23 Dec 83	20.6	24.5	22.8	25.1
24 - 27 Dec 83	16.2			16.6
27 Jan 84				17.9
29 Mar 84			11.9	12.2
06 - 07 Jan 85		16.6	15.4	19.3
28 - 29 Jan 85		21.0	20.8	23.9
16 Dec 85		18.2	17.3	17.8
19 Dec 85				19.7
05 Jan 86		16.9	13.7	16.0
15 Nov 86				19.8
09 Dec 86				20.7
15 Feb 87				19.7
26 Feb 87				17.9
18 Feb 88				19.3
09 Mar 88			13.9	15.6
30 Dec 88				17.5
05 Jan 89			14.5	18.3
22 Jan 89				19.2
09 Dec 89			13.7	13.9
22 Dec 89				18.0
30 Dec 89				18.5
03 Jan 90				18.4
20 Jan 90				21.3
28 Jan 90				18.7
28 Nov 90				19.7
12 Jan 91			21.9	23.1
29 Oct 91			11.6	14.2
04 Dec 91				18.6
02 Mar 92			16.9	19.0
03 Nov 92				21.7
05 Dec 92			17.9	21.5
26 Dec 92			11.7	14.6
18 Jan 93			12.2	13.9
15 Mar 93			12.6	15.3
28 Dec 93			18.8	19.5
31 Dec 93			17.2	22.6
07 Jan 94				20.0
10 Dec 94			13.0	14.8
04 Jan 95				17.5
14 Feb 95			18.4	21.3
05 Apr 95			11.0	12.7
03 Nov 95				17.9
25 Sep 96				18.8
22 Nov 97				17.8
16 Dec 97				19.9

Table 6. The Hmax Populations

	Gumbel Distribution, Method of Moments Hmax (m)									
Return Period										
2	17.8	17.6	19.3	19.4	18.0	18.3	21.2	20.5	20.5	21.2
5	20.6	20.7	21.7	21.7	20.7	20.7	22.8	22.9	22.9	22.8
10	22.3	22.2	23.2	23.2	22.6	21.9	24.0	24.4	24.4	24.0
20	23.9	23.5	24.7	24.6	24.4	23.1	25.1	25.9	25.9	25.2
25	24.4	23.9	25.2	25.1	25.0	23.5	25.5	26.4	26.4	25.6
50	25.9	25.1	26.7	26.5	26.8	24.6	26.6	27.9	27.9	26.8
100	27.4	26.4	28.1	27.8	28.6	25.7	27.7	29.3	29.3	28.0
	Mobil	Mobil	PERD	PERD	CSOWM	CSOWM	AES 40	AES 40	AES 40	AES
								PERD storms	PERD storms *	PERD years *
		Hmax > 17.5		All Hmax > 17.5	All Hmax > 0.5 * max Hs	All Hmax > 17.5	All Hmax > 17.5	Hmax > 17.5	Hmax > 17.5	Hmax > 17.5
	N = 26	N = 18	N = 30	N = 25	N = 60	N = 22	N = 93	N = 28	N = 30	N = 68

	Borgman Distribution, Method of Moments Hmax (m)									
Return Period										
2	17.9	17.4	19.5	18.4	18.0	17.7	21.3	20.6	20.6	21.3
5	20.7	20.8	21.8	21.9	20.4	20.6	22.8	22.9	22.9	22.9
10	22.2	22.2	23.2	23.8	22.0	21.8	23.9	24.4	24.4	24.0
20	23.6	23.4	24.5	25.4	23.4	22.9	24.9	25.6	25.6	25.0
25	24.0	23.7	24.9	26.0	23.8	23.2	25.2	26.0	26.0	25.3
50	25.2	24.8	26.0	27.5	25.1	24.2	26.1	27.2	27.2	26.2
100	26.4	25.8	27.2	28.9	26.3	25.1	27.0	28.3	28.3	27.2
	Mobil	Mobil	PERD	PERD	CSOWM	CSOWM	AES 40	AES 40	AES 40	AES
								PERD storms	PERD storms *	PERD years *
		Hmax > 17.5		All Hmax > 17.5	All Hmax > 0.5 * max Hs	All Hmax > 17.5	All Hmax > 17.5	Hmax > 17.5	Hmax > 17.5	Hmax > 17.5
	N = 26	N = 18	N = 30	N = 25	N = 60	N = 22	N = 93	N = 28	N = 30	N = 68

* "ice" storms included

Table 7. Extreme Value Estimates for Hmax

	Gumbel			Borgman		
Return Period (years)	Mean	Standard Deviation	Coefficient of Variation	Mean	Standard Deviation	Coefficient of Variation
2	19.4	1.41	0.073	19.3	1.56	0.081
5	21.8	1.03	0.047	21.8	1.07	0.049
10	23.2	0.94	0.041	23.2	1.04	0.045
20	24.6	0.94	0.038	24.4	1.02	0.042
25	25.1	0.96	0.038	24.8	1.06	0.043
50	26.5	1.06	0.040	26.0	1.12	0.043
100	27.8	1.15	0.041	27.1	1.20	0.044

Table 8. Statistical Summary of Hmax Estimates from the Ten Data Sets.

7. CONCLUSIONS

The comparison study of the extreme value wave height predictions on the Grand Banks near the Hibernia platform described in this paper lead to the following conclusions:

1. The consistency of the 100 year return extremes is remarkable given the differences in the individual storm hindcasts in the various studies, both in terms of the storm populations and the inter-study differences for the same storms. It is postulated that the range and scatter of these estimates is perhaps the intrinsic uncertainty of extremes obtained using the modern hindcasting approach.

2. At shorter return periods the data sets with more storms obviously provide more realistic extremes because they more correctly reflect the frequencies of storms above the thresholds typically adopted in peaks-over-threshold analyses. Consequently, the AES-40 should give the best shorter return values as an entire 40 year time period was hindcast thus modelling many more of the shorter return period storms.

3. The consistency that is present between the different studies for the same storms comes mainly from the consistency of the hindcast methodology for all of the data sets. All the studies were performed using the Oceanweather family of wave models. All the wind fields were developed by kinematic analysis with a consistent treatment of ship and buoy reports. The AES-40 hindcast used the NCEP Reanalysis Project 10-m wind field for background as opposed to the Cardone (1969) PBL model, but the NCEP winds were chosen from several possible options because it provided wave hindcasts with the least bias.

4. Because the AES-40 is a continuous hindcast it provides much better information for operability estimations since it provides the most reliable estimates of the frequency of occurrence of conditions exceeding various thresholds, particularly lower thresholds, which are critical for weather-sensitive operations

8. REFERENCES

Canadian Climate Centre, 1991: *Wind/wave hindcast extremes for the east coast of Canada, Volume I.* Prepared under contract no. KM169-76678 by MacLaren Plansearch Ltd. and Oceanweather Inc., 109 pages plus Appendices.

Cardone, V.J., D. Szabo and F. Della Stritto, 1989. *Development of wind and wave criteria for Hibernia.* Proceedings 2nd International Workshop on Wave Hindcasting and Forecasting. April 1989, Vancouver, B.C. pp. 75-88.

Cardone, V.J., R.E. Jensen, D.T. Resio, V.R. Swail and A.T. Cox, 1996. *Evaluation of Contemporary Ocean Wave Models in Rare Extreme Events: "Halloween Storm of October, 1991; "Storm of the Century" of March, 1993."* J. Atmos. Ocean. Tech., 13, 1, 198-230.

Cox, A.T., J.A. Greenwood, V.J. Cardone and V.R. Swail, 1995. *An interactive objective kinematic analysis system.* Proceedings 4th International Workshop on Wave Hindcasting and Forecasting, October 16-20, 1995, Banff, Alberta, p. 109-118.

Gumbel, E.J. 1958. *Statistics of Extremes.* Columbia University Press, New York, 375 pp.

Kalnay, E., *et al*, 1996. *The NCEP/NCAR 40-Year reanalysis project.* Bull. Amer. Meteor. Soc., 77, 3, 437-471

Khandekar, M.L., R. Lalbeharry and V.J. Cardone, 1994. *The Performance of the Canadian Spectral Ocean Wave Model (CSOWM) During the Grand Banks ERS-1 SAR Wave Spectra Validation Experiment.* Atmosphere-Ocean, 32, 1, 31-60.

Swail, V.R. and A.T. Cox, 2000. *On the use of NCEP/NCAR reanalysis surface marine wind fields for a long term North Atlantic wave hindcast.* J. Atmos. Ocean. Technol., 17, 532-545.

Swail, V.R., M. Parsons, B.T. Callahan and V.J. Cardone, 1995. *A revised extreme wave climatology for the east coast of Canada.* Proceedings 4th International Workshop on Wave Hindcasting and Forecasting, October 16-20, 1995, Banff, Alberta, p. 81-91.

Swail, V.R., V.J. Cardone and A.T. Cox, 1998. *A Long Term North Atlantic Wave Hindcast.* Proc. 5th International Workshop on Wave Hindcasting and Forecasting, Melbourne, FL, January 26-30, 1998.

Swail, V.R., V.J. Cardone and B.Eid, 1989. *Wind/Wave Hindcast Extremes for the East Coast of Canada.* Proceedings of the 2nd International Workshop on Wave Hindcasting and Forecasting, Vancouver, B.C., April 25-28, 1989.

ONE YEAR COMPARISON OF WAVE HINDCASTS BY BACKWARD RAY TRACING MODEL AND WAM

Yoshio Hatada, Masataka Yamaguchi and Hirokazu Nonaka

Department of Civil and Environmental Engineering
Faculty of Engineering, Ehime University
Matsuyama, Ehime Prefecture, Japan

1. INTRODUCTION

In order to estimate wave climate around the Japanese coastal sea areas based on wave hindcasting, Yamaguchi et al. (1990, 1992, 1995) and Hatada & Yamaguchi (1992, 1997, 1998) have established a long term wave hindcast system in shallow water over several years by use of a backward ray tracing model (Yamaguchi et al. 1987) SPM classified into a category of the first generation model, in cases where the input wind fields on the Pacific Ocean area and the Japan Sea area are calculated through the Bijvoet (1957) wind model from sea-level atmospheric pressure data at irregularly-distributed locations and also are extracted from the ECMWF analysis surface wind data archive. In recent years, the third generation wave model WAM (Gunther et al. 1992) and the ECMWF-WAM analysis wave data archive over several years on the global scale have been released to the public domain, but comparison with long term wave hindcasts of more than one year using the first and second generation models seems not to have been attempted yet at least in the Japanese sea area.

The aim of the study is to hindcast waves over a one-year period of either 1995 or 1997 at deep and shallow water locations around Japan by use of a backward ray tracing model SPM on a grid with high topographical resolution under the ECMWF wind conditions and to compare them with the measurement wave data and the data extracted from the ECMWF-WAM analysis wave data archive which has been constructed under the same wind conditions.

2. WAVE HINDCAST DATA

2.1 *SPM-Hindcast Wave Data*

Input wind data is extracted from the ECMWF analysis surface wind data sets in both 1997 and 1995 where the time and space resolutions are 6 hours and 0.5625 degrees respectively, and is interpolated every 1 hour onto an 80 km distance grid of the Pacific Ocean and a 40 km distance grid of the Japan Sea. The wind and wave grids on the Pacific Ocean have a vertical axis in N-S direction and a horizontal axis in W-E direction, while the Japan sea grids are rotated 45 degrees counterclockwise to make topographical resolution higher with use of the same grid distance, in cases where wind components are rotated as well. The basic equation in SPM is the energy balance equation in shallow water expressed by the Cartesian coordinate system. The source function consists of linear and exponential growth terms, dissipation terms during the following winds and the opposing winds and a linear bottom friction term. Energy dissipation due to wave breaking is estimated by assuming that the directional spectrum component during the growth stage does not exceed a saturated directional spectrum in shallow water. SPM is a frequency and direction-decoupled model. The number of frequency data used in wave hindcasting is 23 ranging from 0.04 to 0.5 Hz and the number of direction data is 36 equally divided on the whole circle. A time splitting method is applied for numerical integration of the basic equation. At the phase of propagation step, either a full ray method for lower frequency components or a piecewise ray method for higher frequency components is utilized. At the phase of growth or decay step, either of their

AUTHOR INDEX TABLE OF CONTENTS

analytical solutions is employed and then energy dissipation due to wave breaking is estimated by use of the saturated spectrum. The open boundary wave condition at the tip of each ray is prescribed by the directional spectrum parameterized with local wind speed and direction. Wind component at wave computation point along a ray is bi-linearly interpolated from wind components at 4 wind grid points surrounding a wave computation point.

SPM follows one hourly variation of directional spectra at a hindcast point through the computation along the refracted rays focusing on the point. Integration of directional spectra yields significant wave height $H_{1/3}$, period $T_{1/3}$ and mean wave direction $\overline{\theta}$. SPM is operated on a nesting grid with high topographical resolution which consists of a 5 km distance grid on the Pacific Ocean or the Japan Sea and a 1 km distance grid on a small sea area including a hindcast point. Figure 1 illustrates the Pacific Ocean area and a small sea area embedded in the large area, where the location of hindcast points is indicated. Also, Figure 2 shows the Japan Sea area and a small sea area which are rotated 45 degrees counterclockwise as mentioned above.

The wave hindcast period is one year, either 1997 or 1995. Since ECMWF wind data gives smaller estimates of wind speed not only on land but also on the coastal sea area presumably due to overestimation of land effect associated with relatively coarse space resolution, the coefficients in the growth and decay terms are empirically tuned according to the local characteristics of ECMWF wind data around each of the hindcast points so as to yield a closer agreement between hindcast and measurement. Wave hindcast points on the Pacific Ocean area are Buoy 21004 station (water depth h= 4860 m) far distant from the western part of the Japanese Mainland and Buoy 22001 (h=140 m) on the East China Sea, Iwakioki station (h= 154 m) of 40 km offshore from the northern part of the Mainland and Kiyanmisaki coastal station (h=51 m) on the Pacific Ocean side of Okinawa Island. At Iwakioki station, wave data was not acquired in 1997 due to withdrawal of the measurement system. Those on the Japan Sea area are B21002 (h=2675 m) situated near central part of the Sea, and the coastal stations of Atsumi (h=45 m) and Matsumae (h=49 m) on the northern part of the Mainland.

2.2 *ECMWF-WAM Wave Data Archive*

ECMWF-WAM wave data archive assimilated with various kinds of measurement data is made on the global scale, in which the time resolution is 6 hours and space resolution is 1.5 degrees in 1995 and 0.5 degrees in 1997. The archive contains 13 kinds of wave information such as significant wave height $H_{1/3}$, mean wave period based on the first spectral moment T_{m01} and mean wave direction $\overline{\theta}$. Significant wave period $T_{1/3}$ is estimated by multiplying an empirical coefficient of

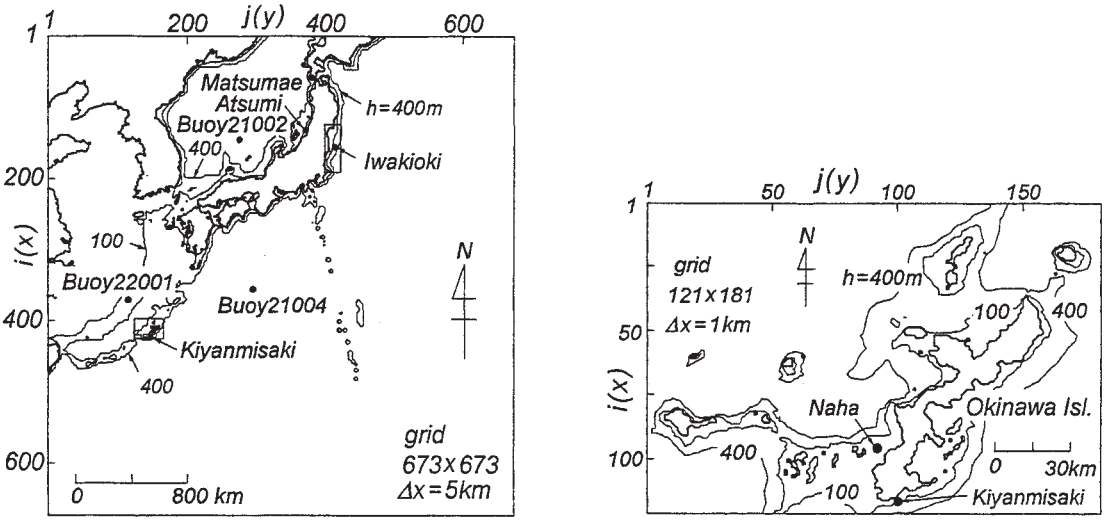

Figure 1 Computation area in the northwestern Pacific Ocean,embedded small sea area and location of hindcast points.

AUTHOR INDEX TABLE OF CONTENTS

1.13 to mean wave period T_{m01}. WAM wave data is extracted at a sea grid point nearest to each of the hindcast points.

Figure 3 gives the 1.5 degrees grid in 1995 and the 0.5 degrees grid in 1997. While the 1.5 degrees grid approximates the Japanese Islands only by 25 grid points, the 0.5 degrees grid in 1997 resolves the Japanese Islands more closely. But, still the grid does not express the presence of Okinawa Island where Kiyanmisaki coastal station is situated. The figure includes the name of individual locations corresponding to the data-extracted

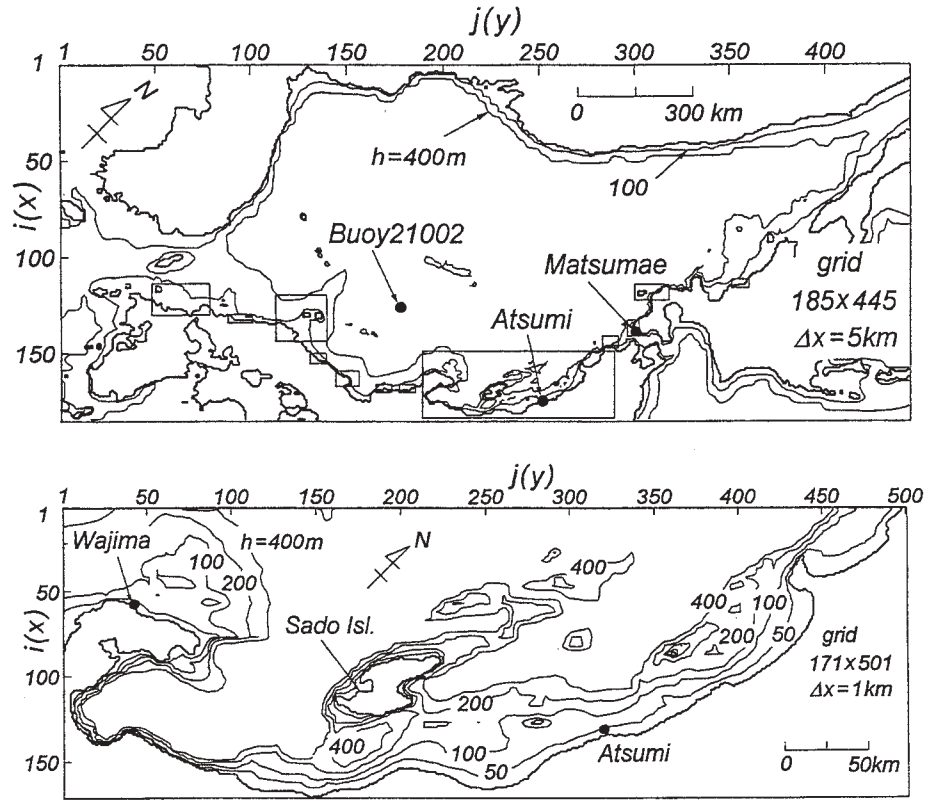

Figure 2 Computation area in the Japan Sea, embedded small sea area and location of hindcast points.

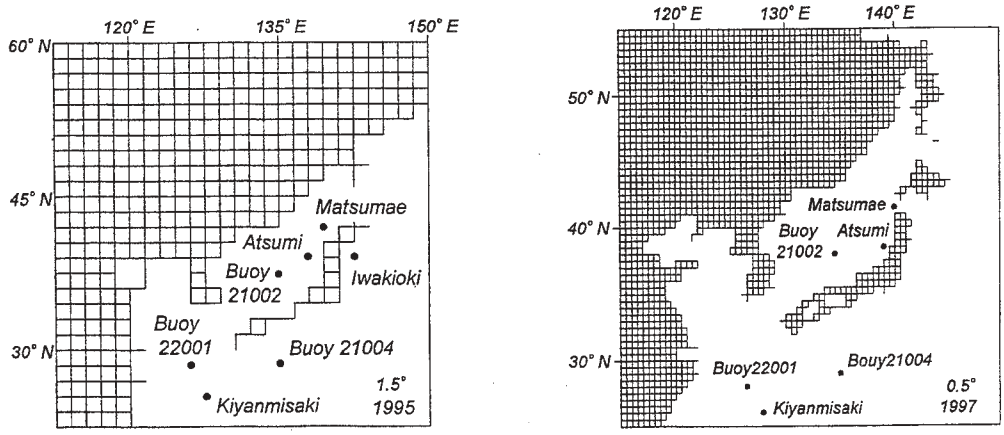

Figure 3 The 1.5 degrees grid in 1995 and 0.5 degrees grid in 1997 for ECMWF-WAM wave data.

AUTHOR INDEX TABLE OF CONTENTS

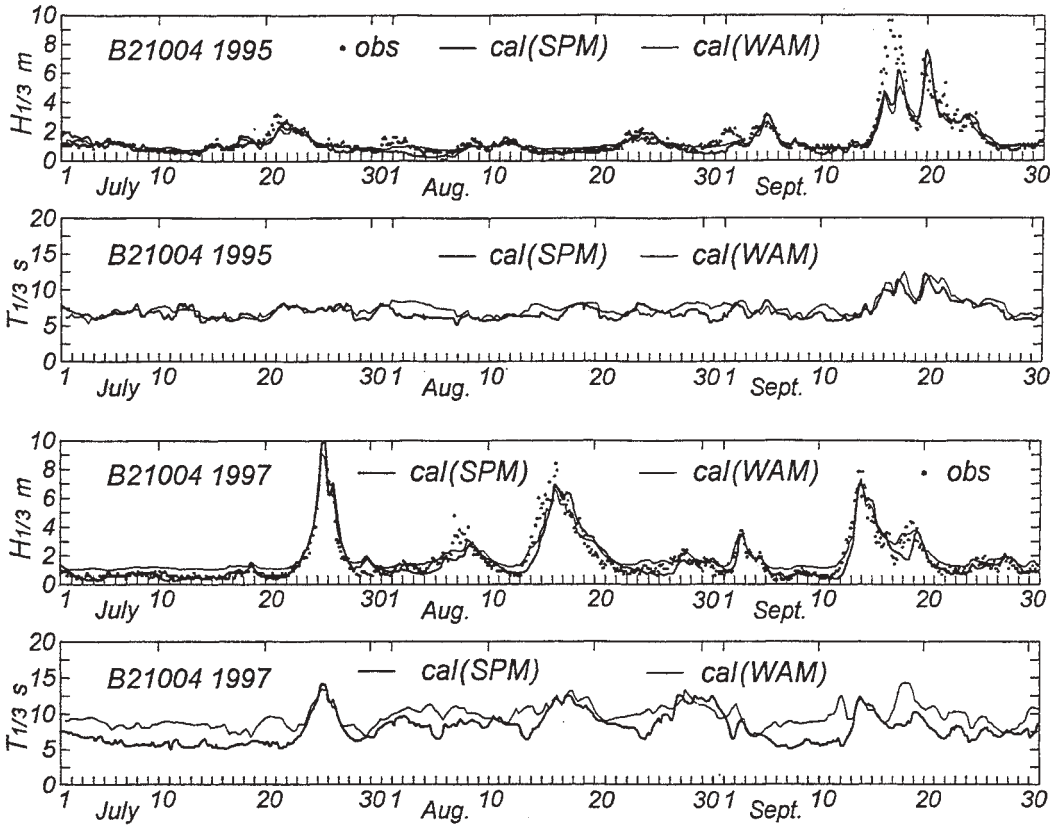

Figure 4 Comparison between hindcast and measurement for time series of wave height and period at Buoy 21004.

sea grid point. It should be noted that the location of coastal stations in WAM wave data is 1.5 degrees in 1995 and 0.5 degrees in 1997 apart from the land grid point.

3. COMPARISON OF HINDCAST AND MEASUREMENT

3.1 *Waves in Open Sea*

Two kinds of hindcast and measurement are compared for both time series and climatic properties of significant wave height and period. Figure 4 indicates hindcast and measurement of wave height and period for 3 months in 1995 and in 1997 at Buoy 21004 on the Pacific Ocean, where measured wave period is not given due to poor data quality. Both hindcasts follow the measurement of wave height fairly well except for some periods of poor correlation during a strong typhoon which is caused by underestimated wind speed in ECMWF wind data. As for wave period, WAM data is in close agreement with SPM data in 1995, but

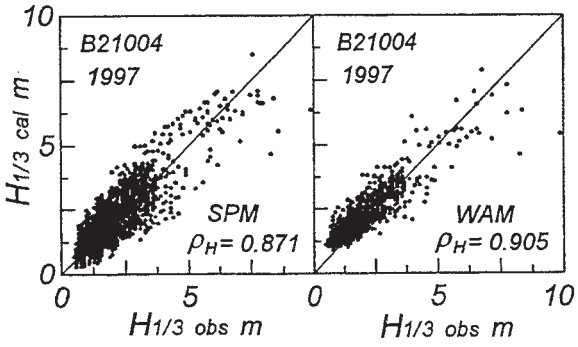

Figure 5 Scatter plot between hindcast and measurement for wave height in 1997 at Buoy 21004.

WAM data is much larger than SPM data in 1997. This suggests that ECMWF-WAM archive in 1997 may include inappropriate wave period data, as will be mentioned in more detail later.
Scatter plot between 3 hourly (SPM) or 6 hourly (WAM) hindcast data and measured data is given in Figure 5. WAM data yields a greater correla-

AUTHOR INDEX TABLE OF CONTENTS

Table 1 Comparison between hindcast and measurement for annual wave climate parameters and error statistics at 3 buoy stations.

location year	data	$\bar{H}$ m	H_{σ} m	p_H	ρ_H	a_{0H}	σ_H m	$\bar{T}$ s	T_{σ} s
B21002	WAM	1.97	1.17	0.367	**0.912**	0.83	0.66	7.36	1.54
1995	SPM	**2.20**	**1.19**	**0.472**	**0.912**	**0.91**	**0.57**	7.20	1.41
	obs	2.32	1.34	0.542					
	WAM	1.54	0.89	0.221	0.894	0.89	0.49	6.90	1.32
1997	SPM	**1.73**	**0.99**	**0.302**	**0.897**	**0.99**	**0.48**	6.58	1.30
	obs	1.64	1.06	0.308					
B21004	WAM	1.85	0.77	0.320	0.827	0.89	**0.55**	7.67	1.08
1995	SPM	**1.98**	**0.92**	**0.415**	**0.832**	**0.97**	**0.55**	7.50	1.04
	obs	1.94	0.98	0.395					
	WAM	2.17	0.99	0.454	**0.905**	**1.00**	**0.56**	8.86	1.40
1997	SPM	**2.07**	**1.14**	**0.412**	0.871	0.98	0.61	7.79	1.33
	obs	1.98	1.22	0.370					
B22001	WAM	1.65	0.67	0.236	**0.832**	0.88	**0.48**	7.27	1.00
1995	SPM	**1.75**	**0.75**	**0.314**	0.828	**0.93**	**0.48**	7.32	0.94
	obs	1.78	0.84	0.353					
	WAM	2.08	**1.15**	**0.378**	0.889	1.02	**0.57**	8.47	1.46
1997	SPM	**2.03**	**1.21**	0.384	**0.891**	**1.01**	**0.57**	7.62	1.37
	obs	1.93	1.18	0.369					

tion coefficient compared to SPM data, which means a smaller scatter of individual data around a linear regression line. But WAM data tends to be greater than measured data in low wave cases and to be smaller in high wave cases, whereas SPM data is in overall agreement with measured data. Table 1 lists yearly-grouped wave climate parameters and error statistics separately estimated from hindcast data and measurement data in 1995 and 1997 at 3 buoy stations. The parameters selected are the mean and standard deviation of wave height ($\bar{H}$, H_{σ}), those of wave period ($\bar{T}$, T_{σ}) and the occurrence rate of high waves greater than 2 m p_H, and the error statistics are the correlation coefficient between hindcast data and measurement data for wave height ρ_H, the slope of a straight line passing the origin best-fitted to correlation between hindcast data and measurement data for wave height in a scatter diagram a_{0H} and the root mean square error (RMSE) of wave height σ_H. It should be noted that a period of measurement data in 1995 at Buoy 21002 on the Japan Sea is restricted to only 3 months from October to December. Also, the index indicating better estimate between SPM data and WAM data is printed in bold-faced type. The following features may be read from the table.

1) As for the mean and standard deviation of wave height ($\bar{H}$, H_{σ}) and the occurrence rate of high waves p_H, SPM yields an estimate closer to the measurement than WAM. In particular, WAM data gives standard deviation H_{σ} smaller than the measurement data.

2) Both the correlation coefficient ρ_H and the slope a_{0H} based on WAM data are closer to 1 in 1997 than in 1995, which means more accurate wave estimation in 1997. This may be due to improved accuracy of ECMWF wind data rather than the use of a grid system with higher space resolution in WAM-based wave hindcast, because SPM data in 1995 and 1997 hindcast using a grid with the same space resolution gives the above-mentioned result.

3) From the aspects of smaller RMSE σ_H, and correlation coefficient ρ_H and slope a_{0H} closer to 1, it can be said that the accuracy of SPM is generally higher than that of WAM.

4) Mean value $\bar{T}$ of wave period based on WAM data in 1997 is far larger than that in 1995. Also, the difference between WAM data and SPM data for mean value $\bar{T}$ of wave period in 1997 is much greater than that in 1995. This suggests that indi-

AUTHOR INDEX TABLE OF CONTENTS

vidual data of mean wave period based on the first moment of spectrum T_{m01} in ECMWF-WAM data archive gives generally larger values.

Figure 6 shows annual variation of monthly-grouped wave climate parameters and error statistics analyzed using SPM data, WAM data and measurement data in 1997 at Buoy 21004 on the Pacific Ocean and Buoy 22001 on the East China Sea where r_H stands for the measurement rate to total run. Either of the hindcast results is in relatively good agreement with the measurement result which shows a remarkable monthly-variation of wave climate parameters associated with rough sea states induced by passage of strong typhoons. But in more detailed aspects, SPM data seems to give closer agreement with the measurement data compared to WAM data, in spite of the fact that the measurement data are assimilated in ECMWF-WAM data. This is confirmed by a correlation plot between hindcast and measurement for individual monthly-wave statistics, as exemplified in Figure 7 indicating the standard deviation of wave height H_σ, in cases where the error statistic are represented by both the correlation coefficient ρ_H

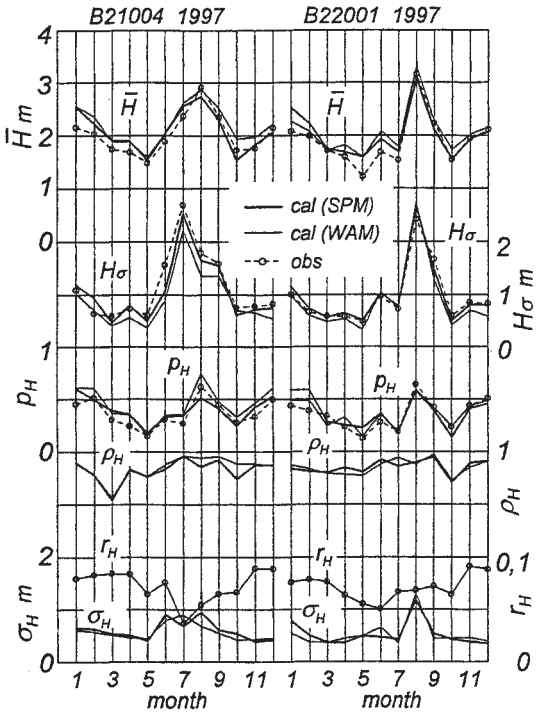

Figure 6 Annual variation of monthly-grouped wave climate parameters and error statistics in 1997 at Buoys 21004 and 22001.

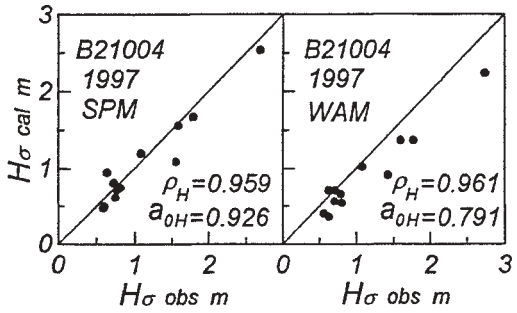

Figure 7 Correlation plot between hindcast and measurement for monthly-grouped standard deviation of wave height in 1997 at Buoy 21004.

Table 2 Error statistics for monthly-grouped wave climate parameters at 3 buoy stations.

location	error	$\bar{H}$		H_σ		ρ_H	
year	statis.	WAM	SPM	WAM	SPM	WAM	SPM
B21002	ρ_H	**1.000**	**1.000**	**0.987**	0.966	0.999	**1.000**
1995	a_{0H}	0.843	**0.946**	0.842	**0.870**	0.678	**0.869**
	ρ_H	0.958	**0.967**	**0.915**	0.907	**0.944**	**0.944**
1997	a_{0H}	0.945	**1.045**	0.826	**0.914**	0.758	**0.980**
B21004	ρ_H	0.919	**0.924**	0.935	**0.958**	0.885	**0.896**
1995	a_{0H}	0.943	**1.011**	0.756	**0.927**	0.832	**1.030**
	ρ_H	**0.957**	0.903	**0.961**	0.959	**0.973**	0.850
1997	a_{0H}	1.086	**1.036**	0.791	**0.926**	1.223	**1.061**
B22001	ρ_H	0.665	**0.828**	0.585	**0.624**	0.662	**0.799**
1995	a_{0H}	0.932	**0.984**	0.757	**0.866**	0.700	**0.893**
	ρ_H	**0.967**	0.929	0.969	**0.983**	**0.923**	0.818
1997	a_{0H}	1.077	**1.047**	**0.972**	1.040	**1.017**	1.032

and the slope of a straight line passing the origin in a correlation diagram a_{0H}.

Table 2 summarizes the error statistics for monthly-grouped climate parameters such as the mean and standard deviation of wave height ($\bar{H}$, H_σ) and the occurrence rate of high waves p_H in 1995 and 1997 at 3 buoy stations. Both the correlation coefficient ρ_H and slope a_{0H} taking a value closer to 1 signify more accurate hindcast data and the index indicating better estimate between WAM data and SPM data is printed in bold-faced type again. In 1995, SPM data provides a more appropriate estimate than WAM data. In 1997, SPM data tends to give lower correlation coefficient than WAM data, whereas SPM data yields slope values closer to 1. These figures suggest that SPM data in 1997 is in collectively better agreement with measurement data compared to WAM data, although each of SPM data is plotted more widely around a correlation line. In other words, WAM data in 1997 tends to give consistently larger or smaller wave height.

In short, it can not be said that WAM wave data has higher accuracy than SPM data, because WAM data tends to give larger estimates in calm sea states and smaller estimates in rough sea states for ocean waves around Japan notwithstanding the use of the most advanced wave model accompanied by assimilation of measurement wave data.

3.2 *Waves in Offshore Waters*

Comparison is made between hindcast data and measurement data in 1995 at Iwakioki station 40 km offshore of the Pacific coast in northern Japan. WAM data at Iwakioki station is obtained at the sea grid point 1.5 degrees apart from the adjacent land grid point and the resulting WAM data might give unreasonable wave information due to overestimated fetches caused by poor space resolution, in cases where wind waves are generated under offshore wind conditions by the northerly strong winds such as winter monsoon winds. For this reason, mean wave direction $\bar{\theta}$ in evaluating wave climate parameters and error statistics is restricted to the open sea directions ranging from 170 to 340 degrees. The mean wave direction of SPM data is used for directional restriction of both wave data sets because of higher correlation with wind direction.

Figure 8 shows comparison of directional occurrence rates of high waves greater than 2 m based on hindcast and measurement, in which direction-restricted wave data is used. SPM data coincides fairly well with the measurement data indicating a high occurrence rate in NE to S directions. But

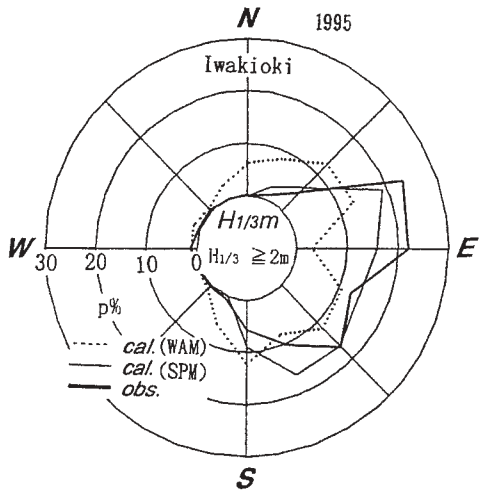

Figure 8 Comparison between hindcast and measurement for direction-grouped occurrence rate of high waves based on direction-restricted analysis at Iwakioki station.

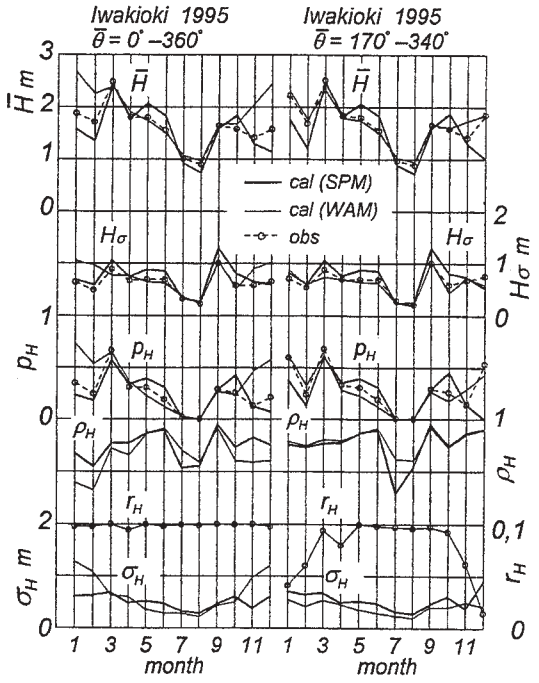

Figure 9 Annual variation of monthly-grouped wave climate parameters and error statistics at Iwakioki station based on both direction-free analysis and direction-restricted analysis.

AUTHOR INDEX TABLE OF CONTENTS

WAM data yields an excessive occurrence rate in N to NE directions and low occurrence rate in SSW to S directions compared to the measurement data. The tendency does not change even in cases where mean wave direction of WAM data ranging from 170 to 340 degrees is applied for compiling direction-limited wave data.

Figure 9 provides a whole year plot of monthly-grouped wave climate parameters and error statistics in the cases of full and limited direction ranges. SPM data hindcast on a grid with high space resolution is in reasonable agreement with the measurement data except for some discrepancy in several months of the year. On the other hand, WAM data is fairly identical with the measurement data during the period of March to October when waves coming from open sea directions are predominant, whereas WAM data gives wave climate parameters far exceeding the measurement-based result and larger error statistics in winter season dominated by northerly offshore winds. Therefore, wave climate statistics on the basis of direction-restricted WAM data come to agree closer with the measurement results through the whole year and the accuracy of WAM data in this case is higher than that of SPM data.

The above-mentioned result suggests that WAM data at an offshore station has higher accuracy than SPM data in cases where the data is restricted to a direction range of open sea but that this is not true for the comparison including mean wave direction data.

3.3 *Waves in Coastal Waters*

Table 3 shows yearly-grouped wave climate parameters and error statistics in 1995 and 1997 at 3 coastal stations. They are Kiyanmisaki station on the Pacific Ocean coast of Okinawa Island, Matsumae and Atsumi stations on the Japan Sea coasts of northern Japan and are situated in about 50 m water depth 2 km offshore of the coast. The wave window is widely opened to predominant wind direction range at both Kiyanmisaki and Atsumi stations, whereas at Matsumae station, a part of the predominant wind directions during the stormy winter season is sheltered by Hokkaido Island. The table including statistics of wave period may make it possible to describe it as follows.

1) SPM data is in good agreement with measurement data for both wave height and wave period irrespective of the measurement station and

Table 3 Comparison between hindcast and measurement for annual wave climate parameters and error statistics at 3 coastal stations.

location year	data	$\overline{H}$ m	H_σ m	p_K	ρ_H	a_{0H}	σ_H m	$\overline{T}$ s	T_σ s	ρ_T	a_{0T}	σ_T s
Kiyanmisaki	WAM	1.43	0.52	0.140	0.358	1.15	0.72	7.67	1.00	**0.539**	1.09	1.34
1995	SPM	**1.05**	**0.55**	**0.052**	**0.698**	**0.94**	**0.43**	**7.35**	**1.24**	0.511	**1.05**	**1.31**
	obs	1.04	0.55	0.049				6.90	1.24			
	WAM	1.81	**0.88**	0.258	0.737	1.26	0.87	8.93	1.29	0.695	1.15	1.90
1997	SPM	**1.20**	0.89	**0.094**	**0.849**	**0.95**	**0.48**	**7.71**	**1.66**	**0.727**	**1.01**	**1.28**
	obs	1.21	0.86	0.099				7.51	1.74			
Matsumae	WAM	1.36	0.97	0.190	0.837	1.23	0.65	6.22	1.26	0.765	1.07	0.97
1995	SPM	**1.02**	**0.75**	**0.100**	**0.890**	**0.95**	**0.37**	**5.88**	**1.25**	**0.850**	**1.02**	**0.69**
	obs	0.99	0.80	0.102				5.75	1.21			
	WAM	1.40	**0.77**	0.181	0.798	1.15	0.60	7.69	**1.12**	0.277	1.27	2.28
1997	SPM	**0.97**	**0.73**	**0.097**	**0.893**	**0.95**	**0.35**	**5.77**	1.24	**0.818**	**1.00**	**0.73**
	obs	0.98	0.75	0.101				5.72	1.17			
Atsumi	WAM	1.34	**1.00**	**0.195**	0.917	**1.00**	0.44	6.51	1.35	0.800	1.06	0.97
1995	SPM	**1.28**	1.13	0.208	**0.925**	1.03	**0.43**	**6.28**	**1.44**	**0.828**	**1.02**	**0.86**
	obs	1.23	1.04	0.179				6.08	1.41			
	WAM	**1.15**	0.90	0.136	**0.930**	0.91	**0.39**	6.91	**1.36**	0.786	1.11	1.18
1997	SPM	1.16	**1.08**	**0.185**	0.920	**0.99**	0.43	**6.13**	1.46	**0.867**	**1.00**	**0.74**
	obs	1.13	1.05	0.178				6.12	1.40			

hindcast year period.

2) WAM data provides excessive estimate compared to the measurement data in both year periods. Wave hindcast with poor space resolution can not properly produce coastal waves measured at Matsumae station where the land is present in a part of the predominant wind directions. At Atsumi station exposed to the Japan Sea, the accuracy of WAM data is rather high for wave height independently of year period but not for wave period.

3) Improvement of the accuracy in WAM data associated with the use of a higher space resolution grid is hardly identified except for partial improvement at Kiyanmisaki station. Also it is noted that a direction-limited analysis of wave climate using WAM data at coastal stations does not give rise to improved estimate of wave climate statistics, differently from the case of offshore waves.

4) WAM wave period data provides rather excessive values compared to the measurement data, particularly in 1997. This implies that the WAM data archive in 1997 may include inappropriate wave period information.

Figure 10 demonstrates annual variation of monthly-grouped wave climate parameters and error statistics in 1997 at Kiyanmisaki station on the Pacific coast and Atsumi station on the Japan Sea coast where both stations are exposed to open sea in predominant wind directions. SPM data hindcast on a nesting grid with high topographical resolution at Kiyanmisaki station is in close agreement with measurement data where waves are high during summer season and low in winter season, while WAM data hindcast with relatively poor space resolution of 0.5 degrees gives excessive mean of wave height $\overline{H}$ and occurrence rate of high waves p_H over the measurement data in several months excluding the typhoon-dominated summer season. This situation does not change even in the case of direction-limited analysis. As a grid system with 0.5 degrees distance can not recognize the presence of Okinawa Island, WAM data substantially corresponds to wave data in deep waters. Consequently WAM data yields a poor estimate for coastal waves at Kiyanmisaki station. On the other hand, not only SPM data but also WAM data give rise to close agreement with the measurement data at Atsumi station on the Japan Sea side. It may be reasonable that SPM data based on hindcast with use of a high space resolution grid under the input wind conditions of high quality produces highly accurate estimates of wind

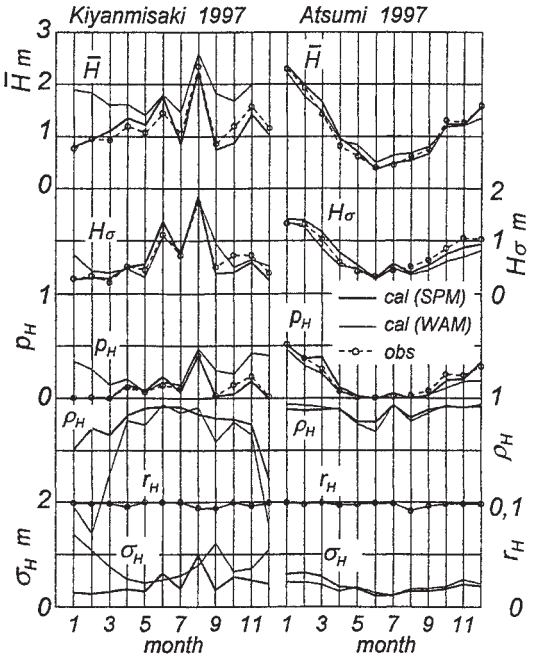

Figure 10 Annual variation of monthly-grouped wave climate parameters and error statistics in 1997 at coastal stations of Kiyanmisaki and Atsumi.

waves-dominated coastal waves in the quasi-closed Japan Sea. But it is beyond our understanding why WAM data based on hindcast with use of a relatively low space resolution grid (1.5 degrees in 1995 and 0.5 degrees in 1997) gives close correlation with the measurement data of coastal waves at several locations along the Japan Sea coasts except for Matsumae which receives a significant land sheltering effect.

4. CONCLUSIONS

The main results drawn from the study are summarized as follows.

1) SPM data based on hindcast with use of a high space resolution grid under ECMWF wind input conditions has high accuracy for long term waves at either of the open sea locations, offshore locations and coastal locations, although SPM classified into the first generation model employs empirically-formulated growth and decay terms.

2) ECMWF-WAM data does not necessarily have higher accuracy over SPM data even for ocean waves in open sea, probably due to a well-known property of WAM which tends to overestimate low waves and underestimate high waves, in spite of

AUTHOR INDEX TABLE OF CONTENTS

the fact that the data is obtained from the application of the most advanced wave model accompanied by assimilated measurement wave data. Also WAM data mostly gives rise to excessive estimate for waves at coastal stations situated within 2 km from the shore because of a poor space resolution grid used in hindcasting.

In short, the accuracy of SPM by use of a grid with high space resolution is comparable to or slightly higher than that of WAM by use of a grid with 1.5 or 0.5 degrees space resolution even at open sea locations, and SPM yields more accurate evaluation than WAM at coastal water locations. We could say that the accuracy of wave hindcast strongly depends on the accuracy of estimated wind fields and topographical resolution rather than the quality of the wave model, particularly in the case of coastal waves.

ACKNOWLEDGEMENTS

The authors give their thanks to the ECMWF which provided ECMWF wind data and ECMWF-WAM wave data sets. Thanks are also due to the Coastal Development Institute of Technology for utilization of NOWPHAS data at Iwakioki station.

REFERENCES

Bijvoet, H. C., 1957: A new overlay for the determination of the surface wind over sea from surface weather charts. KNMI Mededelingen en Verhandelingen, 71, 1-35.

Gunther, H. et al., 1992: The Wamodel cycle 4 (revised version), Deutsches Klima Rechen Zentrum, Technical Report 4, 101.

Hatada, Y. and M. Yamaguchi, 1992: Eight years wave hindcast and analysis of wave climate. Proc. 23rd ICCE, 1, 267-280.

Hatada, Y. and M. Yamaguchi, 1997: Eight years wave hindcast at the coastal area of the East China Sea and estimation of wave climate. Proc. WAVES97, 2, 911-924.

Hatada, Y. and M. Yamaguchi, 1998: A long term wave hindcast system using ECMWF winds. Proc. 26th ICCE, 1, 509-522.

Yamaguchi, M., Y. Hatada and Y. Utsunomiya, 1987: A shallow water wave prediction model at a single location and its applicability. Proc. JSCE, 381/II-7, 151-160 (in Japanese).

Yamaguchi, M., Y. Hatada, M. Ohfuku and K. Nishioka, 1990: Estimation of wave climate along the coast of the Japan Sea based on wave hindcasting. Natural Disas. Sci., 9-3, 18-42 (in Japanese).

Yamaguchi, M., Y. Hatada and T. Hioki, 1992: Applicability of a long term shallow water wave hindcast system to the estimation of wave climate along the coast of the Japan Sea. Natural Disas. Sci., Jour. Japan Soc. Natural Disas. Sci., 11-3, 157-174 (in Japanese).

Yamaguchi, M., Y. Hatada and S. Ohsako, 1995: Applicability of long term shallow water wave hindcast system. Proc. Japanese Coastal Eng., 42, 331-335 (in Japanese).

Long-Range Swell Forecasting Using Source Term Output From Global Wave Models

William C. O'Reilly

U.S. Naval Postgraduate School
bor@coast.ucsd.edu
(510) 595-3425

Paul Wittmann

Fleet Numerical Meteorology and Oceanography Center
wittmann@fnmoc.navy.mil
(831) 656-4526

Abstract

A method for forecasting swell, by propagating global model source term output along great circle routes, is presented. The wave generation, dissipation, and nonlinear transfer source term contributions to each global grid point is estimated at 12 hour intervals. This information is projected along great circle routes to specific forecast sites, effectively bypassing the global model's numerical propagation scheme. This technique has many advantages for swell, including improved predictions of the dispersive arrival of the low frequency energy, more accurate and higher resolution swell directional spectra, and the ability to include blocking by small islands. In addition, by establishing a direct relationship between the wave energy at a specific site and its global grid sources, the methodology can be used to assimilate measured wave frequency spectra into the forecasts in a straightforward manner. An example swell forecast, with and without data assimilation, is provided for a southern hemisphere swell arrival along the California coast in early October, 1999.

SPECTRAL PARTITIONING AS A WAVE HINDCAST VALIDATION TOOL

Jeffrey L. Hanson

The Johns Hopkins University
Applied Physics Laboratory
11100 Johns Hopkins Road
Laurel, MD 20723-6099

ABSTRACT

Ocean surface wave directional spectra typically contain energy contributions from a complex mix of local windsea and swell from distant storms, making them difficult to interpret. Therefore, reduced or 'bulk' wave statistics, such as significant wave height, peak frequency, and mean direction, are often employed for the validation of predictions. Such descriptions lose the identity of the original windsea and swell features and can often mask serious differences between observed and predicted spectra.

Here a fully automated wave partitioning and swell tracking capability is used to investigate third generation Wave Model (WAM) predictions prepared by the U.S. Navy Fleet Numerical Meteorology and Oceanography Center (FNMOC) using winds specified by the Navy Operational Global Atmospheric Prediction System (NOGAPS). The WAM predictions are validated with observations obtained from a Datawell directional waverider buoy deployed in the North Pacific Ocean by the Johns Hopkins University Applied Physics Laboratory (JHU/APL). The spectral representations of individual wave events are captured by a peak isolation routine, with windseas identified by wave age criteria. A separate tracking algorithm identifies swell systems by source and employs gravity wave dispersion to estimate the time and location of each generation event. The results allow a systematic approach to wave validation through comparison of predicted and observed wave systems from specific wind forcing events. Furthermore, the temporal view of evolving wave systems allows quantification of time and direction offsets in the specified winds.

This capability is implemented within the Wave Identification and Tracking System (WITS), an ocean wave analysis package under development at JHU/APL.

A DISCUSSION ON THE DIRECTIONAL DISTRIBUTION OF WIND-GENERATED OCEAN WAVES

Paul A. Hwang, David W. Wang, W. Erick Rogers, and James M. Kaihatu
Oceanography Division, Naval Research Laboratory, Stennis Space Center, MS 39529

1. INTRODUCTION

Measuring the directional distribution of ocean waves is a difficult task in ocean wave research. For the last forty years, the directional distribution of wind-generated waves is assumed to be unimodal. Field measurements using directional buoys or wave staff arrays all claim support of a unimodal directional distribution of a random wind-generated wave field (e.g., Longuet-Higgins 1963; Mitsuyasu et al. 1975; Hasselmann et al. 1980; Donelan et al. 1985). While details of the results vary, the directional models from these field data suggest that under steady wind forcing, waves of all spectral components propagate in the wind direction. The beamwidth of the directional distribution is narrowest near the spectral peak frequency, and increases toward both higher and lower frequencies. With such support of field measurements, unimodal directional distribution function is assumed in all wave spectral models used in scientific and engineering applications.

2. THEORETICAL CONSIDERATIONS

Theoretical analysis of wave dynamics, however, suggests that wave propagation results in bimodal or polymodal directional distributions. At the young wave stage, resonant propagation between winds and waves prevails (Phillips 1957). Because the phase velocities of young waves are slower than the wind speed, in order to maintain in resonance condition waves propagate at oblique angles satisfying $C_p=U_r\cos\theta$, where C_p is the phase velocity of the wave component, U_r is the wind speed at a reference height proportional to the wavelength, and θ is the direction of wave propagation with respect to the wind direction. For young waves, this resonance condition results in two wave systems propagating at oblique angles symmetric to the wind vector (Fig. 1a, b).

Nonlinear wave-wave interaction mechanism also results in a bimodal directional feature of the wave field (Banner and Young 1994). The mechanism of oblique wave generation can be visualized from inspecting the family of curves of the wavenumber components forming a resonant quartet (Fig. 1c). Numerical evaluation has shown that the figure 8 curve dominates the overall interaction effects and is the basis for the discrete interaction approximation (DIA) algorithm used in many nonlinear wave models such as WAM and SWAN (e.g., Hasselmann and Hasselmann 1985; Young and Van Vledder 1993). The nonlinear wave-wave interaction has been shown to be the main mechanism responsible for frequency down shifting during wave growth. Wave energy at the spectral peak is moved out toward both higher and lower frequency components (e.g., Hasselmann et al. 1973). As indicated by the interaction curve, both longer and shorter wave components of the resonant quartet propagate in oblique directions with respect to the dominant wave component from which wave energy is taken away. This scenario is responsible for the robust bimodal directional distribution observed from numerical computations (Banner and Young 1994).

3. EARLIER OBSERVATIONS

Verification of bimodal directional distributions of wave components both above and below spectral peak wavenumber is achieved through directional spectral analysis of 3D surface wave topography of a quasi-steady wind-generated wave field, measured by a high-resolution airborne topographic mapper (ATM, an airborne scanning lidar system) (Hwang et al. 2000a-b). Evidence on the bimodal directional distribution from resonance wind wave generation is not as conclusive. Phillips (1958) suggests that the bimodal feature in the SWOP (Stereo Wave Observation Project, Cote et al. 1960) wavenumber spectrum is due to resonance wind wave generation mechanism. Similar conclusion is given by Jackson et al. (1985) on their directional wavenumber spectra obtained by an airborne imaging radar. In close inspection, the bimodal features observed in the above two datasets are for wave components above the spectral peak wavenumber, and are similar to the observations presented in the airborne scanning lidar dataset. The generation mechanism of this bimodal feature is more likely due to nonlinear wave-wave interaction. A more convincing evidence would be to capture the wave generation at its young stage such that the wave components at the spectral peaks propagating oblique to wind can be observed.

Walsh et al. (1985, 1989) present results from two wave-growth measurements using an airborne scanning radar system. The fetch coverage ranges from less than 100 to over 350 km; the nominal wind speeds are 17 and 12 m/s, respectively. The scanning radar yields continuous 3D surface topography of ocean waves along the flight track. The horizontal resolution (pixel size) of the system is 10 m with an absolute accuracy of ±0.3 m for the elevation measurement. The directional spectra are computed using segments of 10 and 22 km ground distances for the two experiments. One of the interesting results from these continuous measurements is that the peak of the spectrum is not in the wind direction until fetch reaches approximately 150 km. Most of the spectra show only one peak in the directional distribution. They propose that the reason for the oblique angles between wave propagation and wind direction is the slant fetch resulting from complicated coastlines on the upwind region. Long et al. (1994) and Huang (1999) present a reanalysis of these directional spectra. The results show that the angular difference between the wind and wave directions is in agreement with the prediction of Phillips resonance wind wave generation mechanism. They also note that some of the spectra do show two directional lobes, although in contrast to the theoretical prediction of two systems of equal energy, the two-lobe feature is rather asymmetric and in most cases absent. It is suggested that one of the two wave systems may have been suppressed by the ocean swell in the region.

4. EVOLUTION OF SPECTRAL DIRECTIONALITY

Over the years, airborne ranging technology has advanced significantly. Major improvements include global positioning technology, the use of laser to reduce the footprint of the sensor, and the more compact and more powerful computers. The horizontal resolution of the ATM system is 6 m along track and 1.6 m cross track, the vertical resolution is 0.08 m (rms) (Krabill and Martin 1987; Krabill et al. 1995a,b; Hwang et al. 2000a). The ATM system is deployed in the Gulf of Mexico and acquired a dataset of fetch-limited wave evolution under steady wind forcing. As a part of shoaling wave research, the fetch coverage is only 42 km but the higher performance of the system permits accurate spectral computation using data segments of 1.5 km ground distance (Hwang et al. 2000a). As will be shown in the following, the results from this dataset illustrate convincingly the bimodal propagation of dominant waves in a young sea, as predicted by Phillips resonance wind wave generation mechanism.

The ATM wave mapping was performed on November 5, 1998. A steady wind from 330° (NNW) was blowing over a period of more than 12 hours prior to the airborne measurement. The aircraft flew a simple racetrack pattern with two long legs (~ 42 km each) in the wind direction. A light swell from the remnant of Hurricane Mitch propagated into the measurement area from southwest of the Gulf.

Each continuous track (42-km coverage) is divided into segments of 1.5 km length for directional spectral analysis. The swath of the surface topography is approximately 280 m. More details on the data analysis of ATM topographic data have been reported in Hwang et al. (2000a,b). Figure 2 shows a sequence of surface wave topography over the 42-km coverage. The corresponding directional wavenumber spectra for these image segments are shown on the right hand side of the figure. In the nearshore region the wave fronts are almost parallel to the wind direction, indicating that very young waves are propagating normal to, rather than along, the wind direction. As fetch increases waves grow longer and higher, the wave direction also changes from normal to wind to oblique to wind. Since the resonance condition admits two solutions for the propagation angles, $\theta=\pm\cos^{-1}C_p/U_r$, two wave systems symmetric to the wind vector are developed. The surface topography displays a rhomboid pattern from the two systems crossing each other (Fig. 2a). The directional spectra of these waves show two distinct spectral peaks straddling the wind vector, corresponding to $\theta=0$ referenced to the flight track (Fig. 2b). In the present experiment, the two wave systems are not exactly symmetric to the wind, possible due to effects of swell modulation, which is directionally dependent. During the experiment, the angle between swell and wind vectors is approximately 130° (the swell angle is approximately -50° in the coordinates referenced to the flight track). The two wind-generated wave systems (with one wave system aligns almost perpendicular to and the other almost along the swell propagation direction) thus subject to different levels of swell modulation. Qualitatively, a wave system propagating normal to the swell will experience minimal hydrodynamic modulation. In Fig. 2b, the wave system more aligned to the swell (in the region $\theta<0$) shows a much slower directional alignment into the wind as wave grows.

Although the background swell appears to exert a large influence on the directionality of the two wave systems, the effects on the spectral properties are not as severe. Fig. 3 shows an example of the transect spectra along the two peak directions integrated over a 20° beamwidth, with circles for the wave system (more)

aligned with the swell, and crosses for the system almost normal to the swell. For comparison, the omnidirectional spectrum integrated over 180° half-plane is shown with a solid curve. The spectral bandwidth of the modulated wave system is somewhat narrower than the one that is less modulated. The average wavenumbers represented by the square root of the second spectral moment, $k_a = \left(\int k^2 \chi(k) dk / \int \chi(k) dk\right)^{0.5}$, are 0.266, 0.276 and 0.300, respectively, for the modulated transect spectrum, unmodulated transect spectrum, and omnidirectional spectrum shown. The corresponding bandwidths at half-power points of the spectra are 0.065, 0.167, and 0.179, respectively. The variance ratio of the two transect spectra is 1.03. The full track of 42 km is divided into 25 segments. Average over the full track, the ratio of mean wavenumbers of the two transect spectra from each segment with one standard deviation is 1.02±0.053, and the average variance ratio with one standard deviation is 1.00±0.28. For individual cases, this ratio may vary as much as a factor of two. So, even when the orientation of the wind wave propagation may be steered by the swell significantly, the momentum flux from wind to waves appears to be only slightly modified when mild swell is present.

The bimodal directional distribution of these two spectral peaks are very different from the bimodal distributions of the wave components with their wavenumbers higher than the spectral peak wavenumber as presented in Hwang et al. (2000b). Close inspection of the two obliquely propagating systems shows that each system develops bimodal directional distribution of shorter waves above the peak wavenumber. As discussed earlier, we suggest that the bimodal distribution of the peak waves is due to resonance wind wave generation mechanism, and the bimodal distributions of higher wavenumber components are produced by nonlinear wave-wave interaction mechanism.

5. DISCUSSIONS

Clarification of the directional distribution of a random wave field has important implications on remote sensing applications and air-sea interaction studies. For the former, scattering of electromagnetic waves for an active system and radiation for a passive sensor are sensitive to the orientation of the surface roughness, which is composed of surface waves in the ocean. For air-sea interactions, quantitative evaluation of the momentum and energy fluxes between air and water is obviously dependent on the relative direction between winds and waves. Over the past four decades, spectral models assume unimodal directional distributions. Renditions of the ocean surface based on such models do not represent the ocean surface that is shown to be directionally bimodal. For example, field measurements repeatedly report a large crosswind to upwind ratio (R) of the mean square slope components (e.g., Cox and Munk 1954; Hughes et al. 1977). Cox and Munk (1954) report 9 cases of field measurements with natural or manmade slicks suppressing shorter waves. The range of the ratio R is from 0.75 to 1.03. Such large crosswind mean square slope component cannot be explained using unimodal directional spectral models. The calculated result of the upwind and crosswind mean square slope components using bimodal directional distributions (of waves shorter than the peak wavelength) yield substantial improvement in agreement with field measurements (Hwang and Wang 2000). Also, a large crosswind to upwind ratio is expected for the condition of bimodal directional distribution of dominant waves. By definition, if waves travel at 45° from the wind, R=1. As shown in Fig. 2, waves propagating at a large angle from wind are common for a young sea.

The results derived from this study have significant implications on the formulation of the source and sink functions also. For example, the observed obliquely traveling wave systems cannot be reproduced using the conventional wind input functions now serve as standards in numerical models. The observation shown in Fig. 2 suggests that the dynamic ocean surface roughness needs to be considered as a vector quantity, and that the apparent propagation direction of the surface waves reflects the orientation of the roughness elements that are important to the quantification of the surface wind stress. Based on this argument, the surface wind stress can be decomposed into individual components, one for each discernable wave system. For the case shown in Fig. 2, one expects two major stress components along the two wave systems. This concept is tested on a SWAN model simulation (Rogers et al. 2000).

6. SUMMARY

It has been held as a common knowledge that waves propagate in the direction of wind. This concept has been incorporated into the unimodal directional distribution function of all wave spectral models. The formulation of wind input function in equations governing the dynamics of ocean surface waves, such as the source function in the energy or action conservation equation, also assumes that all wave components propagates in the direction of wind. Recent field measurements of 3D ocean surface topography, however, do not support this assumption. For young waves under fetch-limited conditions, the

peak waves are traveling at angles significantly differently from the wind direction. In fact, at very short fetch the dominant wave direction is crosswind rather than along-wind. As fetch increases, two distinct wave systems propagate obliquely to wind can be identified from the crosshatched pattern of the surface topography (Fig. 2a). These results are in good agreement with the prediction of Phillips resonance wind wave generation mechanism. In the present dataset, the propagation directions of the two systems are found to be asymmetric with respect to wind. It is suggested that the directional asymmetry is a result of short wave propagation steered by long waves, possibly a refraction effect by the orbital current. Despite this directional asymmetry, the mean wavenumber and the variance of the two wave systems are similar. As fetch further increases such that the wave propagation velocity is close to the wind velocity, the direction of peak waves coincides with the direction of wind. This range is beyond the 42-km coverage in the present dataset obtained originally for shoaling wave studies.

For waves shorter than the peak wavelength, the directional distribution is also bimodal, forming two lobes symmetric to the peak waves. The mechanism responsible for this bimodal distribution is nonlinear wave-wave interaction (Fig. 1c). Numerical computations of nonlinear wave-wave interaction and spectral analysis of 3D ocean surface topography confirm that the energy extracted from the peak portion of the wave spectrum shifts to oblique components of both longer and shorter portion of the wave spectrum (Banner and Young 1994; Hwang et al. 2000b).

ACKNOWLEDGMENTS

This work is supported by the Office of Naval Research (Naval Research Laboratory Program Element N62435, "Phase Resolved Nonlinear Transformation of Shoaling Waves." NRL Contribution PP/7332--00-0020).

REFERENCES

Banner, M. L., and I. R. Young, 1994: Modeling spectral dissipation in the evolution of wind waves. Part I: Assessment of existing model performance. *J. Phys. Oceanogr.*, **24**, 1550-1571.

Cote, L. J., *et al.*, 1960: The directional spectrum of a wind generated sea as determined from data obtained by the Stereo Wave Observation Project. *Meteor. Papers, New York Univ.*, **2**, W. J. Pierson (ed.), 88 pp.

Cox, C. S., and W. Munk, 1954: Statistics of the sea surface derived from sun glitter. *J. Mar. Res.*, **13,** 198-227.

Donelan, M. A., J. Hamilton, and W. H. Hui, 1985: Directional spectra of wind-generated waves. *Phil. Trans. Roy. Soc. Lond.*, **A315**, 509-562.

Hasselmann, D. E., M. Dunckel, and J. A. Ewing, 1980: Directional wave spectra observed during JONSWAP 1973. *J. Phys. Oceanogr.*, **10,** 1264-1280.

Hasselmann, K. et al., 1973: Measurements of wind wave growth and swell decay during the Joint North Sea Wave Project (JONSWAP). *Deutsch. Hydrogr. Z.*, **A8**, 95 pp.

Hasselmann, S., and K. Hasselmann, 1985: Computations and parameterizations of the nonlinear energy transfer in a gravity-wave spectrum, part 1: A new method for efficient computations of the exact nonlinear transfer integral. *J. Phys. Oceanogr.*, **15**, 1369-1377.

Huang, N. E., 1999: A review of coastal wave modeling: the physical and mathematical problems. In *Advances in Coastal and Ocean Engineering,* Ed. P. L.-F. Liu, World Scientific, Singapore, **4**, 1-20.

Hughes, B. A., H. L. Grant, and R. W. Chappell, 1977: A fast response surface-wave slope meter and measured wind-wave moment. *Deep-Sea Res.*, **24,** 1211-1223.

Hwang, P. A., and D. W. Wang, 2000: Directional distributions and mean square slopes in the equilibrium and saturation ranges of the wave spectrum. *J. Phys. Oceanogr.* (in press).

Hwang, P. A., D. W. Wang, E. J. Walsh, W. B. Krabill, and R. N. Swift, 2000a: Airborne measurements of the wavenumber spectra of ocean surface waves. Part 1. Spectral slope and dimensionless spectral coefficient. *J. Phys. Oceanogr.* (in press).

Hwang, P. A., D. W. Wang, E. J. Walsh, W. B. Krabill, and R. N. Swift, 2000b: Airborne measurements of the wavenumber spectra of ocean surface waves. Part 2. Directional distribution. *J. Phys. Oceanogr.* (in press).

Jackson, F. C., W. T. Walton, and C. Y. Peng, 1985: A comparison of in situ and airborne radar observations of ocean wave directionality. *J. Geophys. Res.*, **90**, 1005-1018.

Krabill, W. B., and C. F. Martin, 1987: Aircraft positioning using global positioning system carrier phase data. *Navig.*, **34**, 1-21.

Krabill, W. B., R. H. Thomas, C. F. Martin, R. N. Swift, and E. B. Frederick, 1995a: Accuracy of airborne laser altimetry over the Greenland ice sheet. *Int. J. Remote Sens.*, **16**, 1211-1222.

Krabill, W. B., R. H. Thomas, K. Jezek, C. Kuivinen, and S. Manizade, 1995b: Greenland ice sheet thickness changes measured by laser altimetry. *Geophys. Res. Lett.*, **22**, 2341-2344.

Long, S. R., N. E. Huang, E. Mollo-Christensen, F. C. Jackson, and G. L. Geernaert, 1994: Directional wind wave development. *Geophys. Res. Let.*, **21**, 2503-2506.

Longuet-Higgins, M. S., D. E. Cartwright, and N.D. Smith, 1963: Observations of the directional spectrum of sea waves using the motions of a floating buoy. *Ocean Wave Spectra,* Prentice Hall, Englewood Cliffs, N. J., 111-136.

Mitsuyasu, H. *et al.*, 1975: Observation of the directional wave spectra of ocean waves using a cloverleaf buoy. *J. Phys. Oceanogr.*, **5**, 750-760.

Phillips, O. M., 1957: On the generation of waves by turbulent wind. *J. Fluid Mech.*, **2**, 417-445.

Phillips, O. M., 1958: On some properties of the spectrum of wind-generated ocean waves. *J. Mar. Res.*, **16**, 231-240.

Phillips, O. M., 1985: Spectral and statistical properties of the equilibrium range in wind-generated gravity waves. *J. Fluid Mech.*, **156**, 505-531.

Rogers, W. E., P. A. Hwang, J. M. Kaihatu, and D. W. Wang, 2000: Modeling bimodal wind-wave propagation resonance. *Proc. 6th Int. Workshop on Wave Hindcasting and Forecasting.*

Walsh, E. J., D. W. Hancock, D. E. Hines, R. N. Swift, and J. F. Scott, 1985: Directional wave spectra measured with the surface contour radar. *J. Phys. Oceanogr.*, **15**, 566-592.

Walsh, E. J., D. W. Hancock, D. E. Hines, R. N. Swift, and J. F. Scott, 1989: An observation of the directional wave spectrum evolution from shoreline to fully developed. *J. Phys. Oceanogr.*, **19**, 670-690.

Young, I. R., and G. Ph. Van Vledder, 1993: A review of the central role of nonlinear interactions in wind-wave evolution. *Phil. Trans. Roy. Soc. Lond.*, **A342**, 505-524.

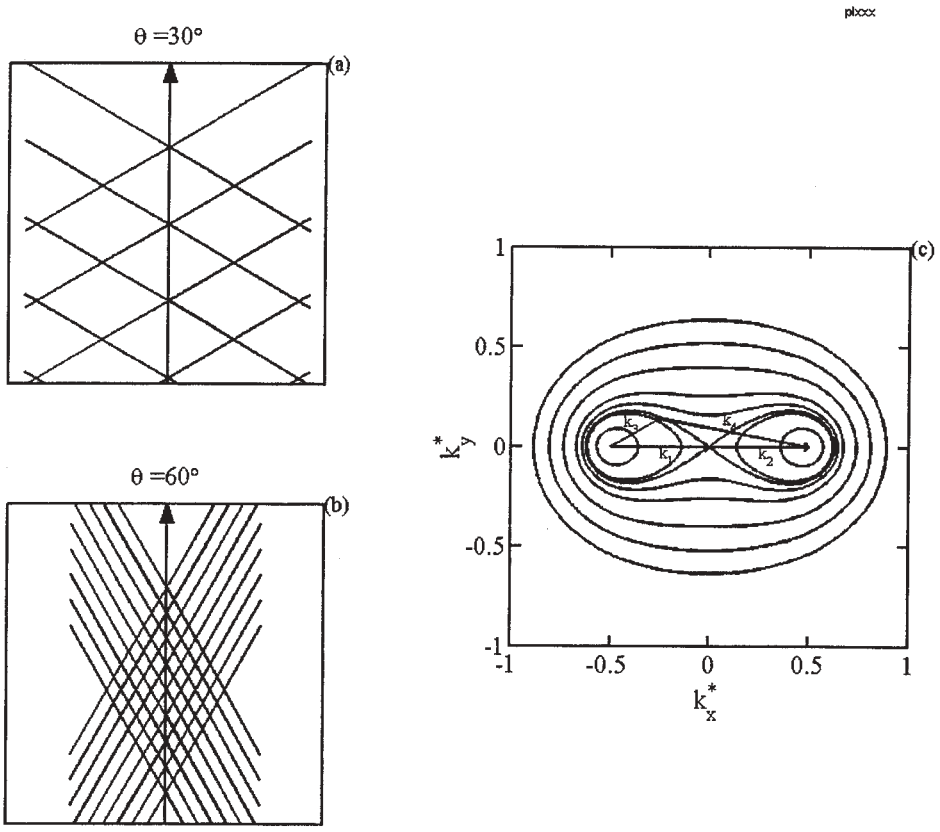

Figure 1. Illustrative sketches of two different mechanisms that produce bimodal directional distribution, (a-b) Phillips resonance wind wave generation mechanism [longer fetch in (a) and shorter fetch in (b)]. The arrow indicates the wind vector. The wave fronts of the two wind-generated wave systems are represented by two sets of parallel lines. (c) Nonlinear wave-wave interaction mechanism. One set of the resonant interaction quartet is show by arrows.

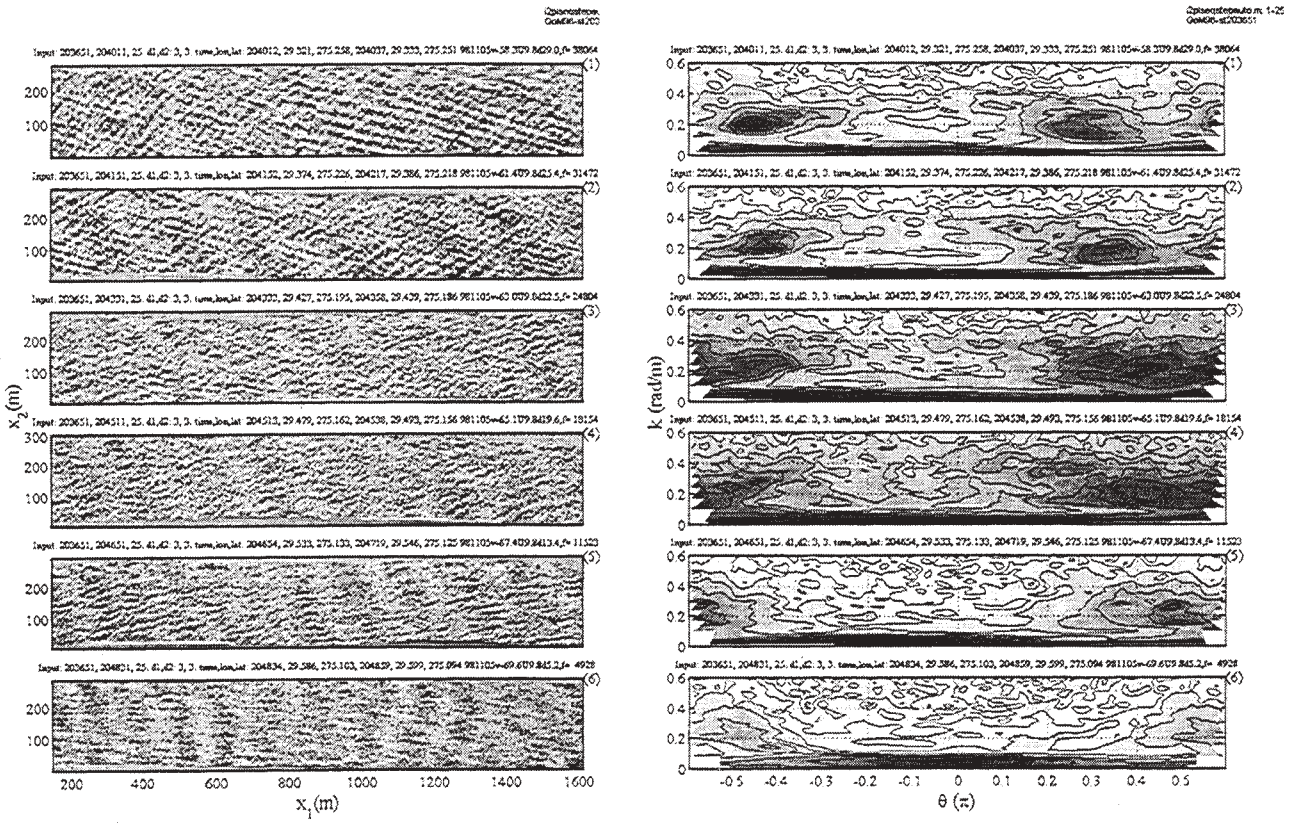

Figure 2. (a) Examples of surface wave topography at six different fetches. Wind is from right to left (offshore fetch-growth condition). (b) The corresponding directional spectra. The wind direction is at θ=0. The fetches for the six cases are 38.1, 31.5, 24.8, 18.2, 11.5 and 4.9 km from top to bottom.

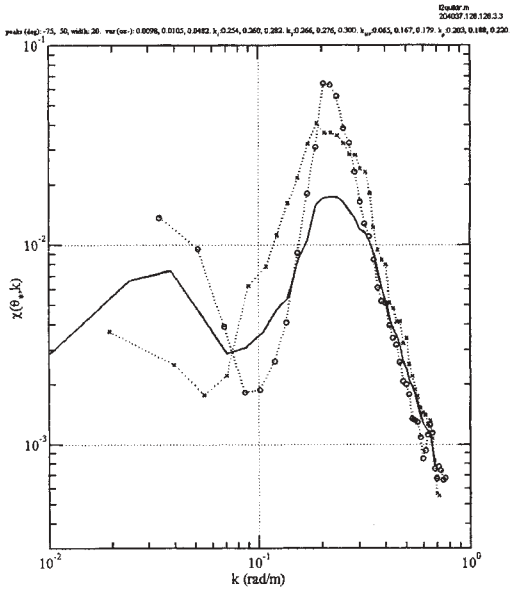

Figure 3. An example of swell modulation on short waves. The wind-generated wave system more aligned to the swell is shown with circles, and the other system that is almost normal to the swell is shown with crosses. The directional beamwidth of integration is 20°. For comparison, the omnidirectional spectrum is shown as solid curve.

Investigations of swell effects on directional characteristics of wind waves using phase-resolved nonlinear models

James M. Kaihatu, David W.C. Wang, Paul A. Hwang and W. Erick Rogers

Oceanography Division, Naval Research Laboratory
Stennis Space Center, MS 39529-5004

1. INTRODUCTION

Recent investigations into the nature of wind wave generation have intimated that the usual presumption of unimodal directional distribution for wind-generated waves may be inaccurate, or at the very least not account for the behavior of very young waves (Hwang et al. 2000; Rogers et al. 2000). Hwang et al. (2000), for example, analyzed airborne topographic mapper (ATM) data from the Gulf of Mexico during a period of offshore winds. In the very nearshore, the waves propagated almost normal to the wind direction. As the fetch increased, the wave directions began to form a bimodal distribution during wave growth and development.

It is hypothesized (Hwang et al. 2000) that the transformation from wind-normal propagation in young waves to wind-aligned older waves is due to resonant interaction between wind and waves (Phillips 1957). Since the phase speeds of young waves are generally smaller than the wind speed, the waves are turned normal to the wind direction to maintain resonance. As the periods (and thus the phase speeds) increase with fetch, the waves turn toward the wave direction. Hwang et al. (2000) saw evidence of this in the Gulf of Mexico ATM data.

Interestingly, while both wind wave spectral peaks approached the wind direction as the fetch increased, one spectral peak did so at a much slower rate than the other. This was thought to be due to the effect of a background swell from Hurricane Mitch, moving in line with the slower moving spectral peak. Additionally, the sea spectral peak moving with the swell is slightly enhanced with respect to that moving normal to the swell. Furthermore it appears that the wind sea propagating in the swell direction (to be referred to as the "in-line wind sea") is less broad in wavenumber space than the wind sea propagating normal to the swell.

This study will outline two phase-resolved wave models and discuss their capabilities for simulating directional spectra evolution. We will then attempt to use the models in some fashion to simulate what is seen in the Gulf of Mexico ATM data.

2. PHASE-RESOLVED FREQUENCY DOMAIN MODEL

To begin this investigation, we use the phase-resolved model of Kaihatu and Kirby (1995), with the improvements described in Kaihatu (2000) and further extended to include directional interactions. This model is a nonlinear frequency-domain model based on the linear parabolic mild-slope equation model REFDIF-S (Kirby and Ozkan 1994). The REFDIF-S model is a "spectral" model but in a different sense than WAM (Komen et al. 1994) or SWAN (Booij et al. 1999), which are expressed in terms of phase-averaged directional spectra. Rather, each frequency-direction component in the initializing spectrum is propagated through the domain with the linear parabolic model simultaneously. The primary difference between the model used here and the REFDIF-S model is the inclusion of nonlinear triads. These triads (three-wave interactions) are more representative of shallow-water nonlinear processes, though both Kaihatu and Kirby (1995) and Kaihatu (2000) demonstrate that overall model performance in deep water is quite good.

The nonlinear terms in the model of Kaihatu and Kirby (1995) do not explicitly account for wave directions, and thus modification is required to incorporate evolution of directional spectra. After modification, the model reads:

$$2i(kCC_g)_n A^m_{n,x} - 2(kCC_g)_n(\bar{k}_n - k_n)A^m_n + i(kCC_g)_{n,x} A^m_n + \left(\frac{3}{2} + \frac{\bar{k}_n}{2k_n}\right)\left[(CC_g)_n A^m_{n,y}\right]_y + \frac{i}{2}\left(\frac{k_{nx}}{k_n^2} + \frac{(kCC_g)_{nx}}{2(k^2CC_g)_n}\right)[(CC_g)_n A^m_{ny}]_y + \frac{i}{k}[(CC_g)_n A^m_{ny}]_{yx} = \Omega \quad (1)$$

where:

$$\Omega = \sum_{l=1}^{n-1}\sum_{p=1}^{M}\sum_{q=1}^{M} RA_l^p A_{n-l}^q \chi + 2\sum_{l=1}^{N-n}\sum_{p=1}^{M}\sum_{q=1}^{M} SA_l^{p*} A_{n+l}^q \phi \quad (2)$$

$$\chi = e^{i\Theta(l,n-l,n)} \quad (3)$$

$$\phi = e^{i\Theta(-l,n+l,n)} \quad (4)$$

$$\Theta(l,n-l,n) = \int \bar{k}_l + \bar{k}_{n-l} - \bar{k}_n dx \quad (5)$$

and where $A^m{}_n$ is the complex amplitude of the wave component with frequency f_n and direction θ_m. There are N total frequency components and M total directions in the spectrum. Subscripts x and y refer to partial differentiation with respect to those coordinates, C is the phase speed, C_g is the group velocity, k is the wavenumber (with the overline referring to an average in the longshore (y) direction), and the interaction coefficients R and S are:

$$R = \frac{g}{\omega_l \omega_{n-l}}[\omega_n^2 k_l k_{n-l} + (k_l + k_{n-l})(\omega_{n-l} k_l + \omega_l k_{n-l})\omega_n] - \frac{\omega_n^2}{g}(\omega_l^2 + \omega_l \omega_{n-l} + \omega_{n-l}^2) \quad (6)$$

$$S = \frac{g}{\omega_l \omega_{n+l}}[\omega_n^2 k_l k_{n+l} + (k_{n+l} - k_l)(\omega_{n+l} k_l + \omega_l k_{n+l})\omega_n] - \frac{\omega_n^2}{g}(\omega_l^2 - \omega_l \omega_{n+l} + \omega_{n+l}^2) \quad (7)$$

where ω is the wave radian frequency. The model (Equation 1) also exists in a form for wave-current interaction. The original model as developed by Kaihatu and Kirby (1995) was typically only run for wave conditions in which multiple directions were not present for each frequency. The incorporation of directional spectra necessitated the double summations on M in order to account for interactions among all components in the directional spectrum.

3. EVOLUTION OF DIRECTIONAL SPECTRA IN THE PRESENCE OF MODULATING SWELL

At present, there is no phase-resolving wave model that can simulate wind-wave generation. However, we are primarily interested in how the propagating wind sea interacts with the swell regardless of the wind. There are two non-exclusive explanations for the behavior of the in-line wind sea spectrum:

a) The swell is acting as an oscillating sea level and current interacting with the wind sea (assumed to be primarily a kinematic effect)

b) The swell is interacting nonlinearly with the wind sea (a dynamic effect).

We create a domain that is $2km$ by $2km$, with a resolution of $2m$ in x and $4m$ in y. The uniform water depth is $30m$. For each model run using Equation 1, the free surface elevation is constructed. This is then subdivided into sixteen subdomains, with a 2D FFT performed on each subdomain. Frequency-directional spectra are then calculated for each subdomain.

We note here that we cannot directly simulate the measured scenario (sea propagating *into* swell), due to the model's parabolic (initial-value) formulation. We also separate the two sea spectra evident in the data into two different model runs, thereby assuming that there is no interaction between them. This was done for computational efficiency; however it is not clear whether this assumption is valid. Despite these *caveats*, however, we feel the resulting simulations might lend insight into the processes at hand.

We use a TMA spectrum (Hughes 1984) with a wrapped mean normal directional distribution (Borgman 1985). The sea spectrum had a peak period T_p=4s, while the monochromatic swell had T=12s. Significant waveheight of the spectra was 0.5m, and the underlying swell (when simulated) was 0.3m. The sea spectra entered the domain at either +45° or -45° to the x axis of the grid, and the swell was set at -45°. All runs used a value of peakedness parameter γ=20 (very narrow banded) and a standard deviation for the directional spread of 5°. As with the separation of the two sea spectra, these values were chosen for computational speed, though broader spectra will be introduced in the future.

To investigate the kinematic effect of the swell on the sea, we deactivate the nonlinear terms in (1) and create a wave-current interaction environment by calculating the orbital velocity and the sea surface elevation of the swell. The sea surface elevation was then added to the constant water depth, and the orbital velocity treated as a current for the sea spectra to encounter. As stated earlier, the linear version of (1) is the REFDIF-S model (Kirby and Ozkan 1994), though the expression including wave-current interaction was not given. The current that is input to the model is assumed to be the depth-averaged current. Taking the expression for orbital velocity of a linear wave (Dean and Dalrymple 1984) and averaging over the depth yields:

$$\bar{u} = \frac{ga}{\omega h} \tanh kh \cos(kx - \omega t) \qquad (8)$$

Since the model is a frequency-domain model, the current field is assumed to be static; thus t=0 in (8).

Figure 1 shows the resulting free surface and directional spectrum (normalized by maximum spectral density) in a sub-domain for a sea spectrum propagating in the same direction as the current from the underlying swell (both at -45°). Figures 1a and 1b show results with the current present, while Figures 1c and 1d depict the case with no current. Since the model is linear, there are no nonlinear interactions present to generate cross-spectral energy transfer. The harmonics of the sea peak that appear in Figure 1 are most likely due to the directional spectrum having been calculated from the spatial 2D FFT of a random wave field. Additionally, the directional spectra were drawn with a logarithmic color map, which helps amplify the peaks. Comparison of Figures 1a and 1c show no discernible differences, but the frequency-direction spectra comparisons (Figures 1b and 1d) reveal that the oscillating current tightens the frequency-direction width at three frequencies relative to the no-current case. This resembles what was found in the Gulf of Mexico ATM data (Hwang et al. 2000).

Figure 2 shows similar results for the case where the sea spectrum is propagating at right angles to the current. The same subdomain is used as before. Figures 2a and 2b depict free surface elevation, wavenumber-direction spectrum, and frequency-direction spectrum (respectively) for the case of oscillating current, while the no-current scenario is shown in Figures 2c and 2d. Unlike the case of an oscillating current colinear with the sea spectrum, however, there is not as much tightening of the directional spectrum at the sea peak due to the current. As in the case shown in Figure 1, however, the oscillating current does shift the high frequency peak toward higher frequencies than is seen in the no-current case. Superposition of Figures 1b and 2b (not shown) reveals a slight asymmetry of the sea spectral peaks about θ=0°. The peak of the sea spectrum running colinearly with the swell is about 3° closer to θ=0° than the peak of the sea spectrum running normally to the swell. The Gulf ATM data showed a swell running directly *into* a wind sea, and a *greater* deviation (about 15°) from the wind direction than the sea propagating normally to the swell. One could conclude that since we are modeling the obverse of this scenario, we are obtaining the obverse results. It to a greater offset than only 3°. Thus, purely kinematic effects might be sufficient to explain all that is seen in the Gulf ATM data with respect to the two sea spectra.

Nonlinear interaction between the frequencies of the sea and underlying swell may also be responsible for the evolution and directional bias of the two sea spectra in the Gulf ATM data. We note that the T=12s swell and the T=4s sea are harmonics and thus subject to triad nonlinear interaction. To test this, we activate the nonlinear terms in (1), and incorporate the swell as an energy component rather than leaving its signature as an oscillating current and undulating water depth. We repeat here that the triad interaction mechanism is represented in this model, so results will likely not translate to discussions of quadruplet interactions. Figure 3 depicts the case in which the sea and swell are propagating in the same direction. Figures 3a and 3b represent the case with no amplified swell (the low-energy T=12s band is part of the original spectrum with T_p=4s), while Figures 3c and 3d show the case in which the T=12s swell is made to have a waveheight of 0.3m. In contrast to the linear kinematic case of Figures 1 and 2, there is a marked difference in the free surface signature shown in Figures 3a and 3c. Additionally, the triad nonlinearity present in the model leads to cross-directional transfers of energy. For example, Figures 3b and 3d (the frequency-direction spectra) show significant energy along both θ=-45° and close to θ=-90°. The amplified swell case shows that the energy in the wind wave spectrum seems to be diminished relative to that in the swell peak (Figure 3d). Additionally some of the spread of energy surrounding the sea spectral peak seems to be reduced with amplified swell. This is contrast to the case of unamplified swell, where energy seems to be distributed equally among all frequencies and the sea spectral peak seems to be somewhat wider (Figure 3b).

Figure 4 depicts a case where the amplified swell and the wind sea are propagating at right angles to each other. The underlying swell can be clearly seen in Figure 4a. Figure 4b (the frequency-directional spectrum) almost appears to be a mirror image of the in-line sea-swell case (Figure 3d), except for the position of the swell peak. However, superposition of Figures 4b and 3d reveal the same 3° difference in angular distance from the zero-angle axis seen in the linear wave-current interaction simulation. The in-line wind sea spectrum is 3° closer to the zero-angle axis than the wind sea spectrum propagating normally to the swell. The sea spectrum and

associated harmonics appear to be lower in energy than the swell, indicating that either the swell is suppressing the sea energy transfer or that the evolution distance is too small for significant energy transfer to take place. This was also seen in the in-line sea spectra. Additionally, the sea spectral peak, while narrowed somewhat with respect to the unamplified swell case, is wider than the case in which the amplified swell is propagating in the same direction as the wind sea.

The results of this model analysis are promising and shed some light on what the Gulf ATM data is depicting (Hwang et al. 2000). However, *both* the kinematic and dynamic analyses show a slight asymmetry in the directional characteristics of the two sea spectra in the presence of swell, and *both* show some suppression of energy in frequency-direction band surrounding the sea in the cases where swell effect is considered. Additionally, the frequency-domain formulation ensures a static depiction of what may be a temporally evolving wave field. The most comprehensive way to simulate this effect would be to utilize a time-dependent model for the free surface evolution.

4. TIME-DEPENDENT EXTENDED BOUSSINESQ MODEL

Probably the best model to use to investigate the effect of the swell on the wind sea is the phase-resolved time domain Boussinesq model FUNWAVE (Wei et al 1995). While standard Boussinesq models (e.g., Rygg 1988) are weakly dispersive and weakly nonlinear, FUNWAVE uses as its base the "extended" Boussinesq model of Nwogu (1993). The "extended" formulation includes a linear dispersion relation for the model that resembles fully-dispersive linear wave theory in deep water. FUNWAVE is a further development in that the nonlinear characteristics of the model include cubic nonlinearity, and has been shown to simulate deep water nonlinearity quite accurately (Kirby and Wei 1994). The Boussinesq equations (in the time domain) are expressed in terms of mass and momentum conservation and have no inherent wave-related parameters. Thus it is able to simulate non-periodic, unsteady flows if forced with an appropriate input condition. Additionally, since the mass and momentum equations are coupled, the model is able to simulate fully-coupled wave-current interaction.

The model is not parabolic; thus it is possible to simulate the case of a sea spectrum propagating against a swell. This involves resetting the source functions in the FUNWAVE code to allow wave propagation from both the upwave and downwave ends, a feature the standard release version of FUNWAVE does not contain. We will revise the code accordingly and will have the corresponding simulations for the conference.

6. SUMMARY

Hwang et al. (2000) analyzed ATM data from the Gulf of Mexico. During the measurement period, a strong offshore wind generated waves which, when analyzed further, contained two directional spectra propagating symmetrically about the wind direction. As the waves continued propagating through the fetch, the two wind sea spectra began to evolve toward the wind direction. During this time a light swell from Hurricane Mitch was propagating through the fetch towards shore and directly opposing one of the wind sea spectra. This wind sea spectra evolved towards the wind direction at a slower rate than that propagating at right angles to the swell, and also evidenced a tighter wavenumber distribution. Hwang et al. (2000) theorized that this was due to a steering effect from the orbital velocities of the underlying swell. Thus we wished to see whether the effect was purely kinematic (wind waves interacting kinematically with the orbital velocities beneath the swell) or dynamic (wind waves interacting nonlinearly with the swell).

We used a phase-resolving model to attempt to investigate the possible reasons for the asymmetry in both wavenumber spread and movement toward the wind direction of the in-line sea spectrum. An improved version of the model of Kaihatu and Kirby (1995) was used; the improvements are detailed in Kaihatu (2000). We first ran the model in linear mode, with the long period swell represented as an oscillating current. A narrow banded TMA spectrum with a narrow directional distribution was used as our initializing spectrum for computational efficiency, and run both in-line and normal to the oscillating current. The results showed that the in-line sea spectrum with the oscillating current activated was indeed narrower in frequency-direction space than either the no-current case or the case of wind sea propagating normal to the swell. Additionally, the directional asymmetry of the two wind sea spectra with respect to (in this case) zero angle is present, with the in-line sea peak about 3° closer to the zero angle axis than the sea peak propagating normal to the swell. In the measured scenario the in-line sea and swell are propagating *into* each other, which results in the in-line sea being 15° further away from the wind direction than the normally-propagating sea. It can be argued that we are modeling the obverse

situation to the field case and obtaining obverse results.

The model was then run with the nonlinearity activated and the swell treated as a wave rather than an oscillating current. The swell was either treated as a low-energy portion of the initializing spectrum, or its amplitude was increased to represent an independently-generated process (in this case, pure swell propagating from another source). Cross-directional transfers of energy away from the primary sea and swell directions were evident in the results. The directional spectra from the case of amplified swell, however, showed that the wind sea and the associated harmonics were consistently of lower energy than the swell. This is in contrast to the case where the swell is a low-energy portion of the sea spectrum; in that case energy appeared to be equally distributed among the energy peaks in the directional spectrum. Additionally, the sea spectra peak propagating in-line with the amplified swell appears to be slightly narrower than that seen in the case of unamplified swell. This sea spectra peak is also narrower than the sea spectra propagating normal to the amplified swell.

The results here are promising; however both the kinematic and dynamic modeling analyses show *both* of the phenomena seen in the Gulf ATM data with respect to wind-wave sea interacting with swell. We then discussed using a time-domain free surface model (FUNWAVE; Wei et al. 1995) to simulate the propagation scenarios seen in the data in a comprehensive manner. Both cubic nonlinear effects and wave-current interaction with the orbital velocities from swell are represented in the model. Some coding changes need to be made in order to effect such a simulation, however, and we endeavor to complete this for the conference presentation.

7. ACKNOWLEDGMENTS

The work is supported by the Office of Naval Research (Naval Research Program Element N62435, "Phase Resolved Nonlinear Transformation of Shoaling Waves," NRL Contribution PP/7320—00-1017). Dr. Qin Chen (University of Delaware) allowed us to use his experimental version of the FUNWAVE code and has answered many ensuing questions; his assistance to this effort is appreciated.

8. REFERENCES

Booij, N., R.C. Ris, and L.H. Holthuijsen. 1999. A third-generation wave model for coastal regions, 1. Model description and validation, *J. Geophys. Res.*, 104, 7649-7666.

Borgman, L.E. 1985. Directional spectrum estimation for the *Sxy* gauges, *Technical report*, Coastal Engineering Research Center, Waterways Experiment Station, Vicksburg, MS, 104p.

Dean. R.G., and R.A. Dalrymple. 1984. *Water wave mechanics for engineers and scientists.* Prentice-Hall, Englewood Cliffs, NJ, 353p. (now available from World Scientific, Inc., Singapore).

Hughes, S.A. 1984. The TMA shallow-water spectrum: description and applications, *Technical report CERC-84-7*, Coastal Engineering Research Center, Waterways Experiment Station, Vicksburg, MS, 24p.

Hwang, P.A., D.W.C. Wang, W.E. Rogers and J.M. Kaihatu. 2000. A discussion on the directional distribution of wind-generated ocean waves, *Proceedings, 6th International Workshop on Wave Hindcasting and Forecasting*, Monterey, CA (this conference).

Kaihatu, J.M. 2000. Improvement of a parabolic nonlinear dispersive wave model, *ASCE J. Wtrway., Port, Coast. and Oc. Engrg.*, in press.

Kaihatu, J.M., and J.T. Kirby. 1995. Nonlinear transformation of waves in finite water depth, *Phys. Fluids*, 7(8), 1903-1914.

Kirby, J.T., and H.T. Ozkan. 1994. Combined refraction/diffraction model for spectral wave conditions: REF/DIF-S, version 1.1, documentation and user's manual, *CACR Report 94-04*, Center for Applied Coastal Research, University of Delaware, Newark, DE, 128p.

Kirby, J.T., and G. Wei. 1994. Derivation and properties of a fully nonlinear model for weakly-dispersive waves, *Proceedings of the International Symposium: Waves – Physical and Numerical Modeling*, Vancouver, B.C., 386-395.

Komen, G.J., L. Cavaleri, M. Donelan, K. Hasselmann, S. Hasselmann, and P.A.E.M. Janssen. 1994. *Dynamics and modeling of ocean waves*, Cambridge University Press, Cambridge, U.K., 531p.

Nwogu, O. 1993. Alternative form of Boussinesq equations for nearshore wave propagation, *J. Wtrway., Port, Coast. and Oc. Engrng.*, 119(6), 618-638.

Phillips. O.M. 1957. On the generation of waves by turbulent wind, *J. Fluid Mech.*, 2, 417-445.

Rogers, W.E., P.A. Hwag, J.M. Kaihatu and D.W.C. Wang. 2000. Modeling bimodal wind-wave propagation resonance, *Proceedings, 6th International Workshop on Wave Hindcasting and Forecasting*, Monterey, CA (this conference).

Rygg, O.B. 1988. Nonlinear refraction-diffraction of surface waves in intermediate and shallow water, *Coast. Engrng.*, 12, 191-211.

Wei, G., J.T. Kirby, S.T. Grilli and R. Subramanya. 1995. A fully nonlinear Boussinesq model for surface waves. Part 1. Highly nonlinear unsteady waves, *J. Fluid Mech.*, 294, 71-92.

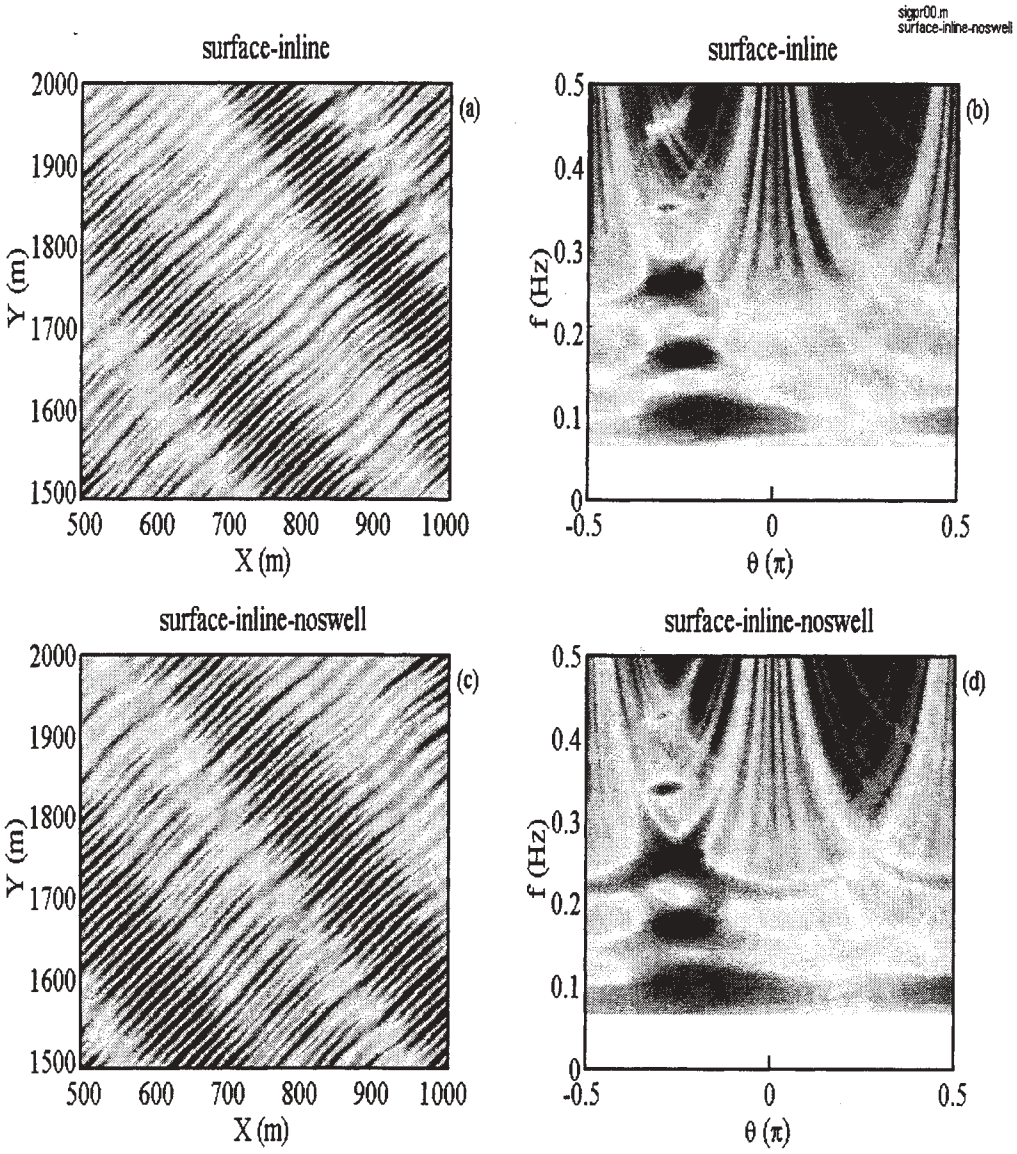

Figure 1. Results of linear model. Sea and swell propagating in line. Top figures show sea interacting with orbital velocity from swell: a) free surface elevation, b) directional spectrum. Bottom figures show sea only: c) free surface elevation, d) directional spectrum.

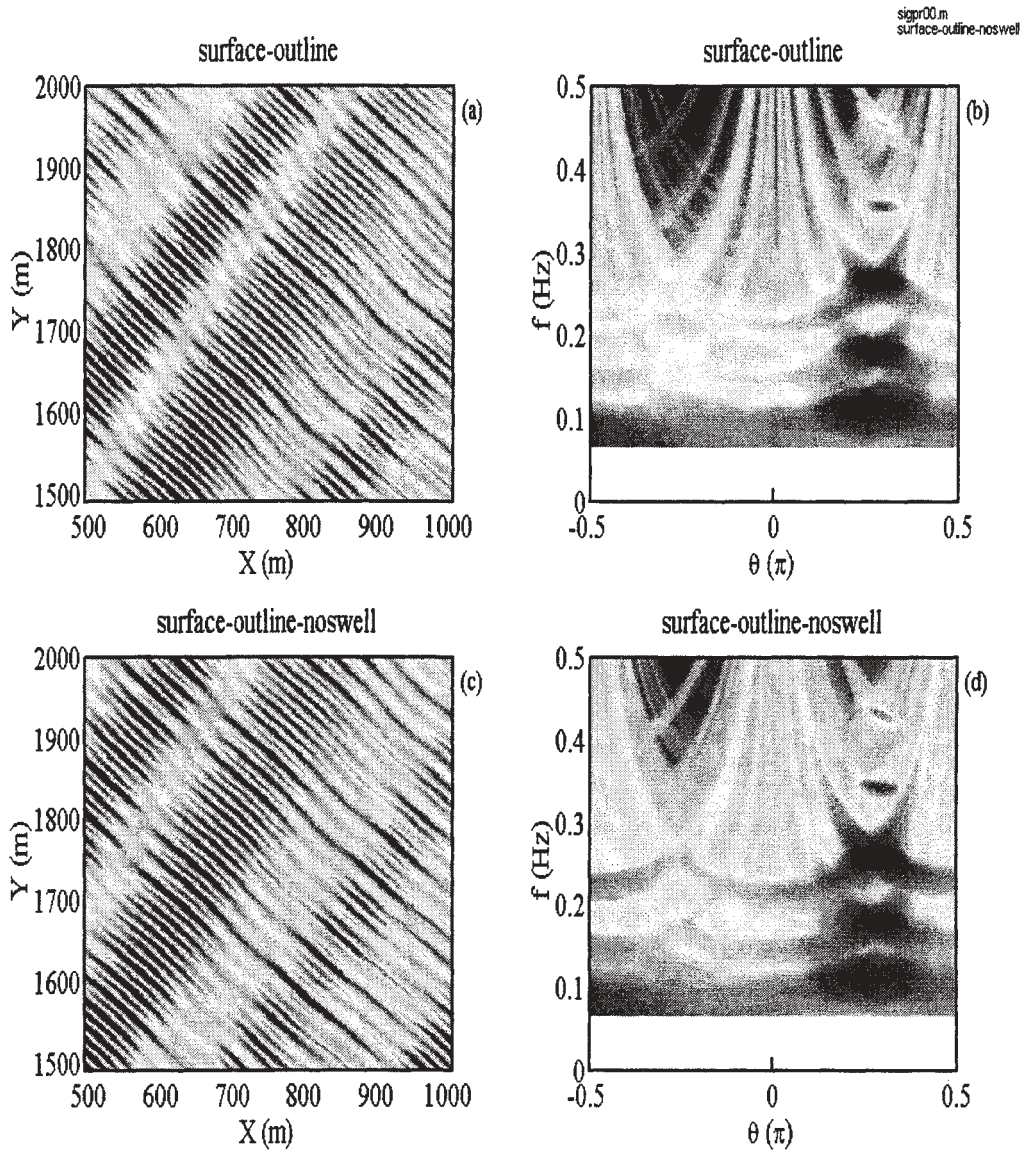

Figure 2. Results of linear model. Sea and swell 90 degrees out of line. Top figures show sea interacting with orbital velocity from swell: a) free surface elevation, b) directional spectrum. Bottom figures show sea only: c) free surface elevation, d) directional spectrum.

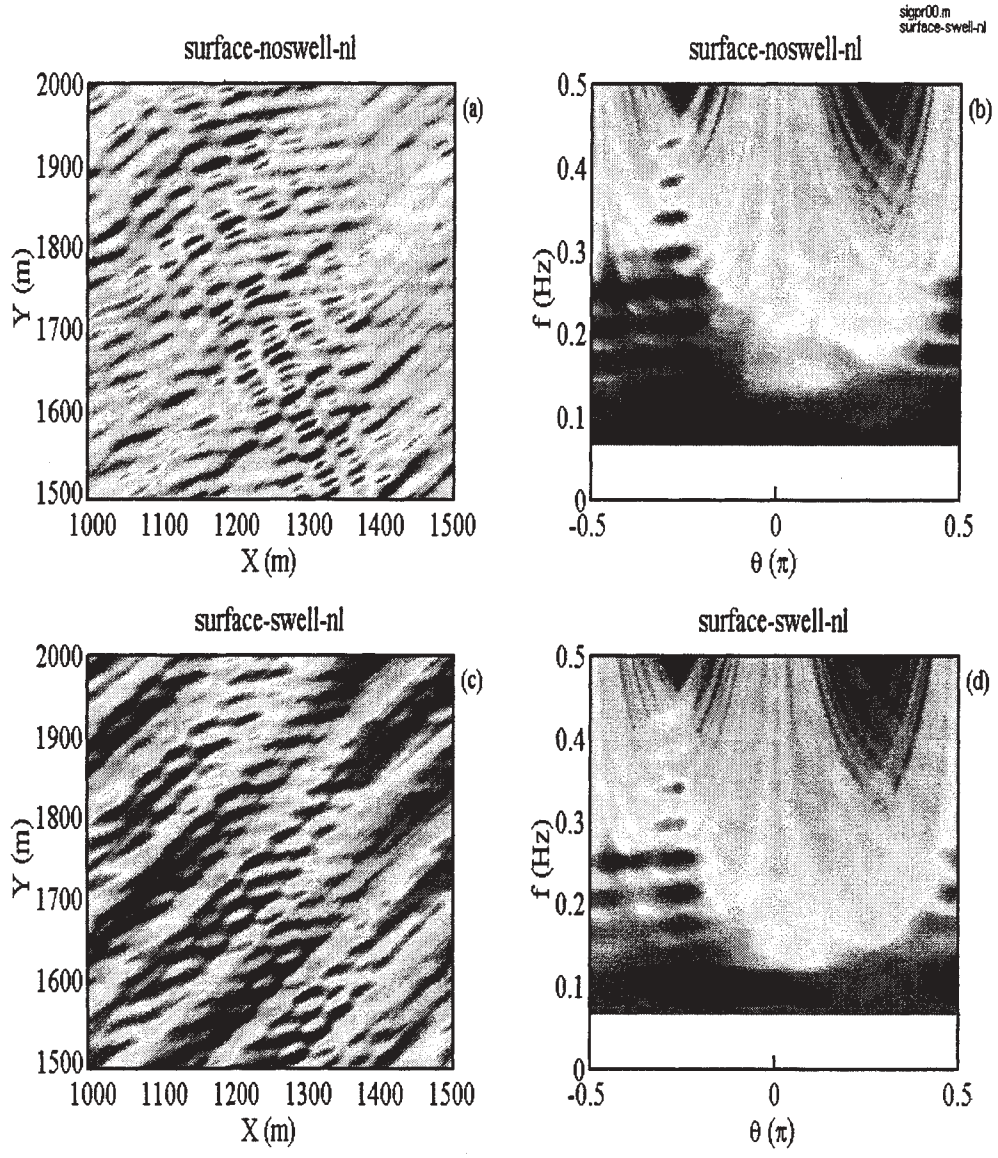

Figure 3. Results of nonlinear model. Sea and swell propagating in line. Top figures show case in which low energy swell is part of sea wavefield: a) free surface elevation, b) directional spectrum. Bottom figures show sea interacting with amplified swell: c) free surface elevation, d) directional spectrum.

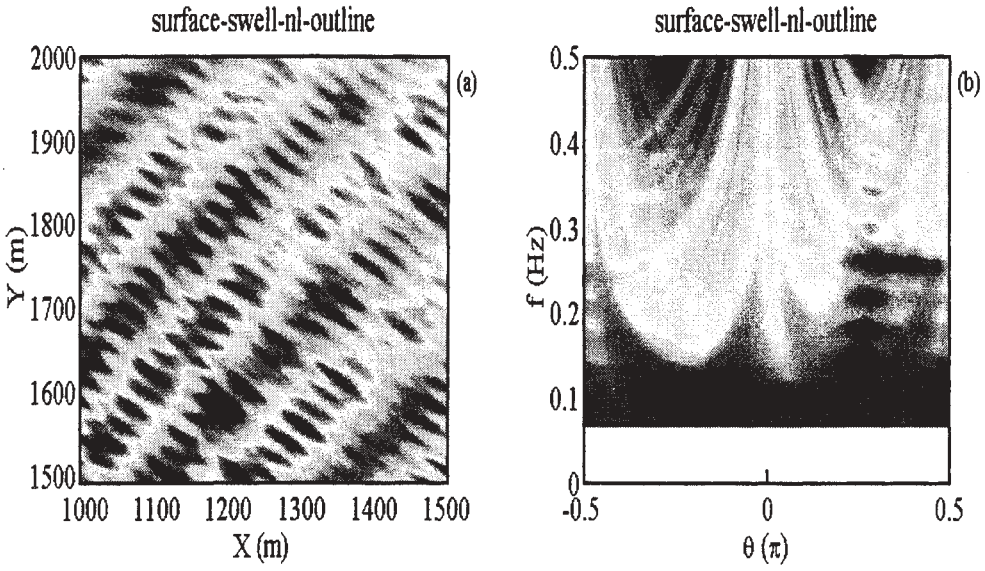

Figure 4. Results of nonlinear model. Sea and swell propagating 90 degrees out of line. Top figures show case in which low energy swell is part of sea wavefield: a) free surface elevation, b) directional spectrum. Bottom figures show sea interacting with amplified swell: c) free surface elevation, d) directional spectrum.

MODELING BIMODAL WIND-WAVE PROPAGATION RESONANCE

W. Erick Rogers, Paul A. Hwang, James M. Kaihatu, and David W. Wang

Oceanography Division, Naval Research Laboratory, Stennis Space Center, MS, USA

1. INTRODUCTION

A high-resolution, airborne topographic mapper was deployed in the Gulf of Mexico on November 5, 1998 during a period of fetch-limited wave conditions (winds directed offshore). A cross-hatched pattern is observed in the free surface disturbances associated with the local sea. In the very nearshore, the wave fronts indicate that wave propagation is almost normal to the wind direction. As fetch increases, waves grow longer and higher, and the wave directions steer to be closer to that of the wind (free surface topography and associated directional spectra are show in Fig. 1). We hypothesize that this is a demonstration of the propagation resonance phenomenon described by Phillips (1957). The propagation resonance condition given by Phillips is satisfied by two solutions:

$$\theta_r = \pm\cos^{-1}(C_p / U_r), \qquad (1)$$

where θ_r is the angle between the wind direction and the wave direction, C_p is the wave phase velocity, and U_r is the wind speed at a reference height proportional to the wavelength (we use $U_r \equiv U_{1/k}$, where k is the component wavenumber). In this study, we attempt to recreate what we observe in the data using a third generation wave model. This type of model is phase-averaged, so processes such as wind input, nonlinear interactions, and wave breaking are represented by energy source/sink terms. The wind input formulations presently used by such models are unimodal, with a peak at θ=0. We replace the unimodal source term with a bimodal source term, with peaks described by (1). It is hoped that further development of this modified source term will allow a more accurate representation of early-stage and short-fetch wave growth by wave models.

2. DATA SET

In data set studied here, the wind was from 310-350° (NNW), with U_{10} of 9.4-10.8 m/s during the four hours prior to the airborne measurement. A light southerly swell is also seen in the topographic data; it is easily distinguished from the fetch-limited local seas. Data was taken along a transect corresponding to a fetch of 0-42km. The lidar data collection system is described in detail in Hwang et al. (2000a,b), and its deployment for this data set is described further in Hwang et al. (2000c).

2.1 Discussion: "Ground Truth"

Though a wave model can often predict wave height and peak frequency with adequate skill, predictions of directional distributions are of more dubious accuracy. To a large extent, this can be blamed on the lack of adequate directional data. Directional data typically come in the form of truncated Fourier series. This information can be very useful to a wave modeler, but some assumptions must be made to convert to actual directional spectra. Thus, these spectra cannot, strictly speaking, be used as ground truth for a model. Free surface topographic data, on the other hand, does provide a ground truth, and therefore provides a useful tool for evaluating or developing the directional capabilities of a numerical model.

3. THE WAVE MODEL

We use the third generation wave model SWAN ("Simulating WAves Nearshore", Booij et al. 1999). It is governed by a form of the two-dimensional hyperbolic wave equation, expressed in terms of the wave action density spectrum:

$$N(x, y, \sigma, \theta) = \frac{E(x, y, \sigma, \theta)}{\sigma}, \qquad (2)$$

where N is wave action density, E is wave energy density, x and y denote geographic location, σ is the relative frequency, and θ is the direction of propagation. Wave action is propagated in geographic and spectral space, while source and sink terms act on the waves. The action balance equation, in horizontal Cartesian coordinates (x,y), can be written as

$$\frac{\partial}{\partial t}N + \frac{\partial}{\partial x}C_{gx}N + \frac{\partial}{\partial y}C_{gy}N + \frac{\partial}{\partial \sigma}C_{\sigma}N + \frac{\partial}{\partial \theta}C_{\theta}N = \frac{S}{\sigma}. \qquad (3)$$

(e.g., Whitham 1974; Phillips 1977; Mei 1983; Hasselmann et al. 1973). Here, t denotes time, C_g is group velocity, C_σ is wave action propagation speed in σ-space, C_θ is propagation speed in θ-space, and S

denotes the total of source and sink terms. The first term represents the local rate of change; the second and third terms represent geographic propagation; the fourth term represents changes to relative frequency (e.g. by nonstationary depth or by currents); the fifth term represents refraction (by depth and currents).

The primary components of S in deep water are

$$S = S_{in} + S_{ds} + S_{nl}, \quad (4)$$

where S_{in} represents input by wind (described below), S_{ds} represents steepness-limited breaking (a tuned closure term, see Komen et al. 1984), and S_{nl} is the model's approximation of four-wave interactions (DIA, Hasselmann et al. 1985). S_{in} has two components:

$$S_{in}(\sigma,\theta) = A + BE(\sigma,\theta). \quad (5)$$

The term A represents linear growth (e.g. Phillips 1957; Cavaleri and Malonotte-Rizzoli 1981; Tolman 1992; Ris 1997):

$$A = \frac{1.5\times10^{-3}}{g^2 2\pi}[U_* \max[0,\cos(\theta_d)]]^4 F, \quad (6)$$

$$F = \exp(-(\sigma/\sigma^*_{PM})^{-4}), \quad (7)$$

$$\sigma^*_{PM} = \frac{0.13g}{28U_*}2\pi, \quad (8)$$

where g is gravity, U_* is the friction velocity, F is a filter, and σ_{PM} is the equilibrium peak frequency for a fully-developed sea state (Pierson and Moskowitz 1964), i.e., duration- and fetch-unlimited conditions.

The term B represents exponential growth (e.g. Miles 1957; Snyder et al. 1981; Komen et al. 1984):

$$B = \max\left[0,0.25\frac{\rho_a}{\rho_w}\left[28\frac{U_*}{C}\cos(\theta_{wv}-\theta_{wd})-1\right]\right]\sigma, \quad (9)$$

where ρ_a and ρ_w are the densities of air and water, and θ_{wv} and θ_{wd} are the directions of the wave component and the wind, respectively.

The values of the free parameters of the breaking term are based on the work of Komen et al. (1984), who used two free parameters to tune the model to match the Pierson and Moskowitz (1964) values for fully-developed conditions. No such tuning has been conducted to match data under fetch-limited conditions; however, SWAN has been compared by Ris (1997) to data and empirical expressions for dimensionless wave energy and peak frequency, and the model is shown to be reasonably accurate.

4. PROPAGATION RESONANCE

Our aim in this paper is to answer the question: "can the development of bimodal directional distribution observed in this data set of 3D surface wave topography be reproduced by incorporating the Phillips propagation resonance (as shown in (1)) into a third generation wind-wave model?". Thus we do not (yet) concern ourselves with issues such as accuracy of model forcing (winds) or tuning the modified model for general usage. With a more thorough data set, it may be possible to a) verify that this bimodality is a consistent feature of a young wave field, b) verify that it is, indeed associated with the resonance mechanism of (1), and c) tune the model such that proper development of directional spectra is achieved under a variety of conditions.

4.1 Kinematics

The kinematics of (1) are quite simple: the crests of a wave will align such that the speed of the crest, measured along the axis of the wind, is identical to the velocity of the wind (at some physically meaningful, reference height). In a phase-average sense, this steering, or realignment, occurs as wave energy satisfying the resonance condition is enhanced, while wave energy not satisfying the condition is diminished (one can expect non-forced short waves to be quickly attenuated).

4.2 Implementation

As a practical matter (for wave modeling purposes) we must allow some energy be transmitted to wave energy with directions slightly different from the resonance-preferred direction(s). We use the $\max(0,\cos^n(\theta))$ form traditional in wave modeling, with n=1, as used in the Snyder et al. (1981) wind input term (9). Thus a modified form of B, replacing θ_{wd} with $\theta_{wd}\pm\theta_r$, would be

$$B = \max\left[0,0.25\frac{\rho_a}{\rho_w}\left[28\beta\frac{U_*}{C}\cos(\theta_{wv}-(\theta_{wd}+\theta_r))-1\right]\right]\sigma$$

$$+\max\left[0,0.25\frac{\rho_a}{\rho_w}\left[28\beta\frac{U_*}{C}\cos(\theta_{wv}-(\theta_{wd}-\theta_r))-1\right]\right]\sigma \quad (10)$$

Here, β is an empirical factor. Komen et al. (1984)) discuss this factor, and use a value of 1.0, noting that it has little effect on results (at least for fully-developed conditions). In order that total stress is

consistent with that of the Komen et al. formula, β should be taken as $\beta = 1/\sqrt{2}$. However, the actual value of β is not important for our purposes, as the actual values of U_* which we use are somewhat arbitrary. We note that β would need to be considered in any subsequent tuning exercise.

We make the linear growth term A bimodal in a manner similar to (10).

4.3 Model input

For model input, we assume deep water, with constant and uniform wind forcing (a reasonable assumption for fetch-limited growth of this scale). Herein, we present results from three simulations of the model with the bimodal source term, using U_{10}=8.5, 10, and 12 m/s, with β=1.0. The simulations are duration-unlimited (steady state).

Though there is a mild swell system apparent in the data, we do not include the swell as boundary forcing, for the simple reason that sea-swell interaction is not represented in the model in a physically meaningful way. To give an example, the dissipation formulation of SWAN, based on WAM cycle 3, is a function of the average steepness of the entire wave spectrum. Thus, whitecapping is reduced by the presence of swell (which is generally not steep). Though it may be argued that swell can indirectly reduce breaking via reduction of roughness and therefore wind input, this is not how the model is formulated. The effect of swell on wind sea growth in the model requires further refinement, so inclusion of swell in the simulation is undesirable if we are interested only in the wind sea portion of the spectrum.

4.4 Model results

Table 1 shows results at a point corresponding to a fetch of about 38km for the original and modified source terms, and compares to data. It is clear from this that, with the original model, there is significant error in the predicted non-directional parameters (T_{peak} and H_{m0}). Thus, a modified model can either match the data, or the original model (not both). To recover the T_{peak} result of the original model, a lower wind speed is needed (8.5m/s). This is expected, as β=1.0 is used in the modified model (and not $\beta = 1/\sqrt{2}$). Figs. 2a, b show the evolution of the directional spectra with fetch for two modified models for comparison to Fig. 1b (U_{10}=10, and 12 m/s). The U_{10}=12 m/s simulation does a reasonably good job of capturing, at least qualitatively, the spectral evolution seen in the data. The spreading of the frequency spectra seems to be underpredicted by the model, while the directional spreading of the lobes is overpredicted. The former is probably (primarily) a direct result of the simplified wind forcing. The latter indicates that a narrower source term might be more accurate, e.g. S_{in}=f(max(0,cos^2(θ))) rather than S_{in}=f(max(0,cos(θ))).

Table 1. Comparison of wave parameters at 38km fetch

Source	T_{peak} (sec)	H_{m0} (m)	θ_{peak} (degrees from primary wind direction)
Lidar data	4.5-5.2	0.9	-80, +50
Original model, U_{10}=10m/s	4.1	1.1	0
Modified model, U_{10}=8.5m/s	4.1	1.2	±25*
Modified model, U_{10}=10m/s	4.3	1.3	±40*
Modified model, U_{10}=12m/s	4.4	1.5	±55

* : the two modes are merged, so the result is unimodal in appearance.

5. DISCUSSION

5.1 Unrepresented Processes

The bimodality observed in the data suggests two possibilities. Either

a) the wave energy is generated, centered at θ_{wv}=θ_{wd} (as a traditional wave model would predict) and quickly steered/transferred to the oblique modes, or

b) the transfer of energy from the wind to the wave system (i.e. the wind input S_{in}) is itself bimodal.

We feel that the latter is the case, and further that the resonance mechanism described by (1) is responsible for the bimodality of dominant waves. Whatever the case may be, it can be said with some certainty that the responsible mechanism is not represented in existing wave models. The traditional mechanism for creating bimodal wave patterns in a wave model is

four-wave interactions, S_{nl}. However, this mechanism does not create bimodality near the spectral peak, as seen in the data, but rather, at the higher and lower ends of the frequency spectrum. Thus this mechanism is tentatively ruled out for explaining the observed bimodal propagation of dominant waves.

There are other processes which, though unlikely to be responsible for the bimodality of the observed spectra, do deserve attention. This is especially true since certain aspects of the data cannot be explained by the resonance mechanism: 1) the waves stay at a cross-wind direction for a longer fetch than would be predicted by the Phillips resonance, and 2) the directional modes of the data are asymmetric with respect to the wind direction. The underlying current field, neglected here, may be important: typically, though most wave models are designed to account for the effects of currents on waves, currents are not included in model forcing, simply because no reliable (and/or adequately resolved) surface current information exists (as in this case). Another issue is the possible hydrodynamic modulation of wind sea by swell, which though perhaps significant, is not faithfully represented in the model. The underlying currents and/or swells is thought to be a likely cause of the asymmetry of the data, since the effect of currents/swell on wind sea is, of course, directionally dependent.

5.2 Fetch-limited Growth Curves

The implementation of the resonance mechanism of (1) in a wave model would have a significant impact on fetch-limited growth curves predicted by the model. Existing models are reasonably effective at matching the Kahma and Calkoen (1992) curve for moderate fetches. Ideally, a modified model, after tuning, would produce, more or less, the same result for such fetches. However, one can expect predictions for shorter fetches to be quite different. Perhaps the most obvious difference would be at the model origin (zero fetch). A traditional model will always predict zero energy at this origin, while the modified model will have energy there, due to waves traveling almost normal to the wind direction and even (due to the cosine distribution of the source term) waves traveling obliquely against the wind direction.

6. SUMMARY

Free surface topography was acquired for a fetch-limited wind growth case in the Gulf of Mexico on Nov. 5, 1998, from which ground truth directional spectra were derived along the fetch axis. In these directional spectra, we observe two directional modes, both oblique to the wind direction (Fig. 1). In this paper we have demonstrated that it is possible to qualitatively recreate this result in a third generation wave model by replacing the unimodal source term with a bimodal source term, with the two peaks being described by the solutions for Phillips propagation resonance, (1). Some unresolved issues remain; the most notable listed here:

1) We believe that this resonance mechanism is the most likely cause of the bimodality of dominant waves and demonstrate how it is possible. However, we do not prove conclusively that this is, in fact, the cause.
2) Frequency distributions predicted by the model are much narrower than that of the data.
3) Directional distributions of the two modes predicted by the model are broader than the data.
4) The two modes in the data are slightly asymmetrical; the cause of this is not clear, though interaction of the wind sea with swell and/or currents is a suspected cause.
5) Any implementation of this mechanism in an operational model would necessitate significant retuning of the model source term(s).

ACKNOWLEDGEMENT

This work is supported by the Office of Naval Research (Naval Research Laboratory Program Element N62435, "Phase Resolved Nonlinear Transformation of Shoaling Waves.", NRL Contribution PP/7320-00-1010).

REFERENCES

Booij, N., R. C. Ris, and L. H. Holthuijsen, 1999: A third-generation wave model for coastal regions, 1, Model description and validation. *J. Geophys. Res.*, **104**, 7649-7666.

Cavaleri, L. and P. Malonotte-Rizzoli, 1981: Wind wave prediction in shallow water: theory and applications. *J. Geophys. Res.*,**86**, No. C11, 10961-10973.

Hasselmann, K., and Coauthors, 1973: Measurements of wind-wave growth and swell decay during the Joint North Sea Wave Project (JONSWAP). *Dtsch. Hydrogr. Z.*, Suppl., **12**, A8.

Hasselmann, S., K. Hasselmann, J. H. Allender, and T. P. Barnett, 1985: Computations and parameterizations of the linear energy transfer in a gravity wave spectrum, II, Parameterizations of the nonlinear transfer for application in wave models. *J. Phys. Oceanogr.*, **15**, 1378-1391.

Hwang, P. A., D. W. Wang, E. J. Walsh, W. B. Krabill, and R. N. Swift, 2000a: Airborne measurements of the wavenumber spectra of ocean

surface waves. Part 1. Spectral slope and dimensionless spectral coefficient. *J. Phys. Oceanogr.* (in press).

Hwang, P. A., D. W. Wang, E. J. Walsh, W. B. Krabill, and R. N. Swift, 2000b: Airborne measurements of the wavenumber spectra of ocean surface waves. Part 2. Directional distribution. *J. Phys. Oceanogr.* (in press).

Hwang, P. A., D. W. Wang, W. E. Rogers, and J. M. Kaihatu, 2000c: A discussion on the directional distribution of wind-generated ocean waves. Proceedings, *6th International Workshop on Wave Hindcasting and Forecasting*, Monterey, California.

Kahma, K. K., and C. J. Calkoen, 1992: Reconciling the discrepancies in the observed growth of wind-generated waves. *J. Phys. Oceanogr.*, **22**, 1389-1405.

Komen, G. J., S. Hasselmann, and K. Hasselmann, 1984: On the existence of a fully developed wind-sea spectrum. *J. Phys. Oceanogr.*, **14**, 1271-1285.

Mei, C. C., 1983: *The applied dynamics of ocean surface waves,* Wiley, New York, 740pp.

Miles, J. W., 1957: on the generation of surface waves by shear flows, *J. Fluid Mech.*, **3**, 185-204.

Phillips, O. M., 1957: On the generation of waves by turbulent wind. *J. Fluid Mechanics*, **2**, 417-445.

Phillips, O. M. 1977: *The dynamics of the upper ocean, 2nd edition,* Cambridge University Press, 336pp.

Pierson, W. J., and L. Moskowitz, 1964: A proposed spectral form for fully developed wind seas based on the similarity theory of S. A. Kitaigorodsii. *J. Geophys. Res.*, **69(24)**, 5181-5190.

Ris, R. C., 1997: *Spectral modeling of wind waves in coastal areas.* Ph.D. thesis, Delft University of Technology, 160pp.

Snyder, R. L., F. W. Dobson, J. A. Elliot, and R. B. Long, 1981: Array measurement of atmospheric pressure fluctuations above surface gravity waves. *J. Fluid Mech.* **102**, 1-59.

Tolman, H. J., 1992: Effects of numerics on the physics in a third-generation wind-wave model, *J. Phys. Oceanogr.*, **22**, No. 10, 1095-1111.

Whitham, G. B., 1974: *Linear and nonlinear waves,* Whiley, New York, 636pp.

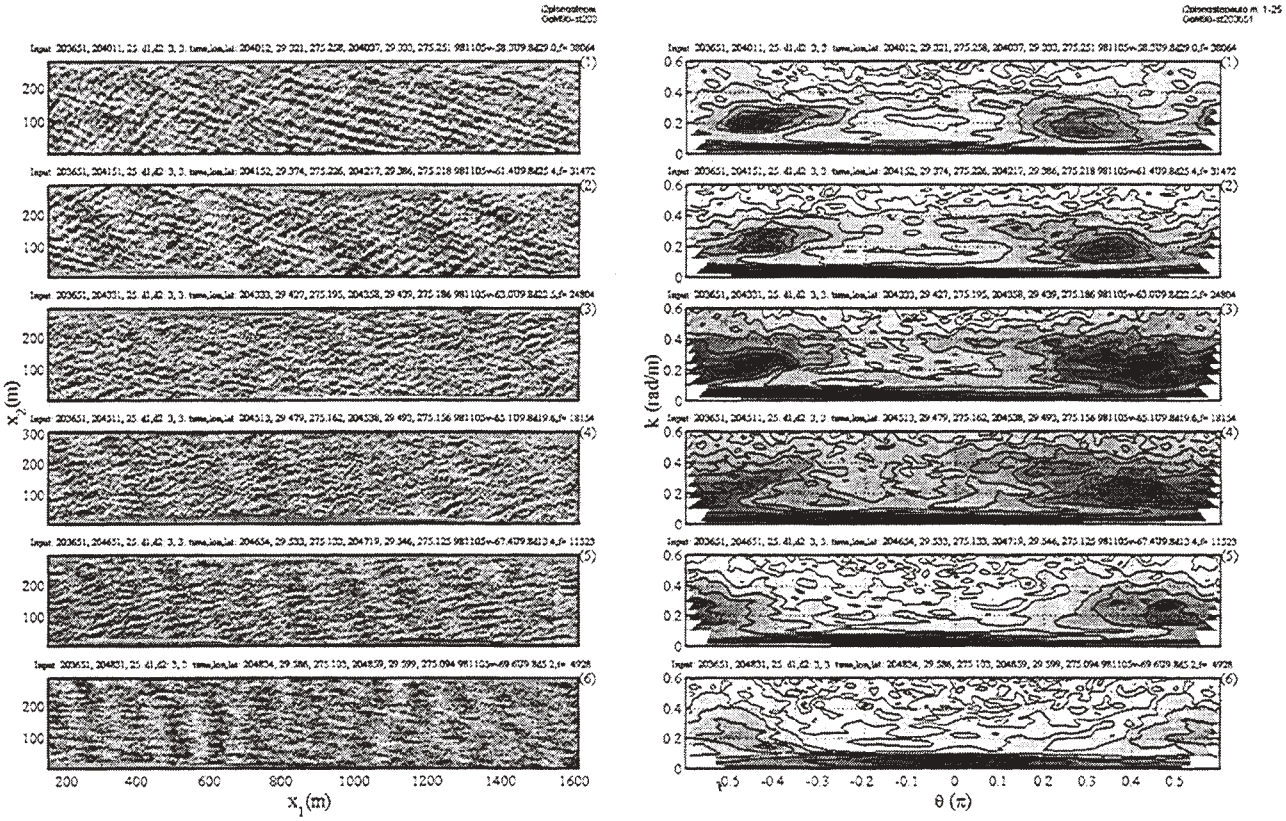

Figure 1. Left diagram: Surface wave topography at six different fetches. Wind is from right to left (offshore fetch growth condition). Right diagram: The corresponding directional spectra. The wind direction is at θ=0. The fetches for the six cases are 38.1, 31.5, 24.8, 18.2, 11.5 and 4.9 km from top to bottom [Hwang et al. 2000c].

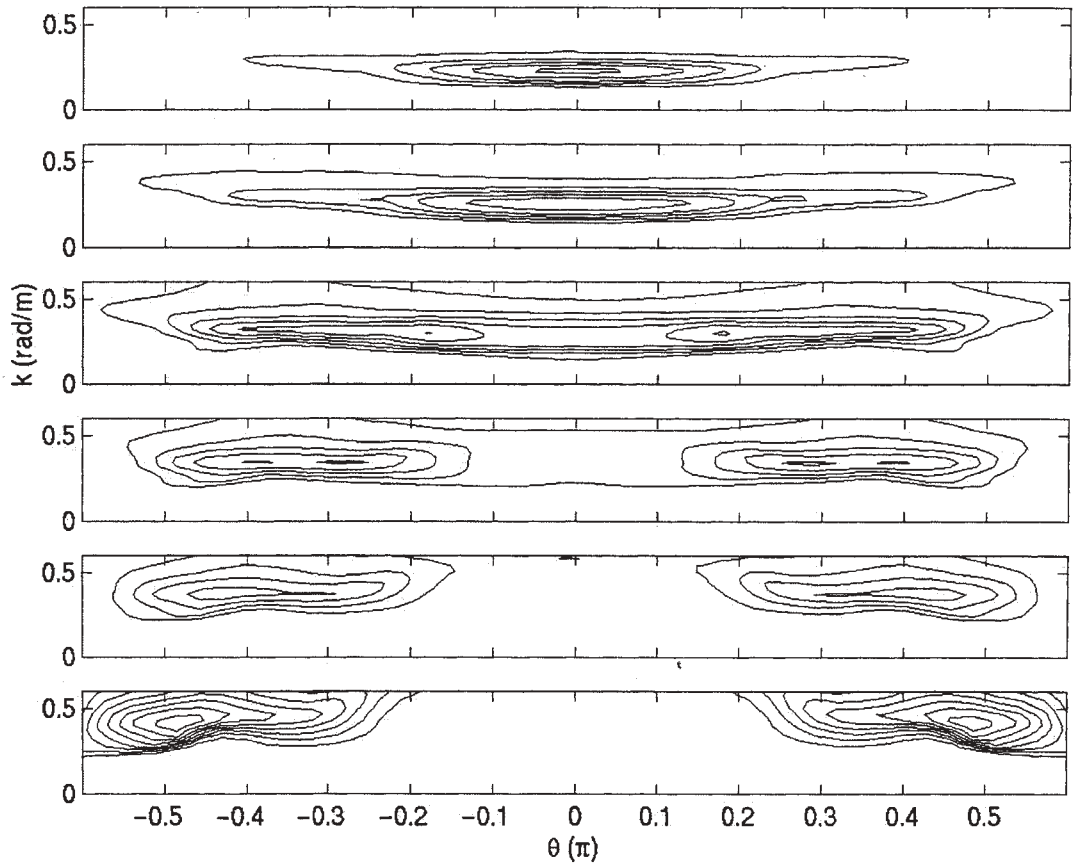

Figure 2a. Directional spectra $S(f,\theta)$ at six locations, corresponding to the locations of lidar measurements in Fig. 1. From top to bottom, fetch is 38.1, 31.5, 24.8, 18.2, 11.5, and 4.9 km. U_{10}=10 m/s.

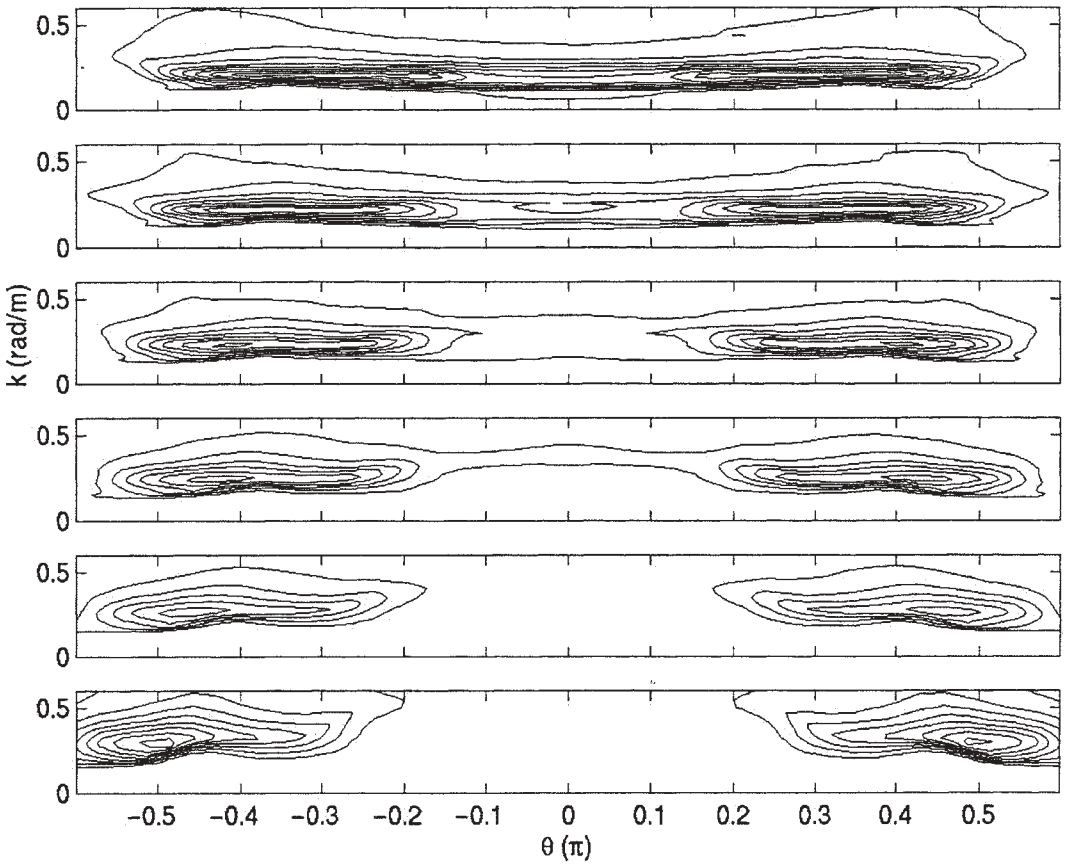

Figure 2b. Directional spectra $S(f,\theta)$ at six locations, corresponding to the locations of lidar measurements in Fig. 1. From top to bottom, fetch is 38.1, 31.5, 24.8, 18.2, 11.5, and 4.9 km. U_{10}=12 m/s.

EXTREME NORTHERLY WIND STORMS IN THE EASTERN MEDITERRANEAN BASIN AND THEIR WAVE IMPACT IN DEEP WATER IN HAIFA BAY

Yochanan Kushnir

Lamont-Doherty Earth Observatory of Columbia University
Palisades, NY 10964, USA

Michael Stiassnie, Dmitry Kunitsa, and Michael Glozman

Coastal and Marine Engineering Research Institute
Deprtment of Civil Engineering, Technion, Israel Institute of Technology
Technion, Haifa 32000, Israel

1. INTRODUCTION

As part of the planning of an expansion of Haifa Harbor, concern has been raised regarding the possibility of rare, but not uncommon, northerly windstorm (hereafter NWS) events. Because the bay does not offer protection from winds and waves arriving from the northerly sector (see Figure 1), human intervention in the form of appropriately engineered breakwaters needs to be taken. Such protection is obviously costly and needs to be carefully considered using reliable design wave statistics. In recent years fully spectral, instrumental wave observations were implemented in Haifa Bay. These can be augmented with reliable numerical wave models that allow the extrapolation of the measurements from the buoy site to the harbor. However the length of the observed wave record is relatively short (6 years) and its statistics need to be supported by other sources to assure correct planning of the harbor. The present study is meant to address this particular concern by building on a much longer record (41-years) of synoptic meteorological data. As explained below, these data are analyzed in two stages to first assess the synoptic conditions that could develop in an extreme NWS and then using the corresponding surface wind evolution to drive a numerical wave model and assess the corresponding wave statistics in the Bay.

2. DATA AND METHODOLOGY

2.1 Wind data

Almost all NWS observed in Haifa Bay occur during winter, which is the stormiest season of the year in the Eastern Mediterranean (EM) region. To determine the distribution of NWS events we use data from the first version of the NCEP/NCAR Climate Data Assimilation System (CDAS-1, Kalnay et al., 1996). The CDAS-1 dataset is based on synoptic meteorological observations (both surface and upper air), which were assimilated into a state-of-the art numerical atmospheric model to produce a spatially uniform representation of both observed and derived variable (those calculated by the model as constrained by the observations) at 6-hour time interval.

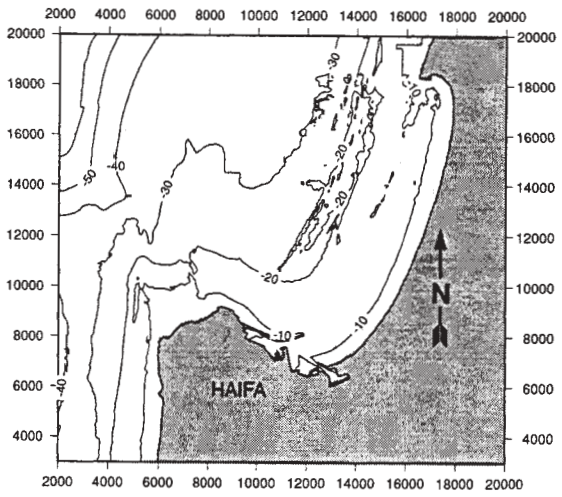

Figure 1: A map of Haifa Bay with bathymetry drawn every 10 m. Vertical and horizontal axes are scaled in meters.

One of the derived variables is a vector representing the wind 10-m above the surface. It is presented on a Gaussian grid with a resolution of 1.875° longitude and approximately 2° latitude. In order to identify all the historical NWS events data at the following 4 grid points are examined:

1. 33.750°E, 33.333°N
2. 35.625°E, 33.333°N
3. 33.750°N, 35.238°N
4. 35.625°E, 35.238°N

These points define a box lying parallel to the coast of Lebanon and Syria, northwest of Haifa Bay (see Figure 3), in the NWS occurrence region. We extracted daily averages of u10 and v10 (west-east and south-north wind components of the 10-m wind vector,

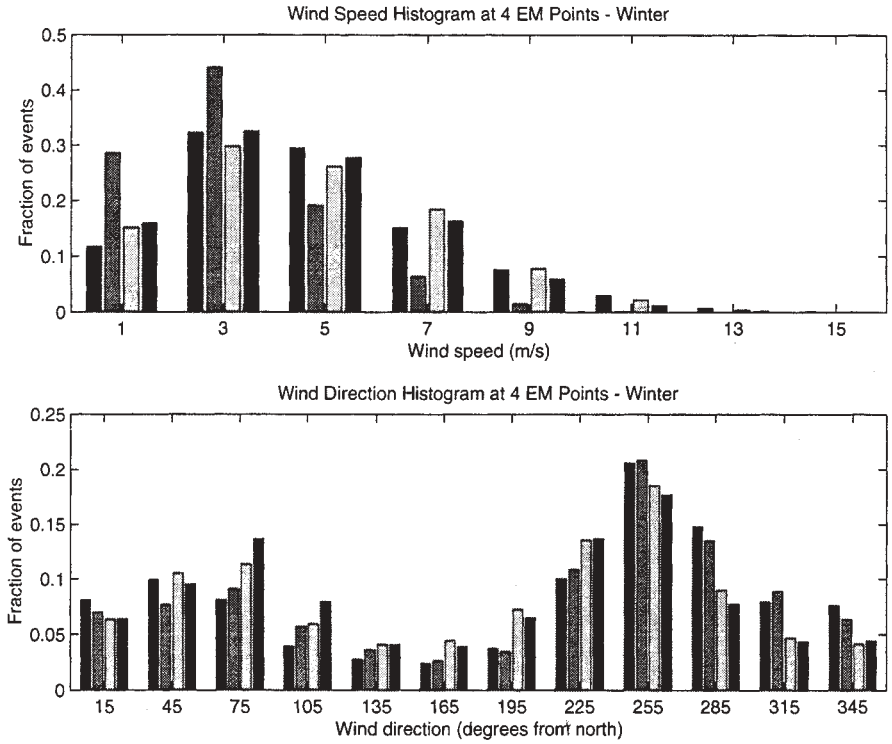

Figure 2: Histogram of CDAS-1 wintertime 10-m surface winds (all directions, 1958-1998) found at the four EM grid points listed in the text above. Top panel is for windspeed in m/s (bin width is 2 m/s centered a 1, 3, 5 etc.) and bottom panel is for wind direction (bin width is 30° centered at 15, 45, 75 etc.). The 4 bars in each bin correspond to points 1-4 in that order, from left to right. Point 2 is second from left.

respectively) at these grid points from the CDAS-1 dataset, for the winter season (defined here as interval between the 1st of November of one year and the 30th of April of the following year). A histogram of daily averaged wind speed and direction at the four grid points is shown in Figure 2. The histograms depict a homogeneous statistics of speeds and direction at grid point 1, 3, and 4. Grid point 2 displays noticeably weaker winds than the other points and we therefore exclude it from the subsequent extreme-value analysis (see below). We attempted to validate the CDAS-1 10-m wind data against actual wind observations in the Haifa Port station. The agreement was reasonable considering the fact that the Port station is not ideally exposed to open sea condition and is affected by the steep topography around the Bay. However, the actual wind data validation (and calibration) was done using the numerical wave model as described below.

2.2. Wave hindcast procedure

An accurate determination of the sea-state at a given point depends on the history of the surface wind field in a relatively large geographical region because both locally formed waves and swell are important. To achieve a depiction of the growth and decay of a NWS in Haifa Bay we forced a third-generation wave model (WAM) of the entire EM basin with the 10-m wind data from CDAS-1. The integration was started from rest (cold start) 3 days prior to the day of maximum windspeed and was forced with the 10-m winds at 6-hour intervals for 7 consecutive days. For the purpose of integrating the model the 10-m wind vectors were linearly interpolated to a high resolution 1/4° grid for the region bounded by the longitudes of 15°E and 36°E, and the latitudes of 30°N and 38.5°N (Figure 3). The hindcast technique is similar to that described in Stiassnie and Kunitsa, (1998 a, b). A complete description of the model and its integration methodology can be found in Kunitsa (1997).

To test the hindcast methodology we integrated the model with observed winds for two NWS events that occurred in the Februarys of 1959 and 1997. The first event (centered on 24 February 1959) is the second largest NWS event in the 41-year wind record. The second event (centered on 4 February 1997) is the 12th largest overall and the second largest in the recent period when instrumental wave data from Haifa and Ashdod are available (Ashdod is a second port city on the coast of Israel, south of Haifa, see Figure 3). A comparison between the hindcast and the observations

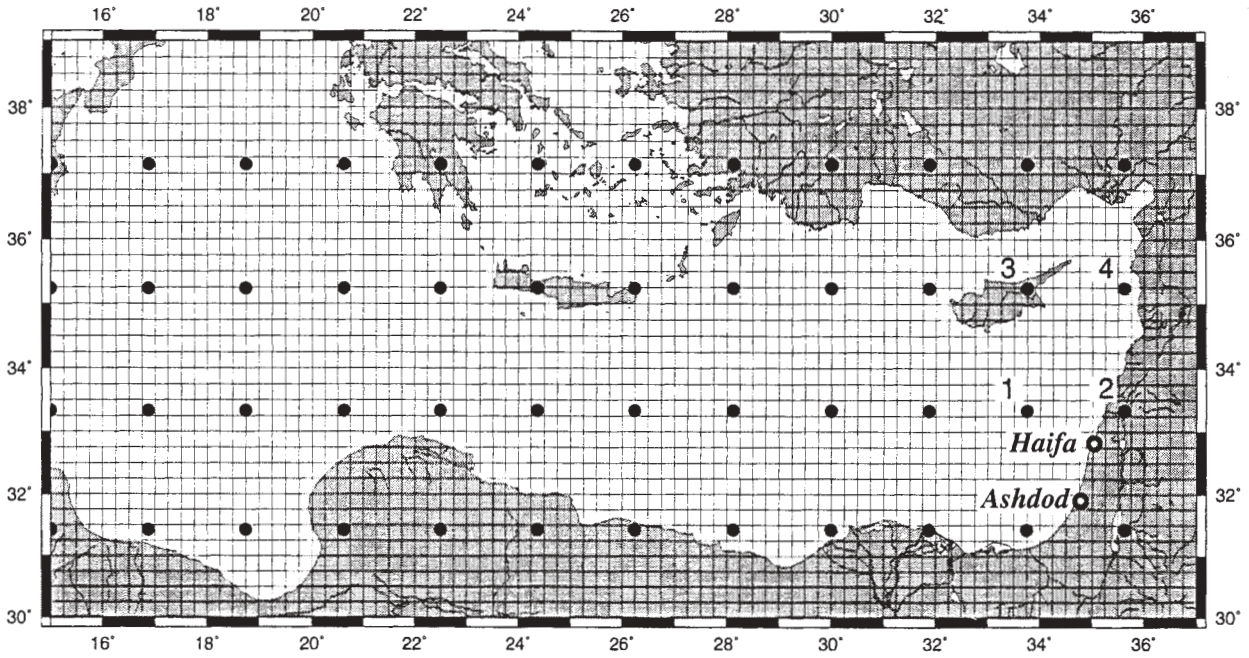

Figure 3: A map of the wave model domain. The model grid is presentedby the verticaland horizontalmesh. The black dots are CDAS-1 10-m wind grid points. The four, numbered grid points north of Haifa are the ones used to determine the storm statistics relevant for Haifa. Open circles mark the ports of Haifa and Ashdod.

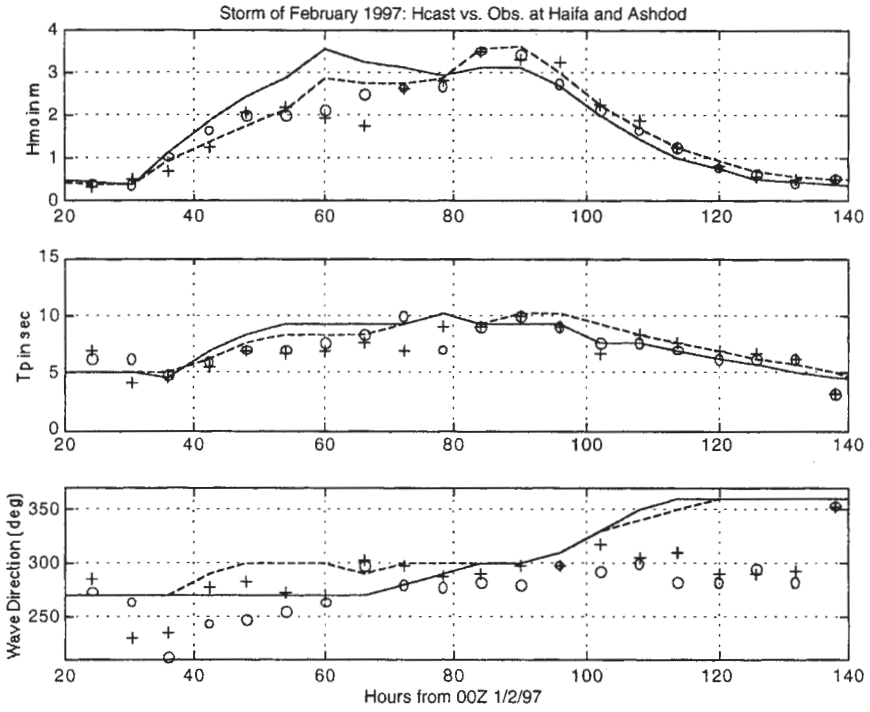

Figure 4: Evolution of the simulated wave field at a deep-water grid point near Haifa (solid line) and Ashdod (dashed lines) during the NWS of February 1997. The WAM was forced with a 6-hourly history of the 10-m wind from CDAS-1, uniformly augmented by a factor of 1.25. The 3 panels (top to bottom) are for significant wave height (Hmo), wave period (Tp), and wave direction, respectively. Instrumental observations are presented by 'o' (Haifa) and '+' (Ashdod). The time axis is in hours measured from 00Z, 1 February 1997 (the beginning of the hindcast run).

at Haifa and Ashdod indicated a need for calibration, as the hindcasted waves were consistently lower than the observed. From scaling arguments (wave height relationship to the square of the windspeed) we concluded that a simple calibration could be achieved by linearly enhancing the CDAS-1 10-m wind by a factor of 1.25. The results from the integration with the calibrated wind of the 1997 NWS event are shown in Figures. 4. They indicate that the simple calibration is excellent for period simulation. The wave heights are overestimate early is the storm evolution but reasonably simulated in the later stages. The simulated wave direction veer too far to the north during the storm decay phase. The event of 1959 (not shown) could only be verified at Ashdod where visual wave observations existed at that time. It also confirms that the simple calibration is equally satisfactory.

2.3 The case study approach

With the observed 10-m wind data, it is possible to force a numerical wave model for the entire CDAS-1 record, and hindcast the conditions during all the 41 winters. However, this would have been a considerable undertaking in time and resources. We therefore adopted a different approach that we shall refer to as the "case-study approach": A statistical extreme-value analysis was performed to project from the wind data the largest expected storm in a 100-year period. The ratio between the projected 100-year maximum and a real historical storm (such as the February 1997 one) was then calculated, and the entire 7-day wind record of that storm was enhanced by that ratio. The WAM was then integrated with the enhanced wind field to determine the waves corresponding to the 100-year storm. This case study approach forms the basis for our historical assessment of the harbor "design wave". Comparing the calculated wave condition with analysis based on the short instrumental wave record forms the final confirmation of the design wave information.

3. SYNOPTIC EVOLUTION OF EM NWS

The case study approach to calculating the design wave would work if all NWS events had a roughly similar synoptic evolution. If different NWS events follow different evolution cycles, their corresponding wave fields could look quite different, due to the non-local dynamics of ocean waves.

To study the evolution of NWS in the EM basin we first identified the largest annual storms, winter-by-winter from 1958 to 1998. The criterion for selecting these events was based on the magnitude and direction of the daily, vector-averaged wind at the points 1, 3, and 4 defined above in Section 2.1. Only winds blowing from the compass sector 310° - 10° were selected. Once these storms were identified we plotted the daily averaged maps of the sea level pressure filed provided in the CDAS-1 dataset, from 3 days before the day of maximum windspeed to 3 days after that. An examination of the 6 storms with average daily windspeed larger than 10 m/s confirmed that the NWS evolution is quite similar in all of these cases. We also examined several weaker NWS events (e.g., the one shown above in Figure 4, when the average speed at the 3 grid points was only 9.1 m/s) and were satisfied with the general similarity of all these events.

The evolution of a typical EM NWS event can be summarized by the 6-panel figure below (Figure 5), which shows the day-by-day composite evolution of the 6 largest storms in the record. The figure was calculated by averaging together day –3 to day +2 of each storm with respect to the day of maximum windspeed.

A NWS event appears to begin (day -3) with a movement of a low-pressure center into Russia with a trough into Turkey and the EM. At the same time the southern part of the EM is under the influence of a weak "Red Sea trough" and the entire western half of the plotted domain is under the influence of a strong high-pressure center. As the northern low-pressure center moves east (days -2 and -1) the trough over the northeastern Mediterranean deepens. This generally results in the intensification of winds from a westerly direction south of Cyprus. The early phase of the NWS thus tends to force waves from a westerly direction (see discussion of wave hindcast experiments below). The development of strong northerly winds north of Haifa occurs when the trough moves into Syria (day 0) and a secondary low-pressure center develops there. These conditions last for another day (day 1) as the trough continues to move east and begins to weaken. This is the time when waves reach their maximum heights and begin to veer northward (see below). On day 2 the storm has weakened considerably and moved out of the area. As we shall see below the concurrent waves continue to veer northward but their height drops quickly as the storm diminishes. The typical NWS event thus appears to be short lived. A rapid intensification of winds is followed by rapid weakening and actual storm conditions last for only 3 days or so.

4. EXTREME-VALUE ANALYSIS

To extrapolate the 41-year storm record and obtain the windspeed value corresponding to a hypothetical 100-year storm, we apply a well-tested extreme-value analysis attributed to Weibull (1939). The Weibull distribution is suitable for wind statistics, in particular when the analysis involves the use of a threshold value (see e.g., Leadbetter et al., 1983). The decision to use

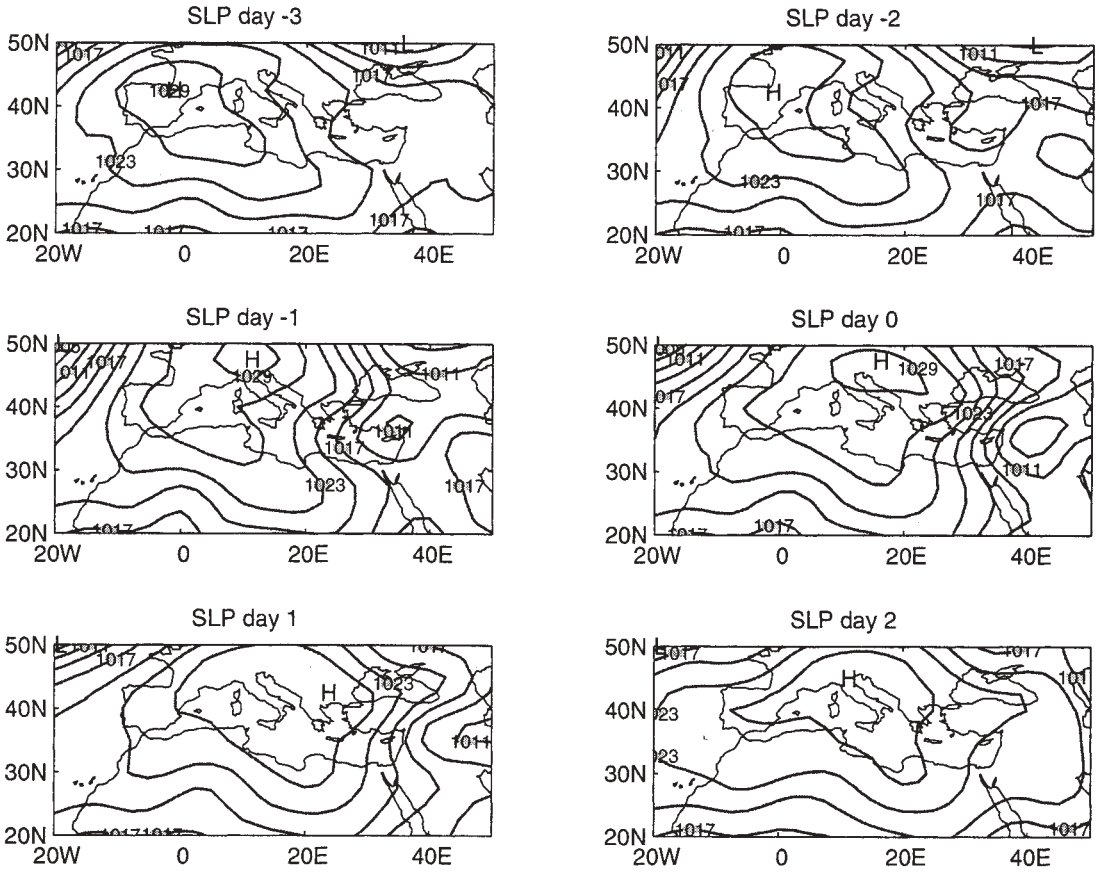

Figure 5: The composite NWS event based on 6 largest storms between 1958 and 1998. A sequence of daily sea level pressure maps is shown. The composite starts 3 days prior to the day of maximum winds in the gridbox north of Haifa Bay and ends 2 days after. Isobars are in mb. with an interval of 3.

the Weibull distribution was based on the superior fit between this distribution function and the data. Other extreme value functions such as the exponential and the Gumbel distribution functions (see Leadbetter et al., 1983) are visibly inferior (not shown). In Figure 6 we plot the annual maximum windspeed data on a diagram with an abscissa scaled according to the cumulative Weibull distribution. Clearly, the fit is extremely good in the strong windspeed end of the diagram. It points at the interesting fact that an event with a probability of occurrence of about 0.01 (a 100 year event) has actually been observed. A check of the list of the largest annual NWS events shows that the largest storm associated with a daily mean windspeed in the gridbox north of Haifa Bay of 12.9 m/s occurred on 11 January 1998. The strength of this storm is just 0.1 m/s short of the 100-year return value based on the parameters of the Weibull fit to our data. The Weibull fit in Fig. 6 shows no indication for the existence of two (or more) different sources of NWS distributions. If this was so, the data would deviate from a single theoretical line in a significant way. This is crucial for the validity of our attempt to use the case study approach.

5. THE 100-YEAR STORM

5.1 Case study with scaled up windspeeds

The Weibull function fit indication that the strongest wind expected in a 100-year record is 13 m/s allows us to calculate a wave hindcast for such event by scaling up accordingly the winds observed during any of the annual storms in the observed record. Application of this methodology to, for example, the storm of February 1997 implies that in addition to the calibration factor of 1.25, the 6-hourly wind data of this storm should be multiplied by a factor of 13/9 (the ratio between the 100-year windspeed and the daily averaged windspeed on 4 February 1997). The maximum wave height (Hmo) in Haifa Bay calculated by WAM is 7.39 m arriving from a compass direction of 280° with a peak period of 13.5 s. An examination of the wave field evolution (which follows with appropriate scaling the solid line in the top panel of Figure 4) indicates that the maximum wave height occurs about one day before maximum northerly windspeed are observed in

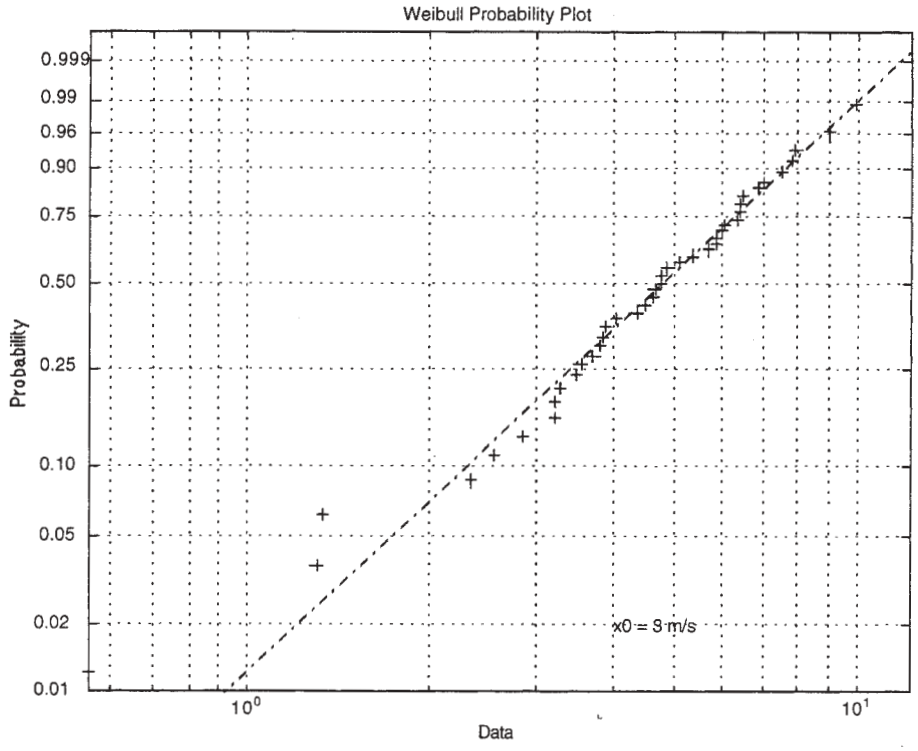

Figure 6: A scatter plot of the maximum, annual, northerly windspeed represented as the excess above a threshold value of 3 m/s, using scaling corresponding to the Weibull CDF. The ordinate is the cumulative probability and the abscissa is the wind speed value above the threshold in m/s. The dashed line is a regression line fitted to the upper and lower quartiles of the data. The slope of the regression line and its zero crossing along the ordinate determine the parameters of the Weibull CDF. The abscissa crossing at a probability value of 0.99 determines the 100-year return value above the threshold. The diagram was produced using the MATLAB Statistics Toolbox (Jones, 1996).

the gridbox north of Haifa Bay. At that stage the sea level pressure field resembles the pattern of day –1 in Figure 5, implying that these large waves result from the strong westerly winds blowing south of Cyprus and the large fetch they display. Notably however, the WAM simulation over estimates the wind speed in this phase in comparison to the observations (shown by '+' in Figure 4). When the northerly wind field reaches a maximum on day 0, the wave heights are lower at an Hmo of about 6 m from a direction of 300°. The wave heights decline steeply less than a day after that. Similar results are obtained by scaling up other large NWS events.

5.2 The storm of 1998

Because the 11 January 1998 NWS has been almost as strong as the estimated 100-year event, it is interesting to compare its observed and numerically calculated wave history with the enhanced 1997 storm described above. The evolution of wave properties between the 8th and the 14th of January 1998 is shown in Figure 7. Application of the linear calibration factor of 1.25 to the CDAS-1 10-m winds results in a hindcast which is somewhat stronger than the observed wave height record, particularly near Haifa, while using the winds as is, results in an underestimate (not shown). Clearly the use of a simple linear adjustment has its disadvantages. However, both model and observations suggest that the waves in this storm are far lower than in the upscaled hindcast of the February 1997 storm. The explanation of that difference is the lack of a westerly wind phase in advance of the 1998 storm. An examination of the synoptic conditions during this event displays a very strong high pressure area over Italy, and a deep Red Sea trough dominating the EM causing strong easterlies over the study area in advance of the NWS. The trough from Europe did not penetrate far enough into the EM region south of Turkey and instead deepened rapidly over Jordan and southern Syria replacing the easterlies with a strong northerly flow.

This evolution explains the rapid rise in wave heights from around 1 m on the 10th of January 1998 to about 3.7 m (observed) and 4.5 m (simulated) by the end of the 11th. Both the rapidity of the trough deepening and absence of westerly swell contributed to the low wave heights. Because most of the observed storms do

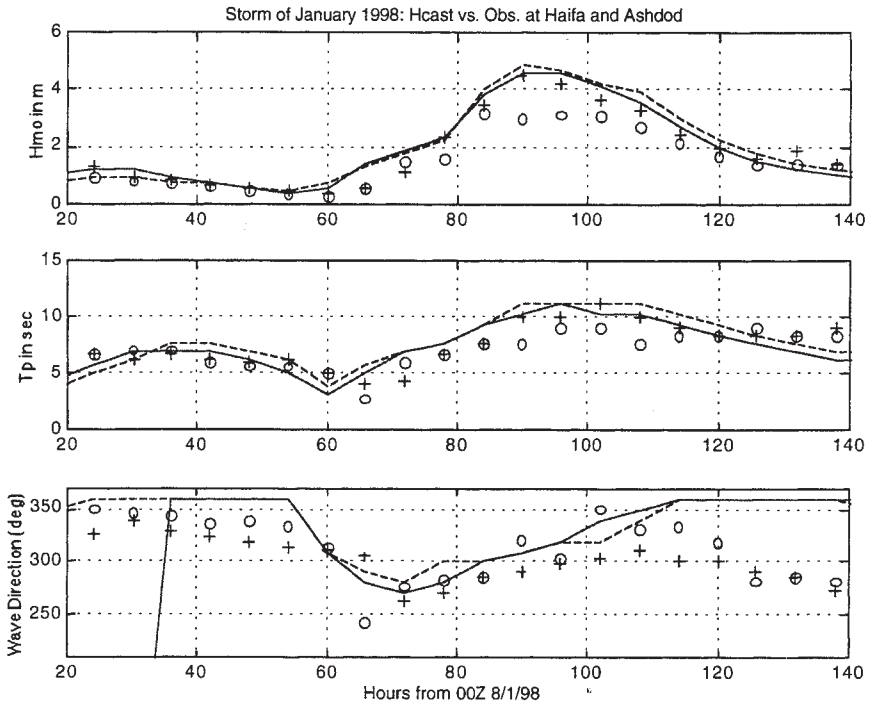

Figure 7: As in Figure 4 but for the NWS event centered on 11 January 1998.

exhibit a westerly wind phase prior to the development of strong northerly winds off the shores of Lebanon and northern Israel, we recommended using the hindcast of the February 1997 storm, enhanced to the level of the 100-year event for the harbor expansion design.

6. SUMMARY

In order to arrive at an estimate of maximum wave heights expected from the north at Haifa Bay and enhance analysis based on a short record of instrumental wave data, we applied a combination of extreme-value analysis and numerical wave hindcasting to a long record of synoptic meteorological observations. The method was designed to provide a picture of the wave field evolution during a hypothetical, extreme northerly wind storm event in the eastern Mediterranean close to the northern coast of Israel but such that is based on realistic situations that occurred in the past.

A 41-year record of 6-hourly analyses of the surface wind field at the 10-m level was used as a data source. The wind data were first analyzed to search for the maximum northerly storm of every winter in the record. Several integrations were then conducted, using the wind data to hindcast the wave history during these storms. The integrations indicated the need for calibration of the wind data against observations and a simple adjustment was adopted for further study that consisted of uniformly augmenting the windspeeds by a factor of 1.25.

The typical evolution of the wave field at Haifa Bay during northerly storms was studied using simulations with calibrated winds. It was found that northerly windstorms are generally short in duration lasting only two to three days. They are often preceded by a strong westerly wind phase that may cause high seas from the west, a direction from which Haifa Harbor is well protected. As the wave field veers northward it also loses energy and the wave height drop rapidly.

The annual maximum northerly-windspeed data were used to project the 100-year event using a Weibull distribution function. The results suggest that it is very rare that storms reach speeds higher than values found in the data record. Wind data corresponding to several historical storms were augmented to the level of the 100-year storm and wave heights were calculated using the numerical wave model. The analysis indicates that under such extreme conditions and during the westerly wind phase waves could reach a significant height of around 7.5 m. When the wave direction turns northerly the significant wave height drops to about 3.5 m. This projection was found consistent with the shorter record of instrumental observations.

The numerical hindcast experiments with winds taken from similar bus non-identical storm events shows that

small differences in storm evolution can cause significant differences in wave statistics at some arbitrary target region. These differences can be attributed to both real differences in synoptic wind conditions and the quality of the wind data. Therefore some degree of subjectivity needs to be taken when applying this methodology for similar situations elswhere.

REFERENCES

Glozman, M. and N. Drimer, 1998: Haifa port development stage B.: Calculation of near port wave climate. CAMERI Report P.N. 504/98, 24pp.

Jones, B., 1996: *Statistics Tollbox for Use with MATLAB, Users Guide.* The MathWorks, Inc., Natick MA.

Kalnay, E., M. Kanamitsu, R. Kistler, W. Collins, D. Deaven, L. Gandin, M. Iredell, S. Saha, G. White, et al., 1996: The Ncep/NCAR 40-Year Reanalysis Project. *Bull. Amer. Meteor. Soc.*, 77, 437-471.

Kunitsa, D., 1997: Application of an advanced forecasting Model to the study of the wave climate at the Israeli coast. MSc. Thesis, Technion, Israel Institute of Technology, Haifa, Israel, 97pp.

Leadbetter, M. R., G. Lindgren and H. Rootzén, 1983: *Extremes and Related Properties of Random Sequences and Processes.* Springer-Verlag, New York, 336 pp.

Stiassnie, M. and D. Kunitsa, 1998a: Wave hindcast study of three characteristic storms in Ashdod area. CAMERI Report P.N. 481/98, 21pp.

Stiassnie, M. and D. Kunitsa, 1998b: Wave hindcast study for the storm of 22-25.2.1959. CAMERI Report P.N. 486/98, 11pp.

Weibull, W., 1939: *A Statistical Theory of the Strength of Materials.* Ingeniors Vetenskaps Akademiens Handlingar, Royal Swedish Institute for Engineering Research. Stockholm, Sweeden, No. 153.

IMPACT OF A SATURATION-DEPENDENT DISSIPATION SOURCE TERM ON THE SKILL OF AN OPERATIONAL WIND-WAVE MODEL

Jose Henrique G. M. Alves[1], Diana J. M. Greenslade[2] and Michael L. Banner[1]

[1] School of Mathematics, University of New South Wales, 2052 Sydney, Australia
[2] Bureau of Meteorology Research Centre, Melbourne, AUstralia

1 INTRODUCTION

Compared to other coastal nations, Australia has one of the longest and most diverse coastlines, containing a wide range of climatic and oceanographic regions. These areas support nearly 90% of Australia's population. A significant part of this coastal population is directly or indirectly involved in activities related to the ocean, which include fishing, offshore petroleum and tourism. Commercial and industrial activities related to the marine environment generate more than AUD$30 billion per year. Sea-state forecasting plays an important role in providing strategic information for the success and safety of many of these activities.

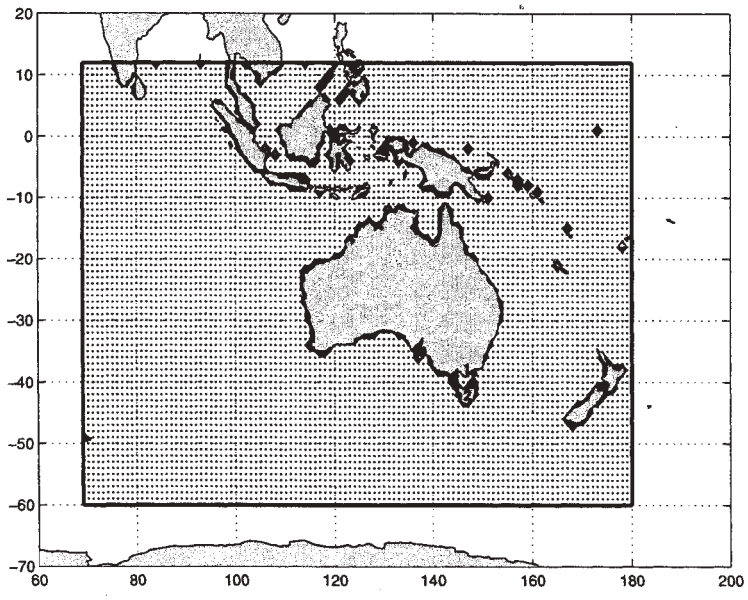

Figure 1: Regional implementation of the AUSWAM model. The numerical grid is shown as an array of black dots at the model resolution of 1 °. Ocean boundaries and coastlines of the numerical grid are indicated by thick continuous lines. Location of validation sites around the Australian coast are indicated by circles and labelled according to the definitions listed in Table 2.

Third-generation spectral wind-wave models are presently the basis of most operational sea-state forecasting systems worldwide. In the Australian Bureau of Meteorology (BoM), sea-state forecasts are generated by the AUSWAM model, a version of the WAM Cycle 4 model (Günther et al., 1992) with the following modifications: (i) a third-order numerical propagation scheme and (ii) source terms from the WAM Cycle 3 model. These two modifications of the standard WAM Cycle 4 release were based on numerical experiments reported in Bender and Leslie (1994) and Bender (1996), as discussed below.

In the absence of depth-induced effects and currents, the governing equation of spectral wave models reduces to the energy balance equation, as follows:

$$\left\{\frac{\partial}{\partial t}+\mathbf{c}_g\cdot\frac{\partial}{\partial \mathbf{x}}\right\}E(f,\theta)=S_{in}+S_{nl}+S_{ds}, \quad (1)$$

where $E(f,\theta)$ is the two-dimensional frequency spectrum, f is wave frequency, θ is wave direction, t is time, $\mathbf{c}_g$ is the wave group velocity, $\mathbf{x}$ is a position vector and the terms on the right-hand-side are source terms accounting for wind input (S_{in}), resonant nonlinear wave-wave interactions (S_{nl}) and dissipation (S_{ds}).

Extensive analytical and observational efforts have led to the development of acceptable parameterizations of S_{in}. In addition, third-generation wave models use robust forms of S_{nl} based on the theory of nonlinear interactions in a homogeneous wave field (Hasselmann, 1962; Zakharov, 1968). Due to the extreme difficulties involved in observing wave breaking and other dissipative processes in the field, dissipation is the least understood physical process driving wave development. Consequently, present models used in operational applications compute spectral dissipation rates through parametric functions developed mostly for tuning purposes.

Based on a conceptual framework for the onset of deep-water wave breaking due to the nonlinear modulation of wave groups, Alves and Banner (2000*b*) propose a new dissipation function that depends nonlinearly on the local azimuthally-integrated saturation spectrum $B = F(k)k^4$, where $F(k)$ is the azimuthally-integrated wavenumber spectrum. This new form of S_{ds} is successfully validated through numerical experiments of fetch-limited wind-wave evolution made with a research model featuring an exact solution for S_{nl} (Alves and Banner, 2000*b*) and an operational wind-wave model (Alves and Banner, 2000*a*).

The present study is a contribution towards testing the Alves-Banner dissipation source term [hereafter represented by the symbol S_{ds}^{ab}] using more realistic two-dimensional wind forcing conditions. For this purpose, S_{ds}^{ab} was implemented into AUSWAM. Performances of model hindcasts using several configurations of the new dissipation function were compared to the operational AUSWAM model setup. Model results were validated against *in situ* observations from two deep water sites off the Australian coast.

This manuscript is structured as follows. Section 2 provides a brief description of the implementation of AUSWAM presently used by the Australian Bureau of Meteorology. Buoy data and validation strategies are described in Section 3. Results are presented in Section 4, which is followed by concluding remarks and a list of references.

2 MODEL DESCRIPTION

The sea-state forecasting system at the Australian Bureau of Meteorology consists of three implementations of the AUSWAM model: (i) a global implementation at 3° spatial resolution; (ii) a regional model with 1° resolution, nested to the global model; and (iii) a mesoscale model running at 0.25° resolution, nested to the regional model. The regional AUSWAM implementation (Figure 1) covers an area from 60°S to 12°N and from 69°E to 180°E. The mesoscale model covers oceanic areas adjacent to the southeast of Australia. Regional and global operational implementations of AUSWAM also include a system to assimilate significant save height H_s observations from the European Remote-Sensing Satellite ERS-2 (Greenslade, 1999).

The AUSWAM model is a modified version of the WAM model. WAM is a third-generation spectral wind-wave model that describes the evolution of the two-dimensional frequency spectrum $E(f,\theta)$ with respect to frequency f and direction θ. Spectral evolution is calculated by integrating the action balance equation in its spherical coordinate form

$$\frac{\partial E}{\partial t}+\cos^{-1}\phi\frac{c_\phi\cos\phi E}{\partial\phi}+ \frac{\partial c_\lambda E}{\partial\lambda}+\frac{\partial c_\theta E}{\partial\theta}= S_{in}+S_{nl}+S_{ds}, \quad (2)$$

where $c_{\phi,\lambda,\theta}$ are components of the group velocity

AUTHOR INDEX TABLE OF CONTENTS

$\mathbf{c}_g = g/4\pi f$ in latitude ϕ, longitude λ and direction θ and S_{in}, S_{nl} and S_{ds} are the wind input, nonlinear interactions and dissipation source functions, respectively. AUSWAM uses the Direct Interaction Approximation (DIA) of S_{nl}, following Hasselmann and Hasselmann (1985), and parameterised S_{in} and S_{ds} source terms consistent with the physics used in the WAM Cycle 3 release.

The wind input source term follows the general form proposed by Snyder et al. (1981):

$$S_{in}(f,\theta) = C_{in} \quad \frac{\rho_{air}}{\rho_{water}} \omega \left(\frac{U_0}{C}\cos\theta - 1\right) E(f,\theta), \tag{3}$$

where $C_{in} = 0.25$ is a constant of proportionality, ρ specifies the density of air or water and U_0 is a scaling wind speed.

The WAM model uses a S_{in} defined in terms of the friction velocity through the relation $U_0 = 28u_*$ (Komen et al., 1984). In the original Snyder et al. (1981) form, the 5m-height wind is used ($U_0 = U_5$). In this study, model validation tests were made with two forms of S_{in} specified in terms of both U_5 and $28u_*$. In the standard AUSWAM operational implementation, whitecap dissipation is computed according to the quasilinear source term proposed by Komen et al. (1984), as follows:

$$S_{ds}^{w3}(f,\theta) = -C_{ds} \quad \left(\frac{\hat{\alpha}}{\hat{\alpha}_{PM}}\right)^m \left(\frac{\omega}{\overline{\omega}}\right)^n \bar{\omega} E(f,\theta), \tag{4}$$

where $\hat{\alpha} = E_{tot}\overline{k}^2$ is an integral steepness parameter and $\overline{k}$ and $\overline{\omega}$ are the mean wavenumber and radian frequency, respectively. In AUSWAM, the value of the dissipation coefficient $C_{ds} = 6.74 \times 10^{-5}$ was set according to Bender and Leslie (1994), while Komen et al. (1984) suggest a somewhat lower constant $C_{ds} = 3.33 \times 10^{-5}$. Other S_{ds} parameters used in AUSWAM were unmodified relative to the standard WAM Cycle 3 release (i.e., $m = 2$ and $n = 2$).

	S_{ds}				
Run code	C_{ds}	m	n	p_∞	B_r
BOM	6.74×10^{-5}	2.0	2.0		
WM3	3.33×10^{-5}	2.65	2.0		
AB1	7.71×10^{-2}	1.3	1.0	0.0	
AB2	2.63	2.0	0.0	4.0	7.5×10^{-3}
AB3	1.91	2.0	0.0	4.0	5.8×10^{-3}
AB4	8.80×10^{-3}	1.0	1.0	4.0	5.0×10^{-3}

Table 1: Summary of run codes and dissipation parameters.

The new dissipation function S_{ds}^{ab} proposed by Alves and Banner (2000*b*) is based on the assumption that spectral dissipation rates of dominant waves are primarily determined by breaking due to the modulation of nonlinear wave groups. This effect is computed through a term that depends nonlinearly on a local measure of wave steepness, represented by the saturation spectrum $B(k,\theta) = F(k,\theta)k^4$. A general expression for S_{ds}^{ab} is given by

$$S_{ds}^{ab}(f,\theta) = -C_{ds} \quad \left(E_{tot}k_p^2\right)^m \left(\frac{k}{\overline{k}}\right)^n \left(\frac{B(k)}{B_r}\right)^{p/2} \omega E(f,\theta), \tag{5}$$

where C_{ds} is a constant setting overall dissipation levels, E_{tot} is the total energy, k_p and $\overline{k}$ are the peak and mean wavenumbers, $B(k) = k^4F(k)$ is the azimuthally integrated spectral saturation parameter, B_r is a reference saturation level, m and n are constant exponents and p, the exponent of the term representing dissipation due to nonlinear group modulation, is given by

$$p = \frac{p_\infty}{2} + \tag{6}$$

$$\frac{p_\infty}{2} \quad \tanh\left\{10\left(\sqrt{\frac{B(k)}{B_r}}-1\right)\right\}.$$

Equation (6) prescribes p as a function that fluctuates between zero and p_∞ whenever the local integrated saturation level $B(k)$ is below or above the threshold saturation value B_r, respectively. The spectral dissipation rates will, therefore, be dominated by the term dependent on the local saturation level whenever $B(k) > B_r$. For values of $B(k) < B_r$, $p \to 0$ and the term $(B(k)/B_r)^{p/2}$ asymptotes to unity. Dissipation rates will then be determined by the remaining terms $(E_{tot}k_p^2)^m$ and $(k/\overline{k})^n$, describing background energy losses.

3 VALIDATION STRATEGY

This study presents a comparison of hindcasts generated by the AUSWAM model using six alternative configurations of S_{ds}, corresponding to the standard AUSWAM dissipation term, an optimised variation of the WAM Cycle 3 term and four variations of the Alves-Banner saturation-dependent form S_{ds}^{ab}. Experiments were labeled with the prefixes BOM, WM3 and AB, respectively. Dissipation parameters used in the six alternative hindcast experiments are summarised in Table 1.

Parameters of S_{ds}^{ab} listed in Table 1 were determined through fetch-limited experiments made with AUSWAM, as described in Alves and Banner (2000*a*). In these experiments, S_{ds}^{ab} was manually tuned to produce model results matching the empirical fetch-limited evolution curves of Kahma and Calkoen (1992) and the fully-developed limits proposed by Alves et al. (2000).

Table 1 shows that the configuration of S_{ds}^{w3} used in the AUSWAM model (run BOM) adopts a constant $C_{ds} = 6.74 \times 10^{-5}$ that is significantly higher than the original constant value $C_{ds} = 3.33 \times 10^{-5}$ from WAM Cycle 3 release (run WM3). This change in C_{ds} was justified on the basis of a wave hindcast study performed by Bender and Leslie (1994) over a one-month period that did not include a validation of the atmospheric model winds used to force the wave model. The specification of this higher dissipation rate level may have resulted from the need to compensate for overpredictions in wind fields generated by the LAPS model.

The configuration of S_{ds}^{w3} used in run WM3 is a slight variation of the original WAM Cycle 3 setup in which the exponent m is increased from 2 to 2.65. This value of m was determined by Monbaliu and Hasselmann (1994) through an automatic model optimisation method. Other dissipation parameters correspond to the original WAM Cycle 3 configuration of S_{ds}^{w3} (i.e., $m = 2$ and $n = 2$).

Label	Code	Location	Hull type	Payload	Position Lat	Position Long	Depth (m)	Wind height	Sample rate (h)
1	55039	Bass Strait	EMI Sensor	Esso	-38.60	148.19	75	44.0	1/6
2	55026	Strahan	Waverider	BoM	-42.08	145.01	100	19.5	1/2

Table 2: Characteristics and locations of wind and wave measurement sites used for model validation. Numbers in the first column correspond to labels in Figure 1. Codes are the World Meteorological Organization (WMO) index numbers.

Wave hindcasts analysed in the present study were generated using wind fields from a 62 day period between March 20 00Z and May 20 00Z 1998. Winds were obtained from analysed data produced by the regional atmospheric model LAPS (Puri et al., 1998) used at the BoM. The performances of the alternative S_{ds} configurations of Table 1 were compared and ranked according to the values of four statistical parameters [bias, root mean square (rms) error, scatter index and correlation coefficient] calculated in relation to H_s and T_p data at the two validation sites (Bass Strait and Strahan) shown in Figure 1. The statistical parameters are defined as follows:

(i) Bias

$$bias = \frac{\sum_{i=1}^{N} M_i - O_i}{N}; \qquad (7)$$

(ii) Root-mean-square error

$$\epsilon_{rms} = \sqrt{\frac{\sum_{i=1}^{N}(M_i - O_i)^2}{N}}; \qquad (8)$$

(iii) Scatter index

$$SI = \frac{\sigma_M}{\overline{O}}; \qquad (9)$$

(iv) Correlation coefficient

$$r = \frac{\sum_{i=1}^{N}(O_i - \overline{O})(M_i - \overline{M})/N}{\sqrt{\sum_{i=1}^{N}(O_i - \overline{O})^2}\sqrt{\sum_{i=1}^{N}(M_i - \overline{M})^2}} \qquad (10)$$

where O_i and M_i represent observed and modelled values, respectively, of either wind speed U_{10}, wind direction θ_U, significant wave height H_s or spectral peak wave period T_p; σ_M is the standard deviation of modelled values; N is the number of observations; and over-bars denote ensemble averages. All statistics were determined by assuming that observations provided the best estimate of the true value of each diagnostic variable.

Model hindcasts were validated against H_s and T_p data from the two sites shown in Figure 1. Table 2 provides a list of their relevant characteristics. Measurements in Bass Strait were made with an electromagnetic induction sensor attached to the leg of an oil platform. In Strahan, measurements were made with a Datawell Waverider buoy. Observations were assumed to be made in deep water. Data from Bass Strait and Strahan, sampled at 10 and 30 min respectively, were reduced to one-hourly intervals by simple averaging. Following the approach of Cardone et al. (1994), the resulting hourly time series were smoothed by averaging three successive observations with weights 1/4, 1/2 and 1/4, to reduce sampling variability. Smoothed hourly time series were finally sub-sampled at three-hourly intervals at times corresponding to the wave model outputs.

Measurements of wind velocity and direction were made at different anemometer heights, as indicated in Table 2. To allow the validation of the hindcast 10m-height wind fields used to force AUSWAM, available observations were converted into corresponding 10m-height winds by assuming a neutrally-stable logarithmic atmospheric boundary layer. Converted U_{10} values were derived using the relation

$$U_z = U_{10}\ln(z/z_0)/\ln(10/z_0), \qquad (11)$$

where the roughness length z_0 was determined from the Charnock relation and the drag coefficient parameterisation proposed by Wu (1982). Although in non-neutral atmospheric stability conditions the wind profile may deviate from this logarithmic profile, measurements of the air-sea temperature differences were not available. As a proper estimation of stability conditions could not be made, neutral stability was assumed.

In most cases, nodes from the regional model grid did not match exactly the location of measurement sites. Because of the relatively coarse resolution of this numerical grid (i.e., 1°) and the proximity of measurement sites to the coast, it was not possible to spatially interpolate the model output into the exact buoy locations, as this would involve nodes over land boundaries. Consequently, model validation was performed using the output from grid nodes nearest to each buoy location.

Both global and regional implementations of AUSWAM were run with the available 62-day LAPS wind-fields. Data assimilation was switched off so that the contrast between different wave model physics options could be emphasised. Initialisation occurred at day 1 the hindcast period with analysed spectra obtained from the BoM operational archives. The global model was run only once with the standard BoM model physics, corresponding to S_{in} and S_{ds} prescribed by equations (3) and (4), respectively. Wave model spectra from the global model at the borders of the regional model were stored and used as boundary conditions for the nested regional model runs. Boundary conditions were, therefore, identical in all regional simulations.

Site	U_{10}					θ_U			
	U_{10}^{obs} m/s	*bias* m/s	ϵ_{rms} m/s	*SI*	r	*bias* deg	ϵ_{rms} deg	*SI*	r
Bass Strait	6.53	0.48	2.15	0.32	0.86	127	74.80	0.38	0.69
Strahan	6.41	1.45	2.79	0.37	0.81	30.99	97.07	0.44	0.54

Table 3: Validation of wind speed U_{10} and direction θ_U at Bass Strait and Strahan during the hindcast period of March 20 to May 20 1998. Listed statistical parameters are bias, root mean square error ϵ_{rms}, scatter index SI and correlation coefficient r. Mean observed values of wind speed U_{10}^{obs} are also indicated.

The propagation time step was set to 20 minutes. Source terms were integrated every 10 minutes. The discrete representation of the two-dimensional frequency spectrum $E(f,\theta)$ consisted of 25 frequency bins logarithmically spaced from 0.0418 Hz to 0.4114 Hz, at intervals of $\Delta f/f = 0.1$, and 12 directional bins with 30° resolution. These general setting were used in both global and regional model runs.

At 1° and 3° spatial grid resolution, very few of the wave model grid points were in water depths of less than 100m. Therefore, the regional and global wave models were run with deep water physics only (i.e., bottom friction and refraction effects were switched off). Modelled wave spectra and diagnostic variables such as significant wave height H_s, mean wave direction θ_m and peak period T_p were stored in output files at 3 model-hour intervals.

The global wave model was forced with 12-hourly hindcast winds at 2.5° spatial resolution, obtained from the global atmospheric model GASP (Seaman et al., 1995) at the BoM. Winds used to force the regional wave model were obtained from the regional atmospheric model LAPS (Puri et al., 1998). Proper U_{10} values were converted from the nearest atmospheric model level via Monin-Obukhov theory with empirical stability functions given by Garrat (1992), in both cases. Furthermore, wind fields were interpolated into hourly intervals and reduced to the required spatial resolution of each model grid. Experiments were performed in a 32 vector processor NEC SX-4 supercomputer, which is largely dedicated to running operational models that produce weather and sea-state forecasts for the Australian region on a 12-hourly basis.

4 RESULTS

Validation statistics of Wind speeds generated by the LAPS model in Bass Strait and Strahan are shown in Table 3. Although the validation statistics shown in Table 3 indicate that the bulk of LAPS model wind fields is not ideal for a critical overall evaluation of wave model performance, model winds in Bass Strait and Strahan were in relatively good agreement with observations. A refined analysis comparing the performance of the saturation-dependent dissipation term S_{ds}^{ab} with the standard AUSWAM configuration using higher quality winds will be provided in a forthcoming paper.

Scatterplots of hindcast and observed H_s and T_p in Bass Strait during the 62-day period of March 20 to May 20 1998 are shown in Figures 2 and 3, respectively. A linear least squares fit through the cloud of co-located data suggests that most alternative experiments generated good hindcast significant wave heights. An exception was run WM3, which produced hindcasts with a strong bias towards overestimating most measurements of H_s. On the other hand, hindcast T_p from all model runs had a consistent trend towards underestimation of measurements greater than approximately 8s.

Table 4 lists the validation statistics corresponding to the Bass Strait hindcasts shown in Figures 2 and 3. Statistics of hindcast H_s indicate a best overall performance of runs BOM, AB1 and AB2. Hindcasts from runs AB3 and AB4 also produced good statistical scores. Run WM3, however, generated hindcast H_s with high positive bias, rms error and scatter index. Although values of bias, rms error and scatter index were comparable to those of hindcast H_s, the correlation coefficients of hindcast T_p were remarkably low (under 0.35 in all cases).

This lower correlation of hindcast T_p values in Bass Strait, which was particularly strong at larger values of this parameter (e.g., $T_p > 8$s), suggests that the ratio between the energy of swell and wind-seas is incorrect in the wave model results. This discrepancy may be associated with at least three factors: (i) the poor specification of swell properties at the external boundary of the regional model grid, (ii) the excessive dissipation of low frequency spectral components in the different specifications of S_{ds} and (iii) the coarse resolution of the regional model grid within Bass Strait. As discussed previously, the first two factors cannot be directly assessed due to the lack of observed wave spectra near the outer regional grid boundaries.

Figure 1 shows that the complex land features within Bass Strait were considerably simplified due to the coarse resolution (1°) of the regional model grid. This misrepresentation does not affect local operational sea-state forecasts, as these are based on the results of a higher resolution (0.25°) meso-scale implementation of AUSWAM covering the southeastern region of the Australian continent in more detail. This implementation, however, was not available for the experiments described in this study.

A visual examination of the available time series of regional hindcasts and observations of T_p generated with alternative forms of S_{ds} revealed that model data within Bass Strait systematically omitted wave events with peak periods typically greater than 12s, usually associated with the occurrence of weak local winds. This combination of higher T_p values with weak local winds is a well-recognised characteristic of swell events. Due to the frequent development of mid-latitude cyclones within the Southern Ocean, these swell systems may often penetrate Bass Strait through its western entrance. This passage, however, is almost completely blocked in the regional model grid, as seen in Figure 1. This numerical boundary may have, consequently, obstructed the passage of swell in the regional simulations, leading to the disagreement between model hindcasts and observations of T_p seen in Table 4 and in Figure 3.

March/May 1998			H_s				T_p			
Location	Mean obs	Run	*bias* m/s	ϵ_{rms} m/s	*SI*	*r*	*bias* sec	ϵ_{rms} sec	*SI*	*r*
Bass Strait	$\overline{H_s^{obs}} = 1.57$m	BOM	-0.16	0.49	0.29	0.86	-1.39	2.81	0.28	0.32
	$\overline{T_p^{obs}} = 8.79$s	WM3	0.37	0.65	0.34	0.85	-0.23	2.40	0.27	0.31
		AB1	-0.12	0.43	0.27	0.87	-1.28	2.58	0.26	0.33
		AB2	0.09	0.42	0.26	0.86	-1.68	2.70	0.24	0.26
		AB3	0.30	0.52	0.27	0.86	-0.97	2.38	0.25	0.25
		AB4	-0.23	0.51	0.29	0.86	-2.67	3.57	0.27	0.13
Strahan	$\overline{H_s^{obs}} = 3.44$m	BOM	-0.73	1.12	0.25	0.77	-2.62	3.67	0.20	0.36
	$\overline{T_p^{obs}} = 12.99$s	WM3	0.53	1.06	0.27	0.80	-0.58	2.30	0.17	0.41
		AB1	-0.41	0.85	0.22	0.79	-1.74	2.75	0.16	0.38
		AB2	-0.38	0.89	0.23	0.77	-3.43	4.06	0.17	0.31
		AB3	0.10	0.79	0.23	0.81	-2.50	3.33	0.17	0.33
		AB4	-1.10	1.40	0.25	0.74	-4.56	5.11	0.18	0.26

Table 4: Validation statistics from hindcasts of significant wave height H_s and peak period T_p provided by AUSWAM at sites 55039 (Bass Strait) and 55026 (Strahan) during the period of March 20 to May 20 1998. Listed statistical parameters are bias, root mean square error ϵ_{rms}, scatter index *SI* and correlation coefficient *r*.

Figures 4 and 5 show the comparisons of hindcast and observed H_s and T_p in Strahan. The difference of results from model runs using alternative S_{ds} configurations is greater than in the data from Bass Strait. Lines of least squares fit through the co-located data suggest that hindcasts of H_s from runs BOM, AB1, AB2 and AB4 systematically underestimated the observations. On the other hand, hindcast H_s produced by run WM3 overestimated the observed values. Only hindcast H_s from run AB3 were in good agreement with the observations, as indicated by their low bias. The general trends seen in the scatterplots of hindcast and observed T_p from Strahan, however, repeat those seen in data from Bass Strait: most model runs underestimated higher values of peak period. An exception were the

results from run WM3, which were in better agreement with observations.

Validation statistics shown in Table 4 indicate that the hindcasts of H_s from run AB3 had the lowest bias and rms error, and thus the best overall performance in both measurement sites. The low scatter index of this model run is, nevertheless, comparable to that of runs AB1 and AB2. These two cases also delivered a good performance in terms of bias and rms error. Runs BOM and AB4 produced significant negative bias and high rms errors. Their scatter-indices, however, were slightly improved relative to run WM3. This latter experiment generated hindcast H_s with considerable positive bias and high rms error.

Run WM3 provided the lowest values of bias in terms of hindcast T_p in both Strahan and Bass Strait. The lowest rms errors in these two locations were associated with runs WM3, AB1 and AB3, while scatter indices of these three test cases and those of runs AB2 were all remarkably low. The poor performance of run AB4 in Strahan and Bass Strait indicates that its configuration of S_{ds}^{ab} may be predicting too much dissipation at wavenumbers lower than the peak. Despite these apparent differences, all model runs correlated poorly with the trends of measured T_p, as suggested by the low values of the parameter r. This generally poor agreement with observations supports the idea that either swell systems are not being properly specified at the AUSWAM model boundaries or, alternatively, that most forms of S_{ds} used in this study predicted dissipation rates that were too high for low wavenumbers. These issues are currently being investigated.

5 CONCLUDING REMARKS

The present study investigates the impact of a new formulation for the dissipation source term S_{ds} on the skill of AUSWAM, the wind-wave model used by the Australian Bureau of Meteorology to produce official sea-state forecasts. The new form of S_{ds} features a nonlinear dependence of spectral dissipation rates on the azimuthally integrated saturation parameter $B(k) = k^4 F(k)$. Model hindcasts of significant wave height H_s and peak period T_p are validated at two measurement sites off the Australian coast. Hindcasts are generated with (i) the standard AUSWAM dissipation term, (ii) an optimised variation of the WAM Cycle 3 term and (iii) four variations of the newly-proposed saturation-dependent form of S_{ds}.

The validation of alternative AUSWAM model hindcasts of H_s and T_p in two validation sites (Strahan and Bass Strait) may be summarised as follows:

- the configuration of S_{ds} used in the standard AUSWAM model setup (run BOM), consisting of the WAM Cycle 3 dissipation function S_{ds}^{w3} with an increased value of the constant C_{ds}, produced hindcasts of H_s and T_p that generally underestimated measured data;

- the alternative configuration of S_{ds}^{w3} used in run WM3 provided the best hindcasts of T_p. This good relative performance is probably related to its stronger nonlinear dependence on the integrated steepness parameter $(E_{tot}\overline{k}^2)^m$. In association with a lower value of C_{ds} relative to the standard AUSWAM configuration, this may have reduced significantly the dissipation levels of old wind seas, leading to a more unconstrained growth of swell components of the wave spectrum. This benefit, however, had as a tradeoff the systematic overestimation of hindcast H_s at both validation sites;

- the aim of run AB1 was to examine the effect of redefining the integral steepness parameter of S_{ds}^{w3} as a function of the peak wavenumber k_p (i.e., the form $E_{tot}\overline{k}^2$ used in S_{ds}^{w3} was replaced by $E_{tot}k_p^2$), as discussed in Alves and Banner (2000*a*). This change may explain why this experiment provided improved hindcast H_s when compared to results of runs BOM and WM3. Hindcasts of T_p from run AB1 were also consistent with observations;

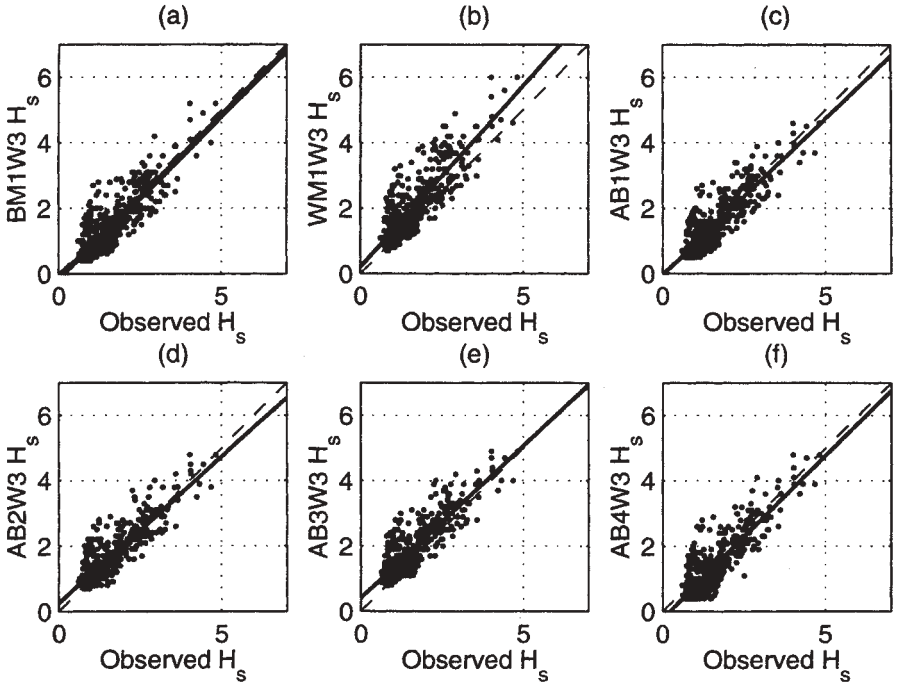

Figure 2: Scatterplots of hindcast and observed significant wave heights H_s in Bass Strait during March 20 to May 20 1998. Model runs are indicated in the vertical axis. Thin dashed lines indicate a perfect 1-to-1 correlation and continuous lines indicate the linear least squares fit through the cloud of co-located data.

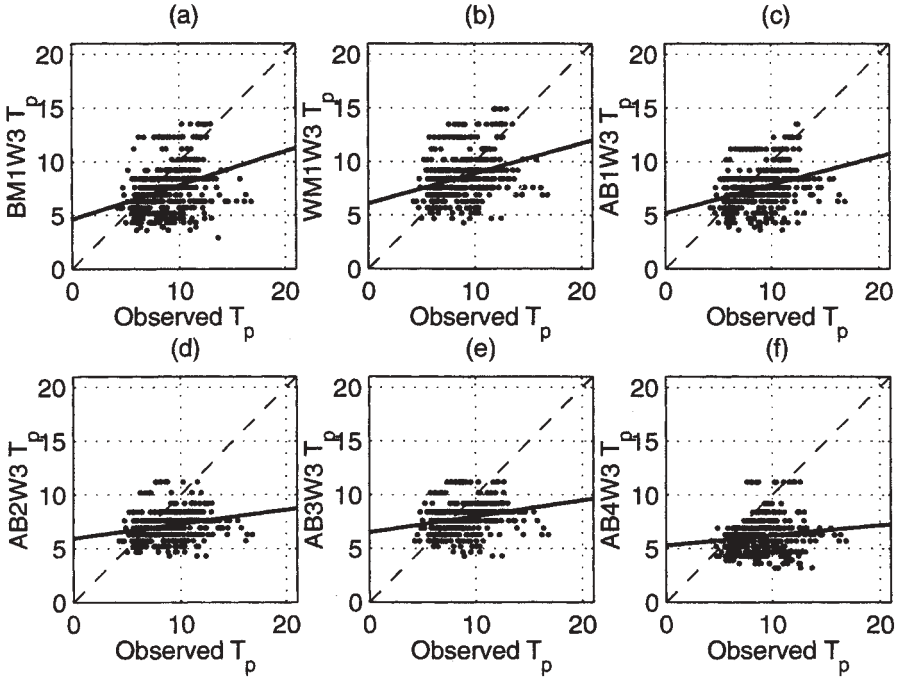

Figure 3: Scatterplots of hindcast and observed significant peak periods T_p in Bass Strait during March 20 to May 20 1998. Model runs are indicated in the vertical axis. Thin dashed lines indicate a perfect 1-to-1 correlation and continuous lines indicate the linear least squares fit through the cloud of co-located data.

- statistics of hindcast H_s from runs AB2 and AB3, made with a strong dependence of S_{ds} on the saturation parameter $B(k)$, were in excellent agreement with measurements. In sta-

tistical terms they were generally superior to cases using the WAM Cycle 3 form of S_{ds} (BOM and WM3). Statistics of hindcast T_p from runs AB2 and AB3, however, indicated that the dissipation rates of spectral components within the swell range predicted by S_{ds}^{ab} may need to be reduced;

- run AB4 produced the most degraded hindcasts of H_s and T_p. This may be a consequence of its stronger dependence on the weighting term $(k/\overline{k})^n = 1$, which increases the dissipation rates at wavenumbers higher than the peak and of incorrect tuning of other dissipation parameters.

These conclusions indicate that the newly-proposed saturation-dependent form S_{ds}^{ab} generally improves the hindcasts of sea-state produced by the AUSWAM model in terms of H_s. Discrepancies in the hindcasts of peak periods, however, indicate that further adjustments are needed in the specification of dissipation rates at wavenumbers lower than the spectral peak. Nevertheless, validation statistics of hindcast T_p from test cases using S_{ds}^{ab} were in the majority of cases better than those associated with the standard AUSWAM setup. These positive results demonstrate the potential benefits of using this new saturation-dependent form of S_{ds} in operational wind-wave models.

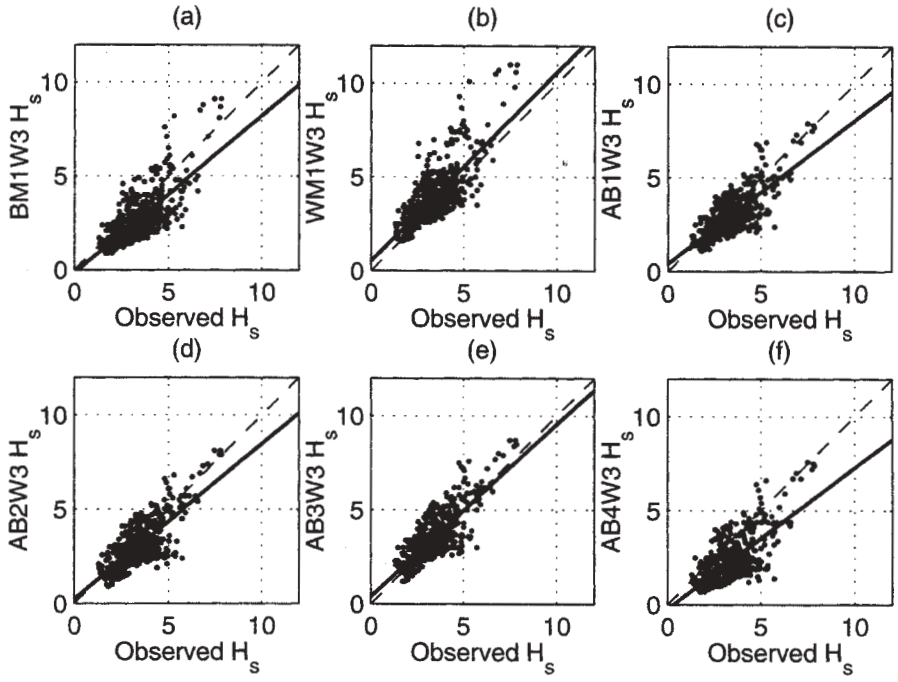

Figure 4: Scatterplots of hindcast and observed significant wave heights H_s in Strahan during the second hindcast period of March 20 to May 20 1998. Model runs are indicated in the vertical axis. Thin dashed lines indicate a perfect 1-to-1 correlation and continuous lines indicate the linear least squares fit through the cloud of co-located data.

6 ACKNOWLEDGEMENTS

The authors acknowledge the Australian Bureau of Meteorology Research Centre (BMRC) for providing the numerical model and the computational resources used in this investigation. This study was part of the doctoral thesis research activities of the first author (J.H.G.M.A.), made possible through a scholarship provided by the Conselho Nacional de Desenvolvimento Cientifico e Tecnologico (CNPq) of Brazil.

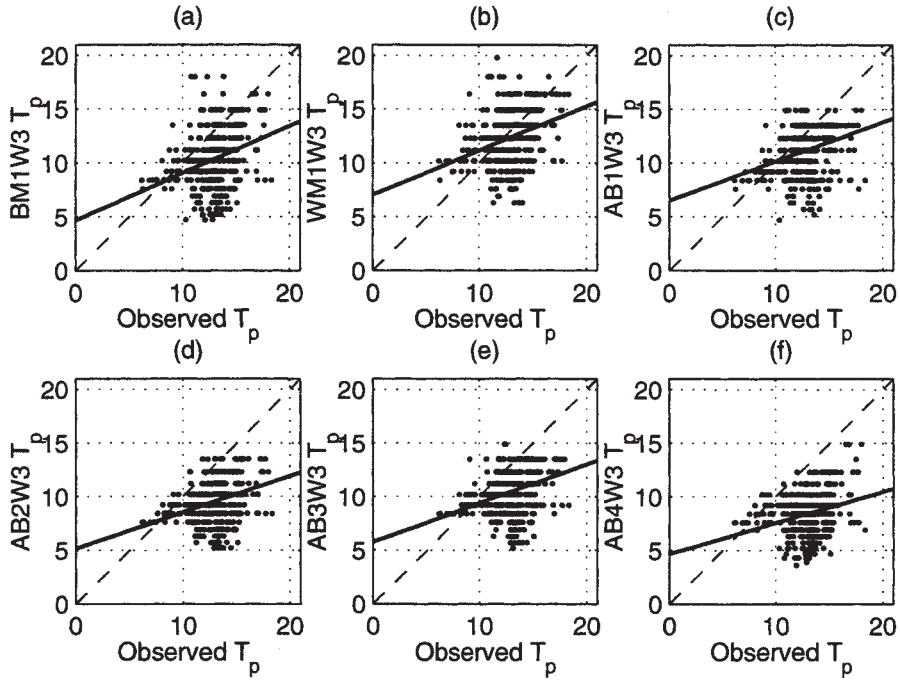

Figure 5: Scatterplots of hindcast and observed significant wave heights (upper panels) and peak periods T_p (lower panels) in Strahan during March 20 to May 20 1998. Model runs are indicated in the vertical axis. Thin dashed lines indicate a perfect 1-to-1 correlation and continuous lines indicate the linear least squares fit through the cloud of co-located data.

REFERENCES

Alves, J. H. G. M. and M. L. Banner (2000*a*), Impact of a saturation-dependent dissipation funciton on wind-wave models: fetch-limited case, *in* '27th International Conference on Coastal Engineering (Abstracts)', Vol. 1, ASCE, Sydney.

Alves, J. H. G. M. and M. L. Banner (2000*b*), 'A saturation-dependent dissipation function for wind-wave modelling applications. Part I: Fetch-limited experiments'. In preparation.

Alves, J. H .G. M., M. L. Banner and I. R. Young (2000), 'Revisiting the asymptotic limits of fully-developed seas', *J. Phys. Oceanogr.* . Submitted.

Bender, L. C. (1996), 'Modification of the physics and numerics in a third-generation ocean wave model', *J. of Atmos. Oceanic Tech.* **13**(3), 726–750.

Bender, L. C. and L. M. Leslie (1994), Evaluation of a third-generation ocean wave model for the australian region, BMRC Research Report 43, Bureau of Meteorology Research Centre, Melbourne, Australia.

Cardone, V. J., H. C. Graber, R. E. Jensen, S. Hasselmann and M. J. Caruso (1994), 'In search of the true surface wind field in SWADE IOP-1: ocean wave modelling perspective', *Global Atm. Ocean Syst.* **3**, 107–150.

Garrat, J. R. (1992), *The atmospheric boundary layer*, University Press, Cambridge. 316pp.

Greenslade, D. (1999), The assimilation of ERS-2 significant wave height data in the Australian wave model, BMRC Research Report 73, Bureau of Meteorology, Melbourne, Australia.

Günther, H., S. Hasselmann and P. A. E. M. Janssen (1992), The WAM model Cycle 4, Technical Report 4, German Climate Research Center - DKRZ, Hamburg.

Hasselmann, K. (1962), 'On the nonlinear energy transfer in a gravity-wave spectrum. Part 1: General theory', *J. Fluid Mech.* **12**, 481–500.

Hasselmann, S. and K. Hasselmann (1985), 'Computations and parameterizations of the nonlinear energy transfer in a gravity-wave spectrum. Part 1: a new method for efficient computations of the nonlinear transfer integral', *J. Phys. Oceanogr.* **15**, 1369–1377.

Kahma, K. and C. J. Calkoen (1992), 'Reconciling discrepancies in the observed growth of wind-generated waves', *J. Phys. Oceanogr.* **22**, 1389–1405.

Komen, G. J., S. Hasselmann and K. Hasselmann (1984), 'On the existence of a fully developed wind-sea spectrum', *J. Phys. Oceanogr.* **14**(8), 1271–1285.

Monbaliu, J. and S. Hasselmann (1994), Optimization of the WAM source functions by direct cost function minimization, *in* G. J. K.et al., ed., 'Dynamics and modelling of wind waves', Cambridge University Press, Cambridge, pp. 442–447.

Puri, K., G. S. Dietachmayer, G. A. Mills, N. E. Davison, R. A. Bowen and L. W. Logan (1998), 'The new BMRC limited area prediction system', *Aust. Met. Mag.* **47**, 203–233.

Seaman, R, W. Bourke, P. Steinle, T Hart, G. Embery, M. Naughton and L. Rikus (1995), 'Evolution of the Bureau of Meteorology's global assimilation and prediction system. Part 1: analyses and initialization', *Aust. Met. Mag.* **44**, 1–18.

Snyder, R. L., F. W. Dobson, J. A Elliot and R. B. Long (1981), 'Array measurements of atmospheric pressure fluctuations above surface gravity waves', *J. Fluid Mech.* **102**, 1–59.

Wu, J. (1982), 'Wind-stress coefficients over the sea surface from breeze to hurricane', *J. Geophys. Res.* **87 (C12)**, 9704–9706.

Zakharov, V. E. (1968), 'Stability of periodic waves of finite amplitude on the surface of a deep fluid', *J. Appl. Mech. Techn. Phys.* **9**, 190–194.

Delft3D Nearshore Wave and Current Predictions Compared with Field Observations

LCDR Bruce Morris and Edward B. Thornton
Oceanography Department, Naval Postgraduate School, Monterey CA 93940
Email: bjmorris@nps.navy.mil
Tel: 831-656-3117
Fax: 831-656-2712

The Delft3D nearshore model is being assessed for transition for use by the U.S. Navy. Predicted waves and currents using the Delft3D model are compared with field data acquired on both planar (La Jolla and Santa Barbara, California) and barred (Duck, North Carolina) beaches. The comparison focuses on the differences of planar and barred beaches, the effects of alongshore variable bathymetry, and tidal modulation of waves and currents over a barred beach. Historically, longshore currents primarily have been modeled assuming alongshore uniformity. On barred beaches, waves break over the bar, reform in the trough and break again on the beach. The longshore currents are predicted to be a maximum over the bar and on the foreshore and a minimum within the trough in response to changes in the radiation stress as the result of wave breaking. However, it was found during the Delilah experiment that the longshore maximum was often in the trough of the barred beach. Putrevu et al., (1995) showed analytically that alongshore pressure gradients induced by small alongshore variation in bottom topography could contribute substantially to longshore current forcing. It is demonstrated that the longshore current maximum in the trough measured during Delilah is due to pressure gradients associated with the non-uniform bathymetry.

Modeled tidal forcing by Delft3D and its effect on longshore current variability is examined. Thornton and Kim (1993) qualitatively showed that depth-dependent breaking wave heights are modulated by time-varying depth due to the tide. The longshore current has a tidal signature in response to the modulated wave forcing. Phases between current and tidal elevation from Delft3D are compared with data from Delilah.

INTERCOMPARISON OF DIFFERENT BOTTOM FRICTION FORMULATIONS IN EXTREME SHALLOW WATER REGIONS.

Roberto Padilla-Hernández
Jaak Monbaliu

Katholieke Universiteit Leuven
Hydraulic Laboratory
De Croylan 2
B-3001 Heverlee
Belgium

1 INTRODUCTION

There are different mechanisms for wave energy dissipation at the bottom, such as energy dissipation through percolation, friction, motion of a soft muddy bottom and bottom scattering. The relative strength of those mechanisms depends on the bottom conditions; type of sediment and the presence or absence of sand ripples, and on the dimensions of such ripples. It appears that the bottom friction is the most important mechanism in sandy coastal regions (Shemdin et al., 1978). Contrary to the situation in deep water, the dynamics of waves in shallow water areas are dominated by their interaction with the bottom. The growth by wind, propagation, non-linear interactions, energy decay and possible the enhancement of whitecapping, are all linked to how the waves interact with the bottom. The energy decay by bottom friction has been a subject of investigation and a large number of dissipation models for bottom friction have been proposed. One of the main problems to advance our knowledge about how to model wind waves in very shallow water was the lack of measurements. To this respect the wave measurements campaign in Lake George, Australia (Young and Verhagen, 1996. Hereafter YV) is as unique as the JONSWAP experiment (Hasselmann et al. 1973). The data obtained from the lake in water of limited depth provide a nearly idealized situation to test and analyze several of the most widely used bottom friction formulations.

The objective of this work is to search for evidence to determine which friction formulation, out of four, performs best. To reach the objective, the numerical wave model SWAN was run with the bottom friction source term as 'unknown' in order to reproduce the Lake George measurements (YV) in the best possible way. Besides the three formulations already present in SWAN (Booij et al. 1999), also the bottom friction formulation by Weber (1989) was used. To this end it was introduced in the SWAN model code. Although all of the individual source terms formulations are open to discussion, it is assumed that the SWAN model computes the energy balance as a whole correctly.

2 THE SWAN WAVE MODEL

The SWAN (Simulation of WAves in Nearshore areas) model is based on the action balance equation. The equation solved by the SWAN model reads

$$\frac{\partial N}{\partial t}+\frac{\partial}{\partial x}(c_x N)+\frac{\partial}{\partial y}(c_y N)+\frac{\partial}{\partial \sigma}(c_\sigma N)+\frac{\partial}{\partial \theta}(c_\theta N)=\frac{S_{tot}}{\sigma} \qquad (1)$$

where $N(\sigma,\theta)$ is the wave action density ($=F(\sigma,\theta)/\sigma$); t is the time; σ is the intrinsic angular frequency; θ is the wave direction; c_x, c_y, are the propagation velocities in geographical x- y-space; and c_σ and c_θ are the propagation velocities in spectral space (frequency and directional space), F is the wave energy density. The first term on the left-hand side of the above equation represents the local rate of change of wave energy density. The second and third terms represent propagation in geographical space. The forth and fifth term represent the shifting of the

AUTHOR INDEX TABLE OF CONTENTS

energy in the frequency space due to variations in depth and currents, and the shifting of energy in the direction space (refraction) respectively. The right hand side represents all effects of generation and dissipation of the waves. The source terms in SWAN include the wave energy growth by wind input S_{in}; wave energy transfer due to wave-wave non-linear interactions S_{nl} (both quadruplets and triads); the decay of wave energy due to whitecapping S_{ds}; bottom friction S_{bf}; and depth-induced wave breaking S_{bk}. A detailed description of the SWAN (Cycle 2) model, the incorporated source terms and the numerical solution method can be found in Ris (1997), Holthuijsen *et al.* (1999) and Booij *et al.* (1999).

3 THE MODELS OF BOTTOM FRICTION DISSIPATION

3.1 *Dissipation of wave energy as a function of bottom stress*

Komen et al. (1994) start with the linearized momentum equation for the bottom boundary layer flow which in the case of pure wave motion (without ambient currents) reads

$$\frac{\partial \mathbf{u}}{\partial t} + \frac{1}{\rho}\nabla p = \frac{1}{\rho}\frac{\partial \boldsymbol{\tau}}{\partial z} \tag{2}$$

where t is time, z is the vertical coordinate, ρ is the density of the water, $\boldsymbol{u}$ and p the Reynolds-average horizontal velocity and pressure, respectively, and $\boldsymbol{\tau}$ the turbulent stress in the wave boundary layer. They obtain an expression for the wave energy dissipation due to bottom friction:

$$S_{bf}(\mathbf{k}) = -\frac{1}{g}\left\langle \frac{\boldsymbol{\tau}}{\rho}\cdot \mathbf{U}_k \right\rangle \tag{3}$$

where the bottom friction depends on the known orbital velocity ($\mathbf{U}_k$) of the waves at the bottom (which considering a turbulent boundary layer is equal to the value at the top of the boundary layer), and on the unknown turbulent bottom stress ($\boldsymbol{\tau}$), the subscript k denote a given wave number.

An exact solution for $\boldsymbol{\tau}$ in eq. (2) (and hence for $S_{bf}(\boldsymbol{k})$ in eq. 3) does not exist, even not for a very simple flow. To overcome the problem, several approaches have been proposed. Most of the approaches result in a turbulent shear stress expressed as a function of a friction coefficient and of a free-stream orbital velocity (orbital velocity at the top of the boundary layer). There are two distinct formulations for $\boldsymbol{\tau}$; the first is to retain a spectral description. The second is to represent the range of frequencies by a single one, for example the peak frequency, resulting in an integral form.

Usually $\boldsymbol{\tau}$ is expressed in a drag law as $\boldsymbol{\tau} = 1/2\rho f_w |\mathbf{U}|\mathbf{U}$ or alternatively as $\boldsymbol{\tau} = 1/2\rho f_w (\mathrm{U})_{rms}\mathbf{U}$, where f_w is a friction coefficient, $\mathbf{U}$ is the wave orbital velocity at the bottom and U_{rms} is the root mean square of the orbital velocity. Taking $C_f = f_w |U|$ results in

$$\boldsymbol{\tau} = \frac{1}{2}\rho C_f \mathbf{U} \tag{4}$$

Substitution of eq. (4) in the dissipation equation (3) yields for wave component with wavenumber $\boldsymbol{k}$:

$$S_{bf}(\mathbf{k}) = -\frac{1}{g}C_f\left\langle (\mathbf{U}_k)^2 \right\rangle \tag{5}$$

The mean square of the bottom velocity, $\left\langle (U_k)^2 \right\rangle$, can be associated with the wave component having the wavenumber $\boldsymbol{k}$. Rewriting the expression (5) in terms of the wave spectrum, one obtains:

$$S_{bf}(\mathbf{k}) = -2C_f \frac{k}{\sinh 2kh} F(\mathbf{k}) \tag{6}$$

where C_f is a dissipation coefficient with the dimension of ms^{-1}, $F(k)$ and $F(\sigma,\theta)$, are the energy-density spectrum and $\boldsymbol{k} = (k_1,k_2) = (k\cos\theta, k\sin\theta)$ is the wavenumber with modulus k and direction θ, and σ is the relative frequency. The different formulations for the bottom friction dissipation differ mainly in the expression given to the dissipation coefficient C_f.

Below the expressions that are currently implemented in the SWAN model (version 40.01, Holthuijsen *et al.* 1999) as well as Weber's formulation for bottom friction dissipation are explained briefly.

3.2 *Expressions for the dissipation coefficient C_f*

The JONSWAP model

This is the simplest expression for bottom dissipation. It was proposed by Hasselmann *et al.* (1973). C_{fJ} is assumed to be constant and is given by

$$C_{fJ} = \frac{\Gamma}{g} \tag{7}$$

where g is the acceleration due to gravity. From the results of the JONSWAP experiment they found a value for Γ of 0.038 m^2s^{-3}. As long as a suitable value for Γ is chosen, this expression performs well in many different conditions. The value for Γ can be different for swell and for wind sea. Bouws and

AUTHOR INDEX TABLE OF CONTENTS

Komen (1983) found that the JONSWAP expression with a value of 0.038 m^2s^{-3} for Γ yields to low dissipation rates for a depth-limited wind sea. They selected a value of 0.067 m^2s^{-3} in order to obtain a correct equilibrium solution for a steady state.

3.2.1 *The Madsen model*

Madsen *et al.* (1988) derived a bottom friction formulation based on the eddy-viscosity concept,

$$C_{fM} = \frac{f_w}{\sqrt{2}} \left\langle U^2 \right\rangle^{1/2} \tag{8}$$

where

$$\left\langle U^2 \right\rangle^{1/2} = \left[\iint \frac{2gk}{\sinh 2kh} F(\sigma,\theta) d\sigma d\theta \right]^{1/2} \tag{9}$$

and f_w is a non-dimensional friction factor estimated by using the formulation of Jonsson (1966):

$$\frac{1}{4\sqrt{f_w}} + \log_{10}\left[\frac{1}{4\sqrt{f_w}} \right] = m_f + \log_{10}\left[\frac{a_b}{K_N} \right] \tag{10}$$

where $m_f = -0.08$, a_b is a representative near-bottom excursion amplitude:

$$a_b = \left[2 \iint \frac{1}{\sinh^2 kh} E(f,\theta) df d\theta \right]^{\frac{1}{2}} \tag{11}$$

and K_N is the bottom roughness length.

3.2.2 *The Collins model*

Hasselmann and Collins (1968) derived a formulation for the bottom friction dissipation. They related the turbulent bottom stress to the external flow by means of a quadratic friction law. The dissipation coefficient they derived reads:

$$C_f = 2c \left\{ \delta_{ij} \langle U \rangle + \left\langle \frac{U_i U_j}{U} \right\rangle \right\} \tag{12}$$

where δ_{ij} is the Kroneker delta function; $\langle\ \rangle$ denotes the ensemble average, U is equal to $\left(U_1^2 + U_2^2\right)^{1/2}$, U_1 and U_2 are the near bottom orbital velocity components. c is a drag coefficient determined experimentally as a function of the bottom roughness. Hasselmann and Collins proposed a value for c equal to 0.015.

Collins (1972) simplified the expression (13) for the dissipation coefficient by leaving out the dependence on the direction of the wave component and by using the total wave induced bottom velocity:

$$C_{fC} = 2c \left\langle U^2 \right\rangle^{\frac{1}{2}} \tag{13}$$

where $\left\langle U^2 \right\rangle$ can be computed from eq. (10). Expression (14) is the one implemented in SWAN model. The value of the drag coefficient c is equal to 0.015.

3.2.3 *The Weber eddy-viscosity model*

Weber's model for the spectral energy dissipation due to friction in the turbulent wave boundary layer is based on the eddy-viscosity concept. In this model the turbulent shear stress is parameterized in analogy with the viscous stress, with the coefficient of molecular viscosity replaced by a turbulent eddy viscosity coefficient.

Solving the Navier-Stokes equations in the turbulent boundary layer and using perturbation theory, Weber derived the following dissipation coefficient.

$$C_{fW} = u^* \left\{ T_k(\xi_0) + T_k^*(\xi_0) \right\} \tag{14}$$

C_{fW} depends on the wave spectrum $F(k)$, the water depth h, and the bottom roughness K_N through the friction velocity u^*, and on the radian frequency through ξ_0.

$$\xi_0 = \left(\frac{4(y_0 + h)\omega}{\kappa u^*} \right)^{\frac{1}{2}} = \left(\frac{4K_N\omega}{30\kappa u^*} \right)^{\frac{1}{2}} \tag{15}$$

The variable ξ_0 reflects the ratio between the roughness length and the boundary layer thickness, which scales with u^*/ω; κ is the von Kármán constant equal to 0.4; (y_0+h) is the theoretical bottom level and T_k is defined as

$$T_k(\xi_0) = -\frac{1}{2}\kappa\xi_0 \frac{Ker'(\xi_0) + iKei'(\xi_0)}{Ker(\xi_0) + iKei(\xi_0)} \tag{16}$$

T_k is a dimensionless complex function and depends on the radian frequency and thus on the wave number through the argument ξ_0. *Ker* + *iKei* is the zero order Kelvin function (Abramowitz and Stegun 1965). The prime denotes the derivative with respect to the argument ξ_0. Details of the derivation of the dissipation coefficient in the eddy viscosity model are given in Weber 1989 and 1991.

4 NUMERICAL EXPERIMENTS

4.1 *Introduction*

In the following numerical experiments the goal is to analyze the performance of the bottom friction formulations of Hasselman *et al.* (1973), the eddy-viscosity model of Madsen *et al.* (1988), the drag law

AUTHOR INDEX TABLE OF CONTENTS

turbulent friction model of Collins (1972) and Weber's (1989) formulation.
A comparison is made of SWAN model output with the data from the Lake George (**YV**). The input files and the data for the SWAN runs are taken from case F41LAKGR of the "Suite 40.01.a of the bench mark tests for the shallow water wave model SWAN Cycle 2, version 40.01 (SBMSWAN)", Delft hydraulics (1999).

4.2 *Statistical analysis*

In order to analyze the results from the SWAN model using the different bottom friction models by comparing them with measurements, a set of statistical parameters following Dingemans (1997) is used:

The *bias*. The difference between the mean of the observations (x_i) and the mean of the model results (y_i)

$$Bias = \overline{X} - \overline{Y} \tag{17}$$

where $Mean = \overline{X} = (\sum_i x_i / N)$, N is the number of data.

The *rmse*. The root mean square error

$$rmse = \left[\frac{1}{N}\sum_i (y_i - x_i)^2\right]^{\frac{1}{2}} \tag{18}$$

The *si*. The scatter index

$$si = \frac{rmse}{\sqrt{\overline{X}\,\overline{Y}}} \tag{19}$$

The *re*. The relative error or index of agreement

$$re = 1 - \frac{N \times rmse^2}{pe} = 1 - \frac{\sum_i |y_i - x_i|^2}{\sum_i (|y_i - \overline{X}| + |x_i - \overline{X}|)^2} \tag{20}$$

The relative error reflects the degree to which the observations are approached by the model results. Willmott (1981) introduced *re* as an index of agreement. (*re=1*, for perfect agreement, normally *0<re<1*). The parameter *pe* is known as the potential variance. In the computations of the different statistical parameters the imposed values of the wave parameters at the grid model boundary are not included in the analysis.

4.3 *Lake George*

4.3.1 *Situation*

The Lake George experiment represents nearly idealized wave growth in depth- and fetch- limited conditions. The lake is fairly shallow with a relative uniform bathymetry (depth about 2m). It is approximately 20 km long and 10 km wide. A series of eight wave gauges were situated along the North-South axis of the lake (Figure 1).

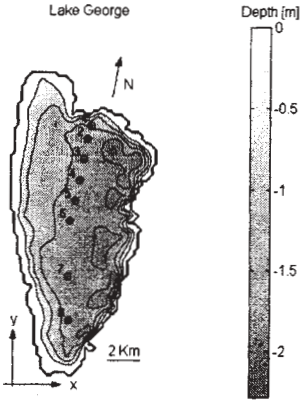

Figure 1. Bathymetry of Lake George and the locations of the eight wave gauges. Depth contour interval is 0.5 m starting from 0.

The bottom is rather smooth (bottom ripples were practically absent) and the bottom material consist of fine clay (Ris, 1997). The wave measurements were carried out during the period from April 1992 until October 1993. Only data for which the wind speed and direction were relatively constant during the 30-minute sampling period have been retained. The criteria used for this selection were that the wind speed should not vary by more than 10% nor should the wind direction turn by more than 10^0 at each side of the alignment of the instrument array (north/south) during the 30-minute sampling period. (For a complete description see **YV**).

4.3.2 *Calibration*

For the computations the three northerly wind cases were selected from the bench mark data set for SWAN (SBMSWAN, case F41LAKGR). These cases are three typical examples, i.e., a low wind speed (U_{10}=6.5 m/s), a medium wind speed (U_{10}=10.8 m/s) and a high wind speed (U_{10}=15.2 m/s). The computations were carried out with SWAN version 40.01 using the WAM Cycle 3 formulations (Booij *et al.* 1999). The triad-wave interactions and depth-induced wave breaking were turned on (default values). For bottom friction formulations one of the above formulations is used. As in Ris (1997), station 1 is taken as the up-wave boundary in the simulation.

AUTHOR INDEX TABLE OF CONTENTS

This avoids uncertainty in the location of the northern shore because of seasonal variation in water depth. Since no directional wave spectrum is available at station 1, the directional distribution of the waves is approximated with a $\cos^2(\theta)$ directional distribution. For the computations a directional resolution of 10^0 and a logarithmic frequency resolution (Δf=0.1f) was chosen between 0.1666 Hz and 2.0 Hz for the low wind case and between 0.125 Hz and 1.0 Hz for the medium and high wind cases. The spatial resolution is 250 m both in x and y direction. To account for seasonal variations in water level, the water level was increased, with respect to the reference bathymetry, over the entire lake with +0.1 m, +0.3 m and +0.27m for the low, medium and high wind case respectively.In order to tune the friction coefficients of every friction model, the third case (high wind speed) was chosen. The combined root mean square error (*rmsec*) for H_s and T_p was taken as the cost function value to be minimized. The definition for the *rmsec* reads

$$rmsec = [rmse(H_s) + rmse(T_P)]/2 \qquad (21)$$

The results using the default value for the friction coefficient in every friction model is taken as a reference (see Table 1). Identical definitions for the combined scatter index (*sic*) and the combined relative error (*rec*) are used, replacing *si* or *re* for *rmse* in eq. 21. Table 1 shows the *rmsec* computed by using the default value for the coefficients and the *rmsec* computed using the optimal values for the coefficients after several runs increasing and decreasing the value of the coefficients. The formulations of Madsen and Weber are easier to tune. For this formulations improvement of *rmsec* leads to improvement for both H_s and T_p. Both parameters H_s and T_p were underestimated using the reference value. This is not the case when using the formulations of JONSWAP and Collins.

Table 1. Friction coefficient values for the different friction models and the resulting *rmsec* for the Lake George case. The coefficients for Madsen and Weber are in mm.

	Default		Optimal	
	Coeff	*rmsec*	Coeff.	*rmsec*
JONSWAP	0.067	0.134	0.030	0.075
MADSEN	50.0	0.306	1.0	0.089
COLLINS	0.015	0.090	0.030	0.088
WEBER	40.0	0.350	0.75	0.088

Once the appropriate values for all friction coefficients were found (see Table 1) the other two selected cases for Lake George were run using these values. It is assumed that the bottom condition did not change.

As can be see in Figure 2 the significant wave height and the peak period are relatively well modeled by SWAN using the four friction models, except at the last three stations in case one. At these stations (from 6 to 8) the wave parameters do not show a monotonic behavior. That can possibly be ascribed to unresolved variation in the wind field. Such variation has been observed by **YV**. Those three stations were therefore eliminated from the statistical calculations for case one only. A small underestimation of T_p can be observed in the medium and low wind cases.

Figure 3 shows the statistical parameters for the three cases using the four bottom friction formulations. The results from SWAN using the different bottom dissipation formulations for C_f are to a certain extent similar. The statistics show that using the formula of Collins, SWAN gives the best approximation for H_s but gives the worst approximation for T_p.

Using the four bottom friction expressions, the largest error for H_s is in the high wind case compared with the other two cases.

This can be partially ascribed to a 'deviation' of the measurements from the monotonic behavior in the locations 2 and 7 as can be seen in Figure 2. Looking at the mean values of *rmse*, *si* and *re* for the three cases (Figure 3), the best performance for H_s corresponds to the use of the Collins formulation and the best performance for T_p corresponds to the Weber formulation. Figure 4 shows the performance of the SWAN using the different bottom friction formulations in function of *rmsec*. As can be seen SWAN has the best performance using Weber's formulation followed by Collins, and then by the JONSWAP and the Madsen formulations. The peak period in the low wind case is very well modeled using the formulation of Weber as can be seen in Figures 2 and 3.

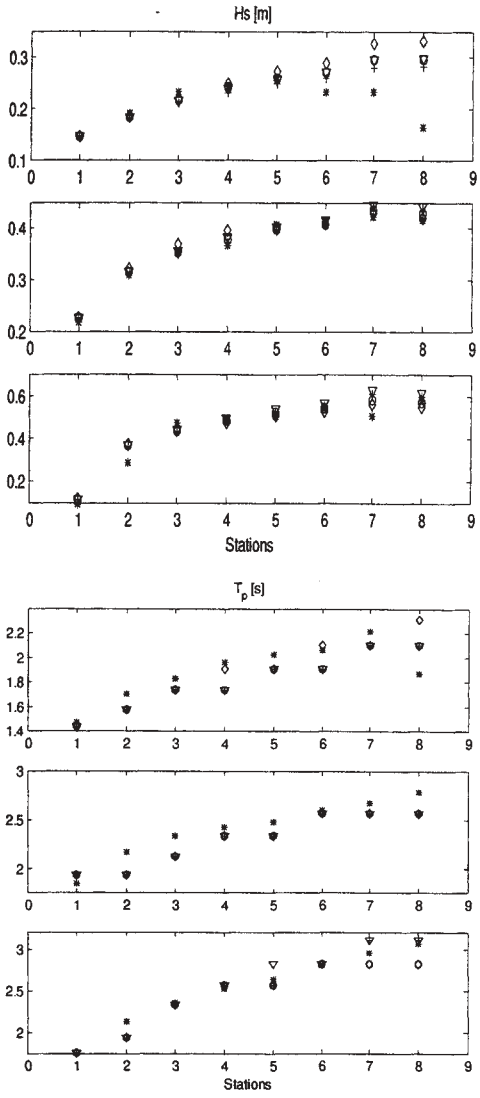

Figure 2. SWAN model results for the different bottom friction formulations (with the optimal value for the friction coefficcients) and observations of the significant wave height (three top panels) and peak period (three botom panels) in nearly ideal generation conditions in Lake George. Observations (*), JONSWAP (+), Madsen (▽), Collins (○) and Weber (◇) formulations.

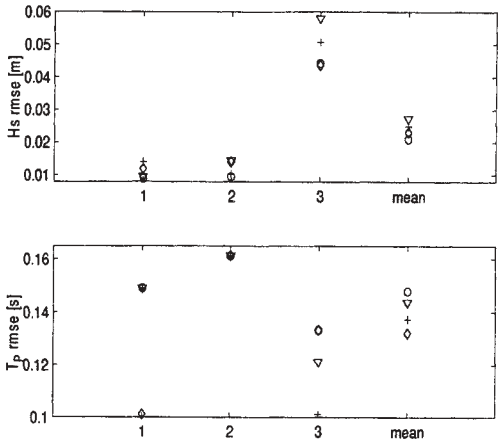

Figure 3. *rmse* for the wave height (top panel) and for the peak period (bottom panel), for the three cases in Lake George. The "mean" case represents the mean value for the three cases. Observations (*), JONSWAP (+), Madsen (▽), Collins (○) and Weber (◇) formulations.

4.3.3 *Depth-limited wave growth*

In order to refine the expressions of Bretschneider (1958) for both non-dimensional energy (ε) and non-dimensional peak frequency (ν), **YV** used their full data set of about 65,000 data points. They found that the asymptotic depth-limited growth can be considered dependent on the non-dimensional depth (δ) only. They found the following limits:

$$\varepsilon = 1.06x10^{-3}\delta^{1.3} \quad (22)$$

$$\nu = 0.20\delta^{-0.375} \quad (23)$$

The non-dimensional parameters are defined as g^2E/U_{10}^4 for the non-dimensional energy (ε), f_pU_{10}/g for non-dimensional peak frequency (ν), gd/U_{10}^2 for non-dimensional depth (δ), g is the gravitational acceleration, E is the total energy of the spectrum, U_{10} is the wind speed measured at a reference height of 10 m, and d is the water depth.

To calculate the depth-limited growth SWAN was run in one-dimensional mode for each of the friction models. Several runs were performed using different depths ranging from 2.5 *m* to 20 *m* and the wind speed was set equal to 20 ms^{-1} (to work in the same non-dimensional depth interval as **YV**).

AUTHOR INDEX TABLE OF CONTENTS

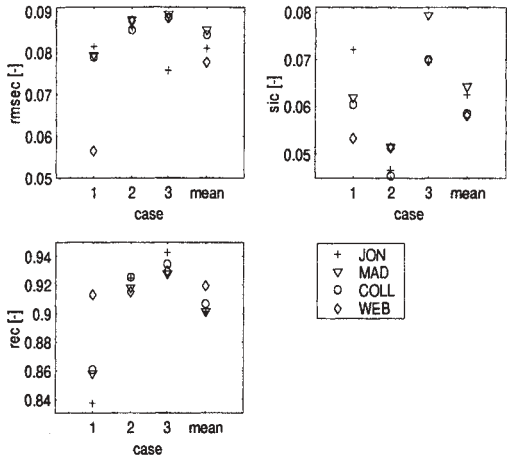

Figure 4. Combined root mean square error *rmsec*, combined scatter index *sic* and the combined relative error *rec* (bottom panels) for the wave height and the peak period. The "mean" case represents the mean values for the three cases in the Lake George wave model runs.

The results were stored for different fetches ranging from 15 km to 15,000 km. The friction coefficients used have the optimal values retained from the tuning runs. The expressions given in Table 2 were computed taking the maximum levels of non-dimensional energy and non-dimensional peak frequency at every non-dimensional fetch of the different runs. Figure 5 shows the different formulas for ε and ν together with the expressions (22) and (23) of **YV**. Table 3 shows the statistics comparing them with the formulas obtained by **YV**. Although all of them give good approximation to the measurements, it is clear that the formula of Weber and Collins give the best results.

The fit to ν curve of **YV** is perfect. Because the good approximation of all formulations to the formula from **YV**, Table 3 confirms that selecting *rmsec* as the parameter to be minimized was a good selection..

Even though **YV** considered that the asymptotic depth-limited energy growth depends on non-dimensional depth only, the numerical results show that the depth-limited growth is a function of the roughness length as well.

Table 1
Friction coefficient values for the different friction models and the resulting *rmsec*. The values in bold are the default and the underlined are the optimal values for the Lake George case.

	$\varepsilon =$	$\nu =$
JONSWAP	$4.1 \times 10^{-3} \delta^{1.76}$	$0.14\delta^{-.47}$
MADSEN	$3.3 \times 10^{-3} \delta^{1.69}$	$0.14\delta^{-.47}$
COLLINS	$1.4 \times 10^{-3} \delta^{1.42}$	$0.20\delta^{-.375}$
WEBER	$1.4 \times 10^{-3} \delta^{1.46}$	$0.20\delta^{-.375}$

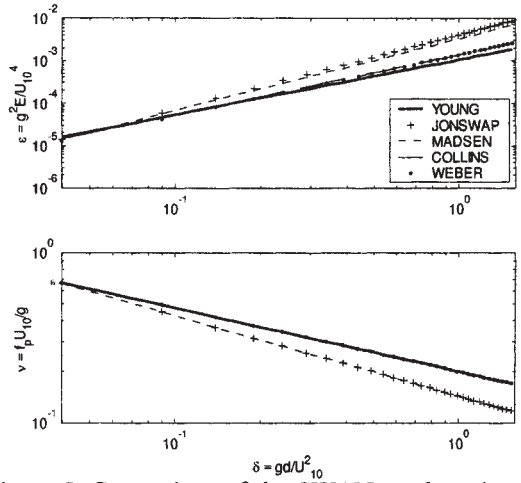

Figure 5. Comparison of the SWAN results using the different bottom friction formulations and the formula from Young and Verhagen (1996) for non-dimensional energy ε (top panel) and non-dimensional peak frequency ν (bottom panel) against non-dimensional depth.

If the bottom friction and bed material were not important in fetch- and depth-limited conditions (as assumed by **YV**), then the value assigned to K_N should not matter and the results would be expected to be the same. This is not the case running the wave model using a different roughness length in the friction dissipation formulation. To exemplify this, the SWAN model was run for depth-limited wave growth with Weber's formulation for bottom friction. Figure 6 shows the results for different values for K_N. Going from larger to smaller values of K_N the ε increases and the ν decreases. Hence one should expect that the curves for ε growth against non-dimensional fetch change as well. This implies that the expression (22) and (23) should take into account the bottom roughness

AUTHOR INDEX TABLE OF CONTENTS

Table 3. Statistics comparing the formulas obtained from SWAN using the different friction formulations against the formula from YV in the case of depth-limited growth.

	Model	JONSWAP	Madsen	Collins	Weber
ε	*bias*	-0.002	-0.001	0.000	0.000
	rmse	0.003	0.002	0.000	0.000
	si	1.969	1.604	0.368	0.380
	re	0.800	0.816	0.958	0.953
ν	*bias*	0.055	0.055	0.000	0.000
	rmse	0.055	0.055	0.000	0.000
	si	0.244	0.244	0.000	0.000
	re	0.950	0.950	1.000	1.000

4.3.4 *Fetch-limited wave growth*

Using their data from Lake George **YV** proposed a generalized form to the shallow water limits for non-dimensional energy (ε) and non-dimensional peak frequency (ν)

$$\varepsilon = 3.64x10^{-3}\left\{\tanh A_1 \tanh\left[\frac{B_1}{\tanh A_1}\right]\right\}^n \qquad (24)$$

$$\nu = 0.133\left\{\tanh A_2 \tanh\left[\frac{B_2}{\tanh A_2}\right]\right\}^m \qquad (25)$$

where

$$A_1 = 0.292^{1/n}\delta^{1.3/n} \qquad (26)$$

$$B_1 = (4.396x10^{-5})^{1/n}\chi^{1/n} \qquad (27)$$

where χ is the non-dimensional fetch. $\chi = gx/U_{10}^2$, x is the distance and

$$A_2 = 1.505^{1/m}\delta^{-0.375/m} \qquad (28)$$

$$B_2 = 16.391^{1/m}\chi^{-0.27/m} \qquad (29)$$

The coefficients n and m control the rate of transition from "deep" to "depth limited" conditions. **YV** performed a non-linear least squares analysis on their selected data set to determine n and m. Their analysis yielded n equal to *1.74* and m equal to *-0.37*. Expression (24) and (25) give a family of curves, one for each value of δ.

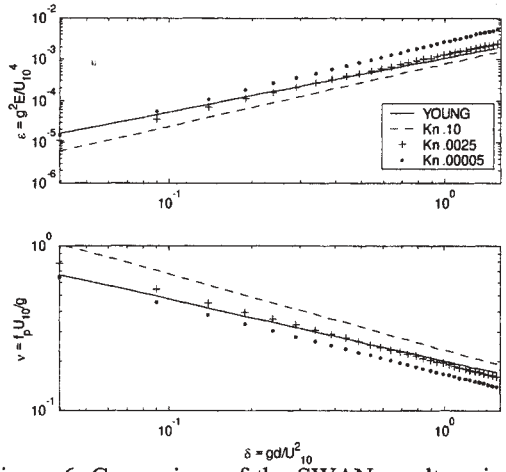

Figure 6. Comparison of the SWAN results using the formulation of Weber with different roughness length (K_N) and the formula from Young and Verhagen (1996) for non-dimensional energy ε (top panel) and non-dimensional peak frequency ν (bottom panel) against non-dimensional depth.

The results from SWAN are compared with the equations given by **YV**. The Figures 7 and 8 show the results from SWAN using the different bottom friction formulations for δ of 0.10 and 0.70 respectively.

The deep water asymptotic form of equations (24) and (25) and the same equations but for shallow water (n equal to *1.74* and m equal to *-0.37*) are also shown. As can be seen from those figures SWAN overestimates the total energy for very short χ.

AUTHOR INDEX TABLE OF CONTENTS

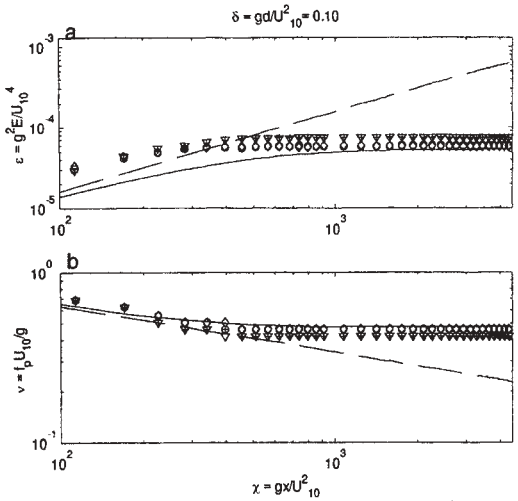

Figure 7. (a) Non-dimensional energy ε and (b) non-dimensional peak frequency ν against non-dimensional fetch for a non-dimensional depth δ of 0.10. The deep water asymptotic form of equations (24) and (25) is shown in dashed line. The same equations but for shallow water as found by **YV** (*n=1.74* and *m=-0.375*) is in solid line. SWAN was run using JONSWAP (+), Madsen (▽), Collins (○) and Weber (◇) formulation.

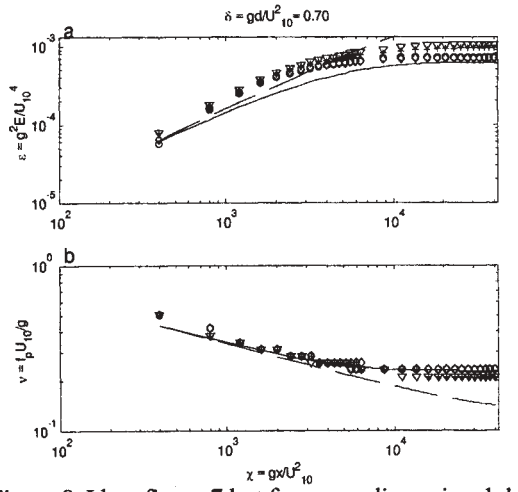

Figure 8. Idem figure 7 but for a non-dimensional depth δ of 0.70. SWAN was run using JONSWAP (+), Madsen (o), Collins (dotted) and Webers (◇) formulations.

In particular, energy growth in the high frequency range (very short fetches) is usually overestimated by SWAN. This overestimation is observed systematically. According with Ris *et al*, (1999) the overestimation of energy at short fetches can be ascribed to the linear wave growth term of Cavaleri and Malanotte-Rizzoli. But in this work the linear growth term was not taken into account. Results from the wave model using the linear wave growth shows no relevant differences with the results without the linear growth term. The observed overestimation of energy should be ascribed to another reason. The search for such reason is however considered beyond the scope of this work.

SWAN with the formulations of Collins and Weber for bottom friction dissipation catched the asymptotic levels of ε and ν given by the expression of **YV** quite well, better that using the expressions of JONSWAP and Madsen. But as can be seen in Figure 8, the wave model reproduces better the levels of non-dimensional energy when using the expression of Weber than when using the expression of Collins.

To quantify the differences between the model results and the expression of **YV** for fetch-limited growth, the wave model was run for a range of values of δ. The four statistical parameters given in section 4.2 are computed.

Figure 9 shows the statistical parameters comparing ε from the wave model results against the ε computed from the **YV** expression (eq. 24) for a range of values of δ.

To calculate the fetch-limited growth SWAN was run in one-dimensional mode for each of the friction models. Several runs were performed using a depth equal to 20 m and wind speed ranging from 10 ms^{-1} to 31.3 ms^{-1} (to work in the non-dimensional depth range from 0.1 to 1.0). The total fetch for every run was 15,000 km with a resolution of 5 km. The fetch to compute the statistical parameters was different for every δ, depending when the energy computed from eq. (24) is constant (until there were no changes in the 7th digit). The fetch range is from 440 km for δ equal to 0.1 to 997 km when δ is equal to 1.0. At small δ SWAN gives results which have almost the same *bias* and *rmse* for the four bottom friction expressions

Figures 10 shows the same as Figure 9 but for ν. In this way Figures 7 and 8 are represented statistically in Figures 9 and 10 as two points at their δ (0.10 and 0.50 respectively).

From Figure 9a and 9b it is evident that results start diverging going to deeper waters. At small δ the *bias* and *rmse* are almost the same.

At higher δ the expressions of JONSWAP and Madsen give the largest *bias* and *rmse*. The formulation of Collins and Weber give smaller *bias* and *rmse*. SWAN gives the smallest *bias* and *rmse* using the expression of Weber. Looking at the *si* and

AUTHOR INDEX TABLE OF CONTENTS

the *re* (Figures 9c and 9d) the results of SWAN using the formula of Weber approach better the ε computed by eq. (24) as can be seen in Figure 9d.

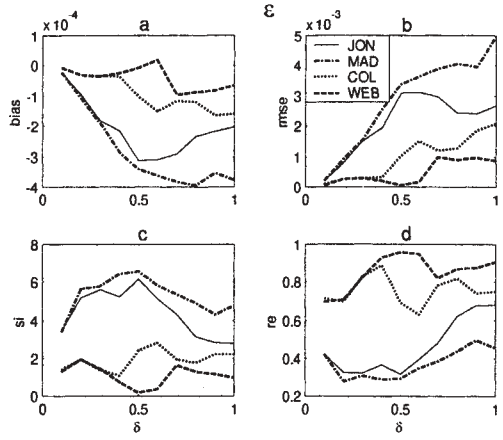

Figure 9. The *bias*, *rmse*, *si* and *re* against non-dimensional depth δ. The comparison is done for wave growth in fetch-limited conditions between the non-dimensional energy ε from SWAN with the different bottom friction dissipation formulations and the formula from Young and Verhagen (1996).

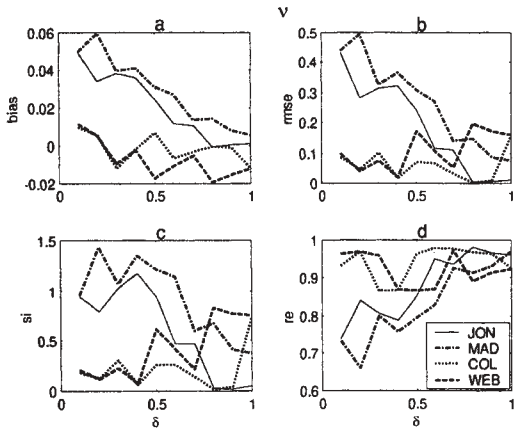

Figure 10: Idem Figure 9 but for non-dimensional frequency.

Figure 10 show the statistics for ν. In contrast with ε, the *bias* and the *rmse* of ν do not start with the same value using the four bottom friction formulations. Contrary to the results for ε, the *bias* and the *rmse* decrease with increasing δ.

The statistical measures for ε indicate that using the expressions of Weber the wave model results approach quit well the values computed from eqs. (24), better than using the other three bottom friction formulations. With respect to ν the wave results are of similar quality when the expressions of Collins and Weber are used and better than when using one of the other two expressions.

One can therefore conclude that in fetch- and depth-limited conditions, the results using the bottom friction dissipation expression of Weber are more consistent.

5 CONCLUSIONS

Weber's model showed the best performance in the cases of depth- and fetch-limited wave growth. In the case of depth-limited wave growth the fit of the calculated curve for the non-dimensional peak frequency to the one obtained by **YV** is as good as perfect. For the non-dimensional energy the statistical values, *rmse*, *si* and *re*, show that the results using Weber's formulation are superior in approaching the equations obtained from **YV**. In the case of fetch-limited wave growth the formulation of Weber showed the best performance in approaching the equations of **YV** derived from the measurements. Running the SWAN model using Weber's formula with different roughness length suggests that in the equations for depth- and fetch-limited wave growth the effect of bottom roughness should be included.

Besides showing the best performance, the formula of Weber has some other advantages. It retains a spectral description making this formulation more reliable for a multi-modal wave spectra. It can in principle be extended to the combined wave-current situation, important in situations where the tidal currents play a significant role in the dynamics of the coastal zone.

Acknowledgments. The first author gratefully acknowledges financial support from the Consejo Nacional de Ciencia y Tecnología (CONACYT, México). We also thank to WL Delft Hydraulics for the SBMSWAN and Ian Young, University of New South Wales, Canberra, Australia for the data of Lake George.

6 LITERATURE

Abramowitz M. and I.A. Stegun, 1965: Handbook of mathematical functions. National Burea of Standars, Washington, DC.

Booij N, R.C. Ris and L. H. Holthuijsen, 1999: A third-generation wave model for coastal region. 1.

Model description and validation. J. of Geophys. Res., 104, (C4), 7649-7666.
Bouws E. and G.J. Komen, 1983: On the balance between growth and dissipation in an extreme, depth limited wind-sea in the southern North Sea, J. Phys. Oceanogr., 13, 1653-1658.
Bretschneider, C. L., 1958: Revised wave forecasting relationships. In: Proc. 6th Conference on Coastal Engineering, Gainesville/Palm Beach/Miami Beach, Fl. ASCE, New York, pp 30-67.
Collins, J.I., 1972: Prediction of shallow water spectra. J. of Geophys. Res., 93 (C1), 491-508.
Dingemans, M.W., 1997: Water Wave Propagation Over Uneven Bottoms. Part 1 Linear wave propagation. Advance Series on Ocean Engineering, Vol. 13. World Scientific.
Hasselmann, K., T.P. Barnett, E. Bouws, H. Carlson, D.E. Cartwright, K. Enke, J.I. Ewing, H. Gienapp, D.E. Hasselmann, P. Kruseman, A. Meerbrug, P. Müller, D.J. Olbers, K. Richter, W. Sell and H. Walden,, 1973: Measurements of wind wave growth and swell decay during the Joint North Sea Wave Project (JONSWAP), Dtsch. Hydrogr. Z., A8(12), 95pp.
Hasselmann, K. and J.I. Collins, 1968: Spectral dissipation of finite-depth gravity waves due to turbulent bottom friction, J. Mar. Res., 26, 1-12.
Holthuijsen L., N. Booij, R. Ris, Ij. G. Haagsma, A.T.M.M. Kieftenburg and R. Padilla-Hernández. 1999: SWAN Cycle 2 version 40.01. User Manual. Delft Univ. of Tech. the Nederlands.
Jonsson, I.G. 1966: Wave boundary layers and friction factors. Proc. 10th Int. Conf Coastal Engineering, ASCE, 127-148.
Komen, G.J., Cavaleri, L., Donelan, M., Hasselmann, K., Hasselmann, S., Janssen, P.A.E.M., 1994: Dynamics and Modelling of Ocean Waves. Cambridge Univ. Press, Cambridge, 532 pp.
Madsen O.S., Y.K. Poon and H.C. Graber, 1988: Spectral wave attenuation by bottom friction: theory. Proc. 21-st Conf. on Coastal Eng. 492-504.
Ris, R.C., 1997: Spectral modelling of wind waves in coastal areas. Ph.D. thesis. Delft University of Technology, the Netherlands.
Ris, R.C., L.H. Holthuijsen and N. Booij, 1999. A third-generation wave model for coastal region. 2. Verification. J. of Geophys. Res., 104, (C4), 7667-7681.
Shemdin, P., K. Hasselmann, S.V. Hsiao and K. Herteirch, 1978. Non-linear and linear bottom interaction effects in shallow water, in Turbulent Fluxes Through the Sea Surface, Wave Dynamics and Prediction, NATO Conf. Ser. V, Vol 1, 347-372
SBMSWAN (Suite 40.01.a of the Benchmark Test for the Shallow Water Wave Model SWAN Cycle 2, version 40.01), 1999. WL Delft Hydraulics. Edited by Delft University of Technology.
Weber, S.L., 1989. Surface gravity waves and turbulent bottom friction. Ph.D. thesis, Univ. of Utrecht, the Netherlands.
Weber, S.L., 1991. Bottom friction for wind sea and swell in extreme depth-limited situations. J. Phys. Oceanogr., 21, 149-172.
Willmott, L.J., 1981. On the validation of models. Physical Geography. 2 (2), 219-232
Young, I.R. and L.A. Verhagen, 1996: The growth of fetch limited waves in water of finite depth. Part 1. Total energy and peak frequency. Coastal Eng., 29, 47-78.

SWELL PROPAGATION IN SHALLOW WATER

Fabrice Ardhuin[1,2], T. H. C. Herbers[1], and W. C. O'Reilly[1]

[1]Oceanography Department, Naval Postgraduate School, Monterey, California, USA
[2]Service Hydrographique et Océanographique de la Marine, Brest, France

1. INTRODUCTION

In shallow water, random surface gravity waves are affected by sea bed features with a wide range of scales. Wave refraction over bottom features with scales much larger than the surface wavelength can induce dramatic variations in wave energy along the coast that are readily observed (e.g. Munk and Traylor, 1947). The effects of refraction on the evolution of wave spectra are generally well understood, and accurately predicted by geometrical optics models (e.g. O'Reilly and Guza, 1993). Smaller scale bottom features (one half to several wavelengths) can cause energy transfers within pairs of wave components that share the same frequency but have different directions. The mechanism for this topographic scattering is the Bragg resonance of wave-wave-bottom triad interactions (Hasselmann, 1966). It has been suggested that back scattering of swell by bottom features with wavelengths about half the surface wavelength may cause the significant swell attenuation observed near the shore (Long, 1973), and play a role in the formation of multiple sand bar systems outside the surf zone (Mei, 1985). However, high resolution bathymetric surveys in the North Sea (Richter et al., 1976) showed that the small depth variability at those intermediate scales could not explain the swell attenuation observed in the JONSWAP experiment (Hasselmann et al., 1973). Scattering of waves by random bottom irregularities is examined in more detail in Ardhuin and Herbers (manuscript submitted to *Journal of Fluid Mechanics*, hereinafter referred to as AH). AH corrected an apparent error in the coupling coefficients between waves and bottom undulations derived by Hasselmann (1966) and Long (1973), extended the theory to a sloping continental shelf, and implemented the scattering mechanism in a regional spectral wave prediction model. Numerical simulations over realistic shelf topography show that back scattering is indeed weak, but forward scattering of waves by longer bottom features, oriented at large oblique angles with respect to the direction of the wave propagation, may increase the directional spread of the wave spectrum in shallow water.

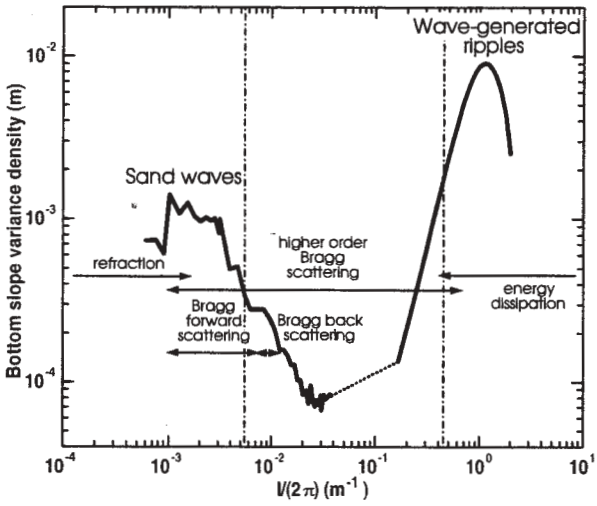

FIG. 1. Omni-directional bottom slope spectrum as a function of the bottom wavenumber l (thick curve). A composite spectrum is shown extrapolating high-resolution bathymetric surveys at larger scales to a crude interpretation of sidescan sonar images of sand ripples at smaller scales. Example wave motion scales, reciprocal wavelength $1/L_w$ and orbital excursion $1/a_b$ are indicated by vertical lines. Typical bottom wavenumber ranges important for different wave-bottom interaction processes are indicated by arrows.

Bottom features with wavelengths between the near-bottom wave orbital excursions and several surface wavelengths can cause higher order Bragg scattering. For example wave-wave-bottom-bottom quartet interactions transfer energy between waves of the same frequency and different directions (Belzons et al., 1991), whereas quartet interactions involving three wave components and one bottom component may transfer energy between waves of

AUTHOR INDEX TABLE OF CONTENTS

different frequencies. Little is known about these higher-order interactions.

Sand ripples with wavelengths slightly smaller than the wave orbital excursions near the seabed (typically of the order of 1 m) can act as roughness elements for the wave orbital motion, and strongly enhance turbulent dissipation of wave energy in the bottom boundary layer. The geological nature of the bed plays an important role in the mobility of sediments under waves, and thus bottom roughness is a function of sediment and wave properties. In contrast to the broad spectrum of bottom irregularities at large scales, sand ripples are much more regular with well-defined wavelengths and a narrow spectrum (figure 1).

The propagation of random waves can be represented in a numerical model by the evolution of the energy spectral density $E(\underline{x},\underline{k},t)$, in wavenumber space ($\underline{k}$), as a function of geographical space ($\underline{x}$) and time (t). Neglecting currents, atmospheric effects and wave-wave interactions, the evolution of E can be described by the energy balance equation:

$$\frac{dE}{dt} = S_{\text{fric}} + S_{\text{Bragg}} \tag{1}$$

where the time derivative follows a wave component along its ray trajectory $[\underline{k}(t),\underline{x}(t)]$, S_{fric} and S_{Bragg} are source terms representing bottom friction and Bragg scattering, respectively.

In previous papers, the effects of bottom friction and Bragg scattering on swell were investigated separately (Ardhuin et al., in press, hereinafter referred to as AHO; AH) using field data from the North Carolina continental shelf (Herbers et al., 2000). These processes cannot be considered independent when waves propagate over large distances. The combined effect of bottom friction and Bragg scattering on swell evolution is the topic of the present paper.

The formulation of the source terms and their local effect on the wave spectrum are described in sections 2 and 3. The wave model CREST (Coupled Rays with Eulerian Source Terms, AHO) used to integrate (1) is described briefly in section 4. Hindcasts of swell propagation across the North Carolina continental shelf are compared with observations from the DUCK94 experiment in section 5, followed by a summary in section 6.

2. BOTTOM FRICTION SOURCE TERM

For sea beds composed of non-cohesive sandy sediments, the dissipation of wave energy in the bottom boundary layer is strongly dependent on the presence of sand ripples formed by the near-bed wave orbital motion. Neglecting currents unrelated to the waves, the bottom boundary layer can be classified in three regimes, based on the ratio of viscous and buoyant forces acting on a sand grain, and represented by the Shields number ψ (e.g. Nielsen, 1981). For small values of ψ, the bottom morphology does not change, thus retaining the history of past wave events and biological activity. In this 'relict roughness' regime wave energy dissipation is minimal as bottom velocities are small and turbulence is weak. As ψ increases past a threshold value ψ_c (typically 0.05 for well-sorted quartz sand) the wave flow intermittently moves surficial sediments, that organize into ripple fields (Nielsen, 1981; Traykovski et al., 1999). These 'active ripples' sharply increase the turbulent dissipation of wave energy as vortices are shed by the orbital flow at the ripple crests. For larger values of ψ the drag coefficient decreases as ripples are eroded. For very large values of ψ (typically $\psi \sim 20\psi_c$, see Li and Amos, 1999) ripples are obliterated and a layer of sediments moves with the water column. Both the thickness of this 'sheet flow' layer and the drag coefficient increase with ψ.

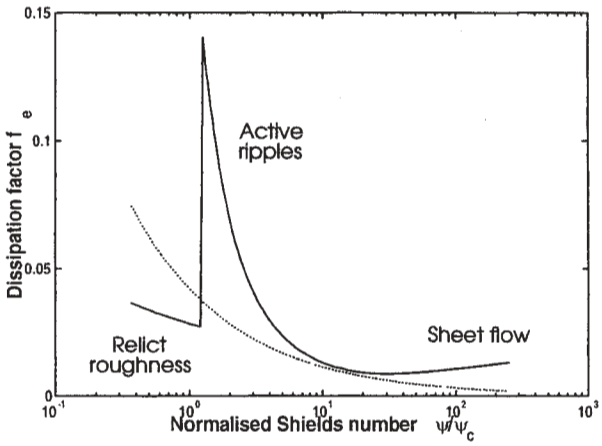

FIG. 2. Dissipation factor for a moveable bed and a swell period of 15 s (solid), is compared to the commonly used JONSWAP parameterization (dotted).

S_{fric} can be parameterized as (e.g. Tolman, 1994)

$$S_{\text{fric}} = -f_e u_b \frac{(2\pi f)^2}{2g\sinh^2(kH)} E, \tag{2}$$

where u_b is $\sqrt{2}$ times the root mean square (r.m.s.) wave orbital velocity at the top of the bottom boundary layer, k is the wavenumber magnitude, H is the local water depth, f is the wave frequency and g is the gravity acceleration. The dissipation factor

AUTHOR INDEX TABLE OF CONTENTS

f_e, shown in figure 2, can be determined from parameterizations of the roughness of ripples (k_r) and sheet flow (k_s) that depend on the near-bed orbital motion and a representative sediment grain diameter (for a review see Tolman, 1994). Comparisons with field data (AHO), showed good agreement for

$$k_r = 0.8\, a_b \left(\frac{\psi}{\psi_c}\right)^{-2.5}, \qquad (3)$$

where a_b is $\sqrt{2}$ times the r.m.s. wave orbital displacement at the top of the bottom boundary layer. The 'optimal' k_r (3) is 48% smaller than Madsen et al.'s (1990) values inferred from laboratory experiments with unidirectional waves. k_s was adopted from Tolman (1994; based on extrapolation of river flows by Wilson, 1989). For $\psi/\psi_c < 1.2$ a constant residual roughness $k_N = 0.01$ m is used, and f_e is limited to a maximum value of 0.3 (Tolman, 1994; Jonsson, 1980).

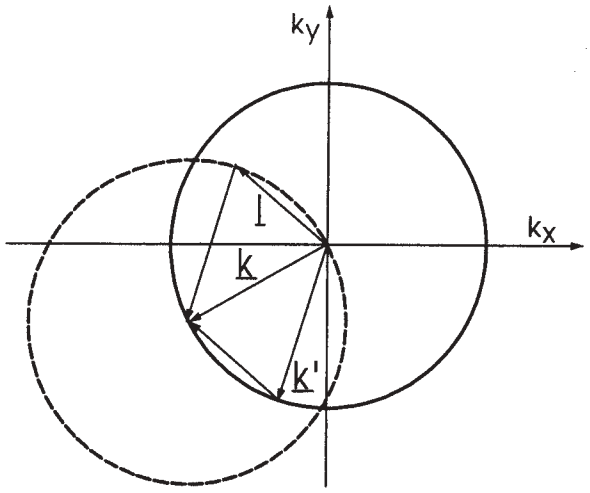

FIG. 3. Resonance condition for Bragg scattering (see text).

3. BRAGG SCATTERING SOURCE TERM

The Bragg scattering source term S_{Bragg}, first introduced by Hasselmann (1966) and Long (1973), was rederived in AH, correcting an apparent factor 4 error in the coupling coefficient:

$$S_{\mathrm{Bragg}}(\underline{k}) = K(f,H) \times \int_0^{2\pi} \cos^2(\theta-\theta')\, F^B(\underline{k}-\underline{k}')\left[E(\underline{k}')-E(\underline{k})\right] d\theta', \qquad (4)$$

$$K(f,H) = \frac{8\pi^2 k^4 f}{\sinh(2kH)\left[2kH+\sinh(2kH)\right]}, \qquad (5)$$

$$\underline{k}' = k(\cos\theta', \sin\theta'), \qquad (6)$$

$$\underline{k} = k(\cos\theta, \sin\theta). \qquad (7)$$

The bottom elevation spectrum F^B is normalized so that $\int_{-\infty}^{\infty}\int_{-\infty}^{\infty} F^B(\underline{l})\, dl_x dl_y$ is the bottom elevation variance.

Two wave components with the same frequency f but different wavenumber vectors $\underline{k}$ and $\underline{k}'$ exchange energy in a resonant triad interaction with the bottom component that has the difference wavenumber $\underline{l} = \underline{k} - \underline{k}'$ (figure 3). For a fixed $\underline{k}$, the resonant combinations of $\underline{k}'$ and $\underline{l}$ lie on two circles in the wavenumber plane (solid and dashed lines in figure 3). The factor $\cos^2\left(\theta-\theta'\right)$ indicates that there is no energy transfer between waves propagating in perpendicular directions. For a given water depth H, $K(f,H)$ has a maximum for an intermediate wave frequency (corresponding to $kH \simeq 1.27$). $K(f,H)$ increases sharply with decreasing water depth (figure 4).

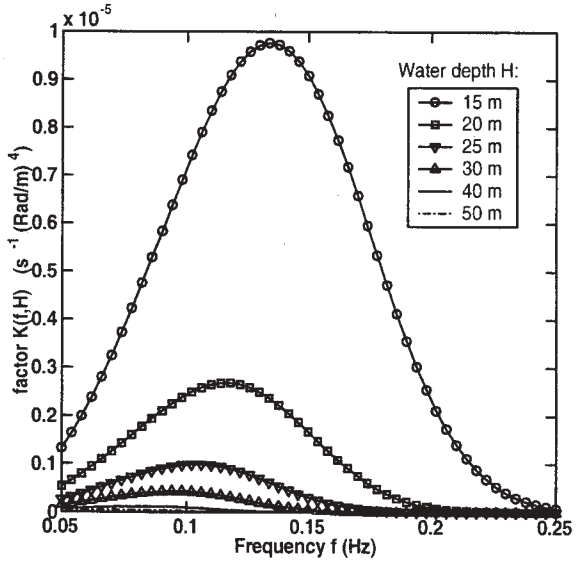

FIG. 4. Values of $K(f,H)$, defined by (5), for representative wave frequencies and continental shelf depths.

AUTHOR INDEX TABLE OF CONTENTS

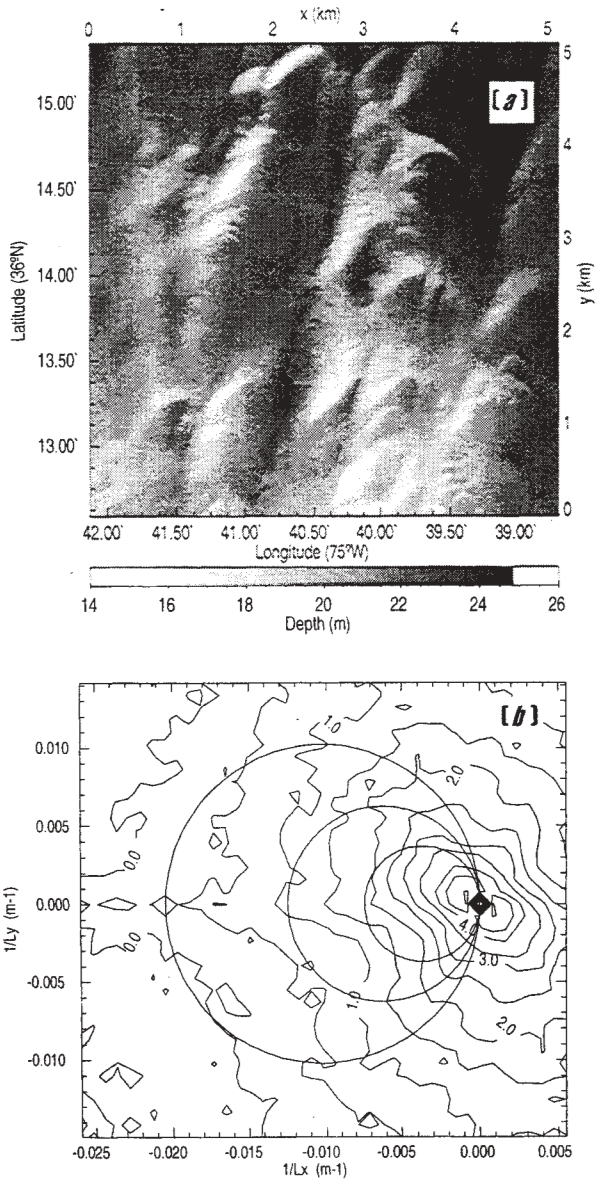

FIG. 5. (a) Multibeam bathymetric survey of a portion of the inner continental shelf off Duck, NC, and (b) contour plot of the corresponding bottom elevation spectrum, the contour values are $\log_{10}\left(4\pi^2 F^B\right)$ with F^B in $\mathrm{m^4 rad^{-2}}$. Circles in (b) indicate the bottom components that interact with waves arriving from the east with frequencies 0.05 (inner circle), 0.12 (middle circle) and 0.25 Hz (outer circle). Axis units 1/Lx and 1/Ly are reciprocal wavelengths.

The bottom spectrum F^B must be determined from high resolution bathymetric surveys. An example is shown in figure 5.

4. IMPLEMENTATION OF THE WAVE MODEL CREST

The hybrid Eulerian-Lagrangian wave model CREST (AHO) with movable bed bottom friction (section 2) and Bragg scattering (section 3) source terms was implemented for the North Carolina shelf region between 35° N and 37° N (Figure 6). The model consists of a precomputation of wave rays and a time integration scheme for the energy balance equation (1).

Wave rays are traced backwards from fixed Eulerian grid points with positions $\underline{x}_i$ to the model boundary, using a regular 6" longitude by 6" latitude bathymetry grid. This grid was derived from the National Ocean Service digital database and additional bathymetric surveys conducted during the DUCK94 experiment (Herbers et al., 2000). The bathymetry was smoothed at a scale of 2 km. The Eulerian model grid, unstructured and much coarser than the bathymetry grid, consists of 329 grid points (figure 6). For each grid point $\underline{x}_i$, rays are initially traced for 162 frequencies, at arrival direction intervals of 0.25°. For each frequency the arrival directions are subsequently bisected (O'Reilly and Guza, 1993) until neighboring rays have directions and positions at the boundary within 2° and 5 km of one another, respectively. If the number of rays for a 3° sector exceeds 500 the bisection is stopped.

The energy balance (1) is integrated in time along the ray trajectories. Along each ray, arriving at $\underline{x}_i$ with a wavenumber vector $\underline{k}$, we define a Lagrangian energy density $E^L(t,\tau)$ as the energy density 'upstream' of $\underline{x}_i$ at time t, where τ is the energy advection time from the local ray position to the grid point $\underline{x}_i$. The spectral densities E^L are averaged over ensembles of rays within finite bands $\underline{k}_j$ of the arrival wavenumbers $\underline{k}$ at $\underline{x}_i$. Here the finite bandwidths (transformed to frequency-direction space) consist of 19 frequency bands spaced exponentially with a 5% increment from 0.05 Hz to 0.12 Hz, and 120 direction bands θ_l spaced linearly over a full circle with a 3 degree resolution.

The full Eulerian energy density spectrum $E\left(\underline{x}_i, \underline{k}_j, t\right)$ at $\underline{x}_i$ is evaluated by combining the average Lagrangian density predictions $E^L(t,0)$ at $\underline{x}_i$ for all bands $\underline{k}_j$. A source term $S\left(\underline{x}_i, \underline{k}_j, t\right)$ is determined at $\underline{x}_i$ from the full Eulerian spectrum and other local parameters (e.g. sediment properties and bottom elevation spectra). S is then interpolated in $\underline{x}$ and $\underline{k}$ space to yield an approximate source term

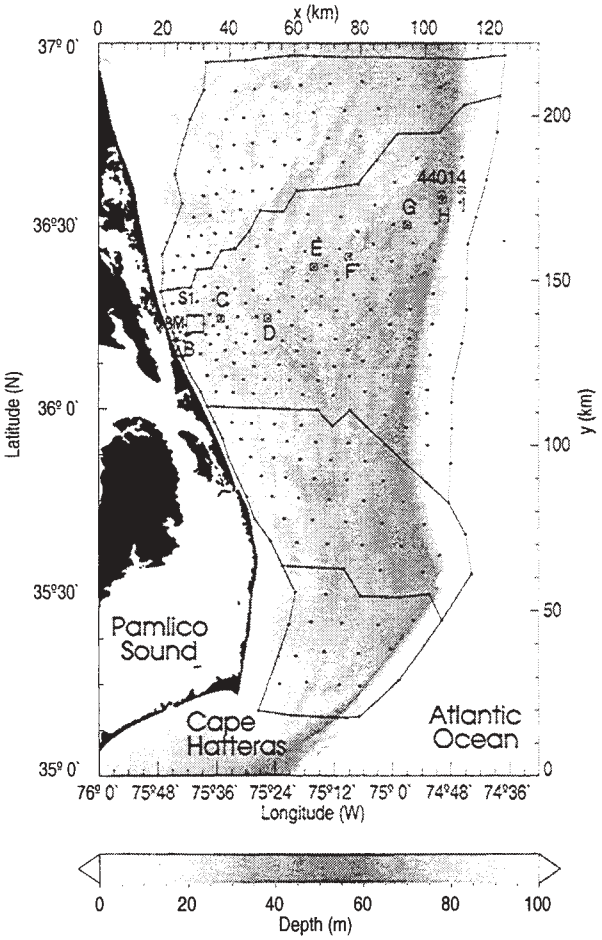

FIG. 6. Bottom topography of the North Carolina continental shelf and model grid (dots). The square marked S1 is the region enlarged in figure 5(a). Other symbols indicate deployment locations of instruments during the DUCK94 experiment, and solid lines are the internal (i.e. subdomains) and external model boundaries.

$S(t,\tau)$ at the local ray positions and wavenumbers which in turn modifies $E^L(t,\tau)$ along the rays. Rays and grid are thus coupled at $\tau = 0$ only (figure 7).

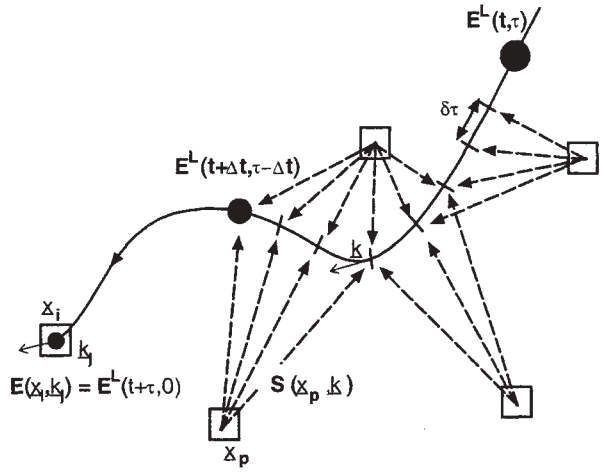

FIG. 7. Schematic of the integration of the Lagrangian energy balance equation from t to $t + \Delta t$ along a single ray (solid curve) using a spatially interpolated source term. Filled circles symbolize the magnitude of the energy density, and dashed arrows indicate the interpolation of the source term from the Eulerian grid (squares) onto the ray at increments $\delta\tau$. See text for further details.

In order to reduce the scattering of rays over large propagation distances, the model domain is subdivided into subdomains that are coupled through their common boundaries. At both internal and external boundaries the energy carried by rays into a domain is obtained by interpolation of the spectra at the boundary grid points.

All interpolation coefficients depend only on the grid geometry and bottom topography, and thus can be precomputed. Using these precomputed coefficients and a time series of wave spectra at the model open boundaries, the energy balance equation is integrated in time. Different numerical schemes are used to integrate S_{fric} (a quasi-linear formulation, AHO), and S_{Bragg} (an eigenvalue decomposition, AH) over a fixed time step $\Delta t = 10$ minutes.

5. FIELD DATA

During the DUCK94 experiment a 100 km cross shelf transect of nine bottom mounted pressure sensors was deployed extending from 12 m depth (site A) to 87 m depth (site I) (Figure 6; Herbers et al. 2000). The instrument deployed at site H in 49 m depth was located within 2 km of 3-m discus buoy

AUTHOR INDEX
TABLE OF CONTENTS

44014 operated by the National Data Buoy Center (NDBC). Between site A and the shore a pressure sensor array was operated in 8 m depth by the Army Corps of Engineers Field Research Facility, Duck, North Carolina. Other instruments on the inner shelf included current meters, thermistors and conductivity sensors in depths ranging from 4 m to 26 m. Data from these instruments show that outside the surf zone the depth-averaged currents are mostly wind-driven with speeds usually in the range 10 to 20 cm s^{-1}, and occasional stronger currents ($>$ 50 cm s^{-1}) in storm conditions (Lentz et al., 1999). These currents are generally much weaker than both the wave speeds and the near-bed orbital velocities of energetic swell in shallow water.

Wave frequency spectra are estimated from the measured bottom pressure records at sites A-I, using a linear theory depth correction. A frequency-directional spectrum $E(f_j, \theta_l)$ is estimated by combining the frequency spectrum obtained from the pressure sensor at site H, with directional distributions estimated from the nearby NDBC buoy cross-spectra using the Maximum Entropy Method (Lygre and Krogstad, 1986). This spectrum, back-refracted from site H to deep water, assuming parallel bottom contours, is used to force the model at the offshore boundary. Additional frequency-directional wave spectra on the inner shelf were estimated from the 8 m depth array near site A (Herbers et al., 1999).

Multibeam sonar bathymetric surveys were conducted during the SHOWEX experiment in November and December 1999 in two 6 km $\times$ 6 km square regions on the inner shelf. These data were processed with the MB-System software (Caress and Chayes, 1995) to obtain 10 m resolution grids. The bathymetry of one of these regions is shown in figure 5 (a), with its location on the shelf is indicated in figure 6. A bottom elevation spectrum (figure 5 b) was estimated using bidimensional Fourier transforms of 1.6 km $\times$ 1.6 km square tiles with 50 % overlap. Although the high-resolution bathymetry data was acquired four years after the wave data, it is consistent, at the larger scales, with older bathymetry data collected by the National Ocean Service (NOS) from 1970 to 1990. In the model hindcasts presented in section 5, the bottom spectrum given by the estimate in figure 5 (b) is taken to be uniform over the entire continental shelf.

Based on core samples collected in 1997 on the inner shelf (Rebecca Beavers, Duke University, personal communication, 1999), and earlier geological data covering the entire shelf (Milliman et al., 1972; Swift and Sears, 1974) we crudely approximate the bottom sediments in the entire area encompassed by the model with a thick uniform layer of fine quartz sand ($s = 2.65$), with a representative grain size $D = 0.15$ mm and a critical Shields number $\psi_c = 0.05$.

5. HINDCASTS

Hindcasts are presented for the period from October 17 to 21, 1994, characterized by well defined swell from the east with significant wave heights H_s ranging from 1 to 3 m, and low wind speeds, gradually decreasing from 10 to 2 m s^{-1} from October 17 to 19, and below 6 m s^{-1} on the following days. The peak period T_p gradually increased from 10 to 15 s between October 17 and 19, before decreasing back to 10 s on October 21.

The model was run both with and without the movable bed bottom friction source term. Runs without the source term isolate the effects of refraction and shoaling in the evolution of wave spectra, and the difference between runs with and without the source term can be used to quantify energy dissipation caused by bottom friction. Another run with both bottom friction and Bragg scattering was performed to asses the combined effects of the two processes.

Predictions of H_s with bottom friction are generally in good agreement with the observed H_s decay (Figure 8 a), while adding Bragg scattering only slightly decreases the wave height. The predicted energy dissipation rates are of the order of 1 W m^{-2}, reducing H_s by up to a factor two. The predicted dissipation is maximum during the morning of October 19 (figures 8 b and 9), when the model predicts active ripples on the entire shelf in depths shallower than 80 m. Because of the decrease of f_e with increasing Shields number (for $\psi/\psi_c < 1.2$, see figure 2), larger waves are expected to be less damped, as supported by the observed weaker decay of 9 m swells from Hurricane Gordon (AHO).

The effects of both source terms on the directional properties of the waves are quantified using standard definitions of the mean wave direction $\overline{\theta}(f)$, taken as the direction of the first-order moment vector $(a_1(f), b_1(f)) = \left[\int_0^{\pi} (\cos\theta, \sin\theta)\ E(f,\theta)\, d\theta\right] / E(f)$, and the directional spread,

$$\sigma_\theta(f) = \left[2 - 2\left(a_1 \cos\overline{\theta} + b_1 \sin\overline{\theta}\right)\right]^{\frac{1}{2}}. \qquad (8)$$

σ_θ ranges from 0 for unidirectional waves, to 81 degrees for isotropic waves. Offshore propagationg waves ($\pi < \theta < 2\pi$) are excluded in the analysis because the predicted back-scattering is weak, and

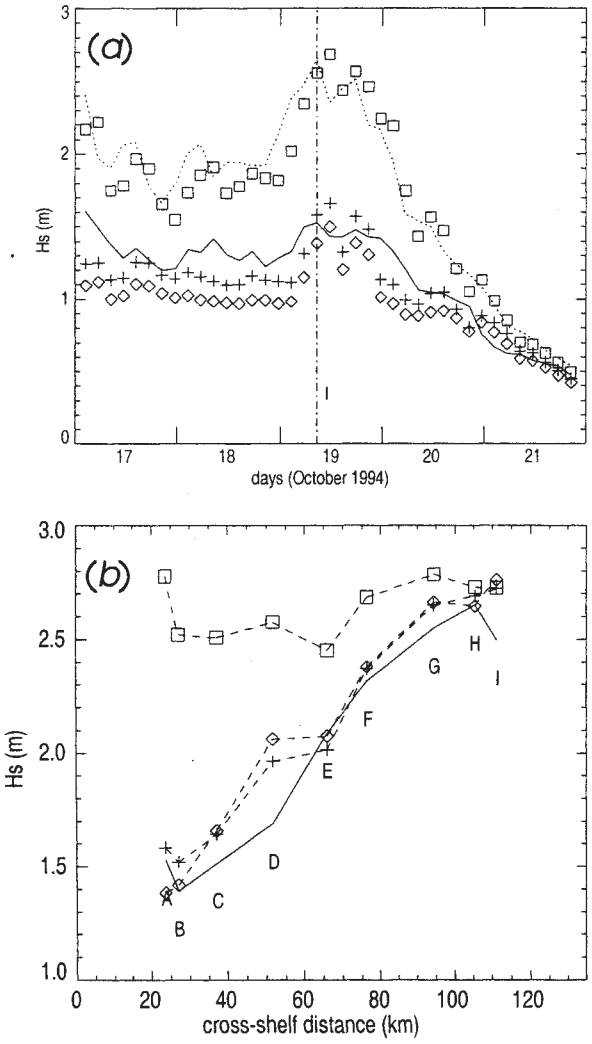

FIG. 8. Observed H_s (——) are compared to model predictions (□: without source terms, +: with bottom friction, ◇: with Bragg scattering and bottom friction). (a) Time series of H_s at site A (H_s offshore is indicated by the dotted curve). (b) cross-shelf variations of H_s at time I (indicated by the vertical dash-dotted line in a).

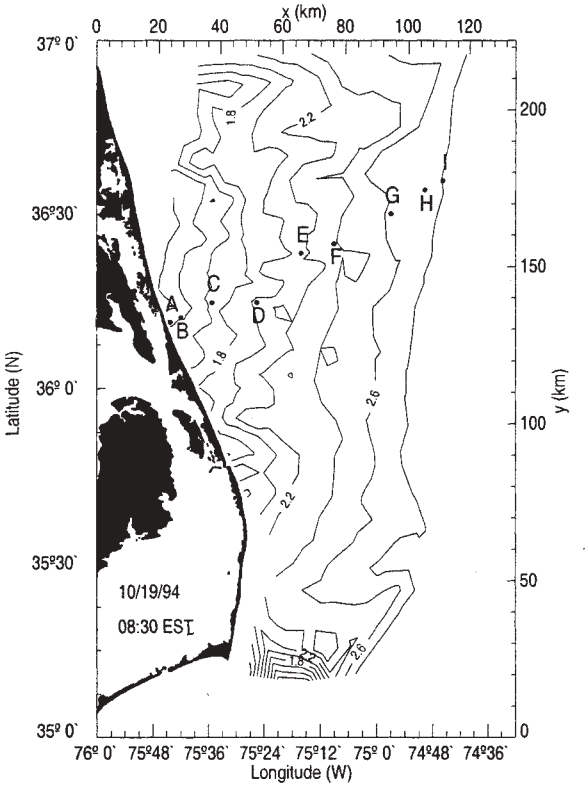

FIG. 9. Contour plot of H_s at time I (see figure 8). Contour values are in meters.

reflection from the beach is not represented in the model. Predictions of $\overline{\theta}$ and σ_θ at the peak frequency f_p are shown in figure 10 and 11.

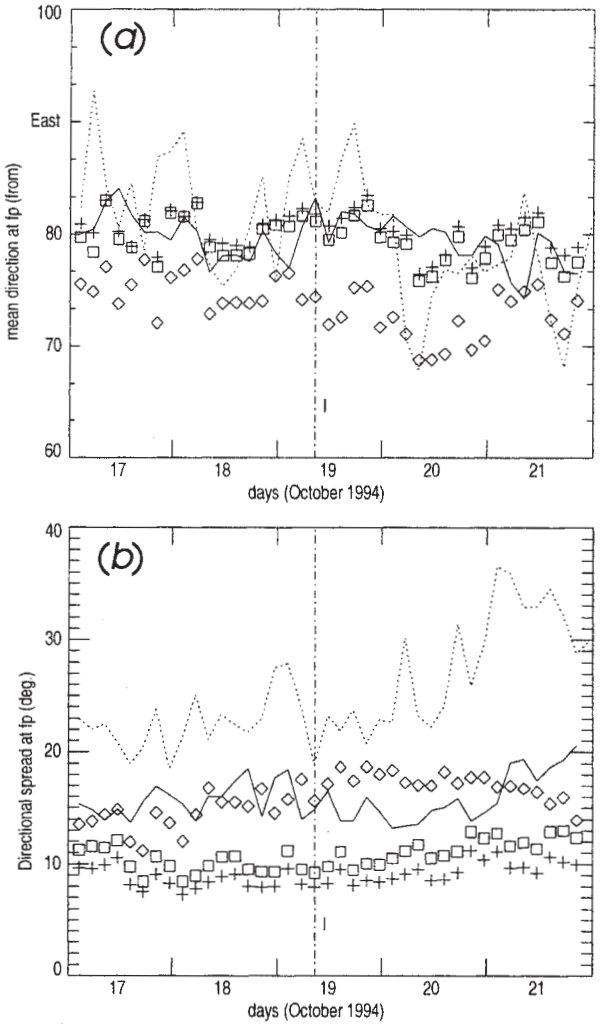

FIG. 10. Time series of (a) $\overline{\theta}$ and (b) σ_θ at the spectral peak frequency f_p, observed (——) and predicted at the 8 m array (□: without source terms, +: with bottom friction, ◇: with scattering and bottom friction). The dotted curves represent observations at the NDBC buoy 44014.

The model without Bragg scattering predicts the expected turning of $\overline{\theta}$ towards the shore-normal direction, owing to refraction by the large scale shelf slope (figures 10 a). The effects of the bottom friction source term on $\overline{\theta}$ are very small. The introduction of Bragg scattering shifts the mean wave direction by an additional 5 to 10 degrees to the north, because the bottom spectrum is not isotropic (figures 5 b). This extra shift is not evident in the observations, suggesting that either the orientation of the bathymetric features in figure (5 a) may not be representative of other parts of the shelf, or other processes, not represented in the model, may be important.

Bragg scattering has a strong effect on the directional spread, increasing σ_θ at the spectral peak by as much as a factor 2 (figure 11 a). Model predictions at the 8 m array without Bragg scattering underestimate σ_θ by 5 to 10 degrees (figure 10 b) whereas predictions with Bragg scattering are generally within a few degrees of the observed σ_θ.

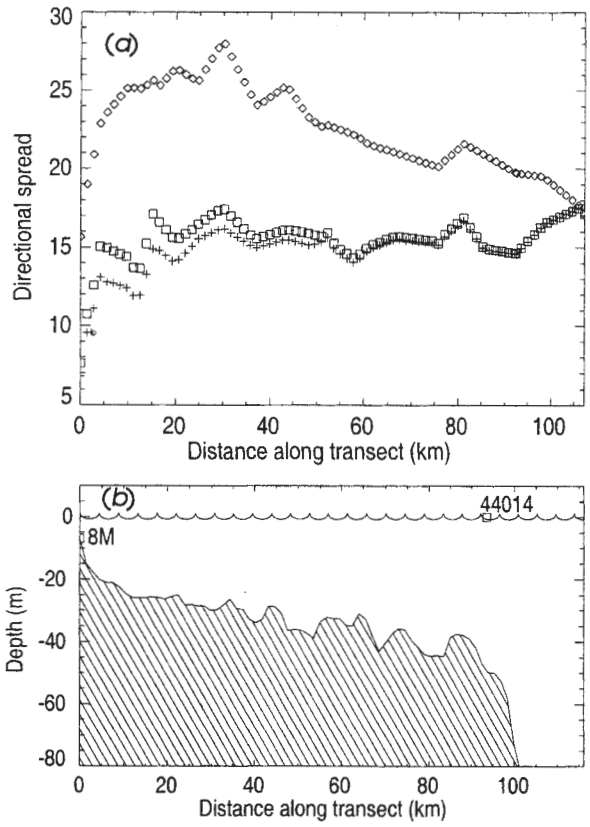

FIG. 11. (a) Predicted variations of σ_θ (f_p) at time I along a cross-shelf transect extending from the 8 m depth array to deep water offshore of NDBC buoy 44014 (same symbols as figure 10), and (b) depth profile with positions of the array (8M) and buoy (44014).

Bottom friction, although locally isotropic in the formulation given by (2), has an indirect effect on the directional spread. Indeed the time it takes the wave energy to cross the continental shelf is longer for waves that propagate at oblique angles. The damping of obliquely propagating waves is therefore enhanced, slightly reducing the directional spread of

waves (figure 10 *b*).

The model results are insensitive to the bathymetry smoothing scale in ray computations, with a typical reduction of $\sigma_\theta\,(f_p)$ by 2 degrees in the predictions presented here using the 2 km smoothed grid compared with predictions using the original 150 m resolution grid.

5. SUMMARY

Comparisons between observations and model predictions of the spectral wave model CREST suggest that the observed strong decay of swell energy across the North Carolina continental shelf is primarily the result of energy dissipation in the boundary layer over a movable sandy bed. The observed mean directions are in good agreement with predicted refraction. However, spectral refraction theory predicts directional spreads on the inner shelf that are about a factor 2 smaller than the observed values, suggesting significant scattering of waves by bottom irregularities. A source term for Bragg scattering, representing the lowest order resonant interactions between waves and bottom undulations, was tested, using a bottom elevation spectrum estimated from high-resolution bathymetric surveys in 15-30 m depth. Including wave-bottom Bragg scattering brings the predicted directional spread on the inner shelf close to observed values, but causes some discrepancies in the mean direction. Although the present calculations are somewhat qualitative, lacking accurate offshore directional wave data and shelf-wide surveys of sediment properties and small scale bathymetry, the results indicate that Bragg scattering plays an important role in the detailed evolution of directional wave spectra in shallow water, whereas moveable bed bottom friction causes variable and sometimes strong wave height decay across wide, shallow and sandy continental shelves.

Acknowledgments. This research is supported by the Coastal Dynamics Program of the Office of Naval Research and by the French Navy Hydrographic and Oceanographic Service. The DUCK94 field data were collected by staff from the Scripps Institution of Oceanography-Center for Coastal Studies and the Naval Postgraduate School. Paul Jessen contributed significantly to the wave and bathymetry data analysis. Additional wave data were provided by the Field Research Facility of the U.S. Army Corps of Engineers Waterways Experiment Station's Coastal Engineering Research Center and the National Data Buoy Center. Permission to use these data is appreciated. Multibeam bathymetry data was acquired on board the Canadian Hydrographic vessel Frederick G. Creed, as part of the Bedford Institute of Oceanography contribution to SHOWEX, with participation of F. Dobson, M. Donelan and H. Graber. T. Stanton instigated the surveys, and his involvement in, and support of the present work are greatly appreciated.

REFERENCES

Ardhuin, F., T. H. C. Herbers, and W. C. O'Reilly, 2000: A hybrid Eulerian-Lagrangian model for spectral wave evolution with application to bottom friction on the continental shelf. *J. Phys. Oceanogr.* In press.

Belzons, M., V. Rey, and E. Guazzelli, 1991: Subharmonic bragg resonance for surface water waves. *Europhysics Letters*, **16**(2), 189–194.

Caress, D. W. and D. N. Chayes, 1995: New software for processing sidescan data from sidescan-capable multibeam sonars. *Proceedings of the IEEE Oceans 95 Conference*, IEEE, 997–1000.

Hasselmann, K., 1966: Feynman diagrams and interaction rules of wave-wave scattering processes. *Review of Geophysics*, **4**(1), 1–32.

———, T. P. Barnett, E. Bouws, H. Carlson, D. E. Cartwright, K. Enke, J. A. Ewing, H. Gienapp, D. E. Hasselmann, P. Kruseman, A. Meerburg, P. Müller, D. J. Olbers, K. Richter, W. Sell, and H. Walden, 1973: Measurements of wind-wave growth and swell decay during the Joint North Sea Wave Project. *Deut. Hydrogr. Z.*, **8**(12), 1–95. Suppl. A.

Herbers, T. H. C., S. Elgar, and R. T. Guza, 1999: Directional spreading of waves in the nearshore. *J. Geophys. Res.*, **104**(C4), 7683–7693.

———, E. J. Hendrickson, and W. C. O'Reilly, 2000: Propagation of swell across a wide continental shelf. *J. Geophys. Res.* In press.

Jonsson, I. G., 1980: A new approach to oscillatory rough turbulent boundary layers. *Ocean Eng.*, **7**, 109–152.

Lentz, S., R. T. Guza, S. Elgar, F. Feddersen, and T. H. C. Herbers, 1999: Momentum balances on the North Carolina inner shelf. *J. Geophys. Res.*, **104**(C8), 18,205–18,226.

Li, M. Z. and C. L. Amos, 1999: Sheet flow and large wave ripples under combined waves and currents: field observations, model predictions and effect on

boundary layer dynamics. *Continental Shelf Research*, **19**, 637–663.

Long, R. B., 1973: Scattering of surface waves by an irregular bottom. *J. Geophys. Res.*, **78**(33), 10,987–11,004.

Lygre, A. and H. E. Krogstad, 1986: Maximum entropy estimation of the directional distribution in ocean wave spectra. *J. Phys. Oceanogr.*, **16**, 2,052–2,060.

Madsen, O. S., P. P. Mathisen, and M. M. Rosengaus, 1990: Movable bed friction factors for spectral waves. *Proceedings of the 22nd international conference on coastal engineering*, ASCE, 420–429.

Mei, C. C., 1985: Resonant reflection of surface water waves by periodic sandbars. *J. Fluid Mech.*, **152**, 315–335.

Milliman, J. D., O. H. Pilkey, and D. A. Ross, 1972: Sediments of the continental margin off the eastern United States. *Geological Society of America Bulletin*, **83**, 1315–1333.

Munk, W. H. and M. A. Traylor, 1947: Refraction of ocean waves: a process linking underwater topography to beach erosion. *Journal of Geology*, **LV**(1), 1–26.

O'Reilly, W. C. and R. T. Guza, 1993: A comparison of two spectral wave models in the Southern California Bight. *Coastal Eng.*, **19**, 263–282.

Richter, K., B. Schmalfeldt, and J. Siebert, 1976: Bottom irregularities in the North Sea. *Deut. Hydrogr. Z.*, **29**(1), 1–10.

Swift, D. J. P. and P. Sears, 1974: Estuarine and littoral depositional patterns in the surficial sand sheet central and southern Atlantic shelf of North America. *Mémoires de l'Institut Géologique du Bassin Aquitain*, **7**, 171–189.

Tolman, H. L., 1994: Wind waves and moveable-bed bottom friction. *J. Phys. Oceanogr.*, **24**, 994–1,009.

Wilson, K. C., 1989: Friction of wave-induced sheet flow. *Coastal Eng.*, **12**, 371–379.

Bed Form Response to Wave and Current Forcing During the Shoaling Waves Experiment, SHOWEX.

Timothy P. Stanton
Oceanography Department, Naval Postgraduate School
Code OC/St, NPS, Monterey, CA 93943
831 656 3144 stanton@oc.nps.navy.mil

Continuous observations of the structure of the bottom boundary layer were made at an inner shelf site for a three month period starting in October 1999 during SHOWEX. An instrumented frame with a high bandwidth data and power cables was deployed at 12m depth offshore from the Army Corp of Engineers Field Research Facility at Duck NC. Measurements on the frame included an upward-looking 5 beam ADCP to profile mean currents and estimate directional wave spectra, a 0.6 cm resolution bistatic coherent doppler profiler which measurement three component velocity profiles to over a 50cm range down to the bed, and a scanned two axis altimeter which measured the bed morphology maps over a 2m cross shore by 1m long shore area with 2cm horizontal and 0.4 cm vertical resolution, every 15 minutes.

Fine, sandy sediments were sampled at this site during the observation period with a mean 0.1mm grain diameter. In this talk two contrasting examples of bedford response to wave and mean current forcing will be shown. The observations will be compared with two models for ripple formation and the resulting wave-induced modulation of bottom friction. The effects of largely long-shore mean currents will also be considered.

NEAR SHORE BORE PROPAGATION AND SPLASHING PROCESSES: GRIDLESS SIMULATIONS.

A. Colagrossi [2], M. Landrini [2] and M.P. Tulin [1]

[1] *Ocean Engineering Laboratory*, UCSB.
[2] INSEAN, *The Italian Ship Model Basin*, Italy.

1 INTRODUCTION

Great advances have taken place in the simulation of water wave propagation by boundary element methods up through the formation of a plunging breaker, both in deep water (Wang, *et al* 1995) and in a shallow water and on beaches (Grilli, *et al* 1997).

However, it has been apparent for some time that new numerical approaches are necessary if we are to gain understanding and to simulate processes in water waves after the jet splashes down, throughout the post-breaking phase in the case of deep water waves, and continually throughout the cyclical splashing phase characteristic of bores, for instance.

The existence of an appropriate numerical approach would immediately surmount the problems which theories have long had to predict the behaviour of highly non-linear flows like bores on beaches, or high amplitude sloshing in containers, or bow waves on ships, using highly idealized mathematical methods. In fact, it is only after seeing the enormously complicated behaviour of the free surface in producing ricochets, backward facing jets, folded shapes, holes, and vortical structures, that a true appreciation of the hydrodynamic complexities can be realized.

In order to be able to simulate the post breaking behaviour of waves around ships and in their wakes, we had proposed at the OEL-UCSB the evolution of an existing gridless, Lagrangian method (SPH), which is well grounded mathematically, and we have subsequently formed an international team to carry out this development and its application, centered at the OEL.

The analysis of the breaking bore presents a natural problem to attack early, because of the availability of reference results, the richness of the fluid dynamics involved and the vigor of its splashing processes.

Actually, some of the mechanisms we have observed studying breaking bores, and which will be presented and extended in the present paper, have also been observed in deep water, both in experiments (Bonmarin 1989), and in recent numerical simulations (Tulin and Landrini 2000).

Here we present new data for breaking bores propagating on water of uniform depth, and running up along beaches with constant slope. The results seem to shed new light on the non-steady process of bore propagation and on the vortical dipole-like structures which are generated and would seem to have great consequence for bottom scouring.

2 NUMERICAL MODELING

In the following, we briefly describe the implementation of a code to study free surface flows (with breaking) based on Smoothed Particle Hydrodynamics (SPH). The method, originally introduced by Lucy (1977), has been greatly enhanced and widened in applications in the last two decades by Monhagan and coauthors (Monaghan 1992). Many theoretical studies have become available to put on a rigorous basis the convergence of the method (see Mas-Gallic and Raviart 1987, Di Lisio *et al.* 1998, Moussa and Villa 2000).

The basic idea is to consider a set of N particles with mass m_j distributed over the bulk of fluid Ω, as in the example of Figure 1. Each particle is characterized by a kernel δ_ϵ: a kind of shape function which is symmetric, regular, nonnegative, and centered on the particle position, Figure 2. The mass and the other physical information carried by each particle are "smoothed" (averaged) through the kernel over its spatial support.

Each particle moves in the force field generated by the whole particle system and the physi-

cal quantities evolve according to suitable evolution laws following from the original differential field equations.

The essential features of the resulting algorithm is the complete absence of a computational grid, and a fully Lagrangian character; see Belytschko *et al.* (1994) for a discussion of Eulerian gridless methods.

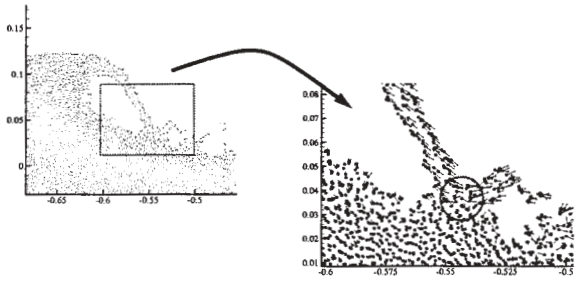

Figure 1: Typical distribution of particles, •, in a free-surface flow. In the enlarged detail, the circle represents the radius of interaction of a generic particle.

2.1 Basic SPH Equations

Let us consider the field $f(\boldsymbol{P})$ of a physical quantity. A regularized representation of $f(\boldsymbol{P})$ is given by the interpolation integral

$$\langle f(\boldsymbol{Q})\rangle = \int_{\Omega} f(\boldsymbol{P})\,\delta_{\epsilon}(\boldsymbol{Q}-\boldsymbol{P})\,d\Omega_P \qquad (1)$$

The parameter ϵ represents a measure of the spreading of the kernel over the space and it is assumed that $\delta_{\epsilon}(\boldsymbol{Q}-\boldsymbol{P})$ converges to a Dirac delta-function as the parameter $\epsilon \to 0$. It is not necessary, though computationally effective, that the kernel has a compact support (*i.e.* it is identically zero beyond a certain distance from the particle). In any event, the choice of the kernel is quite important in determining the stability properties of the discrete method (Morris 1997). In our computations we adopted spline kernels either of third or of fifth order, with 30 to 50 particles inside the interaction radius of each particle (*cf.* the circle in Figure 1). The resulting total number of particles depends on the application considered, in some cases being of order of 10^5.

Upon inserting (1) in the Euler Equations, after some manipulations, we get the following evolution equations for the density ρ_i and the velocity

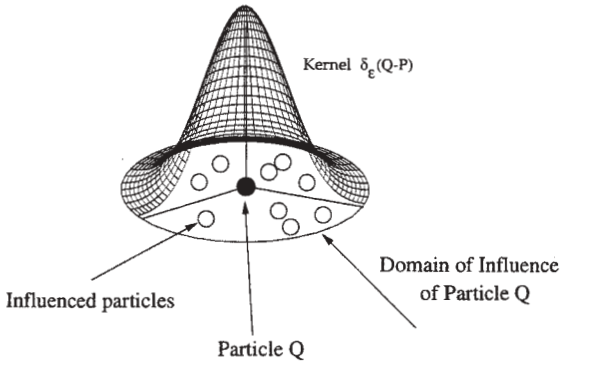

Figure 2: Schematic view of the kernel δ_ε centered on the particle $\boldsymbol{Q}$.

$\boldsymbol{v}_i$ of the $i-$th particle located at point $\boldsymbol{P}_i$:

$$\frac{\mathrm{d}\rho_i}{\mathrm{d}t} = +\sum_{j=1}^{N} m_j\,(\boldsymbol{v}_i-\boldsymbol{v}_j)\cdot\nabla_i\delta_{\epsilon}(\boldsymbol{P}_i-\boldsymbol{P}_j)$$

$$\frac{\mathrm{d}\boldsymbol{v}_i}{\mathrm{d}t} = -\sum_{j=1}^{N} m_j\left(\frac{p_i}{\rho_i^2}+\frac{p_j}{\rho_j^2}\right)\nabla_i\,\delta_{\epsilon}(\boldsymbol{P}_i-\boldsymbol{P}_j)+\boldsymbol{g} \qquad (2)$$

p_i being the pressure. It has to be noted that the fluid has been modeled as a compressible fluid and for real gases an energy equation can be consistently written down. For the present purposes, we will consider a state equation of the form

$$p = B\left(\frac{\rho^{\gamma}}{\rho_0^{\gamma}}-1\right) \qquad (3)$$

with $\gamma = 7$ and B tuned to have a negligible compressibility, Monaghan (1992). In practical computations, the largest density fluctuations are of order $10^{-2}\rho_0$. It is worth stressing that the use of a weakly compressible fluid is not unusual in other fields of computational fluid mechanics and, in the present case, it is essential to avoid a wrong evaluation of the smoothed density field when approaching boundaries. Also to be noted is the symmetric structure of the discretized momentum equation which ensures linear and angular momentum conservation.

Finally, an artificial bulk viscosity term has been introduced in the discretized pressure gradient with the sole purpose to increase the stability properties of the numerical algorithm.

The resulting evolution equations can be

stepped forward in time by any ODE integrator. In the present implementation, a second-order predictor-corrector scheme is adopted with a dynamic choice of the time step according to stability constraints. Kinematic constraints, *i.e.* small distance $\boldsymbol{P}_i - \boldsymbol{P}_j$ between particles with respect to $(\boldsymbol{v}_i - \boldsymbol{v}_j)\delta t$, can require easily an extremely small time step δt (not required by the physics or by the stability). Therefore, we employed an individual time-stepping algorithm to let the particles evolve hierarchically according their own time step (Hernquist and Katz 1989).

Although the particle evolution equations (2) are coupled, the forcing term for each of them can be evaluated independently of the others, and without the solution of an algebraic system (as in most of the discretization method for PDEs). Therefore, the memory requirement is just proportional to the number N of the particles, and the algorithm is well suited for use on parallel computers.

Some more technical details such as fast searching algorithms for efficient particle interaction (which presently requires $N \log N$ operations), enforcement of boundary conditions by ghost particles and renormalization will not be discussed here, though they play a crucial role in the algorithm. More worth stressing is the great potential of this rather "young" method, which is suitable in principle to handle multi-phase flows, weak compressible effects (acoustics), and surface tension. Also, the extension to three-dimensional flows does not suffer theoretical constraints, though it is computationally demanding.

The numerical method described above has been implemented for two-dimensional flows in a code called *SPlasH*. A large variety of applications to violent free-surface flows (notably the dam breaking and sloshing flows with fluid-solid impacts) have been tested, and compared with solutions by other solvers, and will be reported elsewhere.

All the computations presented have been performed by PCs based on Pentium III 700MHz, required 24-72 hours CPU-time and memory never exceeded 50 MBytes.

3 BREAKING BORES

We first study the genesis and the propagation of breaking bores along water of uniform depth. The model problem selected is sketched in Figure 3: the flow starts with a semi-infinite layer of fluid, depth h_0, forced into motion by a vertical piston, moving from left to right with constant speed U. At the beginning of the simulation, a smooth ramp-function for the piston velocity has been used to prevent the irrelevant (for our purposes) formation of a jet at the solid boundary.

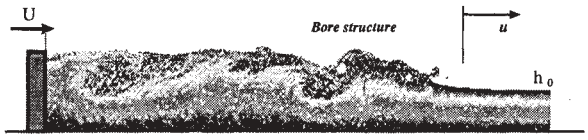

Figure 3: Sketch of the bore generated by a piston moving horizontally with velocity U in a layer of fluid with initial depth h_0.

3.1 Validation

A typical initial evolution is shown in Figure 4 for $U/\sqrt{gh_0} = 0{\cdot}8$. The particles used in the simulation are plotted together with the free surface profiles obtained by a Boundary Element Method (BEM), and are colored according to their initial distance from the bottom; this will make easier the description of the breaking events and readily gives an idea of the strong mixing processes involved. After the piling up of the water against the piston, a long wave starts to propagate with velocity of order $\sqrt{gh_0}$ and soon steepens, overturns and breaks with a large plunging jet impacting onto the underlying free surface. The good agreement between the two solution methods is apparent for all the configurations reported. The breaking of the free surface prevents the BEM to further follow the evolution of the flow field.

Actually, for small $U/\sqrt{gh_0}$, an undular bore would always appear, reconciling the initial unperturbed water level with the higher one behind it, and can be accurately described by boundary integral equation methods. Here we are interested in surface breaking, and we will consider the range $0{\cdot}5 \leq U/\sqrt{gh_0} \leq 0{\cdot}95]$, for which the wave front steepens rapidly, overturns, and evolves into a breaking bore.

For breaking bores the transition from undular-breaking bores and fully developed breaking bores is gradual and, in our simulations, for $F_0 = 1{\cdot}37$ (*cf.* Table 1) we still observe a train of smooth, long undulations downstream of the break-

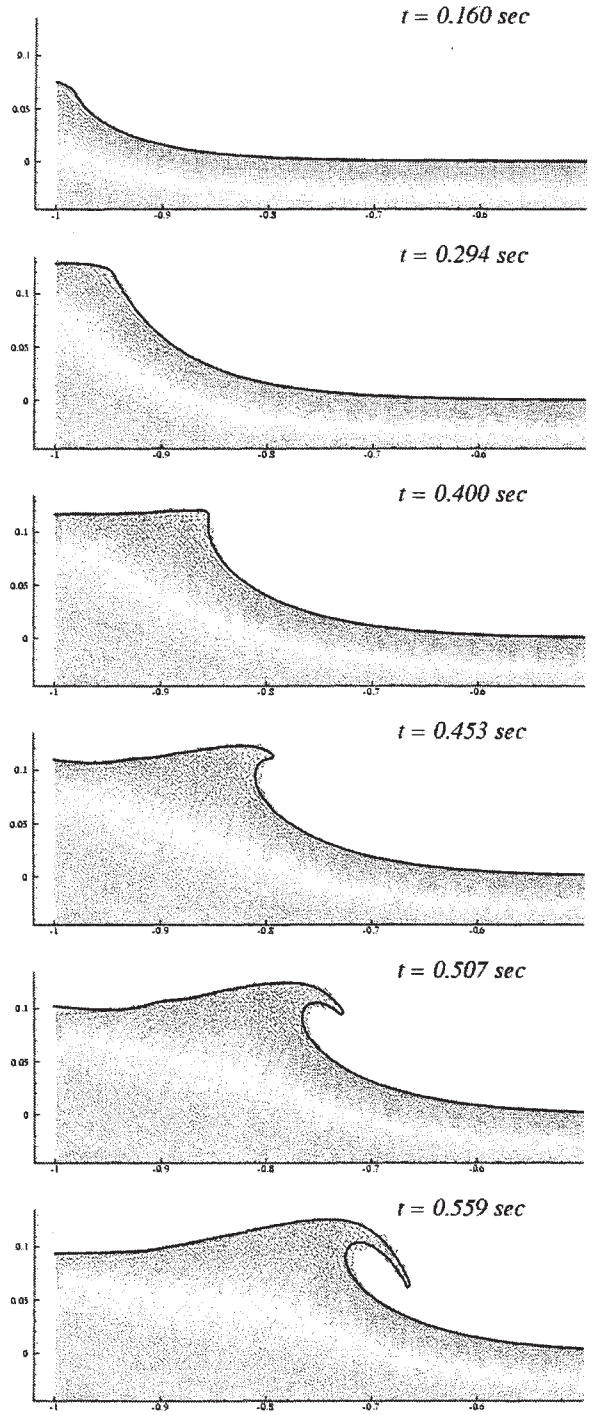

Figure 4: Initial evolution of the free surface motion induced by a vertical piston in steady forward motion, $U/\sqrt{gh_0} = 0{\cdot}8$. The resulting Froude number is $F_0 = 1{\cdot}66$. The coordinate system is moving with the piston, and the unit length equals $10h_0$. The free surface profiles are obtained by BEM (black solid lines). The particles from *SPlasH* computations are colored according to their initial vertical height.

ing front. Increasing the velocity of the piston, the undulations disappear and only fully developed breaking bores are observed. This result is consistent with the observations of Miller (1968), who fixed the transition between undular non-breaking bores and fully developed bores in the range $1{\cdot}35 \leq F_0 \leq 1{\cdot}55$.

After an evolution long enough, the global pattern is characterized by a breaking front moving with constant velocity, separating two layers of water with mean levels h_0 and h_1, downstream and upstream respectively. In this condition, by using mass and momentum conservation, the dimensionless velocity of the bore can be related to the water depths,

$$F_0^2 = (\frac{u_{\text{th}}}{\sqrt{gh_0}})^2 = \frac{1}{2}\left(\frac{h_1}{h_0}\right)\left(1+\frac{h_1}{h_0}\right) . \quad (4)$$

In simulation (as well as in experiments), the front of the bore is not sharply defined. We found that, after an initial transient, the averaged velocity of the front is constant. The data from *SPlasH* simulations are collected in Table 1, and compared with the theoretical prediction (4).

$U/\sqrt{gh_0}$	h_1/h_0	F_0	u_{SPlasH}/u_{th}
0·95	2·12	1·82	1·006
0·9	2·1	1·8	1·000
0·8	1·9	1·66	0·994
0·7	1·8	1·59	1·000
0·6	1·7	1·52	0·980
0·5	1·5	1·37	1·015

Table 1: Comparison between the computed velocity, u_{SPlasH}, of the bore front and the theoretical value, u_{th}, predicted by global mass and momentum conservation, *cf.* Equation (4).

The agreement is generally within 1%, and 2% at maximum. It is perhaps surprising that such good agreement is found from an Euler computation for a flow which is considered highly dissipative.

Our rather accurate results strongly suggest that inertial (Euler) effects may dominate the observable phenomena, including strong mixing of surface water when passing through the bore and the creation of a structured wake continuing considerable kinetic energy in fluctuations.

The model problem under analysis is the same as in Miller's (1968) experiments. Interest-

ingly, he observed (*cf.* his Figure 4) a larger dispersion of the measured velocity u_{front} around the theoretical prediction, with the scattering of measured data increasing extremely for bores with $h_1/h_0 > 2$. The author ascribed this difficulty to the turbulence and aeration of the front, preventing accurate determination of the bore velocities.

3.2 Splash-up cycles and formation of vortical structures

The post-breaking evolution for $F_0 = 1{\cdot}66$ is described thoroughly in Figure 5. At first, attention will be focused on splash-up cycles and on the related genesis of vortical structures. In plot A, the plunging jet has just touched the front face of the free surface, and the closure of the cavity gives rise to first, a clockwise rotating structure, plots B-C. The impinging jet is also feeding the splash-up *I*, plot B, which grows in the form of a mushroom-like upwelling structure, plot C. A second plunging event is already detectable, giving rise to a second clockwise rotating structure, which, with a different rate of growth, assists in the formation of a backward facing jet.

The formation of the mushroom-like structure, and the growth of the backward jet, are essentially related to the gravitational collapse of the mass of water which, deflected upward by the impact, eventually falls down, plots C-D. The further evolution of the backward-facing jet, impacting with the free surface, plot E, results in a counter-clockwise vortex, close to the first one, thus giving origin to a dipole-like structure under the free surface.

In the meantime, the second plunging breaker causes the growth of the splash-up *II*: in plot D a less defined forward plunger is still detectable, while the formation of a second backward facing jet already appears in plot E, eventually leading to a new counter-clockwise vortex, plot G, and forming a second dipole-like structure.

The splash-up *III* in plot F is less vigorous: the forward jet is rather weak and thin and the backward flow, still detectable, is more in the form of a layer of fluid shearing over the clockwise structure originated by *II*. In the following evolution, not shown, we observed other splash-up cycles similar to *III*.

The strength of the backward jet, indeed, determines the type of the interaction with the free surface. Energetic backward jets result in strong counterclockwise vortices, and dipole-like structures are formed, often propagating downwards below the free surface, and somtimes reaching the bottom. Air entrapment is likely to occur, with surface water also captured within the submerging dipole (see the dipole-like structures in plot H). This type of interaction resembles MODE B observed by Bonmarin (*cf.* Bonmarin 1989, Figure 25) for breaking surface waves in deep water. For weaker backward jets, the interaction is more in the form of a layer of fluid surfing on top of the free surface (closer to MODE A in Bonmarin's paper). This is shown in plots G-H where the splash-up *III* divides into forward and backward moving layers, the latter remaining at the surface giving rise to a shear layer. In this case, though vorticity of opposite sign is generated, the dipole structure is not sharply defined, and positive and negative vorticity remain closer to the free surface.

Finally, plots in figure 6 give a closer view of the velocity field in the splash-up regions *I* and *III*, respectively. The first shows better the gravitational collapse leading to the formation of an intense backward-facing jet and to MODE B interaction. This back-flow is weaker for splash-up *III*, resulting in a shearing layer on the top of the left-most clockwise structure, MODE A.

In the above description, the genesis of each vortical region is connected with a folding over of the surface to create a doubly connected region and this is crucial to the generation of vorticity and circulation. At the same time air is entrained, which is not accounted for in these calculations, and which can alter the fine details of the evolution. It can be speculated that the downward motion of the dipole structures is altered by buoyancy effects associated with the bubbly phase entrapped into the rotating cavities. SPH can deal with a fluid of varying density and, in principle, it is possible to include such effects, although the accurate estimation of the actual local change in fluid density through local air entrainment is a problem into itself.

It is not evident how to correlate the unsteadiness of the flow field for different speeds of the forcing piston. The approach we have taken is to count the frequency of creation of the forward splashes. These tend to pair with backward splashes creating dipole-like structures, except when the backward splash is very weak. If N is the number of forward splashes generated in

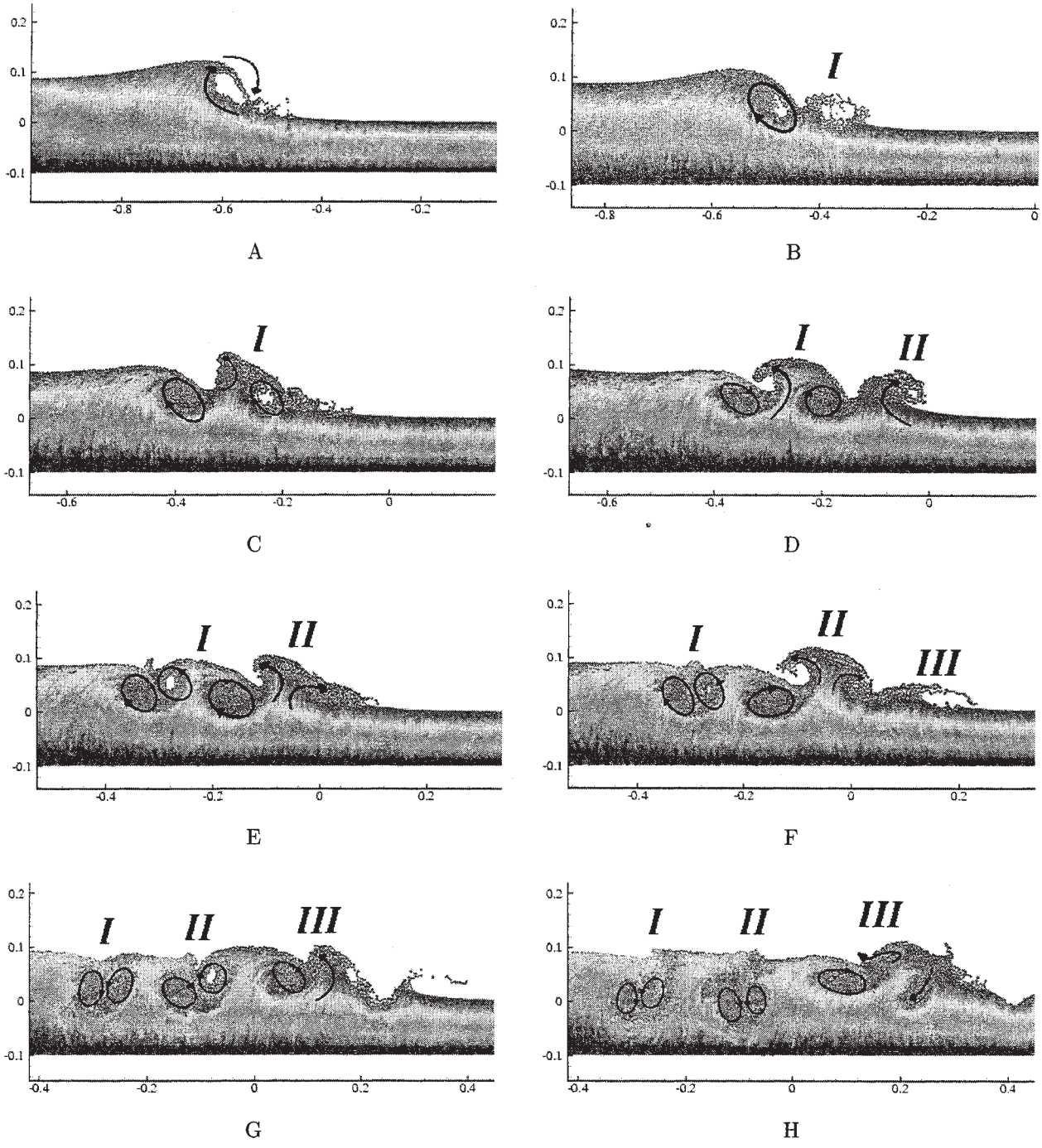

Figure 5: Further evolution of the case presented in Figure 4. Only SPH computations are reported. Plots A through H correspond to t =0·693, 0·853, 1·067, 1·2, 1·28, 1·36, 1·493 and 1·627, respectively. Time is expressed in seconds.

time Δt, the average period of shedding is

$$T_s = \frac{\Delta t}{N},$$

and an appropriate dimensionless period is

$$\overline{T}_s = \frac{T_s u}{h_1 - h_0}.$$

The results of this analysis reveal a value for $\overline{T}_s$ averaging about 4 for the conditions studied:

F_0	0·5	0·6	0·7	0·8	0·95
$\overline{T}_s$	3·7	3·68	4·62	4·2	3·75

An example of the vortical structures generated is given in Figure 7, where the breaking front is followed for $F_0 = 1{\cdot}66$ and the rotational areas, evidenced by the black contours, are numbered in inverse order with respect to their age. Also to be noted is the tendency of the structures to pair during their evolution.

3.3 Impact and ricochet of the plunging jet

The forced breaking bore features repeated plunging events, which is also typical of breaking in shallow water as in the case of wave trains approaching a beach. A detailed description of the first plunging event is instructive, also for deep water breaking waves, and is given through the plots of Figure 8.

In particular, we have chosen the reference configuration in the top-left plot and we have assumed that the jet is formed by those particles within the area delimited by the free surface and the vertical line tangent to the nascent loop beneath the jet. These particles are colored in black. In the following plots the motion of these particles is easily tracked, thanks to the Lagrangian character of the SPH. During the free falling phase, because of mass conservation, the jet is stretched and reduced in thickness. At impact, the jet-particles flow into two separated streams, plot C. One is deflected inside the loop, and the other one contributes to the formation of the splash-up. Up to this point, the plunger is still fed only by fresh particles (colored in red, plot D) which will undergo the same evolution as the black particles. In later stages, the particles earlier entrapped by the clockwise structure, will complete one revolution and (partly) re-contribute to the impinging jet, plots D-E, implying a strong mechanical mixing.

Those particles, earlier entering the splash-up, now evolve into a new plunger and are again split into a portion captured by a second clockwise structure and a remaining one forming the splash-up I in plot C of the previous Figure 5.

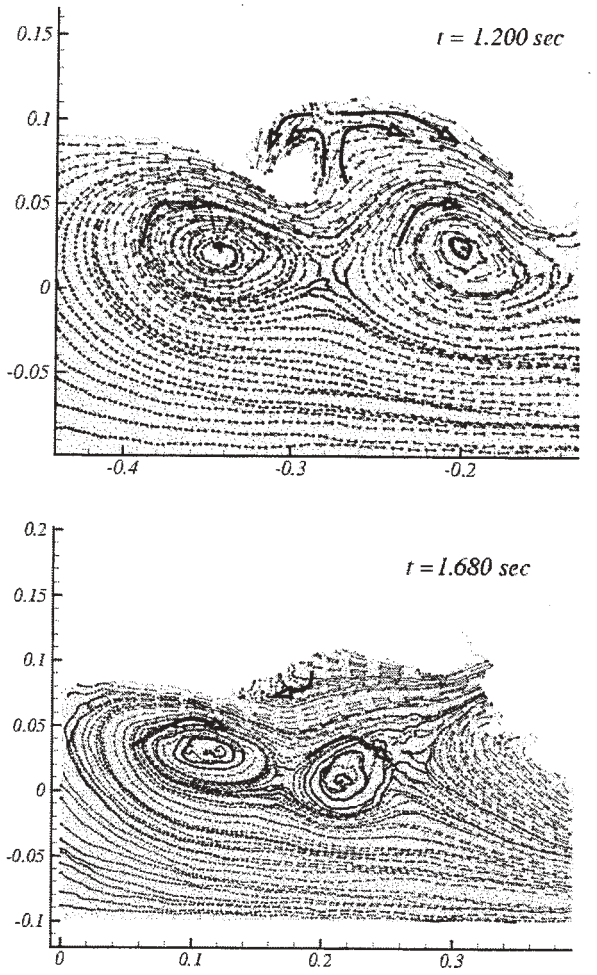

Figure 6: Close view of the velocity field in the splash-up. Top: MODE B interaction for splash-up I in Figure 5. Bottom: MODE A interaction for splash-up III in Figure 5. Black arrowed lines give an indication of the overall direction of motion.

It can be seen, that a portion of the particles originally in the first plunger are now riding on the moving front of the propagating wave, while the others are captured by the cavities and effectively mixed with other portions of fluid. In following cycles, all the tracked particles will be captured by the rotating structures and fresher particles will feed the bore front.

A more quantitative analysis is obtained by the two bottom plots, where the components of the

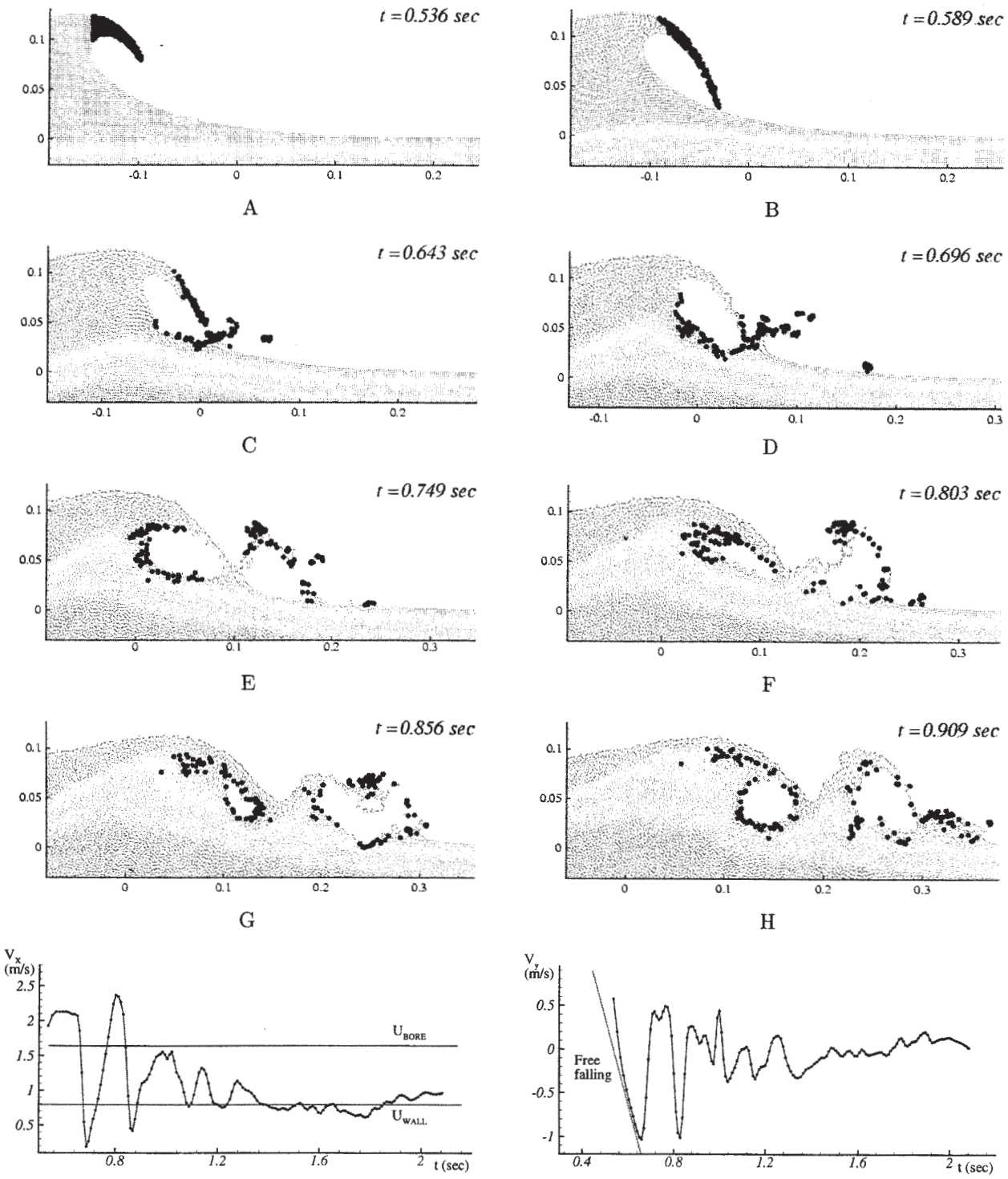

Figure 8: Evolution of the particles originally forming the jet (marked by black symbols). The two bottom diagrams show the time evolution of the horizontal (left) and of the vertical (right) components of the fluid momentum within the jet.

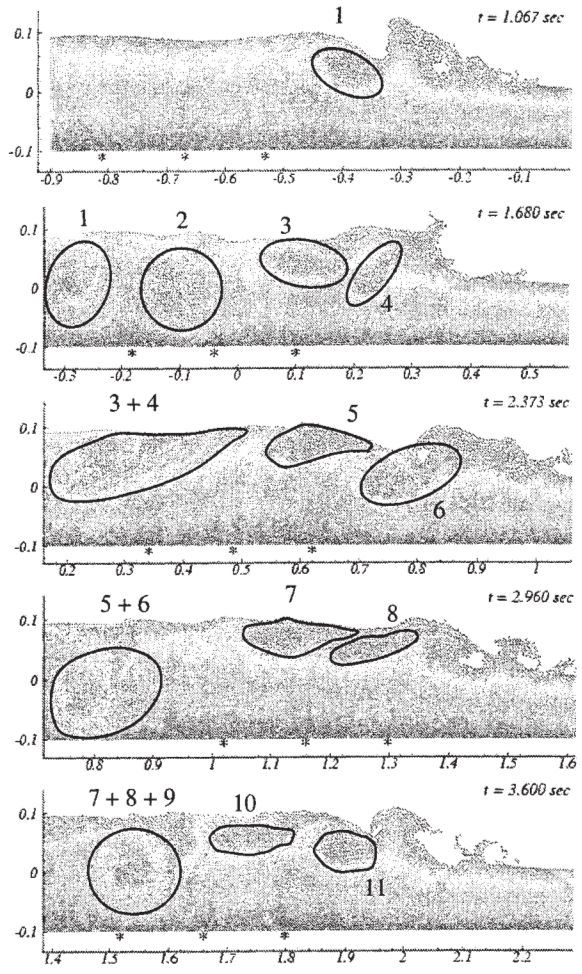

Figure 7: Tracking of vortical structures generated during the splash-up cycles in case of $F_0 = 1{\cdot}66$.

velocity of the center of mass of the jet-particles

$$\boldsymbol{V}_c = \int_{\text{jet}} \rho \boldsymbol{v}\, \mathrm{d}A \Big/ \int_{\text{jet}} \rho\, \mathrm{d}A \qquad (5)$$

are plotted in time. The free fall stage in the first part of the jet-evolution can be clearly seen in the right plot, and accompanied by an almost steady translation in the horizontal direction (*cf.* left plot). The instant of the impact is evidenced by sharp changes of $V_{c,x}, V_{c,y}$. The first drops down to less than 25% of its initial value: this corresponds to the splitting of the jet into two portions with backward and forward motion, balancing each other and thus reducing $V_{c,x}$. The vertical component bounces up, changing in sign, because both portions are moving upward, and then oscillates consistently with the orbital motion of the particles entrapped in the cavities. Eventually, $V_{c,y}$ attains an almost zero value, with small amplitude oscillations related to the orbital motion inside the vortical structures rotating in an uncorrelated way. After some oscillations with decreasing amplitude, due both to the orbital motion and to the multiple splash-up, the horizontal component attains the uniform velocity of the moving piston.

We have analyzed several cases in the range $1{\cdot}37 \leq F_0 \leq 1{\cdot}82$. For larger F_0, a more vigorous formation of the backward plunging jet and MODE B interaction has been observed, with initial formation of stronger dipole-like structures, followed by a predominance of MODE A interaction with vortical regions more confined to the free surface. In the simulation with $F_0 = 1{\cdot}82$, we observed stronger plungers, with splash-up and MODE B interaction. A slower motion of the piston leads to less pronounced splash-up cycles, resulting in weaker vortical structures of opposite sign, mainly due to MODE A interaction. For $F_0 < 1{\cdot}52$, the dipole-like structures are never observed. With the exception of $F_0 = 1{\cdot}82$, MODE B appears connected with the initial breaking events, when the most energetic plungers are generated.

4 BORES ON BEACHES

The problem of the run-up of waves on sloping beaches is widely treated because of its practical importance: coastal erosion, flooding, for example. Here we present some results for fully developed bores climbing up beaches with constant slope. Following Miller (1968), the simulation starts with a piston which, after a smooth acceleration, reaches its final velocity. After a suitable time, the piston stops its forward motion, leaving a breaking bore propagating shoreward, running up, and eventually collapsing down after reaching the shoreline. A sketch of the model problem with the relevant parameters is given in Figure 9.

This evolution is better described in Figure 10, for $U/\sqrt{gh_0} = 0{\cdot}8$ and a beach with constant slope $\alpha = 3°$. In this case, h_0 is the uniform depth before the sudden change in the slope. In the top figure, the bore front is seen propagating along an essentially unperturbed layer of water with decreasing depth. The typical character of the bore, a steep jump reconciling water of different depths, is preserved in the second plot and even in the third, where it has almost reached the shoreline. Thereafter breaking seems to cease, Figure 10 e). It is interesting to observe that the flow, from the shoreline on, resembled that after a dam break: for this,

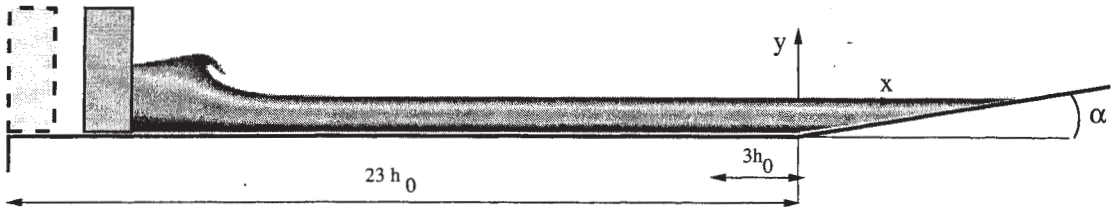

Figure 9: Numerical simulation of a breaking bore climbing an inclined beach. The piston starts to move, and to stop $23h_0$ and $3h_0$, respectively, from the beach.

shallow water theory (Stoker 1957), experiments, and our own numerical simulations, not reported here, show the water front propagating smoothly along the beach without breaking.

Figure 11 presents the flow field patterns for increasing slope of the beach, from bottom up, and the same instant of time from the beginning of the simulation. In particular, for the steepest beach, top plot, the bore has already reached the shoreline and it is on the point to collapse in a way similar to previously shown. For $\alpha = 6°, 3°$ (lower plots), the bore front is increasingly farther and farther from the shoreline. In all cases, the front of the bore is practically located at the same abscissa, showing a limited role of the beach slope in altering the bore celerity. It is remarkable that the structures of the bore front are so similar despite the different beach angles.

Therefore we have to conclude that the bore splashing structure is hardly affected by the beach up until the bore runs out of water ahead of it at the shoreline. Only then does the bore cease, and transition takes place into the dam-break type, advancing wedge flow, above the shoreline.

5 SUMMARY AND RESULTS

A numerical code, *SPlasH*, to simulate flows with breaking and free surface fragmentation has been developed and applied to study the genesis and evolution of breaking bores running on a uniform bottom. The code is based on a gridless particle method, SPH, for the Euler equations and features a Lagrangian character which allows to track in detail the complex dynamics of the breaking bore front.

Splash-up cycles and their connection with the genesis of vortical structures downstream the bore are discussed in detail. The presence of vortical structures of opposite sign is detected and is related to the splash-up mechanics, characterized by the formation of mushroom-like upwelling structures with one branch folding backward and creating circulation of opposite sign with respect to the forward plunging breaker.

A remarkable feature of the observed motion is the complex behaviour of the free surface, in folding over, thereby creating holes, circulation, and vorticity shed into the wakes, forming coherent structures. These result in large scale convection and mixing of fluids, impact on the bottom, and scouring velocities there.

The investigation is extended to the case of breaking bores climbing sloping beaches and the mechanics of propagation through the shoreline is observed. It is striking that the essential character of the bore which propagates through splash-up cycles is preserved up to the shoreline, but that the splashing ceases when the bore reaches the dry beach; after that the front seems to propagate smoothly and without breaking, and resembles the motion after a dam break.

ACKNOWLEDGEMENTS

This work has been supported as part of a program for the simulation of ship breaking waves by the Ship Hydrodynamics Program of ONR under Dr. Ed Rood.

REFERENCES

Belytschko T., Lu Y.Y. and Gu L. (1994), Element free galerkin, *Int. J. Num. Meth. Eng.*, Vol. 37, pp. 229-256.

Bonmarin P. (1989), Geometric properties of deep-water breaking waves, *J. Fluid Mech.*, Vol. 209, pp. 405-433.

Di Lisio R., Grenier E. and Pulvirenti M. (1998),

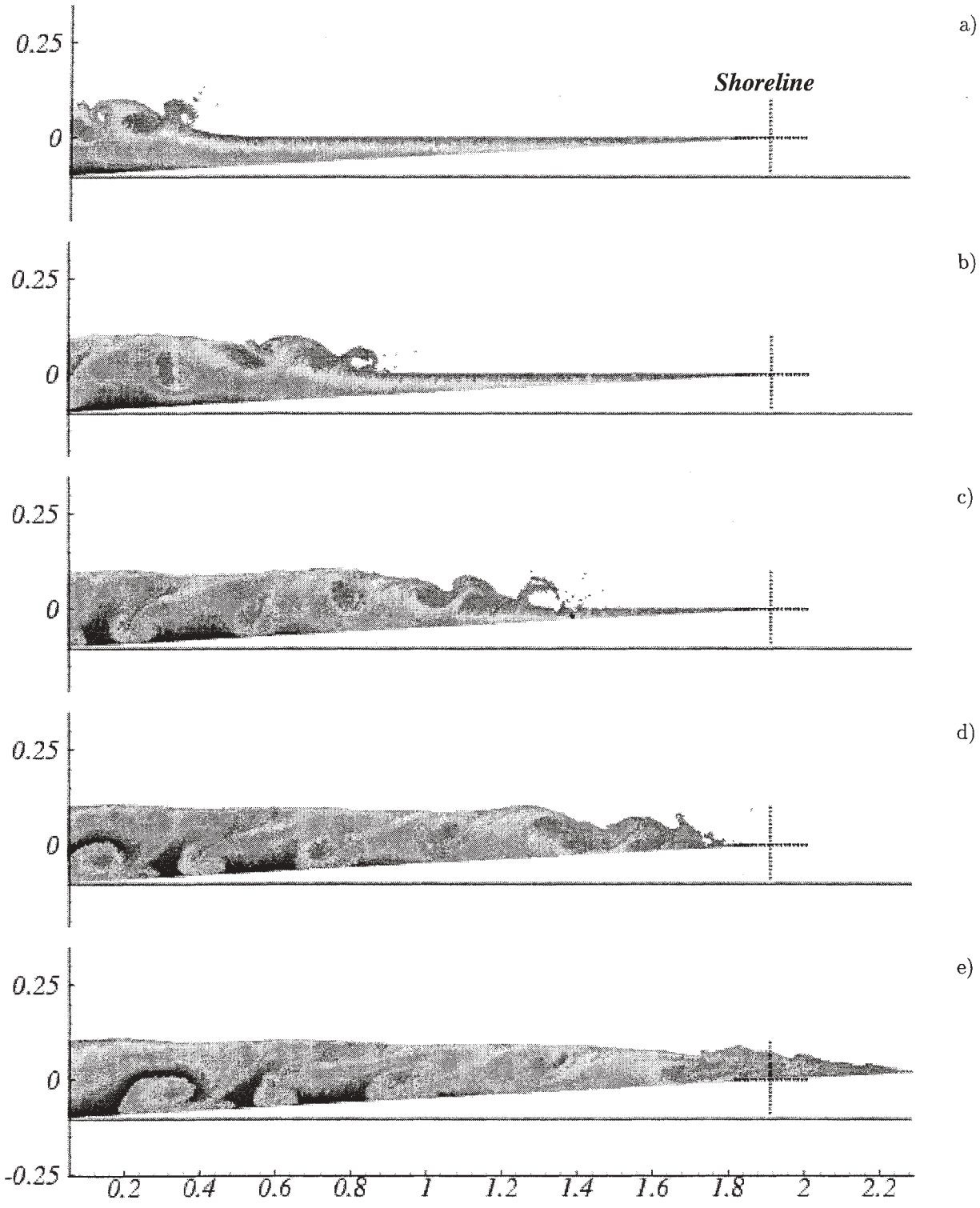

Figure 10: Run-up of bore, $F_0 = 1{\cdot}66$, generated by a piston initially moving with velocity $U/\sqrt{gh_0} = 0{\cdot}8$, along a beach with constant slope $\alpha = 3°$. Crosses mark the shoreline. Time $t\sqrt{g/h_0} = 17$, 19·9, 22·4, 25, 27·7 for a) through e), respectively.

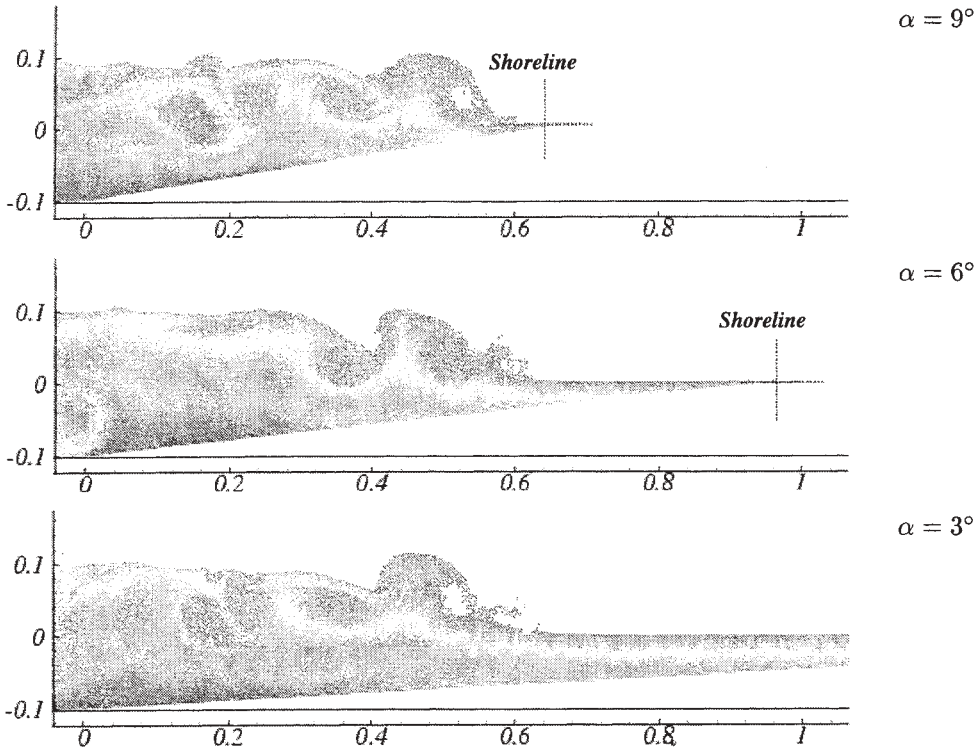

Figure 11: Bore front for decreasing slope, α, of the beach. $U/\sqrt{gh_0} = 0{\cdot}8$ and $t\sqrt{g/h_0} = 18{\cdot}66$. For $\alpha = 9°$, the bore is reaching the shoreline.

The convergence of the SPH Method, *Computers Math. Applic.*, Vol. 35, No. 1/2, pp. 95-102.

Grilli S., Svendsen I.A. and Subramanya R. (1997), Breaking criterion and characteristics for solitary waves on slopes, *J. Waterways, Port, Coastal, and Ocean Engineering*, Vol. 123, pp. 102-112.

Hernquist L. and Katz N. (1989), TREESPH: a unification of SPH with the hierarchical tree method, *The Astrophysical J. Supp. Ser.*, Vol. 70, pp. 419-446.

Keller H.B., Levine D.A. and Witham G.B. (1960), Motion of a bore over a sloping beach, *J. Fluid Mech.*, Vol. 7, pp. 302-315.

Lucy L.B. (1977), A Numerical Approach to the Testing of Fission Hypothesis, *Astronomical Journal*, Vol. 82, No.12, pp. 1013-1024.

Mas-Gallic S. and Raviart P.A. (1987), A Particle Method for First-order Symmetric Systems *Numer. Math.*, Vol. 51, pp. 323-352.

Miller R.L. (1968), Experimental Determination of Run-Up of Undular and Fully Developed Bores. *J. Geophys. Research*, Vol. 73, No. 11, pp. 4497-4510.

Monaghan J.J. (1992), Smoothed Particle Hydrodynamics, *Ann. Rev. Astron. Astroph.*, Vol. 30, pp. 543-574.

Morris J.P. (1997), Stability properties of SPH, *Publ. Astron. Soc. Aust.*, Vol. 13.

Moussa B.B. and Villa J.P. (2000), Convergence of SPH Method for Scalar Nonlinear Conservation Laws, to appear in *SIAM J. Numerical Analysis.*

Peregrine D.H. (1981), The fascination of fluid mechanics, *J. Fluid Mech.*, Vol. 106, pp. 59-80.

Peregrine D.H. (1983), Breaking waves on beaches, *Ann. Rev. Fluid Mech.*, Vol. 15, pp. 149-178.

Stoker J.J. (1957), *Water waves*, London: Interscience Publisher.

Tulin M.P. and Landrini M. (2000), Breaking waves in the ocean and around ships, 23^{rd} Symp. Nav. Hydr., Rouen (Fr).

Wang P., Yao Y. and Tulin M.P. (1995), An efficient numerical tank for nonlinear water waves based on the multi-subdomain approach with BEM, *Int. J. of Numerical Methods in Fluids*, Vol. 20, pp. 1315-1336.

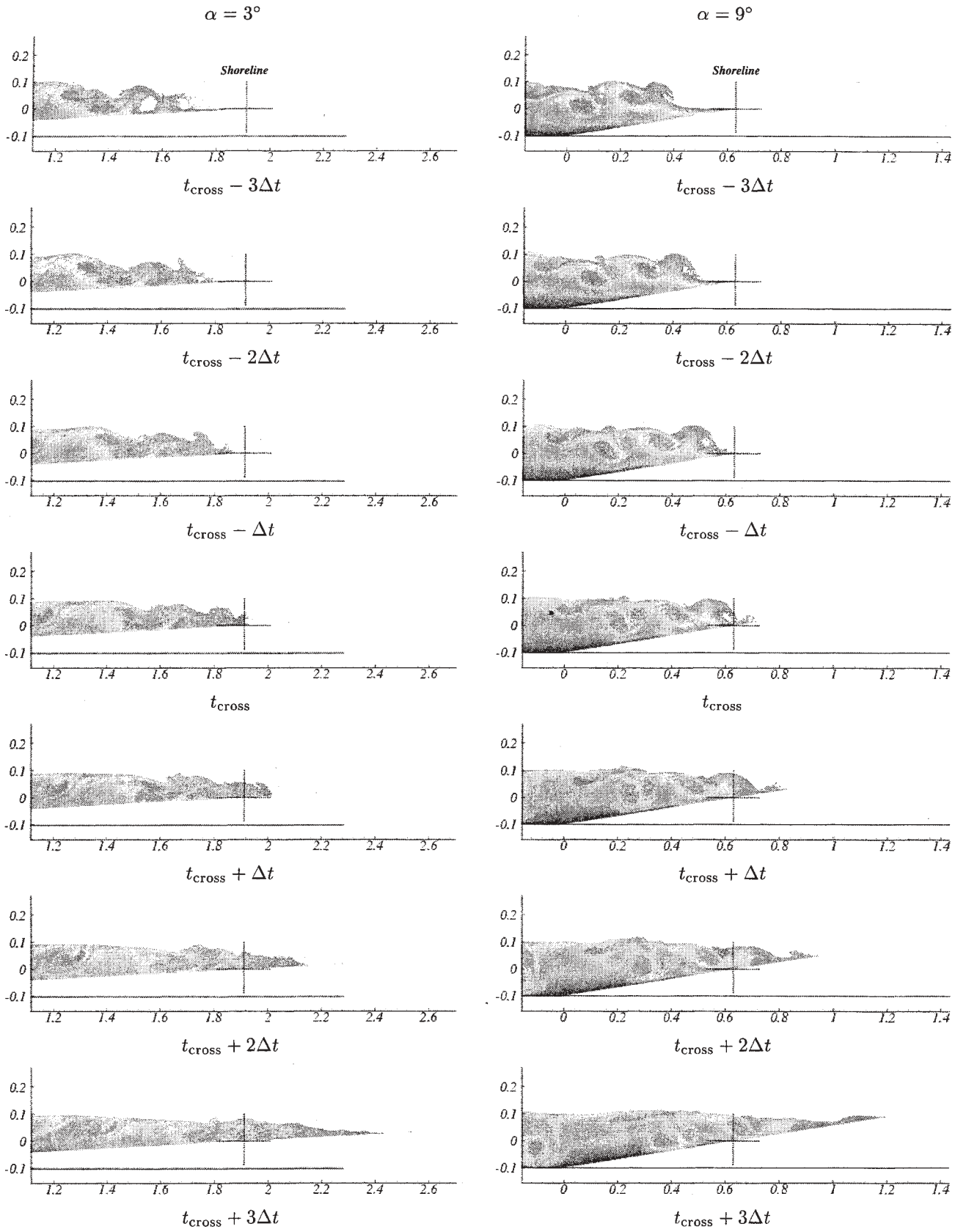

Figure 12: Modification of the bore front while going through the shoreline. $U/\sqrt{gh_0} = 0{\cdot}8$. Left: $\alpha = 3°$, $t_{\text{cross}}\sqrt{g/h_0} = 26{\cdot}13$, $\Delta t\sqrt{g/h_0} = 0{\cdot}53$ Right: $\alpha = 9°$, $t_{\text{cross}}\sqrt{g/h_0} = 18{\cdot}66$, $\Delta t\sqrt{g/h_0} = 0{\cdot}53$.

DEVELOPMENT OF A NEW SOURCE TERM FOR WAVE BREAKING IN SHALLOW WATER

David Hurdle and Gerbrant van Vledder

Alkyon Hydraulic Consultancy & Research
P.O. Box 248, 8300 AE Emmeloord, The Netherlands

1. INTRODUCTION

One of the most important phenomena affecting the wave conditions in shallow coastal areas is energy dissipation by breaking. Existing formulations for wave breaking make use of calibration parameters. The optimal settings of these parameters depend on the wave or bathymetric conditions. This is not practical when using the current generation of wave models because the typical bottom slopes and the wave conditions vary throughout the simulation area. Accurate representation of breaking is not only important to predict the wave height but also to be able to properly represent the non-linear wave-wave interactions, which affect the spectral form and the wave period.

In recent studies, Hurdle and van Vledder (1998), analyzed the results of wave height measurements for a large number of flume tests for bottom slopes between 1:50 and 1:10. They found a way of expressing the data that suggest that it should be possible to derive a formulation for dissipation by wave breaking for which the parameters are independent of both wave steepness and the spectral form. The tests considered covered a wide range of values for the wave steepness and included both single and double peaked spectra.

Furthermore, initial sample calculations for various situations suggested that the rate of dissipation is the same on each depth slope for conditions with the same wave height to depth ratio and the same wave steepness at the beginning of the slope. This suggests that a formulation can be derived which is both independent of the wave steepness and the bottom slope. Such a formulation would be much easier to apply in the current generation of wave models.

This paper describes work to derive a formulation for energy dissipation by wave breaking based on this data set. Further, some behavior in the data set is found which is inconsistent with initial expectations, for example, wave height to depth ratios greater than unity. The possible causes of this behavior and methods to deal with it are briefly discussed.

The procedure to derive the formulation is as follows:

- Express the data in such a way that the wave height to water depth ratio on a known slope follows a clear relationship;
- Parameterise this relationship;
- Derive the source term by incremental differentiation of this relationship.

This method is highly empirical.

2. THE DATA

A series of physical model studies (conducted at a nominal scale of 1:20) were completed by HR Wallingford for the Flood and Coastal Defence with Emergencies Division of the UK Ministry of Agriculture, Fisheries and Food (MAFF) to provide information on wave breaking behavior along the shoreline. Coates et al. (1998) and Hawkes et al. (1998) described this research. Analysis of the measured data was carried out as described by Durand and Allsop (1997). However, this analysis was primarily statistical. Further spectral analysis of the data was carried out by HR Wallingford as part of a study carried out in the Netherlands (see van der Meer et al., 2000).

The experiments were carried out on slopes of 1:10, 1:20, 1:30 and 1:50 with a wave absorbing slope at the end of the tank. In all series there was a flat section at both ends of the sloping section. The first part of the slope in the 1:30 test series had a slope of 1:10.

The wave steepness (defined as H_S / λ_0, where H_S is the energy based significant wave height and λ_0 is the wavelength at deep water based on T_{M-10}) in the tests varied between about 0.001 and 0.04. Double peaked spectra typically had prototype sea and swell peaks with periods of 3s and 11s respectively, although in some tests the swell period was as high as 19s. The wave height to water depth ratio at the foot of the slope generally varied between 0.1 and 0.4. The prototype scale water depth generally varied between 10m at the deep end and 2m at the shallow end for the lowest water level tested. The number of wave probes in most tests was 14, with between 8 and 12 on the sloping part.

3. DATA EXPRESSION

The expression of the data is based on the computation of a nominal value that will be called the "shoaled wave height", denoted H_{SS}. Not too much should be read into the use of this particular parameter. It is only important that it seems to give useful results.

The shoaled wave height is computed on the basis of the wave height and some characteristic wave period at the foot of the constant slope. Further, the water depth at the foot of the slope and the depth at the output point are required. The shoaled wave height is computed on the basis of linear shoaling period as follows:

$$H_{SS} = H_{S0} * \sqrt{C_{G0} / C_{G1}} \qquad (3)$$

Where:

C_G is the wave height at the foot of the slope

H_{S0} is the group velocity of the waves. The subscript 0 indicates the location at the foot of the slope and the subscript 1 the location that the shoaled wave height is to be computed.

In the results presented here, the shoaled wave height was computed on the basis of the spectral wave period T_{M-10}.

Figures 1 to 4 show the measured wave height to water depth ratio plotted against the shoaled wave height to water depth ratio for the slopes 1:10, 1:20, 1:30 and 1:50 respectively. The symbol plotted is coded according to the wave steepness:

- *: wave steepness < 0.01
- +: 0.01 < wave steepness < 0.0225
- o: wave steepness > 0.0225

The wave steepness is that at the foot of the slope.

Further, the results are coded according to the color as follows:

- gray: unimodal spectra;
- black: spectra with two peaks;

Note that only probes on the constant slopes are included in these plots. This means that in the tests for slope 1:30, the probe in the part of the tank with slope 1:10 (probe 13) was not included in the analysis.

Although much of the data seems to be rather well correlated, some clusters of data seem to deviate from the general trend, particularly for the tests on the slope 1:30. Further analysis indicated that these data either come from a particular (malfunctioning) probe or come from five tests (out of the 210).

For the cases where the data is associated with a particular probe, plots of the wave height to depth ratio against distance were made. In all cases a smooth monotonically increasing ratio of wave height to water depth was found with some small amount of noise, except at the above-mentioned probe. Here, large departures from the general trend were found. Because these deviations occurred for a large range of incident wave heights, periods and water levels, it was concluded that they were less likely to be associated with wave behavior in nature than with a badly performing probe (e.g. poor calibration or probe becomes dry with high waves). On this basis the probes were not included in the subsequent procedures to obtain a parametric fit to the data.

Table 1. Cases with results deviating from general trend

Case	H_S (m)	T_{M-10} (s)	Steep-ness (-)
Slope 1:50			
s50d16b_2a.dat	3.083	6.61	0.0290
s50d16b_3a.dat	2.415	6.61	0.0227
Slope 1:30			
s30d12b_1bbis.dat	3.881	7.09	0.0317
s30d12u_hs15s2.dat	3.417	9.88	0.0144
s30d12u_hs2s4.dat	4.260	7.93	0.0279

Table 1 gives some details on the 5 tests with results that deviate from the general trend. There is not any immediately obvious common factor in the tests. Three of the tests were bi-modal and 2 of the tests were uni-modal. They were therefore left out of subsequent procedures to derive a parametric fit but included in statistical analysis of the performance of the method.

4. PARAMETRIC FIT

The form of the fit was selected to fit the data on the four slopes reasonably well. The fit should follow the data reasonably well over the whole range for which data is available. The following formulation was chosen:

$$\frac{H_s}{d} = c_1 \frac{H_{ssh}}{d} + (1 - c_1)\, c_2 \left\{ \tanh\left[\left(\frac{H_{ssh}}{c_2 d} \right)^{1.5} \right] \right\}^{(1/1.5)} \qquad (1)$$

where:

c_1 and c_2 are the parameters to be fit

and H_S is the (measured) wave height at de pth d

Here the depth includes water level changes due to changes in the volume of water in the tank but not due to set-up due to wave dissipation.

The fit was made to minimize the RMS relative error in the predicted value of Hs/d using a standard error minimization routine. The coefficients c_1 and c_2 obtained independently for each bottom slope were then plotted against the slope and the best-fit line drawn through the points. The values of c_1 and c_2 can be related to the slope as follows:

$$c_1 = 1.9 \times slope$$
$$c_2 = 3.45 \times slope + 0.5 \qquad (2)$$

An example of the results of the fitting procedure is shown in Figure 5 for the slope steepness of 1:10. The figure shows the measured significant wave height to depth ratio plotted against the shoaled wave height to depth ratio and the derived parametric relationship. The coding of the points is as described in section 3. The rejected probes and cases have been left out in these plots.

Points with deviations from the parametric fit larger than the experimental accuracy (estimated to be the highest of 10 % or 2mm at model scale) have been circled. It can be seen that the number of points that deviate from the parametric fit by more than the experimental accuracy is very limited.

It should be noted that presenting the wave height to depth ratios generally gives much more insight into the behavior of wave breaking than presenting wave heights. This is because, the wave height to depth ratios are highest at the top of the slope. At the same time, the measured wave height at the top of the slope is low, increasing the percentage measurement error and errors due to variations in the water level. Furthermore, much more has happened at this location. If wave heights are presented, the data points at the top of the slope are all compressed into a small area in the bottom left hand corner of the plot where any disagreement will seem small.

5. EMPIRICAL SOURCE TERM

To demonstrate the method, it is provisionally assumed that the source term will be implemented in wave models that apply linear shoaling theory and that dissipation by bottom friction can be neglected. Then symbolically:

$$S_{tot} = S_b + S_{sh} \qquad (3)$$

Where S_{tot}, S_b and S_{sh} are the total rate of change of significant wave height with distance, and that due to wave breaking and shoaling respectively. These terms can easily be expressed in terms of energy at a later stage. However, for the time being it more intuitive to express them in terms of wave height.

Then, for a given combination of bottom slope, water depth, wave period and wave height, the total source term for the change in wave height can be computed using equations (2) and (3) as described in the following paragraph. The source term for breaking is then simply obtained by subtracting the source term for shoaling from the total source term.

The total source term can be computed as follows:

- Compute the wave height to depth ratio;
- Compute the corresponding shoaled wave height to depth ratio using equations (2) and (3) (we did this using look-up tables);
- Apply small increments (up and down) to the depth, δd, and compute the shoaled wave height at these depths (on the basis of T_{M-10});
- Compute the corresponding distance on the basis the slope, $\delta x = 2\delta d / slope$;
- Use equations (2) and (3) to compute the actual wave height at the two incremental depths, H_{S+} and H_{S-}, from the shoaled wave heights there. The increment in the wave height is then $\delta H_S = H_{S+} - H_{S-}$;
- The total source term for this parameter combination is then given by $\delta H_S / \delta x$

This procedure was carried out for all of the slopes for fixed values of the wave period of 4s and a water depth of 2m. Figure 6 shows the corresponding rate of change of significant wave height with distance against the local wave height to depth ratio. Further, a fit was made to the curves resulting in the dissipation term:

$$\frac{dH_S}{dx} = -0.125\left(\frac{H_S}{d}\right)^4 \qquad (5)$$

This source term is only valid for the wave period 4s. The purpose of this is to illustrate that there seems to be a source term that gives the correct dissipation for all slopes, although for one period. At the time of writing, the scaling of this source term to cover all wave periods is being developed.

6. DISCUSSION

The derivation of the above source term is purely empirical. However, the authors would argue that any method to describe wave breaking is likely to depend on calibration factors determined from measurements. The value of such source terms should be judged on the basis of how well they fit the data.

Shoaled wave height may be computed on the basis of other characteristic wave periods than T_{M-10}. The effect of applying other spectral wave periods was tried (e.g. T_{M-2-1} and T_{M-20}) but was found to have very limited effect on the results. Further, the shoaled wave height was computed spectrally. However, the shoaled wave height computed in this way did not differ significantly from the shoaled wave height computed on the basis of T_{M-10}, even for double peaked spectra. This suggests that any source term derived on the basis of this method for expressing the data will be suitable both for spectral models and for models that work with a representative wave period.

One of the strange aspects of the results is that for the slopes 1:10 and 1:20, the wave height to depth ratio does not seem to approach an upper limit with increasing shoaled wave height to depth ratio. One explanation for this could be that we have used the still water depth without set-up due to wave dissipation. Measured values for the set-up were available for the tests on a slope of 1:10. The inclusion of the set-up when computing the wave height to depth ratios did not have any significant effect either on how well the data fitted or on the lack of upper limit for the wave height to (total) depth ratio.

Another possible explanation could be the generation of low frequency wave energy as the waves approach shallow water. The high frequency waves can propagate into shallow water more effectively during the peak of a low frequency wave. This means that the presence of the low frequency energy may increase the wave energy of higher period that can propagate into shallow water. Further, the scale model tests were carried out without active absorption of the long wave energy at the wave paddle. This means that it is possible that tank resonance occurred in some tests. This has an important implication. That is that the results derived on the basis of these tests should be checked against field measurements or against flume tests where long waves play a less pronounced role. In the field it is likely that the ambient low frequency wave conditions differ considerably from those in a wave tank.

Low frequency tank resonance and the influence of the low frequency waves may also be the explanation for the fact that there is much more scatter in the data for the tests on slopes of 1:20 and 1:30 than for slopes of 1:10 and 1:50.

Examination of the derived source term for a wave period of 4s (see Figure 6) shows that the wave dissipation increases with increasing wave height to depth ratio. However, the dissipation derived from the parametric formulation for each slope reaches an upper limit that depends on the slope. This is the direct consequence of the fact that no upper limit on the wave height to depth ratio was found.

It is worth pointing out that the high values of wave height to water depth ratio were found in rather shallow water, where the wave height is not usually of great interest for design purposes.

7. CONCLUSIONS

A way of expressing measured wave data has been found which makes it easy to derive parametric formulations for the wave height to depth ratio on constant steep slopes. Further, comparison of the dissipation on different slopes suggests that the rate of dissipation can be formulated in terms of the wave height to depth ratio and a single coefficient independent of the bottom slope, the wave period or the spectral form. Such a formulation will be very useful for application in spectral wave models that cover a large area with variable wave steepness and bottom slope.

The formulation works well for the data set examined except in situations with very shallow water with high wave height to depth ratios. A possible explanation for this is the presence of low frequency wave energy. It would be useful to examine whether the same behavior is exhibited in field measurements. If this is the case, it may be necessary to find a way of accounting for the low frequency wave energy when computing the dissipation due to wave breaking (e.g. by using a coupled surf beat model or by increasing the effective water depth).

The work should also be extended for shallower bottom slopes.

REFERENCES

Battjes, J.A., Janssen, J.P.F.M., 1978. Energy loss and set-up due to breaking of random waves. Proc. 16th Int. Conf. Coastal Eng. ASCE, New York, pp. 569-588

Coates, T.T., R.J. Jones and P. Bona, 1998: Wave flume studies on responses to wind / swell and steep approach slopes. Research Report TR 24, HR Wallingford.

Durand N. and N.W.H. Allsop, 1997: Effects of steep bed slopes on depth-limited wave breaking. Proc. Of Waves '97 Conference, November 1997, Virginia Beach, ASCE, New York.

Hawkes, P.J., T.T. Coates and R.J. Jones, 1998: Impact of bi-modal seas on beaches and control structures. Research Report SR 507, HR Wallingford

Van der Meer, J.W., D.P. Hurdle, G.Ph. van Vledder, M.R.A. van Gent, R.C. Ris, 2000: Uni- and bi-modal wave spectra on steep foreshores. Report I230, Infram.

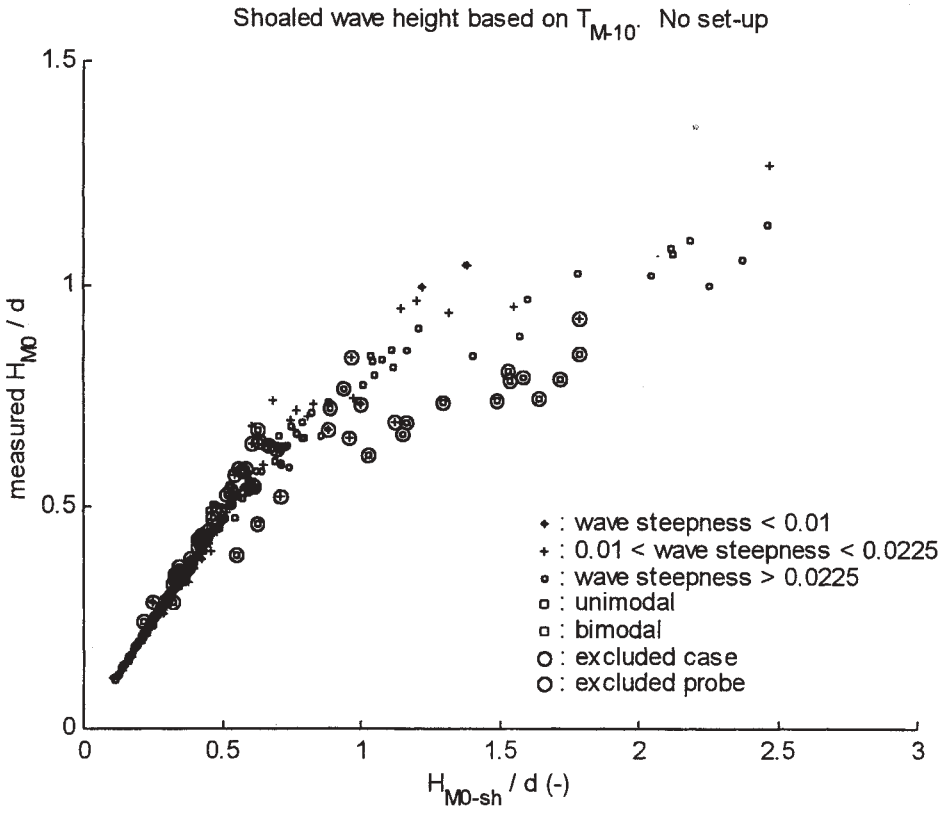

Figure 1. Measured wave height to depth ratio against shoaled wave height to depth ratio for slope 1:10

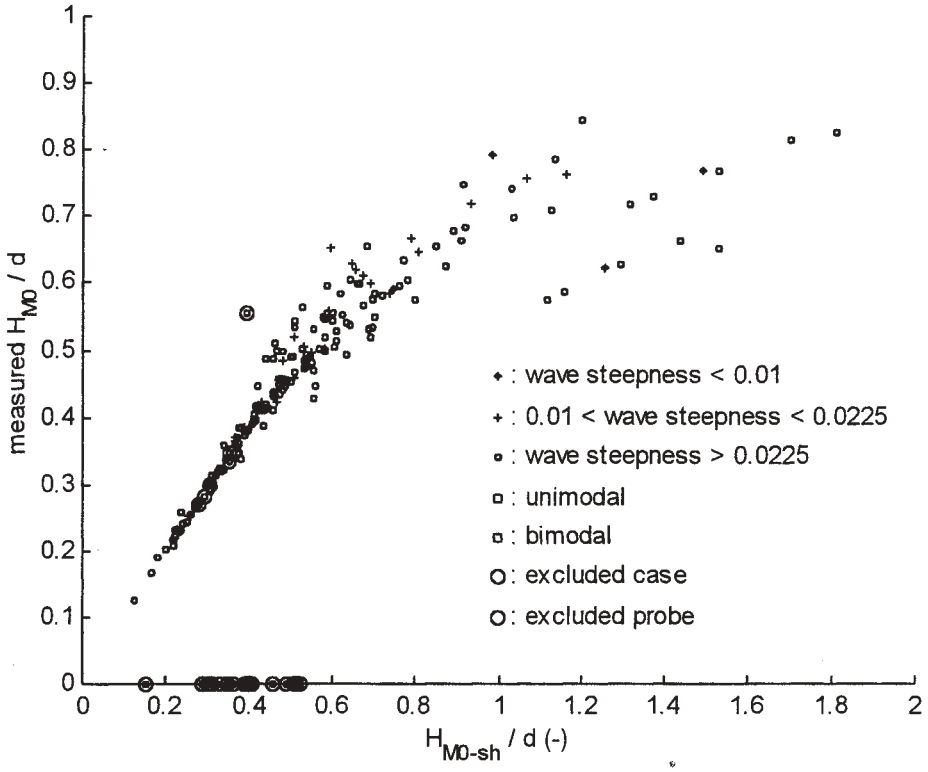

Figure 2. Measured wave height to depth ratio against shoaled wave height to depth ratio for slope 1:20

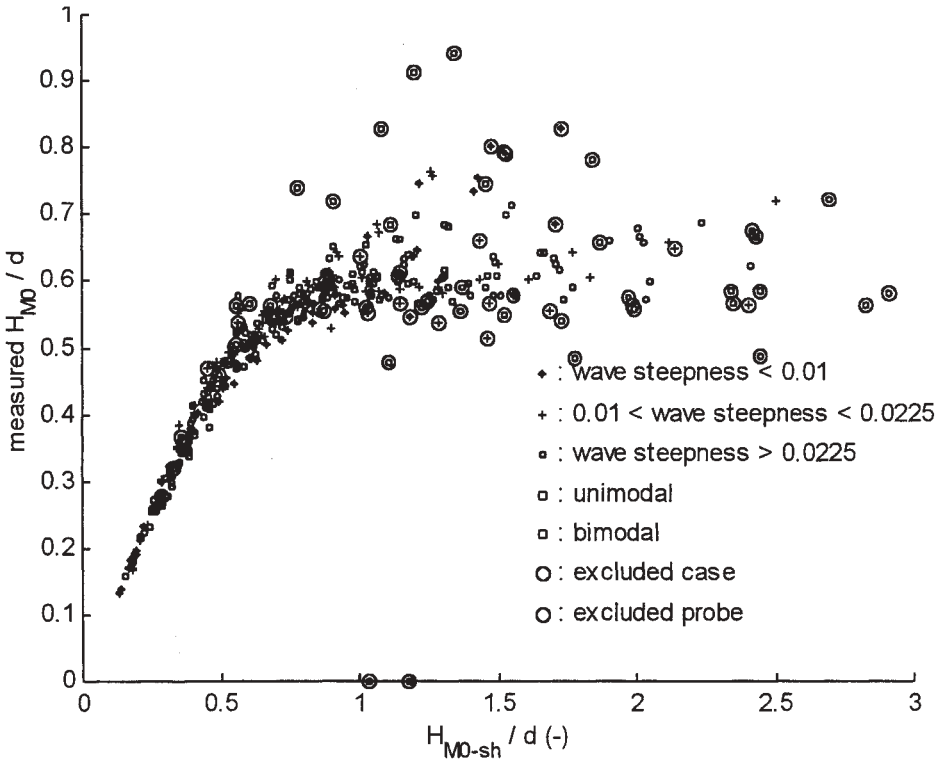

Figure 3. Measured wave height to depth ratio against shoaled wave height to depth ratio for slope 1:30

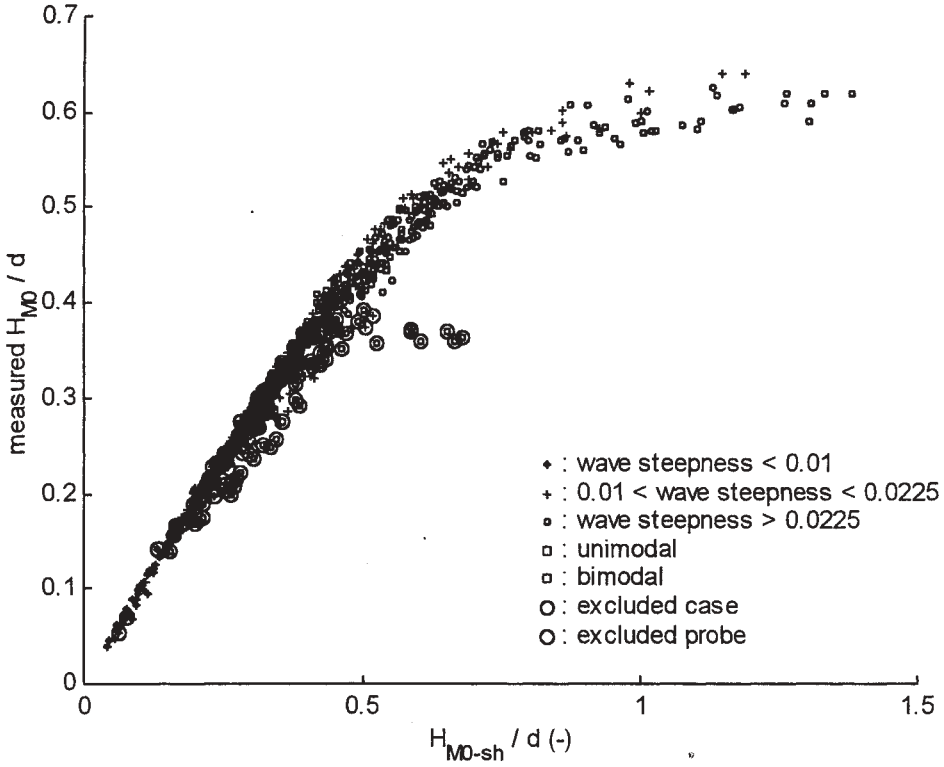

Figure 4. Measured wave height to depth ratio against shoaled wave height to depth ratio for slope 1:50

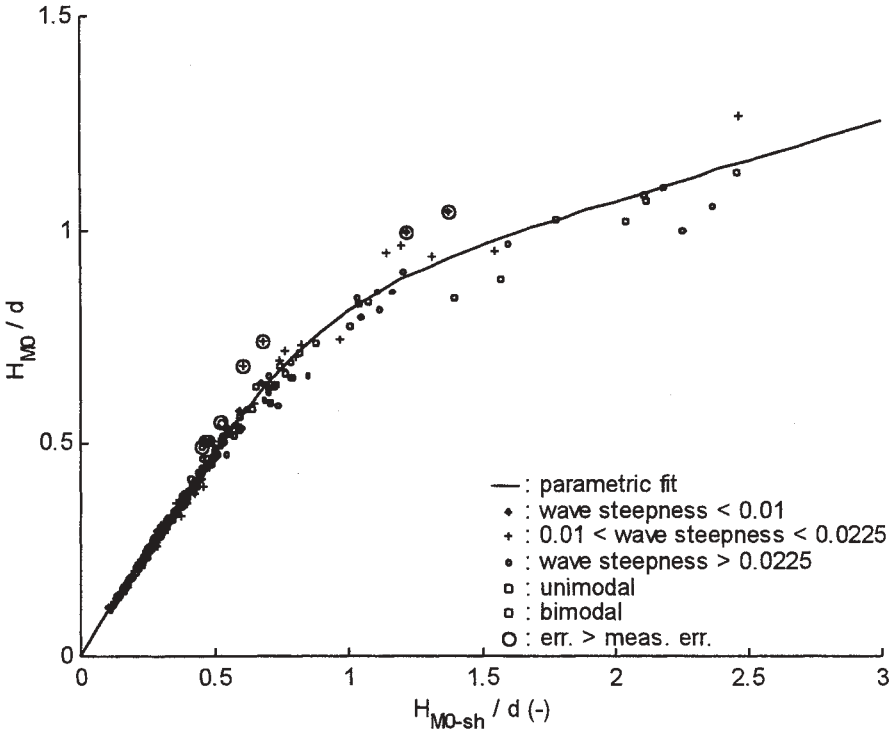

Figure 5. Measured and parametric wave height to depth ratio against shoaled wave height to depth ratio. Slope 1:10.

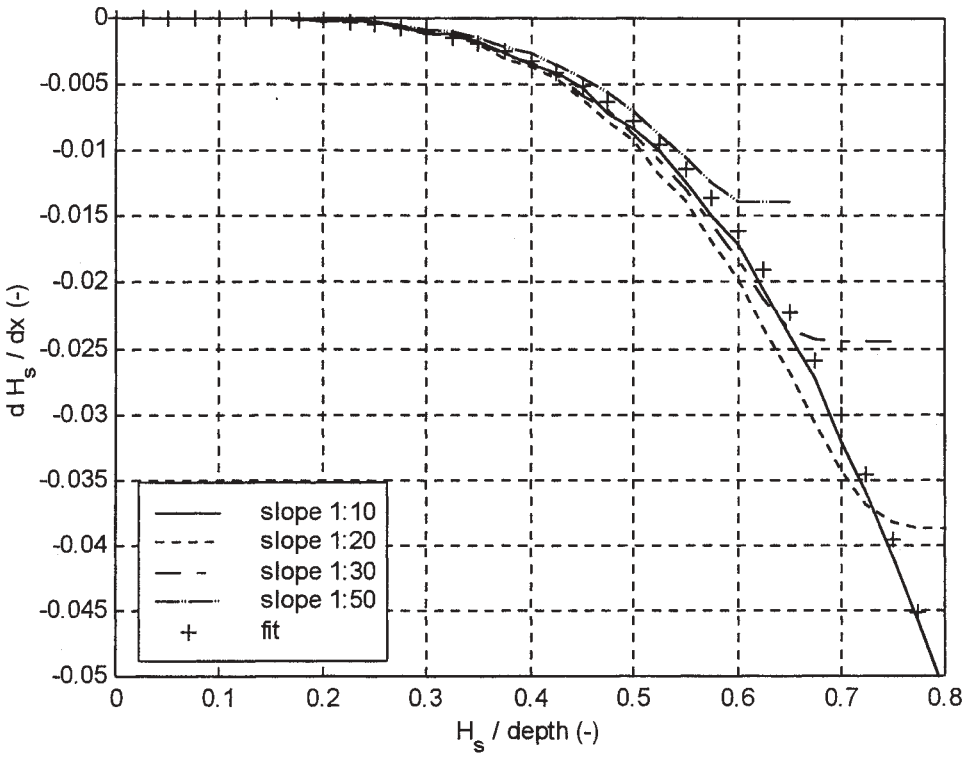

Figure 6. Rate of change of wave height against wave height to depth ratio. Wave period T_{M-10} = 4s

OCEANIC AND NEAR-SHORE WHITECAPPING EFFECTS IN SWAN

L.H. Holthuijsen and N. Booij

Delft University of Technology, Department of Civil Engineering,
Delft, the Netherlands

1. INTRODUCTION

The third-generation wave model SWAN (Booij et al, 1999) has been conceived to compute wave conditions in near-shore areas. The model in its original form is not suited for applications on an oceanic scale because it is not formulated in spherical coordinates and the numerical scheme for propagating wave energy in geographic space is too diffusive. To remedy this shortcoming, SWAN has been modified. These modifications open the possibility to study certain phenomena on widely varying scales such as zooming in from the ocean, across a shelf sea to a coastal region. The example given here is the effect of swell on the whitecapping of wind sea at these different scales in the Indian Ocean (Figs. 1 and 2).

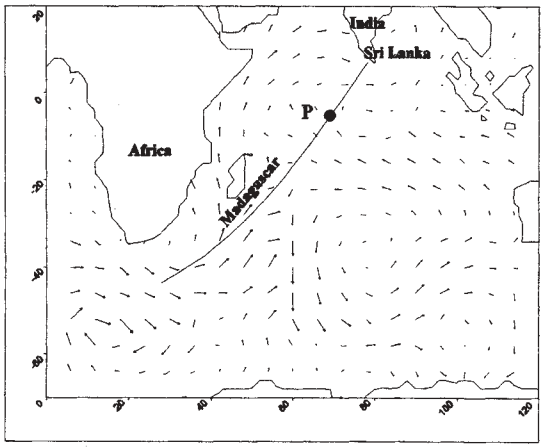

Fig. 1 The Indian Ocean, the storm of this study off Madagascar and the output location P on the swell path to Sri Lanka

2. THE WAVE MODEL

2.1 *Basic equation*

The SWAN wave model is a discrete spectral model based on the spectral action balance equation.

$$\frac{\partial}{\partial t}N + \frac{\partial}{\partial x}c_x N + \frac{\partial}{\partial y}c_y N + \frac{\partial}{\partial \sigma}c_\sigma N + \frac{\partial}{\partial \theta}c_\theta N = \frac{S}{\sigma} \qquad (1)$$

The first term in the left-hand side of this equation represents the local rate of change of action density $N(\sigma,\theta;x,y,t)$, the second and third term represent propagation of action in geographical space (with propagation velocities c_x and c_y in x- and y-direction, respectively). The fourth term represents shifting of the relative frequency due to variations in depths and currents (with propagation velocity c_σ in σ-space). The fifth term represents depth-induced and current-induced refraction (with propagation velocity c_θ in θ-space). The expressions for these propagation speeds are taken from linear wave theory. The term S $(=S(\sigma,\theta))$ at the right hand side of the action balance equation is the source term in terms of energy density representing the effects of generation, dissipation and nonlinear wave-wave interactions. A brief summary of the formulations that are used for the various source terms in SWAN as used for this study are given next.

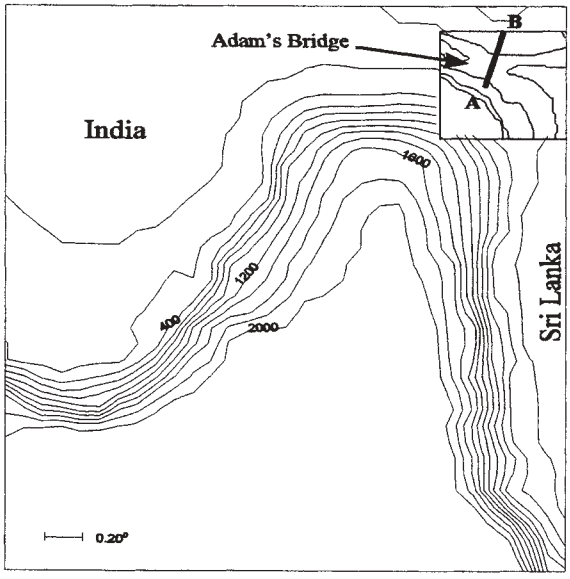

Fig.2 The area between India and Sri Lanka with the transect A-B across Adam's Bridge (depth contours at 200 m depth intervals (main picture) and 10 m (inset).

AUTHOR INDEX TABLE OF CONTENTS

2.2 *Wind input*

Transfer of wind energy to the waves is described in SWAN with a resonance mechanism (Phillips, 1957) and a feed-back mechanism (Miles, 1957). The corresponding source term for these mechanisms is described as the sum of linear and exponential growth:

$$S_{in}(\sigma,\theta) = A + B E(\sigma,\theta) \qquad (2)$$

in which A and B depend on wave frequency and direction, and wind speed and direction. The expression for the term A is due to Cavaleri and Malanotte-Rizzoli (1981) with a filter to avoid growth at frequencies lower than the Pierson-Moskowitz frequency (Tolman, 1992). The expression for the coefficient B is taken from an early version of the WAM model (known as WAM Cycle 3, the WAMDI group, 1988). It is due to Snyder et al.(1981) and rescaled in terms of friction velocity U_* by Komen et al. (1984). The drag coefficient to relate U_* to the driving wind speed at 10 m elevation U_{10} is taken from Wu (1982).

2.3 *Dissipation*

The dissipation of wave energy is represented by the summation of three different contributions: whitecapping $S_{wc}(\sigma,\theta)$, bottom friction $S_b(\sigma,\theta)$ and depth-induced breaking $S_{br}(\sigma,\theta)$.

Whitecapping in SWAN is primarily controlled by the steepness of the waves as the pulse-based model of Hasselmann (1974, as adapted by the WAMDI group, 1988) is used:

$$S_{wc}(\sigma,\theta) = -\eta k E(\sigma,\theta) \qquad (3)$$

with

$$\eta = \tilde{\eta} = -C_{ds}\tilde{s}^{n}\frac{\tilde{\sigma}}{\tilde{k}} \qquad (4)$$

where k is wave number and $\tilde{\sigma},\tilde{k}$ and $\tilde{s}$ denote a mean frequency, a mean wave number and an overall mean wave steepness, respectively (see the Appendix for definitions). C_{ds} and n are empirically estimated coefficients ($C_{ds} = 2.36\times10^{-5}$ and $n = 4$). When in this model swell is added to pure wind sea, the wave steepness $\tilde{s}$ decreases and the value of $\tilde{\sigma}/\tilde{k}$ increases. The net effect is, since $\tilde{\eta}$ is proportional to $\tilde{s}^4$, a sharp decrease of the whitecapping and a consequent sharp increase of the net growth for the wind sea in. This is in contrast to what has been observed (Donelan, 1987; Fig. 3).

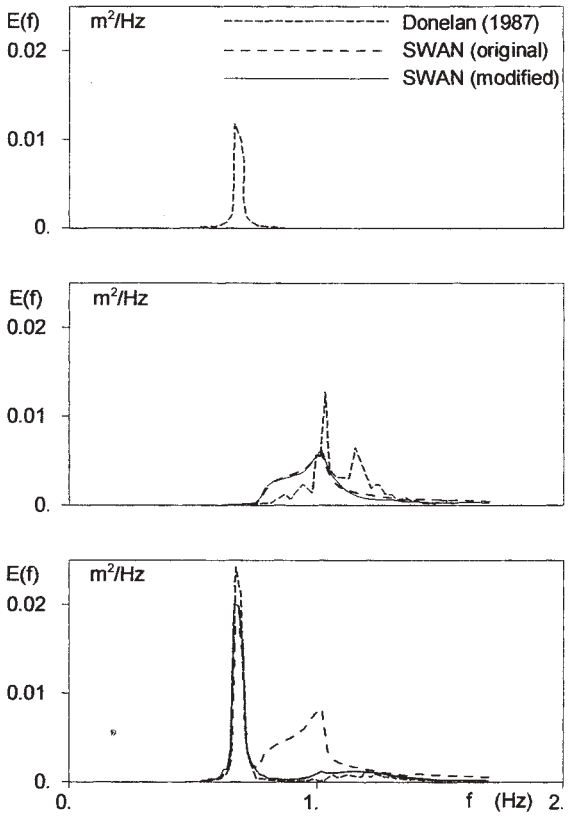

Fig. 3 The spectra observed by Donelan (1987) in a wave flume: mechanically generated low-frequency waves (upper panel), wind generated high-frequency waves (middle panel) and the two wave fields generated simultaneously (lower panel).

Bottom friction is represented for this study as:

$$S_{bfr}(\sigma,\theta) = -C_{bottom}\frac{\sigma^2}{g^2\sinh^2(kd)}E(\sigma,\theta) \qquad (5)$$

in which C_{bottom} is the bottom friction coefficient from Hasselmann et al. (JONSWAP, 1973).

The process of depth-induced wave-breaking is represented essentially with the dissipation of a bore applied to the breaking waves in a random field (Battjes and Janssen, 1978). Eldeberky and Battjes (1995) have formulated a spectral version of this bore model which conserves the spectral shape. Expanding their expression to include directions, the expression that is used in SWAN is:

AUTHOR INDEX TABLE OF CONTENTS

$$S_{br}(\sigma,\theta) = -\frac{D_{tot}}{E_{tot}} E(\sigma,\theta) \qquad (6)$$

in which E_{tot} is the total wave energy and D_{tot} is the rate of dissipation of the total energy due to wave breaking according to Battjes and Janssen (1978). The value of D_{tot} depends critically on the breaking parameter $\gamma = H_{max}/d$ (in which H_{max} is the maximum possible individual wave height in the local water depth d). In the present study a constant value of $\gamma = 0.73$ is used.

2.4 Nonlinear wave-wave interactions

In deep water, quadruplet wave-wave interactions dominate the evolution of the spectrum. They transfer wave energy from the spectral peak to lower frequencies (thus moving the peak frequency to lower values) and to higher frequencies (where the energy is dissipated by whitecapping). In very shallow water, triad wave-wave interactions transfer energy from lower frequencies to higher frequencies often resulting in higher harmonics (Beji and Battjes, 1993; low-frequency energy generation by triad wave-wave interactions is not considered here).

In SWAN the computations of the quadruplet wave-wave interactions are carried out with the Discrete Interaction Approximation (DIA) of Hasselmann et al. (1985). The computations of the triad wave-wave interactions are carried out with the Lumped Triad Approximation (LTA) of Eldeberky (1996).

3. MODIFICATIONS TO THE MODEL

3.1 Whitecapping

As indicated above, in the formulation of whitecapping (Eqs. 3 and 4), swell would enhance net wave growth whereas it should suppress growth (at least in the laboratory conditions of Donelan, 1987). To achieve this we postulate two hypotheses here.

a) For pure wind sea (i.e., in the absence of swell, i.e., low-frequency energy) the whitecapping formulation is correct. The overall steepness in the formulation can then be replaced by the high-frequency steepness, $s_{hf}(\sigma)$ which is the mean steepness of the frequencies above frequency σ (see the Appendix for definitions).

b) The effect of swell is to enhance whitecapping of the short waves due to the steepening of these waves on the crest of the long waves (a surface straining effect; Longuet-Higgins and Stewart, 1966). This is parameterized with the ratio $\beta(\sigma) = s_{hf}(\sigma)/\tilde{s}$.

The formulation that we use for these hypotheses in terms of the pulse model of Hasselmann (1974) is:

$$\eta = \eta^* = C_{ds} f(\beta)\, s_{hf}(\sigma)^4 \frac{\tilde{\sigma}}{\tilde{k}} \qquad (7)$$

with

$$\begin{aligned} f(\beta) &= (\beta - 1)^2 + 1 \quad \text{for} \quad \beta \geq 1 \\ f(\beta) &= 1 \quad \text{for} \quad \beta < 1 \end{aligned} \qquad (8)$$

It can readily been shown that with this modification to account for the low-frequency surface straining effect, swell correctly suppresses wave growth in the experiment of Donelan (1987; Fig. 3).

3.2 Propagation

The numerical scheme for the geographic propagation of the waves in SWAN is an implicit scheme and unconditionally stable. This implies that the computations are not subject to the usual stability criteria. The scheme (BSBT=backward space, backward time) is first order, upwind and therefore rather robust but also very diffusive. This diffusion degrades the accuracy of the model in a number of situations, including those at larger scales (oceans and shelf seas). The diffusiveness of the model was recently reduced by replacing the BSBT scheme with two alternative higher order (implicit) schemes (Rogers et al., 1999, 2000): one for nonstationary applications and one for stationary applications. The first scheme, the S&L scheme, is due to Stelling and Leenderste (1992; with "$Q_0 = 0$, $Q_1 = 1/6$", using their notation). The phase error in this numerical scheme is second order (in Δt) while the diffusion is third-order (proportional to $\Delta t\, \Delta x^2$ and $\Delta t\, \Delta y^2$). Conservation can be proven for the scheme for the general case of geographically varying propagation speeds. Expressions for the numerical growth rate, D (multiplication factor of amplitude per characteristic time scale of the feature to be propagated) and numerical dispersion, C_n/C were calculated, but are quite long and are omitted here. Experimentation with a large number of possible

AUTHOR INDEX TABLE OF CONTENTS

input values for the derived expression for D yielded no unstable combinations. Therefore, the scheme is very likely unconditionally stable. Also, using this scheme suggests that it is unconditionally stable for cases of non-uniform propagation speeds. However, because of the numerical oscillations, there is a practical limitation to the time step with this scheme. To what extent such oscillations are acceptable is very subjective, depending on the tolerance of the model user, the severity of the "shock front" or comparable feature in the wave field, and the resolution of the feature. The great advantage of this scheme is that the high wave numbers in the feature are dampened much stronger than the low wave numbers, generally resulting in a rapid decrease of short oscillations that may be generated during propagation.

Using SWAN on scales where diffusion becomes an issue, implies that the Cartesian description of the geographic space is inadequate and that a formulation on a globe is required (in terms of longitude, λ and latitude, φ). This is readily achieved by replacing x and y by λ and φ and by adjusting the refraction term in the action balance equation to account for great circle propagation:

$$\frac{\partial}{\partial t}N + \frac{\partial}{\partial \lambda}c_\lambda N + (\cos\varphi)^{-1}\frac{\partial}{\partial \varphi}c_\varphi \cos\varphi N + \\ + \frac{\partial}{\partial \sigma}c_\sigma N + \frac{\partial}{\partial \theta}c_\theta N = \frac{S}{\sigma} \qquad (9)$$

The scheme can be made stationary but the resulting scheme cannot be considered a subset of the nonstationary scheme and is, in fact, likely to be unstable. Also, it is important to note that the numerical stencil of this stationary scheme would include downwind points which is incompatible with the up-wind set-up of SWAN. Instead a second-order up-wind scheme (SORDUP) is used for stationary, small-scale computations in which each spatial derivative is determined as the optimal (most accurate) discretization for the numerical stencil with two up-wind grid points (e.g,. *i, i-1, i-2* in the x-direction) using conventional Taylor Series expansion.

4. WHITE-CAPPING EFFECTS ON AN OCEANIC SCALE

The effect of the modified whitecapping on an oceanic scale can be illustrated with a real case. We have arbitrarily chosen a situation in which a storm

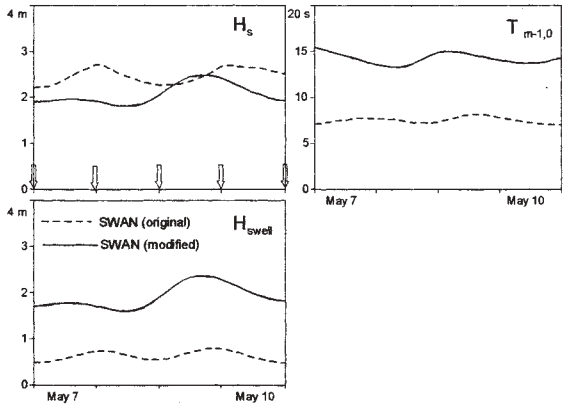

Fig 4. The significant wave height, the swell wave height and the mean wave period at location P of Fig. 1 in May of 1995 (00:00 GMT of every day). Arrows indicate times of spectral output (Fig. 5).

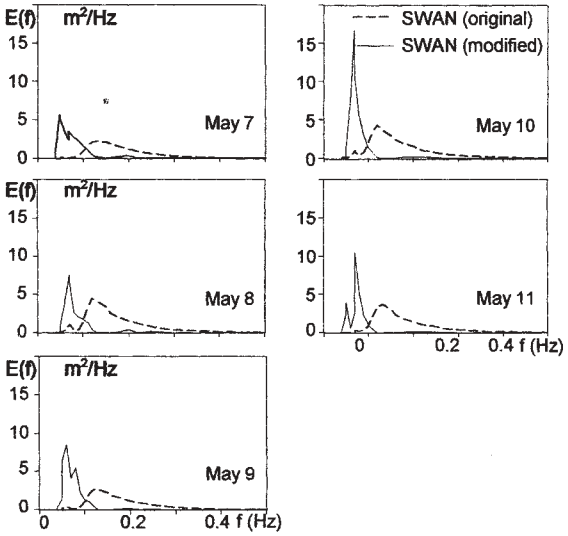

Fig. 5 The computed spectra in the Indian Ocean at location P of Fig. 1 at the times indicated in Fig. 4 (original and modified white-capping).

off Madagascar generates swell that arrives some time later at Sri Lanka (Fig. 1). The nonstationary S&L scheme is applied over the Indian Ocean (the area shown in Fig. 1) with (nested) grids of 2^0, $1/4^0$, $1/10^0$ resolution zooming in on the area south of Sri Lanka. The results in terms of wave height and period off Sri Lanka (location P in Fig. 1) with and without the modified whitecapping are shown in Fig. 4. The differences between the two results are obvious: the significant wave height is only moderately sensitive to the modification in the whitecapping formulation. It is a difference that

AUTHOR INDEX TABLE OF CONTENTS

would not be too obvious in comparisons with observations of the significant wave height (the differences seem to be of the same order as the hindcast error which is typically about 15% for third-generation wave models). The swell wave height and the mean wave period (see Appendix for definitions), however, are very sensitive (Fig. 4). This is also evident in the computed spectra (Fig. 5). Such differences should be very obvious when comparing the model results with observations.

6. WHITE-CAPPING EFFECTS ON A NEAR-SHORE SCALE

We use the same situation as above to illustrate the effect of the modification of the whitecapping on a near-shore scale. To that end we zoom in on the shallow submerged ridge between India and Sri Lanka (Adam's Bridge) and beyond (Fig. 2). For this we use the stationary SORDUP scheme in an even smaller nested area with a $1/100^0$ resolution. The results in terms of wave height and period across Adam's Bridge (locations P1, P2 and P3 in Fig. 6) are shown in Fig. 6. It is obvious from these results that swell is almost absent with the original whitecapping while it is dominant with the modified whitecapping. This is also reflected in the mean wave periods. Again, as in the oceanic case, the significant wave height is not as sensitive. The high-frequency tail of the spectra computed with and without the modification are rather similar (Fig. 7). This is remarkable since one would expect a lower tail with the modified whitecapping (as in the experiment of Donelan, Fig. 3). A repeated computation shows that this unexpected result is due to the triad wave-wave interactions. They generate the two secondary peaks in the computations with the modified whitecapping (swell present) whereas there is no visible effect in the computations with the original whitecapping formulation (swell absent). The high-frequency energy in the latter computations is totally locally generated. The high-frequency tails in both computations are similar but have an entirely different physical origin.

7. CONCLUSIONS

The replacement in the third-generation model SWAN of the BSBT propagation scheme by the S&L scheme (for nonstationary cases) and the SORDUP scheme (for stationary cases) allows computations on a scales varying from the ocean to near-shore areas

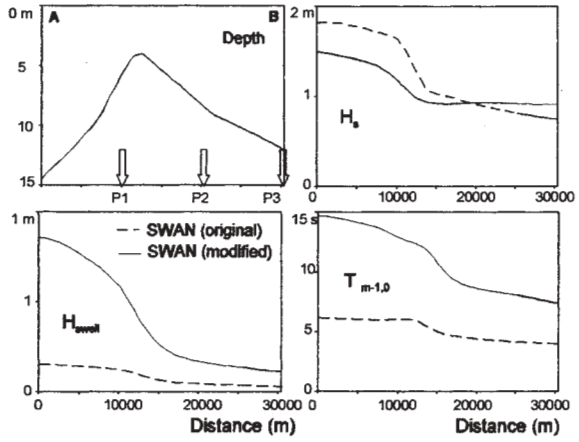

Fig 6. The significant wave height, the swell wave height and the mean wave period across Adam's Bridge (transect A-B of Fig. 2) on May 11th, 1995, 00:00 GMT. Arrows indicate locations of spectral output (Fig. 7).

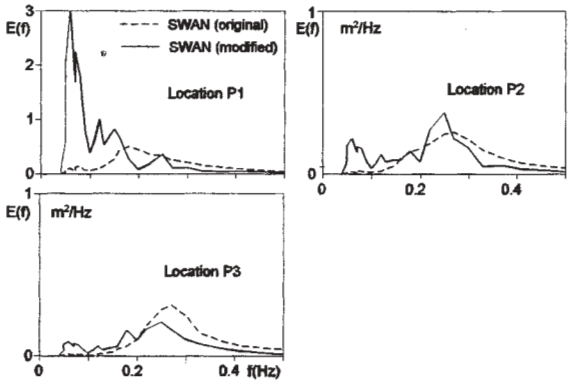

Fig. 7 The computed spectra across Adam's Bridge at locations P1, P2 and P3 of Fig. 6 (original and modified whitecapping).

(optionally in a nesting mode).

The pulse model for white-capping (Hasselmann, 1974; WAMDI, 1988; Komen et al., 1994) can be readily modified to account for the (hypothesised) effect of a low-frequency surface straining on high-frequency whitecapping. This modification causes swell to suppress rather than enhance the growth of wind waves (as in the original formulation). A numerical experiment with this modification included shows good agreement with the laboratory observation of Donelan (1987).

A numerical experiment of swell crossing the Indian Ocean shows that if the hypothesised effect is correct, wind sea would, also on an oceanic scale be suppressed by swell rather than the reverse. This

AUTHOR INDEX TABLE OF CONTENTS

implies that the mean wave period in the oceans would be longer with the modified whitecapping than with the original formulation. The differences are sufficiently obvious that observations of mean wave periods in mixed sea states (wind sea and swell) should indicate the credibility of the hypothesis.

We note that if the straining hypothesis is correct, that the differences in propagation direction of swell and wind sea should be included in the formulation. Moreover, other observations in laboratory conditions have shown that if the swell oppose the wind sea, the growth of the wind sea is enhanced (Mitsuyasu and Yoshida, 1989). An implementation of these aspects in SWAN is currently under investigation.

7. ACKNOWLEDGEMENTS

The authors wish to thank their colleagues Erick Rogers and Jim Kaihatu of the Naval Research Laboratory (Stennis Space Center, MS) and Henri Petit of Delft Hydraulics (Delft, the Netherlands) for their kind permission to report on the new propagation schemes of SWAN before the manuscript in preparation (Rogers et al., 2000) has been published. The work on the propagation schemes was supported by the Advanced Wave Prediction Program of the Office of Naval Research (USA).

8. REFERENCES

Battjes, J.A. and J.P.F.M. Janssen, 1978: Energy loss and set-up due to breaking of random waves, *Proc. 16th Int. Conf. Coastal Engineering*, ASCE, 569-587

Beji, S. and J.A. Battjes 1993: Experimental investigation of wave propagation over a bar, *Coastal Engineering*, 19, 151-162

Booij, N., R.C. Ris and L.H. Holthuijsen, 1999: A third-generation wave model for coastal regions, Part I, Model description and validation, *J.Geoph.Research*, 104, C4, 7649-7666

Booij, N. and L.H. Holthuijsen, 1987: Propagation of ocean waves in discrete spectral wave models, *Journal of Computational Physics*, Vol. 68, No. 2, pp. 307-326

Cavaleri, L. and P. Malanotte-Rizzoli, 1981: Wind wave prediction in shallow water: Theory and applications. *J. Geophys. Res.*, 86, No. C11, 10,961-10,973

Eldeberky, Y. and J.A. Battjes, 1995: Parameterization of triad interactions in wave energy models, *Proc. Coastal Dynamics Conf. '95*, Gdansk, Poland, 140-148

Eldeberky, Y., 1996: Nonlinear transformation of wave spectra in the nearshore zone, *Ph.D. thesis*, Delft University of Technology, Department of Civil Engineering, The Netherlands

Hasselmann, K., T.P. Barnett, E. Bouws, H. Carlson, D.E. Cartwright, K. Enke, J.A. Ewing, H. Gienapp, D.E. Hasselmann, P. Kruseman, A. Meerburg, P. Müller, D.J. Olbers, K. Richter, W. Sell and H. Walden, 1973: Measurements of wind-wave growth and swell decay during the Joint North Sea Wave Project (JONSWAP), *Dtsch. Hydrogr. Z. Suppl.*, 12, A8

Hasselmann. K., 1974: On the spectral dissipation of ocean waves due to whitecapping, *Bound.layer Meteor.*, 6, 1-2, 107-127

Hasselmann, S., K. Hasselmann, J.H. Allender and T.P. Barnett, 1985: Computations and parameterizations of the nonlinear energy transfer in a gravity wave spectrum. Part II: Parameterizations of the nonlinear transfer for application in wave models, *J. Phys. Oceanogr.*, 15, 11, 1378-1391

Komen, G.J., S. Hasselmann, and K. Hasselmann, 1984: On the existence of a fully developed wind-sea spectrum, *J. Phys. Oceanogr.*, 14, 1271-1285

Komen, G.J., Cavaleri, L., Donelan, M., Hasselmann, K., Hasselmann, S. and P.A.E.M. Janssen, 1994: *Dynamics and Modelling of Ocean Waves*, Cambridge University Press, 532 p.

Longuet-Higgins, M.S. and R.W. Stewart, 1960: Changes in the form of short gravity waves on long wind waves and tidal currents, *J. Fluid Mech.*, 8, 565-583

Miles, J.W., 1957: On the generation of surface waves by shear flows, *J. Fluid Mech.*, 3, 185-204

Mitsuyasu, H. and Y. Yoshida, Air-sea interactions under the existence of swell propagating against the wind, Bul. Res. Inst. Appl. Mech., Kyushu Univ. (in Japanese), 63, 47-71, 1989

Phillips, O.M., 1957: On the generation of waves by turbulent wind, *J. Fluid Mech.*, 2, 417-445

Rogers, W.E., J.M. Kaihatu, N. Booij and L.H. Holthuijsen, 1999: Improving the numerics of a third-generation wave action model,

Naval Research Laboratory, NRL/FR/7320-99-9695, 79p.

Rogers, W.E., J.M. Kaihatu, N. Booij and L.H. Holthuijsen, 2000: Arbitrary-scale propagation in a third-generation wind wave model, manuscript in preparation

Snyder, R.L., Dobson, F.W., Elliott, J.A. and R.B. Long, 1981: Array measurement of atmospheric pressure fluctuations above surface gravity waves, *J. Fluid Mech.*, 102, 1-59

Stelling, G. S., and J. J. Leendertse, 1992: Approximation of convective processes by cyclic AOI methods. *Proceedings, 2nd International Conference on Estuarine and Coastal Modeling,* Tampa, Florida, ASCE, 771-782.

Tolman, H.J., 1992: Effects of numerics on the physics in a third-generation wind-wave model, *J. Phys. Oceanogr.*, 22, 10, 1095-1111

WAMDI group, 1988: The WAM model - a third generation ocean wave prediction model, *J. Phys. Oceanogr.*, 18, 1775-1810

Wu, J., 1982: Wind-stress coefficients over sea surface from breeze to hurricane, *J. Geophys. Res.*, 87, C12, 9704-9706

APPENDIX

The significant wave height H_s, the swell wave height H_{swell} and the mean wave period $T_{-1,0}$ are

$H_s = 4\sqrt{m_0}$, $H_{swell} = 4\sqrt{m_{swell}}$ and

$T_{-1,0} = 2\pi\,(m_{-1,0} / m_0)$ respectively in which

$$m_n = \int_0^{\infty} \sigma^n E(\sigma) d\sigma \text{ and } m_{swell} = \int_0^{0.1Hz} E(\sigma) d\sigma$$

and $E(f)$ is the variance density spectrum.

The overall mean frequency $\tilde{\sigma}$, the overall mean wave number $\tilde{k}$ and the overall mean steepness $\tilde{s}$ are

$$\tilde{\sigma} = \left(E_{tot}^{-1} \int_0^{2\pi}\int_0^{\infty} \sigma^{-1} E(\sigma,\theta)\, d\sigma\, d\theta \right)^{-1},$$

$$\tilde{k} = \left(E_{tot}^{-1} \int_0^{2\pi}\int_0^{\infty} k^{-1/2} E(\sigma,\theta)\, d\sigma\, d\theta \right)^{-2} \text{ and}$$

$$\tilde{s} \equiv \tilde{k}\sqrt{E_{tot}}$$

respectively with the total wave energy

$$E_{tot} = \int_0^{2\pi}\int_0^{\infty} E(\sigma,\theta)\, d\sigma\, d\theta.$$

The high-frequency mean steepness $s_{hf}(\sigma)$ is:

$$s_{hf}(\sigma) \equiv k_{hf}(\sigma)\sqrt{E_{hf}(\sigma)}$$

with the high-frequency mean wave number

$$k_{hf}(\sigma) \equiv \left(E_{hf}^{-1} \int_0^{2\pi}\int_{\sigma}^{\infty} k^{-1/2} E(\sigma,\theta)\, d\sigma\, d\theta \right)^{-2}$$

and the high-frequency energy

$$E_{hf}(\sigma) \equiv \int_0^{2\pi}\int_{\sigma}^{\infty} E(\sigma,\theta)\, d\sigma\, d\theta$$

BENCHMARK TESTS OF STWAVE

Jane McKee Smith

Engineer Research and Development Center
Coastal and Hydraulics Laboratory
Vicksburg, Mississippi, USA

1. INTRODUCTION

The U.S. Army Corps of Engineers routinely uses the steady-state coastal spectral wave model STWAVE for nearshore wave generation and transformation. STWAVE has recently been applied to more than 40 ongoing Corps projects, including sites on the US East Coast, West Coast (including Alaska), Gulf of Mexico, and Great Lakes. STWAVE is also under OPTEST at the Naval Oceanographic Office producing real-time wave forecasts in direct support of Naval exercises and operations in the nearshore domain. STWAVE includes the processes of depth and current-induced refraction and shoaling, depth- and steepness-induced wave breaking, and wind-wave growth.

A benchmark data set is being constructed to evaluate the existing version of STWAVE and to assess model upgrades. The benchmarking exercise will be used to identify model strengths and weaknesses and to inter-compare results with other models. The benchmark data set will include measurements of wave-current interaction at tidal inlets, wave growth, and wave breaking. Both lab and field data are included. This paper provides an overview of STWAVE, description of three benchmark comparisons, discussion of results, and summary.

2. STWAVE OVERVIEW

The numerical model STWAVE, version 3.0 (Resio 1987, 1988; Smith et al. 1999, in preparation), was used in the benchmark tests. STWAVE numerically solves the steady-state conservation of spectral action balance along backward-traced wave rays:

$$(C_{ga})_x \frac{\partial}{\partial x}\frac{C_a C_{ga}\cos(\mu-\alpha)E(f,\alpha)}{\omega_r} + (C_{ga})_y \frac{\partial}{\partial y}\frac{C_a C_{ga}\cos(\mu-\alpha)E(f,\alpha)}{\omega_r} = \Sigma\frac{S}{\omega_r} \quad (1)$$

where

C_{ga} = absolute wave group celerity
x,y = spatial coordinates, subscripts indicate x and y components
C_a = absolute wave celerity
μ = current direction
α = propagation direction of spectral component
E = spectral energy density
f = frequency of spectral component
ω_r = relative angular frequency (frequency relative to the current)
S = energy source/sink terms

The source terms include wind input, nonlinear wave-wave interactions, dissipation within the wave field, and surf-zone breaking. The terms on the left-hand side of Equation 1 represent wave propagation (refraction and shoaling), and the source terms on the right-hand side of the equation represent energy growth or decay in the spectrum.

The assumptions made in STWAVE are as follows:

- Mild bottom slope and negligible wave reflection.
- Spatially homogeneous offshore wave conditions.
- Steady waves, currents, and winds.
- Linear refraction and shoaling.
- Depth-uniform current.
- Negligible bottom friction.

STWAVE is a half-plane model, meaning that only waves propagating toward the coast are represented. Waves reflected from the coast or waves generated by winds blowing offshore are neglected. Wave breaking in the surf zone limits the maximum wave height based on the local water depth and wave steepness:

$$H_{mo_{\max}} = 0.1L \tanh kd \qquad (2)$$

where

H_{mo} = zero-moment wave height
L = wavelength
k = wave number
d = total water depth

STWAVE is a finite-difference model and calculates wave spectra on a rectangular grid with square grid cells. The model outputs include zero-moment wave height, peak wave period (T_p), and mean wave direction (α_m) at all grid points and two-dimensional spectra at selected grid points.

The inputs required to execute STWAVE are as follows:

- Bathymetry grid (including shoreline position, grid size, and grid resolution).
- Incident frequency-direction wave spectrum on the offshore grid boundary.
- Current field (optional).
- Tide elevation, wind speed, and wind direction (optional).

The upgrades in STWAVE version 3.0 include calculation of radiation stresses, improved model efficiency (25-40%), an option for inputting a single current field for multiple runs, output of breaking patterns, and an improved Surface-Water Modeling System Graphical User Interface (Brigham Young University Engineering Computer Graphics Laboratory 1997). The next version of the model will include upgrades to the wave generation and wave breaking source terms and additional improvements in efficiency.

3. BENCHMARK DATA SETS

Three benchmark data sets are discussed in this paper. These data sets include Ponce de Leon Inlet, Florida, Willapa Bay, Washington, and Grays Harbor, Washington, all in the United States. These coastal inlet sites provide evaluation of STWAVE for complex bathymetry, wave breaking, and wave-current interaction. An additional data set from the U.S. Army Corps of Engineers Field Research Facility is presently being added to evaluate wind-wave growth. STWAVE is typically applied for coastal processes studies, so the most important evaluation parameters are wave height and wave direction. Data comparisons are made for a variety of incident wave heights, periods, and directions for each data set. For the field cases, a variety of tide elevations and current fields are also included.

3.1 Ponce De Leon Inlet, Florida

Ponce De Leon Inlet is located on the Atlantic Coast of Florida (see King et al. 1999 for more detailed description of the site). The pronounced ebb shoal is displaced to the south of the inlet entrance, and waves tend to focus and break across the shoal. This benchmark case was selected because it includes relatively dense measurements over complex bathymetry.

A 1:100 scale physical model of the inlet was utilized to obtain a wave transformation data set to evaluate wave models (Smith and Harkins 1997). The physical model represents a 4.2-km alongshore by 1.4-km cross-shore reach of the nearshore bathymetry, from the 10.7 mean low water depth contour to the shoreline (Figure 1). Waves were generated with a 27.4-m long, 60-paddle directional spectral wave generator. Directional spectra were generated with a TMA frequency distribution (Bouws et al. 1985) and wrapped normal directional spreading function (Borgman 1990). Fourteen irregular wave cases were run with wave heights of 0.73 m to 1.92 m, peak periods of 8-15 sec, and mean directions of 0, 30, and –30 deg, relative to shore-normal. Wave data were collected with 30 capacitance wave gauges, sampled at 25 Hz. Two gauges were located on the offshore slope of the ebb shoal, two 12-gauge linear arrays with 100-m prototype spacing between gauges were placed on the ebb shoal, and four additional gauges were placed in the inlet entrance. One array was positioned across the outer lobe of the ebb shoal (prototype depths of 4.5 to 7.5 m with +1.07 m tide) and another closer to shore (prototype depths of 3.5 to 4.0 m with tide) (see Figure 1).

The STWAVE bathymetry grid was developed from the templates used to construct the physical model. The STWAVE grid was 380 cells along the shore by 205 cells across the shore with a resolution of 10 m. The input spectra applied at the offshore boundary were the same as the target spectra for the wave generator. Figure 2 shows an example comparison of wave heights calculated by STWAVE to the laboratory measurements (scaled to prototype). The wave heights are focused by 3D structure of the ebb shoal.

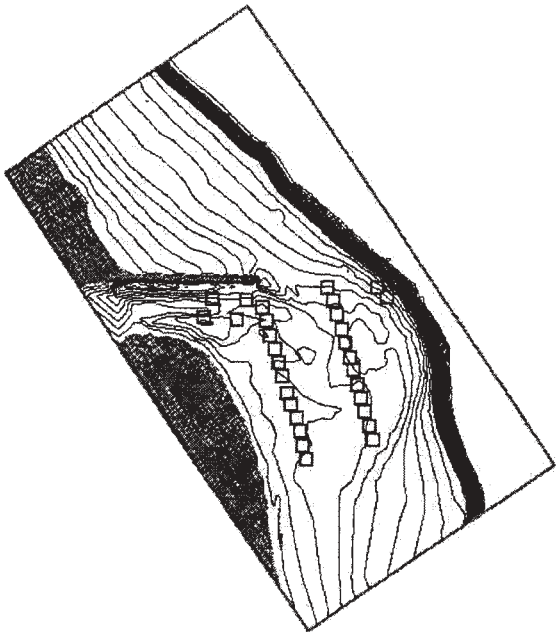

Figure 1. Ponce De Leon Inlet bathymetry (1-m prototype depth contours) and measurement locations

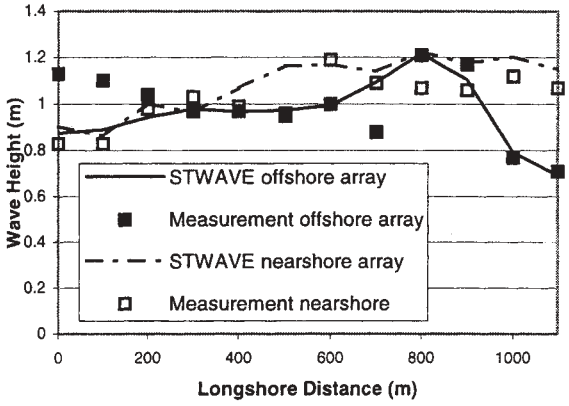

Figure 2. Example of calculated versus measured wave heights for Ponce De Leon Inlet laboratory data (distance measured along the arrays, north to south), incident height is 1 m, peak period is 8 sec, and mean direction is 30 deg (north of shore normal)

Figure 3 shows a scatter plot of calculated versus measured wave heights for all 14 cases for all 30 gauges. In general, wave height is overestimated by the model. To quantify the error for each benchmark case, the bias and root-mean-square (RMS) error are defined:

$$bias = \frac{1}{N}\sum_{i=1}^{N} Y_i - X_i \tag{3}$$

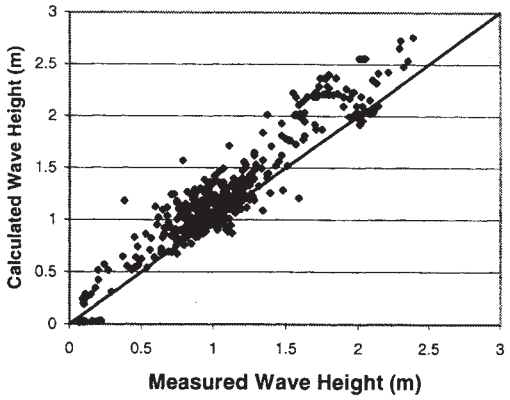

Figure 3. Calculated versus measured wave heights for Ponce De Leon Inlet laboratory data (solid line is perfect agreement)

$$Error_{RMS} = \sqrt{\frac{1}{N}\sum_{i=1}^{N} [Y_i - X_i]^2} \tag{4}$$

where N is the number of data points, Y is the STWAVE-calculated parameter, and X is the measured parameter (wave height or direction). The nondimensional parameters of scatter index (SCI), operational performance index (OPI), and model performance index (MPI) are also defined:

$$SCI = \frac{Error_{RMS}}{\overline{X}} \tag{5}$$

$$OPI = \frac{Error_{RMS}}{X_{incident}} \tag{6}$$

$$MPI = 1 - \frac{Error_{RMS}}{changes_{RMS}} \tag{7}$$

where $\overline{X}$ is the mean measured parameter, $X_{incident}$ is the incident parameter, and $changes_{RMS}$ is defined:

$$changes_{RMS} = \sqrt{\frac{1}{N}\sum_{i=1}^{N} [X_{incident} - X_i]^2} \tag{8}$$

Small values of the SCI and OPI indicate good model to measurement agreement. Values of the MPI near unity indicate good agreement. For the Ponce De Leon laboratory cases, the bias is 0.04 m (model overestimates wave height) and the RMS error is 0.12 m (both is prototype units). The average values of

the performance indices for all cases are: SCI = 0.10, the OPI = 0.11, and the MPI = 0.79.

3.2 Willapa Bay, Washington

Willapa Bay is a natural tidal inlet on the Pacific Coast of Washington. The Bay is a large estuary with a tidal prism of approximately 6 x 10^8 m^3 and an inlet width of 8 km (Jarrett 1976). The entrance is a complex series of shoals and channels (Figure 4). A submerged spit at the northern side of the entrance cyclically grows and breeches. The navigation channel hugs the northern shoreline of the bay, and northern interior shoreline at Cape Shoalwater is eroding at an average rate of 40 m/yr. A bar extends from Leadbetter Point across most of the inlet width with an elevation near mean lower low water. The mean tide range is 2.7 m with peak currents over 2 m/sec. The wave climate is severe, with a yearly average wave height of 2 m and storm heights up to 9 m. Waves within the bay are strongly modulated by the tide and wave dissipation across the bar. This benchmark case was selected because it includes complex bathymetry, wave-current interaction, large tidal range, and wave breaking.

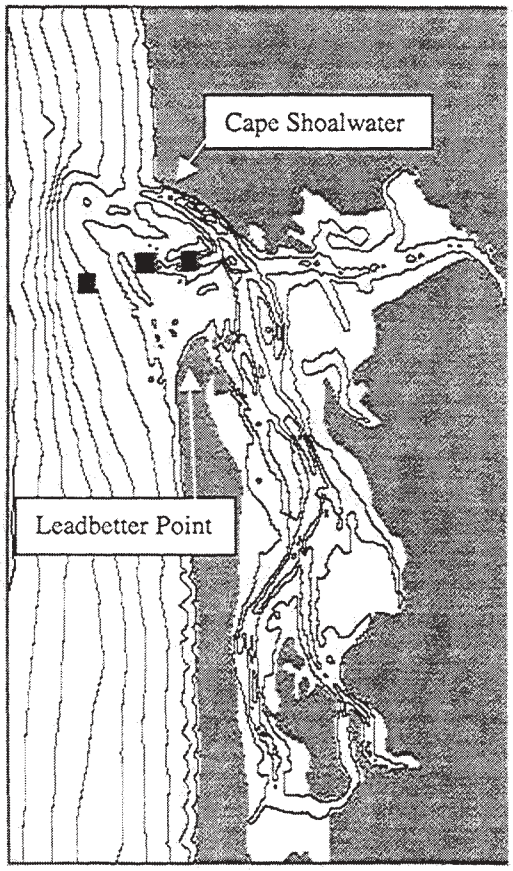

Figure 4. Willapa Bay bathymetry (5-m depth contours) and measurement locations

Directional wave measurements were made at three stations, Station 1 is seaward of the Willapa bar and Stations 2 and 3 are bay-ward of the bar (Figure 4). Wave measurements were made with bottom-mounted pressure gauges and Acoustic Doppler Velocimeters in mean water depths of approximately 10 m. Offshore directional wave measurements were available from the Grays Harbor Buoy at 40-m depth. Measurements were taken from late August through mid November 1998.

The STWAVE grid was developed with bathymetry data compiled from a combination of conventional hydro surveys and a helicopter-based LIDAR survey. The shallowest depths over the Willapa Bar were estimated from local knowledge (Coastal Guard and boat captains). The grid was 301 cells in the across the shore and 511 cells along the shore with a resolution of 100 m. Incident one-dimensional wave spectra from the Gray Harbor Buoy were used to drive the model. The directional distributions measured at the buoy lack sufficient resolution, so a theoretical distribution of the form $\cos^n(\alpha-\alpha_m)$ was applied, where α_m is the mean wave direction from the buoy. The values of n ranged from 4 to 38, with small values (broad directional distribution) applied at higher frequencies and large values (narrow directional distribution) applied at lower frequencies (Thompson et al. 1996).

For applications where wave-current interaction significantly alters the wave height or blocks the waves, current fields are needed as an input to STWAVE. Wave height increases on strong ebb current and decreases on strong flood current. Currents also alter wave direction. The current modifies waves with higher frequencies (shorter periods) more than it does waves with lower frequencies. In addition to shoaling and refraction by currents, wave breaking is also changed by an opposing or following current (L and k change in Equation 2). Wave breaking is enhanced on an opposing current (ebb) and reduced on a following current (flood). If the ebb current is strong, waves with short periods cannot propagate against it, and wave energy is blocked and dissipated. Current fields were generated using the ADCIRC tidal circulation model (Militello et al. 2000). Measured tide elevations were used to specify water levels.

A 6-day benchmark period was selected from the data set (15-20 October 1998) at 2-hour increments. This period was chosen because it covers a large range of incident wave heights (0.9 to 3.3 m) and periods (6 to 16 sec). Figure 5 and 6 show time-history comparisons of wave heights and directions for 15-21 October 1998 for all three stations.

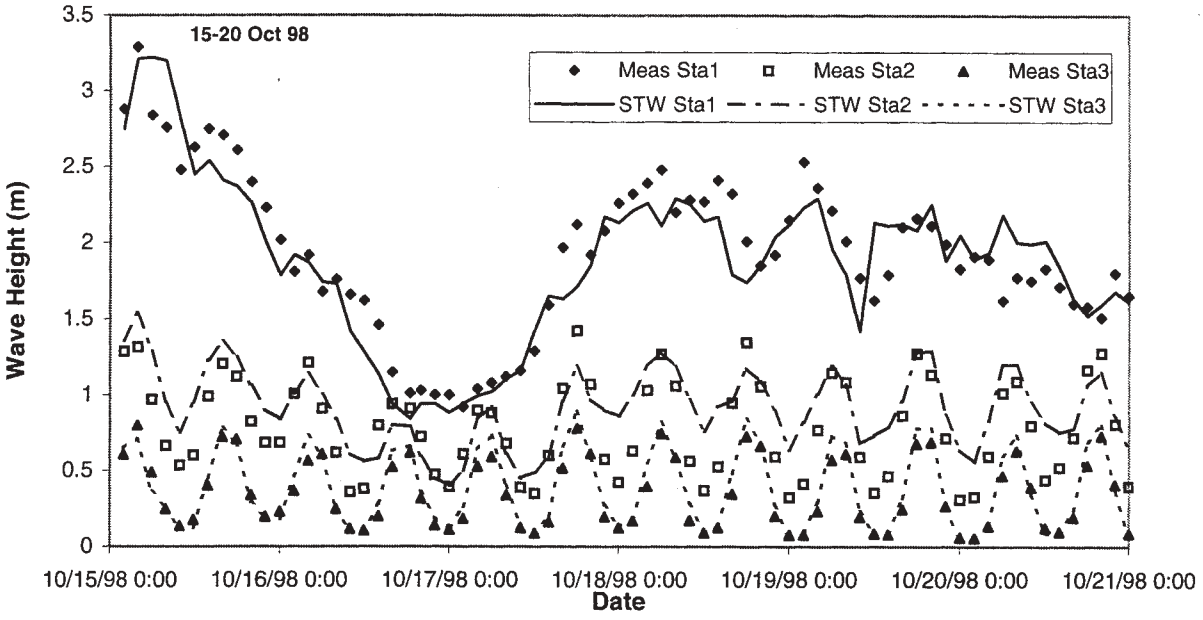

Figure 5. Measured and calculated wave heights at Willapa Bay for 15-21 October 1998

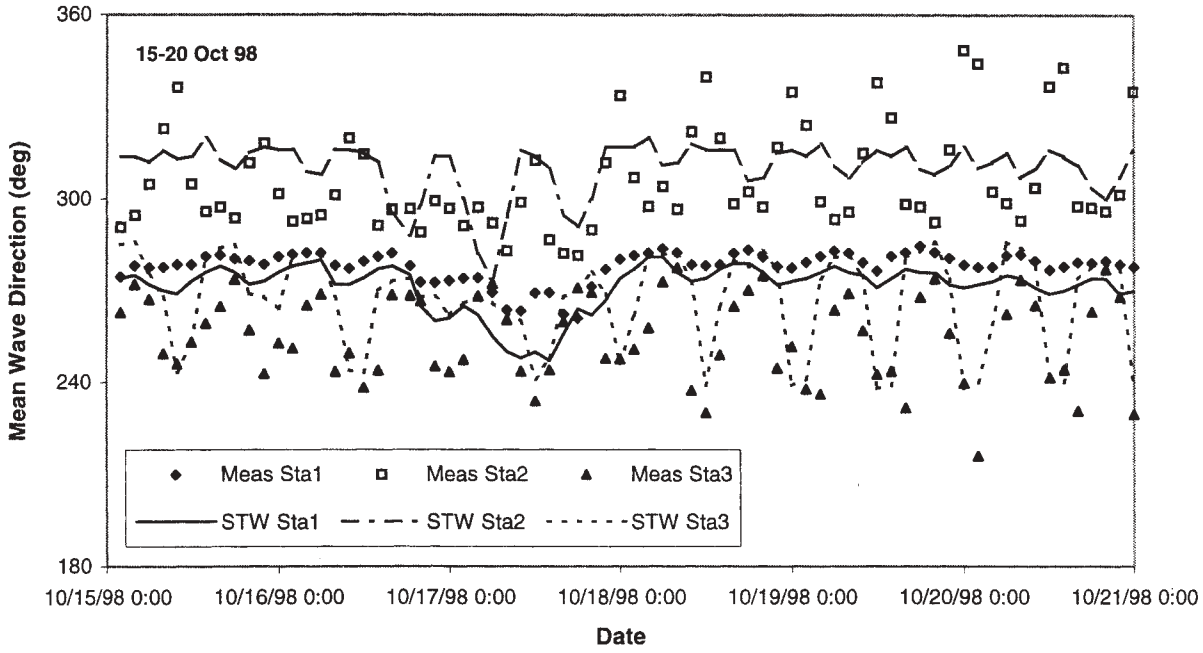

Figure 6. Measured and calculated mean wave directions at Willapa Bay for 15-21 October 1998

The wave height inside Willapa bay is controlled by the water depth over the bar. Nearly continuous depth-limited breaking on the bar leads to an interior wave height modulated by the tide elevation (see Stations 2 and 3 in Figure 5) and having almost no correlation to the incident wave height (compare Stations 1 and 2).

Wave direction in the bay is also controlled by the depth over the bar. At high tide, wave directions at Stations 2 and 3 are 270-290 deg, with most wave energy coming straight over the bar. At low tide, the wave energy reaches Station 2 through the deep navigation channel to the north and thus the wave

directions are more northerly (320-350 deg). The wave energy reaches Station 3 through a relic center channel that is aligned at 220-240 deg. These trends in both wave height and wave direction are well represented in the model. Wave directions at Stations 2 and 3 are less variable in the model than in the measurements, but this is a typical result for measurements when the total energy is relatively low. For the Willapa Bay cases, the bias in wave height is 0.04 m and the RMS error is 0.18 m. STWAVE tends to slightly underestimate the large wave heights (e.g., at Station 1) and overestimate the smaller wave heights (e.g., low tide heights at Station 2). The average values of the performance indices for wave height all three stations are: SCI = 0.21, the OPI = 0.09, and the MPI = 0.91. The bias in wave direction is 3.5 deg and the RMS error is 15 deg. The performance indices are not well suited for wave direction statistics.

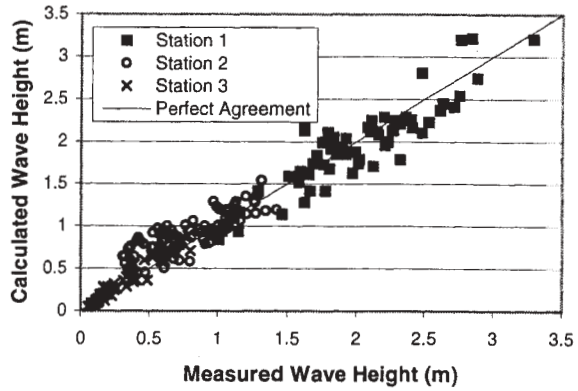

Figure 7. Scatter plot of Willapa Bay wave height

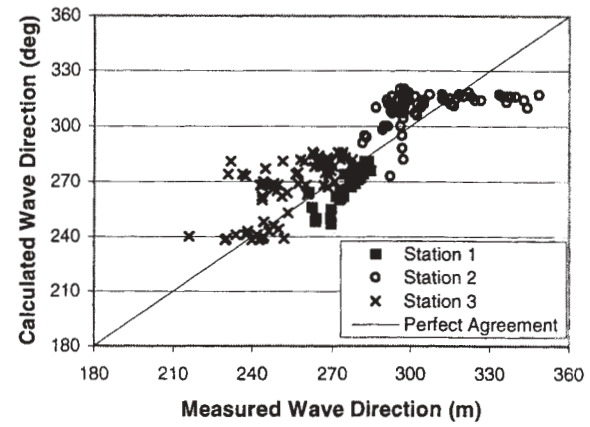

Figure 8. Scatter plot of Willapa Bay wave direction

Figures 7 and 8 are scatter plots of wave height and wave direction. A negative bias for large wave heights and a positive bias for small wave heights can be seen in the scatter plot. The greater variability in the measured directions for Stations 2 and 3 is illustrated in Figure 8.

3.3 Grays Harbor Washington

Grays Harbor is a jettied entrance on the Washington coast, located approximately 30 km north of Willapa Bay. Grays Harbor is exposed to the same severe wave climate and large tidal range as Willapa Bay. The ebb shoal is offset to the north and is of low relief (Figure 9). The navigation channel hugs the south jetty. This benchmark case was selected because it includes complex bathymetry, wave-current interaction, large tidal range, and measurements within the entrance.

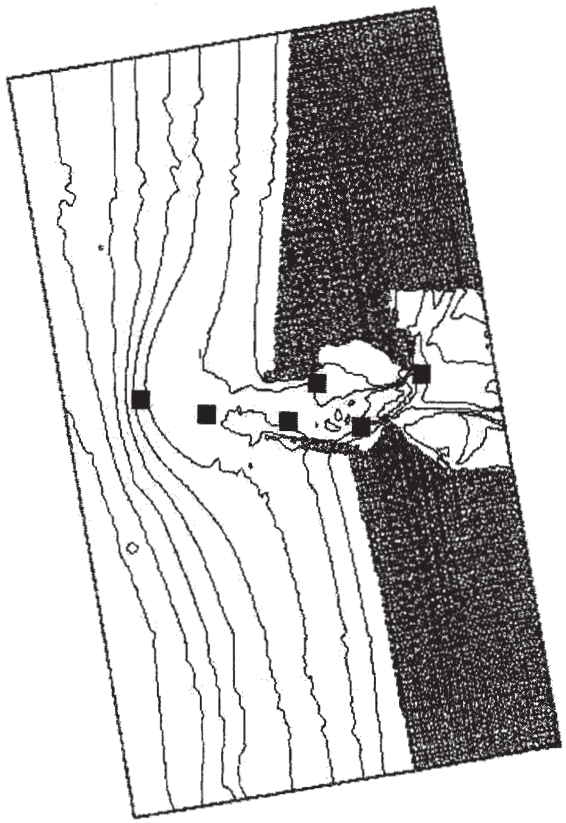

Figure 9. Grays Harbor bathymetry (5-m depth contours) and measurement locations

Directional wave measurements were made at six stations, from the outer edge of the ebb shoal into the bay (Figure 9). The water depths at the gauges are 16.8, 13.7, 12.7, 9.8, 8.6, and 13.4 m mean lower low water (from west to east). Wave measurements were made with bottom-mounted pressure gauges and Acoustic Doppler Velocimeters. Offshore directional wave measurements were available from the Grays

Harbor Buoy at 40-m depth. Measurements were taken from 13 September through 11 October 1999.

The STWAVE grid was compiled from conventional hydro survey data and National Ocean Survey bathymetry. The grid is 171 cells across the shore and 293 cells along the shore with a resolution of 100 m. Incident wave spectra were derived from the Grays Harbor Buoy (located on the offshore grid boundary), as described in Section 3.2 for Willapa Bay. The simulations in the paper were run without wave-current interaction. Current field input will be added later. Water levels were specified from measured tide elevations.

Figures 10 and 11 are time history plots of measured and modeled wave height and mean direction for Station 3 (stations are numbered from west to east) at two-hour increments. Station 3 is representative of the outer three stations, although Station 3 exhibits more variation with tide and current than the outer, Stations 1 and 2. The agreement at the outer stations is reasonably good.

Figures 12 and 13 are time history plots of measured and modeled wave height and mean direction for Stations 5 and 6. Station 5 is representative of Station 4, as well (although Station 4 has greater error, possibly due to the higher noise level of the gauge). For these inner gauges, STWAVE represents the general trends in wave height, but does not reflect the variations (up to 0.5 m) over each tidal cycle. The peaks in wave height are correlated to the ebb current (magnitude up to 1 m/sec). The wave directions calculated at the inner stations are nearly constant because the directional window to reach these stations is small. The measurements show strong variation in the local wave direction as a function of the current. For example, at Station 6, the current is directed approximately northeast on flood and southwest of ebb with a maximum magnitude of approximately 1 m/sec. On flood, the wave directions are generally larger (out of the west-southwest. On ebb, the wave directions are 10 to 20 deg less or out of the southwest. These current-induced wave height and direction variations are not included in the present STWAVE calculations, but will be simulated in the future.

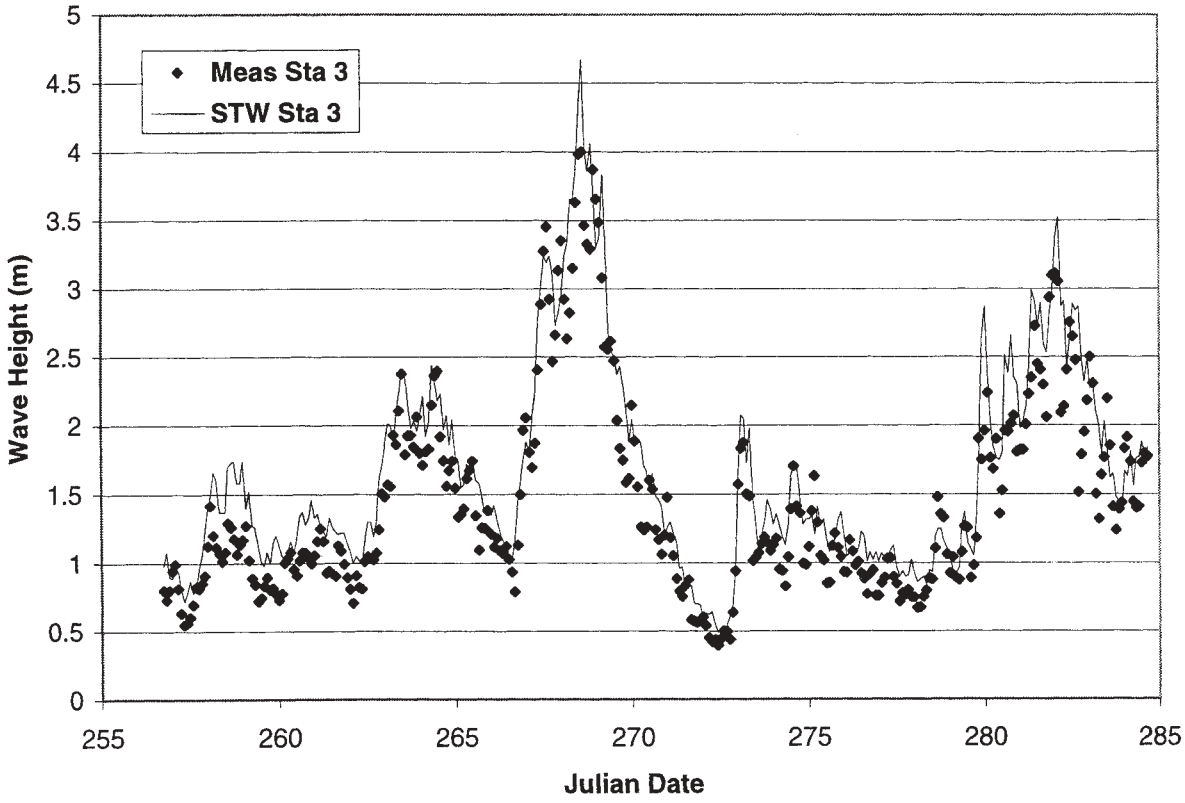

Figure 10. Measured and calculated wave heights at Grays Harbor for Station 3 (13 Sep-11 Oct 1999)

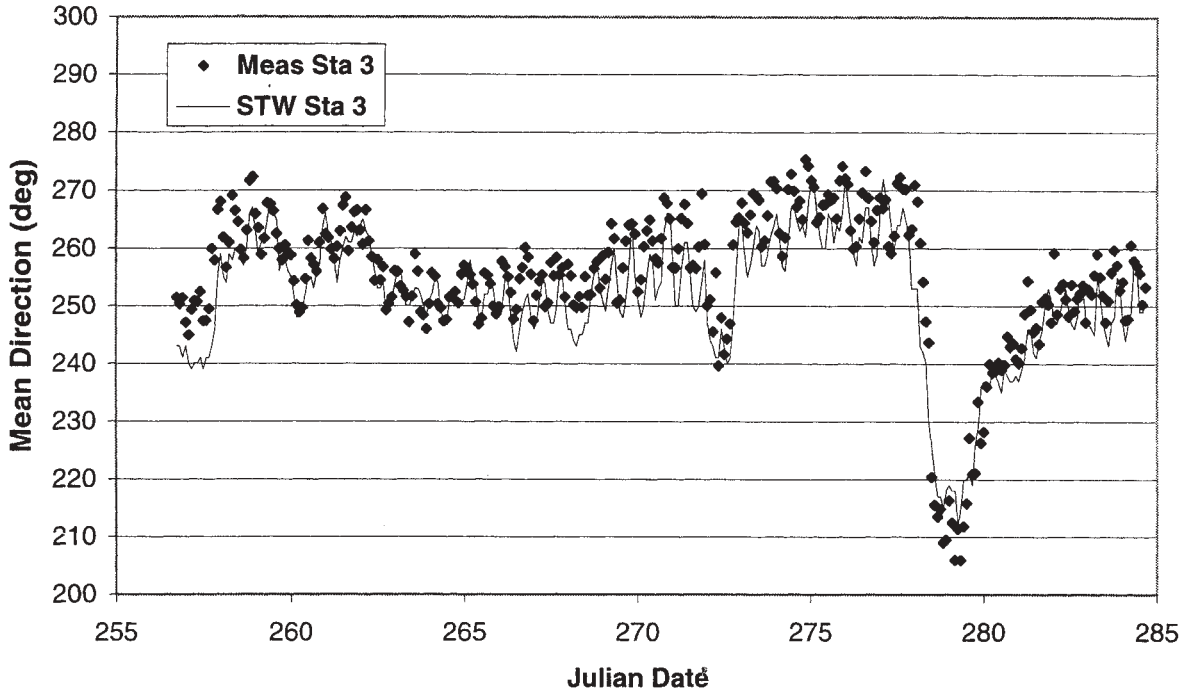

Figure 11. Measured and calculated mean wave directions at Grays Harbor for Station 3 (13 Sep-11 Oct 1999)

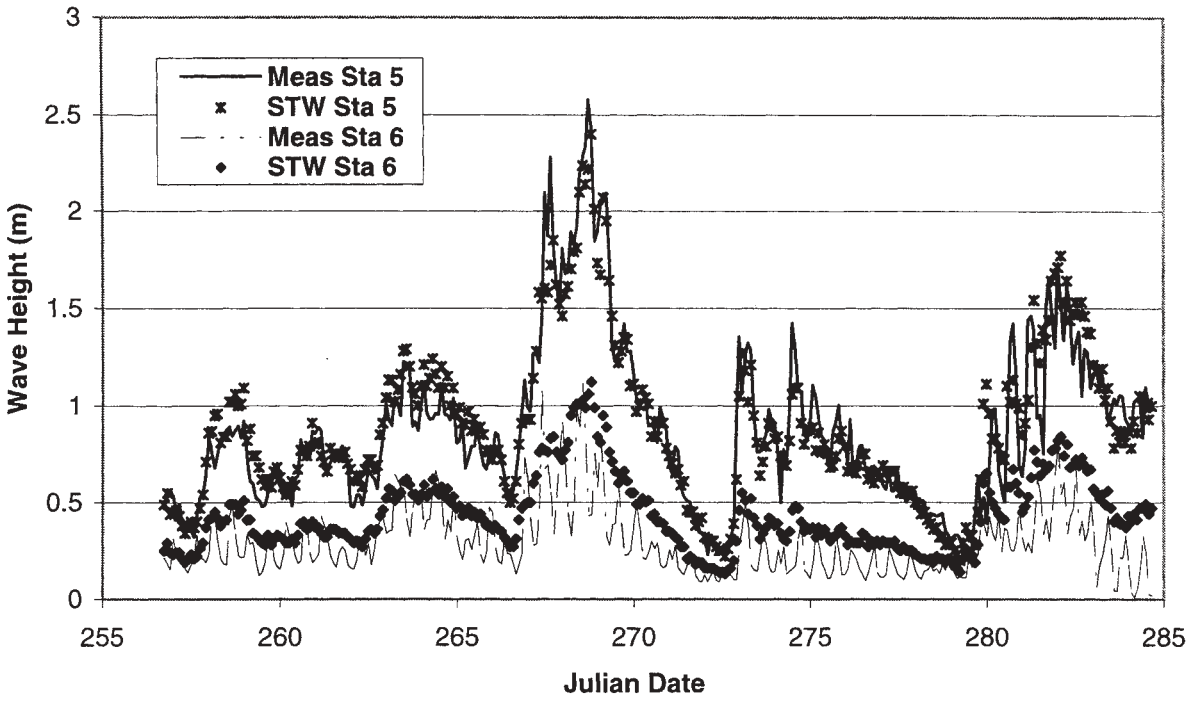

Figure 12. Measured and calculated wave heights at Grays Harbor for Stations 5 and 6 (13 Sep-11 Oct 1999)

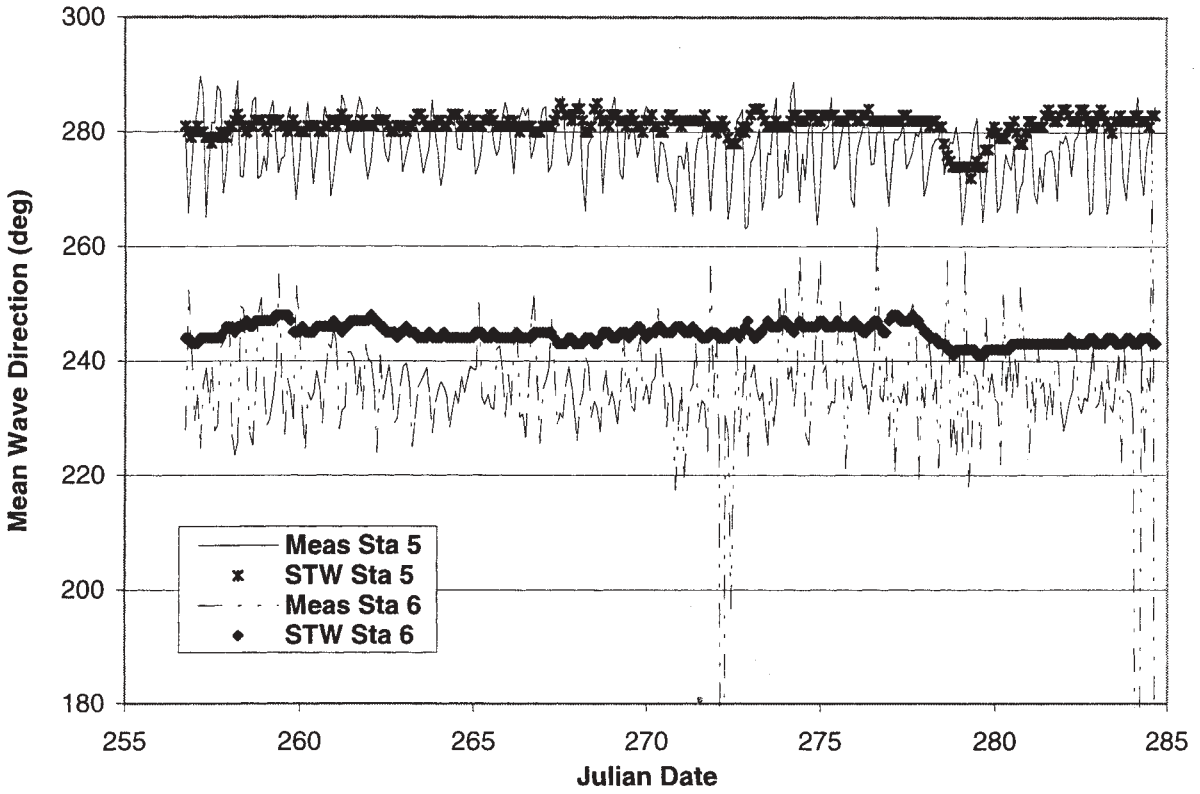

Figure 13. Measured and calculated mean wave directions at Grays Harbor for Stations 5 and 6 (13 Sep-11 Oct 1999)

For the Grays Harbor simulations, the wave height bias is 0.16 m, the RMS error is 0.28 m, and the performance indices are: SCI = 0.20, OPI = 0.36, and MPI = 0.68.

The mean wave direction bias is –1.6 deg and RMS error is 11 deg. Figures 14 and 15 are scatter plots of wave height and direction for all stations. The 10 to 20-deg variation in wave direction induced by the current at the interior stations (Stations 4-6) shows up in the scatter plot are horizontal groupings of points.

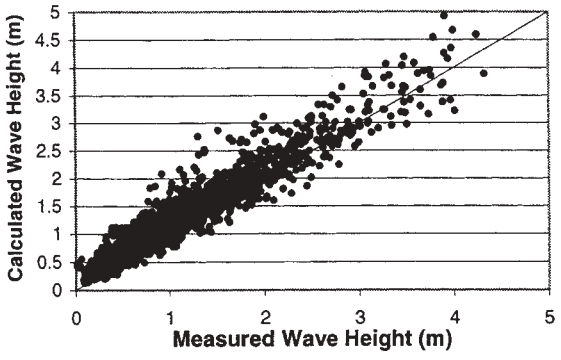

Figure 14. Scatter plot of wave height for Grays Harbor Stations 1-6 (13 Sep-11 Oct 1999)

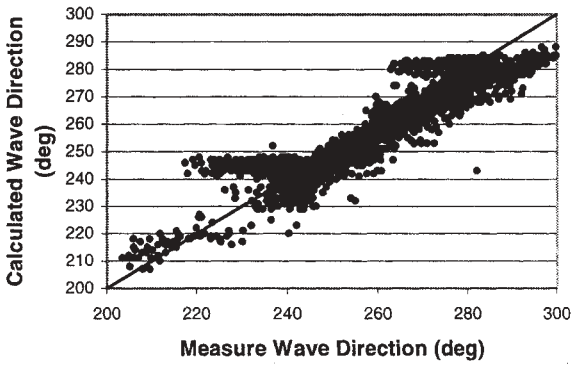

Figure 15. Scatter plot of mean wave direction for Grays Harbor Stations 1-6 (13 Sep-11 Oct 1999)

4. DISCUSSION

The error statistics for the three benchmark data sets are summarized in Table 1. These statistics represent over 3000 data comparisons. The estimated error in measurement of wave height is 10% and in wave direction is 10 deg. The RMS errors in wave height range from 0.12 to 0.22 m. STWAVE tends to overestimate wave height, as shown in positive biases from 0.04 to 0.16 m. Wave direction RMS errors were 11 to 15 deg, with biases of –1.6 to 3.5 deg. The scatter

indices ranged from 0.10 to 0.21, with larger scatter in the field data, where more variability is expected. The operational performance and model performance indices are significantly poorer for the Grays Harbor example. The main reason for the poorer scores is the neglect of currents in the STWAVE simulations. The variations in wave height and direction in the inner gauges are strongly correlated to the current magnitude and direction. Current will added to the Grays Harbor benchmark data set in the near future.

Table 1. Summary of Benchmark Error Statistics

Parameter	Ponce Inlet	Willapa bay	Grays Harbor
H_{mo} bias (m)	0.04	0.05	0.16
H_{mo} $error_{RMS}$ (m)	0.12	0.18	0.22
H_{mo} SCI	0.10	0.21	0.20
H_{mo} OPI	0.11	0.10	0.36
H_{mo} MPI	0.79	0.91	0.68
α bias (deg)	------	3.5	-1.6
α $error_{RMS}$ (deg)	------	15.	11.

The benchmarking results lead to the following conclusions:

- STWAVE reproduces refraction and shoaling over complex bathymetry.
- The wave breaking in STWAVE appears to dissipate too little wave energy over shallow shoals, which results in a positive bias in wave height.
- Although wave-current interaction was calculated in the Willapa Bay data set, wave breaking was the dominant process at Willapa Bay. The Grays Harbor data set indicates that wave height is modulated up to 0.5 m and direction up to 20 deg by the current. The Grays Harbor simulations will be repeated with currents to further test the wave-current interaction capability in the model.

5. SUMMARY

The steady-state spectral wave model STWAVE is routinely used by the U.S. Army Corps of Engineers for nearshore wave modeling. A benchmark data set is being constructed to verify the existing model and assess model upgrades. Three benchmark data sets were presented in this paper: Ponce De Leon Inlet (laboratory), Willapa Bay (field), and Grays Harbor (field). Over 3000 data comparisons were made with the data set. The data set includes complex bathymetry, strong wave breaking, and wave-current interaction.

The results indicate that STWAVE reproduces refraction and shoaling over complex bathymetry with RMS error of 0.12 to 0.22 m. STWAVE appears to dissipate too little wave energy through wave breaking (overestimates wave height). Additional studies of wave-current interaction are needed.

Future work will include revising the Grays Harbor data set to include wave-current interaction and adding wave generation tests to the benchmark data set. Measurements from the U.S. Army Corps of Engineers Field Research Facility are presently being added to evaluate wave generation.

6. ACKNOWLEDGEMENTS

Permission to publish this paper was granted by the Office, Chief of Engineers, U.S. Army Corps of Engineers. This research was conducted under the Wave in Entrance Channels work unit in the Coastal Navigation Hydrodynamics Program of the Coastal and Hydraulics Laboratory, U.S. Army Engineer Research and Development Center. Lori Hadley and Mary Cialone are acknowledged for assistance with benchmark data set compilation and STWAVE simulations. Bruce Ebersole provided useful review comments. Field data collection at Grays Harbor and Willapa Bay was support by the U.S. Army Engineer District, Seattle.

7. REFERENCES

Borgman, L. E. 1990: Irregular ocean waves: kinematics and forces. In *Ocean Engineering Science the Sea*, Vol. 9, Part A (ed. By B. LeMehaute and D.M. Hanes), John Wiley & Sons, NY.

Bouws, E., Gunther, H., Rosenthal, W., and Vincent, C. L. 1985: Similarity of the wind wave spectrum in finite depth waves; 1. Spectral form. *Journal of Geophysical Research*, 90(C1), 975-986.

Brigham Young University Engineering Computer Graphics Laboratory. 1997: Surface-water modeling system reference manual. Brigham Young University, Provo, UT.
http://hlnet.wes.army.mil/software/sms/docs.htp

Jarrett, J. T. 1976: Tidal prism – inlet area relationships. GITI Report 3, U.S. Army Engineer Waterways Experiment Station, Vicksburg, MS.

King, D. B., Smith, J. M., Militello, A., Stauble, D. K., and Waller, T. N. 1999: Ponce De Leon Inlet, Florida Site Investigation, Report 1: Selected Portions of Long

Term Measurements 1995-1997. Technical Report, CHL-99-1, U.S. Army Engineer Waterways Experiment Station, Vicksburg, MS, 147 pp.

Kraus, N. C. 2000: Study of navigation channel feasibility, Willapa Bay Washington. Technical Report ERDC/CHL-00-6, U.S. Army Engineer Research and Development Center, Vicksburg, MS. http://libweb.wes.army.mil/REPORTS/CHL/ERDC-CHL-TR-00-6.pdf

Militello, A., Scheffner, N. W., Bratos, S. M., Brown, M. E., and Fenical, S. 2000: Circulation and transport modeling. Chapter 6 in "Study of navigation channel feasibility, Willapa Bay Washington," Technical Report ERDC/CHL-00-6, U.S. Army Engineer Research and Development Center, Vicksburg, MS.

Resio, D. T. 1987: Shallow-water waves. I: Theory. *Journal of Waterway, Port, Coastal, and Ocean Engineering*, 113(3), ASCE, 264-281.

_____. 1988: Shallow-water waves. II: Data comparisons. *Journal of Waterway, Port, Coastal, and Ocean Engineering*, 114(1), ASCE, 50-65.

Smith, J. M., Resio, D. T., and Zundel, A. K. 1999: STWAVE: steady-state spectral wave model; Report 1: user's manual for STWAVE Version 2.0. Instruction Report CHL-99-1, U.S. Army Engineer Waterways Experiment Station, Vicksburg, MS. ftp://sherlock.cerc.wes.army.mil/pub/stwave/doc/stwaveum2.pdf

Smith, J. M., Sherlock, A. R., and Resio, D. T. in preparation: STWAVE: steady-state spectral wave model; user's manual for STWAVE Version 3.0. Instruction Report, U.S. Army Engineer Research and Development Center, Vicksburg, MS.

Smith, S. J., and Harkins, G. S. 1997: Numerical wave model evaluations using laboratory data. *Proc.*, Waves '97, ASCE, 271-285.

Thompson, E. F., Hadley, L. L., Brandon, W. A., McGehee, D. D., and Hubertz, J. M. 1996: Wave response of Kahului Harbor, Maui, Hawaii. Technical Report CERC-96-11, U.S. Army Engineer Waterways Experiment Station, Vicksburg, MS.

APPLICATION AND VALIDATION OF THE NAVY STANDARD SURF MODEL: SURF 3.1

Theodore R. Mettlach[1], Y. Larry Hsu[2], Marshall D. Earle[1], Daniel A. Osiecki[1]

[1]Ocean Sciences Division, Neptune Sciences, Inc., Slidell, Louisiana 70461 USA
[2]Ocean Dynamics and Prediction Branch, Naval Research Laboratory
Stennis Space Center, Mississippi 39529 USA

1. INTRODUCTION

This paper reviews the results of a comprehensive set of tests conducted by the Naval Research Laboratory (NRL) to validate estimates of surf zone width, wave breaker height, longshore current and breaker characteristics produced by the latest version of the Navy Standard Surf Model (NSSM): SURF 3.1. This version of the model represents a considerable step in surf forecasting accuracy from that of previous versions of the model.

Owing to the importance of NSSM forecast guidance in operational planning and decision making, it is imperative that the model produces reliable results over a wide range of wind and wave conditions. To this end, the model has been tested using data acquired from the following three field experiments during which offshore wave heights ranged from near calm to 3.5 meters:

(1) National Sediment Transport Study (NSTS) experiment conducted at Leadbetter Beach, Santa Barbara, California, in February 1980.
(2) Duck Experiment on Low frequency and Incident-band Longshore and Across-shore Hydrodynamics (DELILAH) conducted in October 1990 at the Field Research Facility (FRF) at Duck, North Carolina.
(3) Duck94 data acquired during October and November 1994 at the FRF.

Model validation was also conducted using data acquired during two laboratory studies:

(1) Laboratory experiments of longshore current conducted by Visser (1991) in a 34.0 m long by 16.6 m wide by 0.7 m deep wave basin of the Delft University of Technology, The Netherlands.
(2) Laboratory experiments of longshore current over a barred beach conducted by Reniers and Battjes (1997) in a 40 m long by 25 m wide by 0.7 m deep wave basin of the Delft University of Technology.

Moreover, results from a long-term study of surf zone width are presented to verify the accuracy of NSSM estimates of surf zone width. We review the Argus video analyses of Mettlach *et al.* (1999), who made several hundred determinations of surf zone width at the FRF from 1 June 1996 to 30 June 1997.

Recently, Hsu *et al.* (2000) have shown that the longshore current estimates from SURF 3.1 have considerably improved by making relatively simple changes to earlier versions of the NSSM. If the bottom friction coefficient in the model is changed to a depth-dependent bottom friction function and horizontal mixing is decreased, the longshore current estimates throughout the majority of the surf zone are properly increased to satisfactorily match measurements. Furthermore, spuriously high currents in very shallow water are eliminated. This is shown using the aforementioned field data. It should be noted that the variable bottom friction function reflects the shoreward increase in friction due to sediment sorting and compensates for the lack of vertical eddy diffusivity in one-dimensional (1-D) models.

2. BRIEF DESCRIPTION OF SURF 3.1

The NSSM has been used extensively throughout the Fleet since it was introduced in the late 1980's (Earle, 1989). It is contained in many Navy oceanographic software libraries. The model was developed because previous surf forecasting techniques were mainly manual techniques based on methods dating to the 1950's that did not adequately consider local shallow water effects. The model is the primary software for Navy operational surf forecasting, but it is also used for systems development and surf climate descriptions. Earle (1999) provides a surf model overview and examples of its applications.

The main surf model inputs are the following:

(1) Wind speed and direction
(2) Wave conditions, either as wave parameters – height, period and direction – or a complete directional wave spectrum.
(3) A nearshore depth profile that extends from above the water level to a depth of about 6 to 8 m.
(4) Tide level with respect to the input depth profile

The input wave conditions and nearshore depth profile are the most important of the four inputs. Input winds produce a contribution to the longshore current and affect the Modified Surf Index (MSI), given below.

Model outputs are the following:

(1) A forecast summary, which lists the surf zone width, the maximum wave height and longshore current in the surf zone, direction of breakers, breaker type, breaker period and the Modified Surf Index (MSI), which is a dimensionless number that characterizes overall surf conditions.
(2) An optional listing of distances offshore, depths, wave heights, wavelengths, percent breaking waves, and longshore currents at regularly spaced intervals throughout the surf zone.

Hsu *et al.* (2000) give a description of the theory, equations and numerical methods in SURF 3.1; thus, only a brief description of the model is given herein. The model is parametric and one-dimensional. Deep-water wave energy is refracted and shoaled to a user-selected starting depth outside of the surf zone. At the model starting depth, the refracted and shoaled directional wave energy distribution is reduced to three physical values: the direction of the vertically averaged wave momentum flux, the root-mean-square wave height H_{rms} and the peak wave frequency.

The direction of the vertically averaged momentum flux is calculated by the method of Higgins *et al.* (1981) using the spectrum of the shoreward-directed momentum flux. An assumption in the surf model is that only one direction from the peak in the energy spectrum is used. Spectra that are bimodal in either frequency or direction or widely spread may produce erroneous directions for model initialization. Small errors in wave direction can produce significant errors in longshore current but have little effect on other surf zone characteristics.

From the starting depth, the model incrementally calculates H_{rms} along a transect that is normal to the beach to the still water level using the local depth and the wave height found at each previous increment. As waves move through the surf zone, the average rate of energy dissipation due to wave breaking and friction balances the gradient of shoreward energy flux. Energy is extracted using the dissipation of a propagating bore modeled after a weighted, Rayleigh-distribution of wave heights (Thornton and Guza, 1983).

The model assumes wave roller dissipation after Lippmann *et al.* (1996), who applied roller theory to a wave transformation model, which produced results consistent with measurements for both a planar and a barred beach. The along shore directed energy in a volume of water through which a wave is passing can be separated into two layers, an upper layer of energy causing turbulent wave breaking which rides over a lower layer of energy producing organized wave motion. The turbulent water above is termed a surface roller. The shear stress between the underlying wave and roller is converted to turbulent kinetic energy that is dissipated into surf. The original idea of a two layer system introduced by Longuet-Higgins and Turner (1974) was refined by Svendsen (1984a,b). Energy throughout the surf zone is refracted using Snell's law.

Longshore current calculations at each increment are based on radiation stress longshore current theory first developed by Longuet-Higgins (1970a,b). The basic model for longshore current V can be reduced to a second order, cross shore-dependent (x) differential equation.

$$\tau_H + \rho \frac{d}{dx}\left(h \mu_t \frac{dV}{dx} \right) - \tau_B + \tau_U = 0 \qquad (1)$$

The first term τ_H represents the momentum flux from waves in the surf zone. The second term gives the horizontal exchange of momentum due to turbulent mixing from the surface to the bottom at depth h. The variable μ_t is the lateral or horizontal eddy viscosity. The density of water is given by ρ. The third term τ_B represents the dissipation of momentum due to bottom friction. The fourth term τ_U gives the generation of momentum from the wind. A detailed description and discussion of the parameterization for each respective term in (1) is given in Hsu *et al.* (2000) and their references. Extensive validation of the longshore current model within SURF 3.1 is required over a wide range of conditions because there is one empirical constant each in the most widely accepted parameterizations of both μ_t and τ_B.

The width of the surf zone is the distance from the edge of the water to the most offshore location where 10 percent of existing waves are estimated to be breaking or broken. The percentage of breaking or broken waves is computed numerically from the integral of a weighted, Rayleigh probability density function integrated over wave heights from zero to $5H_{rms}$. The particular weighting function in the model, from among those existing in the literature, is taken from Thornton and Guza (1983).

The significant wave height H and the longshore current V for MSI calculations are defined to be the highest in the surf zone. The percentage of each breaker type from among spilling, plunging and surging breakers is found from a widely accepted parameterization of wave period, wave height, and bottom slope. Peak wave period is conserved in the surf zone. Breaker angle is found from the direction of the vertically averaged wave momentum flux at the starting depth. MSI is calculated using the criteria given in the *Joint Surf Manual* (Commander, Naval Surface Force, Pacific and Commander, Naval Surface Force, Atlantic, 1987).

The surf model is initialized at a user-defined starting depth, typically 5 to 8 m, with a directional wave spectrum, which may be obtained from direct measurements or from model estimates. The surf model has been initialized with spectra from several wave

models, such as the WAM model (The WAMDI Group, 1988), the Steady State Spectral Wave Model (STWAVE, Smith *et al.*, 1999), the Simulating WAves Nearshore Model (SWAN, Holthuijsen *et al.*, 1999). Allard *et al.* (1998, 1999) have initialized the model with spectra modified by the Refraction and Diffraction Model (REFDIF, Kirby and Dalrymple, 1994).

If the isobaths from offshore to the model starting depth are approximately straight and parallel to the beach, a separate refraction model need not be run. In this case the user selects an option which applies parallel isobath refraction computations to the input wave information.

Because directional wave spectra are not always available to operators of the surf model, the model can be initialized with wave parameters as described by Earle (1989). The user inputs the significant height, peak period and peak direction of incident sea and swell waves. The parameters for sea are used to construct a Pierson-Moskowitz (PM) spectrum (Pierson and Moskowitz, 1964) with the total amount of energy scaled to that of the input significant wave height. The modified PM spectrum is then spread over $\pm 90^{\circ}$ from the input direction using a cosine to the fourth power spreading function. Such modified spectra converge to PM spectra as input heights and periods approach those for fully developed seas. Narrow swell energy components, derived from the input swell wave parameters, are superimposed on the modified PM spectrum.

3. SURF ZONE WIDTH

The *surf zone* as defined in the glossary of the *Joint Surf Manual* is: "The area between [the] outermost breaker[s] and the limit of wave uprush." A weakness in the definition is that no time period over which waves are observed or forecast is indicated. Mettlach *et al.* (1999) proposed the following definition, which was used to produce an improved algorithm for surf zone width estimation:

Surf zone width is the distance from the water edge along a transect normal to the general orientation of the beach to where a trained, conscientious observer sees the seaward limit of depth-induced wave breaking over a period of 10 minutes.

Ten minutes is the same time period over which marine wind observations are taken and typically corresponds to about 100 waves, the number which should be used for surf observations described in the *Joint Surf Manual.*

The surf zone width is important for MSI computations because the highest wave height and strongest longshore current within the surf zone are used to compute MSI. Recently, surf zone width has taken on an added importance with the development of mine countermeasures (MCM) systems that launch rocket propelled explosive nets and lines across the surf zone that fall into the water, explode and neutralize any mines that may exist there. Accurate knowledge of surf zone width is essential for planning the effective, safe execution of such MCM operations.

Three studies of the effectiveness of the model in estimating surf zone width have been made by NRL. The first study was by Mettlach and May (1997) who used Argus (Holland *et al.*, 1997) video images acquired during DELILAH to validate model estimates of MSI. Hsu *et al.* (1997) extended the study to include 20 Argus video images and 9 FRF pier observations of surf zone width. Finally, Mettlach *et al.* (1999) conducted an extensive examination of model-estimated surf zone width compared to over 600 Argus video images acquired at Duck over the 13-month period 1 June 1996 to 30 June 1997.

Figure 1 gives one example of a surf zone width determination. The corresponding depth and video intensity profiles along the transect in Figure 1 are shown in Figure 2, from which is seen obvious wave breaking beginning over the nearshore bar and at the water edge.

For each of the Argus video determinations a corresponding surf model run was made. The most offshore location of a particular percentage of estimated model wave breaking was then correlated to the location of incipient wave breaking from the video. The locations where model-estimated 10 percent wave breaking first occurred were the most highly correlated to and found to have the least error with respect to the location of incipient wave breaking from the Argus video determinations.

Figure 3 is a scatter plot of model-derived estimates of surf zone width compared to video determinations. The accuracy of this relatively simple method for estimating surf zone width is quite high over a wide range of distances. It is interesting to note that the optimal percent breaker threshold has consistently been very close to 10 percent in each of the studies using Argus video determinations.

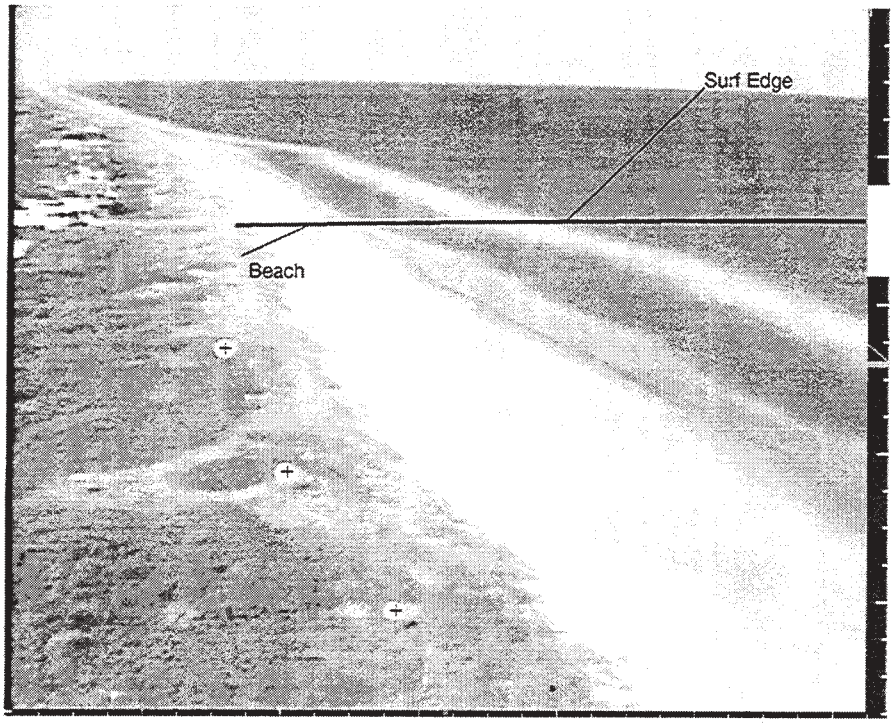

Fig. 1. Argus 10-minute averaged video image acquired 0700 EST 8 November 1996 at Duck. Offshore wave height = 1.1 m. Peak wave period = 8.1 s. Peak wave direction = -38 degrees from shore normal.

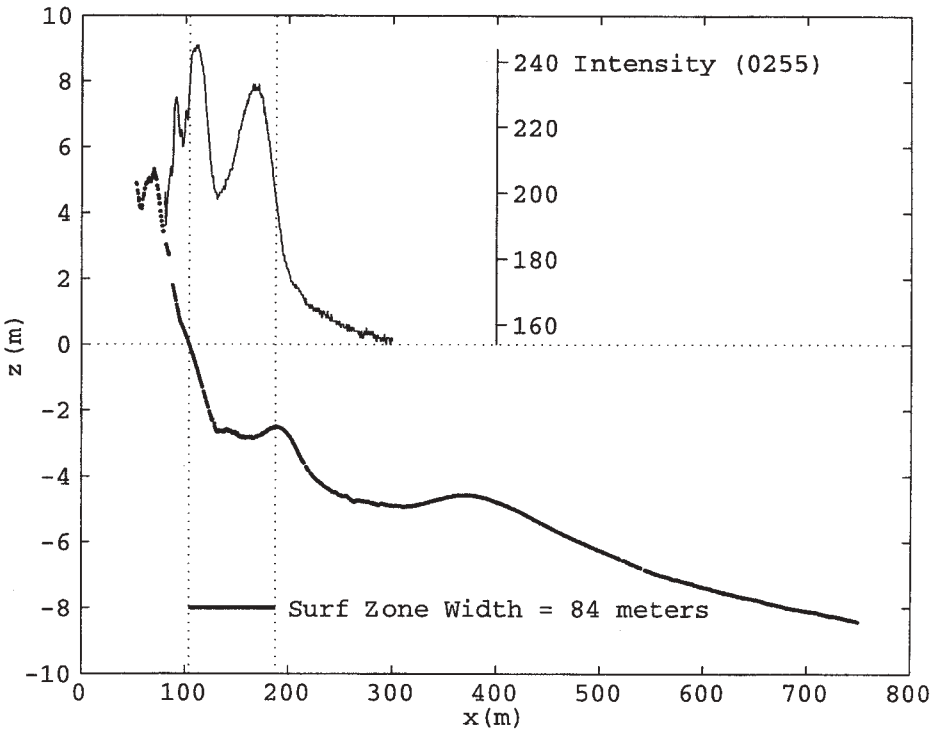

Fig. 2. Profiles of depth z and of 10-minute averaged Argus video intensity (0-255) from image in Figure 1. Depths are relative to the mean 6-min water level during the video acquisition period. The x-axis is the FRF cross-shore coordinate. Scale of video intensity denoted. Right vertical dotted line denotes visually determined surf zone edge.

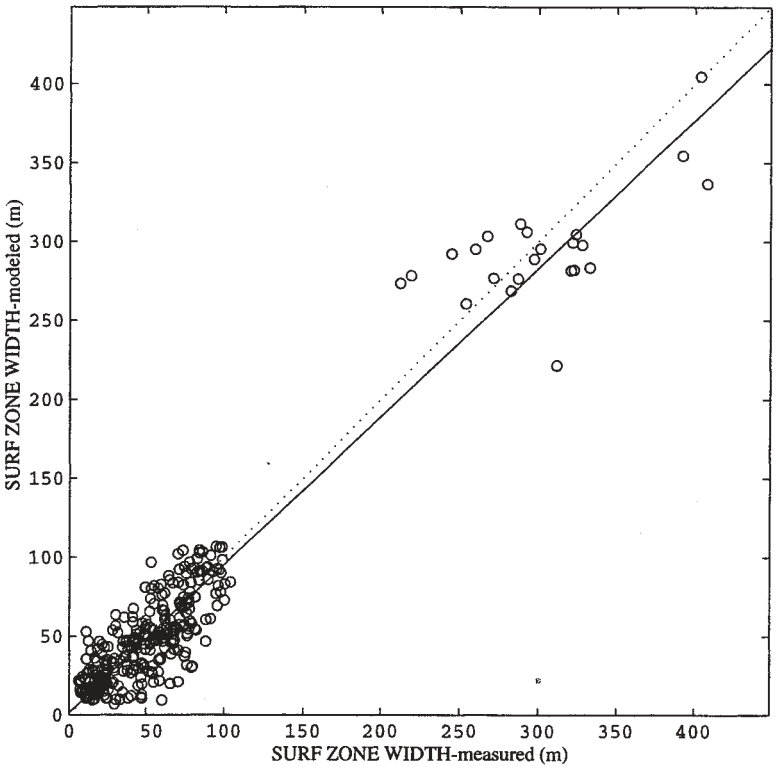

Fig. 3. Scatter plot of video-derived surf zone width versus model estimates. 334 observations. Linear correlation coefficient = 0.96; min error = -90.2 m; mean error = -2.5 m; max error = 61.2 m; standard deviation of the error = 19.1 m; mean fractional error = 8.0%. Solid line is linear regression curve with slope 0.94 and intercept = 1.5 m (Adapted from Mettlach *et al.*, 1999).

4. WAVE HEIGHT AND LONGSHORE CURRENT

The model has been extensively validated with regard to wave height and longshore current by Hsu *et al.* (2000) but model performance using the laboratory data of Visser (1991) and Reniers and Battjes (1997) has never been formally published. In this section the major results of Hsu *et al.* (2000) and of a model comparison to the wave tank data are presented.

4.1 Field Experiments

The wave height and longshore current measurements from DELILAH and Duck94 were combined into a single data set to validate model performance. Surf model runs were initialized using the wave spectra from the 8-m FRF directional wave array, daily mini-grid depth survey data, tide and wind measurements. There were 79 DELILAH cases and 144 Duck94 cases used in the study. The wave height and longshore current estimates nearest in location to corresponding measurements were compared. A scatter plot of measured to modeled wave heights within the surf zone is in Figure 4.

The skill of the model in estimating wave height is quite high from which it is reasonable to assume wave energy dissipation is accurately modeled. The wave dissipation parameterization of Lippmann *et al.* (1996), which is used in SURF 3.1, contains two empirical values. The first is a simple multiplication factor; the second represents the angle of the wave-roller stress vector. Several series of model runs were made using various pairs and the optimal values were found to be nearly the same as those found by Lippmann *et al.* (1996), which are used in the surf model.

As with the wave dissipation parameterization, the solution for the longshore current V given in (1) is dependent on two empirical values. The first governs the amount of lateral or horizontal mixing of momentum and the second is the bottom friction coefficient. As with the wave height validation, a series of surf model runs was made using various values for the empirical coefficients. Figure 5 is a scatter plot of model versus measured longshore current values. The model estimates are derived from runs using the optimal coefficient values.

After the optimal empirical values for wave dissipation and longshore current were found, the model was further tested using the NSTS data set. The statistical accuracy of the model in estimating wave

height and longshore current for the NSTS data set is comparable to that achieved with the DELILAH and Duck94 data set. Figure 6 shows results from a single case and Figures 7 and 8 are scatter plots of the modeled quantities against all corresponding field measurements.

The results of the field data validation of the model reveals a high level of accuracy over a wide range of wave conditions over both planar and barred beaches. The relative accuracy of longshore current is less than both surf zone width and wave height, however, the level of skill is significant.

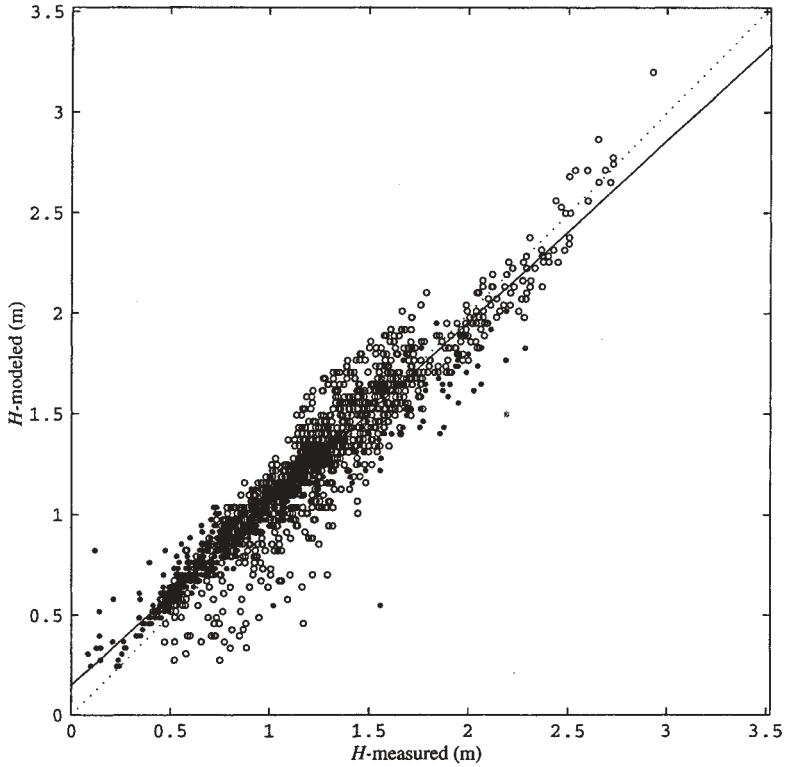

Fig. 4. Scatter diagram of measured versus modeled significant wave heights. Dots denote DELILAH measurements; circles denote Duck94 measurements. 1796 observations. Linear correlation coefficient = 0.95; min error = -1.01 m; mean error = 0.04 m; max error = 0.71 m; standard deviation of the error = 0.15 m; mean fractional error = 6.2%. The solid line is a linear regression curve with slope= 0.90 and intercept = 0.15 m.

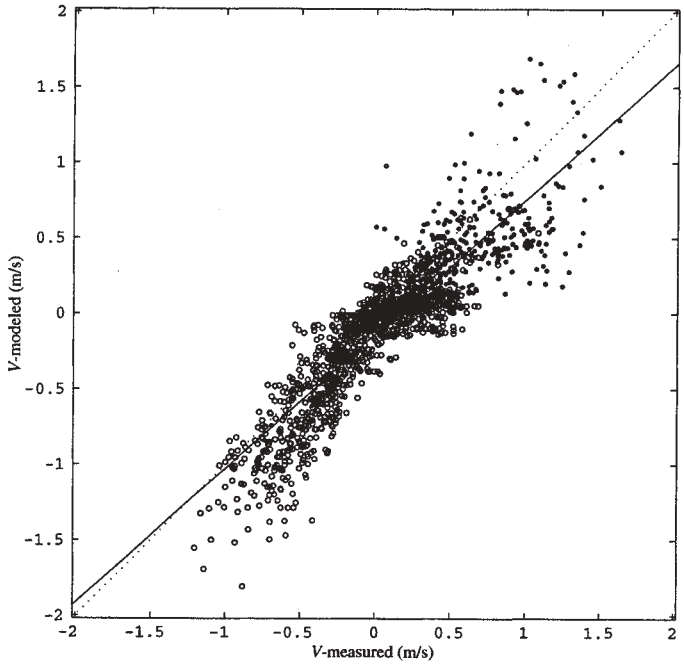

Fig. 5. Scatter plot of measured longshore currents versus the corresponding improved model estimates of current. Dots denote DELILAH measurements; circles denote Duck94 measurements. 1930 observations; linear correlation coefficient = 0.89; min error = -1.06 m/s; mean error=-0.14 m/s; max error = 0.91 m/s; standard deviation of the error = 0.22 m/s; mean fractional error = -17.4 %. The solid line is a linear regression curve with slope = 0.89 and intercept = -0.135 m/s.

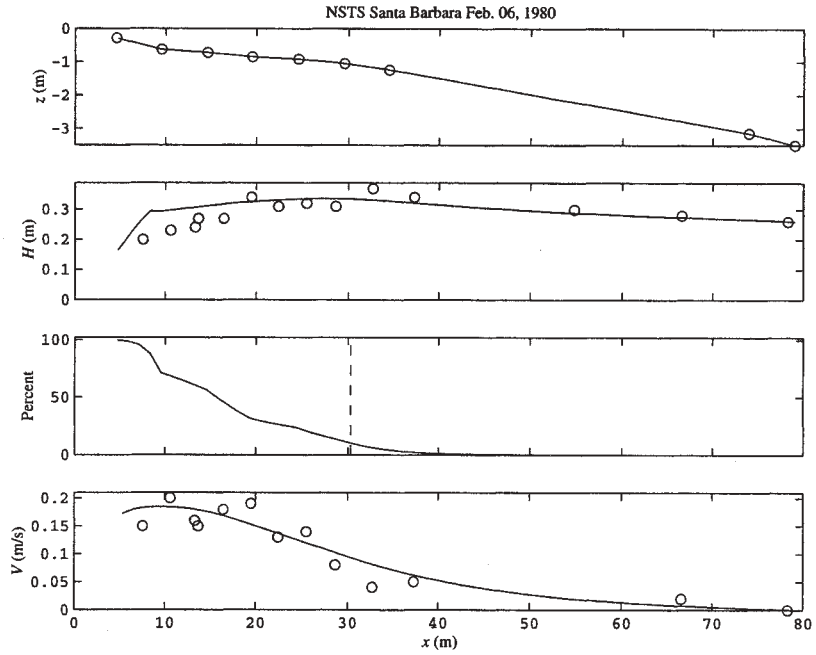

Fig. 6. NSTS Leadbetter Beach, Santa Barbara, California, 6 February 1980: Top panel: interpolated depth from model (solid), measured and input ("o"). Second panel: wave height H from model (solid line) and measured ("o"). Third panel: percentage of broken or breaking waves estimated by model. Dashed vertical line is most offshore point where *Percent* is > 10 percent, which is estimated edge of surf zone. Bottom panel: longshore current V from SURF 3.1 (solid). Measured V denoted ("o"). Offshore wave conditions: H = 0.4 m; peak wave direction = 8 degrees from shore normal; peak wave period = 11.6 s.

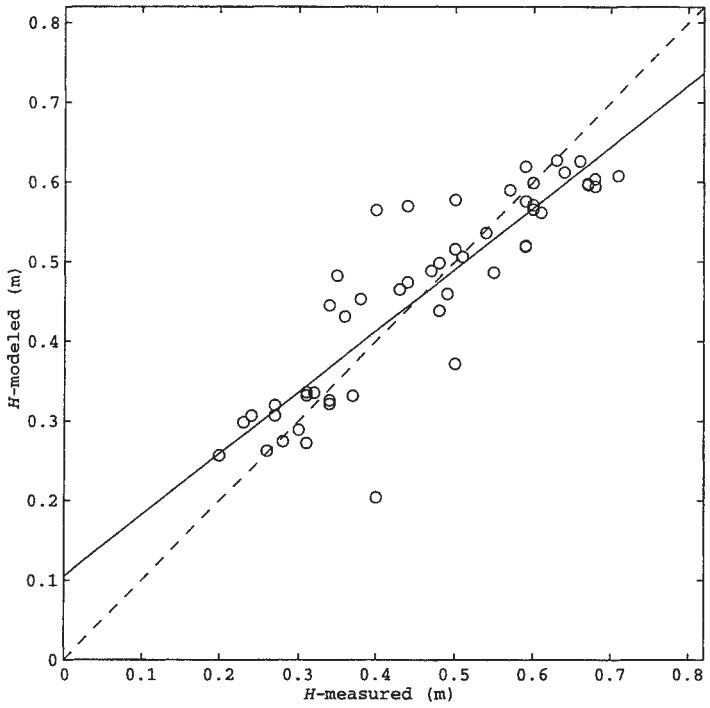

Fig. 7. Scatter diagram of measured significant wave heights versus estimates of wave height: NSTS Santa Barbara--3-6 February 1980. 51 observations. Linear correlation coefficient = 0.89; min error = -0.2 m; mean error = 0.0 m; max error = 0.2 m; standard deviation of the error = 0.07 m; mean fractional error = +2.2%. The solid line is a linear regression curve with slope 0.77 and intercept = 0.10 m.

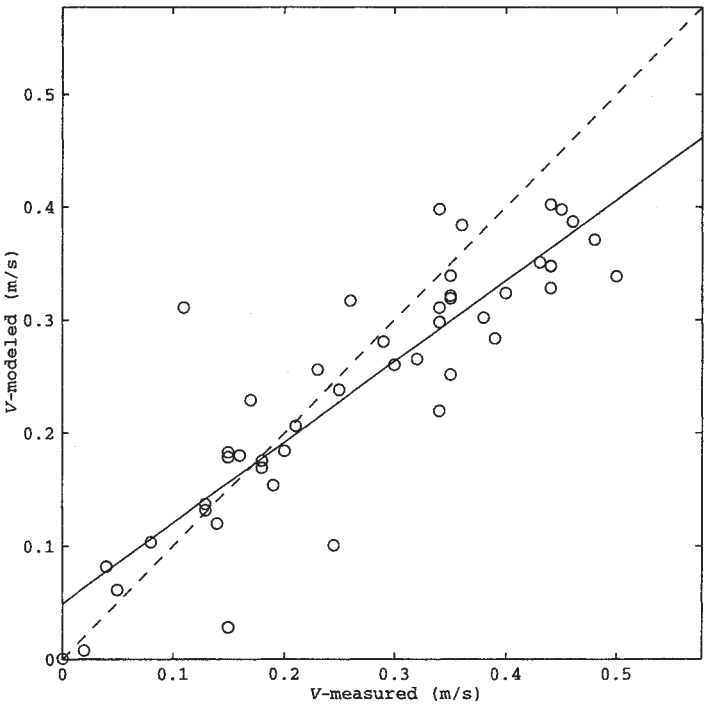

Fig. 8. Scatter diagram of measured longshore current versus estimates of longshore current: NSTS Santa Barbara--3-6 February 1980. 47 observations. Linear correlation coefficient = 0.88; min error = -.2 m/s; mean error = -0.0 m/s; max error = 0.2 m; standard deviation of the error = 0.07 m/s; mean fractional error = -3.3%. The solid line is a linear regression curve with slope 0.71 and intercept = 0.05 m/s.

4.2 Laboratory Experiments

The work of Visser (1991) and Reniers and Battjes (1997) provide important data sets for calibrating the empirical constants in a model and examining phenomena that, in the field, cannot be easily isolated from other processes. Visser's data reveal the importance of bottom friction in estimating longshore current.

Visser produced longshore currents in a large basin by generating obliquely incident waves that broke over a flat, sloped bottom. A pump-driven re-circulation scheme gave currents that were virtually uniform along shore. Each of the eight cases listed in the appendix of Visser (1991) was used in the present study, however only cases 4 and 7 are presented. These two cases were identical except for the type of bottom material used during the experiments: gravel and smooth concrete. The resulting measurements point to the importance of a correct bottom friction coefficient, which is a tunable coefficient in radiation stress-based longshore current models. In Figure 9 the surf model longshore current profile, using the optimal bottom friction coefficient found from the field studies, falls reasonably between the two sets of measurements in that the bottom material at Duck varies from coarse sand on the foreshore to very fine sand seaward of the bar.

A well known characteristic of the longshore current profiles from DELILAH measurements is that the peak in longshore current was not observed to be located over the crest of the bar at Duck but, rather, over the trough shoreward of the bar. Where there is increased wave breaking there should be increased longshore currents due to increased radiation stresses. Since wave breaking is observed generally to occur over the crest of the bar, a peak in longshore current is expected.

Several researchers have attempted to explain this discrepancy by considering along shore variations in depth and wave forcing (e.g. Putrevu and Oltman-Shay, 1995 and Reniers *et al.*, 1995). Figure 10 shows that measured currents in the Delft wave tank are a maximum over the bar, not the trough, where it was during DELILAH. The model adequately matches the laboratory observations of longshore current. The Reniers and Battjes data set is valuable in that from it one may conclude that complications in the longshore current profiles acquired during the DELILAH experiment existed from a source other than simple wave dissipation processes.

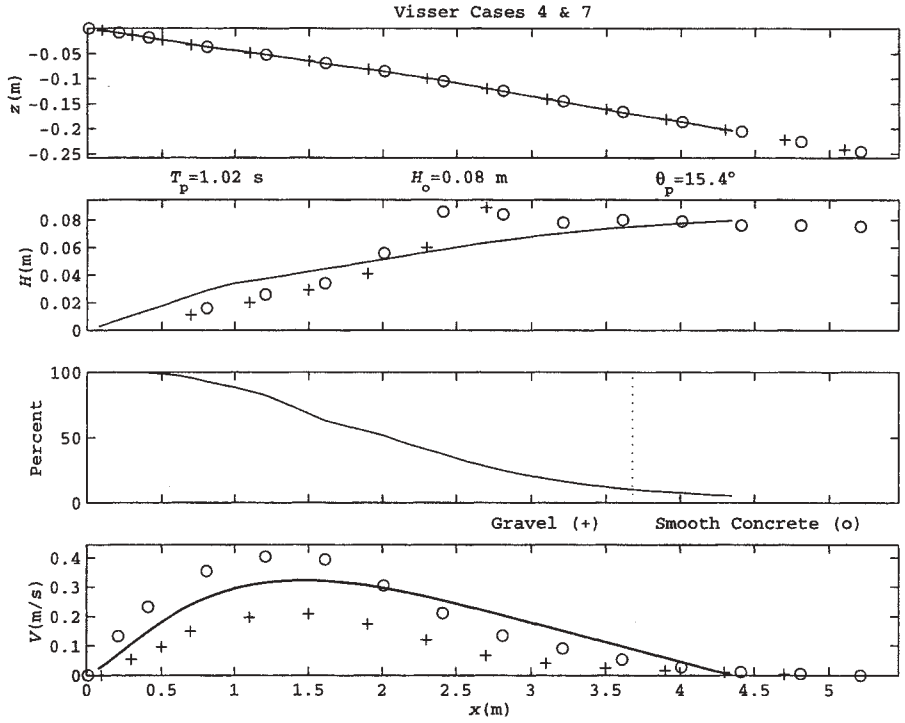

Fig. 9. Visser Cases 4 and 7. Top panels: interpolated depth from model (solid line); measured and input depth ("o" and "+"). Second panel: wave height H from model (solid line) and measured ("o" and "+"). Third panel: percentage of breaking or broken waves estimated by model. Dashed vertical line is most offshore point where *Percent* of breaking waves is > 10 percent, which is edge of surf zone. Bottom panel: longshore current V from model and measured V denoted by "o" and "+". Wave conditions used to initialize model and bottom material noted.

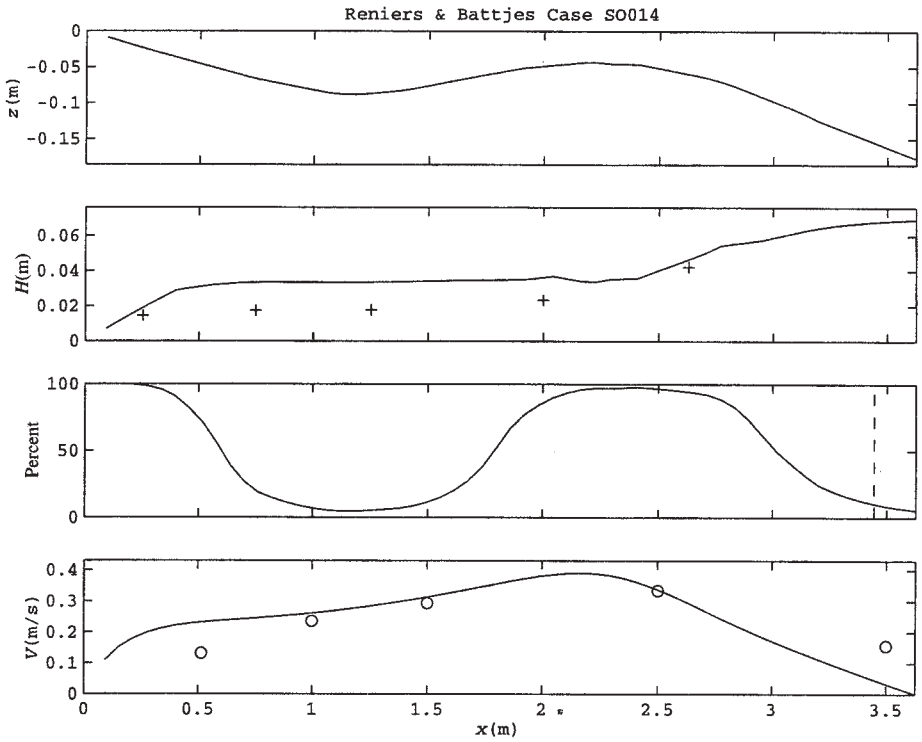

Fig. 10. Reniers and Battjes Case SO014. Top panel: depth z. Second panel: wave height H from model (solid line) and measured ("+"). Third panel: percentage of breaking or broken waves estimated by model. Dashed vertical line is most offshore point where *Percent* is > 10 percent, which is edge of surf zone. Bottom panel: longshore current v from model (solid). Measured V denoted by "o". Wave conditions used to initialize model.

5. SURF MODEL–WAVE MODEL INTERFACE

It is best to initialize the surf model with an *in situ* directional wave spectrum derived from a wave measurement device. However, operational limitations may require that the model be initialized with wave parameters or directional wave spectra from a model. This is especially true for naval operations in denied areas.

Thus, the NSSM has been successfully initialized with directional wave spectra produced by the WAM, STWAVE and REFDIF. In general, the output from any wave model can be used to initialize the NSSM. When using other than direct, real-time spectra from measurements, the resulting accuracy of the surf forecast will rest substantially on the accuracy of the wave model being used, which is often limited by the age, resolution and quality of the bathymetric data used with the wave model.

6. MODEL EXECUTION

In addition to being reasonably accurate over a wide range of conditions, the surf model should also be robust in its execution. This is especially true when using unusual nearshore depth profiles, ranging from the extremely long, flat and shallow to those, which are rough, steeply sloped or irregular.

The Naval Oceanographic Office provided a large collection of nearshore depth surveys from its Beach Survey Chart (BSC) database, which contains beach surveys from many locations in the United States and overseas. A total of 568 depth profiles were input into the model using four different wind, wave and tide conditions for a total of 2,272 runs.

SURF 3.1 successfully produced either a good forecast run or an appropriate diagnostic error message for each of the 2,272 runs. There were no premature terminations or crashes without error messages.

7. CONCLUSION

This paper has reviewed the comprehensive set of validation studies that have been conducted to verify the accuracy of the Navy Standard Surf Model (NSSM) over a wide range of environmental conditions. To our knowledge these are the most extensive tests to have been conducted on any operational surf model.

The expected accuracy of the model has been determined using high quality field and laboratory

data. Accuracy of model estimates of surf zone width and wave height are quite high; accuracy of model estimates of longshore current show significant model skill over a wide range of conditions.

For beaches with complicated bathymetry, SURF 3.1 may not completely describe all of the complex processes in the turbulent surf zone. A 2-D or quasi 3-D approach may be required to produce more accurate longshore current estimates.

8. ACKNOWLEDGEMENTS

The authors thank Professor Edward Thornton of the Naval Postgraduate School, Professor Robert Guza of the Scripps Institution of Oceanography and Dr. Chuck Long of the Field Research Facility for providing the NSTS, DELILAH and Duck94 data sets. Professors A.J.H.M. Reniers and J.A. Battjes of the Delft University of Technology provided the Reniers-Battjes data set. Mr. John Murdock of the Systems Integration Department of the Naval Oceanographic Office provided the BSC depth profiles. This work was sponsored by the Space and Naval Warfare Systems Command under program element 603207N Coastal Wave/Surf Models Project. NRL contribution number: PP/7320-00-1005.

9. REFERENCES

Allard, R.A., Y.L. Hsu, J.M. Smith, M..D. Earle, T.R. Mettlach, and K. Miles, 1998: Use of Coupled Numerical Wave Models to Simulate the Littoral Environment from Deep Water to the Beach, *Proceedings of the 5th Intl. Workshop on Wave Hindcasting and Forecasting*, Melborurne, FL, Jan 26-30, 1998, 187-200.

Allard, R.A., Y.L. Hsu, K. Miles, T. Mettlach and M..D. Earle, 1999: Toward an Operational Coupled Wave/Surf Forecasting System, *Proceedings of the Third Conference on Coastal Atmospheric and Oceanic Prediction Processes*, 3-5 November 1999, New Orleans, LA.

Commander, Naval Surface Force, Pacific and Commander, Naval Surface Force, Atlantic,1987: *Joint Surf Manual*, COMNAVSURFPAC/ COMNAVSURFLANTINST 3840.1B, 02 January 1987, 13 chap., 1 appendix.

Earle, M.D., 1989: *Surf Forecasting Software Scientific Reference Manual*, MEC Corporation report for ASW Oceanography Program Office, Naval Ocean Research and Development Activity (N00014-84-C-0116), 261 pp. (Available from Naval Research Laboratory [Code 7032.2], Stennis Space Center, MS 39529-5004).

Earle, M.D., 1999: Applied and operational surf modeling, *Shore and Beach*, 67, 70-75.

Higgins, A.L., R.J. Seymour and S.S. Pawka, 1981: A compact representation of ocean wave directionality, *Applied Ocean Research*, 3(3), 105-112.

Holland, K.T. R.A. Holman, T.C. Lippmann and J. Stanley, 1997: Practical Use of Video Imagery in Nearshore Oceanographic Field Studies, *IEEE J. Ocean. Eng.*, 22, 81-92.

Holthuijsen, L.H., N. Booij, R.C. Ris, IJ. G. Haagsma, A.T.M.M. Kieftenburg, R. Padilla-Hernandez, 1999: *SWAN Cycle 2 version 40.01 USER MANUAL*, Delft Univ. Tech., Delft, Netherlands, 107 pp.

Hsu, Y.L., T.R. Mettlach, M.E. Earle, E.P. Kennelly, 1997: *Interim Report on Validation of the Navy Surf Model*, NRL/MR/7322—97-8054, October 14, 1997, 233 pp.

Hsu, Y.L., T.R. Mettlach, M.E. Earle, 2000: *Improvement and Validation of the Navy Longshore Current Model*, NRL/FR/7320--00-9927, 46 pp.

Kirby, J.T. and R.A. Dalrymple, 1994: *Combined Refraction/Diffraction Model REF/DIF1, Version 2.5, Documentation and User's Manual, Report 94-22*, CACR Report No. 94-22, Center for Applied Coastal Research, U. Del. Newark, DE, 171 pp.

Lippmann, T.C., A.H. Brookins, and E.B. Thornton, 1996: Wave energy transformation on natural profiles, *Coastal Engineering*, 27, 1-20.

Longuet-Higgins, M.S., 1970a: Longshore Currents Generated by Obliquely Incident Sea Waves, 1, *Journal of Geophysical Research*, 75(33), 6678-6789.

Longuet-Higgins, M.S., 1970b: Longshore Currents Generated by Obliquely Incident Sea Waves, 2, *Journal of Geophysical Research*, 75(33), 6790--6801.

Longuet-Higgins, M.S. and J.S. Turner, 1974: An entraining plume model of a spilling breaker, *J. Fluid Mech*,. 63(1), 1-20.

Mettlach, T. R. and D.A. May, 1997: *The Accuracy of the Navy-Standard Surf Model-Derived Modified Surf Index with and its Sensitivity to Nearshore Bathymeteric Errors.,* NRL/FR/7240—97-9665, October 24, 1997, 34 pp.

Mettlach, T. R., K.T. Holland and D.A. May, 1999: *The Accuracy of Navy Surf Model Estimates of Surf Zone Width with an Examination of the Important Influences on Incipient Wave Breaking,* NRL/FR/,7440--99-9693, September 24, 1999, 46 pp.

Pierson, W.J. Jr. and L. Moskowitz, 1964: A Proposed Spectral Form for Fully Developed Wind Seas Based on the Similarity Theory of S.A. Kitaigorodskii, *J. Geophys. Res.*, 69(24), 5181-5190.

Putrevu, U. and J. Oltman-Shay, 1995: Effect of alongshore nonuniformities on longshore current predictions, *J. Geophys. Res.*, 100(C8), 16,119-16,130.

Reniers, A.J.H.M., E.B. Thornton and T.C. Lippmann, 1995: Longshore currents over barred beaches, *Coastal Dynamics '95: Proceedings of the International Conference on Coastal Research in Terms of Large-Scale Experiments*, Gdansk, Poland, 4-8 September, 1995, ASCE, 413-424.

Reniers, A.J.H.M. and J.A. Battjes, 1997: A laboratory study of longshore currents over barred and non-barred beaches, *Coast. Eng.*, 30, 1-22.

Smith, Jane McKee, D.T. Resio, A.K. Zundel, 1999: *STWAVE: Steady-State Spectral Wave Model, Report 1, User's Manual for STWAVE Version 2.0*, USACE, WES, Instruction Report CHL-99-1, April 1999, 57 pp.

Svendsen, I.A., 1984a: Wave Heights and Set-Up in a Surf Zone, *Coastal Engineering*, 8, 303-329.

Svendsen, I.A., 1984:b Mass Flux and Undertow In A Surf Zone, *Coastal Engineering,* 8, 347-364.

Thornton, E.B and R.T. Guza, 1983: Transformation of Wave Height Distribution, *Journal of Geophysical Research*, 88 (C10),5925-5938.

Visser, P.J., 1991: Laboratory measurements of uniform longshore current, *Coast. Eng.*, 15, 563-591

WAMDI Group, 1988: The WAM Model--A Third Generation Ocean Wave Prediction Model, *J. Phys. Ocean.*, 18, 1775-1810.

Use of Coupled Wave Models to Simulate Near Shore Waves

Chung-Sheng Wu
Office of Science & Technology, National Weather Service
Silver Spring, MD 20910-3280
(O) 1-301-713-1613 x166

Okey George Nwogu
Davidson Laboratory, Stevens Institute of Technology
Hoboken, NJ 07030
(O) 1-201-216- 8217

At Hurricane Opal's landfall near Pensacola, Florida, the high waves riding on the storm surge resulted in total water levels well above the estimated surge levels. A parametric hurricane model using a parametric hurricane wind field is proposed to simulate the spatial and temporal evolution of hurricane waves. The model will be calibrated with field observations of winds and waves measured at buoy locations near the hurricane track. To simulate the changing waves over the various sea bottoms, the model uses multiple grid resolutions for its bathymetry.

The bathymetry near Pensacola is characterized by the presence of a deep canyon. When a hurricane is over deep water, the resolution for the ocean grid is 3 km. The hurricane model will need the radius of maximum winds, the center pressure of the storm, and the storm track, to simulate deep water waves. As the waves approach the continental shelf, the model employs a coastal grid with a resolution of 300 m. This grid will be used to simulate wind wave shoaling and refraction on the shelf. At a depth of about 30 m, the model uses a turbulent bore assumption to calculate breaking wave heights and mean water levels in the surf zone. The model also predicts the wave run-up along the coastline for estimating flooding due to waves. Different choices of modeling coastal seas will be discussed. The impact of the interaction of coastal waves with the near shore bathymetry on marine forecasts will be investigated. Preliminary analysis indicates that the presence of the canyon head guides more energies toward the Panama City Beach.

Session J: Shallow-Water Modeling

WIND WAVES AND SWELL IN LOS ANGELES BAY

Valeri Kalmykov
Reid Nichols

Marine Information Resources Corporation
Ellicott City, Maryland, USA

1. INTRODUCTION

Wave modeling has remained popular in the coastal engineering and oceanography community for nearly three decades. Numerical wave modeling has been described in many papers (e.g., Komen et al, 1994; Wittman and Farrar, 1997; Wittman and O'Reilly, 1998; and Allard et al., 1998) and is usually applied to:

- Characterize small- and large-scale wave fields for ship safety.
- Simulate regime characteristics of ocean waves for known extreme conditions for coastal protection.
- Produce wave maps of local or global regions for long-term analyses.

Accurate wave field data provide information that helps protect property and save lives. Modeling successes can support the marine industry by helping mariners avoid hazardous conditions and mitigate mishaps.

As more powerful computers have been developed, new ideas and capabilities have arisen to improve model resolution and accuracy. For example, we can combine finite difference wave forecast models with finite element models (e.g., Chen and Houston, 1987). In this application finite difference models are used for the open and coastal regions of the ocean. Then, finite-element models may use finite difference model output as a boundary condition to simulate the wave field in a confined bay with a narrow throat.

In this paper we present numerical results obtained through the use of a numerical forecast model in the vicinity of Southern California's Los Angeles-Long Beach coast. Results obtained are to be used as a boundary condition for computation of the wave field in Los Angeles Bay including San Pedro Bay with the help of a finite-element model (see Chen and Houston, 1987).

2. NUMERICAL MODEL

The numerical model used here is the well-known transport equation:

$$\frac{\partial S}{\partial t}+\frac{\partial (SV_x)}{\partial x}+\frac{\partial (SV_y)}{\partial y}=W+N-D-D_h \qquad (1)$$

Initial and boundary (g) values require

$$S\,|_g = S(t=0) = S_0(x,y), \qquad (2)$$

so that on land, spectra are zero and on the open ocean boundary there are swell. On the left hand side of the equation, wave spectra are given by

$$S = S(f,\theta,x,y,t) \qquad (3)$$

where

f = frequency,
θ = angle,
x,y = coordinates,
t = time,
V_x = group velocity + current for x-component, and
V_y = group velocity + current for y- component.

On the right hand side, wind input (W) is taken from Snyder et al (1981). Wind-wave coupling was not considered. The nonlinear term (N) is taken from Hasselmann et al. (1985). The model used an angular step of 11° (i.e., 180°/16) and a frequency step of f_i/f_{i-1} = 0.93, where i = (1,30), and the highest frequency, f_N = 0.4 Hz. Implementation of N is different from the method used in WAM. The dissipation term (D) is taken from Hasselmann (1974). The bottom friction (D_h) term is taken from Tolman (1991).

Numerical schemes used here are explicit and implicit of the first order. The drawback of the first order scheme is large dispersion. One way to overcome this is to use the method of characteristics, which uses a

predetermined wave path dependent on bottom topography and phase velocity. This method is good for swell, but does not apply to wind waves that have directions different from the swell. This is a topic for further model development. The time integration scheme was similar to the one used in WAM. It allows large time steps limited only by stability of the scheme. The time integration scheme is of the second order (e.g., as used in WAM) and is implemented with the help of functional derivatives on the right hand side of the transport equation. By increasing the time step to a reasonably large value of 5 min, the X-resolution extends to 14 km while the Y-resolution extends to 7 km for the lowest frequency of 0.06 Hz. A larger time step is not possible due to scheme instabilities for a given resolution.

Low frequency swell propagates west-southwest from the Pacific Ocean to the Los Angeles coast. The swell period is from 20 to 30 sec with a length scale on the order of a hundred meters. The Pierson-Moscowitz spectrum, multiplied by a small coefficient, was used as an initial spectrum. At the southwestern boundary of the polygon, swell is given as an input from the global WAM model of 0.06 Hz with, amplitude of 0.5 m, and propagation direction to the northeast of the polygon.

For intercomparisons between model and 3-meter discus buoy data, we used output and online data from Station 46025 - CATALINA RDG located at 33.75° N 119.08° W at 21:00 Z on 30 June 1997. The intercomparison location is annotated with an "X" on the following descriptive and intercomparison figures. Longitudes here are shown as 360°-longitude since our starting point at (0,0) is in the lower left corner of the polygon. Northeasterly swell are superimposed on southerly developing wind waves. Such *vis-à-vis* propagation of swell and wind waves should produce intensive wave breaking.

A 51-hour time span covered by the model is presented. It requires 6 hours of CPU time on a 200 MHz Pentium processor using a 5 min time step for 0.06 Hz swell. This frequency is limited by the lowest frequency and spatial resolution. Spectra for the frequency $f>4f_0$ are continued by the tail f^{-5}. The peak frequency is f_0. Spectra beyond the highest frequency were continued by the same tail.

2.1 Los Angeles Coast

The area's coastline is relatively homogenous, consisting of mostly sand beaches and occasional wave-cut cliffs. A dominant manmade feature is the Los Angeles-Long Beach port complex. During summer months, temperature differentials between cool ocean waters and terrestrial areas causes land-seabreeze circulation. During fall months, offshore winds known as "Santannas" impact the area. The seabreezes often combine with prevailing north-westerlies to produce strong onshore winds. Ocean circulation in the area is complex due to the impact of the Channel Islands. Generally, offshore waters flow southerly down the coast with the California Current.

Figures describing the Los Angeles Pacific coast, wind velocity at the beginning of the simulations, wave propagation history, and data intercomparisons are shown below. Figure 1 is a Los Angeles Pacific coastal map. The "X" annotation is the location for computed 3-hour 2-dimensional frequency-angular spectra.
The time interval analyzed here is from 30 June 1997 at 00:00 Z to 1 July 1997 at 06:00 Z. Wind field data were obtained from NOAA. Winds at 40 m were obtained at every degree for the 3-hour period. From these data, wind was extracted over the polygon and linearly interpolated in the X- and Y- directions over the (1/8° x 1/16°) grid. Figure 2 shows this wind and its direction over the polygon at the beginning of the simulation. Similar graphics are available for every 3-hour time period.

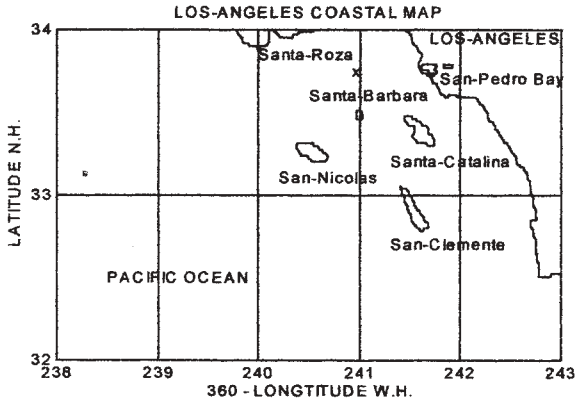

Figure 1. Los Angeles Pacific coastal map. The "X" marks the approximate location of NDBC Station 46025-CATALINA RDG.

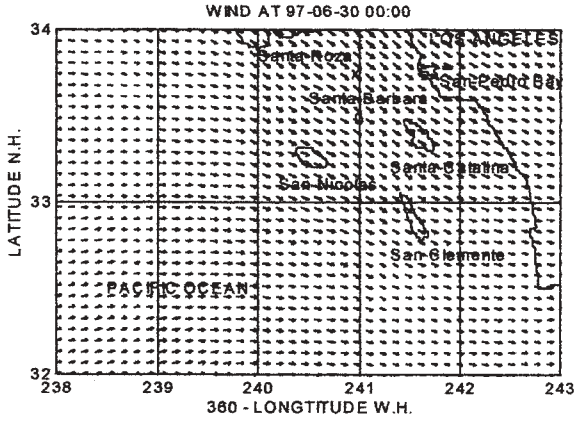

Figure 2. Wind field over Los Angeles Bay (m/s) at 00:00 Z on 30 June 1997.

The polygon has 40 x 32 points in (X,Y) directions. The initial spectra have a peak frequency of 0.3 Hz and 0^0 direction (East), which coincides with wind directions on the western boundary of the polygon. On the south-

AUTHOR INDEX TABLE OF CONTENTS

western boundary the swell have a 17-second period and 0.5 m height. These swell are propagating to the shore from the south-west (i.e., lower left corner of the polygon) towards the wind waves.

Although shallow water was included, only 3% of the grid points were actually shallow as evidenced by the bathymetric data. Therefore, the polygon is valid for deep-water conditions.

Model results are available every 3 hours where wave heights are in meters, average wave directions in degrees, spectral maxima in meters-squared seconds, peak frequency in Hz, and spectra in meters-squared seconds.

2.2. Swell And Wind Waves

Mixed wave field evolution depends on the frequency cutoff for the high-frequency tail. We used frequencies $f>4f_0$, (other approaches use coefficients such as 2, 2.5, 3). This procedure allows or depresses development of the wind waves. Increasing this coefficient causes this numerical scheme to become unstable. A smaller time step should be used to avoid negative spectra. Figure 3 depicts the beginning of the wave evolution where wave heights are determined by the size of the arrow and directions in accordance with the arrowhead. For convenience wave height contours are also depicted. Most wave heights are approximately 0.5 m.

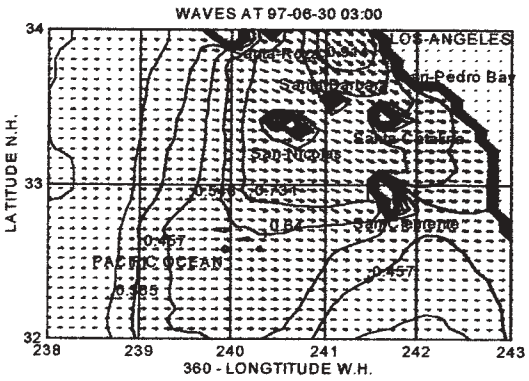

Figure 3. Wave propagation at 03:00 Z on 30 June 1997. Wave heights are in m.

After 3 hours, wind waves and swell divide the polygon almost in half. Later we will show that swell becomes dominant. Figure 4 shows that after 21 hours, wind waves are located only in the shadows of the islands (e.g., Santa-Rosa, Santa-Catalina, and Santa-Barbara). A time period comparison with data from Station 46025 is performed in the next section. On the boundary of wind waves and swell, one would expect to observe wave breaking taking place. Dealing with unstable waves is a good challenge for the numerical scheme.

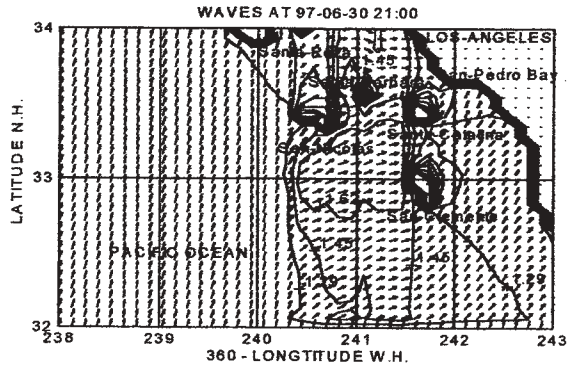

Figure 4. Wave propagation at 21:00 Z on 30 June 1997. Wave heights are in m.

The wave field doesn't demonstrate appreciable changes until the end of the simulation at 06:00 Z on 1 July 1997. Changing features are best observed by inspecting the contours located off San Pedro Bay and seaward of the Channel Islands. Output for 06:00 Z on 1 July 1997 is plotted in Figure 5.

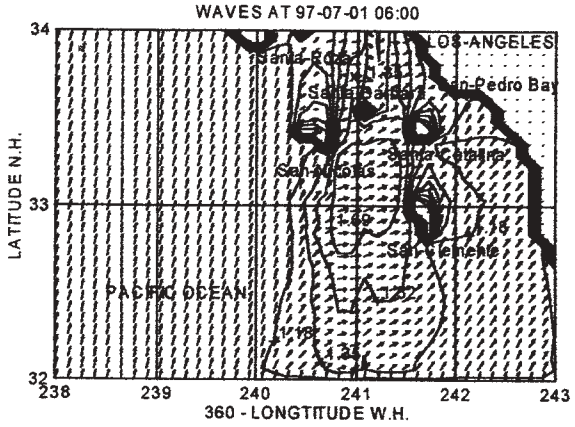

Figure 5. Wave propagation at 06:00 Z on 1 July 1997. Wave heights are in m.

3. MODEL INTERCOMPARISON

Figures 6 and 7 show the intercomparison of simulation output with data from Station 46025 for the area annotated with an "X" in Figure 1. By inspection, one can clearly see on the frequency spectra 0.06 Hz swell and 0.2 Hz wind waves. The variation in the wind peak between simulations and buoy data is probably a Doppler frequency shift. Including drift currents in the simulation may eliminate this, but we did not have access to circulation data. Buoy angular spectra were simply the average wave direction in each frequency bin. Data angles are measured from the north, in the same manner as model data are presented. Some discrepancies between observations and model results

are due to scheme dispersion (i.e., the spectral peak is lower and directions vary by 10°-20°).

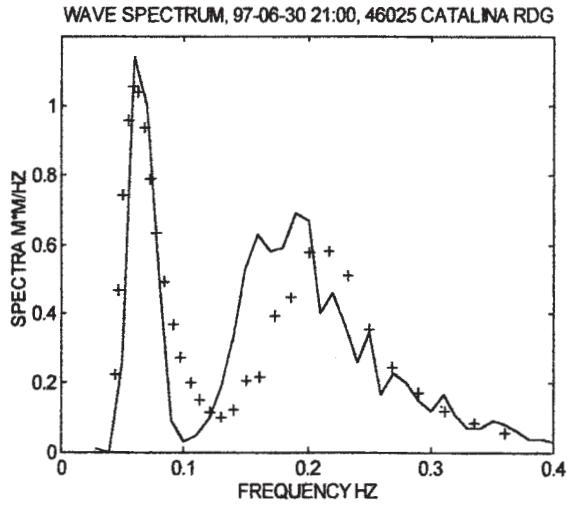

Figure 6. Frequency spectra (m^2s) at 21:00 Z on 30 June 1997. Station buoy data are plotted with a solid line and model output is plotted with "plusses".

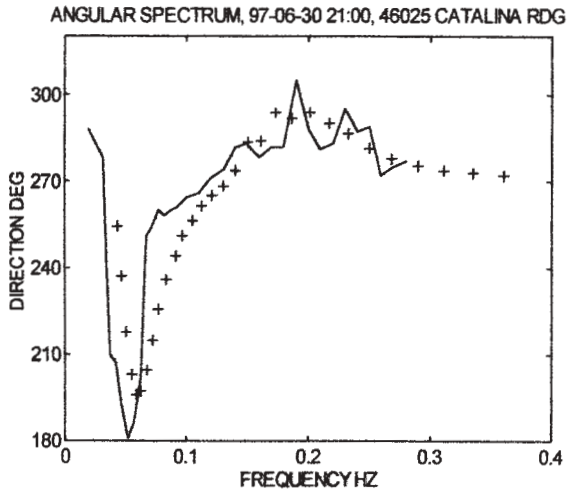

Figure 7. Angular spectra (degrees) at 21:00 Z on 30 June 1997. Station buoy data are plotted with a solid line and model output is plotted with "plusses".

To show the impact of current, notional currents were included in the model. Speed and direction values were necessary to remove frequency shift 0.04 Hz for the wind waves in the frequency spectra on Figure 6. The selected current was 1.2 m/s with direction 70° from the North. As one can see from Figure 8, there is no more frequency shift on the model curve. Because waves are growing while they propagate with currents directed opposite of their direction, the high frequency tail was put at $f>3.5f_0$. The angular spectrum for this case is presented in Figure 9 and remains the same as the one without current that is depicted in Figure 7.

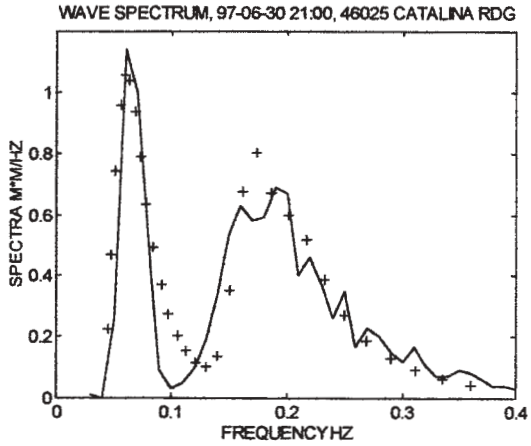

Figure 8. Frequency spectra (m^2s) at 21:00 Z on 30 June 1997. Station buoy data are plotted with a solid line and model output is plotted with "plusses". Currents have been included.

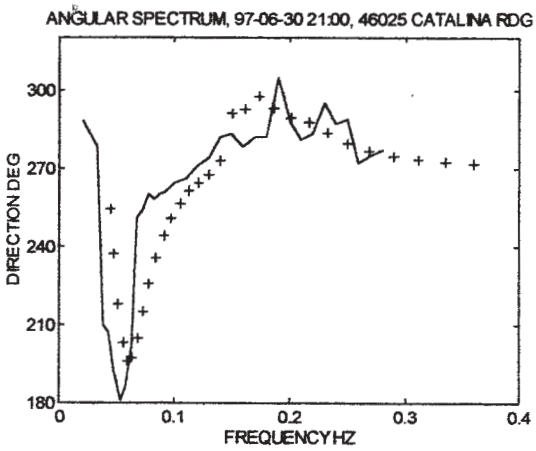

Figure 9. Angular spectra (degrees) at 21:00 Z on 30 June 1997. Station buoy data are plotted with a solid line and model output is plotted with "plusses". Current included.

4. CONCLUSION

One can see that this model successively describes wave evolution in our polygon. We have shown the importance of swell as a boundary condition. For the mixed wave field, results showed a strong dependence on frequencies where we used a high frequency tail. The interactions between swell and wind waves are difficult to describe due to the presence of the Channel Islands. Ocean circulation is also important because wave spectra are sensitive to current speed

and direction values. Future efforts should consider the effect of drift currents.

5. ACKNOWLEDGMENTS

This work extends from opportunities that were made available at Johns Hopkins University and by resources such as archived meteorological and oceanographic data through NOAA's many WWW sites. Encouragement to continue with this wave modeling initiative by research scientists such as Dr. Don Resio is greatly appreciated. Support derived from Marine Information Resources Corporation personnel enhanced the final product.

6. REFERENCES

Allard, R., L. Hsu, M. Collins, J. McKee Smith, M. Earle and K. Miles, 1998: Use of coupled numerical wave and surf models to simulate the littoral environment from deep water to the beach, Naval Research Laboratory Technical Report, NRL/FR/7322--98-9688, Stennis Space Center, MS, 48 pp.

Chen, H.S. and J.R. Houston, 1987: Calculation of water oscillation in coastal harbors, HARBS and HARBD user's manual, CERC Instruction Report No. CERC-87-2. Department of the Army, US Army Corps of Engineers, Vicksburg, MS.

Hasslemann K., 1974: On the spectral dissipation of the ocean waves due to white capping. *Bound.-Layer Meteor.*, **6**, 1, 107-127.

Hasselmann S. and K. Hasselmann, 1985: Computation and parameterizations of the nonlinear energy transfer in a gravity wave spectrum. Part I: A new method for efficient computation of the exact nonlinear transfer integral. *J. Phys. Oceanogr.*, **15**, 11, 1369-1377.

Komen,G., L. Cavaleri, M. Donelan, K. Hasselmann, S. Hasselmann, P. Janssen, 1994: *Dynamics and Modeling of Ocean Waves*. Cambridge University Press, 532 p.

Snyder R.L., F.W. Dobson, J.A. Elliott, R.B. Long, 1981: Array measurement of the atmospheric pressure fluctuations above surface gravity waves. *J. Fluid Mech.*, **102**, 1-59.

Tolman H.L., 1991: A third-generation model for wind waves on slowly varying unsteady, and inhomogenious depth and currents. *J. Phys. Oceanogr.*, **21**, 782-797.

Wittman, P.A. and D.D. Farrer, 1997: Global, regional, and coastal wave predictions, *Mar. Technol. Soc. J.*, **31**, 76-82.

Wittman, P.A. and W.C. O'Reilly, 1998: A coastal swell forecast system, *Proc. MTS/IEEE Oceans Community Conference*, Baltimore, MD, 418-421.

APPLICATION OF SWAN IN MISSISSIPPI SOUND

Y. Larry Hsu, W. Erick Rogers, James M. Kaihatu and Richard A. Allard
Oceanography Division, Naval Research Laboratory
Stennis Space Center, MS, 39529 USA

1. INTRODUCTION

Forecasting conditions in coastal and nearshore regions involves numerical simulation of circulation, waves, and sand-silt sediments. To develop a coastal forecasting system, the Naval Oceanographic Office (NAVOCEANO) at the Stennis Space Center, Mississippi has started the Northern Gulf of Mexico Littoral Initiative (NGLI). The main objectives of NGLI are to implement and validate a circulation-sediment-wave modeling system for the Mississippi Sound and adjoining rivers, bays, and shelf waters. An effort has also been started to develop a water quality component for the modeling system. The final product will be a system that can be utilized by many local, state, and federal agencies for a variety of purposes that deal with military training, research in littoral processes, resource management planning, maximum nutrient loads, and the possible contamination of coastal waters, rivers, and beaches.

This paper reports the preliminary effort of wave simulation part of the NGLI. For this project, a wind wave model with refraction computation is required. Among many possible coastal wave models (e.g. see Ris, 1997), the SWAN (Simulating WAves Nearshore, Booij et al. 1999) model is selected due to its ability to simulate wind wave generation without limitation on wave direction. This feature is critical for driving sediment models. Using buoy wind, a validation study is conducted for a fetch limited case. Additional ongoing modeling and measurement activities are described.

2. AREA OF NGLI PROJECT

The area used in SWAN simulation is shown in Figure 1. It covers the entire Mississippi Sound and Mobile Bay in the North and extends to the shelf break in the South. The stars indicate the location of NDBC (National Buoy Data Center) deep water buoy 42040 (depth 242 m) and shallow water buoy 42007 (depth 13.4 m). The six-second bathymetry created by NAVOCEANO is based on NOS (National Ocean Service) data. For the test case presented here, the bathymetry is re-gridded at 18-second resolution with a grid spacing of 290 m by 189 m. Total grid size is 601 by 341.

3. WIND AND WAVE CONDITIONS

Before the planned measurement data becomes available, SWAN performance under a simplified condition is first evaluated. Examining the wind record from the two NDBC buoys, a case of almost constant wind case in October 1999 is identified. The wind speed and direction from both buoys are plotted in Figure 2. The wind starts low around 5 m/s on 10/19 and increases to 10 m/s around middle of 10/20. Then the wind remains steady near 10 m/s for about one and half days. The wind direction stays essentially constant coming from the North for about two days. This provides an excellent test case for fetch limited condition.

4. MODEL SETUP

The SWAN is run under the non-stationary mode with no incoming waves specified at the boundary. This is justified since the wave condition before the study period is generally below 0.5 m. Wind from buoy 42040 is used to drive the model. In computation, thirty-six angular bands and thirty-six frequency bands are used. Default setting of source and sink terms are used. The computation time step is chosen at 6 minutes; this has been shown to be sufficient even under a rapid changing front condition in this area.

5. RESULTS UNDER A FETCH LIMITED CONDITION

The comparisons of significant wave height and peak period between SWAN and buoy 42040 are shown in Figure 3. Due to the zero initial condition, SWAN takes about 5 hours to spin up to measurement values. The waves grow larger and longer as time passes and reach a peak value of 2 m and 6 second. In general, the wave height curve follows the wind speed curve closely as expected. The agreement between significant wave heights is very good. The peak period from the SWAN is slightly lower than that of the buoy.

6. DISCUSSION

6.1 Bathymetry Resolution

Three days of simulation of the limited fetch case at full grid resolution of 601 by 341 take twelve days on a SUN UltraSPAC-II at 296 M Hz. Due to the heavy demand of computation requirement of SWAN, coarse resolution runs are conducted to study the effect of grid resolution. It is found that no significant change of waves is found even at 81 by 41 grid resolution. This is certainly due to the fact that the offshore traveling waves are short and do not feel the bottom. Therefore, coarser resolution runs can still generate similar results. No general guideline for selecting optimal resolution for a particular situation can be found in the literature. At the end of this project, it is hoped that guidelines for selecting grid resolution based on bathymetry, coastline features and other wave climate parameters can be established.

6.2 Ongoing Modeling and Measurement Activities

There is a need to reduce the computation requirement and to resolve the bathymetry around islands. As shown in Figure 4, a new rotated coarse grid at 1 km resolution and a fine nearshore grid at 250 m resolution are generated for future runs. The wave measurement locations are also plotted in Figure 4. Two NDBC buoys, 42040 and 42007 have been upgraded to directional HIPPY sensor since 8/23/2000. Another NDBC directional buoy 42042 was deployed for three months (8/23 to 11/30). During the September study period (9/1-9/13/2000), a Seabird pressure transducer was deployed at 4 m depth for almost two weeks. The portable directional wave buoy manufactured by Neptune Sciences, Inc. was deployed at various locations inside and outside the Mississippi Sound. The WAM regional wave model has been set up to provide boundary and/or initial conditions for the SWAN. COAMPS wind field of 27 km resolution is used as wind input. Two methods of using WAM directional data in SWAN are possible. In the first method, the WAM directional wave spectra are specified at boundaries using the "BOUNDSPEC SIDE" command in SWAN. In the second method, the direct WAM nesting command "BOUNDNEST2 WAMNEST" is used where the restart binary file from WAM is read as input. Both methods will be explored. The comparison of model results and measurement are being conducted.

7. SUMMARY

Using a fetch limited case, the SWAN has been shown to be a reliable model to provide wave information. The field program of NGLI project offers an unique opportunity for SWAN validation. The ongoing run with COAMPS wind and regional WAM will provide an estimation of SWAN performance under operational conditions.

ACKNOWLEDGEMENT

This work is supported by the Naval Oceanographic Office. This is NRL contribution PP/7320-00-1018.

REFERENCES

Booij, N., R. C. Ris, and L. H. Holthuijsen, 1999: A third-generation wave model for coastal regions, 1, Model description and validation. J. Geophys. Res., 104, 7649-7666.

Ris, R. C., 1997: Spectral modeling of wind waves in coastal areas. Ph.D. thesis, Delft University of Technology, 160pp.

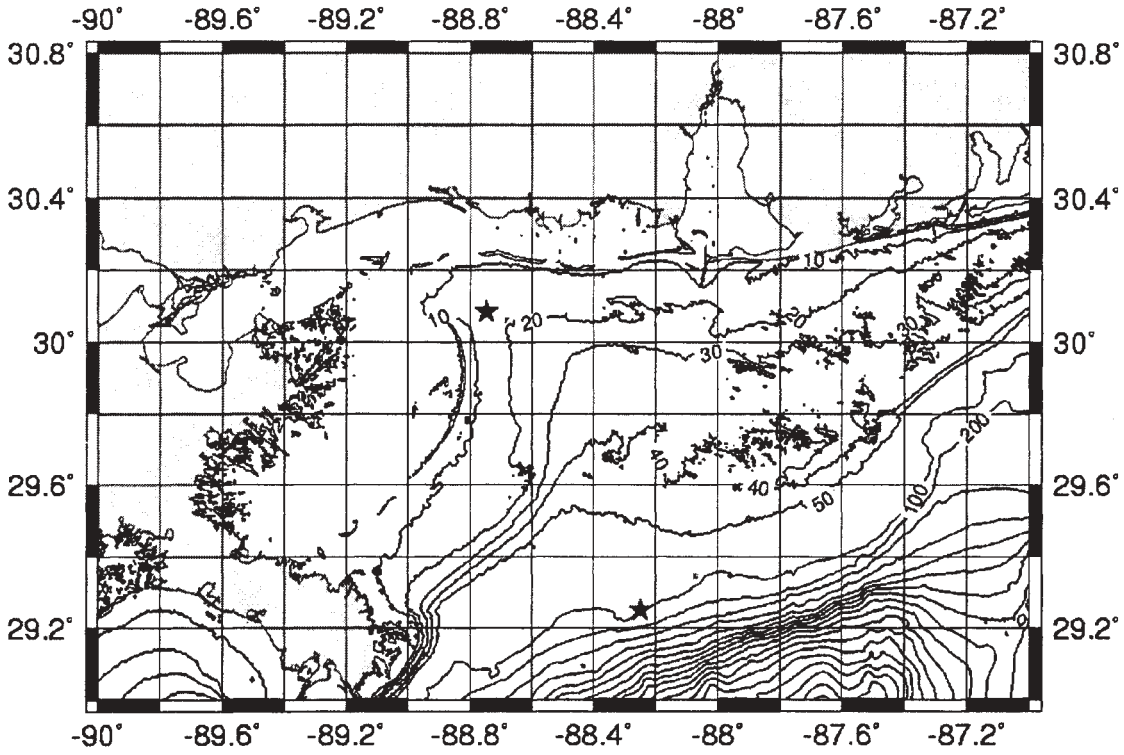

Figure 1. Area Map for NGLI Project. Depth contours are in meters. Stars denote the location for NDBC buoys.

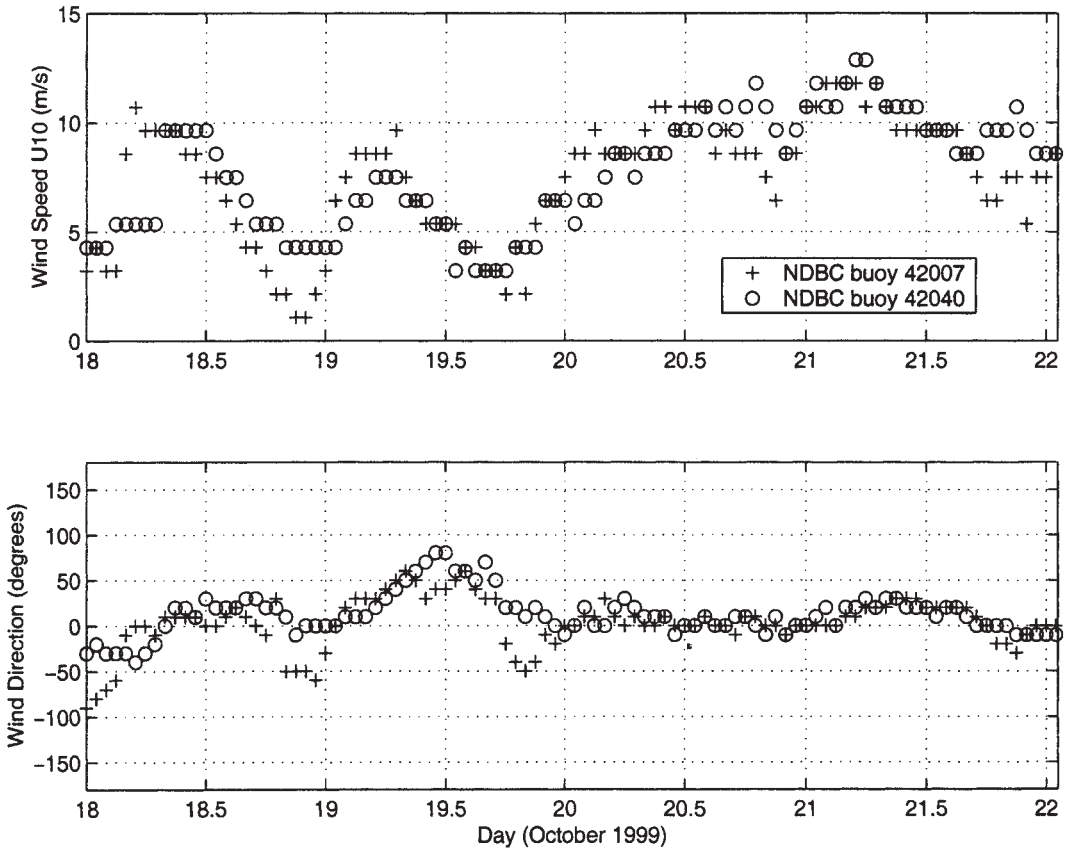

Figure 2. Wind Speed and Direction from NDBC Buoys. Wind direction is relative to the North.

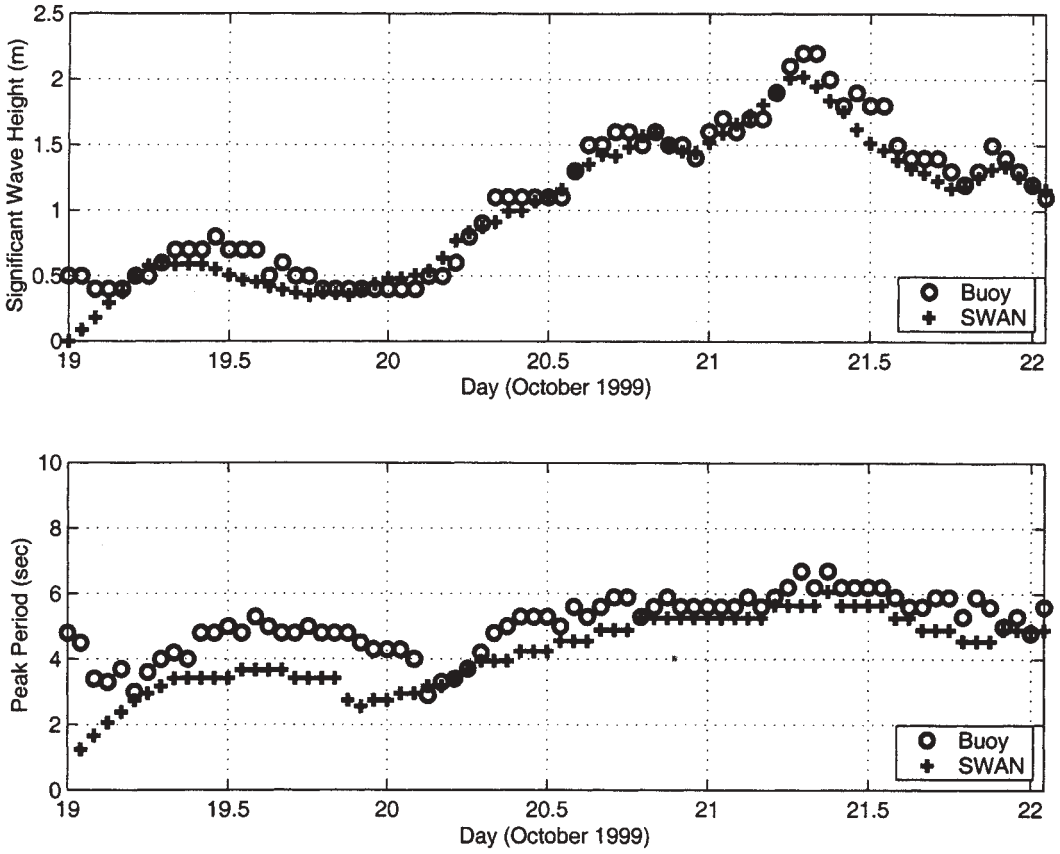

Figure 3. Comparisons of Significant Wave Height and Peak Period Between Buoy 42040 and SWAN.

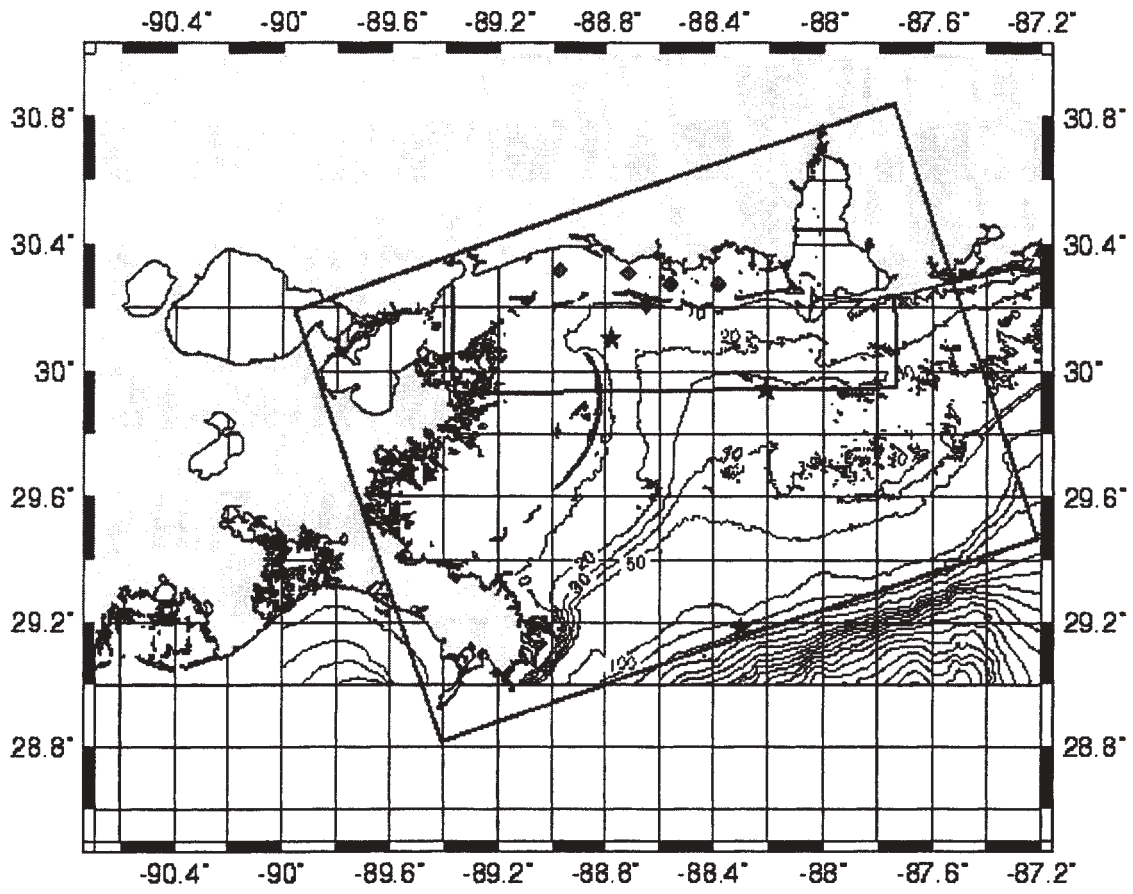

Figure 4. Nested grids for NGLI Project. Symbols denote the measurement locations; Stars: NDBC buoys, Triangle: Seabird pressure transducer, Diamonds: Portable buoy from Neptune Science, Inc.

NONLINEAR MECHANISMS IN A HARBOR/COASTAL WAVE TRANSFORMATION MODEL: ENHANCEMENTS TO CGWAVE

Vijay Panchang, W. Chen, L. Zhao (University of Maine, Orono)
and
Z. Demirbilek (US Army Engineer research & Development Center, Vicksburg)

The mild-slope wave equation is now well-accepted as the method for estimating coastal wave conditions. When solved in its original elliptic form, it can be used to model refraction, diffraction, and reflection arising from bathymetry and structures, with no limitations on the direction of wave scattering. As such, numerical models based on this form be used to simulate wave behavior in domains of complex configurations, such as harbors. An efficient finite-element model called CGWAVE, developed at the University of Maine partially with DoD support, has been rigorously evaluated using several controlled tests and subsequently applied to practical harbor applications (e.g. Oceanside Harbor, Los-Angeles/Long Beach Harbor, Kahului Harbor, Barbers Point Harbor, and others).

This paper describes the incorporation of nonlinear mechanisms in elliptic models. While some nonlinearities may be easily included in simpler models which have constraints on wave scattering angles (e.g. the parabolic approximation model), their incorporation in elliptic models that are suitable for domains of arbitrary shape is more complex. Here the inclusion of two nonlinear processes in CGWAVE is described:

1) Wave-current interaction. Many coastal regions experience high tidal (or other) currents. Wave propagation is influenced by these currents (e.g. waves opposing the currents become larger and vice-versa). Modifications to CGWAVE to include the effect of modelled or measured currents will be presented. Numerical simulations of the hydraulic model experiment recently conducted by Dr. Jane Smith (of the Army WES) will be described. This experiment pertains to waves approaching an inlet with jetties in the presence of ebb currents and allows us to model not only wave-current interaction, but also the effect of wave breaking when opposing currents are present.

2) Wave-wave interaction. By including most of the non-linear terms in the derivation, Kaihatu and Kirby (1995) and Tang and Ouellet (1997) obtained extensions of the CGWAVE model equations that incorporate wave-wave interactions. These are included in the model, thus providing CGWAVE with the same level of non-linearity as that in Boussinesq models (Tang and Ouellet 1997), while simultaneously offering the stability and speed of the CGWAVE matrix solvers and the advantages of finite-element gridding in harbors and complex coastal areas. The model is tested against hydraulic model experiments. Aspects pertaining to practical application will be discussed.

Corresponding Author: Dr. Zeki Demirbilek, US Army Engineer R&D Center, CHL, Halls Ferry Road, Vicksbur, MS 39180. Tel. 601-634-2438.

REFLECTION AND TRANSMISSION OF WAVES NEAR BLOCKING

Ashwini K. Otta

Splash Hydrodynamics
Geomatica Business & Science Park
8316 PT Marknesse, The Netherlands.

1 INTRODUCTION

Waves propagating over a non-uniform current field undergo transformations both in amplitude and shape. One phenomenon of significant interest occurs when waves encounter a strong opposing current and the absolute group velocity nears zero. This is often referred to as wave-blocking.

In a pioneering work, Longuet-Higgins and Stewart (1961) have illustrated the basic principle of wave-current interactions. Subsequently, Bretherton and Garrett (1969) have established the conservation of action flux for waves in the presence of a current, namely

$$\frac{\partial}{\partial t}\frac{E}{\omega_r} + \frac{\partial}{\partial x}\frac{E\left(c_{g_r}+U_c\right)}{\omega_r} = 0 \qquad (1)$$

where

$$\omega_r = \omega - kU_c, \quad c_{g_r} = \frac{1}{2}\frac{\omega_r}{k}\left[1+\frac{2kh}{\sinh\left(2kh\right)}\right] \qquad (2)$$

and energy density of waves per unit surface area in terms of amplitude A is $E = \frac{1}{2}\rho g A^2$. The symbols ω, k, h and U_c denote respectively the angular frequency of the waves, wave number, depth and the ambient current.

The action balance principle, given by (1), predicts that the amplitude of the incident waves goes towards infinity as $\left(c_{g_r}+U_c\right)$ tends toward zero nearer to the blocking point and provides no information regarding the conservation of the action at blocking. This apparent failure of the action balance principle is, however, not inherent with the linear theory. Smith (1975), Stiassnie and Dagan (1979), Shyu and Phillips (1990) and Trulsen and Mei (1993) have presented solution to the wave-field behavior near the blocking point showing that the amplitude of the incident waves remain finite even within the framework of linear theory. Since, linear theory analysis provides the basics for understanding key features at blocking, we summarize some of the main findings here for gravity waves based on the analysis of Shyu and Phillips (1990). Using the deep water assumption, the surface elevation for waves riding on a steady flow $U_c(x)$ can be represented by

$$\eta(x,t) = B_0\mathcal{V}(x)\exp\left(-\frac{1}{2}\int_{x_b}^{x} Q dx\right)\cdot \exp\left(\frac{i}{2}\int_{x_b}^{x}\left(k_1+k_2\right)dx - i\omega t\right) \qquad (3)$$

with B_0 a constant yet to be determined and

$$\mathcal{V}(x) = A_0\mathrm{Ai}(-r) - C_0\mathrm{Ai}'(-r), \qquad (4)$$
$$A_0 = \left(\frac{r}{H}\right)^{1/4}\cos\left(-\frac{1}{2}\int_0^x G/H^{1/2}dx\right)$$
$$C_0 = (rH)^{-1/4}\sin\left(-\frac{1}{2}\int_0^x G/H^{1/2}dx\right)$$

and

$$\frac{2}{3}r^{3/2} = -\int_0^x H^{1/2}dx, \quad H = \frac{1}{4}\left(k_1-k_2\right)^2,$$
$$Q = \frac{3}{U_c}\frac{\partial U_c}{\partial x}, \quad G = i\frac{1}{2}\frac{g'}{U_c^3}\frac{\partial U_c}{\partial x}$$
$$g' = g\cos\theta + \frac{U^2}{R} \quad . \qquad (5)$$

The terms θ and R in (5) refer to the angle and radius of curvature of the surface due to the underlying flow U_c and g' can best be described as the effective gravity experienced by the short waves. x_b is the blocking point defined by $\left(c_{g_r}+U_c\right)=0$. k_1 and k_2 are the two solutions to k in the deep-water dispersion relation

$$\left(\omega - kU_c\right)^2 = gk \qquad (6)$$

AUTHOR INDEX TABLE OF CONTENTS

on the positive k-axis for an adverse current U_c ($U_c < 0$). The lower root k_1 is the wave number of the incident waves and k_2 is that of the reflected waves. At blocking $k_1 = k_2$.

An illustrative simplification of (3), although limited in scope, is obtained by using the asymptotic approximation of the Airy function $\mathrm{Ai}(-r)$ and its derivative $\mathrm{Ai}'(-r)$ for large r, *i.e*,

$$\mathrm{Ai}(-r) \approx \frac{1}{\sqrt{\pi} r^{1/4}} \sin\left(\frac{2}{3} r^{3/2} + \frac{\pi}{4}\right), \qquad (7)$$
$$\mathrm{Ai}'(-r) \approx -\frac{r^{1/4}}{\sqrt{\pi}} \cos\left(\frac{2}{3} r^{3/2} + \frac{\pi}{4}\right)$$

Substitution of (7) into (3) via (4) leads after some algebraic manipulation to the far-field approximation of the surface elevation

$$\begin{aligned} \eta &= B_0 \frac{H^{-1/4}}{2\sqrt{\pi}} \exp\left(-\frac{1}{2}\int_0^x (Q + iG)\, dx\right) \cdot \\ &\quad \sin\left(\int_0^x k_1 dx - \omega t + \frac{\pi}{4}\right) \\ &\quad -B_0 \frac{H^{-1/4}}{2\sqrt{\pi}} \exp\left(-\frac{1}{2}\int_0^x (Q - iG)\, dx\right) \cdot \\ &\quad \sin\left(\int_0^x k_2 dx - \omega t - \frac{\pi}{4}\right) \end{aligned} \qquad (8)$$

The approximation, given by (8), describes separately the incident (k_1 component) and the reflected (k_2 component) wave field and in fact provides a way to specify the arbitrary constant B_0 consistent with the offshore amplitude of an incident train.

In summary, the detailed analysis accounting for a transfer of energy to the second root of the linear dispersion yields a well-bounded amplitude envelope near blocking even in the absence of any dissipative mechanism. The action balance principle holds separately for the two branches away from the blocking point. The wave number of the reflected waves increases with decrease in the strength of the current downstream of the blocking point. While confirming this theoretical analysis for incident waves of small amplitude, experiments by Lai *et al.* (1989), Chawla and Kirby (1998) have highlighted new features such as (a) higher incident waves in some cases lead to appreciable wave transmission beyond the 'linear-theory-predicted' blocking point, (b) wave-period experiences a down-shift (see also Smith *et al.*, 1997).

In the present work, we will explore the features of small waves near blocking over a varying depth and also the effect of nonlinearity as wave height is increased. As a guideline for small waves, we shall use the analytical expression (3). Unfortunately, its validity is limited to deep water waves only. An extension to finite depth does not seem straight-forward. In analogy to (8) an ad-hoc expression for finite-depth may be given by

$$\begin{aligned} \eta(x,t) &= A_i(x) \sin\left(\int_{x_b}^x k_1 dx - \omega t + \frac{\pi}{4}\right) + \\ &\quad A_r(x) \sin\left(\int_{x_b}^x k_2 dx - \omega t - \frac{\pi}{4}\right) \end{aligned} \qquad (9)$$

The corresponding amplitude envelope A_η is given by

$$A_\eta^2 = A_i^2 + A_r^2 + 2A_i A_r \cos\left(\frac{\pi}{2} + \int_{x_b}^x (k_1 - k_2)\, dx\right) \qquad (10)$$

Since the action balance principle holds over finite depth and separately for the two branches away from the blocking point, we expect (9) to hold away from the blocking point if the wave numbers k_1 and k_2 and the amplitudes A_i and A_r are specified from the action-balance principle using the finite-depth dispersion relationship.

2 MODEL FRAMEWORK

2.1 Basic equation

One of our primary concerns is wave-blocking near tidal inlets where strong tidal currents can block rather long waves. We have adopted a higher-order, both in dispersion and nonlinearity, Boussinesq equation (Madsen & Schäffer, 1998) as the mathematical basis to model nonlinear wave-current interactions for such cases. In shorthand notations, this system of two dependent variables elevation η and velocity $\tilde{u}$ is represented by

$$\begin{aligned} &\frac{\partial \eta}{\partial t} + \frac{\partial}{\partial x}\left[\tilde{u}\,(h+\eta) + q_{2,0}\right. \\ &\qquad \left. + q_{2,1} + q_{2,2} + q_{2,3}\right] = 0 \\ &\frac{\partial \tilde{u}}{\partial t} + \frac{1}{2}\frac{\partial}{\partial x}\left(\tilde{u}^2\right) + g\frac{\partial \eta}{\partial x} + \Lambda_{2,0} + \\ &\qquad \Lambda_{2,1} + \Lambda_{2,2} + \Lambda_{2,3} = 0 \end{aligned} \qquad (11)$$

AUTHOR INDEX TABLE OF CONTENTS

where the subscript j in the terms $q_{2,j}$, $\Lambda_{2,j}$ $(j = 0, 1, 2, 3)$ denote the order of nonlinearity in the Boussinesq expansion consistent to $O(kh)^2$. An expansion of these terms in terms of the dependent and non-dependent vaiables may be found in the original article. Additional discussion of the nonlinear properties of this set of equations is included in Otta and Schäffer(1999).

With the the appropriate values for the parameters, the linear dispersion inherent to the system (in the absence of a current) is the Padé [4/4] approximation of the exact $\omega^2 = gk\tanh(kh)$ relationship. Further, considering $\tilde{u}$ as the total velocity including an wave component and an ambient current U_c, shows that the linear dispersion exhibits the Doppler shift to the same degree of accuracy; *i.e.*,

$$\Omega_r^2 = (\Omega - kh \cdot \mathrm{Fr})^2 = (kh)^2 \cdot \frac{1 + \frac{1}{9}(kh)^2 + \frac{1}{945}(kh)^4}{1 + \frac{4}{9}(kh)^2 + \frac{1}{63}(kh)^4} \quad (12)$$

where Fr is the Froud number $U_c/\sqrt{gh}$ and Ω represents the normalized frequency $\omega.\sqrt{h/g}$. The approximation of $(\Omega - kh \cdot \mathrm{Fr})$, given by the square root of the right hand side of (12), is shown along with the exact value in Fig. 1. For a given Froude number $\mathrm{Fr} = U_c/\sqrt{gh}$, the two roots $(kh)_1$ and $(kh)_2$ for the positive kh are obtained from the intersection of the curve with the line given by $\Omega - kh\mathrm{Fr}$. In the exact dispersion relation-

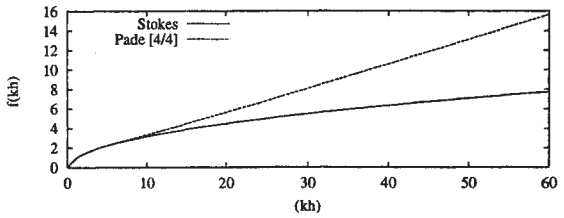

Figure 1: The exact (Stokes) $f(kh) = \sqrt{kh\tanh(kh)}$ and its approximation following Padé [4,4] approximation of linear dispersion relationship.

ship, there is a normalized frequency Ω_{blk} which meets the blocking condition at any (negative) Froude number up to zero. A consequence of the Padé approximation is that this is true only up to the Froude number of 0.26. This is shown in Fig. 2. The agreement of the blocking frequency Ω_{blk} obtained from the exact and the approximate relation is good over [-1.0 ¡ Fr ¿ -0.26]. After that, the approximate relation bifurcates. For

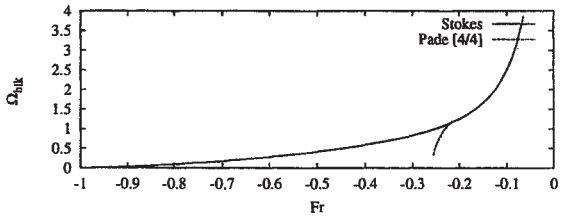

Figure 2: Normalized frequency Ω at the blocking point as a function of the Froude number $U_c/\sqrt{gh}$.

a Forude number lower in magnitude than 0.25, no waves will be blocked in the approximate relationship. For this reason and also the reason of accuracy, the present set of equations should be used only for long waves which are blocked at relatively large froude number.

2.2 Numerical investigation

In the present work, we shall consider only one-dimensional cases of waves encountering a steady, opposing current. Variation in the strength of the current is induced by the depth variation. We shall use the set (11) retaining all the terms. Wave-breaking or bottom friction is not included in this framework. We use a numerical filter operating on the elevation and the velocity to dissipate the very high-frequency waves. To minimize the effect of filtering on the waves of interest an 11-point filtering is used (*e.g.*; Dommermuth and Novikov, 1993). This filter is given by

$$\begin{aligned}\bar{\psi}_j \;=\; & \frac{1}{1024}\left(772\psi_j + 210\left(\psi_{j+1} + \psi_{j-1}\right)\right. \\ & -120\left(\psi_{j+2} + \psi_{j-2}\right) + 45\left(\psi_{j+3} + \psi_{j-3}\right) \\ & \left.-10\left(\psi_{j+4} + \psi_{j-4}\right) + \left(\psi_{j+5} + \psi_{j-5}\right)\right) \quad (13)\end{aligned}$$

The necessity and the consequences of using this filter will be discussed in the context of a numerical example.

In the numerical examples included here we have considered a varying depth from 80 cm offshore to 20 cm on the shelf. For a prescribed discharge rate Q_0, an initial current field is defined through the solution of the continuity equation (assuming vertical distribution of the current to be uniform) and the Bernoulli's equation for the free surface,i.e.

$$U_c\left(h + \eta_c\right) \;=\; 0$$

AUTHOR INDEX TABLE OF CONTENTS

$$\frac{1}{2}{U_c}^2 + g\eta_c = \frac{1}{2}\left(\frac{Q_0}{h_0}\right)^2 \qquad (14)$$

where η_c is the change in the mean water level due to the steady current $U_c(x)$ and h_0 is the undisturbed offshore depth. Experiments with numerical evolution of the current field without any imposed waves show that there is no observable change in the steady current field.

Incident waves according to linear formulations are specified at the left end and are absorbed by a sponge layer on the right. Waves are damped in the sponge layer with respect to the initial steady water level and velocity field defined by the prescribed current field.

3 RESULTS & DISCUSSION

3.1 Small waves and linear theory

First, we consider an incident train of monochromatic waves of offshore amplitude of 0.001 m (1 mm) and period 2 s riding over a current of discharge 0.136 m^2/s (U_c = -0.17 m/s offshore, -0.81 m/s on shelf). Surface elevation is shown in Fig. 3 at three different instants after the start of computation from an initially steady current field. The bottom part of the figure shows the depth variation and the mean water level due to the underlying current. The top two plots show surface elevation with respect to the mean water level while the third plot from the top shows the elevation including the set-down due to the current. The blocking point predicted from the linear theory for this case is 38.85 m at a Froude number of -0.477. At the early stages of evolution of the wave field ($t \leq 40$ s), the top two plot shows the incident wave having reached the blocking point. The dashed line (top plot) showing the amplitude of the incident waves, as predicted from the action balance principle, agrees well up to about two local wave lengths from the blocking point. In consistence with the more detailed theory [expression (3)] mentioned in the introduction, the computed amplitude goes smoothly to zero instead of blowing up as in the action balance theory. We surmise that the existence of the leading edge upstream of the blocking point is due to the existence of the longer waves in the leading edge. With evolution of time, energy of the incident waves is swept downstream by the wave component satisfying the second root of the dispersion relationship. This is shown in third plot of Fig. 3. As this component gets swept downstream, the wave number increases rapidly with the decrease in current strength. In reality, this component suffers viscous or turbulent dissipation due to the large wave number. In the present work, we dissipate the waves through the use of the numerical filter (13). In the absence of other viscous or turbulent dissipation, the use of the filter becomes necessary to stabilize the computation to a longer stage of evolution. The reflected waves, being absorbed by the filtering, disappear from the computed wave field downstream.

A comparison of the computed amplitude envelope with the ad-hoc theoretical expression (10) is provided in Fig. 4. But for the disagreement at the blocking, the two envelopes modulated by the incident and the reflected waves (second branch of the dispersion relationship) agree well. The computations indicate that the wave-amplitude remains finite even without breaking. In fact, the amplitude decreases smoothly from a local maximum to zero. The local maximum is not at the blocking point, but about a two (local) wavelengths preceding the blocking point.

The variation of wave number near the blocking point is shown in Fig. 5. The upper curve shows the wave number of the second branch (k_2 wave). The solid line represents the wave number calculated from the Stokes dispersion relation while the dashed line that from the Padé [4/4] relation. The symbols represent the wave numbers calculated from the computed wave profiles. The agreement of the computed wave number with the first and second roots of the dispersion relationship provide an additional confirmation of the principle of non-singular expression given by (3).

3.2 Effect of higher wave height

To illustrate the nonlinear behavior, we now consider a magnified offshore amplitude of 0.01 m (10 times larger than considered in the previous section). The underlying ambient current and the period remain the same.

Surface profiles at different instants are compared for the two cases in Figs. 6 and 7. For the purpose of this comparison, elevation is defined with respect to the mean set-down due to the

AUTHOR INDEX TABLE OF CONTENTS

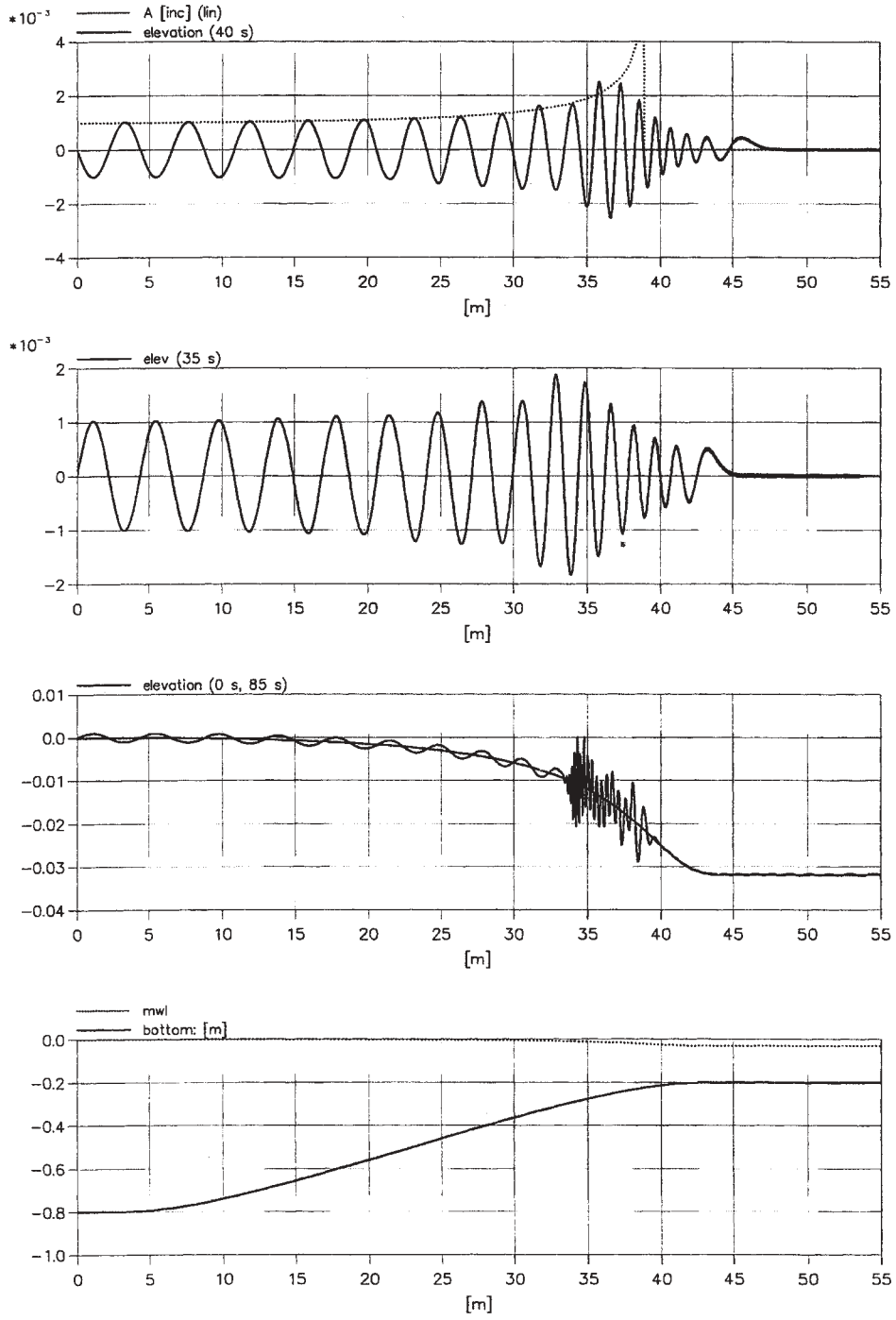

Figure 3: Instantaneous profiles of waves encountering an opposing current.$H = 0.002$m, $T = 2.0$s, $h_0 = 0.8$ m, $h_s = 0.2$m and $Q = -0.136$ m^2/s.

AUTHOR INDEX TABLE OF CONTENTS

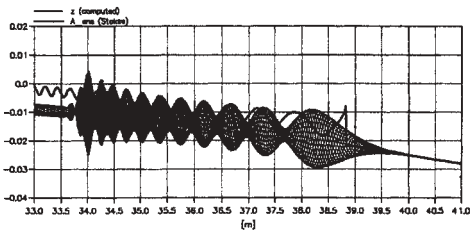

Figure 4: Elevation envelope of waves encountering an opposing current. $H = 0.002$m, $T = 2.0$s, $h_0 = 0.8$ m, $h_s = 0.2$m and $Q = -0.136$ m^2/s.

current. Further, the elevation of the smaller wave height is multiplied by 10 for a direct comparison. The profiles at $t = 40$ s of both the cases are nearly identical (most noticeable difference being the slightly faster phase speed of the higher waves). At this instant, the reflected wave field is not yet developed. At instants later than 90s the incident and reflected trains have become steady for the smaller wave height and the corresponding surface profiles (shown by the solid lines) are identical. However, the leading front for the higher waves (dashed line) exhibits an oscillatory nature.

One of the effects of higher waves is the increase in value of the group velocity. A higher group velocity would result in pushing the blocking point further upstream of the linear-theory-predicted value. The behavior exhibited by the computed profiles is in contrast an oscillating leading edge, the period of oscillation being much longer than the wave period itself. This oscillation is also evident in the time-series of surface elevation at a few points around the 'linear' blocking point (Fig. 8). The elevation shown in this figure is with respect to the initial still water. Thus, the initial set-down in the first stage of the time-series is due to the steady current. The time records at 35 m and 37 m show initially the incident waves which are later modified by the arrival of the reflected energy. The presence of a long wave (accompanied with some short waves) of rather small height (about 5 mm) is worth noting at 41m. Along with these features, wave period at points near the blocking are modified. Since Fourier analysis is not very suitable for detecting irregular and small changes in period (with a relatively short time-record), we have performed a local period calculation based on the interval between two consecutive crests at a given location. The variation in the wave period at different locations is shown in Fig. 9. At 32 m which is not much influenced by the reflected waves (due to the explicit use of a numerical filter) the period remains nearly unchanged. But, closer to the blocking point the wave period is strongly modulated.

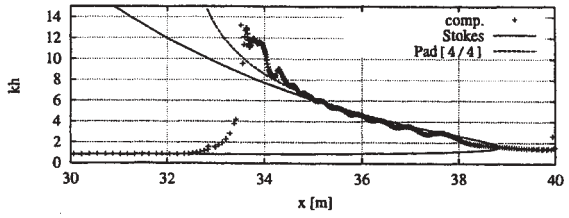

Figure 5: Wave number variation for the case shown in Fig. 4.

3.3 Variation with current gradient

In the previous example, the most noticeable features with increase in wave height were the oscillation of the leading edge and the change in wave period. The evidence of any energy being transmitted beyond the blocking point was not strong. With identical wave parameters (period of 2 s and wave heights of 0.002 m, 0.01 m and 0.02 m), Fig. 10 shows the computed profiles where a milder opposing current of discharge $Q_0 = -0.120$ m^2/s has been used. Depth variation is the same in all cases.

The bottom plot of the figure shows instantaneous surface profiles for the smallest height. The waves are blocked near 42.5 m in confor-

AUTHOR INDEX TABLE OF CONTENTS

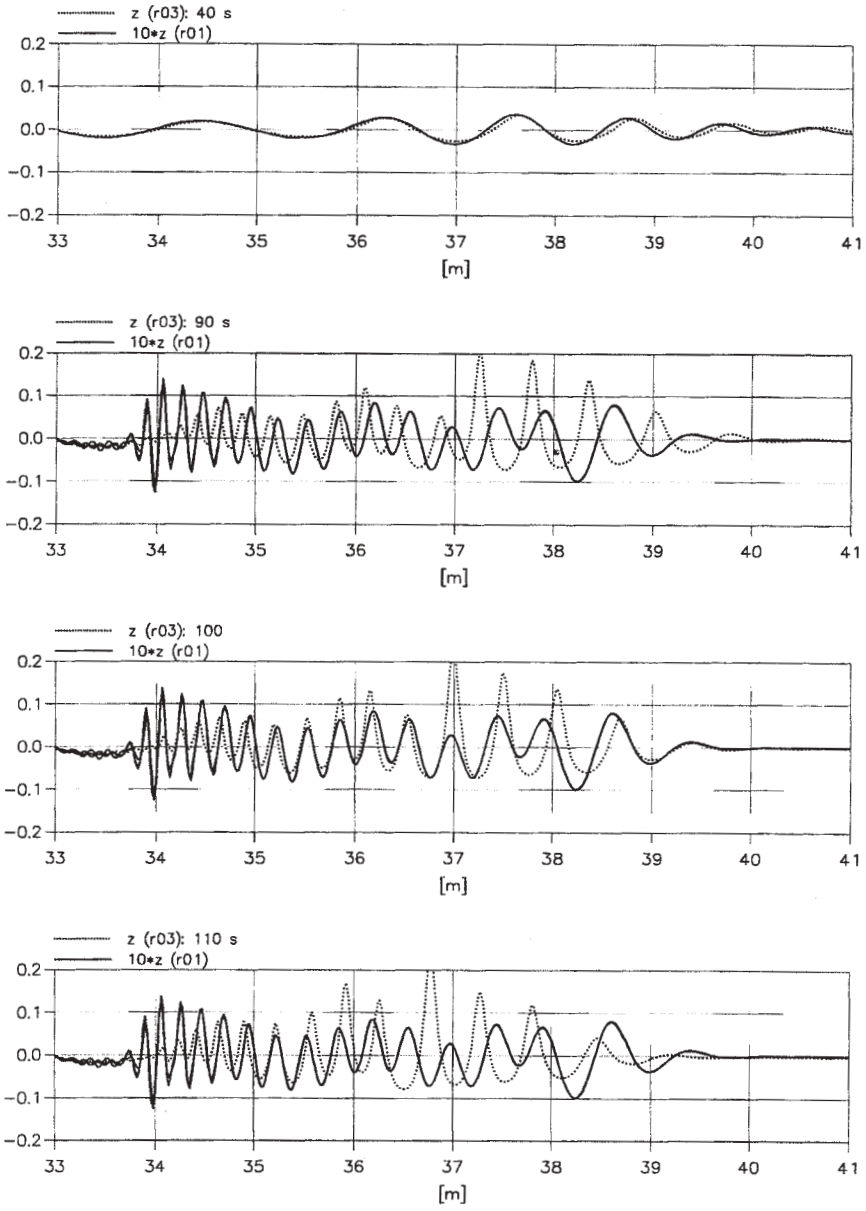

Figure 6: Continued on the next page.

AUTHOR INDEX TABLE OF CONTENTS

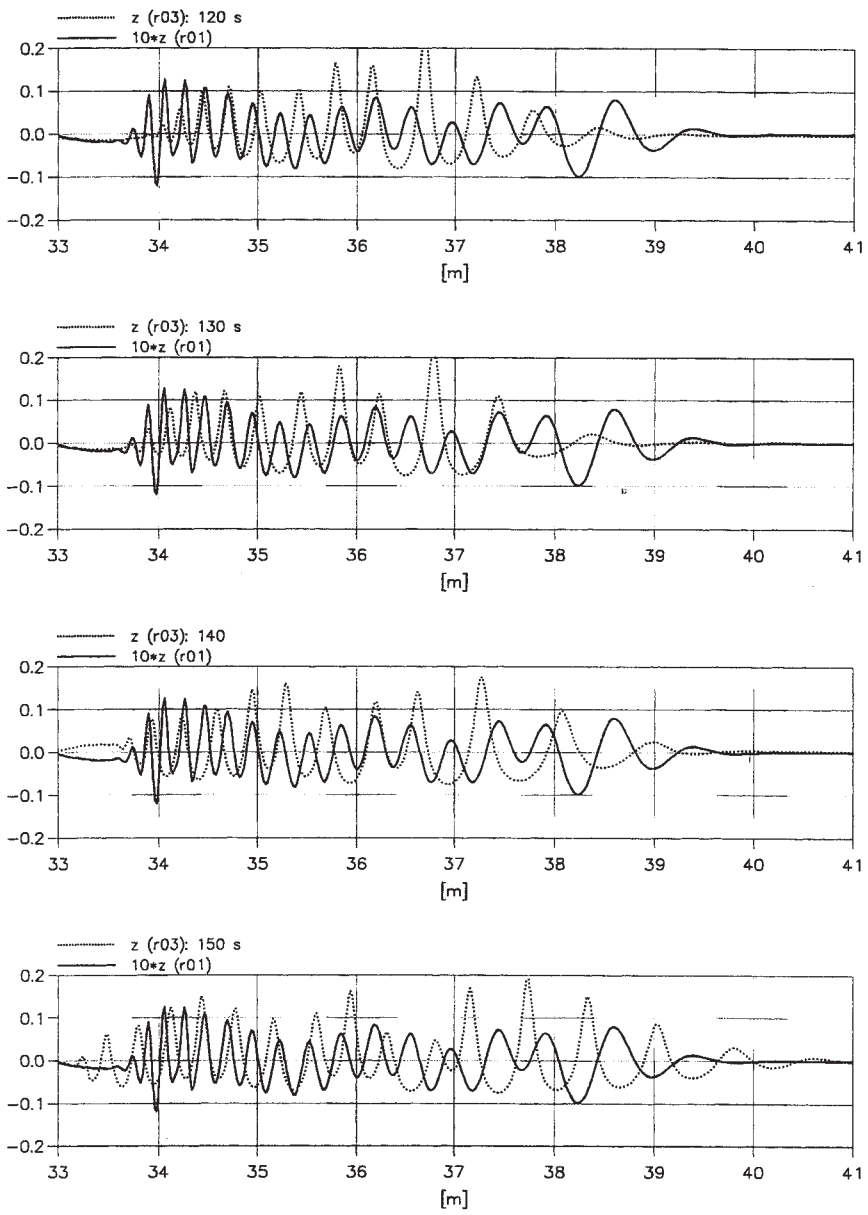

Figure 7: Surface elevation of waves encountering an opposing current. $T = 2.0$s, $h_0 = 0.8$ m, $h_s = 0.2$m and $Q_0 = -0.136$ m^2/s. Solid line: $H_i = 0.002$m, dashed line: $H_i = 0.02$m. Profiles at instants 40 s, 90 s, 100 s, 110 s, 120 s, 130 s, 140 s, 150 s.

AUTHOR INDEX TABLE OF CONTENTS

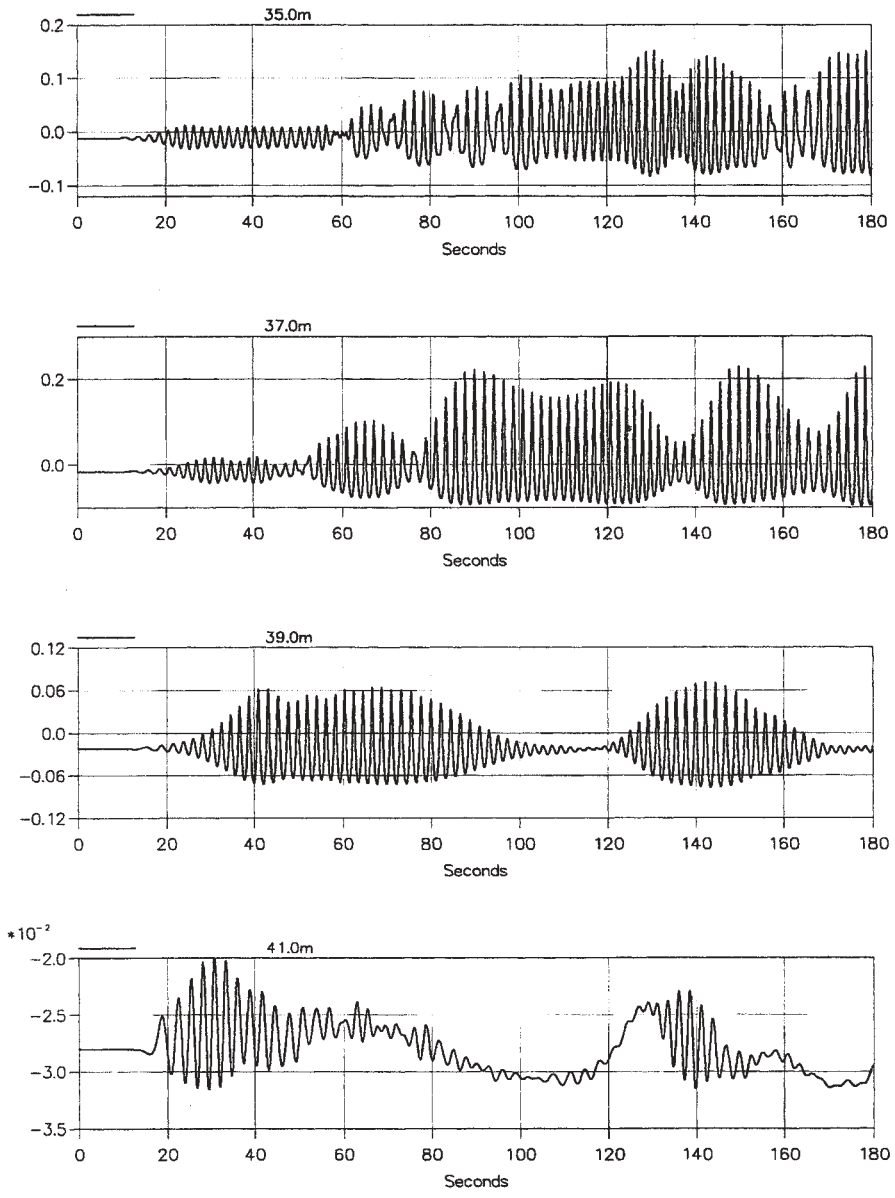

Figure 8: Time-series of surface elevation at a few points. $T = 2.0$s, $h_0 = 0.8$ m, $h_s = 0.2$m and $Q = -0.136$ m^2/s. $H_i = 0.02$ m.

AUTHOR INDEX TABLE OF CONTENTS

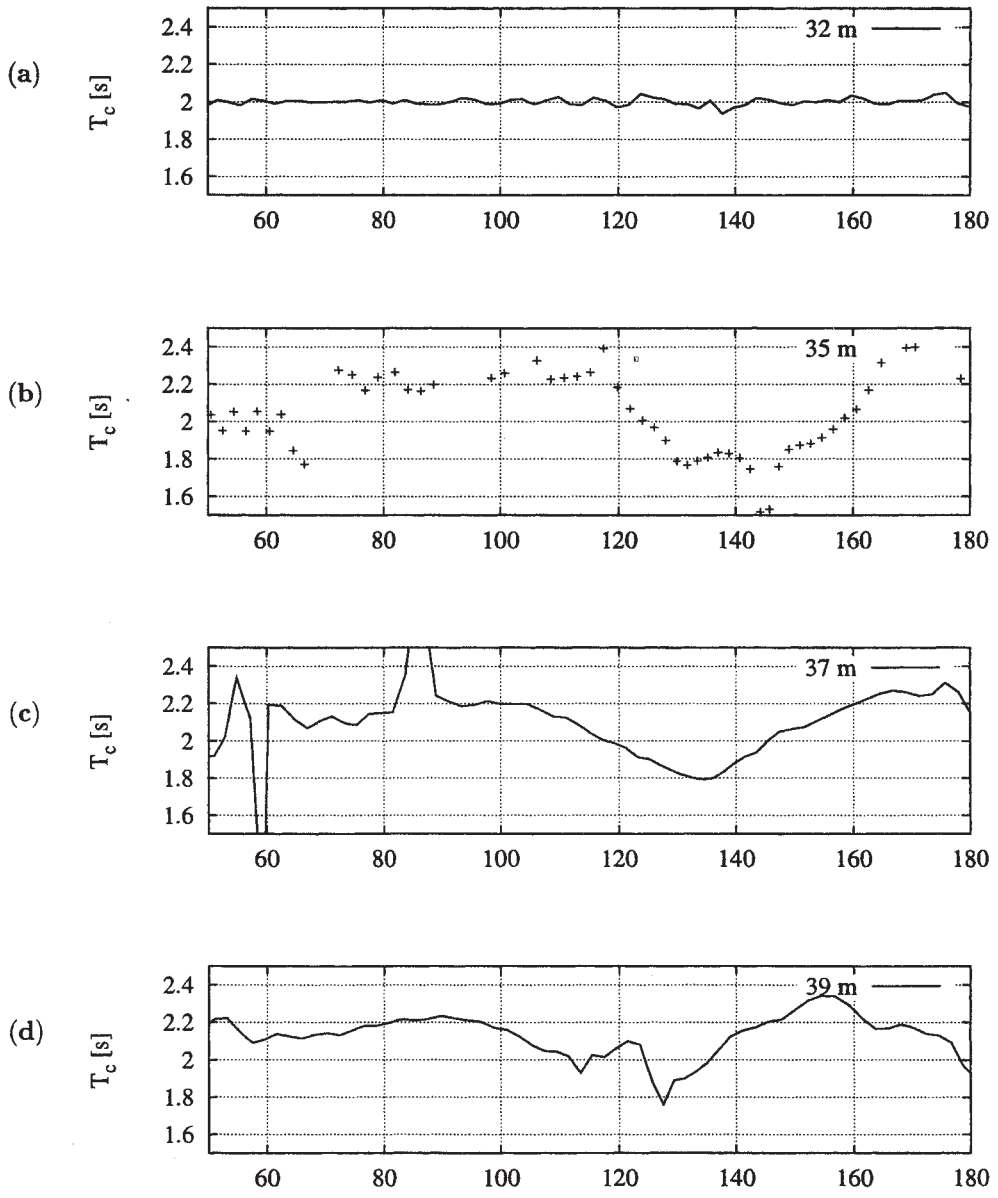

Figure 9: Wave period computed from time separation between successive crests.$T = 2.0$s, $h_0 = 0.8$ m, $h_s = 0.2$m and $Q = -0.136$ m^2/s. $H_i = 0.02$ m.

AUTHOR INDEX TABLE OF CONTENTS

mance with the linear theory. Features associated with this case are identical to the results for the small wave height against the more adverse current of $Q_0 = -0.136$ m^2/s discussed in the previous section. With increase in wave height, however, transmission of energy beyond the blocking point is clearly evident. Secondly, the ratio of the transmitted amplitude to the incident amplitude is seen to be much higher for $H_i = 0.02$ m than for $H_i = 0.01$ m. This indicates that the underlying mechanism is nonlinearly dependent on the wave height.

4 SUMMARY & CONCLUSION

Time-domain computations using a higher-order Boussinesq model have been used to investigate blocking of waves against an adverse current over a varying depth. The features of wave-blocking embedded in the equations used are first put in perspective with the action balance principle and an analytical expression based on deep-water linear theory (*e.g.*, Shyu and Phillips, 1990) through a numerical example of very small waves. In this example, complete blocking of the waves takes place due to a strong adverse current. Marked differences from the 'linear-theory' behavior are found to occur with increase in wave height. Among the noticeable features, for the strong current barrier ($Q_0 = -0.136$ m^2/s) the leading edge exhibits an oscillating blocking point, the period of oscillation being much longer than the wave period. Long-wave undulations of smaller amplitude are observed upstream of the blocking point. For the milder barrier of $Q = -0.120$ m^{2}m/s significant transmission of the short waves are observed. Analysis shows that in both cases the wave period around the 'blocking point' changes from the period of the specified incident waves. This observation is based on wave period defined by the time-separation between two successive crests in the time-record of surface elevation at a given location.

Frequency down-shift of monochromatic and irregular waves in the presence of an adverse current has been observed from experimental measurements by Lai *et al.* (1989), Smith *et al.* (1997) and Chawla and Kirby (1998). Chawla and Kirby (1998) have also given experimental evidence of wave transmission beyond the blocking point. Further, they hypothesize and establish to some extent that side-band instability is a mechanism behind the observed frequency down-shift and transmission of waves beyond the blocking point. From Gerber (1987), one may conclude that the side-band (Benjamin-Feir) instability criteria are essentially the same in the presence of a current if one uses the local wave number and amplitude (which are influenced by the current gradient). Thus in deep and intermediate water condition (as for the experiments of Lai *et al.*, 1989 and Chawla and Kirby, 1998) side-band instability may be a possible mechanism. The nonlinear equations used in the present work include cubic terms and may incorporate side-band instability. However, no formal analysis of the equations has been done as yet in this regard. For the numerical examples presented here, local kh of the incident waves is lower than 1.33 for most part of the propagation reaching to only 1.7 (for the stronger current) at the blocking. Thus, side-band instability being a dominant factor behind the nonlinear features observed in the present examples is questionable. On the other hand, there is evidence in the numerical data that a weak long wave is generated. It is our hypothesis that the underlying ambient current is modulated by a wave-induced current. In shallower water, the wave-induced current gets stronger. Our present analysis is lacking at this stage to set any further claim to this hypothesis.

Wave-breaking, bottom friction and surface dissipation of very short waves have not been accounted for in the present computations. For wave heights of practical importance, breaking is likely to play a role. First, breaking may reduce the nonlinearity and hence the intensity of the mechanisms causing transmission of the waves. Secondly, as in experiments without an ambient current (Melville, 1982; Tulin and Waseda, 1999) breaking may be expected to be a factor behind frequency down-shift.

REFERENCES

Bretherton, F.P. & C.J.R. Garrett (1969). Wavetrains in inhomogenous moving media, *Proc. Roy. Soc. A*, 302: 529.

Chawla, A. & J.T. Kirby (1998). Experimental study of wave breaking and blocking on

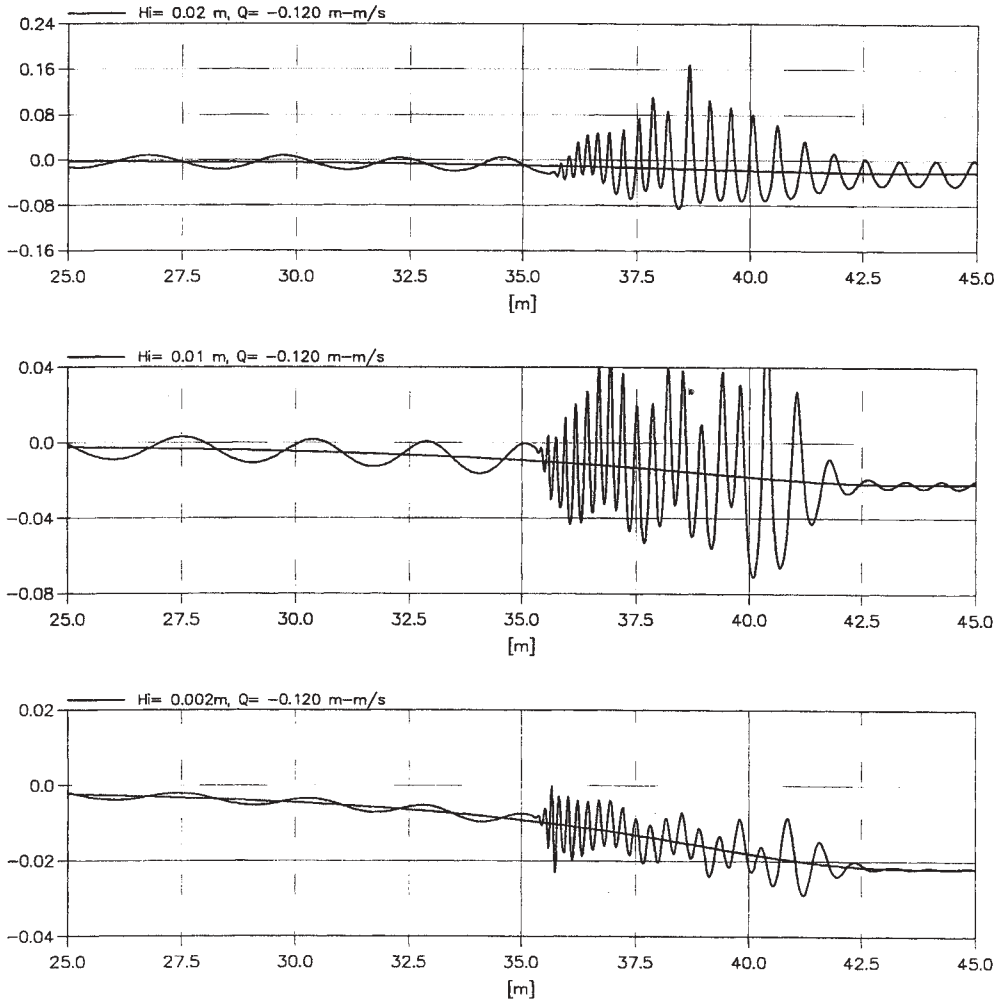

Figure 10: Instantaneous profiles of waves encountering an opposing current. $H = 0.002$m, 0.01 m and 0.02 m. $T = 2.0$s, $h_0 = 0.8$ m, $h_s = 0.2$m and $Q = -0.120$ m^2/s.

AUTHOR INDEX TABLE OF CONTENTS

opposing currents, *Proc. 26th Conf. Coastal Engg.*, Copehagen.

Dommermuth, D.G. and E.A. Novikov (1993). Direct-numerical and large-eddy simulations of turbulent free-surface flows, *Sixth Int. Conference on Numerical Ship Hydrodynamics*, Iowa City.

Gerber, M (1987). The Benjamin-Feir instability of a deep-water Stokes wavepacket in the presence of a non-uniform medium, *J. Fluid Mech.*, (176): 311-332.

Lai, R.J., S.R. Long & N.E. Huang (1989). Laboratory studies of wave-current interaction: kinematics of the strong interaction, *J. Geophysical Research*, 94:16201-16214.

Longuet-Higgins, M.S. & R.W. Stewart (1961). The Changes in amplitude of short gravity waves on steady non-uniform currents, *J. Fluid Mech.*, (10): 529-549.

Madsen, P. & H.A. Schäffer(1998). Higher-order Boussinesq-type equations for surface gravity waves - derivation and analysis, *Phil. Trans. of the Royal Society*, series A, 356: 3123-3184.

Melville, W.K. (1982). The instability and breaking of deep-water waves, *J. Fluid Mech.*, (115): 165-185.

Otta, A.K. & H.A. Schäffer(1999). Finite-amplitude analysis of some Boussinesq-type equations, *Coastal Engineering*, 36: 323-341.

Shyu, J & O.M. Phillips (1990). The blockage of gravity and capillary waves by longer waves and currens, *J. Fluid Mech.*, (217): 115-141.

Smith, J.M., D.T. Resio & C.L. Vincent (1997). Current-induced breaking at an idealized inlet, *Proc. of Coastal Dynamics' 97*, edited by E. Thornton, 993-1002.

Smith, R. (1975). The reflection of short gravity waves on a non-uniform current, *Math. Proc. Camb. Phil. Soc.*, (78): 517-525.

Stiassnie, M. & S. Dagan (1979). Partial reflexion of water waves by non-uniform adverse currents, *J. Fluid Mech.*, (92): 119-129.

Trulsen, K. & C.C. Mei (1993). Double reflection of capillary/gravity waves by a non-uniform current: a boundary-layer theory, *J. Fluid Mech.*, (251): 239-271.

Tulin, M.P. and Waseda, T. (1999). Laboratory observations of wave group evolution, including breaking effects, *J. Fluid Mech.*, (378): 197-232.

IMPROVED METHOD FOR OBTAINING THE INTEGRATION SPACE FOR THE COMPUTATION OF NONLINEAR QUADRUPLET WAVE-WAVE INTERACTIONS

Gerbrant van Vledder

Alkyon Hydraulic Consultancy & Research
P.O. Box 248, 8300 AE Emmeloord, The Netherlands

1. INTRODUCTION

Non-linear quadruplet wave-wave interactions play an important role in the evolution of wind waves (Young and Van Vledder, 1993). Although an accurate integral description of these interactions exists for more than 28 years (Hasselmann 1962, see also Zakharov, 1998), the computation thereof is hampered by the complexity of its functional form and its computational demands.

The basic equation describing these interactions is known as the Boltzmann integral or kinetic equation. Various methods have been developed to approximate the Boltzmann integral, such as narrow peak approximations (e.g., Fox, 1976) and parametric schemes (e.g. Barnett, 1968, Young 1988). These methods, however, failed since they have an insufficient number of degrees of freedom to represent all components in a discrete wave spectrum. This shortcoming was solved in 1985 by the introduction of the Discrete Interaction Approximation (DIA) by Hasselmann et al. (1985). This enabled the development of third generation wave prediction models like the WAM model (WAMDIG, 1988) and the SWAN model (Booij et al., 1999).

The DIA, however, has some shortcomings which hamper the further development of third generation wave prediction models. A number of known shortcomings are:

- A comparison with exact method fails for many types of spectra;
- spectral width too large, i.e. in comparison with measurements (Forristall and Ewans, 1998) and compared to exact computations;
- the DIA produces too much transfer towards higher frequencies, requiring limiters in numerical integration methods .
- the present implementation uses a crude depth scaling in finite depth.

Still, the DIA contributed significantly to the development of third-generation wave prediction models.

By providing an accurate and fast method for computing the nonlinear quadruplet wave-wave interactions, wave evolution characteristics will improve and more attention can be given to the development of the other source terms.

To improve the situation various approaches are being explored by various research groups. Four of these approaches are mentioned here. The first approach is to speed up the computation of the 'exact' solution for computing the Boltzmann integral. The second approach is based on extending the DIA with more basic quadruplet wave-wave configurations. The third method is the application of a diffusion operator (Pushkarev and Zakharov, 2000), and the fourth method is based on a neural network approach which is 'trained' by results of exact computations (Krasnopolsky and Tolman, 2000).

In this paper some developments are presented of the first method. To that end the solution technique of Webb, Resio and Tracy (WRT), as described by Resio and Perrie (1991), is used for solving the Boltzmann equation. A key element in the WRT method is the repeated solution of a closed line integral in wave number space. In this paper attention is given to an explicit method for computing the closed lines or loci in deep and finite depth water.

2. THE WEBB-RESIO-TRACY TECHNIQUE FOR SOLVING THE BOLTZMANN INTEGRAL

The Boltzmann integral describes the rate of change of action density of a particular wave number due to resonant interactions between pairs of 4 wave numbers. To interact these wave numbers must satisfy the following conditions:

$$\vec{k}_1 + \vec{k}_2 = \vec{k}_3 + \vec{k}_4 \qquad (1)$$

$$\omega_1 + \omega_2 = \omega_3 + \omega_4 \qquad (2)$$

in which ω_j the radian frequency and $\vec{k}_j$ the wave number. The frequency and the wave number are related by the dispersion relation $\omega^2 = gk\tanh(kd)$, where g is the gravitational acceleration and d the water depth. The rate of change of action density n_1 at wave number $\vec{k}_1$ due to all quadruplet interactions involving $\vec{k}_1$ is given by:

$$\frac{\partial n_1}{\partial t} = \iiint G\left(\vec{k}_1,\vec{k}_2,\vec{k}_3,\vec{k}_4\right)\times\delta\left(\vec{k}_1+\vec{k}_2-\vec{k}_3-\vec{k}_4\right) \times\delta\left(\omega_1+\omega_2-\omega_3-\omega_4\right) \times\left[n_1n_3\left(n_4-n_2\right)+n_2n_4\left(n_3-n_1\right)\right]d\vec{k}_2d\vec{k}_3d\vec{k}_4 \qquad (3)$$

The term G is a complicated coupling coefficients for which expressions have been given by Herterich and Hasselmann (1980) and Zakharov (1998).

In the method of Webb-Resio-Tracy a number of transformations are made to remove the delta functions. A key element in the WRT method is to consider the integration space for each ($\vec{k}_1,\vec{k}_3$) combination:

$$\frac{\partial n_1}{\partial t} = \int d\vec{k}_3 T\left(\vec{k}_1,\vec{k}_3\right) \qquad (4)$$

in which the function T is given by:

$$T(\vec{k}_1,\vec{k}_3) = 2\iint d\vec{k}_2d\vec{k}_4G\left(\vec{k}_1,\vec{k}_2,\vec{k}_3,\vec{k}_4\right)\delta(\vec{k}_1+\vec{k}_2-\vec{k}_3-\vec{k}_4) \times\delta\left(\omega_1,\omega_2,\omega_3,\omega_4\right)\cdot\theta\left(\left|\vec{k}_1-\vec{k}_4\right|-\left|\vec{k}_1-\vec{k}_3\right|\right) \times\left[n_1n_3\left(n_4-n_2\right)+n_2n_4\left(n_3-n_1\right)\right] \qquad (5)$$

in which:

$$\theta(x) = \begin{cases} 1 & \text{if} \quad x>0 \\ 0 & \text{if} \quad x<0 \end{cases} \qquad (6)$$

and

$$x = \left|\vec{k}_1-\vec{k}_4\right|-\left|\vec{k}_1-\vec{k}_3\right| \qquad (7)$$

The $\theta(x)$ function determines a section of the integral which is not defined due to the assumption that $\vec{k}_1$ is closer to $\vec{k}_3$ than $\vec{k}_2$.

The crux of the Webb consists of using a local coordinate system (n, s) along the locus.

To that end the (k_{2x},k_{2y}) coordinate system is replaced by a $(\vec{s},\vec{n})$ coordinate system along the locus. After some transformations the transfer integral can then be written as a closed line integral:

$$T\left(\vec{k}_1,\vec{k}_3\right) = \tilde{N}G\left|\frac{\partial W\left(\vec{s},\vec{n}\right)}{\partial n}\right|^{-1}\theta\left(\vec{k}_1,\vec{k}_3,\vec{k}_4\right) \times\left[n_1n_3\left(n_4-n_2\right)+n_2n_4\left(n_3-n_1\right)\right]d\vec{s} \qquad (8)$$

In which G is the coupling coefficient and $|\partial W/\partial n|^{-1}$ the inverse of the gradient term. The latter term can be rewritten in term of the x- and y-components of the wave number k_2:

$$\left|\frac{\partial W\left(\vec{s},\vec{n}\right)}{\partial n}\right|^{-1} = \left|\nabla W\left(k_{2x},k_{2y}\right)\right|^{-1} \qquad (9)$$

The delta functions in Eq. (5) determine a region in wave number space along the integration should be carried out. For a given ($\vec{k}_1,\vec{k}_3$) wave number combination the resonance condition for the radian frequencies can be written as:

$$W\left(\vec{k}_2\right) = 0 = \omega_1+\omega\left(\vec{k}_2\right)-\omega_3-\omega\left(\vec{k}_1+\vec{k}_2-\vec{k}_3\right) \qquad (10)$$

Following Tracy and Resio (1982) the variables Q and $\vec{P}$ are introduced:

$$Q = \omega_1-\omega_3 \qquad (11)$$

$$\vec{P} = \vec{k}_1-\vec{k}_3 \qquad (12)$$

Then the wave number $\vec{k}_4$ can be written as :

$$\vec{k}_4 = \vec{k}_1-\vec{k}_3+\vec{k}_2 = \vec{P}+\vec{k}_2 \qquad (13)$$

The locus equation is obtained in terms of the wave number $\vec{k}_2$ by solving the so-named locus equation:

$$W\left(\vec{k}_2,d\right) = Q+\Omega\left(\vec{k}_2,d\right)-\Omega\left(\vec{P}+\vec{k}_2,d\right) = 0 \qquad (14)$$

in which $\omega_j = \Omega\left(\vec{k}_j,d\right)$ is the general expression for the dispersion relation. In finite depth $\Omega\left(\vec{k},d\right)$ is given by the linear dispersion relation:

$$\omega^2 = gk\tanh(kd) \tag{15}$$

The solution of Eq. (14) results in an egg-shaped contour for all possible $\vec{k}_2$ wave numbers in wave number space. Using the resonance conditions, all possible $\vec{k}_4$ wave numbers can be found by a simple translation formation over the vector $\vec{P}$:

$$\vec{k}_4 = \vec{k}_2 + \vec{P} \tag{16}$$

An example of a locus for $\vec{k}_2$ and $\vec{k}_4$ is given in Figure 1.

In the following section expressions are given for computing the gradient term for deep and finite depth water.

3. THE GRADIENT TERM

The gradient term $\left|\nabla W\left(k_{2x}, k_{2y}\right)\right|$ can be expressed as:

$$|\nabla W| = \left|\left(\frac{\partial W}{\partial x}\right)^2 + \left(\frac{\partial W}{\partial y}\right)^2\right|^{1/2} \tag{17}$$

For finite depth the gradient term can be computed as follows. First we have:

$$\frac{\partial W}{\partial x} = \frac{\partial}{\partial x}\Omega\left(\vec{k}_2, d\right) - \frac{\partial}{\partial x}\Omega\left(\vec{k}_2 + \vec{P}, d\right) \tag{18}$$

$$\frac{\partial W}{\partial y} = \frac{\partial}{\partial y}\Omega\left(\vec{k}_2, d\right) - \frac{\partial}{\partial y}\Omega\left(\vec{k}_2 + \vec{P}, d\right) \tag{19}$$

in which

$$\frac{\partial\Omega\left(\vec{k}_2, d\right)}{\partial x} = \frac{\sqrt{g}}{2\Omega\left(\vec{k}_2, d\right)}\frac{k_{2x}}{k_2}\left[\tanh\left(k_2 d\right) + \frac{k_2 d}{\cosh^2\left(k_2 d\right)}\right] \tag{20}$$

$$\frac{\partial\Omega\left(\vec{k}_2, d\right)}{\partial y} = \frac{\sqrt{g}}{2\Omega\left(\vec{k}_2, d\right)}\frac{k_{2y}}{k_2}\left[\tanh\left(k_2 d\right) + \frac{k_2 d}{\cosh^2\left(k_2 d\right)}\right] \tag{21}$$

$$\frac{\partial\Omega\left(\vec{k}_2 + \vec{P}, d\right)}{\partial x} = \frac{\sqrt{g}}{2\Omega\left(\vec{k}_2 + \vec{P}, d\right)}\frac{k_{2x} + P_x}{\left|\vec{k}_2 + \vec{P}\right|} \times\left[\tanh\left(\left|\vec{k}_2 + \vec{P}\right| d\right) + \frac{\left|\vec{k}_2 + \vec{P}\right| d}{\cosh^2\left(\left|\vec{k}_2 + \vec{P}\right| d\right)}\right] \tag{22}$$

$$\frac{\partial\Omega\left(\vec{k}_2 + \vec{P}, d\right)}{\partial y} = \frac{\sqrt{g}}{2\Omega\left(\vec{k}_2 + \vec{P}, d\right)}\frac{k_{2y} + P_y}{\left|\vec{k}_2 + \vec{P}\right|} \times\left[\tanh\left(\left|\vec{k}_2 + \vec{P}\right| d\right) + \frac{\left|\vec{k}_2 + \vec{P}\right| d}{\cosh^2\left(\left|\vec{k}_2 + \vec{P}\right| d\right)}\right] \tag{23}$$

For deep water $\tanh \to 1$ and $\cosh \to \infty$ the above equations reduce to:

$$\frac{\partial\Omega\left(\vec{k}_2\right)}{\partial x} = \frac{\sqrt{g}k_{2x}}{2k_2^{3/2}} \tag{24}$$

$$\frac{\partial\Omega\left(\vec{k}_2\right)}{\partial y} = \frac{\sqrt{g}k_{2y}}{2k_2^{3/2}} \tag{25}$$

$$\frac{\partial\Omega\left(\vec{k}_2 + \vec{P}\right)}{\partial x} = \frac{\sqrt{g}\left(k_{2x} + P_x\right)}{2\left|\vec{k}_2 + \vec{P}\right|^{3/2}} = \frac{\sqrt{g}k_{4x}}{2k_4^{3/2}} \tag{26}$$

$$\frac{\partial\Omega\left(\vec{k}_2 + \vec{P}\right)}{\partial y} = \frac{\sqrt{g}\left(k_{2y} + P_y\right)}{2\left|\vec{k}_2 + \vec{P}\right|^{3/2}} = \frac{\sqrt{g}k_{4y}}{2k_4^{3/2}} \tag{27}$$

The same result was also obtained by Tracy and Resio (1982) by application of the chain rule for differentiation, except for the factor $\sqrt{g}$ which they left out in their equation.

4. CHARACTERISTICS OF THE LOCUS

In this section a number of characteristics of the locus equation are presented. For given values of the wave numbers $\vec{k}_1$ and $\vec{k}_3$ the locus function $W\left(\vec{k}_2\right)$ can be considered as 2d function in wave number space. An example of this function is given in Figure 2 in the form of a contour plot. The contour line for z=0 is the locus satisfying the resonance conditions. The symmetry axis is also shown in Figure 2.

Symmetry axis

As can be seen in Figure 2, the locus function $W\left(\vec{k}_2\right)$ has a symmetry axis through the origin and in line with the $\vec{P}$ vector. This is shown mathematically by writing both the wave number $\vec{k}_2$ and difference vector $\vec{P}$ in polar coordinates:

$$\vec{k}_2 = \begin{pmatrix} k_{2x} \\ k_{2y} \end{pmatrix} = k_2 \begin{pmatrix} \cos(\theta) \\ \sin(\theta) \end{pmatrix} \tag{28}$$

and

$$\vec{P} = \begin{pmatrix} P_x \\ P_y \end{pmatrix} = P \begin{pmatrix} \cos(\theta_P) \\ \sin(\theta_P) \end{pmatrix} \tag{29}$$

Substitution of the Eqs. (28) and (29) in the locus equation gives:

$$\begin{aligned} W(k_2,\theta) = Q + \Omega\left(\left| k_2 \begin{pmatrix} \cos(\theta) \\ \sin(\theta) \end{pmatrix} \right|, d \right) \\ -\Omega\left(\left| P \begin{pmatrix} \cos(\theta_P) \\ \sin(\theta_P) \end{pmatrix} + k_2 \begin{pmatrix} \cos(\theta) \\ \sin(\theta) \end{pmatrix} \right|, d \right) \end{aligned} \tag{30}$$

Elaboration of this expression and collecting the squared cosine and sine terms gives:

$$\begin{aligned} W(k_2,\theta) = Q + \Omega(k_2, d) \\ -\Omega\left(\left| P^2 + k_2^2 + 2P\cos(\theta_P - \theta) \right|^{1/2}, d \right) \end{aligned} \tag{31}$$

Since $\cos(\theta) = \cos(-\theta)$ it is evident from Eq.(31) that the locus function is symmetric around the line with angle θ_P. It is noted here that expression (31) gives an explicit relation for the angle θ for a given value of the wave number k_2. This property will be used below to compute the trajectory of the locus in wave number space.

Other characteristics of the locus equation are determined along the symmetry axis. The variation of the locus function along the symmetry axis is shown in Figure 3. Below a number of characteristics of the locus function along this line are given.

Maximum

The maximum value of the locus function occurs at a point on the symmetry axis where $\vec{k}_2 = -\vec{P}$.

Substitution of this value into the locus equation gives:

$$W_{max} = W\left(-\vec{P}\right) = Q + \Omega\left(\left|\vec{P}\right|\right) \tag{32}$$

The minimum value of the locus function occurs at the origin where $\vec{k}_2 = 0$, yielding:

$$W_{min} = W(0) = Q - \Omega\left(\left|\vec{P}\right|\right) \tag{33}$$

The position of the maximum is indicated in Figure 3 with the symbol k_p

Limiting value

The limiting value W_{lim} for $\vec{k}_2 \to \infty$ or $\vec{k}_2 \to -\infty$ of the locus equation is

$$W_{lim} = Q \tag{34}$$

The limiting value is indicated in Figure 3 with a dashed line.

Zero crossings for deep water

Two other points of interest are the points where the locus crosses the symmetry axis. For deep water analytic expressions can be found for these points by considering the variation of the wave number k_2 along the symmetry axis. For deep water the locus equation can be rewritten as (dividing by the common factor $\sqrt{g}$):

$$q + k_2^{1/2} - \left(\left|\vec{P} + \vec{k}_2\right|\right)^{1/2} = 0 \tag{35}$$

in which

$$q = k_1^{1/2} - k_3^{1/2} \tag{36}$$

For the case that that $\left|\vec{k}_3\right| > \left|\vec{k}_1\right|$ we have $q < 0$ and the vectors $\vec{P}$ and $\vec{k}_2$ are co-linear but with opposite directions. This implies that Eq. (35) can be written as:

$$q + k_2^{1/2} = \left|P - k_2\right|^{1/2} \tag{37}$$

This equation can be rewritten as:

$$q^2 + 2qk_2^{1/2} + k_2 = \pm(P - k_2) \tag{38}$$

This equation has two solutions for the wave number magnitude k_2. The first solution is found for:

$$q^2 + 2qk_2^{1/2} + k_2 = -P + k_2 \tag{39}$$

yielding:

$$k_B^{q<0} = \left(\frac{-P - q^2}{2q} \right)^2 \tag{40}$$

The second solution follows from:

$$q^2 + 2qk_2^{1/2} + k_2 = P - k_2 \tag{41}$$

which can be rewritten as

$$2k_2 + 2qk_2^{1/2} + q^2 - P = 0 \tag{42}$$

This equation is quadratic in $k_2^{1/2}$, and it has the following valid solution:

$$k_A^{q<0} = \left(\frac{-q + \sqrt{2P - q^2}}{2} \right) \tag{43}$$

Similar expressions can be found for the case that $q > 0$. The zero-crossing points are indicated in Figure 3 with circles.

Zero crossings for finite depth water

For finite depth, no explicit expressions can be derived to compute the points where the locus crosses the symmetry axis. In that case an iterative zero-crossing method has to be applied to find these points.

5. METHODS FOR TRACING THE LOCUS

In this Section two methods are described for determining the trajectory of the locus in wave number space. Since the trajectory of a locus is used as the path of integration for the determination of a contribution to the nonlinear transfer, it is desirable to have control of the number of points and spacing of the discrete points on a locus. The number of points on a locus affects the accuracy of the line integral over the locus, and the spacing of the points may be important for certain types of integration techniques of the line integral.

Radial solution from point in locus

Resio and Tracy (1982) introduced a radial solution technique to compute the position of the locus in wave number space. To that end they choose a point inside the locus and point rays radially outwards at equidistant angles. Next, they compute iteratively the crossing point of such a line with the locus, defined as the point on this line where the locus function is zero. In this way the position locus can be estimated at a pre-set number of points. Since for deep water the locus is symmetric, only half the points need to be computed, followed by mirror imaging of these points.

Mathematically, this procedure can be written as follows. For a given point $\vec{k}_0$ inside the locus all points on a ray at an angle θ can be written as:

$$\vec{k}_2 = \vec{k}_0 + \lambda \begin{pmatrix} \cos(\theta) \\ \sin(\theta) \end{pmatrix} \tag{44}$$

Substitution of Eq.(44) into the general locus equation gives:

$$W\left(\vec{k}_2, d; \lambda, \theta\right) = Q + \\ +\Omega\left(\left[\left(k_{0x} + \lambda\cos(\theta)\right)^2 + \left(k_{0y} + \lambda\sin(\theta)\right)^2 \right]^{1/2}, d \right) + \\ -\Omega\left(\begin{bmatrix} \left(\{k_{0x} + P_x\} + \lambda\cos(\theta)\right)^2 + \\ \left(\{k_{0y} + P_y\} + \lambda\sin(\theta)\right)^2 \end{bmatrix}^{1/2}, d \right) = 0 \tag{45}$$

using $\vec{s} = \begin{pmatrix} \cos(\theta) \\ \sin(\theta) \end{pmatrix}$ Eq.(45) can be written as:

$$W\left(\vec{k}_2, d; \lambda, \theta\right) = Q + \Omega\left(\left[k_0^2 + \lambda^2 + 2\lambda \vec{k}_0 \vec{s} \right]^{1/2}, d \right) + \\ -\Omega\left(\left[k_0^2 + P^2 + 2\vec{k}_0 \vec{P} + \lambda^2 + 2\lambda\left(\vec{k}_0 + \vec{P}\right)\vec{s} \right]^{1/2}, d \right) = 0 \tag{46}$$

For deep water, Resio and Tracy use the point $\vec{k}_m$ located halfway the minimum and maximum wave number on the symmetry axis. For finite depth, they use the point $\vec{k}_P = -\vec{P}$, at the peak value of the locus function. The results of both methods are illustrated in the Figures 4 and 5. Taking the origin in the middle of the locus generally results in more uniformly distributed points.

For finite depth, the locus becomes flattened and the radial method becomes inaccurate, especially when the peak value is chosen as the origin. This is illustrated in the Figures 6 and 7 for both methods of choosing the origin. As can be seen in these figures the step size between the points on the locus is not constant, but varies with position along the locus.

Polar solution from origin

For deep water an explicit solution to the locus equation can be found by using polar coordinates. The first step is to write both the wave number $\underset{\sim}{k}_2$ and the vector $\underset{\sim}{P}$ in polar co-ordinates:

$$\underset{\sim}{k}_2 = \begin{pmatrix} k_{2x} \\ k_{2y} \end{pmatrix} = k_2 \begin{pmatrix} \cos(\theta) \\ \sin(\theta) \end{pmatrix} \tag{47}$$

and

$$\underset{\sim}{P} = \begin{pmatrix} P_x \\ P_y \end{pmatrix} = P \begin{pmatrix} \cos(\theta_p) \\ \sin(\theta_p) \end{pmatrix} \tag{48}$$

Substitution of the expressions (47) and (48) into the locus equation gives

$$\begin{aligned} W(k_2,\theta) = q + k_2^{1/2} - \Big(\big(k_2\cos(\theta) + P\cos(\theta_p)\big)^2 + \\ + \big(k_2\sin(\theta) + P\sin(\theta_p)\big)^2 \Big)^{1/4} \\ = 0 \end{aligned} \tag{49}$$

after some algebra this expression reduces to:

$$q + k_2^{1/2} = \left(k_2^2 + P^2 + 2k_2 P\cos(\theta - \theta_p)\right)^{1/4} \tag{50}$$

Isolating the cosine term gives:

$$\cos(\theta - \theta_p) = \frac{\left(q + k_2^{1/2}\right)^4 - k_2^2 - P^2}{2k_2 P} \tag{51}$$

and solving for θ gives:

$$\theta = \theta_p \pm \operatorname{acos}\left(\frac{\left(q + k_2^{1/2}\right)^4 - k_2^2 - P^2}{2k_2 P} \right) \tag{52}$$

Finally, the angle θ in Eq. (52) is substituted in Eq. (47) to obtain the wave number vector $\underset{\sim}{k}_2$.

Thus, by varying the wave number magnitude k_2 between the minimum and maximum value, all points on the locus can be found by an explicit expression. For finite depth the locus equation can be rewritten as:

$$\begin{aligned} W(k_2,\theta,d) &= Q + \Omega\left(\underset{\sim}{k}_2, d\right) - \Omega\left(\left|\underset{\sim}{k}_2 + \underset{\sim}{P}\right|\right) \\ &= Q + \sqrt{g k_2 \tanh(k_2 d)} - \sqrt{g k \tanh(k d)} \end{aligned} \tag{53}$$

in which

$$\begin{aligned} k &= \left(\big(k_2\cos(\theta) + P\cos(\theta_p)\big)^2 + \big(k_2\sin(\theta) + P\sin(\theta_p)\big)^2 \right)^{1/2} \\ &= \left(k_2^2 + P^2 + 2k_2 P\cos(\theta - \theta_p)\right)^{1/2} \\ &= k_2(\theta) \end{aligned} \tag{54}$$

Combining the equations (53) and (54) gives:

$$\omega = Q + \sqrt{g k \tanh(k_2 d)} = \sqrt{g k \tanh(k d)} \tag{55}$$

Eq. (55) can be considered as a dispersion relation in which the wave number k must be obtained for the radian frequency ω on the left side of Eq. (55) and the water depth d.

To obtain all the points on the locus, the value of the wave number magnitude k_2 is varied between its minimum and maximum value. For each value of k_2 the corresponding value for k is obtained from Eq. (55) using an iterative procedure or using an explicit method, such as a high order Padé approximation (see Hunt, 1979). Next the angle θ is obtained from Eq.(54). as:

$$\theta = \theta_p \pm \operatorname{acos}\left(\frac{k^2 - k_2^2 - P^2}{2k_2 P} \right) \tag{56}$$

In the last step the points on the locus are retrieved by substituting the angles in Eq. (47). Examples of the polar method are shown in the Figures 8 and 9 for deep water and finite depth water respectively.

Adaptive stepping

In the case the polar method is applied with constant steps along the symmetry axis, the points are not distributed uniformly along the locus. This can clearly be seen in the Figures 8 and 9. To obtain regularly spaced point along the locus an adaptive stepping method is applied.

The distance Δs_i between succeeding two points on the locus with radii k_i and $k_i + \Delta k_i$ and angles θ_i and θ_{i+1} are related via the cosine rule:

$$(\Delta s_i)^2 = k_i^2 + (k_i + \Delta k_i)^2 - 2k_i(k_i + \Delta k_i)\cos(\theta_i - \theta_{i-1}) \quad (57)$$

If a constant spacing ds is required the difference wave number Δk_i and stet Δs_i along the locus for step i can be estimated on the basis of the previous step from Eq. (57). This results in an estimate of the step size :

$$\Delta k_i \approx \Delta k_{i-1} \frac{ds}{\Delta s_i} \quad (58)$$

Applying Eq. (58) a two or three times results in a regular distribution of points on the locus. This is illustrated in Figure 10.

6. DISCUSSION

In this paper an analysis has been method of wave number loci that are used in the WRT technique of computing the nonlinear quadruplet wave-wave interactions. Important characteristic of the wave number locus have been described. These characteristics are used in two methods for the computation of the wave number loci. The first method is a radial method and its requires an iterative process to determine the location of the locus. The second method using polar coordinates to explicitly compute the position of the locus.

Comparison of the two method for finite depth cases yields that the polar method is better suited for finite depth cases.

Application of an explicit method for computing the position of the loci instead of an iterative method gives more accurate results.

To have more control on the spacing of the points along the locus an adaptive methods has been developed to enable an equi-distant spacing of points on the locus.

The spacing of the points is important for certain types of integration techniques of the line integral. For example simple (adaptive) integration techniques require an equi-distant spacing with constant weights. More advanced integration techniques, such as a Gaussian-method require that the points spaced according to some rule with unequal weights.

The impact of such integration techniques on the accuracy and efficiency of the computation of the nonlinear transfer rate has not been explored in this study. These results will be reported elsewhere.

It is noted here that Eq. (52) can also be obtained by geometric considerations for solving the resonance conditions, as described by Khatri and Young (1999).

Acknowledgement

This study was sponsored by the Office of Naval Research under contract N00014-98-C-0009.

7. REFERENCES

Barnett, T.P., 1968: On the generation, dissipation and prediction of ocean wind waves. J. Geophys. Res., Vol. 73, 513-529.

Booij, N., L.H. Holthuijsen and R.C. Ris, 1999: A third-generation wave model for coastal regions. 1. Model description and validation. J. Geophys. Res., Vol. 104, No. C4, 7649-7666.

Forristall, G.Z., and KC. Ewans, 1998: Worldwide measurements of directional wave spreading. Journal of Atmospheric and Oceanic Technology., Vol. 15, 440-469.

Hasselmann, K., 1962: On the non-linear transfer in a gravity wave spectrum, 2, Conservation theory, wave-particle correspondence, irreversibility, J. *Fluid Mechanics*, Vol. 15, No. 385-398.

Hasselmann, S., and K. Hasselmann, 1981: A symmetric method of computing the nonlinear transfer in a gravity wave spectrum, Hamburger. Geophys. Einzelschr., A, 52, 138 pp.

Herterich, K., and K. Hasselmann, 1980: A similarity relation for the nonlinear energy transfer in a finite-depth gravity-wave spectrum. J. Fluid. Mech., Vol. 97, 215-224.

Hasselmann, S., K. Hasselmann, J.H. Allender and T.P. Barnett, 1985: Computations and parameterisations of the nonlinear energy transfer in

a gravity wave spectrum. Part 2: Parameterisations of the nonlinear energy transfer for application in wave models. J. Phys. Oceanogr., Vol. 15, 1378-1391.

Hunt, J.N., 1979: Direct solution of the wave dispersion equation, Journal of the Waterway, Port, Coastal and Ocean Division, ASCE, Vol. 105, No. WW4, 457-459.

Khatri, S.K., and I.R. Young, 1999: A new technique to evaluate nonlinear wave interactions for ocean wave prediction models. Proc. 5th Int. Conf. On Coastal and Port Engineering in Developing Countries. Cape Town, 19-23 April 1999, 159-169.

Krasnopolsky, V. and H.L. Tolman, 2000: personal communication.

Pushkarev, A., and V.E. Zakharov, 1999: personal communication.

Resio, R.T., and W. Perrie, 1991: A numerical study of nonlinear energy fluxes due to wave-wave interactions. Part 1: Methodology and basic results. J. Fluid Mech., Vol. 223, 609-629.

Tracy, B., and D.T. Resio, 1982: Theory and calculation of the nonlinear energy transfer between sea waves in deep water. WES Rep. 11, US Army Engineer Waterways Experiment Station, Vicksburg, MS.

WAMDI group, S. Hasselmann, K. Hasselmann, E. Bauer, L. Bertotti, V.J. Cardone, J.A. Ewing, J.A. Greenwood, A. Guillaume, P.A.E.M. Janssen, G.J. Komen, P. Lionello, M. Reistad and L. Zambresky, 1998: The WAM model – a third generation ocean wave prediction model. J. Phys. Oceanography, Vol. 18, No. 12, 1775-1810.

Webb, D.J., 1978: Non-linear transfers between sea waves. Deep-Sea Research, Vol. 25, 279-298.

Young, I.R., 1988: A shallow water spectral wave model. J. Geophys. Res., Vol. 93, 5113-5129.

Young, I.R., and G.Ph. van Vledder, 1993: The central role of nonlinear wave interactions in wind-wave evolution. Philos. Trans. R. Soc. London, 342, 505-524.

Zakharov, V.E, 1998: Statistical theory of gravity and capillary waves on the surface of the finite-depth fluid. Proc. UITAM symposium (Nice, 1998), special issue of the European Journal Mechanics.

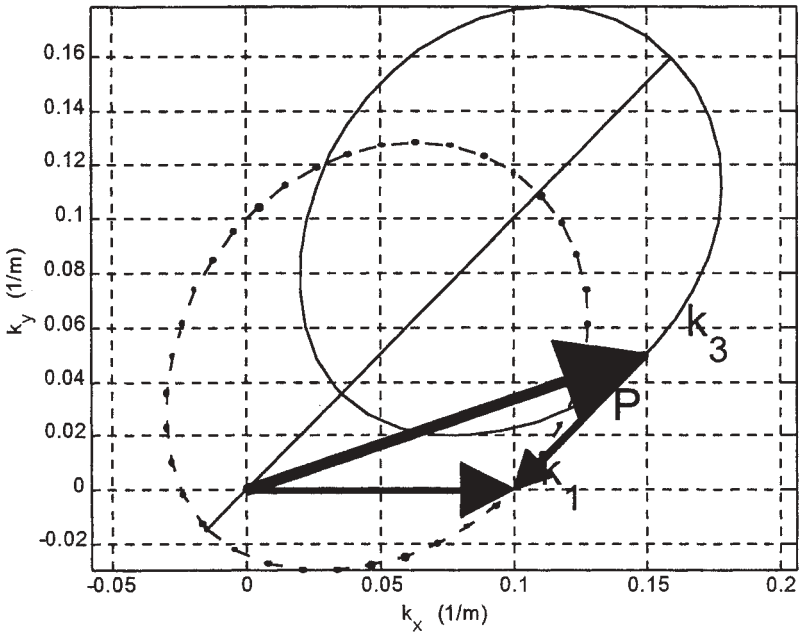

Figure 1. Example of the loci for the wave numbers $\vec{k}_2$ and $\vec{k}_4$ for $\vec{k}_1 = (0.1, 0)$ and $\vec{k}_3 = (0.15, 0.05)$..

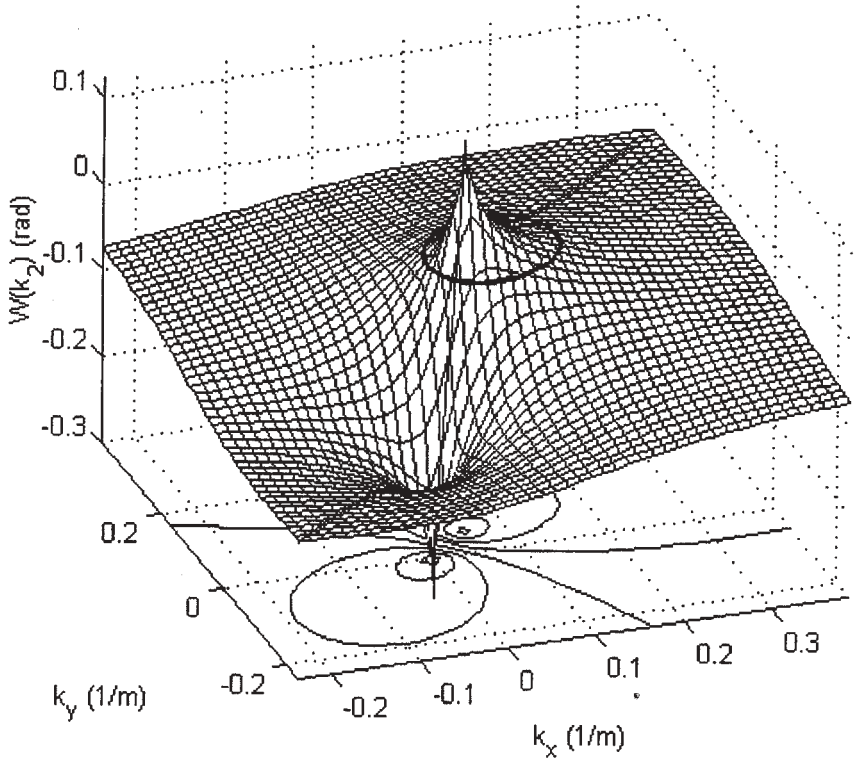

Figure 2. Mesh plot of locus function as a function of the wave number $\vec{k}_2$ for the wave numbers $\vec{k}_2$ and $\vec{k}_4$ for $\vec{k}_1 = (0.1, 0)$ and $\vec{k}_3 = (0.15, 0.05)$.. The locus for $\vec{k}_2$ is shown by the solid line around the peak value. The symmetry axis is shown by the solid line.

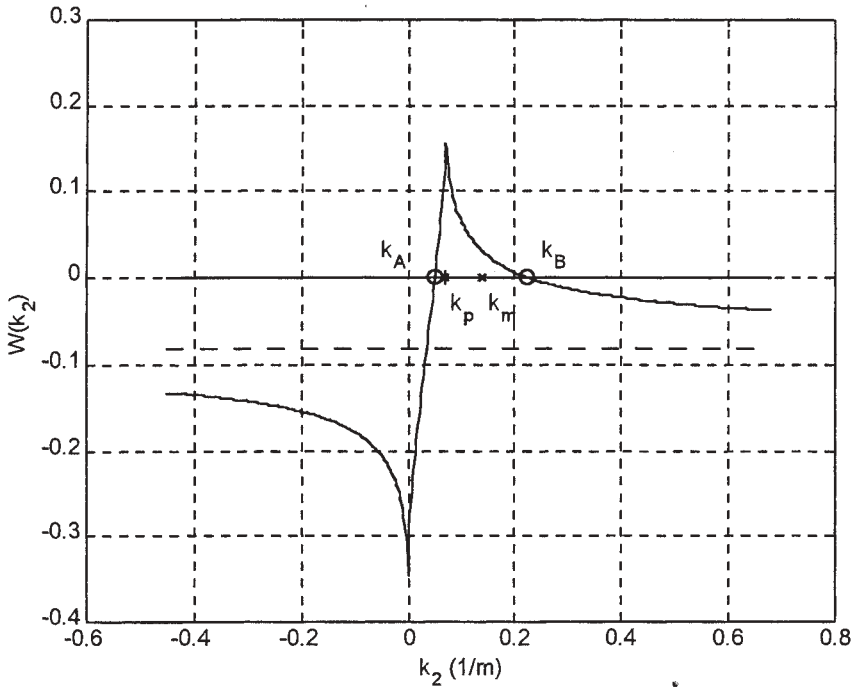

Figure 3. Variation of the locus function as a function of wave number $\vec{k}_2$ along the symmetry axis for $\vec{k}_2$ for the wave numbers $\vec{k}_2$ and $\vec{k}_4$ for $\vec{k}_1 = (0.1, 0)$ and $\vec{k}_3 = (0.15, 0.05)$. The limiting value is indicated with the dashed line.

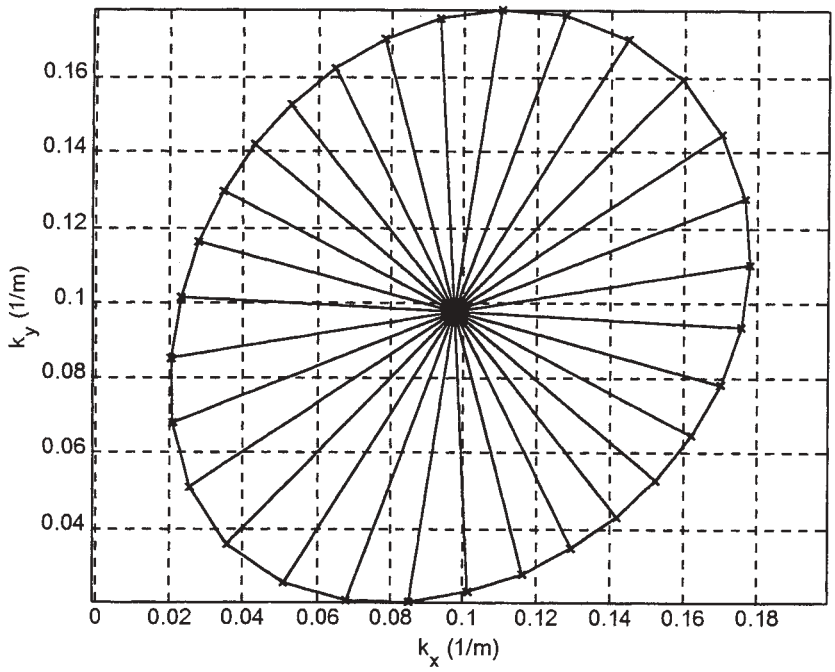

Figure 4: Example of a deep water locus for wave number $\vec{k}_2$ obtained with the radial method by choosing the mid-point k_m as origin for Based on $\vec{k}_1 = (0.1, 0)$ and $\vec{k}_3 = (0.15, 0.05)$. The number of points on the locus is 30.

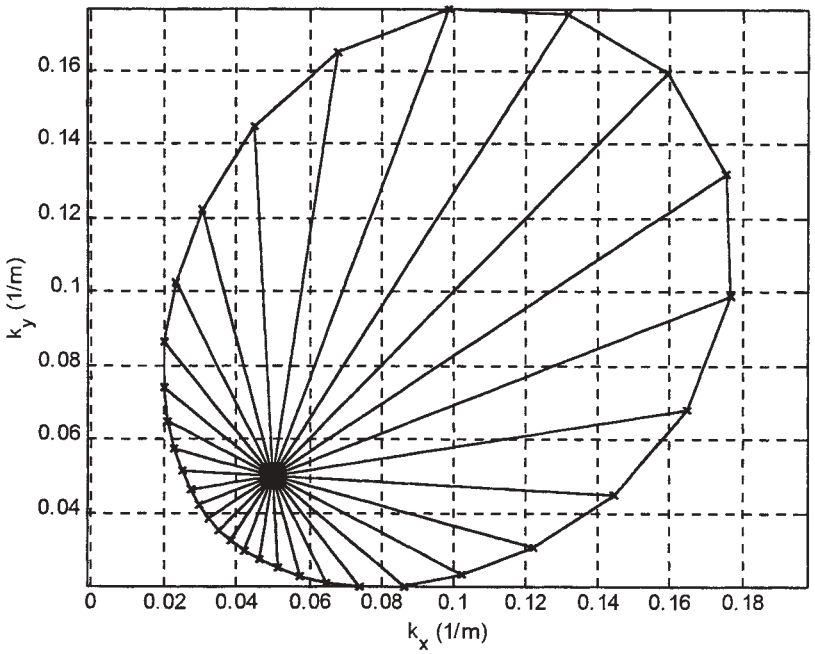

Figure 5: Example of a deep water locus for wave number $\vec{k}_2$ obtained with the radial method by choosing the peak wave number k_p as origin for Based on $\vec{k}_1 = (0.1, 0)$ and $\vec{k}_3 = (0.15, 0.05)$. The number of points on the locus is 30.

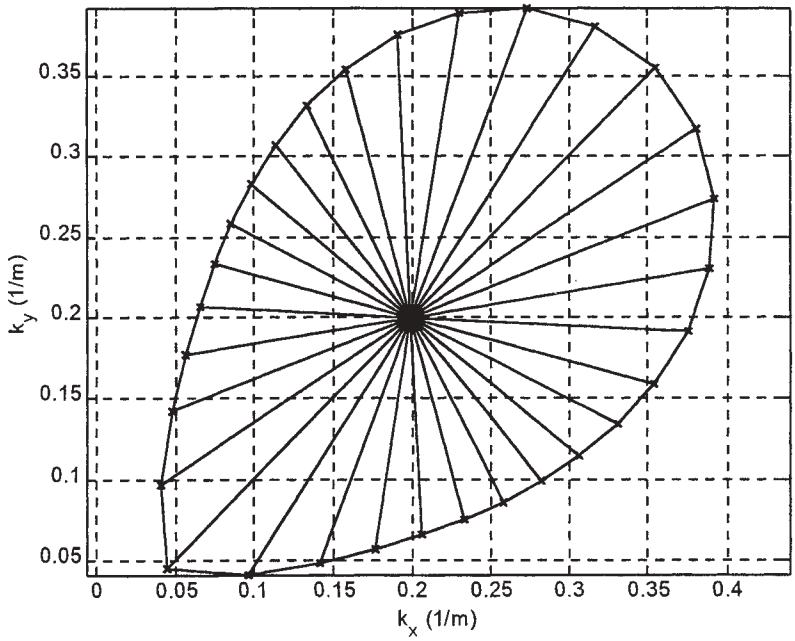

Figure 6: Example of a finite depth (d=1.5m) locus for wave number $\vec{k}_2$ obtained with the radial method by choosing the mid-point k_m as origin for Based on $\vec{k}_1 = (0.1, 0)$ and $\vec{k}_3 = (0.15, 0.05)$. The number of points on the locus is 30.

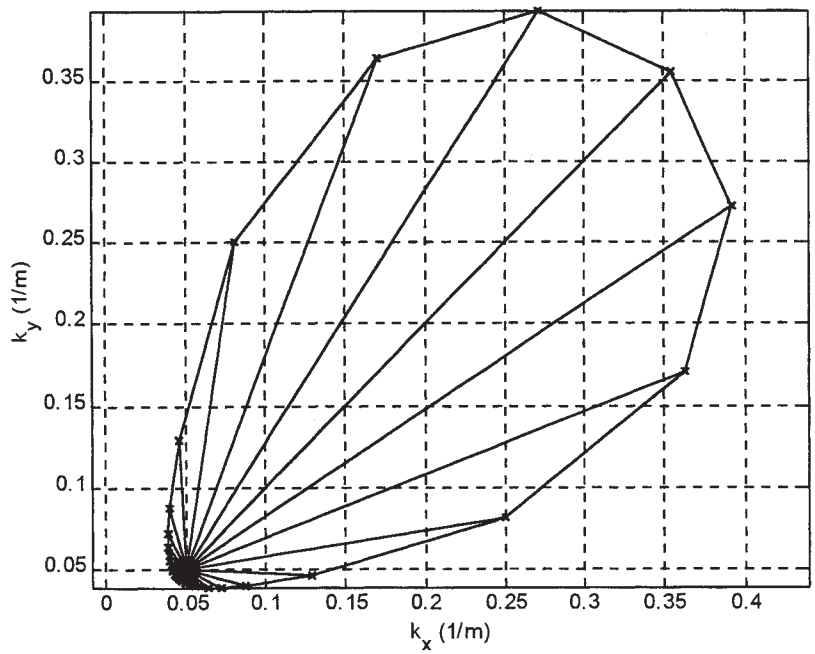

Figure 7: Example of a finite depth (d=1.5 m) locus for wave number $\vec{k}_2$ obtained with the radial method by choosing the peak wave number k_p as origin for Based on $\vec{k}_1 = (0.1, 0)$ and $\vec{k}_3 = (0.15, 0.05)$. The number of points on the locus is 30.

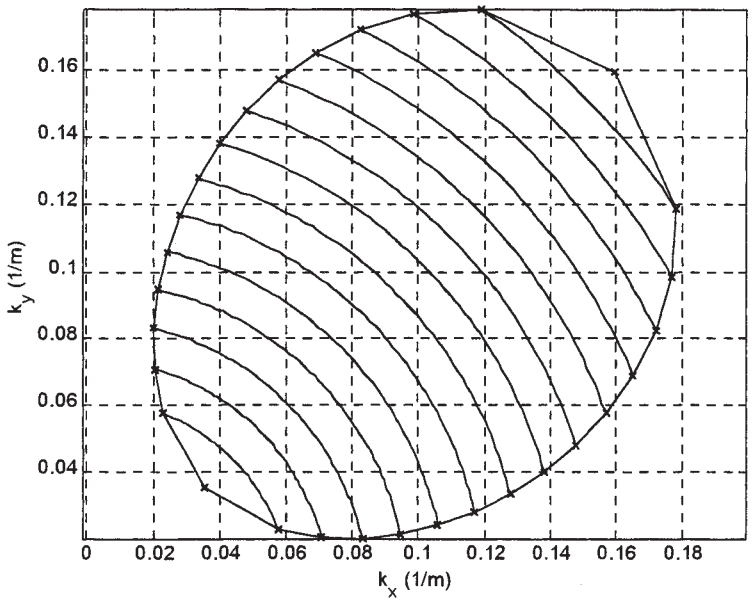

Figure 8: Example of a deep water locus for wave number $\vec{k}_2$ obtained with the polar method. Based on $\vec{k}_1 = (0.1, 0)$ and $\vec{k}_3 = (0.15, 0.05)$. The number of points on the locus is 30.

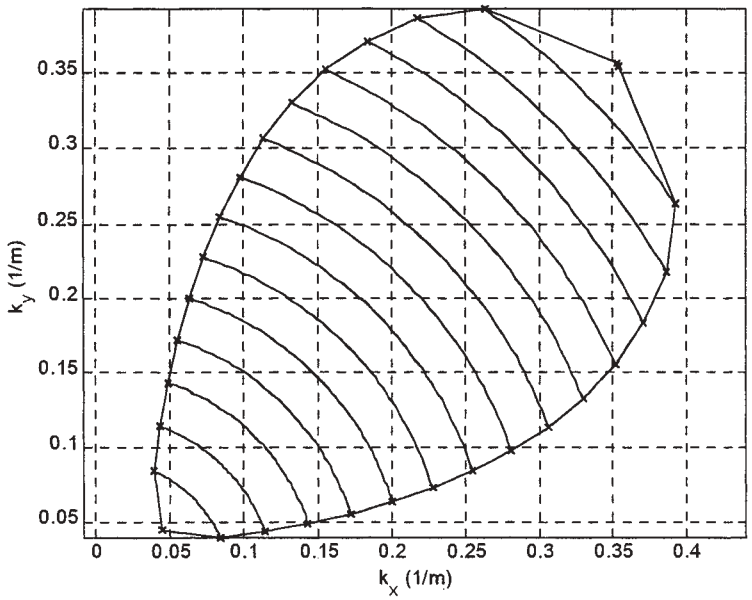

Figure 9: Example of a finite depth (d=1.5 m) locus for wave number $\vec{k}_2$ obtained with the polar method. Based on $\vec{k}_1 = (0.1, 0)$ and $\vec{k}_3 = (0.15, 0.05)$. The number of points on the locus is 30.

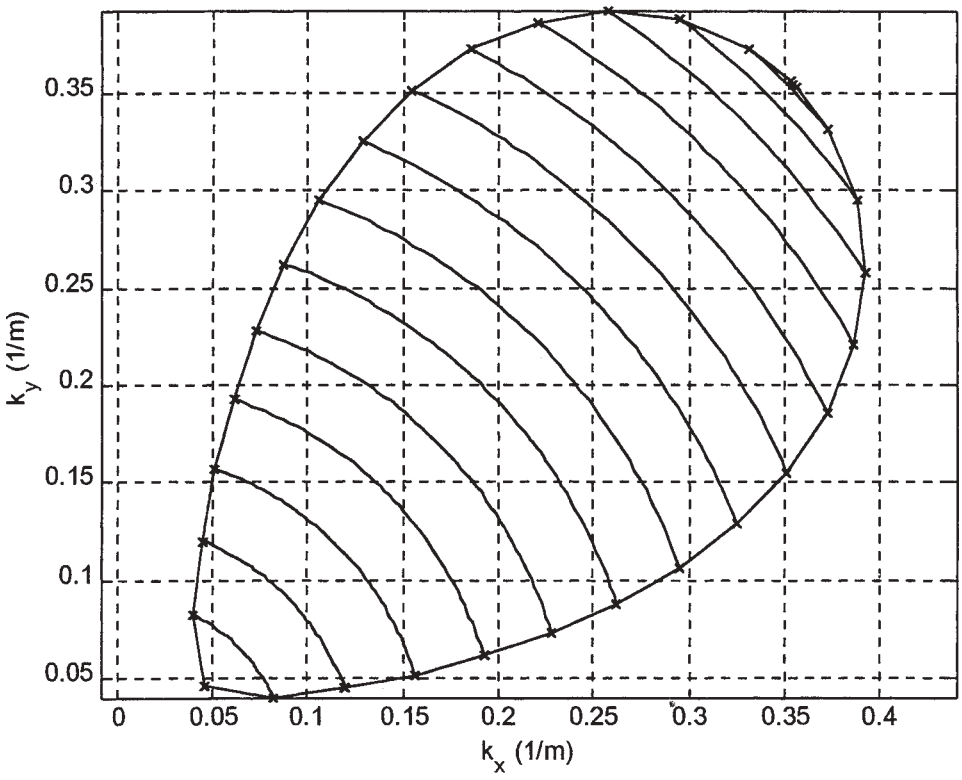

Figure 10: Example of a finite depth (d=1.5 m) locus for wave number $\vec{k}_2$ obtained with the polar method obtained with adaptive stepping to get equi-distant points on the locus. Based on $\vec{k}_1 = (0.1, 0)$ and $\vec{k}_3 = (0.15, 0.05)$. The number of points on the locus is 30.

A STUDY OF LONG WAVE AND SHORT WAVE INTERACTIONS BY USING A NEW SPECTRUM MODEL

Ray-Qing Lin[1] and Weijia Kuang[2]

[1] Seakeeping Department, David Taylor Model Basin
Naval Surface Warfare Center, Carderock Division,
West Bethesda, Maryland, USA 20817-5700

[2] Joint Center for Earth System Technology, University of Maryland
Baltimore County, Maryland, USA 21250

1. INTRODUCTION

Phillips (1960) first identified that at least 4 gravity waves could interact resonantly in deep oceans. Frelich and Guza (1984) suggested that three-gravity interactions dominate in shallow water under the shallow water assumptions. Lin and Perrie (1997) pointed out that at least 4 gravity waves interactions are required to satisfy the resonant conditions for all water depths. However, in the extremely shallow water, the 4-comparable gravity wave interactions do not satisfy the resonant conditions: the new resonant conditions require one long wave interacting with three local wind waves. The shallow water assumptions neglect very low frequency waves, leading to an entirely different mechanism. The three wave interactions can be resonant only when they are parallel, e.g. two opposite edge waves interact with one complete reflected gravity wave (Hasselmann,, 1967). But Zakharov and Shulman (1980) proved that the nonlinear coefficients of parallel wave interactions equal to zero. The non-parallel three wave interactions can only be considered as quasi-resonant interactions. One question arises on whether quasi-resonant interactions could dominate resonant wave-wave interactions.

The existing nonlinear wave-wave interaction models could not answer the above question because they are based on resonant 4-wave interaction theories. The "exact solution" by Hasselmann and Hasselamn (1981), Discrete Integration Approximation (Hasselmann and Hasselmann, 1985), Resio and Tracy (1998) are based on the Boltzmann Integration theory and apply to very weakly 4-wave interactions ($\varepsilon \leq 0.06$ and $kh \geq 0.7$). The Reduce Integration Approximation (RIA) by Lin and Perrie (1999) is based on the Hamiltonian Variation Principle and applies also to weakly 4-wave interactions ($\varepsilon \leq 0.3$ and $kh \geq 0.3$).

In this study, we attempt to use the new spectrum wave model (Lin and Kuang, 2000) to address this issue. The model can be applied to study finite amplitude wave interactions in arbitrary water depth. In this model, resonant modes as well as non-resonant modes are all included. In particular, arbitrary number of wave-wave interactions are considered, such as 2-wave, 3-wave, etc.. The maximum number n of the waves are determined by the truncation level in the model. For example, we use n=128 for this study. We intend to compare the nonlinear transfer rates due to long wave and gravity wave interactions with those due to comparable gravity wave interactions in shallow water. By this we may pinpoint the dominant mechanism of wave-wave interactions in shallow water. In the study, we choose a swell as the long wave interacting with local waves. We also specify that the wave steepness $\varepsilon \leq 0.3$ to avoid the effect of higher order wave-wave interactions. The new wave-wave interaction model is 4 times faster than RIA method and 3-order of magnitude faster than the "exact solution" by Hasselmann and Hasslemann (1981).

The mathematical formulations of the model are summarized in Section 2. In section 3, we analyze the differences among the nonlinear transfer rates due to one long wave interacting with three gravity waves and those due to the three comparable gravity wave interactions. Discussions are presented in Section 4.

2. MATHEMATICAL MODEL OF FINITE AMPLITUD WAVE-WAVE INTERACTIONS

The basic equations of the model are those governing the surface waves, i.e. the continuity equation, the dynamical equation at the water surface and the

boundary conditions for the waves. With appropriate scaling, these equations can be written in the following non-dimensional forms:

$$\alpha^2\nabla_h^2\varphi+\frac{\partial^2\varphi}{\partial z^2}=0,\qquad -1\le z\le\xi\,, \tag{1}$$

$$\frac{\partial\varphi}{\partial t}+\frac{1}{2}(\nabla_h\varphi)^2+\frac{1}{2}(\frac{\partial\varphi}{\partial z})^2+\xi=0,\quad \text{at } z=\xi \tag{2}$$

$$\frac{\partial\xi}{\partial t}+\alpha^2(\nabla_h\xi)\cdot(\nabla_h\varphi)=\frac{\partial\varphi}{\partial z},\quad \text{at } z=\xi \tag{3}$$

$$\frac{\partial\varphi}{\partial z}=0,\quad \text{at } z=-1 \tag{4}$$

where φ is the non-dimensional velocity potential, ξ is the normalized free surface elevation and

$$\alpha^2\equiv h/L \tag{5}$$

is the ratio of the water depth (h) and the typical horizontal length scale (L) of the system. For the mathematical details, we refer the reader to Lin and Kuang (2000).

When the wave amplitudes are very small, the nonlinear terms in (1)-(4) can be ignored. This linearized system admits the following wave solutions:

$$\begin{cases}\varphi=b_1\exp[i(\omega t+\vec{k}\cdot\vec{r})]\cosh\alpha k(1+z)/\cosh\alpha k,\\ \omega=\sqrt{\alpha k\tanh\alpha k},\\ k=\sqrt{k_x^{\,2}+k_y^{\,2}},\end{cases} \tag{6}$$

where $\vec{k}=k_x\hat{x}+k_y\hat{y}$ is the horizontal wave vector and ω is the frequency of the waves. By (4), we have

$$\xi=-\frac{\partial\varphi}{\partial t}\Big|_{z=0}=-i\omega b_1\exp[i(\omega t+\vec{k}\cdot\vec{r})=a_1 \tag{7}$$

$$\exp[i(\omega t+\vec{k}\cdot\vec{r})],$$

where

$$b_1\equiv\frac{ia_1}{\omega}. \tag{8}$$

For numerical modeling, we apply a pseudo-spectral method to solve (2) and (3): we expand the potential velocity φ and the free surface elevation ξ in Fourier series:

$$\xi=\sum_{m,n}a_{m,n}(t)\exp(i\omega t+k_mx+k_ny)+c.c., \tag{9}$$

$$\varphi=\sum_{m,n}b_{m,n}(t)\exp(i\omega t+k_mx+k_ny)+c.c., \tag{10}$$

where *c.c.* describe the complex conjugate parts. The (non-dimensional) discrete wave numbers (k_m,k_n) are determined by the truncation level $(m\le M,n\le N)$ of the expansions (9)-(10) and by the dimensional peak wave number $\tilde{k}_p$ (i.e. the wave number corresponding to the peak energy spectrum) of the initial wave energy spectrum. For a given dimensional peak wave number $\tilde{k}_p$, we select an integer N_1 such that the horizontal length scale

$$L=\frac{\pi N_1}{\tilde{k}_p}. \tag{11}$$

The non-dimensional wave numbers (k_m,k_n) in the expansions (9) and (10) are defined as

$$k_n=n\pi,\qquad \text{for } n=0,\pm1,\pm2,\cdots,\pm N. \tag{12}$$

By (11) and (12), k_n at $n=N_1$ is the corresponding non-dimensional peak wave number.

The nonlinear terms in (2) and (3) are first evaluated at collocation points. The corresponding spectral coefficients are then obtained via FFT.

The (non-dimensional) energy E of the waves are given by

$$E=\frac{1}{2}\int_{-1}^{\xi}dz[\alpha^2(\nabla_h\varphi)^2+(\frac{\partial\varphi}{\partial z})^2]+\frac{1}{2}\xi^2. \tag{13}$$

With the expansion (9)-(10), we may obtain that

$$E=\sum_{m,n}\mathrm{Re}(\hat{e}_{m,n})\cos\theta_{m,n}-In(\hat{e}_{m,n})\sin\theta_{m,n}\equiv\sum_{m,n}e_{m,n}, \tag{14}$$

where $\hat{e}_{m,n}$ is the solution of Eq. (13) and $\theta_{m,n} \equiv \tan^{-1}(k_m / k_n)$ is the phase angle for the mode (m, n).

The (non-dimensional) energy transfer rate is approximated as

$$\frac{de_{m,n}}{dt} \approx \frac{e_{m,n}(t+\Delta t) - e_{m,n}(t)}{\Delta t}. \qquad (15)$$

Therefore, for a given initial state $\{a_{mn}(t_0), b_{mn}(t_0)\}$, we can evaluate the energy distribution and the energy transfer rate at any given time t.

3. MODEL RESULTS:

Our new model includes multiple wave-wave interactions, as shown in the expansions (9)-(10). The multiplicity is governed by the truncation level (M, N) in numerical modeling. Apart from general non-resonant wave modes, the model includes the interactions of 4-resonant wave interactions, and all other possible resonant wave interactions (*e.g.* 5-resonant wave interactions, etc.) within the truncation level. This is a substantial improvement from the existing nonlinear source functions, such as DIA and "Exact-Solutions" (Masada, 1980; Hasselmann and Hasselmann, 1981; Resio and Perrie, 1991, Hasimoto et al, 1998; Lin and Perrie, 1999) which include only 4-resonant wave interactions.

Although our new model differs greatly from the existing nonlinear source functions, we expect that it should yield similar solutions when the water is deep or shoaling and the normalized wave steepness is small (the 4-resonant wave interactions dominate). To demonstrate this, we choose an initial energy distribution (see Figure 1) and select $N_1 = 7$. The truncation level is $M = N = 128$. In our benchmarking test, the effective $\varepsilon \equiv ak_p \frac{3 + \tanh^2 k_p h}{4 \tanh^3 k_p h}$ varies from 0.072 to 0.158 (correspondingly $k_p h$ varies from 8.4 to 0.697), well within the weakly nonlinear interaction regime.

Figure 1 shows an initial energy density spectrum (JONSWAP Spectrum) with the angle spreading $\cos^4(\theta_j - \theta_0)$, where $\theta_0 = 0^0$. The lines A, B, C, ..., F in the figure represent the angles 0^o, 15^o, 30^o, ..., 90^o. The angle 0^o is in the down wind direction.

The numerical results are shown in Figure 2, where the one-dimensional nonlinear transfer rates for $k_p h \approx 0.697$, 0.851, 1.066, 1.791, 8.40, (with $ak_p \approx 0.072$) are given by the lines A, B, C, D, E, and F. In Figure 2(a) are the results by RIA, and in Figure 2(b) are the results by our new model. We may observe that the results agree well. The results obtained by RIA also agrees well with Hasselmann and Hasslemann (1981) and Resio and Tracy (1998).

To study the dominant wave-wave interactions in various water depths, we use $\varepsilon \approx 0.28$ ($k_p h \approx 0.35$) in shallow water and $\varepsilon \approx 0.016$ ($k_p h \approx 8.4$) in deep water. These parameters are within the weakly nonlinear analysis regime. Another requirement for weakly nonlinear interactions is that the initial wave amplitudes must be much smaller than those in Figure 1 for shoaling water. Figure 3 shows the initial spectrum for this part of study. The lines A, B, C, D, E, and F in Figure 3 are similar to those in Figure 1: in (a) is the single peak spectrum with the peak frequency $f_p \approx 1.444hz$; in (b) is the single peak spectrum with $f_p \approx 0.1hz$; (c) is the double peak spectrum, the sum of the spectrums in (a) and in (b).

Figure 4 shows the nonlinear transfer rates in deep water: the lines A, B, C, D, E, and F are the results corresponding to the lines A, B, C, D, E, and F in Figure 3: (a) the results for the initial spectrum in Figure 3a and (b) the results for the initial spectrum in Figure 3c. We may observe that the nonlinear transfer rates in Figure 4b are about 5 times greater than those in Figure 4a. This is because the double peak spectrum has much greater significant wave heights. Figure 5 is similar to Figure 4, but for the nonlinear transfer rates in shallow water. The nonlinear transfer rates in Figure 5a are about 5 times greater than those in Figure 4a. However, the nonlinear transfer rates in Figure 5b are about one order of magnitude greater than those in Figure 4b and in Figure 5a. This suggests that the nonlinear transfer rates due to a long wave interacting with short waves increase rapidly as the water depth decreases. The nonlinear transfer rates due to a long wave interacting with three gravity waves are significantly greater than the total nonlinear transfer rates due to all other wave-wave interactions in shallow water, including resonant modes, such as 4-comparable wave-wave interactions (they are still

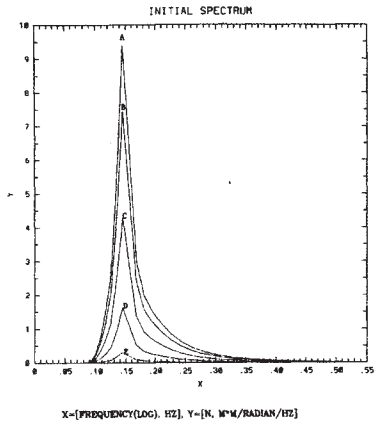

Figure 1. The symmetric JONSWAP gravity wave spectrum ($\gamma = 3.3$) with the angle spreading $\cos^4(\theta - \theta_j)$ is the two-dimensional spectrum with the lines A, B, C, …,G for the angles 0°, 15°, 30°, …, 90° (0° is the down wind direction and $\theta_j = 0$).

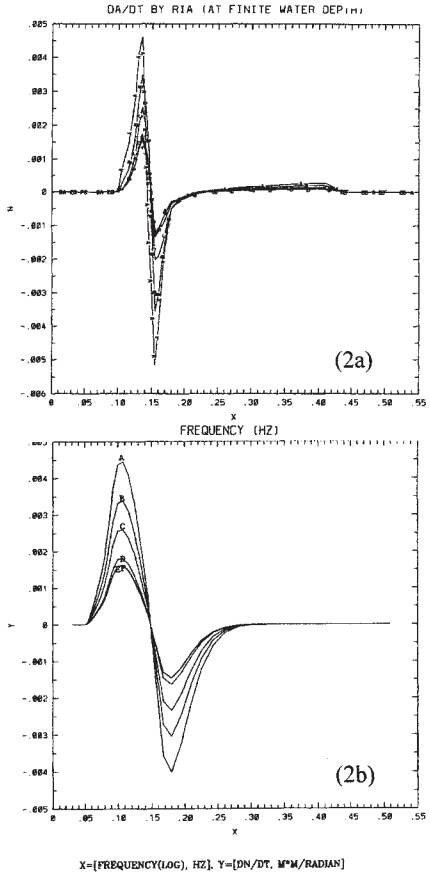

Figure 2.. The one-dimensional transfer rates for deep and shoaling water, lines A, B, C, D, E, and F, represent $k_p h \approx$ 0.697, 0.851, 1.066, 1.719, 3.369 and 8.40, and $ak_p \approx 0.072$; (a) by RIA, and (b) by our new model.

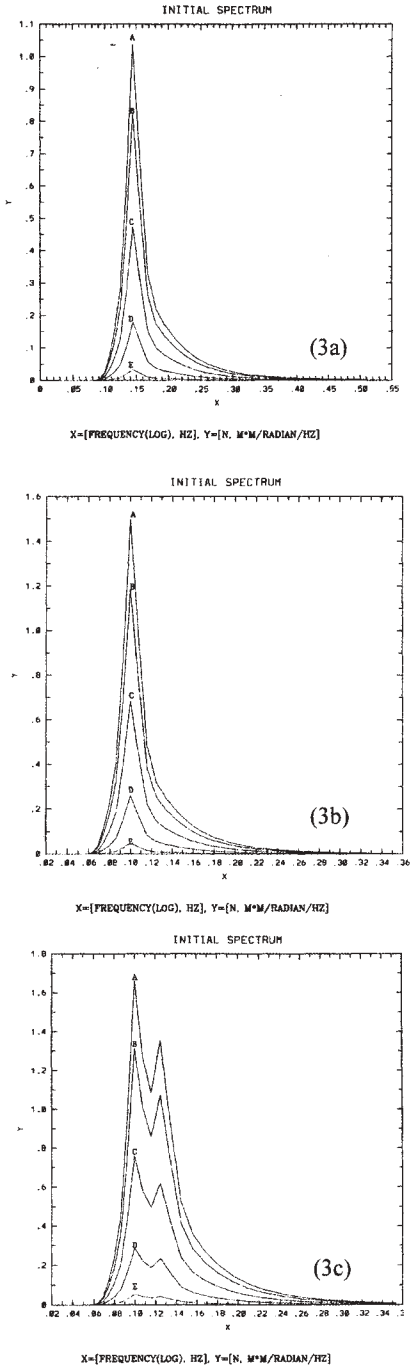

Figure 3.. This figure is the same as Figure 1 except wave amplitudes, peak frequency may different; (a) single peak initial spectrum, $f_p \approx 0.1444hz$; (b) single peak initial spectrum, $f_p \approx 0.1hz$; (c) double peak spectrum, which is equal to spectrum in (a) plus spectrum in (b).

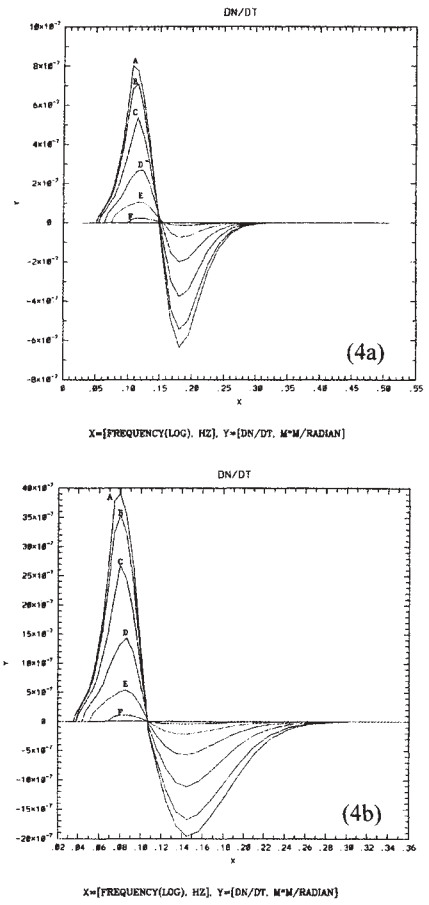

Figure 4 shows the nonlinear transfer rates in deep water ($k_p h \approx 8.4$), where the lines A, B, C, D, E, F and G are associated with the lines A, B, C, D, E, F and G in Figure 3 respectively; (a) the initial spectrum is in Figure 3(a); (b) the initial spectrum is in Figure 3(c).

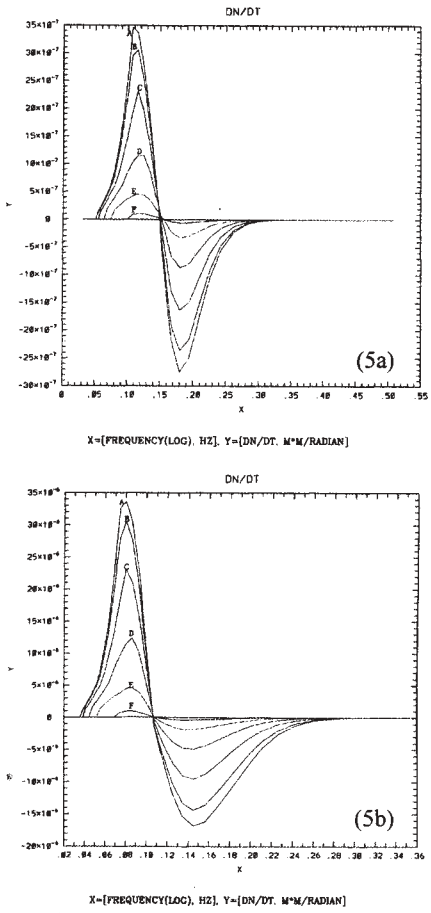

Figure 5. This is the same as figure 4, except it is in shallow water ($k_p h \approx 0.35$).

significant when $k_p h \approx 0.35$) and 5-wave interactions, and all non-resonant wave-wave interactions.

4. DISCUSSIONS

We present in this paper the numerical results on the nonlinear energy transfer rates with our new wave-wave interaction model. This model is based on a pseudo-spectral method, i.e. the potential velocity φ and the free surface elevation ξ are expanded in Fourier series (9)-(10). The nonlinear interaction in (2)-(3) are then evaluated at collocation points. The corresponding nonlinear interaction coefficients are obtained via FFT. This new model is benchmarked with RIA (one of the existing models on nonlinear wave-wave interactions) and the results agree well with those of the existing models for weakly nonlinear wave-wave interactions.

Our new model can be applied to both weakly and strongly nonlinear wave-wave interactions in arbitrary water depth. In particular, the model includes not only 4-resonant wave interactions (which are dominant in deep water and in shoaling water for small wave amplitudes $\varepsilon \leq 0.3$), but also higher order resonant wave-wave interactions and non-resonant wave-wave interactions within the truncation level.

Our numerical results show that in shallow water, the nonlinear transfer rates due to one long wave

interacting with 3-local wind waves are much larger than those due to other wave-wave interactions, including those due to the quasi-resonant 3-wave interactions (Frelich and Guza, 1984). This suggests that the dominant mechanism in shallow water is one long wave and 3-local wave interactions, not the quasi-resonant 3-wave interactions, supporting the previous studies (Lin and Perrie,1997). Therefore, our studies indicate that the shallow water assumption in which low frequency (long) waves are neglected could lead to entirely different mechanisms. This is consistent with the well-known physics: at least four waves are needed for resonant interactions in all water depths (Phillips, 19??).

ACKNOWLEDGEMENTS

One of us (R.L.) is supported by the grant from Office of Naval Research under ILIR program though the David Taylor Model Basin, Naval Surface Warfare Center, Carderock Division. Another (W.K.) is supported by NASA Solid Earth and Natural Hazard program and by NSF CSEDI program.

REFERENCES

Frelich, M. H., and R. T. Guza, 1984: Nonlinear effects on shoaling surface gravity waves. Philos. Trans. Roy. Soc. London, A, 311, 1-41.

Hasselmann, K., 1967: A criterion for nonlinear wave stability. J. Fluid mech. 30, Part 4, 737-739.

Hasselmann, S., K. Hasselmann, 1981: A symmetrical method of computing the nonlinear transfer in a gravity-wave spectrum. Hamb. Geophys. Einzelschriften Reihe A Wiss. Abhand, 52, 138pp.

Hasselmann, S. and K. Hasselmann, 1985: Computation and parameterizations of the nonlinear energy transfer in a gravity-wave spectrum. Part I. A new method for efficient computations of exact nonlinear transfer integral. J. Phys. Oceanogr., 15, 1369-1377.

Lin , R.-Q. and W. Perrie, 1997: A new coastal wave model, Part III. Nonlinear wave-wave interaction for wave spectral evolution. J. Phys. Oceanogr., 27, 1813-1826.

Lin, R.-Q. and W. Perrie, 1999: Wave-wave interactions in finite water. J. Geophys. Res., 104, No. C5, 11193-11213.

Lin, R.-Q., and W. Kuang, 2000: Nonlinear wave-wave interactions for finite amplitude in arbitrary water depth. Submitted to JPO.

Phillips, O. M., 1960: On the dynamics of unsteady gravity waves of finite amplitude. J. Fluid Mech., 9, 193-217.

Resio, D. and W. Perrie, 1991: A numerical study of nonlinear energy fluxes due to wave-wave interactions. Part I. Methodology and basic results, J. Fluid Mech., 223, 603-6129.

Resio, D. and B. Tracy, 1998: A weakly nonlinear wave-wave interaction model. An international competition in "Base Enhancement Wave Prediction" workshop.

Zakharov, V. E., and E. Shulman, 1980: Degenerative dispersion law, motion invariants and kinetic equation, Phys. D, 21, 192-202.

EFFECT OF WIND WAVE SPECTRUM FLUCTUATIONS ON NON-LINEAR SPECTRUM EVOLUTION

IGOR V. LAVRENOV

State Research Center of the Russian Federation - Arctic and Antarctic Research Institute, Bering 38, 199397, St.Petersburg, Russia, e-mail: lavren@aari.nw.ru.

INTRODUCTION

The wind waves are a non-stationary probability process. The evolution of the wind wave field, as it is shown by the experimental data, occurs in a wide range of spatial - temporal scales. The wave period is the shortest temporary scale ($\tau_1 \approx$ 1—10 s). The wave movements connected with the group wave structure are the second temporary scale ($\tau_2 \approx 10-15\tau_1$). The so-called "quasioscillations" can be referred to the third temporal fluctuation scale of sea surface. They are fairly well traced in changes of the frequency spectrum form and in its parameters even for stable conditions of wave development (Efimov and Soloviev 1984, Andreev 1988; Zaslavskii and Krasitskii, 1993; Bitner-Gregersen and Gran, 1983). The quasioscillation periods are approximately equal from 5 to 20 min. The scale estimation of these periods an be accepted as $\tau_3 \approx 10^3$ s. This phenomenon well known as SIWEH (smoothed instantaneous wave energy history) was described in the papers (Zaslavskii and Krasitskii 1993, Bitner-Gregersen and Gran 1983, Mase 1989, Sand 1982). It clearly revealed in changes of wave dispersion (see Fig.1) and frequency spectrum (see Fig.2). The quasioscillation reveals the following estimated features:

- measured wave values have various spectral densities and wave dispersions;
- spectral maximum frequency ω_{max} has approximately the same value in different parts of wave record;
- the greatest spectral density fluctuations are exhibited in the vicinity of spectral maximum (Fig.2).

The effect of wind wave parameter fluctuation on the non-linear spectrum evolution is studied by numerical solution of the Hasselmann (1962) equation with the periodically changing term.

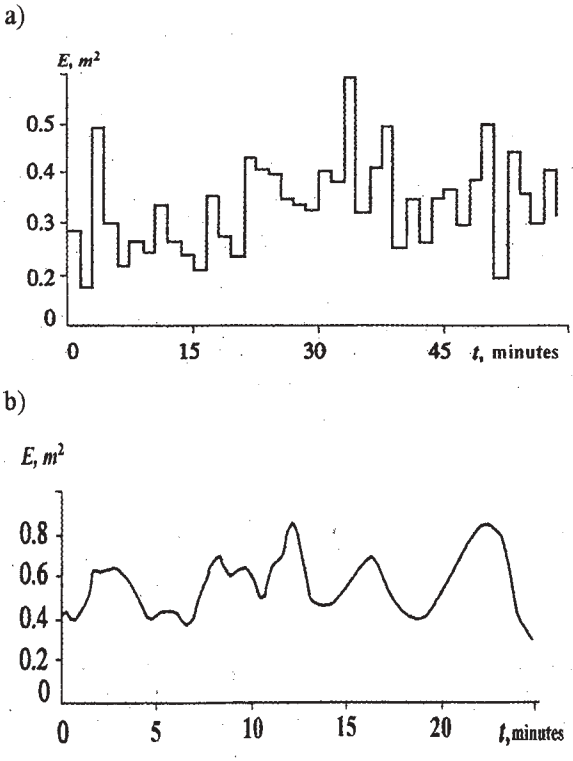

Fig 1. Experimental data of the wave energy quasioscillations: a) Zaslavskii and Krasitskii, (1993); b) Andreev, (1988).

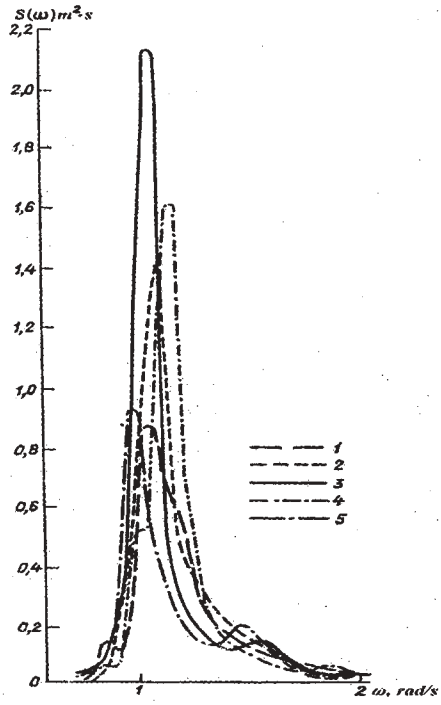

Figure 2. Spectral density fluctuations of developing waves (1–5) calculated for wave record 3.5 min long intervals (Andreev, 1988).

PROBLEM FORMULATION AND SOLUTION METHOD

Using the results of paper (Zaslavskii and Krasitskii, 1993), the elementary approximation of spectral density with quasioscillations can be presented as an approximation of the JONSWAP spectrum (Hasselman et al., 1973) with periodic spectral density maximum changes. This spectrum variation can be presented as:

$$S(\omega,\varphi,\omega_{\max},t)= S_J(\omega,\varphi) \quad \gamma^{\mu\sin(2\pi/\tau)f(\omega)}, \quad (1)$$

where $S(\omega,\varphi,\omega_{\max},t)$ is the frequency-angular spectrum; $S_J(\omega,\varphi)$ is JONSWAP spectrum, γ is the spectrum peakness parameter, μ is the relative oscillation amplitude of spectral maximum; τ_3 is a period of oscillations. The temporal dependence of spectrum enhancement could be defined as $\tilde{\gamma}=\gamma^{(1-\mu\sin(2\pi/\tau))}$.

The non-linear spectrum evolution with quasioscillations is to be studied by solving the following equation:

$$\frac{\partial S}{\partial t} = G_{nl}(S)-Sf_2(\omega)\cos(2\pi t/\tau), \quad (2)$$

where $f_2(\omega)=\mu \quad f(\omega) \quad \ln(\gamma)2\pi/\tau$; $G_{nl}(S)$ is the integral of non-linear interaction in the wind wave spectrum computed relatively $S(\omega,\varphi)$. It should be noted that in case when $G_{nl}(S)$ is equal zero, the equation (2) produces the spectrum solution (1). On the other hand if oscillations are excluded ($f_2(\omega)=0$) the traditional non-linear evolution of spectrum is described by the equation (2).

Generally the expression for the integral of non-linear energy transfer is written as follows (Hasselmann, 1962):

$$G_{nl}(N)=\iiint T(\mathbf{k},\mathbf{k}_1,\mathbf{k}_2,\mathbf{k}_3)\,\delta(\mathbf{k}+\mathbf{k}_1-\mathbf{k}_2-\mathbf{k}_3)\,\delta(\omega+\omega_1-\omega_2-\omega_3) \times\{N_2N_3(N+N_1)-N_1N(N_2+N_3)\}d\mathbf{k}_1\,d\mathbf{k}_2\,d\mathbf{k}_3 \quad (3)$$

where $N_i=N(\mathbf{k}_i)$ is the spectral density of wave action; $T(\mathbf{k},\mathbf{k}_1,\mathbf{k}_2,\mathbf{k}_3)$ is the kernel function of the non-linear interaction between wave components; $\delta(\mathbf{k})$ and $\delta(\omega)$ are the Diraque delta-functions describing the interaction resonance conditions between four wave components.

In order to solve the problem correctly the quasioscillation period should be large enough for the waves "to have time" to interact, the latter being determined by the characteristic time of phase intermixing (Yuen and Lake, 1987):

$$\frac{1}{\tau_{pb}}\approx\omega''(k)(\Delta k)^2, \quad (4)$$

where Δk is the wave spectrum width.

The value τ_{pb} appears to be equal to several spectrum maximum periods. The condition of applicability of the method can be written as: $\tau_{pb}<<\tau_3$. It should be noted that in this case the quasioscillation period can be smaller or of the same order with an evaluation of the characteristic time of non-linear waves evolution $\tau_{nl}\sim\tau$. Using Eq.3 the value τ_{nl} can be estimated 3 as:

$$\frac{1}{\tau_{nl}}\approx\frac{TN^2}{\omega''(k)(\Delta k)^2}, \quad (5)$$

Now the kinetic Eq. 2 is to be solved numerically. It is necessary to ensure that the temporal step Δt of numerical integration is much smaller than oscillation period τ. In this case the numerical solution can take into account correctly the spectral density quasioscillation. The period τ should be less than the specified time of the non-linear spectrum evolution $\Delta t<<\tau<\tau_4$. So it is necessary to solve Eq. 2 for the large time scale ($t\succ\succ\tau_4$) using sufficiently small time step Δt. The numerical computation of non-linear energy transfer demands considerable CPU time. To solve the problem efficient algorithm proposed by I.Lavrenov (1998), based on the numerical integrating method of the highest precision is used. Eq. 2 is solved numerically by the two-step predictor-corrector method allowing to obtain an accurate numerical solution. The time step of numerical integration was equal to 12.5s, which made it possible to conduct numerical integration up to the 10^5 s time interval.

RESULTS OF NUMERICAL SIMULATION

In numerical simulation the value of parameter μ is assumed to be equal to 0.9 that provided periodic oscillations of spectrum enhancement (1) ranging from 1.1 to 9.7 with a mean value γ = 3.3. The oscillation periods are 10, 20 and 40 min. respectively. The calculation results of the frequency spectra for μ=0.9 at different moments t (for different values of spectrum peackness $\tilde{\gamma}$) are presented in Fig. 3a. The spectral density values are normalized by the maximum spectrum value for $\tilde{\gamma}=33$. The non-linear transfer function normalized by its maximum value for $\tilde{\gamma}=33$ is presented for the different

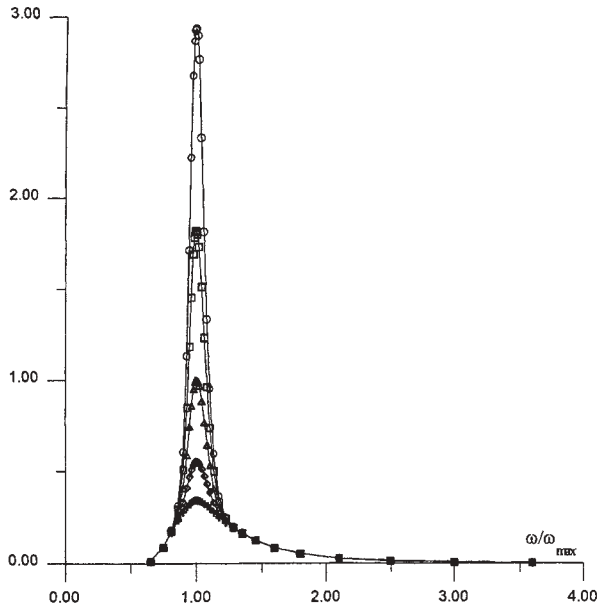

Fig. 3a.

Numerical calculations of frequency spectra normalised by maximum spectrum value at $\tilde{\gamma} = 3.3$ for $\tilde{\gamma} = 1.1$ (+); $\tilde{\gamma} = 1.8$ (◊); $\tilde{\gamma} = 3.3$ (Δ); $\tilde{\gamma} = 5.9$ ( ); $\tilde{\gamma} = 9.7$ (O)

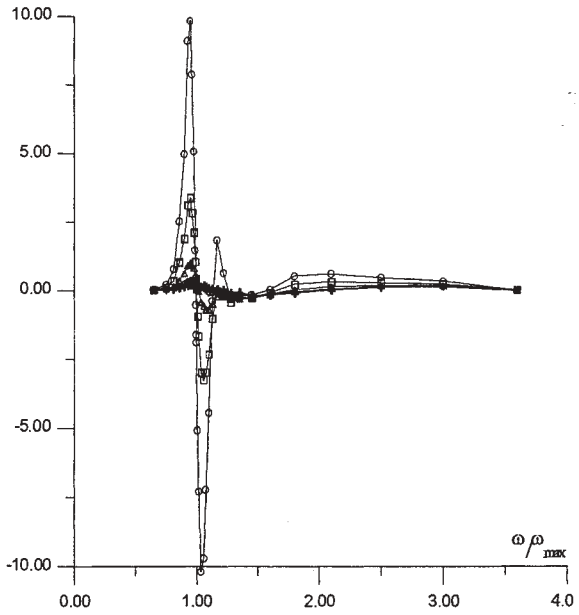

Fig.3b

Non-linear energy transfer functions normalised by its maximum value at $\tilde{\gamma} = 3.3$.

$\tilde{\gamma}$ in Fig. 3b. The relative values of non-linear transfer function differ significantly compared to the corresponding spectral density ones. This is an evidence of the proportion between the spectral density and the non-linear energy transfer function is significantly non-linear. Changes of spectrum influence do not only influence significantly the non-linear energy transfer maximum, but result in changes of non-linear transfer function in general as well.

The computed changes of the frequency spectral maximum ω_{max} for four calculation versions are presented in Fig. 4 for the case of absence of the spectral oscillations (i.e. $\mu = 0.0$) and for three cases with oscillations of different periods equal to 10, 20 and 40 min respectively. The non-linear energy transfer produces an average spectrum displacement to the low frequency range. However, the mean evolution speed of frequency maximum differs significantly, when the oscillation spectrum peakness is taken into account. Thus in the "oscillation absence" case the spectrum maximum frequency decreases monotonically from the initial value of $\omega^0_{max} = 1.88$ rad s^{-1} to ω_{max} = 1.75 rad s^{-1} for t =10^{4}s, to ω_{max} = 1.60 rad s^{-1} for $t = 3 \cdot 10^4$ s, and to ω_{max} = 1.47 rad s^{-1} for t = 10^5 s. In the presence of oscillations the spectrum maximum frequency decreases from its initial value to ω_{max} = 1.60 rad s^{-1} for t =10^{4}s, to ω_{max} =1.43 rad s^{-1} for $t = 3 \cdot 10^4$ s and to ω_{max} = 1.30 rad s^{-1} for t =10^5 s. Oscillations result in a faster decrease of the spectrum maximum frequency. The period of oscillation (for the used values) does not effect significantly on the general tendency. As soon as the spectrum maximum frequency is the most conservative parameter, the comparison of these results show the essential influence of oscillations on the non-linear spectrum evolution speed. The average speed of spectral maximum displacement is increased more than 3-fold. The numerical simulations show that the average velocity of the spectral maximum displacement depends directly on the quasioscillation amplitude of the spectral maximum.

PARAMETRISATION OF QUASIOSCILATION IN WIND WAVE MODELS

Modern wind wave mathematical models usually produce the approximation of frequency-angular spectrum averaged by a synoptic period $t \approx 3 \div 6$ hours. The spectrum variations appearing at smaller time periods τ_3 are not taken into consideration. As it is shown the fluctuations of the wind wave field result in significant changes of the spectrum form and its evolution. That is why it is important to take the effect into account.

Now an average analytical estimate of the non-linear energy transfer in the cyclically changed peackness is to be obtained. Numerical results shows that the non-linear transfer value is proportional to spectrum maximum in the power of two $G_{nl}(S) \sim S_{\max}^2$. Assuming that the maximum frequency $\omega_{\max}$ does not change within one cycle, and spectral peak value changes as $S_{\max}(t) \sim \gamma^{\mu \sin(2\pi t/\tau)}$, integration of the non-linear transfer value within one quasioscillation period, produces the average as follows:

$$\left\langle G_{nl} \right\rangle = \frac{1}{\tau} \int_0^{\tau} G_{nl}(S(t))\, dt = \tilde{G}_{nl}\, I_0(p), \quad (6)$$

where $\tilde{G}_{nl}$ is non-linear transfer without quasioscillations $(\mu = 0)$, I_0 is the modified Bessel function of the first order, the parameter p is determined as $p = 2\mu \ln(\gamma)$. Assuming that $\mu = 1.0$ and $\gamma = 33$, it is possible to derive $p \approx 2.39$ (i.e. $p>1$). Using the Bessel function asymptotic formula:

$$I_0(p) \approx \frac{e^p}{\sqrt{2\pi p}} \left(1 + \frac{1^2}{1!8p} + \frac{1^2 \cdot 3^2}{2!(8p)^2} + \ldots \right) \quad (7)$$

values $I_0 \approx 3.05$ can be obtained for the specific parameter.

It can be pointed out that the spectrum mean over 1 (+) — without oscillations; 2 (◊) — 10 min oscillation period; 3 (Δ) — 20 min period; 4 (•) — 40 min period. the period for quasioscillations determined as (1) differs from its corresponding value, computed for "no oscillation case" $(\mu = 0)$. The mean spectrum is equal to

$$\langle S \rangle = \tilde{S} \cdot I_0(p/2), \quad (8)$$

where $\tilde{S}$ is the spectrum value without quasioscillations $(\mu = 0)$. In (8) the factor is equal to $\cdot\, I_0(p/2) \approx 1.38$. If the non-linear energy transfer for mean spectrum is recalculated, the value is increased up to 1.92 times. It is 1.59 times less than non-linear energy transfer with quasioscillations.

A simplified approximation of the relative increase of non-linear energy transfer due to quasioscillations can be derived from the ratios (7) and (8):

$$\left\langle G_{nl} \right\rangle \approx F(p)\, G_{nl}(\langle S \rangle), \quad (9)$$

where $F(p) = \dfrac{I_0(p)}{I_0^2(p/2)}$, $p = 2\mu \ln(\gamma)$.

F as a function of μ in Fig. 5 for various values of the parameter γ is presented. The function F is increases monotonically with growing μ and parameter γ. The value F is equal to 1.0 for $\gamma = 1.0$. The relative increase of non-linear energy transfer

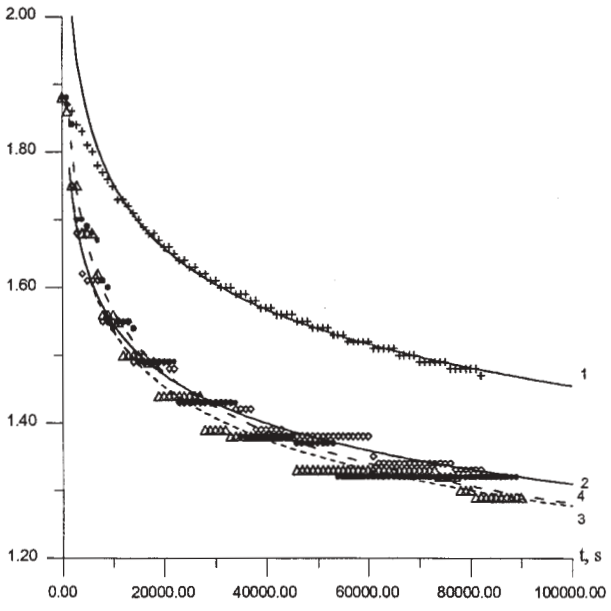

Fig 4.

Evolution of spectrum frequency maximum $\omega_{\max}$ for different period quasioscillations:

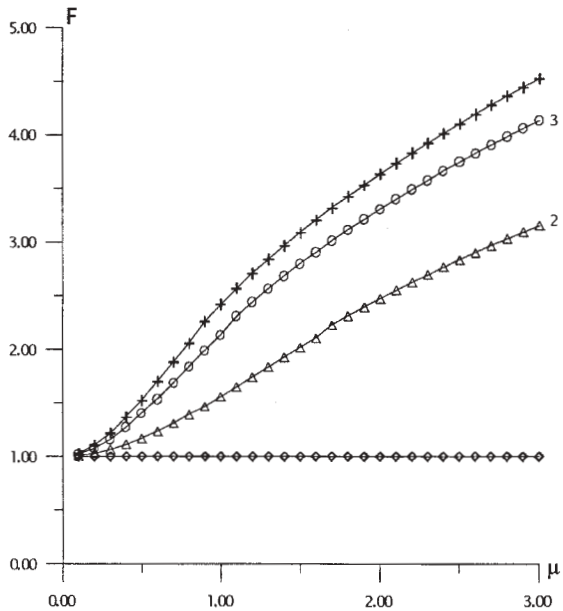

Fig 5.

Proportion between the function F and parameter μ for different values of average spectrum peakness of γ: 1(◊) — γ=1.0; 2(Δ) — γ=3.3; 3(o) — γ=7.0; 4(+) — γ=

10.0.

does not depend on the quasioscillation period but it is governed by the oscillation amplitude of the spectral maximum μ and the average spectrum peakness γ.

CONCLUSION

The influence of the wind wave parameter fluctuation on the non-linear spectrum evolution is estimated by solving numerically the kinetic equation taking into account the non-linear interaction in the wave spectrum. The non-linear energy transfer is calculated using an original numerical integrating method of the highest accuracy (Lavrenov 1998). The results of numerical simulation shows that wind wave parameter fluctuation produces a significant increase effect of the non-linear wave spectrum evolution. The present study results in a parameterisation, which makes it possible taking into account this effect in spectral wind wave models.

Acknowledgement. The paper is supported by the INTAS-666 (1999) project "Estimation of extreme metoocean events" and by the Federal Objective Programm-3 "World Ocean" of the Russian Federation

REFERENCES

Andreev, B.M., 1988: Variability of spectral characteristics of wave developing. Theoretical foundations and calculation methods of wind waves. L.: Gidrometeoizdat, 75—81.

Bitner-Gregersen, E., and S .Gran, 1983: Local properties of sea waves derived from a wave record. *Appl. Ocea Res.*, **5**, No. 4, 210—214.

Efimov V.V. and Y.P.Soloviev 1984 Low frequency sea level oscillations and gwind waves group structure. *Izv. Acad. Sci. USSR. Atmos. and Oceanic Phys.*,. **20**, No. 10. 985-994.

Hasselmann, K., 1962: On the non-linear energy transfer in a gravity wave spectrum. Part I. *J.Fluid Mech.*, **12**, 481—500.

Hasselmann, K. 1963 On the non-linear energy transfer in a gravity wave spectrum. Part 2. *J.Fluid Mech.* **15**, 273—281.

Lavrenov, I.V.,1998: Mathematical modelling of wind waves at non-uniform ocean. St.Petersburg, Gidrometeoizdat, 1—500.

Mase, H.,1989: Goupiness factor and wave height distribution. *J. Wat., Port, Coast and Ocean Eng.*, **115**, No. 1, 105—121.

Sand, S., 1982: Wave grouping described by bundled long waves. *Ocean Eng.* (Gr. Brit.), **9**, No. 6, 567—579.

Yuen, G. and A. Lake, 1987: Nonlinear dynamics of gravitational waves in deep water. M.: Mir, 1—180.

Zaslavskii, M.M. and V.P. Krasitskii, 1993: About wave fluctuations of wind waves spectrum parameters. *J. Okeanologia*, **33**, No. 1, 21—26.

SOME NEW RESULTS OF NON-LINEAR ENERGY TRANSFER IN WIND WAVE SPECTRUM

IGOR V. LAVRENOV

State Research Centre of the Russian Federation - Arctic and Antarctic Research Institute, Bering 38, 199397, St.Petersburg, Russia, e-mail: lavren@aari.nw.ru.

1.INTRODUCTION

For the first time the problem of the non-linear energy transfer in wind wave spectrum was formulated by K Hasselmann (1962,1963) and V.Zakharov (1968). According to their theory the non-linear evolution of the wave action was described by the kinetic equation:

$$\frac{\partial N(\vec{k})}{\partial t}=\iiint T(\vec{k},\vec{k}_1,\vec{k}_2,\vec{k}_3)\,\delta(\vec{k}+\vec{k}_1-\vec{k}_2-\vec{k}_3)\,\delta(\sigma+\sigma_1-\sigma_2-\sigma_3)\times$$
$$\times\{N_2N_3(N+N_1)-N_1N(N_2+N_3)\}d\vec{k}_1d\vec{k}_2d\vec{k}_3 \qquad (1.1)$$

where $N_i=N(\vec{k}_i)$ – is a spectral density of wave action, $T(\vec{k},\vec{k}_1,\vec{k}_2,\vec{k}_3)$ – are matrix elements of four resonance interaction, $\delta(\vec{k})$ and $\delta(\sigma)$ - are delta functions. They describe the resonance condition between the four wave components :

$$\vec{k}+\vec{k}_1=\vec{k}_2+\vec{k}_3 \qquad (1.2\bullet)$$
$$\sigma+\sigma_1=\sigma_2+\sigma_3. \qquad (1.2b)$$

The main peculiarity of the equation (1.1) is a preservation of the following quantities:
- total wave action:

$$A=\int N(\vec{k})\,d\vec{k}, \qquad (1.3a)$$

- total energy:

$$E=\int\sigma\,N(\vec{k})\,d\vec{k}, \qquad (1.3b)$$

and total momentum:

$$\vec{K}=\int\vec{k}\,N(\vec{k})\,d\vec{k} \qquad (1.3c)$$

K Hasselman proved the existence of the integral (1.3) in 1965.. Later on a study of the non-linear energy transfer was carried out to elaborate the collision integral estimation (1.1) Thus some effective numerical schemes were worked out and the main integral features were investigated in a number of papers (Hasselmann S. and Hasselmann K 1981;1985; Komen et al. 1994; Komatsu and Masuda 1996; Masuda 1981; Lavrenov 1991, 1998; Lavrenov and • • ampo-Torres 1999; Polnikov 1989, 1990,1993; Resio and Perrie 1991; Snyder et al. 1993; Webb 1978 etc.).
But still not enough attention has been paid to the problem of analytical and numeric study of the kinetic equation (1.1). Among the stationary analytical solution the following one is as as "thermodynamical":

$$N=\left(a+b\omega+\vec{c}\vec{k}\right)^{-1} \qquad (1.4)$$

where a, b and $\vec{c}$ are constants. The solution (1.4) reduces the integral value to be equal to zero.
The investigation of equation solution (1.1) remains an important and difficult problem. The main progress in its analytical study was achieved by V. Zakharov et al (1966, 1981, 1982,1983). A solution of the stationary analytical spectra of the equation (1.1) was derived for the angle isotropic case and infinite frequency range [0,∞]. Analytical methods of the equation solution were developed further in the papers (Zaslavskii 1989, 2000) based on "the narrow directional approximation". According to M.Zaslavskii (2000), the evolution equation (1.1) can be presented as self-similar solutions. The frequency spectral dependence was found out to be equal to $S(\sigma)\sim\sigma^{-13/2}$ (for $\sigma>\sigma_p$, where σ_p is a peak spectrum frequency), frequency spectral maximum evolution was estimated as $\sigma_p\propto t^{-1/11}$, angular narrowness in the vicinity of spectral maximum was $D.\ \cong 1$. But sorry to say the confidential equations used by M.Zaslavskii (2000) did not provide a complete study of the whole evolution equation. His self- similar spectrum approximation did not satisfy the energy preservation law.
There are not so many papers devoted to the problem of the numerical simulation of the evolution equation (1.1). In a papers (Polnikov 1990,1999) it is shown that spectral angular form does not depend on the initial spectral form and the integral spectral parameters vary within narrow bands for a large time scale of the non-linear evolution. The effect is considered to be an establishing one of the self-similar spectral form and confirmed by the analytical estimations (Zaslaskii 2000).
The problem of a self-similar solution seemed to have been solved. But in a paper (Komatsu and Masuda 1996) the numerical solutions differed from the results (Ponikov 1990, Zaslavskii 2000). The deference is not only in another spectral tail frequency dependence but also in the integral parameters. Thus as it is presented the numerical result provides the following

approximation $S(\sigma) \sim \sigma^{-4}$ (for $\sigma > 1.5\sigma_p$ and $\sigma > 1.5\sigma_p$). And still the problem remains unsolved and can be formulated this way: is there an exact self-similar form of the spectrum? And then: if the answer is positive, what are the values of its parameters?

There is an attempt to solve the problems in this paper. It contains the following Sections: a time scale of non-linear spectrum evolution is considered in the second Section. The Section 3 deals with problem initial condition and describes the numerical algorithm. The numerical results for the JONSWAP spectrum are presented in the 4th Section A problem of self-similar frequency spectrum approximations is discussed in the 5th Section.

2. TIME SCALE OF ESTABLISHING SELF-SIMILER SOLUTION

In this paper the T time scale of spectral non-linear evolution is considered, on which the non-linear energy transfer exchanges fully a spectral form. It should not depend on the initial spectrum detail. It is possible to get an estimation of the time scale by dividing the total wave action (1.3a) by an effective value of the action flux F_n determining by the preservation law of the total wave action:

$$\frac{\partial N(\vec{k})}{\partial t} + div_{\vec{k}} \vec{F}_n = 0, \qquad (2.1)$$

where $\vec{F}_n$ is a vector of the action flux. According to the paper (Polnikov 1999) the T value can be estimated with the help of the a ratio of a spectral maximum N_p to a maximum of the non-linear transfer $(\partial N/\partial t)$.

$$T \cong N_p / (\partial N / \partial t)_p . \qquad (2.2)$$

In order to get the estimation • one can transfer from the wave action spectrum $N(\mathbf{k})$ to frequency-angular spectrum $S(\sigma,\theta)$ using the formula:

$$N(\vec{k})d\vec{k} \propto \frac{1}{\sigma} S(\vec{k})d\vec{k} \propto \frac{g^3}{2\sigma^4} S(\sigma,\theta)d\sigma d\theta , \qquad (2.3)$$

where $\sigma^2 = gk$ is a deep water dispersion relation. An application of the spectrum $S(\sigma,\theta)$ allows to get the reliable estimation as far as its form is well known. For the typical values $\sigma_{max} = 1$ ràà/s, $S_{max} = 0.2 m^2 s$ it is possible to get

$$T \cong 10^5 \tau \qquad (2.4)$$

where $\tau = 2\pi / \sigma_{max}$ is a period of the initial spectral maximum.

Thus an nonlinear evolution establishing of a self-similar spectral form happens at the time scale larger then estimation (2.4) at least at one or two orders: $\tilde{t} = t/\tau \succ\succ T/\tau$.

3. PROBLEM INITIAL CONDITIONS AND NUMERICAL ALGORITHM

3.1 Initial conditions

Non-linear energy spectrum evolution should be computed for the most typical initial frequency-angular approximations $S(\sigma,\theta)$ such as:

$$S(\sigma,\beta) = S(\sigma)\, Q(\sigma,\beta), \qquad (3.1)$$

where $S(\sigma)$ is the frequency spectrum; $Q(\sigma,\beta)$ is the angular distribution.

The frequency approximation is used in the form of the *JONSWAP* spectrum (Hasselmann. et al.1973):

$$S(\omega) = \alpha \; g^2 \sigma^{-5} e^{-\frac{5}{4}\left(\frac{\sigma_{max}}{\sigma}\right)^4} \gamma^{\exp\left[-(\sigma-\sigma_{max})^2/(2\sigma_J^2\sigma_{max}^2)\right]}, \qquad (3.2)$$

where

$$\sigma_J = \begin{cases} 0.07 & at \;\; \tilde{\sigma} \le 1; \\ 0.09 & at \;\; \tilde{\sigma} > 1; \end{cases}$$

$\tilde{\sigma} = \dfrac{\sigma}{\sigma_{max}}$, σ_{max} - is a maximum of the initial spectrum.

The energy angular distribution is used consecutively in the form of two approximations, one of them being an ordinary cosine energy dependence:

$$Q(\sigma,\beta) = \begin{cases} \left[\dfrac{\pi\Gamma(n_\beta+1)}{2^{n_\beta}\Gamma^2\left((n_\beta/2+1)\right)}\right]^{-1} \cos^{n_\beta}(\beta-\bar{\beta}) \; at \; |\beta-\bar{\beta}| \le \pi/2 \\ 0 \text{ at } |\beta-\bar{\beta}| \ge \pi/2 \end{cases} \qquad (3.3)$$

The second angular distribution is used in the next following form:

$$Q_J(\sigma,\beta) = \left[2^{2s-1}\pi\Gamma^2(s+1)/\Gamma(2s+1)\right]\cos^{2s}((\beta-\bar{\beta})/2), \qquad (3.4)$$

Non-linear energy spectrum evolution is computed for these initial frequency-angular approximations $S(\sigma,\theta)$. In the process of computation the main parameters are estimated including the frequency width B, defined as

$$B = \int S(\sigma)d\sigma / S(\sigma_p)\sigma_p , \qquad (3.5)$$

where $S(\sigma) = \int_{-\pi}^{\pi} S(\sigma,\beta)d\beta$, σ_p is a frequency maximum of the time-evaluating spectrum.

and the directional width D:

$$D(\sigma) = S(\sigma,\theta_p)/S(\sigma), \qquad (3.6)$$

Series of initial spectrum parameters γ, n_β, $2s$ and initial value B and D defined at the general direction: $D_p = D(\sigma_p) = S(\sigma_p,\theta_p)/S(\sigma_p)$ are presented in a Table 1.

Table 1

Values of the initial spectrum parameters

γ	$2s$=2		n_β=2		n_β=8	
	B	D_p	B	D_p	B	D_p
1.0	0.69	0.32	0.69	0.64	0.69	1.16
3.3	0.34	0.32	0.34	0.64	0.34	1.16
7.0	0.25	0.32	0.25	0.64	0.25	1.16

3.2 Numerical algorithm

Establishment of a self-similar spectral form, controled by the non-linear energy transfer, demands to produce computation for time scale which is larger than estimation (2.4) at least at one or two orders $\tilde{t} = t/\tau \succ 10^6 \div 10^7$. The main problem is that the numerical computation of the integral (1.1) takes a lot of CPU time. It means that an algorithm of non-linear energy transfer computations should be very fast. To solve the evolution equation the integral (1.1) is to be computed thousand times to reach the estimated time scale of spectrum evolution. That is why the most optimal algorithm is used in the present study. I.Lavrenov (1991,1998) has developed such algorithm with a help of numerical method of integration of the highest precision.

A numerical solution of the evolution equation (1.1) is carried out using the Semi-implicit method (WAMDI group 1988, Lavrenov 1998). It should be noted that a traditional method of numerical integration usually leads to numerical instabilities at the high frequency spectral range. It demanded to use a small time step of numerical integration and apply special limits on numerical solution and on a value of the source function (Lavrenov 1998, Tolman 1992). Sorry to say, these methods can disturb the energy preservation. It leads to misinterpretation of physical results. But a utilization of the semi-implicit numerical method do not produce any instabilities for relatively large time steps of numerical integration (Lavrenov 1998) and there is no need to use any limits.

The numerical accuracy and the preservation of the main integrals (1.3) were controlled in the process of computation. So a numerical error of the total energy preservation did not exceed 10 per cent and the error of the total momentum estimation did not exceed 25 per cent in comparison to its initial values.

4. NUMERICAL RESULTS

4.1 Numerical results of spectra evolution

Numerical results for an initial condition (3.2) – (3.3) with $\gamma = 3.3$ and $n = 2$ for four different time moments: $\tilde{t} \cong 0, 10^3, 10^5, 10^7$ respectively are presented in Fig.3-6. Numerical simulation results of the relative frequency-angular spectrum values in polar co-ordinate system, where a radius- vector is a relative frequency value $\tilde{\sigma} = \sigma/\sigma_p$, are presented in Fig.3a-3d. The spectrum time evolution, which results in a moon-like form is shown in the figures. The spectrum becomes more narrow in the vicinity of the spectral maximum and wider at the high and low frequency range.

Two dimensional non-linear transfer values for the same steps of wave evolution are presented in Fig. 4a-4d. The non-linear evolution changes the spectrum form and shifts frequency maximum to lower frequencies. The non-linear energy transfer function is changed to a larger extend in comparison with the spectrum. It becomes narrower with concentration intensity in the vicinity of the spectral maximum. The frequency spectrum for the same evolution time steps is presented in Fig. 5. The spectrum is proportional to $\sim \sigma^{16.3}$ at the low frequency range $\sigma_p \succ \sigma$ and it is proportional to $\sim \sigma^{-6.1}$ within the range $\sigma_p \prec \sigma \prec 1.5\sigma_p$ The spectrum decreases in such a way $\sim \sigma^{-2.6}$ at the larger frequencies . $\sigma \succ 1.5\sigma_p$

An evolution of the parameter D (3.6) for different time moments is presented in Fig.6. The parameter D value becomes larger and equals to 1.33 in the vicinity of the spectral maximum, and it gets smaller at low and high frequency ranges. It is an evidence of spectral spectral isotropisation within these frequency ranges.

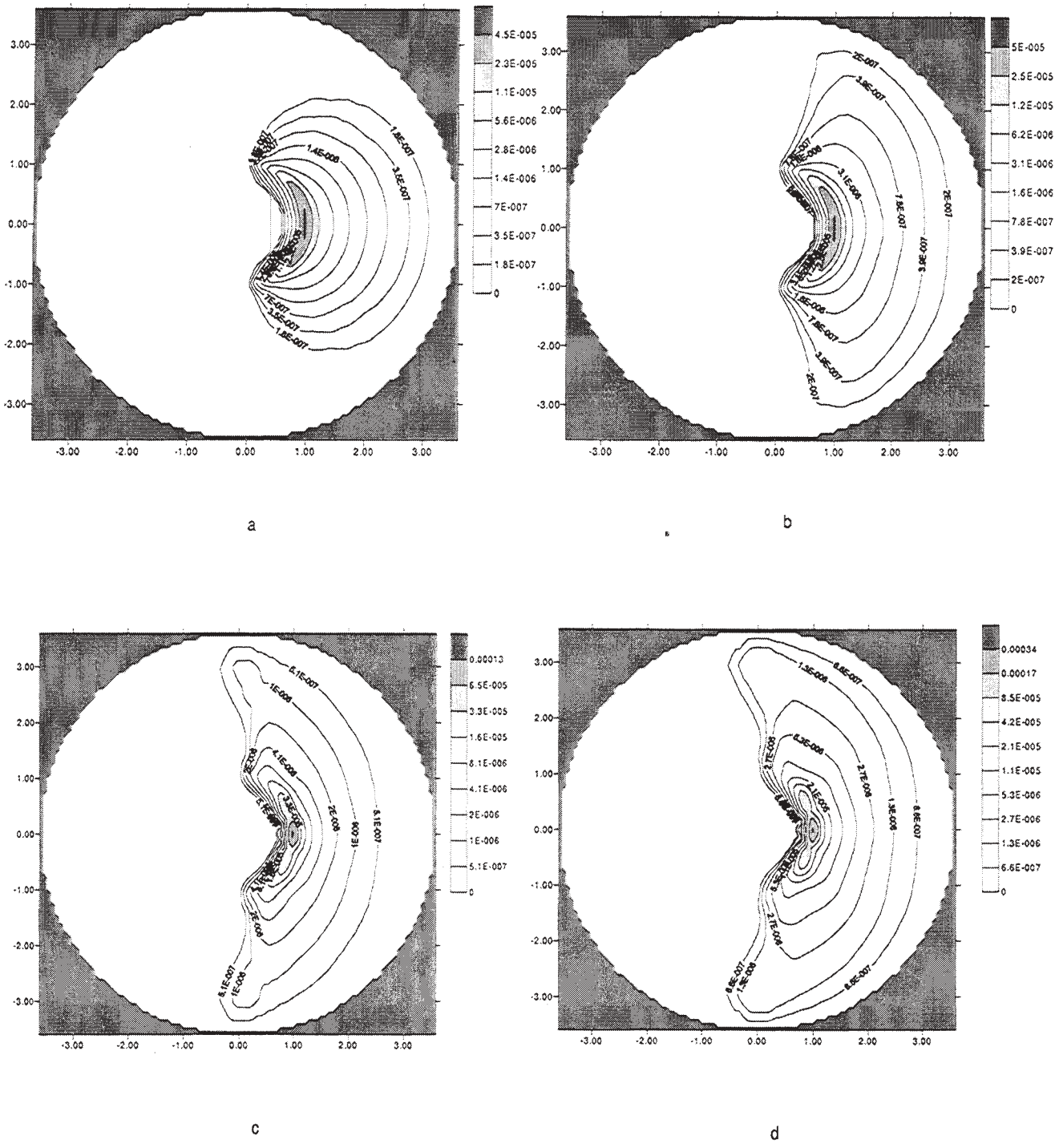

Fig.3
Non-linear two dimensional spectrum evolution
with the initial spectrum value (3.2) - (3.3) and $\gamma = 3.3, n = 2$ at different time moments:
a)- . $\tilde{t} = 0$, b)- $\tilde{t} = 10^3$, c)- $\tilde{t} = 10^5$, d)- $\tilde{t} = 10^7$

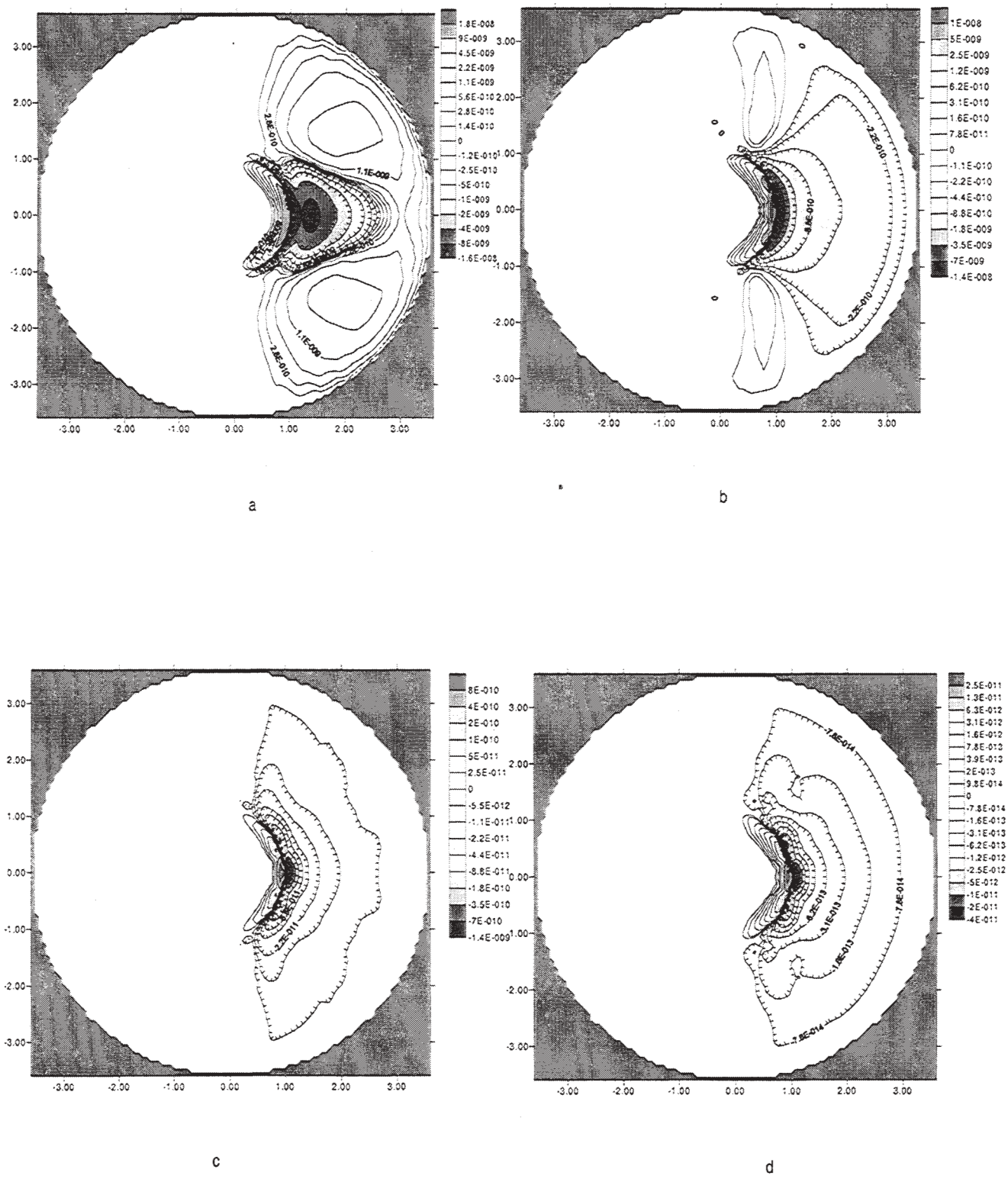

Fig.4
Two dimensional non-linear energy transfer function evolution
with the initial value (3.2) - (3.3) and $\gamma = 3.3, n = 2$ at different time moments:
a)- . $\tilde{t} = 0$, b)- $\tilde{t} = 10^3$, c)- $\tilde{t} = 10^5$, d)- $\tilde{t} = 10^7$

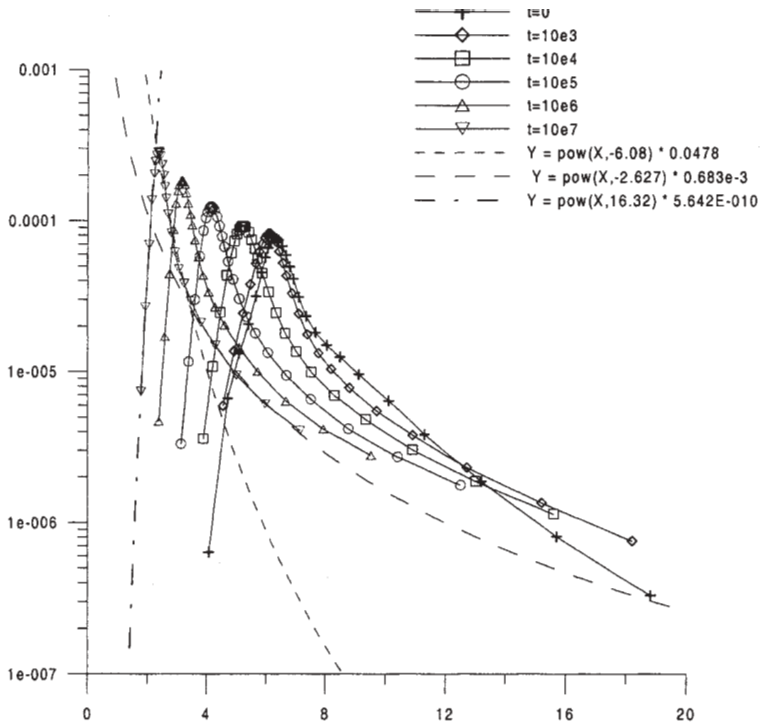

Fig.5
Frequency spectrum evolution
with the initial value (3.2) - (3.3) and $\gamma = 3.3, n = 2$ at different time moments:
a)- . $\tilde{t} = 0$, b)- $\tilde{t} = 10^3$, c)- $\tilde{t} = 10^5$, d)- $\tilde{t} = 10^7$

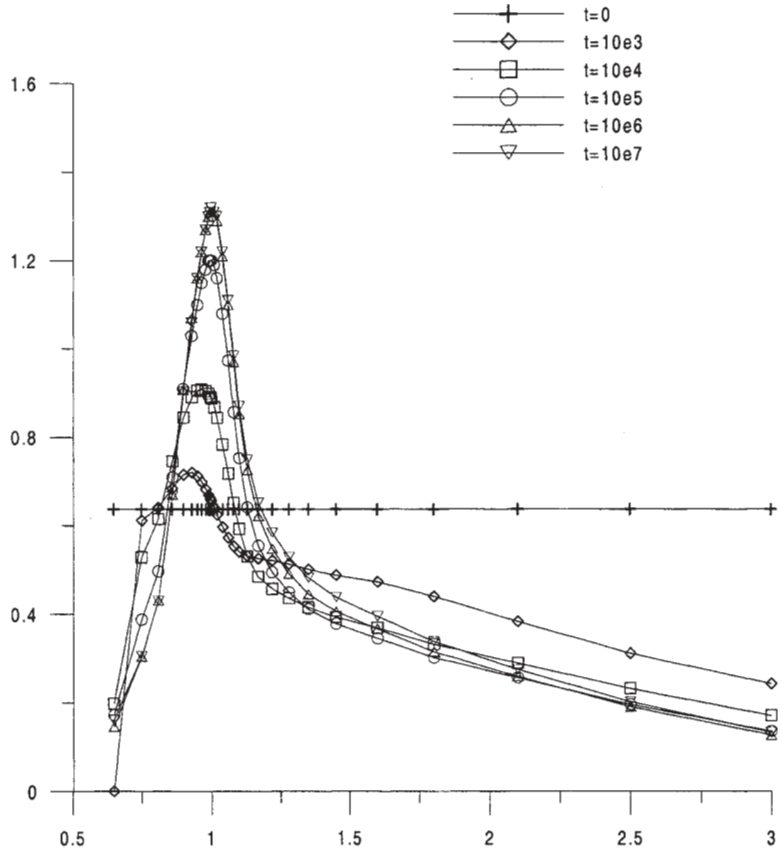

Fig.6
Evolution of parameter D
with the initial value (3.2) - (3.3) and $\gamma = 3.3, n = 2$ at different time moments:
a)- . $\tilde{t} = 0$, b)- $\tilde{t} = 10^3$, c)- $\tilde{t} = 10^5$, d)- $\tilde{t} = 10^7$

The similar results for the initial frequency-angular spectrum (3.2) and (3.4) with $\gamma = 3.3, \quad 2s = 2$ for the following steps of evolution $\tilde{t} \cong 0, 10^4, 10^6, 10^7$ are presented in Fig.7-10. It is interesting to note that at the time moment $\tilde{t} \le 10^4$ the frequency-angular spectrum (Fig.7) varies in such a way that it becomes more isotropic as it is mentioned in the paper (Lavrenov and Ocampo, 1999). It becomes more smooth and round. But later on (at $\tilde{t} \ge 10^5$) it transforms in a more directional form. So the previous suggestion about the spectrum becoming isotropic with initial angular approximation (3.4) is disproved. The spectrum becomes more narrow in a vicinity of its maximum and is wider at low and high frequencies.

An important feature of the nonlinear energy transfer (Fig.8) is the presence of an area with positive values at the direction opposite to the main one of the wave propagation. Due to action of the nonlinear energy transfer the spectrum becomes more isotropic at the first stages of the evolution. Later on this non-linear energy transfer positive area disappears with the spectrum becoming more directional and moving to the low frequency range.

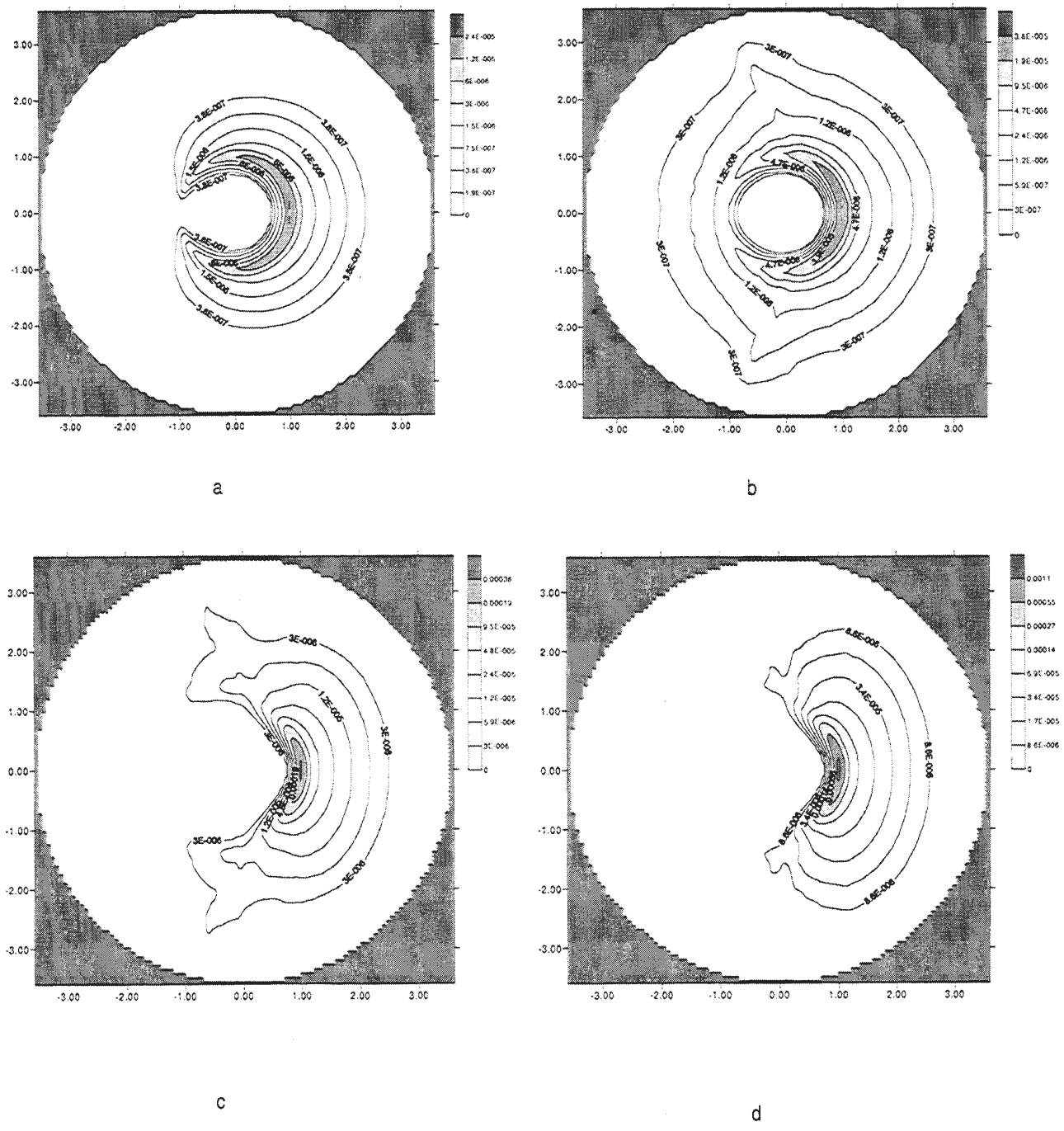

Fig.7
Non-linear two dimensional spectrum evolution
with the initial value (3.2) - (3.4) and $\gamma = 3.3, 2s = 2$ at different time moments:

a)-. $\tilde{t}=0$, b)- $\tilde{t}=10^3$, c)- $\tilde{t}=10^6$, d)- $\tilde{t}=10^7$

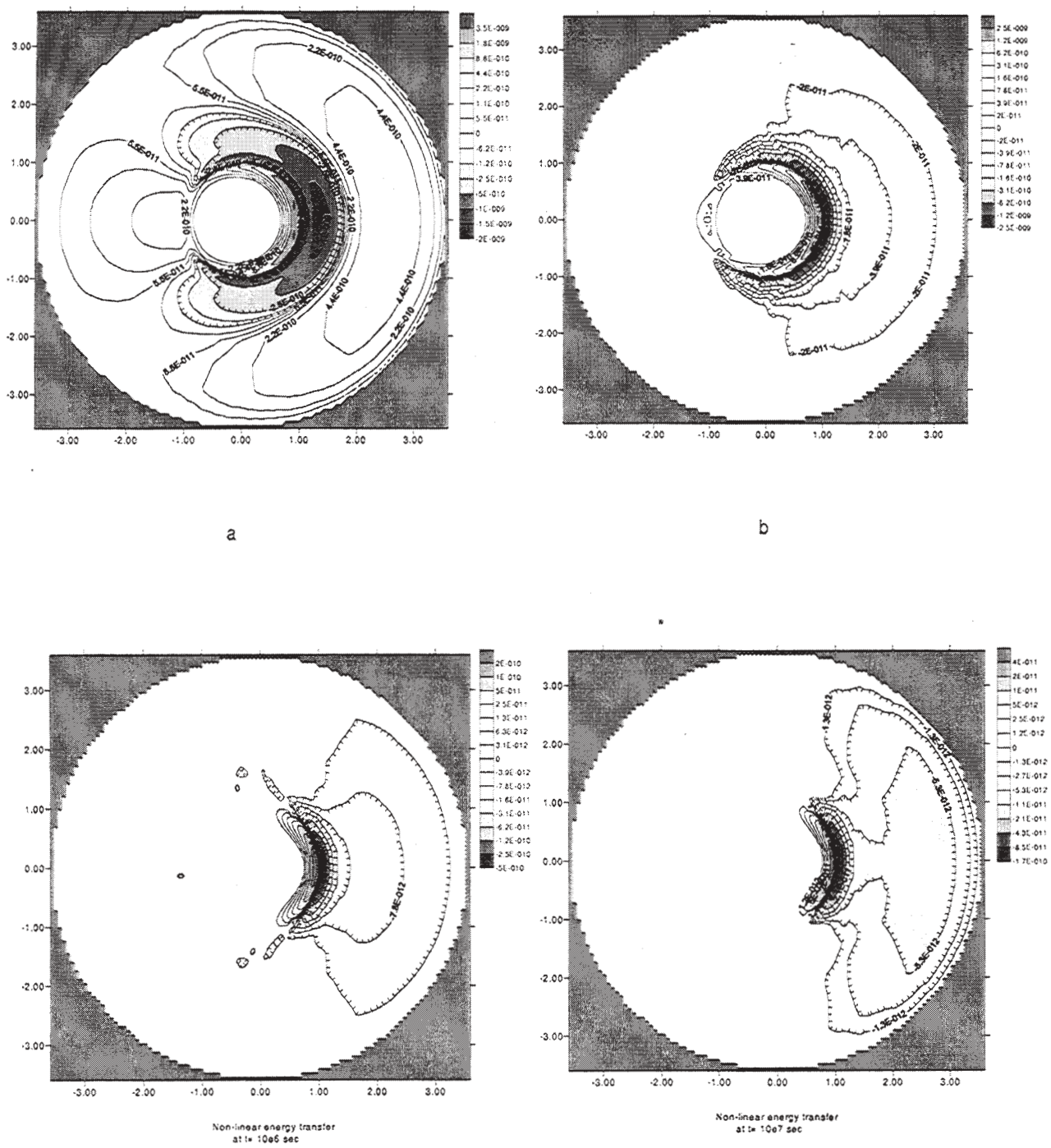

Fig.8
Two dimensional non-linear energy transfer function evolution
with the initial value (3.2) - (3.4) and $\gamma = 3.3,\ 2s = 2$ at different time moments:
.a)- $\tilde{t}=0$, b)- $\tilde{t}=10^3$, c)- $\tilde{t}=10^6$, d)- $\tilde{t}=10^7$

The frequency spectrum is proportional to $S \sim \sigma^{17.}$ at the low frequency range $\sigma_p \succ \sigma$ (Fig.9). The spectrum is proportional to $\sim \sigma^{-6.2}$ within the range $\sigma_p \prec \sigma \prec 1.5\sigma_p$. It decreases in a such way $\sim \sigma^{-3.7}$ at the high frequency range approximately the same as in

AUTHOR INDEX TABLE OF CONTENTS

the isotropic power spectrum (Section 3).

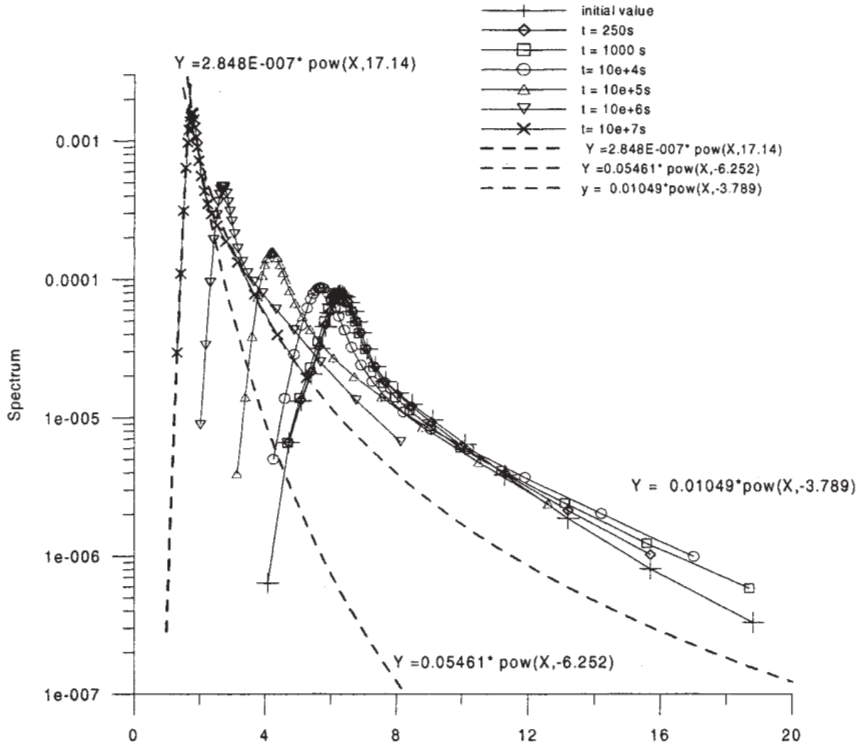

Fig.9
Frequency spectrum evolution
with the initial value (3.2) - (3.4) and $\gamma = 3.3, 2s = 2$ at different time moments:
.a) $\tilde{t} = 0$, b) $\tilde{t} = 10^3$, c) $\tilde{t} = 10^5$, d) $\tilde{t} = 10^7$

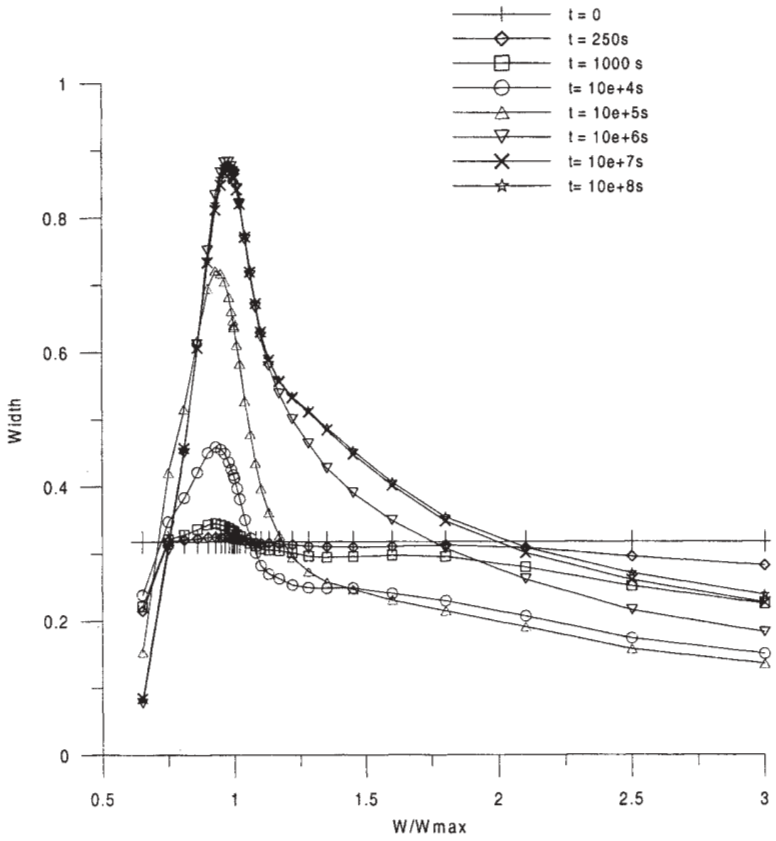

Fig.10
Evolution of the parameter D in time
with the initial value (3.2) – (3.3) and $\gamma = 3.3, n = 2$ atr different time moments:

.a) $\tilde{t}=0$, b) $\tilde{t}=10^3$, c) $\tilde{t}=10^5$, d) $\tilde{t}=10^7$

4.2 Numerical results of integral parameter evolution

The function D (Fig.10). describing the angular narrowness increases in the vicinity of the spectral maximum as it is seen in the previous case (Fig.6). But the function value is smaller

The numerical solutions for all initial spectra (see Tabl. 1) for time duration up to $\tilde{t}=10^7-10^8$ are obtained. The frequency maximum evolution $\sigma_p=\sigma_p(t)$ for all these cases is presented in Fig.11. The frequency maximum shifts to the lower frequency range in this way: $\sigma_p(t)\sim t^{0.1}$

Time evolution of the parameter $B=B(t)$ for all initial conditions is presented in Fig.12. The most important feature of the parameter $B=B(t)$ is the fact that it approaches to the same similar value for all initial conditions. It is approximately equal to $B\approx 1/3$. (the "Law of $1/3$").

As it is shown by the numerical results, not only the parameter B, but also the parameter D_p approach to some constant values for all initial spectra. The digital final values of the parameters B and D_p for the all initial spectra conditions are presented in the Table 2.

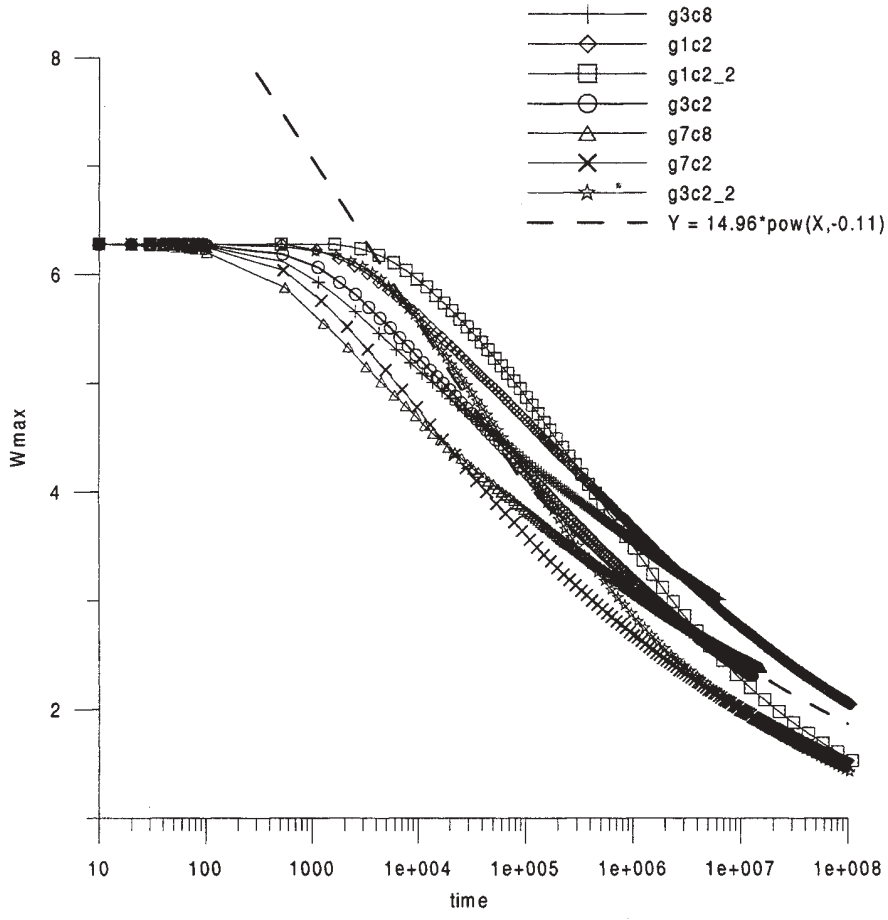

Fig.11

Frequency maximum evolution for different initial spectra parameters

(see Tabl.1)

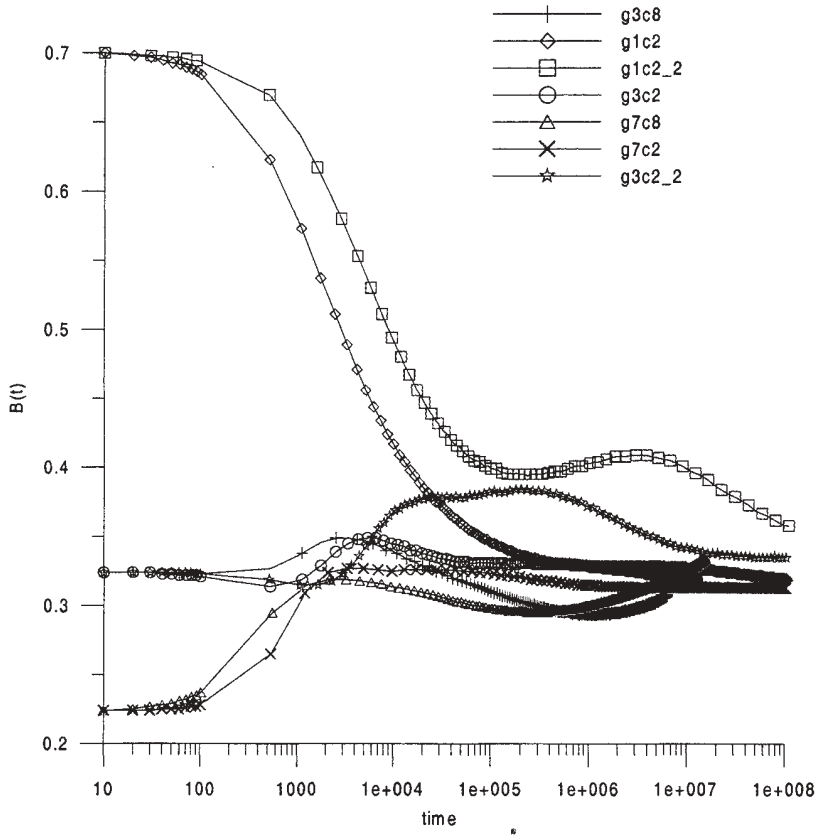

Fig. 12

Parameter • time evolution for different initial spectra

Table 2

Final values of the parameters B and D_p for all initial spectra conditions

γ	$2s=2$		$n_\beta=2$		$n_\beta=8$	
	B	$D_{\max}$	B	$D_{\max}$	B	$D_{\max}$
1.0	0.358	0.988	0.328	1.31	0.330	1.29
3.3	0.342	0.899	0.320	1.32	0.321	1.12
7.0	0.342	0.963	0.313	1.31	0.326	1.09

5. INTERMIDIATE SELF-SIMILAR FREUQENCY SPECTRUM APPROXIMATION

As it is shown by the numerical result, the spectrum reveals itself as a self-similar solution at large time of non-linear evolution. It is possible to assume that the frequency spectrum does not depend on the features of the initial spectrum, but it should depends on the frequency maximum σ_p, time t, total energy E and wave action A. Thus the frequency spectrum S can be presented as a following function

$$S = S(\sigma, \sigma_p, t, E, A) \qquad (5.1)$$

Using the Π - theorem (Barenblatt, 1984) it is possible to define self-similar approximation as a function of undimensional parameters in the following form:

$$\frac{\sigma\, S(\sigma)}{E} = F\left(\frac{\sigma}{\sigma_p}, t\sigma_p, \frac{A\sigma_p}{E}\right) \qquad (5.2)$$

where E – is a total energy, F is a function to be defined.

The number of variables in (5.2) can be diminished using the dependence between frequency maximum and time $\sigma_p = \sigma_p(t)$. In order to satisfy to numerical result in the main frequency range $0.5\sigma_p \prec \sigma < 1.5\sigma_p$, the function F can be defined in the following way:

$$F = (n+1)\left(\frac{\sigma_p}{\sigma}\right)^n \exp\left(-\frac{n+1}{n}\left(\frac{\sigma_p}{\sigma}\right)^n\right) \quad (5.3)$$

where n is a new undimensional parameter, which is a function of the value $n = n(A\sigma_p/E)$. As it is shown by the numerical results, the value n is estimated as $n \approx 5 \div 7$. It should be noted that integrating the spectrum (A.1) with (A.2) within the frequency range gives the total energy value E. . It provides the total energy preservation in the process of non-linear spectrum evolution with frequency maximum variation $\sigma_p = \sigma_p(t)$.

In order to define the n value, the total wave action A can be used as a moment of the –1 power:

$$A = m_{-1} = \int_0^\infty \sigma^{-1} S(\sigma) d\sigma = E\sigma_p^{-1}\left[\frac{n+1}{n}\right]^{-1/n} \Gamma\left(1+\frac{1}{n}\right) \quad (5.4)$$

where $\Gamma(n)$ is the gamma-function. For $n \geq 4$, the value A is estimated as:

$$A \cong E\sigma_p^{-1} e^{-C/n} \quad (5.5)$$

where • is the Eiler's constant • $=0.5772157$.

The value A preserves itself and the parameter n slowly varies in the process of changing the frequency maximum:

$$n \approx -C/\ln(A\sigma_p/E) \quad (5.6)$$

Using the approximation (A.1) with (A.2), the frequency narrowness parameter (3.5) can be defined as:

$$B = E/S(\sigma_p)\sigma_p = \exp\left(\frac{n+1}{n}\right)\Big/(n+1) \quad (5.7)$$

Due to changing the n parameter from 4 to 8, the value B is varied within the range from 0.69 to 0.34. This estimation approximately correspondences with the numerical results, obtained in the paper.

Thus it can be assumed that the expression (5.2) with (5.3)-(5.6) describes the intermediate self-similar approximation of the frequency spectrum. It preserves the total energy and the wave action.

CONCLUSION

The problem of non-linear spectral evolution based on the K.Hasselman's equation is solved for a large time of evolution. In order to solve the problem the most optimal numerical algorithm of the non-linear energy transfer computation (Lavrenov 1991,1998) is used. It is shown that the non-linear spectrum evolution can be described by variation of different features. The numerical results allow to reveal some general features common for all cases of the spectrum evolution. They can be defined as:

1) due to action of the non-linear energy transfer all frequency–angular spectra approach in time to some general form depending on the initial conditions with its spectrum maximum shifts to a low frequency range;
2) the most definite features are revealed for frequency spectrum $S(\sigma)$ and function of the angular narrowness $D(\sigma)$;
3) the sharp peak maximum with enough steep low and high frequency ranges is shown in the frequency spectra $S(\sigma)$, with a low frequency range $\sigma \prec \sigma_p$ approximated by the dependence $S(\sigma) \sim \sigma^{-16.5\pm0.5}$, whereas within the range $\sigma_p \prec \sigma \prec 1.5\sigma_p$ the spectrum is approximated as $S(\sigma) \sim \sigma^{-6,5\pm0.5}$;
4) the frequency spectrum decreases as $S(\sigma) \sim \sigma^{-3,2\pm0.5}$ at the high frequency range $\sigma \succ 1.5\sigma_p$, with the frequency power depending on the angular energy distribution of the initial spectrum;
5) the frequency narrowness of the value • is established as 0.33 ±0.02 ("the Law of $1/3$") and is practically not dependent on an initial spectral form;
6) the function of the angular narrowness $D(\sigma)$ reveals a sharp maximum in the vicinity of the frequency spectral maximum, with its value becoming smaller at the range of low and high frequency ranges;
7) the maximum of the parameter D_p is established within the range : $D_p = 0.9 \div 1.3$, depending on the initial angular narrowness $D_p(t=0)$...

As it is shown by the numerical computation results the self-similar spectrum is established in the process of the non-linear evolution. It is revealed as an establishment of the parameter values B and D_p, and a total form of the spectrum. It has two main domains: a sharply defined peak and a slow decreasing high frequency tail. It should be noted that the Kolmogorov's spectrum $S(\sigma) \sim \sigma^{-4.0}$, numerically found out in the paper (Kamutsu and Masuda 1996), is not realised in all initial conditions. Using these numerical results a simplified intermediate self-similar frequency spectrum approximation is offered (5.2). This approximation descries the main features of the non-linear spectrum evolution and provides a preservation of the total energy and wave action.

Acknowledgement. The author is thankful to Dr.V.Polnikov for fruitful discussion. The paper is supported by the INTAS-666 (1999) "Estimation of Extreme Metoocean Events" Project and by the "World Ocean" Federal Objective Programm-III of the Russian Federation.

REFERENCE

Hasselmann K. On the non-linear energy transfer in a gravity wave spectrum. Part 1. 1962 - *J.Fluid Mech.*,Vol.12. p.481—500.

Hasselmann K. 1965 On the nonlinear energy transfer in a gravity-wave spectrum. Conservation theorem, wave particle correspondence, irreversibility - *J. Fluid Mech.*Vol.15. p.273—281.

Hasselmann, K. et al., 1973: Measurements of wind-waves growth and swell decay during the Joint North Sea Wave Project (JONSWAP). Hamburg: Deutsch. Hydrogr. Inst, p.1—95.

Hasselmann, S., K. Hasselmann, 1981: A symmetrical method of computing the nonlinear transfer in a gravity wave spectrum. - *J. Hamburger Geophys. Einzelschrifte*, A **52**.

Hasselman, S., K. Hasselman, 1985: Computations and parametrizations of the non-linear energy transfer in gravity-wave spectrum. Part 1. A new method of the nonlinear energy transfer integral. *J.Phys. Oceanogr.* , **15**, p.1369-1377.

Komatsu K., Masuda A. 1996 A new Scheme of Nonlinear Energy Transfer among Wind Waves: RIAM Method – Algorithm and Perfomance - *Journal of Oceanology.*, V. 52. p. 509-537.

Komen G.J., Cavaleri L., Donelan M., Hasselmann K., Hasselmann S., Janssen P.A.E.M. 1994 Dynamics and Modelling of Ocean Waves. —Cambridge: University Press, 532 p.

Lavrenov I.V., 1991a: Non-linear interaction in rips spectrum. - *Izv. Acad. Sci. USSR. Atmos. and Oceanic Phys.*, **27**, No. 4, 438—447. Lavrenov, I.V.,

1991b: Non-linear evolution of wave spectrum in shallow water area - *Izv. Acad. Sci. USSR. Atmos. and Oceanic Phys.*, **27**, No. 12, 1373—1378.

Lavrenov I. V., 1998: Mathematical modelling of wind waves at non-uniform ocean. St.Petersburg, Gidrometeoizdat, p.1—500 (in Russian).

Lavrenov I.V., • • ampo-Torres F.J. 1999 Non-linear energy generation of waves opposite to the wind direction. – The wind-driven air-sea interface. Proceedings of the the symposium on the wind-driven air-sea interface. Sydney, Australia, 11-15 January 1999, 141-150p.

Masuda A. 1981 Non-linear energy transfer between wind waves - J. Phys. Oceanogr.Vol.10., p.2082—2093

Polnikov, V.G. 1989: Calculation of non-linear energy transfer by surface gravitational waves spectrum. - *Izv. Acad. Sci. USSR. Atmos. and Oceanic Phys.*, Vol. **25**, 1214—1225.

Polnikov, V.G. 1990: Numerical study of the kinetic equation for surface gravity waves. - *Izv. Acad. Sci. USSR. Atmos. and Oceanic Phys.*, Vol. **26**, N2, 168—176.

Polnikov, V.G. 1993: Numerical formation of flux spectrum of surface gravity waves. - *Izv. Acad. Sci. USSR. Atmos. and Oceanic Phys.*, Vol. **29, N6, p.** 1214—1225.

Polnikov, V.G. 1999: Numerical study of the equation of non-linear swell in the directional approximation.- *Izv. Acad. Sci. USSR. Atmos. and Oceanic Phys.*, Vol. 35, N3, p.364-370.

Resio, D. and W. Perrie, 1991: A numerical study of non-linear energy flux due to wave-wave interaction. Part 1. Methodology and basic results.- *J. Fluid Mech.*, **223**, 603—629.

Snyder, R.L., W.C. Thacker, K. Hasselmann, S. Hasselmann and G. Barzel, 1993: Implementation of an efficient scheme for calculating nonlinear transfer from wave-wave interaction.- *J. Geoph. Res.*, **98**, 14507—145245.

Tolman H.L. 1992 Effects of numeric on the physics in a third –generation wind wave model. – *Journal f Physical Oceanography*, 22, p.1095-1111.

WAMDI group "The WAM model — a third generation ocean wave prediction model" 1988 - *J.Phys.Ocean.* Vol.12., p..1775—1810.

Webb D.J. 1978 Non-linear transfer between sea waves - *Deep-Sea Research* .Vol.25. p.279—298.

Zakharov, V.Ye., 1968: Stability of periodic waves of final amplitude on a deep liquid surface. - *PMTF*, **2**, 86—94.

Zakharov V.E. and Filonenko N.N. 1966. The energy spectrum for stochastical oscillation of fluid surface. - *Doklady Acad. Nauk SSSR*, 170, N6,, p.1292-1295.

Zakharov V.E., Smilga A.V. 1981 About quasi-onedimentional spectrum of weak turbulence . *JATF* , 18 N4, p.1318-1326.

Zakharov, V.E. and Zaslavskii, M.M. (1982) The kinetic equation and Kolmogorov's spectra in the weakly turbulent theory of wind waves. *Izv. AN SSSR, ser. Physics of Atmosph. and Ocean,* v. 18, N 9, p.970-979.

Zakharov, V.E. and Zaslavskii, M.M. (1983) Dependence of wave parameters on wind speed, duration of its action, and fetch in a weakly-turbulent theory of wind waves. Ibid., v. 19, N 4, p. 406-416.

Zaslavskii • .• . 1989 About narrow directional approach of the kinetic equation for wind wave.- *Izv. AN SSSR ser. Physics of Atmosph. and Ocean,* v. 25, N 4, p.402-410.

Zaslavskii • .• . 2000 Non-linear evolution of swell spectrum. - *Izv. AN RAS, ser. Physics of Atmosph. and Ocean,* v. 36, N 2, p.275-283.

On conservation of the constants of motion in the models of nonlinear wave interaction.

A.Pushkarev, V.Zakharov

1. Introduction

One of the central problem of the development of the operational models for sea-wave prediction is an adequate description of nonlinear wave interaction. So far, the most solidly justified approach to this description is the use of the kinetic equation for the spectral density of wave action first derived by K.Hasselmann in 1962. Since this time, several codes for numerical simulation of nonlinear wave interaction were developed (Webb 1978, Masuda 1980, Hasselmann and Hasselmann 1981, Resio and Perrie 1991, Polnikov 1994, Lavrenov 1998, Komatsu and Masuda 1996, Van Vledder 1999, etc).

Nonlinear wave interaction is described by a complicated nonlinear integral operator and its numerical simulation is a tricky problem. All existing algorithms for its simulation are cumbersome and time consuming. So far, they are too slow to be directly used in practical operational models of wave prediction. Therefore, the development of faster approximate models of the nonlinear wave interaction is a very urgent problem.

The mostly common approximate model is DIA (Discrete Interaction Approximation), known also as the WAM method. Hasselmann and Hasselmann offered it in 1985. In this model, the integral operator in S_{nl} is replaced by a sum consisting of few discrete terms. Zakharov and Pushkarev proposed quite another approximate model, based on the use of the nonlinear diffusion operator in 1999.

To estimate the quality of an approximate model one should compare its prediction with the results of numerical simulation in the framework of the "exact" kinetic equation. To make this comparison reliable on should be sure that the " exact" model is good enough to be a paragon for such test. Actually, the real criteria for examination of quality of such models are absent.

Different schemes for numerical solution of the Hasselmann kinetic equation give qualitatively similar, but quantitatively slightly different results, and there was no so far a standard way for estimation of their reliability. This circumstances makes the problem of construction of fast approximate models of nonlinear wave interaction difficult and uneasy. One cannot believe in an approximate model if one cannot compare it with a real good standard for calibration.

Meanwhile there is a natural way for examination of numerical method for solution of the wave kinetic equation. This is the control of conservation of the basic constants of motion - wave action, energy, and two components of momentum. Similar approach is widely used in applied mathematics in the case when physical situation is described by conservative ordinary or partial differential equations.

In the case of nonlinear wave interaction, the situation is more complicated. It is described by not differential, but by the integral operator, which is non-local in the k-space. Any scheme of numerical integration of the kinetic equation operates in some finite domain of this space, always bounded in frequency and sometimes limited in angle. Integrals of motion, contained in any bounded domain are not conserved; the non-linear wave interaction carries them out of the domain. Due to non-locality of the S_{nl} operator, this leakage cannot be interpreted just as a flux through a boundary of the domain. The loss of the motion constants from finite domains is not a mathematical abstraction. Its is a real and a very strong physical effect. In many cases, the transport of motion constants is the major mechanism defining shape of spectra. For instance, a typical asymptotic behavior of energy spectrum at large frequency $\mathrm{E}_f \propto f^{-4}$ is the result of constant transport of wave energy to the large frequency region.

In this article, we propose a modified method of calculation of conservation of the motion constant in finite domain making possible to take into consideration the leakage outside a domain. We call it "clean

test", which allows accurate estimation of the quality of any algorithms for numerical solution of the wave kinetic equation.

2. Are the constants of motion really conserved?

In the absence of pumping from the wind and dissipation the Hasselmann equation reads:

$$\frac{\partial n}{\partial t} = S_{nl} \tag{2.1}$$

$$S_{nl} = \int |T_{kk_1k_2k_3}|^2 \, \delta(k + k_1 - k_2 - k_3)\delta(\omega_k + \omega_{k_1} + \omega_{k_2} + \omega_{k_3}) \times (n_{k_1} n_{k_2} n_{k_3} + n_k n_{k_2} n_{k_3} - n_k n_{k_1} n_{k_2} - n_k n_{k_1} n_{k_3}) dk_1 dk_2 dk_3 \tag{2.2}$$

It is considered that equation preserves the following constants of motion

$$N = \int n d\vec{k} \text{ - Wave action} \tag{2.3}$$

$$E = \int \omega_k n_k d\vec{k} \text{ - Energy} \tag{2.4}$$

$$\vec{M} = \int \vec{k} n_k d\vec{k} \text{ - Momentum} \tag{2.5}$$

Are these constants really constant? To prove conservation of these integrals, one must prove validity of following identities:

$$\frac{\partial N}{\partial t} = \int S_{nl} d\vec{k} = 0 \tag{2.6}$$

$$\frac{\partial E}{\partial t} = \int \omega_k S_{nl} d\vec{k} = 0 \tag{2.7}$$

$$\frac{\partial \vec{M}}{\partial t} = \int \vec{k} S_{nl} d\vec{k} = 0 \tag{2.8}$$

These identities are trivial if one can change the order of integration by different k_i. If this operation is possible, one can transform, for instance, the expression (2.7) to the form

$$\int \omega_k S_{nl} dk = \int (\omega_k + \omega_{k_1} + \omega_{k_2} + \omega_{k_3}) \delta(k + k_1 - k_2 - k_3) \delta(\omega_k + \omega_{k_1} + \omega_{k_2} + \omega_{k_3}) n_{k_1} n_{k_2} n_{k_3} dk_1 dk_2 dk_3 \tag{2.9}$$

As it is known from the classical calculus, the operator of change of the integration order in improper integrals is allowed if the integrand decays fast enough at infinity. Let us consider this question in detail.

In equation (2.2), as well as in formulae (2.3)-(2.9), the integration is going on the infinite domain. In reality, both in experiment and in computer modeling the domain of integration is finite. Thus to check the identities (2.6)-2.8) we should first consider a finite domain. This is a quite nontrivial procedure. Suppose that the domain of integration is finite

$$|k| < p \tag{2.10}$$

One can denote

$$n_k^p = \begin{cases} n_k, |k| < p \\ 0, |k| > p \end{cases} \tag{2.11}$$

By plugging n_k^p instead of n_k into S_{n1} one get by definition $S_{n1} \to S_{n1}^{(p)}$. Apparently integrand in $S_{n1}^{(p)}$ has bounded support and change of order of integration is permitted at any value of p. Hence

$$\begin{aligned} \int S_{nl}^{(p)} dk &= \int_{|k|<p} S_{nl}^{(p)} dk + \int_{|k|>p} S_{nl}^{(p)} dk = 0 \\ \int \omega_k S_{nl}^{(p)} dk &= \int_{|k|<p} \omega_k S_{nl}^{(p)} dk + \int_{|k|>p} \omega_k S_{nl}^{(p)} dk = 0 \\ \int \vec{k} S_{nl}^{(p)} dk &= \int_{|k|<p} \vec{k}\omega_k S_{nl}^{(p)} dk + \int_{|k|>p} \vec{k} S_{nl}^{(p)} dk = 0 \end{aligned} \tag{2.12}$$

Let us denote

$$N^p = \int_{|k|<p} n dk\,, \quad E^p = \int_{|k|<p} \omega_k n_k dk\,, \quad \vec{M}^p = \int_{|k|<p} \vec{k} n_k dk$$

Now one can find balance of the motion constants in the domain $|k| < p$

$$\begin{aligned} \frac{\partial N^{(p)}}{\partial t} &= \frac{\partial}{\partial t} \int_{|k|<p} n_k dk = \int_{|k|<p} S_{nl}^{(p)} dk = -\int_{|k|>p} S_{nl}^{(p)} dk = -Q(p) \\ \frac{\partial E^{(p)}}{\partial t} &= \frac{\partial}{\partial t} \int_{|k|<p} \omega_k n_k dk = \int_{|k|<p} \omega_k S_{nl}^{(p)} dk = -\int_{|k|>p} \omega_k S_{nl}^{(p)} dk = -P(p) \\ \frac{\partial \vec{M}^{(p)}}{\partial t} &= \frac{\partial}{\partial t} \int_{|k|<p} \vec{k} n_k dk = \int_{|k|<p} \vec{k} S_{nl}^{(p)} dk = -\int_{|k|>p} \vec{k} S_{nl}^{(p)} dk = -\vec{K}(p) \end{aligned} \tag{2.13}$$

Last integrals in (2.13) can be calculated by the use of identity (2.11). In (2.13) Q, P and $\vec{K}$ are the values of the "losses" of the constants of motion. One can present S_{nl} in the following form

$$S_{nl}(k) = F_k - \gamma_k n_k \tag{2.14}$$

$$F_k = \int |T_{kk_1k_2k_3}|^2 \delta(\omega_k + \omega_{k_1} + \omega_{k_2} + \omega_{k_3}) \delta(\vec{k} + \vec{k}_1 + \vec{k}_2 + \vec{k}_3) \times n_{k_1} n_{k_2} n_{k_3} dk_1 dk_2 dk_3 \tag{2.15}$$

$$\gamma_k = \int |T_{kk_1k_2k_3}|^2 \delta(\omega_k + \omega_{k_1} + \omega_{k_2} + \omega_{k_3}) \delta(\vec{k} + \vec{k}_1 + \vec{k}_2 + \vec{k}_3) \times (n_{k_1} n_{k_2} + n_{k_1} n_{k_3} - n_{k_2} n_{k_3}) dk_1 dk_2 dk_3 \tag{2.16}$$

By definition

$$S_{nl}^{p}(k) = F_k^{(p)} - \gamma_k^{(p)} n_k^p \tag{2.17}$$

$$F_k^{(p)} = \int\limits_{|k_1|<p,|k_2|<p,|k_3|<p} |T_{kk_1k_2k_3}|^2 \delta(\omega_k + \omega_{k_1} + \omega_{k_2} + \omega_{k_3}) \delta(\vec{k} + \vec{k}_1 + \vec{k}_2 + \vec{k}_3) \times n_{k_1} n_{k_2} n_{k_3} dk_1 dk_2 dk_3 \tag{2.18}$$

$$\gamma_k^{(p)} = \int\limits_{|k_1|<p,|k_2|<p,|k_3|<p} |T_{kk_1k_2k_3}|^2 \delta(\omega_k + \omega_{k_1} + \omega_{k_2} + \omega_{k_3}) \delta(\vec{k} + \vec{k}_1 + \vec{k}_2 + \vec{k}_3) \times (n_{k_1} n_{k_2} + n_{k_1} n_{k_3} - n_{k_2} n_{k_3}) dk_1 dk_2 dk_3 \tag{2.19}$$

One should mention that $S_{nl}^{p}(k) \neq 0$ at $|k| \rhd p$. As far as $n_k^p = 0$ at $|k| \rhd p$, one has:

$$S_{nl}(k) = F_k^p, \; |k| \rhd p \tag{2.20}$$

Formula (2.20) is extremely important. It expresses the following clear physical fact: the income term F_k^p is nonzero far beyond the domain of $|k| < p$ where the wave spectrum is concentrated. Meanwhile $F_k^p \neq 0$ only in a finite domain. Indeed, vector $\vec{k}$ satisfies the conditions

$$\vec{k} = \vec{k}_2 + \vec{k}_3 - \vec{k}_1 \tag{2.22}$$

$$\omega_k = \omega_{k_2} + \omega_{k_3} - \omega_{k_1} \tag{2.23}$$

and $|k_1| < p, |k_2| < p, |k_3| < p$.

Conditions (2.22), (2.23) can be satisfied only for

$$|k| < p_{\max} \tag{2.24}$$

Here $p_{\max} = f(p)$ - some upper limit depending on a shape of ω_k. One can get some apriori estimate for $p_{\max}$. From (2.22) one can get

$$p_{\max} < 3p \tag{2.25}$$

From (2.23) one obtains

$$\omega_{p_{\max}} < 2\omega_p \tag{2.26}$$

More accurate estimate for $p_{\max}$ is defined by ω_k and depends on the depth. On the infinite depth $\omega_k = \sqrt{gk}$ and $p_{\max}$ is achieved if

$$\vec{k}_2 = \vec{k}_3,\ \vec{k}_1 = -\frac{1}{4}\vec{k}_2,\ |\vec{k}_2| = p \tag{2.27}$$

In this case

$$p_{\max} = \frac{9}{4}p \tag{2.28}$$

$$\omega_{p_{\max}} = \frac{3}{2}\omega_p \tag{2.29}$$

Introducing polar coordinates in $\vec{k}$ -pane, we have the following expressions for losses (rates of leakage) of the constants of motion from the domain $|k| > p$

$$\begin{aligned}
Q(p) &= \int_p^{p_{\max}} pdp \int_0^{2\pi} F^p(p,\theta)d\theta \\
P(p) &= \int_p^{p_{\max}} p\omega_p dp \int_0^{2\pi} F^p(p,\theta)d\theta \\
K_x(p) &= \int_p^{p_{\max}} p^2 dp \int_0^{2\pi} F^p(p,\theta)\cos\theta d\theta \\
K_y(p) &= \int_p^{p_{\max}} p^2 dp \int_0^{2\pi} F^p(p,\theta)\sin\theta d\theta
\end{aligned} \tag{2.30}$$

3. Clean test for integrals conservation

Now we can answer the question about real conservation of the integrals. If the domain is finite, they are never preserved. It is obvious from (2.30) that in all cases

$$Q(p) > 0,\ P(p) > 0 \tag{3.1}$$

Thus, wave action and energy always leak out of the domain $|k| < p$. In most cases, wave spectrum is concentrated in the right half-plane $-\frac{\pi}{2} < \theta < \frac{\pi}{2}$, $\cos\theta > 0$. In this situation $K_x(p) > 0$, the sign of $K_y(p)$ can be arbitrary.

Suppose again that

$$n_k = 0,\ |k| > p \tag{3.2}$$

We showed that

$$\frac{\partial n}{\partial t} = S_{nl}^{(p)}(k) = F^{(p)}(k) > 0 \tag{3.3}$$

if $|k| < p_{\max}$.

Hence, from physical viewpoint condition (3.2) is artificial. If it is satisfied in the initial moment of time, it will be immediately violated. In the close moment of time δt

$$n = n_0 + S_{nl}^p(k) \cdot \delta t \tag{3.4}$$

n becomes positive in the whole domain $|k| < p_{\max}$.

Anyway, the consideration we performed is useful. It can be used as a foundation for a "clean" test for all codes for numerical solution of the kinetic wave equation.

If condition (3.2) is satisfied

$$\frac{\partial n}{\partial t} = 0 \quad \text{if } |k| > p_{\max} \tag{3.5}$$

Hence

$$\begin{aligned}
&\frac{\partial}{\partial t} \int_{|k|<p_{\max}} S_{nl}^p dk \Big|_{t=0} = 0 \\
&\frac{\partial}{\partial t} \int_{|k|<p_{\max}} \omega_k S_{nl}^p dk \Big|_{t=0} = 0 \\
&\frac{\partial}{\partial t} \int_{|k|<p_{\max}} \vec{k} S_{nl}^p dk \Big|_{t=0} = 0
\end{aligned} \tag{3.6}$$

Conditions (3.6) can be rewritten in polar coordinates as

$$\begin{aligned}
&\frac{\partial}{\partial t} \int_0^{p_{\max}} p dp \int_0^{2\pi} S_{nl}^{(p)} d\theta \Big|_{t=0} = 0 \\
&\frac{\partial}{\partial t} \int_0^{p_{\max}} \omega_p p dp \int_0^{2\pi} S_{nl}^{(p)} d\theta \Big|_{t=0} = 0 \\
&\frac{\partial}{\partial t} \int_0^{p_{\max}} p^2 dp \int_0^{2\pi} S_{nl}^{(p)} \cos\theta d\theta \Big|_{t=0} = 0 \\
&\frac{\partial}{\partial t} \int_0^{p_{\max}} p^2 dp \int_0^{2\pi} S_{nl}^{(p)} \sin\theta d\theta \Big|_{t=0} = 0
\end{aligned} \tag{3.7}$$

Condition (3.7) can be relatively easily checked for any numerical code used for solution of the kinetic equation. To check the quality of the code one should put the initial data $n_k > 0$ at $|k| < p_{\max}$. Expansion of the integration domain is the price to be paid for nonlocality of the four-wave interactions.

Relations (2.13) can be generalized to the case when there is the interaction with wind and damping. Now kinetic equation (2.1)-(2.2) reads

$$\frac{\partial n}{\partial t} = S_{nl} + \beta_k n_k \tag{3.9}$$

where β_k is growth-rate of the instability or the damping depending on the sign. Equations (2.6)-(2.8) now should be replaced by the following relations:

$$\begin{aligned} \frac{\partial N}{\partial t} &= \int \beta_k n_k dk \\ \frac{\partial E}{\partial t} &= \int \omega_k \beta_k n_k dk \\ \frac{\partial \vec{M}}{\partial t} &= \int \vec{k} \beta_k n_k dk \end{aligned} \tag{3.10}$$

Relations (3.10) are formal and for a finite domain should be deciphered in a proper way. To do that one can assume

$$\beta_k = -A\,,\ A \to \infty\,,\ |k| \rhd p$$

In the domain $|k| \rhd p$ one can neglect the time derivative $\frac{\partial n}{\partial t}$ and put

$$S_{nl} - \beta_k n_k = F_k^p - (\gamma_k + A) n_k = 0$$

As far as $\gamma_k << A$, one can consider approximately ($|k| \rhd 1$)

$$n_k = \frac{F_k^{(p)}}{A} \tag{3.11}$$

By plugging (3.11) into (3.10) one notice that the value of A is cancelled from the equations, taking the form

$$\begin{aligned} \frac{\partial N^p}{\partial t} &= -\int_{|k|<p} \beta_k n_k dk - Q \\ \frac{\partial E^p}{\partial t} &= -\int_{|k|<p} \omega_k \beta_k n_k dk - P \\ \frac{\partial \vec{M}}{\partial t} &= -\int_{|k|<p} \vec{k} \beta_k n_k dk - \vec{K} \end{aligned} \tag{3.12}$$

Equations (3.12) are the balance equations which also could be used to control numerical codes. One should either specially program the calculation of the losses $Q, P, \vec{K}$ or extend the integration domain to $|k| = p_{\max}$.

4. Estimates for integral losses.

Suppose that spectral density of wave action $n(k)$ has the maximum at $k \approx k_0$ and $p >> k_0$. Let us estimate in this limit the losses Q, P and $\vec{K}$. Integrals (2.30) consist of two parts. One part is given by integration in a small domain $p' \cong p + \delta p$, $\delta p \le k_0$. In this domain, integration by k_1, k_2 is performed over the vicinity of the spectral maximum k_0. Thus

$$\begin{aligned} Q &= Q^{(1)} + Q^{(2)} \\ P &= P^{(1)} + P^{(2)} \\ \vec{K} &= \vec{K}^{(1)} + \vec{K}^{(2)} \end{aligned} \tag{4.1}$$

Here

$$\begin{aligned} Q^{(1)} &\cong \frac{n(p)n^2(k_0)}{\omega(k_0)} \cdot \left|T_{p,k_0,p,k_0}\right|^2 k_0^6 \\ P^{(1)} &\cong \frac{\omega(p)}{\omega(k_0)} n(p)n^2(k_0) \cdot \left|T_{p,k_0,p,k_0}\right|^2 k_0^6 \\ K^{(1)} &\cong \frac{p}{\omega(k_0)} n(p)n^2(k) \cdot \left|T_{p,k_0,p,k_0}\right|^2 k_0^6 \end{aligned} \tag{4.2}$$

Other part of contribution in (4.1) is given by integration in the domain $p' \cong p$. In this case, all wave vectors in (2.18) have the same order of magnitude. Hence

$$\begin{aligned} Q^{(2)} &\cong \frac{n^3(p)}{\omega(p)} \cdot \left|T_{p,p,p,p}\right|^3 p^6 \\ P^{(2)} &\cong n^3(p)\left|T_{p,p,p,p}\right|^3 p^6 \\ K^{(2)} &\cong \frac{p}{\omega(p)} n^3(p) \cdot \left|T_{p,p,p,p}\right|^2 p^6 \end{aligned} \tag{4.3}$$

We consider now the case of deep fluid. In this case $\omega(p) \cong g^{1/2} p^{1/2}$

$$\begin{aligned} T(p,p,p,p) &\cong p^3 \\ T(p,k_0,p,k_0) &\cong k_0^2 p \end{aligned} \qquad k_0 << p \tag{4.4}$$

We will consider that $n(k)$ is a powerlike function

$$n(k) \cong k^{-s} \tag{4.5}$$

Comparing $Q^{(1)}$ and $Q^{(2)}$ one see that for the case $S > 19/4$ $Q^{(1)} << Q^{(2)}$. The same is correct for other constants of motion. Finally, one obtains

$$\begin{aligned} Q &\cong p^{23/2-3s} \\ P &\cong p^{12-3s} \\ K &\cong p^{25/2-3s} \end{aligned} \tag{4.6}$$

Now we can answer the question about real conservation of the motion constants. All motion constants conserve if

$$n(k) < Ck^{-25/6} \text{ at } k \to \infty \tag{4.7}$$

5. Kolmogorov spectra and their experimental confirmation.

It is known since 1966 (Zakharov, Filonenko) that the stationary equation

$$S_{nl} = 0 \tag{5.1}$$

has isotropic powerlike solutions

$$n_k^{(1)} = C_1 k^{-23/6} \tag{5.2}$$

$$n_k^{(2)} = C_2 k^{-4} \tag{5.3}$$

The physical meaning of this solution becomes clear after plugging (5.2) into (4.6). For $s = 23/6$ Q is the constant while P and K grow in time. Hence, (5.2) is a Kolmogorov spectrum, corresponding to constant flux of wave action from large to small wavenumbers. For such type of asymptotic neither N, E or $\overrightarrow{M}$ are "real" constants of motion.

If $s = 4$ $Q \cong p^{-1/2}$. In this case $Q \to 0$ at $p \to \infty$, and wave action is "a real" constant of motion. Meanwhile, in this case $P = const$. Hence, (5.3) is a Kolmogorov spectrum describing permanent leakage of energy to large wavenumbers. In terms of spectral density of energy spectra (5.2)-(5.3) read

$$E_\omega^{(1)} = a_1 Q^{1/3} \omega^{-11/3} \tag{5.4}$$

$$E_\omega^{(2)} = a_2 P^{1/3} \omega^{-4} \tag{5.5}$$

Here a_1, a_2 are unknown Kolmogorov constants. One can formulate a conjecture that a general physically relevant solution equation

$$n_k = p^{1/3} k^{-4} F\left(\frac{Q}{P}(gk)^{1/2}, \frac{K}{P}(gk)^{-1/2}\right) \tag{5.6}$$

where F is an unknown function of two variables. It can be found explicitly in heuristic "diffusive" model of S_{nl} (Zakharov, Pushkarev 1999).

The spectrum ω^{-4} has the long history. Zakharov and Filonenko found it analytically as a well-hidden exact solution of equation (5.1) in 1966. Both authors lived in the USSR and were not allowed to travel abroad and report their results on international conferences. That was one reason why the paper of Zakharov and Filonenko, published in the leading Russian scientific journal (Doklady Academii Nauk) was almost not noticed.

There was another reason too. In 1958, O.Phillips offered that the spectrum of wind-driven waves is defined completely by wave breaking and has a universal form

$$\varepsilon_\omega \approx \alpha g^2 \omega^{-5} \tag{5.7}$$

Here α is the dimensionless "Phillips constant".

The very idea of Phillips was seminal and productive. A we understand now, situations when spectra of wave turbulence are defined completely by local singularities is rather common (see, for instance, Zakharov, Dias, Pushkarev, Guyenne 2000).

According to original idea of Phillips, spectrum (5.7) is automatically established at $\omega > \omega_0$, where ω_0 is a characteristic frequency of the spectral maximum. All spectral dynamics is just evolution $\omega_0 = \omega_0(t) \to 0$ at $t \to \infty$. In spite of its elegance and simplicity, the initial conjecture of Phillips is not confirmed by experiments. By definition

$$\int_0^\infty \varepsilon_\omega d\omega = \langle \eta^2 \rangle = H^2 \tag{5.8}$$

By integration of (5.7) one obtain

$$H^2 \cong \frac{\alpha g^2}{4\omega^4} \cong \frac{\alpha g^2}{4(2\pi)^4} T^4$$

or

$$H \propto T^2 \tag{5.9}$$

Here $T = 2\pi/\omega_0$ - characteristic period of energy containing waves.

Relation (5.9) can be checked experimentally. It was Yoshiaki Toba who did it. In 1972-73, he published a set of articles, summarizing his long-time experiments on the wind-wave channel in Sendai University. He found that, instead of (5.9), another relation holds:

$$H \propto T^{3/2} \tag{5.10}$$

Moreover, the Phillips constant, supposed to be universal and not depending on the wind velocity, happened to be proportional to the " friction velocity" u_*, characterizing the momentum transfer from air to sea. These facts can be naturally explained if one assume that instead of (5.7), the spectrum has a form

$$\varepsilon_\omega = \beta g u_* \omega^{-4} \tag{5.11}$$

Here β is another dimensionless constant (Toba's constant). Toba made careful measurements of the spectrum tale and found that formula (5.9) describes the spectral asymptotic very well. He found experimentally that the value of β is:

$$\beta = 6.2 \cdot 10^{-2} \tag{5.12}$$

We must stress that Toba was completely unaware about the paper of Zakharov and Filonenko.

After pioneering works of Toba experimental confirmation of ω^{-4} spectrum are mounted. Just a list of authors who observed this asymptotic is impressive: among them Kawai at al. 1977, Kahma 1981, Forristall 1981, Battjes at al 1986, Donelan, Hamilton and Hui 1985, Donelan and Pierson 1987. In 1985 O.Phillips, summarizing all experimental data, criticized his early theory (which, in our opinion, is still a sample of outstanding scientific intuition) and agreed that ω^{-4} is a reality.

Another approach for confirmation of the ω^{-4} spectrum is the numerical experiment. Several groups (see Masuda and Komatsu 1980, 1996; Resio and Perrie 1991; Polnikov 1994, 2000) observed a universal effect. If the initial data in equation (2.1)-(2.2) decay like ω^{-5}, very soon its asymptotic behavior changes to ω^{-4}.

In this connection, we would like to mention especially works of the group of D.Resio. They did not only follow formation of the ω^{-4} spectrum, but also calculated fluxes of energy at $k \to \infty$ and checked that for ω^{-4} the flux is constant in ω.

In conclusion, one can say that the spectrum ω^{-4} is definitely confirmed now by both many experiments as well as many numerical simulation arguments. The spectrum $\omega^{-11/3}$ also is confirmed quite well, but this point is beyond the scope of this article.

5. Why ω^{-4} not ω^{-5}?

The battle between ω^{-4} and ω^{-5} could look strange for a person outside of a narrow community of S_{nl} experts. Nevertheless, this argument makes a serious sense. It is enough to compare the value of the energy loss P in (4.6) for both spectra. For $\varepsilon_\omega \cong \omega^{-4}$ and $s = 4$, P is the constant. . For $\varepsilon_\omega \cong \omega^{-5}$ $s = 9/4$, $P \cong p^{-3/2} \to 0$ at $p \to \infty$.

Another words, for $\varepsilon_\omega \cong \omega^{-5}$ the energy in the wave ensemble is conserved, while in the case $\varepsilon_\omega \cong \omega^{-4}$ it leaks out with a constant rate. This is a very critical difference. Just an elementary analysis of the observational data contradicts the idea that both wave action and energy are conserved. Indeed, all experiments show that the spectral maximum moves in the process of "maturing " to the low wave numbers. At the same time, the spectrum in the asymptotic area $\omega >> \omega_0$ stays almost constant. As far as quanta of waves loose their energy, moving from high to low frequency region, the outlined facts are compatible with the fact of permanent loss of wave energy, existence of the constant flux of energy to high ω and, as a result, to the ω^{-4} asymptotic at $\omega \to \infty$.

Summarizing the facts, one can say that the asymptotic $\varepsilon_\omega \cong \omega^{-5}$ in the weak turbulent regime is a contradiction to the energy conservation law.

Said Aristotle: "You are friend Plato, but the truth is more valuable". We can say
" You are a friend Dr.... but the conservation of energy is more important".

Acknowledgments.

The authors are grateful for the support of US ARMY under the grant DACA 39-99-C-0018 and ONR, under the grant N00014-98-1-0439.

We would like to express our special gratitude to Dr. Donald Resio for numerous discussions.

References

Dias F., Guyenne P., Pushkarev A.N., Zakharov V.E. Wave turbulence in one-dimensional models, Preprint N2000-4, Centre de Mathematiques et del leur Applications, E.N.S.de CACHAN, pp.1-48, 2000

Battjes J.A., Stive M.J. Calibration and verification of a dissipation model for random breaking waves. J.Geophys.Res., 90(C5), pp.9159-9167, 1986.

Donelan M.A., Hamilton J. and Hui W.H. Directional spectra of wind-generated waves, Phil.Trans.Roy.Soc. London, A315, pp.509-562, 1985.

Forristall J.Z. Measurements of a saturated range in ocean wave spectra, J.Geophys.Res., 86, pp.8075-8084, 1981.

Hansen C., Katsaros K.B., Kitaigorodskii S.A., Larsen S.E. The dissipation range of wind-wave spectra observed on a lake, Journ. Phys.Oceanogr., 20, pp.1264-1277, 1990.

Hashimoto N., Tsukuya H. and Nakagawa Y. Numerical computations of the nonlinear energy transfer of gravity-wave spectra in finite water depth, Coastal Engineering Journal, 40, N1, pp.23-40, 1998.

Hasselmann, K. On the nonlinear energy transfer in a gravity wave spectrum. Part 1, J.Fl.Mech., 12 , pp.481-500, 1962.

Hasselmann, K. On the nonlinear energy transfer in a gravity-wave spectrum. Part 2., J.Fl.Mech., 15, pp.273-281, 1963.

Hasselmann S., Hasselmann K., Komen J., Janssen P., Ewing J. and Cardone V. The WAM model – a third generation ocean wave prediction model. J.Phys.Oceanogr., 18, pp. 1775-1810, 1958.

Hasselmann S. and Hasselmann K. , A symmetrical method of computing the nonlinear transfer in a gravity wave spectrum. Hamburger Geophys. Einzelschrifte., Hamburg, p.52-172, 1981.

Hasselmann S., Hasselmann K. and Bartnett T. Computation and parameterization of the nonlinear transfer in a gravity wave spectrum. Part II. J.Phys.Oceanogr., 15, pp.1378-1391, 1985.

Kahma K.K. A study of the growth of the wave spectrum with fetch, J.Phys.Oceanogr., 11, pp.1503-1515, 1981.

Kawai S., Okada K. and Toba Y. Field data support of three-second power law and $gu_*\sigma^{-4}$ spectral form for growing wind waves., J.Oceanog.Soc.Japan, 33, pp.137-150, 1977.

Kitaigorodskii S.A. On the theory of equilibrium range in the spectrum of wind-generated gravity waves, J.Phys.Oceanogr., 13, N5, pp.816-827, 1983.

Kitaigorodskii S.A. The equilibrium ranges in wind-wave spectra in wave dynamics and radio probing of the ocean surface, Ed. by O.M. Phyllips and K.Hasselmann. Plenum Press Corp., pp.9-40, 1986.

Komatsu K. and Masuda A. A new scheme of Nonlinear Energy Transfer among wind waves: RiAM method – algorithm and performance, Journal of Oceanography, 32, pp.509-537, 1996.

Lavrenov I.V. Mathematical modeling of wind waves in spatially inhomogeneous ocean, Gidrometeoizdat, Sankt-Petersburg, 1998.

Masuda A., Nonlinear energy transfer between wind waves. J.Phys.Oceanogr., 23, pp.1249-1258, 1980.

Phillips O.M. The equilibrium range in the spectrum of wind-generated waves. J.Fl.Mech., 4, pp. 426-434, 1958.

Phillips O.M. Spectral and statistical properties of the equilibrium range in wind-generated gravity waves. J.Fl.Mech., 156, pp. 505-531, 1985.

Polnikov V. Numerical modeling of the constant flux spectra for surface gravity waves in the case of angular anysotropy, Wave Motion, 1008, pp.1-12, 2000.

Polnikov V. Numerical modeling of the flux energy formation for surface gravity waves, J.Fl.Mech., 278, pp.289-291, 1994.

Resio D.T. and Perrie W.A. Implication of an f^{-4} equilibrium range for wind-generated waves. J.Phys.Oceanogr., 2, pp.193-204, 1989.

Resio D. and Perrie W. A numerical study of nonlinear energy fluxes due to wave-wave interactions. Part I. Methodology and basic results, J.Fl.Mech., 223, pp.603-629, 1991.

Tracy B.A. and Resio D.T. Theory and calculation of the nonlinear transfer between sea wave in deep water wave information studies. Report of US Army Engineer Waterway Experimental Station, Vicksburg, MS, 1982.

Toba Y. Local Balance in the air-sea boundary processes. I, J.Oceanog.Soc.Japan, 28, pp.109-120, 1972.

Toba Y. Local balance in the air-sea boundary processes. II, J.Oceanog.Soc.Japan, 29, pp.70-75, 1973.

Toba Y. Local balance in the air-sea boundary processes. III. On the spectrum of wind waves. J.Oceanog.Soc.Japan, 29, pp.209-220, 1973.

Zakharov V.E., Lvov V.S. and Falkovich J. Kolmogorov spectra of wave turbulence, Springer-Verlag, 1992.

Zakharov V.E. and Filonenko N.N. The energy spectrum for stochastic oscillation of a fluid surface, Doklady Akademii Nauk, 170, pp.1292-1295, 1966.

Zakharov V.E. and Zaslavskii M.M. The kinetic equation and Kolmogorov spectra in the weak-turbulence theory of wind waves, Izv.Atm.Ocean.Phys., 18, pp.747-753, 1982.

Zakharov V.E., Pushkarev A.N. Diffusion model of interacting gravity waves on the surface of deep fluid, Nonlin.Proc.Geophys., 6, pp.1-10, 1999.

Van Vledder G., Private communication

Webb D.J. Non-linear transfer between sea waves. Deep Sea Research, 25, pp.279-298, 1978.

NONLINEAR DYNAMICS OF ROGUE WAVES

M. Onorato, A. R. Osborne and M. Serio

Dipartimento di Fisica Generale dell'Università
Via Pietro Giuria 1, Torino 10125, Italy

1. INTRODUCTION

Ever since man ventured into the sea there have been countless reports of "giant", "freak" or "rogue" waves in the ocean. The mechanism of freak wave generation has become an issue of principal interest due to their potentially devastating effects on offshore structures and ships. An important contribution to observations of this phenomenon is the paper by Captain Mallory [1974] who reports on 11 oil tankers that were extensively damaged by giant waves off the south-east coast of South Africa. By examining weather charts, Mallory showed that when the incidents occurred, waves generated by the wind were travelling in a direction opposite to the prevailing currents. Linear caustic theory provides a basis for freak wave generation, i.e. events of extreme wave amplitude can be created by the presence of ocean currents or bottom topography that can cause wave energy to focus in a small area. This theory and its development for the formation of freak waves are discussed in detail in a recent paper by White and Fornberg [1998]. Even though the linear theory is well accepted and physically plausible, it is also well known, but less understood that exceptionally large waves can occur in the open ocean away from currents or particular topography.

Our interest in the phenomena of rogue waves was recently awakened by a North Sea measurement program conducted by Statoil (the Norwegian national oil company) [Haver and Karunakaran, 1998] in which a number of freak waves have been measured (we define a freak wave to be a wave that exceeds the significant wave height by a factor of 2.2 [Dean, 1996]). The largest of the measured waves was 26 m crest-to trough, but amazingly, the significant wave height was only 11 m. On the basis of gaussian statistics, one rarely expects to encounter a measured wave train with a maximum wave that exceeds about twice the significant wave height. The fact that the 26 m wave was more than 2.2 times the significant wave height suggests the occurrence of a very extraordinary event.

Following the ideas of other recent authors [Trulsen and Dysthe, 1996], [Henderson, et al, 1999], we conjecture that freak waves can be produced by *nonlinear self modulation of a slowly modulated wave train*. A detailed analysis of the experimental data from Statoil reveals a number of parameters that might be important for the generation of freak waves (see [Trulsen and Dysthe, 1996]). In particular two parameters seem to be fundamental: the *wave steepness* and the *bandwidth of the wave number spectrum*. Under the hypothesis of small steepness and narrow bandwidth, the resulting amplitude modulation equation (derived from the Euler equations) is the Nonlinear Schroedinger equation.

The aim of this paper is to consider the self modulational instability, and therefore the NLS equation in infinite water, as the starting point for investigating the formation of freak waves. Our approach is herein supported by (i) extensive numerical simulations of the NLS equation in 1+1 and higher order equations [Dysthe, 1978], and (ii) detailed studies on rogue wave analytical solutions of NLS using the inverse scattering transform.

The majority of previous work conducted on problems governed by the Benjamin-Feir instability relates to *small amplitude modulations,* results which are well understood and robust from a physical and mathematical point of view. It is still unclear, however, how freak waves are generated via this instability mechanism in more realistic oceanic conditions, i. e. in sea states characterized not by a simple monochromatic wave perturbed by two small side-bands, but instead by a complex spectrum whose perturbation of the carrier wave cannot be viewed as being small. We have therefore performed many numerical simulations for which we have used initial conditions characterized by the JONSWAP spectrum. These results were then compared with the ones from linear simulations. We discuss how the generation of freak waves in a random sea state is more likely to occur for large values of the Philips parameter, α, and the so-called "enhancement" parameter, γ. Our main focus herein is *not* to attempt to model ocean waves, but instead to study leading order effects using the nonlinear Schroedinger equation. Research at higher order suggests that the results given herein are indicative of many physical phenomena in the primitive equations themselves [Henderson, et al, 1999].

The paper is organized as follows: In Sec. 2 weakly nonlinear envelope equations which can be derived from the Euler equations are briefly

discussed. Sec. 3 contains the numerical methods we have employed for the nonlinear Schroedinger and Dysthe equations. We give the results of a number of simulations in which freak waves occur. In Sec. 4 we give theoretical predictions for the maximum amplitude reached by a freak wave. Sec. 5 discusses the formation of freak waves in random sea states.

2. NONLINEAR DYNAMICS OF THE ENVELOPE FUNCTION OF A NARROW BANDED WAVE TRAIN

In this Section we briefly recall the hypothesis under which the nonlinear dynamical envelope equations are derived from the primitive equations of motion. We consider the fluid to be inviscid, irrotational and the waves are assumed to propagate along the x direction. The vertical coordinate is z and the depth is considered to be infinite. The nonlinear envelope equations are obtained by employing an harmonic expansion of the velocity potential ϕ and the surface displacement ζ (for a formal and complete derivation of NLS equation see for example Mei, [1983]):

$$\phi = \bar{\phi} + \frac{1}{2}\left(A e^{i\vartheta+z} + A_2 e^{2(i\vartheta+z)} + \ldots + c.c.\right), \tag{1}$$

$$\zeta = \bar{\zeta} + \frac{1}{2}\left(B e^{i\vartheta} + B_2 e^{2(i\vartheta)} + \ldots + c.c.\right), \tag{2}$$

where $c.c.$ denotes the complex conjugate and $\vartheta = kx - \omega t$. $\bar{\phi}$, $\bar{\zeta}$, A, A_2, B and B_2,..., are functions of the slow modulations. The next step is to Taylor expand the boundary conditions, substitute eq. (1) and eq. (2) into the primitive equations and to make the following assumptions:

$$k_o a_o = O(\varepsilon) \tag{3}$$

$$\Delta k / k_o = O(\varepsilon), \tag{4}$$

where a_o is the wave amplitude and k_o is the modulation wave number. Under these hypotheses, neglecting terms of the order of ε^4, the envelope is described by the well-known nonlinear Schroedinger equation:

$$A_t + i\frac{\omega_o}{8k_o^2} A_{xx} + i\frac{1}{2}\omega_o k_o^2 |A|^2 A = 0. \tag{5}$$

This equation was pioneered by Zakharov [1968], Benney and Roskes [1969] and Hasimoto and Ono [1972]. A plane wave solution of the NLS equation is known to be unstable to a modulation perturbation. This instability, first discovered by Benjamin and Feir [Benjamin and Feir, 1967], has been investigated numerically and experimentally in a series of papers whose main results are collected in the review by Yuen [1982]. Moreover, from a mathematical point of view, the NLS equation, just as for the Korteweg-deVries, is integrable by the *Inverse Scattering Transform* (IST) and has soliton solutions [Tracy, 1984; Tracy and Chen, 1988]; the Lax pair for NLS was found by Zakharov and Shabat [1972].

In order to compare theoretical results with point-wise measurements (obtained as a time series), where a slow variation of wave groups occurs from an hypothetical point at zero *fetch*, we employ the following transformation (see Lo and Mei [1985]:

$$A = a_o A', \qquad \phi = \omega a_o^2 \phi',$$

$$\varepsilon\omega\gamma\left(\frac{2k}{\omega}x - t\right) = \tau, \quad \varepsilon^2 kx = x', \tag{6}$$

The nondimensional form of the NLS equation for space evolution is then given by (primes have been omitted for brevity):

$$A_x + iA_{tt} + i|A|^2 A = 0. \tag{7}$$

In the frame of reference of eq. (7), the variable x corresponds to the distance over which the wave group has advanced and t is the negative of time elapsed. This equation corresponds to a time-like Nonlinear Schroedinger equation (TNLS) which solves a *boundary value problem*: given the temporal evolution of $A(0,t)$ at some location $x = 0$, eq. (7) determines the wave motion over all space and time, $A(x,t)$.

2.1 Higher Order Envelope Equations

One question that we want to answer is the following: if the NLS equation is a good model for the generation of freak waves, do higher order equations also support freak wave solutions? If the expansion of the Euler equations is continued up to the next order, the Dysthe equation [1978] is obtained. Using transformation (6) on the form of the dimensional equation, the higher order equation reads:

$$A_x + i\gamma^2 A_{tt} + i|A|^2 A + \varepsilon\left(8|A|^2 A_t + 4iA\phi_t|_{z=0}\right) = 0 \tag{8}$$

$$4\bar{\phi}_{tt} + \bar{\phi}_{zz} = 0 \qquad -h < z < 0 \tag{9}$$

$$\bar{\phi}_z = \left(|A|^2\right)_t \qquad z = 0 \tag{10}$$

$$\bar{\phi}_z = 0 \qquad z = -h \tag{11}$$

We will call this set of equations the Dysthe-Lo-Mei equation (DLM). Two motivations led us to use the variables and coordinate system defined by Lo and Mei: (i) the evolution of the waves can be directly compared with experimental time series from open sea measurements or wave tank facilities (this issue will be reported in a separate paper), (ii) the higher order equations simplifies, rendering the numerical computation easier with respect to the original form of the equation (compare eq. (2.4) in Dysthe [1978] with eq. (8) in this paper).

The linear stability analysis for the Dysthe equation has been reported on in different papers (see for example [Dysthe, 1978, Janssen, 1983, Brinch-Nielsen and Jonsson, 1986]). The major founding is that the higher order term in eq. (8), $A\bar{\phi}_x$, which couples the wave envelope with the potential flow has the property of reducing the region of instability. For $\varepsilon = 0$ the results from the NLS instability curve is recovered, while for small values of ε, the instability region becomes smaller and the growth rate reduces. The result, at least for $\varepsilon < 0.2$, is remarkably accurate when compared with the stability diagram obtained by Crawford et al., [1981] based on the Zakharov equation. The second higher order term $|A|^2 A_x$ does not bring any changes in the linear stability analysis and its only effect is to allow the solution to be asymmetric starting with a symmetric initial condition.

3. FREAK WAVES FROM MONO-CHROMATIC INITIAL CONDITIONS

We have solved numerically the prescribed equations in their time-like form. The numerical scheme adopted is basically the one described by Lo and Mei, [1985], that uses a split-step Fourier approach. The linear and nonlinear terms are separately treated at each time step. A mid-point finite difference approximation is used for advancing A in x. For the linear part, the exact solution is found using the Fourier Transform. The most delicate point of the integration is the calculation of $\bar{\phi}_t$ in the nonlinear part of the equation. Using eqs. (8), (9), (10) and (11), it is straightforward to show that for infinitely deep water the potential is related to the envelope in the following way:

$$\bar{\phi} = F^{-1}\left[\frac{|A|^2}{2\omega}\right] \qquad (12)$$

where F^{-1} is the Fourier operator. The derivatives with respect to t are calculated using the FFT algorithm.

We have performed a series of simple numerical simulations for finding initial conditions suitable for generating freak waves. We have started all numerical simulations in this Section with a simple sinusoidal wave perturbed by two sidebands. Even though it is well known that such a situation is a pure idealization of a real sea surface state, the simulations we show are very instructive and are an indispensable exercise before advancing to more complex cases. In these simple simulations our main idea is to produce waves of very high amplitude with respect to the background state. The starting point is the experimental data reported in [Trulsen and Dysthe, 1996] where a 26 meter high wave is recorded in a sea state of 11 meters. The dominant frequency of the full time series was estimated to be around f_o=0.074 Hz and the wave steepness, ε, was 0.14. Taking into account these parameters we have run the NLS and the DLM equations for a variety of cases with the following initial condition for the surface amplitude:

$$\zeta(x=0,t) = \left[a_o + \delta\cos\left(\frac{2\pi}{T}t\right)\right]\cos(2\pi f_o t) \qquad (13)$$

In order to reproduce a situation which is physically interesting we choose exactly the parameters obtained from the experimental data in the North Sea, i.e. a_o=5.5 m, f_o=0.074 Hz. In the simulations the parameter δ was selected to be 1/10 of the amplitude of the carrier. As will be shown in the next Section, the choice is not general as previously thought and different values of δ can lead to very different maximum wave amplitudes. The period of the perturbation T was varied from 67.5 s to 405 s which corresponds respectively to Tf_o=5 and Tf_o=30. Note that increasing T basically corresponds to setting the side-bands closer to the carrier wave in the Fourier representation. In Fig. 1 we show the evolution of a monochromatic wave for Tf_o=10 from a numerical simulation of the TNLS equation.

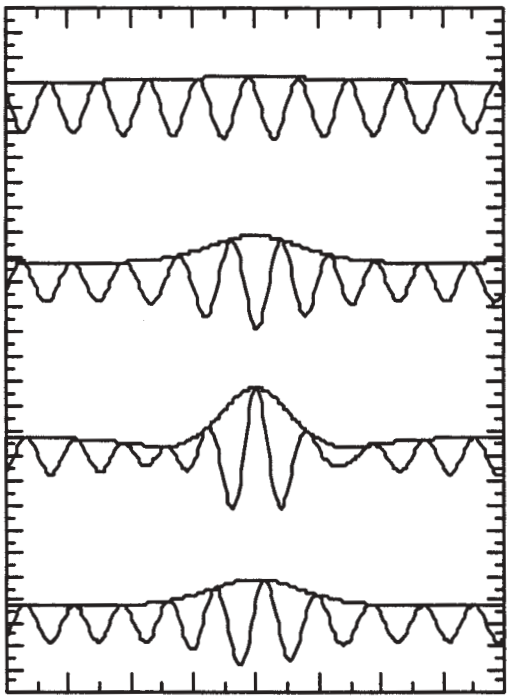

Figure 1. Time series at different *fetch* (x=0, 1250, 1900, 2250 m) of the envelope and the associate wave surface from TNLS numerical simulation, T=135 s. Details on the initial conditions are reported in the text.

The envelope, as expected, begins to grow, and reaches a maximum at *fetch* x = 1900 m. Then the wave decreases its amplitude and repeat its cycle. The maximum amplitude reached is 13.8 m, which corresponds to 2.5 times the initial amplitude. A second example with Tf_o=15 is shown in Fig. 2.

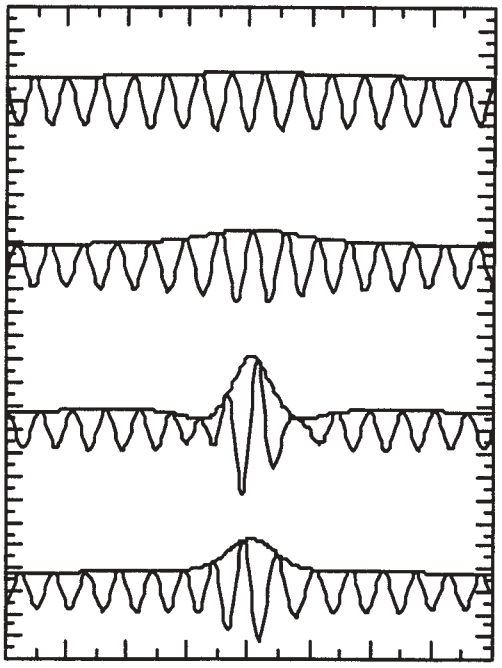

Figure 2. Time series at different *fetch* (x=0, 1250, 2050, 2250 m) of the envelope and the associate free surface from a TNLS numerical simulation, T =202 s. Details on the initial conditions are reported in the text.

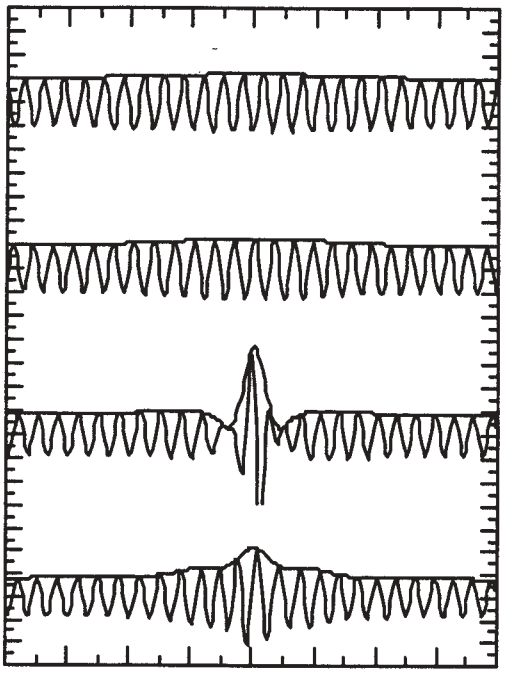

Figure 3. Time series at different *fetch* (x=0, 1250, 2550, 2900 m) of the envelope and the associate free surface from a TNLS numerical simulation, T =336 s. Details on the initial conditions are reported in the text.

The early stage of the evolution is more or less the same as Fig. 1 with the main difference that, in the present case, the wave reaches a maximum amplitude greater than in the previous case. The last case, shown in Fig. 3, corresponds to Tf_o=30. The amplitude of the wave becomes even greater (18.7 m) with respect to the previous two cases (as the length of the perturbation increases, the maximum amplitude increases) but the evolution is slower (the maximum amplitude is obtained at x= 2550 m.

Similar results, as shown in Fig. 4, can be achieved using the DLM equation. The simulation has been started using exactly the same initial conditions as in Fig. 2. At variance with NLS, the envelope from DLM simulations moves with a non constant group velocity, becomes asymmetric and its evolution is slower (the maximum amplitude is obtained at fetch =2250 m for DLM and 2050 m for TNLS). Besides these effects, the higher order terms reduce slightly the maximum amplitude.

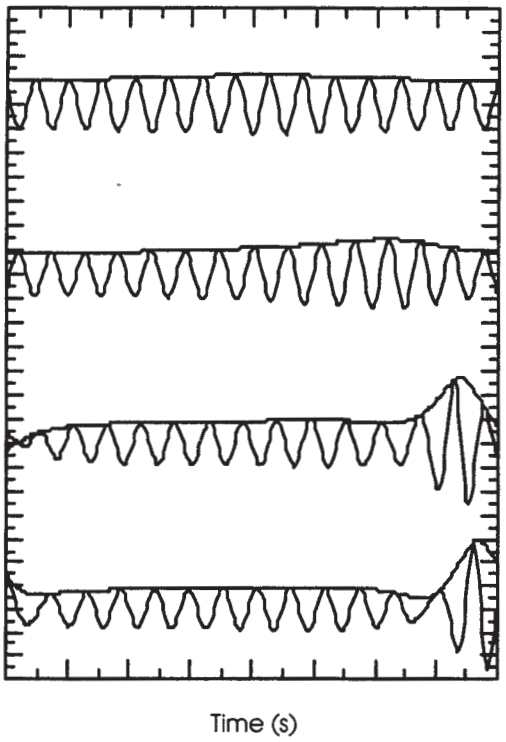

Figure 4. Time series at different *fetch* (x=0, 1250, 2050, 2250 m) of the envelope and the associate wave surface from numerical simulation of DLM equation with T=202 s. Details on the initial conditions are reported in the text.

4. RESULTS FROM INVERSE SCATTERING THEORY

We have derived a simple formula for the maximum amplitude of an unstable mode of the NLS equation. The main idea is the following. For typical numerical examples and laboratory experiments one normally considers a small amplitude perturbation, δ, of a carrier, a_o, with wavelength, $k_o = 2\pi / L_o$, and frequency $\omega = \sqrt{gk_o}$. The modulation wavelength and wave number are respectively L and $\Delta k = 2\pi / L$. It is possible to compute the IST of a complex wave form (single degree of freedom) solution of the NLS equation in terms of an eigenvalue which is purely imaginary, $\lambda = i\lambda_o$, [Its and Kotljarov, 1976, Osborne, et al., 2000]. If one assumes the restriction $0 < \lambda_o < a_o$, then the modulations are initially small provided that δ is small. The main results are that the wave number, Δk, for infinitesimal amplitude unstable modes, is given by (we assume that the carrier wave amplitude is unity, $a_o = 1$):

$$\Delta k = \frac{2\pi}{L} = -2\sqrt{1+\lambda^2} + O(\delta) \qquad (14)$$

We have computed this expression from appropriate loop integrals to leading order in perturbation amplitude δ. The maximum amplitude of the unstable mode during its evolution is given by:

$$A_{\max} = 1 + 2\lambda_o \qquad (15)$$

The result has been computed from the ϑ-function solution of NLS; the generic form for this formula is: $A_{\max} = 1 + 2\lambda_I$, where λ_I is the imaginary part of the eigenvalue. Thus the maximum amplitude has the formula (use $\lambda_I = i\lambda_o$) in (14); eliminate λ_o from (14) and (15) to get:

$$\frac{A_{\max}}{a_o} = 1 + 2\sqrt{1 - \left(\frac{\pi}{L}\right)^2} \qquad (16)$$

Now, if we let the carrier wave amplitude be an arbitrary number a_o (instead of a_o=1), and rearranging eq. (16) we obtain:

$$\frac{A_{\max}}{a_o} = 1 + 2\sqrt{1 - \left(\frac{1}{2\sqrt{2}\varepsilon N}\right)^2}, \qquad (17)$$

where N is given by $k_o / \Delta k$ and corresponds to the number of waves under the perturbation and to the inverse of the bandwidth parameter that was supposed to be small in the derivation of the envelope equations. For the TNLS equation (see eq. (7)) which gives the evolution in space (instead of in time), it is straightforward to show that, for infinitely deep water, the maximum amplitude reached by the wave is given by:

$$A_{\max} = 1 + 2\sqrt{1 - \left(\frac{1}{\sqrt{2}\varepsilon N}\right)^2}, \qquad (18)$$

where now $N = \omega_o / \Delta\omega$. These results are particularly interesting because they tell us that, the steepness of the wave and the wavelength or the period of the perturbation are fundamental for estimating the maximum amplitude of a freak wave.

In order to verify our numerical results in Fig. 5 we show the maximum amplitude of the wave divided by a_o as a function of N from eq. (18) with ε=0.1 and from numerical experiments described in the previous Section. The values of the amplitude of the perturbation were fixed at $\delta = 10^{-4}$.

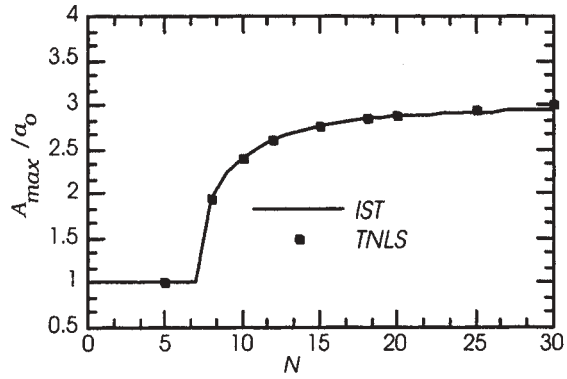

Figure 5. Normalized maximum wave amplitude as a function of the number of waves under the perturbation. Solid line is obtained from IST theory and dots are from numerical simulations of TNLS.

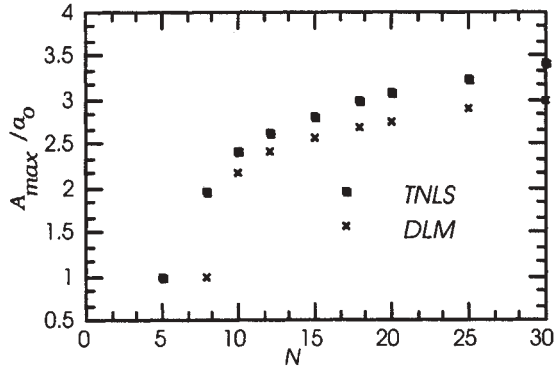

Figure 6. Normalized maximum wave amplitude for the TNLS (dots) and the DLM (crosses) equations as a function of the number of waves under the perturbation.

As expected, good agreement is achieved. In the same plot, the maximum amplitude for the Dysthe equation is reported. As already mentioned in the previous Section, the amplitudes from the Dysthe equation are smaller with respect to the NLS equation. Moreover, the region of instability for the DLM equation is restricted with respect to the TNLS equation: for $N=8$ the TNLS equation is unstable and the waves grow to a normalized amplitude of 2 while the DLM equation is stable and there is no growth.

4.1 The effect of the amplitude of the perturbation

The linear stability analysis is based on the assumption that the amplitude of the perturbation is small. When dealing with numerical simulations one question that arises is how "small" must be the amplitude of the perturbation to be considered small. As an example, we show in Fig. 7 some results with two numerical simulations of the TNLS starting with two *small* initial conditions. The first one is the same as the one that led to Fig. 6 with $\delta = 10^{-4}$ and the second one is with $\delta = 10^{-1}$. While for small values of N the two curves are almost indistinguishable, for large N, the large perturbation amplitude leads to the formation of a higher amplitude waves. In Fig. 8 we show the evolution of the maximum amplitude for amplitude perturbations that range from $\delta = 10^{-1}$ to $3 \cdot 10^{-1}$ at different N on a semi-logarithmic scale.

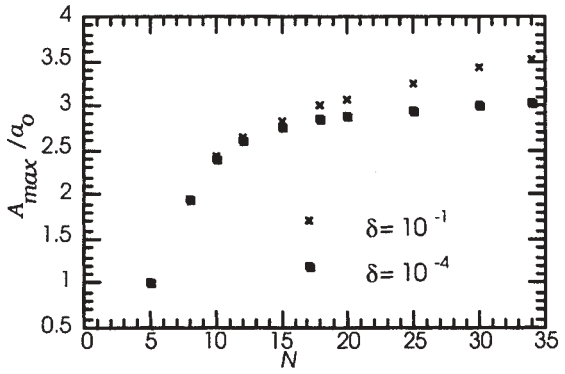

Figure 7. Effect of the amplitude of the perturbation on the maximum amplitude as a function of the number of waves under the perturbation.

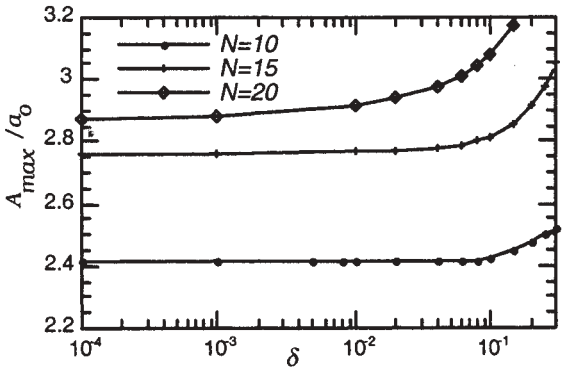

Figure 8. Effect of the amplitude of the perturbation on the maximum amplitude as a function of the amplitude perturbation for different values of N.

The maximum amplitude remains more or less constant up to 10^{-2} and then a rapid growth, especially for large N, is encountered. The results just shown are very interesting because they represent a first attempt to understand more realistic oceanic situations. In open seas one rarely finds small amplitude perturbations. IST theory for the NLS equation has provided important results concerning the maximum amplitude in the case of $\delta << 1$ and at the moment we have no analytical prediction for larger perturbations. Using a numerical code for IST, it is possible to understand in greater detail the NLS dynamics in terms of the unstable modes in the complex plain. These results will be reported in a separate paper [Osborne, et al. 2000].

5. FREAK WAVES IN RANDOM SEAS

In this Section our attention is focused on freak wave generation in numerical simulations of the NLS equation where we assume initial conditions described by the JONSWAP power spectrum [Hasselmann, et al., 1976]:

$$P(f)=\frac{\alpha}{f^5}\exp\left[-\frac{4}{5}\left(\frac{f_o}{f}\right)^4\right]\gamma^{\exp\left[\frac{(f-f_0)^2}{2\sigma_o^2 f_0^2}\right]} \qquad (19)$$

Here σ_o=0.07 if $f \le f_o$ and σ_o=0.09 if $f > f_o$. Our use of the JONSWAP formula is based upon the established result that developing storm dynamics are governed by this spectrum for a range of the parameters [Komen, et al. 1994]. The constants α, γ and σ_o were originally obtained by fitting experimental data from the international JONSWAP experiment conducted during 1968-69 in the North Sea. Here f_o is the dominant frequency, γ is the "enhancement" coefficient and α is the Phillips parameter [Komen, et al. 1994]. All of the JONSWAP parameters depend on the stage of wave development and probably are all interdependent on one other in a non trivial manner. For a recent description of these topics see [Babanin and Soloviev, 1998] and references cited therein. Accepted values of α range from 0.0081 to 0.02 and values of γ lie in the range 1 to 10. For γ=1 and α=0.0081 the spectrum reduces identically to that of Pierson and Moskowitz [Komen, et al., 1994] which describes a fully developed sea state, i.e. one which has evolved over infinite time and space. For $f = f_o$, the expression $E = \gamma^{\exp[-]}$ is effectively equal to the value of γ and, as f moves away from f_o in either direction, E tends rapidly to unity. Therefore as γ increases, the spectrum becomes higher and narrower around the spectral peak. In Fig. 1 we show the JONSWAP spectrum for different values of γ (γ=1, 5, 10) for f_o=0.1 *Hz* and α=0.0081.

The major finding we would like to discuss with regard to our numerical simulations is that, as γ and α grow, the nonlinearity becomes more important and the probability of the formation of freak waves increases. Our results have been achieved by considering the NLS equation as the *simplest* nonlinear evolution equation for describing deep-water wave trains. We have performed numerical simulations using the JONSWAP spectrum to determine the initial conditions. Since the analytical form of the spectrum is given as a function of frequency, the analysis is carried out by considering the TNLS equation (see eq. (7)). Initial conditions for the free surface elevation $\zeta(t)$ have been constructed as the following random process [Osborne, 1982]:

$$\zeta(0,t)=\sum_{n=1}^{M} C_n \cos(2\pi f_n t-\phi_n) \qquad (20)$$

where ϕ_n are uniformly distributed random numbers on the interval $(0, 2\pi)$ and $C_n=\sqrt{2P(f_n)\Delta f_n}$, where $P(f)$ is the JONSWAP spectrum given in (19). In Fig. 10 we show the initial condition that has been used. The dominant frequency and the Phillips parameter of the initial wave train were set respectively to 0.1 Hz and α=0.02. A large amplitude wave appears in the simulation and in order to better visualize it, in Fig. 11 we show a time series of the free surface $\zeta(t)$ at x=1550 m. A freak wave of about 18.5 m in a random wave train with significant wave height of H_s=6.9 m is evident at time t=140 s.

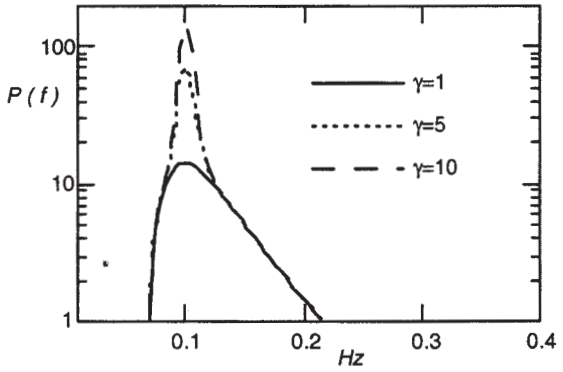

Figure 9. The JONSWAP spectrum for γ =1 (dashed line), γ =5 (dotted line), γ =10 (solid line) with f_o=0.1 Hz and α=0.0081.

We point out that the same simulation, not reported here for brevity, with exactly the same initial conditions, has been performed after deleting the nonlinear term in the TNLS equation. No waves fulfilling the freak wave threshold ($H_{max} > 2.2\ H_s$) were found. In this second simulation, the Benjamin-Feir instability cannot occur and "freak" waves could occur only via a simple superposition of Fourier modes. This result indicates that, in our simulations, nonlinearity plays an important role in the dynamics of freak wave generation.

In order to give additional quantitative results we have performed more that 300 simulations of the TNLS equation. The simulations have been performed in dimensional units in the following way. An initial time series of 250 seconds has been computed from the JONSWAP spectrum for different values of α (from α=0.0081 to α=0.02) and γ (γ=1, 4, 10). To increase the number of statistical events we made computer runs with 10 different sets of random phases, ϕ_n.

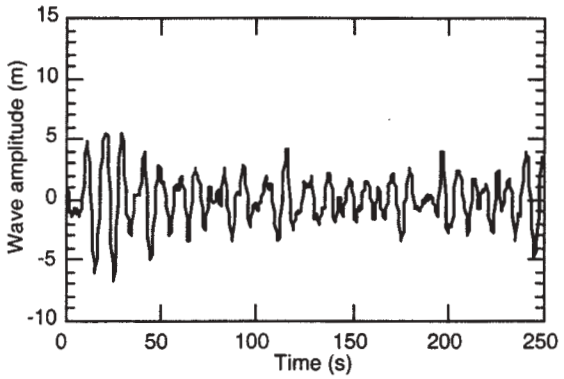

Figure 10. Free surface elevation $\zeta(t)$ at $x=0$ generated through a linear superposition of random phase waves with JONSWAP power spectrum.

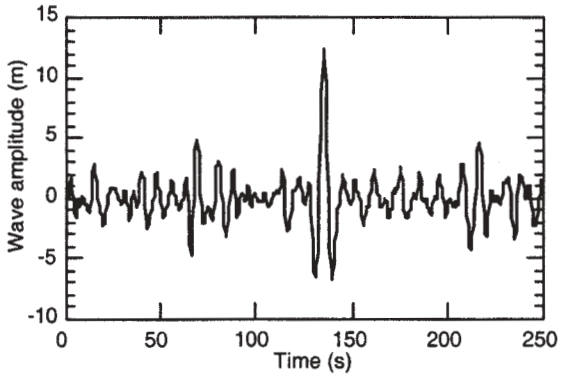

Figure 11. Free surface elevation $\zeta(t)$ at $x=1550$ m obtained integrating the TNLS equation.

The time series were then evolved according to the TNLS for a distance of 10 km, saving the output every 10 m. From an experimental point of view this approach corresponds to setting 1000 probes along the wave propagation direction (one every 10 m) and measuring each time series for 250 s at a sampling frequency of 2.05 Hz. The significant wave height, H_s, of each realization has been computed; the highest wave, H_{max}, has been found and the ratio H_{max}/H_s has been calculated. In order to verify that our findings are indeed a consequence of the nonlinear dynamics, we have also computed exactly the same simulations using the *linear* version of the TNLS equation, i.e. the term $|A|^2 A$ was set identically to zero. The summary of the results are shown in Fig. 12, 13. Fig. 12 corresponds to $\gamma=1$. A horizontal line at $H_{max}/H_s=2.2$ indicates the threshold that arbitrarily discriminates the height rogue waves. For the Pierson Moskowitz spectrum ($\gamma=1$ and $\alpha=0.0081$) only one realization in the 10 considered shows a "rogue" wave with $H_{max}/H_s=2.25$. For higher values of α only a few of the realizations show waves with H_{max}/H_s slightly greater than 2.2. From the plot it is clear that the effects of nonlinearities are rather small for this case ($\gamma=1$). Among all the 50 linear simulations performed with $\gamma=1$, we have encountered a number of large amplitude waves but none exceeds 2.2 H_s.

For $\gamma=4$, see Fig. (13), the physical picture becomes much more interesting: while in the linear simulations there are no freak waves, 50% of the nonlinear simulations performed show at least one freak wave.

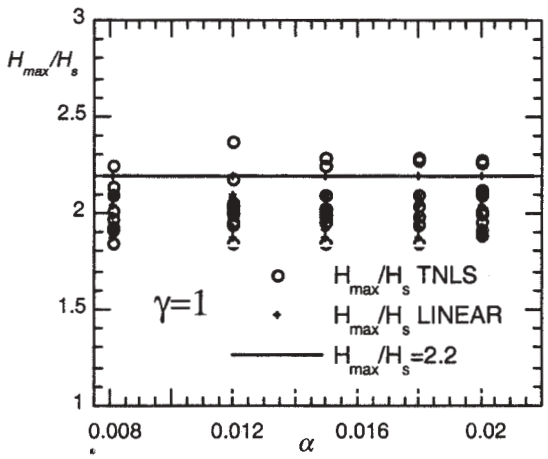

Figure 12. H_{max}/H_s as a function of α for $\gamma=1$. Circles and crosses correspond respectively to the nonlinear (TNLS) and linear simulations. For each value of α, 10 different realizations corresponding to 10 different sets of random numbers have been performed.

For $\gamma=10$ the picture is qualitatively the same and therefore the graphs are not reported here. Thus there is clear evidence from our simulations that increasing γ increases the probability of freak wave occurrences; high values of γ do not, however, guarantee the presence of a giant wave. One concludes that the local properties of the wave trains are presumably of fundamental importance for understanding the formation of freak waves. In actual fact it may well happen that the Benjamin-Feir instability mechanism is satisfied only in a small temporal portion of the full wave train, giving raise to a local instability and therefore to the formation of a freak wave. From a theoretical point of view all these results can probably be better understood and explained in terms of the discrete unstable modes of the NLS equation whose integrability properties and the inverse scattering transform provide a unique way of approaching the problem, the scope of a future paper. IST can be viewed as a kind of generalized Fourier analysis and it will be indeed interesting to analyze time series to obtain the requisite properties of the rogue wave components in real world situations.

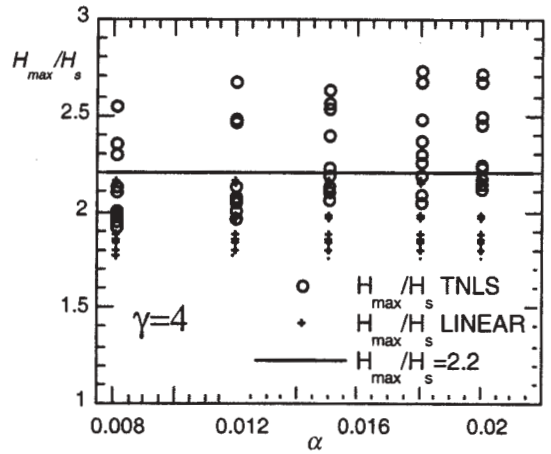

Figure 13. H_{max} / H_s as a function of α for γ =4. Circles and crosses correspond respectively to the nonlinear (TNLS) and linear simulations. For each value of α, 10 different realizations corresponding to 10 different sets of random numbers have been performed.

6. SUMMARY AND CONCLUSIONS

We have considered the envelope equations (the NLS and DLM equations) as the fundamental leading order equations for studying the generation of freak waves. Numerical simulations starting from a monochromatic wave perturbed by two side-bands indicate that large amplitude waves can appear as a self focusing process without the need of currents or particular topography. We have also shown numerically that as the side-bands are moved towards the carrier wave freqency, larger freak waves appear. For such simple initial conditions we have exploited the integrability properties of the NLS equation to find a simple analytical form that predicts the maximum wave height reached by a monochromatic wave with a given *steepness* and *sideband perturbation*.

Attention has also been given to more complex and realistic situations such as those charatcterized the JONSWAP power spectrum. This work provides a first attempt to study the influence of nonlinearity on the prediction of large amplitude waves in random sea states. Numerical simulations of random waves governed by the dynamics of the NLS equation for the JONSWAP power spectrum have provided insight into this problem. We have shown that as γ and α increase the effects of nonlinearity become more important: therefore freak waves that result as a modulation instability are more probable to occur in a physical situation where γ and α are large. More than 150 simulations using the *linear* NLS equation have been performed and no freak waves were found. This result is in stark contrast to the large number of freak waves (50) appearing in the nonlinear simulations. From a physical point of view, we are aware of the fact that the NLS equation overestimates the region of instability and the maximum wave amplitude with respect to higher order models [Dysthe, 1978], especially for ε greater than 0.1. Furthermore it is well known that the NLS equation is formally derived from the Euler equations under the assumption of a narrow-banded process. Nevertheless, in spite of these deficiencies in the NLS equation, we believe that our results provide new important physical insight into the generation of freak waves. Simulations with higher order models [Dysthe, 1978] or directly with the fully nonlinear equations of motion will be required in order to confirm these results. Wave tank experiments will also be very useful in this regard. We thank Sverre Haver of Statoil for providing us with North Sea data.

M. O. was supported by Assegno di Ricerca from the Università di Torino. This work was supported by the Office of Naval Research of the United States of America. Italian University funds (60 %) are also acknowledged

REFERENCES

Babanin, A. V. and Soloviev, Y. P. J. Phys. Oceanogr. 28, 563-576, (1998).

Benjamin, T. B. and Feir, J. E. "The disintegration of wave trains on deep water. Part 1. Theory", J. Fluid Mech. 27, 417-430, (1967).

Benney, D. J. and Roskes, G. J. "Wave instabilities", Studies Appl. Math. 48 377-385, (1969).

Brinch-Nielsen, U. and Jonsson, I. G. "Fourth order evolution equations and stability analysis for Stokes waves in arbitrary depth", Wave Motion 8, 455-472, (1986).

Crawford, D. R. ,Lake, B. M., Saffman, P. G. and Yuen, H. C. "Stability of weakly nonlinear deep-water waves in two and three dimensions", J. Fluid Mech. 105 , 177-191, (1981).

Dysthe, K. B. "Note on a modification to the nonlinear Schroedinger equation for application to deep water waves", Proc. R. Soc. Lond. A 369, 105-114, (1979).

Hasimoto, H. and Ono, H. "Nonlinear modulation of gravity", J. Phys. Soc. Japan 33, 805-811, (1972).

Hasselmann, K., Ross, D. B., Muller, P. and Sell, W. J. Phys. Oceanogr. 6, 200-228, (1976).

Haver, S. and D. Karunakaran, "Probabilistic Description of Crest Heights of Ocean Waves," *Proc. of the 5th Int. Workshop on Wave Hindcasting and Forecasting*, Melbourne, Florida, pp. 451-466, 1998.

Henderson, K. L., Peregrine D. H. and Dold, J. W., Wave Motion 29 , 341-361, (1999).

Its A. R. and Kotljarov, V. P. Dokl. Akad. Nauk. Ukain SSR Ser. A 11, 965, (1976).

Janssen, P. A. "On a fourth-order envelope equation for deep-water waves", J. Fluid Mech. 126, 1-11, (1983).

Komen, G. J.,. Cavaleri, L., Donelan, M., Hasselmann, K., Hasselmann S. and Janssen, P. A. Dynamics and modelling of ocean waves, Cambridge University Press, (1994).

Lo, E. and Mei, C. C. "A numerical study of water-wave modulation based on a higher-order nonlinear Schroedinger equation", J. Fluid Mech. 150, 395-416, (1985).

Mallory, J. K. "Abnormal waves on the south east coast of South Africa", Intl. Hydrog. Rev. 51, 99-129, (1974).

Mei, C. C. The Applied Dynamics of Ocean Surface Waves, J. Wiley & Sons, New York (1983).

Osborne, A. R., Onorato, M., Serio M. in preparation, (2000).

Osborne, A. R., Topics in Ocean Physics, Proceedings of the Int. School E. Fermi, 515-550, (1982).

Tracy, E. Topics in nonlinear wave theory with applications, Ph.D. Thesis, University of Maryland (1984); E. R. Tracy and H. H. Chen, Phys. Rev. A **37**, 815 (1988).

Trulsen, K Dysthe, K. B. "Freak Waves - A three-dimensional wave simulation", Proc. 21st Symp. on Naval Hydrodynamics, National Academy Press, 550-560, (1996).

White B. S. and Fornberg, B "On the chance of freak waves at sea" Fluid Mech. 335, 113-138, (1998).

Yuen, H. "Nonlinear Dynamics of Deep-Water Gravity Waves". Adv. Appl. Mech. 22, 67-229, (1982).

Zakharov, V. E. "Stability of periodic waves of finite amplitude on the surface of deep fluid", J. Appl. Mech. Tech. Phys. 9, 190-194, (1968).

Zakharov, V. E. and Shabat, A. B. "Exact theory of two dimensional self-focusing and one dimensional self-modulation of waves in nonlinear media", Sov. Phys JETP 34, 62-9, (1972).

WIND WAVE SOURCE TERMS: CONSTRAINTS RELATED TO NONLINEAR ENERGY FLUXES

Donald Resio, Charles Long, Barbara Tracy ERDC-CHL
Linwood Vincent NRL-Stennis

1. Introduction

Over 15 years ago, third-generation wave modeling arose with the advent of the WAM model (Hasselmann et al.,1985). This model was extremely successful for a prototype version of a new class of model and was adopted by many forecast centers around the globe. Lately, however, attention has been drawn to certain performance characteristics which create problems in applications. Significant modifications to the WAM model have produced new versions (cycles) of WAM and have led to a new third-generation model, WAVEWATCH III (Tolman, 1991; Tolman and Chalikov, 1996). This latter model has been shown in some studies to reduce problems recognized in WAM runs and has been adopted for use within the major forecast centers of the US Navy and the National Weather Center (NOAA). This new model has been explicitly formulated to minimize errors via empirical modifications to wind source functions and improved propagation methods. It should be recognized, however, that modifications of such types are inevitably linked to the veracity of the winds used in the testing. Consequently, other forecast centers, which use different wind fields and different comparison metrics, still maintain that the performance of the WAM model is as good or better than other models available today.

Disagreement over model performance is not new, nor is it confined to third-generation models. For many years before the advent of third-generation models, developers and users of first- and second-generation models debated their relative performance. Here again the source of disagreement could typically be linked to potential inaccuracies in the wind fields and to the performance metrics utilized. Only a small set of existing results from field studies is almost universally agreed upon. Essentially all of these empirical findings come from fetch-limited wave measurements of the type initially developed by Mitsuyasu (1968) and Hasselmann et al. (1973) and subsequently supplemented by Donelan (1985), Kahma (1981), and others.

Fetch-limited wave growth characteristics used to calibrate wave models are typically represented by nondimensional relationships between simple parameters of the wave field and fetch, i.e.

$$1. \quad E_n = m_1 x_n^{m_2}$$

and

$$2. \quad f_{pn} = m_3 x_n^{m_4}$$

where E_n is the nondimensional energy, f_{pn} is the nondimensional peak frequency, x_n is the nondimensional fetch, and m_1, m_2, m_3, and m_4 are empirical coefficients determined from measured data. The definitions of these nondimensional parameters is as usual

$$3. \quad E_n = \frac{g^2 E_0}{u^4}$$

$$4. \quad f_{pn} = \frac{g f_p}{u}$$

and

$$5. \quad x_n = \frac{gx}{u^2}$$

where g is gravity, u is a "suitable" reference wind speed, E_0 is total wave energy, f_p is spectral peak frequency, and x is the fetch.

Our understanding of the basic physics of wave generation has been relatively constant for slightly over twenty five years now. Certain details continue to evolve, such as the finding that the equilibrium range is f^{-4} rather than f^{-5} in wave spectra and the exact form of the input and dissipation source terms; but the fundamental form of all functional wave models still encompasses the effects of three source terms: nonlinear (quartet) interactions, wind input, and wave dissipation due to breaking. In fact, the

AUTHOR INDEX
TABLE OF CONTENTS

performance of first- and second-generation models which parameterize the effects of spectral balances in a fashion consistent with this physics has been shown to be at least as good as that of third generation models in some applications. Consequently, such models have been adopted for use by the US Army Corps of Engineers in their hindcast studies, by the UK Meteorological Office for their forecast studies, and by companies in the private sector such as Oceanweather, Inc.

We see from the above discussion that, in spite of a concerted effort within the international wave prediction community, that third-generation models have not yet lived up to their early promise of improved wave predictions. An important factor in this lack of progress is the lack of clear calibration/validation guides for detailed balance models. Instead, model calibrations have been primarily based either on the ability of the sum of the source terms to produce some relatively simple fetch-limited results or calibrations with a particular set of wind fields. Additionally, typical comparison metrics (such as scatter indices, rms errors, and biases) give more weight to periods of time with small wave heights, since such waves usually dominate wave climates. On the other hand, whether wave predictions are used for ship routing, offshore or coastal structural design, estimating coastal sediment transport rates, or even warning hazards for local recreational users, it is the top 10% of the population that is usually of primary interest.

The purpose of this paper is to develop some additional constraints on wave source terms which can be used to improve 1) our understanding of spectral wave generation processes and 2) our ability to constrain the behavior of individual source terms rather than a sum of source terms.

2. Theoretical Perspective

From the classic works of Hasselmann (1962) and Zakharov (1968), it can be shown that the lowest order interaction resulting in permanent energy transfers in a homogeneous wave field involve interactions among four waves within a spectrum. Resio et al. (2000) have shown that, in spite of the fact that very different approaches were used in their derivations, the resulting equations, including the interaction (coupling) coefficients in finite depth, are exactly equivalent. This remarkable agreement between these two very different analyses of nonlinear interactions within a wave field lend even more credence to their results. Thus, a logical starting point for understanding wave generation physics is to establish characteristic constraints on source/sink balances within wave spectra related to these interactions. The work of Young and Van Vledder (1993) was a good step in this direction, but stopped short of formulating quantitative constraints on individual source terms.

Most past investigators have relied on calculations of the rate of change of action density or energy density in their analyses of nonlinear wave-wave interactions. For the case of the rate of change of action density at a fixed vector wavenumber, $\underline{k}$. As shown by Resio et al. (2000), a modified form of Webb's (1978) integral, including finite-depth effects, can be written as

$$6.\quad \frac{\partial n(\underline{k}_1)}{\partial t} = \iint\oint C^2(\underline{k}_1,\underline{k}_2,\underline{k}_3,\underline{k}_4)\, D^3 \left|\frac{\partial W}{\partial \underline{n}}\right|^{-1} d\underline{s}\,dk_3 k_3 d\theta$$

where the $\underline{k}_i$ are the interacting wavenumbers, $n(\underline{k}_i)$ is the action density at $\underline{k}_1$, C^2 is the interaction (coupling) coefficient, D^3 is the density function within the integral (consisting of sums of triplets of action densities), $\underline{s}$ and $\underline{n}$ are coordinates along and orthogonal to resonant interaction loci given by

$$7.\quad W = \omega_1+\omega_2-\omega_3-\omega_4 = 0$$

where the ω_i are the radial frequencies related to the interacting wavenumbers via the dispersion relationship

$$8.\quad \omega^2 = gk\tanh(kh)$$

where h is the local water depth and k is the magnitude of $\underline{k}$. The finite-depth version of equation 6 has recently been termed the Webb-Resio-Tracy (WRT) method for calculating nonlinear source functions.

Equation 6 is useful since, when converted to the appropriate form, it provides a direct estimate of the rate of change of energy, action, or momentum within a spectrum. Figure 1 shows the results for a standard JONSWAP integral in a 20-meter water depth. Such information is useful since it can be directly added to wind input and wave breaking source terms to provide a detailed picture of the expected evolution of spectral densities.

As shown by Resio and Perrie (1991) a potentially more useful form for understanding the effects of nonlinear interactions is the energy flux form for the above equations.

In this paper, we will adopt a slightly different version of the flux equation than that used by Resio and Perrie. Given a small band of wavenumbers centered around wavenumber k (i.e. a thin annulus in vector wavenumber space as shown in Figure 2), the energy flux into this band from higher wave numbers can be written as

$$9.\ \Gamma^{-}(k+\frac{\delta k}{2}) = \int_0^{\infty}\int_0^{2\pi}\omega \int_{k-\delta k/2}^{k+\delta k/2}\int_0^{2\pi} T(k,k') \, H(k'-k)\, H(T(k,k'))\, dk\ k\ d\theta\ dk'\ k'\ d\theta'$$

where T(k,k') is given by

$$10.\ T(k,k') = \oint C^2(\underline{k}_1,\underline{k}_2,\underline{k}_3,\underline{k}_4)\, D^3 \left|\frac{\partial W}{\partial \underline{n}}\right|^{-1} d\underline{s}$$

for all interaction loci such that $\underline{k}+\underline{k}'=\underline{k}''+\underline{k}'''$ and $\omega+\omega'=\omega''+\omega'''$. Similarly three other fluxes can be considered: the energy flux into this band from lower frequencies

$$11.\ \Gamma^{+}(k-\frac{\delta k}{2}) = \int_0^{\infty}\int_0^{2\pi}\omega \int_{k-\delta k/2}^{k+\delta k/2}\int_0^{2\pi} T(k,k') \, H(k-k')\, H(T(k,k'))\, dk\ k\ d\theta\ dk'\ k'\ d\theta'$$

the energy flux out of this band into higher frequencies,

$$12.\ \Gamma^{+}(k+\frac{\delta k}{2}) = \int_0^{\infty}\int_0^{2\pi}\omega \int_{k-\delta k/2}^{k+\delta k/2}\int_0^{2\pi} T(k,k') \, H(k'-k)\, H(-T(k,k'))\, dk\ k\ d\theta\ dk'\ k'\ d\theta'$$

and finally the flux out of this band into lower frequencies,

$$13.\ \Gamma^{-}(k-\frac{\delta k}{2}) = \int_0^{\infty}\int_0^{2\pi}\omega \int_{k-\delta k/2}^{k+\delta k/2}\int_0^{2\pi} T(k,k') \, H(k-k')\, H(-T(k,k'))\, dk\ k\ d\theta\ dk'\ k'\ d\theta'$$

In equations 9 and 11-13, H(.) is the Heaviside function defined as

$$14.\quad H(x) = 1 \quad for \quad x \geq 0$$
$$= 0 \quad for \quad x < 0$$

and the Γ's denote fluxes. The "+" superscripts denote fluxes from low to high wavenumbers, and the "-" superscripts denote fluxes from high to low wavenumbers, usually referred to as the inverse fluxes. If the ω term were left out of the above integrals, action fluxes rather than energy fluxes would be calculated. If k's were substituted for the ω's, momentum fluxes could be calculated.

Conventional source terms of the form given by equation 6 can be recovered from equations 9-13 via the relationship between the flux divergence and these integrals,

$$15.\ \frac{\partial F(k)}{\partial t} = \frac{\Gamma^{+}(k-\delta k/2) - \Gamma^{+}(k+\delta k/2)}{\delta k} + \frac{\Gamma^{-}(k+\delta k/2) - \Gamma^{-}(k-\delta k/2)}{\delta k}$$

where F(k) is the energy density in a wavenumber basis. Using the dispersion relationship to convert from

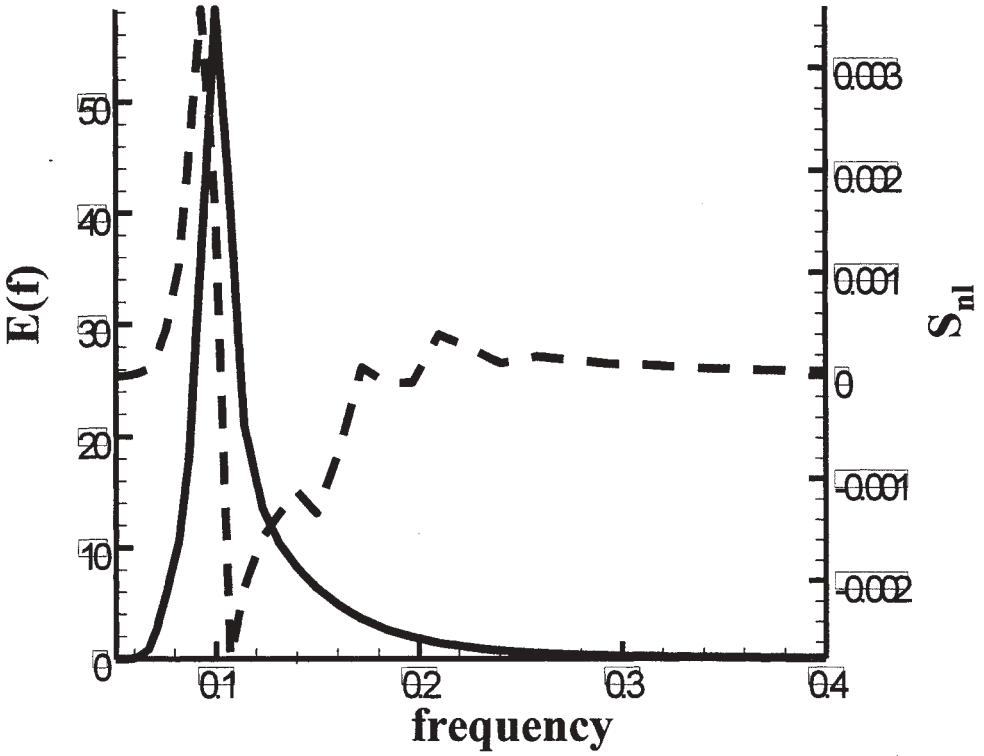

Fig. 1 S_{nl} for JONSWAP Spectrum with $f_p = 0.1$ Hz at 20-m Depth

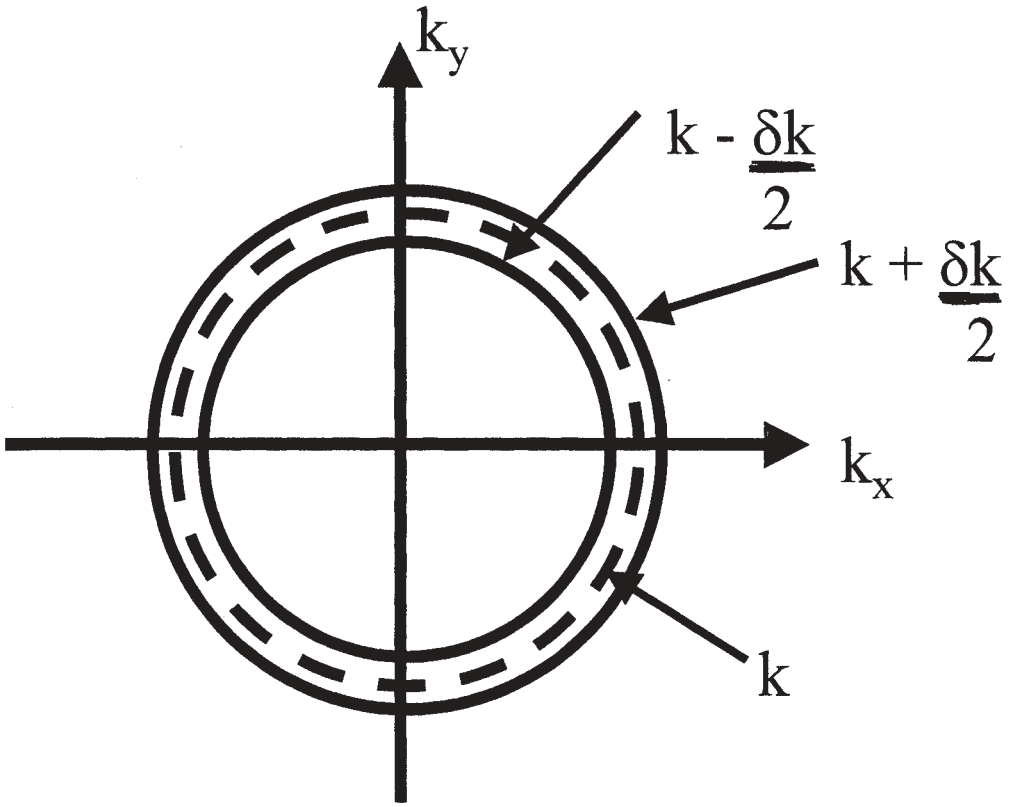

Fig. 2 Region for Flux Calculations

wavenumbers to frequencies, similar quantities can be calculated for energy density in the more conventional energy density in frequency basis, E(f).

3. Numerical Simulations and Results

The WRT form for the arbitrary-depth Boltzmann integral was modified to contain estimates of all of the fluxes defined above. Previous theoretical (Zakharov, 1968), numerical (Resio and Perrie, 1991; Resio et al., 2000), and field (Donelan et al., 1985; Resio et al., 2000) studies have all shown that wave spectra in deep and shallow water should contain equilibrium ranges of the form

$$16. \quad F(k) \sim \beta k^{-5/2}$$

where β is a dimensional constant. This is equivalent to an f^{-4} equilibrium range for E(f) in deep water. Consequently, it is not appropriate to use f^{-5}-based formulations such as the Pierson-Moskowitz or the JONSWAP spectrum as the basis for accurate studies of nonlinear interactions. For the case of finite depth, it is counterproductive to use frequency-based spectra at all, since it removes much of the simplicity of wavenumber-based spectra. Consequently, a spectrum of the form

$$16. \quad F(k) = \beta\, G(k/k_p)\, k^{-5/2}$$

where k_p is the wavenumber of the spectral peak and G is a dimensionless shape function given by

$$18. \quad G(k/k_p) = \gamma^{\exp(-q)} \qquad k \geq k_p$$
$$= k^{5/2}\gamma^{\exp(-q)} \qquad k < k_p$$

where γ is the peakedness parameter and q is specified equivalently to the peakedness formulations used in the standard JONSWAP spectrum, including the standard definitions and values for σ_a and σ_b. It should be noted that this places the peakedness within a frequency-based formulation.

For simplicity a constant angular spreading function is used here, i.e.

$$19. \quad F(k,\theta) = F(k)\,Z(\theta)$$

where $Z(\theta)$ is given by

$$20. \quad Z(\theta) = \frac{1}{S_0}\cos^s(\theta)$$

with S_0 defined as

$$21. \quad S_0 = \int_0^{2\pi} \cos^s(\theta)\, d\theta$$

Figure 3 shows the fluxes for a spectrum of the form given by equation 17 for the case of s=4 and γ=3. Three properties of the fluxes are of most interest here. First, as expected the fluxes become quite constant in the equilibrium range. Second, the fluxes are strongly divergent near the spectral peak, with the inverse fluxes becoming dominant in this region. And, third, there is a point slightly past the spectral peak at which the fluxes and inverse fluxes are equal to each other. If we define a frequency, f_0, as the first frequency past the spectral peak at which this occurs, it provides a means to factor out the wave-wave interactions from the detailed-balance source terms.

We will assume here that the value of β in the equilibrium range depends only on a reference wind speed, consistent with the arguments of Kitaigorodskii (1961,1985) and the findings of Donelan et al. (1985). For this case, the rate of gain of energy within the spectrum can be written as

$$22. \quad \frac{\partial E_0}{\partial t}\Big|_1 = \int_0^{f_0} [S_{in}(f) + S_{ds}(f)]\, df - \frac{\partial E_0}{\partial f_0}\Big|_1 \frac{\partial f_0}{\partial t}$$

for the region of the spectrum from 0 to f_0, where $S_{in}(f)$ and $S_{ds}(f)$ are the wind input and wave dissipation source terms, respectively. For the region of the spectrum higher than f_0, we have

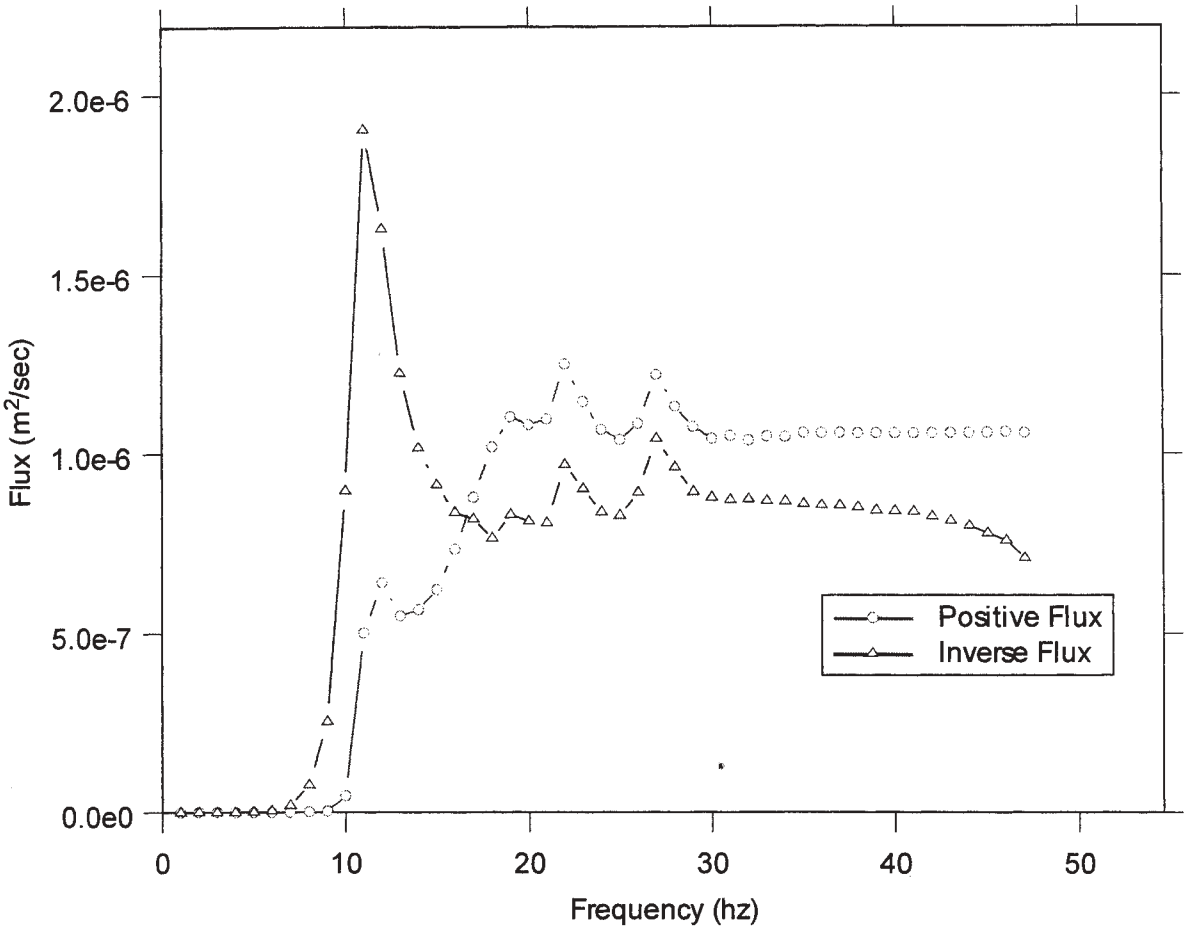

Fig. 3 Calculated Positive and Inverse Fluxes

$$23. \quad \frac{\partial E_0}{\partial t}\Big|_2 = \frac{\partial E_0}{\partial f_0}\Big|_2 \frac{\partial f_0}{\partial t}$$

where the subscripts "1" and "2" refer to the low-frequency and high-frequency side of the spectrum in Figure 4.

Also shown in Figure 4 is a depiction of the local balances which one can derive from this spectral partitioning. Here it is assumed that dissipation (wave breaking) is much weaker than wind input in the vicinity of the spectral peak, which should certainly be the case at least up to nearly fully-developed conditions. Since the last term on the right hand side of equation 22 is exactly equal to the term on the right hand side of equation 23, the rate of gain of energy within the spectrum can be written as a function of wind input only, provided that f_0 has a parameterizable behavior in terms of f_p. It is clear that within region 1 the role of nonlinear interactions is only to shape the spectrum, since they can make no net contribution to total energy. Thus, spectral peakedness is expected to be dependent on a balance between wind input, which will be an almost symmetric function centered on f_p, and the nonlinear source term, which is a strongly asymmetric function around f_p.

In region 2, the equilibrium range will be built by the wind input over the range from f_0 to some point where the total fluxes (positive and inverse) become much larger than the local wind input. This happens because the fluxes are essentially a constant for all frequencies above f_0 while local wind inputs have the form

$$24. \quad \frac{\partial E(f)}{\partial t} = Rfu^2 E(f)$$

where R is an empirical constant. Since E(f) diminishes as f^{-4} in deep water and as $f^{-5/2}$ as an asymptotic limit in very shallow water, the wind source term will diminish in proportion to frequency to some negative power. Therefore, as frequency increases, it takes a smaller and smaller variation in equilibrium range densities to allow the divergence in nonlinear fluxes to balance the wind input. In this context, energy levels within the equilibrium range will have the following balance with the wind inputs

$$25. \quad \int_{f_0}^{f_{eq}} Rfu^2 E(f)\, df \approx (\lambda^+ - \lambda^-)\beta^3$$

which states that there will be an approximate balance between the cumulative wind input into the region between f_0 and f_{eq} (where f_{eq} is defined as the frequency which starts the equilibrium range) and the net fluxes out of this region. This will be true if wave dissipation is much smaller in this region than wind input. The parameters λ^+ and λ^- refer to constants which satisfy the equations

$$26. \quad \Gamma^+ = \lambda^+ \beta^3$$

and

$$27. \quad \Gamma^- = \lambda^- \beta^3$$

where β is defined in equation 16. In this context, the λ's represent Komolgorov constants for the energy fluxes. For the case of an isotropic spectrum, the λ values should be constant; however, as seen in Figure 5, the values increase as the angular spreading decreases (i.e. "s" increases). Since the magnitude of the fluxes can be strongly influenced by triplets in the vicinity of the maximum energy density at the central wave angle, this is not too surprising. Figure 5 was obtained via careful numerical simulations that included variations in both the peakedness function and the angular spreading function. Only the angular spreading function significantly affected fluxes in the equilibrium range.

A simple integration of equation 25 for the deep-water case shows that we should have

$$28. \quad \beta = \left[\frac{R\beta'(f_{eq}^{-2} - f_0^{-2})}{2(\lambda^+ - \lambda^-)}\right]^{1/3} u$$

where β' is defined as

$$29. \quad E(f) = \beta' u f^{-4}$$

for the equilibrium range in a frequency representation.

This implies that there should be a linear relationship between wind speed and the spectral parameter β. Equation 29 is relatively well accepted for deep water

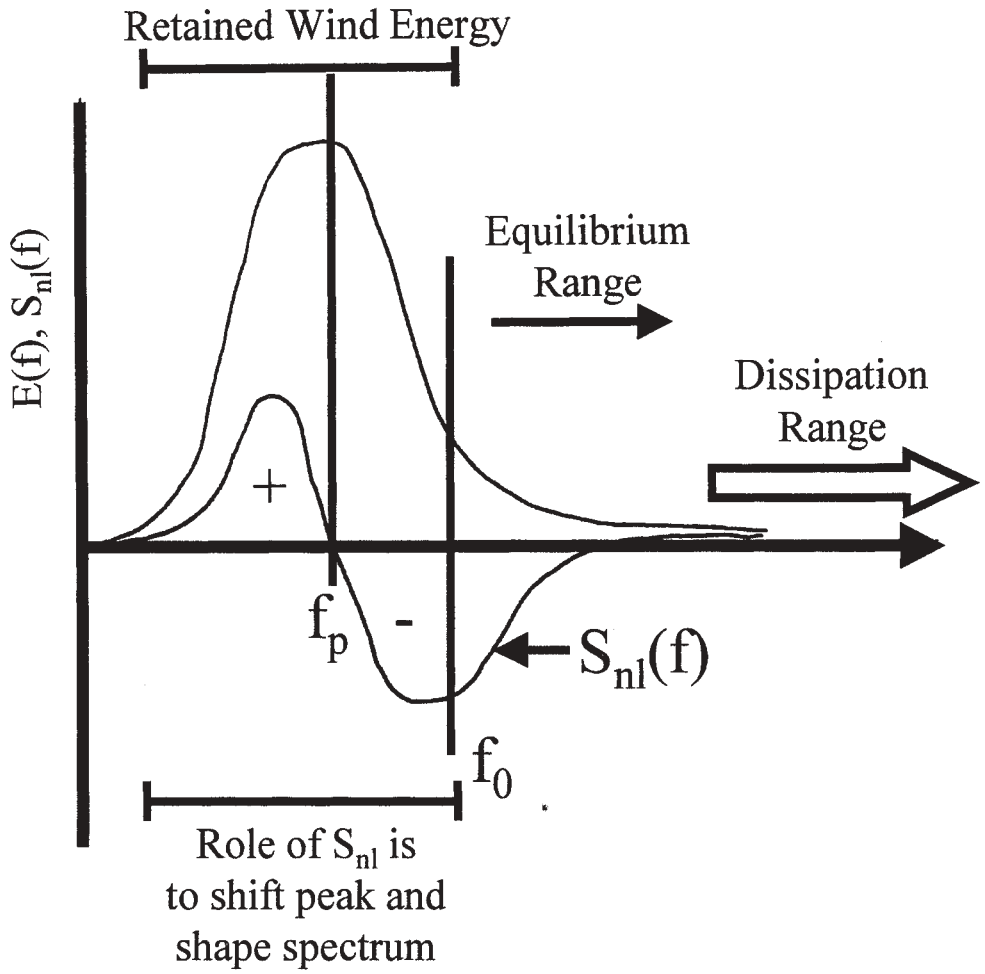

Fig. 4 Definable Spectral Regions

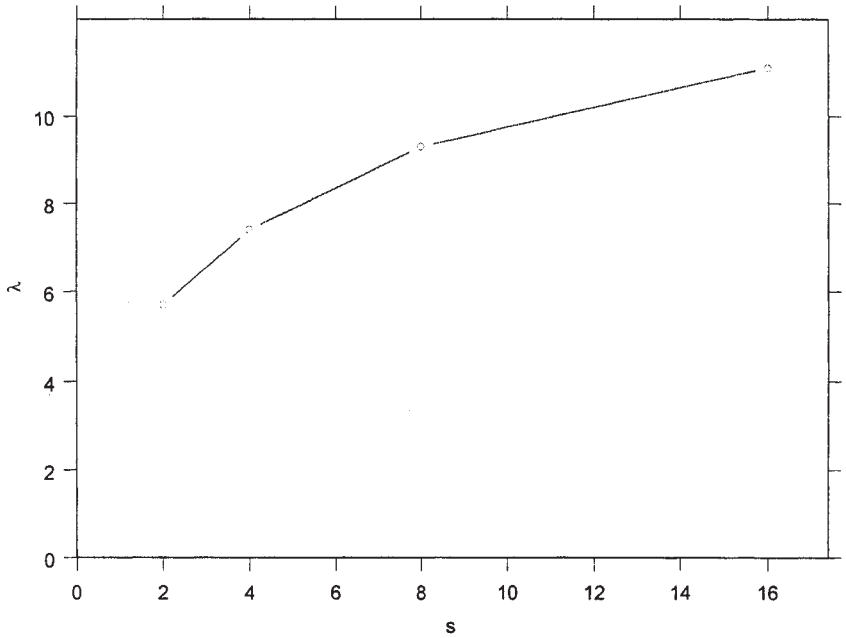

Fig. 5 Behavior of Flux Constant as a Function of Angular Spreading

waves (see for example Donelan et al., 1985) and some work has been done to extend this relationship into shallow water (Bouws et al.(1985), Miller and Vincent (1990). However, little has been done to establish a theoretical link between the deep and shallow water cases.

Figure 6 contains wave data from three sites plotted against measured wind speeds. The data come from Lake George (depths 1-2 meters), the end of the pier at CHL's Field Research Facility (FRF) in Duck, North Carolina (depths 6-8 meters), and the waverider off the coast of the FRF (depths 18.5-20 meters). The wind speed parameter used here is the wind speed a constant fraction of the spectral peak wave length above the water surface (Resio et al., 1999). This wind reference level provided the highest correlation (0.81) between the β's and the wind speeds from all three sites. The degree of agreement shown in Figure 6 suggests that the interaction between winds and waves in the equilibrium range in shallow water is not a strong function of depth. Thus, given information on the angular spreading in actual wave spectra, a relatively independent check on the wind input function can be made using equation 28.

In region 1, the rate of gain of energy can be determined via equation 22. A simple integration for a wind input function of the same form used above can be written as

$$30. \quad \frac{\partial E_0}{\partial t} = \int_{z_1 f_p}^{z_2 f_p} Ru^2 E(f)\, df$$

where z_1 and z_2 are dimensionless constants, where $z_1 f_p$ is the low-frequency limit of the energy-containing frequencies near the spectral peak and $z_2 f_0$ is equal to f_0. It is clear that the rate of input will depend strongly on the energy levels near the spectral peak, which depends on the peakedness of the spectrum, and the size of the integration domain, which depends on the values of z_1 and z_2.

Figure 7 shows a plot of z_2 versus peakedness. As was the case for the previous simulations, both angular spreading and peakedness was varied but only one of the factors (in this case peakedness) was found to significantly affect the results. Interestingly, Figure 7 indicates that there are two conflicting influences on the integral given in equation 30. First, as peakedness goes up, the value of E(f) near the spectral peak increases, so the integral might be expected to increase as a function of peakedness. On the other hand, as the peakedness increases the integration domain diminished, tending to make the overall integral smaller. Detailed analysis of this integral is currently underway, but is beyond the scope of this paper.

4. Summary and Discussion

Results shown here show that it may be possible to partition wave generation processes into two important regions, a spectral peak region and the equilibrium range. It is anticipated that a third region, one where dissipation dominates the spectral form will occur at some frequency above the equilibrium range; however, the analysis to develop this argument was not made as part of this paper. Interestingly, these findings are in approximate agreement with the similarity arguments of Kitaigorodskii (1961) made some 40 years ago. The findings of this paper only show how to quantify these ranges and that individual source term balances should be able to be isolated within these regions. The findings here are also consistent with those of Young and Van Vledder (1993) who argued that nonlinear interactions should play a very dominant role in developing spectral energies and source term balances.

This work is the first step toward establishing clear guidelines for the calibration of source terms for detailed-balance wave models. A second paper is planned which will treat this topic.

5. REFERENCES

Bouws, E., Gunther, H., Rosenthal, W., and C.L. Vincent, 1985: Similarity of the wind wave spectrum in finite-depth water, part 1: Spectral form, J. Geophys. Res., v. C90, 1653-1658.

Donelan, M.A., Hamilton, J., and W.H. Hui, 1985: Directional spectra of wind generated waves, Phil. Trans.Roy. Soc. London, v. A315, 509-562.

Hasselmann, K.,1962: On the nonlinear energy transfer in a gravity wave spectrum, part 1: general theory, J. Fluid Mech., v. 12, 481.

Hasselmann, K., Barnett, T.P., Bouws, E., Carlson, H., Cartwright, D.E., Enke, K., Ewing, J.A., Gienapp, H. Hasselmann, D.E., Kruseman, P. Meeburg, A., Muller, P, Olbers, D.J., Richter, K., Sell, W., and H. Walden, 1973: Measurements of wind-wave growth and swell decay during the Joint North Sea Wave Project (JONSWAP), Dtsch. Hydrogr. Z., Suppl. A, v. 8, 95p.

Hasselmann, S., Hasselmann, K., Allender, J.H., and T.P. Barnett, 1985: Computations and parameterizations of the nonlinear energy transfer in a gravity wave spectrum,

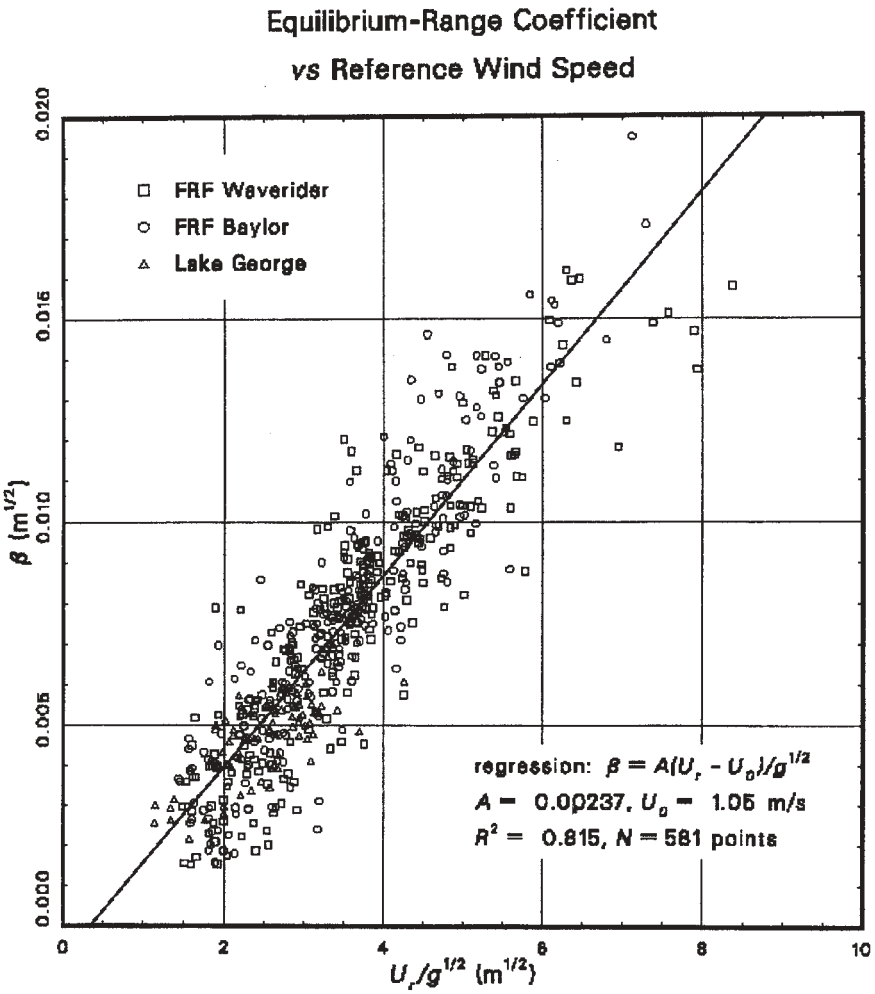

Fig. 6 Lake George and Duck, NC, Data

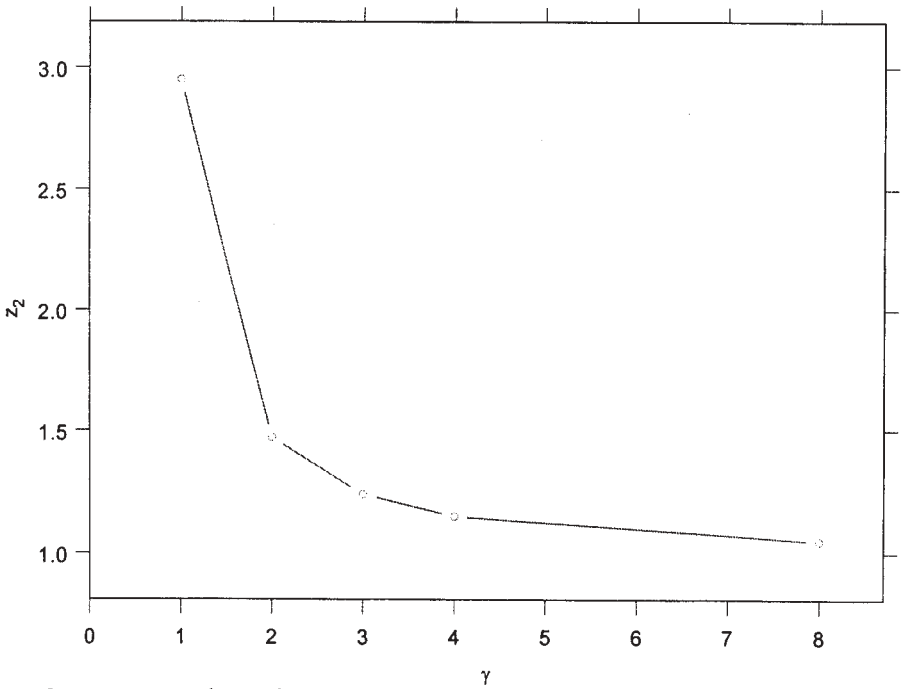

Fig. 7 Behavior of f_0 as a Function of Peakedness

AUTHOR INDEX
TABLE OF CONTENTS

Part 2: Parameterizations of non-linear transfers for applications in wave models, J. Phys. Oceanogr, v. 15., 1378-1391.

Kahma, K.K., 1981: A study of the growth of the wave spectrum with fetch, J.Phys. Oceanogr., v. 11, 1503-1515.

Kitaigorodskii, S.A., 1962: Application of the theory of similarity to the analysis of wind-generated water waves as a stochastic process, Bull. Acad. Sci. USSR Geophys., Ser. no. 1, 73p.

Kitaigorodskii, S.A., 1983: On the theory of the equilibrium range in the spectra of wind-generated waves, J. Phys. Oceanogr., v. 13, 816-827.

Miller, H.C. and C.L. Vincent, 1990: The FRF spectrum, TMA scaling with Kitaigorodskii's f^{-4} scaling, J. Waterway Port Coast Engr, v. 116, 57-78.

Mitsuyasu, H., 1968: On the growth of the spectrum of wind-generated waves, 1., Rep. Res. Inst. Mech., Kyushu Univ.,v. 16, 251-264.

Resio, D.T. and W. Perrie, 1991: A numerical study of nonlinear fluxes due to wave-wave interactions: Part I, Methodology and Basic Results, J. Fluid Mech., v. 223, 603 -629.

Resio, D.T., Swail, V.R., Jensen, R.E., and V.J. Cardone, 1999: Wind speedscaling in fully-developed seas, J. Phys. Oceanogr., 1801-1811.

Resio, D.T., Rassmussen, J., Tracy, B.A., and C.L. Vincent, 2000: Nonlinear energy fluxes and shallow-water wave spectra, accepted for publication in J. Geophys. Res.

Tolman, H.L., 1991: A third-generation model for wind waves on slowly varying, unsteady, and inhomogeneous depths and currents, J.Phys. Oceanogr., v. 21, 782-797.

Tolman, H.L. and D. Chalikov, 1996: Source terms in a third-generation wind wave model, J. Phys. Oceanogr., v 26, 2497- 2518.

Webb, D.J., 1978: Nonlinear transfers between sea waves, J. Deep Sea Res., v. 25, 279-298.

Young, I.R. and G.Ph. van Vledder, 1993: A review of the central role of nonlinear interactions in wind-wave evolution, Phil. Trans. Roy. Soc. London, v. 342, 505-524.

Zakharov, V.E., 1968: Stability of periodic waves of finite amplitude on the surface of a deep fluid, J.Appl. Mech.Techn. Phys., v. 9, 190-194.

A NOWCAST TOOL TO ASSESS WAVE PARAMETERS IN COASTAL AREAS

Carlos Ventura Soares[1], Eugen Rusu[2], Emanuel F. Coelho[1], António A. Pires Silva[3], Oleg Makarynskyy[4]

1. Instituto Hidrográfico, IH, Marinha, Rua das Trinas 49, 1249-093 Lisboa, PORTUGAL
2. Galati University, ROMANIA – presently at IH, PORTUGAL
3. Instituto Superior Técnico, IST, Av. Rovisco Pais, 1049-001 Lisboa, PORTUGAL
4. Odessa Hydrometeorological Institute, UKRAINE – presently at IST, PORTUGAL

1. INTRODUCTION

For coastal environmental and ocean engineering applications the availability of realistic data of the sea wave field is most important for the safe design and operation of marine structures and installations, as well as for the control of the sediment transport and the study of the nearshore wave climate. Running numerical models being able to produce forecast products of the oceanographic data can also make available in a useful time scale the environmental support necessary for various military operations and to conduct to a rapid environmental assessment of a tactically significant area. An adequate evaluation of the wave conditions in a near real time is therefore of essential importance in the coastal engineer applications as well as in the military landing operations. In the present paper a methodology is proposed for environmental assessment taking into account the non-linear effects that are most important in shallow water. Starting from buoy data, as input, SWAN spectral model is used to predict the results to a specific area. Then, fully using its high performances in integration between computations and visualization effects, the wave data are processed in the MATLAB environment.

2. THEORY OF SWAN

SWAN (acronym for Simulation WAves Nearshore) is a numerical wave model designed to obtain realistic estimates of wave parameters in coastal areas, lakes and estuaries from given wind, bottom, and current conditions. The model is based on the action balance equation (or energy balance in the absence of currents) with sources and sinks. The SWAN model has been developed at the Delft University of Technology, Department of Civil Engineering, Delft, the Netherlands, Ris et al (1998). It was released in the public domain and can be downloaded from the Internet. In SWAN the following wave propagation processes are implemented: propagation through geographic space, refraction due to bottom and current variations, shoaling due to bottom and current variations, blocking and reflections by opposing currents, transmission through or blockage by sub-grid obstacles. It also accounts for the dissipation effects due to whitecapping, bottom friction and wave breaking. Diffraction and reflection are not modeled in SWAN, so it should not be used in areas where wave height variations are large within a horizontal scale of a few wavelengths. Because of this, the wave field computed by SWAN will generally not be accurate in the immediate vicinity of obstacles and certainly not in harbors. The depth and currents (if present) are input to SWAN. The propagation in SWAN is rather diffusive. SWAN should therefore not be used in domains larger than 25 km.

The waves are described with the two-dimensional wave action density spectrum, even when nonlinear phenomena dominate (e.g., in the surf zone). The rationale for using the spectrum in such highly nonlinear conditions is that, even in such conditions it seems possible to predict with reasonable accuracy this spectral distribution of the second order moment of the waves (although it may not be sufficient to fully describe the waves statistically). The spectrum that is considered here is the action density spectrum $N(\sigma,\theta)$ rather than the energy density spectrum $E(\sigma,\theta)$ since in the presence of currents, action density is conserved whereas energy density is not (e.g., Whitham, 1974). The independent variables are the relative frequency σ (as observed in a frame of reference moving with the action propagation velocity) and the wave direction θ (the direction normal to the wave crest of each spectral component). The action density is equal to the energy density divided by the relative frequency: $N(\sigma,\theta) = E(\sigma,\theta)/\sigma$. The evolution of the wave spectrum is described by the spectral action balance equation, which for Cartesian coordinates is (e.g., Hasselmann et al., 1973):

AUTHOR INDEX TABLE OF CONTENTS

$$\frac{\partial}{\partial t}N+\frac{\partial}{\partial x}c_x N+\frac{\partial}{\partial y}c_y N+ \\ +\frac{\partial}{\partial \sigma}c_\sigma N+\frac{\partial}{\partial \theta}c_\theta N=\frac{S}{\sigma}. \quad (1)$$

The first term in the left-hand side of this equation represents the local rate of change of action density in time, the second and third term represent propagation of action in geographical space (with propagation velocities c_x and c_y in x- and y-space, respectively). The fourth term represents shifting of the relative frequency due to variations in depths and currents (with propagation velocity c_σ in σ-space). The fifth term represents depth-induced and current-induced refraction (with propagation velocity c_θ in θ-space). The expressions for these propagation speeds are taken from linear wave theory (e.g., Whitham, 1974; Mei, 1983; Dingemans, 1997). The term $S = S(\sigma,\theta)$ at the right hand side of the action balance equation is the source term in terms of energy density representing the effects of generation, dissipation and nonlinear wave-wave interactions. A brief summary of the formulations that are used for the various source terms in SWAN is given next.

Transfer of wind energy to the waves is described with the resonance mechanism of Phillips (1957) and the feedback mechanism of Miles (1957). The corresponding source term for these mechanisms is commonly described as the sum of linear and exponential growth:

$$S_{in}(\sigma,\theta) = A + BE(\sigma,\theta), \quad (2)$$

in which A and B depend on wave frequency and direction, and wind speed and direction. The effects of currents are accounted for in SWAN by using the apparent local wind speed and direction. The expression for the term is due to Cavaleri and Malanotte-Rizzoli (1981) with a filter to avoid growth at frequencies lower than the Pierson-Moskowitz frequency (Tolman, 1992). Two optional expressions for the coefficient B are used in the model. The first is taken from an early version of the WAM model (known as WAM Cycle 3, the WAMDI group, 1988). It is due to Snyder et al. (1981), rescaled in terms of friction velocity U_0 by Komen et al. (1984). The drag coefficient to relate U_0 to the driving wind speed at 10m elevation U_{10} is taken from Wu (1982). The second expression for B in SWAN is taken from the most recent version of the WAM model (known as WAM Cycle 4, Komen et al., 1994). It is due to Janssen (1991a) and it accounts explicitly for the interaction between the wind and the waves by considering atmospheric boundary layer effects and the roughness length of the sea surface. The corresponding set of equations is solved (as in the WAM model) with the iterative procedure of Mastenbroek et al. (1993).

The dissipation term of wave energy is represented by the summation of three different contributions: whitecapping $S_{ds,w}(\sigma,\theta)$, bottom friction $S_{ds,b}(\sigma,\theta)$ and depth-induced breaking $S_{ds,br}(\sigma,\theta)$.

Whitecapping is primarily controlled by the steepness of the waves. In presently operating generation wave models, the whitecapping formulations are based on the pulse-based model of Hasselmann (1974), as adapted by the WAMDI group (1988):

$$S_{ds,w}(\sigma,\theta) = -\Gamma\tilde{\sigma}\frac{k}{\tilde{k}}E(\sigma,\theta), \quad (3)$$

where Γ is a steepness dependent coefficient, k is wave number and $\tilde{\sigma}$ and $\tilde{k}$ denote a mean frequency and a mean wave number, respectively (cf. the WAMDI group, 1988). Komen et al. (1984) estimated the value of Γ by closing the energy balance of the waves in fully developed conditions. This implies that this value depends on the wind input formulation that is used. Since two expressions are used for the wind input in SWAN, also two values for Γ are used. The first is due to Komen et al. (1984, as in Cycle 3 of the WAM model). It is used in SWAN when the wind input coefficient B of Komen et al. (1984) is used. The second expression is an adaptation of this expression based on Janssen (1991a; as in Cycle 4 of the WAM model; see Janssen, 1991b; Günther et al., 1992). It is used when the wind input term B of Janssen (1991a) is used. Young and Banner (1992) and Banner and Young (1994) have shown that the results of closing the energy balance in this manner depend critically on the choice of a high-frequency cut-off frequency above which a diagnostic spectral tail is used. In SWAN this cut-off frequency is different from the one used in the WAM model. Differences in the growth rates between the WAM model and SWAN are therefore to be expected.

Depth-induced dissipation may be caused by bottom friction, by bottom motion, by percolation or by back-scattering on bottom irregularities (Shemdin et al., 1978). For continental shelf seas with sandy bottoms, the dominant mechanism appears to be bottom friction (e.g., Bertotti and Cavaleri, 1994) which can generally be represented as:

$$S_{ds,b}(\sigma,\theta) = -C_{bottom}\frac{\sigma^2}{g^2\sinh^2(kd)}E(\sigma,\theta), \quad (4)$$

in which C_{bottom} is a bottom friction coefficient. A large number of models have been proposed since the pioneering paper of Putnam and Johnson (1949). Hasselmann et al. (JONSWAP, 1973) suggested to use

an empirically obtained constant. It seems to perform well in many different conditions as long as a suitable value is chosen (typically different for swell and wind sea; Bouws and Komen, 1983). A nonlinear formulation based on drag has been proposed by Hasselmann and Collins (1968) which was later simplified by Collins (1972). More complicated, eddy viscosity models have been developed by Madsen et al. (1988) and by Weber (1989, 1991a, 1991b). Considering the large variations in bottom conditions in coastal areas (bottom material, bottom roughness length, ripple height etc.), there is no field data evidence to give preference to a particular friction model (Luo and Monbaliu, 1994). For this reason, the simplest of each of these types of friction models has been implemented in SWAN: the empirical JONSWAP model of Hasselmann et al. (1973), the drag law model of Collins (1972) and the eddy-viscosity model of Madsen et al. (1988). The effect of a mean current on the wave energy dissipation due to bottom friction is not taken into account in SWAN. The reasons for this are given by Tolman (1992b) who argues that state-of-the-art expressions vary too widely in their effects to be acceptable. He found that the error in finding a correct estimate of the bottom roughness length scale has a much larger impact on the energy dissipation rate than the effect of a mean current. The expression that is used in SWAN for modeling the depth-induced wave breaking is:

$$S_{ds,br}(\sigma,\theta) = -\frac{D_{tot}}{E_{tot}} E(\sigma,\theta), \qquad (5)$$

in which E_{tot} is the total wave energy and D_{tot} is the rate of dissipation of the total energy due to wave breaking according to Battjes and Janssen (1978). Adding a quadratic dependency on frequency as suggested by Mase and Kirby (1992, supported by Elgar et al., 1997) seems to have no noticeable effect on the SWAN results.

3. SIMULATIONS WITH SWAN IN THE COASTAL ENVIRONMENT OF PORTUGAL

To measure the wind wave climatology off the Portuguese coast a permanent network of wave stations along the coast was established and is maintained by Instituto Hidrografico (IH). These stations include directional buoys and their respective data collection systems. At the present time five stations are operating along the Portuguese continental coast and two off Madeira Islands. In the present work only the Sines buoy, placed at Lat = 37° 55' 16" N, Long = 008° 55' 44" W, depth = 87 meters was used. Moreover, in the last years the IH deploys pressure sensors aiming to obtain additional information about current and wave conditions close to the surf zone and to assess the quality of the numerical estimations.

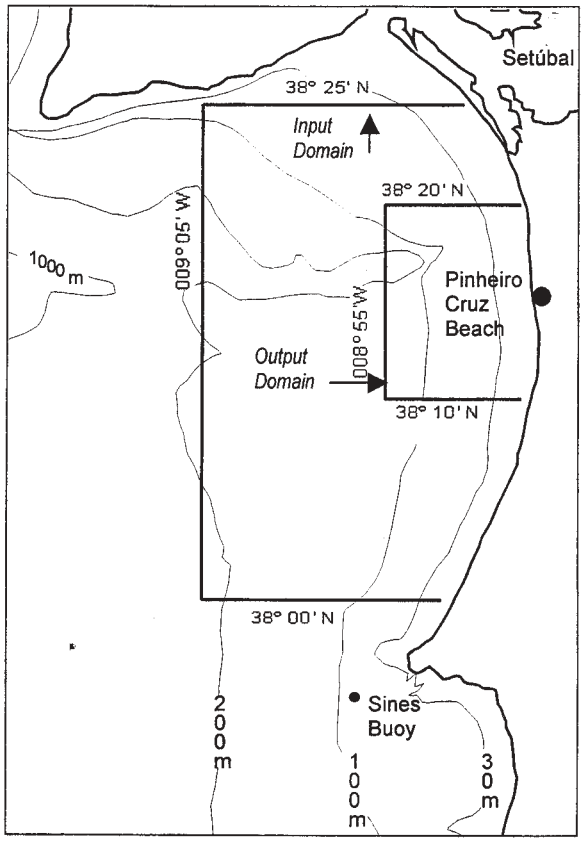

Fig. 1
The area Pinheiro da Cruz and the initial scheme

To obtain directional information, the co and quad-spectra of the heave and slope time series are first estimated, using FFT techniques. These spectra are then used to derive five coefficients of the Fourier series expansion of the directional distribution function. From these coefficients it is possible to estimate the mean wave direction and the directional spread. The usual non-directional parameters are also evaluated from the spectral information, the characterization of the wave climate being based on the following parameters: significant wave height, mean period, peak period and mean direction at peak period. The field for experiments was the area Pinheiro da Cruz in the vicinity of Sines wave buoy (Figure 1).

Pinheiro da Cruz beach is a sandy-cliff stretch, south of Lisbon and nearby Setubal, with its cord aligned with North to South direction. Incoming swell is basically W/NW defining a regular pattern almost all the year. The bathymetry is regular with parallel contours to the coastline except in the East Point of the Setúbal canyon. SWAN implementation over this area has been done

AUTHOR INDEX TABLE OF CONTENTS

testing different schemes and model input domains (the initial one is represented in Figure 1) in order to obtain wave parameters in the model output domain.
A digital model of the ocean floor was used as bottom boundary condition. Deep-water wave parameters obtained from the "Waverider" wave buoy at Sines, were then used to define the external boundary condition. Winds and tides were also introduced as forcing functions. Several model runs were made to characterize dominant features of swell, namely in storm conditions.
A pressure sensor was deployed at 10-meter depth during winter 1999/2000 at the Pinheiro da Cruz beach to assess the quality of the wave parameter estimates nearshore. A fair agreement was obtained between observed and modeled data. (Pires Silva et al. 2000).

4. A WAVE NOWCAST TOOL

The results delivered by SWAN are subsequently processed in the MATLAB environment using for this an original interactive interface, which consists of subroutines with the structure of script M-files. These files can be classified into three categories according to their functions. In the first are included subroutines necessary for setting the global variables and import the data into the MATLAB environment (as Mat-files). Since the interface was designed as an extension to SWAN it could be used almost in any scheme of running the model. For these reasons some global variables were introduced to describe the characteristics of the experiment (the dimensions and positions of the grids used, the number of meshes, etc).
The second are command subroutines having different functions as evaluation of wave data in any point of the domain, main wave parameter variation along any line selected from the sea field, global data assessment, evaluation of the 1 or 2-D frequency spectrum and prediction of the surf-zone conditions. Finally, in the third category are included the auxiliary files which are mainly used for interpolations or for plotting maps and isolines. The direction of the information flux propagating from SWAN to MATLAB and then to the final outputs is suggested in Fig. 3. Once the data transfer is finished the rapid environmental assessment procedure could begin and it consists mainly of four phases.
Phase I - Local data evaluation. In this phase using the map of the area any point or line in the field can be chosen to evaluate the values of the wave variables.

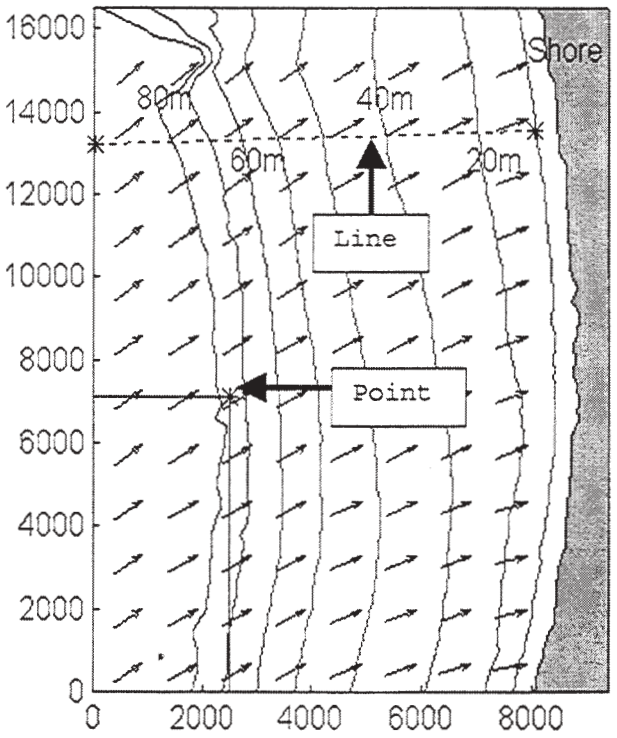

Fig. 2
The wave field analyzed and two examples of locations

In Fig.2 two arbitrary locations (for a point and respectively a line) are presented and in Fig.4 and 5 the respective values of the main wave variables (and their variation), as they are delivered instantaneously by the corresponding command file. All examples in the figures presented refer to the wave conditions registered in 11 February 1994. For the case of the point, it is also made a comparison with the maximum value of the respective variable in the field. The numerical values are also provided and they are given in table 1 for both the point and line selected.
Since the MATLAB interface was designed to use the same numerical scheme as SWAN, namely bilinear interpolation between the points of the computational grid, no difference occurs between the results processed in the MATLAB environment and those delivered in the same locations directly by SWAN. As in SWAN, the interpolation of spectra was made using a bin-by-bin interpolation procedure in order not to be caused reduction of the spectral peak. It is an interpolation where the spectra are first normalized by average frequency and direction then interpolated and then transformed back. Subsequently the software can provide the isolines, as showed in the map (Fig.2) and the distribution of the wave variables along them.

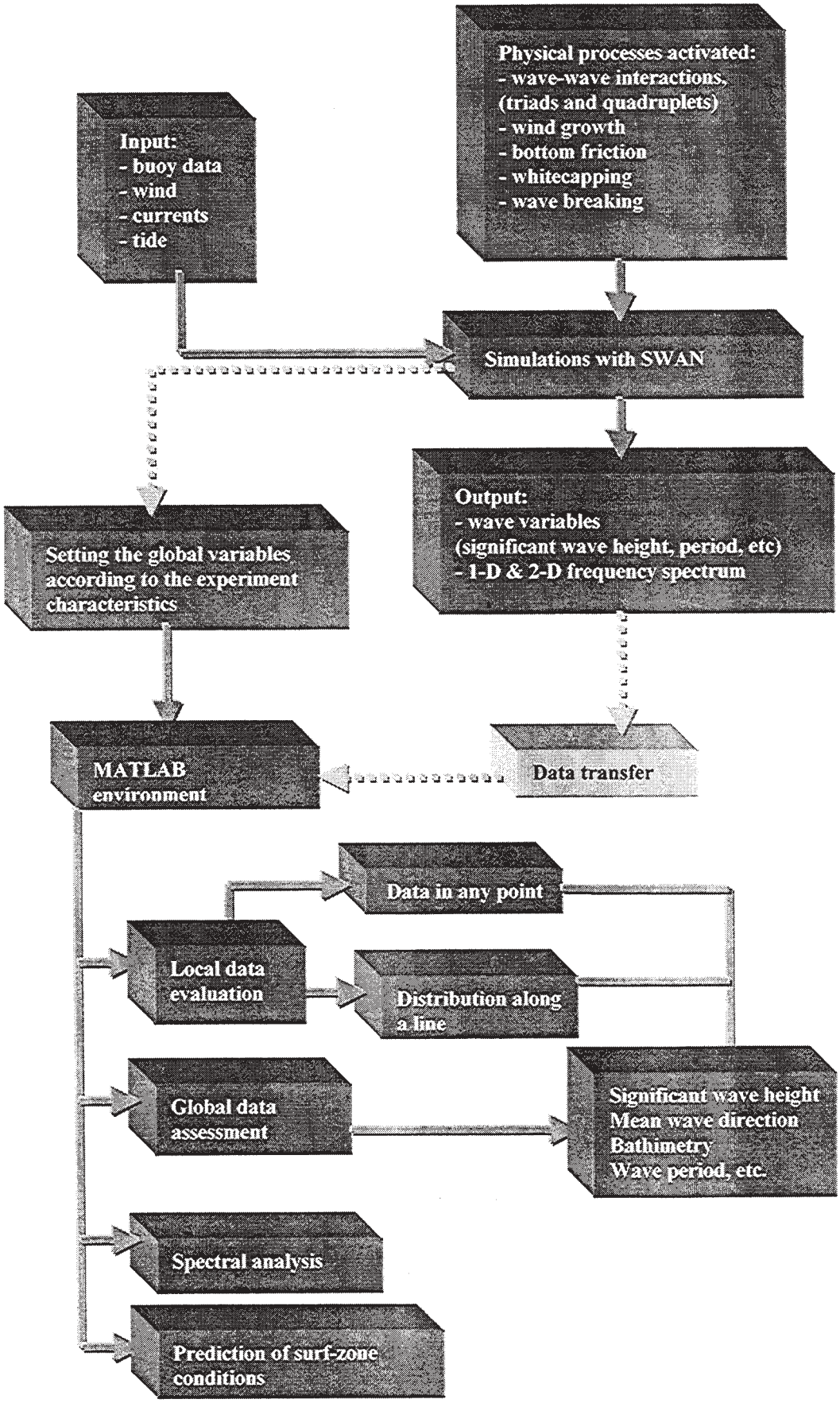

Fig. 3
Description of the proposed wave assessment procedure

Table 1
The values of the wave variables in the located point (a) and respectively along the located line (b) (case registered in 11.02.1994)

Case	X (m)	Y (m)	H_S (m)	TM01 (s)	WD (m)	DIRW (°)
a) point	2518.2	7112.9	3.49	9.89	-74.61	257.15
b) Line Point number						
1	21.71	13209.7	3.68	9.96	-120.07	254.21
2	911.78	13248.41	3.63	9.89	-135.78	254.59
3	1801.85	13287.12	3.42	9.59	-78.96	254.64
4	2619.92	13325.83	3.33	9.53	-51.87	253.92
5	3581.99	13364.54	3.30	9.57	-41.27	253.87
6	4472.06	13403.25	3.29	9.67	-34.14	254.90
7	5362.12	13441.96	3.27	9.76	-28.52	256.11
8	6252.19	13480.67	3.26	9.85	-23.71	257.12
9	7142.26	13519.38	3.29	10.01	-17.93	257.96
10	8032.33	13558.09	Surf-zone	Surf-zone	-5.97	Surf-zone
11	8922.4	13596.8	Shore	Shore	+10	Shore

Table 2
Maximum values of the waves variables and their location (case registered in 11.02.1994)

NR	Wave variable	Notation	Dimension	Value	X (m)	Y (m)
1	Significant wave height	H_S	m	3.73	600	13530
2	Mean absolute wave period	TM01	s	12.82	8600	1850
3	Water depth	WD	m	-243.55	0	12540
4	Variance	V	m^2	231.84	8200	1815
5	Wave direction (mean value)	DIRW	Degrees	256	-	-
6	Directional spreading	DSPR	Degrees	24.65	0	11220
7	Frequency spreading	FSPR	Hz	0.65	8600	10560
8	Wave length	WLEN	m	112.67	800	0
9	Wave steepness	STEE	-	0.05	8400	12210

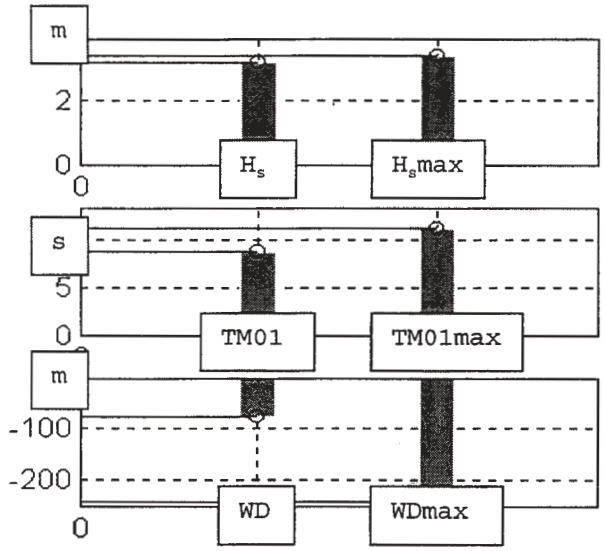

Fig. 4
The values of the wave variables in the elected point

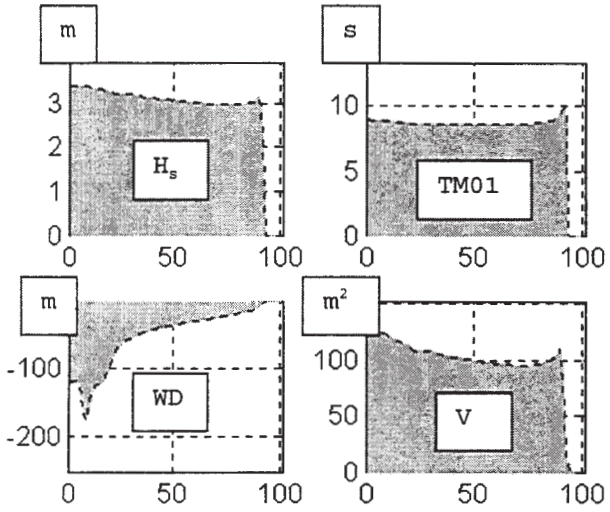

Fig. 5
The distribution along the selected line of the variables (in the abscises are the point numbers, from 1 to 100)

Phase II – Global data evaluation. In this phase a global assessment of the wave conditions is made concerning the entire area of interest. This phase gives an overview of the distribution of the wave variables in the sea field and allows an evaluation of the wave data accuracy. It also helps in correction of the initial and (or) of the boundary conditions, as well as to evaluate the optimal combination of the physical processes activated. In figure 2 can be seen the distribution of the wave direction in the field also and in table 2 the maximum values of the wave parameters and their location in the field.

Phase III - Spectral data evaluation. In this phase both the 1 and 2-D frequency spectrum are evaluated. In the second case the interface makes also possible the identification of both the directional and the frequency spectra distributions.

Phase IV – Surf-zone conditions.

The prediction of surf-zone conditions is another component of the wave nowcasting tool.

To model the energy dissipation in random waves due to depth-induced breaking, the bore-based model of Battjes & Janssen (1978) is used by SWAN. The mean rate of energy dissipation per unit horizontal area due to wave breaking D_{tot} is expressed as:

$$D_{tot} = -\frac{1}{4}\alpha_{BJ} Q_b \left(\frac{\bar{\sigma}}{2\pi}\right) H_m^2, \qquad (6)$$

in which α_{BJ} =1, H_m is the maximum wave height that can exist at the given depth and Qb is the fraction of breaking waves:

$$\frac{1-Q_b}{\ln Q_b} = -8\frac{E_{tot}}{H_m^2}. \qquad (7)$$

Following the variations of some wave parameters towards to the shore the imminence of the breaking process is given in two ways. A local maximum (is the case of the significant wave height and the variance) or a drastically increase (is the case of the dissipation and the fraction of breakers). Consequently, the location of the breaking line was found using these two different approaches (the significant wave height approach and the energy dissipation approach) by estimating the local maximum or respectively a drastically increase in the variation of the variable. The results are quite similar. The main characteristics of the breaking line are presented in figure 6. These are the variations along the breaking line of the distance to shore, the significant wave height and the water depth.

Breaking waves have been classified as spilling, plunging, collapsing or surging, depending on the way in which they break. Spilling breakers break gradually and they are characterised by white-water at the crest. Plunging breakers curl over a crest with a plunging forward of the mass of water at the crest. Surging breakers built up as if to form a plunging breaker but the base of the wave surges up to the beach before the crest can plunge forward. The term collapsing breaker is used to describe breakers in the transition from plunging to surging,. The breaker-type prediction usually uses the inshore form of Iribarren number, which combines the beach slope S with the wave steepness:

$$\xi_b = \frac{S}{(H_b / L_\infty)^{1/2}}, \qquad (8)$$

where H_b is the significant wave height of the breakers.

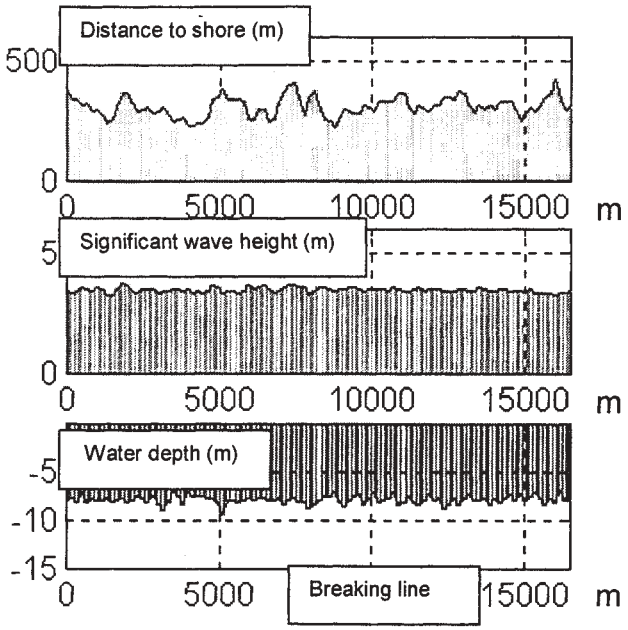

Fig. 6
The breaking line characteristics

In reference to this parameter the breaking-type classification is the following: $\xi_b \leq 0.4$-spilling; $0.4 < \xi_b \leq 2.4$-plunging; $2.4 < \xi_b \leq 3.1$-collapsing and $\xi_b > 3.1$ –surging.
Taking into account the characteristics of the beach in the area Pinheiro da Cruz, all the cases analyzed up to now were spilling breaking-type. The variation of the Iribarren parameter along the breaking line is given in figure 7.

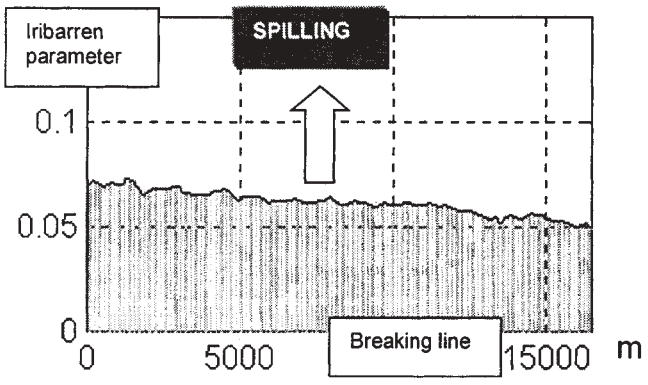

Fig. 7
Identification of the breaking type

In the analysis of wave transformations as they progress from deep water towards the shore and of wave decay in the surf-zone a special role is played by the breaking ratio:

$$\gamma_b = \frac{H_b}{h_b}, \tag{9}$$

where h_b is the water depth. If the linear theory is used the empirical formula derived by Kaminsky & Kraus (1993):

$$\gamma_b = 1.20 \xi_\infty^{0.27}, \tag{10}$$

which gives dependence for the ratio of wave breaking and the deep-water form of the Iribarren number. In figure 8 it is presented a comparison between the variation of the breaking ratio along the breaking line, computed from the spectral model, as explained above, and computed from equation (10).
The results are sensible different, applying the linear theory the average value of the breaking ratio is $\gamma_{bl}=0.56$ while the computed value is $\gamma_{bc}=0.40$. On the other hand the computed results using model output data are very close of those obtained by Thornton & Guza (1983), $\gamma_b=0.42$ at Torrey Pines Beach, California which is a fine sand beach that is gently sloping with minimal development of bars and troughs, similar to the Pinheiro da Cruz beach.

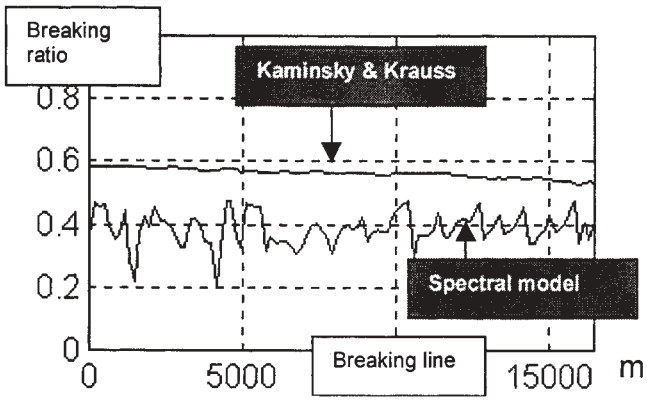

Fig. 8
Variation of the breaking ratio

In figure 9 is given the variation of the number of wave fronts in the surf along the shoreline which was computed with the formula:

$$\sum_{i=1}^{NF(j)} C_i(j) T(j) \approx S_W(j) \tag{11}$$

For computing the celerity in the surf-zone was used the relationship given by Thornton and Guza (1983), considering it constant during a period time:

AUTHOR INDEX TABLE OF CONTENTS

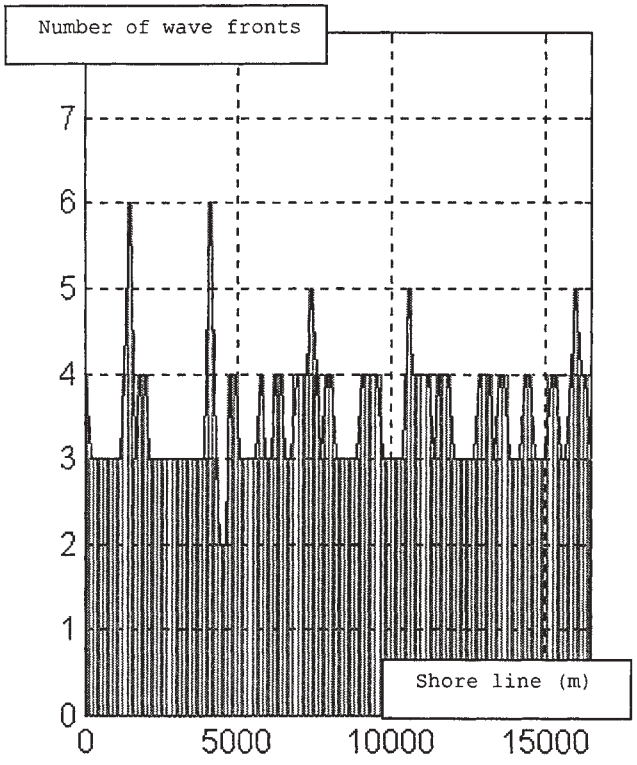

Fig. 9
Distribution of the number of fronts in the surf

$$C_i(j) \approx 1.15\sqrt{gh_i(j)}. \qquad (12)$$

Finally, in order to exemplify other type of applications using these methods, correlation diagrams described by figure 10 are proposed for the processed area. 25 different energetic cases were analyzed in order to estimate dependence between the total variance at the buoy and the characteristics of the breaking process. The minimum, average and maximum values were evaluated in every case.

5. FINAL CONSIDERATIONS

Wave parameters in coastal areas are commonly estimated by wave models capable to account for shallow water effects. The SWAN (Simulating Waves Nearshore) is a stochastic spectral model (phase averaged) which can be applied on a shallow water environment. The model accounts for shoaling, refraction and dissipation. Diffraction is not considered. The SWAN is being implemented for Pinheiro da Cruz, an open sandy beach in the Portuguese West Coast with a North to South orientation. Incoming swell is basically W/NW defining a regular pattern almost all the year. Pressure sensor data was obtained nearshore to verify the model results.

Based on the SWAN typical outputs a nowcast operational model was designed, using a MATLAB graphical interface, in order to make available, in a user-friendly way, wave parameters for the referred coastal area (significant wave height, mean wave direction, wave period, etc). Spectral data analysis can also be performed. In addition, wave-breaking characteristics can be estimated based on SWAN output and linear theory formulations.

This operational tool can be used not only in prediction of the coastal and nearshore wave climate (shallow waters) but also in transport sediments studies, coastal management and military landing operations support.

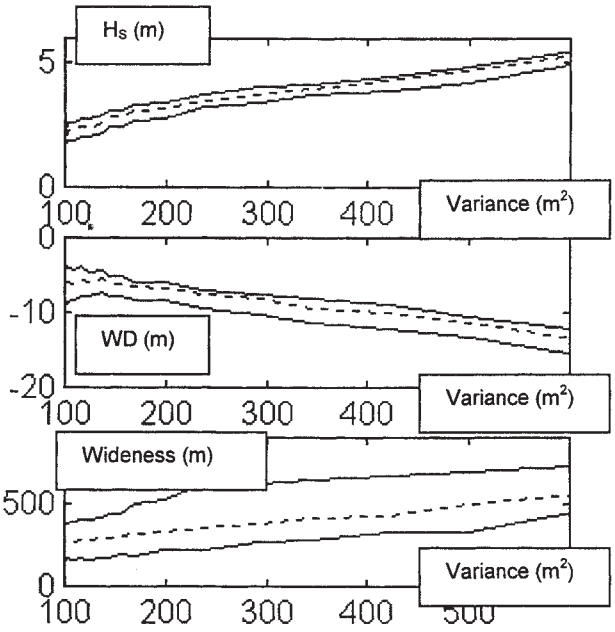

Fig. 10
Correlation diagram offshore-surf

6. ACKNOWLEDGMENT

This work was developed on the scope of the research project PAMMELA that is supported by a grant from the Portuguese Ministry of Defense Program "The Environment and Defense". The Instituto Hidrográfico of the Portuguese Navy is gratefully acknowledged for making available the bathymetry and wave buoy data. Eugen Rusu acknowledges a post-doc fellowship from NATO "Science Programme" and Oleg Makarynskyy acknowledges a post-doc fellowship from "Fundação para a Ciência e Tecnologia".

7. REFERENCES

Banner, M.L. and Young, I.R., 1994: Modeling spectral dissipation in the evolution of wind waves. Part I: Assessment of existing model performance, J. Phys. Oceanogr., 24, No. 7, 1550-1571.

Battjes, J.A. and Janssen, J.P., 1978: Energy loss and set-up due to breaking of random waves, Proc.16 Th Int. Conf. Coastal Engineering, ASCE, 569-587.

Bertotti, L and Cavaleri, L., 1994: Accuracy of wind and wave evaluation in coastal regions, Proc. 24 Th Int. Conf. Coastal Engineering, ASCE, 57-67.

Bouws, E. and Komen, G.J., 1983: On the balance between growth and dissipation in an extreme, depth-limited wind-sea in the southern North Sea, J. Phys. Oceanogr., 13, 1653-1658.

Collins, J.I., 1972: Prediction of shallow water spectra, J. Geophys. Res., 77, No. 15, 2693-2707.

Dingemans, M.W., 1997: Water wave propagation over uneven bottoms. Part 1 -linear wave propagation, Advanced Series on Ocean Engineering, 13, World Scientific, 471.

Elgar, S., Guza, R.T., Raubenheimer, B., Herbers T.H.C., and Gallagher, E.L., 1997: Spectral evolution of shoaling and breaking waves on a barred beach, J. Geophys. Res., 102, C7, 15797-15805.

Günther, H., Hasselmann, S., and Janssen, P.A.,1992: The WAM model Cycle 4 (revised version), Deutsch. Kaminski, G. and Krauss, N.C., 1993: Evaluation of depth-limited wave breaking criteria. Waves 193, Amer. Soc. Civil Engrs., 180-193.

Klim. Rechenzentrum, Techn. Rep. No. 4, Hamburg, Germany.

Hasselmann, K. and Collins, J.I., 1968: Spectral dissipation of finite-depth gravity waves due to turbulent bottom friction, J. Mar. Res., 26, 1-12.

Hasselmann, K., Barnett, T.P., Bouws, E., Carlson, H., Cartwright, D.E., Enke, K., Ewing, J.A., Gienapp, H., Hasselmann, D.E., Kruseman, P., Meerburg, A., Müller, P., Olbers, D.J., Richter, K., Sell, W. and Walden, H., 1973: Measurements of wind-wave growth and swell decay during the Joint North Sea Wave, Project (JONSWAP), Dtsch. Hydrogr. Z. Suppl., 12, A8.

Janssen, P.A., 1991a: Quasi-linear theory of wind-wave generation applied to wave forecasting, J.Phys. Oceanogr., 21, 1631-1642.

Janssen, P.A., 1991b: Consequences of the effect of surface gravity waves on the mean airflow, Int. Union of Theor. and Appl. Mech. (IUTAM), Sydney, Australia, 193-198.

Komar, P.D., 1998: Beach processes and sedimentation Library of Congress Cataloging-in-Publication Data, Prentice-Hall Inc., New Jersey, 545p.

Komen, G.J., Hasselmann, S. and Hasselmann, K., 1984: On the existence of a fully developed wind-sea spectrum, J. Phys. Oceanogr., 14, 1271-1285.

Luo, W. and Monbaliu, J., 1994: Effects of the bottom friction formulation on the energy balance for gravity waves in shallow water, J. Geophys. Res., 99, C9, 18,501-18,511.

Madsen, O.S., Poon Y.K. and Graber, H.C., 1988: Spectral wave attenuation by bottom friction: Theory, Proc. 21 Th Int. Conf. Coastal Engineering, ASCE, 492-504.

Mase, H. and Kirby, J.T., 1992: Hybrid frequency-domain KdV equation for random wave transformation, Proc. 23 Th Int. Conf. Coastal Engineering, ASCE, 474-487.

Mastenbroek, C., Burgers, G. and Janssen, P.A., 1993: The dynamical coupling of a wave model in a storm surge model through the atmospheric boundary layer, J. Phys. Oceanogr., 23, 1856-1866.

Mei, C.C., 1983: The applied dynamics of ocean surface waves, Wiley, New York, 740.

Miles, J.W., 1957: On the generation of surface waves by shear flows, J. Fluid Mech., 3, 185-204.

Phillips, O.M., 1957: On the generation of waves by turbulent wind, J. Fluid Mech., 2, 417-445.

Pires Silva, A.A., Makarynskyy, O., Monbaliu, J , Soares C. V., and Coelho, E. F., 2000: Modeling wave transformation in a open beach on the west coast of Portugal, Workshop coastal wave meeting. Univ. Politecnica, Barcelona.

Putnam, J.A. and Johnson, J.W., 1949: The dissipation of wave energy by bottom friction, Trans. Am. Geoph. Union, 30, 67-74.

Ris, R.C., Booij, N., Holthuijsen, L.H., Padilla-Hernandez, R. and Haagsma, IJ.G. 1998: User Manual for SWAN version 30.75, Delft University of Technology, Delft, The Netherlands, 103p.

Shemdin, P., Hasselmann, K. Hsiao S.V. and Herterich, K., 1978: Non-linear and linear bottom interaction effects in shallow water, in: Turbulent Fluxes through the Sea Surface, Wave Dynamics and Prediction, NATO Conf. Ser., V, 1, 347-372.

Snyder, R.L., Dobson, F.W., Eliot, J.A. and Long, J.B., 1981: Array measurement of atmospheric pressure fluctuations above surface gravity waves, J. Fluid. Mech. 102, 1-59.

Thornton, E.B. and Guza, R.T., 1983: Transformation of wave height distribution, J. Geophys. Res., 88, C10, 5925-5938.

Tolman, H.L., 1992: An evaluation of expressions for the wave energy dissipation due to bottom friction in the presence of currents, Coastal Engineering, 16, 165-179.

Weber, S.L., 1991a: Bottom friction for wind sea and swell in extreme depth-limited situations, J. Phys. Oceanogr., 21, 149-172.

Whitham, G.B., 1974: Linear and nonlinear waves, Wiley, New York, 636.
Young, I.R., and Banner, M.L., 1992: Numerical Experiments on the evolution of fetch limited waves, Int.Union of Theor. and Appl. Mech. (IUTAM), Sydney, Australia, 267-275.

A LONG-TERM WAVE HINDCAST FOR THE NEW ZEALAND COAST

Richard Gorman

National Institute of Water and Atmospheric Research, Ltd,
Hamilton, New Zealand

Andrew Laing

National Institute of Water and Atmospheric Research, Ltd,
Wellington, New Zealand

1. INTRODUCTION

Knowledge of the wave climate is an essential ingredient in understanding sediment movement in the coastal zone and in planning coastal structures and activities. There are several requirements for the wave data forming such a climatology. (1) The duration of the record should be at least several years, to capture annual variation, and preferably extend through more than a single phase of the El Niño/Southern Oscillation. (2) Spatial variation along the full extent of the relevant coast should be represented. (3) Directional information is needed (for example, to allow both the direction and magnitude of longshore sediment transport to be estimated).

For the New Zealand coast, numerical modelling is at present the only practical way of meeting all of these requirements. Historical records from in situ measurements, typically with waverider buoys, provide only patchy coverage at a few sites, with long-term (> 1 year) and directional data being especially limited (Laing, 1993). In recent years, satellite data have become available, but is restricted by available satellite orbits and repeat cycles, and does not provide directional information.

The need for long-term numerical wave hindcasting in New Zealand waters has been addressed using the WAM model. This has been implemented on a grid covering the wave-generating regions influencing the New Zealand coast. The model has been applied to create a 15-year wave hindcast (1979 to 1993), making use of the available satellite and in situ data for calibration and verification.

In this paper we describe the wave model used in the study, then discuss methods used to extract relevant wave statistics at the coast. Some results are then presented, principally as occurrence statistics for the coasts of New Zealand's main islands.

2. A NEW ZEALAND REGIONAL WAVE MODEL

The third generation WAM wave model (WAMDIG, 1988) describes the evolution of a two-dimensional ocean wave spectrum $F(f,\theta,x,y,t)$. This represents the energy density of the wave field broken down by wave frequency f and propagation direction θ, at each position (x,y) in the model grid and time t of the simulation.

In its present form (Cycle 4) the model accommodates the processes of generation by wind stress, propagation with refraction by the seabed and/or currents, four-wave nonlinear interactions, and dissipation by white-capping and bottom friction. Each of these processes is explicitly incorporated in the model equations describing the evolution of the wave spectrum.

For hindcasting wave conditions in the New Zealand region, a rectangular grid was established covering latitudes 80°S to 10S° and longitudes 100°E to 220°E (140°W) at 2° resolution. This region centres on New Zealand, extending westward beyond Australia's Indian Ocean coast, southward to the Antarctic, and into the Pacific Ocean as far as the Marquesas Islands in the north-east corner of the grid (Figure 1). Spectra were computed at 12 equally spaced propagation directions and 25 logarithmically spaced frequencies, between f_1 = 0.0417 Hz and f_{25} = 0.4518 Hz.

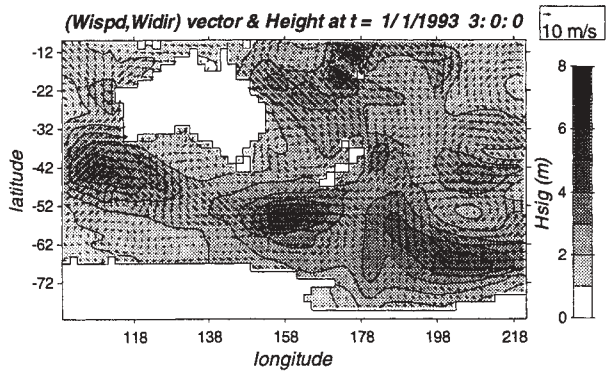

Figure 1. Example output from the wave model, showing wind vectors and the distribution of wave height over the 2°×2° New Zealand regional grid, at 03:00UT on 1/1/1993.

Refraction due to currents or bathymetry was not included. However bathymetric data are still required to locate dry cells. These were taken from the U.S. National Oceanic and Atmospheric Administration's ETOPO5 database (NOAA, 1988), which provides global bathymetry at 5 minute resolution.

3. THE 15 YEAR HINDCAST

Wind data were sourced from the European Centre for Medium-Range Weather Forecasts (ECMWF) reanalysis data set. Wind fields are available on a 1.125° latitude/longitude grid at 10 m elevation. The data are provided at the analysis times of 00, 06, 12 and 18 hours Universal Time (UT) on each day. A key feature of these wind fields is that they have been generated in a consistent way over all the years of the record.

The model was run from 00:00 hours (UT) on 1/1/1979 to 18:00 hours UT on 31/12/1993. Wave statistics over the entire grid were output to binary files at 3 hourly intervals. A set of 38 model cells, including all those adjacent to the New Zealand coast (Figure 2), were selected for which full directional spectra were also filed at 3 hour intervals.

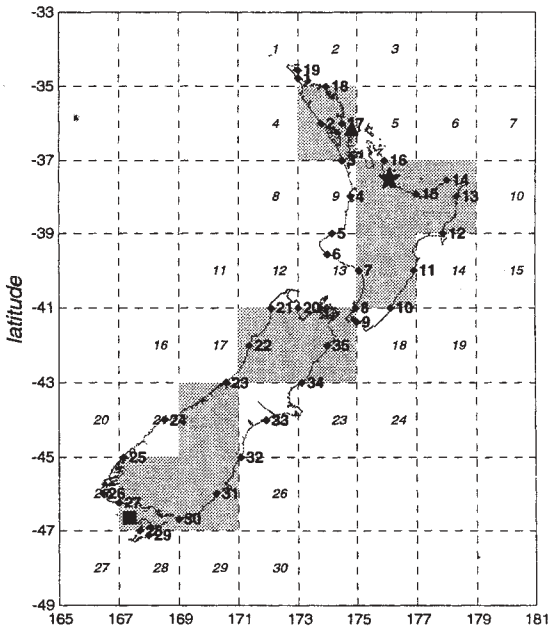

Figure 2. Map showing the model grid and output sites for coastal wave statistics. The model computes directional spectra at each cell of the 2°×2° grid, except dry cells (shaded), but full spectra are only saved to file at selected cells, numbered in italics. In postprocessing, wave statistics are derived at coastal sites, marked by diamonds and boldface numerals. Each of these sites is located 5 km offshore. Statistics were also computed at the Foveaux Strait (■), Katikati (★) and Mangawhai (▲) buoy sites.

The wave model output provides a full directional spectrum $F(f,\theta,x,y,t)$ at the centre of each wet 2°×2° square in the grid. For validation against buoy data and for the study of coastal processes, we

require wave conditions at specific locations along the actual coastline, rather than 1° offshore from the nominal "blocky" coast represented in the model. We also need to resolve wave directions to longshore and cross-shore components relative to the local alignment of the true coast. Therefore some further processing was required.

As a first step, a "raw" spectrum at the site of interest was obtained from the spectra in the model output cells by bilinear interpolation, using up to three of the nearest model grid cells. No extrapolation was used, so that all interpolation weights were positive.

The resulting directional spectra will still have a poor representation of waves from directions affected by the limited fetch from the coastline. For a typical output point, within a few kilometres of the coast, the model will overestimate the spectrum in approximately half the model wave directions, for which the true fetch is much less than half a grid cell width. This overestimate can be improved by filtering to limit the spectral components from these directions to be no greater than the JONSWAP spectrum (Hasselmann et al., 1973) appropriate for the local wind speed and fetch. A set of positions was first located on the coastline, each representing the closest point of the coast to the output site at 5° direction increments (Figure 3). The fetches to these positions were then averaged over the 30° direction bins of the model spectra with $\cos\theta$ weighting to produce an effective fetch for each bin. Direction bins with long fetches (i.e. not intersecting the New Zealand coast) were not modified.

The local coastline orientation was also found by linear regression on those 5° resolution coastline points lying within 20 km of the output site.

From the directional spectrum, a 1-dimensional spectrum can be obtained by integrating over propagation directions:

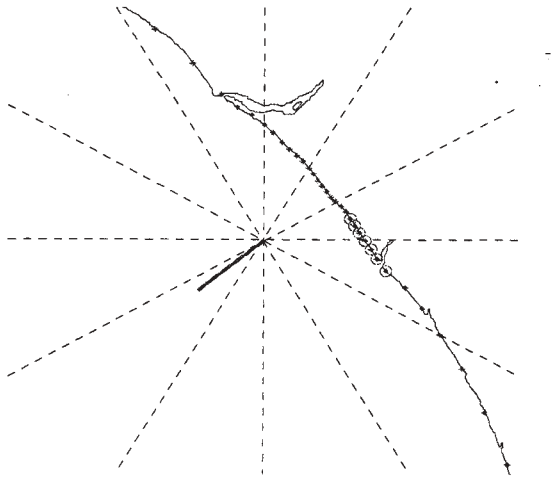

Figure 3. Example of the fetch computation method. The output site is at the centre of the diagram, with dashed lines marking discrete model wave directions, at 30° intervals. The point on the coastline nearest the buoy along each direction at 5° increments was found (✱). The mean offshore direction (solid line) was found by linear regression from these points. The effective fetch for each model direction was then computed by a $\cos\theta$ weighted average over points within the direction bin (marked here by circles for the 90°±15° bin, as an example).

$$S(f) = \int_0^{2\pi} F(f,\theta)d\theta \,. \qquad (1)$$

From this, spectral moments

$$M_j = \int_0^{\infty} df \; f^j S(f) \qquad (2)$$

are computed for integer values of j. The zeroth moment, for example, gives the total energy in the spectrum, from which the significant height can be computed

$$H_s = 4\sqrt{M_0} \,. \qquad (3)$$

The mean frequency

$$f_{mean} = M_1 / M_0 \qquad (4)$$

is defined from the first moment, while a measure of mean direction

$$\theta_{mean} = \arctan\left(\frac{S_0}{C_0}\right) \qquad (5)$$

can also be derived using directional moments

$$C_0 = \int_0^{\infty} df \int_0^{2\pi} d\theta \, F(f,\theta)\cos\theta\,, \qquad (6)$$

$$S_0 = \int_0^{\infty} df \int_0^{2\pi} d\theta \, F(f,\theta)\sin\theta\,. \qquad (7)$$

The flux of wave energy is a vector quantity obtained from the product of group velocity and spectral density (or wave energy). Using wave angle θ' relative to the local coast orientation, we have resolved this into onshore and longshore components

$$\begin{Bmatrix} P_{onsh} \\ P_{long} \end{Bmatrix} = \tfrac{1}{8}\rho g \times \int_0^{\infty} df \int_0^{2\pi} d\theta \, C_g(f,\infty) F(f,\theta) \begin{Bmatrix} \cos\theta' \\ \sin\theta' \end{Bmatrix} \qquad (8)$$

Here $C_g(f,d)$ is the group velocity for waves of frequency f in water of depth d, ρ is the density of water and g is gravitational acceleration. The longshore direction has been defined so that a positive flux is directed to the left facing shoreward, i.e. clockwise around the island.

4. VALIDATION WITH BUOY DATA

The establishment and testing of this model has been previously reported in more detail with validation information (Gorman and Laing, 2000). This includes comparison of the hindcast with data from wave buoys near Foveaux Strait and at Katikati (Macky et al., 1995) (Figure 2). It was found that the model was able to closely match the main wave events in 153 days of the Foveaux Strait record (Figure 4). There was a correlation of 0.81 between buoy and model height estimates, with a bias (model - data) of -4 cm and scatter index (root-mean-square error as a fraction of the mean) of 0.22. Filtering out fetch-limited components has reduced the bias from +17 cm as well as improving the correlation (0.76) and scatter index (0.25). These verification results were very similar to those obtained by Laing (1992), who applied a second-generation model over a similar region. Results for f_{mean} were also nearly identical, with both hindcasts achieving a bias of +0.017 Hz and scatter index of 0.23. The present simulation achieved a higher correlation (0.56) than the 0.43 found by Laing (1992).

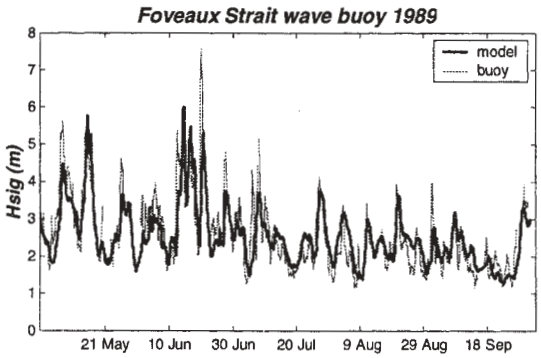

Figure 4. Significant wave height at a wave buoy site near Foveaux Strait as simulated by the wave model and as measured by the buoy over 153 days of the instrument deployment. The buoy data has been averaged over three-hour intervals matching the model output times.

For the Katikati buoy, correlations between hindcast and buoy wave heights averaged 0.84 over the three years, and the mean bias was +9 cm, compared with 0.51 and +64 cm respectively for unfiltered model output (Gorman and Laing, 2000). The average correlation for f_{mean} was 0.72.

Both of these buoy sites are relatively unaffected by refraction. The Foveaux Strait buoy was in approximately 100 m water depth, and the Katikati

buoy in 34 m depth, but on a relatively straight and open stretch of coast.

In areas of more complex local bathymetry, a site-specific refraction transformation would be needed for accurate estimates of shallow-water wave statistics. For example, model results were compared with data from a 1996 wave buoy deployment at Mangawhai on the North Island northeast coast (Gorman and Laing, 2000). The buoy site was in approximately 30 m depth in a location partly protected by several offshore islands (Figure 5). As a result, wave heights from the nearest cell of the 2° regional model greatly overestimate the measured values (Figure 6).

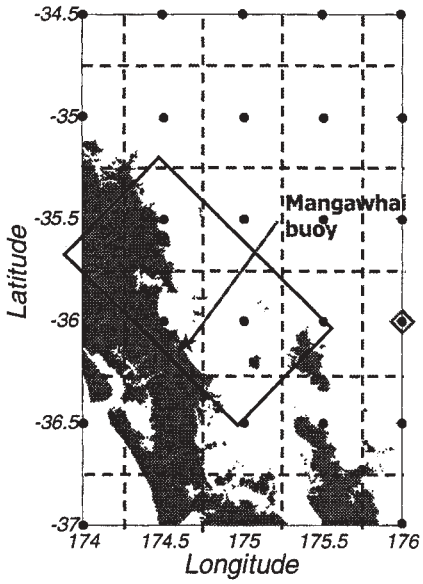

Figure 5. Location map for modelling grids used to hindcast wave conditions at the Mangawhai buoy site. The WAM model was first run on the 2° grid (nearest cell indicated ◊), which was then nested to a 0.5° grid (•). Refraction modelling on a grid oriented 45° from True North was then used to derive a transformation from WAM spectra offshore to the inshore buoy site.

To provide a better nearshore estimate, a nested WAM simulation was carried out on a grid covering latitudes 52°S to 30° and longitudes 160°E to 186°E (174°W) at 0.5° resolution (Figure 5). Results from this simulation were then applied at the offshore boundary of a rectilinear grid at 1.06 km spacing oriented at 45° from True North (Figure 5), using the wave refraction model WBEND (Black and Rosenberg, 1992) to estimate wave conditions at the buoy site. This provided a much-improved hindcast of significant wave height (Figure 6) compared to direct application of the 2° WAM result. It should be noted that much of the discrepancy (typically of order 50%) of the improvement is provided by nesting to the 0.5° grid.

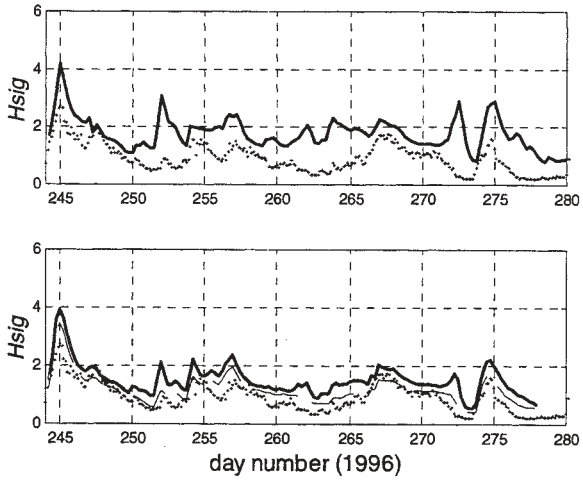

Figure 6. Significant wave height measured at the Mangawhai wave buoy (+), compared with: (top panel) the hindcast on the 2° regional grid, (bottom panel) the WAM model hindcast at the nearest cell of the 0.5° New Zealand regional grid (solid line). Statistics obtained by applying a shoaling transformation to the WAM hindcast spectra are also shown (dashed line).

5. HINDCAST STATISTICS

One of the main aims of the hindcast is to provide coverage of wave conditions along the full extent of the New Zealand coastline. To this end, a set of sites along the coast was chosen, generally placed at one-degree intervals of latitude or longitude, to provide a thorough coverage of the exposed coastline (Figure 2). These points lie on the digitised World Vector Shoreline (Soluri and Woodson, 1990) obtained from the US Geological Survey. The sites for wave output were located 5 km in a nominal offshore direction (N, NE, E, SE, S, SW, W or NW, depending on the local orientation) from the respective coastal sites.

Directional wave spectra were computed at these positions, using interpolation and filtering for limited fetch, as described above. No local refraction modelling was carried out, however, as most sites are on relatively open coasts.

Wave roses derived from the full 15-year hindcast are shown in Figure 7. Wave statistics are represented by segments with length proportional to occurrence. The segments are aligned in the direction *towards* which the waves travel, and broken down by wave height into ranges 0-1m (white), 1-2m (light grey), 2-4m (dark grey) and >4m (black). For clarity, only every third site is shown. The strong influence of swell generated by westerly winds in the Southern Ocean is apparent in the trend to larger wave heights on the west coasts than the east coasts of both main islands. The most energetic climate is found on the Southland and Fiordland coasts in the south and southwest respectively of the South Island.

Symmetrical distributions of longshore flux were produced on the northern part of the North Island West Coast (sites 1-3), which is aligned approximately normal to the predominant swell from the south-west (Figure 8(a)). But further south on this coast, strongly asymmetric flux distributions are seen, with positive (northward) fluxes north of the Taranaki Peninsula (sites 4 and 5), and negative fluxes on the southern side (sites 6 and 7) (Figure 8(b, c)). This pattern of fluxes would tend to move sediments sourced from Mt Taranaki away in both directions.

A similar division occurs around West Cape (site 26), at the southern limit of the South Island's West Coast, but with higher flux magnitudes than on the North Island (Figure 8(d, e)). As a result, there is a preponderance of northward fluxes on both the west and east coasts of the South Island (Figure 8(d, f)). The south-east coast of the North Island (sites 10-13) also show a net northward flux, while further north, wave fluxes are both weaker and more neutrally balanced (Figure 8(g, h)).

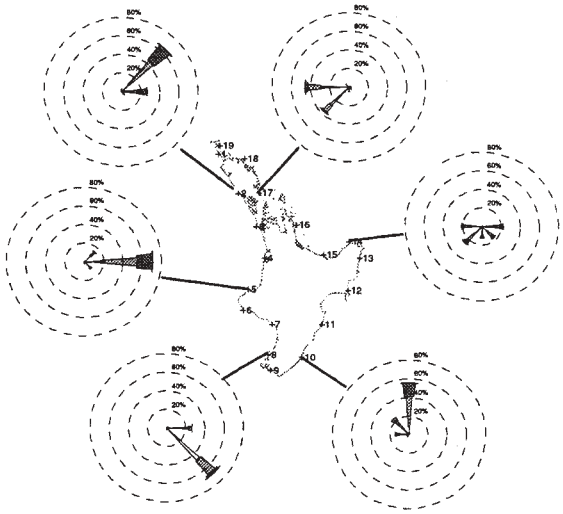

Figure 7 (a). Wave roses derived from the hindcast for every third coastal output site around the North Island coast. Wave occurrence is binned by direction and significant wave height, in ranges 0-1, 1-2, 2-4, >4 m.

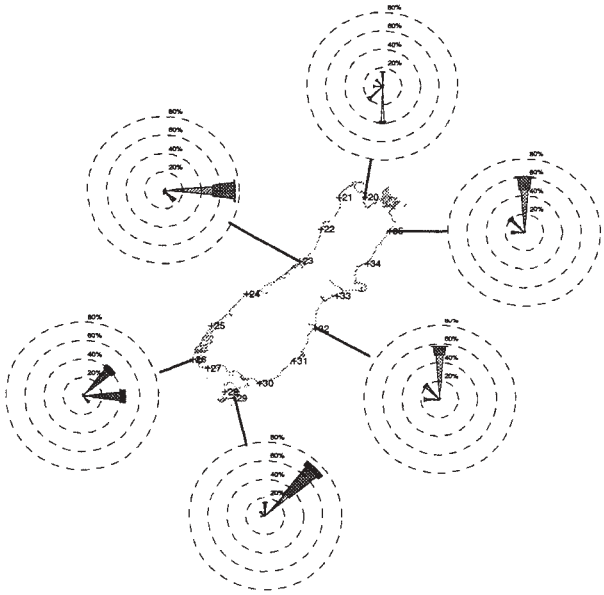

Figure 7 (b). Wave roses derived from the hindcast for every third coastal output site around the South Island coast. Wave occurrence is binned by direction and significant wave height, in ranges 0-1, 1-2, 2-4, >4 m.

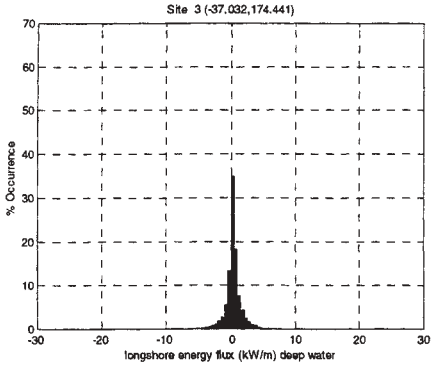

Figure 8(a). Occurrence statistics for the longshore component of wave energy flux hindcast at coastal site 3 (North Island West Coast - Auckland).

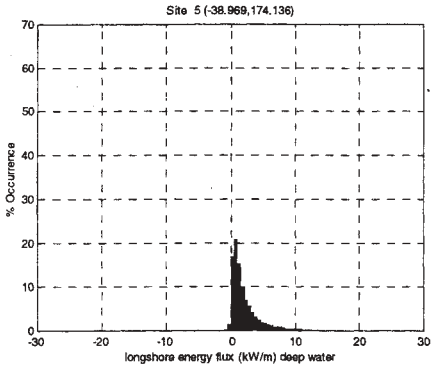

Figure 8(b). Occurrence statistics for the longshore component of wave energy flux hindcast at coastal site 5 (North Island West Coast - North Taranaki Bight).

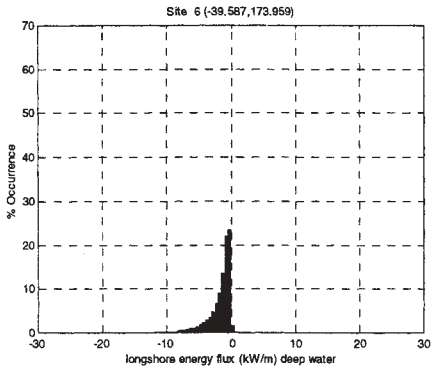

Figure 8(c). Occurrence statistics for the longshore component of wave energy flux hindcast at coastal site 6 (North Island West Coast - South Taranaki Bight).

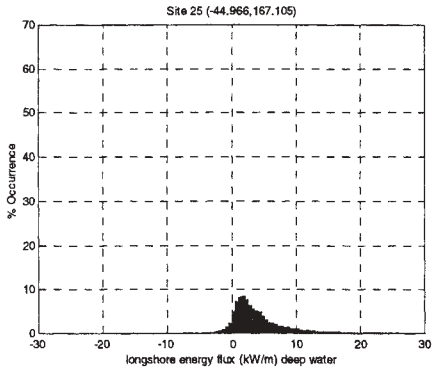

Figure 8(d). Occurrence statistics for the longshore component of wave energy flux hindcast at coastal site 25 (South Island West Coast - Milford Sound).

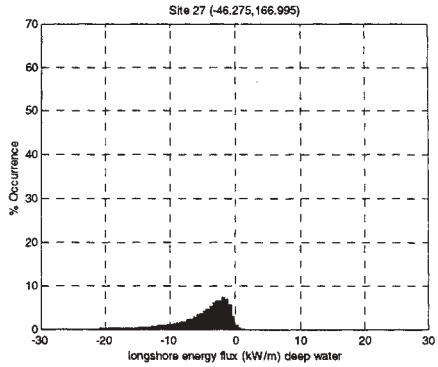

Figure 8(e). Occurrence statistics for the longshore component of wave energy flux hindcast at coastal site 27 (South Island South Coast - Puysegur).

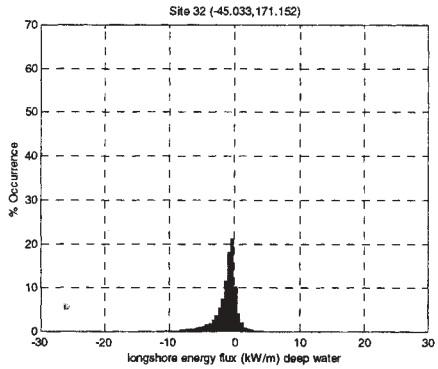

Figure 8(f). Occurrence statistics for the longshore component of wave energy flux hindcast at coastal site 32 (South Island East Coast - Oamaru).

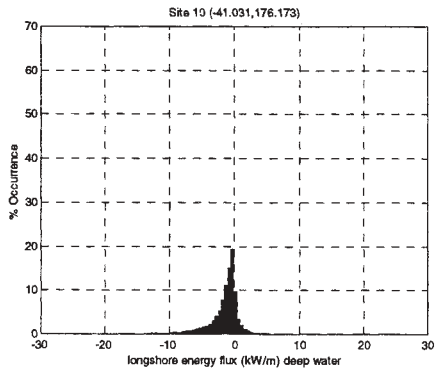

Figure 8(g). Occurrence statistics for the longshore component of wave energy flux hindcast at coastal site 10 (North Island East Coast - Castle Pt).

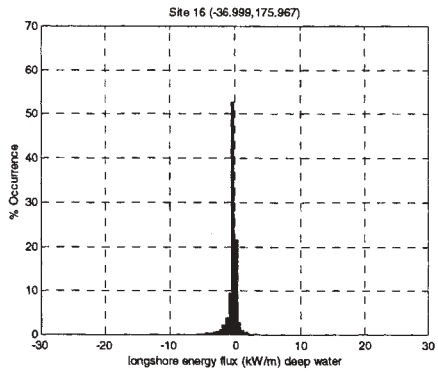

Figure 8(h). Occurrence statistics for the longshore component of wave energy flux hindcast at coastal site 16 (North Island East Coast - Coromandel Peninsula).

The hindcast data also allow us to investigate seasonal variation. Plotting monthly means through the year at site 3 (Figure 9) shows the largest waves in the southern winter and spring, for which there is a strong onshore component but only a weak net positive flux. In autumn the typical wave direction shifts to provide a more distinct positive (northward) flux, although the onshore component is considerably weaker than the typical winter/spring values.

Monthly means computed from the coastal site statistics can be examined for longer-term variations, such as those associated with the ENSO cycle. For example, the austral summers of 1982-83 and 1991-92 produced slightly smaller wave heights than average on the North Island northeast coast (Figure 10(b)). These times coincided with strong El Niño events, shown by strongly negative values of the Southern Oscillation Index (Figure 10(c)). Any corresponding influence on the west coast was much less discernible (Figure 10(a)).

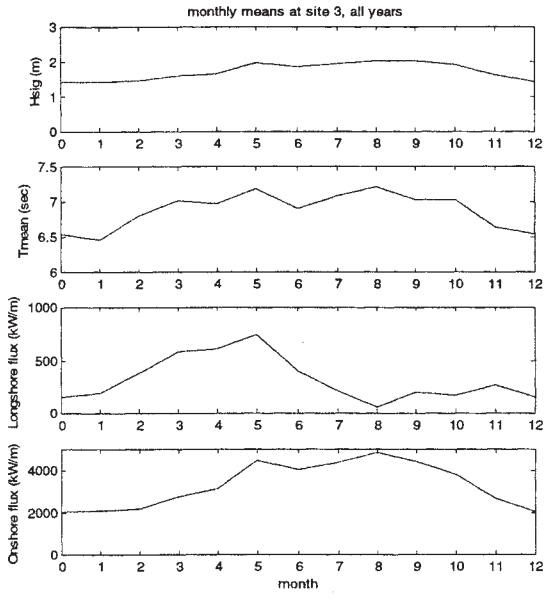

Figure 9. Seasonal variation of wave statistics at site 3 (North Island West Coast - Auckland) obtained by taking monthly means over all years. From top to bottom: significant height, mean period, longshore and onshore components of wave energy flux (in deep water).

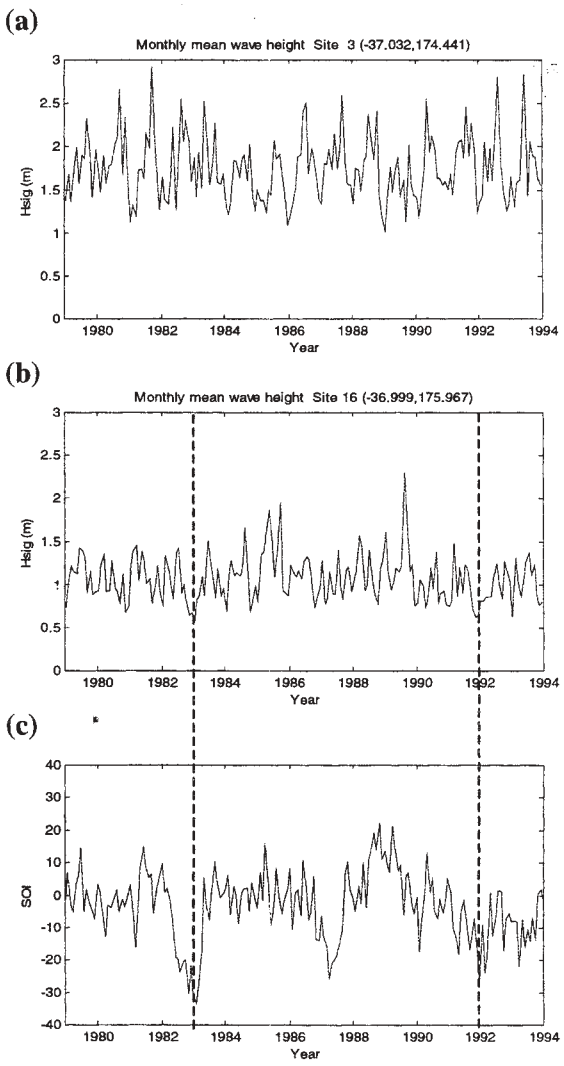

Figure 10. Monthly mean significant wave height (a) at coastal site 3 (North Island West Coast - Auckland) and (b) at site 16 (North Island East Coast - Coromandel Peninsula). The variation of the Southern Oscillation Index over the same period is shown in panel (c).

6. CONCLUSIONS

The WAM model has been used to hindcast the generation and propagation of deep-water waves incident on the New Zealand coast over a 15-year period (1979-93). The model was forced using winds taken from the European Centre for Medium Range Weather Forecasting (ECMWF) re-analysis dataset. After interpolation and filtering to account for limited fetch, the hindcasts compared satisfactorily with data from two wave buoys,

exposed to the different wave climates of the Southern Ocean and the subtropical Pacific.

From the hindcast, wave occurrence statistics were computed for coastal sites distributed along the New Zealand coastline. The distribution of longshore wave energy flux is of particular interest for studies of large scale sediment motion. It was noted that the predominance of swell from the Southern Ocean results in a generally northward energy flux, with magnitude decreasing from south to north. This pattern is modified by large-scale coastal features such as the Taranaki Peninsula, on the south coast of which there is locally a southward flux.

7. ACKNOWLEDGEMENTS

This work was carried out with support from the Public Good Science Fund (Contract No. C01618). We thank BTW Associates and NIWA staff members Graham Macky, Geoff Latimer, Sandra Kingsland and Warren Thompson for assistance in providing wave data, and ECMWF for providing wind data.

8. REFERENCES

Black, K.P. and Rosenberg, M.A., 1992. Semi-empirical treatment of wave transformation outside and inside the breaker line. Coastal Engineering, 16: 313-345.

Gorman, R.M. and Laing, A.K., 2000. Bringing wave hindcasts to the New Zealand coast, International Coastal Symposium 2000, Rotorua, New Zealand.

Hasselmann, K. et al., 1973. Measurements of wind-wave growth and swell decay during the joint North Sea Wave Project (JONSWAP). Dtsch. Hydrogr. Z., A 8(12): 95 pp.

Laing, A.K., 1992. A spectral model for the sea-state with explicit forcing terms. Applied Ocean Research, 14: 341-351.

Laing, A.K., 1993. Estimates of wave height data for New Zealand waters by numerical modelling. New Zealand Journal of Marine and Freshwater Research, 27: 157-175.

Macky, G.H., Latimer, G.J. and Smith, R.K., 1995. Wave climate of the Western Bay of Plenty, New Zealand, 1991-93. New Zealand Journal of Marine and Freshwater Research, 29(3): 311-327.

NOAA, 1988. Digital relief of the Surface of the Earth. 88-MGG-02, NOAA, National Geophysical Data Center, Boulder, Colorado.

Soluri, E.A. and Woodson, V.A., 1990. World Vector Shoreline. International Hydrographic Review, LXVII(1).

WAMDIG – the WAM Development and Implementation Group, 1988. The WAM Model - a third generation ocean wave prediction model. J. Phys. Oceanogr., 18(12): 1775-1810.

HIGH RATES OF WAVE GROWTH FROM STORMS AFFECTING THE EAST COAST OF NEW ZEALAND

Andrew Laing

National Institute of Water and Atmospheric Research,
Wellington, New Zealand

Richard Gorman

National Institute of Water and Atmospheric Research,
Hamilton, New Zealand

1. INTRODUCTION

High rates of wave growth are a regular feature of wave measurements on the east coast of New Zealand. This coast is sheltered from the prevailing westerly and southwesterly conditions that sustain an energetic wave climate on the west coast of the country. However, a prominent feature of the wave climate along the east coast is south-southeast storms which affect the coast from Otago to East Cape. These are often heralded by the passage of an intense cold front up the east coast of the country with a sudden change in wind direction and a substantial drop in air temperature (Smith et al. 1991).

Synoptic winds over the east coast of the country are predominantly offshore, and in such conditions waves are generally modest. After the passage of a cold front, the coast is exposed to southerly or southeasterly wind events. The onset of these events is generally delineated by a wind change. Thus, whilst the fetches to the south are not limited by any geographical constraints, wave growth is usually duration limited. However, it is also often much faster than that expected from duration-limited storms.

In Figure 1 the wave record for a site near Wellington shows a succession of events with significant wave heights often exceeding 3 m. These punctuate an otherwise relatively low sea state, with significant wave heights of less than 1.5 m. The figure also shows wind direction measured at Wellington Airport at the same time. The direction invariably shifts to southerly (150°-200°) at the point of rapid rise in wave height or just preceding it. The zero-crossing periods from the record indicate low values during the onset of these events, indicating freshly generated windsea, with higher periods characteristic of swell, during the dying stages of the events. This is often accompanied by a reversal of the wind to northerly.

It is also notable in Figure 1 that during some events the wave growth is extremely rapid. During June 14, the significant wave height rose from 0.56 m to 2.73 m within 2.0 hours. The southerly change at Wellington brought winds from 7 ms^{-1} rising to 13 ms^{-1} during this period. The wave period during this time was modest, indicating active wave generation rather than a sudden influx of swell. The wave growth during such events appears to be considerably more rapid than normal for duration limited wave generation.

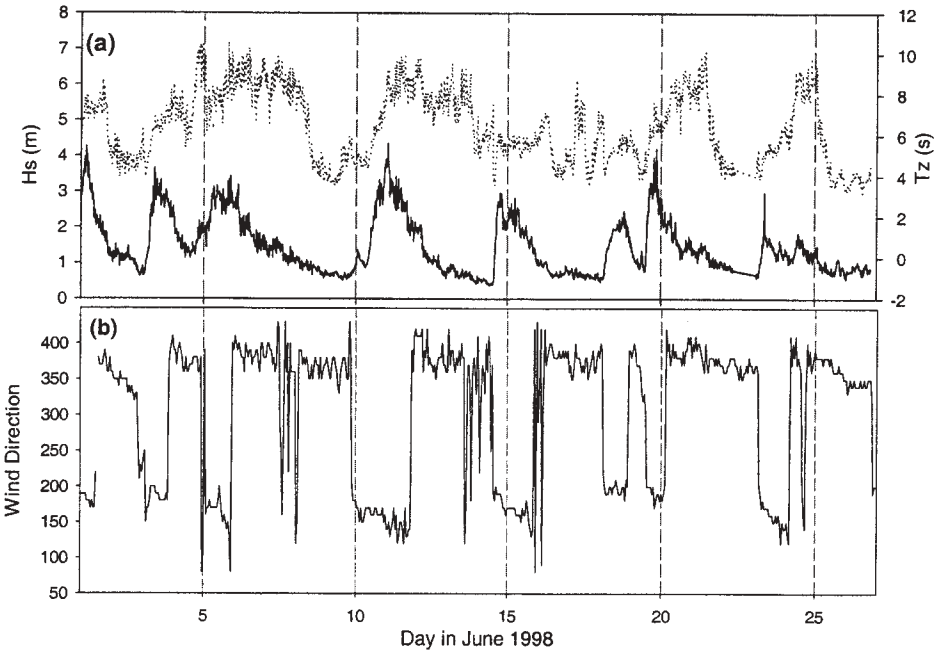

Figure 1 – (a) Wave conditions near Wellington during June 1998. The significant wave height (solid line) and zero-crossing period (dotted line) are shown. The wind directions at Wellington Airport are shown in (b). Directions in the northeast quarter have had 360° added.

The rapid onset of high sea-states is a potential hazard for mariners, coastal operators and private recreational users of coastal waters. This paper describes some of these events, a possible mechanism for the accelerated wave growth and simulates the wave growth using a numerical wave model.

2. WAVE AND WIND OBSERVATIONS

In 1995 the National Institute of Water and Atmospheric Research (NIWA) moored a Waverider buoy in 44 m of water at 41.403°S, 174.846°E, off Baring Head, outside the entrance to Wellington Harbour (see Figure 2). The site is exposed to the south and southeast, with unobstructed fetches down the east coast of South Island. The deployment has continued through to 2000, and there are now nearly 5 years of data for this site.

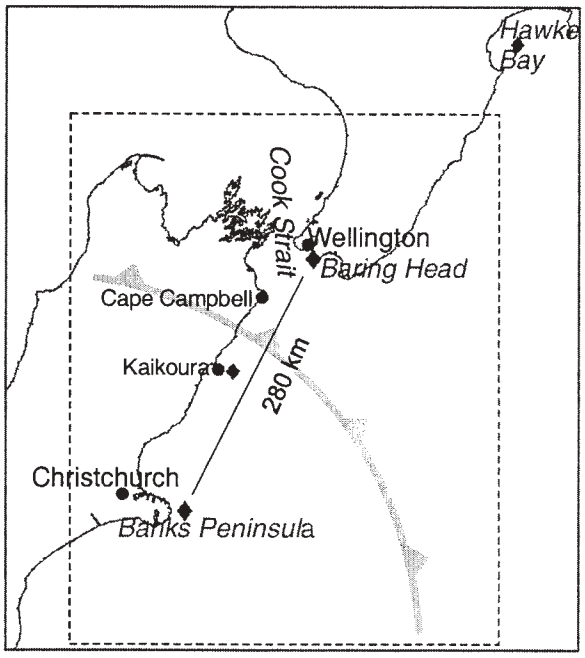

Figure 2 – The central east coast of New Zealand showing the study area and sites of wave (diamonds) and wind (circles) measurements. The dashed lines show the domain for the wave model.

In February 1999 a directional wave buoy was deployed at 43.753°S 173.251°E, 10 km off the eastern end of Banks Peninsula (see Figure 2). The instrument is moored in 74 m of water with a clear exposure to all significant fetches. Other deployments in recent years have also occurred off Kaikoura (for 2 months in winter 1996) and more recently in Hawke Bay (from December 1998). This paper will be limited to the use of data from Baring Head and Banks Peninsula.

Wind data were extracted from the NIWA climate database. The hourly observations comprise 10-minute averages for the period just prior to the hour. Directions are in the meteorological convention, i.e. direction from which the wind blows. A number of stations are available on the east coast. Those referenced in this paper are shown in Figure 2. The key data are from Wellington Airport, but winds from Christchurch Airport, Kaikoura and Cape Campbell are also used to monitor progress of southerly changes.

3. DURATION-LIMITED WAVE GROWTH

Duration-limited wave growth is difficult to measure. Observations of wave growth from a calm sea, under the influence of a steady wind are non-existent. In limited fetch conditions there are a few landmark field studies that have provided the data which underpin our modern expectations of wave growth. In particular, the results of the JONSWAP (Joint North Sea Wave Project) study (Hasselmann et al. 1973) are commonly used as a benchmark for fetch-limited wave growth and to calibrate and validate wave models. Numerical models that have proven themselves against these data are also usually accepted as reasonably replicating wave growth under duration-limited conditions. The most precise research model with explicit representation of the physics of wave generation and decay and full calculation of weakly nonlinear wave-wave interactions is the EXACT-NL model. This is essentially the WAM model (WAMDI, 1994) extended to include full calculation of the nonlinear wave-wave interactions (Hasselmann and Hasselmann, 1985).

A number of other studies have lead to the development of nomograms for wave growth. These are usually derived from empirical parameterisations of wave observations. Hasselmann et al. (1976) developed a parametric model based on the JONSWAP results and this is the basis of the Hybrid Parametric (HYPA) model of Gunther et al. (1979). The JONSWAP data are also the basis of nomograms developed for the Shore Protection Manual (CERC, 1984). It is noted that the wind dependence in these relationships (ie. in CERC, 1984) is based on a wind stress factor which is defined as $0.73U^{1.23}$, where U is a windspeed corrected for stability of the lower atmosphere.

Groen and Dorrestein (1976) have also developed graphical guidance for estimating wave growth under fetch and duration-limited conditions. These are based on the 10-m wind U_{10}, and have been widely adopted for practical wave forecasting (see WMO, 1998).

Unfortunately, even in idealised test cases numerical wave models perform differently, as exemplified in the Sea Wave Modelling Project (SWAMP, 1985). As part of that study a number of wave models were inter-compared for duration-limited growth. For most of the evolution, models predict exponential growth for non-dimensional energy as a function of

non-dimensional duration. Fitting simple curves to these data makes it possible to compare the results with the manual methods of CERC (1984) and Groen and Dorrestein (1976) (GD).

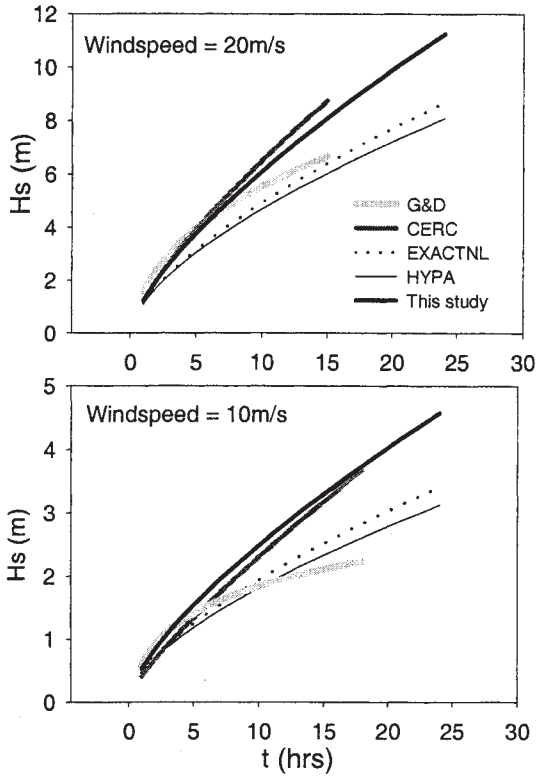

Figure 3 – Duration-limited growth of significant wave height (H_s) at (a) 10 ms^{-1} and (b) 20 ms^{-1}. Exponential curves have been fitted to the EXACT-NL and HYPA models, but the CERC and GD values have been plotted directly. The growth curve selected for this study is also shown.

In Figure 3, duration-limited wave growth is illustrated for several numerical and empirical models. For this study a high theoretical growth rate was targeted to ensure a conservative threshold against which to assess the observed wave growth. The simple exponential growth form was adopted. This is couched in terms of the non-dimensional total energy $\tilde{E} = \frac{g^2 E}{u_*^4}$, and duration $\tilde{t} = \frac{gt}{u_*}$, where g is the gravitational constant, t is duration (s), E is the total variance (m^2) and u_* is the friction velocity. The significant wave height $H_s = 4\sqrt{E}$, and u_* is derived from the 10-m wind by $u_* = \sqrt{C_d} U_{10}$, assuming neutral stability and a drag coefficient $C_d = 1.83 \times 10^{-3}$. The resulting form for growth of total energy is

$$\tilde{E} = (1.8 \times 10^{-4} \tilde{t})^{1.4}. \quad (1)$$

This describes duration-limited growth. The corresponding curves plotted in Figure 3 indicate that it exceeds the growth rate from the numerical models, and is at the upper limits of growth suggested by empirical models. It is noted that the fit has been tuned to fit mid-growth stages and that it varies for different windspeeds. In particular, as sea-states approach full development the growth eases and the exponential form is no longer applicable.

4. OBSERVATIONS OF RAPID GROWTH

In Figure 1 the observations suggest that the wave growth at Baring Head near Wellington is very rapid. A number of other cases are now presented and compared with the theoretical duration-limited wave growth.

Firstly, in Figure 4 examples of two events associated with southerly changes are presented in which the growth matches theoretical predictions. The first (Figure 4(a)) occurred on the January 4th, 1997. The southerly change at Wellington airport indicated winds climbing to 14 ms^{-1}. Assuming this windspeed, and an initial significant wave height of 1.1 m, the growth is seen to match the actual observations at Baring Head. Similarly on

November 7, 1996, winds rose to 10.5 ms^{-1} and starting from a significant wave height of 0.5 m the theoretical growth is again matched by the observations.

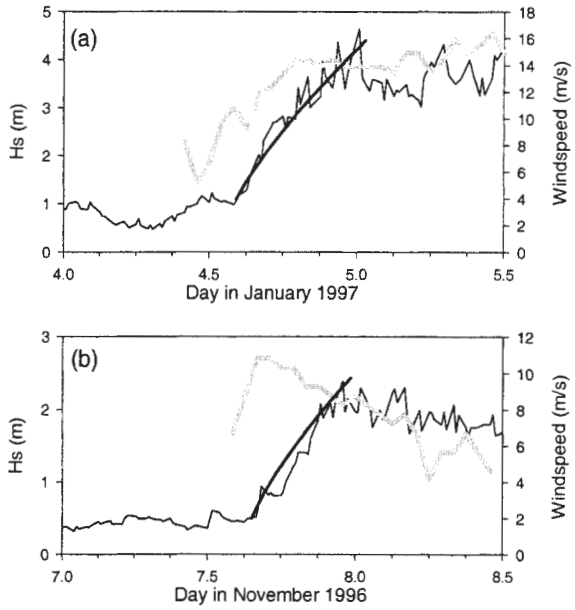

Figure 4 – Wave growth following two southerly change events at Wellington. The solid thin line shows the significant wave height (Hs) at Baring Head, the thick grey line shows the windspeed at Wellington Airport and the solid thick line shows the theoretical wave growth. The windspeed is only plotted after the direction turns southerly.

However, there are quite a number of occasions when the growth clearly exceeds expectations. In Figure 5 six of these are illustrated. In all cases the expected growth is projected from the actual time of the southerly change. The wind used to estimate this growth rate is the average for the period immediately after the wind reaches its peak following the change. This windspeed is noted for each case in Table 1. In general it is higher than the wind that would cause local wave growth. This will give a conservative measure of the excess growth above expected local generation. The significant wave height at the time of the southerly change is used as the initial sea-state for the estimates.

Table 1 details wind and wave key parameters during each event. In none of the cases was there any substantial pre-existing swell component (i.e. anything greater than 1.0 m). The table shows the time taken for a given change in significant wave height (Δt) and the time which the theoretical growth curve would predict ($\Delta t(U)$). It is clear that the six cases all exhibit excess wave growth for the observed windspeed. The peak periods for the wave spectra are also similar to those expected for waves generated from the observed windspeed. In all cases they are well within the range of values for waves growing under the influence of the given windspeed. Therefore, the waves are characteristic of freshly generated waves, but the generation mechanism is not simple duration-limited wind forcing.

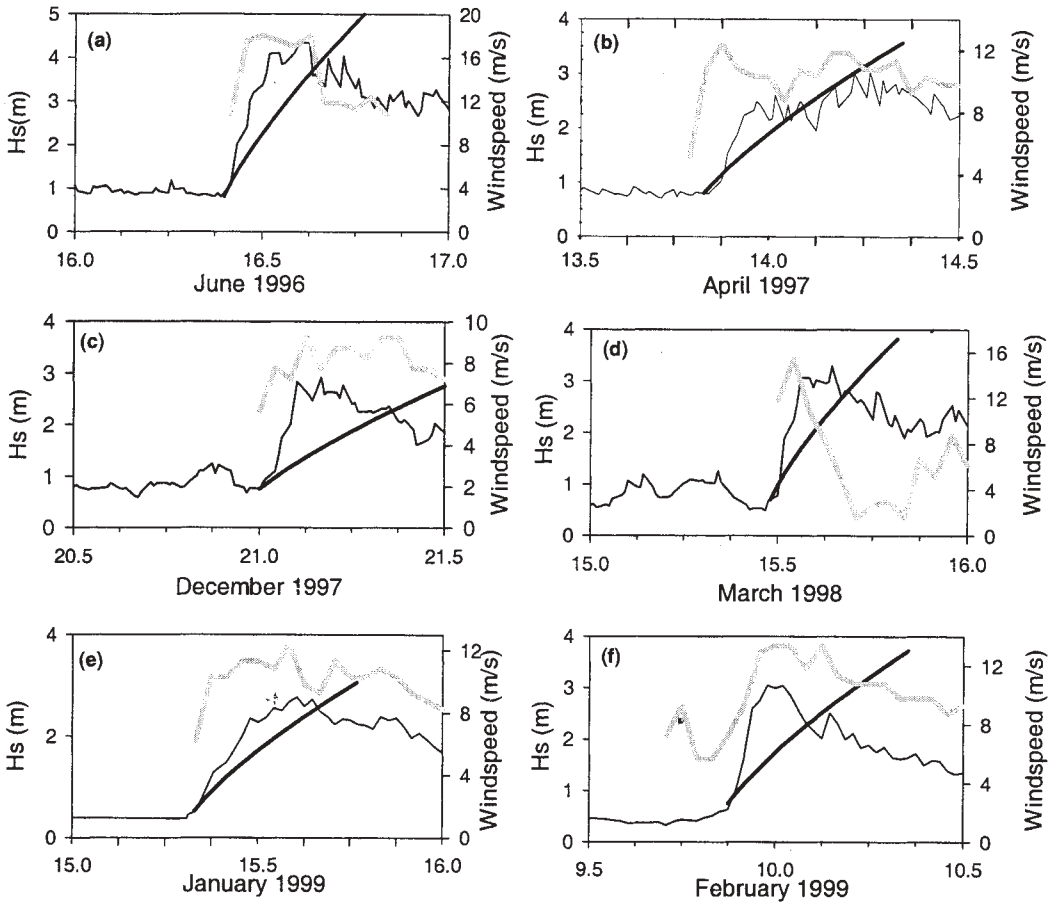

Figure 5 – Wave growth observed at Baring Head near Wellington, following southerly changes. The six events occurred on (a) June 16, 1996, (b) April 13, 1997, (c) December 21, 1997, (d) March 15, 1998, (e) January 15, 1999, and (f) February 9, 1999. Lines are as for Figure 4.

Table 1 – Wind and wave parameters for high-growth rate events near Wellington. For each event the parameters shown (rows) are: ΔH_s, the change in significant wave height; Δt, the time over which this change takes place; U, the windspeed adopted for the event; $\Delta t(U)$, the duration for this change derived from the windspeed; T_p, the peak period; and $T_{p,max}$ (U), the maximum feasible peak period for the given windspeed.

	June 16 1996	*April 13 1997*	*Dec. 21 1997*	*Mar. 15 1998*	*Jan.15 1999*	*Feb.9 1999*	*July 8 1999*
ΔH_s (m)	3.2	1.4	2.1	2.5	1.9	2.4	2.1
Δt (hrs)	3.0	2.0	2.7	2.3	3.5	3.5	3.0
U (ms^{-1})	17.5	12.0	9.0	15.0	11.0	12.0	13.4
$\Delta t(U)$ (hrs)	9.0	5.5	12.0	6.0	7.5	8.5	6.0
T_p (s)	7.5	6.8	6.5	7.0	6.5	7.7	8.0
$T_{p,max}$ (U) (s)	12.8	8.8	6.6	11.0	8.0	8.8	9.8

5. GROWTH FROM A MOVING FETCH

The third-generation numerical wave model WAM (WAMDIG, 1988) describes the evolution of sea-state as a two-dimensional ocean wave spectrum. In its present form (Cycle 4) the model accommodates the processes of generation by wind stress, propagation with refraction by the seabed and/or currents, four-wave nonlinear interactions, and dissipation by white-capping and bottom friction. Each of these processes is explicitly incorporated in the model equations describing the evolution of the wave spectrum.

The model was used here to simulate wave growth in response to a fetch moving up the east coast of South Island. A rectangular grid was established on a latitude-longitude grid bordered by latitudes 44.5°S and 40S° and longitudes 172°E and 177°E, with gridpoints at 5-minute intervals. This region covers the area within the dashed lines in Figure 1. Spectra were computed at 12 equally spaced propagation directions and 25 logarithmically spaced frequencies, between f_1 = 0.0417 Hz and f_{25} = 0.4518 Hz.

Windfields were defined for a small fetch 150 km long and 100 km wide moving up the east coast of South Island. The wind direction was set at 210°. The centre of the fetch was initially located at 43.5°S, 173.5°E and translated in the direction of the wind (towards 30°). The speed of the fetch was varied from 0 ms^{-1} to 10 ms^{-1}.

Time series of wave statistics were generated for the gridpoint closest to the buoy site at Baring Head (see Figure 1). Two sets of results were generated, for winds within the fetch of 10 ms^{-1} and 20 ms^{-1}. Separate simulations were made for a stationary fetch immediately upwind of the site. Figure 6 shows these results, with wave growth measured from the time that the front (leading edge of the fetch) arrived at the buoy site.

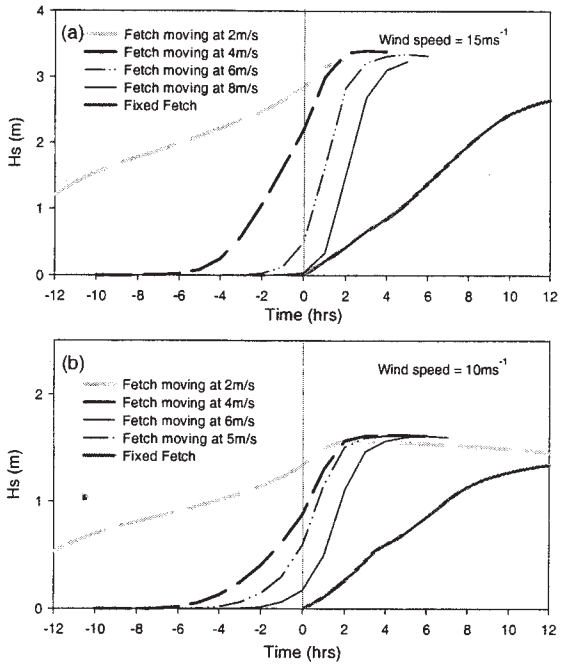

Figure 6 – Wave evolution at the Baring Head buoy site from WAM simulations with (a) wind of 15 ms^{-1} and (b) 10 ms^{-1}. Time series of significant wave height (Hs) are shown for moving fetch and fixed fetch scenarios. Time is measured from the instant at which the front of the fetch arrives at the site.

It is clear that the growth rate is affected considerably by the progression of the front. Slow movement allows swell to escape from the fetch and reach the site ahead of the front, slowly building the sea-state until the front arrives. A surge in the growth can sometimes be noted just after the wind reaches the site. As the speed of the fetch approaches 6 ms^{-1} the rate of growth has increased significantly and for wind speed of 15ms^{-1} the significant wave height rises 2.3 m in the 2 hours immediately after arrival of the front. This is very

similar to the rises measured at the site for a similar windspeed in the case shown in Figure 5(d).

For a stationary fetch over the site, the model simulates simple duration-limited growth. However, the growth will be lower than that represented by the curves in Figure 3 since the fetch is also limited in length and width.

6. ENHANCED DURATION

When a fetch moves in the same direction as the wind within the fetch, the wind-sea will propagate with the fetch. The effect is to sustain windstress over the growing sea and to enhance growth. The speed of the storm affects the enhancement. This phenomenon is reflected in both the observations and the model simulations of the present study.

For the cases in Table 1 the fronts, and the southerly fetches immediately following them, progress up the east coast of South Island at an average speed of 8.5 ms^{-1}. The passage is not always regular, but it is observed that the wind change at Wellington often occurs about 9 hours after the change at Christchurch. Measurements also show that the peak period for waves just following the climax of these events is typically T_p = 9 s. At the point of highest total energy, the seas are rapidly evolving and the peak period is a little lower, in the range 6.5 s to 8 s (Table 1). The associated group velocity is 7 ms^{-1}. Since the energy of a wave field travels at the group velocity ($c_g = \frac{gT_p}{4\pi}$, for peak period T_p) we observe that the energy flux in wave field is nearly keeping pace with the moving fetch. In these cases the climax of the storm is often within 2 hrs - 3 hrs after the wind change, which coincides almost exactly with the time predicted from the peak of the spectrum (T_p = 9 s).

This condition of near-resonance between wave energy flux and the motion of the fetch, U_{fetch}, increases the effective duration of wind over the fetch. The condition can be expressed as

$$U_{fetch} \approx c_g . \qquad (2)$$

The modelling in section 5 supports the observations. For the short (150 km) fetch of those simulations, T_p reached 7 s under a stationary fetch with 15ms^{-1} winds. However for a moving fetch T_p reached 8.5 s. This corresponds to a group velocity of 6.6 ms^{-1}. Figure 6(a) reflects the maximum growth rates achieved just after onset of the wind (t=0) for fetch movement of 6 ms^{-1}. For the simulations at windspeeds of 10 ms^{-1} T_p reached 5.2 s for a stationary fetch and 6.3 S for a moving fetch. The latter corresponds to a group velocity of 5 ms^{-1}. Figure 6(b) reflects a maximum growth rate achieved just after onset of the wind for fetch movement of 5 ms^{-1}.

As the fetch moves over any given site the stage of growth of the waves also rises rapidly. This is accompanied by a rapid rise in the peak period. Consider the event on July 8, 1999 (see Table 1 and Figure 7). Prior to the onset of the southerly, there was a low swell with peak period of 12 s -14 s and H_s of less than 0.9 m. As the southerly increased to 13.4 ms^{-1} the spectrum became bimodal, with a low-period peak associated with the fresh wave growth and a long-period swell peak (12 s). The low-period peak rose to 6 s within 2 hours and to over 8 s within a further 2 hours. Under simple duration-limited growth it would take considerably longer: 4

hrs (using CERC, 1984) or 10 hrs (using WMO, 1998) for the peak period to increase from 6 s to 8 s.

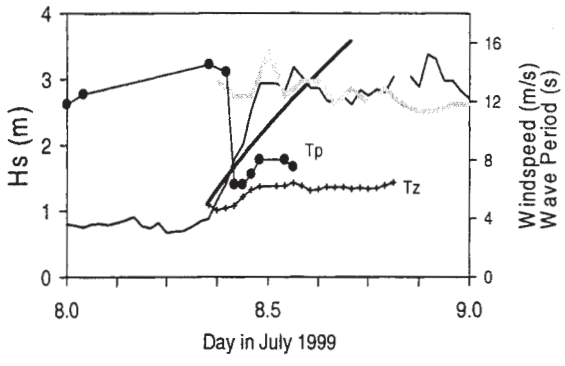

Figure 7 – Wave evolution during the July 8, 1999 event. Time series are shown for significant wave height (Hs, medium solid line), peak period (Tp, line with closed circles), zero-crossing period (Tz, line with "+") and windspeed (thick grey line). Windspeed and wave periods are measured against the right-hand axis). The thick solid line shows the theoretical wave growth.

For this event, wave data were also available off Banks Peninsula (Figure 1). Figure 8 shows the time series of significant wave height at both Baring Head and Banks Peninsula along with the windspeeds during the southerly event. It was noted that the change occurred at Wellington 6 hrs (±2 hrs) after Christchurch (280 km distant) and 3 hrs and 1 hr respectively after the change at Kaikoura (153 km) and Cape Campbell (63 km). The progress of the front was therefore reasonably steady, although it may have accelerated as it moved north.

The Banks Peninsula data have lower temporal resolution (3-hourly) than the Baring Head data (half-hourly). It is clear that there is a sudden rise in wave heights at both sites immediately following the passage of the front, but the wave data from Banks Peninsula do not resolve whether the growth rate at that site is as rapid as that at Baring Head. The increase in significant wave height is lower (1.3 m cf 2.3 m) and the wave height after the passage of the front is also lower (2.6 m cf 3.4 m), consistent with further development occurring as the southerly fetch moves up the coast to Wellington.

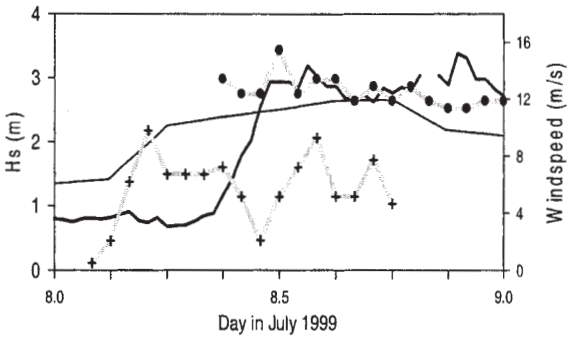

Figure 8 – Evolution of Hs at Banks Peninsula (thin solid line) and Baring Head (thick solid line) for July 8, 1999. The windspeeds at Wellington and Christchurch are shown as thick grey lines (with circles and crosses respectively), and are measured against the right-hand axis.

7. CONCLUSIONS

Wave growth associated with fronts moving up the east coast of New Zealand is often rapid, with increases of up to 3 m in significant wave height occurring within 2 to 3 hours. Such rapid onset of high sea-states is a potential hazard for mariners, coastal operators and private recreational users of coastal waters.

Wave observations near Wellington indicate that although the waves are characteristic of freshly generated wind-seas, the growth rates exceed those expected under simple duration-limited wave evolution. A likely factor is the matching between the motion of the front and the advection of wave energy generated from the fetch immediately behind the front. The timing of the storm peaks at Wellington is also consistent with the waves being

under constant forcing during their passage up the east coast of South Island.

Simulations of a simple moving fetch using the numerical wave model WAM produce growth rates similar to those measured. Maximum growth occurs just after the onset of wind at the site if the fetch speed matches the group velocity for the peak of the spectrum.

8. ACKNOWLEDGEMENTS

This study has been funded from the Public Good Science Fund under contract CO1X0015. We would like to thank TranzRail for commissioning wave measurements at Baring Head, and the Canterbury Regional Council for their support in maintaining the wave measuring facility off Banks Peninsula. Special thanks are also due to Warren Thompson, Sandra Kingsland, Kathy Walter, Andrew Harper and Malcolm Greig for maintaining the instruments and supplying the wave data.

9. REFERENCES

CERC, 1984: Shore Protection Manual Volume 1. Publ. U.S. Dept of the Army, Waterways Experimental Research Station, Coastal Engineering Research Center. U.S. Govt. Printing Office.

Groen, P. and R. Dorrestein, 1976: Zeegolven. K.N.M.I. opstellen op oceanografisch en maritiem meteorologisch gebied, No 11, 124pp.

Gunther, H., W. Rosenthal, T.J. Weare, B.A. Worthington, K. Hasselmann and J.A. Ewing, 1979: A hybrid parametrical wave prediction model. J. Geophys. Res., 84(C9), 5727-5738.

Hasselmann, K., T.P. Barnett, E. Bouws, H. Carlson, D.E. Cartwright, K. Enke, J.A. Ewing, H. Gienapp, D.E. Hasslemann, P. Kruseman, A. Meerburg, P. Muller, D.J. Olbers, K. Richter, W. Sell and H. Walden, 1973: Measurements of wind wave growth and swell decay during the Joint North Sea Wave Project (JONSWAP). Deutchen Hydrographischen Zeitschrift, Suppl. A8, No12.

Hasselmann, K., D.B. Ross, P. Muller and W. Sell, 1976: A parametric wave prediction model. J. Phys. Oceanogr., 6, 200-228.

Hasselmann, S. and K. Hasselmann, 1985: Computations and parameterisations of the nonlinear energy transfer in a gravity wave spectrum. Part 1: A new method for efficient computations of the exact nonlinear transfer integral. J. Phys. Oceanogr., 15(11), 1369-1377.

The SWAMP group, 1985: Ocean Wave Modelling. Publ. Plenum Press, New York, 256pp.

WAMDI (Hasselmann, S., K. Hasselmann, E. Bauer, P.A.E.M. Janssen, G.J. Komen, L. Bertotti, P. Lionello, A. Guillaume, V.C. Cardone, J.A. Greenwood, M. Reistad, L. Zambresky, L. and J.A. Ewing, 1988. The WAM model - a third generation ocean wave prediction model. J. Phys. Oceanogr., 18(12), 1775-1810.

Smith, R.K., R.N. Ridley, M.A. Page, J.T. Steiner, and A.P. Sturman, 1991. Southerly changes on the East Coast of New Zealand. Mon. Weather Rev., 119, 1259 – 1282.

WMO, 1998. Guide to wave analysis and forecasting. Publ. World Meteorological Organisation, WMO – No 702, 159pp.

The Perils of Coastal Wave Simulations in High Latitude Domains using 3G Spectral Wave Modeling

R.E. Jensen
Engineer Research and Development Center
Coastal and Hydraulics Laboratory
3909 Halls Ferry Rd.
Vicksburg, MS 39180-6199
(601)-634-2101
email: jensenr@wes.army.mil

Abstract:

The estimation of nearshore wave conditions is a difficult undertaking for open coastal sites. Spatial changes in the directional spectrum combined with temporal changes in the wind fields result in the interplay between the active source term mechanisms and effects of the local bathymetry. In addition to these standard mechanisms, in the high latitude environment ice ridge movement becomes a major factor influencing the local wave climate. The complexities are further increased considering the net effect of *far-field wave* activity, the generation of wind-seas from tropical cyclones creating low frequency swells. A long-term wave climatology is produced along the Alaskan coastline north of 67.5° N latitude for the *open water season* generally lasting 6 months. This makes for a very interesting study, where the combined effect of locally generated wind-seas produced in the Chukchi Sea distant swells from the Bering Sea, north pacific derived from typhoons as well as the movement of the ice ridge. The paper (and presentation) will summarize the modeling technology used, *lessons-learned* in the simulation, as well as comparisons to observations.

Theoretical and observational study of the response of wave directions to changing wind directions for inhomogeneous wave fields

Li Luping Huang Peiji Chen Xueying

First Institute of Oceanography . SOA Qingdao 266061, P.R.China

Abstract

Based on the wave energy balance equation, through considering the wave propagation term, i.e. $\nabla \cdot [Cg(f,\theta)E(f,\theta)] \neq 0$, the time scale of the directional response of wind waves is derived for inhomogeneous wave fields. The new results show that observational wave data from a single point can not provide enough information to deal with the directional response for inhomogeneous wave fields due to the lack of advection and an instrument array should be used for observation analysis study. The observations of wind waves measured by an instrument array in a closed small water body are analyzed, and the results indicate that the scatter of the dimensionless response time scales between theoretical calculations and observations is large, but through using the moving average method in the same intervals of $|\theta_w - \theta_0|$, the averages of the nondimensional time scale of the response obtained from theoretical calculations and observations have strongly linear relationships. It is pointed out that the response time scale is random and statistics should be used for data analysis. Several tests show that the theoretical calculation method for directional response presented in this paper is also consistent with published observations.

1. Introduction

Information of wave directions is of great importance to many ocean engineering problems. The characteristics of wave directions are poorly understood due to lack of theoretical researches and observations. Because the directional response of wind waves to turning winds is important for assessing numerical wave model performance, recently many authors have studied the directional characteristics of waves using different approaches and presented some models for the response of wave directions to changing wind directions (Gunther et al. 1985; Hasselmann et al. 1980; Holthuijsen et al. 1984, 1987, 1988, Li Luping et al. 1991,1992, Van Vledder et al. 1987,1993). This response has become a very important topic because of its significance in theoretical researches and numerical wave modeling. But the models presented so far have been hardly able to describe the behavior of the change in wave directions and can only be used in homogeneous wave fields. The observed time scales scatter largely when plotted as a

function of the dimensionless wave energy.

Theoretically, Holthuijsen et al. (1984,1987,1988) derived a relaxation model for the response of wave directions to changing wind directions with the mean wave direction obtained from measurements with a pitch and roll buoy, that is,

$$\theta_0 = \arctan(\frac{b_1}{a_1})$$

in which

$$b_1 = \int_0^{\infty}\int_0^{2\pi} \sin\theta E(f,\theta)d\theta df, \qquad a_1 = \int_0^{\infty}\int_0^{2\pi} \cos\theta E(f,\theta)d\theta df.$$

The locally changing rate of the wave direction θ_0, determined as the time derivative of the above equation, can be written as

$$\frac{\partial\theta_0}{\partial t} = \frac{1}{m_0}\frac{\partial m_0}{\partial t}\cdot\sin(\theta_w - \theta_0)$$

in which $m_0 = \int_0^{\infty} E(f)df$ is the total wave energy. This result is derived on two rather crude assumptions: 1.the shapes of the directional distributions of $E(f,\theta)$ and $S(f,\theta)$ are frequency independent, equal to one another and symmetric around θ_0 and θ_s, respectively; 2. the source function is centered around the wind direction θ_w such that $\theta_s = \theta_w$. This result means that the time scale of the response can be estimated from the rate of wave growth. Under the same assumptions for directional distributions as those made by Holthuijsen et al., Li Luping et al. (1991,1992) derived a model for the response of wave directions to changing wind directions on the basis of the wave energy balance equation. With the directional distributions of the wave energy and the source function: $D(\theta) = \frac{2}{\pi}\cos^2(\theta - \theta_0)$ and $D'(\theta) = \frac{2}{\pi}\cos^2(\theta - \theta_w)$, on the wave energy balance equation in a homogeneous field, the locally changing rate of the mean wave direction can be derived:

$$\frac{\partial\theta_0}{\partial t} = \frac{1}{m_0}\frac{\partial m_0}{\partial t}\cdot\frac{\sin(\theta_w - \theta_0)}{2\cos(\theta_w - \theta_0)}$$

This result supports the conclusion mentioned above, that is, the time scale of the response can be estimated from the rate of wave growth, but their concepts are different.

In the derivation above, the propagation term of waves is not considered, that means that the wave field should be homogeneous. And in this case, it is easy to see that the time scale of the response can be obtained from single position wave observations. Many authors presented lots of results of observations about the time scale of the response, and all of these results are from single position observation data. The analysis of the data shows that the time scales of response are scatter largely due to inhomogeneity of wave

fields, as pointed out by Holthuijsen et al.. That means that the condition of the homogeneous wave field is hardly satisfied for observation study.

In order to deeply understand the response of wave directions to changing wind directions, we study the directional response of waves through considering the wave propagation term in the wave energy balance equation, that is, $\nabla \cdot [Cg(f,\theta)E(f,\theta)] \neq 0$, based on the wave energy balance equation. The theoretical results show that the inhomogeneity of wave fields plays an important role on the time scale of the response, and for the observational study an instrument array should be used to provide the inhomogeneity information. For the simplest inhomogeneous wave fields, We carried out an array wave observation in a reservior near Qingdao city. The analysis shows that the time scales of the response for theoretical calculations and observations are almost random because the wind directions always change their directions in a large sector. A moving average method with $|\theta_w - \theta_0| = 20^\circ$ and a step length=2.5° is used to analyze the time scales of the response, so that theoretical results agree fairly well with observations.

Section 2 describes the theoretical model for inhomogeneous wave fields. Section 3 describes test of the theoretical model. Section 4 describes the observation and data analysis for inhomogeneous wave fields. Conclusions are section 5.

2.The response model for inhomogeneous wave fields

2.1 Theoretical derivation

On the basis of the wave energy balance equation, we have

$$\frac{\partial E(f,\theta)}{\partial t} + \nabla \cdot \left[Cg(f,\theta)E(f,\theta)\right] = S(f,\theta) \qquad (1)$$

where $E(f,\theta)$ - two dimensional spectrum;

$Cg(f,\theta)$ -energy propagation velocity of frequency f and in the direction θ in the x-y space;

$S(f,\theta)$ -source function;

∇ -second order partial differential operator in the x-y space.

In the following derivation, as Holthuijsen et al. did, it is supposed that: (1) the shapes of the directional distribution of the two-dimensional spectrum $E(f,\theta)$ and the source function $S(f,\theta)$ are frequency independent, equal to one another and symmetric around θ_0 and θ_s, respectively; (2) the source function is centered around the wind direction θ_w such that $\theta_s = \theta_w$. According to these assumptions. We have:

$$E(f,\theta) = E(f) \cdot D(\theta),$$

$$S(f,\theta) = S(f) \cdot D'(\theta),$$

and for the directional energy distribution, it is reasonable to choose:

$$D(\theta)=\frac{2}{\pi}\cos^2(\theta-\theta_0),$$

$$D'(\theta)=\frac{2}{\pi}\cos^2(\theta-\theta_w),$$

for developing wind waves.

For all frequencies and any directional sector centered around θ_w, Eq.(1) can be written as:

$$\int_{\theta_w-\alpha}^{\theta_w+\alpha}\int_0^{\infty}\left\{\frac{\partial E(f,\theta)}{\partial t}+\nabla\cdot[Cg(f,\theta)E(f,\theta)]\right\}\mathrm{d}f\mathrm{d}\theta=\int_{\theta_w-\alpha}^{\theta_w+\alpha}\int_0^{\infty}S(f,\theta)\mathrm{d}f\mathrm{d}\theta. \tag{2}$$

In deep water, the propagation term $Cg(f,\theta)$ can be written as

$$Cg(f,\theta)=\frac{g}{4\pi f}(\cos\theta,\sin\theta). \tag{3}$$

After some straightforward manipulations and through using the following approximate formula:

$$\frac{\partial}{\partial x}\int_0^{\infty}\frac{g}{4\pi f}E(f)df\approx\frac{\partial}{\partial x}\frac{gm_0}{4\pi f_p},$$

$$\frac{\partial}{\partial y}\int_0^{\infty}\frac{g}{4\pi f}E(f)df\approx\frac{\partial}{\partial y}\frac{gm_0}{4\pi f_p},$$

where f_p is the spectral peak frequency.

From Eq.(2) the local rate of the change of the mean wave direction can be derived:

$$\frac{\partial\theta_0}{\partial t}\approx\frac{1}{m_0}\frac{\partial m_0}{\partial t}\cdot\frac{\sin(\theta_w-\theta_0)}{2\cos(\theta_w-\theta_0)}-\frac{\cos\alpha^{-1}}{m_0\sin 2(\theta_w-\theta_0)}\cdot\nabla\cdot\left[Cg(f_p,\theta_w)m_0\sin^2(\theta_w-\theta_\partial)\right] \tag{4}$$

in which $Cg(f_p,\theta_w)=\frac{g}{4\pi f_p}(\cos\theta_w,\sin\theta_w)$

Eq.(4) shows that in inhomogeneous wave fields the changing rate of the mean wave directions is related to the inhomogeneity of wave fields and the integral interval α. This is obviously reasonable because the effect of inhomogeneity of wave fields on the response of wave directions is different for different regions.

The total contribution of the inhomogeneity of wave fields can be obtained if $\alpha=\pi$. Then, we have:

$$\frac{\partial \theta_0}{\partial t} \approx \frac{1}{m_0}\frac{\partial m_0}{\partial t}\cdot\frac{\sin(\theta_w-\theta_0)}{2\cos(\theta_w-\theta_0)}+\frac{\partial}{\partial D}\left[Cg(f_p)m_0\right]\times$$
$$\times\frac{\cos^2(\theta_w-\theta_0)}{2m_0\sin(\theta_w-\theta_0)}+\frac{3}{2}Cg(f_p,\theta_w)\nabla\theta_0 \tag{5}$$

in which $\frac{\partial}{\partial D}$ is the local change along the wind direction.

The following equation is used:

$$\frac{\partial \theta_0}{\partial t}=\frac{1}{\tau}\sin(\theta_w-\theta_0) \tag{6}$$

where τ is the time scale of the response, then

$$\frac{1}{\tau}=\frac{1}{\tau_1}+\frac{1}{\tau_2}+\frac{1}{\tau_3} \tag{7}$$

where

$$\tau_1=2\left(\frac{1}{m_0}\frac{\partial m_0}{\partial t}\right)^{-1}\cos(\theta_w-\theta_0) \tag{8}$$

$$\tau_2=\left\{\frac{\partial}{\partial D}\left[Cg(f_p)m_0\right]\right\}^{-1}\frac{2m_0\sin^2(\theta_w-\theta_0)}{\cos^2(\theta_w-\theta_0)} \tag{9}$$

$$\tau_3=\frac{2}{3}\left[Cg(f_p,\theta_w)\nabla\theta_0\right]^{-1}\sin(\theta_w-\theta_0) \tag{10}$$

Therefore, the time scales of the response can be divided into three parts in inhomogeneous wave fields: 1. the contribution of the response in homogeneous situations, which has been studied; 2. the influence of the inhomogeneity of wave energy distributions; 3. the influence of the inhomogeneity of the mean wave direction distributions. Theoretically it is suggested that the inhomogeneity of wave fields plays an essential role in this response.

2.2 The response model for fetch-limited wave fields

For homegeneous and stationary wind fields, the fetch-limited wave fields are considered as the simplest inhomogeneous wave fields. In this case the relationship of wind wave growth (Wen et al .1989) can be written as:

$$\tilde{H}_s=5.5\times10^{-3}\tilde{x}^{0.35}, \tag{11}$$

$$\tilde{T}_s=0.55\tilde{x}^{0.233}, \tag{12}$$

$$\tilde{t} = 29.8\tilde{x}^{0.767}, \tag{13}$$

where $\tilde{H}_s$ -dimensionless significant wave height $\tilde{H}_s = \frac{H_s g}{U_{10}^2}$,

$\tilde{T}_s$ -dimensionless significant wave period $\tilde{T}_s = \frac{T_s g}{U_{10}}$,

$\tilde{t}$ -dimensionless time $\tilde{t} = \frac{tg}{U_{10}}$,

$\tilde{x}$ -dimensionless fetch $\tilde{x} = \frac{xg}{U_{10}^2}$,

U_{10} - the mean wind speed at 10m above the sea level.

In order to compare with other results ,the friction wind speed U_* is used to dimensionlize the parameters mentioned above and the theoretical time scales of the response is quantitatively estimated. In this case the dimensionless time scale $\tau^* = \frac{g\tau}{U_*}$, the dimensionless peak frequency $f_P^* = \frac{f_p U_*}{g}$,in which f_p is the peak frequency, and $\frac{1}{f_p} = 1.05T_s$. The friction wind speed is $U_*^2 = C_d U_{10}^2$,the friction coefficient(Wu, 1982) is $C_d = (a + bU_{10}) \times 10^{-3}$ in which $a = 0.8$, $b = 0.065$. Therefore, after dimensionlized, equation(8) can be written as

$$\tau^*_1 = a(U_{10}) f_p^{*-3.29} \cdot [2\cos(\theta_w - \theta_0)], \tag{14}$$

in which $a(10) = 0.1125$, $a(20) = 0.1718$.

That means that because of the use of the friction wind speed, the theoretical response time scales relate to not only the turning angle of the wind but also the wind speed. Fig.1 gives the relationship between τ_1^* and f_p^*.

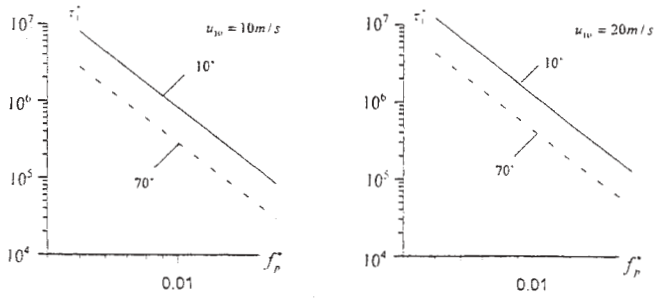

Fig.1 The relationship between dimensionless time scale τ_1^* and dimensionless peak frequency f_p^* for homegeneous wave fields

Fig.1 shows that the dimensionless time scale τ_1^* increases with the increase of wind speed. It means that for high wind speed the rate of the turning of wave directions decreases, and for low wind speed the rate of the turning of wave directions increases. This result is reasonable. Because for high wind speed the friction coefficient between air and sea increases and the friction wind speed also increases, the air current near the surface of the sea can not rapidly change its direction with the upper air current due to the influence of the friction. Therefore, when the wind changes its direction in a situation of a high wind speed the rate of the change in wave directions decreases. But for low wind speed the friction coefficient between air and sea decreases and the friction wind speed also decreases, therefore the air current near the surface of the sea rapidly changes its direction with the change in the upper air current. This makes the rate of the change in wave directions increase.

Fig.1 also shows that the turning angles of the wind direction affect the time scale of the response. From Eq.(14) it is known that although the effect of the wind speed and the turning angle of the wind direction on the response time scale is small in order of magnitude, it is reasonable to consider this effect in the research on the response of wave direction to changing wind directions.

Eq.(9) can be written as

$$\tau_2^* = b(U_{10}) f_p^{*-3.29} tg^2(\theta_w - \theta_0), \tag{15}$$

in which $b(10) = 0.159$, $b(20) = 0.243$.

Fig.2 gives the relationship between τ_2^* and f_p^*.

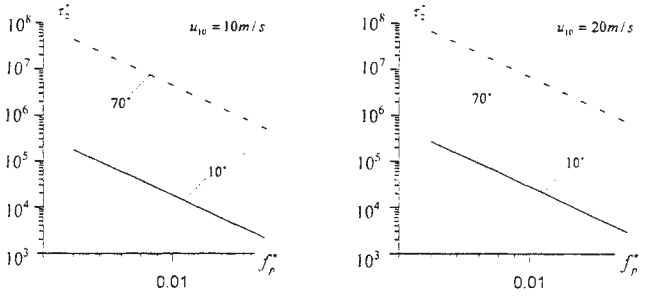

Fig.2 The relationship between dimensionless time scale τ_2^* and dimensionless peak frequency f_p^* for inhomogeneous wave fields

Fig.2 shows that the change of the dimensionless time scale with wind speed due to the inhomogeneity of the distribution of the wave energy is almost the same as the result of homogeneous wave fields, but the effect of the turning angles of wind directions on τ_1^* and τ_2^* is contrary. Especially, the change of the turning angles of wind directions can make the dimensionless time scales increase or decrease several orders of magnitude. In other words, the turning angle of wind direction must be considered in the research

on the response of wave directions to changing wind directions due to the inhomogeneity of wave energy distribution.

Fig.3 gives the relatiouship between $\frac{\tau_2^*}{\tau_1^*}$ and the turning angle of wind directions.

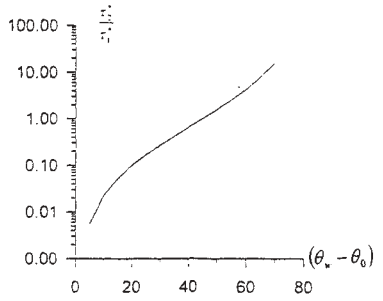

Fig.3 The relationship between $\frac{\tau_2^*}{\tau_1^*}$ and the turning angle of wind directions $|\theta_w - \theta_0|$

The results mentioned above are derived from the wave energy balance equation and have important practical significance.

In the situation of homogeneous wind fields, while turning the wind directions, wave fields are hardly homogeneous; at this time, the calculated time scale of the response from observational data should be the total time scale of the response τ^*. Based on Eq.(14) and (15), it is easy to calculate τ_1^* and τ_2^* if wind speeds, wind directions and spectral peak frequencies are given, and further to calculate the total time scale of the response τ^*. In other words, the test of the theoretical model presented in this paper is easily done.

Eq.(10) stands for the change in time scale of the response due to inhomogeneity of the mean wave direction distributions. In fetch-limited wave fields, before the turning of the wind directions the mean wave direction do not change with fetch, although the dimensionless spectral peak frequencies and dimensionless wave energy change with fetch, that is, the distribution of wave directions is homogeneous. After the turning of the wind directions the mean wave directions would be influenced by fetch, but we don't know the law of the change in the mean wave directions theoretically, the time scale of the response of this term can not be quantitatively estimated in this study. However, because the turning of wind directions is generally not large, it is expected that the effect of the fetch on the time scale would not be large even if the fetch do influence the mean wave directions, that is, $\frac{\partial \theta_0}{\partial \tilde{\chi}}$ is very small and τ_3^* is large. It is considered that it is reasonable to ignore the contribution of the inhomogeneity of the mean wave direction to the response in the study of the effect of

AUTHOR INDEX TABLE OF CONTENTS

inhomogeneities of wave fields on the directional response. Eq.(7) then reduces to the following equation:

$$\frac{1}{\tau^*} = \frac{1}{\tau_1^*} + \frac{1}{\tau_2^*} \tag{16}$$

3.Test of the theoretical model

3.1 fitting with Holthuijsen's observations

If wave fields satisfy with Eq.(11)-Eq.(13), the total dimensionless time scale of the response of wave directions to changing wind directions should equal the dimensionless time scale of the response of the observations. Gao et al.(1993) presented that the rate of change of the mean wave direction should be determined by the angle between $\theta_{\frac{\partial F}{\partial t}}$, the mean direction of the rate of change of the spectrum, and θ_0. They introduced the notation $\theta_{\frac{\partial F}{\partial t}}$ rather than θ_w to indicate the effect of advection on change of mean wave directions. Gao et al. used their new method to reanalyze observations made by Holthuijsen et al. and we used Eq.(16) to reanalyze Holthuijsen's observations. The comparisons among our theoretical results , Gao's results and Holthuijsen's observations are shown in table 1.

Table 1 The comparisons of the response time scales among our theoretical results τ_{Li}^*, Gao's results τ_a^*,and Holthuijsen's obserortions τ_{ob}^*

序号	H_s/m	f_m/HZ	θ_{wave}	$U_{10}/m\cdot s^{-1}$	θ_{wind}	$f_p^*/10^{-3}$	m_0^*	U_*	$\tau_a^*/10^5$	$\tau_{Li}^*/10^5$	$\tau_{ob}^*/10^5$
1	0.90	0.24	202	7.9	234	7.0	724	0.286	8.4	5.13	6.29
2	2.42	0.16	340	12.6	330	8.3	532	0.51	2.0	0.39	0.55
3	2.42	0.17	235	15.0	215	1.03	220	0.63	1.4	0.82	0.88
4	0.95	0.23	190	11.3	218	10.0	141	0.44	2.8	1.5	3.6
5	1.56	0.16	218	8.5	234	5.1	1530	0.312	5.3	4.0	1.92
6	1.67	0.18	271	11.2	314	8.4	456	0.437	4.7	5.4	5.7
7	0.71	0.27	246	10.2	263	11	130	0.39	0.82	0.65	0.81
8	1.21	0.20	351	9.9	018	7.7	439	0.375	4.6	3.0	3.04

Fig.4 gives the relationship between dimensionless response time scales, i.e., Holthuijsen's observations τ_{ob}^*, Gao's calculated results τ_a^*, and theoretical values τ_{Li}^* in this study and spectral peak frequencies. Fig.5 gives the correlation between τ_{ob}^* and τ_a^* (correlation coefficient R=0.65) and that between τ_{ob}^* and τ_{Li}^* (correlation coefficient R=0.81). These results demonstrate that the fitting between the results

presented by this paper and observations is better than the fitting between Gao's results and observations. As Gao et al. pointed out, among the published observations, only the data of Holthuijsen seem to be available for reanalysis.

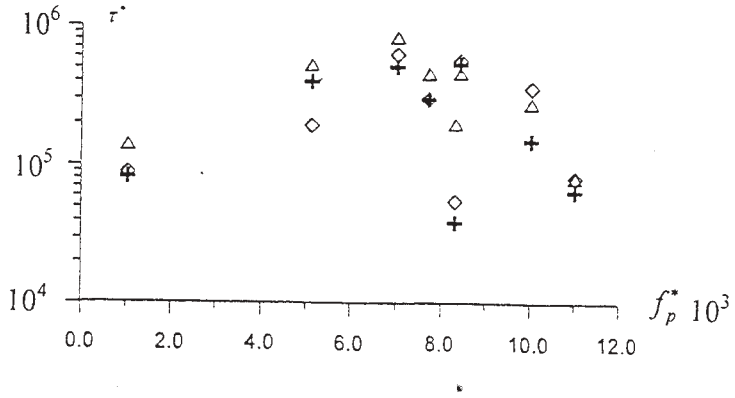

Fig.4 The comparison of the relationship between nondimensional time scale of the response and nondimensional spectral peak frequency.

Holthuijsen's observations ◇, Gao's calculations △, theoretical values in this study+.

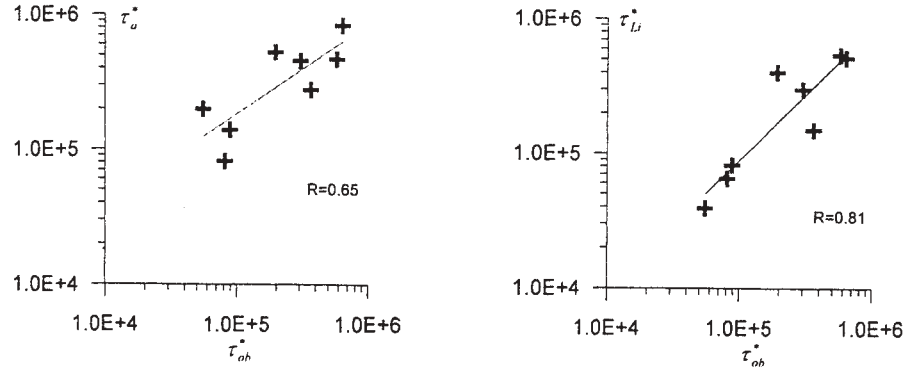

Fig.5 The correlation between Hothuijsen's observations τ_{ob}^* and Gao's calculations τ_a^* and the correlation between Holthuijsen's observations τ_{ob}^* and theoretical values τ_{Li}^* in this study.

3.2 The comparison between Gao's results from WAM model and theoretical values in this study

Gao et al. pointed out that the WAM model can successfully predict the directional characteristics of wind waves in the condition of changing wind direction. They use the WAM model to compute the time scales of the response for fetch-limited wind waves with 60° of the turning angle of wind directions and 15°, 30° and 45° of the turning angles of the mean wave directions under the action of wind speed 20m/s and show that the use of $\cos^{2s}(\theta/2)$ directional distribution can not get better improvement than the use of $\cos^{2}(\theta)$ directional distribution.

Table 2 gives the comparison of the nondimensional time scales at two nondimensional peak frequencies with 60 of a turning angle of suddenly changing wind directions between the theoretical values in this study and Gao's numerical envelopes under the action of wind speed 20m/s.

Table 2. The comparison between theoretical values in this study and Gao's numerical envelopes.

		f_p^*=0.008	f_p^*=0.014	$\theta_w - \theta_0$
Theoretical values in this study	τ^*	9.62×10^5	1.53×10^5	45°
	τ^*	5.07×10^5	8.04×10^4	30°
	τ^*	1.26×10^5	2.01×10^4	15°
	Average value	5.31×10^5	8.45×10^4	
Gao's numerical envelopes	Upper	6.1×10^5	9.3×10^4	
	Lower	2.3×10^5	3.7×10^4	
	Average value	4.2×10^5	6.5×10^4	

Table 2 shows that the fitting between theoretical values in this study and Gao's numerical results is good. However, in the process of the response, the theoretical values of the time scale decrease with the turning of the mean wave directions, it is indicated that the contributions of the inhomogeneities of wave fields to the response continually increase with the turning of the mean wave direction toward the direction of the wind. The change of the directional response time scales with time can not be reflected in Gao's numerical results.

3.3 Qualitative test with Diane Masson's results

Diane Masson's observations(1990) show that the response of wave directions to changing wind directions strongly depend on frequencies, and the mean wave directions for high frequencies firstly turn to the wind directions, but the mean wave directions for the frequency bands controlled by low frequency swell are not affected by turning winds.

He pointed out that the wave fields are no longer homogeneous during observation, the time scales of the response relate to wind speed, and the turning angles of the wind directions also powerfully influence the

response of wave directions. These views mentioned above support the theoretical results in this study. However, the mean wave direction in this paper is the mean direction of directional spectra and is not the mean direction at any frequency in Diane Masson's study. The comparisons show that Diane Mosson's results do not agree with our results.

It should be emphasized that the data mentioned above are from single point wave measurements. According to Eq.(9), the time scale of the response τ_2 can be calculated out only on the data from an instrument array . In order to do comparisons with observations from single point measurement, the fetch-limited wave growth relationship, that is, Eq.(11)-Eq.(13) are used. Therefore, if the theoretical results are really tested, the data presented by an instrument array must be used.

4. Observation and data analysis of directional response for inhomogeneous wave fields

Instrument array wave measurements were carried out in a reservoir in winter 1999 (From 0000 3 January to 2300 11 January in local time). The figure of the dam of the reservior likes a ellipse with a long axis of 4km and a short axis of 3km.The datasets contained 96 observations (17 minute duration each at one-hour intervals). The observation array was placed along the south-east dam. The wave observation array consist of two wave gauges and a directional wave pressure sensior Seapac, which is produced by Woods Hole Institute Instrument Company.

The draft of the wave gauge arrangement is shown in Fig.6

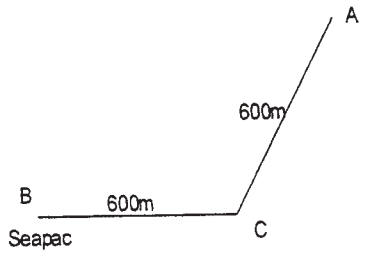

Fig.6 The draft of the arrangement of gauges for a wave array

B.Seapac; A, C, Wave gauges; BC=CA=600 m

During the observation the wave gauge at A point refused to work ,and no data at A point can be used. The wind observation were carried out with a conventional cup anemometer and a wind vane at 10 m elevation on the water surface. The former measured wind direction with degree, and the later measured the 16 directors of wind directions, that is, ENE, NE, ...etc. Because the differences of the wind direction

measured with these instruments is quite large, all of the measured data are analyzed. The total dataset reached 192 observations. In the data processing , according to the expression of the turning rate of the mean wave direction derived theoretically for inhomogeneous wave fields, i.e. Eq.(5), the time scales of the response τ^*_{obs} can be calculated from the measurements of the wind directions and the mean wave directions based on $\frac{\partial \theta_0}{\partial t} = \frac{1}{\tau_{obs}} \sin(\theta_w - \theta_0)$, and the time scales of the response τ^*, as the theoretical value can be computed from total wave energy, spectral peak frequency, wind direction and mean wave direction based on the right of Eq.(5).

However, the comparisons between observational dimensionless time scales τ^*_{obs} and theoretical values τ^* show that the scatter is considerable, and the scatter diagram between τ^*_{obs} and τ^*, and the dimensionless peak frequency is divergent and the fitting lines of τ^*_{obs} and τ^* obtained with the method of least squares exhibit a lower correlation coefficient although they are closed. These results can not be improved through choosing some criterion. During the observation, We noticed that the wind directions were always changing with time and the determination of the wind directions was not objective and dependent on the opinion of observers. Therefore, in our opinion, the time scales of the response are random and statistical methods should be used in processing of theoretical calculations and observations.

In the following statistical analysis, the observations are used only for developing wind waves, that is, $\frac{\partial m_0}{\partial t} > 0$ and $|\theta_w - \theta_0| < 90°$; as for the requirement of the observed wave direction changing towards the observed wind direction, it is not considered because the wind direction easy changes. Even more, in the analysis of data, the smoothed averages of theoretical and observational values with $|\theta_w - \theta_0| = 20°$ and a step width 2.5° are used. The results show that the theoretical nondimensional response time scales and observational nondimensional response time scales have strongly linear relationship. Fig.7 gives the results of their fitting. The correlation coefficients are 0.85 and 0.96 seperately, due to using different theoretical calculations at B point and C point. For each interval of $|\theta_w - \theta_0| = 20°$, there exist 13 values on the average.

Because there are strongly correlation between theoretical dimensionless time scales and observational values, it means that the observations can be calculated by the theoretical model in this study. Fig.8 gives the results of approximation in the mean. That is, the averages of theoretical nondimensional time scales and observational nondimenszonal time scales changes with increasing the intervals between wind directions and wave directions.

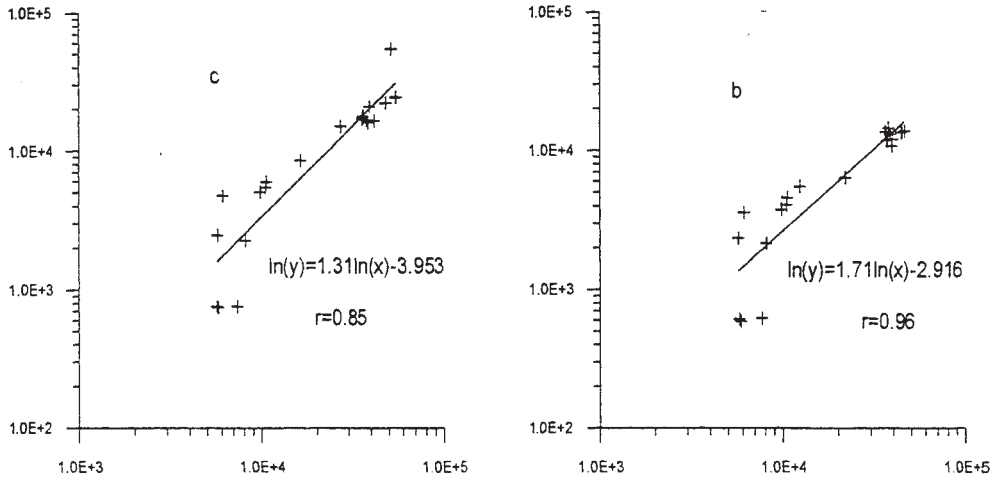

Fig 7. The scatter diagram between dimensionless response time scales τ^*_{obs} and τ^* after smoothed average. Lateral coordinate τ^*_{obs}, longitudial coordinate τ^*

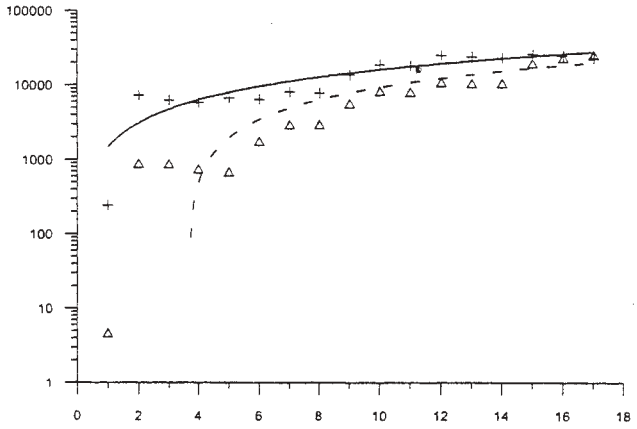

Fig.8 The results of approximation in the mean

+ observations △theoretical calculations

solid line-observations, broken line-theoretical calculations

Fig.8 shows that the differences between observations and theoretical calculations is getting small with increasing intervals of $|\theta_w - \theta_0|$ and the the total average of all of observation is 0.257×10^5 and the total average of all of theoretical calculations is 0.145×10^5. Their total averages are fairly closed. The ratio of τ_2^* / τ_1^* obtained based on observations and that obtained based on Wen's wave growth relationship in fetch-limited conditions are considered to be mutually consistant, considering the difference between the wave growth in a closed small water body and that in fetch-limited conditions in the sea. Fig.9 give the comparison between this study and the results from Eq.(14) and Eq.(15)

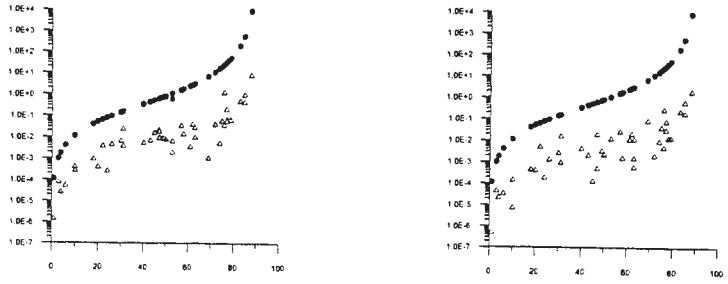

Fig.9 The comparison of the ratio of τ_2^* / τ_1^*.

•: Calculations based on Wen's wave growth in fetch-limited conditions

△: calculations based on the observations in this study

5. Conclusion

In this study, the directional response of wind waves to changing wind directions for inhomogeneous wave fields is derived based on the wave energy balance equation. Because of considering the advection term, the time scales of the response derived also include the effect of inhomogeneity of both wave energy distribution and mean wave direction distribution besides the contribution of wave energy growth. It is pointed out that for observational study an array wave gauges should be used instead of single gauge in order to get the information of inhomogeneous wave fields. Such array wave measurements carried out in a small closed water area. The uncertainties of wind directions are found during the observation and are considered to be adversely affecting the results. The observations and theoretical calculations show that the time scales of the response are random; the comparisons both between observations and theoretical calculations and between τ_{obs}^* and f_p^* show large scatter. However, their smoothed averages and their total average are rather consistant. The theoretical model in this paper is tested with published data and the time scales from theoretical calculations are agreement fairly well with published data.

Acknowledgment

This work was financially supported by the National Science Foundation of China (No.49776282).

References

[1] Diane Masson. Observations of the response of sea waves to veering winds. J. Phys Oceanogr, 1990, 20:1876～1885

[2] Gunther H, Rosenthal W, Dunckel M. The response of surface gravity waves to changing wind directions. J Phys Oceanogr, 1981, 11: 718～728

[3] Gao Quanduo, Gerbrand Komen. Directional response of ocean waves to changing wind direction. J Phys Oceanogr, 1993, 23: 1561～1566

[4] Hasselmann D E, Dunckel M, Ewing J A. Directional wave spectra observed during JONSWAP 1973. J Phys

Oceanogr，1980，10: 1264～1280

[5]Holthuijsen L H, Smith D R. An evaluation of model estimation of ocean wave directions. Ocean Engng，1988，15，2: 127～137

[6] Holthuijsen L H，Kuik A J, Mosselman E. The response of wave directions to changing wind directions. J Phys Oceanogr. 1987，7, 7: 845～853

[7] Jackson F C, Jensen R E. Directional response of wind waves to a large wind shift. J phys Oceanogr，1991，29，4: 2829～2843

[8] Li Luping. The effect of the inhomogeneity of wave fields on the response of wave directions to Changing wind directions. J. of Oceanography of Huang hai & Bohai Seas, China 1996, 14(4):21-26 in Chinese.

[9] Li Luping，Gong Bin. A model for the response of wave directions to changing wind directions for random breaking waves. IUTAM Breaking Waves Symposium. Sydney，1991，207～217

[10] Li Lupng，Gong Bin. A model for the response of wave direction in slowly turning wind fields. Acta Oceanologica Sinica，1991，11, 4: 499～508

[11] Wen S C. zhang D C. Chen B H, et al. Parameters in wind wave frequency spectra and their bearings on spectrum forms and growth. Acta Oceanologica Sinica, 1989, 8, 1:15~39

[12] Wu J.，Wind-stress coefficient over sea surface from breeze to hurricane. J Geophys. Res，1982. 87(C12): 9704～9706

[13] Vledder G Ph van, Holthuijsen L H. Waves in turning wind fields. Twenty-First Coastal Engineering Conference，1988，Vol.602～611

[14] Vledder G Ph Van, Holthuijsen L H. The Directional response of ocean waves to turning winds. J Phys Oceanogr，1993，23: 177～192

BED FORM RESPONSE TO WAVE AND CURENT FORCING DURING THE SHOALING WAVES EXPERIMENT, SHOWEX.

Timothy P. Stanton
Oceanography Department, Naval Postgraduate School, Monterey, CA 93943, USA

1. INTRODUCTION

Several recent observational studies suggest that in the absence of local wind forcing, dissipation in the bottom boundary layer can result in the loss of a large fraction of longer period wave energy. For example, Herbers et al, 2000, measured cross-shelf wave energy levels offshore from Duck, N.C., on a day with no significant wave forcing and strong, 2.5m significant wave heights offshore. A comparison between the inshore energy and that predicted by a propagation model with refraction only showed that only 25% of the offshore wave variance reached in the inshore station in these energetic conditions. There is therefore great interest in correctly modeling wave dissipation in the bottom boundary layer to correctly predict this cross-shelf attenuation term.

The Shoaling Waves Experiment is an ONR-funded program designed to study processes affecting the propagation of waves in coastal regions. As part of this effort, continuous observations of the structure of the bottom boundary layer were made at an inner shelf site for a three month period starting in October 1999. An instrumented frame equipped with a high bandwidth data and power cables was deployed at 12m depth offshore from the Army Corp of Engineers Field Research Facility at Duck NC. Measurements on the frame included an upward-looking 5 beam ADCP to profile mean currents and estimate directional wave spectra, a 0.6 cm vertical resolution bistatic coherent doppler profiler (Stanton 1996) which measured three component velocity profiles over a 50cm range down to the bed, and a scanned two axis altimeter which measured the bed morphology maps over a 1.5m cross shore by 1m long shore area with 2cm horizontal and 0.2 cm vertical resolution, every 15 minutes. All the instruments were mounted on a 4m long frame orientated long-shore supported by two 7cm diameter pipes jetted into the sand at the end of the frame. This observation system was designed to measure wave and current forcing, the 3D bed form response to forcing, and the three component velocity structure of the wave and mean current boundary layer to allow direct estimation of the oscillatory stresses and shears across the thin oscillatory boundary layer in the presence of mean currents.

Continuous measurements were obtained with these instruments over most of the three month field program, spanning a wide range of forcing conditions. Fine, sandy sediments were sampled at this site several times during the observation period, and a size analysis consistently showed a mean 0.1mm grain diameter, sandy bed composition.

In the following analysis a storm event has been selected to illustrate the observed forcing and bed response over a two day period. Strong long-shore, low frequency currents were associated with all the storms observed during the experiment, so a preliminary comparisons with wave forced and wave plus current forced empirical models are presented.

2. WAVE FORCING

Wave Height density spectra were estimated every 30 minutes from a high precision Paroscientific pressure transducer on the instrument frame. The 2 Hz sampled data had a linear wave transformation applied to estimate the surface elevation out to 0.5 Hz frequency. Figure 1 shows the spectra timeseries over a two day interval starting on yearday 315, prior to the arrival of an energetic frontal weather system. A gray scale wave-height energy spectral timeseries shows the rapid development of local seas from 3 second period to energetic 8 second

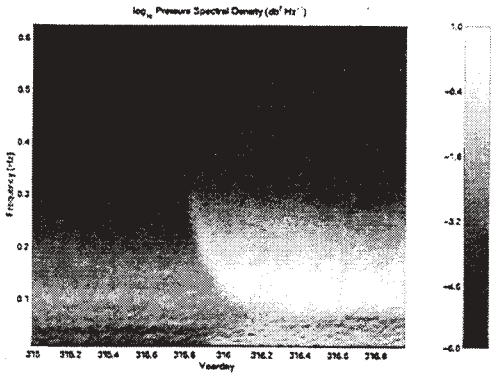

Figure 1. A two day spectral timeseries of log10 wave height spetral density measured at the 12m SHOWEX BBL instrument array. The rapidly evolving sea / swell system can be seen staring at the end of yearday 315.

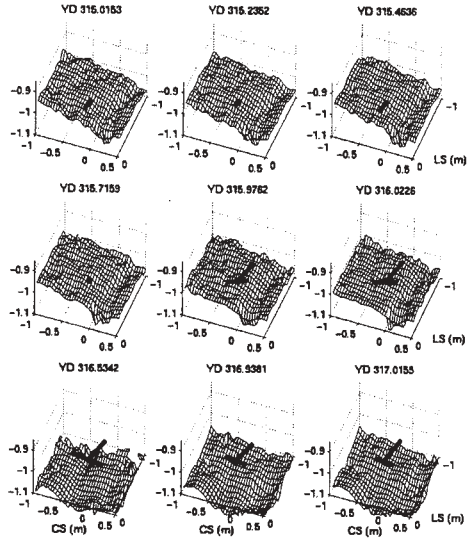

Figure 3. A subsample of 9 bedform maps measured by the scanned X/Y altimeter at the 12m BBL site for the same period as Figure 1. Mean and wave current forcing are shown as the bar vectors on each map (see text). The maps show a 1.5m cross-shore by 1m long shore area of the bed.

waves with superimposed local seas by early on yearday 316 (all times are UT). The wave forcing slowly decreased over the following two days.

3. BED FORM RESPONSE

A subsampled timeseries of the bed morphology sampled near the center of the 4m wide instrument frame is shown in Figure 2. The raster-scanned range and attitude angle data from the scanned acoustic altimeter have been transformed into a vertical coordinate system, and objectively analyzed onto a 1.5cm scale grid with a 5cm lateral smoothing scale, which limits the finescale resolution of the system to ~>3cm features. The surfaces plotted in Figure 2 represent the distance from the altimeter head to the bed, and so have an arbitrary vertical offset.

The local forcing is represented on each plot by the standard deviation of the currents as the double-sided bar vector, while the mean current vector is shown as the solid bar vector above each surface. The first four maps show little change (at the scale shown) of the bedforms until both the mean and wave forcing rapidly increases by yearday 315.97 when the large scale cross-shore slope which dominates the early bedform maps starts to level out. At this time, the distinct valley at cross-shore distance +0.2m remains, but by yearday 316.5 the long cross-shore slope and this feature have been replaced by a O(1m) single cycle waveform on the 0m long-shore end of the map, and a slight long-shore depression.

These 3D bedform sequences are dominated by long wavelength, irregular features with short longshore scales, rather than long-crested long-shore ripple fields frequently seen at coastal shelf sites. The bedform changes with forcing also show rapid movement and formation of these large scale features at the maxima of the forcing, followed by very slow evolution at lower forcing levels. It is hypothesized that these are characteristic of bedforms forced by both oscillatory wave displacements and strong mean currents.

The cross-shore evolution of the bed with mean and oscillatory currents are summarized in a 30 minute sampled timeseries of a cross-shore line near the center of the bed maps in Figure 3. The cross-shore sense is the opposite of the map sequence in Figure2. This representation better shows small-scale changes

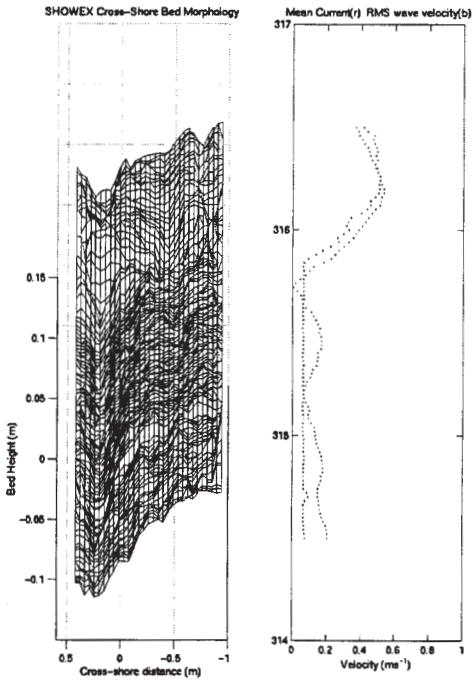

Figure 3. The left panel shows the evolution of a cross-shore transect of the bed near the center of the X/Y altimeter bed maps for the same 2 day period shown in Figure 1. The right panel shows the corresponding mean and RMS oscillatory current levels just above the oscillatory bottom boundary layer.

in the bed with time. At the start of the sequence ~ 1cm amplitude, 30-40 cm wavelength ripples are superimposed on the surface of the large cross-shore scaled feature only partially sampled by the scanning altimeter. Small scale changes, near the resolution of the acoustic-based system occur until the bed quickly flattens out near the end of yearday 315, then rapidly reforms into evolving bedforms with dominant scales of 70 to 100 cm. It is important to note that since the bedforms have distinctly 3 dimensional character, the scales inferred from the single cross-shore transect in Figure 3 are subject to significant error.

4. COMPARISOSN WITH BEDFORM MODELS

A range of laboratory and field observations have been used to develop

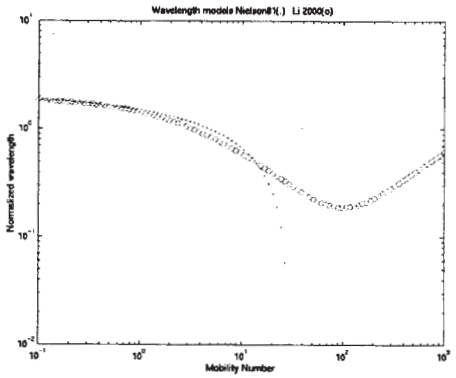

Figure 4. The predicted wavelength normalized by orbital displacement vs. mobility number for a wave only model proposed by Neilson, 1981, (. symols), and by a waves + current model by Khelifa and Oullet, 2000 (o symbols).

predictive models for the evolution bedforms forced by surface gravity waves. Experimental approaches have centered on laboratory investigations using oscillating water tunnels and flumes, leading to a range of empirical formulations of bedform response (see for example Mogridge et al, 1994). This previous work has modeled bed evolution in the presence of mean flows, oscillatory flows, and more recently combined oscillatory and mean flows. Here two models for the prediction of ripple wavelength are considered. The first is a laboratory based formula for oscillatory flow by Nielson (1981) and has been widely tested by other researchers:

$$\frac{2\lambda}{d_w} = 2.2 - 0.345\psi_w^{0.34}$$

where λ is the predicted ripple wavelength normalized by the orbital displacement d_w and ψ_w is the oscillatory mobility number

$$\psi_w = \frac{U_w^2}{(s-1)gD}$$

where U_w is the rms oscillatory velocity just outside the wave boundary layer, s is the sediment density ratio to water, and D is the median sediment diameter. This formulation is limited to wave mobility numbers < 230.

This empirical model been modified by Khelifa and Oullet, 2000, for the case of an

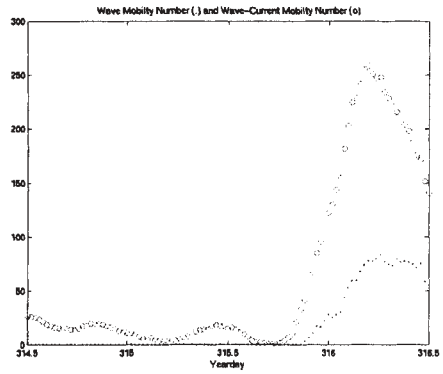

Figure 5. A timeseries of wave only (. symbols) and wave plus current (o symbols) mobility number for the same two day timeseries as Figure 1.

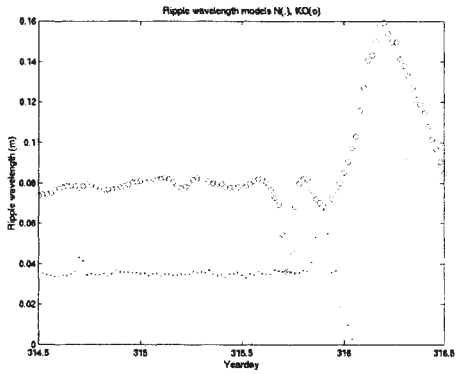

Figure 6. A two day timeseries of predicted ripple wavelength based on the wave only model (. symbols) and wave plus current model (o symbols) for the same period as the previous figures.

oscillatory velocity plus a mean current using fits to data from a wave basin which had a mean current at selected, non parallel directions to the oscillatory flow. The modified wave-current (wc) wavelength predictor is

$$\frac{2\lambda}{d_{wc}} = 1.9 + 0.08Ln^2(1+\psi_{wc}) - 0.74Ln(1+\psi_{wc})$$

where the mobility number and orbital displacements now include the vector contributions of mean currents to the oscillatory flow.

The form of these predictions can be seen in Figure 4, where the wave only prediction has been limited to it's valid range. The combined wave and current prediction shows an upturn at a mobility number of ~100.

A timeseries plot of the wave only and wave plus current mobility number is shown Figure 5 for the same time interval as Figures 2 and 3. Clearly the large longshore mean currents make a significant difference in the second mobility estimate, and clearly cannot be ignored. As the wave and current forcing increase during yearday 316, the ψ_w values reach 100, while ψ_{wc} exceeds 250. Predicted ripple wavelengths are shown in Figure 6 for the same two day timeseries. Pedicted wavelengths for the wave only model are close to the resolution of the 3D measurement throughout the timeseries, and are beyond the valid range of mobility number for the Neislon model during the higher forcing during yearday 316. The Khelifa – Oullet (KO) model with the wave plus current forcing predicts 8 to 16 cm cross-shore wavelengths for these conditions. Comparisons with the SHOWEX observations at the Duck site are not encouraging, with small amplitude ripples of 30 50 cm being observed during the low forcing conditions, and 1m ripples with significant 3D form seen during the stronger forcing periods.

5. CONCLUSIONS

A two day section of the SHOWEX wave and current forcing with bed morphological response has been shown . The unique 3 dimensional bedform timeseries reveal significant long-shore structure and the presence of large (not fully resolved at the 1.5m measurement scale) bed forms through much of the timeseries, which are left as relict forms following strong forcing events.

Comparisons with two empirical ripple wavelength models did not provide satisfying predictions of the field observations when observed forcing and sediment characteristics were applied to the models, but the trends in the models are encouraging, and provide a starting point for further model development for inner shelf regions forced episodically by strong waves and large mean currents.

6. ACKNOWLEDGEMENTS

This research was supported by the office of Naval Research Coastal Sciences program under contract N0001400WR30016. The field work involved a large group of staff through the 2 month deployment including the cooperative with Tom Herber's group. Rob Wyland designed the mechanical components in the sled system and Jim Stockel programmed most of the data acquisition and processing software. Logistical support was provided by the Field Research Facility of the Army Corps of Engineer Waterways Experiment Stations's Coastal Engineering Research Center. Their support in this programs is appreciated.

7. REFERENCES

Herbers, T. H. C., E. J. Hendrickson and W. C. O'Reilly, 2000: Propagation of swell across a wide continental shelf. J. Geophy. Res., 105(C8), 19729-19737.

Khelifa, A., and Y. Ouellet, 2000. Prediction of sand ripple geometry under waves and currents. J. Waterway, Port, Coastal and Ocean Enginr., 12614-22.

Mogridge, G. R., M. H. Davies, and D. H. Willis, 1994: Geometry prediction for wave-generated bedforms. Coast. Engrg., 22, 255-286.

Neilson, P., 1981. Dynamics and geometery of wave-generated ripples. J. Gephys. Res., 86(C7), 6467-6472.

Stanton, T. P., 1996. Probing ocean wave boundary layers with a hybrid bistatic / monostatic Coherent Acoustic Doppler Profiler. Proceedings of the Microstructure Sensors in the Ocean Workshop, Mt Hood, October 1996.